A Multifrequency Study of the Magellanic Clouds

Evan Johnston Crawford

A thesis submitted for the degree of

Doctor of Philosophy

at

University of Western Sydney

May 2015

Dedication

To my family, Sarah, Emily, Abigale and Elliott for always being there and understanding me.

To my parents, in-laws and grandparents for their patience, understanding and encouragement.

And finally dedicated to the memory of those who are no longer with us, Kevin Miles, Judy Queen, Jim Lear and Tom Crawford, for their unwavering faith that I would succeed.

Acknowledgements

This Thesis uses data from the Australia Telescope Compact Array and the Parkes Telescope.

> The Australia Telescope Compact Array and Parkes radio telescope are parts of the Australia Telescope National Facility which is funded by the Commonwealth of Australia for operation as a National Facility managed by CSIRO.
>
> This thesis includes archived data obtained through the Australia Telescope Online Archive (`http://atoa.atnf.csiro.au`).

I thank the Magellanic Clouds Emission Line Survey (MCELS) team for access to the optical images. I acknowledge the many contributions of R.C. Smith, F. Winkler of CTIO and other members of the MCELS team.

This Thesis uses data from XMM-Newton.

> Based on observations obtained with XMM-Newton, an ESA science mission with instruments and contributions directly funded by ESA Member States and NASA.
>
> The *XMM-Newton* project is supported by the Bundesministerium für Wirtschaft und Technologie/Deutsches Zentrum für Luft- und Raumfahrt (BMWI/DLR, FKZ 50 OX 0001) and the Max-Planck Society.

This Thesis uses data from the Chandra X-ray Observatory.

> The scientific results reported in this Thesis are based in part on observations made by the Chandra X-ray Observatory.

I also wish to thank my collaborators for their input, encouragement and assistance during my candidature: M. Balbo, J. Ballet, I. S. Bojičić, P. Bordas, L. M. Bozzetto, E. Bozzo, T. Brantseg, D. A. H. Buckley, B. J. Cahall, K. O. Cajko, Y.-H. Chu, M. J. Coe, M. Cohen, J. D. Collier, A. Y. De Horta, C. DeRoo, J. Dickel, D. Drašković, M. Ehle, C. Ferrigno, M. D. Filipović, T. J. Galvin, S. A. Griffith, C. K. Grimes, M.-H. Grondin, R. A. Gruendl,

F. Haberl, D. Hatzidimitriou, K. Heitritter, J. L. Hora, J. Horner, A. Hughes, R. Indebetouw, P. A. Jones, P. J. Kavanagh, A. R. Kosakowski, R. Kothes, S. Kotuš, K. E. Kraemer, S. Laine, P. Maggi, R. L. McEntaffer, A. Mendik, M. Meixner, S. Mereghetti, W. C. Millar, J. P. Napier, A. N. O'Brien, J. M. Oliveira, R. A. Owen, T. G. Pannuti, Q. A. Parker, L. Pavan, J. L. Payne, W. Pietsch, S. D. Points, G. Pühlhofer, W. A. Reid, T. P. Robitaille, Q. Roper, M. Sasaki, M. Sewiło, N. Seymour, B. Sharma, B. Shiao, J. D. Simon, G. C. Sloan, R. C. Smith, E. R. Sommer, W. D. Staggs, L. Stella, F. H. Stootman, M. Stupar, R. Sturm, L. A. Tauber, A. Tiengo, N. F. H. Tothill, D. Urošević, Y. van Loon, R. Walter, B. Wardlaw, G. L. White, R. Williams, G. F. Wong, and P. R. Wood.

The work presented in this thesis is, to the best of my knowledge and belief, original except as acknowledged in the text.

I hereby declare that I have not submitted this material, either in full or in part, for a degree at this or any other

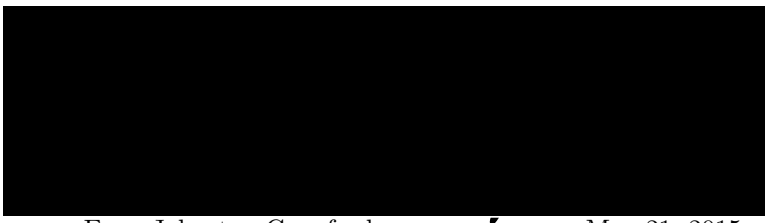

Evan Johnston Crawford May 21, 2015

Contents

List of Tables

List of Figures

Abstract

This project examines the variety and nature of the radio sources in the Magellanic Clouds reprocessing recent and archival high sensitivity radio-continuum observations from the Australia Telescope Compact Array, using newly developed techniques and other large-scale surveys. This higher resolution and quality study creates a new complete catalogue of discrete and extended sources in the Magellanic Clouds, identifying background sources, Planetary Nebulae, and Supernova Remnants.

List of Abbreviations

$\boldsymbol{\alpha}$	Spectral index: defined as $S_\nu \propto \nu^\alpha$ where S is flux density and ν is frequency
ATCA	Australia Telescope Compact Array
ATNF	Australia Telescope National Facility
CCD	Charge Coupled Device
CSIRO	Commonwealth Scientific and Industrial Research Organisation
CSM	Circumstellar Material
CTIO	Cerro Tololo Inter-American Observatory
DEC	Declination
ESA	European Space Agency
eV	electronvolt: 1 eV $\approx 1.6 \times 10^{-19}$ J
EPIC	European Photon Imaging Camera
Hii	HII region
IR	Infrared
ISM	Interstellar Medium
Jy	Jansky, a unit of spectral flux density: 1 Jy $\equiv 10^{-26}$ W m^{-2} Hz^{-1}
LMC	Large Magellanic Cloud
MOST	Molonglo Observatory Synthesis Telescope
MCELS	Magellanic Clouds Emission Line Survey
NASA	National Aeronautics and Space Administration
$\boldsymbol{M_e}$	Electron Mass: 1 $M_e \approx 9.1 \times 10^{-31}$ kg

$M_\odot$	Solar Mass: 1 $M_\odot \equiv 1$ solar mass $\simeq 1.99 \times 10^{30}$ kg
MC	Magellanic Cloud
pc	parsec: 1 pc $\simeq 3.09 \times 10^{16}$ m
PN	Planetary Nebula
PNe	Planetary Nebulae
RA	Right Ascension
SMC	Small Magellanic Cloud
SN	Supernova
SNe	Supernovae
SNR	Supernova Remnant
VLA	Very Large Array
XMM-Newton	X-ray Multi-Mirror Mission – Newton an ESA X-ray Observatory
XRB	X-Ray Binary

Publications

During the course of the candidature the following refereed journal articles have been published, the four papers that form the basis of this thesis are marked with an asterix (*):

1. Payne, J. L., Filipović, M. D., Millar, W. C., Crawford, E. J., De Horta, A. Y., Stootman, F. H., and Urošević, D. (2008a). Optical Spectra of Radio Planetary Nebulae in the Large Magellanic Cloud. *Serbian Astronomical Journal*, 177:53–59

   Citations: 4

2. *Crawford, E. J., Filipović, M. D., De Horta, A. Y., Stootman, F. H., and Payne, J. L. (2008a). Radio-Continuum Study of the Supernova Remnants in the Large Magellanic Cloud - An SNR with a Highly Polarised Breakout Region - SNR J0455-6838. *Serbian Astronomical Journal*, 177:61–66

   Citations: 16

3. Payne, J. L., Tauber, L. A., Filipović, M. D., Crawford, E. J., and De Horta, A. Y. (2009). The 100 Strongest Radio Point Sources in the Field of the Large Magellanic Cloud at 1.4 GHz. *Serbian Astronomical Journal*, 178:65–70

   Citations: 2

4. Filipović, M. D., Cohen, M., Reid, W. A., Payne, J. L., Parker, Q. A., Crawford, E. J., Bojičić, I. S., De Horta, A. Y., Hughes, A., Dickel, J., and Stootman, F. (2009). Radio planetary nebulae in the Magellanic Clouds. *MNRAS*, 399:769–777

   Citations: 15

5. Cajko, K. O., Crawford, E. J., and Filipović, M. D. (2009). Multifrequency Observations of One of the Largest Supernova Remnants in the Local Group of Galaxies, LMC - SNR J0450-709. *Serbian Astronomical Journal*, 179:55–60

   Citations: 19

6. *Crawford, E. J., Filipović, M. D., Haberl, F., Pietsch, W., Payne, J. L., and De Horta, A. Y. (2010). Multi-frequency study of Local Group supernova remnants. The curious case of the Large Magellanic Cloud SNR J0528-6714. *A&A*, 518:A35

   Citations: 14

7. Filipović, M. D., Crawford, E. J., Jones, P. A., and White, G. L. (2010). Radio-Continuum Jets Around the Peculiar Galaxy Pair ESO 295-IG022. *Serbian Astronomical Journal*, 181:31–37

8. Bozzetto, L. M., Filipović, M. D., Crawford, E. J., Bojičić, I. S., Payne, J. L., Medik, A., Wardlaw, B., and De Horta, A. Y. (2010). Multifrequency Radio Observations of a SNR in the LMC. The Case of SNR J0527-6549 (DEM L204). *Serbian Astronomical Journal*, 181:43–49

   Citations: 10

9. Bojičić, I. S., Filipović, M. D., and Crawford, E. J. (2010). SMC SMP 24: A Newly Radio-Detected Planetary Nebula in the Small Magellanic Cloud. *Serbian Astronomical Journal*, 181:63–68

   Citations: 4

10. Millar, W. C., White, G. L., Filipović, M. D., Payne, J. L., Crawford, E. J., Pannuti, T. G., and Staggs, W. D. (2011). Optical spectra of supernova remnant candidates in the Sculptor Group galaxy NGC 300. *Ap&SS*, 332:221–239

    Citations: 3

11. Owen, R. A., Filipović, M. D., Ballet, J., Haberl, F., Crawford, E. J., Payne, J. L., Sturm, R., Pietsch, W., Mereghetti, S., Ehle, M., Tiengo, A., Coe, M. J., Hatzidimitriou, D., and Buckley, D. A. H. (2011). IKT 16: a composite supernova remnant in the Small Magellanic Cloud. *A&A*, 530:A132

    Citations: 14

12. Wong, G. F., Filipović, M. D., Crawford, E. J., De Horta, A. Y., Galvin, T., Drašković, D., and Payne, J. L. (2011a). New 20-cm Radio-Continuum Study of the Small Magellanic Cloud: Part I - Images. *Serbian Astronomical Journal*, 182:43–52

    Citations: 9

13. *Crawford, E. J., Filipović, M. D., De Horta, A. Y., Wong, G. F., Tothill, N. F. H., Drašković, D., Collier, J. D., and Galvin, T. J. (2011). New 6 and 3-cm Radio-Continuum Maps of the Small Magellanic Cloud. Part I - The Maps. *Serbian Astronomical Journal*, 183:95–102

    Citations: 4

14. Wong, G. F., Filipović, M. D., Crawford, E. J., Tothill, N. F. H., De Horta, A. Y., Drašković, D., Galvin, T. J., Collier, J. D., and Payne, J. L. (2011b). New 20-cm Radio-Continuum Study of the Small Magellanic Cloud: Part II - Point Sources. *Serbian Astronomical Journal*, 183:103–106

    Citations: 6

15. Haberl, F., Sturm, R., Filipović, M. D., Pietsch, W., and Crawford, E. J. (2012c). SXP 1062, a young Be X-ray binary pulsar with long spin period. Implications for the neutron star birth spin. *A&A*, 537:L1

    Citations: 26

16. Grondin, M.-H., Sasaki, M., Haberl, F., Pietsch, W., Crawford, E. J., Filipović, M. D., Bozzetto, L. M., Points, S., and Smith, R. C. (2012). XMMU J0541.8-6659, a new supernova remnant in the Large Magellanic Cloud. *A&A*, 539:A15

    Citations: 11

17. Bozzetto, L. M., Filipović, M. D., Crawford, E. J., Haberl, F., Sasaki, M., Urošević, D., Pietsch, W., Payne, J. L., De Horta, A. Y., Stupar, M., Tothill, N. F. H., Dickel, J., Chu, Y.-H., and Gruendl, R. (2012b). Multifrequency study of the Large Magellanic Cloud supernova remnant J0529-6653 near pulsar B0529-66. *MNRAS*, 420:2588–2595

    Citations: 14

18. De Horta, A. Y., Filipović, M. D., Bozzetto, L. M., Maggi, P., Haberl, F., Crawford, E. J., Sasaki, M., Urošević, D., Pietsch, W., Gruendl, R., Dickel, J., Tothill, N. F. H., Chu, Y.-H., Payne, J. L., and Collier, J. D. (2012). Multi-frequency study of supernova remnants in the Large Magellanic Cloud. The case of LMC SNR J0530-7007. *A&A*, 540:A25

    Citations: 15

19. Bozzetto, L. M., Filipović, M. D., Crawford, E. J., Payne, J. L., De Horta, A. Y., and Stupar, M. (2012c). Radio continuum observations of LMC SNR J0550-6823. *Rev. Mexicana Astron. Astrofis.*, 48:41–46

    Citations: 15

20. Galvin, T. J., Filipović, M. D., Crawford, E. J., Tothill, N. F. H., Wong, G. F., and De Horta, A. Y. (2012a). 20 cm VLA Radio-Continuum Study of M31 - Images and Point Source Catalogues. *Serbian Astronomical Journal*, 184:41–68

    Citations: 1

21. Bozzetto, L. M., Filipović, M. D., Crawford, E. J., De Horta, A. Y., and Stupar, M. (2012a). Multifrequency Radio Observations of SNR J0536-6735 (N 59B) with Associated Pulsar. *Serbian Astronomical Journal*, 184:69–76

    Citations: 6

22. Wong, G. F., Crawford, E. J., Filipović, M. D., De Horta, A. Y., Tothill, N. F. H., Collier, J. D., Drašković, D., Galvin, T. J., and Payne, J. L. (2012a). New 6 and 3-cm Radio-Continuum Maps of the Small Magellanic Cloud: Part II - Point Source Catalogue. *Serbian Astronomical Journal*, 184:93–95

    Citations: 4

23. Haberl, F., Filipović, M. D., Bozzetto, L. M., Crawford, E. J., Points, S. D., Pietsch, W., De Horta, A. Y., Tothill, N., Payne, J. L., and Sasaki, M. (2012a). Multi-frequency observations of SNR J0453-6829 in the LMC. A composite supernova remnant with a pulsar wind nebula. *A&A*, 543:A154

    Citations: 6

24. Galvin, T. J., Filipović, M. D., Crawford, E. J., Wong, G., Payne, J. L., De Horta, A., White, G. L., Tothill, N., Drašković, D., Pannuti, T. G., Grimes, C. K., Cahall, B. J., Millar, W. C., and Laine, S. (2012b). Radio-continuum study of the Nearby sculptor group galaxies. Part 1: NGC 300 at λ=20 cm. *Ap&SS*, 340:133–142

    Citations: 3

25. Maggi, P., Haberl, F., Bozzetto, L. M., Filipović, M. D., Points, S. D., Chu, Y.-H., Sasaki, M., Pietsch, W., Gruendl, R. A., Dickel, J., Smith, R. C., Sturm, R., Crawford, E. J., and De Horta, A. Y. (2012). Multi-frequency study of supernova remnants in the Large Magellanic Cloud. Confirmation of the supernova remnant status of DEM L205. *A&A*, 546:A109

    Citations: 9

26. Bozzetto, L. M., Filipović, M. D., Urošević, D., and Crawford, E. J. (2012d). Radio-Continuum Observations of Small, Radially Polarised Supernova Remnant J0519-6902 in the Large Magellanic Cloud. *Serbian Astronomical Journal*, 185:25–33

    Citations: 7

27. Wong, G. F., Filipović, M. D., Crawford, E. J., Tothill, N. F. H., De Horta, A. Y., and Galvin, T. J. (2012b). New 20-cm Radio-Continuum Study of the Small Magellanic Cloud: Part III - Compact HII Regions. *Serbian Astronomical Journal*, 185:53–64

Citations: 1

28. Kavanagh, P. J., Sasaki, M., Points, S. D., Filipović, M. D., Maggi, P., Bozzetto, L. M., Crawford, E. J., Haberl, F., and Pietsch, W. (2013). Multiwavelength study of the newly confirmed supernova remnant MCSNR J0527-7104 in the Large Magellanic Cloud. *A&A*, 549:A99

Citations: 4

29. De Horta, A. Y., Collier, J. D., Filipović, M. D., Crawford, E. J., Urošević, D., Stootman, F. H., and Tothill, N. F. H. (2013). Radio confirmation of Galactic supernova remnant G308.3-1.4. *MNRAS*, 428:1980–1985

Citations: 4

30. Oliveira, J. M., van Loon, J. T., Sloan, G. C., Sewiło, M., Kraemer, K. E., Wood, P. R., Indebetouw, R., Filipović, M. D., Crawford, E. J., Wong, G. F., Hora, J. L., Meixner, M., Robitaille, T. P., Shiao, B., and Simon, J. D. (2013). Early-stage young stellar objects in the Small Magellanic Cloud. *MNRAS*, 428:3001–3033

Citations: 14

31. Bozzetto, L. M., Filipović, M. D., Crawford, E. J., Sasaki, M., Maggi, P., Haberl, F., Urošević, D., Payne, J. L., De Horta, A. Y., Stupar, M., Gruendl, R., and Dickel, J. (2013). Multifrequency study of SNR J0533-7202, a new supernova remnant in the LMC. *MNRAS*, 432:2177–2181

Citations: 9

32. O'Brien, A. N., Filipović, M. D., Crawford, E. J., Tothill, N. F. H., Collier, J. D., De Horta, A. Y., Wong, G. F., Drašković, D., Payne, J. L., Pannuti, T. G., Napier, J. P., Griffith, S. A., Staggs, W. D., and Kotuš, S. (2013). Radio-continuum study of the nearby Sculptor group Galaxies. Part 2: NGC 55 at λ=20, 13, 6 and 3 cm. *Ap&SS*, 347:159–168

Citations: 2

33. Sturm, R., Drašković, D., Filipović, M. D., Haberl, F., Collier, J., Crawford, E. J., Ehle, M., De Horta, A., Pietsch, W., Tothill, N. F. H., and Wong, G. (2013a). Active galactic nuclei behind the SMC selected from radio and X-ray surveys. *A&A*, 558:A101

Citations: 2

34. Filipović, M. D., Horner, J., Crawford, E. J., Tothill, N. F. H., and White, G. L. (2013). Mass Extinction and the Structure of the Milky Way. *Serbian Astronomical Journal*, 187:43–52

    Citations: 2

35. Pavan, L., Bordas, P., Pühlhofer, G., Filipović, M. D., De Horta, A., O'Brien, A., Balbo, M., Walter, R., Bozzo, E., Ferrigno, C., Crawford, E., and Stella, L. (2014a). The long helical jet of the Lighthouse nebula, IGR J11014-6103. *A&A*, 562:A122

    Citations: 7

36. Pavan, L., Bordas, P., Pühlhofer, G., Filipović, M. D., De Horta, A., O'Brien, A., Crawford, E., Balbo, M., Walter, R., Bozzo, E., Ferrigno, C., and Stella, L. (2014b). The Puzzling Jet and Pulsar Wind Nebula of Igr J11014-6103. *International Journal of Modern Physics Conference Series*, 28:60172

37. Bozzetto, L. M., Kavanagh, P. J., Maggi, P., Filipović, M. D., Stupar, M., Parker, Q. A., Reid, W. A., Sasaki, M., Haberl, F., Urošević, D., Dickel, J., Sturm, R., Williams, R., Ehle, M., Gruendl, R., Chu, Y.-H., Points, S., and Crawford, E. J. (2014b). Multifrequency study of a new Fe-rich supernova remnant in the Large Magellanic Cloud, MCSNR J0508-6902. *MNRAS*, 439:1110–1124

    Citations: 4

38. De Horta, A. Y., Sommer, E. R., Filipović, M. D., O'Brien, A., Bozzetto, L. M., Collier, J. D., Wong, G. F., Crawford, E. J., Tothill, N. F. H., Maggi, P., and Haberl, F. (2014b). Multi-frequency Observations of a Superbubble in the LMC: The Case of LHA 120-N 70. *AJ*, 147:162

    Citations: 3

39. Bozzetto, L. M., Filipović, M. D., Urošević, D., Kothes, R., and Crawford, E. J. (2014a). Radio-continuum study of Large Magellanic Cloud supernova remnant J0509-6731. *MNRAS*, 440:3220–3225

    Citations: 4

40. Galvin, T. J., Filipović, M. D., Tothill, N. F. H., Crawford, E. J., O'Brien, A. N., Seymour, N., Pannuti, T. G., Kosakowski, A. R., and Sharma, B. (2014). Radio-continuum study of the nearby sculptor group galaxies. Part 3: NGC 7793 at λ=12.2, 6 and 3 cm. *Ap&SS*, 353:603–611

    Citations: 1

41. *Crawford, E. J., Filipović, M. D., McEntaffer, R. L., Brantseg, T., Heitritter, K., Roper, Q., Haberl, F., and Urošević, D. (2014). HFPK 334: An Unusual Supernova Remnant in the Small Magellanic Cloud. *AJ*, 148:99

42. De Horta, A. Y., Filipovic, M. D., Crawford, E. J., Stootman, F. H., Pannuti, T. G., Bozzetto, L. M., Collier, J. D., Sommer, E. R., and Kosakowski, A. R. (2014a). Radio-Continuum Emission from the Young Galactic Supernova Remnant G1.9+0.3. *Serbian Astronomical Journal*, 189:41–51

    Citations: 2

43. Roper, Q., McEntaffer, R. L., DeRoo, C., Filipovic, M., Wong, G. F., and Crawford, E. J. (2015). X-ray Spectroscopy of Potential Small Magellanic Cloud Type Ia Supernova Remnants and Their Environments. *ApJ*, 803:106

Citation data has been taken from NASA's Astrophysics Data System Bibliographic Services (Eichhorn 1994)[1], and is correct at the time of printing.

[1] `http://www.adsabs.harvard.edu/`

Part I

Overarching Statement

Chapter 1

Introduction

1.1 The Magellanic System

The Magellanic Clouds (MCs), comprising of the Large Magellanic Cloud (LMC) (Fig. 1.1) and the Small Magellanic Cloud (SMC) (Fig. 1.2), less than a tenth of our Galaxy in size, are irregular dwarf galaxies orbiting close to our own Galaxy (at distances of 179,000 (di Benedetto 2008) and 210,000 (Hilditch et al. 2005) light years respectively) covering an angular size on the sky of about 36 square degrees. Figure 1.3 provides a schematic view of the MCs positions in relation to our own galaxy. Some of the interesting objects within the MCs are diffuse nebulae, globular and open clusters, planetary nebulae (PNe) and supernova remnants (SNRs). The recent supernova 1987A occurred in the LMC.

The stars in the MCs provide the nearest examples of young intermediate-to-low chemical abundance (low metallicity environment) stellar populations and this suggests that star formation in the LMC is a recent phenomenon, and is occurring because of the tidal force disruption caused by our own Galaxy. Therefore dynamics and the consequences of the interaction of the LMC with our Galaxy, and the LMC–SMC interactions are of great interest.

The close and known proximity of the MCs provides us with excellent opportunity to investigate the interstellar medium, dynamics, star formation, evolution processes and related polarisation and magnetic fields. The lower dust to gas ratio than our own Galaxy, provides an important understanding of a different interstellar medium (ISM).

1.2 Research Question

This project sets out to study the MCs in all available wavebands, with a particular emphasis on the centimetre radio-continuum. This project will study both the large and small scale structure of the two galaxies.

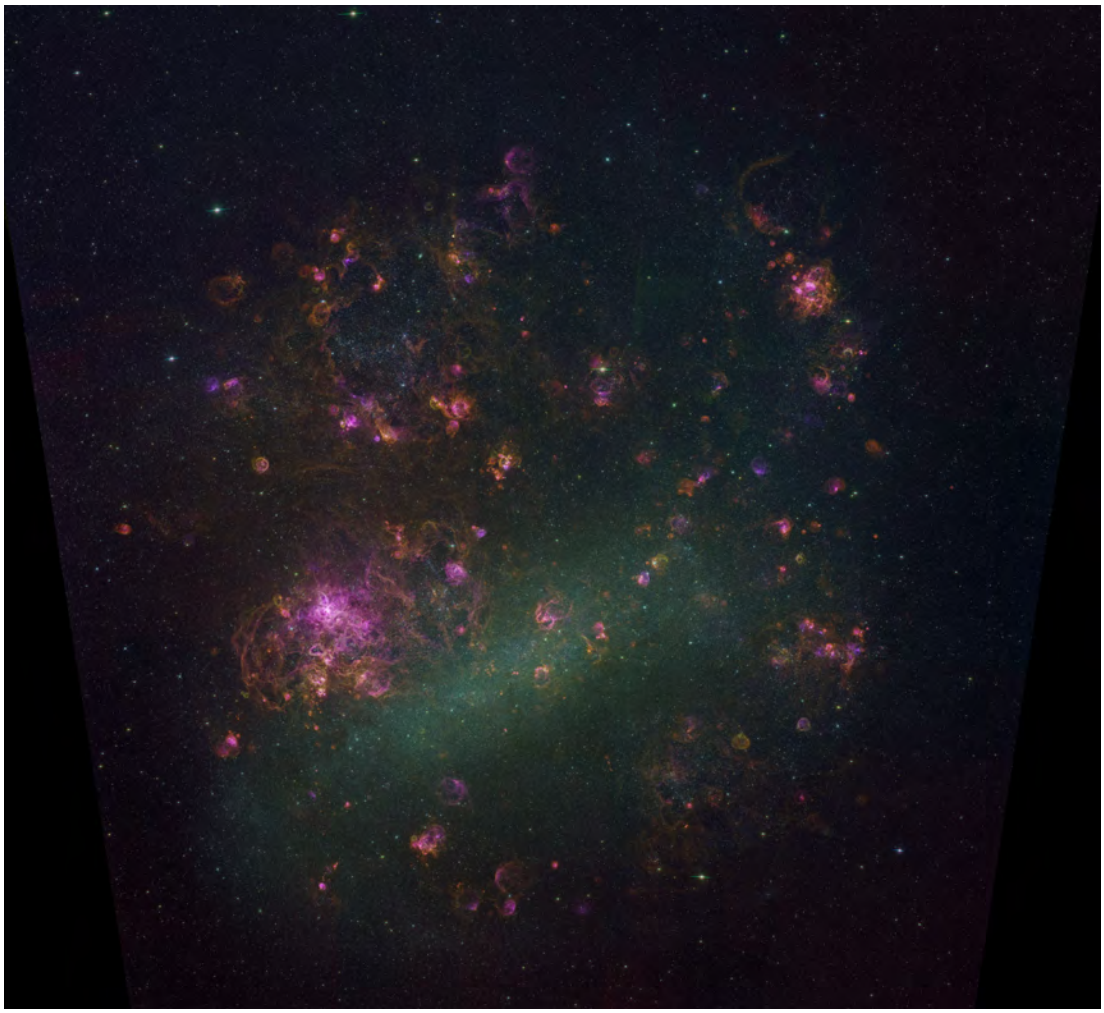

Figure 1.1 The MCELS optical survey of the LMC.

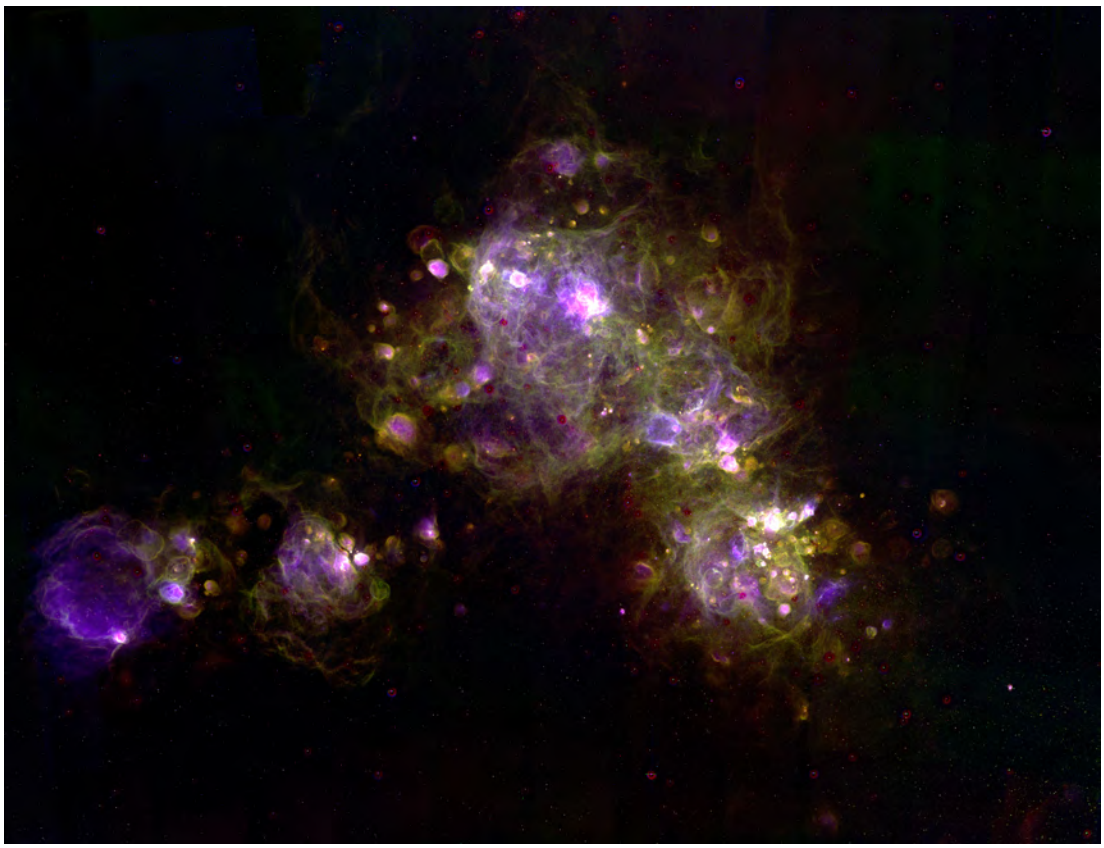

Figure 1.2 The MCELS optical survey of the SMC.

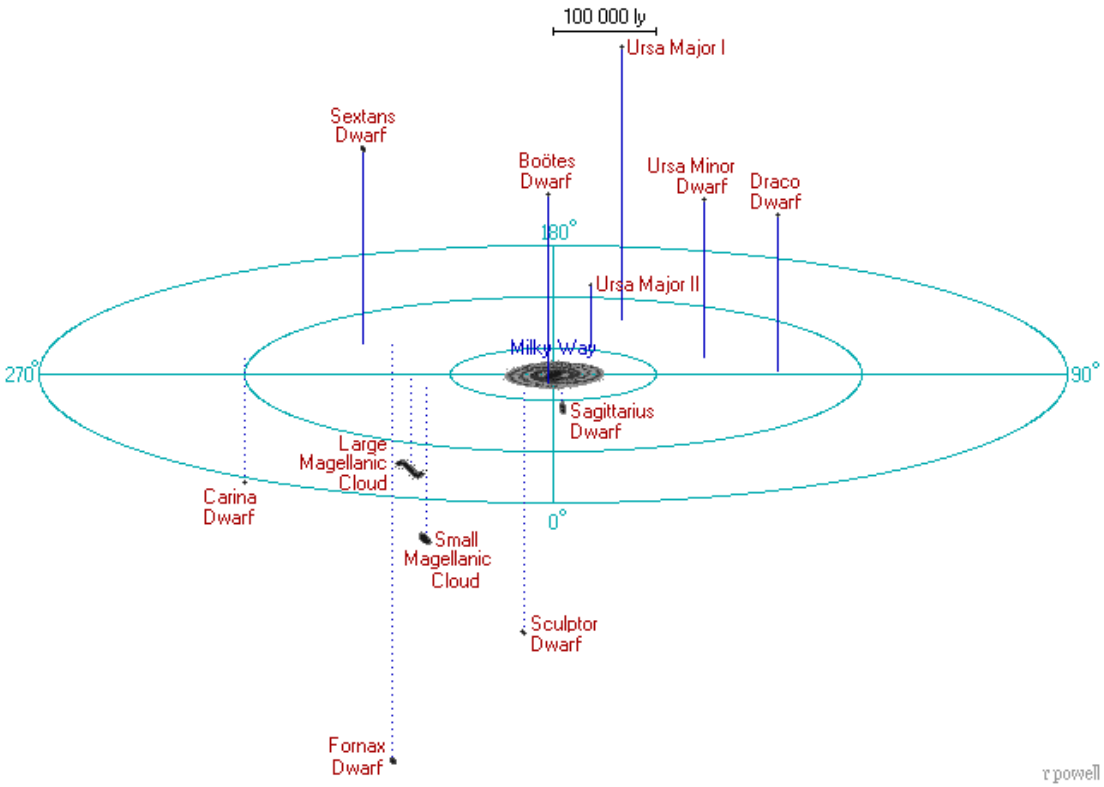

Figure 1.3 The Milky Way and its satellite Galaxies, (image taken from Powell (2006)).

1.2.1 Large Scale Structure of the Magellanic Clouds

In studying the large scale structure, the following have been realised:

- Produce the highest resolution and sensitivity radio-continuum maps of the SMC to date, by combining and stacking all available and relevant observations of the MCs.
- Produce catalogues of objects in the fields of the LMC and SMC, and attempt to characterise these objects.

1.2.2 Small Scale Structure of the Magellanic Clouds

In studying the small scale structure, the following have been realised:

- Using the large scale data, select a sample of SNRs and PNe, for further study.
- Generate new and reprocess existing data on these objects.
- Make comparisons between Infrared (IR), optical, X-Ray and radio-continuum.

1.3 Project Significance

The maps will be of great importance to the Astrophysical community, providing a basis for further analysis, and a reference for other types of study.

The catalogues will contain the most complete sample of a galaxy's population of objects, allowing for accurate statistics.

The known distance to the MC allows us to study the evolution of classes of objects, for example SNRs and PNe, covering the whole population.

Chapter 2

Overview of Achievements

2.1 Outline of Achievements

There are two themes that my research builds on, the large scale and the smaller scale of the Magellanic Clouds. The large scale is the survey work, the smaller scale individual objects such as SNRs and PNe.

The two are related as they lead from the large scale work is used to select the most interesting small scale features.

2.2 Large Scale Structure of the Magellanic Clouds

In the past two decades, several Parkes, Molonglo Observatory Synthesis Telescope (MOST) and Australia Telescope Compact Array (ATCA) moderate resolution surveys of the Magellanic Clouds (MCs) have been completed (Filipović et al. 1998).

Deep ATCA and Parkes radio-continuum and snap-shot surveys of the Small Magellanic Cloud (SMC) were conducted at 1.42, 2.37, 4.80 and 8.64 GHz by Filipović et al. (2002), achieving sensitivities of 1.8, 0.4, 0.8 and 0.4 mJy/beam respectively. These surveys were conducted in mosaic mode with between 35 and 320 separate pointings using 5 antennae in the 375-m array configuration. The maps have angular resolutions of 98″, 40″, 30″ and 20″ at the frequencies listed above.

Similarly, in the LMC, there are three major surveys at 1.42 GHz (Hughes et al. 2007, Fig. 2.1) and 4.8/8.64 GHz (Dickel et al. 2005, Figs. 2.2 and 2.3).

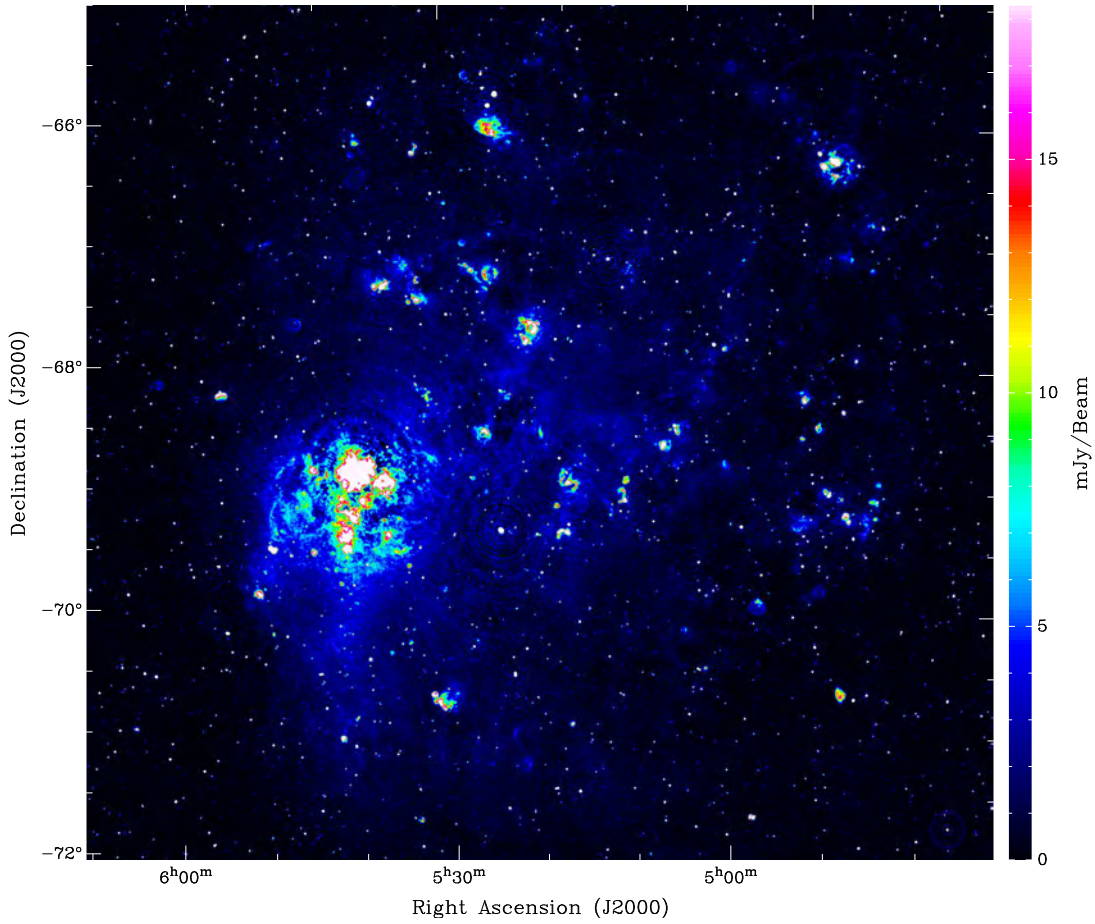

Figure 2.1 The Large Magellanic Cloud survey at 1.42-GHz

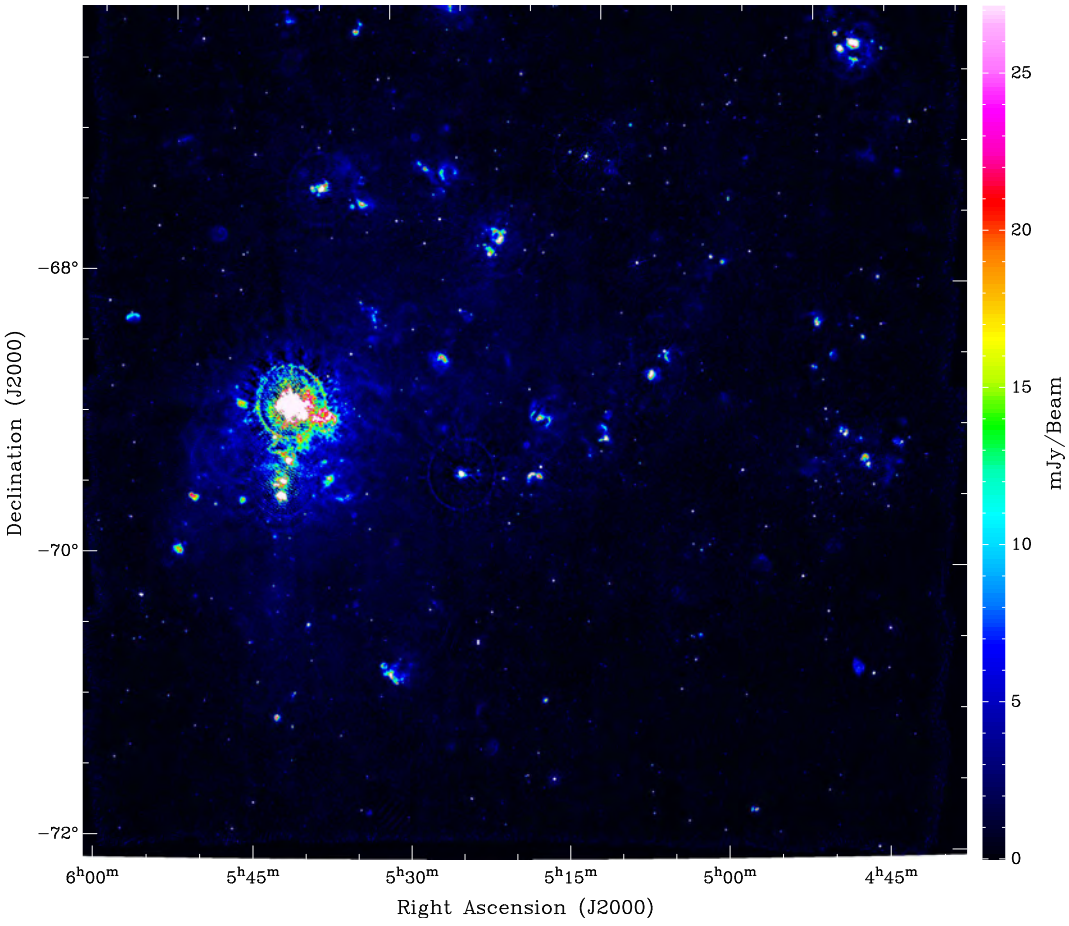

Figure 2.2 The Large Magellanic Cloud survey at 4.8-GHz

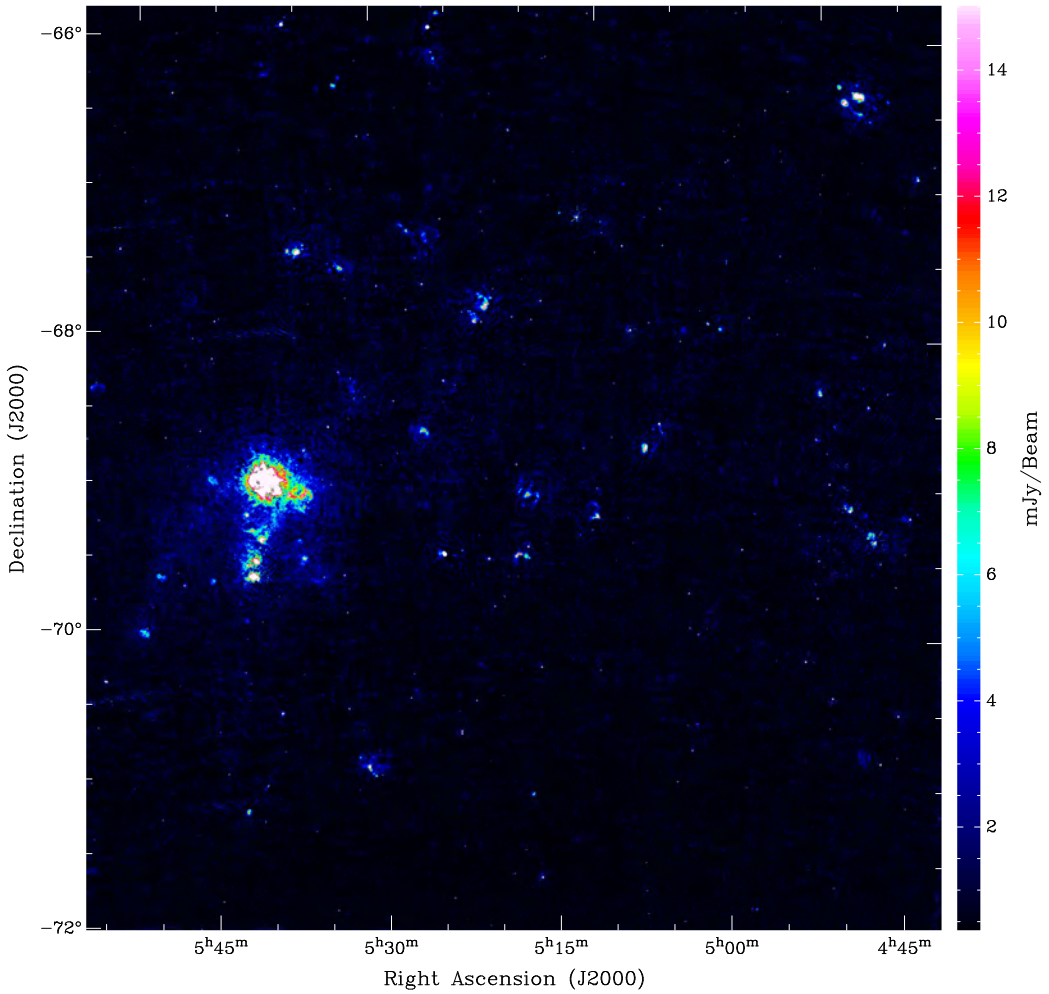

Figure 2.3 The Large Magellanic Cloud survey at 8.64-GHz

2.2.1 Wide-field Imaging Techniques

When the area to be imaged exceeds the field of view of the telescope, a mosaic must be made (Holdaway 1999). There are two methods for assembling a mosaic: Image each field and combine the images at the end; or combine the data at the beginning and image them jointly. The field-by-field approach has the advantage that it has modest processing requirements. However, not all available information in the data is utilised. The downside to the joint approach is a huge increase in the processing time and complexity.

The biggest problem with a wide-field image is that the dirty beam has sidelobes. This allows strong sources to contaminate large maps, as the primary beam is only modelled to a certain distance, and thus their consideration is standard deconvolution algorithms ends at this distance. The solution to this problem is to use the "peeling" technique first detailed in Hughes et al. (2007). Essentially, the techniques of self-calibration and source subtraction are used to correct for off-axis sources and thus reduce the artefact levels.

The interferometer images only sample the Fourier plane down to the shortest baseline — the largest scale structures are missed (Sault et al. 1996; Stanimirovic et al. 1999; Holdaway 1999; Stanimirovic 2002). To correct for this deficiency, "zero-spacing" data from a large single dish (for example the Parkes telescope) observations should be incorporated into the images.

2.2.2 The Peeling Technique

When imaging individual fields, selecting the area to be imaged is straightforward, simply image all the emission that effects the pointing, and let the deconvolution algorithm take care of the side lobes. Figure 2.4 is a good example of this. Figure 2.5 is an example of a less well behaved field, that will be used to illustrate the peeling process. There is a reasonably bright source to the north that requires a 64% larger image to account for the sidelobes. Figure 2.6 shows the same image with the primary beam correction applied, notice that although there are no sidelobes the bright northern source is outside the final image. If this field had been imaged with the same size as Figure 2.4 the result would be Figure 2.7. The green lines hi-light the grating artefact left behind by not including the northern source in the deconvolution, which for a single pointing would be trivial to do, however in a jointly deconvolved mosaic this is not possible, as you can only image your fields to the half power point of the beam, i.e. where the image is blanked in Figures 2.4, 2.5 and 2.7.

The solution is to apply the peeling technique. The first step is to model (using CLEAN) the emission in the area of the primary field of view. This model is used to subtract this emission from the visibility data, the result of which is seen in Figure 2.8.

Then the technique of self calibration is used on any emission outside the primary field

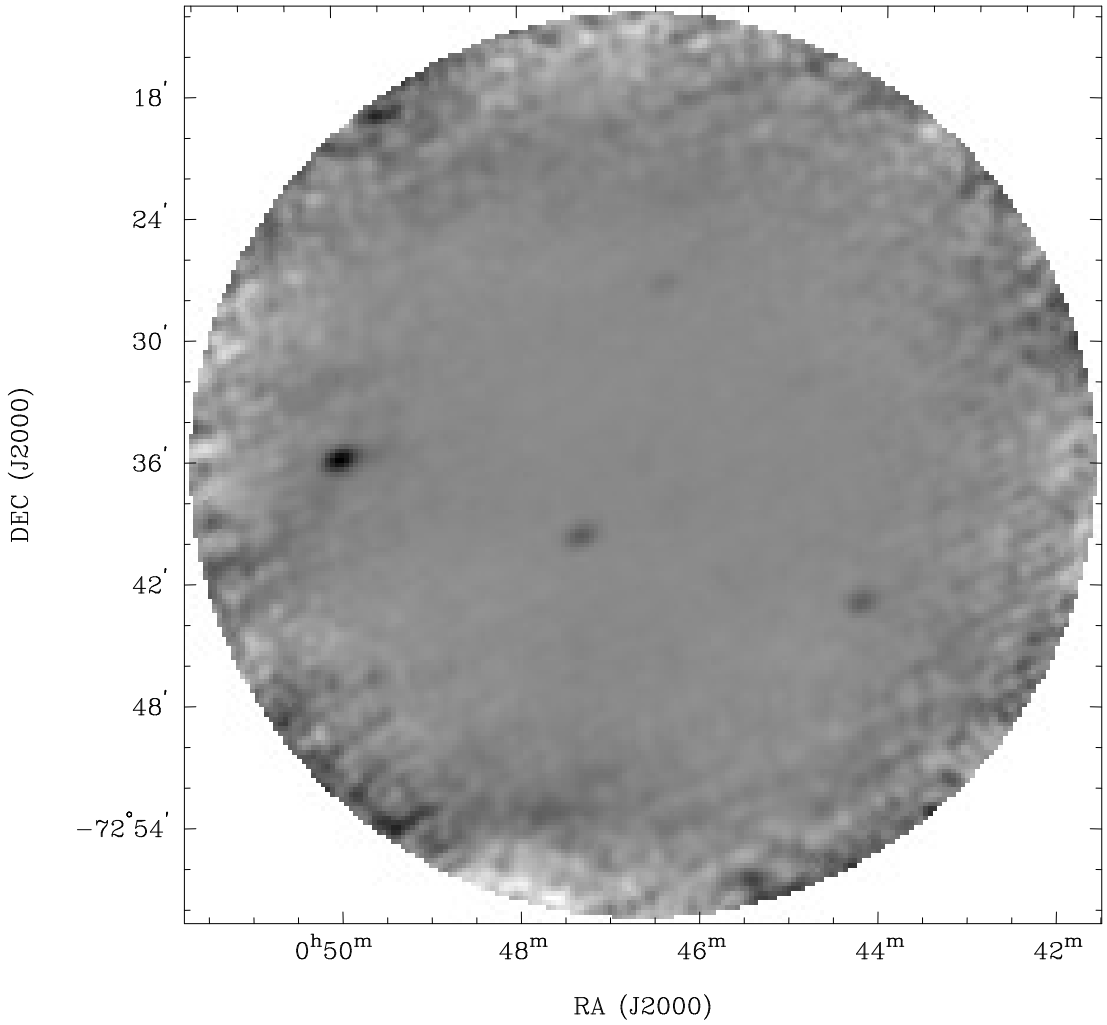

Figure 2.4 A well behaved mosaic field with primary beam correction, taken from the mosaic presented in Chapter 3.

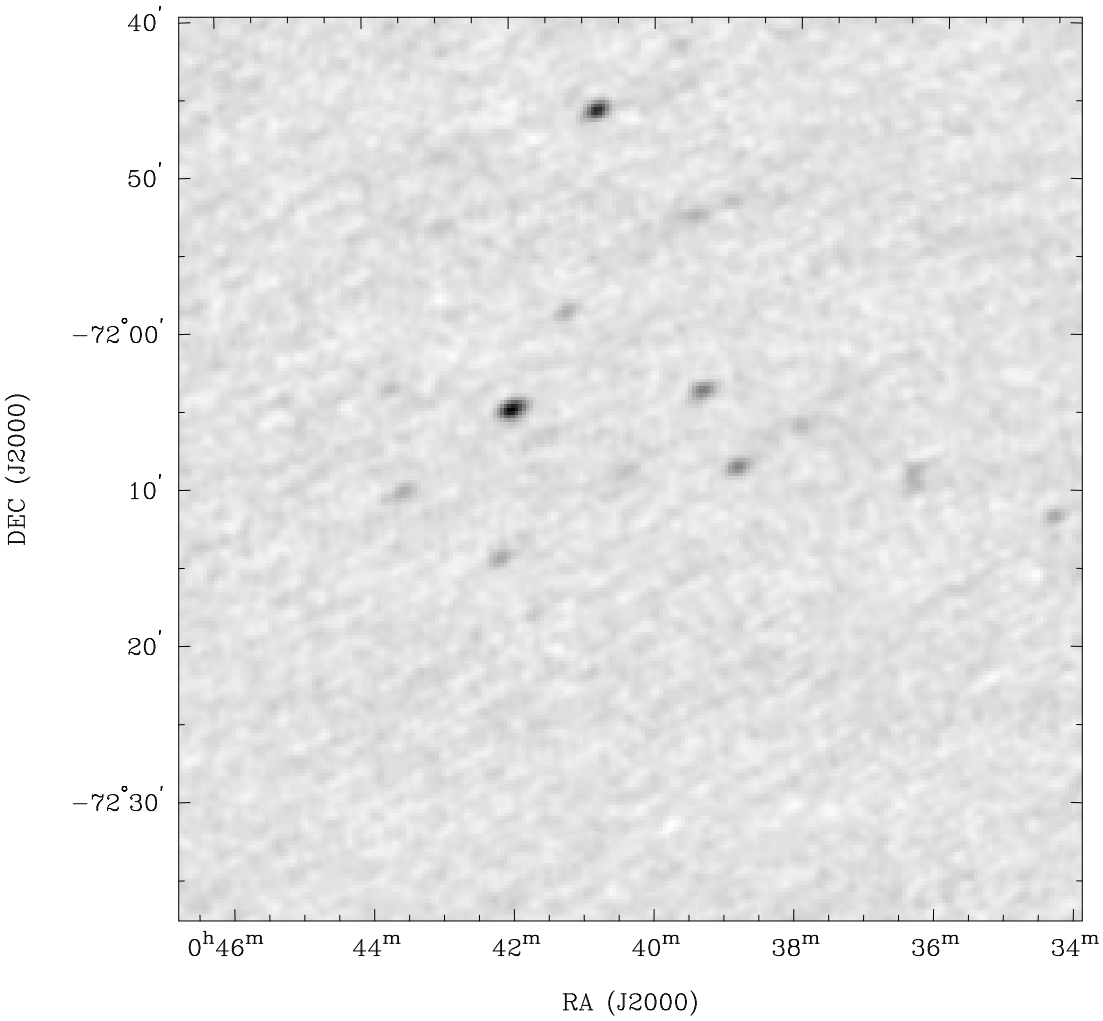

Figure 2.5 A less well behaved mosaic field without primary beam correction, taken from the mosaic presented in Chapter 3. Note the bright source in the north.

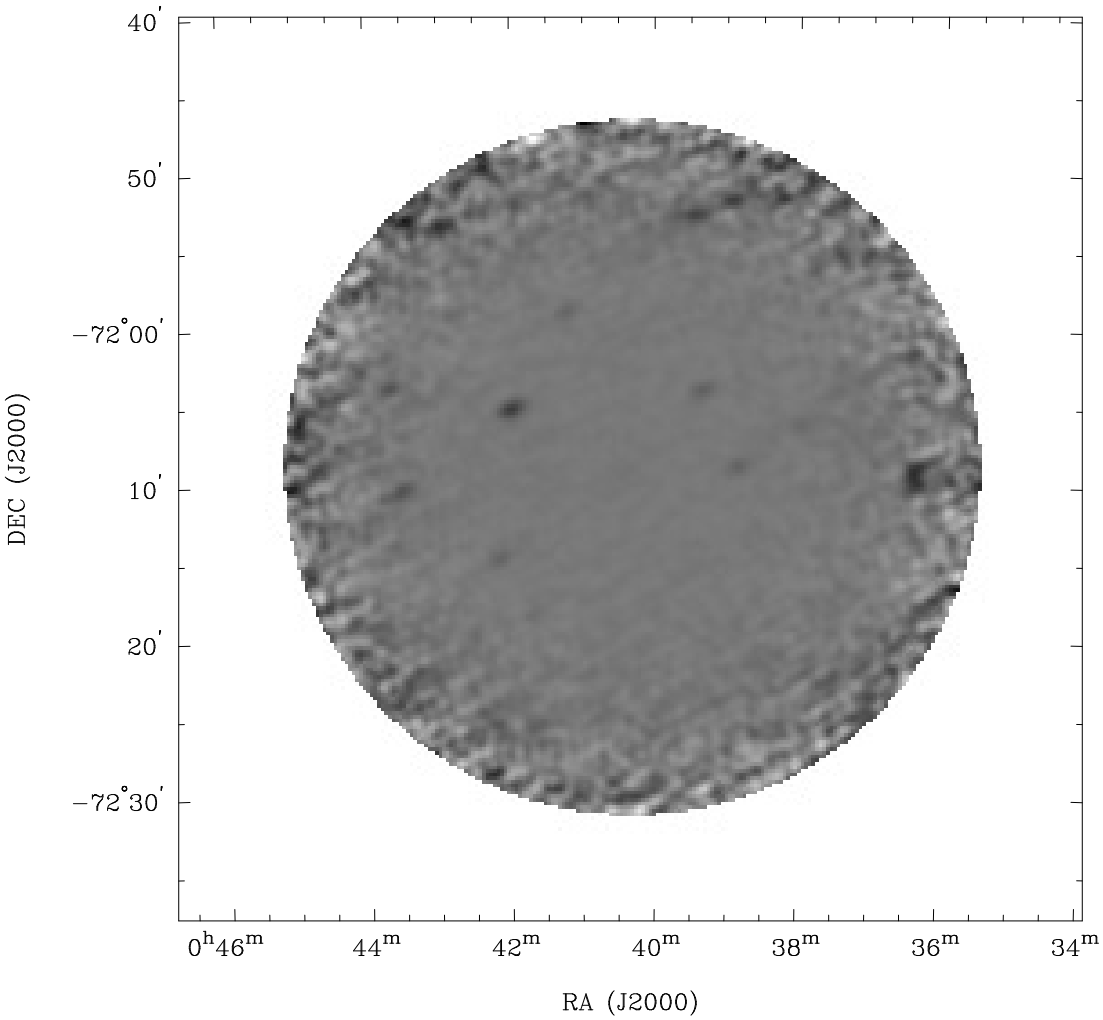

Figure 2.6 Figure 2.5 with primary beam correction.

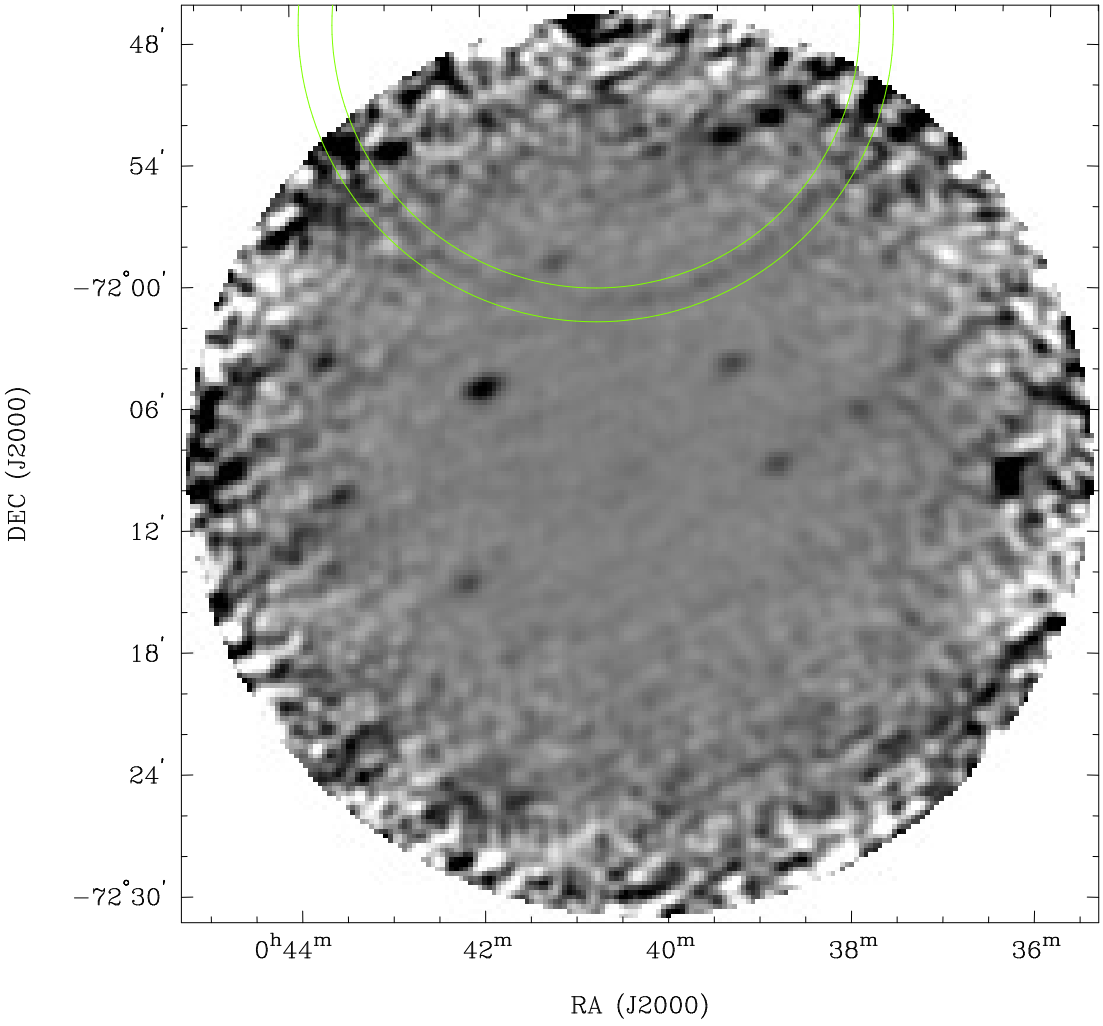

Figure 2.7 Figure 2.5 with primary beam correction, imaged with the same dimensions as 2.4, taken from the mosaic presented in Chapter 3. The green lines emphasise the artefact left behind from not including the source to the north in the deconvolution.

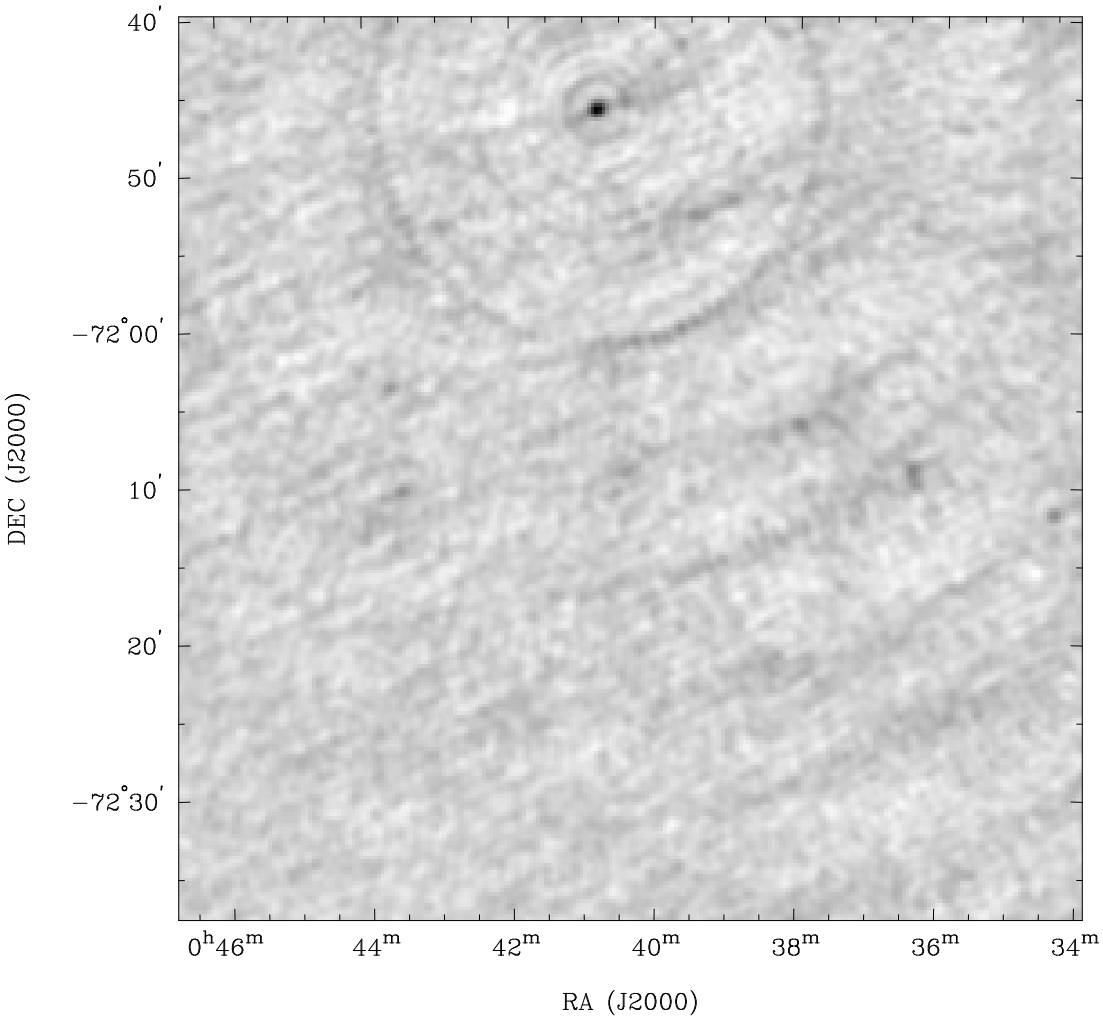

Figure 2.8 The field of Figure 2.5 with central emission subtracted. Note now the periodic rings around from the source in the north.

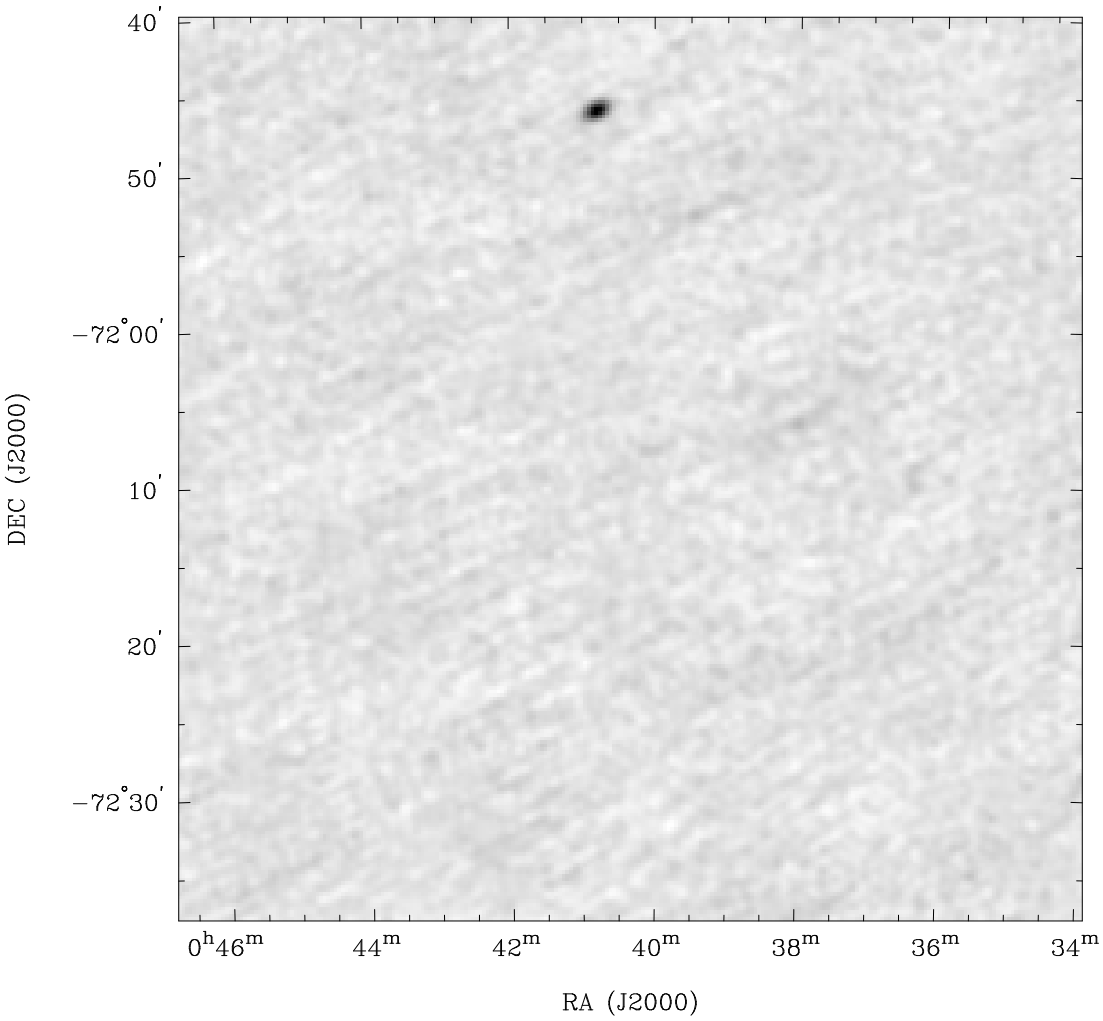

Figure 2.9 The field of Figure 2.5 with the outside emission self calibrated. Note now the periodic rings around from the source in the north have disappeared.

of view. The result of this process is seen in Figure 2.9. Once this is satisfactory then self calibration solution is applied to the data and then the outside emission is subtracted from the visibility data. Once the outside emission is subtracted then the self-calibration solution is removed from the data, and finally the emission inside the primary filed of view is added back to the visibilities. The results of this process are shown in Figure 2.10. A final self calibration of the data may be done if necessary.

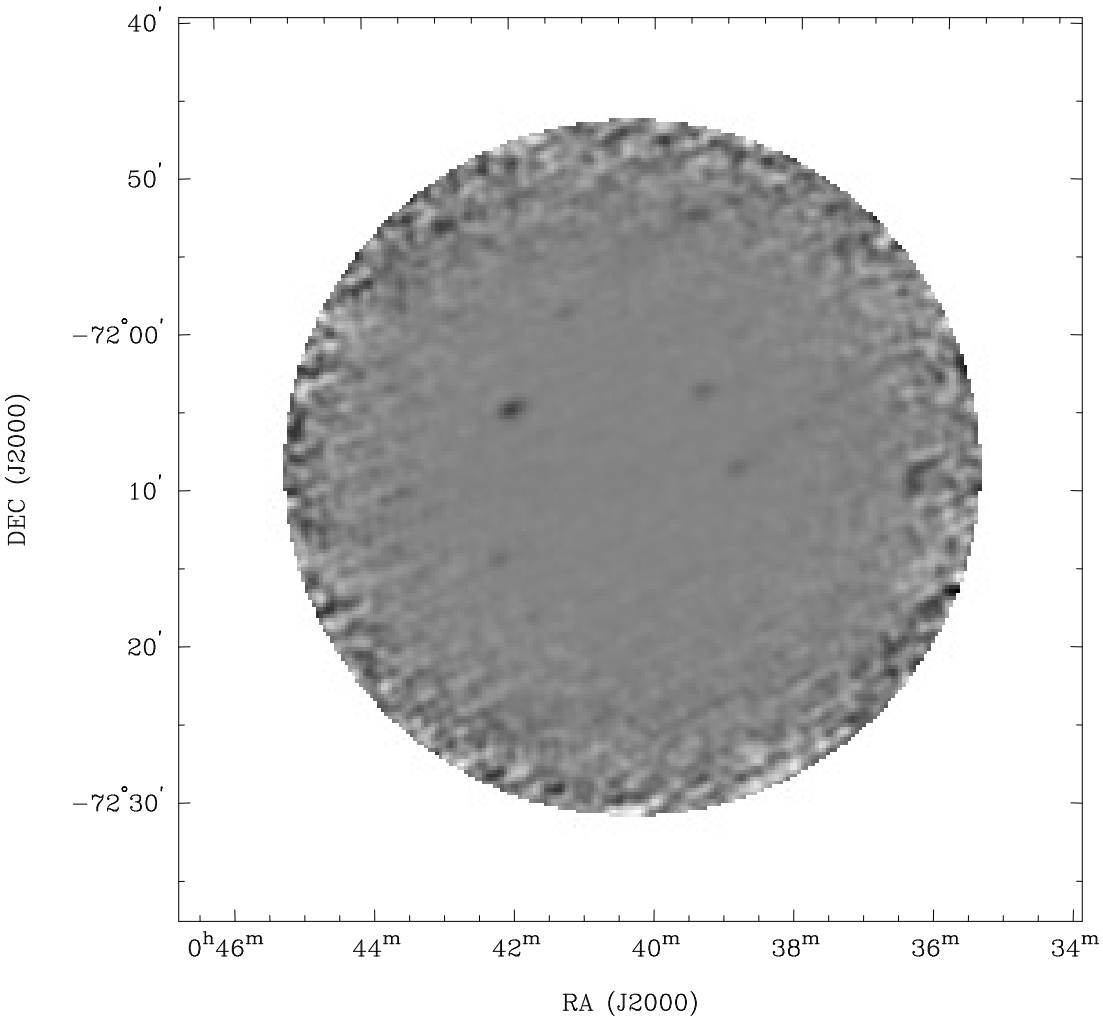

Figure 2.10 The field of Figure 2.5 after the peeling process. Note that the artefacts seen in Figure 2.7 are no longer present.

2.2.3 The New Maps

This work constructed new images that all employ the peeling technique first described in Hughes et al. (2007) and detailed in Section 2.2.2. This technique allows for correction of off-axis effects and reduces artefact levels. These new images represent a significant advancement over the previous ones processed with more traditional techniques.

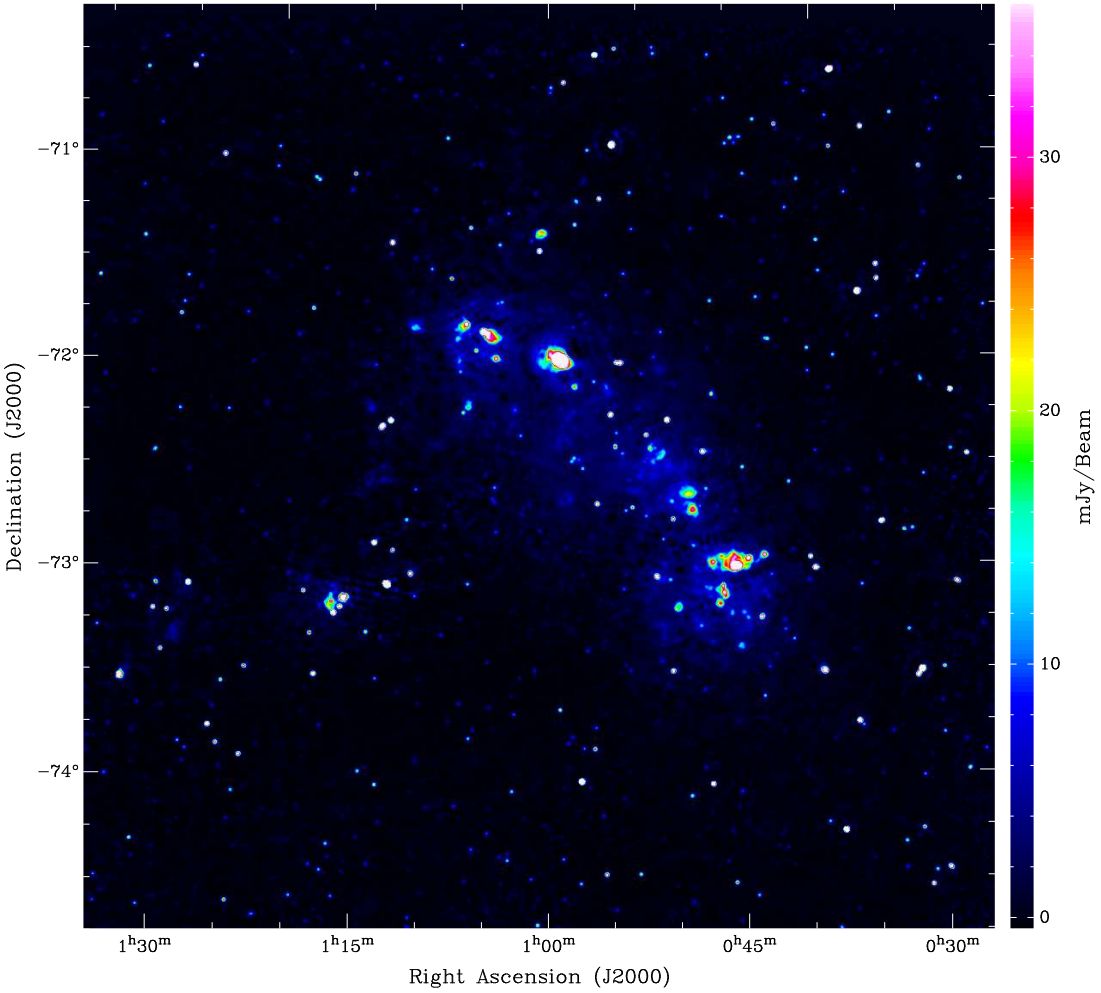

Figure 2.11 The Small Magellanic Cloud survey at 2.37-GHz

"Zero-spacing" data from Parkes observations has been incorporated into all of the new survey images. However, some older Parkes observations have high noise levels and were not planned as compliments to the ATCA surveys and thus do not cover the same regions. There are plans for new Parkes Telescope observations to rectify these shortcomings.

These maps have been used to investigate the overall structure of both the LMC and SMC. At the same time I was investigating the distributions of SNRs and PNe across both clouds. The major result is that all these groups of objects follow the hypothesised spiral arm structure (Filipović et al. 1998) in the LMC, and are in the main body grouping of the SMC.

The new 13 (Fig. 2.11), 6 (Fig. 2.12) and 3-cm (Fig. 2.13) radio-continuum maps of the SMC, were created with the "peeling" technique and a joint deconvolution. The maps have resolutions of 60″ 30″ and 20″ and r.m.s. noise of 0.7, 0.7 and 0.8 mJy/beam at 13, 6 and 3 cm, respectively, and are (at the time of publication) both the highest resolution and most sensitive maps of the SMC.

Most of this work was originally presented as Crawford et al. (2011) reproduced in Chapter 3.

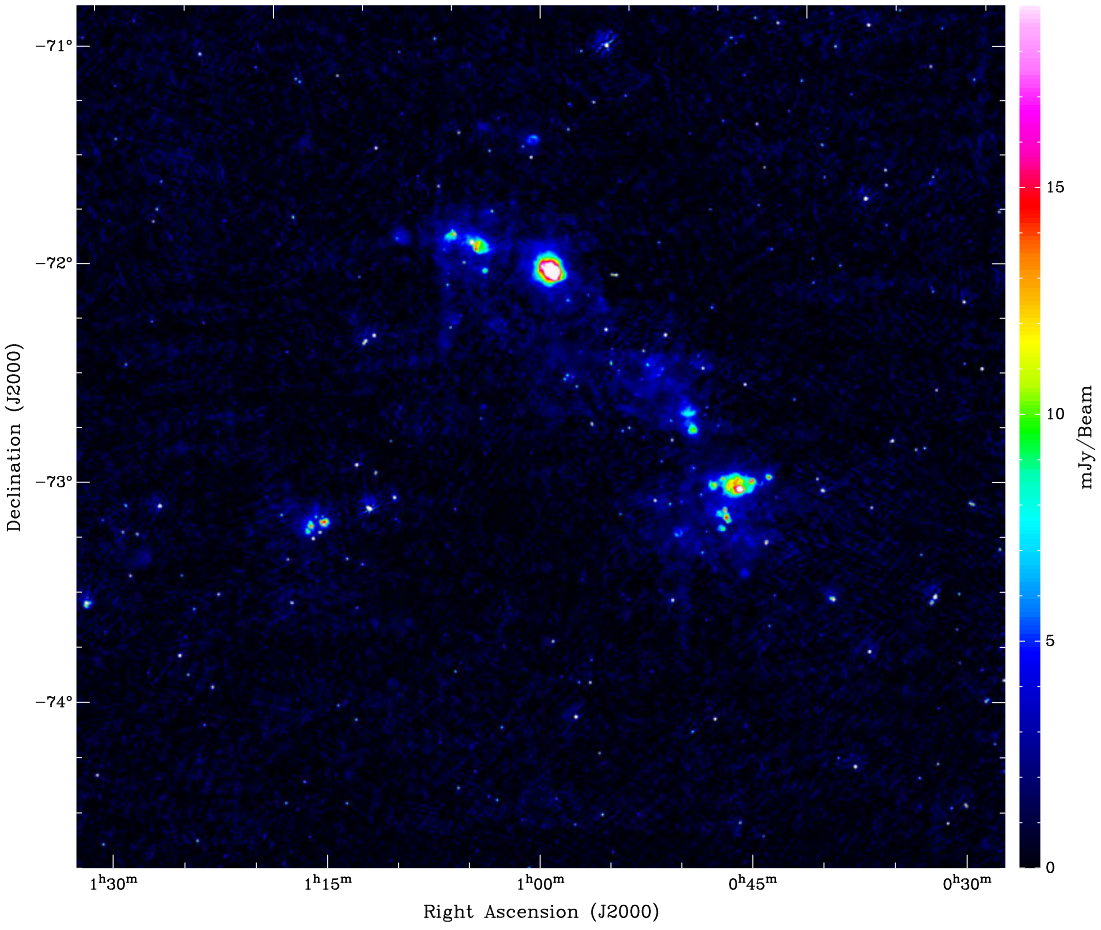

Figure 2.12 The Small Magellanic Cloud survey at 4.8-GHz

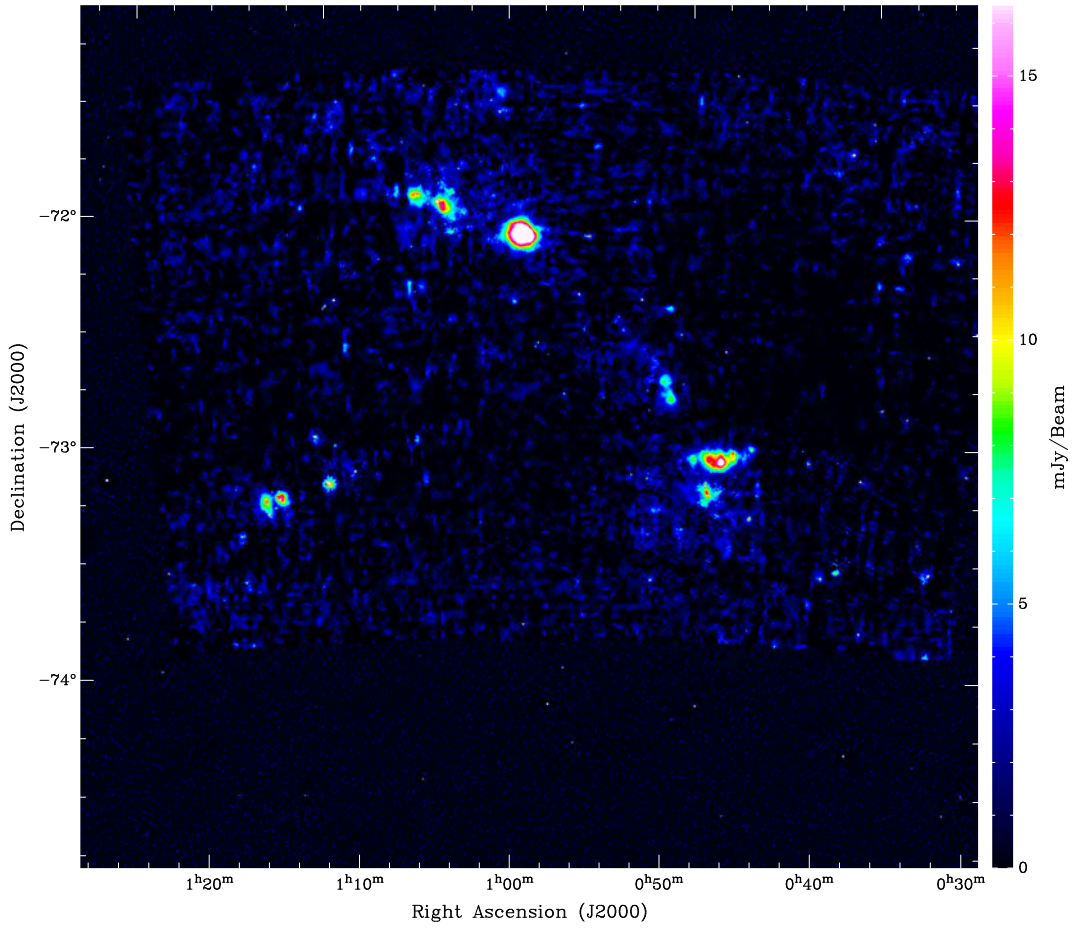

Figure 2.13 The Small Magellanic Cloud survey at 8.64-GHz

These maps are also being used for future studies of the SMCs radio source population and overall extended structure.

The techniques and expertise developed in this project have been used and passed on to the Wong et al. (2011a, reproduced in Sec. A.10) 20 cm survey of the SMC and resulting catalogues (Wong et al. 2011b, 2012a,b, reproduced in Sec. A.11 A.19 & A.24), the Galvin et al. (2012a, reproduced in Sec. A.17) survey and catalogue of M31, the Galvin et al. (2012b, reproduced in Sec. A.21) survey and catalogue of NGC 300, O'Brien et al. (2013, reproduced in Sec. A.29) survey and actalogue of NGC 55, and the Galvin et al. (2014, reproduced in Sec. A.37) survey and catalogue of NGC 7793.

2.3 Small Scale Structure of the Magellanic Clouds

2.3.1 Supernova Remnants

The study of supernova remnants (SNRs) in nearby galaxies is of major interest in order to understand the multi-frequency output of more distant galaxies, and to understand the processes that proceed on local interstellar scales within our own Galaxy. Unfortunately, the distances to many Galactic remnants are uncertain by a factor of ~ 2 (eg. Johanson and Kerton 2009; Green 2009a,b), leading to a factor of ~ 4 uncertainty in luminosity and of ~ 5.5 in the calculated energy release of the initiating supernova (SN).

It is feasible to obtain a nearly complete sample of SNRs in the MCs and not only study the global properties of the sample but also study the subclasses in detail (e.g., sorted by X-ray and radio morphology or by progenitor SN type). Toward this goal, I have identified new SNRs using combined optical, radio, and X-ray observations.

SNRs reflect a major process in the elemental enrichment of the interstellar medium (ISM). Multiple supernova explosions over space-time generate super-bubbles typically hundreds of parsecs in extent. Both are among the prime drivers controlling the morphology and the evolution of the ISM. Pulsar wind nebulae (PWN) offer further information, as the SNR shell and PWN together provide unique constraints and insights into the ISM. Their properties are therefore crucial to the full understanding of the galactic matter cycle.

This study mostly confirms the standard SNR evolutionary track (Woltjer 1972), based on an analysis of SNR studies that I am a contributor, that is Crawford et al. (2008a, 2010, 2014, reproduced in Chaps. 4, 5 & 6), Cajko et al. (2009, reproduced in Sec. A.4), Bozzetto et al. (2010, 2012a,b,c,d, 2013, 2014a,b, reproduced in Secs. A.6, A.18, A.14, A.16, A.23, A.28, A.36 & A.34), Owen et al. (2011, reproduced in Sec. A.9), Grondin et al. (2012, reproduced in Sec. A.13), De Horta et al. (2012, 2013, 2014b,a, reproduced in Secs. A.15, A.26, A.35 & A.38),

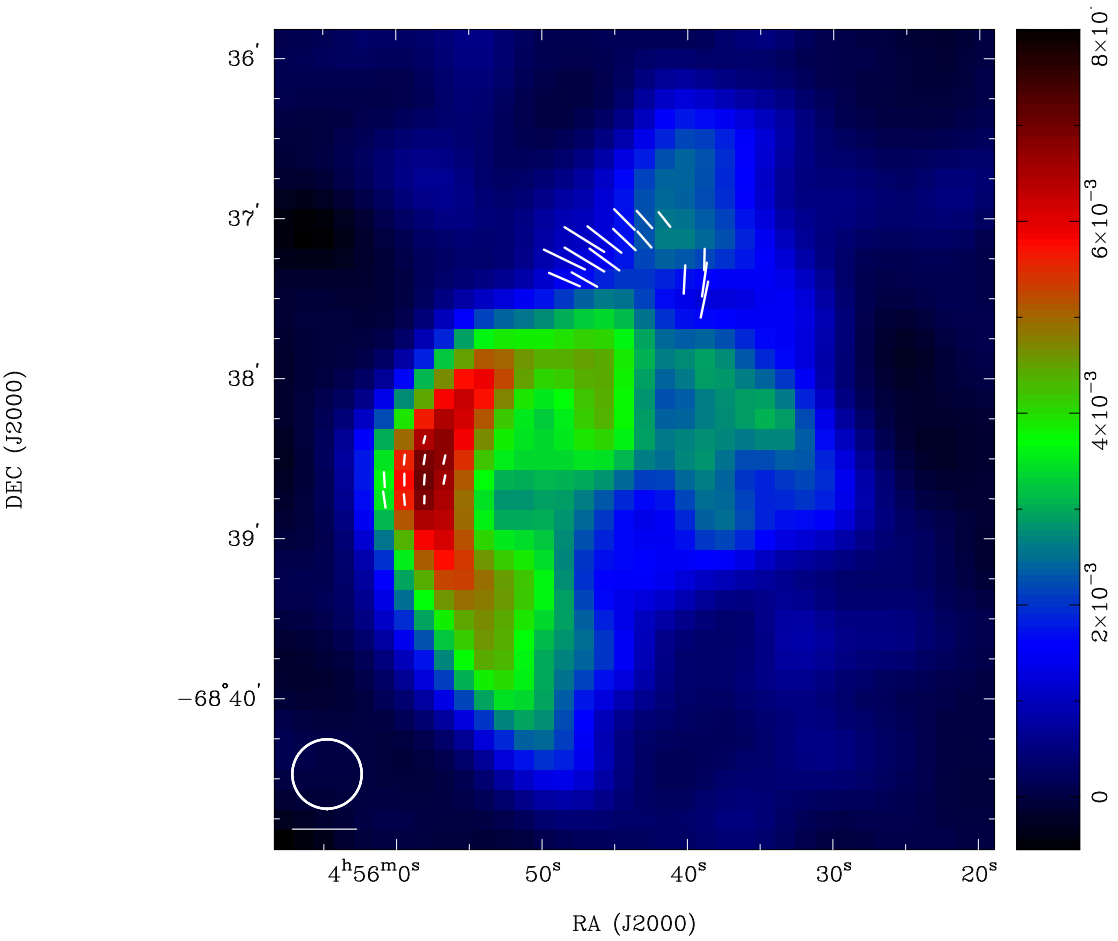

Figure 2.14 ATCA observations of SNR J0455–6838 at 6 cm (4790 MHz) overlaid with fractional polarised intensity. The white circle in the lower left corner represents the synthesised beam of 26″, and the white line below the circle is a polarisation vector of 100%. The sidebar quantifies the pixel map and its units are Jy/beam.

Haberl et al. (2012a, reproduced in Sec. A.20), Maggi et al. (2012, reproduced in Sec. A.22), Kavanagh et al. (2013, reproduced in Sec. A.25), and Roper et al. (2015, reproduced in Sec. A.39).

However this study focuses on the non-typical SNRs, that is SNRs that do not fully conform to the standard evolutionary model.

2.3.1.1 The case of LMC SNR J0455–6838

The first SNR J0455–6838 (Fig. 2.14), features regions of high polarisation, including one region that was unusually strong (∼70%) that corresponds to the "breakout" region in the north. A diameter of $215'' \times 156'' \pm 5''$, a complex spectral index $\alpha = -0.81 \pm 0.18$ were also measured. This work was originally presented as Crawford et al. (2008a) and reproduced in Chapter 4.

2.3.1.2 The case of LMC SNR J0528–6714

The second SNR J0528–6714, exhibits luminous radio-continuum emission, but is one of the unusual and rare cases without detectable optical and very faint X-ray emission (initially detected by ROSAT and listed as object [HP99] 498). We used new multi-frequency radio-continuum surveys and new optical observations at Hα, [S II] and [O III] wavelengths, in combination with XMM-Newton X-ray data, to investigate the SNR properties and to search for a physical explanation for the unusual appearance of this SNR. It was found that this object is a typical older SNR with a radio spectral index of $\alpha = -0.36 \pm 0.09$ and a diameter of D = 52.4 ± 1.0 pc. Regions of moderate and somewhat irregular polarisation were detected which are also indicative of an older SNR. Using a non-equilibrium ionisation collisional plasma model to describe the X-ray spectrum, temperatures kT of 0.26 keV were determined for the remnant. The low temperature, low surface brightness, and large extent of the remnant all indicate a relatively advanced age. The near circular morphology indicates a Type Ia event.

This study revealed one of the most unusual cases of SNRs in the Local Group of galaxies, a luminous radio SNR without optical counterpart and, at the same time, very faint X-ray emission. While it is not unusual to not detect an SNR in the optical, the combination of faint X-ray and no optical detection makes this SNR very unique. This is in contrast to the M 33 findings of Long et al. (2010), where no SNR is found with X-ray and radio emission, but not seen in optical. This work was originally presented as Crawford et al. (2010) and reproduced in Chapter 5.

2.3.1.3 The case of SMC SNR HFPK 334

New Australia Telescope Compact Array (ATCA) radio-continuum and *XMM-Newton*/*Chandra X-ray Observatory* (CXO) observations of the unusual supernova remnant SNR J0528–6714in the Small Magellanic Cloud (SMC) are presented. The remnant follows a shell type morphology in the radio-continuum and has a size of $\sim$20 pc at the SMC distance. The X-ray morphology is similar, however, we detect a prominent point source close to the center of the SNR exhibiting a spectrum with a best fit powerlaw with a photon index of $\Gamma = 2.7 \pm 0.5$. The nature of this central point source is ambiguous and cannot be directly associated with the remnant. The high temperature, nonequilibrium conditions in the diffuse region suggest that this gas has been recently shocked and point toward a younger SNR with an age of $\lesssim$ 1800 years. With an average radio spectral index of $\alpha = -0.59 \pm 0.09$ we find that an equipartition magnetic field for the remnant is $\sim$90 μG, a value typical of younger SNRs in low-density environments. Also, we report detection of scattered radio polarisation across the remnant at 20 cm, with a peak fractional polarisation level of 25$\pm$5%.

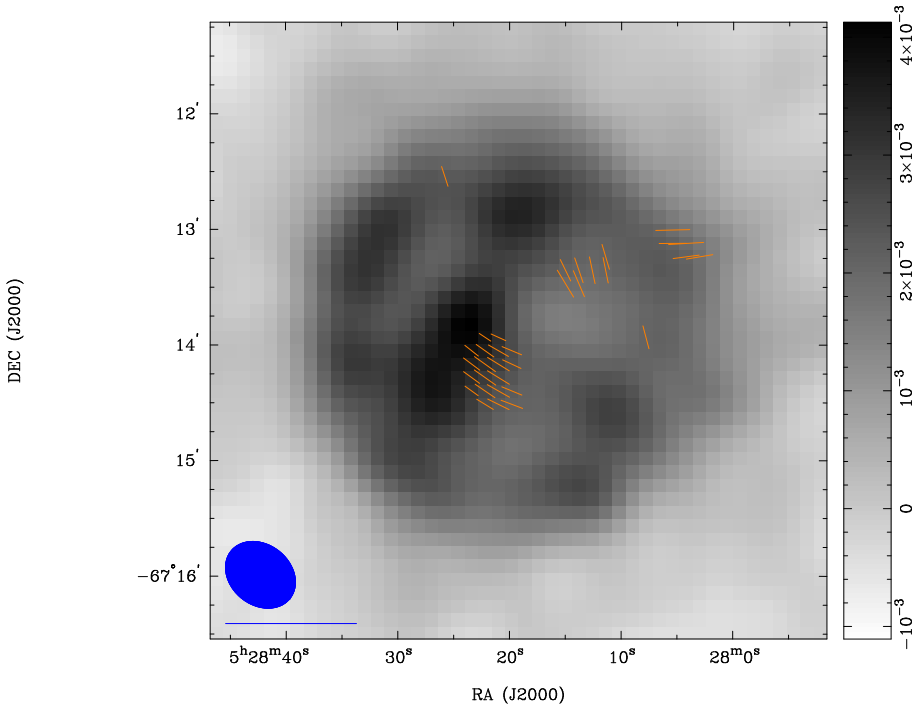

Figure 2.15 ATCA observations of LMC SNR J0528–6714 at 6 cm (4790 MHz) overlaid with fractional polarised intensity. The ellipse in the lower left corner represents the synthesised beam of 39″×31″, and the line below the ellipse is a polarisation vector of 100%. The sidebar quantifies the pixel map and its units are Jy/beam.

This work was originally presented as Crawford et al. (2014) and reproduced in Chapter 6.

2.3.2 Planetary Nebulae

The last stage of the evolution of stars starts when the nuclear fuel in its core is exhausted. The majority of stars (∼95% of all stars in our Galaxy) will gradually evolve by casting off their envelopes through a series of bursts in luminosity. When the gravo-thermal stability is achieved again, the almost fully revealed dense and hot core will continue to evolve toward a white dwarf (WD) phase. The hot core will trough the extreme input of mechanical and electromagnetic energy, start to shape and ionise previously ejected layers of gas. These layers, now in the form of glowing symmetric nebulosities, are called planetary nebulae (PNe). PNe are among the most complex, varied and fascinating of celestial phenomena. They extremely potent astrophysical probes by virtue of their strong emission lines, and are powerful indicators of parent's galaxy star-forming history (Maciel and Costa 2003).

Earlier work, Filipović et al. (2009, Reproduced in Sec. A.3) reported the first confirmed extragalactic radio-continuum detection of 15 PNe in the Magellanic Clouds (MCs). Prior to this study, a tentative radio detection of only three extragalactic PNe have been reported in the literature (Zijlstra et al. 1994; Dudziak et al. 2000). The Small Magellanic Cloud (SMC) PNe sample appear to be unusually strong radio emitters. Based on the radio-continuum properties

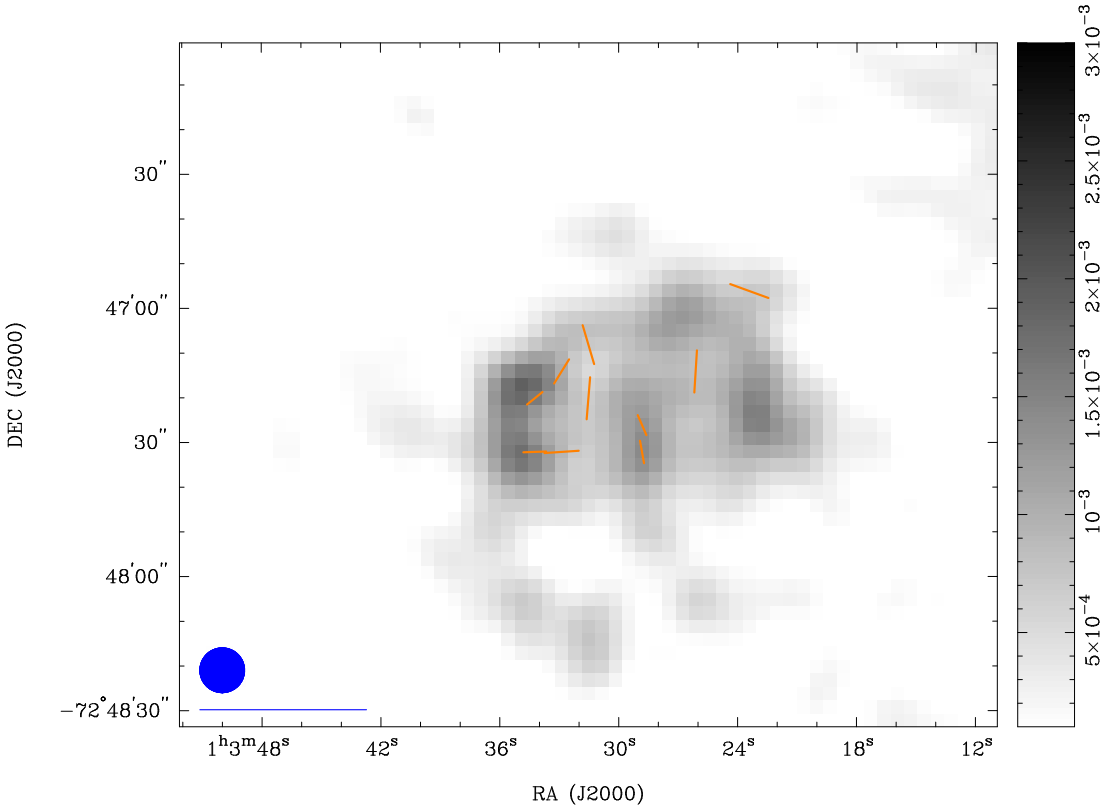

Figure 2.16 ATCA observations of HFPK 334 at 20 cm (1384 MHz) overlaid with fractional polarised intensity. The ellipse in the lower left corner represents the synthesised beam of 10″ and the line below the ellipse is a polarisation vector of 100%. The peak polarisation is estimated to ∼25±5%. The sidebar quantifies the pixel map in units of Jy/beam.

Table 2.1 Planetary Nebulae in the Large Magellanic Cloud, with 5500 MHz and 9000 MHz fluxes where detected, along with spectral index ($S \propto \nu^{\alpha}$).

Name	R.A. (J2000)	DEC (J2000)	S_{5500} (mJy)	S_{9000} (mJy)	α
SMP-LMC-3	04:42:23.96	-66:13:01.6	0.89	–	–
SMP-LMC-8	04:50:13.13	-69:33:56.8	1.10	1.29	0.33
SMP-LMC-13	04:59:59.97	-70:27:41.4	0.60	–	–
SMP-LMC-52	05:21:23.83	-68:35:33.4	1.39	1.34	-0.08
SMP-LMC-61	05:24:35.99	-73:40:40.2	1.41	–	–
SMP-LMC-63	05:25:26.00	-68:55:53.7	1.70	1.26	-0.61
SMP-LMC-66	05:28:40.97	-67:33:39.0	0.60	–	–
SMP-LMC-67	05:29:15.65	-67:32:47.5	0.69	–	–
SMP-LMC-73	05:31:21.86	-70:40:45.3	1.43	1.53	0.14
SMP-LMC-78	05:34:21.24	-68:58:25.1	1.74	1.58	-0.20
SMP-LMC-85	05:40:30.79	-66:17:37.2	1.59	1.76	0.22
SMP-LMC-87	05:41:07.97	-72:42:08.2	0.54	–	–
SMP-LMC-92	05:47:04.56	-69:27:34.0	1.61	1.40	-0.28
SMP-LMC-98	06:17:35.36	-73:12:34.6	2.06	1.65	-0.46
SMP-LMC-100	06:22:55.50	-72:07:40.9	0.70	–	–
SMP-LMC-71	05:30:33.14	-70:44:37.8	0.37	–	–
SMP-LMC-1	04:38:34.86	-70:36:43.1	0.89	–	–
SMP-LMC-15	05:00:52.72	-70:13:41.1	0.65	–	–
SMP-LMC-19	05:03:41.11	-70:13:53.3	0.38	–	–
SMP-LMC-29	05:08:03.26	-68:40:15.9	0.79	–	–
SMP-LMC-33	05:10:09.38	-68:29:54.5	0.77	–	–
SMP-LMC-37	05:11:03.00	-67:47:58.7	0.57	–	–
SMP-LMC-38	05:11:23.56	-70:01:57.5	0.76	–	–
SMP-LMC-53	05:21:32.79	-67:00:04.5	0.85	–	–
SMP-LMC-58	05:24:20.62	-70:05:01.1	0.65	–	–
SMP-LMC-6	04:47:38.99	-72:28:20.6	0.79	–	–
SMP-LMC-76	05:33:56.14	-67:53:08.3	0.87	–	–
SMP-LMC-79	05:34:17.22	-74:19:35.0	0.57	–	–
SMP-LMC-81	05:35:20.89	-73:55:30.0	0.99	–	–
SMP-LMC-99	06:18:58.06	-71:35:50.0	0.82	–	–
SMP-LMC-21	05:04:51.96	-68:39:09.3	0.82	–	–

of radio-bright Galactic PNe the expected (theoretical) radio flux densities at the distance of the LMC/SMC are up to ∼2.5 and ∼2.0 mJy at 1.4 GHz, respectively. It was found that one of the new radio PNe in the SMC has a flux density of 5.1 mJy at 1.4 GHz, several times higher than NGC 7027, the most radio-luminous known Galactic PN.

Building on this earlier work (Payne et al. 2008a; Filipović et al. 2009; Bojičić et al. 2010, Reproduced in Secs. A.1, A.3, & A.7) additional observations were undertaken with Australia Telescope Compact Array (ATCA) on 28th–30th Novemver 2010, with an array configuration 6A, at wavelengths of 6 and 3 cm (ν=5500 and 9000 MHz). The observations were done in so called "snap-shot" mode, totaling ∼30 minutes of integration over a 12 hour period. Source B1934-638 was used to calibrate the flux scale and bandpass, 0530-727 was used as a phase calibrator for LMC PNe.

The following new fluxes were found for the sample of LMC PNe are presented in Table 2.1.

Part II

Lead Author

Refereed Journal Papers[1]

[1] All articles presented in this part have been refereed and appear in a ERA recognised journal. The text is presented unchanged, save for renumbering of the figures and tables, but the formatting has been harmonised with the rest of the thesis. Figures and tables have been re-numbered for consistency.

Chapter 3

Paper I

Apart from formatting changes the following text originally appeared as:
Crawford, E. J., Filipović, M. D., De Horta, A. Y., Wong, G. F., Tothill, N. F. H., Drašković, D., Collier, J. D., and Galvin, T. J. (2011). New 6 and 3-cm Radio-Continuum Maps of the Small Magellanic Cloud. Part I - The Maps. *Serbian Astronomical Journal*, 183:95–102

New 6 and 3-cm Radio-continuum maps of the Small Magellanic Cloud. Part I – The Maps

E. J. Crawford, M. D. Filipović, A. Y. De Horta, G. F.Wong, N. F. H. Tothill, D. Drašković, J. D. Collier, T. J. Galvin

3.1 Summary

We present new 6 and 3-cm radio-continuum maps of the Small Magellanic Cloud (SMC), created with the "peeling" technique and a joint deconvolution. The maps have resolutions of 30″ and 20″ and r.m.s. noise of 0.7 and 0.8 mJy/beam at 6 and 3 cm, respectively. These maps will be used for future studies of the SMC's radio source population and overall extended structure.

3.2 Introduction

In the past two decades, several Parkes, Molonglo Observatory Synthesis Telescope (MOST) and Australia Telescope Compact Array (ATCA) moderate resolution (∼arcmin) surveys of the Magellanic Clouds (MCs) have been completed (Filipović et al. 1998).

Deep ATCA and Parkes radio-continuum and snap-shot surveys of the Small Magellanic Cloud (SMC) were conducted at 20, 13, 6 and 3 cm by Filipović et al. (2002), achieving

Table 3.1 ATCA Projects used.

Project Code	Dates Observed
C1604	Jun 2007
C1207	February 2005 & 2006
C882	Jun 2000
C859	March 2007
C634	October 1997

sensitivities of 1.8, 0.4, 0.8 and 0.4 mJy/beam respectively. These surveys were conducted in mosaic mode with between 35 and 320 separate pointings using 5 antennae in the 375-m array configuration, with short-spacing information from single-dish Parkes observations. The maps have angular resolutions of 98″, 40″, 30″ and 20″ at the respective wavelengths listed above. Recently, we published a set of new high resolution (few-arcsec) radio-continuum mosaic images of the SMC at 20 cm created by combining observations from ATCA and Parkes (Wong et al. 2011a). The latest images of the SMC at 6 and 3 cm were presented by Dickel et al. (2010, 2005). These maps display significant artefacts due to the way they were constructed as linear mosaics of individually cleaned images. By jointly deconvolving these data with other archival data we were able to obtain significantly improved maps of the SMC.

3.3 Imaging Techniques

When the area to be imaged exceeds the field of view of the telescope, a mosaic must be made. There are two methods for assembling a mosaic: Image each field and combine the images at the end; or combine the data at the beginning and image them jointly. The field-by-field approach has the advantage that it has modest processing requirements. However, not all available information in the data is utilised. The downside to the joint approach is a huge increase in the processing time and complexity.

A further problem with wide field imaging is the effect of "off-axis" sources. A source that is outside the primary beam of the telescope can still influence the response of the receiver. The solution to this problem is to use the "peeling" technique detailed in Hughes et al. (2007). Essentially, the techniques of self-calibration and source subtraction are used to correct for off-axis sources and thus reduce the artefact levels.

The interferometer images only sample the Fourier plane down to the shortest baseline — the largest scale structures are missed. To correct for this deficiency, archival "zero-spacing" data from Parkes (a large single dish) observations (Filipović et al. 1997) have been incorporated into all of the new survey images. However, these observations do not cover the whole field of the ATCA observations. The Parkes data also have much higher r.m.s. noise than the ATCA data.

3.4 Data Reduction Technique and Results

The majority of archival data used come from ATCA project C1207 (Dickel et al. 2010), available in calibrated form[1]. A search of the Australia Telescope Online Archive[2] yielded four more projects that cover the SMC at 6 and 3 cm (Table 3.1). All data were inspected, peeled if necessary, and then combined into a single "dirty map". The SDI clean algorithm (Sault and Killeen 2006) was used to deconvolve the images, which were then restored. The new maps are presented with and without zero-spacing data in Figs. 3.1 to 3.4. The resolutions are $30''$ and $20''$ and the sensitivities of the ATCA data are 0.7 and 0.8 mJy/beam at 6 cm (Fig. 3.1) and 3 cm (Fig. 3.3), respectively. The r.m.s. noise levels in Figs. 3.2 and 3.4 are dominated by the additional noise of the single dish data (Filipović et al. 1997).

As only project C1207 was designed as a survey of the entire region, the maps suffer from nonuniform sensitivity, a consequence of differing integration times at each pointing. Figures 3.5 & 3.6 demonstrate how the sensitivity changes across the field.

All these images can be downloaded from `http://spacescience.uws.edu.au/mc/smc/`

3.5 Acknowledgements

The Australia Telescope Compact Array and Parkes radio telescope are parts of the Australia Telescope National Facility which is funded by the Commonwealth of Australia for operation as a National Facility managed by CSIRO. This paper includes archived data obtained through the Australia Telescope Online Archive (`http://atoa.atnf.csiro.au`). We used the KARMA and MIRIAD software package developed by the ATNF.

[1] `http://www.atnf.csiro.au/research/smc_ctm/`
[2] `http://atoa.atnf.csiro.au`

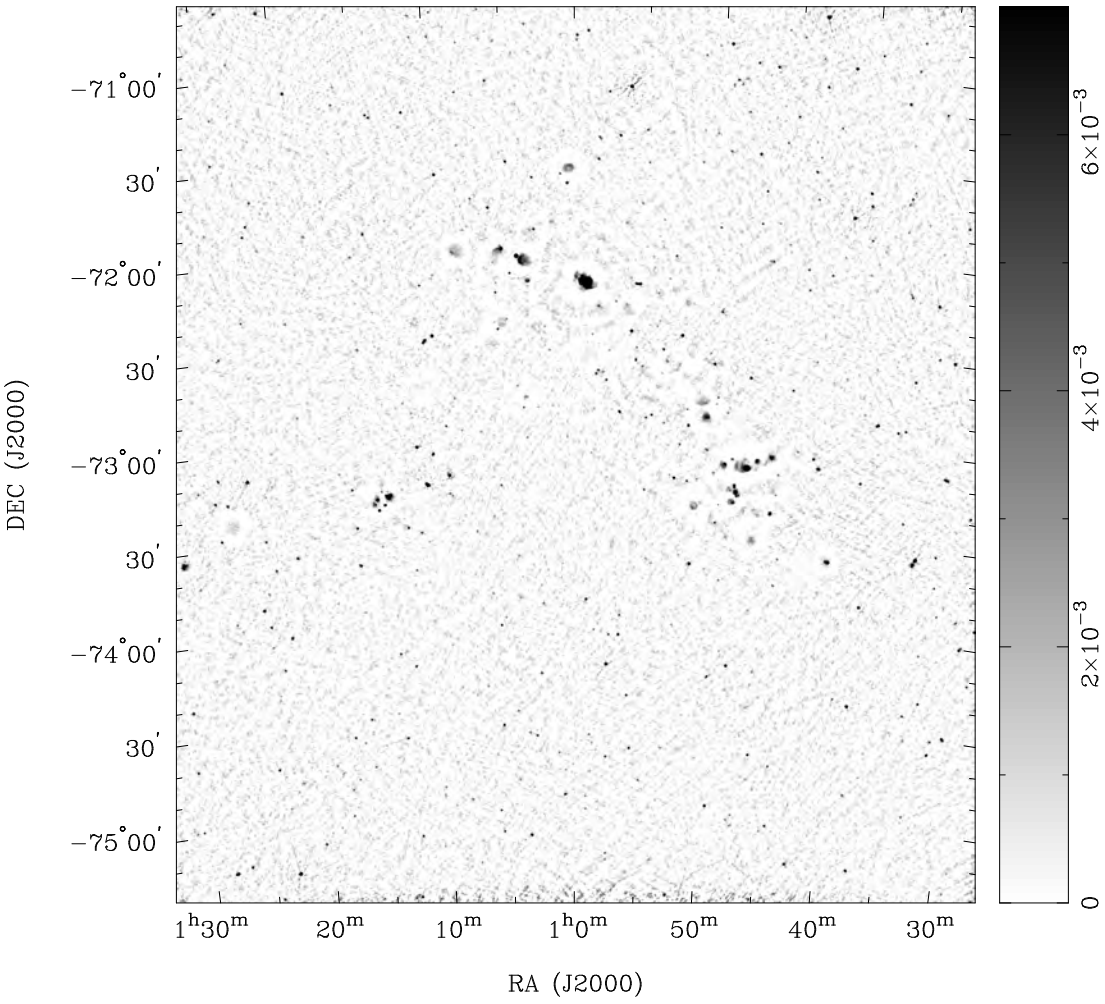

Figure 3.1 The SMC at 6 cm without zero-spacing data. The map has a resolution of 30″. The sidebar gives the intensity scale in units of Jy/beam.

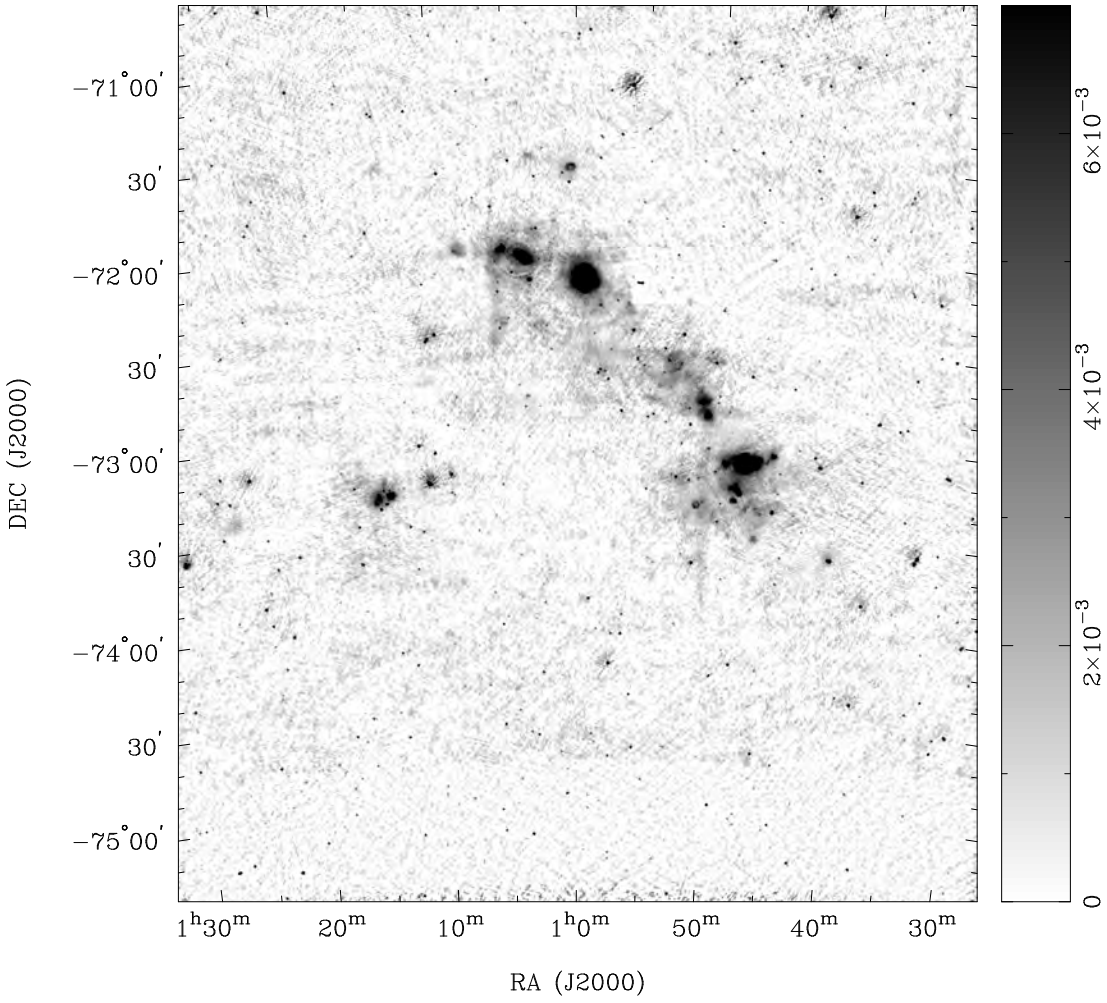

Figure 3.2 The SMC at 6 cm with zero-spacing data. The map has a resolution of 30″. The sidebar gives the intensity scale in units of Jy/beam. The zero-spacing data does not cover the same spatial area as the interferometer data.

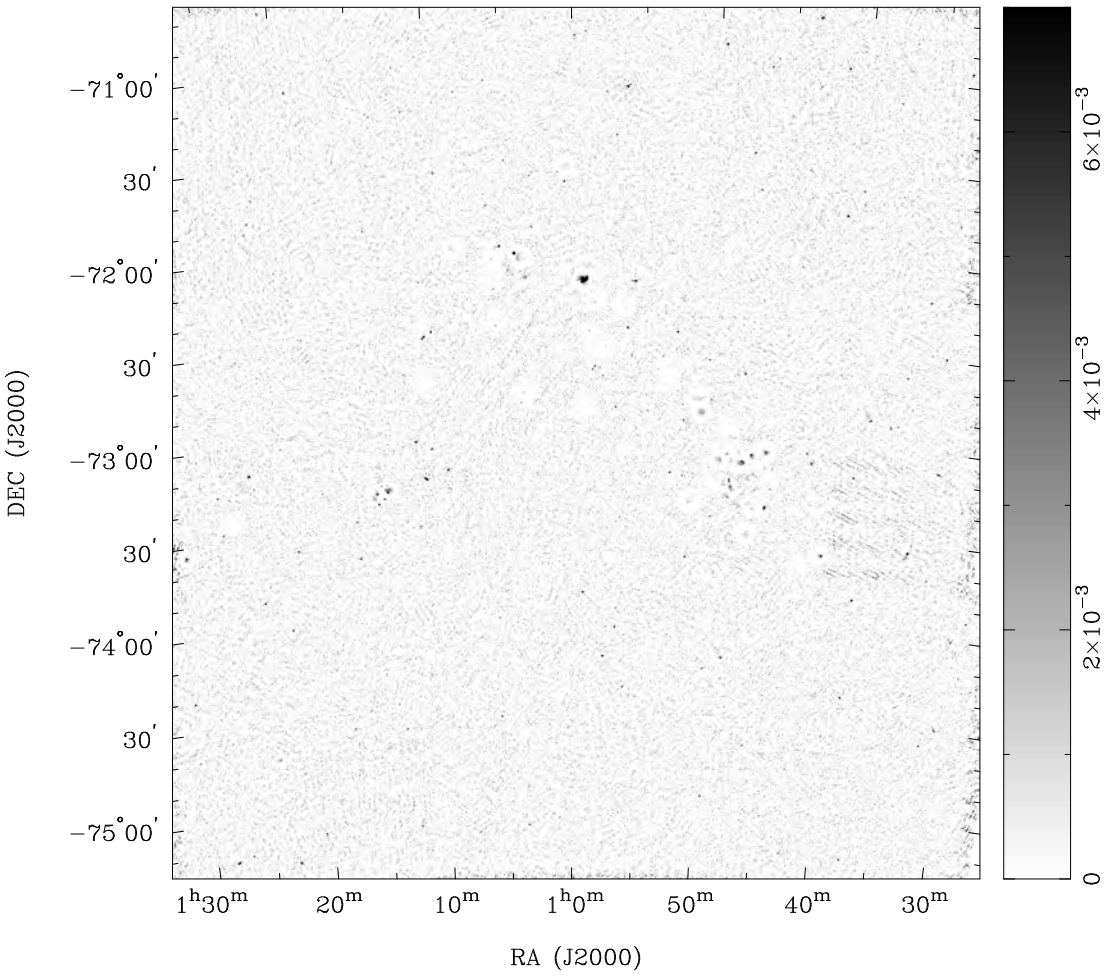

Figure 3.3 The SMC at 3 cm without zero-spacing data. The map has a resolution of 20″. The sidebar gives the intensity scale in units of Jy/beam.

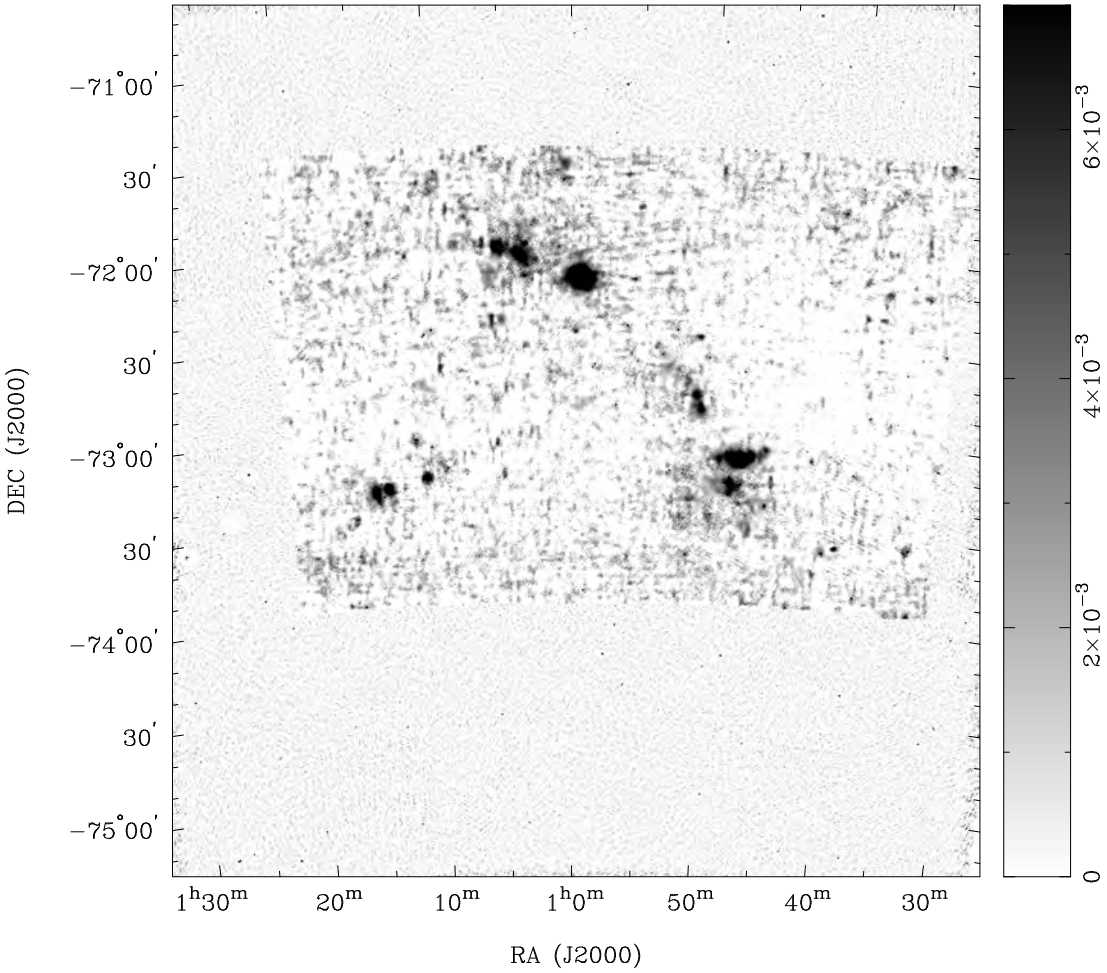

Figure 3.4 The SMC at 3 cm with zero-spacing data. The map has a resolution of 20″. The sidebar gives the intensity scale in units of Jy/beam. The zero-spacing data does not cover the same spatial area as the interferometer data.

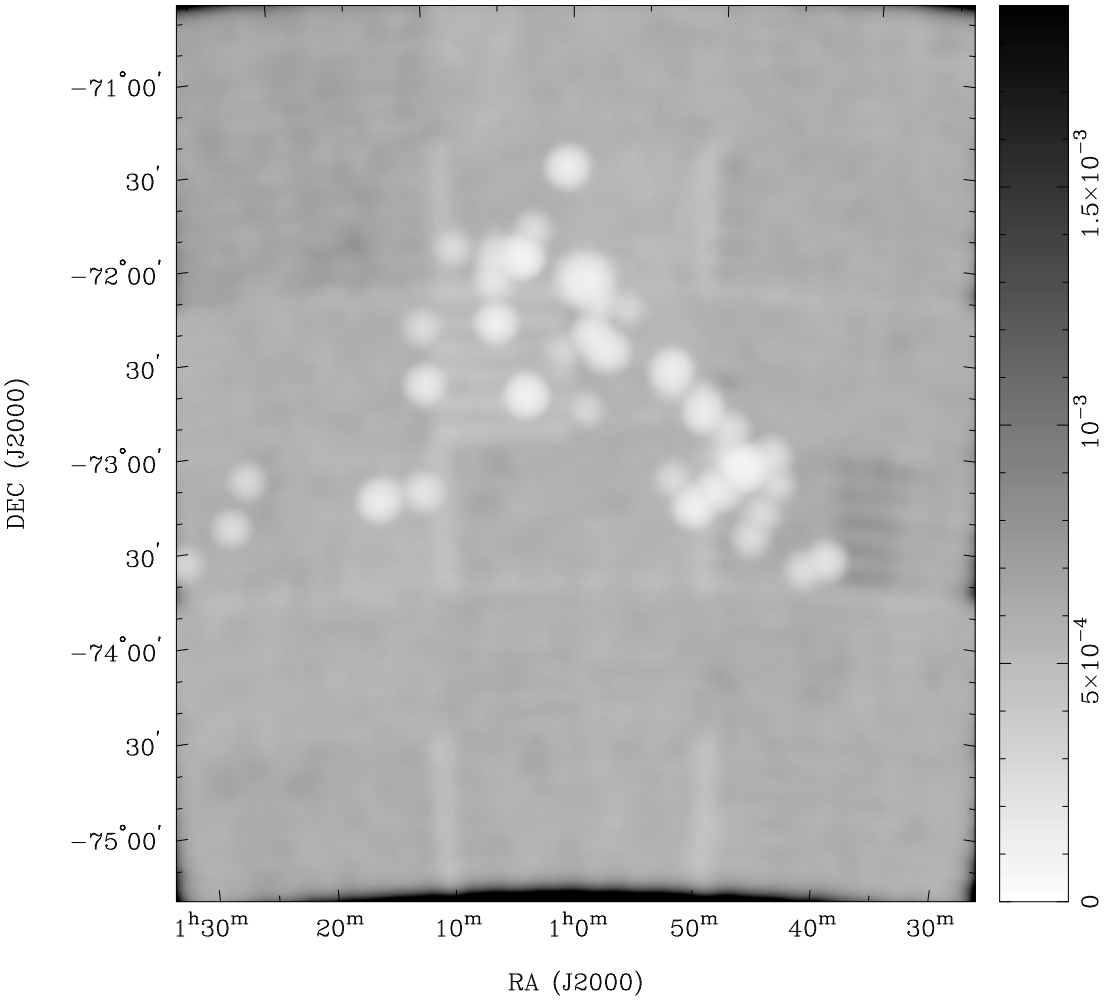

Figure 3.5 Theoretical r.m.s. sensitivity map of the 6 cm data used in this study in Jy/beam. Lighter areas indicate higher sensitivity.

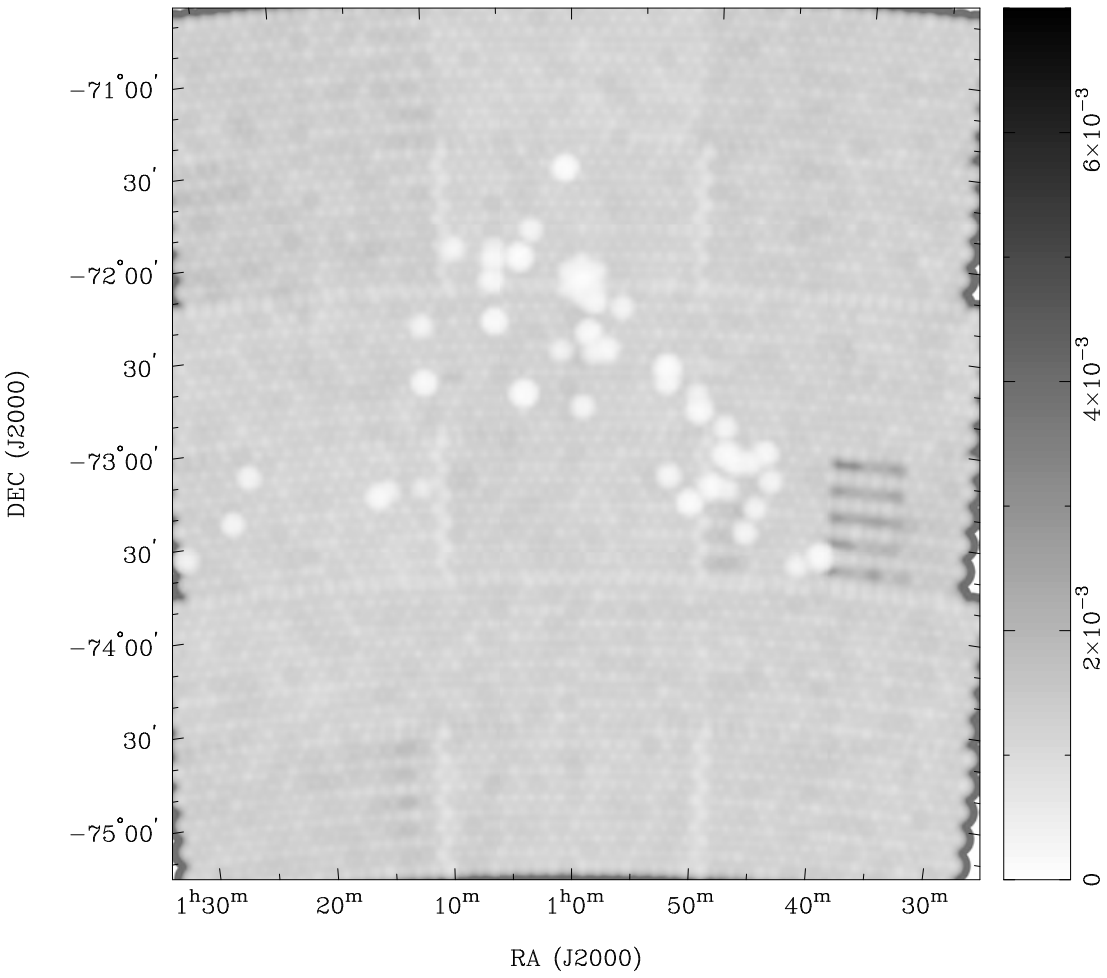

Figure 3.6 Theoretical r.m.s. sensitivity map of the 3 cm data used in this study in Jy/beam. Lighter areas indicate higher sensitivity.

Chapter 4

Paper II

Apart from formatting changes the following text originally appeared as:
Crawford, E. J., Filipović, M. D., De Horta, A. Y., Stootman, F. H., and Payne, J. L. (2008a). Radio-Continuum Study of the Supernova Remnants in the Large Magellanic Cloud - An SNR with a Highly Polarised Breakout Region - SNR J0455-6838. *Serbian Astronomical Journal*, 177:61–66

Radio-Continuum Study of the Supernova Remnants in the Large Magellanic Cloud – An SNR with a Highly Polarised Breakout Region – SNR J0455–6838.

E. J. Crawford, M. D. Filipović, A. Y. de Horta, F. H. Stootman, and J. L. Payne.

4.1 Summary

We present the results of new moderate resolution ATCA observations of SNR J0455–6838. We found that this SNR exhibits a mostly typical appearance with rather steep and curved α=–0.81±0.18 and D=43×31±1 pc. Regions of high polarisation were detected, including unusually strong (∼70%) region corresponding to the northern breakout. This detection of strong polarisation in breakout regions has not been observed in any other SNR.

4.2 Introduction

The Large Magellanic Cloud (LMC), with its low foreground absorption and relative proximity of 50kpc (Hilditch et al. 2005), offers the ideal laboratory for the study of a complete sample of supernova remnants (SNRs) in great detail. The proximity enables detailed spatial studies of the remnants in the sample, and the accurately known distance allows for analysis of the energetics of each remnant. In addition, the wealth of wide-field multiwavelength data available,

from radio maps to optical emission-line images and broad band photometry to global X-ray mosaics, provides information about the contexts and environments in which these remnants are born and evolve.

It is possible to obtain a relatively complete sample of SNRs in the LMC and not only study the global properties of the sample but also study the subclasses in detail (e.g., sorted by X-ray and radio morphology or by progenitor SN type). Toward this goal, we have been identifying new SNRs using combined optical, radio, and X-ray observations. There are over 40 confirmed SNRs in the LMC and another 35-40 candidates (Payne et al. 2008b)

Here, we report on radio-continuum observation of a previously known and intriguing SNR SNR J0455–6838. It was initially classified as an SNR based on observations made by the Mills Cross telescope at the Molonglo Radio Observatory at 408MHz (Mathewson and Clarke 1973). Further confirmation comes from the Einstein X-Ray survey by Long et al. (1981) (named LHG 2) and Wang et al. (1991) (named W 3). Mathewson et al. (1983)) catalogued SNR J0455–6838 as B0455–68.7 based on their optical observations, reporting an estimated size of $217'' \times 183''$. Filipović et al. (1998) added further confirmation, with a set of radio continuum observations (with the Parkes telescope) over a wide frequency range. Blair et al. (2006) report no detection at far ultraviolet (FUV) wavelengths. Haberl and Pietsch (1999) (named SNR as HP 915) and Williams et al. (1999a) discuss the X-Ray properties of SNR J0455–6838 based on ROSAT observations. Most recently Payne et al. (2008b) presented optical spectroscopy of a wide range of LMC SNRs including SNR J0455–6838. They found an enhanced [SII]/Hα ratio of 0.6 typical for SNRs.

4.3 Observation Data

We observed SNR J0455–6838 with the Australia Telescope Compact Array (ATCA) on 6$^{\text{th}}$ April 1997, with an array configuration EW375, at wavelengths of 6 and 3 cm (ν=4790 and 8640 MHz). The observations were done in so called "snap-shot" mode, totaling $\sim$1 hour of integration over a 12 hour period. Source 1934-638 was used for primary calibration and source 0530-727 was used for secondary calibration. The MIRIAD (Sault and Killeen 2006) and KARMA (Gooch 2006) software packages were used for reduction and analysis. More information about observing procedure and other sources observed during this session can be found in Bojičić et al. (2007) and Crawford et al. (2008b).

Images were prepared, cleaned and deconvolved using MIRIAD tasks. Baselines formed with the 6$^{\text{th}}$ ATCA antenna were excluded, as the other five antennas were arranged in a compact configuration. The 6-cm image (Fig. 4.1) has a resolution of $26''$ and the r.m.s noise is estimated

to be 0.2 mJy/beam. Similarly, the 3-cm image (Fig. 4.2(a)) has a resolution of 26″ and the r.m.s noise is estimated to be 0.3 mJy/beam. The 3-cm image resolution of 26″ was chosen to compliment the 6-cm image, and was used in the preparation of Figs. 4.2 and 4.3.

4.4 Results and Discussion

The remnant has a classical horseshoe morphology centered at RA(J2000)=$4^h55^m45.7^s$, DEC(J2000)=–68°38′52.9″ with a diameter of 215″×156″±5″ (43×31±1 pc), excluding the breakout region to the north. This is reasonably consistent with the optical size reported by Mathewson et al. (1983). The X-ray size of 366″ × 168″ reported by Williams et al. (1999a), seems to include the breakout region to the north, and when removed our diameters are in agreement.

The breakout region to the north is not usually seen in SNRs. Williams et al. (1999b) indicated that they may have a significant role in SNR evolution. They report a northern and southern breakout, however we only detect the northern one.

Flux density measurements were made at 6 and 3 cm, resulting in values of 115 mJy and 30 mJy respectively (Table 4.1), although our data seems to suffer from "short-spacing" effects and some flux may have been missed. Using the 21-cm mosaic image described in Hughes et al. (2007), we made a new measurement of the flux density of SNR J0455–6838, with a value of 289 mJy. A spectral index (defined as $S \propto \nu^{\alpha}$) was plotted using the flux densities in Table 4.1 (Fig. 4.3(b)) and estimated to be $\alpha = -0.81 \pm 0.18$, which is very steep for SNRs (Filipović et al. 1998). The previous spectral index estimate was based solely on single dish data, and was $\alpha = -0.43 \pm 0.05$ (Filipović et al. 1998). As shown in Fig. 4.3(b), we note that the 3 and 6 cm points are low compared to the others, and indicates that a simple model does not accurately describe the data, and that a higher order model is needed. This is not unusual given that several other SNR's exhibit this "curved" spectra (Filipović et al. 1998). Noting the breakdown of the power law fit at shorter wavelengths, we decomposed the spectral index estimate into two components the first (α_1) between 73 and 13 cm, and the second (α_2) 13 and 3 cm. The first component $\alpha_1 = -0.35 \pm 0.08$ is a very good fit and typical for an SNR, whereas the second $\alpha_2 = -1.52 \pm 0.39$, is a poor fit, and indicates that non-thermal emission is is no longer the dominant emission mechanism at the shorter wavelengths. Although the low flux at 3 cm (and to a lesser extent 6 cm) could cause the large deviations, an underestimate of up to ∼50% would still lead to a "curved" spectrum.

From our spectral index map (Fig. 4.3(a)) we can see a very steep gradient of spectral index, caused by the lower than expected 3-cm flux density. Comparing our radio-continuum images

Table 4.1 Integrated Flux Density of SNR J0455–6838.

S_I	73 cm	36 cm	21 cm	13 cm	6 cm	3 cm
SNR J0455–6838	410 mJy	380 mJy	289 mJy	229 mJy	115mJy	33 mJy
Reference	Clarke et al. 1976	Mills et al. 1984	This Work	Filipović et al. 1996	This Work	This Work

with ROSAT HRI X-ray images of Williams et al. (1999a, Fig. 1v) shows a correlation between radio and X-ray emission, as X-ray emission may be dominated by non-thermal emission.

Linear polarization images for each frequency were created using Q and U parameters. While we detect no reliable polarization at 3-cm, the 6-cm image reveals some very unusually strong linear polarisation. Without reliable polarisation measurements at the second frequency we could not determine the Faraday rotation.

The mean fractional polarisation at 6-cm was calculated using flux density and polarisation:

$$P = \frac{\sqrt{S_Q^2 + S_U^2}}{S_I} \cdot 100\% \tag{4.1}$$

where S_Q, S_U and S_I are integrated intensities for the Q, U and I Stokes parameters. Our estimated peak value is $P \sim 70\%$ in the breakout region, where the total intensity is relatively low. This could be due to the breakout interacting with the interstellar medium. This effect has not been seen before as SNRs with clear breakouts are rare, nor has such strong polarisation been seen, even in strongly polarised SNRs. Along the brightest section of the shell the polarisation is relatively uniform, and quite strong at approximately 20% (Fig. 4.1), as would be expected from non-thermal SNRs. This relatively high level of polarisation is (theoretically) expected for an SNR with a radio spectrum ($\sim$0.5) this steep (Rohlfs and Wilson 2004; Urošević and Milogradov-Turin 2007).

4.5 Conclusion

We conducted the highest resolution observations to date of SNR J0455–6838. From these observations we found a diameter of $215'' \times 156'' \pm 5''$, a complex spectral index $\alpha = -0.81 \pm 0.18$ and interesting polarisation features associated with the brightest region of the SNR and the northern breakout region.

4.6 Acknowledgements

We used the KARMA software package developed by the ATNF. The Australia Telescope Compact Array is part of the Australia Telescope which is funded by the Commonwealth of Australia

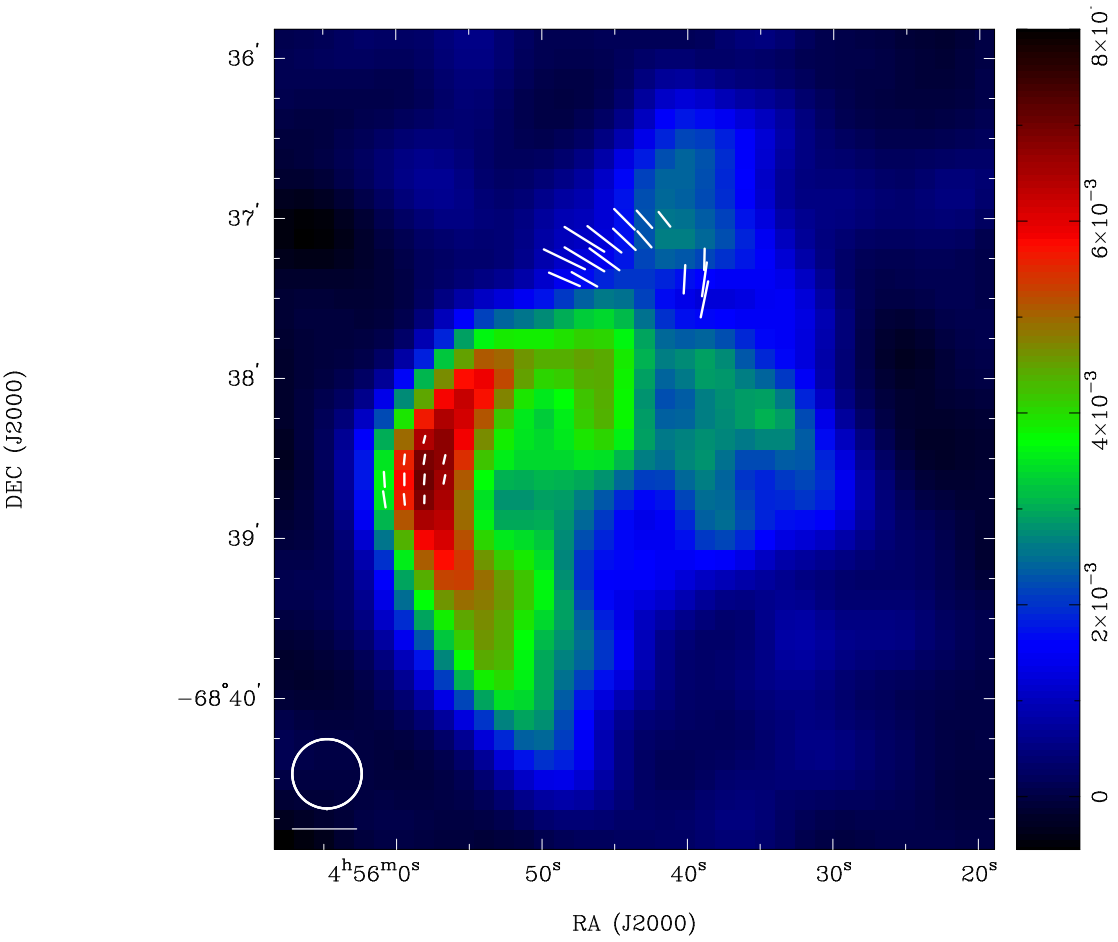

Figure 4.1 ATCA observations of SNR J0455–6838 at 6 cm (4790 MHz) overlaid with fractional polarised intensity. The white circle in the lower left corner represents the synthesised beam of 26″, and the white line below the circle is a polarisation vector of 100%. The sidebar quantifies the pixel map and its units are Jy/beam.

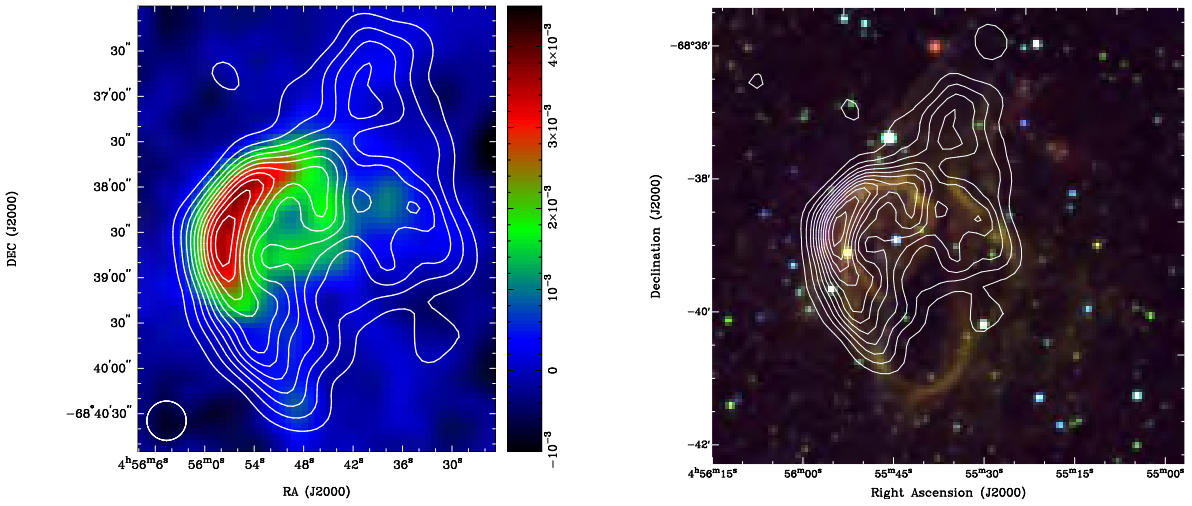

Figure 4.2 (a)ATCA 3-cm observations of SNR J0455–6838, overlaid with 6-cm contours. The white circle in the lower left corner represents the 3 cm (8640 MHz) synthesised beam of 26″. The sidebar quantifies the pixel map and its units are Jy/beam. (b) MCELS composite optical image (RGB = H_α,[SII],[OIII]) image overlaid with ATCA 6-cm contours. The contours on both images are 3–33σ in 3σ steps.

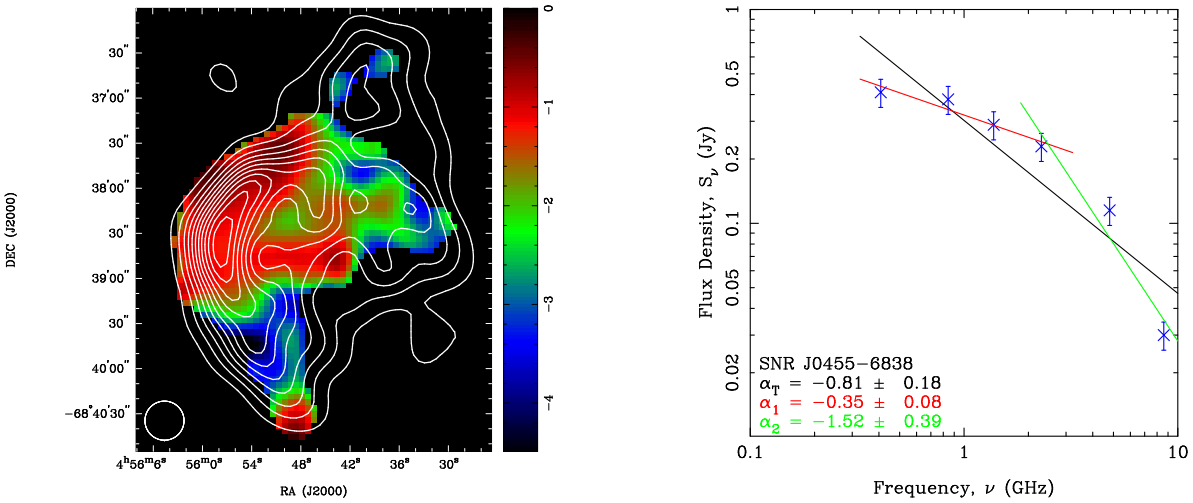

Figure 4.3 (a) Spectral index map of SNR J0455–6838 overlaid with 6 cm (4790 MHz) contours. The contours are the same as Fig. 4.2. The white circle in the lower left corner represents the synthesised beam of 26″. The sidebar quantifies the pixel map, representing the spectral index. (b) Radio-continuum Spectrum of SNR J0455–6838.

for operation as a National Facility managed by CSIRO. We thank the Magellanic Clouds Emission Line Survey (MCELS) team for access to the optical images.

Chapter 5

Paper III

Apart from formatting changes the following text originally appeared as:
Crawford, E. J., Filipović, M. D., Haberl, F., Pietsch, W., Payne, J. L., and De Horta, A. Y. (2010). Multi-frequency study of Local Group supernova remnants. The curious case of the Large Magellanic Cloud SNR J0528-6714. *A&A*, 518:A35

Multi-frequency study of Local Group supernova remnants. The curious case of the Large Magellanic Cloud SNR J0528-6714.

E. J. Crawford, M. D. Filipović, F. Haberl, W. Pietsch, J. L. Payne, and A. Y. de Horta.

5.1 Abstract

Context The SNRs known in the Local Group show a variety of morphological structures that are relatively uncorrelated in the different wavelength bands. This variety is probably caused by the different conditions in the surrounding medium with which the remnant interacts.

Aims Recent ATCA, XMM-Newton and MCELS observations of the Magellanic Clouds (MCs) cover a number of new and known SNRs which are poorly studied, such as SNR J0528–6714. This particular SNR exhibits luminous radio-continuum emission, but is one of the unusual and rare cases without detectable optical and very faint X-ray emission (initially detected by ROSAT and listed as object [HP99] 498). We used new multi-frequency radio-continuum surveys and new optical observations at Hα, [S II] and [O III] wavelengths, in combination with XMM-Newton X-ray data, to investigate the SNR properties and to search for a physical explanation for the unusual appearance of this SNR.

Methods We analysed the X-ray and Radio-Continuum spectra and present multi-wavelength morphological studies of this SNR.

Results We present the results of new moderate resolution ATCA observations of SNR J0528–6714. We found that this object is a typical older SNR with a radio spectral index of $\alpha = -0.36 \pm 0.09$ and a diameter of D = 52.4 ± 1.0 pc. Regions of moderate and somewhat irregular polarisation were detected which are also indicative of an older SNR. Using a non-equilibrium ionisation collisional plasma model to describe the X-ray spectrum, we find temperatures kT of 0.26 keV for the remnant. The low temperature, low surface brightness, and large extent of the remnant all indicate a relatively advanced age. The near circular morphology indicates a Type Ia event.

Conclusions Our study revealed one of the most unusual cases of SNRs in the Local Group of galaxies – a luminous radio SNR without optical counterpart and, at the same time, very faint X-ray emission. While it is not unusual to not detect an SNR in the optical, the combination of faint X-ray and no optical detection makes this SNR very unique.

5.2 Introduction

The Large Magellanic Cloud (LMC), with its low foreground absorption and relative proximity of ∼50 kpc (di Benedetto 2008), offers the ideal laboratory for the detailed study of a complete sample of objects such as supernova remnants (SNRs). The proximity enables detailed spatial studies of the remnants, and the accurately known distance allows for analysis of the energetics of each remnant. In addition, the wealth of wide-field multiwavelength data available, from radio maps to optical emission-line images and broad-band photometry to global X-ray mosaics, provides information about the contexts and environments in which these remnants are born and evolve.

It is possible to obtain a relatively complete sample of SNRs in the LMC and not only study the global properties of the sample but also study the subclasses in detail (e.g., sorted by X-ray and radio morphology, diameter or by type of the supernova progenitor). Toward this goal, we have been studying SNRs in the Magellanic Clouds (MCs) in greater detail using combined optical, radio, and X-ray observations. Today we know over 40 confirmed SNRs in the LMC and another 35-40 candidates (Payne et al. 2008b).

Here, we report on multi-frequency observations of a previously known and intriguing LMC supernova remnant. SNR J0528–6714 was initially suggested as a candidate by Turtle and Mills (1984). Mathewson et al. (1985) classified it as an SNR based on observations made with the

Molonglo Radio Observatory, at 36 cm (ν=843 MHz), and they noted no optical counterpart. Filipović et al. (1998) added further confirmation, with a set of radio-continuum observations (with the Parkes telescope) over a wide frequency range and estimated a steep spectrum with powerlaw index $\alpha = -0.79 \pm 0.15$. Blair et al. (2006) observed SNR J0528–6714 but reported no detection at far-ultraviolet (FUV) wavelengths. Haberl and Pietsch (1999) associated an X-ray counterpart to this radio SNR from *ROSAT* PSPC observations. According to the entry number in their catalogue, the ROSAT source is named [HP99] 498.

5.3 Observational Data

5.3.1 The ATCA radio-continuum observations

We observed SNR J0528–6714 with the Australia Telescope Compact Array (ATCA) on 6$^{\rm th}$ April 1997, with an array configuration EW375, at wavelengths of 6 and 3 cm (ν=4790 and 8640 MHz). The observations were done in so called "snap-shot" mode, totaling ∼1 hour of integration over a 12 hour period. Source 1934-638 was used for primary calibration and source 0530-727 was used for secondary calibration. The MIRIAD (Sault and Killeen 2006) and KARMA (Gooch 2006) software packages were used for data reduction and analysis. More information about the observing procedure and other sources observed during this session can be found in Bojičić et al. (2007), Crawford et al. (2008a,b) and Cajko et al. (2009).

Baselines formed with the 6$^{\rm th}$ ATCA antenna were excluded, as the other five antennas were arranged in a compact configuration. The 6 cm image (Fig. 5.1) has a resolution of $39'' \times 31''$ at position angle 50° and the r.m.s noise is estimated to be 0.4 mJy/beam. Due to the signal to noise restrictions and the size of the remnant, no reliable image could be prepared at 3 cm.

We also used all available radio-continuum images of the LMC. These are composed of observations at several radio frequencies having moderate resolution at 36 cm (ν=843 MHz, MOST; Turtle and Amy 1991) and 20 cm (ν=1400 MHz, ATCA; Hughes et al. 2007).

5.3.2 *XMM-Newton* observations and data reduction

XMM-Newton serendipitously observed SNR J0528–6714 on 28$^{\rm th}$ January 2007, for a total of about 20 ks (observation ID 0402000601) at an off-axis angle of ∼6′. The observation was performed with the EPIC instruments (PN and two MOS cameras, Strüder et al. 2001; Turner et al. 2001) in imaging read out mode. Thin optical blocking filters were used to optimise observations of the target, the supersoft X-ray source candidate RX J0529.4−6713 (Kahabka et al. 2008) which is associated with the planetary nebula SMP L69. The data were analysed using the analysis package XMMSAS version 8.0.0. After removal of intervals with

high background activity, we obtained a net exposure time of 17.3 ks (EPIC-PN).

For morphology studies in comparison with radio-continuum and optical images *XMM-Newton* EPIC images were produced in the standard energy bands 0.2−0.5 keV, 0.5−1.0 keV, 1.0−2.0 keV and 2.0−4.5 keV. The images show faint diffuse emission at the position of the SNR and a point-like source near its centre at RA(J2000)=$5^h28^m17.9^s$, DEC(J2000)=–67°14′01″ (statistical error 1″, systematic uncertainty 2–3″).

To investigate if the point-like source is related to the SNR we extracted spectra for both sources separately. For the point-like source we used a circular extraction region with 20″ radius. For the SNR the outer radius of the extraction region (centre at RA(J2000)=$5^h28^m19.8^s$, DEC(J2000)=–67°14′21″) was 100″, excluding a circle around the point-like source with radius 25″. EPIC X-ray spectra were extracted for PN (single + double pixel events, corresponding to a PATTERN 0−4 selection) and MOS (PATTERN 0−12), excluding bad CCD pixels and columns (FLAG 0). We used XSPEC[1] version 12.5.1 for spectral modelling. The three EPIC spectra from the SNR were fitted simultaneously, allowing only a renormalisation factor to account for cross-calibration uncertainties between the instruments and area losses for the MOS extraction as the region covered by the SNR is near the edge of the inner MOS CCD in both cameras. To account for photo-electric absorption by interstellar gas, two hydrogen column densities were used. The first represents the foreground absorption in the Milky Way, fixed at 6×10^{20} cm^{-2} assuming elemental abundances of Wilms et al. (2000). The second considers the absorption in the LMC (with metal abundances set to 0.5 solar as typical of the LMC; Russell and Dopita 1992). The statistical quality of the spectra was sufficient to fit one-component thermal plasma emission models. For the supernova remnant we used a single-temperature non-equilibrium ionisation collisional plasma (NEI) model (in XSPEC, see Borkowski et al. 2001, and references therein) with metal abundances fixed to 0.5 solar, yielding acceptable χ^2 values. Results from similar modelling of X-ray spectra from SNRs in the SMC were published by van der Heyden et al. (2004) and Filipović et al. (2008), allowing direct comparison.

5.3.3 The MCELS optical surveys of the LMC

The Magellanic Cloud Emission Line Survey (MCELS) was carried out from the 0.6 m University of Michigan/CTIO Curtis Schmidt telescope, equipped with a SITE 2048×2048 CCD, which gave a field of 1.35° at a scale of 2.4″ pixel^{-1}. Both the LMC and SMC were mapped in narrow bands corresponding to Hα, [O III] (λ=5007 Å), and [S II] (λ=6716, 6731 Å), plus matched red and green continuum bands that are used primarily to subtract most of the stars from the images to reveal the full extent of the faint diffuse emission. All the data have been

[1] http://heasarc.gsfc.nasa.gov/docs/xanadu/xspec/

Table 5.1 Integrated Flux Density of SNR J0528–6714.

Frequency (MHz)	843	1400	4800
Wavelength (cm)	36	20	6
S_I (mJy)	125±10	122±5	69±5
Reference	Mathewson et al. 1984	This work	This work

flux-calibrated and assembled into mosaic images, a small section of which is shown in Fig. 5.5. Further details regarding the MCELS are given by Smith et al. (2006), Winkler et al. (in preparation) and at http://www.ctio.noao.edu/mcels/.

Additional observations were attempted on 25$^{\rm th}$ September 2009, using the 1.9-meter telescope and Cassegrain spectrograph at the South African Astronomical Observatory (SAAO) in Sutherland. While the observing conditions were good, we did not detect any emission from SNR J0528–6714.

5.4 Results

5.4.1 Radio-continuum

The remnant has a circular appearance centered at RA(J2000)=$5^h28^m18.5^s$, DEC(J2000)=–67°13′49.2″ with a diameter of 216″±5″ (52.4±1.0 pc). This is reasonably consistent with its X-ray extent as indicated in Fig. 5.4 where the 3σ radio-continuum contour is drawn on an X-ray image. The point-like X-ray source is located very close to the centre of the radio emission while the diffuse X-ray emission is brighter on the south-eastern side.

A flux density measurement was made at 6 cm, resulting in a value of 69±5 mJy (Table 5.1). Using the 20 cm mosaic image described in Hughes et al. (2007), we made a new estimate of the flux density of SNR J0528–6714, with a value of 122 ± 5 mJy. A spectral index (defined as $S \propto \nu^{\alpha}$) using the flux densities in Table 5.1 is estimated to α=–0.36±0.09 (Fig. 5.2), which is indicative of older SNRs (Filipović et al. 1998). We note that the 36 cm and 6 cm observations are only interferometer measurements, whereas the 20 cm observations consist of both single dish and interferometer measurements. This could lead to a flux density underestimate at these two wavelengths. Previous spectral index estimates were based solely on single dish data, (α=–0.79±0.15; Filipović et al. 1998). We note that this is a highly confused region, and that as our new estimate uses higher resolution data than Filipović et al. (1998), we have been able to exclude the confusing sources from the spectral index estimate.

Linear polarization images at 6 cm were created using stokes Q and U parameters. This image reveals regions of moderate and somewhat irregular polarisation within the SNR. Without

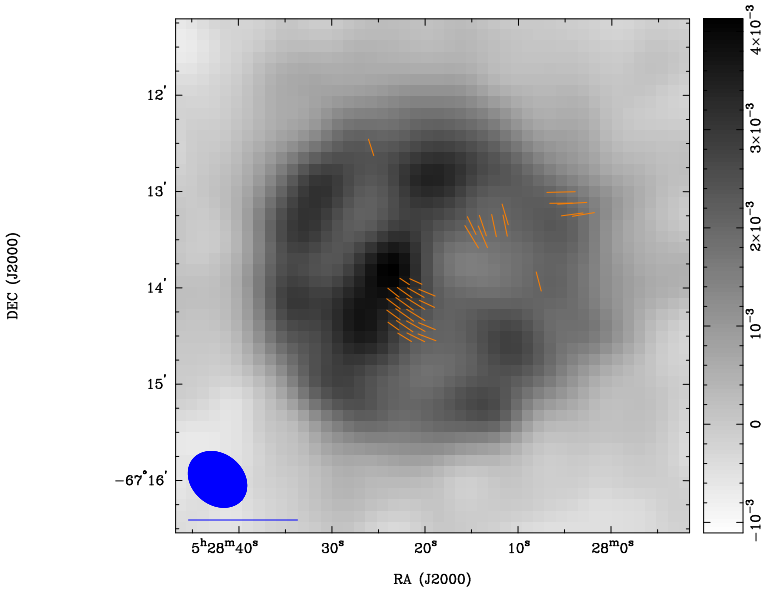

Figure 5.1 ATCA observations of SNR J0528–6714 at 6 cm (4790 MHz) overlaid with fractional polarised intensity. The ellipse in the lower left corner represents the synthesised beam of $39'' \times 31''$, and the line below the ellipse is a polarisation vector of 100%. The sidebar quantifies the pixel map and its units are Jy/beam.

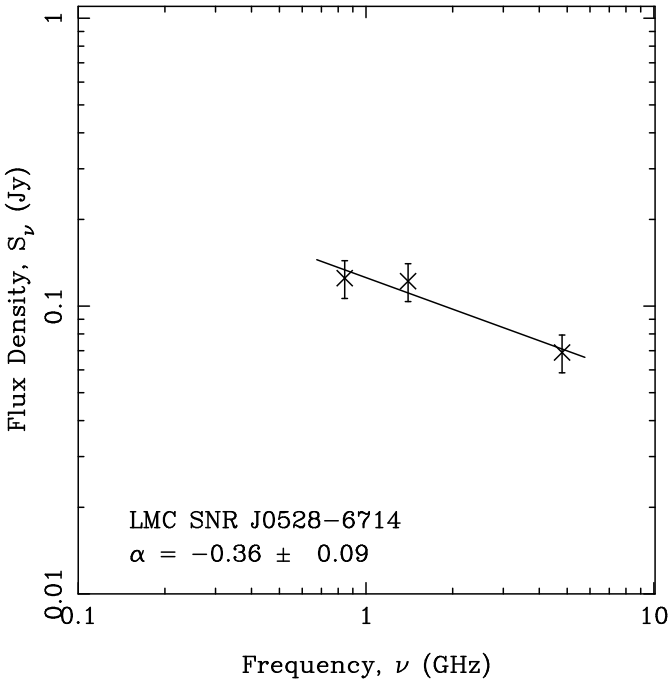

Figure 5.2 Radio-continuum spectrum of SNR J0528–6714.

reliable polarisation measurements at a second frequency we could not determine the Faraday rotation, and thus cannot deduce the magnetic field strength.

The mean fractional polarisation at 6 cm was calculated using flux density and polarisation:

$$P = \frac{\sqrt{S_Q^2 + S_U^2}}{S_I} \cdot 100\% \tag{5.1}$$

where S_Q, S_U and S_I are integrated intensities for the Q, U and I Stokes parameters. Our estimated peak value is $P \sim 20\%$ just off the centre of the remnant. Along the shell there is a pocket of uniform polarisation, at approximately 15% (Fig. 5.1), possibly indicating varied dynamics along the shell. This unordered polarisation is consistent with the appearance of an older SNR.

5.4.2 X-Ray

The EPIC spectra of the SNR (excluding the central source) are plotted in Fig. 5.3 together with the best-fit NEI model. The derived model parameters (LMC absorption, temperature kT and ionisation time scale τ) are summarised in Table 5.2 together with inferred fluxes and luminosities. Flux and luminosity are given for the 0.2–2 keV band, determined from the EPIC-PN spectrum (which has the best statistics with a count rate of 0.056 counts s^{-1}). The intrinsic source luminosity with total N_H set to 0 assumes a distance of 50 kpc to the LMC. The relatively large errors in the derived LMC absorption lead to large uncertainties in the (absorption corrected) luminosities for the soft X-ray spectrum of the SNR. Therefore, we give a luminosity range derived from fits with LMC N_H fixed at the lower and upper 90% confidence values. Similarly we derive a confidence range for the emission measure EM.

Spectra extracted from the point-like source near the centre of the SNR yield low counting statistics and only a spectrum from EPIC-PN data with 5 bins between 0.3 and 2 keV could be obtained. The shape of the spectrum is similar to that of the SNR and we therefore used the same model for a fit to the PN spectrum. The resulting best fit values for absorption column density and temperature are somewhat higher than derived for the SNR, but consistent within the statistical errors. It remains unclear if the point-like source is caused by a (somewhat hotter) knot in the emission of the SNR or unrelated to it. No foreground star, which could have a similar X-ray spectrum, is found near the X-ray position.

The spectrum of SNR J0528–6714 is characterised by a high absorption and a low temperature. Considering its large extent and low surface brightness, it is most likely an older remnant. The low temperature is similar to 3 SMC SNRs (van der Heyden et al. 2004; Filipović et al. 2008), and cooler than any known bright LMC SNR (Williams et al. 2004; Williams and Chu

Table 5.2 Spectral fits to the EPIC spectra of SNR J0528–6714 with an absorbed NEI model.

PN exp. [10^3 s]	LMC N_H [10^{21}cm^{-2}]	kT [keV]	τ [10^8 s cm^{-3}]	F_x [erg cm^{-2} s^{-1}]	L_x [erg s^{-1}]	EM [cm^{-3}]	χ^2_r	dof
17.3	$2.9^{+2.2}_{-1.0}$	$0.26^{+0.17}_{-0.12}$	$6^{+3.5}_{-2}$	1.1×10^{-13}	$9.6^{+43}_{-5.0}\times10^{35}$	$7.4^{+65}_{-4.7}\times10^{58}$	1.26	77

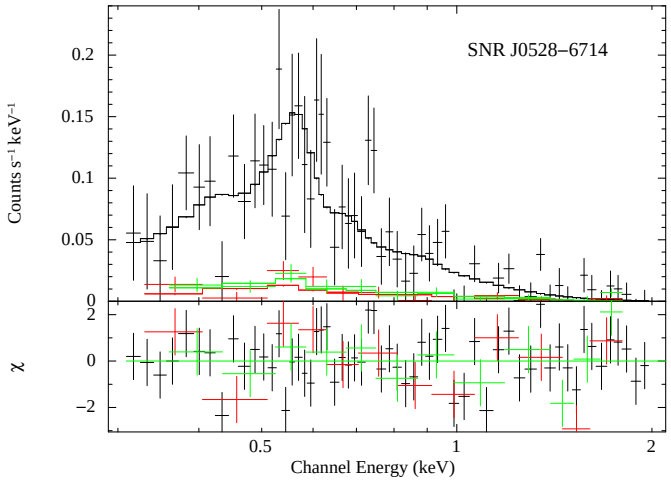

Figure 5.3 EPIC spectra of SNR J0528–6714 ([HP99] 498). The best fits using a single-temperature NEI model are plotted as histograms (black: PN, red: MOS1, green: MOS2).

2005; Borkowski et al. 2006; Bamba et al. 2006).

5.4.3 Optical

There is no obvious association between any emission in the Hα, [S II] or [O III] bands and SNR J0528–6714 (Fig.5.5), confirming the earlier observation of Mathewson et al. (1985). The high-density group of stars KMHK 943 (Kontizas et al. 1990) is visible on the eastern rim of the SNR J0528–6714. Martayan et al. (2006) report several B and Be stars in this region. These other objects, and their interaction with the interstellar matter (ISM), could explain the lack of an optical counterpart to SNR J0528–6714. Also, we cannot exclude the possibility of a dark cloud in the line of sight.

5.5 Discussion and Conclusions

We have analysed our new and archival *XMM-Newton*, MCELS and ATCA observations in the direction to the SNR J0528–6714. We conducted the highest resolution X-ray and radio-continuum observations to date of SNR J0528–6714. From radio observations we found a diameter of 52.4±1.0 pc, at the top end of the size distribution (Badenes et al. 2010), a radio-continuum spectral index α=–0.36±0.09, which is indicative of an older SNR (Filipović et al.

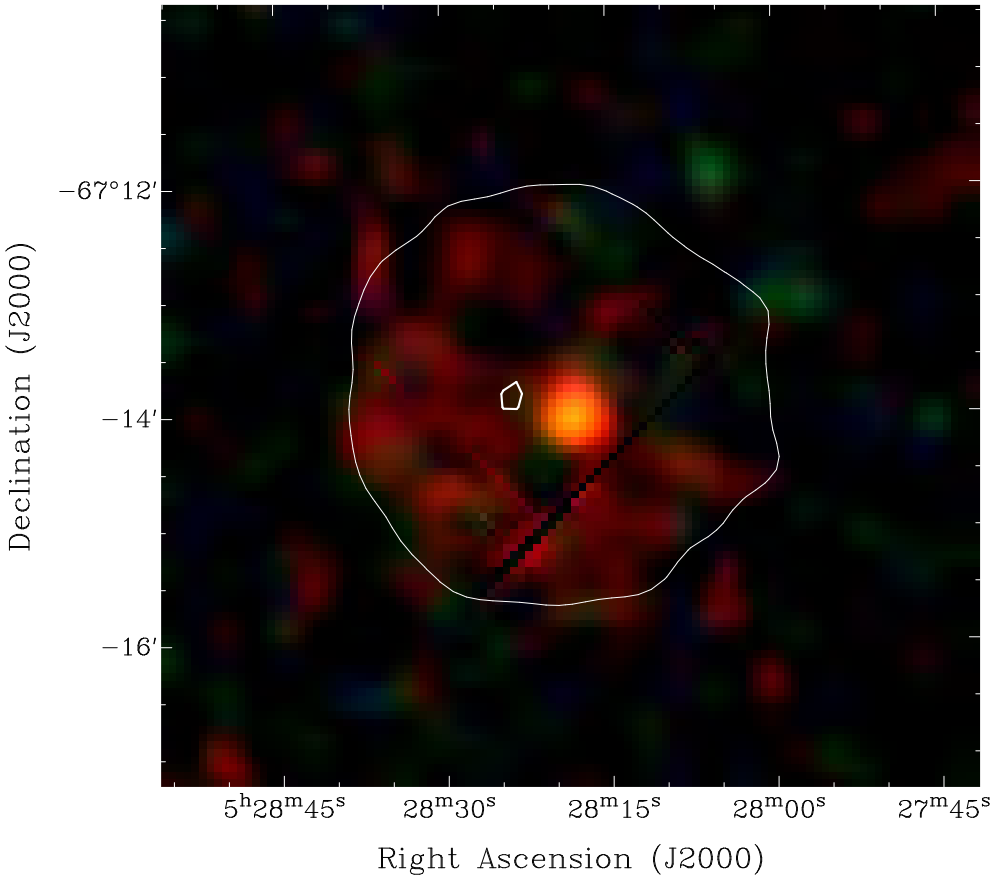

Figure 5.4 *XMM-Newton* false colour image (red corresponds to X-ray intensity in the 0.2−1.0 keV band, green to 1.0−2.0 keV and blue to 2.0−4.5 keV) of SNR J0528–6714 overlaid with an ATCA 6 cm 3σ (1.2 mJy) and 10σ (4.0 mJy) radio-continuum contours.

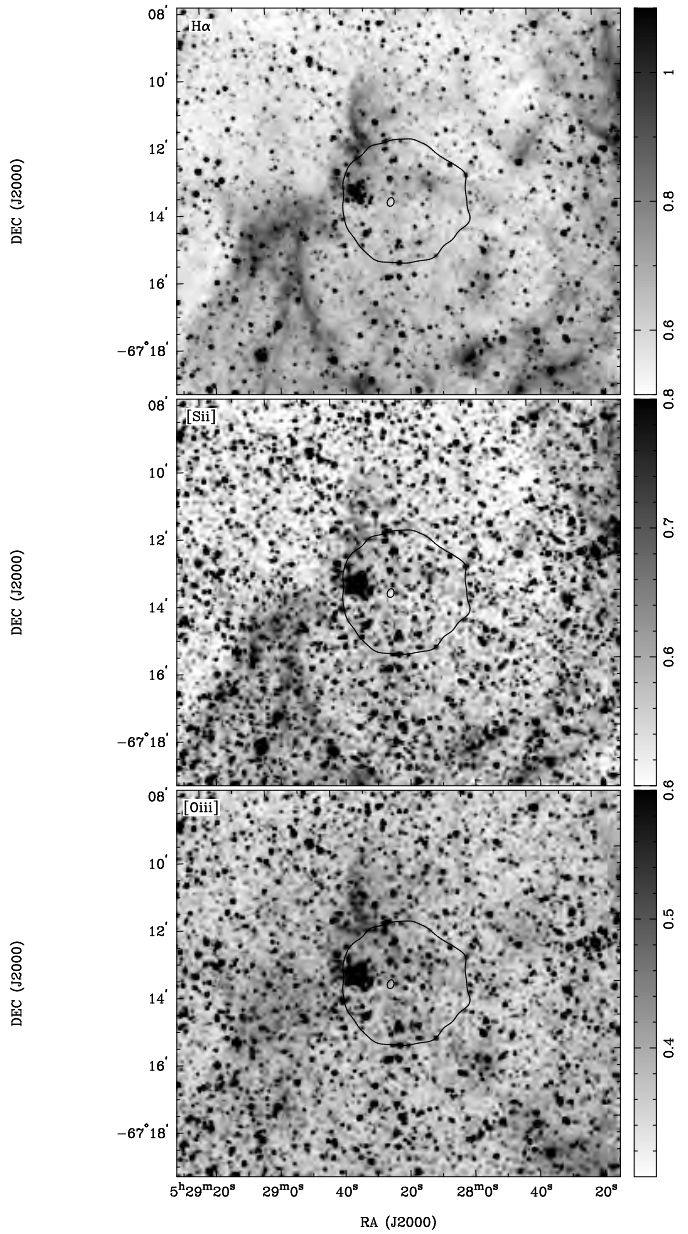

Figure 5.5 MCELS Hα(top), [S II](Middle) and [O III](bottom) images of SNR J0528–6714 overlaid with an ATCA 6 cm 3σ (1.2 mJy) and 10σ (4.0 mJy) radio-continuum contours.

1998). The unordered polarisation features, most likely due to a weakening of the remnants magnetic field, also indicate an older age for SNR J0528–6714. The almost perfectly circular appearance, along with the lack of radial symmetry classifies this object as a Type Ia SN event (Lopez et al. 2009).

However, the most unusual feature is the lack of any optical counterpart and very faint X-ray emission (Filipović et al. 2008; Bilikova et al. 2007, and the references therein). While it is not unusual to not detect an SNR in the optical, (Filipović et al. 2001; Stupar et al. 2004, 2005), the combination of faint X-ray and no optical detection is rare. This is in contrast to the M 33 findings of Long et al. (2010), where no SNR is found with X-ray and radio emission, but not seen in optical. This may imply possible observational bias towards the optical techniques of SNR detection in external galaxies where the resolution (and therefore sensitivity) may play dominant role in SNR identification. Also, Long et al. (2010) found significant number of M 33 SNRs with similar (or lower) X-ray energies then SNR J0528–6714 but their radio-continuum brightness is not exceedingly high as in case of SNR J0528–6714.

We detect regions of moderate and somewhat irregular polarisation with maximum fractional polarisation of 15%. Also, we argue that as with the majority of other SNRs in the MCs, this intriguing SNR is most likely in the adiabatic phase of its evolution (Payne et al. 2008b).

The nature of the point-like X-ray source near the center of the remnant remains unclear. It does not coincide with the maximum radio intensity which is found somewhat off-center to the East. It is also unclear if the radio maximum is truly a point source or just enhanced emission from the shell. This, and the lack of hard X-ray emission make the explanation that SNR J0528–6714 is a Pulsar Wind Nebula (PWN) very unlikely. Also, there is no reported radio pulsar in this region (Manchester et al. 2005).

5.6 Acknowledgements

The *XMM-Newton* project is supported by the Bundesministerium für Wirtschaft und Technologie/Deutsches Zentrum für Luft- und Raumfahrt (BMWI/DLR, FKZ 50 OX 0001) and the Max-Planck Society. We used the Karma/MIRIAD software packages developed by the ATNF. The Australia Telescope Compact Array is part of the Australia Telescope which is funded by the Commonwealth of Australia for operation as a National Facility managed by the CSIRO. We acknowledge the many contributions of R.C. Smith, F. Winkler of CTIO and other members of the MCELS team. We were granted observation time at the South African Astronomical Observatory (SAAO) and wish to thank them for their kind help and accommodations. Travel to the SAAO was funded by Australian Government AINSTO AMNRF grant number 09/10-O-03.

We thank the referee for their excellent comments that improved this manuscript.

Chapter 6

Paper IV

Apart from formatting changes the following text originally appeared as:
Crawford, E. J., Filipović, M. D., McEntaffer, R. L., Brantseg, T., Heitritter, K., Roper, Q., Haberl, F., and Urošević, D. (2014). HFPK 334: An Unusual Supernova Remnant in the Small Magellanic Cloud. *AJ*, 148:99

HFPK 334: An unusual Supernova Remnant in the Small Magellanic Cloud

E. J. Crawford, M. D. Filipović, R. L. McEntaffer, T. Brantseg, K. Heitritter, Q. Roper, F. Haberl and D. Urošević

6.1 Abstract

We present new Australia Telescope Compact Array (ATCA) radio-continuum and *XMM-Newton*/*Chandra X-ray Observatory* (CXO) observations of the unusual supernova remnant HFPK 334 in the Small Magellanic Cloud (SMC). The remnant follows a shell type morphology in the radio-continuum and has a size of ∼20 pc at the SMC distance. The X-ray morphology is similar, however, we detect a prominent point source close to the center of the SNR exhibiting a spectrum with a best fit powerlaw with a photon index of $\Gamma = 2.7 \pm 0.5$. This central point source is most likely a background object and cannot be directly associated with the remnant. The high temperature, nonequilibrium conditions in the diffuse region suggest that this gas has been recently shocked and point toward a younger SNR with an age of $\lesssim 1800$ years. With an average radio spectral index of $\alpha = -0.59 \pm 0.09$ we find that an equipartition magnetic field for the remnant is ∼90 μG, a value typical of younger SNRs in low-density environments. Also, we report detection of scattered radio polarisation across the remnant at 20 cm, with a peak fractional polarisation level of 25±5%.

6.2 Introduction

The study of supernova remnants (SNRs) in nearby galaxies is of major interest in order to understand the multi-frequency output of more distant galaxies, and to understand the processes that proceed on local interstellar scales within our own Galaxy. Unfortunately, the distances to many Galactic remnants are uncertain by a factor of ~ 2 (eg. Johanson and Kerton 2009; Green 2009a,b), leading to a factor of ~ 4 uncertainty in luminosity and of ~ 5.5 in the calculated energy release of the initiating supernova (SN). At an assumed distance of ~ 60 kpc (Hilditch et al. 2005), the Small Magellanic Cloud (SMC) is one of the prime targets for the astrophysical research of objects, including SNRs. These remnants are located at a known distance, yet close enough to allow a detailed analysis.

SNRs reflect a major process in the elemental enrichment of the interstellar medium (ISM). Multiple supernova explosions over space-time generate super-bubbles typically hundreds of parsecs in extent. Both are among the prime drivers controlling the morphology and the evolution of the ISM. Pulsar wind nebulae (PWN) offer further information, as the SNR shell and PWN together provide unique constraints and insights into the ISM. Their properties are therefore crucial to the full understanding of the galactic matter cycle.

Today, a total number of 24 classified SNRs are known in the SMC (Haberl et al. 2012c,b; Filipović et al. 2008; van der Heyden et al. 2004, and references therein). This represents the most complete sample of SNRs in any galaxy. There is one confirmed PWN in the SMC, IKT 16 (Owen et al. 2011), and at least three other candidate PWNs, HFPK 334, DEM S5 and IKT 4. The other 20 SNRs range from the very young 1E0102 at 1400 years old to the very old HFPK 419 at 50000 years old (Haberl et al. 2012c), giving an unparalleled insight into the evolution of of SNRs and their environment.

Kahabka et al. (1999) first detected HFPK 334 with Röntgensatellit (*ROSAT*), and list it as source 179 in their catalogue. Haberl et al. (2000) used advanced data processing and additional available data to extend the Kahabka et al. (1999) catalogue and noted that HFPK 334 was extended at 13 cm. It was Filipović et al. (2008) that provided the first conformation that HFPK 334 was an SNR, albeit an unusual SNR with detectable radio and X-ray emission, but no optical emission (Payne et al. 2007). They also noted a possible central source, leading them to suggest that it may be a PWN, possibly the first (at the time) detected in the SMC. Here, we present new follow-up radio-continuum observations with the Australia Telescope Compact Array (ATCA). This is in addition to previous higher frequency study of Filipović et al. (2008). We also present new *Chandra* X-ray observations, together with archival *XMM-Newton* observations of the SMC SNR HFPK 334. Therefore we present a new insight on HFPK 334 and clarify the nature of the central point source suggested in previous studies

(Filipović et al. 2008).

6.3 Observations

6.3.1 The ATCA radio-continuum observations and data reduction.

We observed HFPK 334 with the ATCA on 2009 January 5 using the 6C array, and on 2009 February 4 using the EW352 array at wavelengths of 20 and 13 cm ($\nu = 1384$ and 2367 MHz). The observations were done in an interleaved mode, totaling ∼4 hours of integration over a 12-hr period. Source 1934-638 was used for primary calibration and source 0252-712 was used for secondary calibration. The MIRIAD (Sault et al. 1995) and KARMA (Gooch 1996) software packages were used for data reduction and analysis. Images were formed using MIRIAD's multi-frequency synthesis algorithm (Sault and Wieringa 1994) and natural weighting. They were deconvolved with primary beam correction applied. The same procedure was also used for both Q and U Stokes parameter maps. The mean fractional polarisation at 20 cm was calculated using flux density and polarisation:

$$P = \frac{\sqrt{S_Q^2 + S_U^2}}{S_I} \cdot 100\% \tag{6.1}$$

where S_Q, S_U and S_I are integrated intensities for Q, U and I Stokes parameters.

The 20 cm image (Figure 6.1) has a resolution of $10''$ and an r.m.s. noise of 0.2 mJy/beam. A matched 13 cm image was produced, with an r.m.s. noise of 0.3 mJy/beam and used in the calculation of the spectral index.

6.3.2 *XMM-Newton* observations and data reduction

HFPK 334 was serendipitously observed during an *XMM-Newton* observation of a candidate supersoft source in the direction of the SMC. The observation (Obs. Id. 0402000101) was performed on 2006 October 3 and further details about instrument setups and data quality can be found in Haberl and Pietsch (2008). Using data from this observation, Filipović et al. (2008) classified the source as a new candidate SNR (plerionic) and presented images (their Fig. 5) and X-ray spectra obtained by the European Photon Imaging Camera (EPIC). However, their spectral analysis of the SNR spectra did not consider the contribution of a point source near the centre of the remnant, which was revealed in follow-up *Chandra* observations with superior spatial resolution (see §6.3.3 below).

Therefore, we re-extracted the EPIC-pn (Strüder et al. 2001) spectra using the *XMM-Newton* Science Analysis System (SAS) version 11.0.0. To obtain the best statistics we selected

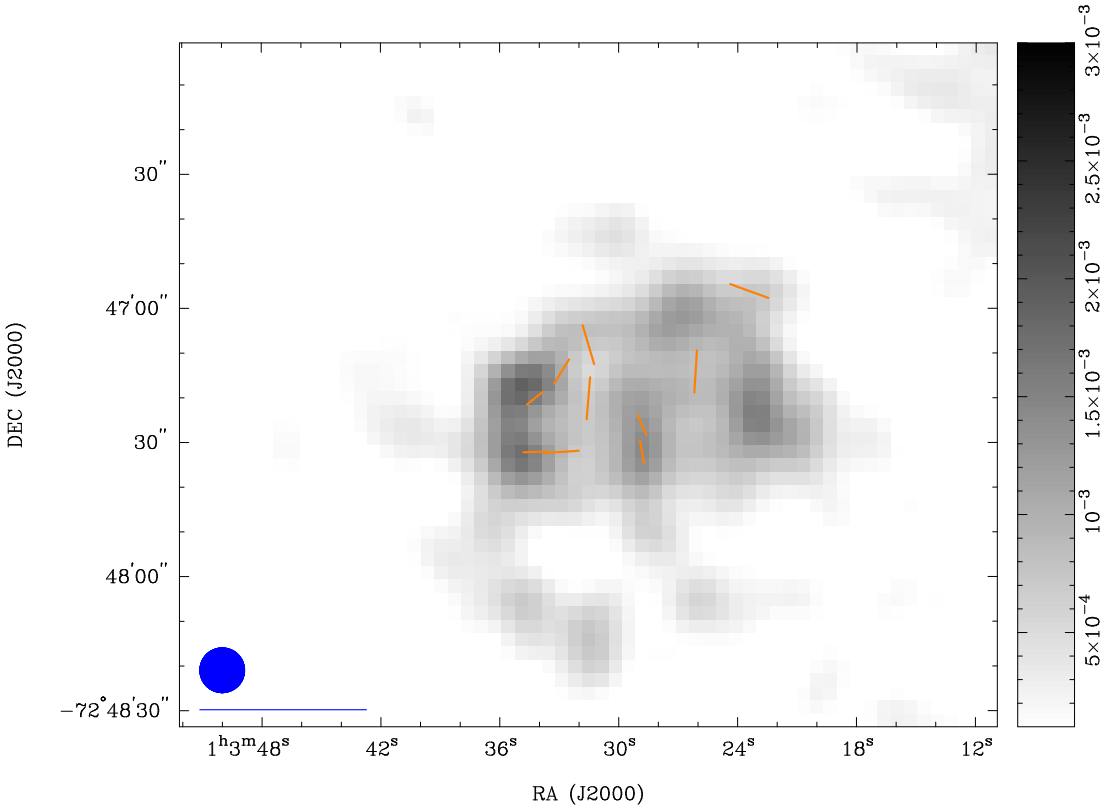

Figure 6.1 ATCA observations of HFPK 334 at 20 cm (1384 MHz) overlaid with fractional polarised intensity. The ellipse in the lower left corner represents the synthesised beam of 10″ and the line below the ellipse is a polarisation vector of 100%. The peak polarisation is estimated to ∼25±5%. The sidebar quantifies the pixel map in units of Jy/beam.

single- and double-pixel events with quality flag 0 and binned the source spectrum to a minimum of 20 counts per bin. Source counts were extracted from an ellipse with a size of $40'' \times 30''$, while the background was selected from a nearby source-free circular region with $60''$ radius. The net exposure time was 17.5 ks.

6.3.3 The *Chandra* X-ray observations and data reduction

Dedicated X-ray observations of HFPK 334 were carried out with the *Chandra* X-ray observatory on 2010 December 9 (Obs. Id. 11821) as part of the guaranteed time program available at MPE. The observation was made using ACIS-S and totalled 28.55 ksec. The level 1 data were reprocessed to level 2 with standard processing procedures in the *Chandra* Interactive Analysis of Observations (CIAO, v 4.4; Fruscione et al. 2006) software package with current calibration data from the *Chandra* Calibration Database (CALDB, v.4.4.2). Good time intervals, charge transfer inefficiency, and time-dependent gain variations were accounted for. The extracted spectra were background-corrected using adjacent regions of the chip that were devoid of emission. The effective exposure time after removing bad events is 28.19 ksec.

The raw data are shown in Figure 6.2. The image has been binned to $\sim 2''$ pixels and Gaussian-smoothed over a 3-pixel kernel. The scale ranges from 0.2–90 counts/bin. Due to the low average count rate of 0.017 cts/sec, we treat the diffuse emission as a single region. The red, elliptical region on the right side of Figure 6.2 encompasses a point source near the center of the remnant. This region is determined using *wavdetect* in CIAO (Freeman et al. 2002). This tool finds sources in the data set by correlating the image with "Mexican Hat" wavelet functions. The tool then draws an elliptical region around the detected source out to a specified number of standard deviations. In the present case, the detection scales used are 1 and 2 pixels, and the red region size in Figure 6.2 is 3σ where σ is the uncertainty in the intensity distribution of the detected point source given the point spread function (PSF) of *Chandra*. We use the CIAO tool *mkpsfmap* to determine the expected *Chandra* PSF at the location of the point source. The extraction region we use for spectral analysis is larger to ensure all point source photons are included. We use an elliptical region centered on the source, at $01^{\rm h}03^{\rm m}28\overset{\rm s}{.}896$ $-72^\circ47'28.35''$, and twice the size of the 3σ error contour with axes of 4.7×4.3 pixels or $2.3'' \times 2.1''$. The remainder of the emission from HFPK 334 exists in a diffuse nebula surrounding the point source. The ellipse labelled "Source" in Figure 6.2 is the extraction region used for this diffuse emission, with axes of $42'' \times 49''$. The 6σ error ellipse used as the extraction region for the point source has been excluded from these data prior to fitting.

Spectra for each of these regions are extracted using the *specextract* tool in CIAO. This tool automatically creates ancillary response files and redistribution matrix files for each region.

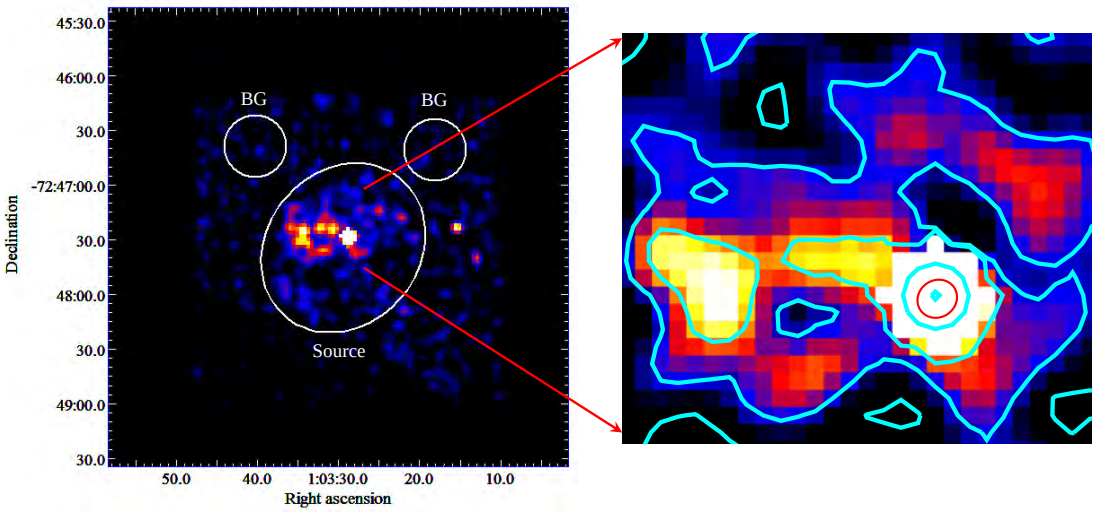

Figure 6.2 *Left*–Image of the raw data from the *Chandra* ACIS S2 CCD. The data have been binned to 2″ pixels and Gaussian-smoothed with a 3-pixel kernel radius to a final scale of 0.2–90 counts/pixel. The white ellipsoidal region labeled "Source" is used for spectral analysis with regions labeled "BG" serving as background subtraction regions. *Right*–A close-up of the central emission using the same binning and smoothing parameters. Cyan contours outline the emission at 1.0, 1.8, 2.5, 20, and 40 counts per pixel. The red ellipse is the 6 sigma error ellipse for the point source position, as detected using the CIAO tool *wavdetect*.

A background for the diffuse emission is created from the two circular regions shown on the exterior of the remnant. For the point source the background used is an elliptical annulus surrounding the extraction region with the intent of subtracting any diffuse emission that may be confusing the source spectrum. The outer bound of this background annulus measures 11.5×10.6 pixels (15σ) with an inner bound consistent with the extraction region. The spectral resolution obtained by *Chandra* is ∼5–20 ($E/\Delta E$) over the energy band used, 0.5–8.0 keV. Data below 0.5 keV and above 8.0 keV are not used, owing to a combination of uncertain ACIS calibration and lack of flux. For the diffuse emission, data above 2.0 keV is consistent with zero in the *Chandra* data. The data are binned to at least 20 counts per bin to allow the use of Gaussian statistics.

6.4 X-Ray Spectral Fitting

To analyze the extracted spectra, we use the X-ray spectral fitting software, XSPEC (Arnaud 1996), and the CIAO modelling and fitting package, Sherpa (Freeman et al. 2001).

6.4.1 *Chandra*

The superior spatial resolution of *Chandra* allows us to separate the X-ray spectra of the point source and the extended emission from the SNR. For the point source extraction we attempt a variety of fits that examine a range of possibilities for the nature of the emission. These include

a powerlaw model to see if the emission is consistent with a pulsar wind nebula (PWN), neutron star, or background AGN, and blackbody and neutron star atmosphere models to test for the presence of a compact central object (CCO). We apply these models to the *Chandra* data since we cannot extract a point source separately from the diffuse emission in the *XMM-Newton* data.

In the diffuse region, if the emission is caused by shock-heating of the ejecta or interstellar medium (ISM), we expect to see prominent emission lines. Depending on the plasma density and the time since it has been shocked, we expect the emitting material to be in either collisional ionization equilibrium (CIE; if the plasma has high density or was shocked a long time ago) or in nonequilibrium ionization (NEI). We use the *xsvnei* model for nonequilibrium conditions (Borkowski et al. 1994, 2001; Hamilton et al. 1983; Liedahl et al. 1995). This model simulates a single-temperature plasma uniformly shocked at a specific time in the past. Although this assumption is very simplified, as SNR plasmas contain a wide range of temperatures and ionization timescales, our data is of insufficient quality to provide meaningful constraints on the more physically realistic *xsvpshock* or *xsvsedov* models, which account for the range of temperatures and ionization timescales produced by the passage of a plane-parallel (*xsvpshock*) or spherical (*xsvsedov*) model. We therefore treat the plasma temperature and ionization timescale obtained with this model as average values. We replace the default *xsvnei* line list with an augmented list developed by Kazik Borkowski that includes more inner shell processes especially for the Fe-L lines (Badenes et al. 2006). For equilibrium conditions we use the *xsvapec* model, which uses an updated version of the ATOMDB code (v2.0.1; Smith et al. 2001; Foster et al. 2011) to model the emission spectrum. We include a second temperature component to these fits if it is determined statistically relevant as inferred from an F-test (probabilites < 0.05 indicate a statistical improvement given the additional component). In addition, we investigate the significance of a contribution from a non-thermal component by including the *xssrcut* and/or *xspowerlaw* models in the diffuse region (Reynolds and Keohane 1999; Reynolds 1998).

To account for interstellar absorption along the line of sight, the above models are convolved with two photoelectric absorption models (*xsphabs*), one of which is held at our Galactic column density along this line of sight, $N_H = 2.8 \times 10^{20}$ cm^{-2} (a high resolution foreground H I map was kindly provided by Erik Müller, see also Müller et al. (2003)), with solar abundances, and the other allowed to vary to account for absorption in the SMC at SMC abundances. The SMC abundances are taken from Russell and Dopita (1992) and relative to solar are: He 0.83, C 0.13, N 0.05, O 0.15, Ne 0.19, Mg 0.24, Si 0.28, S 0.21, Ar 0.16, Ca 0.21, Fe 0.20, and Ni 0.40. Emission line lists in the 0.5–2.0 keV energy range for plasmas with temperatures $kT \sim$0.09–2.0 keV show that the emission is dominated by highly ionized states of C, N, O, Ne, and Fe with

contributions from Mg and Si. The spectral fits begin with all abundances frozen to SMC levels. A given element is allowed to vary if it significantly improves the fit. Dielectronic recombination rates are taken from Mazzotta et al. (1998) with solar abundances from Wilms et al. (2000) and cross-sections from Balucinska-Church and McCammon (1992).

6.4.2 Simultaneous *Chandra*/*XMM-Newton* analysis

To better constrain our fit parameters we perform simultaneous fitting of *Chandra* ACIS and *XMM-Newton* EPIC-pn data in Xspec. The spatial resolution of *XMM-Newton* is insufficient to extract the point source and diffuse emission separately. However, the additional data may further constrain the physical properties of the source. Also, flux variations between the different epochs of the *Chandra* and *XMM-Newton* data may indicate variability in the central source. The fit data consist of three inputs: the point source extraction from *Chandra*, the diffuse emission extraction from *Chandra*, and the entire source in the *XMM-Newton* data. The parent fit model is the same as that found for the *Chandra* data, a non-equilibrium ionization model for the diffuse component with an additional powerlaw component for the point source. Each component is allowed a separate photoelectric absorbing column in the LMC with a global, galactic absorption also applied with a frozen value of $N_H = 2.8 \times 10^{20}$ cm^{-2}, as described above [*phabs*×(*phabs*×*vnei*+*phabs*×*powerlaw*)]. The three data sets are fit simultaneously with the parent model using the following method: the *Chandra* point source is fit with the thermal model normalization set to 0; the *Chandra* diffuse source is fit with the powerlaw norm set to 0; the *XMM-Newton* data norms for both components are allowed to vary; all thermal models have their abundances, absorbing column, ionization parameter, temperature, and normalization linked; all powerlaw models have their absorbing column, and photon index linked; the *Chandra* point source powerlaw norm is frozen to its best fit value while the *XMM-Newton* powerlaw norm is thawed to investigate variability. We performed various iterations of freezing/thawing various parameters to find the tightest parameter constraints, e.g. thawing the *Chandra* point source powerlaw norm, but find no additional limitations. Furthermore, these additional fit parameters do not result in a lower reduced χ^2. The final fit with the best statistic and parameter constraints is shown in Table 6.1.

6.5 Discussion

6.5.1 Radio

HFPK 334 has a clumpy appearance, with a knot of emission at the centre, which lead Filipović et al. (2008) to suggest that it was likely to contain a PWN, centered at $01^{\rm h}03^{\rm m}29\overset{\rm s}{.}5$ $-72°47'20''$

Table 6.1. Best fit parameters for the spectra from different extraction regions

Region	χ^2/dof	$N_{H,PL}$ [a] (10^{22}cm^{-2})	$N_{H,vnei}$ [b] (10^{22}cm^{-2})	Γ	kT (keV)	τ [c] (10^9 cm^{-3}s)	$norm_{PL}$ $10^{-5}A$[d]	$norm_{vnei}$ $10^{-5}B$[e]
Point source	13/19	0.8±0.4	···	2.7±0.5	···	···	5±2	···
Diffuse emission	18.0/19	···	<0.5	···	1^{+3}_{-1}	6±3	···	5^{+21}_{-2}
Combined[f]	84/89	0.8±0.1	$0.1^{+0.3}_{-0.1}$	2.8±0.2	$1.3^{+1}_{-0.8}$	7^{+5}_{-2}	8±1[g]	$6^{+0.2}_{-2}$

[a]Absorption column in the SMC along the line of sight to the point source.

[b]Absorption column in the SMC along the line of sight to the diffuse emission.

[c]Ionization timescale, defined as $n_e t$, where t is the time since the plasma was shocked.

[d]Normalization parameter. $A = 1$ photon keV^{-1} cm^{-2} s^{-1} at 1 keV.

[e]Normalization parameter. $B = [10^{-14}/(4\pi D^2)] \int n_e n_H dV$, where D is the distance to the SMC (60 kpc) and the integral is the volume emission measure.

[f]This is a parallel fit with *XMM-Newton*, *Chandra* point source, and *Chandra* diffuse emission data sets.

[g]Normalization parameter for the *XMM-Newton* data. The *Chandra* data are set to the best fit normalization.

Note. — Quoted errors are 90% confidence intervals for the parameter in question.

with the enclosing remnants extent of $70'' \times 40''$ (20×12 pc) at PA=–70°. Using the flux density measurements and images of Filipović et al. (2008) along with our new measurements at 20 cm and 13 cm of 26.9±1.3 mJy and 18.9±1.5 mJy respectively, we estimate a spectral index $\alpha = -0.59 \pm 0.09$ where $S_\nu \propto \nu^\alpha$. This estimate includes emission from the entire remnant and central object.

We also created an image from just the longest ATCA baselines (i.e. those to ATCA antenna 6), which shows no indication of a central point source, to a 3σ detection limit of ~ 0.3 mJy. However, the extended radio emission aligns well with the diffuse X-ray emission (Figure 6.3).

Linear polarisation images were also formed, as shown in Figure 6.1. The polarised emission is unordered, with a maximum of 25±5%, and indicates a random magnetic field. We note that this order of polarisation from HFPK 334 is relatively high when compared to other SNRs in the MCs for which the typical range is 0–20%(Crawford et al. 2008a,b, 2010; Cajko et al. 2009; Bozzetto et al. 2010, 2012a,c,d,b, 2013, 2014a,b; Grondin et al. 2012; De Horta et al. 2012, 2014c; Haberl et al. 2012a; Maggi et al. 2012; Kavanagh et al. 2013).

With a radio surface brightness of 0.36×10^{-20} W m^{-2} Hz^{-1} sr^{-1}, and a diameter of ∼20 pc, the position of HFPK 334 on the surface brightness-diameter diagram of Berezhko and Völk (2004, their Figure 6), leads us to infer an explosion energy to be in the order of 2×10^{51} ergs. We calculate an equipartition magnetic field of ~ 90 μG (Arbutina et al. 2012) which is high for an MC SNR (Bozzetto et al. in prep). Assuming a strong shock passing through the ISM one can expect magnetic field of up to ~ 20 μG (the SMC magnetic field is $\sim 3\mu$G Mao et al. (2008)). Another mechanism, so called amplification of the magnetic field (added to simple compression by the shock) is therefore necessary to explain such a high magnetic field of 90 μG. The amplification of magnetic field is process driven by very fast shocks of

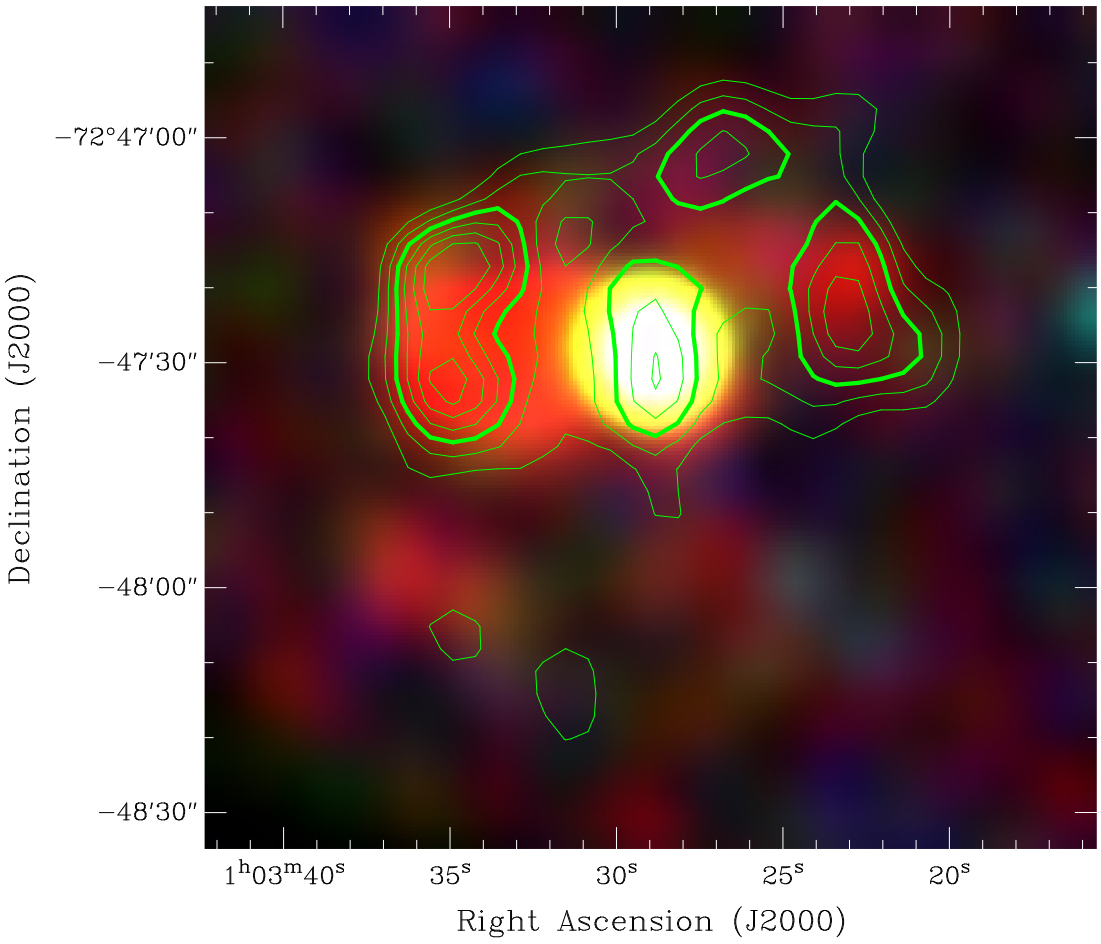

Figure 6.3 *Chandra* three colour composite (red: 0.3–1.0 keV (soft), green: 1.0–2.0 keV (medium), blue: 2.0–6.0 keV (hard)) smoothed with a Gaussian width to match 20 cm radio image. The radio contours are 0.6–1.6 mJy/beam in 0.2 mJy/beam steps.

young SNRs. Because of this, a spectral index of −0.59, the location in the surface brightness-diameter diagram, and moderate amplification (strong amplification would lead to a field of a few hundred μG (Telezhinsky et al. 2012)) of magnetic field suggesting that this SNR is on somewhat younger age i.e. <5000 yr.

6.5.2 X-Ray

The best fit parameters for the two *Chandra* regions are given in Table 6.1. The point source region is best fit by a powerlaw with photon index $\Gamma = 2.7 \pm 0.5$. The fit is shown overlaid on the data in Figure 6.4. Attempts at fitting the point source spectrum with other possible models, such as blackbody and neutron star atmosphere to test for a leftover compact object, were generally reasonable but the absorbing column is poorly constrained. A neutron star atmosphere model, *nsa* in Xspec, resulted in a fit statistic of $\chi^2/dof = 15.3/19$ and an effective temperature of $\log T = 6.5$, but the absorbing column was low, with an upper limit of 3×10^{20} cm^{-2}.

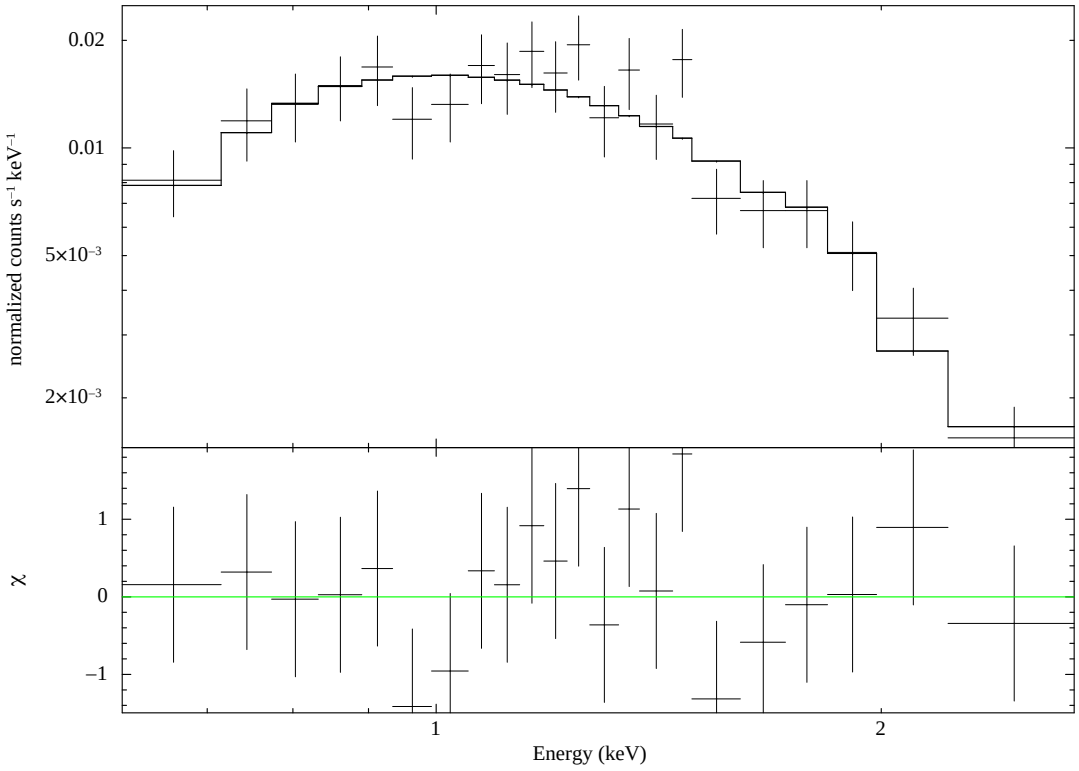

Figure 6.4 *Chandra* spectrum extracted from the point source region with the best fit powerlaw model overlaid.

We also model the spectrum using the *bbody* model resulting in a fit statistic of $\chi^2/dof = 17.5/19$ and temperature of $kT \sim 0.4$ keV. Again, the absorbing column is ill-constrained, with an upper limit of 1.6×10^{21} cm^{-2}. Using the energy band common to both *Chandra* and *XMM-Newton*, 0.5–4.0 keV, we can calculate the fluxes and luminosities for these models. The

flux values are consistent and range from 7.5×10^{-14} erg cm^{-2} s^{-1} to 8.7×10^{-14} erg cm^{-2} s^{-1} for the various models resulting in luminosities from 3.3×10^{34} erg s^{-1} to 3.8×10^{34} erg s^{-1} assuming a 60 kpc distance to the object.

The X-ray position of the central point source is $01^{\rm h}03^{\rm m}28\overset{\rm s}{.}896$ $-72°47'28.35''$. We find a faint (I_{mag}=20.849 and V_{mag}=21.628) object in OGLE survey (Udalski et al. 1998) at a distance of $\sim$1.52″. As the 2σ error of our X-ray positional estimate is in order of 1.4″ and OGLE positional error is $\sim$0.2″ we claim that this is fully consistent with an association (according to the cumulative Rayleigh distribution the probability for the counterpart to be found within 1.5″ is 88%). We calculate the optical to X-ray flux ratio to be 0.91, indicating background object, a foreground star would have a ratio less than -1 and a foreground neutron star would have a ratio greater than 4 (Maccacaro et al. 1988; Haberl 2004; Sturm et al. 2013b).

The diffuse emission region cannot be described by a powerlaw and is best fit with a nonequilibrium thermal plasma at a temperature of $kT = 1^{+3}_{-1}$ keV. This fit is shown in Figure 6.5. The fit could not be improved with variable abundance of any element or combinations thereof.

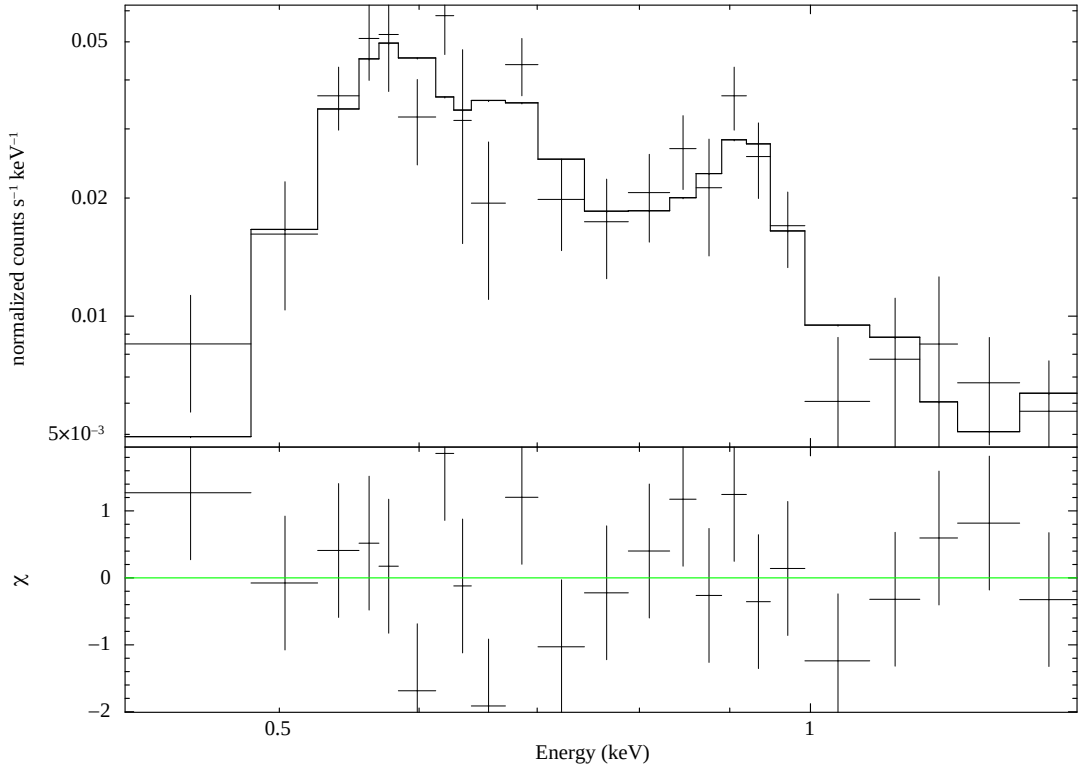

Figure 6.5 *Chandra* spectrum extracted from the diffuse emission region with the best fit thermal model overlaid.

The results of the combined fit are also given in Table 6.1. In addition to the powerlaw component for the point source, a nonequilibrium plasma is again found as the best explanation for the diffuse emission. This thermal component has a temperature comparable to that found when considering *Chandra* data alone. The additional *XMM-Newton* data allow for tighter

constraints on the temperature and ionization parameter for the thermal plasma, and normalizations for both components. However, the combined fit is still not improved by thawing any elemental abundances. The best fits to these data are shown in Figure 6.6.

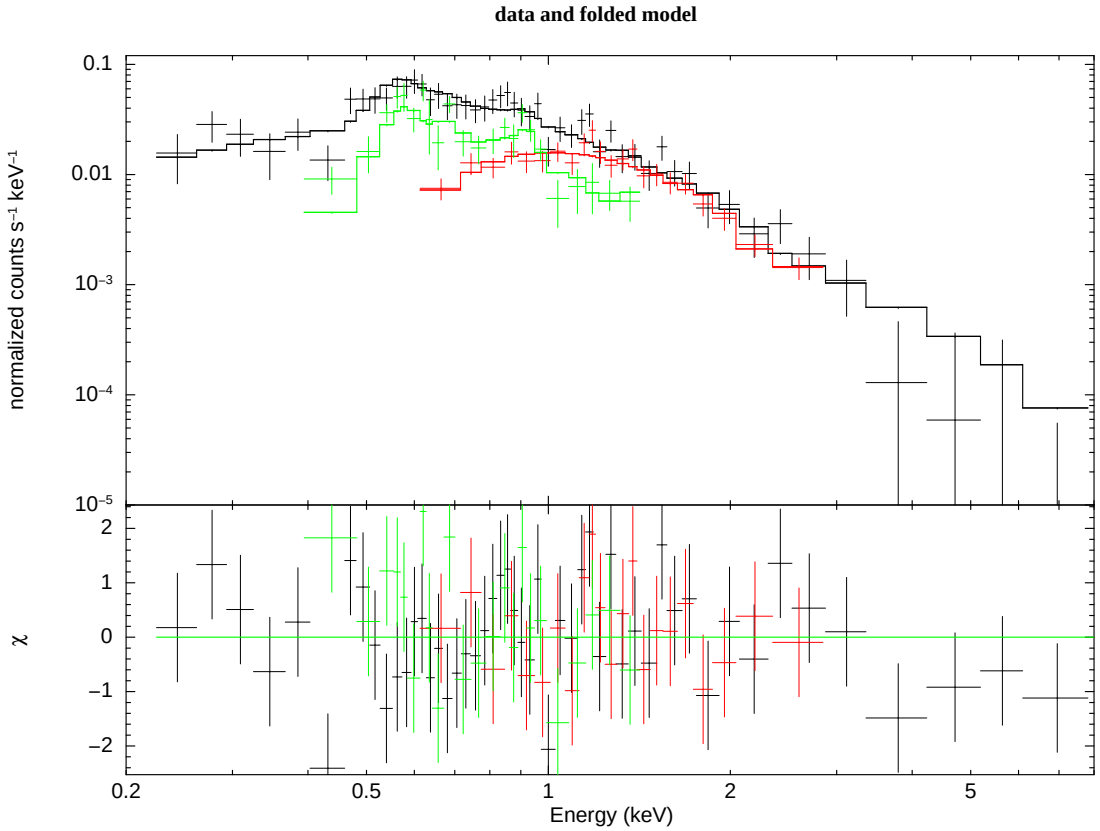

Figure 6.6 Co-fit *Chandra* (point source – red, diffuse emission – green) and *XMM-Newton* (black) spectra with best fit model overlaid.

The spectral index of the high energy emission, $\alpha = 2.7 \pm 0.5$, is high, but given the large error bars, barely consistent with the range expected if the emission was arising from a PWN. Given a lack of plerionic remnants in the SMC we can use the LMC for comparison. PWN containing remnants in the LMC typically have a lower index: $\alpha = 1.0 \pm 0.2$ in SNR 0453-68.5 (McEntaffer et al. 2012); $\alpha = 0.4 - 1.4$ for a series of annular regions encompassing the PWN of SNR 0540-69.3 (Petre et al. 2007); $\alpha = 1.2 \pm 0.3$ in N 206 (SNR 0532-71.0) (Williams et al. 2005); $\alpha = 0.57^{+0.05}_{-0.06}$ for DEM L241 (Bamba et al. 2006); and $\alpha \sim 1.2 - 1.6$ over several regions from N 157B (Chen et al. 2006). At SMC distance the calculated luminosity would be consistent with that expected expected from a PWN. Even though a PWN fits in nicely with the picture of a young SNR and the powerlaw fit was statistically best, the photon index is more compatible with an AGN interpretation, which typically have typical $\Gamma \sim 1.5 - 2.1$ (Ishibashi and Courvoisier 2010).

As shown in Table 6.1, the thermal and powerlaw components of the combined fits have

different column densities. We expect that if the point source were associated with the surrounding SNR, the two components would have consistent absorbing columns. The significantly higher column density of the point source implies that it is an unrelated background source.

The powerlaw fit was reasonable even though we allowed the normalization to vary between the *XMM-Newton* and *Chandra* data. We did not detect significant flux variability. The best fit norm for the *XMM-Newton* data is higher than that for the *Chandra* data but just consistent with one another at the limits of the 90% confidence interval. Higher significance data are required to properly constrain the flux over multiple epochs to determine if flux variability is present.

The high temperature, nonequilibrium conditions in the diffuse region suggest that this gas has been recently shocked and point toward a younger SNR. Calculations of shock velocity and density support this conclusion. Solving the Rankine-Hugoniot relations in the strong shock case for a monatomic plasma ($\gamma = 5/3$), gives the post-shock temperature as a function of shock velocity, $kT = (3/16)\mu m_p v^2$. We assume that the plasma is fully ionized, so $\mu = 0.6$ and $n_e = 1.2 n_H$ This equation makes the implicit assumption that $T_e \sim T_{ion}$. This is not necessarily the case for shock-heated plasmas (Ghavamian et al. 2007), so our calculated velocities may be taken as a lower bound. The calculated velocity at the best fit temperature is ~ 1100 km/sec, significantly decelerated from the initial blast wave velocity (> 5000 km/s), but still very fast. It does not appear that the diffuse emission is from particularly dense material even though it is probably dominated by shock-heated ISM as suggested by the SMC ISM abundances in the fit. The density is found using the *norm* parameter for the diffuse component, where $norm = [10^{-14}/(4\pi D^2)] \int n_e n_H dV$. The integral contains the emission measure for the plasma which is dependent on the density and total emitting volume. A value of 60 kpc is used for D and we assume that $n_e = 1.2 n_H$. We use the volume of a sphere with a radius equal to the average of the major and minor axes of the elliptical region used for extraction. We also include a filling factor, f, such that $V = 4/3\pi R^3 f$. The resulting electron density is $0.09/\sqrt{f}$ cm^{-3} supporting a low-density environment. Given that the filling factor is always less than 1, and most likely for this remnant much less than 1, this density is a lower limit and most likely larger. The low-density may explain the high temperature, nonequilibrium conditions and a conclusion of a young SNR may be premature. However, we can estimate the age of the remnant from the τ parameter since $\tau = n_e t$, where t is this timescale. This calculation yields a shock time of $1800\sqrt{f}$ years, thus supporting a lower age for this object. Finally, it is quite possible that this diffuse emission cannot be explained using a single set of plasma conditions. There is a need for higher signal-to-noise data to enable more detailed spatially resolved spectroscopy.

6.6 Conclusions

HFPK 334 is a young shell-type radio/X-Ray SNR with no optical or IR counterpart. The most striking feature of this SNR is the bright central object seen only in our X-ray observations. We argue that this central object with the best fit powerlaw $\Gamma = 2.7 \pm 0.5$, could not be definitely associated with the remnant, as either a pulsar or compact central object. Therefore we propose that the central point source is a background object. The remnant itself appears as quite young, < 1800 years, and our estimates of the remnant magnetic field ($\sim$90 μG) also favours younger age. The somewhat higher temperature and nonequilibrium conditions in the diffuse region suggest that this gas has been recently shocked. We report detections of scattered regions showing moderately high orders of polarisation at 20 cm, with a peak value of $\sim$25$\pm$5%, indicating the magnetic field is unordered.

6.7 Acknowledgments

The Australia Telescope Compact Array is part of the Australia Telescope National Facility which is funded by the Commonwealth of Australia for operation as a National Facility managed by CSIRO. The scientific results reported in this article are based on observations made by the *Chandra X-ray Observatory* (CXO). Based on observations obtained with *XMM-Newton*, an ESA science mission with instruments and contributions directly funded by ESA Member States and NASA. This research is supported by the Ministry of Education, Science and Technological Development of the Republic of Serbia through project No. 176005.

References

Arbutina, B., Urošević, D., Andjelić, M. M., Pavlović, M. Z., and Vukotić, B. (2012). Modified Equipartition Calculation for Supernova Remnants. *ApJ*, 746:79.

Arnaud, K. A. (1996). XSPEC: The First Ten Years. In Jacoby, G. H. and Barnes, J., editors, *Astronomical Data Analysis Software and Systems V*, volume 101 of *Astronomical Society of the Pacific Conference Series*, page 17.

Badenes, C., Borkowski, K. J., Hughes, J. P., Hwang, U., and Bravo, E. (2006). Constraints on the Physics of Type Ia Supernovae from the X-Ray Spectrum of the Tycho Supernova Remnant. *ApJ*, 645:1373–1391.

Badenes, C., Maoz, D., and Draine, B. T. (2010). On the size distribution of supernova remnants in the Magellanic Clouds. *MNRAS*, 407:1301–1313.

Balucinska-Church, M. and McCammon, D. (1992). Photoelectric absorption cross sections with variable abundances. *ApJ*, 400:699.

Bamba, A., Ueno, M., Nakajima, H., Mori, K., and Koyama, K. (2006). A detailed observation of a LMC supernova remnant DEM L241 with XMM-Newton. *A&A*, 450:585–591.

Berezhko, E. G. and Völk, H. J. (2004). The theory of synchrotron emission from supernova remnants. *A&A*, 427:525–536.

Bilikova, J., Williams, R. N. M., Chu, Y.-H., Gruendl, R. A., and Lundgren, B. F. (2007). Supernova Remnants in the Magellanic Clouds. IX. Multiwavelength Analysis of the Physical Structure of N49. *AJ*, 134:2308–2317.

Blair, W. P., Ghavamian, P., Sankrit, R., and Danforth, C. W. (2006). Far Ultraviolet Spectroscopic Explorer Survey of Magellanic Cloud Supernova Remnants. *ApJS*, 165:480–511.

Bojičić, I. S., Filipović, M. D., and Crawford, E. J. (2010). SMC SMP 24: A Newly Radio-Detected Planetary Nebula in the Small Magellanic Cloud. *Serbian Astronomical Journal*, 181:63–68.

Bojičić, I. S., Filipović, M. D., Parker, Q. A., Payne, J. L., Jones, P. A., Reid, W., Kawamura, A., and Fukui, Y. (2007). Multifrequency study of the Large Magellanic Cloud supernova remnant (SNR) B0513-692 and new SNR candidate J051327-6911. *MNRAS*, 378:1237–1247.

Borkowski, K. J., Hendrick, S. P., and Reynolds, S. P. (2006). Dense, Fe-rich Ejecta in Supernova Remnants DEM L238 and DEM L249: A New Class of Type Ia Supernova? *ApJ*, 652:1259–1267.

Borkowski, K. J., Lyerly, W. J., and Reynolds, S. P. (2001). Supernova Remnants in the Sedov Expansion Phase: Thermal X-Ray Emission. *ApJ*, 548:820–835.

Borkowski, K. J., Sarazin, C. L., and Blondin, J. M. (1994). On the X-ray spectrum of Kepler's supernova remnant. *ApJ*, 429:710–725.

Bozzetto, L. M., Filipović, M. D., Crawford, E. J., Bojičić, I. S., Payne, J. L., Medik, A., Wardlaw, B., and De Horta, A. Y. (2010). Multifrequency Radio Observations of a SNR in the LMC. The Case of SNR J0527-6549 (DEM L204). *Serbian Astronomical Journal*, 181:43–49.

Bozzetto, L. M., Filipović, M. D., Crawford, E. J., De Horta, A. Y., and Stupar, M. (2012a). Multifrequency Radio Observations of SNR J0536-6735 (N 59B) with Associated Pulsar. *Serbian Astronomical Journal*, 184:69–76.

Bozzetto, L. M., Filipović, M. D., Crawford, E. J., Haberl, F., Sasaki, M., Urošević, D., Pietsch, W., Payne, J. L., De Horta, A. Y., Stupar, M., Tothill, N. F. H., Dickel, J., Chu, Y.-H., and Gruendl, R. (2012b). Multifrequency study of the Large Magellanic Cloud supernova remnant J0529-6653 near pulsar B0529-66. *MNRAS*, 420:2588–2595.

Bozzetto, L. M., Filipović, M. D., Crawford, E. J., Payne, J. L., De Horta, A. Y., and Stupar, M. (2012c). Radio continuum observations of LMC SNR J0550-6823. *Rev. Mexicana Astron. Astrofis.*, 48:41–46.

Bozzetto, L. M., Filipović, M. D., Crawford, E. J., Sasaki, M., Maggi, P., Haberl, F., Urošević, D., Payne, J. L., De Horta, A. Y., Stupar, M., Gruendl, R., and Dickel, J. (2013). Multifrequency study of SNR J0533-7202, a new supernova remnant in the LMC. *MNRAS*, 432:2177–2181.

Bozzetto, L. M., Filipović, M. D., Urošević, D., and Crawford, E. J. (2012d). Radio-Continuum Observations of Small, Radially Polarised Supernova Remnant J0519-6902 in the Large Magellanic Cloud. *Serbian Astronomical Journal*, 185:25–33.

Bozzetto, L. M., Filipović, M. D., Urošević, D., Kothes, R., and Crawford, E. J. (2014a). Radio-continuum study of Large Magellanic Cloud supernova remnant J0509-6731. *MNRAS*, 440:3220–3225.

Bozzetto, L. M., Kavanagh, P. J., Maggi, P., Filipović, M. D., Stupar, M., Parker, Q. A., Reid, W. A., Sasaki, M., Haberl, F., Urošević, D., Dickel, J., Sturm, R., Williams, R., Ehle, M., Gruendl, R., Chu, Y.-H., Points, S., and Crawford, E. J. (2014b). Multifrequency study of a new Fe-rich supernova remnant in the Large Magellanic Cloud, MCSNR J0508-6902. *MNRAS*, 439:1110–1124.

Cajko, K. O., Crawford, E. J., and Filipović, M. D. (2009). Multifrequency Observations of One of the Largest Supernova Remnants in the Local Group of Galaxies, LMC - SNR J0450-709. *Serbian Astronomical Journal*, 179:55–60.

Chen, Y., Wang, Q. D., Gotthelf, E. V., Jiang, B., Chu, Y.-H., and Gruendl, R. (2006). Chandra ACIS Spectroscopy of N157B: A Young Composite Supernova Remnant in a Superbubble. *ApJ*, 651:237–249.

Clarke, J. N., Little, A. G., and Mills, B. Y. (1976). The Molonglo radio source catalogue 4 - The Magellanic cloud region. *Australian Journal of Physics Astrophysical Supplement*, 40:1–71.

Crawford, E. J., Filipović, M. D., De Horta, A. Y., Stootman, F. H., and Payne, J. L. (2008a). Radio-Continuum Study of the Supernova Remnants in the Large Magellanic Cloud - An SNR with a Highly Polarised Breakout Region - SNR J0455-6838. *Serbian Astronomical Journal*, 177:61–66.

Crawford, E. J., Filipović, M. D., De Horta, A. Y., Wong, G. F., Tothill, N. F. H., Drašković, D., Collier, J. D., and Galvin, T. J. (2011). New 6 and 3-cm Radio-Continuum Maps of the Small Magellanic Cloud. Part I - The Maps. *Serbian Astronomical Journal*, 183:95–102.

Crawford, E. J., Filipović, M. D., Haberl, F., Pietsch, W., Payne, J. L., and De Horta, A. Y. (2010). Multi-frequency study of Local Group supernova remnants. The curious case of the Large Magellanic Cloud SNR J0528-6714. *A&A*, 518:A35.

Crawford, E. J., Filipović, M. D., McEntaffer, R. L., Brantseg, T., Heitritter, K., Roper, Q., Haberl, F., and Urošević, D. (2014). HFPK 334: An Unusual Supernova Remnant in the Small Magellanic Cloud. *AJ*, 148:99.

Crawford, E. J., Filipović, M. D., and Payne, J. L. (2008b). Radio Continuum Study of the Large Magellanic Cloud - SNR J0519-6926. *Serbian Astronomical Journal*, 176:59–63.

De Horta, A. Y., Collier, J. D., Filipović, M. D., Crawford, E. J., Urošević, D., Stootman, F. H., and Tothill, N. F. H. (2013). Radio confirmation of Galactic supernova remnant G308.3-1.4. *MNRAS*, 428:1980–1985.

De Horta, A. Y., Filipović, M. D., Bozzetto, L. M., Maggi, P., Haberl, F., Crawford, E. J., Sasaki, M., Urošević, D., Pietsch, W., Gruendl, R., Dickel, J., Tothill, N. F. H., Chu, Y.-H., Payne, J. L., and Collier, J. D. (2012). Multi-frequency study of supernova remnants in the Large Magellanic Cloud. The case of LMC SNR J0530-7007. *A&A*, 540:A25.

De Horta, A. Y., Filipovic, M. D., Crawford, E. J., Stootman, F. H., Pannuti, T. G., Bozzetto, L. M., Collier, J. D., Sommer, E. R., and Kosakowski, A. R. (2014a). Radio-Continuum Emission from the Young Galactic Supernova Remnant G1.9+0.3. *Serbian Astronomical Journal*, 189:41–51.

De Horta, A. Y., Sommer, E. R., Filipović, M. D., O'Brien, A., Bozzetto, L. M., Collier, J. D., Wong, G. F., Crawford, E. J., Tothill, N. F. H., Maggi, P., and Haberl, F. (2014b). Multi-frequency Observations of a Superbubble in the LMC: The Case of LHA 120-N 70. *AJ*, 147:162.

De Horta, A. Y., Sommer, E. R., Filipović, M. D., O'Brien, A., Bozzetto, L. M., Collier, J. D., Wong, G. F., Crawford, E. J., Tothill, N. F. H., Maggi, P., and Haberl, F. (2014c). Multi-frequency observations of a superbubble in the LMC: The case of LHA 120-N 70. *ArXiv e-prints*.

di Benedetto, G. P. (2008). The Cepheid distance to the Large Magellanic Cloud and NGC 4258 by the surface brightness technique and improved calibration of the cosmic distance scale. *MNRAS*, 390:1762–1776.

Dickel, J. R., Gruendl, R. A., McIntyre, V. J., and Amy, S. W. (2010). A 4.8 and 8.6 GHz Survey of the Small Magellanic Cloud: The Images. *AJ*, 140:1511–1518.

Dickel, J. R., McIntyre, V. J., Gruendl, R. A., and Milne, D. K. (2005). A 4.8 and 8.6 GHz Survey of the Large Magellanic Cloud. I. The Images. *AJ*, 129:790–804.

Dudziak, G., Péquignot, D., Zijlstra, A. A., and Walsh, J. R. (2000). A radio-continuum and photoionization-model study of the two planetary nebulae in the Sagittarius dwarf galaxy. *A&A*, 363:717–732.

Eichhorn, G. (1994). An Overview of the Astrophysics Data System. *Experimental Astronomy*, 5:205–220.

Filipović, M. D., Bohlsen, T., Reid, W., Staveley-Smith, L., Jones, P. A., Nohejl, K., and Goldstein, G. (2002). An ATCA radio-continuum study of the Small Magellanic Cloud - I. Source catalogues at 1.42, 2.37, 4.80 and 8.64 GHz. *MNRAS*, 335:1085–1090.

Filipović, M. D., Cohen, M., Reid, W. A., Payne, J. L., Parker, Q. A., Crawford, E. J., Bojičić, I. S., De Horta, A. Y., Hughes, A., Dickel, J., and Stootman, F. (2009). Radio planetary nebulae in the Magellanic Clouds. *MNRAS*, 399:769–777.

Filipović, M. D., Crawford, E. J., Jones, P. A., and White, G. L. (2010). Radio-Continuum Jets Around the Peculiar Galaxy Pair ESO 295-IG022. *Serbian Astronomical Journal*, 181:31–37.

Filipović, M. D., Haberl, F., Winkler, P. F., Pietsch, W., Payne, J. L., Crawford, E. J., De Horta, A. Y., Stootman, F. H., and Reaser, B. E. (2008). New XMM-Newton observations of supernova remnants in the Small Magellanic Cloud. *A&A*, 485:63–70.

Filipović, M. D., Haynes, R. F., White, G. L., and Jones, P. A. (1998). A radio continuum study of the Magellanic Clouds. VII. Discrete radio sources in the Magellanic Clouds. *A&AS*, 130:421–440.

Filipović, M. D., Horner, J., Crawford, E. J., Tothill, N. F. H., and White, G. L. (2013). Mass Extinction and the Structure of the Milky Way. *Serbian Astronomical Journal*, 187:43–52.

Filipović, M. D., Jones, P. A., and Aschenbach, B. (2001). Vela Z-so young and so exotic. In Holt, S. S. and Hwang, U., editors, *Young Supernova Remnants*, volume 565 of *American Institute of Physics Conference Series*, pages 267–270.

Filipović, M. D., Jones, P. A., White, G. L., Haynes, R. F., Klein, U., and Wielebinski, R. (1997). A radio continuum study of the Magellanic Clouds V. Catalogues of radio sources in the Small Magellanic Cloud at 1.42, 2.45, 4.75, 4.85 and 8.55 GHz. *A&AS*, 121:321–326.

Filipović, M. D., White, G. L., Haynes, R. F., Jones, P. A., Meinert, D., Wielebinski, R., and Klein, U. (1996). A radio continuum study of the Magellanic Clouds. IVa. Catalogue of radio sources in the Large Magellanic Cloud at 2.30GHz (λ=13cm). *A&AS*, 120:77–81.

Foster, A. R., Smith, R. K., Ji, L., and Brickhouse, N. S. (2011). AtomDB v2.0: Atomic Data for X-ray Astrophysics. In *2010 NASA Laboratory Astrophysics Workshop*, page C2.

Freeman, P., Doe, S., and Siemiginowska, A. (2001). Sherpa: a mission-independent data analysis application. In Starck, J.-L. and Murtagh, F. D., editors, *Society of Photo-Optical Instrumentation Engineers (SPIE) Conference Series*, volume 4477 of *Society of Photo-Optical Instrumentation Engineers (SPIE) Conference Series*, pages 76–87.

Freeman, P. E., Kashyap, V., Rosner, R., and Lamb, D. Q. (2002). A Wavelet-Based Algorithm for the Spatial Analysis of Poisson Data. *ApJS*, 138:185–218.

Fruscione, A., McDowell, J. C., Allen, G. E., Brickhouse, N. S., Burke, D. J., Davis, J. E., Durham, N., Elvis, M., Galle, E. C., Harris, D. E., Huenemoerder, D. P., Houck, J. C., Ishibashi, B., Karovska, M., Nicastro, F., Noble, M. S., Nowak, M. A., Primini, F. A., Siemiginowska, A., Smith, R. K., and Wise, M. (2006). CIAO: Chandra's data analysis system. In *Society of Photo-Optical Instrumentation Engineers (SPIE) Conference Series*, volume 6270 of *Society of Photo-Optical Instrumentation Engineers (SPIE) Conference Series*.

Galvin, T. J., Filipović, M. D., Crawford, E. J., Tothill, N. F. H., Wong, G. F., and De Horta, A. Y. (2012a). 20 cm VLA Radio-Continuum Study of M31 - Images and Point Source Catalogues. *Serbian Astronomical Journal*, 184:41–68.

Galvin, T. J., Filipović, M. D., Crawford, E. J., Wong, G., Payne, J. L., De Horta, A., White, G. L., Tothill, N., Drašković, D., Pannuti, T. G., Grimes, C. K., Cahall, B. J., Millar, W. C., and Laine, S. (2012b). Radio-continuum study of the Nearby sculptor group galaxies. Part 1: NGC 300 at λ=20 cm. *Ap&SS*, 340:133–142.

Galvin, T. J., Filipović, M. D., Tothill, N. F. H., Crawford, E. J., O'Brien, A. N., Seymour, N., Pannuti, T. G., Kosakowski, A. R., and Sharma, B. (2014). Radio-continuum study of the nearby sculptor group galaxies. Part 3: NGC 7793 at λ=12.2, 6 and 3 cm. *Ap&SS*, 353:603–611.

Ghavamian, P., Laming, J. M., and Rakowski, C. E. (2007). A Physical Relationship between Electron-Proton Temperature Equilibration and Mach Number in Fast Collisionless Shocks. *ApJ*, 654:L69–L72.

Gooch, R. (1996). Karma: a Visualization Test-Bed. In Jacoby, G. H. and Barnes, J., editors, *Astronomical Data Analysis Software and Systems V*, volume 101 of *Astronomical Society of the Pacific Conference Series*, page 80.

Gooch, R. (2006). *Karma Users Manual*. Australia Telescope National Facility.

Green, D. A. (2009a). A revised Galactic supernova remnant catalogue. *Bulletin of the Astronomical Society of India*, 37:45–61.

Green, D. A. (2009b). A catalogue of galactic supernova remnants (http://www.mrao.cam.ac.uk/surveys/snrs/).

Grondin, M.-H., Sasaki, M., Haberl, F., Pietsch, W., Crawford, E. J., Filipović, M. D., Bozzetto, L. M., Points, S., and Smith, R. C. (2012). XMMU J0541.8-6659, a new supernova remnant in the Large Magellanic Cloud. *A&A*, 539:A15.

Haberl, F. (2004). AXPs and X-ray-dim isolated neutron stars: recent XMM-Newton and Chandra results. *Advances in Space Research*, 33:638–644.

Haberl, F., Filipović, M. D., Bozzetto, L. M., Crawford, E. J., Points, S. D., Pietsch, W., De Horta, A. Y., Tothill, N., Payne, J. L., and Sasaki, M. (2012a). Multi-frequency observations of SNR J0453-6829 in the LMC. A composite supernova remnant with a pulsar wind nebula. *A&A*, 543:A154.

Haberl, F., Filipović, M. D., Pietsch, W., and Kahabka, P. (2000). A ROSAT PSPC catalogue of X-ray sources in the SMC region. *A&AS*, 142:41–57.

Haberl, F. and Pietsch, W. (1999). A ROSAT PSPC catalogue of X-ray sources in the LMC region. *A&AS*, 139:277–295.

Haberl, F. and Pietsch, W. (2008). XMM-Newton observations of the Small Magellanic Cloud: X-ray outburst of the 6.85 s pulsar XTE J0103-728. *A&A*, 484:451–455.

Haberl, F., Sturm, R., Ballet, J., Bomans, D. J., Buckley, D. A. H., Coe, M. J., Corbet, R., Ehle, M., Filipović, M. D., Gilfanov, M., Hatzidimitriou, D., La Palombara, N., Mereghetti, S., Pietsch, W., Snowden, S., and Tiengo, A. (2012b). The XMM-Newton survey of the Small Magellanic Cloud. *A&A*, 545:A128.

Haberl, F., Sturm, R., Filipović, M. D., Pietsch, W., and Crawford, E. J. (2012c). SXP 1062, a young Be X-ray binary pulsar with long spin period. Implications for the neutron star birth spin. *A&A*, 537:L1.

Hamilton, A. J. S., Sarazin, C. L., and Chevalier, R. A. (1983). X-ray line emission from supernova remnants. I - Models for adiabatic remnants. *ApJS*, 51:115–147.

Hilditch, R. W., Howarth, I. D., and Harries, T. J. (2005). Forty eclipsing binaries in the Small Magellanic Cloud: fundamental parameters and Cloud distance. *MNRAS*, 357:304–324.

Holdaway, M. A. (1999). Mosaicing with Interferometric Arrays. In Taylor, G. B., Carilli, C. L., and Perley, R. A., editors, *Synthesis Imaging in Radio Astronomy II*, volume 180 of *Astronomical Society of the Pacific Conference Series*, page 401.

Hughes, A., Staveley-Smith, L., Kim, S., Wolleben, M., and Filipović, M. (2007). An Australia Telescope Compact Array 20-cm radio continuum study of the Large Magellanic Cloud. *MNRAS*, 382:543–552.

Ishibashi, W. and Courvoisier, T. J.-L. (2010). X-ray power law spectra in active galactic nuclei. *A&A*, 512:A58.

Johanson, A. K. and Kerton, C. R. (2009). H I Absorption Spectra Toward Magpis Supernova Remnant Candidates. *AJ*, 138:1615–1621.

Kahabka, P., Haberl, F., Pakull, M., Millar, W. C., White, G. L., Filipović, M. D., and Payne, J. L. (2008). Faint super-soft X-ray sources in XMM-Newton Large Magellanic Cloud fields. *A&A*, 482:237–245.

Kahabka, P., Pietsch, W., Filipović , M. D., and Haberl, F. (1999). A ROSAT PSPC X-ray survey of the Small Magellanic Cloud. *A&AS*, 136:81–94.

Kavanagh, P. J., Sasaki, M., Points, S. D., Filipović, M. D., Maggi, P., Bozzetto, L. M., Crawford, E. J., Haberl, F., and Pietsch, W. (2013). Multiwavelength study of the newly confirmed supernova remnant MCSNR J0527-7104 in the Large Magellanic Cloud. *A&A*, 549:A99.

Kontizas, M., Morgan, D. H., Hatzidimitriou, D., and Kontizas, E. (1990). The cluster system of the Large Magellanic Cloud. *A&AS*, 84:527–547.

Liedahl, D. A., Osterheld, A. L., and Goldstein, W. H. (1995). New calculations of Fe L-shell X-ray spectra in high-temperature plasmas. *ApJ*, 438:L115–L118.

Long, K. S., Blair, W. P., Winkler, P. F., Becker, R. H., Gaetz, T. J., Ghavamian, P., Helfand, D. J., Hughes, J. P., Kirshner, R. P., Kuntz, K. D., McNeil, E. K., Pannuti, T. G., Plucinsky, P. P., Saul, D., Tüllmann, R., and Williams, B. (2010). The Chandra ACIS Survey of M33: X-ray, Optical, and Radio Properties of the Supernova Remnants. *ApJS*, 187:495–559.

Long, K. S., Helfand, D. J., and Grabelsky, D. A. (1981). A soft X-ray study of the Large Magellanic Cloud. *ApJ*, 248:925–944.

Lopez, L. A., Ramirez-Ruiz, E., Badenes, C., Huppenkothen, D., Jeltema, T. E., and Pooley, D. A. (2009). Typing Supernova Remnants Using X-Ray Line Emission Morphologies. *ApJ*, 706:L106–L109.

Maccacaro, T., Gioia, I. M., Wolter, A., Zamorani, G., and Stocke, J. T. (1988). The X-ray spectra of the extragalactic sources in the Einstein extended medium sensitivity survey. *ApJ*, 326:680–690.

Maciel, W. J. and Costa, R. D. D. (2003). PN and Galactic Chemical Evolution (invited review). In Kwok, S., Dopita, M., and Sutherland, R., editors, *Planetary Nebulae: Their Evolution and Role in the Universe*, volume 209 of *IAU Symposium*, page 551.

Maggi, P., Haberl, F., Bozzetto, L. M., Filipović, M. D., Points, S. D., Chu, Y.-H., Sasaki, M., Pietsch, W., Gruendl, R. A., Dickel, J., Smith, R. C., Sturm, R., Crawford, E. J., and De Horta, A. Y. (2012). Multi-frequency study of supernova remnants in the Large Magellanic Cloud. Confirmation of the supernova remnant status of DEM L205. *A&A*, 546:A109.

Manchester, R. N., Hobbs, G. B., Teoh, A., and Hobbs, M. (2005). The Australia Telescope National Facility Pulsar Catalogue. *AJ*, 129:1993–2006.

Mao, S. A., Gaensler, B. M., Stanimirović, S., Haverkorn, M., McClure-Griffiths, N. M., Staveley-Smith, L., and Dickey, J. M. (2008). A Radio and Optical Polarization Study of the Magnetic Field in the Small Magellanic Cloud. *ApJ*, 688:1029–1049.

Martayan, C., Frémat, Y., Hubert, A.-M., Floquet, M., Zorec, J., and Neiner, C. (2006). Effects of metallicity, star-formation conditions, and evolution in B and Be stars. I. Large Magellanic Cloud, field of NGC 2004. *A&A*, 452:273–284.

Mathewson, D. S. and Clarke, J. N. (1973). Supernova remnants in the Large Magellanic Cloud. *ApJ*, 180:725–738.

Mathewson, D. S., Ford, V. L., Dopita, M. A., Tuohy, I. R., Long, K. S., and Helfand, D. J. (1983). Supernova remnants in the Magellanic Clouds. *ApJS*, 51:345–355.

Mathewson, D. S., Ford, V. L., Tuohy, I. R., Mills, B. Y., Turtle, A. J., and Helfand, D. J. (1985). Supernova remnants in the Magellanic Clouds. III. *ApJS*, 58:197–200.

Mazzotta, P., Mazzitelli, G., Colafrancesco, S., and Vittorio, N. (1998). Ionization balance for optically thin plasmas: Rate coefficients for all atoms and ions of the elements H to NI. *A&AS*, 133:403–409.

McEntaffer, R. L., Brantseg, T., and Presley, M. (2012). SNR 0453-68.5: An Asymmetric Remnant and its Plerion in the Large Magellanic Cloud. *ApJ*, 756:17.

Millar, W. C., White, G. L., Filipović, M. D., Payne, J. L., Crawford, E. J., Pannuti, T. G., and Staggs, W. D. (2011). Optical spectra of supernova remnant candidates in the Sculptor Group galaxy NGC 300. *Ap&SS*, 332:221–239.

Mills, B. Y., Turtle, A. J., Little, A. G., and Durdin, J. M. (1984). A new look at radio supernova remnants. *Australian Journal of Physics*, 37:321–357.

Müller, E., Staveley-Smith, L., Zealey, W., and Stanimirović, S. (2003). High-resolution HI observations of the Western Magellanic Bridge. *MNRAS*, 339:105–124.

O'Brien, A. N., Filipović, M. D., Crawford, E. J., Tothill, N. F. H., Collier, J. D., De Horta, A. Y., Wong, G. F., Drašković, D., Payne, J. L., Pannuti, T. G., Napier, J. P., Griffith, S. A., Staggs, W. D., and Kotuš, S. (2013). Radio-continuum study of the nearby Sculptor group Galaxies. Part 2: NGC 55 at λ=20, 13, 6 and 3 cm. *Ap&SS*, 347:159–168.

Oliveira, J. M., van Loon, J. T., Sloan, G. C., Sewiło, M., Kraemer, K. E., Wood, P. R., Indebetouw, R., Filipović, M. D., Crawford, E. J., Wong, G. F., Hora, J. L., Meixner, M., Robitaille, T. P., Shiao, B., and Simon, J. D. (2013). Early-stage young stellar objects in the Small Magellanic Cloud. *MNRAS*, 428:3001–3033.

Owen, R. A., Filipović, M. D., Ballet, J., Haberl, F., Crawford, E. J., Payne, J. L., Sturm, R., Pietsch, W., Mereghetti, S., Ehle, M., Tiengo, A., Coe, M. J., Hatzidimitriou, D., and Buckley, D. A. H. (2011). IKT 16: a composite supernova remnant in the Small Magellanic Cloud. *A&A*, 530:A132.

Pavan, L., Bordas, P., Pühlhofer, G., Filipović, M. D., De Horta, A., O'Brien, A., Balbo, M., Walter, R., Bozzo, E., Ferrigno, C., Crawford, E., and Stella, L. (2014a). The long helical jet of the Lighthouse nebula, IGR J11014-6103. *A&A*, 562:A122.

Pavan, L., Bordas, P., Pühlhofer, G., Filipović, M. D., De Horta, A., O'Brien, A., Crawford, E., Balbo, M., Walter, R., Bozzo, E., Ferrigno, C., and Stella, L. (2014b). The Puzzling Jet and Pulsar Wind Nebula of Igr J11014-6103. *International Journal of Modern Physics Conference Series*, 28:60172.

Payne, J. L., Filipović, M. D., Millar, W. C., Crawford, E. J., De Horta, A. Y., Stootman, F. H., and Urošević, D. (2008a). Optical Spectra of Radio Planetary Nebulae in the Large Magellanic Cloud. *Serbian Astronomical Journal*, 177:53–59.

Payne, J. L., Tauber, L. A., Filipović, M. D., Crawford, E. J., and De Horta, A. Y. (2009). The 100 Strongest Radio Point Sources in the Field of the Large Magellanic Cloud at 1.4 GHz. *Serbian Astronomical Journal*, 178:65–70.

Payne, J. L., White, G. L., and Filipović, M. D. (2008b). Long-slit optical spectroscopy of Large Magellanic Cloud radio supernova remnants. *MNRAS*, 383:1175–1194.

Payne, J. L., White, G. L., Filipović, M. D., and Pannuti, T. G. (2007). An ATCA radio-continuum study of the Small Magellanic Cloud - V. Long-slit optical spectroscopy of supernova remnants and confirmation of a new candidate supernova remnant. *MNRAS*, 376:1793–1804.

Petre, R., Hwang, U., Holt, S. S., Safi-Harb, S., and Williams, R. M. (2007). The X-Ray Structure and Spectrum of the Pulsar Wind Nebula Surrounding PSR B0540-69.3. *ApJ*, 662:988–997.

Powell, R. (2006). An atlas of the universe. *http://www.atlasoftheuniverse.com/*.

Reynolds, S. P. (1998). Models of Synchrotron X-Rays from Shell Supernova Remnants. *ApJ*, 493:375.

Reynolds, S. P. and Keohane, J. W. (1999). Maximum Energies of Shock-accelerated Electrons in Young Shell Supernova Remnants. *ApJ*, 525:368–374.

Rohlfs, K. and Wilson, T. L. (2004). *Tools of radio astronomy*. Springer, Berlin.

Roper, Q., McEntaffer, R. L., DeRoo, C., Filipovic, M., Wong, G. F., and Crawford, E. J. (2015). X-ray Spectroscopy of Potential Small Magellanic Cloud Type Ia Supernova Remnants and Their Environments. *ApJ*, 803:106.

Russell, S. C. and Dopita, M. A. (1992). Abundances of the heavy elements in the Magellanic Clouds. III - Interpretation of results. *ApJ*, 384:508–522.

Sault, B. and Killeen, N. (2006). *Miriad Users Guide*. Australia Telescope National Facility.

Sault, R. J., Staveley-Smith, L., and Brouw, W. N. (1996). An approach to interferometric mosaicing. *A&AS*, 120:375–384.

Sault, R. J., Teuben, P. J., and Wright, M. C. H. (1995). A Retrospective View of MIRIAD. In Shaw, R. A., Payne, H. E., and Hayes, J. J. E., editors, *Astronomical Data Analysis Software and Systems IV*, volume 77 of *Astronomical Society of the Pacific Conference Series*, page 433.

Sault, R. J. and Wieringa, M. H. (1994). Multi-frequency synthesis techniques in radio interferometric imaging. *A&AS*, 108:585–594.

Smith, C., Points, S., and Winkler, P. F. (2006). *NOAO Newsletter*, 85:6–7.

Smith, R. K., Brickhouse, N. S., Liedahl, D. A., and Raymond, J. C. (2001). Collisional Plasma Models with APEC/APED: Emission-Line Diagnostics of Hydrogen-like and Helium-like Ions. *ApJ*, 556:L91–L95.

Stanimirovic, S. (2002). Short-Spacings Correction from the Single-Dish Perspective. In Stanimirovic, S., Altschuler, D., Goldsmith, P., and Salter, C., editors, *Single-Dish Radio Astronomy: Techniques and Applications*, volume 278 of *Astronomical Society of the Pacific Conference Series*, pages 375–396.

Stanimirovic, S., Staveley-Smith, L., Dickey, J. M., Sault, R. J., and Snowden, S. L. (1999). The large-scale HI structure of the Small Magellanic Cloud. *MNRAS*, 302:417–436.

Strüder, L., Briel, U., Dennerl, K., Hartmann, R., Kendziorra, E., Meidinger, N., Pfeffermann, E., Reppin, C., Aschenbach, B., Bornemann, W., Bräuninger, H., Burkert, W., Elender, M., Freyberg, M., Haberl, F., Hartner, G., Heuschmann, F., Hippmann, H., Kastelic, E., Kemmer, S., Kettenring, G., Kink, W., Krause, N., Müller, S., Oppitz, A., Pietsch, W., Popp, M., Predehl, P., Read, A., Stephan, K. H., Stötter, D., Trümper, J., Holl, P., Kemmer, J., Soltau, H., Stötter, R., Weber, U., Weichert, U., von Zanthier, C., Carathanassis, D., Lutz, G., Richter, R. H., Solc, P., Böttcher, H., Kuster, M., Staubert, R., Abbey, A., Holland, A., Turner, M., Balasini, M., Bignami, G. F., La Palombara, N., Villa, G., Buttler, W., Gianini, F., Lainé, R., Lumb, D., and Dhez, P. (2001). The European Photon Imaging Camera on XMM-Newton: The pn-CCD camera. *A&A*, 365:L18–L26.

Stupar, M., Filipović, M. D., Jones, P. A., and Parker, Q. A. (2005). Radio continuum observations of the galactic supernova remnant Vela Z (G266.2-1.2). *Advances in Space Research*, 35:1047–1051.

Stupar, M., Filipović, M. D., and Parker, Q. A. (2004). Radio continuum observations of Vela Z. In Paillé, J.-P., editor, *35th COSPAR Scientific Assembly*, volume 35 of *COSPAR Meeting*, page 2434.

Sturm, R., Drašković, D., Filipović, M. D., Haberl, F., Collier, J., Crawford, E. J., Ehle, M., De Horta, A., Pietsch, W., Tothill, N. F. H., and Wong, G. (2013a). Active galactic nuclei behind the SMC selected from radio and X-ray surveys. *A&A*, 558:A101.

Sturm, R., Haberl, F., Pietsch, W., Ballet, J., Hatzidimitriou, D., Buckley, D. A. H., Coe, M., Ehle, M., Filipović, M. D., La Palombara, N., and Tiengo, A. (2013b). The XMM-Newton survey of the Small Magellanic Cloud: The X-ray point-source catalogue. *A&A*, 558:A3.

Telezhinsky, I., Dwarkadas, V. V., and Pohl, M. (2012). Particle spectra from acceleration at forward and reverse shocks of young Type Ia Supernova Remnants. *Astroparticle Physics*, 35:300–311.

Turner, M. J. L., Abbey, A., Arnaud, M., Balasini, M., Barbera, M., Belsole, E., Bennie, P. J., Bernard, J. P., Bignami, G. F., Boer, M., Briel, U., Butler, I., Cara, C., Chabaud, C., Cole, R., Collura, A., Conte, M., Cros, A., Denby, M., Dhez, P., Di Coco, G., Dowson, J., Ferrando, P., Ghizzardi, S., Gianotti, F., Goodall, C. V., Gretton, L., Griffiths, R. G., Hainaut, O., Hochedez, J. F., Holland, A. D., Jourdain, E., Kendziorra, E., Lagostina, A., Laine, R., La Palombara, N., Lortholary, M., Lumb, D., Marty, P., Molendi, S., Pigot, C., Poindron, E.,

Pounds, K. A., Reeves, J. N., Reppin, C., Rothenflug, R., Salvetat, P., Sauvageot, J. L., Schmitt, D., Sembay, S., Short, A. D. T., Spragg, J., Stephen, J., Strüder, L., Tiengo, A., Trifoglio, M., Trümper, J., Vercellone, S., Vigroux, L., Villa, G., Ward, M. J., Whitehead, S., and Zonca, E. (2001). The European Photon Imaging Camera on XMM-Newton: The MOS cameras : The MOS cameras. *A&A*, 365:L27–L35.

Turtle, A. J. and Amy, S. W. (1991). The Molonglo 843 MHz Survey of the Magellanic Clouds. In Haynes, R. and Milne, D., editors, *The Magellanic Clouds*, volume 148 of *IAU Symposium*, page 114.

Turtle, A. J. and Mills, B. Y. (1984). Supernova remnant searches at Molonglo. *Proceedings of the Astronomical Society of Australia*, 5:537–540.

Udalski, A., Szymanski, M., Kubiak, M., Pietrzynski, G., Wozniak, P., and Zebrun, K. (1998). The Optical Gravitational Lensing Experiment. BVI Maps of Dense Stellar Regions. I. The Small Magellanic Cloud. *Acta Astron.*, 48:147–174.

Urošević, D. and Milogradov-Turin, J. (2007). *Teorijske osnove radio-astronomije (Theoretical fundamentals of Radio Astronomy)*. Faculty of Mathematics, Belgrade.

van der Heyden, K. J., Bleeker, J. A. M., and Kaastra, J. S. (2004). Synoptic study of the SMC SNRs using XMM-Newton. *A&A*, 421:1031–1043.

Wang, Q., Hamilton, T., Helfand, D. J., and Wu, X. (1991). The detection of X-rays from the hot interstellar medium of the Large Magellanic Cloud. *ApJ*, 374:475–495.

Williams, R. M. and Chu, Y.-H. (2005). Supernova Remnants in the Magellanic Clouds. VI. The DEM L316 Supernova Remnants. *ApJ*, 635:1077–1086.

Williams, R. M., Chu, Y.-H., Dickel, J. R., Gruendl, R. A., Seward, F. D., Guerrero, M. A., and Hobbs, G. (2005). Supernova Remnants in the Magellanic Clouds. V. The Complex Interior Structure of the N206 Supernova Remnant. *ApJ*, 628:704–720.

Williams, R. M., Chu, Y.-H., Dickel, J. R., Gruendl, R. A., Shelton, R., Points, S. D., and Smith, R. C. (2004). Supernova Remnants in the Magellanic Clouds. IV. X-Ray Emission from the Largest Supernova Remnant in the Large Magellanic Cloud. *ApJ*, 613:948–955.

Williams, R. M., Chu, Y.-H., Dickel, J. R., Petre, R., Smith, R. C., and Tavarez, M. (1999a). Supernova Remnants in the Magellanic Clouds. III. an X-Ray Atlas of Large Magellanic Cloud Supernova Remnants. *ApJS*, 123:467–485.

Williams, R. M., Chu, Y.-H., Dickel, J. R., Smith, R. C., Milne, D. K., and Winkler, P. F. (1999b). Supernova Remnants in the Magellanic Clouds. II. Supernova Remnant Breakouts from N11L and N86. *ApJ*, 514:798–817.

Wilms, J., Allen, A., and McCray, R. (2000). On the Absorption of X-Rays in the Interstellar Medium. *ApJ*, 542:914–924.

Woltjer, L. (1972). Supernova Remnants. *ARA&A*, 10:129.

Wong, G. F., Crawford, E. J., Filipović, M. D., De Horta, A. Y., Tothill, N. F. H., Collier, J. D., Drašković, D., Galvin, T. J., and Payne, J. L. (2012a). New 6 and 3-cm Radio-Continuum Maps of the Small Magellanic Cloud: Part II - Point Source Catalogue. *Serbian Astronomical Journal*, 184:93–95.

Wong, G. F., Filipović, M. D., Crawford, E. J., De Horta, A. Y., Galvin, T., Drašković, D., and Payne, J. L. (2011a). New 20-cm Radio-Continuum Study of the Small Magellanic Cloud: Part I - Images. *Serbian Astronomical Journal*, 182:43–52.

Wong, G. F., Filipović, M. D., Crawford, E. J., Tothill, N. F. H., De Horta, A. Y., Drašković, D., Galvin, T. J., Collier, J. D., and Payne, J. L. (2011b). New 20-cm Radio-Continuum Study of the Small Magellanic Cloud: Part II - Point Sources. *Serbian Astronomical Journal*, 183:103–106.

Wong, G. F., Filipović, M. D., Crawford, E. J., Tothill, N. F. H., De Horta, A. Y., and Galvin, T. J. (2012b). New 20-cm Radio-Continuum Study of the Small Magellanic Cloud: Part III - Compact HII Regions. *Serbian Astronomical Journal*, 185:53–64.

Zijlstra, A. A., van Hoof, P. A. M., Chapman, J. M., and Loup, C. (1994). Radio and infrared emission from a [WC]-type planetary nebula in the LMC. *A&A*, 290:228–234.

Appendix A

Related Refereed Journal Papers[1]

A.1 Related Paper 1

Payne, J. L., Filipović, M. D., Millar, W. C., Crawford, E. J., De Horta, A. Y., Stootman, F. H., and Urošević, D. (2008a). Optical Spectra of Radio Planetary Nebulae in the Large Magellanic Cloud. *Serbian Astronomical Journal*, 177:53–59

My contribution to this paper was to assist in the preparation of the radio data. This is a 10% contribution.

[1] All articles presented in this part have been refereed and appear, or will appear in a ERA recognised journal.

Serb. Astron. J. № 177 (2008), 53 - 59
DOI: 10.2298/SAJ0877053P

UDC 524.37-355.3 : 524.722.3
Original scientific paper

OPTICAL SPECTRA OF RADIO PLANETARY NEBULAE IN THE LARGE MAGELLANIC CLOUD

J. L. Payne[1], M. D. Filipović[2], W. C. Millar[1], E. J. Crawford[2], A. Y. De Horta[2], F. H. Stootman[2] and D. Urošević[3]

[1] *Centre for Astronomy, James Cook University Townsville QLD, 4811, Australia*

E–mail: *snova4@msn.com*

[2] *University of Western Sydney, Locked Bag 1797 Penrith South, DC, NSW 1797, Australia*

[3] *Department of Astronomy, Faculty of Mathematics, University of Belgrade Studentski trg 16, 11000 Belgrade, Serbia*

(Received: July 9, 2008; Accepted: August 19, 2008)

SUMMARY: We present 11 spectra from 12 candidate radio sources co-identified with known planetary nebulae (PNe) in the Large Magellanic Cloud (LMC). Originally found in Australia Telescope Compact Array (ATCA) LMC surveys at 1.4, 4.8 and 8.64 GHz and confirmed by new high resolution ATCA images at 6 and 3 cm ($4''/2''$), these complement data recently presented for candidate radio PNe in the Small Magellanic Cloud (SMC). Their spectra were obtained using the Radcliffe 1.9-meter telescope in Sutherland (South Africa). All of the optical PNe and radio candidates are within $2''$ and may represent a population of selected radio bright sample only. Nebular ionized masses of these objects are estimated to be as high as 1.8 $M_{\odot}$, supporting the idea that massive PNe progenitor central stars lose much of their mass in the asymptotic giant branch (AGB) phase or prior. We also identify a sub-population (33%) of radio PNe candidates with prominent ionized iron emission lines.

Key words. planetary nebulae: individual: SMP L8, SMP L25, SMP L33, SMP L39, SMP L47, SMP L62, SMP L74, SMP L75, SMP L83, SMP L84, SMP L89

1. INTRODUCTION

Planetary nebulae (PNe) are one of the most important processes giving rise to and sustaining the chemical evolution of galaxies, contributing about half of the overall enrichment of the interstellar medium. They are the product of lower-mass stars where the central-star and nebular masses are only about 0.6 and 0.3 $M_{\odot}$, respectively. However, detection of white dwarfs in open clusters suggests the main-sequence mass of PNe progenitors can be as high as 8 $M_{\odot}$ (Kwok 1994). Because they contain the products of the nuclear reactions occurring in the later stages of stellar evolution, they have high levels of helium, nitrogen, oxygen and carbon. Their expansion into the interstellar environment carries these products into the galactic disk. It is very likely that PNe are a greater contributer to the galactic N/O abundance than super-

novae remnants. The over-abundance of these elements in typical PNe allows us to support the confirmation of a candidate PN with optical spectra by measuring abundance ratios of these elements. Optical spectral requirements for the confirmation of PNe have been summarised very nicely by Reid and Parker (2006). Classically, PNe can be identified by a [O III]5007Å:[O III]4959Å:Hβ intensity ratio near 9:3:1. This can be relaxed when the intensity of [N II]6583Å is greater than Hα. In that case, a strong [O III] line has been often detected along with the high excitation He II4686Å line hardly seen in H II regions. Generally, the [O II]3727Å doublet is seen in PNe, as well as [Ne III]3869Å, [Ar III]7135Å and He I6678Å lines. [S II]6717, 6731Å are usually present but not significant when compared to Hα.

The study of extra-Galactic PNe is crucial to the understanding of PNe in general. Observations of Galactic PNe are hampered by the uncertain distances. While the population of nearby Galactic PNe is not small, we can drastically expand our understanding of Galactic PNe by studying PNe in other, nearby galaxies, such as the Magellanic Clouds (MCs).

In this paper we present optical spectra of 11 PNe that co-identify with radio PNe candidates recently found in the Large Magellanic Cloud (LMC). Spectra of four (4) PNe with radio counterparts were recently presented for the Small Magellanic Cloud (SMC) in Payne et al. (2008). Section 2 details our spectral observations and reduction methods used to calibrate the data analysed in Section 3. The paper concludes with some final comments and a brief summary as presented in Section 4.

2. OBSERVATIONS

The first radio PNe candidate of this series was reported in Payne et al. (2004). Since, ∼17 have been found within a few arcseconds of known optical PNe in the direction of the Magellanic Clouds (Filipović et al., in prep.). This includes at least 12 LMC sources from Australia Telescope Compact Array (ATCA) observations, complemented with short-spacings using Parkes data and reduced using the MIRIAD software suite to create mosaic images at 1.4 GHz (Hughes et al. 2007), and 4.8, 8.64 GHz (Dickel et al. 2005). Recent followup ATCA observations at 4.8 and 8.64 GHz give much higher resolutions ($4''/2''$) and appear to confirm that most are bright radio counterparts within $2''$ of known optical PNe. The number and flux densities of these candidate radio PNe are unexpected given the distance of the LMC of ∼ 50 kpc (Alves 2004). This may well modify our current understanding of PNe, including their progenitor mass and evolution.

Here, we present optical spectra for the radio candidates shown in Fig. 1 and listed in Table 1. For each, we give its radio name, position (adopted from the highest available frequency), difference of radio and optical positions, radio spectral index, 4.8 GHz flux density, estimated ionized mass and optical counterpart PNe names. These known optical PNe have been found in surveys including Sanduleak et al. (1978) and Read and Parker (2006). From Table 1, we also note that our spectral indices support the general belief that PNe are dominant thermal radio emitters.

Spectral observations were conducted in January 2008, using the 1.9-meter telescope and Cassegrain spectrograph at the South African Astronomical Observatory (SAAO) in Sutherland. We used grating number 7 (300 lpmm) to obtain spectra between 3500 and 6200 Å having a resolution of 5 Å. For these, the slit size was $1.5'' \times 1.5'$ with a spatial resolution of $0.74''$ pixel^{-1}. Exposure times were limited to 800 s with a positional accuracy of $< 1''$.

Data reduction included bias subtraction and flat-field correction using the IRAF software package. Extraction (task 'extractor'), including background sky subtraction, of data allowed the creation of one-dimensional spectra, with wavelength calibrated using standard lines from a CuAr arc. Flux calibration was applied using the spectrometric standard star EG 21. Observing conditions were fair with seeing limited to $>1''$ but varied throughout the night.

3. SPECTRAL ANALYSIS

If one assumes that these PNe have a relatively symmetric uniform density, it may be possible to crudely estimate their ionized mass ($M_{\rm i}$):

$$M_{\rm i} = 282(D_{\rm kpc})^2 F_5 (n_{\rm e})^{-1} M_{\odot}, \qquad (1)$$

where $D_{\rm kpc}$ is distance (kpc), F_5 is radio flux density at ∼ 5 GHz (Jy) and $n_{\rm e}$ represents assumed electron density (10^3 cm^{-3}) (Kwok 2000). Table 1 lists an ionized mass estimate for each PN based on the given flux densities at 4.8 GHz. These values, as high as 1.8 $M_{\odot}$, imply our selected radio bright objects may have higher nebular ionized masses than previously expected.

We used IRAF's task SPLOT to view and analyze our spectra. Only fluxes from spectral lines visually distinct from the baseline rms (∼ 10^{-15} ergs cm^{-2} s^{-1} Å^{-1}) were selected for inclusion in Table 2. For each PNe, Table 2 lists the relative flux densities (using EG21) and 90% confidence intervals of common lines within our spectral range. These lines include the [O II]3727Å doublet, [Ne III]3869Å, H$\beta\lambda$4861Å and [O III]4363, 4959, 5007Å. All values are shown at their rest wavelengths.

Table 1. Radio PN candidates in the LMC with available spectra from our study. ΔP represents the distance between radio and optical positions. SMP refers to Sanduleak et al. (1978). Spectral index (α) is defined here as $S_\nu \propto \nu^\alpha$, where S_ν is the flux density at frequency ν. Ionized mass (M_i) assumes an electron density (n_e) of 10^3 cm^{-3}.

No.	ATCA Radio Source Name	R.A. (J2000.0)	Dec. (J2000.0)	ΔP (arcsec)	$\alpha \pm \Delta\alpha$	$S_{4.8\mathrm{GHz}}$ (mJy)	M_i ($M_\odot$)	Optical PN Name
1	LMC J045013-693352	04 50 13.28	–69 33 52.7	1″	—	—	—	SMP L8
2	LMC J050624-690320	05 06 24.22	–69 03 20.1	1″	0.2±0.3	2.1	1.5	SMP L25
3	LMC J051009-682955	05 10 09.38	–68 29 55.1	1″	—	—	—	SMP L33
4	LMC J051142-683459	05 11 42.11	–68 34 59.1	1″	—	—	—	SMP L39
5	LMC J051954-693104	05 19 54.51	–69 31 04.5	2″	0.0±0.2	2.1	1.5	SMP L47
6	LMC J052455-713255	05 24 55.31	–71 32 55.0	1″	–0.2±0.2	2.1	1.5	SMP L62
7	LMC J053329-715227	05 33 29.09	–71 52 27.2	2″	–0.7±0.3	1.1	0.8	SMP L74
8	LMC J053346-683643	05 33 46.90	–68 36 43.0	2″	—	—	—	SMP L75
9	LMC J053620-671807	05 36 20.69	–67 18 07.9	< 1″	–0.3±0.2	0.9	0.6	SMP L83
10	LMC J053653-715339	05 36 53.46	–71 53 39.3	2″	—	—	—	SMP L84
11	LMC J054237-700930	05 42 37.17	–70 09 30.4	2″	–0.1±0.2	2.6	1.8	SMP L89

Table 2. Spectral analysis of known optical PNe co-incident with radio sources. Flux densities are given in units of 10^{-14} ergs cm^{-2} s^{-1} and include 90 % confidence intervals. Electron temperature (T_e) assumes an electron density (n_e) of 10^3 cm^{-3}. There is no correction for extinction.

Name	[O II] 3727Å	[Ne III] 3869Å	[O III] 4363Å	Hβ 4861Å	[O III] 4959Å	[O III] 5007Å	Hγ/Hβ	E(B–V)	T_e (K)
SMP L8	—	51.0±1.0	18.4±0.6	35.4±0.9	70.8±0.9	207.3±1.0	0.7	–0.9	49760
SMP L25	118.5±1.1	185.5±1.0	26.1±1.1	144.4±1.0	380.5±1.0	1110.0±0.9	0.7	–0.9	16430
SMP L33	86.9±1.1	33.9±0.9	2.8±0.8	16.1±1.0	68.0±1.0	198.1±1.0	0.8	–1.2	13039
SMP L39	10.7±1.0	—	—	0.9±0.9	3.7±0.9	11.1±0.9	—	—	—
SMP L47	1112.0±1.2	676.0±1.1	36.5±1.0	124.1±0.9	395.3±1.0	1183.0±1.0	0.7	–0.9	19056
SMP L62	6.1±1.2	11.3±1.0	3.9±0.9	21.3±1.0	77.8±0.8	236.7±1.0	0.4	0.6	14039
SMP L74	14.5±1.2	14.0±0.9	2.6±1.1	13.8±0.9	57.1±0.9	172.5±1.0	0.5	–0.2	13409
SMP L75	—	12.3±1.0	1.8±1.2	18.7±0.9	57.5±0.9	173.1±1.0	1.0	–1.6	11696
SMP L83	—	9.0±1.0	3.3±1.5	10.1±1.1	28.7±0.9	85.5±1.0	0.5	–0.3	21941
SMP L84	—	—	1.8±1.1	11.5±1.0	25.8±0.9	78.8±0.9	—	—	16473
SMP L89	1203.0±1.1	1279.0±1.1	116.1±1.4	181.2±0.9	685.6±1.0	1954.0±1.0	1.1	–1.9	30492

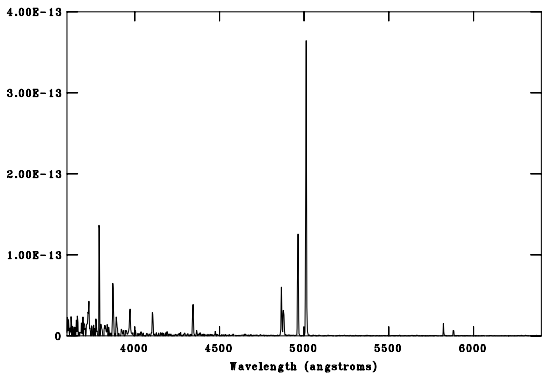

Fig. 1a. *Optical spectrum of SMP L8 coincident with J045013-693352.*

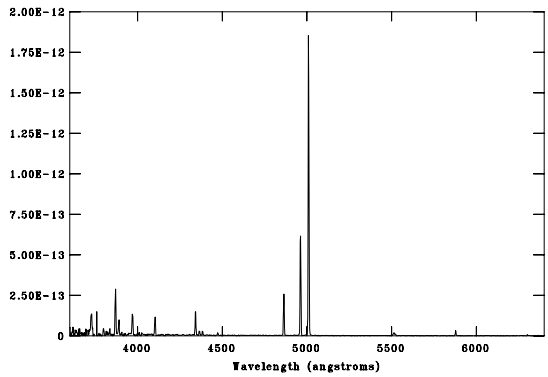

Fig. 1b. *Optical spectrum of SMP L25 coincident with J050624-690320.*

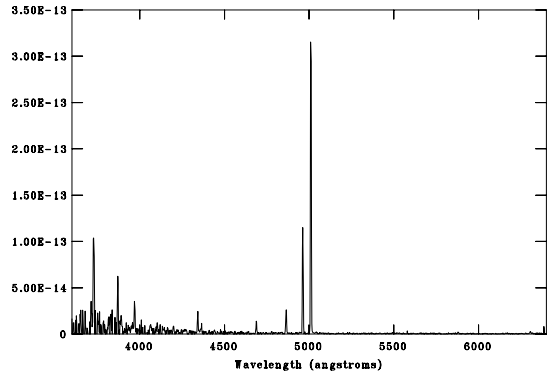

Fig. 1c. *Optical spectrum of SMP L33 coincident with J051009-682955.*

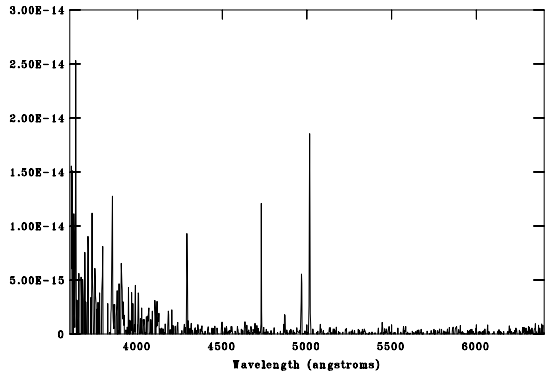

Fig. 1d. *Optical spectrum of SMP L39 coincident with J051142-683459.*

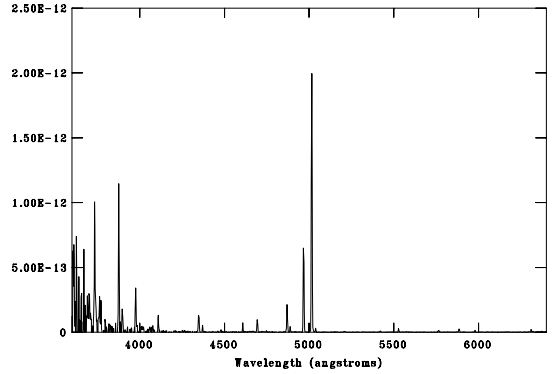

Fig. 1e. *Optical spectrum of SMP L47 coincident with J051954-693104.*

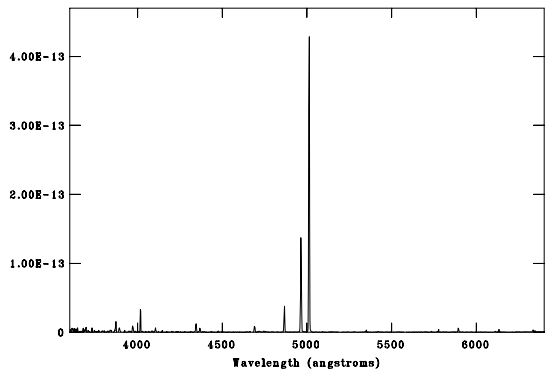

Fig. 1f. *Optical spectrum of SMP L62 coincident with J052455-713255.*

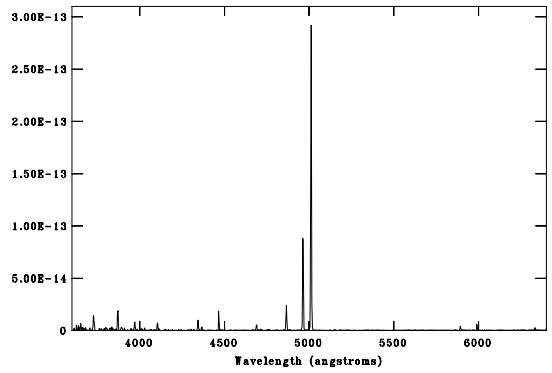

Fig. 1g. *Optical spectrum of SMP L74 coincident with J053329-715227.*

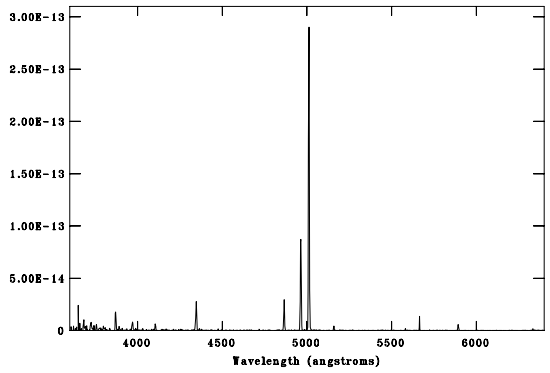

Fig. 1h. *Optical spectrum of SMP L75 coincident with J053346-683643.*

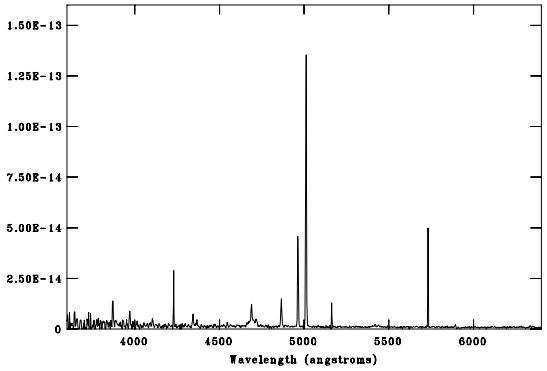

Fig. 1i. *Optical spectrum of SMP L83 coincident with J053620-671807.*

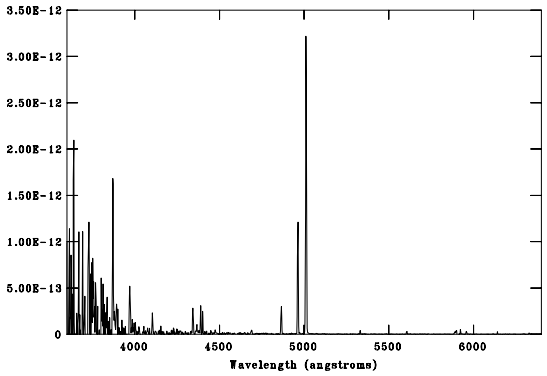

Fig. 1k. *Optical spectrum of SMP L89 coincident with J054237-700930.*

Extinction may be calculated using the Balmer emission lines: Hα6563Å, Hβ4861Å, Hγ4340Å and Hδ4102Å. Noting that our spectral range does not include Hα6563Å and that there is increased noise in many of the spectra near the Hδ4102Å line, we estimate Balmer decrements as Hγ/Hβ. Characteristic extinction curves are given by Osterbrock and Ferland (2006) and expected intrinsic Balmer decrements are based on Case B recombination[1]. Table 2 lists individual values for E(B–V) based on these decrements. We cannot accurately measure the Hγ4340Å line for SMP L39 and

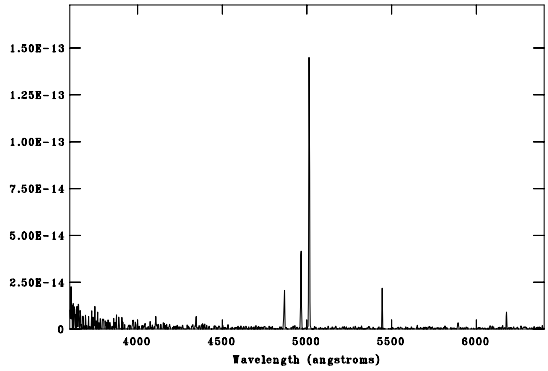

Fig. 1j. *Optical spectrum of SMP L84 coincident with J053653-715339.*

SMP L84 because of baseline noise (Fig. 1). Of the available decrements, the calculated extinctions are zero or less for all but one. Thus, three electron temperatures (T_e) (SMP L39, SMP L62 and SMP L84) given in Table 2 may be affected, but their uncorrected values are reasonable, given the values are dependent on the [O III] forbidden line ratio having a maximum interval of 644Å.

The 90% confidence errors reported in Table 2 are based on line measurement; we do not account for absolute photometric errors. Line measurement errors were calculated using Monte-Carlo simulation techniques found in the task SPLOT for a sample number of 100 and measured rms sensitivity. This 1σ value was multiplied by 1.64 to estimate a 90% confidence interval for each flux density.

Ions including [O III] and [N II] have energy-level structures that produce emission lines from different excitation energies. The relative rates of excitation depend very strongly on temperature and may be used to measure T_e. The only practical probe for the measurement of electron temperature in our case is the [O III] forbidden line ratio[2]. We list electron temperatures in Table 2 for each of our nebulae, based on this [O III] ratio.

Since our spectral range excluded the [S II]6717, 6731Å lines needed to calculate electron densities, we assume a n_e of 10^3 cm^{-3} for this selected radio sample[3]. We base this approximate value on PNe averages found in Stanghellini and Kaler (1989) and estimate T_e using the Space Telescope Science Data Analysis System task NEBULAR.TEMDEN, based on a five-level atom approximation from De Robertis et al. (1987).

[1] An approximation characterized by large optical depth, where every Lyman-line photon is scattered many times and is eventually converted into lower-series photons.

[2] Defined as $\frac{\lambda 4959+\lambda 5007}{\lambda 4363}$.

[3] While the [O III] forbidden line ratio algorithm uses electron density, it should be noted that even a factor of 100 from the assumed 10^3 cm $^{-3}$ in electron density affects the calculated temperature by only a few hundred K at most.

Table 3. Ionized abundances for [O II], [O III] and [Ne III] given in N(X) / N(H^+) as determined by NEBULAR.IONIC.

Name	$O^+ \times 10^{-4}$ 3727Å Blend	$O^{+2} \times 10^{-4}$ 5007Å Line	$Ne^{+2} \times 10^{-5}$ 3869Å Line
SMP L8	—	0.08	0.36
SMP L25	0.06	0.65	2.50
SMP L33	0.86	1.90	8.13
SMP L39	—	—	—
SMP L47	0.46	0.58	7.27
SMP L62	0.04	1.40	1.63
SMP L74	0.15	1.79	3.58
SMP L75	—	1.96	3.66
SMP L83	—	0.39	0.87
SMP L84	—	—	—
SMP L89	—	0.28	3.65

Ion abundances are presented in Table 3, computed using NEBULAR.IONIC. This program determines ionic concentrations with respect to H^+ ions based on the flux (on a scale Hβ = 100) and the wavelength of a selected emission line. Comparison with values obtained for Galactic PNe, such as those presented by Bohigas (2001), suggest they are not unusual.

Table 4. Spectra containing prominent ionized [forbidden] iron emission lines (1 = flux much greater than Hβ; 2 = flux about equal to Hβ; 3 = flux much less than Hβ).

Name	Iron Emission Lines
SMP L39	[Fe II]4287Å(1)
SMP L83	[Fe V]4227Å(1)
	[Fe VII]5721Å(1)
SMP L84	[Fe VI]5427Å(2)

Figs. 1a through 1k show our one-dimensional spectra for each PNe listed in Table 2. These spectra have typical emission lines which we highlight here. In addition to the expected [O II], [O III] and Balmer lines, we note that several reveal a [Ne III]3869Å line (SMP L8, SMP L25, SMP L33, SMP L47, SMP L62, SMP L74, SMP L75, SMP L83 and SMP L89) common in PNe. Many also have a blend at 3968Å representing [Ne III]/Hϵ (SMP L25, SMP L33, SMP L47 and SMP L89). Other lines include He I3889, 4026, 4471, 5876Å and He II4686Å.

SMP L39, SMP L83 and SMP L84 show an assortment of ionized iron emission lines including [Fe II]4287Å, [Fe V]4227Å, [Fe VI]5427Å and [Fe VII]5721Å (see Table 4). In the previous paper (Payne et al. 2008), we also noted that JD10 in the SMC had a predominant [Fe III]4881Å line. This seemed unusual since the abundance of iron in PNe is scarcely studied, due to its relative faintness (Perinotto et al. 1999). Therefore, we are identifying a sub- population of PNe with prominent ionized iron lines that warrant further verification and study.

4. CONCLUDING REMARKS AND SUMMARY

Most observed PNe have nebular masses of only 0.3 $M_\odot$, although the main-sequence mass of PNe progenitors can be as high as 8 $M_\odot$ (Kwok 1994). The PNe studied here may represent a predicted "missing-mass link", belonging originally to a system possessing up to an 8 $M_\odot$ or higher central star. Given values of radio flux density at $\sim$ 5 GHz, we suggest that the ionized nebular mass of these PNe could be as high as 1.8 $M_\odot$ assuming an average density of 10^3 cm^{-3}.

High rates of mass loss that continue for an extended fraction of a AGB's lifetime can allow a significant fraction of the star's mass to be accumulated. This may result in the formation of a circumstellar envelope (CSE) or halo. If the transition from the AGB to PN stage is short, then such CSEs could have a significant effect. Perhaps our radio observations select for high mass PNe, since the quantity of ionized mass present is directly related to radio flux density.

Our combined observations suggest that a population of PNe in the MCs have bright radio counterparts, with nebular electron temperatures within a reasonable range given instrument resolution and sensitivity. Ionized abundances of [O II], [O III] and [Ne III] are not unusual. While most have typical spectra, at least a third have prominent forbidden ionized iron lines.

Acknowledgements – This paper uses observations made from the South African Astronomical Observatory (SAAO). Travel to the SAAO was funded by Australian Government, AINSTO AMRFP grant number 07/08-O-11. We thank the Serbian Ministry for Science for support (Projects 146012 and 146016). We also used the KARMA software package developed by the ATNF. The Australia Telescope Compact Array is part of the Australia Telescope which is funded by the Commonwealth of Australia for operation as a National Facility managed by CSIRO. IRAF is distributed by the National Optical Astronomy Observatories, which are operated by the Association of Universities for Research in Astronomy, Inc., under cooperative agreement with the National Science Foundation.

REFERENCES

Alves, D. R.: 2004, *New Astronomy Review*, **48**, 659.
Bohigas, J.: 2001, *Rev. Mex. Astron. Astrofis.*, **37**, 237.
De Robertis, M. M., Dufour, R., Hunt, R.: 1987, *J. Roy. Astron. Soc. Canada*, **81**, 195.
Dickel, J. R., McIntyre, J. J., Gruendl, R. A., Milne, D. K.: 2005, *Astron. J.*, **129**, 790.
Hughes, A., Staveley-Smith, L., Kim, S., Wolleben, M., Filipović, M. D.: 2007, *Mon. Not. R. Astron. Soc.*, **382**, 543.

Jacoby, G. H., De Marco, O.: 2002, *Astron. J.*, **123**, 269.
Kwok, S.: 1994, *Publ. Astron. Soc. Pacific*, **106**, 344.
Kwok, S.: 2000, "The Origin and Evolution of Planetary Nebulae", Cambridge University Press, Cambridge, p. 51.
Kwok, S.: 2005, *J. Kor. Astron. Soc.*, **38**, 271.
Osterbrock, D. E., Ferland, G. J.: 2006, "Astrophysics of Gaseous Nebulae and Active Galactic Nuclei (second edition)". University Science Books, Sausalito, p. 180.
Payne, J. L., Filipović, M. D., Crawford, E. J., de Horta, A. Y., White, G. L., Stootman, F. H.: 2008, *Serb. Astron. J.*, **176**, 65.
Payne, J. L., Filipović, M. D., Reid, W., Jones, P. A., Staveley-Smith, L, White, G. L.: 2004, *Mon. Not. R. Astron. Soc.*, **355**, 44.
Perinotto, M., Bencini, C. G., Pasquali, A., Manchado, Rodriguez Espinosa, J. M., Stanga, R.: 1999, *Astron. Astrophys.*, **347**, 967.
Reid, W. A., Parker, Q. A.: 2006, *Mon. Not. R. Astron. Soc.*, **373**, 521.
Sanduleak, N., MacConnell, D. J., Philip, A. G. Davis: 1978, *Publ. Astron. Soc. Pacific*, **90**, 621.
Stanghellini, L., Kaler, J. B.: 1989, *Astrophys. J.*, **343**, 811.

ОПТИЧКИ СПЕКТРИ РАДИО ПЛАНЕТАРНИХ МАГЛИНА У ВЕЛИКОМ МАГЕЛАНОВОМ ОБЛАКУ

J. L. Payne[1], M. D. Filipović[2], W. C. Millar[1], E. J. Crawford[2], A. Y. De Horta[2], F. H. Stootman[2] and D. Urošević[3]

[1] *Centre for Astronomy, James Cook University Townsville QLD, 4811, Australia*

E–mail: *snova4@msn.com*

[2] *University of Western Sydney, Locked Bag 1797, Penrith South DC, NSW 1797, Australia*

[3] *Department of Astronomy, Faculty of Mathematics, University of Belgrade Studentski trg 16, 11000 Belgrade, Serbia*

УДК 524.37-355.3 : 524.722.3
Оригинални научни рад

У овој студији представљамо прелиминарне резултате спектралне анализе 11 (од познатих 12) радио кандидата за планетарну маглину у Великом Магелановом Облаку (ВМО). Оптичка посматрања приказана овде урађена су са Радклиф 1.9-m телескопом (Садерленд, Јужна Африка). Ових 11 радио планетарних маглина оригинално су откривене у нашим ранијим радио-прегледима ВМО направљеним Аустралијским Телескопом Компактног Поља (ATCA) на 20, 6 и 3 cm, а такође су потврђене додатним посматрањима високе резолуције на 6 и 3 cm ($4''/2''$). Оптичке и радио-позиције ових 11 кандидата за радио планетарне маглине у ВМО су удаљене мање од $2''$ и највероватније представљају подпопулацију планетарних маглина изражених као веома сјајни радио-објекти. Јонизоване масе ових маглина су прорачунате на до 1.8 $M_\odot$, што даље подржава постојање планетарних маглина са масивним (до 8 $M_\odot$) прогениторским централним звездама које губе већи део своје масе у АГБ фази или чак пре ове фазе. Такође смо идентификовали и подпопулацију (33%) радио планетарних маглина са проминантним емисионим линијама гвожђа.

A.2 Related Paper 2

Payne, J. L., Tauber, L. A., Filipović, M. D., Crawford, E. J., and De Horta, A. Y. (2009). The 100 Strongest Radio Point Sources in the Field of the Large Magellanic Cloud at 1.4 GHz. *Serbian Astronomical Journal*, 178:65–70

My contribution to this paper was to create the initial list of sources, and then some of the crossmatching. This is a 10% contribution.

Serb. Astron. J. № 178 (2009), 65 - 70
DOI: 10.2298/SAJ0978065P

UDC 52–13–77 : 524.722.3
Professional paper

THE 100 STRONGEST RADIO POINT SOURCES IN THE FIELD OF THE LARGE MAGELLANIC CLOUD AT 1.4 GHz

J. L. Payne[1], L. A. Tauber[1], M. D. Filipović[2], E. J. Crawford[2] and A. Y. De Horta[2]

[1] *Centre for Astronomy, James Cook University*
Townsville QLD, 4811, Australia

E–mail: *snova4@msn.com*

[2] *University of Western Sydney, Locked Bag 1797*
Penrith South, DC, NSW 1797, Australia

(Received: January 19, 2009; Accepted: January 26, 2009)

SUMMARY: We present the 100 strongest 1.4 GHz point sources from a new mosaic image in the direction of the Large Magellanic Cloud (LMC). The observations making up the mosaic were made using Australia Telescope Compact Array (ATCA) over a ten year period and were combined with Parkes single dish data at 1.4 GHz to complete the image for short spacing. An initial list of co-identifications within $10''$ at 0.843, 4.8 and 8.6 GHz consisted of 2682 sources. Elimination of extended objects and artifact noise allowed the creation of a refined list containing 1988 point sources. Most of these are presumed to be background objects seen through the LMC; a small portion may represent compact H II regions, young SNRs and radio planetary nebulae. For the 1988 point sources we find a preliminary average spectral index (α) of –0.53 and present a 1.4 GHz image showing source location in the direction of the LMC.

Key words. Radio Continuum: galaxies – Magellanic Clouds – Catalogs

1. INTRODUCTION

The Large Magellanic Cloud (LMC) is a galaxy that, from our vantage point, appears as a nearly face-on spiral. It is an ideal location to study and to develop our understanding of radio sources such as supernova remnants (SNRs), H II regions, planetary nebulae, and X-ray binaries and their interactions. More distant radio sources that include active galaxies can also be seen in the direction of the LMC. These sources, that are not in the LMC, must also be identified and distinguished from those within the LMC.

We present a description and analysis of our data in Section 2, and the results in Section 3. Concluding remarks with a brief discussion are presented in Section 4.

2. OBSERVATIONS AND ANALYSIS

During October 1994 and February 1995, the LMC was surveyed in mosaic mode, centred at 1.4 GHz (bandwidth 128 MHz), using the Australia Telescope Compact Array (ATCA). This survey divided the LMC into 12 regions, each containing 112 pointing centres. Each pointing centre was observed approximately 115 times (ranging from 95 to 140) for 15 s. The data were reduced using the MIRIAD software suite (Sault and Killeen 2006). Data from the

64-m Parkes radio telescope (Filipović et al. 1995) of the same region at 1.401 GHz (λ=21 cm) were used to fill in the missing short spacing allowing large-scale structure to be resolved. The Parkes data were obtained in the 1990's with beamwidth of 16.6′ and rms noise of 30 mJy beam^{-1}. As described in Hughes et al. (2006, 2007), the resulting combined 21-cm mosaic image of the LMC has a resolution of $\sim 40''$ and a sensitivity of ~ 0.3 mJy beam^{-1}. Hughes at al. (2007) developed a pioneering technique for the more efficient cleaning of the side-lobes which are mainly created by strong sources such as 30 Doradus.

Similar ATCA/Parkes mosiac images have been created from observations at 4.8 and 8.6 GHz (λ=6 and 3 cm) during the period between 2001 and 2003 by Dickel et al. (2005). Their 4.8 GHz image has a FWHM of 33″ while the 8.6 GHz image has a FWHM of 20″. Our analysis of these images shows a rms noise of 0.36 and 0.55 mJy beam^{-1} at 4.8 and 8.6 GHz, respectively. The original data were also re-processed by A. Hughes using the same technique as discussed in Hughes et al. (2007).

In our analysis, we also make use of radio surveys at 843 MHz made with the Molonglo Observatory Synthesis Telescope (MOST). This survey of the Magellanic Clouds has an angular resolution of 45″ and a sensitivity of 0.7 mJy beam^{-1}. Since this image covers the largest portion of sky second only to the 1.4 GHz image, its area represents the boundary limits for our catalogue. For more details, see Turtle and Amy (1991).

The above radio images were analyzed one by one using the IMSAD task, which is part of the MIRIAD software suite. We initially selected all 1.4 GHz point sources with gaussian peak fluxes greater than 5σ (1.5 mJy beam^{-1}). The resulting list from IMSAD were compared to those obtained using the 843 MHz, 4.8 and 8.6 GHz images with their respective 3σ cutoff values. A preliminary point source catalogue was obtained for those 1.4 GHz sources having at least one co-identification within 10″ at another frequency. The extent of the catalogue limited by the MOST observation region is RA (J2000)=$06^h11^m00^s$ to $04^h29^m00^s$ and DEC(J2000)=– $64^0 59' 00''$ to –$72^0 49' 30''$. This initial list contained 2682 objects.

Each source was numbered and labeled using Karma's KVIS tool, which allowed for individual inspection. Sources that were extended at 1.4 GHz were excluded as well as those sources that appeared to be noise artefacts. The search area included the central portion of the LMC, although most sources there were extended, not appearing to be consistent with being point sources.

Using these latest images of the LMC we have found co-identifications with 56 previously identified radio SNRs from Filipović et al. (1998) and an additional 20 candidate SNRs based on location, radio intensity, size and morphology. More details about the LMC SNRs study will be presented in the follow-up papers.

3. RESULTS

Using the methods described above, we were able to create a refined list containing 1988 sources. 1.4 GHz flux densities (based on peak flux) range from 1.5 mJy to 1.5 Jy. Using available flux densities (S_ν) at all frequencies (ν), individual spectral indices ($S_\nu \propto \nu^\alpha$) for each source were determined. From these we determined an average spectral index (α) of -0.53 (SD= 0.93). Further analysis will most likely narrow this range as this list is compared to other known sources within the LMC.

In Fig. 1, we show a histogram of the spectral indices for the strongest 100 point sources in our catalog. For these sources we see a symmetric curve indicating that the majority of them have indices between –0.8 and –1.0. The values range between indices of 0.2 and –2.2 and compare reasonably to a similar histogram of background objects in the direction of the SMC as shown in Fig. 1 of Payne et al. (2004).

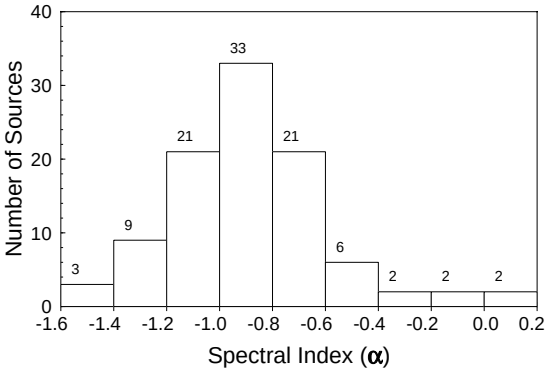

Fig. 1. *Histogram of spectral indices for the strongest 100 point radio sources in the field of the LMC. Only one object is outside of this graph range at α=–2.2.*

Table 1 gives source position (J2000; given in R.A. and Dec.), flux densities at 1.4 GHz, 843 MHz, 4.8 GHz and 8.6 GHz (given in Jy) and corresponding radio spectral index for the strongest 100 objects in the field of the LMC at 1.4 GHz. We show their positions in Fig. 2 (crosses). As expected, these sources cover the transparent region of the LMC evenly.

The expected background integral source count at 1.4 GHz was obtained by interpolating polynominial fits (log N – log S) given by Wall (1994). These fits give the predicted number of background sources in the observed field. For 1.4 GHz, given a 5σ cut-off of 1.5 mJy and a sky coverage of ~ 32 square degrees[1], we expect to find 1960 background sources. This compares well to the 1988 sources reported here, especially since further comparisons with catalogs at other wavelengths will most likely eliminate a few more sources.

[1]This represents the transparent region of the 843 MHz map in the direction of the LMC.

Table 1. Catalogue of the strongest 100 point sources in the field of the LMC at 1.4 GHz.

R.A. (J2000.0)	Dec. (J2000.0)	1.4 GHz (Jy)	843 MHz (Jy)	4.8 GHz (Jy)	8.6 GHz (Jy)	Spectral Index (α)
05:15:37.55	-67:21:28.1	1.477	2.27	0.5502	0.3548	–0.80
06:00:05.11	-70:38:34.0	0.4854	0.9202	–	–	–1.26
05:45:54.05	-64:53:34.8	0.4593	0.6791	–	–	–0.77
05:28:10.63	-65:03:52.8	0.4487	0.6484	–	–	–0.73
05:16:41.55	-71:49:05.3	0.3528	0.4766	0.1591	0.1144	–0.62
04:49:03.04	-70:52:04.6	0.3395	0.5204	0.1342	0.09757	–0.73
05:32:54.25	-72:31:54.7	0.3013	0.4891	–	–	–0.96
05:15:24.12	-65:58:41.1	0.2962	0.5108	0.07576	0.03643	–1.13
06:01:11.33	-70:36:08.3	0.2347	0.3005	–	–	–0.49
05:29:30.11	-72:45:28.6	0.2294	0.262	–	–	–0.26
05:16:37.78	-72:37:07.6	0.2224	0.323	–	–	–0.74
05:52:05.93	-68:14:41.3	0.2219	0.3716	0.06859	0.04017	–0.96
05:29:51.49	-67:49:33.2	0.2121	0.3251	–	0.04381	–0.86
05:44:27.14	-71:55:26.7	0.209	0.3359	0.05635	0.02649	–1.10
04:46:11.45	-72:05:11.7	0.1865	0.2755	–	–	–0.77
06:00:02.78	-71:42:06.2	0.1825	0.3193	–	–	–1.10
06:01:35.23	-69:55:45.2	0.1788	0.2933	–	–	–0.98
05:05:01.10	-66:45:18.2	0.1751	0.3338	0.04099	0.01991	–1.21
05:43:15.13	-68:06:52.0	0.1686	0.3298	0.03978	0.02182	–1.17
05:33:44.77	-72:16:24.4	0.1554	0.1701	–	–	–0.18
05:52:34.69	-66:40:41.6	0.1456	0.2902	–	–	–1.40
04:49:38.98	-65:05:02.0	0.1436	0.2409	–	–	–1.02
05:12:13.41	-72:32:47.4	0.1414	0.4356	–	–	–2.20
05:55:16.04	-67:20:51.1	0.1388	0.2429	–	–	–1.10
04:37:44.59	-72:27:50.0	0.1354	0.1933	–	–	–0.70
05:22:29.45	-70:37:55.0	0.1336	0.2112	0.04991	0.03348	–0.79
04:37:04.43	-71:48:19.6	0.1321	0.2365	–	–	–1.15
04:59:40.36	-69:55:03.7	0.1268	0.2037	0.03978	0.01401	–1.11
05:59:57.73	-71:20:36.0	0.1258	0.2581	–	–	–1.42
04:36:55.13	-69:30:33.1	0.1256	0.1943	–	–	–0.86
04:56:08.72	-70:14:33.8	0.1256	0.1903	0.1527	0.1294	–0.09
04:58:45.37	-72:50:24.7	0.1229	0.157	–	–	–0.48
05:44:38.33	-65:34:54.2	0.1201	0.218	–	–	–1.18
04:44:51.16	-67:46:36.2	0.1198	0.1967	–	–	–0.98
04:45:12.98	-65:47:07.9	0.1148	0.1737	–	–	–0.82
05:56:32.25	-71:29:06.0	0.1109	0.1804	0.03382	0.02142	–0.93
05:01:39.04	-66:25:25.4	0.1094	0.1045	0.04726	0.02491	–0.63
05:18:40.68	-65:36:14.8	0.1087	0.2151	–	–	–1.35
04:44:16.21	-68:42:11.8	0.1081	0.1571	–	–	–0.74
05:51:30.41	-69:16:31.0	0.1063	0.1736	0.03496	0.02236	–0.89
04:38:51.46	-68:22:58.5	0.1049	0.1641	–	–	–0.88
05:05:51.39	-69:51:17.4	0.1012	0.1487	0.05908	0.04966	–0.46
06:00:35.26	-70:12:18.4	0.09992	0.1434	–	–	–0.71
05:08:31.35	-67:06:16.4	0.09891	0.1666	0.03379	0.02128	–0.88
05:47:45.43	-67:45:06.2	0.0956	0.1548	0.05575	0.03996	–0.55
05:05:36.10	-70:05:14.8	0.09407	0.1571	0.02918	0.01682	–0.96
05:00:36.49	-72:06:23.5	0.09076	0.1406	0.03057	0.01716	–0.90
06:04:36.08	-71:02:23.6	0.09023	0.1273	–	–	–0.68
05:05:31.12	-65:55:15.7	0.08999	0.1409	0.03114	0.01756	–0.89
05:04:02.36	-72:03:45.5	0.08952	0.132	0.03226	0.01587	–0.90

Table 1. Catalogue of the strongest 100 point sources at 1.4 GHz (Continued).

R.A. (J2000.0)	Dec. (J2000.0)	1.4 GHz (Jy)	843 MHz (Jy)	4.8 GHz (Jy)	8.6 GHz (Jy)	Spectral Index (α)
05:05:39.65	-71:07:40.2	0.08849	0.138	0.03396	0.01994	–0.82
05:51:40.46	-68:43:09.5	0.08817	0.1457	0.02994	0.02247	–0.82
06:01:41.28	-72:38:32.5	0.0864	0.1225	–	–	–0.69
05:43:17.55	-66:26:55.6	0.08633	0.05501	0.09289	0.09518	0.19
04:40:08.66	-71:57:18.2	0.08249	0.1083	–	–	–0.54
04:53:37.89	-68:29:27.8	0.08134	0.1089	0.05749	0.05211	–0.31
04:43:18.45	-66:52:04.9	0.07911	0.1038	–	–	–0.54
05:21:27.37	-65:21:40.3	0.0778	0.126	–	–	–0.95
04:43:15.50	-66:02:48.5	0.07735	0.1349	–	–	–1.10
04:51:19.90	-72:21:07.4	0.07439	0.1242	–	–	–1.01
05:41:32.78	-67:06:15.7	0.07283	0.1241	0.0225	0.01355	–0.95
05:56:13.83	-69:23:31.7	0.07255	0.1179	–	–	–0.96
05:07:10.63	-71:44:04.8	0.07184	0.1414	0.009675	–	–1.56
05:36:36.32	-67:07:35.0	0.07069	0.1199	0.02514	–	–0.89
05:54:22.23	-67:54:50.8	0.06796	0.1138	–	–	–1.02
04:55:51.47	-69:02:10.4	0.06759	0.07879	–	0.09049	0.09
05:09:31.11	-67:31:16.0	0.06748	0.09819	0.02745	0.02201	–0.66
04:58:46.33	-67:05:38.5	0.06663	0.1061	0.02556	0.01788	–0.77
05:48:45.09	-65:53:49.6	0.06527	0.1097	0.01753	0.007036	–1.16
05:31:24.31	-65:16:34.0	0.06496	0.1088	–	–	–1.02
04:42:11.81	-68:10:03.9	0.0645	0.08777	–	–	–0.61
05:46:44.39	-66:41:14.2	0.06351	0.1038	0.02143	0.01385	–0.87
05:46:36.81	-72:05:54.8	0.06315	0.08177	0.03052	0.01494	–0.70
05:32:53.02	-67:09:42.0	0.06214	0.099	0.02105	0.0115	–0.92
05:07:35.95	-71:52:34.6	0.06178	0.1044	0.01883	0.01067	–0.98
05:19:28.01	-65:27:03.6	0.06149	0.1033	–	–	–1.02
05:49:01.77	-71:20:11.4	0.0607	0.09022	0.02295	0.01599	–0.75
05:07:17.62	-66:56:46.8	0.06061	0.1001	0.0193	0.01044	–0.96
04:53:33.06	-70:40:27.2	0.05927	0.1036	0.02467	0.01444	–0.82
05:55:01.85	-69:51:46.5	0.05892	0.1053	0.01232	–	–1.24
05:52:08.74	-70:31:30.2	0.05886	0.1049	0.01428	0.007234	–1.15
04:52:56.95	-65:28:13.7	0.05784	0.09686	–	–	–1.02
05:42:41.91	-66:02:57.5	0.0578	0.08926	0.02161	0.01046	–0.90
05:06:34.32	-67:56:43.7	0.05736	0.09587	0.01923	0.01353	–0.85
05:55:11.20	-69:47:51.4	0.05732	0.09435	0.01808	0.009905	–0.96
05:41:27.27	-67:39:52.5	0.05719	0.1076	0.01316	–	–1.21
05:02:27.66	-65:57:11.7	0.05633	0.09523	0.01758	0.007245	–1.07
05:14:07.63	-70:40:58.1	0.05559	0.09152	0.0139	0.004549	–1.26
05:21:27.62	-67:07:23.3	0.05531	0.08736	0.02026	0.01078	–0.88
05:56:53.22	-68:22:28.4	0.0546	0.1028	–	–	–1.25
05:20:22.04	-72:44:44.7	0.05448	0.09054	–	–	–1.00
05:12:30.38	-68:28:05.8	0.05408	0.07479	0.02454	0.01354	–0.72
05:10:27.20	-69:32:09.1	0.05404	0.08677	0.01762	0.01143	–0.88
05:18:13.26	-71:38:07.3	0.05333	0.07372	0.02262	0.01212	–0.76
05:46:59.84	-65:35:00.9	0.05322	0.09416	–	–	–1.12
05:51:05.04	-71:06:10.2	0.05313	0.09359	0.01655	0.01005	–0.96
05:10:57.94	-65:29:34.2	0.05311	0.0727	–	–	–0.62
06:03:47.39	-69:29:43.2	0.05301	0.08889	–	–	–1.02
04:58:37.24	-67:12:44.2	0.0523	0.9973	0.01316	0.003353	–1.39
05:04:09.69	-67:01:10.8	0.05176	0.1005	0.0117	0.00481	–1.29

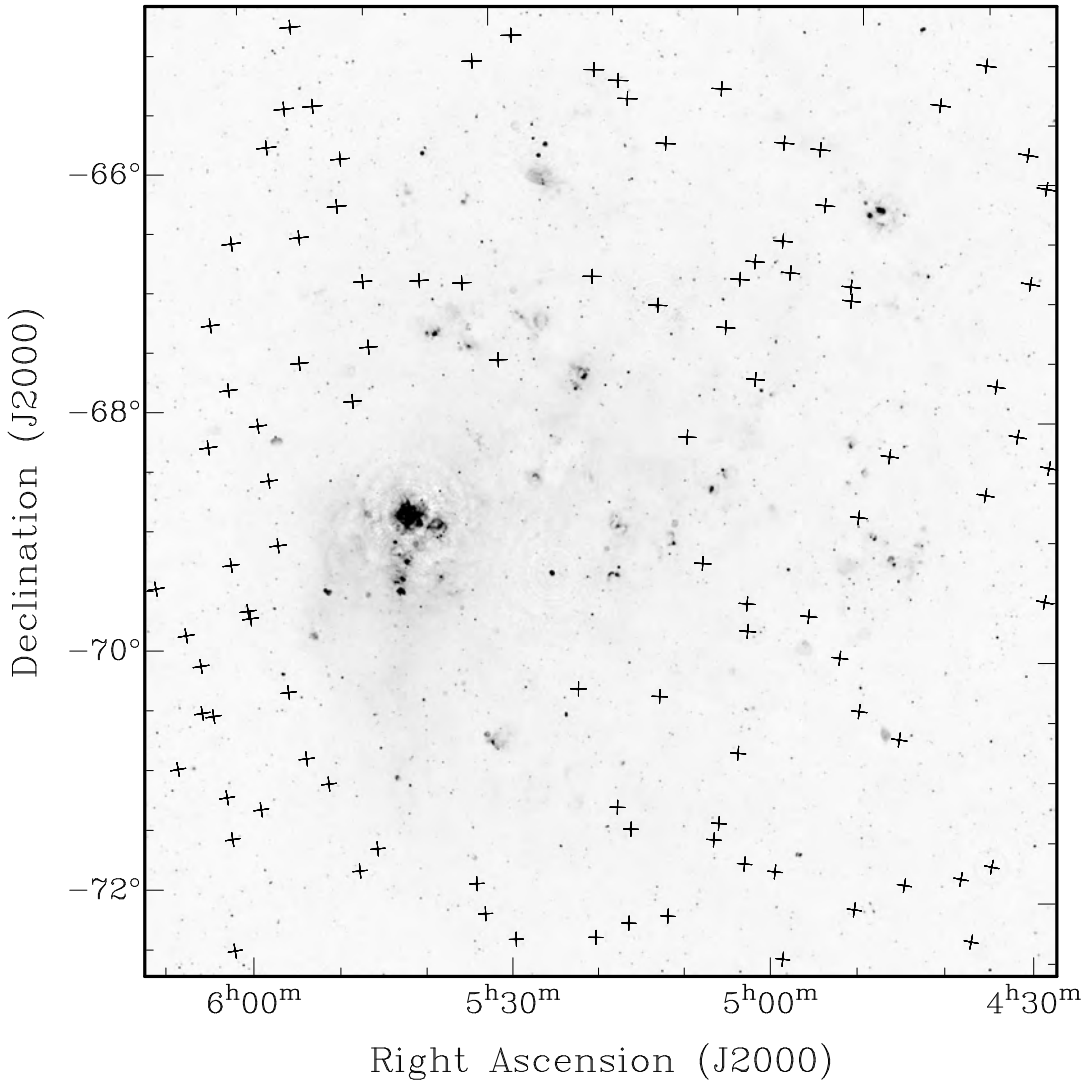

Fig. 2. *Strongest 100 radio point sources (crosses) overlying the 1.4 GHz radio image of the LMC. This image has a sensitivity of* ~ 0.3 *mJy beam*$^{-1}$ *and a resolution of 40″.*

4. CONCLUDING REMARKS AND SUMMARY

As the LMC is relatively transparent in radio, background radio galaxies and quasars are seen throughout except for the densest regions. Most likely, some of these objects may alternatively represent compact H II regions, microquasars, small SNRs and radio planetary nebulae. Comparisons with catalogues including these objects will be necessary before the completion of the final catalogue.

We present here the strongest 100 sources from a preliminary analysis of a 1.4 GHz ATCA/Parkes mosiac image created by Hughes et al. (2007). The refined list contains 1988 point objects having an average spectral index of –0.53; this list will be the subject of a future more comprehensive paper.

Acknowledgements – We used the Karma / MIRIAD software package developed by the ATNF. The Australia Telescope Compact Array is part of the Australia Telescope, which is funded by the Commonwealth of Australia for operation as a National Facility managed by CSIRO.

REFERENCES

Dickel, J. R., McIntyre, V. J., Gruendl, R. A., Milne, D.: 2005, *Astron. J.*, **129**, 790.
Filipović, M. D., Haynes, R. F., White, G. L., Jones, P. A.: 1998, *Astron. Astrophys. Suppl. Series*, **130**, 421.
Filipović, M. D., Haynes, R. F., White, G. L., Jones, P. A., Klein, U., Wielebinski, R.: 1995, *Astron. Astrophys. Suppl. Series*, **111**, 311.
Hughes, A., Staveley-Smith, L., Kim, S., Wolleben, M., Filipović, M. D.: 2007, *Mon. Not. R. Astron. Soc.*, **382**, 543.
Hughes, A., Wong, T., Ekers, R., Staveley-Smith, L., Filipović, M., Maddison, S., Fukui, Y., Mizuno, N.: 2006, *Mon. Not. R. Astron. Soc.*, **370**, 363.
Payne, J. L., Filipović, M. D., Reid, W., Jones, P. A., Staveley-Smith, L., White, G. L.: 2004, *Mon. Not. R. Astron. Soc.*, **355**, 44.
Sault, B., Killeen, N.: 2006, MIRIAD Users Guide, Australia Telescope National Facility.
Turtle, A. J., Amy, S. W.: 1991, *IAU Symp.*, **148**, 114.
Wall J. V.: 1994, *Aust. J. Phys.*, **47**, 625.

100 НАЈСНАЖНИЈИХ ТАЧКАСТИХ РАДИО-ИЗВОРА У ВЕЛИКОМ МАГЕЛАНОВОМ ОБЛАКУ НА 1.4 GHz

J. L. Payne[1], L. A. Tauber[1], M. D. Filipović[2], E. J. Crawford[2] and A. Y. De Horta[2]

[1] *Centre for Astronomy, James Cook University*
Townsville QLD, 4811, Australia

E–mail: *snova4@msn.com*

[2] *University of Western Sydney, Locked Bag 1797*
Penrith South, DC, NSW 1797, Australia

УДК 52–13–77 : 524.722.3
Стручни чланак

У овој студији представљамо 100 најснажнијих тачкастих радио-извора са наше нове мозаик слике Великог Магелановог Облака (ВМО) на фреквенцији од 1.4 GHz. Посматрања коришћена у овој студији сакупљена су у последњих 10 година на ATCA телескопу, а такође су допуњена са подацима добијеним са Паркс 64-м телескопа. Иницијална листа објеката у кругу од $10''$ на фреквенцијама од 0.843, 4.8 и 8.6 GHz састоји се од 2682 радио-извора. Елиминацијом нетачкастих објеката и артефаката шума дошло се до редукованог каталога од 1988 тачкастих радио-објеката. Већина ових објеката су највероватније позадински објекти, као што су квазари или активна галактичка језгра, која се виде кроз прозрачне делове ВМО. Веома мали проценат ових објеката представља објекте у самом ВМО као што су HII региони, млади остаци супернових и радио-планетарне маглине. Нашли смо да је средњи спектрални индекс за ових 100 најснажнијих радио-извора $\alpha = -0.53$. Такође представљамо и расподелу ових 100 објеката у пољу ВМО на 1.4 GHz.

A.3 Related Paper 3

Filipović, M. D., Cohen, M., Reid, W. A., Payne, J. L., Parker, Q. A., Crawford, E. J., Bojičić, I. S., De Horta, A. Y., Hughes, A., Dickel, J., and Stootman, F. (2009). Radio planetary nebulae in the Magellanic Clouds. *MNRAS*, 399:769–777

My contribution was to assist in the data collection and analysis. This is a 10% contribution.

Mon. Not. R. Astron. Soc. **399,** 769–777 (2009) doi:10.1111/j.1365-2966.2009.15307.x

Radio planetary nebulae in the Magellanic Clouds

M. D. Filipović,[1⋆] M. Cohen,[2] W. A. Reid,[3] J. L. Payne,[1] Q. A. Parker,[3] E. J. Crawford,[1] I. S. Bojičić,[3] A. Y. De Horta,[1] A. Hughes,[4,5] J. Dickel[6] and F. Stootman[1]

[1]*University of Western Sydney, Locked Bag 1797, Penrith South DC, NSW 1797, Australia*
[2]*Radio Astronomy Laboratory, University of California, Berkeley, CA 94720, USA*
[3]*Department of Physics, Macquarie University, Sydney, NSW 2109, Australia*
[4]*Swinburne University of Technology, Hawthorn, VIC 3122, Australia*
[5]*CSIRO Australia Telescope National Facility, PO Box 76, Epping, NSW 1710, Australia*
[6]*Department of Physics and Astronomy, University of New Mexico, 800 Yale Blvd NE, Albuquerque, NM 87131, USA*

Accepted 2009 June 24. Received 2009 June 23; in original form 2009 March 30

ABSTRACT

We report the extragalactic radio-continuum detection of 15 planetary nebulae (PNe) in the Magellanic Clouds (MCs) from recent Australia Telescope Compact Array+Parkes mosaic surveys. These detections were supplemented by new and high-resolution radio, optical and infrared observations which helped to resolve the true nature of the objects. Four of the PNe are located in the Small Magellanic Cloud (SMC) and 11 are located in the Large Magellanic Cloud (LMC). Based on Galactic PNe the expected radio flux densities at the distance of the LMC/SMC are up to ∼2.5 and ∼2.0 mJy at 1.4 GHz, respectively. We find that one of our new radio PNe in the SMC has a flux density of 5.1 mJy at 1.4 GHz, several times higher than expected. We suggest that the most luminous radio PN in the SMC (N S68) may represent the upper limit to radio-peak luminosity because it is approximately three times more luminous than NGC 7027, the most luminous known Galactic PN. We note that the optical diameters of these 15 Magellanic Clouds (MCs) PNe vary from very small (∼0.08 pc or 0.32 arcsec; SMP L47) to very large (∼1 pc or 4 arcsec; SMP L83). Their flux densities peak at different frequencies, suggesting that they may be in different stages of evolution. We briefly discuss mechanisms that may explain their unusually high radio-continuum flux densities. We argue that these detections may help solve the 'missing mass problem' in PNe whose central stars were originally 1–8 $M_{\odot}$. We explore the possible link between ionized haloes ejected by the central stars in their late evolution and extended radio emission. Because of their higher than expected flux densities, we tentatively call this PNe (sub)sample – 'Super PNe'.

Key words: planetary nebulae: general – Magellanic Clouds – infrared: galaxies – radio-continuum: galaxies – radio continuum: ISM.

1 INTRODUCTION

Planetary nebulae (PNe) possess ionized, neutral, atomic, molecular and solid states of matter in diverse regions with different temperature, density and morphological structure. Their physical environments range in temperature from 10^2 K to greater than 10^6 K. Although these objects radiate from the X-ray to the radio, detected structures are influenced by selection effects due to intervening dust and gas, instrument sensitivity and distance (see the more specific discussions by Dgani & Soker 1998; Kwok 2005).

Radio-continuum surveys of PNe in the MCs potentially offer a flux-limited sample that could provide absolute physical attributes such as fluxes, emission measures and spectral energy distributions (SEDs) (e.g. Zijlstra, van Hoof & Perley 2008). These in turn are relevant to the major issues of PN evolution, although MC PNe provide very limited information on morphology.

Most known PNe are weak thermal radio sources, and although morphologies of these radio objects are similar to their optical counterparts, radio interferometric observations allow us to image the structure of a PNe's ionized component. A spherically symmetric uniform-density PNe has an ionized mass, $M_{\rm i}$, that can be expressed as

$$M_{\rm i} = 282\,(D_{\rm kpc})^2\,F_5(n_{\rm e})^{-1}\,{\rm M}_{\odot}, \quad (1)$$

⋆E-mail: m.filipovic@uws.edu.au

where $D_{\rm kpc}$ is distance (kpc), F_5 is radio flux density at 5 GHz (Jy) and $n_{\rm e}$ represents electron density (cm^{-3}) derived from forbidden-line ratios (Kwok 2000). In cases where the PNe distance is unknown, this equation can be inverted to provide a crude but useful distance estimate (Mezger & Henderson 1967, Appendix A, equation A14). For example, adopting a 5 GHz flux density of 25 mJy and $T_{\rm e} = 10^4$ K gives an ionized gas mass of $0.0022 \times D_{\rm kpc}^{2.5}\,{\rm M}_\odot$. Assuming a mean PNe ionized mass of 0.1 to 0.25 $\rm M_\odot$ allowed Cohen et al. (2005) to estimate that the distance to G313.3+00.3 lies between 4.6 and 6.6 kpc. However, this distance range may not be always valid as equation (1) may not be always applicable. For example, some PNe such as NGC 7027, the brightest PN in the radio sky, exhibit an ionized mass of 0.057 $\rm M_\odot$ (Beintema et al. 1996). At the other extreme, large PNe have masses up to 0.5 $\rm M_\odot$ or sometimes well above.[1] Therefore, we point that equation (1) is valid only if PN is optically thin, but this will be true in the large majority of cases.

The study of extragalactic PNe has the advantage that their distance is known with much greater certainty than those of Galactic PNe. Centimetre radio emission from PNe can also be used to estimate interstellar extinction by comparing radio and optical Balmer-line fluxes (Luo, Condon & Yin 2005). The study of radio PNe at a known distance allows us to better understand the properties of PNe in our own Galaxy, and ultimately to refine methods of estimating their distances. We also point out that PNe may even reflect conditions inherent in their host galaxies. However, there is consistency in the bright-end cut-off of the PN Luminosity Function (PNLF) regardless of the galaxy type (Herrmann et al. 2008).

We present the first complete sample ($S_i > 1.5$ mJy) in the radio continuum of confirmed extragalactic PNe. Further analysis depends heavily on a variety of new, high-resolution and time-consuming observations which are underway.

2 RADIO DATA

The large majority of known Galactic PNe are weak but detectable radio-continuum objects. Their thermal radio emission is a useful tracer of nebular ionization. Because centimetre-wavelength radiation is not extinguished by dust grains, the observed emission should be a good representation of the conditions in the PNe. For these reasons, large-scale radio surveys, surveys of nearby galaxies such as the MCs, may serve as a perfect example for the detection of radio-continuum PNe outside of our own Milky Way.

In the past decade, several Australia Telescope Compact Array (ATCA) moderate-resolution surveys of the MCs have been completed. Deep ATCA and Parkes radio-continuum (Filipovic et al. 1995, 1997) and snap-shot surveys of the Small Magellanic Cloud (SMC) were conducted at 1.42, 2.37, 4.80 and 8.64 GHz by Filipović et al. (2002, 2005) and Payne et al. (2004), achieving sensitivities of 1.8, 0.4, 0.8 and 0.4 mJy beam^{-1}, respectively. The maps have angular resolutions of 98 arcsec, 40 arcsec, 30 arcsec and 15 arcsec at the frequencies listed above. New complete mosaics of the SMC at 4.80 and 8.64 GHz (both at sensitivities of 0.5 mJy beam^{-1}) have recently been completed by Dickel et al. (2009) and Filipovic et al. (2009). Also, Mao et al. (2008) presented a new 20-cm ATCA mosaic survey of the SMC with a resolution of 18×11 arcsec^2, which is well suited for initial PNe detection as the PNe appear as point sources.

For the Large Magellanic Cloud (LMC), a new moderate-resolution (40 arcsec; sensitivity $\sim$0.6 mJy beam^{-1}) ATCA+Parkes survey by Hughes et al. (2006, 2007) and Payne et al. (2009) at 1.4 GHz ($\lambda = 20$ cm) complements ATCA+Parkes mosaic images at 4.8 and 8.64 GHz obtained by Dickel et al. (2005). For these observations, the 4.8 GHz total intensity image has a full width at half-maximum (FWHM) of 33 arcsec while the 8.64 GHz image has a FWHM of 20 arcsec. Both have sensitivities of $\sim$0.5 mJy beam^{-1} and positional uncertainties for all three radio-continuum maps of the LMC are less than 1 arcsec.

In addition to the ATCA+Parkes surveys, we also searched the 843 MHz Sydney University Molonglo Sky Survey [SUMSS; resolution $\sim$45 arcsec, sensitivity $\sim$2 mJy; Bock, Large & Sadler 1999] for sources co-incident with known catalogued PNe. We also searched the specific MOlonglo Synthesis Telescope (MOST) observations of the SMC presented by Turtle et al. (1998).

From these mosaic surveys a collection of targets was selected for follow up observation. In several sessions since 2006, we have observed five of these PNe with the ATCA (project C1604) in 'snap-shot' mode at 4.8 and 8.64 GHz achieving resolutions as high as 1 arcsec. With this resolution, we expect that the larger PNe, such as SMP L83, might be resolved, but most PNe will still appear unresolved. These five PNe are marked with an asterisk (*) in Table 1 (Column 1).

3 METHOD AND RESULTS

The radio-continuum surveys described in Section 2 were initially searched within 2 arcsec of known optical PNe for co-identifications. In the SMC, PNe lists given by Morgan (1995, his table 3) and Jacoby & De Marco (2002, their table 4) contain a total of 139 PNe. We found four radio sources (3 per cent) that were spatially coincident with the PNe: JD 04 (Fig. 1, left-hand panel), SMP S11 (Fig. 2; left-hand panel), SMP S17 (Fig. 1; right-hand panel) and N S68 (Fig. 2; right-hand panel). For more details see Table 1. We refer to the PNe using the names listed in Jacoby & De Marco (2002). Three other previously classified PNe, MA 1796, MA 1797 (Meyssonnier & Azzopardi 1993) and MG 2 (Morgan 1995), also appear to be coincident with the corresponding radio sources. However, Stanghellini et al. (2003) found that these three sources are in fact ultra-compact H II regions and not bona fide PNe. We also note that the radio flux densities for these three objects are much higher than reported here for MC radio PNe. Another previously classified PN in the SMC known as JD 26 was also detected across the range of our radio frequencies but after close examination we re-classified this object as an H II region.

Within the LMC, we found 11 co-identifications using optical PNe catalogues presented by Leisy et al. (1997) and Reid & Parker (2006a,b). The catalogue by Leisy et al. (1997) contains accurate positions and finding charts for $\sim$280 LMC PNe compiled from all major surveys prior to 1997. More recent catalogues presented by Reid & Parker (2006a,b) identify $\sim$629 LMC PNe and PNe candidates, classified into three groups: True (T), Likely (L) and Possible (P). All of our 11 co-identifications are classified type 'T'. We note that there are 11 other radio-continuum sources in the LMC previously classified by Reid & Parker (2006a) as PNe or candidates. Namely, two sources were classified as true (RP 1534 and RP 105), three as likely (RP 872, RP 993 and RP 1541) and six as possible (RP 641, RP 1113, RP 1495, RP 1716, RP 1933 and RP 2194). Reid & Parker (2009) eliminated RP 1534 and RP 105

[1] Masses up to 4 $\rm M_\odot$ are achievable due to the interstellar medium (ISM) sweep-up (Wareing, Zijlstra & O'Brien 2007), the outer shell comes to a stand-still when the ejected mass has been swept up about 10 times.

Table 1. Radio PN candidates in the SMC and LMC. Asterisk (⋆) in Column 1 indicates that PN is observed with the ATCA high-resolution mode at 6/3 cm. The positions given in Columns 2 and 3 are from the detection at highest radio frequency. The errors in flux densities at all frequencies (Columns 4–8) are flux dependent and they are <10 per cent (Filipović et al., in preparation). Optical fluxes (Column 11) are taken from Reid & Parker (in preparation). Optical diameter (Column 12) is taken from Shaw et al. (2006) except for SMP L25 and L33.

ATCA radio source name	RA (J2000.0)	Dec. (J2000.0)	$S_{843\,\mathrm{MHz}}$ (mJy)	$S_{1.4\,\mathrm{GHz}}$ (mJy)	$S_{2.37\,\mathrm{GHz}}$ (mJy)	$S_{4.8\,\mathrm{GHz}}$ (mJy)	$S_{8.64\,\mathrm{GHz}}$ (mJy)	$\alpha \pm \Delta\alpha$	MIR/ $S_{1.4\,\mathrm{GHz}}$	Hα flux (10^{-13} erg cm^{-2} s^{-1})	Optical D (arcsec)	Optical[a] PN name
SMCPN J004336-730227	00 43 36.54	−73 02 27.1	5.9	5.1	5.0	4.4	3.1	-0.3 ± 0.2	3	–	?	JD 04
SMCPN J004836-725802⋆	00 48 36.58	−72 58 02.0	–	1.9	2.0	2.6	2.4	$+0.1 \pm 0.2$	25	–	?	SMP S11
SMCPN J005156-712442	00 51 55.20	−71 24 42.5	–	1.4	<1.2	1.5	<1.2	$+0.1 \pm 0.4$	7	–	?	SMP S17
SMCPN J005842-722716⋆	00 58 42.89	−72 27 16.5	2.0	2.3	3.5	4.1	4.2	$+0.4 \pm 0.2$	22	–	?	N S68
LMCPN J045013-693352	04 50 13.28	−69 33 52.7	<1.5	<1	–	<1.5	2.2	–	22	–	?	SMP L8
LMCPN J050624-690320	05 06 24.22	−69 03 20.1	<1.5	1.8	–	2.1	2.4	$+0.2 \pm 0.3$	11	12.43	0.44×0.40	SMP L25
LMCPN J051009-682955	05 10 09.38	−68 29 55.1	<1.5	<1	–	<1.5	1.8	–	9	5.563	0.69×0.53	SMP L33
LMCPN J051142-683459	05 11 42.11	−68 34 59.1	<1.5	2.3	–	<1.5	<1.5	–	3	1.940	0.60×0.55	SMP L39
LMCPN J051954-693104⋆	05 19 54.51	−69 31 04.5	2.3	2.2	–	2.1	2.3	0.0 ± 0.2	10	8.635	0.45×0.32	SMP L47
LMCPN J052009-695339⋆	05 20 09.62	−69 53 39.4	<1.5	1.6	–	1.5	<1	-0.1 ± 0.4	11	9.428	0.40×0.35	SMP L48
LMCPN J052455-713255	05 24 55.31	−71 32 55.0	<1.5	2.5	–	2.1	1.8	-0.2 ± 0.2	3	14.82	0.59×0.41	SMP L62
LMCPN J053329-715227	05 33 29.09	−71 52 27.2	4.0	3.0	–	<1.5	<1.5	-0.6 ± 0.4	–-	–	0.79×0.63	SMP L74
LMCPN J053620-671807⋆	05 36 20.69	−67 18 07.9	2.4	1.6	–	0.9	0.7	-0.5 ± 0.2	1	5.375	3.98×3.63	SMP L83
LMCPN J053653-715339	05 36 53.46	−71 53 39.3	<1.5	1.6	–	<1.5	<1.5	–	2	–	0.57×0.48	SMP L84
LMCPN J054237-700930	05 42 37.17	−70 09 30.4	<1.5	3.1	–	2.6	2.8	-0.1 ± 0.2	9	7.201	0.51×0.45	SMP L89

[a]Explanation of abbreviations used: JD – Jacoby & De Marco (2002) and SMP – Sanduleak et al. (1978).

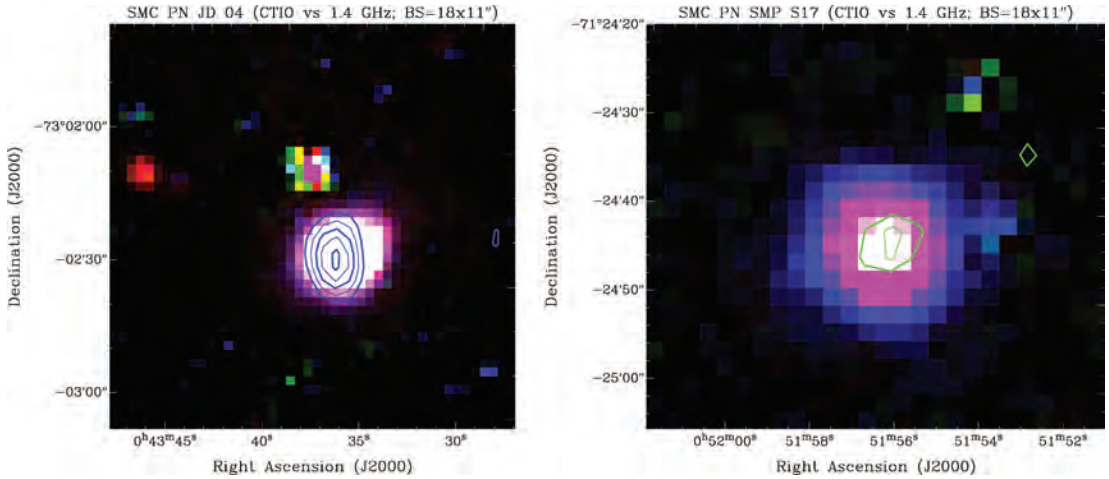

Figure 1. A composite optical image (RGB = Hα, [S II] and [O III], respectively, all continuum-subtracted) of two SMC PNe – JD04 (left-hand panel) and SMP S17 (right-hand panel) – overlaid with 1.4 GHz contours from Mao et al. (2008) mosaic survey. This optical image is from the Magellanic Cloud Emission Line Survey (MCELS) (Winkler et al., in preparation). The radio-continuum contours are from 1 mJy beam^{-1} in steps of 0.5 mJy beam^{-1}. The synthesized beam of 1.4 GHz survey is 18 × 11 arcsec^2. The larger optical extent of these two PNe is due to faint AGB haloes.

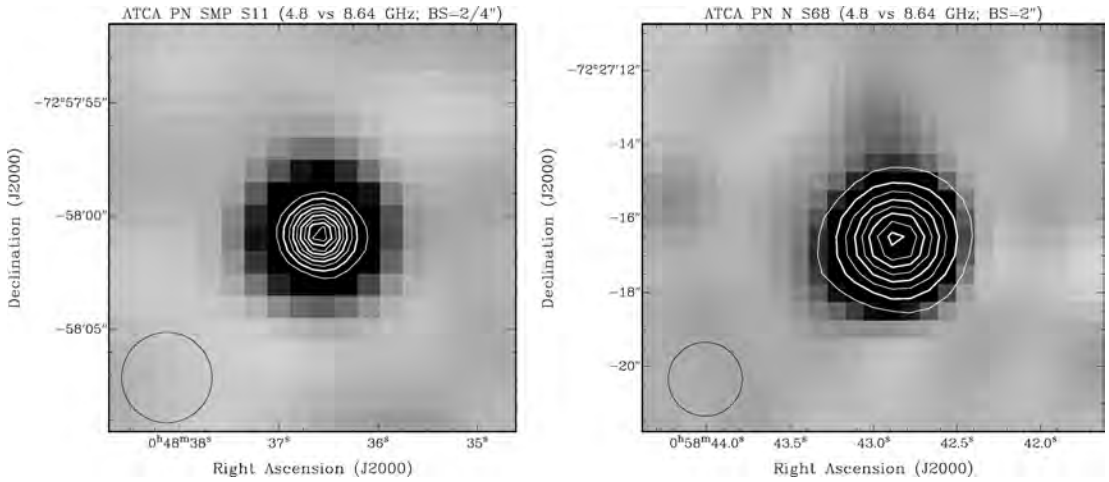

Figure 2. ATCA high-resolution radio-continuum images of two SMC PNe – SMP S11 (left-hand panel) and N S68 (right-hand panel). Grey scale images are at 4.8 GHz and overlaid contours are from 8.64 GHz observations. The radio-continuum contours from 8.64 GHz observations are at both images from 0.5 mJy beam^{-1} in steps of 0.5 mJy beam^{-1}. All images have rms noise (1σ) of the order of ∼0.1 mJy beam^{-1}. Both synthesized beams are circular (2/4 arcsec), and they are displayed as a black circle in the bottom left corner.

as being true PNe when the MIR data were examined. Eight of these 11 point sources have significantly higher than expected flux densities, in the range of 10–15 mJy, at 1.4 GHz. By applying multi-frequency criteria to these 11 candidates, including the higher than expected flux density, they were found to be compact H II regions. We suggest that an upper limit on radio flux density be included as a new parameter in the multi-frequency PNe selection criteria. More details about this post-facto classification will be given below and in our subsequent papers.

Finally, high-resolution imaging and spectra from a recent *Hubble Space Telescope* (*HST*) survey of 59 PNe in the MCs (Shaw et al. 2006) have 10 (all in the LMC) radio PNe matches (see Table 1, Column 11), displaying a wide range of morphologies. We note that our four PNe radio-continuum detections in the SMC are not yet observed with the *HST*.

We employed the 'shift technique' in order to estimate the possibility of false detections. We offset the positions of known optical PNe by 30 arcmin in each of four directions (±RA and ±Dec.) and counted the number of spurious identifications. We find only one false detection per Cloud, implying that at the most one of the cross-identification in each Cloud that we report here occurred by chance.

Table 1 summarizes our 15 radio detections coincident with known LMC and SMC PNe. We list ATCA radio source name, radio positions (J2000), flux densities at 843 MHz, 1.4 GHz, 2.37 GHz, 4.8 GHz and 8.64 GHz, spectral index [which is defined as α in $S_\nu \propto \nu^\alpha$, where (S_ν) is flux density and (ν) is frequency] and error, flux density ratio between *Spitzer* MIR at 8 μm and $S_{1.4\,\mathrm{GHz}}$, optical flux, optical diameter (arcsec) and optical name. None of these sources can be considered radio extended, given our radio resolutions and their expected sizes at the distance of the MCs. All 15 radio detections are within 1 arcsec of the best optical positions.

3.1 *Spitzer* detections and mid-infrared properties

True radio detections of MC PNe are dependent on accurate optical and IR identifications as PNe. For example, Sanduleak, MacConnell & Philip (1978) note that a faint star with strong Hα emission can

be misconstrued as a PN if its continuum lies below the sensitivity of the detector. Ultra-compact H II regions have also been confused with PNe and their paper lists examples of both in the LMC and in the SMC. Some of the optical counterparts among our radio-continuum PN candidates could, therefore, be confused with ultra-compact H II regions as shown by Stanghellini et al. (2003).

Compact H II regions and Symbiotics constitute a major contaminant in the search for PNe at all frequencies. However, the mid-infrared morphologies and false colours of H II regions are distinct from those of PNe (Cohen et al. 2007a,b). H II regions that are classified as compact or even ultra-compact are associated with MIR structures such as multiple filaments and/or haloes. Unlike PNe, the MIR morphology of H II regions is highly irregular. Their false colours [using IRAC bands 2 (4.5 μm), 3 (5.8 μm), 4 (8 μm) as blue, green and red, respectively] are generally white, indicative of thermal emission by warm dust grains rather than of fluorescent polycyclic aromatic hydrocarbon bands or molecular hydrogen lines that cause many PNe to appear orange or red.

We have cut out small regions of *Spitzer* IRAC images around each of the catalogued PNe with potential radio detections. For the LMC, these come from the enhanced products of the SAGE Legacy program (PID 20203) available at the Spitzer Science Center (SSC). For the SMC we downloaded the SSC IRAC mosaics recently available from the SMC SAGE Legacy program (PID 40245). Combining the above techniques with detailed scrutiny of the optical spectra (Reid & Parker 2006a) we have been able to reclassify the brightest radio detections of PNe candidates (those with flux densities above 10–15 mJy) in both Clouds as coming from H II regions rather than PNe.

Jacoby & De Marco (2002) list JD 04, SMP S11, SMP S17 and N S68 as previously known SMC PNe in their table 4, recovered by their 'blinking' technique using images obtained with an [O III] filter (on-band) and a nearby continuum filter (off-band). They identified objects as PNe if their diameters were less than 10 arcsec and the [O III] on-band image flux exceeded twice the off-band flux. We also detect these four objects in our *Spitzer* images and confirm the status for two (JD 04 and SMP S17) as bona fide PNe. The other two objects (SMP S11 and N S68) appear to have somewhat larger MIR/radio continuum (RC) ratio (see Section 4.2) and from the MIR perspective each could also be an ultra-compact H II region or an unusual PN.

SMP L8, 25, 33, 39, 47 (Fig. 3), 48 (Fig. 4), 62, 74 (Fig. 5), 83 (Fig. 6), 84 and 89 are originally listed as LMC PNe by Sanduleak et al. (1978) based on deep blue and red sensitive objective-prism plates taken from the Curtis Schmidt telescope at the Cerro Tololo Inter-American Observatory. These were originally obtained for other unrelated programs, and objects with no evidence of a continuum were selected. Nine of these 11 were confirmed spectroscopically by Reid & Parker (2006b), whilst the other three lie outside their sampled field. Shaw et al. (2006) presented comprehensive *HST* high resolution (spectra and images) of eight out of 11 LMC radio-continuum PNe. All 15 radio-continuum PNe detections exhibit canonical optical spectra leaving us in no doubt that they are indeed optical PNe. These criteria include the relative sizes and morphologies of nebulae in Hα and red continuum; the contrast between nebular and ambient Hα emission; and the presence and intensity ratios in the optical spectrum of forbidden lines, characteristic of PNe but not seen in H II regions. These are the attributes described by Reid & Parker (2006b). More than 10 of our radio detections are also confirmed as PNe from *HST* imaging (Shaw et al. 2006). Also, in the meantime, two other LMC PNe (SMP L25 and SMP L33) were observed with the *HST*. Bernard-Salas et al. (2008, 2009) have presented two *Spitzer* spectroscopic studies of a sample of 25 MC PNe from which we report here radio continuum for four objects (SMP L8, 62, 83 and SMP S11).

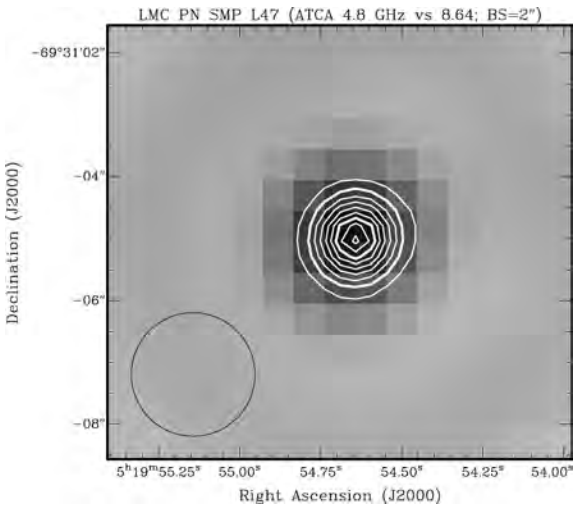

Figure 3. ATCA high-resolution radio-continuum image of the LMC PNe – SMP L47. Grey scale image is at 4.8 GHz and overlaid contours are from 8.64 GHz. The radio-continuum contours are from 0.3 mJy beam^{-1} in steps of 0.2 mJy beam^{-1}. Both images' rms noise (1σ) is of the order of $\sim$0.1 mJy beam^{-1}. The synthesized beam is circular (2 arcsec), and it is displayed as a black circle in the bottom left corner.

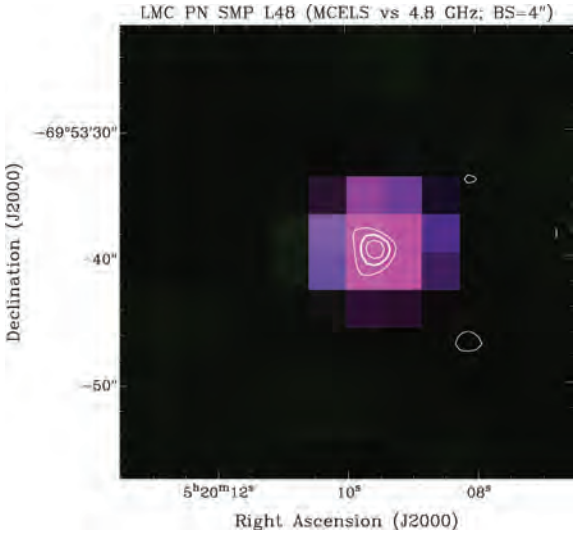

Figure 4. The MCELS image of the LMC PNe SMP L48 overlaid with the ATCA high-resolution radio-continuum image at 4.8 GHz. The radio-continuum contours are from 0.75 mJy beam^{-1} in steps of 0.25 mJy beam^{-1}. The synthesized beam of the radio image is 4 arcsec and the rms noise (1σ) is $\sim$0.25 mJy beam^{-1}. We note the large optical extent which is due to the PN faint AGB haloes.

3.2 Other radio-continuum extragalactic PNe and PNe candidates

Zijlstra et al. (1994) have reported a radio [WC]-type planetary nebula in the LMC named SMP L58 (Sanduleak et al. 1978) having flux densities of 0.79 and 0.84 mJy at 4.8/8.64 GHz, respectively (based on the well-calibrated ATCA 1993 June observations). We did not detect SMP L58 in any of our LMC mosaic radio surveys as

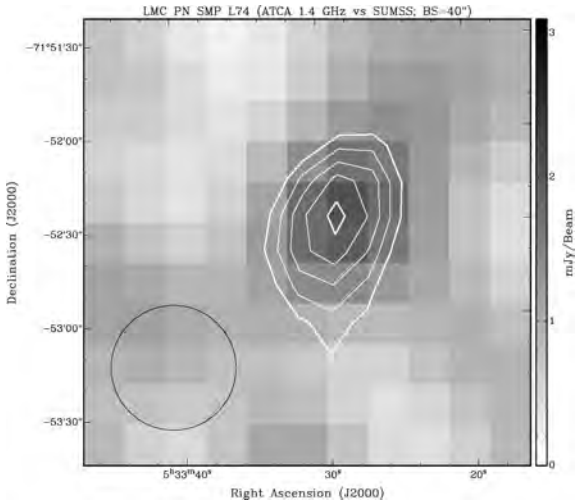

Figure 5. ATCA low-resolution radio-continuum image of the LMC PNe – SMP L74. Grey scale image is at 1.4 GHz and overlaid contours are from 843 MHz (SUMSS) observations. The radio-continuum contours are from 2 mJy beam^{-1} in steps of 0.5 mJy beam^{-1}. The 1.4 GHz image rms noise (1σ) is of the order of $\sim$0.6 mJy beam^{-1} and SUMSS $\sim$1 mJy beam^{-1}. Our 1.4 GHz image synthesized beam is circular (40 arcsec), and it is displayed as a black circle in the bottom-left corner.

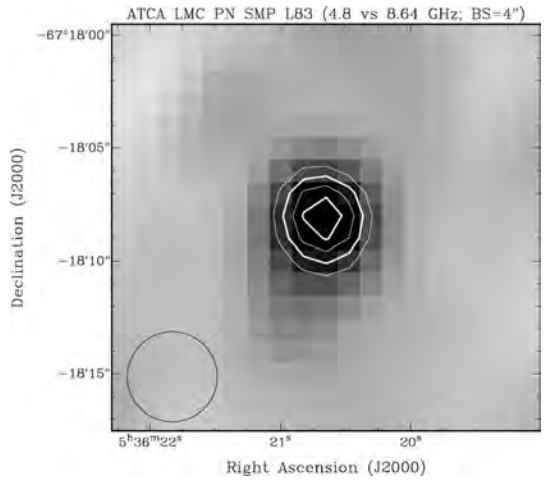

Figure 6. ATCA high-resolution radio-continuum image of the LMC PNe SMP L83. Grey scale image is at 4.8 GHz and overlaid contours (8.64 GHz) are from 0.3 mJy beam^{-1} in steps of 0.1 mJy beam^{-1}. Both images' rms noise (1σ) is of order of $\sim$0.1 mJy beam^{-1}. The synthesized beam is circular (4 arcsec), and it is displayed as a black circle in the bottom left corner.

our detection limits ($3\sigma = 1.5$ mJy) are well above SMP L58 flux densities. These two radio fluxes imply a spectral index of about 0.1 ± 0.3.

Our non-detection of this PN highlights the difficulty of radio observations of extragalactic PNe, even with the most recent ATCA techniques. SMP L58 is sufficiently bright among MC PNe that it was originally detected by *IRAS* at 25 μm at a level of 220 mJy (Loup et al. 1997), with an estimated error of ±25 per cent. The SAGE detection of this PN in the MIPS 24-μm band corresponds to 190 ± 5 mJy (Hora et al. 2008), consistent with no change in MIR emission over the intervening almost two decades. The 8.0-μm flux densities in both SAGE epochs (3 months apart) were 37 mJy. That would imply a large MIR/RC ratio of $\sim$47 if we took a flat spectrum to 1 GHz from Zijlstra et al. (1994) average 4.8/8.65 GHz flux densities or our own measurements. This rather large ratio points to more like H II region nature than a PN. However, Bernard-Salas et al. (2009) present the *Spitzer* spectrum, and conclude that the dust is carbonaceous, and thus the H II region nature can therefore be excluded, further highlighting the difficulty of positively identifying PNe even given multi-wavelength data.

We also note two radio PNe detections in the Sagittarius dwarf galaxy (Dudziak et al. 2000). When scaled to the distance of the LMC ($\sim$1 mJy at 4.8 GHz) neither of these PNe would be detectable in our surveys.

4 DISCUSSION

4.1 Expected flux density at the distance of the MCs

PNe within the MCs should not have measurable radio emission much above the sensitivity limits of our present generation data. For example, scaling up the radio fluxes from the very distant (6.6 kpc) Galactic PNe G313.3+00.3 (Cohen et al. 2005), it would have flux densities of 0.6 and 0.4 mJy at 1.384 and 2.496 GHz at the distance of the LMC. Another example is the very luminous Galactic PN NGC 6302. If we adopt expansion distance estimates by Meaburn et al. (2008) of 1.17 ± 0.14 kpc and flux density of 3.1 Jy from Casassus et al. (2007) then this PNe would have a 4.80-GHz flux density at the distance of the LMC of $\sim$1.7 mJy and the SMC of $\sim$1.2 mJy. It is widely accepted (e.g. Zijlstra 1990) that the strongest radio PNe in the Galactic Bulge, at a distance of 8.5 kpc, show an upper cut-off flux density of 65 mJy. Scaling this to the distance of the LMC gives an expected flux density of 1.9 mJy and for the SMC of 1.3 mJy.

Probably the most luminous Galactic PNe at present is NGC 7027, at a distance of 980 ± 100 pc (Zijlstra et al. 2008), it would have a 4.80-GHz flux density (5.6 Jy at its radio peak in 1987.34) at the distance of the LMC of $\sim$2.2 mJy and the SMC of 1.5 mJy. NGC 7027 is fading, and the original peak flux will have been higher than the current value, although by how much is uncertain. Assuming that a PN central star (CS) has a highest likely luminosity of 2×10^4 L$_\odot$ (if higher, the object would evolve too quickly through the PN phase to be detectable), which is about twice that of NGC 7027, suggests a peak LMC radio flux of up to 3 mJy. A further correction factor is needed for the stellar temperature: the radio flux of an optically thick PN varies by up to a factor of 2 during its evolution, caused by the changing stellar temperature (which affects the number of ionizing photons) (Zijlstra et al. 2008). According to Zijlstra (private communication), this may add another 25–50 per cent to the peak radio flux. However, very few PNe would be expected to show such values. Almost half of our sample presented here (seven out of 15) have similar or significantly higher flux densities (up to 4.1 mJy of the SMC PN N S68) at 4.8 GHz than projected values for NGC 7027. This suggests that the most radio luminous PNe such as N S68 may represent an upper (or close to upper) limit in radio-peak emission. At present, this SMC PN (N S68) is a factor of $\sim$3 more luminous than Galactic PN NGC 7027.

In general, we have found much higher flux densities than expected in both MCs PNe; e.g. LMCPN J054237-700930 (SMP L89) with a 1.4-GHz value of 3.1 mJy (±10 per cent) and SMCPN J004336-730227 (JD 04) with 5.1 mJy at 1.4 GHz. We note that three out of four detections in the SMC are surprisingly stronger (by up to a factor of 3) than their LMC and Galactic cousins even though the SMC is some 10 kpc further away than the LMC. While these are small sample statistics one could ask why is the SMC

PN sample brighter than the LMC? Could we be missing even more brighter LMC ones? However, the existence of the observable infrared emission for the four of the five detected SMC PNe implies that the dust in the shell must be relatively dense and close to the CS in order to be efficiently heated. The major part of the detected radio-continuum emission most likely originates from the dense ionized shell (<0.1 pc) which is, at the distance of 60 kpc, much smaller than our 8.64 GHz synthesized beam. The radio spectrum distribution of JD 04 is fairly flat throughout the observed radio frequency range. However, N S68, SMP S17 and SMP S11 demonstrate a mild but distinctive drop in the flux density towards the lower frequencies which is very likely the effect of the increased optical depth. The spectral index estimate for the N S68 in the $\lambda = 13$ cm range agrees with the value predicted by the unbounded wind shell model of 0.6 (Wright & Barlow 1975). Following the CS evolutionary model of Schoenberner (1981), it can be seen that high core mass CS are travelling through the heating part of the HR diagram much faster than the low-mass CS. The CS with a mass of 0.84 $M_{\odot}$ will pass through the heating stage almost 10 times quicker than the CS with 0.6 $M_{\odot}$ (Schoenberner 1993). At the same time, the number of ionizing photons ($\lambda < 912$ Å) is significantly larger for the high-mass CS (e.g. a 0.65 $M_{\odot}$ CS will produce almost three times more ionizing photons than CS with 0.6 $M_{\odot}$ mass). Therefore, assuming that the SMC CS mass distribution is shifted towards 0.65 $M_{\odot}$, it is reasonable to assume that the sudden drop in the radio-continuum flux density and consequent gap between the bright detected objects and the sensitivity limit (see Section 4.3) could be caused by the quick recombination phase when the ionizing source is 'turned off'. However, this model will also imply higher densities ($>10^4$) in the ionized shell and therefore characteristically optically thick radio-continuum emission at the lower frequencies.

4.2 MC PNe properties and selection criteria

We estimate spectral indices for 11 of the sources shown in Table 1 (Column 9). Despite the rather large estimated errors, most of our samples are within the expected ($-0.3 < \alpha < +0.3$) range. These large errors are most likely due to the low flux density levels of the associated detections. We cannot determine more accurate spectral indices without observations of higher spatial resolution and sensitivity, but we assume that PNe emission is predominantly thermal. However, thermal emission also characterizes compact H II regions. We point out that the radio-continuum flux densities peak at different frequencies and in most cases the spectral index cannot be described as a straight line. We compared corresponding PNe Hα fluxes (Reid & Parker, in preparation) with radio/IR and found no obvious correlation. Also, our 10 radio LMC PNe detections observed with the *HST* exhibit a wide range of diameters from very small (∼0.08 pc or 0.32 arcsec; SMP L47) to very large (∼1 pc or 4 arcsec; SMP L83; Fig. 6).

While one cannot classify radio sources based solely on spectral index, we note that two of our radio-continuum PNe (SMP L74 and SMP L83; Figs 5 and 6) have a very steep spectrum ($\alpha = -0.6 \pm 0.4$ and $\alpha = -0.5 \pm 0.2$) implying non-thermal emission, although the error in the index is large. We point out that Peña et al. (2004) report on large variability in the optical star in SMP L83, which may be responsible for the steeper spectral index. Similarly steep spectral indices may originate from supernova remnants (SNRs) and background sources such as active galactic nuclei and/or quasars. We exclude these possibilities as they would have very different characteristics at other frequencies such as X-ray and optical. Also, these may exhibit similar physical process as the Galactic PN associated with V1018 Sco and GK Per with spectral index of −0.8. Cohen et al. (2006) attributed this rather steep spectrum to the collision between the fast and slow winds in this nebula and neither is normally classified as PN.

Nor is the ratio of MIR to radio flux densities, MIR/RC, uniquely diagnostic for individual objects. The MIR/RC ratios for the MCs are based on MIR flux densities at 8.0 μm and radio-continuum values at 1.4 GHz. These are given in Table 1 (Column 10). If there are data, but not at 1.4 GHz, then we assume a flat radio spectrum. The median value for 137 Galactic PNe gives the MIR/RC ratio as 4 ± 1 (Cohen et al., in preparation). Very large values, such as 50–300, suggest optically thick radio emission regions (Cohen et al. 2007a); diffuse H II 25 (Cohen et al. 2007b); ultra-compact H II 42 (Murphy et al., in preparation). The 14 MCs MIR/RC ratios have a median value of 9 ± 2, consistent with the Galactic sample (the formal difference between the median values for MC and Galactic PNe has less than 2σ significance). An absent ratio in Table 1 indicates no MIR detection.

Although the primary emission mechanism of PN is thermal, Dgani & Soker (1998) presented a revised model of the PNe emission mechanism after the discovery of an inner region of non-thermal radio emission in the 'born-again' PNe, A30. They assumed that the fast wind from the CS carries a very weak magnetic field. Interactions of the wind with dense condensations trap magnetic field lines for long periods and stretch them, leading to a strong magnetic field. As the fast wind is shocked, relativistic particles form and interact with the magnetic field to create non-thermal emission. None the less, the flux density from this mechanism for PNe in the MCs would be exceedingly low, less than 1 μJy at the distance of the SMC.

Villaver, Stanghellini & Shaw (2007) have found that the average CS mass of a sample of 54 PNe located in the LMC is 0.65 ± 0.07 $M_{\odot}$, slightly higher than reported for those in the Galaxy. They attributed this difference to the lower metallicity in the LMC (on average by half) than in our Galaxy. This naturally raises the question: do MCs PNe evolve differently when compared to their Galactic cousins?

Zijlstra (2004) proposed that low-metallicity stars evolve to higher final masses. There has been no convincing confirmation of this (see Gesicki & Zijlstra 2007 for a discussion of the accuracy of mass determinations.) However, our results presented here suggest that this effect is present for the brightest sources. Also, one could interpret this as evidence for a more recent epoch of strong star formation in the MCs, leading to an overabundance of high-mass CS PNe.

Our radio PNe detections (Table 1) represent only ∼3 per cent of the optical PNe population of the MCs. Whatever the emission mechanism, we are selecting only the strongest radio-continuum emitters, possibly at a variety of different stages of their evolution (Vukotic et al. 2009). A much higher percentage of known Galactic PNe have radio counterparts [e.g. from ∼1300 PNe from Kerber et al. (2003) ∼60 per cent have been detected at 6 cm and ∼70 per cent at 20 cm] (Bojičić et al., private communication; Condon & Kaplan 1998; Luo et al. 2005), presumably because they are much closer.

4.3 PN central star properties

Most PNe have CS and nebular masses of only about 0.6 and 0.3 $M_{\odot}$, respectively. Detection of white dwarfs in open clusters suggests that the main-sequence mass of PNe progenitors can be as high as 8 $M_{\odot}$ (Kwok 1994). Our preliminary spectroscopic study

contained three of four SMC and 10 of 11 LMC radio-detected PNe (Payne et al. 2008a,b) and suggests that nebular electron temperatures are also within the expected range assuming an average density of 10^3 cm^{-3}. Given the values of radio flux density at ∼5 GHz, we estimated that the ionized nebular mass of these 13 MCs PNe may be 2.6 $M_\odot$ or greater. However, forbidden lines are insensitive to high densities and one might question whether the [S II] densities should be applied to the radio region.

This study suggests that the MC PNe detected in the radio continuum may represent a predicted link to the 'missing-mass' problem associated with systems possessing a 1–8 $M_\odot$ CS. If a high rate of mass loss continues for an extended fraction of the asymptotic giant branch (AGB) Star's lifetime, a significant fraction of a star's original mass can be accumulated in a circumstellar envelope (CSE). If the transition from the AGB to PNe stage is short, then such CSEs could have a significant influence on the formation of PNe, resulting in the detection of optical AGB haloes. The presence of these haloes has been known since the 1930s (Duncan 1937).

We consider the notion that our ATCA observations may be detecting the extended radio counterparts of these AGB haloes, presumed to be composed of weakly ionized material. However, the peak radio flux in a PN occurs while the nebula is optically thick for ionizing radiation, meaning only a fraction (in most cases a small fraction) of the circumstellar matter would be ionized. Once the ionized mass increases above (>0.1 $M_\odot$), the radio flux decreases quite rapidly as the nebulae become optically thin. Therefore, we conclude that haloes are very weak in the radio and cannot be detected in the MCs with the current observations. Although the ionized mass will increase at a much later stage, when the ISM interaction region merges with the PN (Wareing et al. 2007), at this time the expected radio flux will be very low indeed.

While most of the MC SNRs flux densities are much higher then these 15 PNe (see Bojičić et al. 2007; Crawford, Filipovic & Payne 2008a; Crawford et al. 2008b; Filipović et al. 2008, for a small sample of MC SNR flux densities), they are still a bit more luminous than their galactic counterparts 'prompting' us to call these sources Super PNe or mini-SNRs. While obvious differences remain between the two classes, the physical processes within these two groups (PNe versus SNRs) are perhaps not too dissimilar, if one takes into consideration the fact that older SNRs shock fronts are isothermal in nature.

5 CONCLUSION AND FUTURE OBSERVATIONS

We present the first 15 extragalactic radio PNe – all in the MCs. At least 10 of these candidates can currently be positively identified as a PN via a high-resolution optical (*HST*) imaging. All 15 radio-continuum objects examined here exhibit typical PN characteristics, i.e. canonical optical spectra and MIR properties leaving us no doubt that they are bone fide. Assuming they are radio PNe, their higher than expected flux densities at lower frequencies are most likely related either to environmental factors and/or selection effects. We tentatively call this PNe (sub)sample 'Super PNe'.

We are presently conducting high-resolution (∼1 arcsec) ATCA observations of all these 15 PNe candidates using a variety of frequencies and arrays. We also plan further optical confirmations of these PNe using high-resolution [O III] images from the *HST*.

ACKNOWLEDGMENTS

We used the KARMA/MIRIAD software packages developed by the ATNF. The Australia Telescope Compact Array is part of the Australia Telescope which is founded by the Commonwealth of Australia for operation as a National Facility managed by the CSIRO. MC thanks NASA for funding his participation in this work through ADP grant NNG04GD43G and JPL contract 1320707 with UC Berkeley. We thank the Magellanic Clouds Emission Line Survey (MCELS) team for access to the optical images. We thank the referee (Albert Zijlstra) for his excellent comments that have greatly improved this manuscript.

REFERENCES

Beintema D. A. et al., 1996, A&A, 315, L253
Bernard-Salas J., Pottasch S. R., Gutenkunst S., Morris P. W., Houck J. R., 2008, ApJ, 672, 274
Bernard-Salas J., Peeters E., Sloan G. C., Gutenkunst S., Matsuura M., Tielens A. G. G. M., Zijlstra A. A., Houck J. R., 2009, ApJ, 699, 1541
Bock D. C.-J., Large M. I., Sadler E. M., 1999, AJ, 117, 1578
Bojičić I. S., Filipović M. D., Parker Q. A., Payne J. L., Jones P. A., Reid W., Kawamura A., Fukui Y., 2007, MNRAS, 378, 1237
Casassus S., Nyman L.-Å., Dickinson C., Pearson T. J., 2007, MNRAS, 382, 1607
Cohen M. et al., 2005, ApJ, 627, 446
Cohen M., Chapman J. M., Deacon R. M., Sault R. J., Parker Q. A., Green A. J., 2006, MNRAS, 369, 189
Cohen M. et al., 2007a, MNRAS, 374, 979
Cohen M. et al., 2007b, ApJ, 669, 343
Condon J. J., Kaplan D. L., 1998, ApJS, 117, 361
Crawford E. J., Filipovic M. D., de Horta A. Y., Stootman F. H., Payne J. L., 2008b, Serbian Astron. J., 177, 61
Crawford E. J., Filipovic M. D., Payne J. L., 2008a, Serbian Astron. J., 176, 59
Dgani R., Soker N., 1998, ApJ, 499, L83
Dickel J. R., McIntyre V. J., Gruendl R. A., Milne D. K., 2005, AJ, 129, 790
Dickel J., Gruendl R. A., McIntyre V., Amy S., Milne D., 2009, in van Loon J. T., Oliveira J. M., eds, IAU Symp. Vol. 256, The Magellanic System: Stars, Gas, and Galaxies. Cambridge Univ. Press, Cambridge, p. 14
Dudziak G., Péquignot D., Zijlstra A. A., Walsh J. R., 2000, A&A, 363, 717
Duncan J. C., 1937, ApJ, 86, 496
Filipovic M. D., Haynes R. F., White G. L., Jones P. A., Klein U., Wielebinski R., 1995, A&AS, 111, 311
Filipovic M. D., Jones P. A., White G. L., Haynes R. F., Klein U., Wielebinski R., 1997, A&AS, 121, 321
Filipović M. D., Bohlsen T., Reid W., Staveley-Smith L., Jones P. A., Nohejl K., Goldstein G., 2002, MNRAS, 335, 1085
Filipović M. D., Payne J. L., Reid W., Danforth C. W., Staveley-Smith L., Jones P. A., White G. L., 2005, MNRAS, 364, 217
Filipović M. D. et al., 2008, A&A, 485, 63
Filipovic M. D. et al., 2009, in van Loon J. T., Oliveira J. M., eds, IAU Symp. Vol. 256. The Magellanic System: Stars, Gas, and Galaxies. Cambridge Univ. Press, Cambridge, p. PDF–8
Gesicki K., Zijlstra A. A., 2007, A&A, 467, L29
Herrmann K. A., Ciardullo R., Feldmeier J. J., Vinciguerra M., 2008, ApJ, 683, 630
Hora J. L. et al., 2008, AJ, 135, 726
Hughes A., Staveley-Smith L., Kim S., Wolleben M., Filipović M., 2007, MNRAS, 382, 543
Hughes A., Wong T., Ekers R., Staveley-Smith L., Filipovic M., Maddison S., Fukui Y., Mizuno N., 2006, MNRAS, 370, 363
Jacoby G. H., De Marco O., 2002, AJ, 123, 269
Kerber F., Mignani R. P., Guglielmetti F., Wicenec A., 2003, A&A, 408, 1029
Kwok S., 1994, PASP, 106, 344
Kwok S., 2000, The Origin and Evolution of Planetary Nebulae. Cambridge Univ. Press, Cambridge
Kwok S., 2005, J. Korean Astron. Soc., 38, 271
Leisy P., Dennefeld M., Alard C., Guibert J., 1997, A&AS, 121, 407

Loup C., Zijlstra A. A., Waters L. B. F. M., Groenewegen M. A. T., 1997, A&AS, 125, 419
Luo S. G., Condon J. J., Yin Q. F., 2005, ApJS, 159, 282
Mao S. A., Gaensler B. M., Stanimirović S., Haverkorn M., McClure-Griffiths N. M., Staveley-Smith L., Dickey J. M., 2008, ApJ, 688, 1029
Meaburn J., Lloyd M., Vaytet N. M. H., López J. A., 2008, MNRAS, 385, 269
Meyssonnier N., Azzopardi M., 1993, A&AS, 102, 451
Mezger P. G., Henderson A. P., 1967, ApJ, 147, 471
Morgan D. H., 1995, A&AS, 112, 445
Payne J. L., Filipović M. D., Reid W., Jones P. A., Staveley-Smith L., White G. L., 2004, MNRAS, 355, 44
Payne J. L., Filipovic M. D., Crawford E. J., de Horta A. Y., White G. L., Stootman F. H., 2008a, Serb. Astron. J., 176, 65
Payne J. L., Filipovic M. D., Millar W. C., Crawford E. J., de Horta A. Y., Stootman F. H., Urosevic D., 2008b, Serb. Astron. J., 177, 53
Payne J. L., Tauber L. A., Filipovic M. D., Crawford E. J., de Horta 2009, Serbian Astron. J., 178, 65
Peña M., Hamann W.-R., Ruiz M. T., Peimbert A., Peimbert M., 2004, A&A, 419, 583
Reid W. A., Parker Q. A., 2006a, MNRAS, 365, 401
Reid W. A., Parker Q. A., 2006b, MNRAS, 373, 521
Reid W. A., Parker Q. A., 2009, in van Loon J. T., Oliveira J. M., eds, IAU Symp. Vol. 256. The Magellanic System: Stars, Gas, and Galaxies. Cambridge Univ. Press, Cambridge, p. 36
Sanduleak N., MacConnell D. J., Philip A. G. D., 1978, PASP, 90, 621
Schoenberner D., 1981, A&A, 103, 119
Schoenberner D., 1993, Acta Astron., 43, 297
Shaw R. A., Stanghellini L., Villaver E., Mutchler M., 2006, ApJS, 167, 201
Stanghellini L., Villaver E., Shaw R. A., Mutchler M., 2003, ApJ, 598, 1000
Turtle A. J., Ye T., Amy S. W., Nicholls J., 1998, Publ. Astron. Soc. Aust., 15, 280
Villaver E., Stanghellini L., Shaw R. A., 2007, ApJ, 656, 831
Vukotic B., Urosevic D., Filipovic M. D., Payne J. L., 2009, A&A, in press (doi:10.1051/0004-6361/200911807)
Wareing C. J., Zijlstra A. A., O'Brien T. J., 2007, MNRAS, 382, 1233
Wright A. E., Barlow M. J., 1975, MNRAS, 170, 41
Zijlstra A. A., 1990, A&A, 234, 387
Zijlstra A. A., 2004, MNRAS, 348, L23
Zijlstra A. A., van Hoof P. A. M., Chapman J. M., Loup C., 1994, A&A, 290, 228
Zijlstra A. A., van Hoof P. A. M., Perley R. A., 2008, ApJ, 681, 1296

This paper has been typeset from a TEX/LATEX file prepared by the author.

A.4 Related Paper 4

Cajko, K. O., Crawford, E. J., and Filipović, M. D. (2009). Multifrequency Observations of One of the Largest Supernova Remnants in the Local Group of Galaxies, LMC - SNR J0450-709. *Serbian Astronomical Journal*, 179:55–60

My contribution was to assist in the data analysis. This is a 40% contribution.

Serb. Astron. J. № 179 (2009), 55 - 60 **UDC 524.722.3 : 524.354–77**
DOI: 10.2298/SAJ0979055C Original scientific paper

MULTIFREQUENCY OBSERVATIONS OF ONE OF THE LARGEST SUPERNOVA REMNANTS IN THE LOCAL GROUP OF GALAXIES, LMC – SNR J0450–709

K. O. Čajko[1], E. J. Crawford [2], M. D. Filipović[2]

[1] *Faculty of Sciences, University of Novi Sad*
Trg Dositeja Obradovića 4, 21000 Novi Sad, Serbia
E–mail: *tinacaj@gmail.com*

[2] *School of Computing and Mathematics, University of Western Sydney*
Locked Bag 1797, Penrith South DC, NSW 1797, Australia
E–mail: *e.crawford@uws.edu.au, m.filipovic@uws.edu.au*

(Received: July 16, 2009; Accepted: September 2, 2009)

SUMMARY: We present the results of new Australia Telescope Compact Array (ATCA) observations of one of the largest supernova remnants, SNR J0450–709, in the Local Group of galaxies. We found that this Large Magellanic Cloud (LMC) object exhibits a typical morphology of an old supernova remnant (SNR) with diameter D=102×75±1 pc and radio spectral index α=– 0.43±0.06. Regions of high polarisation were detected with peak value of ∼40 %.

Key words. ISM: supernova remnants – Magellanic Clouds – Radio Continuum: ISM – Polarisation – ISM: individual objects : SNR J0450–709

1. INTRODUCTION

The Magellanic Clouds (MCs) are one of the most favorable places for investigations of objects such as supernova remnants (SNRs). Beside their position, close to the South Pole, they are found in one of the coldest parts of the radio sky allowing us to investigate and detect radio emission without interruptions from Galactic foreground radiation (Haynes et al. 1991). The MCs are located out of the Galactic plane and thus the influence of dust, gas and stars is small, making detailed investigations of SNRs possible. The Large Magellanic Cloud (LMC) at a distance of 50 kpc (Hilditch et al. 2005), allows for analysis of the energetics of each remnant.

SNRs are usually characterised by their strong and predominately non-thermal emission that they emit at radio wavelengths. They have typical spectral index of $\alpha \sim -0.5$ defined by $S \propto \nu^{\alpha}$. SNRs have very important influence on the interstellar material (ISM). Appearances of shell-like filaments are very often perturbed by interaction with and non-homogeneous structure of the ISM. SNRs dictate behavior, structure, morphology and evolution of the ISM. But on the other hand, the evolution of SNRs is dependent on the environment which surrounds them.

Here we report on new moderate-resolution radio-continuum observations of SNR J0450–709, one of the largest SNRs in the Local Group of Galaxies. It was initially classified as SNR by Mathewson et al. (1985), based on optical obser-

vations (Hα) and, later, on radio-continuum survey with MOlonglo Synthesis Telescope – MOST. McGee et al. (1972) named this source MC 11 in their 4800 MHz MCs catalogue, but didn't attempt to classify it. Clarke et al. (1976) also included SNR J0450–709 in their 408 MHz MC4 catalogue. Wright et al. (1994) catalogued SNR J0450–709 as PMN J0450–7050 based on their observations within Parkes-MIT-NRAO (PMN) surveys at 4850 MHz. Filipović et al. (1995, 1996) added further confirmation with a set of radio-continuum observations (with Parkes telescope) over a wide frequency range. Filipović et al. (1998a), using *ROSAT* All Sky Survey (RASS) observations, did not detect X-ray emission from SNR J0450–709. Neither the *ROSAT* PSPC nor HRI observations covered the area of SNR J0450–709. Blair et al. (2006) reported detection at far ultraviolet wavelengths based on FUSE (Far Ultraviolet Spectroscopic Explorer) satellite, and labelled SNR as D90401. As very faint object SNR J0450–709 is detected at [CIII] and [OVI] wavelengths.

The [SII]/Hα ratio is 0.7, which according to Mathewson et al. (1985) satisfies one of the selection criteria for the large diameter class of SNRs. Hα emission from SNR J0450–709 shows typical well evolved shell-like appearance. Filipović et al. (1998b) presented Parkes low resolution multifrequency analysis and estimated spectral index as $\alpha = -0.39 \pm 0.08$. Williams et al. (2004) added high resolution XMM-Newton X-ray results. Most recently, Payne et al. (2008) presented optical spectroscopy of a wide range of LMC SNRs including SNR J0450–709. They found an enhanced [SII]/H$_\alpha$ ratio of 0.5 typical for SNRs.

2. OBSERVATIONAL DATA

We observed SNR J0450–709 with the Australia Telescope Compact Array (ATCA) on 6$^{\rm th}$ April 1997, with an array configuration EW375, at wavelengths of 8640 and 4800 MHz (λ=3 and 6 cm). Baselines formed with the 6$^{\rm th}$ ATCA antenna were excluded, as the other five antennas were arranged in a compact configuration. The observations were carried out in the so called "snap-shot" mode, totaling ∼1 hour of integration over a 12 hour period. Source PKS B1934-638 was used for primary calibration and source PKS B0530-727 for secondary calibration. The MIRIAD (Sault and Killeen 2006) and KARMA (Gooch 2006) software packages were used for reduction and analysis. More information on the observing procedure and other sources observed in this session can be found in Bojičić et al. (2007) and Crawford et al. (2008a,b).

Images were prepared, cleaned and deconvolved by means of the MIRIAD tasks, using multifrequency synthesis (Sault and Wieringa 1994). The 4800 MHz image (Fig. 1) has a resolution of $21'' \times 19''$ and an estimated r.m.s. noise of 0.5 mJy/beam. As the remnant is larger than the primary beam response ($5'$) at 8640 MHz no reliable image could be prepared.

3. RESULTS AND DISCUSSION

The remnant has a shell like morphology centered at RA(J2000)=$4^{\rm h}\,50^{\rm m}\,33\overset{\rm s}{.}4$, DEC(J2000)=$-70°50'43\overset{''}{.}5$ with a diameter of $420'' \times 310'' \pm 5''$ ($7' \times 5\overset{'}{.}16$ or $101.8 \times 75.2 \pm 1$ pc), which is in agreement with optical diameter of $6.5' \times 4\overset{'}{.}7$ reported by Williams et al. (2004). We note that it is elongated in north-south direction and "clump" along its western side (see Fig. 1 and Fig. 2).

Flux density measurements were made at 4800 MHz resulting in a value of 0.448 Jy. New measurements were also made at 843 MHz (from the LMC MOST image), 1400 MHz and 8640 MHz (both from the mosaics presented by Filipović et al. 2009 and Hughes et al. 2007). Using values of flux densities obtained from the observed frequencies in Table 1, a spectral index was plotted (Fig. 4) and estimated to be $\alpha = -0.43 \pm 0.06$, confirming the non-thermal nature of this object as the still dominant emission mechanism. However, our value is slightly "flatter" in comparison with typical and estimated value of -0.5 for SNRs (Mathewson et al. 1985).

Urošević and Pannuti (2005) showed models for two cases when SNRs could produce significant amount of thermal emission. Further on, they discuss the contribution of that thermal emission to the radio-continuum spectral index make-up of SNR. Urošević and Pannuti (2005) derived flatter empirical $\Sigma - D$ relation which is in a good agreement with previous modified theoretical relations. Discrepancies between theoretically derived and empirically measured $\Sigma - D$ relations may be partially explained by taking into account thermal emission at radio frequencies from SNRs at particular evolutionary stages and located in particular environments. In the case of SNR J0450–709, this may indicate an older age for the remnant where contribution of thermal component could be significant, similar to the example given in Urošević et al. (2007) and elaborated on in Onić and Urošević (2008). Also, SNR J0450–709 is most likely expanding in a denser and warmer medium of $n \sim 1 - 10\,{\rm cm}^{-3}$.

We note that the point at 408 MHz (Table 1; Fig. 4) lies slightly off the line of best fit. This is most likely due to an older data (1970-ties) processing. Particularly in this case it may overestimate flux density due to a clean bias effect. We estimate that the combined flux density errors from all radio images used in this study, are less than 10% at each given frequency.

Linear polarisation image for SNR J0450–709 at 4800 MHz is shown on Fig. 3. Regions of fractional polarisation are quite strong. They are designated with polarisation vectors located at north-west side of the shell. Linear polarisation images for each frequency were created using Q and U parameters. While we do not have any measurements at 8640 MHz, the 4800 MHz image reveals some strong linear polarisation. Without reliable polarisation measurements at another wavelength, we could

not determine the Faraday rotation. The mean fractional polarisation at 4800 MHz was calculated using flux density and polarisation:

$$P = \frac{\sqrt{S_Q^2 + S_U^2}}{S_I} \cdot 100\% \qquad (1)$$

where S_Q, S_U and S_I are integrated intensities for Q, U and I Stokes parameters. Our estimated peak value is $P \cong 40\%$. Along the shell there is a pocket of uniform polarisation possibly indicating varied dynamics along the shell. This unordered polarisation is consistent with the appearance of an older SNR.

Table 1. Integrated Flux Density of SNR J0450–709.

	S_I (0.408 GHz)	S_I (0.843 GHz)	S_I (1.4 GHz)	S_I (4.8 GHz)	S_I (8.64 GHz)
SNR J0450–709	1470 mJy	837.3 mJy	643.7 mJy	448 mJy	360 mJy
Reference	Clarke et al. 1976	Mills et al. 1984	This Work	This Work	This Work

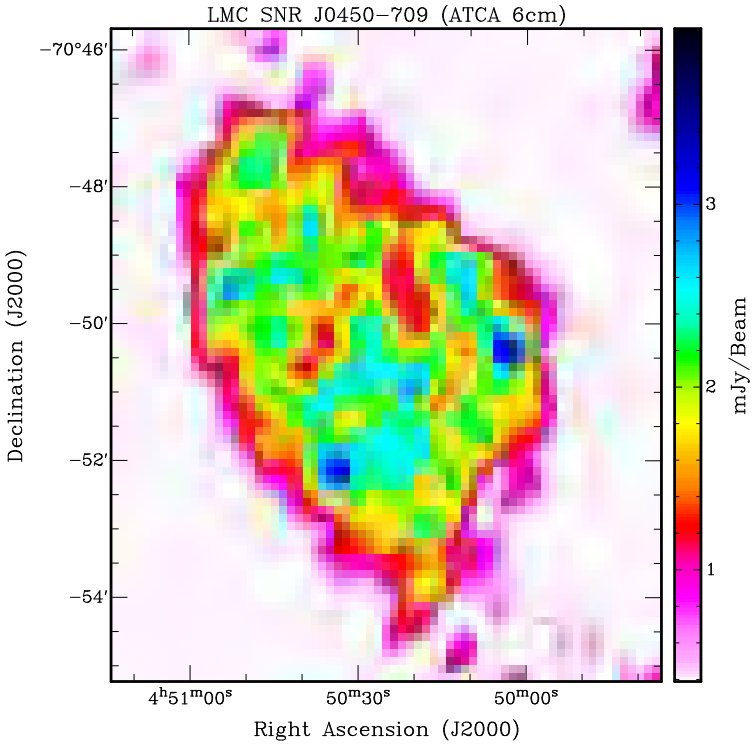

Fig. 1. *ATCA observations of SNR J0450–709 at 4800 MHz (6 cm). The side bar quantifies the pixel map and its units are mJy/beam.*

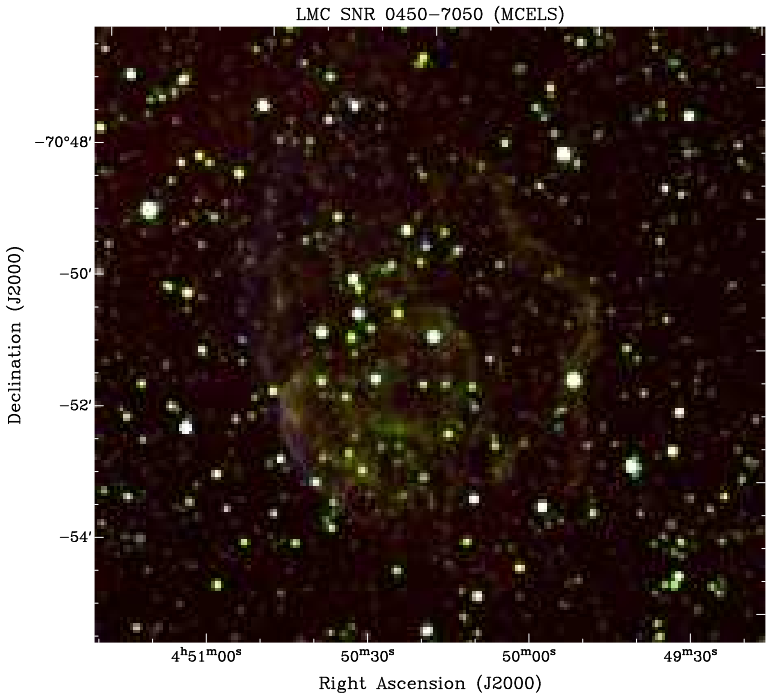

Fig. 2. *MCELS composite optical image* (RGB =H_α,[SII],[OIII]) *of SNR J0450–709.*

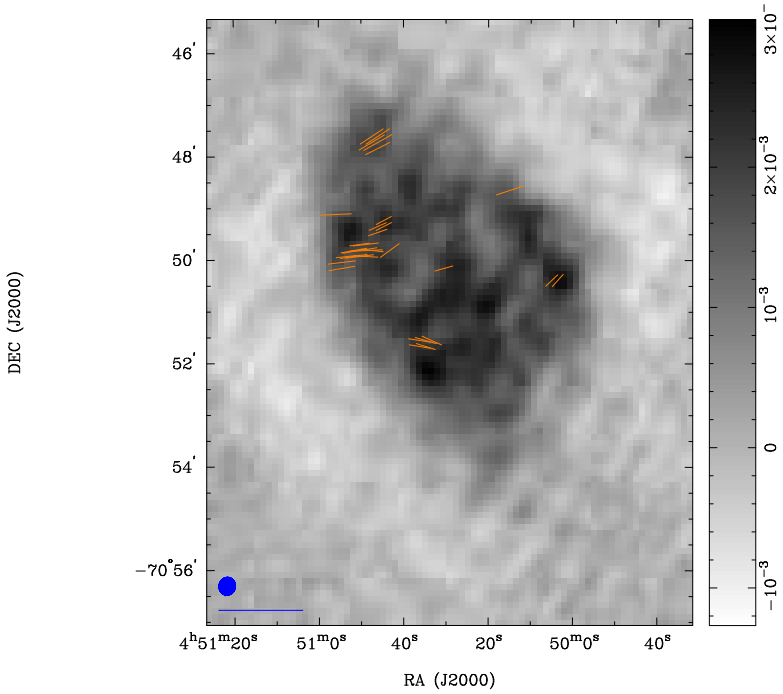

Fig. 3. *ATCA observations of SNR J0450–709 at 4800 MHz (6 cm). The blue circle in the lower left corner represents the synthesised beam-width of 21″×19″, and the blue line below the circle is a polarisation vector of 100%. The sidebar quantifies the pixel map and its units are Jy/beam.*

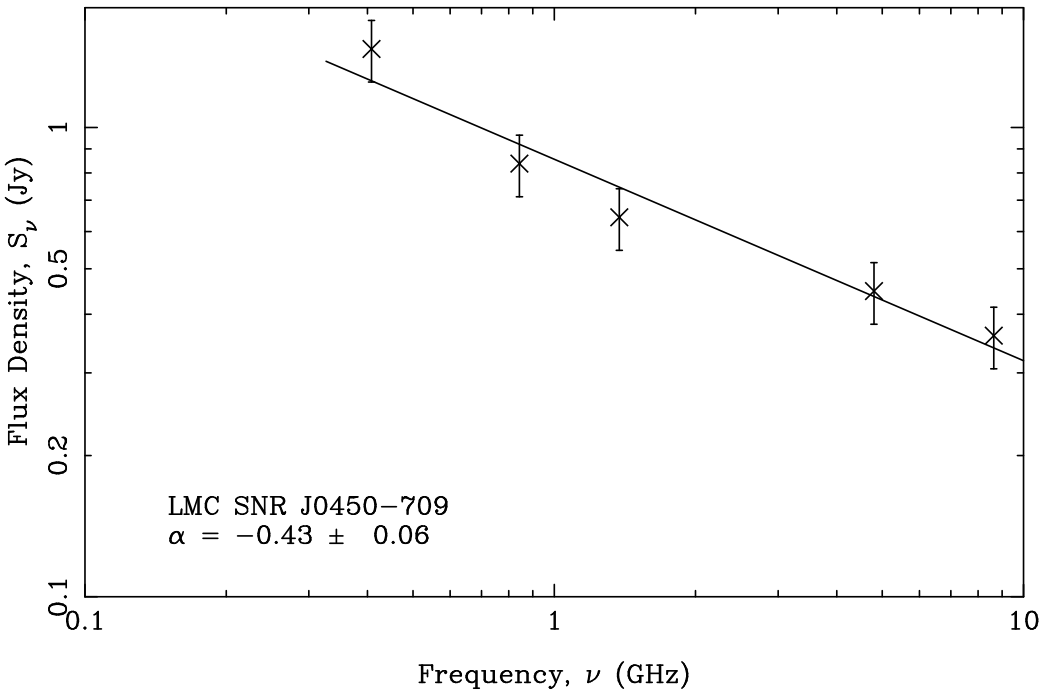

Fig. 4. *Radio-continuum spectrum of SNR J0450–709.*

4. CONCLUSION

We analysed one of the largest SNRs in the Local Group of Galaxies – SNR J0450–709. Here, the new radio-continuum observations of this SNR together with the multi-frequency analysis are presented. From these new observations, we found SNR diameter of 101.8×75.2±1 pc, spectral index of α=–0.43±0.06 and relatively strong level of linear polarisation with peak value of $\sim$ 40%. We concluded that these are all indicators of an older SNR.

Acknowledgements – We used the KARMA software package developed by the ATNF. The Australia Telescope Compact Array is part of the Australia Telescope which is funded by the Commonwealth of Australia for operation as a National Facility managed by CSIRO. We thank the Magellanic Clouds Emission Line Survey (MCELS) team for access to the optical images.

REFERENCES

Blair, W. P., Ghavamian, P., Sankrit, R., Danforth, C. W.: 2006, *Astron. Astrophys. Suppl. Series*, **165**, 480.

Bojičić, I. S., Filipović, M. D., Parker, Q. A., Payne, J. L., Jones, P. A., Reid, W., Kawamura, A., Fukui, Y.: 2007, *Mon. Not. R. Astron. Soc.*, **378**, 1237.

Clarke, J. N., Little, A. G., Mills, B. Y.: 1976, *Aust. J. Phys. Astrophys. Suppl.*, **40**, 1.

Crawford E. J., Filipović, M. D. and Payne, J. L.: 2008 *Serb. Astron. J.*, **176**, 59.

Crawford E. J., Filipović, M. D., De Horta, A. Y., Stootman, F. H., Payne J. L.: 2008, *Serb. Astron. J.*, **177**, 61.

Filipović, M. D., Haynes, R. F., White, G. L., Jones, P. A., Klein, U., Wielebinski, R.: 1995, *Astrophys. J. Suppl. Series*, **111**, 331.

Filipović, M. D., White, G. L., Haynes, R. F., Jones, P. A., Meinert, D., Wielebinski, R., Klein, U.: 1996, *Astrophys. J. Suppl. Series*, **120**, 77.

Filipović, M. D., Pietsch, W., Haynes, R. F., White, G. L., Jones, P. A., Wielebinski, R., Klein, U., Dennerl, K., Kahabka, P., Lazendić, J. S.: 1998a, *Astron. Astrophys. Suppl. Series.* **127**, 119.

Filipović, M. D., Haynes, R. F., White, G. L., Jones, P. A.: 1998b, *Astron. Astrophys. Suppl. Series.* **130**, 421.

Filipović M. D., Crawford E. J., Hughes A., Leverenz H., de Horta A. Y., Payne J. L., Staveley-Smith L., Dickel J. R., Stootman F. H., White G. L.: 2009, in van Loon J. T., Oliveira J. M., eds, *IAU Symposium Vol. 256 of IAU Symposium*, pp PDF8.

Gooch, R.: 2006, Karma Users Manual, ATNF, Sydney.

Haynes et al.,: 1991, *Astron. Astrophys.*, **252**, 456.

Hilditch, R. W., Howarth, I. D., Harries, T. J.: 2005, *Mon. Not. R. Astron. Soc.*, **357**, 304.

Hughes, A., Staveley-Smith, L., Kim, S., Wolleben, M., Filipović, M. D.: 2007, *Mon. Not. R. Astron. Soc.*, **382**, 543.

Mathewson, D. S., Ford, V. L., Tuohy, I. R., Mills, B. Y., Turtle A. J., Helfand, D. J.: 1985, *Astrophys. J. Suppl. Series*, **58**, 197.
McGee, R. X., Brooks, J. W., Batchelor, R. A.: 1972, *Aust. J. Phys*, **25**, 581.
Mills, B. Y., Turtle, A. J., Little, A. G., Durdin, J. M.: 1984, *Aust. J. Phys.*, **37**, 321.
Onić, D., Urošević D.: 2008, *Serb. Astron. J.*, **177**, 67.
Payne, J. L., White, G. L., Filipović, M. D.: 2008, *Mon. Not. R. Astron. Soc.*, **383**, 1175.
Sault, R., Killeen, N.: 2006, Miriad Users Guide, ATNF, Sydney.
Sault, R. J., Wieringa, M. H.: 1994, *Astron. Astrophys. Suppl. Series*, **108**, 585.
Urošević, D., Pannuti, T. G.: 2005, *Astroparticle Physics*, **23**, 577.
Urošević, D., Pannuti, T. G., Leahy, D.: 2007, *Astrophys. J.*, **655**, L41.
Williams, R. M., Chu, Y.-H., Dickel, J. R., Gruendl, R.A., Shelton, R., Points, S.D., Smith, R. C.: 2004, *Astrophys. J*, **613**, 948.
Wright, A. E., Griffith, M. R., Burke, B. F., Ekers, R. D.: 1994, *Astrophys. J. Suppl. Series*, **91**, 111.

МУЛТИФРЕКВЕНЦИОНА ПОСМАТРАЊА ЈЕДНОГ ОД НАЈВЕЋИХ ОСТАТАКА СУПЕРНОВИХ У ЛОКАЛНОЈ ГРУПИ ГАЛАКСИЈА – LMC SNR J0450–709

K. O. Čajko[1], E. J. Crawford[2] M. D. Filipović[2]

[1] *Faculty of Sciences, University of Novi Sad*
Trg Dositeja Obradovia 4, 21000 Novi Sad, Serbia

E–mail: *tinacaj@gmail.com*

[2] *School of Computing and Mathematics, University of Western Sydney*
Locked Bag 1797, Penrith South DC, NSW 1797, Australia

E–mail: *e.crawford@uws.edu.au, m.filipovic@uws.edu.au*

УДК 524.722.3 : 524.354–77
Оригинални научни рад

У овој студији представљамо нове ATCA резултате радио-посматрања у континууму остатка супернове у Великом Магелановом Облаку – SNR J0450–709. Нашли смо да овај остатак супернове има љускасту морфологију која је типична за старије остатке супернових. Измерена вредност радио спектралног индекса износи $\alpha = -0.43 \pm 0.06$, а дијаметра $D = 101.8 \times 75.2 \pm 1$ парсека. Детектовали смо релативно висок степен поларизације где максимална вредност износи око 40%.

A.5 Related Paper 5

Filipović, M. D., Crawford, E. J., Jones, P. A., and White, G. L. (2010). Radio-Continuum Jets Around the Peculiar Galaxy Pair ESO 295-IG022. *Serbian Astronomical Journal*, 181:31–37

My contribution was to assist in the data analysis. This is a 20% contribution.

Serb. Astron. J. № 181 (2010), 31 - 37 **UDC 524.7–77**
DOI: 10.2298/SAJ1081031F Original scientific paper

RADIO-CONTINUUM JETS AROUND THE PECULIAR GALAXY PAIR ESO 295-IG022

M. D. Filipović[1], E. J. Crawford[1], P. A. Jones[2,3] and G. L. White[1,4]

[1] *University of Western Sydney, Locked Bag 1797, Penrith South DC, NSW 1797, Australia*
E–mail: *m.filipovic@uws.edu.au, e.crawford@uws.edu.au*

[2] *School of Physics, University of New South Wales, Sydney, NSW 2052, Australia*
E–mail: *pjones@phys.unsw.edu.au*

[3] *Departamento de Astronomía, Universidad de Chile, Casilla 36-D, Santiago, Chile*

[4] *Faculty of Science, Charles Sturt University, Wagga Wagga, Australia*

(Received: September 17, 2010; Accepted: November 2, 2010)

SUMMARY: We report new radio-continuum observations with the Australia Telescope Compact Array (ATCA) of the region surrounding the peculiar galaxy pair ESO 295-IG022 at the centre of the poor cluster Abell S0102. We observed this cluster at wavelengths of λ=20/13 and 6/3 cm with the ATCA 6 km array. With these configurations, we achieved a resolution of $\sim 2''$ at 3 cm which is sufficient to resolve the jet-like structure of $\sim 3'$ length detected at 20 cm. From our new high resolution images at 6 and 3 cm we confirm the presence of a double jet structure, most likely originating from the northern galaxy (ESO 295-IG022-N), bent and twisted towards the south. We found the spectral index of the jet to be very steep (α=–1.32). No point source was detected that could be associated with the core of ESO 295-IG022-N. On the other hand, ESO 295-IG022-S does not show any jet structure, but does show a point radio source. This source has variable flux and spectral index, and appears to be superposed on the line-of-sight of the jets (seen at 20-cm) originating from the northern galaxy ESO 295-IG022-N. Finally, regions of very high and somewhat well ordered polarisation were detected at the level of 70%.

Key words. Galaxies: clusters: individual: Abell S0102 – Galaxies: individual: ESO 295-IG022 – Galaxies: interactions – Galaxies: jets – Radio continuum: galaxies – X-rays: galaxies

1. INTRODUCTION

Merging and interacting galaxies are often found in galaxy clusters. Such interactions and mergers provide a valuable insight into the evolution of both the cluster and the embedded galaxies, thus underpinning the most current theories of cluster and galaxy formation and evolution. As an example, it is now well established that radio jets interact with the intracluster medium (ICM) providing energy to the ICM. It is shown by Rafferty et al. (2006) and Bîrzan et al. (2007) that the synchrotron ages of the radio jet lobes are generally less than the X-ray ages of the cluster cavities; suggesting that the cavities

are being pumped by the energy supplied by the jet. In their study, they compared the size of the cavities (determined from X-ray data) with the size of the lobes (found on radio maps) and concluded that the lower radio frequencies maps are a better tool (than the higher frequency maps) to study the several hundred million year history of active clusters.

A prime example of a complex, merging and interacting system of galaxies within a cluster has been discovered by Read et al. (2001). They reported a prominent (bipolar) radio source with jets embedded in the poor galaxy cluster Abell S0102 (Abell et al. 1989) (also known as EDCC 494; Lumsden et al. 1992) at a redshift of z=0.054824 (Bica et al. 1991). The ESO 295-IG022 galaxy pair also coincides with Abell S0102 and was classified as a merging galaxy system by Bica et al. (1991).

Read et al. (2001) suggested two possible scenarios for the appearance of radio-continuum jet/s. One is a "single galaxy" model with two jets coming out of either ESO 295-IG022-S or ESO 295-IG022-N and with the other galaxy seen superimposed on the jet structure. For this scenario they suggest the southern galaxy (ESO 295-IG022-S) as the "origin" of the bipolar radio jets which extend south about 95″ (≈ 100 kpc at the distance of ESO 295-IG022), and to the north about ≈ 80″. The northern termination is positional coincidence with the northern galaxy ESO 295-IG022-N.

The alternatively scenario suggested by Read et al. (2001) is that the emission emanates from the northern galaxy ESO 295-IG022-N and that there is a positional coincidence with a similar jet structure associated with ESO 295-IG022-S. This second, and less likely scenario, requires the northern and southern galaxies to produce their own substantive jets. In this two jet model, Read et al. (2001) estimate projected lengths of up to 100 kpc, with velocities of at least 1000 km s^{-1}, and explain the bending of the jets as being due to ESO 295-IG022-S moving through the ICM at ~ 190 km s^{-1}.

The ROSAT PSPC observations of Read et al. (2001) indicate relatively cool diffuse X-ray emission from Abell S0102 consistent with group or poor cluster emission. This emission, when compared with the radio jets, is suggestive of channeling effects taking place that might create the so-called cavities where jets are able to punch holes in the ICM and displace the X-ray emitting gas, as is seen in other galaxy groups/clusters such as Hydra A (Wise et al. 2007), Abell 2204 (Sanders et al. 2009) or Abell 1446 (Douglass et al. 2008).

Our aim was to use Australia Telescope Compact Array (ATCA) high-resolution radio-continuum observations to resolve the jet structure of this Abell cluster, and to better determine the relationship between the optical galaxies and radio-continuum/X-ray (anti)correlation. In this paper, we present new ATCA radio results of this cluster area at 6 and 3 cm. In Section 2, we describe our radio-continuum observations and data analysis. The results of this analysis are given in Section 3. Finally, we summarise our findings in Section 4.

2. OBSERVATIONS AND DATA ANALYSIS

The Abell S0102 region was initially observed as a part of the ATCA observations of the NGC 300 area (ATCA project C828) at wavelengths of 20 and 13 cm (ν=1384 and 2496 MHz) with a 6A array giving angular resolutions of 6″ and 4″ (see Figs. 1 and 2). More information regarding these observations can be found in Payne et al. (2004). As the Abell S0102 positions are well down the primary beam pattern of the ATCA, we have applied a primary beam correction using the standard techniques in the MIRIAD software package (Sault and Killeen 2010).

We again observed Abell S0102 with the ATCA on October 9, 2000 (ATCA project C913), with an array configuration 6A, at wavelengths of 6 and 3 cm (ν=4800 and 8640 MHz). These observations were undertaken in the so-called full synthesis mode and total ∼10.5 hours of integration over a 12 hour period. Source 1934-638 was used for primary calibration and source 0048-427 was used for secondary calibration. The MIRIAD (Sault and Killeen 2010) and KARMA (Gooch 2006) software packages were used for data reduction and analysis.

The 6 cm image (Figs. 2 and 3) has a resolution of 4″×3″ at position angle 2° and the r.m.s noise is estimated to be 0.1 mJy/beam. Similarly, the 3 cm image was constructed with a resolution of 2.2″×1.6″ and r.m.s noise of 0.1 mJy/beam (Fig. 4).

Additional archival λ = 6 cm ATCA data from December 13, 1991 (ATCA project C133), centred on ESO 295-IG022 were found. These observations are only ∼20 minutes of fairly low sensitivity observations, and were only to determine the ESO 295-IG022-S flux and position. Finally, we note recent (January 17, 2010), Burnett et al. (2010) ATCA CABB observations with some significant calibration problems, from which they managed to extract integrated flux densities for the main feature of ESO 295-IG022-S. We report their results in our Table 1 (also see Fig. 5c).

Two prominent radio features are seen at 13 and 6 cm – the "core/s" and "jet/s". The radio point source (J005546-372427: at RA(J2000)=$00^h55^m46.58^s$, DEC(J2000)=–37°24′27.7″) is coincident with the southern galaxy (ESO 295-IG022-S). The "jet" – named J005547-372320 (at RA(J2000)=$00^h55^m47.31^s$, DEC(J2000)=–37°23′20.6″) appears to be associated with the optical counterpart ESO 295-IG022-N (positions from the 6 cm observations).

The frequency-dependent integrated flux densities (S) of J005547-372320 and J005546-372427 features are given in Table 1 and shown in Fig. 5. We point out that we do not detect the jets at 3 cm because of the very steep radio spectrum of the jets, however, this steep spectral index ($\alpha = -1.32 \pm 0.14$; see Fig. 5a) may be the result of the missing flux of

the short spacings at the higher radio-continuum frequencies (6 and 3 cm).

The integrated flux density of J005547-372320 was determined as the sum of the flux density in a box around ESO 295-IG022-N and that of the two twisted jet features. The integrated flux density of the central point-like radio source coincident with ESO 295-IG022-S was determined using the two-dimensional elliptical Gaussian fitting algorithm within the MIRIAD software package. The spectral index distribution of this object is shown in Figs. 5b and 5c. We emphasise that the integrated flux at 20 cm of the ESO 295-IG022 source in our February 28, 2000 observations agrees well with the flux density from the VLA NVSS and that reported by Read et al. (2001). We estimate the integrated flux density errors for all our images to be less than 10%.

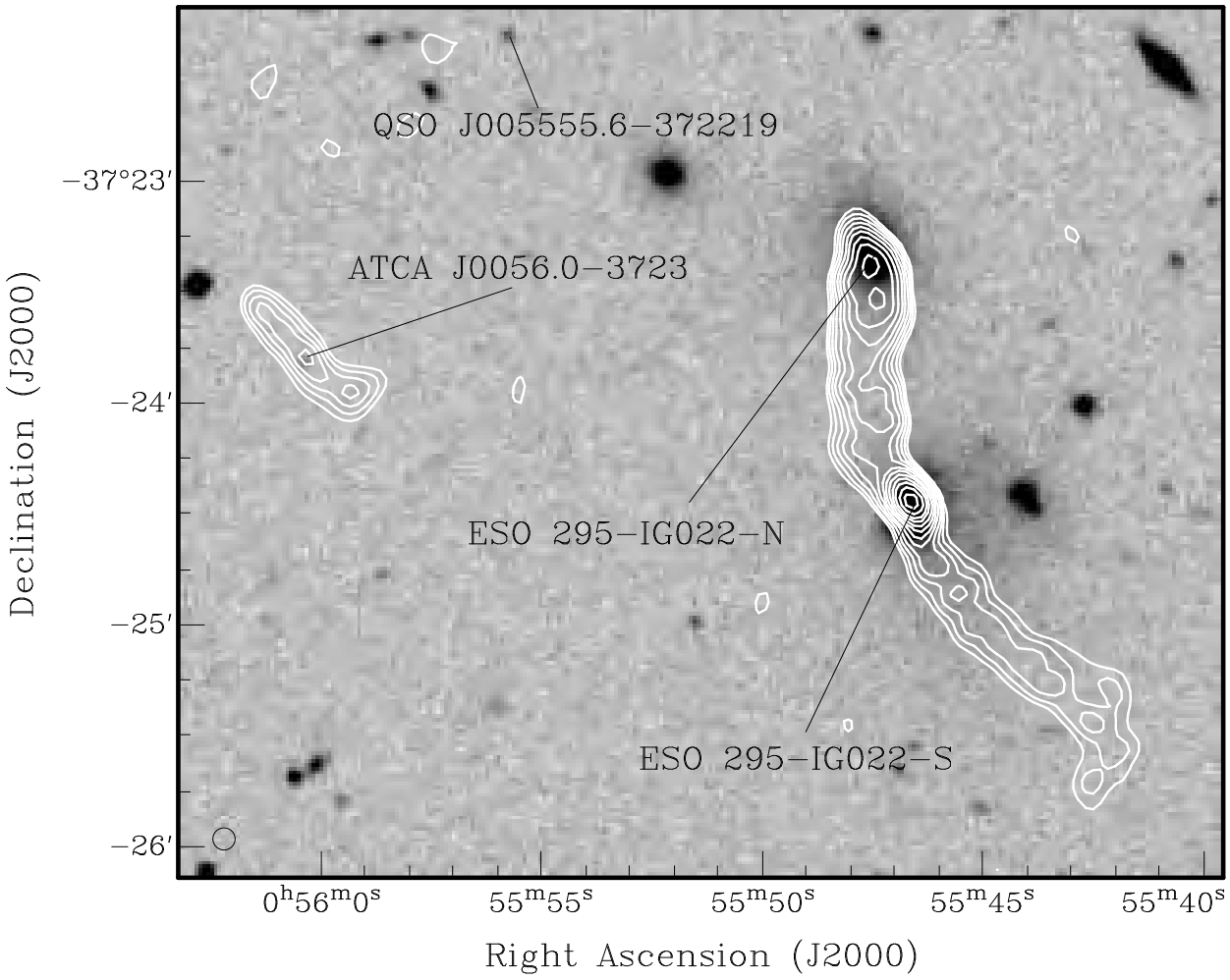

Fig. 1. *Digital Sky Survey (red) image of the Abell S0102 cluster central region overlaid with primary beam corrected 20 cm ATCA radio-continuum contours. The synthesised beam of the ATCA observation is 6″ × 6″ (see circle, lower left corner) with r.m.s. noise (1σ) of 0.06 mJy. Contours increase by factors of* $\sqrt{2}$ *from 0.5 mJy/beam. This picture is adapted from Read et al. (2001).*

Table 1. Radio-continuum integrated flux densities (S) of the two radio features within Abell S0102. Our new spectral index (α) estimates are based on two observing sessions from 2000 while Burnett et al. (2010) is also shown in Column 8.

ATCA Radio Name	Other Name	Obs. Date	$S_{20\,\mathrm{cm}}$ (mJy)	$S_{13\,\mathrm{cm}}$ (mJy)	$S_{6\,\mathrm{cm}}$ (mJy)	$S_{3\,\mathrm{cm}}$ (mJy)	$\alpha \pm \Delta\alpha$	Reference
J005547-372320	ESO 295-IG022-N	28/02/2000	80.0	42.5		–	-1.32 ± 0.14	Read et al. (2001)
J005547-372320	ESO 295-IG022-N	09/10/2000			15.5	–		This paper
J005546-372427	ESO 295-IG022-S	13/12/1991			32.6			Read et al. (2001)
J005546-372427	ESO 295-IG022-S	28/02/2000	47.0	63.9			-0.11 ± 0.14	Read et al. (2001)
J005546-372427	ESO 295-IG022-S	09/10/2000			48.6	41.1		This paper
J005546-372427	ESO 295-IG022-S	17/01/2010	18.2		74.0	67.0	$+0.78 \pm 0.31$	Burnett et al. (2010)

3. RESULTS AND DISCUSSION

In comparing our various radio-continuum images with optical Digital Sky Survey 2 (DSS2) images (Figs. 1, 2, 3 and 4), we see some striking features in and around the central Abell S0102 cluster galaxy pair, ESO 295-IG022. From the higher resolution image at 13 and 6 cm (Figs. 2 and 3), the southern peak appears quite compact and NOT a knot in the jet. The compact nature of this source is supported by our 2000 observations of ESO 295-IG022-S that give a flat spectrum of $\alpha = -0.11 \pm 0.14$ (Fig. 5b). This spectral index is, however, significantly different from $\alpha = +0.78 \pm 0.31$ found in 2010 by Burnett et al. (2010) (Fig. 5c) and we note that the flux density values for Burnett et al. (2010) are higher than ours by a factor of ∼1.6 at the higher frequencies (6 and 3 cm) but substantively lower than that of Read et al. (2000) by a factor of ∼0.4 at the lower (20 cm) frequency. We are, therefore, assuming that the source is both of flat spectrum and variable, and interpret the inconsistencies of flux density as a consequence of either variability (over two decades) or the loss of flux due to the missing spacings in the data set/s.

As pointed by Read et al. (2001), the galaxy ESO 295-IG022-S has a complex optical morphology with two nuclei ≈ 6″ (i.e. 6.5 kpc) apart. This may be a merging pair or a NGC 5128 type object seen at great distance. The bright and compact northernmost radio knot at 3 cm (RA(J2000)=$00^h55^m46.57^s$, DEC(J2000)=$-37°24'27.5''$) lies within ∼ 1″ of the northern component of ESO 295-IG022-S (Fig. 4) and, given the positional errors of both the optical and radio data (both ≈1″), it seems sensible to interpret the point radio source as coincident with ESO 295-IG022-S and emanating from the AGN core of the northern component of that galaxy.

The scenario put forward by Read et al (2000), that ESO 295-IG022-S is the origin of the observed (20 cm) jets, is therefore unlikely. We do not find the jet structure asymmetric as the northern jet is much brighter than the southern. Combining this with the compact and potentially variable nature of the radio source and its identification with a component of ESO 295-IG022-S. We argue that the jet structure most likely originates from ESO 295-IG022-N and not from ESO 295-IG022-S as suggested by Read et al (2000). This is therefore probably a rare, but not too unlikely random line of sight coincidence.

The 6 cm twin jet of the northern source (Fig. 3) is nicely coincident with an optical object which is an extended and elliptical galaxy. We point out the lack of a point radio source which could be associated directly with ESO 295-IG022-N but see the

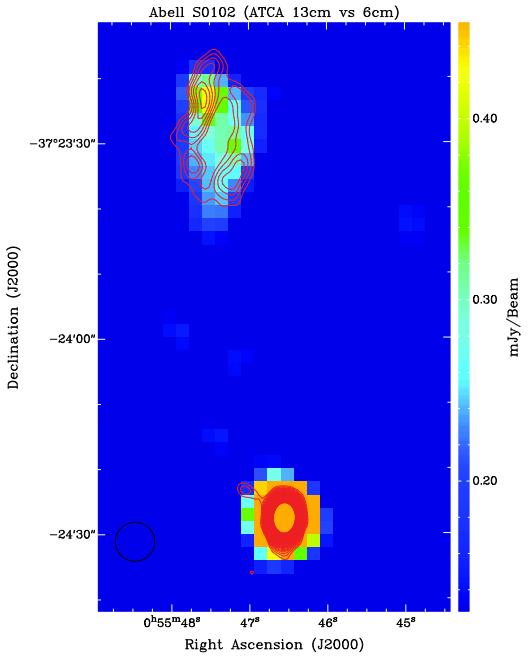

Fig. 2. *ATCA 13-cm image of the Abell S0102 cluster central region overlaid with primary beam corrected 6-cm ATCA radio-continuum contours. The synthesized beam of the ATCA observation is 4″ × 3″ (see circle, lower left corner) with r.m.s. noise (1σ) of 0.1 mJy. Contours increase by factors of 2.5σ from 0.5 mJy/beam.*

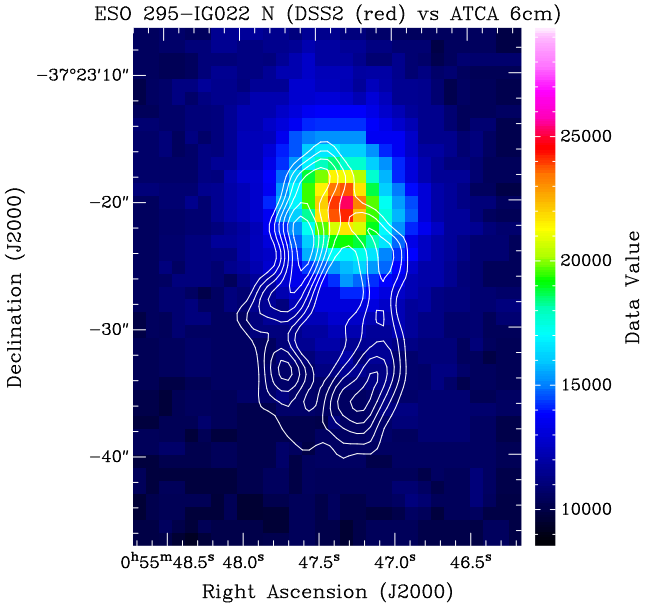

Fig. 3. *Digital Sky Survey (red) image of the ESO 295-IG022-N region overlaid with primary beam corrected 6-cm ATCA radio-continuum contours. Contours are the same as in Fig. 2.*

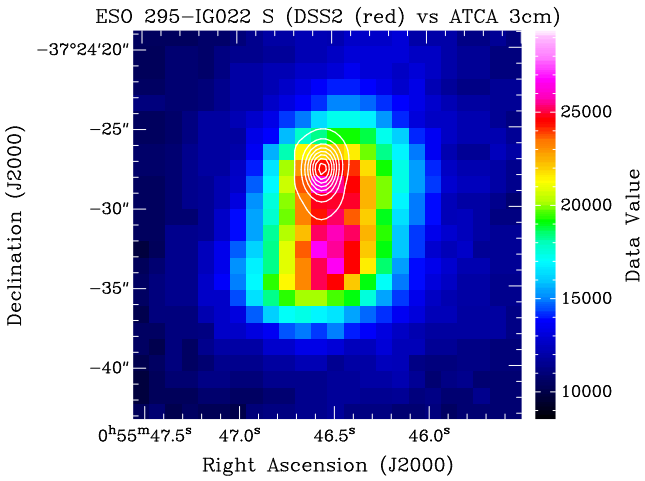

Fig. 4. *Digital Sky Survey (red) image of the ESO 295-IG022-S region overlaid with primary beam corrected 3-cm ATCA radio-continuum contours. The synthesized beam of the ATCA observation is 2.2″ × 1.6″ with r.m.s. noise (1σ) of 0.1 mJy. Contours increase by factors of 50σ from 1.5 mJy/beam.*

twin-jet nature of the jet near ESO 295-IG022-N as a defining feature (this is not seen in the 13 cm image with lower resolution). As radio cores are often much weaker than the jets, the non detection of a core in ESO 295-IG022-N is not too surprising (see Jones et al. 1994; cores typically <1% of jets). Finally, our spectral index estimate for this jet feature is quite steep with $\alpha = -1.32 \pm 0.14$ (Fig. 5a). This steep spectral index may be an explanation for not detecting the jet features in our 3 cm image. However, the steep spectral index is, at least in part, due to the missing flux at higher resolution/frequency. McAdam et al. (1988) reported discovery of radio source PKS 0427-53 interacting with IC 2082 and the cluster medium. The morphology of this radio AGN looks very similar to ESO 295-IG022-S. Even the size of PKS 0427-53 jets of 160 kpc is similar to ESO 295-IG022-S jets estimate of 180 kpc.

The linear polarisation image of Abell S0102 at 6 cm is illustrated in Fig. 6. This linear polarisation image was created using Q and U parameters. Regions of fractional polarisation are quite strong at the southern side of the Abell S0102 cluster with polarisation vectors aligned with the observed jets from ESO 295-IG022-N. We could not determine the Faraday rotation and magnetic field without polarisation measurements at the second wavelength of 3 cm. The mean fractional polarisation at 6 cm was calculated using flux density and polarisation:

$$P = \frac{\sqrt{S_Q^2 + S_U^2}}{S_I} \cdot 100\% \qquad (1)$$

where S_Q, S_U and S_I are integrated intensities for Q, U and I Stokes parameters. Our estimated peak polarisation value is $P \cong 72\% \pm 15\%$ at 6 cm. Along the northern part of the jet there is a pocket of uniform polarisation at approximately 70% (Fig. 6) possibly indicating a varied dynamics along the jet. We speculate that in the mid part of the jet, some twisting of the two bended jets may produce a poorly ordered polarisation as can be seen also in Fig. 6. This strong and ordered polarisation is among the strongest ever observed in a large scale AGN.

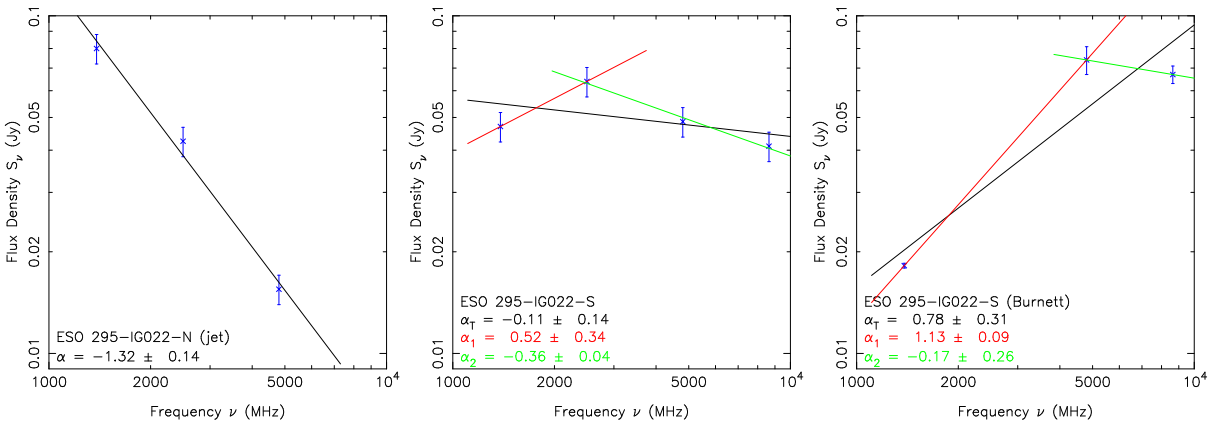

Fig. 5. *Spectral index distribution of the radio features within the Abell S0102. (a) Jet structure associated with ESO 295-IG022-N based on the ATCA 2010 observations (b) ESO 295-IG022-S based on our ATCA 2000 observations (c) ESO 295-IG022-S from Burnett et al. (2010). For (b) and (c) α_T is the fit including all points; α_1 and α_2 are fits using a subset of the points.*

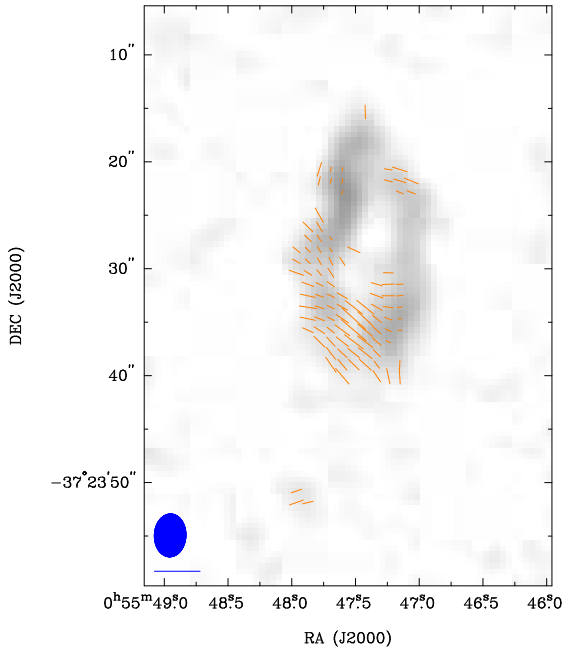

Fig. 6. *ATCA observations of ESO 295-IG022-N at 6 cm (4.8 GHz). The blue circle in the lower left corner represents the synthesised beamwidth of 4″×3″ and the blue line below the circle is a polarisation vector of 100%.*

We note that ESO 295-IG022-N is typical of narrow angle tail radio galaxies which are commonly found in rich Abell clusters. While it looks like the emission is weak, the second tail is now seen well.

4. SUMMARY

We present new high resolution images at various radio-continuum frequencies of the peculiar galaxy pair ESO 295-IG022 at the centre of the poor cluster Abell S0102. The most likely interpretation is that the double jet structure originates from the northern galaxy (ESO 295-IG022-N), which then bends and twists towards the south. We detected strong polarised emission of $\sim 70\%$ from the AGN jets. Also, the spectral index of jet filaments is very steep (α=–1.32) indicating the presence of strong magnetic fields. No point source was detected that could be associated with the core of ESO 295-IG022-N.

On the other hand, ESO 295-IG022-S does not show any jet structure, but does have a radio point source with variable flux and spectral index. This appears to be superposed in the line-of-sight of the 20-cm jets, which most likely originate from the northern galaxy ESO 295-IG022-N. We emphasis that the more sensitive and higher resolution radio-continuum observations of this Abell cluster would help to reveal the real nature of this complex system.

Acknowledgements – We used the KARMA/MIRIAD software package developed by the ATNF. The Australia Telescope Compact Array is part of the Australia Telescope which is funded by the Commonwealth of Australia for operation as a National Facility managed by CSIRO. PAJ acknowledges partial support from Centro de Astrofísica FONDAP 15010003 and the GEMINI-CONICYT FUND. We thank the referee for numerous helpful comments that have greatly improved the quality of this paper.

REFERENCES

Abell, G. O., Corwin, H. G., Olowin, R. P.: 1989, *Astrophys. J. Suppl. Series*, **70**, 1.
Bica, E. L. D., Pastoriza, M. G., Maia, M., da Silva, L. A. L., Dottori, H.: 1991, *Astron. J.*, **102**, 1702.
Bîrzan, L., McNamara, B. R., Carilli, C. L., Nulsen, P. E. J., Wise, M. W.: 2007, in: Heating versus Cooling in Galaxies and Clusters of Galaxies, ESO Astrophysics Symposia. Springer-Verlag Berlin Heidelberg, 115.
Burnett, C., Lonsdale, N., Pearce, K.: 2010, ATNF Summer Student Symposium, http://www.atnf.csiro.au/internal/meetings/2010/0008.html
Douglass, E. M., Blanton, E. L., Clarke, T. E., Sarazin, C. L., Wise, M. W.: 2008, *Astrophys. J.*, **673**, 763.
Gooch, R.: 2006, Karma Users Manual, Australia Telescope National Facility.
Jones, P. A., McAdam, W. B., Reynolds, J. E.: 1994, *Mon. Not. R. Astron. Soc.*, **268**, 602.
Lumsden, S. L., Nichol, R. C., Collins, C. A., Guzzo, L.: 1992, *Mon. Not. R. Astron. Soc.*, **258**, 1.
McAdam, W. B., White, G. L., Bunton, J. D.: 1988, *Mon. Not. R. Astron. Soc.*, **235**, 425.
Payne, J. L., Filipović, M. D., Pannuti, T. G., Jones, P. A., Duric, N., White, G. L., Carpano, S.: 2004, *Astron. Astrophys.*, **425**, 443.
Rafferty, D. A., McNamara, B. R., Nulsen, P. E. J., Wise, M. W.: 2006, *Astrophys. J.*, **652**, 216.
Read, A. M., Filipović, M. D., Pietsch, W., Jones, P. A.: 2001, *Astron. Astrophys.*, **369**, 467.
Sanders, J. S., Fabian, A. C., Taylor, G. B.: 2009, *Mon. Not. R. Astron. Soc.*, **393**, 71.
Sault, B., Killeen, N.: 2010, MIRIAD users Guide, ATNF.
Wise, M. W., McNamara, B. R., Nulsen, P. E. J., Houck, J. C., David, L. P.: 2007, *Astrophys. J.*, **659**, 1153.

РАДИО-КОНТИНУУМ МЛАЗЕВИ У ОКОЛИНИ НЕОБИЧНОГ ПАРА ГАЛАКСИЈА ESO 295-IG022

M. D. Filipović[1], E. J. Crawford[1], P. A. Jones[2,3] and G. L. White[1,4]

[1] *University of Western Sydney, Locked Bag 1797, Penrith South DC, NSW 1797, Australia*

E–mail: *m.filipovic@uws.edu.au, e.crawford@uws.edu.au*

[2] *School of Physics, University of New South Wales, Sydney, NSW 2052, Australia*

E–mail: *pjones@phys.unsw.edu.au*

[3] *Departamento de Astronomía, Universidad de Chile, Casilla 36-D, Santiago, Chile*

[4] *Faculty of Science, Charles Sturt University, Wagga Wagga, Australia*

УДК 524.7–77

Оригинални научни рад

У овој студији представљамо нове ATCA радио-континуум резултате посматрања региона у окружењу необичног пара галаксија ESO 295-IG022 у центру слабог јата Abell S0102. Посматрања су вршена са 6 км конфигурацијом на таласним дужинама од $\lambda = 20/13$ и $6/3$ цм. Резолуција је $\sim 2''$ на 3 цм што је довољно за разлучивање структуре у облику млаза од $\sim 3'$ дужине оргинално детектоване на 20 цм. Користећи наша нова радио-посматрања потврђујемо постојање два млаза која су настала из северније галаксије (ESO 295-IG022-N). Оба млаза су савијена и увијена према јужној галаксији (ESO 295-IG022-S). Радио спектрални индекс млаза насталог из северне галаксије (ESO 295-IG022-N) је веома стрм ($\alpha = -1.32$) што без обзира на непостојање централног тачкастог објекта потврђује изворност Активног Галактичког Језгра (АГЈ). Са друге стране, (ESO 295-IG022-S) је тачкасти радио објекат те са променљивим флуксом и спектралним индексом указује на центар АГЈ који је пројектован на линију посматрања млазева (виђених на 20 цм) насталих из северне галаксије ESO 295-IG022-N. Детектовали смо правилно организован и веома висок степен поларизације где максимална вредност износи око 70%.

A.6 Related Paper 6

Bozzetto, L. M., Filipović, M. D., Crawford, E. J., Bojičić, I. S., Payne, J. L., Medik, A., Wardlaw, B., and De Horta, A. Y. (2010). Multifrequency Radio Observations of a SNR in the LMC. The Case of SNR J0527-6549 (DEM L204). *Serbian Astronomical Journal*, 181:43–49

My contribution was to assist in the data analysis. This is a 10% contribution.

Serb. Astron. J. № 181 (2010), 43 - 49 **UDC 524.722.3 : 524.354-77**
DOI: 10.2298/SAJ1081043B Original scientific paper

MULTIFREQUENCY RADIO OBSERVATIONS OF A SNR IN THE LMC. THE CASE OF SNR J0527–6549 (DEM L204)

L. M. Bozzetto, M. D. Filipović, E. J. Crawford, I. S. Bojičić, J. L. Payne, A. Mendik, B. Wardlaw and A. Y. De Horta

School of Computing and Mathematics, University of Western Sydney
Locked Bag 1797, Penrith South DC, NSW 1797, Australia

E–mail: *m.filipovic@uws.edu.au*

(Received: July 14, 2010; Accepted: September 3, 2010)

SUMMARY: We present a detailed study and results of new Australia Telescope Compact Array (ATCA) observations of supernova remnant SNR J0527–6549. This Large Magellanic Cloud (LMC) object follows a typical supernova remnant (SNR) horseshoe morphology with a diameter of D=(66×58)±1 pc which is among the largest SNRs in the LMC. Its relatively large size indicates older age while a steeper than expected radio spectral index of α=– 0.92±0.11 is more typical of younger and energetic SNRs. Also, we report detections of regions with a high order of polarization at a peak value of ∼54%±17% at 6 cm.

Key words. ISM: supernova remnants – Magellanic Clouds – Radio Continuum: ISM – Polarization – ISM: individual objects: SNR J0527–6549

1. INTRODUCTION

The Large Magellanic Cloud (LMC) contains one of the most vigorous star forming regions, (such as 30 Dor) in our Local Group of galaxies. Located at a distance of 50 kpc (Di Benedetto 2008), it is one of the best galaxies to study supernova remnants (SNRs) due to the favourable position in the direction toward the South Pole. As well as its viewing position, the LMC is also located in one of the coldest areas of the radio sky which allows us to observe radio emission without the interruption from Galactic foreground radiation. In addition to this, the LMC resides outside of the Galactic plane and, therefore, the influence of dust, gas and stars is negligible.

Predominately non-thermal emission is a well-known characteristic of SNRs in the radio-continuum. Although SNRs have a typical radio spectral index of $\alpha \sim -0.5$ defined by $S \propto \nu^{\alpha}$, this can significantly change, due to the fact of the wide variety of types of SNRs in various environments (Filipović et al. 1998a). The ISM's morphology, structure, behaviour and evolution can be attributed to SNRs and, in turn, this heavily impacts the evolution of SNRs, as they are dependant on the environment in which they reside.

Here, we report on new radio-continuum and optical observations of previously, poorly studied, SNR J0527–6549. The observations, data reduction and imaging techniques are described in Section 2. The astrophysical interpretation of newly obtained moderate-resolution total intensity and polarimetric image in combination with the existing Magellanic Cloud Emission Line Survey (MCELS) images is discussed in Section 3.

2. OBSERVATIONAL DATA

2.1. Previous observations of SNR J0527–6549

SNR J0527–6549 was initially classified as an SNR based on the Einstein X-ray survey by Long et al. (1981) (named LHG 39). Mathewson et al. (1983) catalogued SNR J0527–6549 based on their optical observations reporting an estimated optical size of $237'' \times 212''$ ($57\times51\pm1$ pc; using 50 kpc as the distance to the LMC). They also studied this object using MOlonglo Synthesis Telescope (MOST) survey. This SNR showed in Clarke et al. (1976) 408 MHz MC4 catalogue as a distinctive point-like radio source whose integrated flux density was later re-measured by Mathewson et al. (1983) to be of 260 mJy. Mills et al. (1984) detected this source with specific MOST pointings and indicated a spectral index α=–0.45. However, Filipović et al. (1998b) reported a flatter spectral index α=–0.2±0.1.

An optically identified object at this position was also listed in the Davies et al. (1976) catalogue of nebular complexes in the Magellanic Clouds as emission nebulae — DEM L204. Chu and Kennicutt (1988) classified SNR J0527–6549 to belong to Population II? (with '?' indicating uncertain classification) group with very distant (non-influential) stellar association of LH 53 at some 340 pc. Filipović et al. (1998b), using *ROSAT* All Sky Survey (RASS) observations, detected X-ray emission from SNR J0527–6549 (LMC RASS 213). Filipović et al. (1998a) added a further confirmation with a set of single dish Parkes radio-continuum observations on a wide frequency range (Filipović et al. 1995, 1996). Blair et al. (2006) reported a marginal detection only in C III at far ultraviolet wavelengths based on FUSE (Far Ultraviolet Spectroscopic Explorer) satellite. Finally, Haberl and Pietsch (1999) (named SNR as HP 180) discuss the X-Ray properties of SNR J0527–6549 based on ROSAT PSPC observations. Most recently, Payne et al. (2008) presented optical spectroscopy of a wide range of LMC SNRs including SNR J0527–6549. They found an enhanced [SII]/H_α ratio of 0.8 typical of SNRs.

2.2. New observations of SNR J0527–6549

We observed SNR J0527–6549 with the Australia Telescope Compact Array (ATCA) on 2nd October 1997 using the array configuration EW375 at wavelengths of 3 and 6 cm (ν=8640 and 4800 MHz). Baselines formed with the 6th ATCA antenna were excluded, as the other five antennas were arranged in a compact configuration. The observations were carried out in the so called "snap-shot" mode, totaling ∼1 hour of integration over a 12 hour period. Source PKS B1934-638 was used for the primary calibration and source PKS B0530-727 was used for the secondary (phase) calibration. The MIRIAD (Sault and Killeen 2010) and KARMA (Gooch 2006) software packages were used for reduction and analysis. More information on the observing procedure and other sources observed in this session/project can be found in Bojičić et al. (2007), Crawford et al. (2008a,b, 2010) and Čajko et al. (2009).

Images were formed using the MIRIAD multi-frequency synthesis (Sault and Wieringa 1994) and natural weighting. They were deconvolved using the CLEAN and RESTOR algorithms with the primary beam correction applied using the LINMOS task. A similar procedure was used for both U and Q Stokes parameter maps. Because of the low dynamic range (signal to noise ratio between the source flux and 3σ noise level) self-calibration could not be applied. The 6 cm image (Fig. 1) has a resolution $41.4''\times30.3''$ at PA=0° and an estimated r.m.s. noise 0.15 mJy/beam. Similarly, we made an image of SNR J0527–6549 at 3 cm (Fig. 1) with resolution $22.9''\times16.5''$ (PA=0°).

We also used the Magellanic Cloud Emission Line Survey (MCELS) that was carried out with the 0.6 m University of Michigan/CTIO Curtis Schmidt telescope, equipped with a SITE 2048 × 2048 CCD, which gave a field of 1.35° at a scale of $2.4''$ pixel^{-1}. Both the LMC and SMC were mapped in narrow bands corresponding to Hα, [O III] (λ=5007 Å), and [S II] (λ=6716, 6731 Å), plus matched red and green continuum bands that are used primarily to subtract most of the stars from the images to reveal the full extent of the faint diffuse emission. All the data have been flux-calibrated and assembled into mosaic images, a small section of which is shown in Figs. 2 and 3. Further details regarding the MCELS are given by Smith et al. (2006) and at http://www.ctio.noao.edu/mcels. Here, for the first time, we present optical images of this object in combination with our new radio- continuum data.

3. RESULTS AND DISCUSSION

The remnant has a typical horseshoe morphology (Fig. 1) centered at RA(J2000)=$5^h27^m54.9^s$, DEC(J2000)=–65°49′49.2″ with a measured diameter of $271''\times240''\pm4''$ ($66\times58\pm1$ pc) at 6 cm. We used the KARMA tool KPVSLICE to estimate the SNR J0527–6549 extension at (6 cm image) the 3σ noise level (0.45 mJy) along the major (NE) (Fig. 4) and minor (NW) axis (PA=45°). We note that our estimate of the major diameter is significantly larger (∼34″) than the previously measured by Mathewson et al. (1983). We attribute this to the SNR NE extension detected in [O III] that was not seen in any other optical wavebands (see Fig. 3; right panel). However, our measurements are in a better agreement with radio diameters (61×56 pc) previously reported by Mills et al. (1984). The MCELS images are showing a particularly strong [O III] emission around the North, North East (NE) and North West (NW) part of the shell. Especially, in the NW direction where SNR J0527–6549 extends to $325''\pm4''$ (78 ± 1 pc) diameter which is significantly more than at radio or other optical frequencies (Fig. 3; right panel). Also, we note a prominent Hα emission towards the southern part of SNR that is probably causing a shell brightening at that end. Overall, the optical and radio-continuum emissions follow each other.

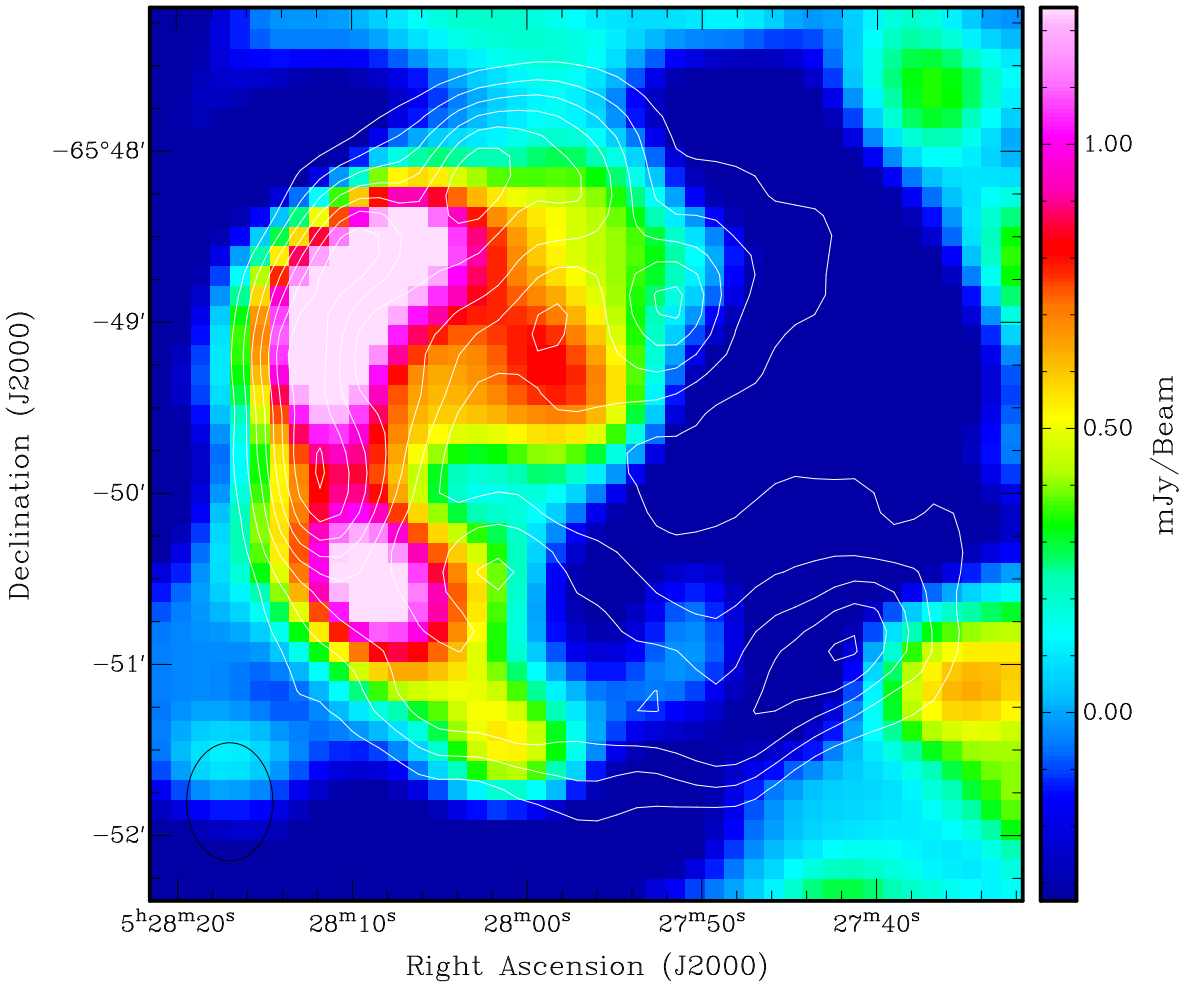

Fig. 1. *ATCA observations of SNR J0527–6549 at 3 cm (8.6 GHz) overlaid with 6 cm (4.8 GHz) contours. The contours are 3, 5, 7, 9, 11, 13, 15 and 17σ. The black circle in the lower left corner represents the synthesised beamwidth (at 6 cm) of 41.4″×30.3″. The sidebar quantifies the pixel map and its units are mJy/beam.*

In order to estimate the spectral energy distribution for this object, we use our new integrated flux density measurements at various radio frequencies with 408 MHz measurement by Mathewson et al. (1983), 843 MHz measurement by Mills et al. (1984) as well as at 1400 MHz (from the mosaics presented by Filipović et al. (2009) and Hughes et al. (2007)). We list these flux density measurements at various frequencies in Table 1 and then plot the SNR J0527–6549 spectral index (α) in (Fig. 5). The overall radio-continuum spectral index of SNR J0527–6549 is unusually steep (α=–0.92±0.11) given that this is most likely an older (evolved) SNR, due to its rather large size of ∼66 pc. Usually, a steep gradient like this would suggest a much younger and energetic SNR. However, in this case, the steepness can be contributed to the fact of missing short spacings at higher radio-continuum frequencies (4800 and 8640 MHz) and, therefore, a missing flux. Specifically at 3 cm (where the ATCA primary beam is ∼300″) this SNR edges would be positioned close to the primary beam boundary where the flux tends to significantly uncertain. We also note that this may indicate that a simple model does not accurately describe the data, and that a higher order model is needed. This is not unusual, given that several other Magellanic Clouds SNR's exhibit this "curved" spectra (Crawford et al. 2008b). Noting the breakdown of the power law fit at shorter wavelengths, we decomposed the spectral index estimate into two components, one (α_1) between 73 and 20 cm, and the other (α_2) between 6 and 3 cm. The first component, α_1= – 0.51±0.08, is a very good fit and typical of an SNR, whereas the second, α_2=–1.60±0.34, is a poor fit, and indicates that non-thermal emission can be described by different populations of electrons with different energy indices. Although the low flux at 3 cm (and to a lesser extent at 6 cm) could cause the large deviations, an underestimate of up to ∼50% would still lead to a "curved" spectrum.

Table 1. Integrated Flux Density of SNR J0527–6549.

ν (MHz)	λ (cm)	R.M.S (mJy)	Beam Size ($''$)	S_{Total} (mJy)	Reference
408	73	—	156×156	260	Mathewson et al. (1983)
843	36	1.5	43×43	166	Mills et al. (1984)
1400	20	1.5	45.0×45.0	140	This Work
4800	6	0.15	41.4×30.2	38.4	This Work
8640	3	0.17	22.9×16.5	15.0	This Work

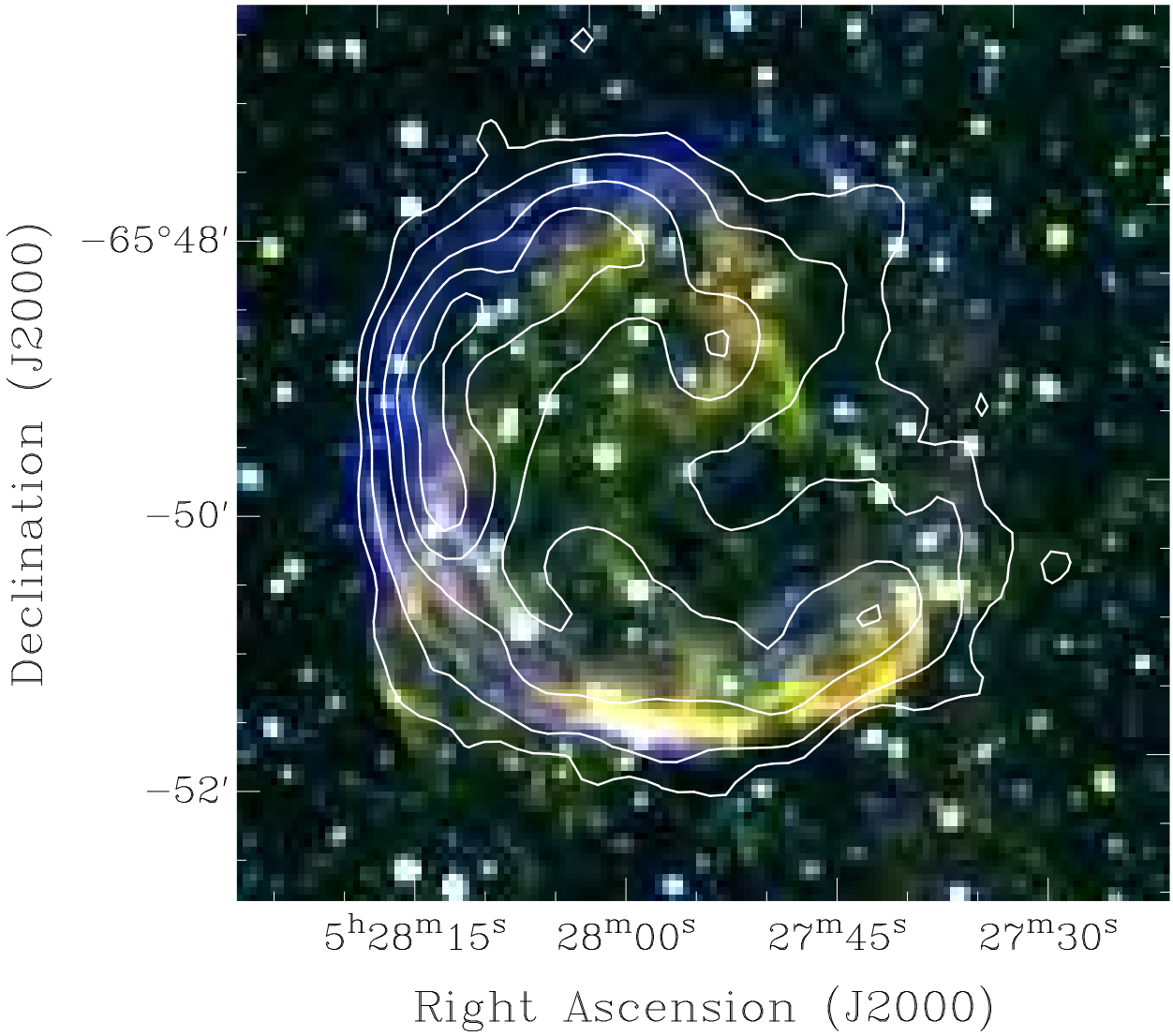

Fig. 2. *MCELS composite optical image (RGB =Hα,[SII],[OIII]) of SNR J0527–6549 overlaid with 6 cm contours. The contours are 1, 3, 7, 11 and 15σ.*

Such a curved spectrum, shown in Fig. 5, can be explained using the so-called diffuse shock acceleration (DSA) theory coupled with the effect of synchrotron losses within the finite emission region. If the thin region near the shock discontinuity is not resolved by the telescope beam, the observed emission includes some flux from electrons which have been diffused away from the place of effective acceleration and lose a significant amount of energy via the synchrotron emission. As these losses are more severe for higher energy electrons, we expect this to steepen the observed synchrotron spectrum. For details see Heavens and Meisenheimer (1987), Longair (2000, and references therein).

The linear polarization images for each frequency were created using parameters Q and U (Fig. 6). The 6 cm image reveals some strong linear polarization, greater than with various other LMC SNRs (Bojičić et al. 2007, Crawford et al. 2008a,b, Čajko et al. 2009, Crawford et al. 2010). The mean fractional polarisation at 6 cm was calculated using the flux density and polarisation:

$$P = \frac{\sqrt{S_Q^2 + S_U^2}}{S_I} \cdot 100\% \qquad (1)$$

where S_Q, S_U and S_I are integrated intensities for Stokes parameters Q, U and I. Our estimated peak value is 54%±17% at 6 cm and no reliable detection at 3 cm. Along the shell there is a very strong uniform polarisation coinciding with the total peak intensity located at the north-west side of the shell. We note that SNR J0527–6549 exhibits one of the strongest polarisations observed so far in the LMC averaged at approximately 50% (Fig. 6) as would be expected from the non-thermal SNRs. This relatively high level of polarization is (theoretically) expected for an SNR with a radio spectrum of around or less than −0.5 (Rolfs and Wilson 2003). Possibly, this may indicate varied dynamics along the shell. Without reliable polarisation measurements at a second frequency we could not determine the Faraday rotation, and thus cannot deduce the magnetic field strength.

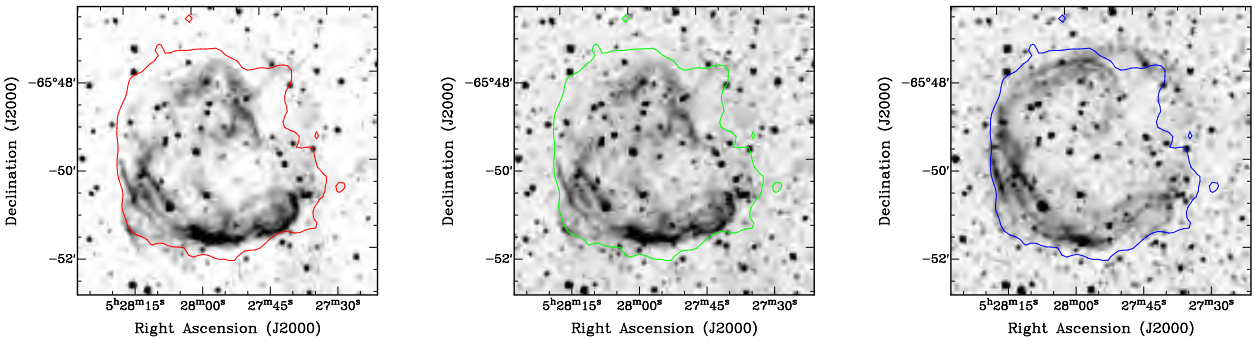

Fig. 3. *MCELS optical images (Hα (Left), [S II] (Middle), [O III] (Right)) of SNR J0527–6549 overlaid with a single 1σ 6 cm contour.*

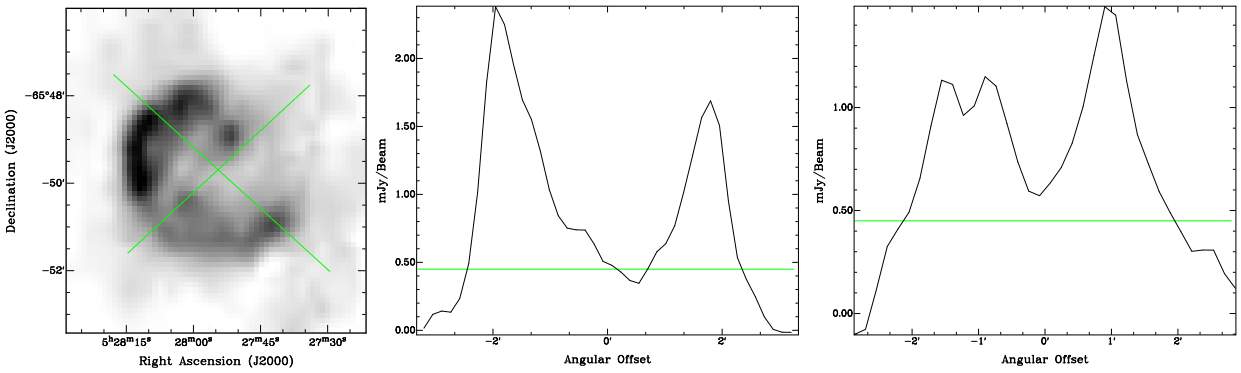

Fig. 4. *The left image shows the major and minor axis, with the major axis starting at the NW corner and the minor axis starting at the SW corner. The center image shows the I-Profile of the major axis with the 3σ line shown. The right image shows the I-Profile of the minor axis with the 3σ line shown.*

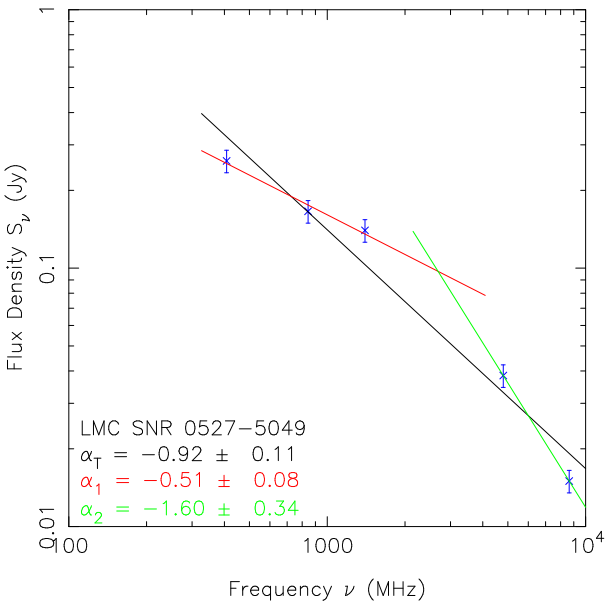

Fig. 5. *Radio-continuum spectrum of SNR J0527–6549.*

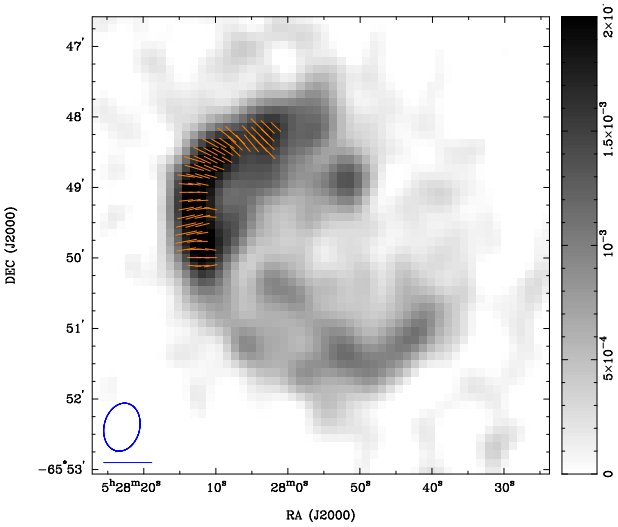

Fig. 6. *ATCA observations of SNR J0527–6549 at 6 cm (4.8 GHz). The blue circle in the lower left corner represents the synthesised beamwidth of 41.4″×30.3″, and the blue line below the circle is the polarization vector of 100%. The sidebar quantifies the pixel map and its units are Jy/beam.*

4. CONCLUSION

We conducted the highest resolution radio-continuum and optical observations to date of SNR J0527–6549. From this analysis, we confirmed this object as a bona-fide SNR with a relatively large diameter of 271″×240″±4″ (66×58±1 pc), a complex spectral index (α = –0.92±0.11), strong polarisation of ∼54%±17%, as well as strong circular optical [O III] emission.

Acknowledgements – We used the KARMA software package developed by the ATNF. The Australia Telescope Compact Array is a part of the Australia Telescope which is funded by the Commonwealth of Australia for operation as a National Facility managed by CSIRO. We thank the Magellanic Clouds Emission Line Survey (MCELS) team for access to the optical images. We were granted observation time at the South African Astronomical Observatory (SAAO) and wish to thank them for their kind help and accommodations. Travel to the SAAO was funded by Australian Government ANSTO AMNRF grant number 09/10-O-03. We thank the referee (D. Urošević) for numerous helpful comments that have greatly improved the quality of this paper.

REFERENCES

Blair, W. P., Ghavamian, P., Sankrit, R., Danforth, C. W.: 2006, *Astrophys. J. Suppl. Series*, **165**, 480.

Bojičić, I. S., Filipović, M. D., Parker, Q. A., Payne, J. L., Jones, P. A., Reid, W., Kawamura, A., Fukui, Y.: 2007, *Mon. Not. R. Astron. Soc.*, **378**, 1237.

Čajko, K. O., Crawford, E. J., Filipović, M. D.: 2009, *Serb. Astron. J.*, **179**, 55.

Chu, Y-H., Kennicutt, R. C.: 1988, *Astron. J.*, **96**, 1874.

Clarke, J. N., Little, A. G., Mills, B. Y.: 1976, *Aust. J. Phys. Astrophys. Suppl.*, **40**, 1.

Crawford, E. J., Filipović, M. D. and Payne, J. L.: 2008a, *Serb. Astron. J.*, **176**, 59.

Crawford, E. J., Filipović, M. D., De Horta, A. Y., Stootman, F. H., Payne, J. L.: 2008b, *Serb. Astron. J.*, **177**, 61.

Crawford, E. J., Filipović, M. D., Haberl, F., Pietsch, W., Payne, J. L., De Horta, A. Y.: 2010, *Astron. Astrophys.*, **518**, A35.

Davies, R. D., Elliott, K. H., Meaburn, J.: 1976, *Mem. R. Astron. Soc.*, **81**, 89.

Di Benedetto, G. P.: 2008, *Mon. Not. R. Astron. Soc.*, **390**, 1762.

Filipović, M. D., Haynes, R. F., White, G. L., Jones, P. A., Klein, U., Wielebinski, R.: 1995, *Astron. Astrophys. Suppl. Series*, **111**, 331.

Filipović, M. D., White, G. L., Haynes, R. F., Jones, P. A., Meinert, D., Wielebinski, R., Klein, U.: 1996, *Astron. Astrophys. Suppl. Series*, **120**, 77.

Filipović, M. D., Haynes, R. F., White, G. L., Jones, P. A.: 1998a, *Astron. Astrophys. Suppl. Series*, **130**, 421.

Filipović, M. D., Pietsch, W., Haynes, R. F., White, G. L., Jones, P. A., Wielebinski, R., Klein, U., Dennerl, K., Kahabka, P., Lazendić, J. S.: 1998b, *Astron. Astrophys. Suppl. Series*, **127**, 119.

Filipović, M. D., Crawford, E. J., Hughes, A., Leverenz, H., de Horta, A. Y., Payne, J. L., Staveley-Smith, L., Dickel, J. R., Stootman, F. H., White, G. L.: 2009, in van Loon J. T., Oliveira J. M., eds, *IAU Symposium Vol. 256*, PDF8.

Gooch, R.: 2006, Karma Users Manual, ATNF, Sydney.
Haberl, F., Pietsch, W.: 1999, *Astron. Astrophys. Suppl. Series.* **139**, 277.
Heavens, A. F., Meisenheimer, K.: 1987, *Mon. Not. R. Astron. Soc.*, **225**, 335.
Hughes, A., Staveley-Smith, L., Kim, S., Wolleben, M., Filipović, M. D.: 2007, *Mon. Not. R. Astron. Soc.*, **382**, 543.
Long, K. S., Helfand, D. J., Grabelski, D. A.: 1981, *Astrophys. J.*, **248**, 925.
Longair, M. S.: 2000, High Energy Astrophysics (vol. 2), Cambridge University Press.
Mathewson, D. S., Ford, V. L., Dopita, M. A., Tuohy, I. R., Long, K. S., Helfand, D. J.: 1983, *Astrophys. J. Suppl. Series*, **51**, 345.
Mills, B. Y., Turtle, A. J., Little, A. G., Durdin, J. M.: 1984, *Aust. J. Phys.*, **37**, 321.
Payne, J. L., White, G. L., Filipović, M. D.: 2008, *Mon. Not. R. Astron. Soc.*, **383**, 1175.
Rolfs, K., Wilson, T.: 2003, "Tools of Radio Astronomy 4ed.", Springer, Berlin.
Sault, R. J., Killeen, N.: 2010, Miriad Users Guide, ATNF, Sydney.
Sault, R. J., Wieringa, M. H.: 1994, *Astron. Astrophys. Suppl. Series*, **108**, 585.
Smith, C., Points, S., Winkler, P. F.: 2006, *NOAO Newsletter*, **85**, 6.

МУЛТИФРЕКВЕНЦИОНА РАДИО-ПОСМАТРАЊА ОСТАТКА СУПЕРНОВЕ У ВЕЛИКОМ МАГЕЛАНОВОМ ОБЛАКУ. СЛУЧАЈ SNR J0527–6549 (DEM L204)

L. M. Bozzetto, M. D. Filipović, E. J. Crawford, I. S. Bojičić, J. L. Payne, A. Mendik, B. Wardlaw and A. Y. De Horta

School of Computing and Mathematics, University of Western Sydney
Locked Bag 1797, Penrith South DC, NSW 1797, Australia

E–mail: *m.filipovic@uws.edu.au*

УДК 524.722.3 : 524.354-77
Оригинални научни рад

У овој студији представљамо нове ATCA резултате посматрања у радио-континууму за остатак супернове у Великом Магелановом Облаку – SNR J0527–6549. Овај објект је типичан остатак супернове са потковичастом морфологијом. Измерена вредност дијаметра износи D=(66×58)±1 парсека. Ово је један од највећих остатака супернових у Великом Магелановом облаку. Димензије остатка указују да је то старији објект, док је спектрални индекс ($\alpha = -0.92 \pm 0.11$) веома стрм и повремено се среће код млађих остатака. Детектовали смо висок степен поларизације чак и до 54%±17% (мерења на 6-цм).

A.7 Related Paper 7

Bojičić, I. S., Filipović, M. D., and Crawford, E. J. (2010). SMC SMP 24: A Newly Radio-Detected Planetary Nebula in the Small Magellanic Cloud. *Serbian Astronomical Journal*, 181:63–68

My contribution was to assist in the data analysis. This is a 30% contribution.

Serb. Astron. J. № 181 (2010), 63 - 68 **UDC 524.722.7 : 524.37–77**
DOI: 10.2298/SAJ1081063B Preliminary report

SMC SMP 24: A NEWLY RADIO-DETECTED PLANETARY NEBULA IN THE SMALL MAGELLANIC CLOUD

I. S. Bojičić, M. D. Filipović and E. J. Crawford

University of Western Sydney, Locked Bag 1797, Penrith South DC, NSW 1797, Australia
E–mail: *i.bojicic@uws.edu.au*

(Received: September 16, 2010; Accepted: September 27, 2010)

SUMMARY: In this paper we report a new radio-continuum detection of an extragalactic planetary nebula (PN): SMC SMP 24. We show the radio-continuum image of this PN and present the measured radio data. The newly reduced radio observations are consistent with the multi-wavelength data and derived parameters found in the literature. SMC SMP 24 appears to be a young and compact PN, optically thick at frequencies below 2 GHz.

Key words. planetary nebulae: individual: SMC SMP 24 – Magellanic Clouds – Radio Continuum: ISM

1. INTRODUCTION

The importance of the radio-continuum properties of planetary nebulae (PNe) has been recently reinstated by the report of the radio-continuum observations of PNe in the Magellanic Clouds (Filipović et al. 2009). The comprehensive multifrequency study, based on Australia Telescope Compact Array+Parkes mosaic surveys of Magellanic Clouds (MCs) (Hughes et al. 2006, 2007, Payne et al. 2004, 2009, Filipović et al. 1995, 1997, 2002, 2005, 2008), helped to reveal the true nature of more than 50 PN candidates in MCs as compact H II regions. Also, based on our radio data, Reid and Parker (2010) were able to re-classify three ultra-bright PNe (previously classified as 'true' PNe) as contaminants due to their strong radio fluxes. Our MCs radio PN detections represent only ∼3 % of the optical PN population of the MCs. Most likely, we are selecting only the strongest radio-continuum emitters, possibly at a variety of different stages of their evolution (Vukotić et al. 2009).

Prior to this study, a radio detection of only three extragalactic PNe have been reported in the literature (Zijlstra et al. 1994, Dudziak et al. 2000). Based on the radio-continuum properties of radio-bright Galactic PNe the expected radio flux densities at the distance of the Large Magellanic Cloud (LMC) and the Small Magellanic Cloud (SMC) are up to ∼2.5 and ∼2.0 mJy, respectively at 1.4 GHz. While the LMC sample conforms with the radio luminosity limit predicted from Galactic PNe, the SMC PN sample appears to be unusually strong radio emitter.

The known and well refined distances to the LMC/SMC provide a large opportunity for accurate evaluation of important physical properties for PNe such as ionised masses and electron densities. Also, a statistically significant sample of radio detected extragalactic PNe will allow the construction and examination of the bright end of the radio PN luminosity function (PNLF) and comparison with established theoretical and empirical PNLFS of MCs obtained at other wavelengths (Jacoby et al. 1990, Mendez et al. 1993, Stanghellini 1995, Jacoby and De Marco 2002, Ciardullo et al. 2002).

Therefore, we initiated a deep, 6 cm radio-continuum, survey which will attempt to detect and accurately measure the radio-continuum flux densities of 50+ MCs PNe. As the first step in this project we thoroughly examined the archived Australia Telescope Compact Array (ATCA) data (the Australia Telescope Online Archive[1]) in order to find out if any of the objects have already been observed and to estimate upper flux limits for the prepared sample. In this paper, we report the radio detection of SMC SMP 24 (hereafter SMP 24), found in the ATCA's archival deep observation of the SMC supernova remnant SNR 0101-7226 conducted in 1993/1994 by Ye et al. (1995).

2. MULTIWAVELENGTH DATA

SMP 24 (LHA 115 – N S70; Henize, 1956) is an SMC PN located approximately 2 arcmin north of the N S66 giant star-forming complex. From its appearance in Hα and [O III] spectral lines, Stanghellini et al. (2003) designated this PN as an elliptical with a possible faint halo. The authors reported a flux calibrated intensity in the Hβ line, optical extinction ($c_{H\beta}$), and relative intensities of several bright spectral lines. Also, the photometric radii of the nebula and the nebular dimensions, measured from the 10% brightness contour, have been reported. They determined the electron density $\log n_e \approx 3.1$ from [S II]$\lambda\lambda$6716,6731 lines and calculated ionised mass of the nebula ($M_i \approx 0.86\ M_\odot$). It is important to note that the reported ionised mass, calculated using the Eq. (6) from Boffi and Stanghellini (1994), is by a factor of 2.8 and 4 larger than the average mass of the rest of the PNe from the SMC and LMC sample reported in this paper, respectively. From the [O II] electron density diagnostic (I(λ3726.0)/I(λ3728.8), Stanghellini et al. (2009) and Shaw et al. (2010) reported a significantly higher electron density $\log n_e \approx 3.4$ for this PN of. Assuming the rest of the parameters used by Stanghellini et al. (2003) remains the same, the new electron density estimate will half the ionised mass to $M_i \approx 0.4$. The newly obtained mass is in a much better agreement with the rest of the SMC PN sample. We tabulated the reported data relevant to this study in Table 1.

SMP 24 is observed as a part of spectroscopic observations of 25 MCs PNe conducted with the *Spitzer Space Telescope* Infrared Spectrograph (Bernard-Salas et al. 2009). The presence of hydrogenated amorphous carbon molecules (HACs) in this PN, is interpreted by the authors as an evidence of the early evolutionary stage. The SMP 24 central star is characterised by a very low ionisation potential, also noticed by Stanghellini et al. (2009) (EC 1-2). Also, this PN is detected in the Spitzer Survey of the Small Magellanic Cloud (S^3MC: Bolatto et al. 2007), which imaged the star-forming body of the SMC in all seven MIPS and IRAC wave bands. Measured flux densities from the B band to the 70 μm band (where the PN is not detected) are tabulated in Table 2.

Table 1. SMP 24: Multi-wavelength data and parameters compiled from the literature.

Parameter			Reference
RA(2000)	00 59 16.6		1
DEC(2000)	-72 02 00.8		1
$\log F(H\beta : \lambda 4861)$	-12.66	$(\frac{ergs}{cm^2 s})$	2
$c(H\beta)$	0.047		2
R_{phot}	0.20	(arcsec)	2
θ	0.38	(arcsec)	2
T_e	11620^{+910}_{-740}K	(K)	3
$\log n_e$	3.4(3.1†)	(cm^{-3})	3(2)
M_{ion}	0.4 (0.86†)	($M_\odot$)	4(2)
$n(He^+)/n(H^+)$	0.097±0.011		5

References: 1) Jacoby and De Marco (2002), 2) Stanghellini et al. (2003), 3) Shaw et al. (2010), 4) this paper, 5) Idiart et al. (2007)

3. 20 cm DETECTION OF SMP 24

SMP 24 was observed by T. Ye, S. Amy, L. Ball and J. Dickel with the ATCA as a part of the project C281 over two 12 hour sessions on 25th August 1993 and 10th February 1994. Two complementary array configurations at 20/13 cm (ν=1377/2377 MHz) were used – 1.5B and 6B. However, SMP 24 is positioned some $\sim 18'$ from the pointing centre and therefore appeared outside of the primary beam of the 13 cm observations. The source 1934-638 was used for the primary calibration and the source 0252-712 as the secondary calibrator. More information on observing procedure and other sources observed during these sessions can be found in Ye et al. (1995).

The MIRIAD (Sault and Killeen 2010) and KARMA (Gooch 2006) software packages were used for reduction and analysis. The initial high-resolution image was produced from the full dataset and using the MIRIAD multi-frequency synthesis (Sault and Wieringa 1994) and natural weighting. The obtained 20 cm image has a resolution $7.0'' \times 6.6''$

Table 2. SMP 24: IR data compiled from the literature.

Band	B	V	I	J	H	K	3.6 μm	4.5 μm	5.8 μm	8.0 μm	24 μm	70 μm
F_λ(mJy)	0.878	1.622	0.395	0.473	0.534	0.902	1.870	2.252	3.813	9.292	28.028	<(10×)5

[1]http://atoa.atnf.csiro.au/

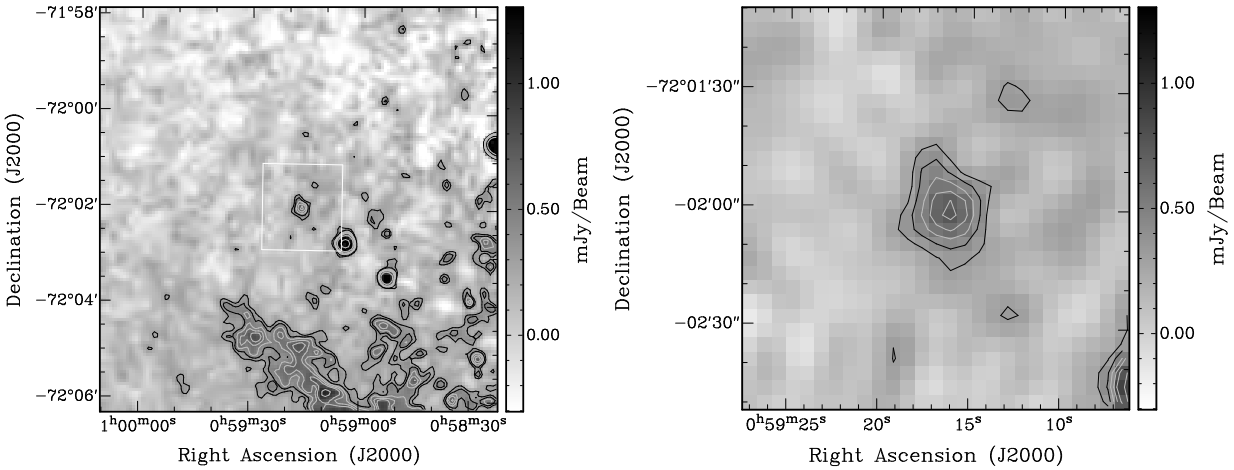

Fig. 1. *Radio-continuum total intensity images of SMP 24 overlaid with contours at: 0.3, 0.4 (black), 0.5, 0.6, 0.7, 1 and 2 mJy (grey). The white box in the left panel indicates the zoom region which is presented on the right. The beam size is shown at the bottom left corner of each of the images.*

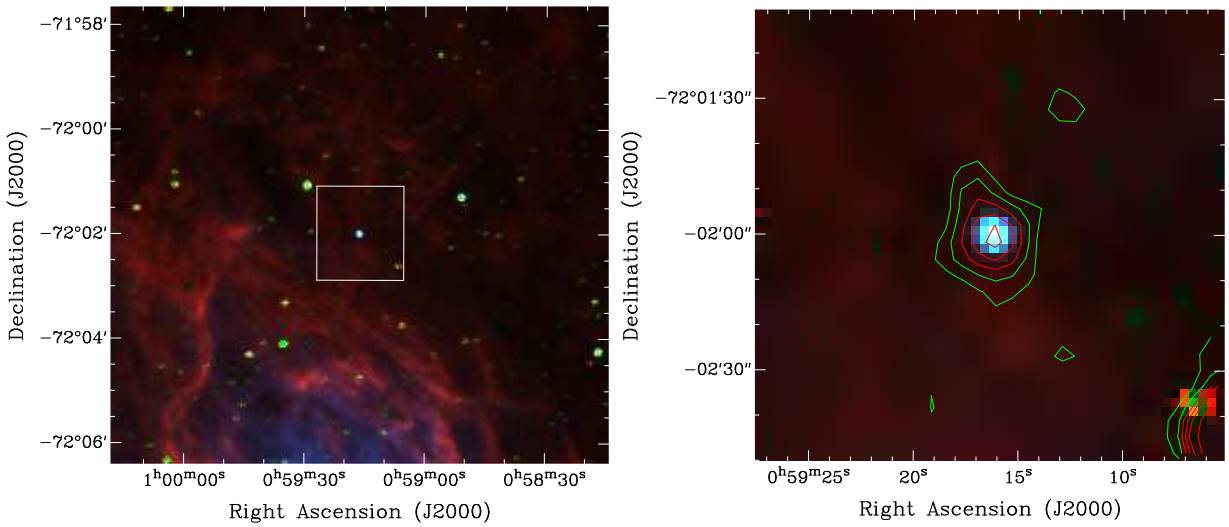

Fig. 2. *Colour composite (RGB) images of the SMP 24 region with Hα in green, [O III] in blue, and [S II] in red, and with arbitrary intensity scaling.* **Left***: The 8×8 arcmin region of the SMC where SMP 24 is located. The PN can be seen in the centre of the field as a distinctive blue point source. The white box indicates the "zoom" region which is presented on the right. The part of the star forming region N 66 can be seen to the South of the PN.* **Right***: A radio-continuum contour map of SMP 24 superposed on the MCELS colour composite image. Contours are at: 0.3, 0.4 (dark green), 0.5, 0.6, 0.7, 1 and 2 mJy (red).*

at PA=42.6° and an estimated r.m.s. noise 0.05 mJy beam^{-1} which is significantly better than Ye et al. (1995) of 0.1 mJy beam^{-1}. We attribute this difference to a slightly different cleaning technique and a careful flagging of very noisy observational data. The new high-resolution and high-sensitivity analysis of these observations will be presented in the future papers.

However, due to the effect of the decreasing phase stability with increasing baseline length, which could affect the position and the flux density estimate of faint, point like sources, we created an additional "low-resolution" total intensity image by excluding long baselines (i.e. without correlations with Antenna 6). The excerpts from this "low-resolution" map, which is used in this study, are presented in Fig. 1. The map has a resolution 15.3″×14.4″ at PA=39.8° and an estimated local r.m.s. noise 0.1 mJy beam^{-1} measured from the ∼8′×8′ box centred on the SMP 24.

To confirm the positional correlation between the newly found radio source and SMP 24, we created a colour composite (RGB) image of the SMP 24 region using data from the Magellanic Cloud Emission Line Survey (MCELS: Smith and The MCELS Team 1999). Fig. 2 (Left) represents the region of

the SMC centred on SMP 24. The PN can be seen in the centre of the field as a distinctive blue point source. In Fig. 2 (Right) we show a radio-continuum contour map of SMP 24 superposed on the MCELS colour composite image. From Fig. 2, it can be seen that the peak flux in the radio domain appears to be well correlated with the peak flux in the optical line emission.

The position and the peak flux density of the SMP 24 was determined by fitting a two-dimensional Gaussian to the restored and beam-corrected total intensity map. We used the MIRIAD's task IMFIT with a clip level of 5 σ (where σ is the measured local r.m.s. noise). All pixels below the clipping level were excluded from the fitting process. The error in the measured peak flux density is estimated as a quadrature sum from the local noise level (0.1 mJy beam^{-1}) and the uncertainty in the gain calibration (10%). However, due to the non-linear systematic errors which can arise from a large distance from the phase centre and a low signal to noise ratio (e.g. CLEAN bias), we applied additional 30% of uncertainty in the final flux density estimate. The results and the parameters used in the fitting procedure are presented in Table 3.

Table 3. SMP 24: ATCA radio-continuum data.

Parameter		
Frequency	1337	MHz
Synth. Beam	15×14	(arcsec)
local r.m.s. noise (σ)	0.1	(mJy beam^{-1})
Peak Flux	0.73±0.13	(mJy beam^{-1})
Flux Density	0.7±0.4	(mJy)
RA(2000)	00 59 16.3	
DEC(2000)	-72 01 59.9	

4. DISCUSSION

The presented multi-wavelength data is in a good agreement with the suggestion that SMP 24 is a very young PN (Bernard-Salas et al. 2009). The 20 cm peak flux density observed in this PN corresponds to the low limit for the radio surface brightness temperature of $\sim 4.3 \times 10^3$ K (assuming the upper limit of $\theta \approx 0.38$) for the angular diameter. This implies an optically thick or at least partially optically thick radio-continuum emission at 20 cm. The same implication can also arise from a comparison between the measured radio flux density and the flux derived from the Hβ emission line. Due to the same dependence on the nebular density, it is expected that the centimeter radio-continuum emission and Balmer lines emission are well correlated (see Pottasch 1984, Eq. IV-26). From parameters tabulated in Table 1 (F(Hβ), c(Hβ), T_e and $n(He^+)/n(H^+)$), we estimated flux of 1.1 mJy at 1.4 GHz. Although within the uncertainty range, this 40% deviation from the measured 1.4 GHz radio-continuum flux indicates that the self-absorption by the nebula is important in this frequency band and implies an existence of a significant density stratification (where the reported $\log n_e \approx 3.4$ cm^{-3} is probably only the average).

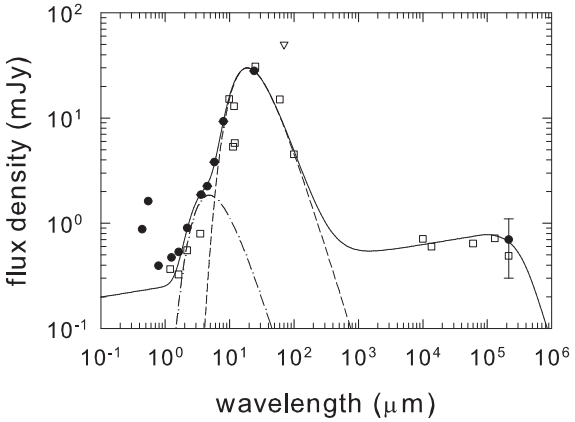

Fig. 3. *SED of SMP 24 from B band to radio frequencies. Dashed line represents the best fit to the FIR band with the black body (BB) approximation. The dot-dashed line represents the best fit (BB approximation) to the empirical distribution in NIR and MIR bands. The summed SED of the radio-continuum, dust and the hot dust is plotted with solid line. The triangle represents the detection limit in the 70 μm band. Overplotted boxes represent the observed SED of a young Galactic PN IC 418, scaled to the distance of the SMC (see text for more details).*

The empirical and modelled spectral energy distributions (SED) of SMP 24 are presented in Fig. 3. Since only one observation is available in the radio-continuum band, we roughly estimated the position of the turnover (critical) frequency using the obtained brightness temperature at 20 cm. From T_b=T_e(1-$e^{-\tau_\nu}$), we found an average optical depth of $\tau_{20cm} = 0.47$ at 20 cm. The critical frequency (ν_c) can now be found from $\tau_\nu = (\nu/\nu_c)^{-2.1}$ (Pottasch 1984). From these two points we constructed the SED for SMP 24 using the simple approximation of the uniformly ionised region with constant density and constant electron temperature (see Eq. (4) in Sharova 2002).

Assuming that SMP 24 is a young planetary nebula, we expect its central star still be closely surrounded by the ejected dusty envelope. In order to estimate the dust temperature (T_d), we fitted a blackbody spectrum to the far IR (FIR) data. It is important to note that the R_{phot} measurement from Stanghellini et al. (2003) is used as an estimate for the angular diameter of the emitting dust. Also, no attempt was made to estimate the optical depth in IR bands. The best fit is obtained with $T_d \approx 270$ K (Fig. 3: dashed line). However, to better reproduce the observed SED down to 1 μm, we fitted additional hot dust component in the mid and near IR bands (MIR and NIR, respectively) with estimated $T_{hd} \approx 1000$ K (dot-dashed line) and with the same

approximations used for the FIR band. The summed SED of the radio-continuum, the dust and hot dust was plotted in Fig. 3 with solid line. The MIR to radio ratio for this object is found to be ~ 12 which is in accord with a range of values expected for the PNe (Cohen and Green 2001, Cohen et al. 2007).

For comparison, we overplotted the observed radio-continuum to IR SED of young Galactic PN IC 418 scaled to the distance of SMC. Observational data are from Meixner et al. (1996), Guzmán et al. (2009), Pazderska et al. (2009) and Vollmer et al. (2010) and with adopted distance to this PN of 1.3 kpc (Guzmán et al. 2009). This object is already used by Bernard-Salas et al. (2009) for a comparison with the SMC PN SiC feature (broad feature from 9 to 13 μm seen regularly in carbon stars but very rarely in Galactic PNe). IC 418 is a bright and young C-rich Galactic PN with well defined ring structure with angular diameter of ~ 12 arcsec (~ 0.25 arcsec scaled to the SMC distance). It is surrounded by a low-level ionised halo and embedded into a large molecular envelope (Taylor et al. 1989, Hyung et al. 1994). As can be seen from Fig. 3, IC 418 shows a clear similarity in SED with SMP 24.

5. SUMMARY

In this paper, we presented a detection of radio-continuum emission from the SMC PN: SMP 24. This object is a radio luminous PN with estimated flux density of 0.7±0.4 mJy at 1.4 GHz ($\sim$ 2.7 Jy scaled to the distance of 1 kpc). Because of the relatively high brightness temperature at 1.4 GHz and the significant difference between the measured radio-continuum flux and that predicted from Hβ, we conclude that the ionised shell of this PN is very likely optically thick (or partially optically thick) at frequencies below 2 GHz. However, it is important to note that, in order to properly examine radio-continuum properties of this PN, the additional, multi-frequency radio-continuum data are needed. This PN is scheduled to be observed in our ATCA-based follow-up observations of MC's PNe.

We discussed the evolutionary stage and spectral energy distribution of this SMC PN in the light of the available multi-wavelength data and from the evident similarities with a young and well studied Galactic PN IC 418. SMP 24 appears to be a young PN with a dynamic age of <1000 yr. The ionised gas and the hot dust are very likely still located in the same region, close to the central star. We believe that our future high resolution and high sensitivity radio-continuum observations of SMP 24 will help to reveal some of its intrinsic physical properties (e.g. emission measure, physical size and mass of the ionised shell).

Acknowledgements – We used the KARMA and MIRIAD software package developed by the ATNF. The Australia Telescope Compact Array (/ Parkes telescope / Mopra telescope / Long Baseline Array) is part of the Australia Telescope which is funded by the Commonwealth of Australia for operation as a National Facility managed by CSIRO. We thank the Magellanic Clouds Emission Line Survey (MCELS) team for access to the optical images. This research has made use of the SIMBAD database and VizieR catalogue access tool, operated at CDS, Strasbourg, France. We were granted the observation time at the South African Astronomical Observatory (SAAO) and wish to thank them for their kind help and accommodations. Travel to the SAAO was funded by the Australian Government ANSTO AMNRF grant number 09/10-O-03. This research has been supported by the University of Western Sydney research grant (project number 20721.80758).

REFERENCES

Bernard-Salas, J., Peeters, E., Sloan, G. C., Gutenkunst, S., Matsuura, M., Tielens, A. G. G. M., Zijlstra, A. A. and Houck, J. R.: 2009, *Astrophys. J.*, **699**, 1541.

Boffi, F. R. and Stanghellini, L.: 1994, *Astron. Astrophys.*, **284**, 248.

Bolatto, A. D., Simon, J. D., Stanimirović, S., van Loon, J. T., Shah, R. Y., Venn, K., Leroy, A. K., Sandstrom, K., Jackson, J. M., Israel, F. P., Li, A., Staveley-Smith, L., Bot, C., Boulanger, F. and Rubio, M.: 2007, *Astrophys. J.*, **655**, 212.

Ciardullo, R., Feldmeier, J. J., Jacoby, G. H., Kuzio de Naray, R., Laychak, M. B. and Durrell, P. R.: 2002, *Astrophys. J.*, **577**, 311.

Cohen, M. and Green, A. J.: 2001, *Mon. Not. R. Astron. Soc.*, **325**, 531.

Cohen, M., Parker, Q. A., Green, A. J., Murphy, T., Miszalski, B., Frew, D. J., Meade, M. R., Babler, B., Indebetouw, R., Whitney, B. A., Watson, C., Churchwell, E. B. and Watson, D. F.: 2007, *Astrophys. J.*, **669**, 343.

Dudziak, G., Péquignot, D., Zijlstra, A. A. and Walsh, J. R.: 2000, *Astron. Astrophys.*, **363**, 717.

Filipović, M. D., Haynes, R. F., White, G. L., Jones, P. A., Klein, U., Wielebinski, R.: 1995, *Astron. Astrophys. Suppl. Series*, **111**, 311.

Filipović, M. D., Jones, P. A., White, G. L., Haynes, R. F., Klein, U., Wielebinski, R.: 1997, *Astron. Astrophys. Suppl. Series*, **121**, 321.

Filipović, M. D., Bohlsen, T., Reid, W., Staveley-Smith, L., Jones, P. A., Nohejl, K., Goldstein, G.: 2002, *Mon. Not. R. Astron. Soc.*, **335**, 1085.

Filipović, M. D., Payne, J. L., Reid, W., Danforth, C. W., Staveley-Smith, L., Jones, P. A., White, G. L.: 2005, *Mon. Not. R. Astron. Soc.*, **364**, 217.

Filipović, M. D. et al.: 2008, in van Loon J. T., Oliveira J. M., eds, IAU Symp. **256**, The Magellanic System: Stars, Gas, and Galaxies. Cambridge Univ. Press, Cambridge, PDF8.

Filipović, M. D., Cohen, M., Reid, W. A., Payne, J. L., Parker, Q. A., Crawford, E. J., Bojičić, I. S., de Horta, A. Y., Hughes, A., Dickel, J. and Stootman, F.: 2009, *Mon. Not. R. Astron. Soc.*, **399**, 1098.

Gooch, R., 1996, in G. H. Jacoby and J. Barnes ed., Astronomical Data Analysis Software and Systems, **101** of *Astron. Soc. of the Pacific Conf. Series*, p. 80.
Guzmán, L., Loinard, L., Goḿez, Y. and Morisset, C.: 2009, *Astron. J.*, **138**, 46.
Henize, K. G.: 1956, *Astrophys. J. Suppl. Series*, **2**, 315.
Hughes, A., Staveley-Smith, L., Kim, S., Wolleben, M., Filipović, M.: 2007, *Mon. Not. R. Astron. Soc.*, **382**, 543.
Hughes, A., Wong, T., Ekers, R., Staveley-Smith, L., Filipović, M., Maddison, S., Fukui, Y., Mizuno, N.: 2006, *Mon. Not. R. Astron. Soc.*, **370**, 363.
Hyung, S., Aller, L. H. and Feibelman, W. A.: 1994, *Publ. Astron. Soc. Pacific*, **106**, 745.
Idiart, T. P., Maciel, W. J. and Costa, R. D. D.: 2007, *Astron. Astrophys.*, **472**, 101.
Jacoby, G. H., Ciardullo, R. and Walker, A. R.: 1990, *Astrophys. J.*, **365**, 471.
Jacoby, G. H. and De Marco, O.: 2002, *Astron. J.*, **123**, 269.
Meixner, M., Skinner, C. J., Keto, E., Zijlstra, A., Hoare, M. G., Arens, J. F. and Jernigan, J. G.: 1996, *Astron. Astrophys.*, **313**, 234.
Mendez, R. H., Kudritzki, R. P., Ciardullo, R. and Jacoby, G. H.: 1993, *Astron. Astrophys.*, **275**, 534.
Oskinova, L. and Brown, J. C.: 2003, in S. Kwok, M. Dopita, and R. Sutherland ed., Planetary Nebulae: Their Evolution and Role in the Universe **209** of IAU Symposium, 425.
Payne, J. L., Filipović, M. D., Reid, W., Jones, P. A., Staveley-Smith, L., White, G. L.: 2004, *Mon. Not. R. Astron. Soc.*, **355**, 44.
Payne, J. L., Tauber, L. A., Filipović, M. D., Crawford, E. J., de Horta, A.: 2009, *Serb. Astron. J.*, **178**, 65
Pazderska, B. M., Gawroński, M. P., Feiler, R., Birkinshaw, M., Browne, I. W. A., Davis, R., Kus, A. J., Lancaster, K., Lowe, S. R., Pazderski, E., Peel, M. and Wilkinson, P. N.: 2009, *Astron. Astrophys.*, **498**, 463.
Pottasch, S. R.: 1984, in: Planetary nebulae - A study of late stages of stellar evolution. **107** of Astrophysics and Space Science Library, D. Reidel.
Reid, W. A. and Parker, Q. A.: 2010, *Mon. Not. R. Astron. Soc.*, **405**, 1349.
Sault, R. J., Killeen, N.: 2010, Miriad Users Guide, ATNF, Sydney.
Sault, R. J., Wieringa, M. H.: 1994, *Astron. Astrophys. Suppl. Series*, **108**, 585.
Sharova, O. I.: 2002, *Astron. Astrophys. Transactions*, **21**, 271.
Shaw, R. A., Lee, T., Stanghellini, L., Davies, J. E., García-Hernández, D. A., García-Lario, P., Perea-Calderón, J. V., Villaver, E., Manchado, A., Palen, S. and Balick B.: 2010, *Astrophys. J.*, **717**, 5622.
Smith, R. C., Team, T. M.: 1999, in Y.-H. Chu, N. Suntzeff, J. Hesser and D. Bohlender ed., New Views of the Magellanic Clouds **190** of IAU Symposium, 28.
Stanghellini, L.: 1995, *Astrophys. J.*, **452**, 515.
Stanghellini, L., Lee, T.-H., Shaw, R. A., Balick, B. and Villaver, E.: 2009, *Astrophys. J.*, **702**, 733.
Stanghellini, L., Shaw, R. A., Balick, B., Mutchler, M., Blades, J. C. and Villaver, E.: 2003, *Astrophys. J.*, **596**, 997.
Taylor, A. R., Gussie, G. T. and Goss, W. M.: 1989, *Astrophys. J.*, **340**, 932.
Vollmer, B., Gassmann, B., Derrière, S., Boch, T., Louys, M., Bonnarel, F., Dubois, P., Genova, F., Ochsenbein, F.: 2010, *Astron. Astrophys.*, **511**, A53.
Vukotić, B., Urošević, D., Filipović, M. D., Payne, J. L.: 2009, *Astron. Astrophys.*, **503**, 855.
Ye, T. S., Amy, S. W., Wang, Q. D., Ball, L. and Dickel, J.: 1995, *Mon. Not. R. Astron. Soc.*, **275**, 1218.
Zijlstra, A. A., van Hoof, P. A. M., Chapman, J. M. and Loup, C.: 1994, *Astron. Astrophys.*, **290**, 228.

SMC SMP 24: НОВА РАДИО ПЛАНЕТАРНА МАГЛИНА У МАЛОМ МАГЕЛАНОВОМ ОБЛАКУ

I. S. Bojičić, M. D. Filipović and E. J. Crawford

University of Western Sydney, Locked Bag 1797, Penrith South DC, NSW 1797, Australia
E–mail: *i.bojicic@uws.edu.au*

УДК 524.722.7 : 524.37–77
Претходно саопштење

У овој студији представљамо нове ATCA резултате посматрања у радио-континууму вангалактичке планетарне маглине: SMC SMP 24. Нова радио-посматрања су конзистентна са посматрањима на осталим таласним дужинама и параметрима нађеним у досадашњим истраживањима. SMC SMP 24 је највероватније млада и компактна планетарна маглина, оптички густа на фреквенцијама испод 2 GHz.

A.8 Related Paper 8

Millar, W. C., White, G. L., Filipović, M. D., Payne, J. L., Crawford, E. J., Pannuti, T. G., and Staggs, W. D. (2011). Optical spectra of supernova remnant candidates in the Sculptor Group galaxy NGC 300. *Ap&SS*, 332:221–239

My contribution was to assist in the data analysis. This is a 5% contribution.

Astrophys Space Sci (2011) 332: 221–239
DOI 10.1007/s10509-010-0556-y

ORIGINAL ARTICLE

Optical spectra of supernova remnant candidates in the Sculptor Group galaxy NGC 300

William C. Millar · Graeme L. White · Miroslav D. Filipović · Jeffrey L. Payne · Evan J. Crawford · Thomas G. Pannuti · Wayne D. Staggs

Received: 3 September 2010 / Accepted: 27 November 2010 / Published online: 9 December 2010

Abstract We present moderate-resolution (<5 Å) long-slit optical spectra of 51 nebular objects in the nearby Sculptor Group galaxy NGC 300 obtained with the 2.3 meter Advanced Technology Telescope at Siding Spring Observatory, Australia. Adopting the criterion of $[\mathrm{S\,II}]_{\mathrm{Total}}$:H$\alpha \geq 0.4$ to confirm supernova remnants (SNRs) from optical spectra, we find that of 28 objects previously proposed as SNRs from optical observations, 22 meet this criterion with six showing $[\mathrm{S\,II}]_{\mathrm{Total}}$:H$\alpha$ of less than 0.4. Of 27 objects suggested as SNRs from radio data, four are associated with the 28 previously proposed SNRs. Of these four, three (included in the 22 above) meet the criterion. In all, 22 of the 51 nebular objects meet the $[\mathrm{S\,II}]_{\mathrm{Total}}$:H$\alpha$ criterion as SNRs while the nature of the remaining 29 objects remains undetermined by these observations.

Keywords Supernova remnants · Galaxies: individual: NGC 300 · Galaxies: ISM

W.C. Millar (✉) · M.D. Filipović
Centre for Astronomy, James Cook University, Townsville, Queensland 4811, Australia
e-mail: wmillar@grcc.edu

W.C. Millar
Grand Rapids Community College, 143 Bostwick N.E., Grand Rapids, MI, 49503, USA

G.L. White · M.D. Filipović · J.L. Payne · E.J. Crawford
University of Western Sydney, Locked Bag 1797, Penrith South DC, NSW 1797, Australia

T.G. Pannuti · W.D. Staggs
Department of Earth and Space Sciences, Space Science Center, 235 Martindale Drive, Morehead State University, Morehead, KY 40351, USA

1 Introduction

The spectral identification of supernova remnants (SNRs) was pioneered in a series of papers by Mathewson and Clarke (1972, 1973a, 1973b, 1973c) where narrow-band optical interference filters, centered on Hα and the [S II] ($\lambda\lambda$ 6717, 6731 Å) doublet, were used to differentiate between primordial hydrogen and heavy metal contaminated ejecta of a SNR. This technique depended on the strength of the [S II] lines in SNRs being about the same strength as the Hα lines, probably due to shock fronts in the expanding SNR shell, which in H II regions would not exist. The [S II] lines should be at least an order of magnitude weaker than the Hα line in H II regions as compared to SNRs (Mathewson and Clarke 1972). The Hα filters are often was not able to remove the [N II] (λ 6584 Å) line which is adjacent to the Hα line. In some SNRs this line can be a strong as the Hα itself. An emission region was classified as an SNR if it contained a (non-thermal) radio source and the Hα + [N II] to [S II] ratio was less than two (Mathewson and Clarke 1972).

Dodorico et al. (1978) pointed out the possibility of confusion between possible SNRs and H II regions as well as between SNRs and shells of ionized gas originating as a consequence of supersonic stellar winds. They presented arguments based on observations of SNRs and H II regions within the Galaxy and within the Large Magellanic Cloud to show how SNRs can be identified within M33 when $[\mathrm{S\,II}]_{\mathrm{Total}}$:H$\alpha \leq 0.4$. Fesen et al. (1985) found that [O I] $\lambda\lambda$ 6300, 6364 Å, [O II] λ 3727 Å and [O III] $\lambda\lambda$ 4959, 5007 Å are often all simultaneously strong in SNRs and this can be used to differentiate SNRs from H II regions in cases where $[\mathrm{S\,II}]_{\mathrm{Total}}$:H$\alpha$ is borderline.

As we are located in the dusty disk of the Milky Way, the study of SNRs is hampered by the extinction and reddening effects of the interstellar medium (ISM) which impairs our

Table 1 Gross properties of NGC 300

Property	Value	Reference
Hubble type	SA(s)d	Tully and Fisher (1988)
		de Vaucouleurs et al. (1991)
R.A. (J2000.0)	$00^h54^m53.48^s$	NED
Dec. (J2000.0)	$-37°41'03.8''$	NED
Galactic latitude	$-77.17°$	NED
Radial velocity	144 km/s (Solar)	Puche et al. (1990)
		Karachentsev et al. (2003)
Inclination	46°	Tully and Fisher (1988)
	42.6°	Puche et al. (1990)
Distance	2.1 Mpc	Freedman et al. (1992)
	2.02 Mpc	Freedman et al. (2001)
	1.88 Mpc	Bresolin et al. (2005);
		Gieren et al. (2005)
Observed diameter (D_{25})	20.2 arcmin	Tully and Fisher (1988)
Observed diameter (UV isophotes)	21.9×15.5 arcmin	Gil de Paz et al. (2007)
Galaxy Diameter	22.6 kpc, at 2.1 Mpc	Based on Gil de Paz et al. (2007)
Mass (HI)	2.4×10^9 $M_\odot$	Tully and Fisher (1988)
N_H column density	2.97×10^{20} cm^{-2}	Read et al. (1997)

Note: NED = NASA/IPAC Extragalactic Database (http://nedwww.ipac.caltech.edu/)

ability to see Galactic SNRs at wavelengths other than radio. However, observing SNRs in nearby galaxies—particularly in face-on galaxies with high Galactic latitude—reduces absorption by both the host galaxy and our own (Matonick and Fesen 1997; Pannuti et al. 2000). Surveys of SNRs in the Local Group galaxies and galaxies within some nearby clusters have resulted in samples that are free from biases. A list of over 450 optical SNRs found in external galaxies is given by Urošević et al. (2005), Matonick and Fesen (1997) and Pannuti et al. (2007).

Finding new SNRs is a task best carried out using multiple wavelength surveys (mainly X-ray, optical and radio) rather than a single wavelength survey (see Filipović et al. 1998, 2008; Lacey and Duric 2001; Payne et al. 2006). Radio-continuum observations using one frequency cannot uniquely identify SNR candidates, clearly differentiate SNRs from other nebulous objects or contend with the confusion that arises due to the presence of background sources (namely distant AGNs). An example of the most recent work in multiple wavelength observations of extra-galactic SNRs (M 33) is presented by Long et al. (2010).

In this paper we present moderate-resolution (<5 Å) long-slit optical spectra for 51 nebular objects in the nearby Sculptor Group galaxy NGC 300. Dodorico et al. (1980) first published optical observations of SNRs in this galaxy. None of the 7 candidates published in that paper match any of the 51 candidates discussed here. The 51 candidates studied here were chosen from those published by Blair and Long (1997, hereafter BL97) and Payne et al. (2004, hereafter P04). Table 1 provides a brief list of the characteristics of NGC 300 following Payne et al. (2004, hereafter P04); a more complete list is provided by Kim et al. (2004). NGC 300 is a type SA(s)d galaxy with an angular extent of $21.9' \times 15.5'$ (based on UV isophotes, Gil de Paz et al. 2007). An image of NGC 300 is presented in Fig. 1: this galaxy has been classified as flocculent—that is, its arms are poorly defined and it features many giant H II regions which are evidence of many star formation episodes (Read and Pietsch 2001, hereafter RP01). The similarity of angular size between NGC 300 and other nearby spiral galaxies that have been studied (such as M 33 and other members of the Sculptor Group, such as NGC 7793) lead us to conclude that NGC 300 is a typical, normal spiral galaxy (BL97).

We adopt the long accepted $[S\,II]_{Total}$:Hα line flux density ratio to distinguish between a SNR and either a H II region or a planetary nebula (PN). This criterion—if the $[S\,II]_{Total}$:Hα ratio is ≥ 0.4 the object is assumed to be a SNR, if <0.2 the object is more likely to be a H II region or a PN—has been used many times for galaxies in the Local Group and other nearby galaxies (for example BL97; Matonick and Fesen 1997; McNeil and Winkler 2006; Payne et al. 2007, 2008a, 2008b). As described previously, the physical processes thought to create this criterion are well understood (BL97 and references therein).

Because of its low inclination angle (measured to be between 43° and 46°; Tully and Fisher 1988 and Puche et al. 1990) and its high Galactic latitude (−77.17°, Table 1), observations of NGC 300 entail very low internal extinction (Butler et al. 2004) and foreground reddening ($E(B-V) = 0.013$ mag, Bland-Hawthorn et al. 2005).

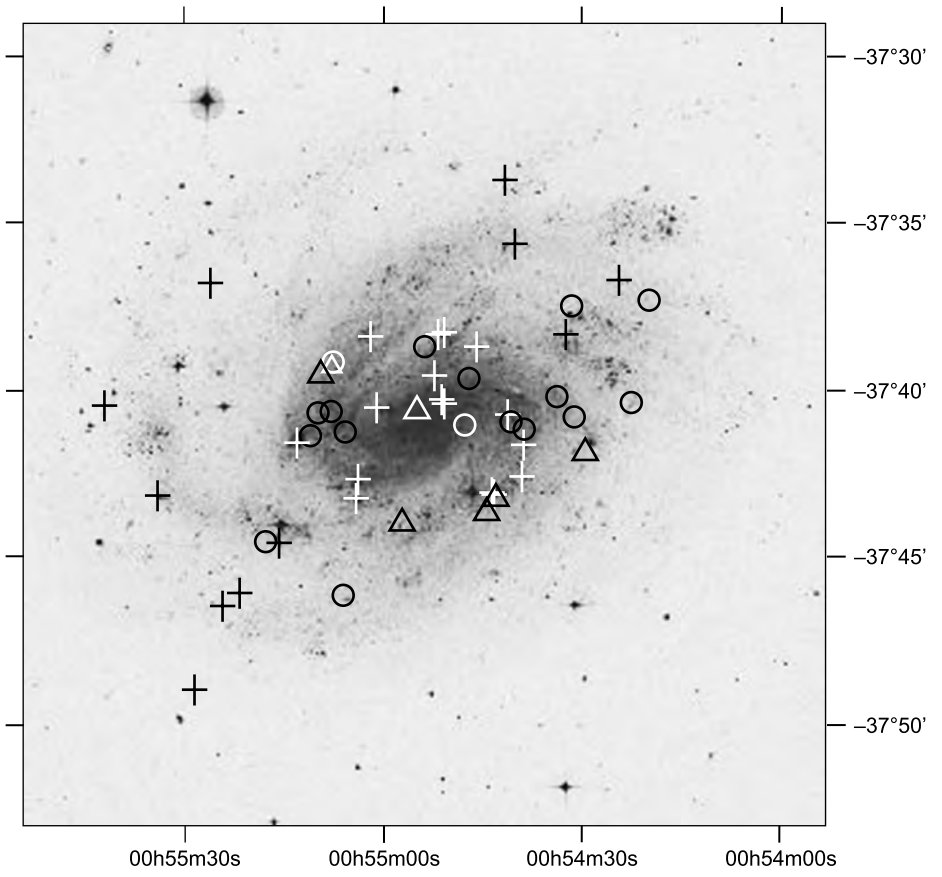

Fig. 1 A DSS image of NGC 300 with the positions (in J2000.0 coordinates) indicated of the 51 SNRs and candidate SNRs considered by the present study. Radio sources (SNRs and SNR candidates only) from P04 are shown with crosses. Optical candidates with line ratios measured with long-slit spectra (from BL97) are shown as *circles* and optical candidates with line ratios measured by interference filters (BL97) are shown with *triangles*. Symbols are *black* or *white* only for increased contrast. (Southern sky DSS image, Royal Observatory Edinburgh, Anglo-Australian Observatory, California Institute of Technology)

For studies of this galaxy, most authors have adopted distances of 2.0–2.1 Mpc (BL97; Freedman et al. 1992, 2001) though recent distance measurements based on observations of Cepheid variables have favoured a nearer distance of 1.88 Mpc with an error of 3% (Bresolin et al. 2005; Gieren et al. 2005). For the present paper, we have adopted a distance of 2.1 Mpc to be consistent with previous observations (BL97, P04). The corresponding linear scale is 10.2 pc arcsec^{-1}.

The observations and the corresponding (optical and X-ray) data reduction are presented in Sect. 2. The results of this analysis are presented in Sect. 3 including notes on individual objects. We confirm 22 objects as SNRs while the nature of the remaining 29 objects remains uncertain. Finally, in Sect. 4, we summarize our main results.

2 Observations and data reduction

2.1 Optical data

The positions (J2000.0) of all 51 SNRs and SNR candidates observed are given in Table 2 and are shown in Fig. 1. Optical spectra of all the sources were obtained in August of 2006 using the 2.3 m ($f/17.9$) Advanced Technology Telescope at Siding Spring Observatory, Australia, and the Dual-Beam Spectrograph (DBS, Rodgers et al. 1988). The slit width was 1 arcsec and a 4 arcmin decker was adopted. The wavelength domain used was 5400 Å to 9000 Å (from which we extracted data between 6300 Å and 6800 Å).

Most objects were observed twice, once with the DBS slit aligned in Declination (position angle, PA $= 0°$) and again with the slit aligned in Right Ascension (PA $= 90°$). A few objects were surrounded by interesting structure (in DSS2-Red) and observations were made with the slit positioned at the appropriate angle. Telescope pointing was confirmed by comparing the DBS slit camera image with pointing charts prepared from the DSS2-Red.

The observations reported here used only the red arm of the DBS. The grating used was the 316R (316 lines/mm) which is blazed at 6° 48′. This grating gives a resolution of 4.1 Å (170 km s^{-1}). Used here at a Grating Angle of 3° 49′, the 316R grating gives a central wavelength $\lambda_{\rm cent}$ of 7200 Å. The DBS's SiTE CCD camera has dimensions (1752 × 532 pixels, with pixels of 15 μm). All spectra were 600 second exposures returning a typical background (sky) level of ∼30–60 counts per pixel and a center of spectra level of ∼400–600 counts per pixel.

Data reduction and analysis was performed using the Image Reduction and Analysis Facility (IRAF) software package, with Starlink's Figaro cosmic ray cleaner, and Brent Miszalski's "Planetary Nebula Extraction" package for IRAF. All line flux densities were measured with the DEBLEND function of IRAF's SPLOT task. Data reduction included bias subtraction, flat-field correction and wavelengths calibration using standard NeAr arc-lamp lines. The star EG274 was the photometric standard (Stone and Baldwin 1983; Baldwin and Stone 1984; Hamuy et al. 1994) for flux density calibration.

2.2 X-ray data

To complement our optical spectroscopic observation of SNRs in NGC 300, we also analyzed an archival X-ray observation made of this galaxy with the Chandra X-ray Observatory (Weisskopf et al. 2002). This observation made use of the High Resolution Camera (HRC-I) (Murray et al. 2000) which can attain an angular resolution of approximately 0.4 arcseconds. Data for this observation (ObsID 7072—centered at RA(J2000) = $00^{h}55^{m}10^{s}$, DEC(J2000) = $-37°38'55''$) was downloaded and reduced using standard tools available in the Chandra Interactive Analysis of Observations (CIAO) package (Fruscione et al. 2006) Version 4.0.1. The CIAO tool "acis_process_events" was run to apply the latest calibration files: in addition, the dataset was filtered based on grade and status to create a new level = 2 event file (that is, events were removed that did not have a good grade or had one or more of the STATUS bits set to 1). The good time intervals and a light curve was generated to search for background light flares during the observation. The effective exposure time of the final image after processing was 15.19 kiloseconds and the corresponding energy range is 0.3–10.0 keV. To detect sources in this field of view, we ran the tool "wavedetect," which is a wavelet-based algorithm used for source detection (Freeman et al. 2002): a total of 31 sources were detected to a limiting unabsorbed luminosity of approximately 10^{37} ergs/sec (assuming a distance of 2.1 Mpc to NGC 300, a column density of $N_H = 3.08 \times 10^{20}$ cm^{-2} and a Raymond-Smith thermal plasma emission model with a temperature $kT = 0.5$ keV and solar abundance ratios).

From these 31 sources, only two discrete X-ray sources were found to match the positions (to within $2''$ or less) of known SNRs in NGC 300. These particular SNRs are the optically-identified SNRs N300-S10 and N300-S26. The associations between the X-ray sources and these optically-identified SNRs have been presented in previous works (P00, P04). We estimate the absorbed (unabsorbed) luminosities (over the energy range of 0.3–10.0 keV) for the HRC-detected X-ray counterparts to S10 and S26 to be 2.7×10^{37} (3.5×10^{37}) and 1.1×10^{37} (1.5×10^{37}), respectively. These luminosities were calculated using the tool PIMMS[1] Version 3.9i assuming a Galactic column density $N_H = 3.08 \times 10^{20}$ cm^{-2} toward NGC 300 and a thermal bremsstrahlung model with a temperature of $kT = 0.5$ keV. Unfortunately, because of the short exposure time of the observation, the limiting unabsorbed luminosity of approximately 1×10^{37} ergs sec^{-1} is too high to detect X-ray emission from the large majority of SNRs associated with NGC 300.

3 Analysis and results

As described previously, at optical wavelengths, SNRs are identified primarily by the flux density ratio of [S II]:Hα. When this ratio is greater than 0.4, the nebula is considered to be as a SNR and the presence of some other optical spectral lines may lend support to the classification. Table 3 is the collected multi wavelength observations for the 51 objects of Table 2 as selected principally from P04 and BL97. Tables 3, 4 and 5 are divided into three sections according to the results of our observations. The first is "SNRs" which are those objects for which our observations resulted in a $[\mathrm{S\,II}]_{\mathrm{Total}}$:H$\alpha \geq 0.4$. The second is those objects which did not meet this requirement and the third is those objects for which we obtained no spectrum. In Table 3; Column 1 is the source name adopted by BL97 and Column 2 is the radio source name from P04, based on the J2000 position. Columns 3 and 4 give the radio data for the sources with Column 5 listing the nature of the source proposed by P04. Columns 6 through 9 show X-ray observations and Columns 10 through 12 show previous optical observations. There is no standard designation style for X-ray sources, so X-ray nomenclatures in Columns 6 through 9 are tied to individual papers.

Column 3 gives the radio spectral index from Very Large Array (VLA) observations at 1465 and 4885 MHz as reported in P00. Column 4 shows the radio spectral index as reported in P04. These values are based on flux densities obtained at 1347, 1448, 2496 and 4860 MHz at the Australia Telescope Compact Array (ATCA, P04) or the VLA (P00).

Column 5 gives the object type proposed by P04 based on their radio spectral index of Column 4. Sources are classified as candidate radio SNRs if the spectral index α[2] of the radio emission is in the range $-0.8 \leq \alpha \leq -0.2$ and if it is co-identified with an X-ray source. This range is based on a statistical average of the spectral indices of over 270 Galactic SNRs (Trushkin 1998). P04 also classified radio SNRs taking in account their association with known optical SNR, OB association or H II region. Other object types proposed by P04 are "snr"—radio SNR candidate;

[1] http://cxc.harvard.edu/toolkit/pimms.jsp.

[2] Where α is defined as $S \propto \nu^{\alpha}$.

Table 2 Positions (J2000.0) of the selected 51 SNRs and SNR candidates in the NGC 300

1	2	3	1	2	3
Object name	Position (J2000.0)		Object name	Position (J2000.0)	
	RA (h m s)	Dec (° ′ ″)		RA (h m s)	Dec (° ′ ″)
J005423-373648	00 54 23.84	−37 36 48.4	N300-S1	00 54 19.21	−37 37 23.96
J005431-373825	00 54 31.91	−37 38 25.9	N300-S2	00 54 21.85	−37 40 27.11
J005438-374144	00 54 38.16	−37 41 44.2	N300-S3	00 54 28.86	−37 41 53.32
J005438-374240	00 54 38.49	−37 42 40.5	N300-S4	00 54 30.62	−37 40 53.75
J005439-373543	00 54 39.61	−37 35 43.4	N300-S5	00 54 30.99	−37 37 33.96
J005440-374049	00 54 40.68	−37 40 49.7	N300-S6	00 54 31.91	−37 38 25.68
J005441-373348	00 54 41.05	−37 33 48.9	N300-S7	00 54 33.17	−37 40 16.90
J005442-374313	00 54 42.70	−37 43 13.3	N300-S8	00 54 38.17	−37 41 14.88
J005443-374311	00 54 43.11	−37 43 11.0	N300-S9	00 54 40.20	−37 41 02.12
J005445-373847	00 54 45.39	−37 38 47.1	N300-S10	00 54 40.87	−37 40 48.73
J005450-374030	00 54 50.28	−37 40 30.0	N300-S11	00 54 42.54	−37 43 14.16
J005450-373822	00 54 50.30	−37 38 22.4	N300-S12	00 54 43.86	−37 43 39.08
J005450-374022	00 54 50.73	−37 40 22.2	N300-S13	00 54 46.60	−37 39 44.32
J005451-373826	00 54 51.16	−37 38 26.1	N300-S14	00 54 47.15	−37 41 07.63
J005451-373939	00 54 51.79	−37 39 39.6	N300-S15	00 54 53.32	−37 38 48.24
J005500-374037	00 55 00.58	−37 40 37.4	N300-S16	00 54 54.46	−37 40 35.46
J005501-373829	00 55 01.49	−37 38 29.9	N300-S17	00 54 56.68	−37 43 57.70
J005503-374246	00 55 03.50	−37 42 46.0	N300-S18	00 55 01.39	−37 39 18.17
J005503-374320	00 55 03.66	−37 43 20.1	N300-S19	00 55 05.41	−37 41 21.04
J005512-374140	00 55 12.70	−37 41 40.3	N300-S20	00 55 05.68	−37 46 13.35
J005515-374439	00 55 15.40	−37 44 39.2	N300-S21	00 55 07.15	−37 39 15.17
J005521-374609	00 55 21.35	−37 46 09.6	N300-S22	00 55 07.50	−37 40 43.20
J005523-374632	00 55 23.95	−37 46 32.4	N300-S23	00 55 09.10	−37 39 32.61
J005525-373653	00 55 25.82	−37 36 53.8	N300-S24	00 55 09.48	−37 40 46.21
J005528-374903	00 55 28.25	−37 49 03.3	N300-S25	00 55 10.68	−37 41 27.13
J005533-374314	00 55 33.87	−37 43 14.6	N300-S26	00 55 15.46	−37 44 39.11
J005541-374033	00 55 41.94	−37 40 33.5	N300-S27	00 55 17.54	−37 44 36.65
			N300-S28	00 55 33.76	−37 43 13.13

"snr†"—SNR based on spectral index only; "H II"—H II region; "hii"—possible H II region; "BKG"—background radio source or "bkg"—possible background radio source.

All SNRs emit soft X-rays resulting from heated gas inside the expanding shock front (Aller 1991; Osterbrock and Ferland 2006). The identification of potential SNRs at X-ray wavelengths is based on spectral fits to the observed emission using thermal bremsstrahlung models. X-ray emission can also occur from SNRs by virtue of an embedded pulsar or neutron star (e.g. Gaensler et al. 2003). X-ray emission from SNR candidates is usually fitted to models (temperature and particle density) of these emission types to verify the candidacy.

Columns 6 through 9 show data reported by four papers of X-ray point sources in positional agreement with those sources observed in this paper. Data comes from Read et al. (1997, hereafter RPS97), Read and Pietsch (2001, hereafter RP01), P04 and Carpano et al. (2005, hereafter C05), respectively.

Data in Columns 6 and 7 were generated from observations made with the ROSAT X-ray observatory while data in Column 8 are from results obtained with observations made with the XMM-Newton observatory. In addition, we have further investigated putative associations between X-ray sources and SNRs through the analysis of an archival Chandra HRC-I observation of NGC 300 (also see Sect. 2.2).

Column 10 indicates if the source is visible as a nebulous object on the DSS2-Red survey. Column 11 gives the ratio of [S II] to Hα line flux density as reported by BL97. The values in parenthesis are from Table 3A of BL97 and are based on interference filter images, otherwise they are from Table 4A of BL97 and are based on long-slit spectra.

Table 3 Previous observations of the selected objects

1	2	3	4	5	6	7	8	9	10	11
Object designation		Radio observations			X-ray observations				Optical observation (BL97)	
Optical	Radio	Spectral index (P00)	Spectral index (P04)	Proposed object (P04)	RPS97 label data	RP01 label data	P04 label data	C05 label data	DSS2-Red	[S II]:Hα
SNRs										
N300-S1									No	0.68
N300-S2								#79	Yes	0.77
N300-S4									Yes	0.99
N300-S5									Yes	0.68
N300-S6	J005431-373825			SNR	#1	P29	XMM2		Yes	0.96
N300-S7									Yes	0.72
N300-S8									Yes	0.61
N300-S9									Yes	0.67
N300-S12									Yes	(0.52)
N300-S13									Yes	0.98
N300-S14									Yes	0.83
N300-S15									Yes	0.74
N300-S16									Yes	(0.70)
N300-S17									Yes	(0.69)
N300-S19								#123	Yes	0.90
N300-S20									Yes	1.00
N300-S22									Yes	0.57
N300-S24									No	0.83
N300-S26	J005515-374439			SNR/H II	#10	P49	XMM9	#34	Yes	1.03
N300-S25									Yes	0.80
N300-S27									Yes	1.05
N300-S28	J005533-374314			SNR/H II				#151	Yes	0.72

Table 3 (*Continued*)

1	2	3	4	5	6	7	8	9	10	11
Object designation		Radio observations			X-ray observations				Optical observation (BL97)	
Optical	Radio	Spectral index (P00)	Spectral index (P04)	Proposed object (P04)	RPS97 label data	RP01 label data	P04 label data	C05 label data	DSS2-Red	[S II]:Hα
Other objects (H II Regions?)										
	J005438-374144	< 1.1	−0.8	SNR/H II					Yes	
	J005438-374240	< 1.5		snr/H II					Yes	
	J005439-373543		−0.4	snr†					No	
					36.66, 82.8, 0.10	0.87, −0.33	1.27, −0.63, −0.99	−0.17, −0.58		
						4.8, 25.4	1.63, −0.58, −1.00	1.03, 5.03		
	J005441-373348			bkg/snr			XMM4		Yes	
							1.39, +0.84, +0.94		Yes	
							0.72, +0.31, +0.62		Yes	
	J005442-374313		−0.9	SNR/H II					Yes	(0.66)
	J005443-374311	−0.6	−0.6	SNR/H II					Yes	
	J005445-373847		−0.3	SNR/H II					Yes	
	J005450-374030	−0.6	−0.5	SNR/H II					Yes	
	J005450-373822		−0.2	SNR/H II					Yes	
	J005450-374022		−0.3	SNR/H II					Yes	
	J005451-373826		−1.2	SNR/H II					Yes	
	J005451-373939	−0.4	−0.1	SNR/H II					Yes	
	J005500-374037		−0.4	SNR/H II					Yes	
	J005501-373829		−0.9	SNR					Yes	
	J005503-374246	−0.2	−0.4	SNR/H II					Yes	
	J005503-374320	−1.0	−0.7	SNR/H II					Yes	
	J005512-374140	−0.4	−0.7	SNR/H II					Yes	
N300-S3									No	(0.40)
N300-S10	J005440-374049		−0.5	SNR	#4	P38	XMM3	#12	Yes	0.47
N300-S11	J005442-374313?		−0.9	SNR/H II					Yes	(0.66)
N300-S18									Yes	0.71
N300-S21									Yes	(0.59)
N300-S23									Yes	(0.46)
No signal										
	J005423-373648		−0.7	snr†					No	
	J005521-374609		−1.0	bkg/snr					No	
	J005523-374632		−0.9	bkg/snr					No	
	J005525-373653		−1.0	bkg/snr					No	
	J005528-374903		−0.6	snr†					No	
	J005541-374033			snr			XMM10		No	
							2.35, −0.76, −0.88		No	
							1.08, −0.88, −0.93		No	

Table 4 The integrated line flux density measurements

1	2	3	4	5	6	7	8
Designation		Hα λ 6563 Å	[N II] total	[S II] total		[O I] total	Diameter
Radio	Optical	(10^{-15} ergs cm^{-2} s^{-1})	(10^{-15} ergs cm^{-2} s^{-1})	(10^{-15} ergs cm^{-2} s^{-1})	$[S\,II]_{Total}$:Hα	(10^{-15} ergs cm^{-2} s^{-1})	(pc)
SNRs							
	N300-S1[a]	1.3	0.25	0.57	0.46 ± 0.29	2.1	38
	N300-S2	11	3.7	8.1	0.72 ± 0.39	3.3	69
	N300-S4	7.0	3.0	6.5	0.93 ± 0.04	5.1	150
	N300-S5	8.4	2.4	4.7	0.56 ± 0.47	2.2	…[b]
J005431-373825	N300-S6	4.2	1.2	2.9	0.69	0.22	44
	N300-S7	5.2	2.1	3.0	0.57 ± 0.41	2.7	31
	N300-S8	5.0	1.9	2.9	0.58 ± 0.06	2.6	49
	N300-S9	37	12	20	0.53 ± 0.23	4.0	83
	N300-S12	2.3	1.2	1.7	0.73 ± 0.27	2.4	22
	N300-S13	1.9	1.1	1.8	0.91 ± 0.05	1.0	35
	N300-S14	2.3	1.8	2.5	1.08 ± 0.24	1.5	41
	N300-S15	3.0	1.0	1.7	0.57 ± 0.39	0.90	12
	N300-S16	2.2	2.0	2.1	0.94 ± 0.06	1.1	57
	N300-S17	4.2	1.6	4.1	0.96 ± 0.15	1.4	65
	N300-S19	9.4	3.8	6.6	0.70 ± 0.42	0.90	30
	N300-S20	2.3	0.71	1.8	0.79 ± 0.11	0.28	48
	N300-S22	2.9	1.1	1.3	0.46 ± 0.38	1.0	75
	N300-S24	2.7	0.86	1.7	0.64 ± 0.13	0.66	100
	N300-S25	16	4.7	8.7	0.54 ± 0.40	1.8	80
J005515-374439	N300-S26[a]	26	11	23	0.86 ± 0.67	11	31
	N300-S27	6.5	1.7	4.2	0.64 ± 0.48	1.1	66
J005533-374314	N300-S28[a]	69	13	31	0.45 ± 0.15	6.5	63

Table 4 (*Continued*)

1	2	3	4	5	6	7	8
Designation		Hα λ 6563 Å	[N II] total	[S II] total		[O I] total	Diameter
Radio	Optical	(10^{-15} ergs cm^{-2} s^{-1})	(10^{-15} ergs cm^{-2} s^{-1})	(10^{-15} ergs cm^{-2} s^{-1})	[S II]$_{Total}$:Hα	(10^{-}15 ergs cm^{-2} s^{-1})	(pc)
Other objects (H II regions?)							
J005438-374144		80	15	13	0.17 ± 0.07	3.2	
J005438-374240		39	8.5	10	0.25 ± 0.02	3.4	
J005439-373543		5.9	1.4	1.6	0.27	5.2	
J005440-374049	N300-S10	105	32	36	0.35 ± 0.15	4.9	
J005441-373348[a]		1.7	0.34	0.62	0.36	1.5	
J005442-374313		250	48	49	0.19 ± 0.07		
J005443-374311		290	58	53	0.18 ± 0.09		
J005445-373847		130	20	14	0.11 ± 0.03		
J005450-374030		140	46	43	0.32 ± 0.12	8.1	24
J005450-373822		200	40	44	0.22 ± 0.14	7.9	
J005450-374022		84	28	32	0.38 ± 0.31	4.5	130
J005451-373826		140	30	36	0.26 ± 0.16	2.2	
J005451-373939[a]		100	16	10	0.10 ± 0.18	0.51	
J005500-374037		53	17	13	0.25 ± 0.09	2.1	
J005501-373829		6.4	1.5	2.3	0.35 ± 0.12	1.1	31
J005503-374246		150	24	20	0.14 ± 0.04	1.3	
J005503-374320		270	53	41	0.15 ± 0.08	1.6	
J005512-374140		240	27	19	0.08 ± 0.02	0.95	
	N300-S3	51	10	12	0.24 ± 0.31	4.2	26
J005440-374049	N300-S10	105	32	36	0.35 ± 0.15	4.9	
	N300-S11	1670	39	50	0.30 ± 0.12	6.9	150
	N300-S18[a]	5.0	1.5	1.6	0.32 ± 0.32	0.44	69
	N300-S21	2.1	0.72	0.78	0.37 ± 0.30	0.35	41
	N300-S23	29	7.2	9.1	0.31 ± 0.08	1.3	43
No signal[c]							
J005423-373648							
J005521-374609							
J005523-374632							
J005525-373653							
J005528-374903							
J005541-374033							

[a]Very low faint spectrum recorded

[b]Gaussian fit returned value too small to be deconvolved with reference star

[c]No observed spectral lines

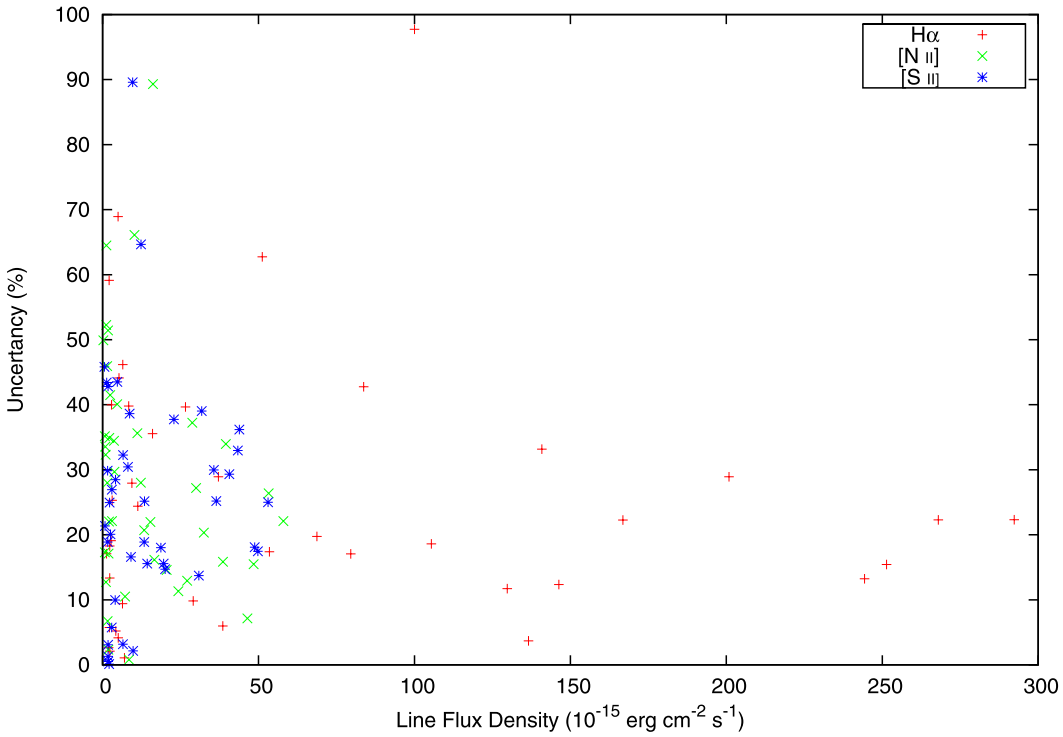

Fig. 2 The standard errors (expressed as a percentage) in the means (SEMs) of the multiple flux density measurements in the individual spectral lines as a function of flux density of that line. The noise independent uncertainty is about 22%. Details are given in the text

For approximately half of the spectra collected the length along the decker of the Hα line (λ 6563 Å), and the [N II] ($\lambda\lambda$ 6548, 6583 Å) and [S II] ($\lambda\lambda$ 6716, 6732 Å) lines were essentially the same, indicating that the emission regions were of approximately the same physical size. Reduction of these spectra followed standard procedures.

For spectral lines where the Hα, [N II] and [S II] lines differ in length (indicating a possible different physical size for the emitting regions) extraction was done so as to ensure that the line ratio was not dominated by extracted Hα emission from the background.

Table 4 gives the integrated line flux densities for all objects in Table 3. The first two columns are the designation of the SNR or SNR candidate in P04 (Column 1) or BL97 (Column 2). Also listed is the integrated Hα line (6563 Å) flux density (Column 3); the total, integrated [N II] line (6548 Å + 6583 Å) flux density (Column 4); the total, integrated [S II] line (6716 Å + 6731 Å) flux density (Column 5); the ratio of $[\mathrm{S\,II}]_{\mathrm{Total}}$:H$\alpha$ (Column 6); the total, integrated [O I] line (6300 Å + 6364 Å) flux density (Column 7); and the Hα diameter of the object (Column 8).

With a few exceptions, each object was observed at least twice and these multiple observations allow the direct computation of the uncertainties in flux densities of each line. Figure 2 shows the standard errors (expressed as a percentage) in the means (SEMs) of the individual flux densities for each spectral line in Table 4 as a function of flux density of that line. Here, the noise independent uncertainty (of about 22%) and the noise dependent component are clearly delineated. The envelope of uncertainties in Fig. 2 is defined by:

$$\Delta \mathrm{L} = \sqrt{0.15\mathrm{L} + 0.05\mathrm{L}} \tag{1}$$

where ΔL is the uncertainty in the flux density of each individual line and L is the flux density of that line in units of 10^{-15} ergs cm^{-2} s^{-1}. The formal uncertainties in the line flux density values of Columns 3, 4 and 5 of Table 4 are defined by this relationship.

The uncertainty in the $[\mathrm{S\,II}]_{\mathrm{Total}}$:H$\alpha$ (Column 6 of Table 4) is governed by the uncertainties in the flux densities of the individual lines, and is about 8% for ratios close to unity and about 20% for ratios tending towards zero. For the smaller values of $[\mathrm{S\,II}]_{\mathrm{Total}}$:H$\alpha$ the uncertainty is made larger by the increased uncertainty in the weaker [S II] lines.

A comparison of the line ratios reported here with those of BL97 (Fig. 2) shows consistency between our results and the results presented by BL97, but with a small (of order 10%) bias (with BL97 greater than the current work) and an indication that this bias is induced by the size of the source as well as the selection of the type of extraction used (see above). As one would expect, the bias is also dependent on the strength of the lines, caused by the rising noise component in the line flux density for very weak lines.

Table 5 Summary of results

1	2	3	4	5	6
Optical object	Radio object	Object type (P04)	Object type (BL97)	[S II]$_{Total}$:Hα	Diameter (pc)
SNRs					
N300-S1			SNR	0.46 ± 0.29	38
N300-S2			SNR	0.72 ± 0.39	69
N300-S4			SNR	0.93 ± 0.04	150
N300-S5			SNR	0.56 ± 0.47	...[a]
N300-S6	J005431-373825	SNR	SNR	0.69	44
N300-S7			SNR	0.57 ± 0.41	31
N300-S8			SNR	0.58 ± 0.06	49
N300-S9			SNR	0.53 ± 0.23	83
N300-S12			SNR	0.73 ± 0.27	22
N300-S13			SNR	0.91 ± 0.05	35
N300-S14			SNR	1.08 ± 0.24	41
N300-S15			SNR	0.57 ± 0.39	12
N300-S16			SNR	0.94 ± 0.06	57
N300-S17			SNR	0.96 ± 0.15	65
N300-S19			SNR	0.70 ± 0.42	30
N300-S20			SNR	0.79 ± 0.11	48
N300-S22			SNR	0.46 ± 0.38	75
N300-S24			SNR	0.64 ± 0.13	100
N300-S25			SNR	0.54 ± 0.40	80
N300-S26	J005515-374439	SNR/H II	SNR	0.86 ± 0.67	31
N300-S27			SNR	0.64 ± 0.48	66
N300-S28	J005533-374314	SNR/H II	SNR	0.45 ± 0.15	63
Other objects (H II regions?)					
	J005438-374144	SNR/H II		0.17±0.07	
	J005438-374240	snr/H II		0.25±0.02	
	J005439-373543	snr†		0.27	
	J005441-373348	bkg/snr		0.36	
	J005442-374313	SNR/H II		0.19±0.07	
	J005443-374311	SNR/H II		0.18±0.09	
	J005445-373847	SNR/H II		0.11±0.03	
	J005450-374030	SNR/H II		0.32±0.12	
	J005450-373822	SNR/H II		0.22±0.14	
	J005450-374022	SNR/H II		0.38±0.31	130
	J005451-373826	SNR/H II		0.26±0.16	
	J005451-373939	SNR/H II		0.10±0.18	
	J005500-374037	SNR/H II		0.25±0.09	
	J005501-373829	SNR		0.35±0.12	31
	J005503-374246	SNR/H II		0.14±0.04	
	J005503-374320	SNR/H II		0.15±0.08	
	J005512-374140	SNR/H II		0.08±0.02	
N300-S3			SNR	0.24±0.31	26
N300-S10	J005440-374049	SNR	SNR	0.35±0.15	63
N300-S11			SNR	0.30±0.12	150
N300-S18			SNR	0.32±0.32	69
N300-S21			SNR	0.37±0.30	41
N300-S23			SNR	0.31±0.08	43
No signal					
	J005423-373648	snr†			
	J005521-374609	bkg/snr			
	J005523-374632	bkg/snr			
	J005525-373653	bkg/snr			
	J005528-374903	snr†			
	J005541-374033	snr			

[a]Gaussian fit returned a value too small to be deconvolved

3.1 Measurement of the supernova remnant diameter

Column 7 of Table 4 is our measured diameter of the SNR. We have attempted to estimate the linear diameter of the SNR or SNR candidate by fitting a Gaussian profile to the Hα, [N II] and [S II] lines along the decker orthogonal to the wavelength directions. The image scale of the SiTE detector is 0.78 arcseconds per channel which corresponds to 7.7 pc per channel at the adopted distance of NGC 300 (2.1 Mpc). Each spectral line was then deconvolved with the standard star for that night to give a diameter of the source in parsecs. The full-width half-maximum (FWHM) diameters are given in Column 7 of Table 4.

For the optical candidates published in BL97, a comparison of our diameter measurements with those in BL97 does not show good correlation ($r^2 = 0.02$). This, we believe, is not the result of any problem with our data or that of BL97, rather that the data sets are limited by the seeing which is of approximately the same size as the object itself. Our measured diameters indicate an average size of 54 ± 22 pc, and on this basis, we note that there are only three objects (N300-S4, N300-S11 and N300-S24; where N300-S4 and N300-S24 are confirmed SNRs) that are worthy of being noted as large objects at 150 pc, 150 pc and 100 pc respectively. Sources of this size may be superbubbles rather than a single SNR.

In addition, we have looked for large Hα diameters relative to smaller [N II], [S II] or [N II] + [S II] diameters, as indications of an embedded SNR in H II regions. There is only one object that might stand a solid statistical analysis—N300-S6—where the Hα is larger than the [S II] by a factor of 2.6 and the combined [N II] + [S II] is larger by 2.2. However, BL97 report the same diameter as us: therefore, either the S II diameter reported by BL97 or our Hα diameter measurement is an overestimate. Further work at higher angular resolution is required to better determine the diameters of these objects.

3.2 Overall results

The SNR candidates published in BL97 where originally found using Hα and [S II] interference filters on the 2.5 m du Pont Telescope at Las Campanas. Surveys of this type preferentially find objects with large $[S\,II]_{Total}$:Hα ratios. As confirmation, moderate-resolution long-slit spectra were obtained by BL97 for 21 of their 28 candidates using the Modular Spectrograph and the line flux density measurements are presented in BL97 as Table 4A. We obtained satisfactory spectra for all 28 candidates and confirm 22 (78%) as optical SNRs based on the $[S\,II]_{Total}$:Hα.

Figure 3 shows examples of spectra of objects which meet the $[S\,II]_{Total}$:H$\alpha \geq 0.4$ criterion and are therefore labeled as SNRs in our results. Figure 4 shows examples of spectra for objects which do not meet the criteria. A summary for our results is given in Table 5. On the basis of the above definition we confirm 22 objects as SNRs. Of the 27 radio objects suggested as SNRs by P04, we confirm only three (11%). These three radio sources are positionally linked to three of the SNRs listed in BL97.

Figure 5 shows a plot of the $[S\,II]_{Total}$:Hα values for all objects which returned data. We can see a trend for objects which are below 0.4 to have greater Hα emissions, lending support to these objects appearing as H II regions rather than SNRs at optical wavelengths. Figure 6 shows a plot of [N II] flux against Hα flux. This plot shows a fairly consistent ratio of $[N\,II]_{Total}$:Hα of 0.3 across both groups of objects. Figure 7 shows a plot of [O I] flux against Hα flux. The plot shows a consistent value of [O I] emission from both object groups, with greater Hα emission from the "other" objects. Because [O I] flux is associated with SNR shock fronts it may be possible that the emission from the "other sources" is caused by shock fronts created by SNRs that are visible only in radio, being buried within H II regions.

3.3 Notes on individual radio objects

3.3.1 J005431-373825

The radio source J005431-373825 is associated with the optical object N300-S6 and thus has both radio and optical emission. The line ratio of 0.69 confirms this object as a SNR. This SNR also shows hard X-ray emission (C05).

3.3.2 J005438-374144

There is a faint optical object at the position of this radio source which was previously classified as SNR by P04. The spectrum shows a $[S\,II]_{Total}$:Hα ratio of 0.17 with an error of 0.07. On the basis of this we do not confirm this object as a SNR although this source may be a radio SNR hidden within an H II region.

3.3.3 J005440-374049

The radio source J005440-374049 (N300-S10) was observed three times (once more after the main runs, with PA = 45°) because of the interesting structure seen on the DSS2-Red. All three observations return a line ratio of <0.4. Our diameter measurement for this object reveal it to be 63 pc, significantly larger than BL97 who describe it as very compact (16 pc). Based on the proposed radio and optical identification from P04 and BL97, our X-ray identification (also see Sect 2.2) and the $[S\,II]_{Total}$:Hα of <0.4, we classify this object as a candidate SNR.

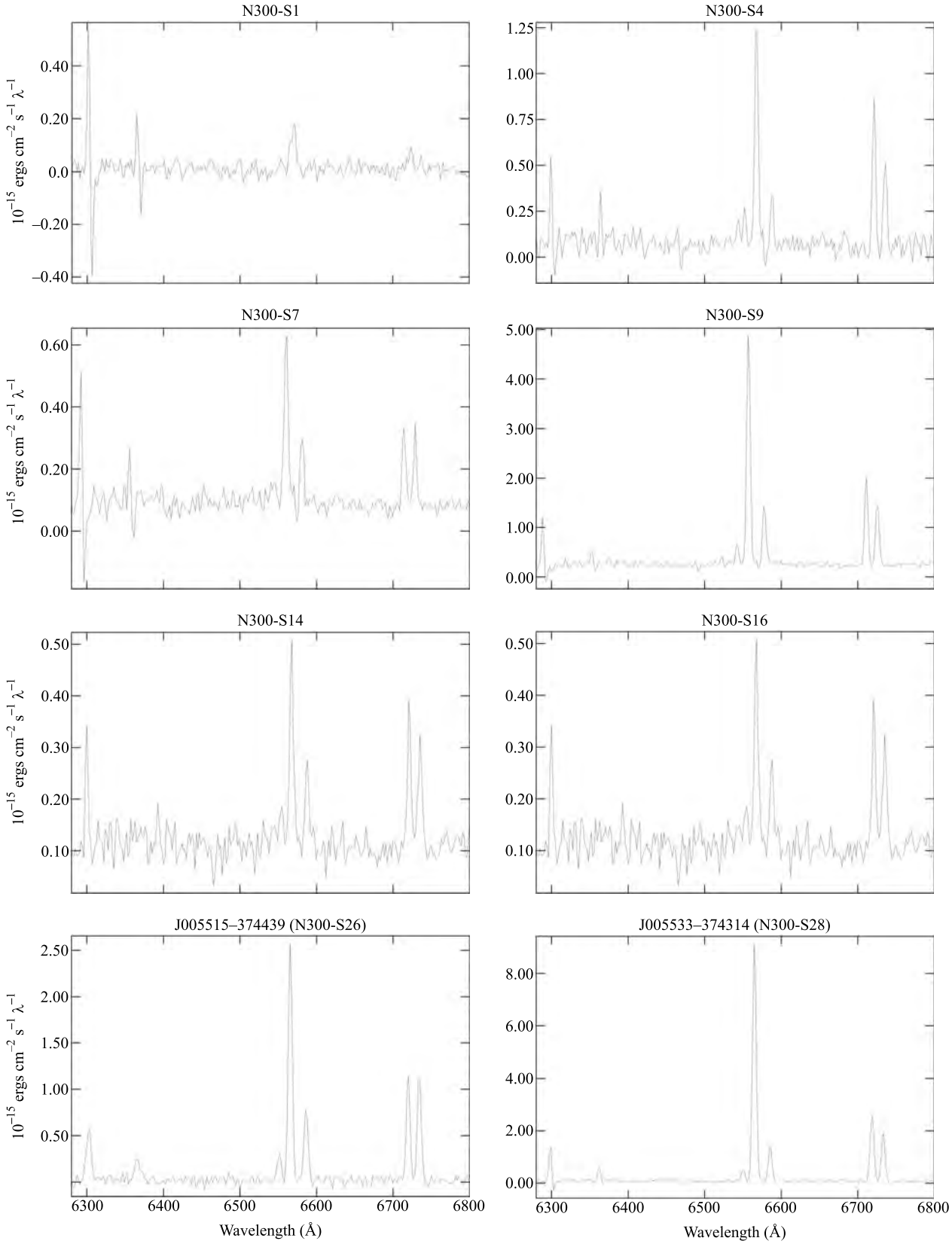

Fig. 3 Example spectra of objects meeting the $[S\,II]_{Total}$:Hα >0.4 criterium and are therefore labeled as SNRs in our results

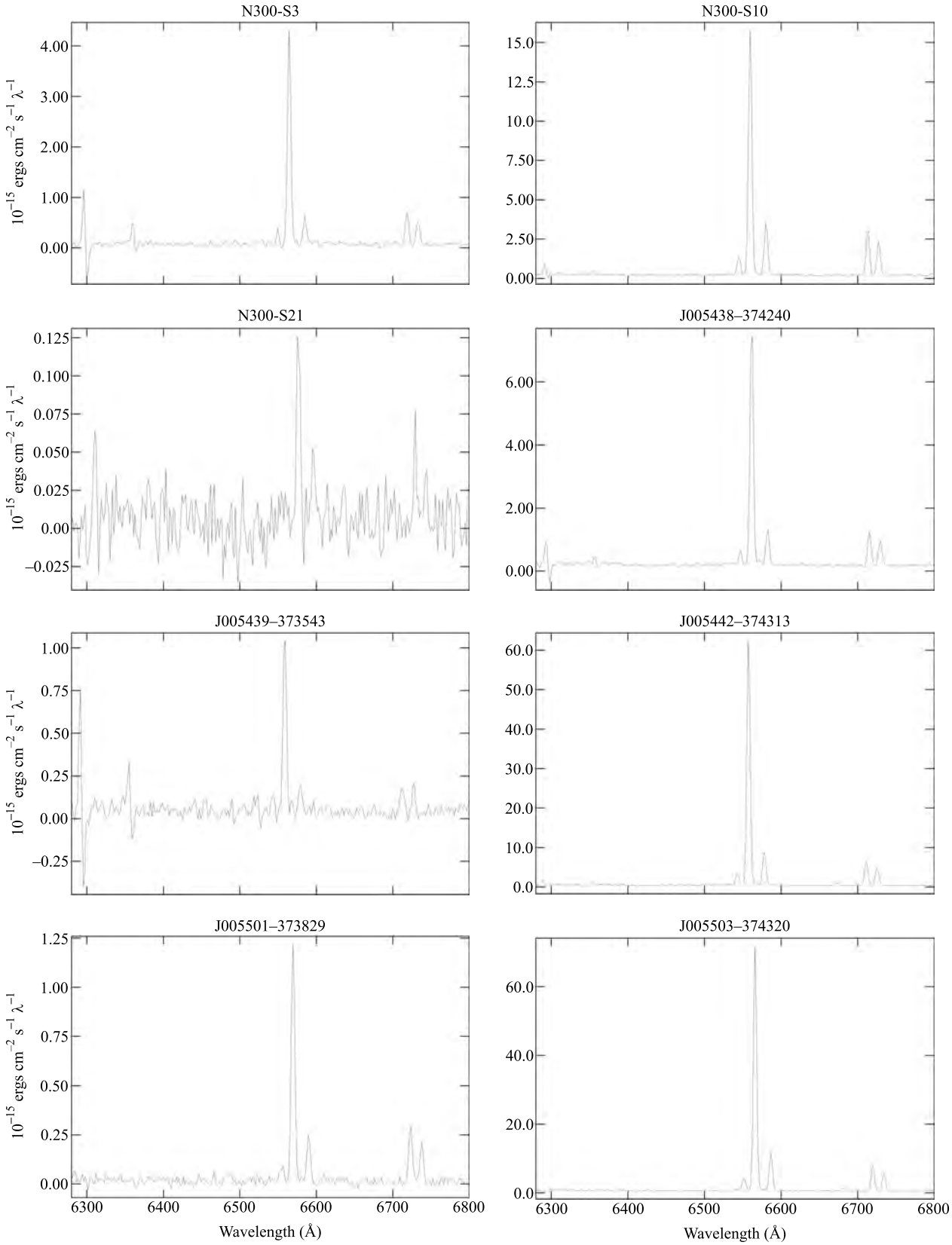

Fig. 4 Example spectra of objects which did not meet the $[S\,II]_{Total}$:Hα > 0.4 criterium and are therefore labeled as "other objects" in our results

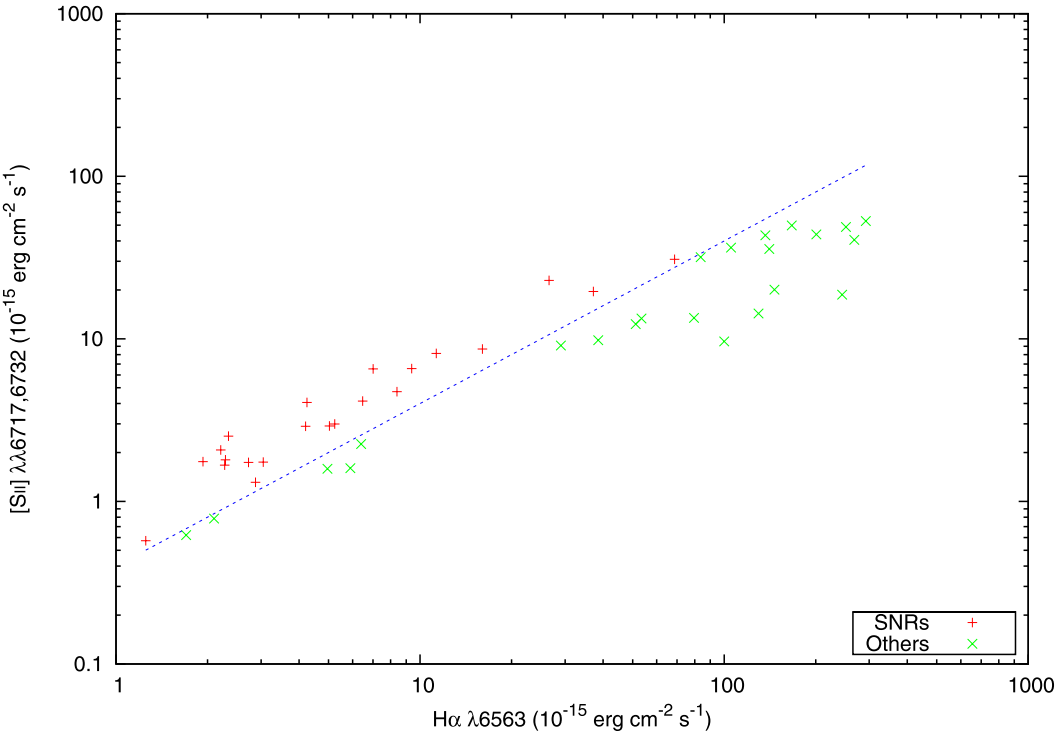

Fig. 5 A plot of [S II]$_{\text{Total}}$:Hα values for the objects we label as SNRs and "other objects." The scales were made logarithmic to make the data points more visible. The *dashed line* represents a [S II]$_{\text{Total}}$:Hα of 0.4

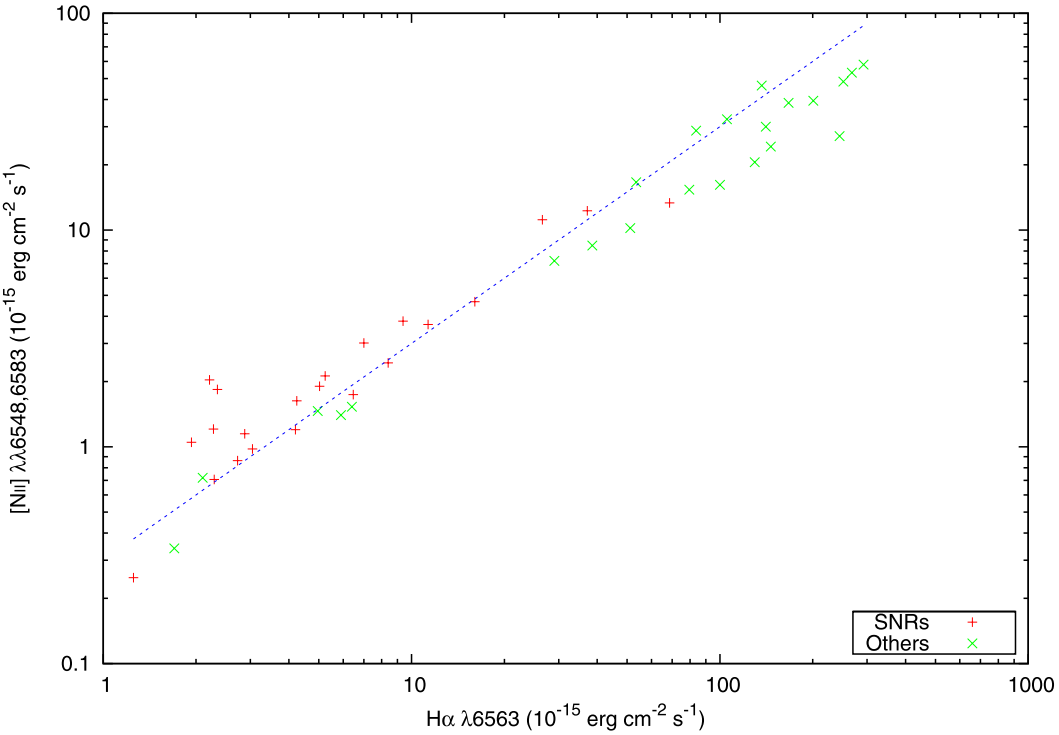

Fig. 6 A plot of [N II] vs. Hα flux values for the objects we label as SNRs and "other objects." The scales were made logarithmic to make the data points more visible. The plot shows a consistent nitrogen-hydrogen ratio of roughly 0.3 (indicated by the *dashed line*) across both groups of objects

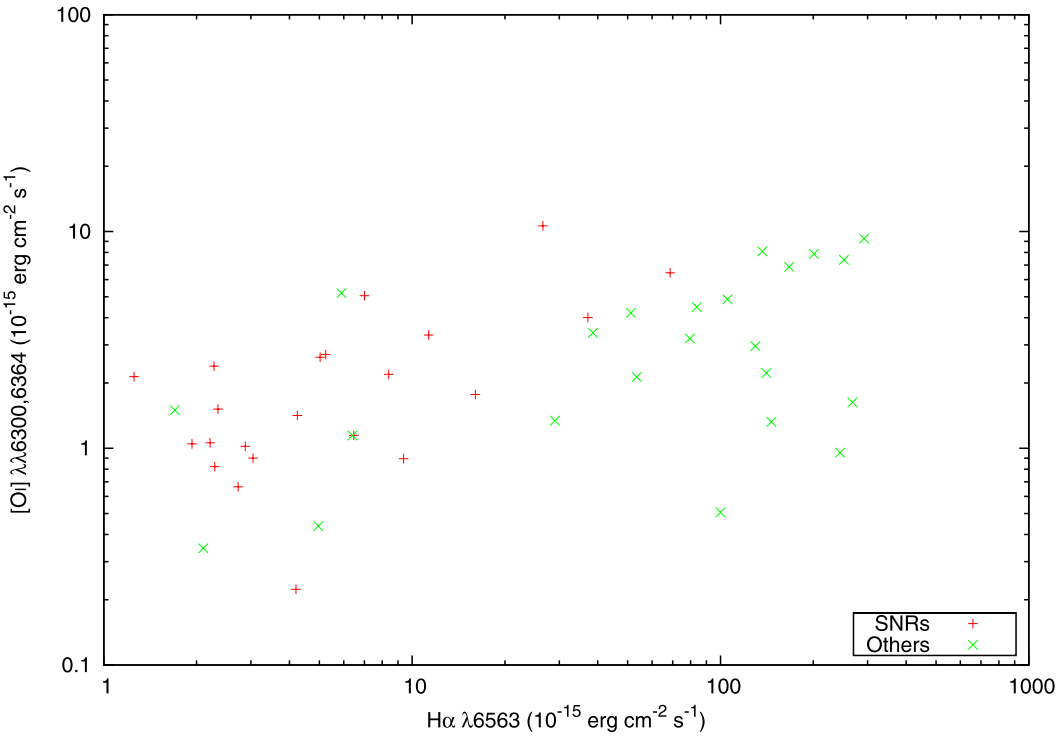

Fig. 7 A plot of [O I] vs. Hα flux values for the objects we label as SNRs and "other objects." The scales were made logarithmic to make the data points more visible. The plot shows a consistent value of [O I] emission from both object groups, with greater Hα emission form the "other" objects. Because [O I] flux is associated with SNR shock fronts it may be possible that the emission from the "other objects" is caused by shock fronts created by SNRs that are visible only in radio, being buried within H II regions

3.3.4 J005441-373348

We did not see any optical emission from this source but it was observed in X-rays as XMM4 by P04 and as source #54 in Carpano et al. (2005). As these papers have noted, this object is probably a background source.

3.3.5 J005442-374313 and J005443-374311

The sources J005442-374313, J005443-374311 and N300-S11, are in the same line of sight and may be located near to each other. They also have similar optical spectra and $[S\,II]_{Total}$:Hα ratios (Table 6). N300-S11 was observed in both P00 and BL97 and identified as an SNR in BL97. P00 searched for X-ray and radio emissions from this source but no definitive counterparts could be identified. X-ray source #161 in the catalog given by Carpano et al. (2005) is nearby, but not within the positional uncertainties given in the respective papers. With these data, these objects remain candidate "radio" or "optical" SNRs and their physical association is still questionable. Table 6 gives the positional agreement between these sources and source #161 from Carpano et al. (2005) X-ray Source Catalog.

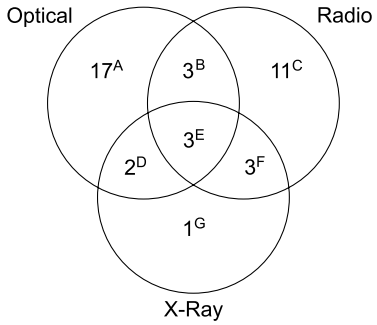

Fig. 8 Venn diagram showing the intersection of selected sets of SNRs for NGC 300. The letter superscript on each value corresponds to the "Venn Region" column of Table 7

3.3.6 J005450-374030 and J005450-374022

Radio sources J005450-374030 and J005450-374022 are 10.3 arcseconds ($\sim$100 pc) from each other. The $[S\,II]_{Total}$:Hα for these objects are 0.32 ± 0.12 and 0.38 ± 0.31 respectively. They may be two radio emission regions within the same (perhaps older and larger) SNR or simply two neighboring candidate radio SNRs.

Table 6 Three neighboring sources

1	2	3	4	5	6
Source	J0054424313-37	J0054434311-37	N300-S11	Carpano # 161	$[S\,II]_{Total}$:Hα
J005442-374313		6.57, 66.3	2.73, 27.6	20.3, 205	0.282 ± 0.003
J005443-374311	6.57, 66.3		9.23, 93.2	25.2, 254	0.237 ± 0.002
N300-S11	2.73, 27.6	9.23, 93.2		18.9, 191	0.317 ± 0.003

Note: The distance between each pair of sources is given in arcseconds and then in parsecs

Table 7 Sources placed in the Venn diagram of Fig. 8

Venn region	Source count	Designations
A	17	N300-S1, S4, S5, S7–S9, S12–S17, S20, S22, S24, S25, S27
B	3	J005450-374030, J005450-374022, J005501-373829
C	11	J005438-374144, J005442-374313 (N300-S11?), J005443-374311, J005445-373847, J005450-373822, J005451-373826, J005451-373939, J005500-374037, J005503-374246, J005503-374320, J005512-374140
D	2	N300-S2 (C79), N300-S19 (C123)
E	3	N300-S6 (J005431-373825, C69), N300-S26 (J005515-374439, C34), N300-S28 (J005533-374314, C151)
F	3	C60 (SNR5-R4), C72 (SNR3-R3), N300-S10 (J005440-374049, C12)
G	1	C20 (SNR15-X11)

N300-S (or just S) refers to BL97 optically selected SNRs. SNR refers to P00 radio (-R) and X-ray (-X) SNRs. J refers to P04 (ATCA) radio SNRs. C refers to Carpano et al. (2005) X-ray SNRs

3.3.7 J005501-373829

J005501-373829 is on the western edge of a large region of optical emission (dim in DSS2-Red but bright in DSS; perhaps indicating a strong component of reflected emission). This object has radio (P04) emission but its optical emission has $[S\,II]_{Total}$:Hα of 0.35 ± 0.12. We also note the proximity of the OB association AS_082 (Pietrzyński et al. 2001) which is cross-referenced by those authors to H II region 115 in Deharveng et al. (1988) catalog.

3.3.8 J005515-374439

The radio source J005515-374439 is associated with N300-S26 and has $[S\,II]_{Total}$:Hα of 0.86 ± 0.67. We confirm this source as a bona-fide SNR. It is on the edge of a small, circular, faint object visible in both DSS2-Red and DSS images. This SNR has proximity to OB association AS_107, H II region 141 and also to P04's XMM9 X-ray source. Also, Carpano et al. (2005) lists N300-S26 as a soft X-ray source (#34). From our complementary HRC X-ray observations of this object we confirmed a discrete X-ray source within 2 arc seconds of the radio position. For more details see Sect. 2.2.

3.3.9 J005533-374314

J005533-374314 (associated with N300-S28) has a measured $[S\,II]_{Total}$:Hα of 0.45 ± 0.15 and an optical counterpart with an estimated size of 63 pc, which in both DSS2-Red and DSS has a two-lobed shape. The radio emission is southeast of the center of the lobes. J005533-374314 may be linked to the OB association AS_113 and H II region 159. C05 found an X-ray source at this location (#151). Better optical imaging and further X-ray observations of this SNR will prove beneficial.

3.4 Sources with no measurable spectrum

We did not detect a measurable level of Hα and/or [S II] flux against the background noise from the following sources: J005423-373648, J005521-374609, J005523-374632, J005525-373653, J005528-374903, and J005541-374033. The nature of these sources is thus uncertain.

P04 suggests the two radio sources J005423-373648 and J005528-374903 as low confidence SNR candidates. The other P04 sources in the above list have radio emission which would not exclude them as possible SNRs. Given the data and discussion in P04, failure to detect an optical emission spectrum typical of SNRs is consistent with the P04 expectations.

3.5 The multi-wavelength properties of the SNRs

In P00, P04, Long et al. (2010), Pannuti et al. (2007) and Pannuti et al. (2010, in preparation), Venn diagrams were

used to show the number of "radio," "optical," and "X-ray" SNRs in NGC 300, M 33 and NGC 7793. In Fig. 8, we create a new diagram using results from this paper and papers P04, P00 and Carpano et al. (2005, 2006). The SNRs included within each region are listed in Table 7.

The majority of the SNRs (29 out of 40) are identified with emission in only one wavelength region. We note also the low numbers of multiple-frequency and high-energy SNRs; there are only six SNRs detected in both radio and optical wavelengths and only three detected in all three wavelength regions. One SNR was detected in X-ray wavelengths only, and nine SNRs detected in X-ray wavelengths.

Our results are somewhat similar to the M 33 findings of Long et al. (2010) and in NGC 7793 (Pannuti et al. 2010, in preparation) where a large number of optical-only SNRs are identified. This may imply a possible observational bias towards the optical techniques of SNR detection in external galaxies where the resolution (and sensitivity) may play a dominant role in SNR identification. Further to this argument, Dopita et al. (2010a, 2010b) showed that the $[\mathrm{S\,II}]_{\mathrm{Total}}$:H$\alpha$ is a very "sharp" tool in the case of two other nearby galaxies (M 83 and NGC 4214) where they use very advanced Hubble Space Telescope (HST) imaging and spectroscopy. Therefore, we note that the population in the Venn cells is probably of little astrophysical consequence as it is determined by selection effects and the sensitivity limits of the present radio, optical and X-ray surveys. Details of these limits are given in P04, Pannuti et al. (2007) and BL97, and by C05 for the X-ray observations reported here.

It is accepted (Filipović et al. 1998) that all SNRs will emit some thermal radiation at all of these wavelengths. In addition, most SNRs exhibit non-thermal properties in radio and a handful of SNRs in X-rays. However, the amount of emission at each band is the subject of numerous studies, and it is generally understood that the emission is determined by the SN event itself and the ISM in which it occurs. These two variables lead to a wide range of observed structural and emission properties when SNRs are studied over the full electromagnetic spectrum, and no standard spectrum over all wavelengths exists for SNRs.

Compounding these variations are the selection effects that have been introduced. The radio observations of P04 have preferentially selected all sources with spectral index below -0.2 (a safer spectral index selection cut-off value would be -0.5), which probably excludes half of the SNRs available at these wavelengths, and selects preferentially the non-thermal objects. Similarly, the filter-based optical selection of BL97 preferentially selects objects with strong [S II]. This again is a safe choice for locating SNRs, but will miss older objects or the [O III] dominated objects that are perhaps present at the 10 to 15% level (Stupar et al. 2008). It is clear that further studies conducted with instruments featuring improved sensitivity will result in the detection of more SNRs within each wavelength region thus increasing the populations of individual cells of the Venn diagram.

To complete this study we investigated the dependence of the $[\mathrm{S\,II}]_{\mathrm{Total}}$:H$\alpha$ with distance from the galactic nucleus. We found no statistically-significant dependence.

4 Summary

It is not surprising that we found only a few radio SNR candidates exhibiting the established $[\mathrm{S\,II}]_{\mathrm{Total}}$:H$\alpha$. At the distance to this galaxy (2.1 Mpc), with this slit width ($1''$) and the seeing spread along the decker, we are sampling about 100 square parsecs per "line." Thus, each spectral line contains the light from $\sim$50 000 field stars as well as the emission from the nebula. Although $[\mathrm{S\,II}]_{\mathrm{Total}}$:H$\alpha \geq 0.4$ may be fine for galaxies of the Local Group, it may not be the best tool for detecting distant extra-galactic SNRs unless we use the highest resolution telescopes such as the HST. We summarize our findings as follows:

1. We obtained moderate resolution optical spectra of 51 nebular objects in the Sculptor Group galaxy NGC 300. Of the 51 objects, 4 were proposed as SNR candidates in both optical and radio observations, 24 are proposed SNR candidates from optical spectra and 23 are SNR candidates from radio spectra.
2. We find 22 objects meeting the accepted $[\mathrm{S\,II}]_{\mathrm{Total}}$:H$\alpha$ as SNRs, with the nature of the remaining 29 objects either unclear or unknown. A slight bias (of order 10%) appears between our $[\mathrm{S\,II}]_{\mathrm{Total}}$:H$\alpha$ for the optical candidates compared to a previous observation of these same objects (BL97).
3. We created a Gaussian fit of the image of the nebular object across the spectroscope's slit to estimate the diameter of the candidate SNRs. Comparison of our diameter measurements does not show good correlation with previous size estimates (BL97).
4. We also found 31 X-ray sources in this galaxy, 2 of which are positionally linked to nebulae meeting the accepted $[\mathrm{S\,II}]_{\mathrm{Total}}$:H$\alpha$ ratio as SNRs.

Acknowledgements We thank the Australian National University Research School of Astronomy and Astrophysics (RSAA) for the use of their 2.3 m Advanced Technology Telescope. We used the NOAO (National Optical Astronomical Observatory) IRAF (Image Reduction and Analysis Facility) software package, with Brent Miszalski's extractor task for IRAF, and the Figaro software package from the Starlink Project. IRAF is distributed by the National Optical Astronomy Observatories, which are operated by the Association of Universities for Research in Astronomy, Inc. (AURA), under cooperative agreement with the National Science Foundation. We also used the KARMA software package.

References

Aller, L.H.: Atoms, Stars, and Nebulae. Cambridge University Press, Cambridge (1991)

Baldwin, J.A., Stone, R.P.S.: Mon. Not. R. Astron. Soc. **206**, 241 (1984)

Blair, W.P., Long, K.S.: Astrophys. J. Suppl. Ser. **108**, 261 (1997)

Bland-Hawthorn, J., Vlajić, M., Freeman, K.C., Draine, B.T.: Astrophys. J. **629**, 239 (2005)

Bresolin, F., Pietrzyński, G., Gieren, W., Kudritzki, R.P.: Astrophys. J. **634**, 1020 (2005)

Butler, D.J., Martínez-Delgado, D., Brandner, W.: Astron. J. **127**, 1472 (2004)

Carpano, S., Wilms, J., Schirmer, M., Kendziorra, E.: Astron. Astrophys. **443**, 103 (2005)

Carpano, S., Wilms, J., Schirmer, M., Kendziorra, E.: In: Wilson, A. (ed.) The X-ray Universe 2005. ESA Special Publication, vol. 604, p. 445 (2006)

de Vaucouleurs, G., de Vaucouleurs, A., Corwin, H.G. Jr., Buta, R.J., Paturel, G., Fouque, P.: Third Reference Catalogue of Bright Galaxies. Springer, New York (1991)

Deharveng, L., Caplan, J., Lequeux, J., Azzopardi, M., Breysacher, J., Tarenghi, M., Westerlund, B.: Astron. Astrophys. Suppl. Ser. **73**, 407 (1988)

Dodorico, S., Benvenuti, P., Sabbadin, F.: Astron. Astrophys. **63**, 63 (1978)

Dodorico, S., Dopita, M.A., Benvenuti, P.: Astron. Astrophys. Suppl. Ser. **40**, 67 (1980)

Dopita, M.A., Blair, W.P., Long, K.S., Mutchler, M., Whitmore, B.C., Kuntz, K.D., Balick, B., Bond, H.E., Calzetti, D., Carollo, M., Disney, M., Frogel, J.A., O'Connell, R., Hall, D., Holtzman, J.A., Kimble, R.A., MacKenty, J., McCarthy, P., Paresce, F., Saha, A., Silk, J., Sirianni, M., Trauger, J., Walker, A.R., Windhorst, R., Young, E.: Astrophys. J. **710**, 964 (2010a)

Dopita, M.A., Calzetti, D., Maíz Apellániz, J., Blair, W.P., Long, K.S., Mutchler, M., Whitmore, B.C., Bond, H.E., MacKenty, J., Balick, B., Carollo, M., Disney, M., Frogel, J.A., O'Connell, R., Hall, D., Holtzman, J.A., Kimble, R.A., McCarthy, P., Paresce, F., Saha, A., Walker, A.R., Silk, J., Sirianni, M., Trauger, J., Windhorst, R., Young, E.: Astrophys. Space Sci. **330**, 123 (2010b)

Fesen, R.A., Blair, W.P., Kirshner, R.P.: Astrophys. J. **292**, 29 (1985)

Filipović, M.D., Haynes, R.F., White, G.L., Jones, P.A.: Astron. Astrophys. Suppl. Ser. **130**, 421 (1998)

Filipović, M.D., Haberl, F., Winkler, P.F., Pietsch, W., Payne, J.L., Crawford, E.J., de Horta, A.Y., Stootman, F.H., Reaser, B.E.: Astron. Astrophys. **485**, 63 (2008)

Freedman, W.L., Madore, B.F., Hawley, S.L., Horowitz, I.K., Mould, J., Navarrete, M., Sallmen, S.: Astrophys. J. **396**, 80 (1992)

Freedman, W.L., Madore, B.F., Gibson, B.K., Ferrarese, L., Kelson, D.D., Sakai, S., Mould, J.R., Kennicutt, R.C. Jr., Ford, H.C., Graham, J.A., Huchra, J.P., Hughes, S.M.G., Illingworth, G.D., Macri, L.M., Stetson, P.B.: Astrophys. J. **553**, 47 (2001)

Freeman, P.E., Kashyap, V., Rosner, R., Lamb, D.Q.: Astrophys. J. Suppl. Ser. **138**, 185 (2002)

Fruscione, A., McDowell, J.C., Allen, G.E., Brickhouse, N.S., Burke, D.J., Davis, J.E., Durham, N., Elvis, M., Galle, E.C., Harris, D.E., Huenemoerder, D.P., Houck, J.C., Ishibashi, B., Karovska, M., Nicastro, F., Noble, M.S., Nowak, M.A., Primini, F.A., Siemiginowska, A., Smith, R.K., Wise, M.: In: Proc. SPIE, vol. 6270. SPIE Press, Bellingham (2006)

Gaensler, B.M., Hendrick, S.P., Reynolds, S.P., Borkowski, K.J.: Astrophys. J. Lett. **594**, 111 (2003)

Gieren, W., Pietrzyński, G., Soszyński, I., Bresolin, F., Kudritzki, R.P., Minniti, D., Storm, J.: Astrophys. J. **628**, 695 (2005)

Gil de Paz, A., Boissier, S., Madore, B.F., Seibert, M., Joe, Y.H., Boselli, A., Wyder, T.K., Thilker, D., Bianchi, L., Rey, S., Rich, R.M., Barlow, T.A., Conrow, T., Forster, K., Friedman, P.G., Martin, D.C., Morrissey, P., Neff, S.G., Schiminovich, D., Small, T., Donas, J., Heckman, T.M., Lee, Y., Milliard, B., Szalay, A.S., Yi, S.: Astrophys. J. Suppl. Ser. **173**, 185 (2007)

Hamuy, M., Suntzeff, N.B., Heathcote, S.R., Walker, A.R., Gigoux, P., Phillips, M.M.: Publ. Astron. Soc. Pac. **106**, 566 (1994)

Karachentsev, I.D., Grebel, E.K., Sharina, M.E., Dolphin, A.E., Geisler, D., Guhathakurta, P., Hodge, P.W., Karachentseva, V.E., Sarajedini, A., Seitzer, P.: Astron. Astrophys. **404**, 93 (2003)

Kim, S.C., Sung, H., Park, H.S., Sung, E.C.: Chin. J. Astron. Astrophys. **4**, 299 (2004)

Lacey, C.K., Duric, N.: Astrophys. J. **560**, 719 (2001)

Long, K.S., Blair, W.P., Winkler, P.F., Becker, R.H., Gaetz, T.J., Ghavamian, P., Helfand, D.J., Hughes, J.P., Kirshner, R.P., Kuntz, K.D., McNeil, E.K., Pannuti, T.G., Plucinsky, P.P., Saul, D., Tüllmann, R., Williams, B.: Astrophys. J. Suppl. Ser. **187**, 495 (2010)

Mathewson, D.S., Clarke, J.N.: Astrophys. J. Lett. **178**, 105 (1972)

Mathewson, D.S., Clarke, J.N.: Astrophys. J. **179**, 89 (1973a)

Mathewson, D.S., Clarke, J.N.: Astrophys. J. **180**, 725 (1973b)

Mathewson, D.S., Clarke, J.N.: Astrophys. J. **182**, 697 (1973c)

Matonick, D.M., Fesen, R.A.: Astrophys. J. Suppl. Ser. **112**, 49 (1997)

McNeil, E.K., Winkler, P.F.: Bull. Am. Astron. Soc. **38**, 80 (2006)

Murray, S.S., Austin, G.K., Chappell, J.H., Gomes, J.J., Kenter, A.T., Kraft, R.P., Meehan, G.R., Zombeck, M.V., Fraser, G.W., Serio, S.: In: Truemper, J.E., Aschenbach, B. (eds.) Proc. SPIE, vol. 4012, p. 68. SPIE Press, Bellingham (2000)

Osterbrock, D.E., Ferland, G.J.: Astrophysics of Gaseous Nebulae and Active Galactic Nuclei. University Science Books, Sausalito (2006)

Pannuti, T.G., Duric, N., Lacey, C.K., Goss, W.M., Hoopes, C.G., Walterbos, R.A.M., Magnor, M.A.: Astrophys. J. **544**, 780 (2000)

Pannuti, T.G., Schlegel, E.M., Lacey, C.K.: Astron. J. **133**, 1361 (2007)

Payne, J.L., Filipović, M.D., Pannuti, T.G., Jones, P.A., Duric, N., White, G.L., Carpano, S.: Astron. Astrophys. **425**, 443 (2004)

Payne, J.L., Filipović, M.D., White, G.L.: Supernovae: one millennium after SN1006. In: 26th Meeting of the IAU, Joint Discussion 9, 17–18 August 2006, Prague, Czech Republic, JD09, #45 **9** (2006)

Payne, J.L., White, G.L., Filipović, M.D., Pannuti, T.G.: Mon. Not. R. Astron. Soc. **376**, 1793 (2007)

Payne, J.L., White, G.L., Filipović, M.D.: Mon. Not. R. Astron. Soc. **383**, 1175 (2008a)

Payne, J.L., Filipović, M.D., Crawford, E.J., de Horta, A.Y., White, G.L., Stootman, F.H.: Serb. Astron. J. **176**, 65 (2008b)

Pietrzyński, G., Gieren, W., Fouqué, P., Pont, F.: Astron. Astrophys. **371**, 497 (2001)

Puche, D., Carignan, C., Bosma, A.: Astron. J. **100**, 1468 (1990)

Read, A.M., Pietsch, W.: Astron. Astrophys. **373**, 473 (2001)

Read, A.M., Ponman, T.J., Strickland, D.K.: Mon. Not. R. Astron. Soc. **286**, 626 (1997)

Rodgers, A.W., Conroy, P., Bloxham, G.: Publ. Astron. Soc. Pac. **100**, 626 (1988)

Stone, R.P.S., Baldwin, J.A.: Mon. Not. R. Astron. Soc. **204**, 347 (1983)

Stupar, M., Parker, Q.A., Filipović, M.D.: Mon. Not. R. Astron. Soc. **390**, 1037 (2008)

Trushkin, S.A.: Bull. Spec. Astrophys. Obs. **46**, 62 (1998)

Tully, R.B., Fisher, J.R.: Catalog of Nearby Galaxies. Cambridge University Press, Cambridge (1988)

Urošević, D., Pannuti, T.G., Duric, N., Theodorou, A.: Astron. Astrophys. **435**, 437 (2005)

Weisskopf, M.C., Brinkman, B., Canizares, C., Garmire, G., Murray, S., Van Speybroeck, L.P.: Publ. Astron. Soc. Pac. **114**, 1 (2002)

A.9 Related Paper 9

Owen, R. A., Filipović, M. D., Ballet, J., Haberl, F., Crawford, E. J., Payne, J. L., Sturm, R., Pietsch, W., Mereghetti, S., Ehle, M., Tiengo, A., Coe, M. J., Hatzidimitriou, D., and Buckley, D. A. H. (2011). IKT 16: a composite supernova remnant in the Small Magellanic Cloud. *A&A*, 530:A132

My contribution was to assist in the data analysis. This is a 10% contribution.

A&A 530, A132 (2011)
DOI: 10.1051/0004-6361/201116586

Astronomy & Astrophysics

IKT 16: a composite supernova remnant in the Small Magellanic Cloud⋆

R. A. Owen[1], M. D. Filipović[2], J. Ballet[1], F. Haberl[3], E. J. Crawford[2], J. L. Payne[2], R. Sturm[3], W. Pietsch[3], S. Mereghetti[4], M. Ehle[5], A. Tiengo[4], M. J. Coe[6], D. Hatzidimitriou[7,8], and D. A. H. Buckley[9]

[1] Laboratoire AIM, IRFU/Service d'Astrophysique – CEA/DSM – CNRS – Université Paris Diderot, Bat. 709, CEA-Saclay, 91191 Gif-sur-Yvette Cedex, France
e-mail: richard.owen@cea.fr
[2] University of Western Sydney, Locked Bag 1797, Penrith South DC, NSW 1797, Australia
[3] Max-Planck-Institut für extraterrestriche Physik, Giessenbachstrasse, 85741 Garching, Germany
[4] INAF, Istituto di Astrofisica Spaziale e Fisica Cosmica Milano, via E. Bassini 15, 20133 Milano, Italy
[5] XMM-Newton Science Operations Centre, ESAC, ESA, PO Box 50727, 28080 Madrid, Spain
[6] School of Physics and Astronomy, University of Southampton, Highfield, Southampton SO17 1BJ, UK
[7] Department of Astrophysics, Astronomy and Mechanics, Faculty of Physics, University of Athens, Panepistimiopolis, GR15784 Zografos, Athens, Greece
[8] Foundation for Research and Technology Hellas, IESL, Greece
[9] South African Astronomical Observatory, PO Box 9, 7935 Observatory, Cape Town, South Africa

Received 26 January 2011 / Accepted 16 March 2011

ABSTRACT

Aims. IKT 16 is an X-ray and radio-faint supernova remnant (SNR) in the Small Magellanic Cloud (SMC). A previous X-ray study of this SNR found a hard X-ray source near its centre. Using all available archival and proprietary *XMM-Newton* data, alongside new multi-frequency radio-continuum surveys and optical observations at Hα and forbidden [SII] and [OIII] lines, we aim to constrain the properties of the SNR and discover the nature of the hard source within.
Methods. We combine *XMM-Newton* datasets to produce the highest quality X-ray image of IKT 16 to date. We use this, in combination with radio and optical images, to conduct a multi-wavelength morphological analysis of the remnant. We extract separate spectra from the SNR and the bright source near its centre, and conduct spectral fitting of both regions.
Results. We find IKT 16 to have a radius of 37 ± 3 pc, with the bright source located 8 ± 2 pc from the centre. This is the largest known SNR in the SMC. The large size of the remnant suggests it is likely in the Sedov-adiabatic phase of evolution. Using a Sedov model to fit the SNR spectrum, we find an electron temperature kT of 1.03 ± 0.12 keV and an age of ≈14700 yr. The absorption found requires the remnant to be located deep within the SMC. The bright source is fit with a power law with index $\Gamma = 1.58 \pm 0.07$, and is associated with diffuse radio emission extending towards the centre of the SNR. We argue that this source is likely to be the neutron star remnant of the supernova explosion, and infer its transverse kick velocity to be 580 ± 100 km s^{-1}. The X-ray and radio properties of this source strongly favour a pulsar wind nebula (PWN) origin.

Key words. Magellanic Clouds – ISM: supernova remnants

1. Introduction

To date, ∼275 SNRs have been identified in the Galaxy (Green 2009). The majority of these are detected as steep spectrum ($\alpha \sim -0.5$ where $S_\nu = \nu^\alpha$) extended radio synchrotron sources. Acceleration of the synchrotron electrons to GeV–TeV energies occurs at the shock boundary (Reynolds & Chevalier 1981). The ambient gas is heated at the shock to X-ray emitting temperatures (Shklovskii 1968; Grader et al. 1970; Chevalier 1977), and radiative cooling of the gas in slower shocks produces optical emission in Hα, [S] and [O] lines (Fesen et al. 1985). Observations of the thermal X-ray and optical emission can be used to derive fundamental properties such as the age of the remnant and the local gas density. Unfortunately, the study of Galactic SNRs is impeded by two factors. The high absorption in the direction of many of these sources means that only radio emission is detected and much of the broad-band information is lost. In addition, the distance measurements to sources within the Galaxy are often uncertain by a factor of two, leading to an uncertainty of a factor of 4 in luminosity and 5.5 in supernova explosion energy (Borkowski et al. 2001). It is therefore desirable to find populations of SNRs in nearby galaxies at known distances, so that their properties can be determined with greater certainty.

The Small Magellanic Cloud (SMC) is a very good target for study, as its proximity (60 kpc, Karachentsev et al. 2004) allows the morphology of SNRs and SNR candidates to be resolved while the low foreground Galactic absorption column (6×10^{20} cm^{-2}, Dickey & Lockman 1990) permits detection of emission in optical and soft X-ray bands. 23 sources classified as SNRs have been discovered in the SMC (Filipović et al. 2005; Payne et al. 2007). Most of these have been found with associated soft X-ray emission, exhibiting a variety of morphological structures. A synoptic study of the X-ray properties of thirteen of these remnants was completed by

⋆ Based on observations obtained with *XMM-Newton*, an ESA science mission with instruments and contributions directly funded by ESA Member States and NASA.

Table 1. Details of the *XMM-Newton* observations covering IKT 16 used in this study.

Observation ID	Start date (yyyy-mm-dd)	Filter[a] pn/MOS1/MOS2	Pointing co-ordinates RA (J2000)	Dec (J2000)	Useful exposure (ks) pn	MOS 1	MOS2	Off-axis angle (arcmin)
0018540101	2001-11-20	M/M/M	$00^h59^m26.8^s$	$-72°09'55''$	23.4[b]	18.1[b]	18.0[b]	9.3
0084200101	2002-03-30	T/M/M	$00^h56^m41.7^s$	$-72°20'11''$	8.8	10.0	10.3	8.0
0110000201	2000-10-17	M/M/M	$00^h59^m26.0^s$	$-72°10'11''$	14.3[b]	16.7[b]	16.8[b]	9.1
0212282601	2005-03-27	C/M/M	$00^h59^m26.8^s$	$-72°09'54''$	0.0	3.8	3.8	9.3
0304250401	2005-11-27	M/M/M	$00^h59^m26.8^s$	$-72°09'54''$	15.9	17.4[b]	17.4[b]	9.3
0304250501	2005-11-29	M/M/M	$00^h59^m26.8^s$	$-72°09'54''$	14.9	16.5[b]	16.6[b]	9.3
0304250601	2005-12-11	M/M/M	$00^h59^m26.8^s$	$-72°09'54''$	10.6	16.4[b]	16.2[b]	9.3
0500980201	2007-06-06	T/M/M	$01^h00^m00.0^s$	$-72°27'00''$	14.8	23.2	23.9[b]	11.8
0601210801	2009-10-09	T/M/M	$00^h56^m15.5^s$	$-72°21'55''$	23.0[b]	24.6	24.6[b]	10.4

Notes. [(a)] T = thin filter, M = Medium filter, C = Filter-wheel Closed; [(b)] observation used for spectral analysis.

van der Heyden et al. (2004, hereafter VDH04). Filipović et al. (2008) presented *XMM-Newton* results from another three known and one candidate remnant. These studies found that the majority of SMC SNRs are likely in the Sedov-adiabatic phase of evolution.

IKT 16 was discovered as a candidate supernova remnant in the SMC by Inoue et al. (1983) using *Einstein*, and its identity as a shell-type SNR was confirmed through radio and Hα analysis (Mathewson et al. 1984). VDH04 included this remnant as part of their study of SMC SNRs. Using the earliest *XMM-Newton* observation, they found it to be X-ray faint, and its properties were hence poorly constrained. A region of harder X-ray emission close to the centre of the remnant, whose source was unclear, was also reported.

Nine *XMM-Newton* observations covering IKT 16 now exist, giving an eightfold increase in exposure time. In this paper we present a study of IKT 16 and the object located towards its centre using X-ray data from *XMM-Newton*, radio data from the Australia Telescope Compact Array (ATCA) and optical images from the Magellanic Clouds Emission Line Survey (MCELS). In Sect. 2, we outline the procedures used to reduce and analyse *XMM-Newton* data. We also discuss complementary radio and optical data. In Sect. 3, we present the results of spatial and spectral analysis of IKT 16 and the X-ray hard object inside it. In Sect. 4, we discuss the derived properties of IKT 16 and speculate on the nature of the hard source. We present our conclusions in Sect. 5.

2. Observations and data reduction

2.1. X-ray observations

XMM-Newton has observed IKT 16 serendipitously with EPIC in full-frame mode on 9 occasions between 2000 and 2009, at off-axis angles between 8′ and 12′. Eight of the nine observations were used for analysis, with one (obsid 0212282601) discarded due to persistent high background. Details of the observations are shown in Table 1.

Data reduction was based on SAS v10.0.0[1]. Datasets were screened for periods of high background through the creation of full-field single event (PATTERN = 0) lightcurves above 10 keV (with an upper limit of 12 keV for pn data). MOS data were excluded when the count-rate in a 25 s bin exceeded 0.4 count s^{-1}, with pn data excluded above 0.5 count s^{-1}. These thresholds were selected based on quiescent levels in the observations. After filtering, useful exposure times range between 9 and 25 ks.

For each observation, images and exposure maps were created in several energy bands: 0.3−0.8 keV, 0.8−1.2 keV and 1.2−2.0 keV for production of 3-colour X-ray images, and 0.3−1.0 keV for a broader-band soft X-ray image. We used data from single and double pixel events in the pn camera (patterns 0−4) and single to quadruple pixel events in MOS cameras (patterns 0−12). The selection FLAG = 0 was used to exclude spurious data from bad pixels, hot columns and chip gaps, and the pixel size was set at $4'' \times 4''$. A constant particle rate, estimated from the corners of each image not exposed to the sky, was subtracted from each image. The images for each camera were then co-added using the SAS task *emosaic* in order to account for differences in pointing direction between the observations, and the exposure maps were added in the same way. Finally, the mosaic image for each camera was divided by the relevant exposure map and the images from the three cameras summed to produce a flat-field image suitable for further spatial analysis.

Spectral analysis was performed on 15 exposures (3 pn, 5 MOS1 and 7 MOS2), selected on the basis of exposure time and position on the detector. When studying extended sources, it is necessary to be careful in defining source and background areas to extract. In this case there are two areas of interest: the central source (detected as a point source in our X-ray observations) located at RA(J2000) = $00^h58^m16.7^s$ Dec = $-72°18'06''$ and the remainder of the supernova remnant. The shock boundary of the SNR is well-described by a circular region centred on RA = $00^h58^m22.4^s$ Dec = $-72°17'52''$ with a radius of $128 \pm 8''$, with the error due to uncertainty in the best fit circle radius. We therefore defined two source regions for each observation: a 20″ radius area centred on the bright source and a 128″ radius area centred on our best estimate of the centre of the SNR, excluding the previously defined source area. These extraction regions are shown in Fig. 1 (top left). For the first region, a background region was extracted from a nearby position on the same CCD outside the SNR. For the second, a nearby background region of similar size to the source region was found such that the average exposure time for source and background regions was the same. This was done to ensure that the contributions from the cosmic X-ray background (vignetted by the telescope) and particle background (not vignetted to first order) remained in the correct proportion when applied to the source spectrum. The SAS tasks *arfgen* and

[1] Science Analysis Software, http://xmm.esac.esa.int/sas/

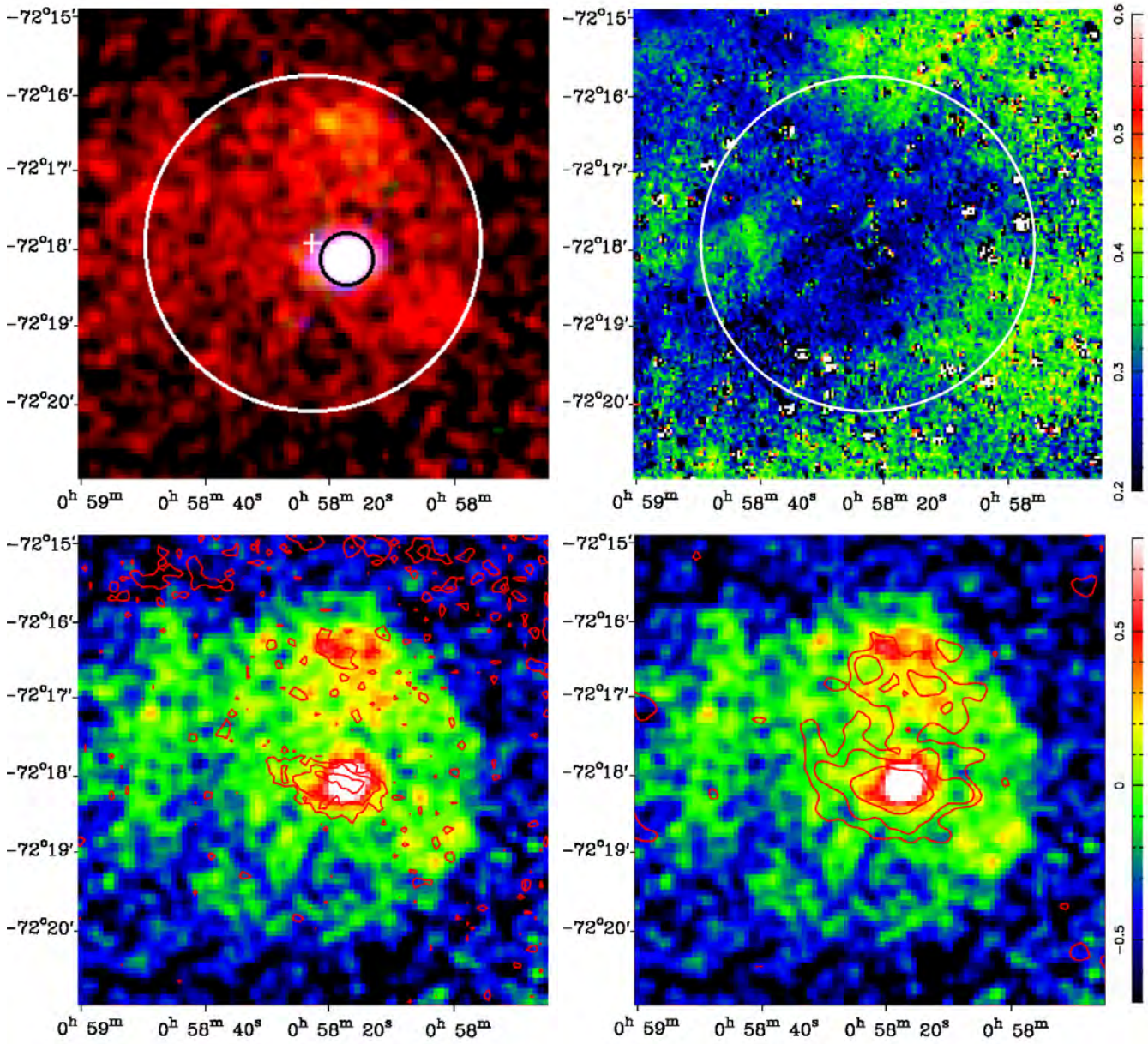

Fig. 1. *Top left*: lightly smoothed RGB *XMM-Newton* EPIC image of IKT 16 (R = 0.3–0.8 keV, G = 0.8–1.2 keV, B = 1.2–2.0 keV). The two regions marked are those used for spectral analysis for the SNR (white circle) and the bright source (black circle). The centre of the remnant is marked with a cross. The image is binned in 4″ × 4″ pixels, and is displayed logarithmically with a dynamic range of 20. *Top right*: MCELS [S]/Hα ratio of IKT 16. The image is binned in 2″ × 2″ pixels. The white circle indicates the extent of the SNR. *Bottom left*: lightly smoothed soft X-ray image (0.3–1 keV) overlaid with high-resolution 20 cm (1400 MHz) ATCA radio contours. The contours are at levels of 0.07, 0.14 and 0.28 mJy beam^{-1}. The X-ray image is displayed logarithmically with a dynamic range of 20, and the X-ray colour bar is shown in units of log(pn+MOS) ct/pixel/20 ks. *Bottom right*: soft X-ray map overlaid with 3 cm (8640 MHz) ATCA radio contours. The contours are at levels of 0.25, 0.5 and 1.0 mJy beam^{-1}. The beam sizes for the radio observations are shown in Table 2.

rmfgen were used to generate appropriate auxiliary response files (ARF) and response matrix files (RMF) for each observation, and the counts in adjacent spectral bins were summed to a minimum of 20 counts per bin using the Ftool[2] *grppha*.

2.2. Optical observations

The Magellanic Cloud Emission Line Survey (MCELS) was carried out using the University of Michigan/CTIO Curtis Schmidt telescope. Using narrow band filters corresponding to Hα(6563 Å), [S](6724 Å) and [O](5007 Å) line emission, plus red and green continuum bands (used to subtract most of the stars from the images), images of diffuse structure across both Magellanic Clouds have been produced with an angular resolution of 2.4″/pixel. An image of the [S]/Hα ratio across the remnant is presented in Fig. 1 (top right). Further information about the MCELS is given in Smith et al. (2000).

Integral field spectroscopy (IFS) was performed on 3 November, 2010 at Siding Springs Observatory using the 2.3-m Advanced Technology Telescope and its Wide Field Spectrograph (WiFeS). WiFeS provides a 25″ × 38″ field with 0.5″ per pixel spatial sampling along each of 25″ × 1″ slits. The output format match two 4096 × 4096 pixel CCD detectors in each camera individually optimized for the blue and red ends of

[2] http://heasarc.gsfc.nasa.gov/ftools/

Table 2. Radio integrated flux density of IKT 16.

ν (MHz)	λ (cm)	Beam size (arcsec)	$S_{\rm Total}$ (Jy)	$S_{\rm Source}$ (Jy)	$S_{\rm SNR}$ (Jy)	Telescope/Project
843	36	44.9×43	0.087	0.045	0.042	MOST
1371	20	7.05×6.63	0.071	0.039	0.032	C281
2378	13	7.02×6.58	0.058	0.038	0.020	C281
4798	6	30×30	0.041	0.033	0.008	C634, Parkes
8640	3	20×20	0.030	0.028	0.002	C634, Parkes

the spectrum. The 900 s single exposure was made in the central region of IKT 16 at position angle (east of north) 90 degrees under clear skies with seeing estimated at 1″. The exposure was made in classical equal mode[3] using the RT560 beam splitter and 3000 Volume Phased Holographic (VPH) gratings. For these gratings, the blue (708 lines mm^{-1}) range includes 3200−5900 Å while the red (398 lines mm^{-1}) range includes 5300−9800 Å. The data were reduced using the WiFeS data reduction pipeline based on NOAO (National Optical Astronomy Observatory) IRAF software. This data reduction package was developed from the Gemini IRAF package (McGregor et al. 2003). The pipeline consists of four primary tasks: *wifes* to set environment parameters, *wftable* to convert single extension FITS file formats to multi-extension FiTS ones and create file lists used by subsequent steps, *wfcal* to process calibration frames including bias, flat-field, arc and wire; and *wfreduce* to apply calibration files and create data cubes for analysis.

2.3. Radio observations

We have extracted all archival radio-continuum observations of IKT 16 using the Australia Telescope Compact Array (ATCA) comprising observations at 4 radio wavelengths: 20, 13, 6 and 3 cm for ATCA (Dickel et al. 2001; Filipović et al. 2002; Payne et al. 2004; Filipović et al. 1997). In addition we make use of the Molonglo Observatory Synthesis Telescope (MOST) SMC survey at 36 cm (843 MHz) (Turtle et al. 1998). The beam size for these observations ranges from 7″ to 45″. IKT 16 was also observed with the ATCA as a part of projects C281 and C634. More information about observing procedure and other sources observed during these sessions can be found in Bojičić et al. (2007), Bojičić et al. (2010) and Crawford et al. (2008). Soft X-ray images of IKT 16 overlaid with 3 cm and high-resolution 20 cm radio contours are shown in Fig. 1, and the integrated flux densities detected from our radio observations of the SNR are shown in Table 2. The error in the measured integrated flux density (for the whole system and the bright source) is estimated as a quadrature sum from the local noise level (0.1 mJy beam^{-1}) and the uncertainty in the gain calibration (10%). For the SNR region (excluding the bright source) the error is calculated by adding the errors for the other two extraction regions in quadrature.

3. Results

3.1. X-ray

3.1.1. Morphology

Figure 1 shows a 3-colour X-ray (0.3−0.8 keV, 0.8−1.2 keV and 1.2−2.0 keV) image of IKT 16, along with radio images from ATCA and optical data from MCELS. The X-ray images are lightly smoothed with a Gaussian kernel of width 4″. We define the boundary of the SNR to be where the surface brightness of the X-ray emission abruptly falls to the background level. Using this definition, the radius of the remnant is estimated to be 128″ ± 8″, with the error resulting from a 2-pixel uncertainty in fitting a circular region to the edge of the X-ray emission. At the assumed distance of the SMC (60 kpc), this corresponds to a radius of 37 ± 3 pc, consistent with being an older remnant in the Sedov phase of evolution (Cox 1972). The measured radius makes it the largest known SNR in the SMC. The shock boundary is well-defined in the north and west of the SNR, where the diffuse X-ray emission is strongest. In the region of strongest emission to the north of the remnant, we also find the X-ray emission to be slightly harder than its surroundings. More tenuous emission is observed to the east of the remnant, and there is some evidence for greater extension of the SNR in this direction. Depending on the direction of measurement, the linear radius of the SNR varies between 122″ (in the N-S direction) and 144″ (NE-SW), implying that the remnant is not perfectly circular on the sky. These deviations are relatively small and our simplification of the geometry of the system does not have a large effect on the results we obtain. These variations do however lead to uncertainty in the position of the SNR centre, which limits the precision with which we can measure the dynamics of the system.

The bright source observed inside the SNR shell is significantly harder than the emission from the rest of the remnant, as seen in the 3-colour image and its X-ray spectrum (in Sect. 3.1.2). We find no evidence for this source being extended in *XMM-Newton* measurements. We therefore limit its maximum X-ray extent to the FWHM of the detector (6″), which is 1.7 pc at the distance of the SMC. Assuming that the SNR shell can be described as spherically symmetric, the position of the bright source is offset from the centre of the shell by 30″ ± 8″ (with the error mostly due to uncertainty in the position of the SNR centre). Not taking into account possible projection effects, this corresponds to a linear distance of 8 ± 2 pc. We note that the bright source has been previously identified in a 9 ks *Chandra* observation (OBSID 2948; Evans et al. 2010). The *Chandra* X-ray position is consistent with that found here, but due to the extremely short observation time and large off-axis angle in that observation, the errors on the *XMM-Newton* position are smaller. The observation also suggests that the source may be slightly extended (with an extent of 1.1″ ± 0.6″). A longer on-axis observation is necessary to constrain this value precisely.

3.1.2. Spectral analysis

Spectral analysis was performed using XSPEC v12.5.1 (Arnaud 1996). For each of the relevant observations, source and background spectra were extracted as described in the previous section. All 15 spectra extracted for each of the two extraction regions were fitted simultaneously, allowing only for a renormalisation factor between observations from different cameras. To account for photoelectric absorption by interstellar gas, two absorption components were used in fitting: a *phabs* component fixed at the foreground Galactic value of 6×10^{20} erg s^{-1} (Dickey & Lockman 1990) assuming elemental abundances of Wilms et al. (2000), and a variable absorption (*vphabs*) component to account for absorption inside the SMC. This second component has metal abundances fixed at 0.2 solar, as is typical in the SMC (Russell & Dopita 1992).

X-ray emission from the central region was fit with an absorbed power-law, and emission from the remainder of the SNR

[3] This is a principal WiFeS data accumulation mode in which data were accumulated in the red and blue cameras on the source for equal times.

Table 3. Parameters of the best-fit model to SNR and bright source regions.

Region	SMC absorption 10^{21} cm^{-2}	Power-law cont. photon index normalization	Sedov model shock T (keV) normalization	Sedov model Ion. time (10^{10} cm^{-3} s)	Goodness of fit χ^2/d.o.f.	Unabsorbed L_X[a] 0.5–10 keV (10^{35} erg s^{-1})
SNR	3.4(f)	1.58(f) 1.0×10^{-5}(f)	1.03 ± 0.12 $1.4 \pm 0.3 \times 10^{-4}$	6.1	1103/1032	1.6 ± 0.4
Bright source	3.4 ± 0.6	1.58 ± 0.07 $3.4 \pm 0.4 \times 10^{-5}$	1.03(f) 3.6×10^{-6}(f)	6.1(f)	150/137	1.6 ± 0.2

Notes. [(a)] Includes correction for spillover of bright source photons into SNR extraction area and vice versa.
(f) Parameter fixed for consistency between fit regions.

was fit with a Sedov model (Borkowski et al. 2001). Due to the relatively broad point spread function of the *XMM-Newton* EPIC detector, we estimate that for a point source, ~25% of the source counts will fall outside an extraction region of 20″. Therefore, an extra power-law component is introduced to the SNR fit, with index fixed to that obtained through fitting the central region and normalization set to account for this spillover. Similarly, as the central extraction region encompasses 2.5% of the overall SNR region, an appropriately scaled Sedov component is added to the central source model, with parameters fixed to those derived for the SNR.

The free parameters of the Sedov model are the mean shock temperature, electron temperature just behind the shock front, metal abundances, ionization age (electron density behind the shock front multiplied by the remnant age) and normalization. Providing that the SNR has spherical symmetry and is in the Sedov phase of evolution, the fits obtained can be used to estimate several physical parameters. Using the distance to the SNR (D) and radius (R in m, assuming a distance of 60 kpc), volume of X-ray emitting material (V in m^3), normalization derived from the XSPEC fit (N), shock temperature (T_S in keV) and baryon number per hydrogen atom ($r_m \approx 1.4$, assuming a helium/hydrogen ratio of 0.1), it is possible to derive the electron density (n_e), age of the remnant (t_{dyn}), total emitting mass (M), initial explosion energy (E_0) and ionization age (I_t) through the following system of equations (VDH04, from Borkowski et al. 2001):

$$n_e = \sqrt{\frac{3D^2N}{10^{-24}R^3}},\ \mathrm{m}^{-3} \tag{1}$$

$$t_{dyn} = \frac{1.3 \times 10^{-14}R}{\sqrt{T_S}},\ \mathrm{yr} \tag{2}$$

$$M = 5 \times 10^{-31} m_p r_m n_e V,\ M_\odot \tag{3}$$

$$E_0 = 2.64 \times 10^{-8} T_s R^3 n_e,\ \mathrm{erg} \tag{4}$$

$$I_t = 4 \times 10^{-6} n_e t_{dyn},\ \mathrm{m}^{-3}\mathrm{s} \tag{5}$$

We note that our distance estimate of 60 kpc to IKT 16 may not be entirely accurate due to the large line of sight extent of the SMC, which is measured to be 4–6 kpc in this region of the galaxy (Subramanian & Subramaniam 2009). Errors in the distance measurement will also impact the measured radius of the SNR ($\propto D$) and its volume ($\propto D^3$), and the physical properties derived from the above system of equations will be affected.

Details of the best fit spectra obtained are given in Table 3 and the combined pn and MOS spectra for both extraction regions are shown in Fig. 3. Due to the limited quality of the spectral data, shock and electron temperatures are assumed to be the same (valid as an evolved SNR should be approaching electron-ion equilibration). The metal abundances in the fits are fixed at 0.2 solar for the same reason. Since lines, whose presence is required to fit the ionization age, are not easily discernable in the X-ray spectrum, this parameter was calculated based on the above system of equations. Spectral fitting was then repeated with the calculated ionization age to derive new Sedov parameters, and this process was repeated until convergence was achieved. The best fit physical parameters from the Sedov model fit are shown in Table 4. The best fit models found require a significant absorption component within the SMC in addition to foreground Galactic absorption. We initially left this absorption as a free parameter for both regions. In this case, we find the best fit Sedov model for the SNR to have an electron temperature of 0.71 keV with absorption inside the SMC of 4.6×10^{21} cm^{-2} ($\chi^2 = 1100.7/1032$), outside the error bounds of the absorption found in the bright source spectrum. Setting the SNR absorption at the level found for the bright source does not significantly worsen the fit ($\chi^2 = 1103.2/1033$), but it does alter the best fit temperature (see Table 3). We fix the absorption in the SNR to the level of the bright source, as is expected if the two emission regions are physically connected, and derive the Sedov parameters for the SNR based on this fit (see Table 4). If we instead fix the absorption for the bright source at the level found for the SNR, we obtain a significantly worse fit for this component ($\chi^2 = 164/138$). In this case, we find the power-law index of the source to be somewhat steeper ($\Gamma = 1.74 \pm 0.08$). For both components, the average flux across all observations is measured to be 2.7×10^{-13} erg cm^{-2} s^{-1} (0.5–10 keV), corresponding to an unabsorbed luminosity of 1.6×10^{35} erg s^{-1}. The flux for both components is found to be constant between observations to within 15%. There is thus no evidence for any long-term variability of the point source.

The X-ray spectrum of the bright source within the SNR is typical of many astrophysical sources. The possible nature of this source will be discussed in Sect. 4.2.

3.2. Optical

Using data from MCELS, we find that the [S]/Hα ratio found in the SNR is ~0.25 (Fig. 1, top right), significantly below the standard "minimum" ratio typically found in radiative shocks. This implies that there is no evidence for radiative shocks around

Table 4. Physical properties of IKT 16 from best fit Sedov model.

Parameter	Units	This paper	VDH04
Temperature	keV	1.03	1.76
Radius	pc	37	29
Electron density	cm^{-3}	0.03	0.05/0.04[a]
Dynamical age	yr	14 700	7500
Swept-up mass	$M_\odot$	232	124
Explosion energy	10^{51} erg	1.2	3.4

Notes. [(a)] VDH04 derive electron and proton densities separately, assumed to be approximately the same here.

the SNR. In known SMC SNRs, this ratio is typically found to be higher than 0.4 (Payne et al. 2007).

Similar results are found from analysis of the central region of IKT 16. Using QFitsView3[4], a one-dimensional spectrum of the diffuse region excluding all visible stars was created (Fig. 4). Analysis required the identification of cosmic rays on the 2-dimensional spectra while the IRAF task *splot* allowed determination of emission line counts based on gaussian fits. Standard errors were calculated based on an average rms noise of 600 counts; propagation of error methods were used for the addition or division of line fluxes. Using this method, we find a [S]/Hα ratio of 0.23 with a 2.1% error. It is quite possible that there are very faint nebulae interspersed between the stars that do not meet the criteria for shocked regions. We cannot exclude the possibility of an HII region being present in the line of sight.

3.3. Radio

The available radio images show IKT 16 to be a very radio-weak SNR. There is evidence of faint diffuse radio structure throughout the remnant. The images are dominated by a source corresponding to the X-ray bright source, which appears to extend a distance of ~30″ towards the centre of the remnant. There is no evidence for a radio point source located within this emission. Table 2 shows the integrated flux density measurements at frequencies from 843–8640 MHz. The overall radio spectrum (Fig. 2) is well-described by a power-law with index $\alpha = -0.45 \pm 0.02$. The radio spectral index of the central source is found to be flatter (-0.19 ± 0.02) than that of the SNR itself (-0.97 ± 0.35). The SNR spectral index is unusually steep, especially given that IKT 16 is most likely an older (evolved) SNR, due to its rather large size. Usually, a steep gradient like this would suggest a much younger and more energetic SNR. However, in this case, the steepness can be contributed to missing short spacings at higher radio-continuum frequencies (4800 and 8640 MHz) and therefore missing flux. Specifically at 8640 MHz (where the ATCA primary beam is ~300″) this SNR edges would be positioned close to the primary beam boundary where the flux tends to be significantly uncertain. We note that if we omit the two highest frequency data points from the SNR fit, the radio spectral index is –0.72, which is more in line with that found in other SNRs in the SMC (Filipović et al. 2005).

[4] Written by Thomas Ott and freely available at `www.mpe.mpg.de/ott/dpuser/index.html`

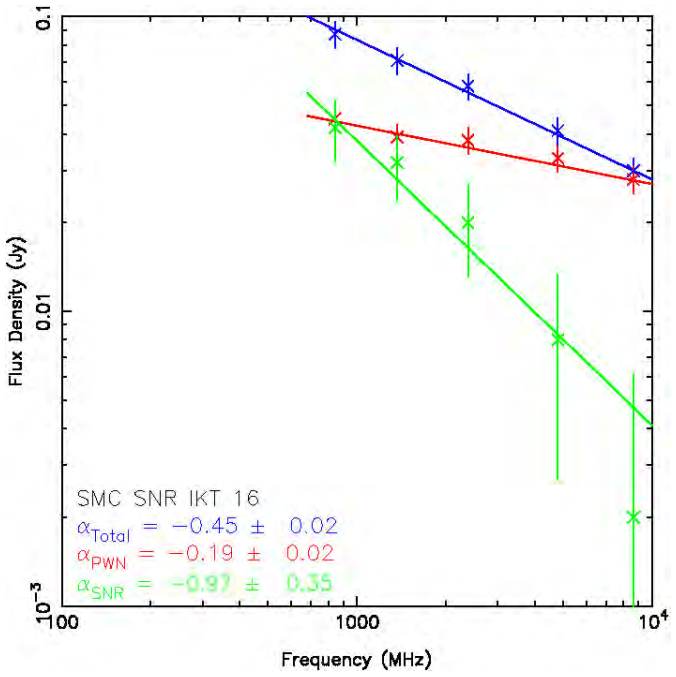

Fig. 2. Radio spectra of the entire SNR (blue), the bright source near the centre of the remnant (red) and the remainder of the remnant (green), constructed from radio observations at 5 frequencies using MOST and ATCA. The best fit power-law fits are shown, and the data is also shown in Table 2.

4. Discussion

The only significant study of the X-ray properties of this remnant to date has been completed by VDH04. The *XMM-Newton* observations covering IKT 16 since publication of this paper have significantly improved the available statistics. This allows us to examine the properties of the SNR more accurately, as well as enabling study of the nature of the bright source located close to its centre.

4.1. Properties of the SNR

In the analysis of IKT 16 conducted by VDH04, the bright source emission area was excluded from analysis, and the remaining emission was fit with both a single-temperature non-equilibrium ionization (NEI) model and a Sedov model. As we have shown, simply excluding the source emission area may not produce an accurate measure of the properties of the SNR, since ~25% of the flux detected through this method will be from the point source. As this source is significantly harder than the SNR as a whole, this unduly influences the results obtained. Additionally, the previous study estimates the radius of the SNR to be 100″ compared with 128″ here. The new estimate is based on mosaicing of all available observations, through which the X-ray shock boundary is more clearly defined in all directions. This changes the estimate of the X-ray emitting volume, which also affects the derived Sedov parameters.

The Sedov properties obtained for both studies are shown in Table 4. The properties we find justify our use of the Sedov approximation, as the swept-up mass significantly exceeds the ejecta mass but radiative cooling has not occurred yet. The parameters we derive are significantly different from those in VDH04. The temperature we find is cooler, which we attribute to the different methods of dealing with the point source mentioned in the previous paragraph. Along with our larger estimate

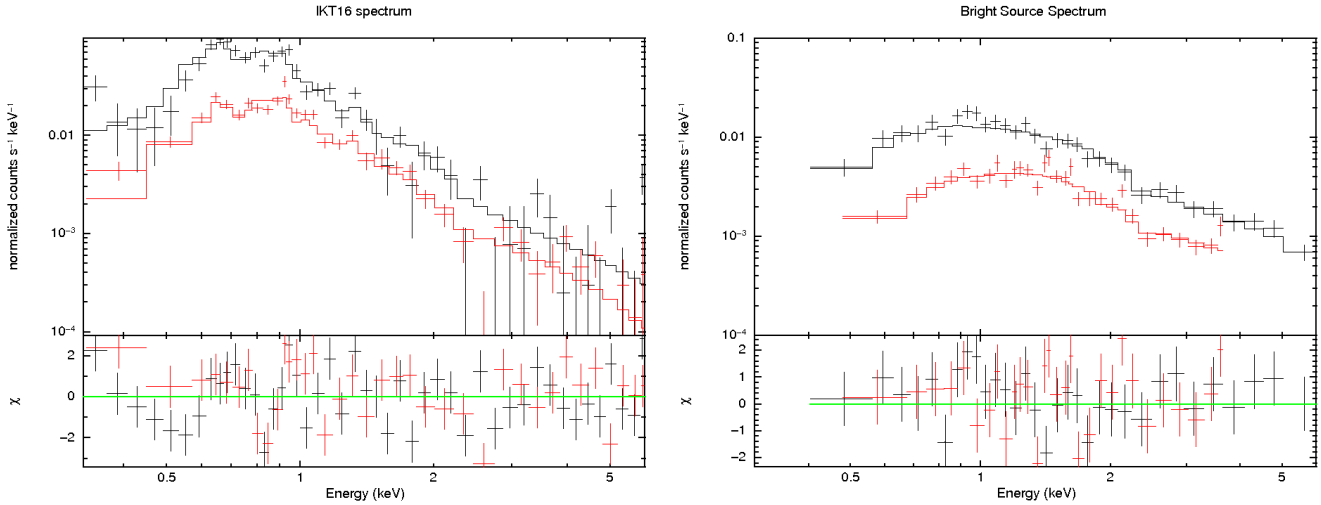

Fig. 3. EPIC spectra from IKT 16 (*left*) and the bright source located near its centre (*right*). In both cases the solid line corresponds to the best-fit spectral model (see text and Table 3), with the upper line showing the combined spectra from pn observations and the lower line combined spectra from MOS1 and MOS2 observations. The χ^2 residuals with respect to the best-fitting model are also shown.

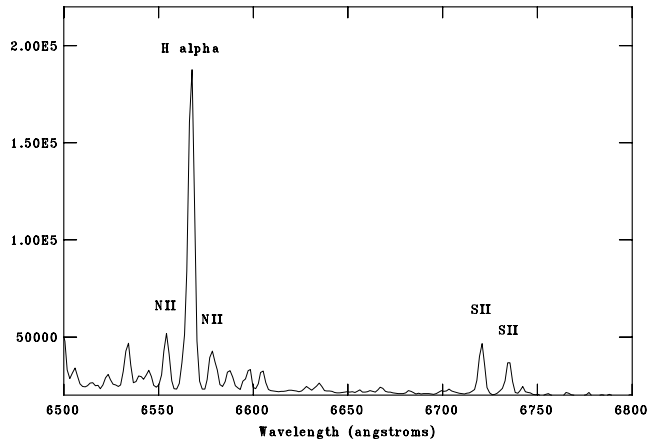

Fig. 4. WiFeS spectra of the central region of IKT 16.

of the radius of the remnant, this leads to a higher dynamical age, larger swept-up mass and lower initial explosion energy (as expected from Eqs. (1)–(4)). In order to test whether this explains the difference in our results, we attempted to fit the SNR emission region with a Sedov model without accounting for spillover from the bright source. We find a good fit (χ^2 = 1099/1032) with a higher shock temperature of 1.30 ± 0.20 keV. This is consistent with the value found by VDH04 (1.76 ± 0.65 keV). VDH04 noted that the initial explosion energy appears high in comparison to typical SNRs, which they suggest is due to the remnant resulting from collapse of a massive star within a low-density circumstellar cavity. Our estimate of the explosion energy (~10^{51} erg s^{-1}) is much more in line with that derived for other SNRs in the SMC.

Compared with other SNRs in the SMC, IKT 16 is notably X-ray faint and is detected at higher electron temperature (~1.0 keV vs. ~0.2 keV). While this is the largest confirmed SNR in the SMC there are several larger cousins in the Large Magellanic Cloud (LMC) (Cajko et al. 2009; Klimek et al. 2010). The radio emission from the SNR is also found to be faint (32 mJy at 1400 MHz; Table 2). The large size of the remnant, considering that it is still in the Sedov phase of evolution, suggest that the density of the SNR environment is low. This may also contribute to its X-ray and radio faintness. The low density implied is consistent with a SNR explosion inside a wind blown bubble, which are typically found inside molecular clouds. Such sites are associated with massive star formation, which would increase the likelihood of this system being a core-collapse SNR and the central source being associated with it. Muller et al. (2010) have carried out a survey of CO emission across the northern SMC, finding a series of molecular clouds near the position of IKT 16. Their presence strongly supports this scenario. The apparent X-ray faintness of the remnant may be additionally enhanced by high absorption attenuating the soft X-ray signal. Using a map of HI density from Stanimirović et al. (1999), the total column density of the SMC in the direction of IKT 16 is 5.7 × 10^{21} cm^{-2}. The value we derive from spectral fitting is ≈60% of this value, indicating that IKT 16 is located deep within the SMC.

The soft X-ray image shows that the distribution of X-ray emission appears somewhat uneven inside the remnant, with more emission observed towards the northern shock boundary than to the south. The radio images also show more emission to the north of the remnant. The 3-colour X-ray image (Fig. 1, top left) suggests that the X-ray emission in the north may be at a higher temperature than in the rest of the remnant. This may be due to a combination of several factors, including fluctuations in the SMC absorption column, a higher concentration of SNR ejecta increasing the local metallicity or true variations in the plasma temperature of the ISM. Due to the limited X-ray statistics, it is not possible to carry out spatially resolved spectral analysis to investigate this further.

4.2. Nature of the bright source

The X-ray spectrum of the bright source is consistent with that of several different astrophysical objects, including X-ray binary systems, pulsar wind nebulae and background active galactic nuclei. Here, we attempt to discriminate between these possibilities.

In fitting a power law model to the source, a significant absorption component is required in addition to foreground Galactic absorption. This suggests that it is not a Galactic object located along the line of sight.

It is possible, however, that the source is a background AGN. The average power-law photon index of a type I AGN is measured to be ~1.9 (Pounds et al. 1990), somewhat softer than what we see here. However, the absorption required in our spectral fit ($3.4 \pm 0.6 \times 10^{21}$ cm^{-2}) is significantly lower than that of the SMC along our line of sight, making this unlikely. We therefore attempted to fit a more complex model commonly found to fit AGN spectra: a power law plus a 0.1 keV black body component (Turner & Pounds 1989). Here, we find a reasonable fit with an extra absorption component of $3 \pm 1 \times 10^{21}$ cm^{-2}. The X-ray flux detected in this model is $\sim 3 \times 10^{-13}$ erg cm^{-2} s^{-1}.

Studies of type I AGN typically show the fluxes in X-ray (0.5−10 keV) and optical bands to lie within approximately an order of magnitude of each other (Maccacaro et al. 1988). For a source with this observed X-ray flux, we therefore expect there to be an optical counterpart at a V magnitude of between 14.8 and 20.8. We searched the Optical Gravitational Lensing Experiment (OGLE) (Udalski et al. 1998) and Magellanic Clouds Photometric Survey (Zaritsky et al. 2002) to try to find the optical counterpart. The closest match found to the X-ray position (searching down to a V band optical magnitude of 21.5) is at a distance of 2.5″, 2 times the combined errors in optical and X-ray positions. However, the two closest optical sources in the catalogue have optical colours consistent with stars within the SMC. The closest source with optical colours atypical for a main sequence star is at a distance of 3.2″, still within 3 sigma of our X-ray source position. This is a possible optical counterpart to our source.

We can also estimate the probability of finding a background AGN coincident with the SNR position. Studies of the $\log N - \log S$ distribution of AGN (e.g. Rosati et al. 2002) show that above our estimate of the unabsorbed X-ray flux of this object ($\sim 4 \times 10^{-13}$ erg cm^{-2} s^{-1}, 0.5–10 keV) we expect to find 3 AGN per square degree of the sky. The probability of finding one such source within 30″ of the centre of IKT 16 is 0.07%. Although we are unable to rule out an AGN origin for this source, we conclude that it is statistically unlikely. We assume from this point that the source is located inside the SMC.

As shown in Sect. 3, the SNR shell is well-described by a circle of radius 128″. Presuming that the well-defined profile of the western shock boundary can be used to find the centre of the remnant, the bright source is located ≈30 ± 8″ (a transverse distance of 8 ± 2 pc) away from this point. Providing it is associated with the supernova event, it has traversed this distance in the dynamical age of the remnant (14 700 yr), at an average speed of 580 ± 100 km s^{-1}. The direction of travel is not necessarily perpendicular to us, so this is a lower limit. However, unless the direction of travel is significantly out of this plane, the velocity of the object will not be much greater than this value. Asymmetry in SNR explosions typically gives the resulting compact object a random space velocity of 350–550 km s^{-1} (Lyne & Lorimer 1994), so it is reasonable to suggest that the bright X-ray source is related to this object. There are two known objects which may produce the emission observed: a pulsar wind nebula or a microquasar.

Pulsar wind nebulae (PWNe) are generated by dissipation of a pulsar's rotational energy through relativistic winds, producing synchrotron emission visible in radio to X-ray bands. For a review of the properties of these systems, see Gaensler & Slane (2006). ~50 PWNe have been observed in the Galaxy and the LMC, and the majority are associated with known SNRs ("Composite" SNR, Kaspi et al. 2006). The X-ray spectrum of known PWNe is well-described by a power-law of index ranging between $\Gamma \sim 1.1$–2.3 (Cheng et al. 2004), consistent with the power law fit found here. The measured X-ray luminosity of 1.6×10^{35} erg s^{-1} is also similar to that of known PWNe in the Galaxy and the LMC (e.g. Gaensler et al. 2003b; Porquet et al. 2003; Slane et al. 2004). In our observations, the maximum extension of the X-ray source was found to be 6″, which corresponds to a radius of ~1 pc at the distance of the SMC. Gelfand et al. (2009) find that in the spherically symmetric case, a pulsar wind nebula inside a Sedov-phase remnant at an age of 15 kyr should be undergoing compression due to the SNR reverse shock to a radius of <1 pc. This would be detected as a point source in *XMM-Newton* observations, consistent with our measurements. The radius measured in the *Chandra* observation is 0.3 ± 0.2 pc, consistent with this scenario. In this case, the movement of the source away from the centre of the SNR shell implies that spherical symmetry no longer holds, but as the distance travelled is only ~10% of the shell diameter, this scenario may still be valid. Unfortunately, the limited spatial resolution of *XMM-Newton* and the distance to the SMC (60 kpc) preclude identification of a central pulsar, which would confirm the identity of this source as a pulsar wind nebula. The relatively low X-ray flux also prevents us from conducting timing analysis to search for pulsations.

The ATCA images in Fig. 1 show the source to have a radio extent of ~40″ × 30″, elongated in the direction of the centre of the remnant. This extent is significantly greater than that observed in X-rays. This may be due to the longer cooling time for radio emission compared to that of X-ray emission. The radio emission may therefore trace the path of the nebula as it moves from the centre of the SNR, as is observed in "relic" PWN (e.g. Vela X, Frail et al. 1997). The radio spectral index of this source is measured to be ~ -0.2, consistent with the typical radio spectrum found in PWNe (Gaensler & Slane 2006). The absence of a radio point source in this emission rules out the presence of an established radio pulsar. However, confirmed PWNe (e.g. LMC SNR B0453-685 and LMC SNR N 206; Gaensler et al. 2003a; Williams et al. 2005; Crawford et al., in prep.) have been found where the central pulsar is not detected in radio observations, so this does not discount a PWN origin.

The other possibility we consider here is a microquasar travelling through the SMC, where the extended radio emission is due to optically thin synchrotron radiation in relativistic jets. The X-ray emission in this case would come from an X-ray binary (XRB) system with a power-law of index 1.5–2.2, with radio jets observed at a spectral index between −0.8 and −0.4 (e.g. Fender 2006; Hannikainen et al. 2006). The X-ray power-law slope is consistent with this scenario, but the radio spectrum is somewhat flatter than expected ($\alpha \sim -0.2$). If it is associated with the SNR, and providing the western shock boundary can be used to estimate the original site of the supernova explosion, the velocity we infer for this object (580 ± 100 km s^{-1}) is very high compared with the average kick velocity for even Low-Mass X-ray Binary (LMXB) systems (180 ± 80 km s^{-1}; Brandt & Podsiadlowski 1995). In fact, the majority of known microquasars are High-Mass X-ray Binary (HMXB) systems, for which the corresponding typical kick velocity is 50 km s^{-1} (also from Brandt & Podsiadlowski 1995). It is possible that the object may be within the SMC but not associated with the SNR, in which case this velocity measurement is not applicable. The relative stability of the X-ray flux between observations is somewhat unexpected, as many X-ray binary systems will exhibit state changes on a timescale of 10 years. From the available X-ray and radio evidence, we conclude that it is unlikely that the bright source is a microquasar. We note that no LMXB systems

are currently known in the SMC, and they are very rare in the Galaxy. This also decreases the likelihood of this scenario.

On the basis of current observations, it is most likely that the source is a PWN. However, we cannot entirely rule out a microquasar or AGN. A future deep *Chandra* observation will be able to determine the X-ray extent of this source accurately, and will thus conclusively determine its nature.

5. Conclusions

We have carried out analysis of the spatial and spectral properties of the SMC SNR IKT 16, using archive and proprietary data from *XMM-Newton*, radio data from ATCA and optical images from MCELS. The properties of the SNR are consistent with it being in the Sedov-adiabatic phase of evolution. The dynamic age of the remnant and initial explosion energy are typical of the population of SNRs in the SMC.

We find the X-ray point source near the centre of IKT 16 to be non-thermal, with an X-ray spectral index of ∼1.6. This source is coincident with a radio source which extends a distance of ∼30″ in the direction of the centre of the SNR. We conclude that the X-ray source is unlikely to be a background AGN, due to the small probability of spatial coincidence with the SNR and the absence of an obvious optical counterpart. Two astrophysical objects are considered which may explain the X-ray and radio emission observed: a pulsar wind nebula or microquasar. The flatness of the radio spectrum, the one-sided morphology of the radio emission and inferred velocity of the source strongly favour a PWN origin, which may be confirmed by a future *Chandra* observation. If this is the case, IKT 16 is the second largest such system (after the Vela SNR) found to date.

Acknowledgements. The *XMM* project is supported by the Bundesministerium für Wirtschaft und Technologie/Deutsches Zentrum für Luft- und Raumfahrt (BMWI/DLR, FKZ 50 OX 0001) and the Max-Planck Society. R.S. acknowledges support from the BMWI/DLR grant FKZ 50 OR 0907. S.M. and A.T. acknowledge financial contribution from the agreement ASI-INAF I/009/10/0. We used the Karma/MIRIAD software packages developed by the ATNF. The Australia Telescope Compact Array is part of the Australia Telescope which is funded by the Commonwealth of Australia for operation as a National Facility managed by the CSIRO. We thank the Magellanic Clouds Emission Line Survey (MCELS) team for access to the optical images. We thank the anonymous referee for their comments, which have helped to improve this manuscript significantly.

References

Arnaud, K. A. 1996, in Astronomical Data Analysis Software and Systems V, ed. G. H. Jacoby, & J. Barnes, ASP Conf. Ser., 101, 17
Bojičić, I. S., Filipović, M. D., Parker, Q. A., et al. 2007, MNRAS, 378, 1237
Bojičić, I. S., Filipović, M. D., & Crawford, E. J. 2010, Serb. Astron. J., 181, 63
Borkowski, K. J., Lyerly, W. J., & Reynolds, S. P. 2001, ApJ, 548, 820
Brandt, N., & Podsiadlowski, P. 1995, MNRAS, 274, 461
Cajko, K. O., Crawford, E. J., & Filipović, M. D. 2009, Serb. Astron. J., 179, 55
Cheng, K. S., Taam, R. E., & Wang, W. 2004, ApJ, 617, 480
Chevalier, R. A. 1977, ARA&A, 15, 175
Cox, D. P. 1972, ApJ, 178, 159
Crawford, E. J., Filipović, M. D., & Payne, J. L. 2008, Serb. Astron. J., 176, 59
Dickel, J. R., Williams, R. M., Carter, L. M., et al. 2001, AJ, 122, 849
Dickey, J. M., & Lockman, F. J. 1990, ARA&A, 28, 215
Evans, I. N., Primini, F. A., Glotfelty, K. J., et al. 2010, ApJS, 189, 37
Fender, R. 2006, Jets from X-ray binaries, ed. W. H. G. Lewin, & M. van der Klis, 381
Fesen, R. A., Blair, W. P., & Kirshner, R. P. 1985, ApJ, 292, 29
Filipović, M. D., Jones, P. A., White, G. L., et al. 1997, A&AS, 121, 321
Filipović, M. D., Bohlsen, T., Reid, W., et al. 2002, MNRAS, 335, 1085
Filipović, M. D., Payne, J. L., Reid, W., et al. 2005, MNRAS, 364, 217
Filipović, M. D., Haberl, F., Winkler, P. F., et al. 2008, A&A, 485, 63
Frail, D. A., Bietenholz, M. F., Markwardt, C. B., & Oegelman, H. 1997, ApJ, 475, 224
Gaensler, B. M., & Slane, P. O. 2006, ARA&A, 44, 17
Gaensler, B. M., Hendrick, S. P., Reynolds, S. P., & Borkowski, K. J. 2003a, ApJ, 594, L111
Gaensler, B. M., Schulz, N. S., Kaspi, V. M., Pivovaroff, M. J., & Becker, W. E. 2003b, ApJ, 588, 441
Gelfand, J. D., Slane, P. O., & Zhang, W. 2009, ApJ, 703, 2051
Grader, R. J., Hill, R. W., & Stoering, J. P. 1970, ApJ, 161, L45
Green, D. A. 2009, Bull. Astron. Soc. India, 37, 45
Hannikainen, D. C., Wu, K., Stevens, J. A., et al. 2006, Chin. J. Astron. Astrophys. Suppl., 6, 010000
Inoue, H., Koyama, K., & Tanaka, Y. 1983, in Supernova Remnants and their X-ray Emission, ed. J. Danziger, & P. Gorenstein, IAU Symp., 101, 535
Karachentsev, I. D., Karachentseva, V. E., Huchtmeier, W. K., & Makarov, D. I. 2004, AJ, 127, 2031
Kaspi, V. M., Roberts, M. S. E., & Harding, A. K. 2006, Isolated neutron stars, ed. W. H. G. Lewin, & M. van der Klis, 279
Klimek, M. D., Points, S. D., Smith, R. C., Shelton, R. L., & Williams, R. 2010, ApJ, 725, 2281
Lyne, A. G., & Lorimer, D. R. 1994, Nature, 369, 127
Maccacaro, T., Gioia, I. M., Wolter, A., Zamorani, G., & Stocke, J. T. 1988, ApJ, 326, 680
Mathewson, D. S., Ford, V. L., Dopita, M. A., Tuohy, I. R., Mills, B. Y., & Turtle, A. J. 1984, ApJS, 55, 189
McGregor, P. J., Hart, J., Conroy, P. G., et al. 2003, in SPIE Conf. Ser. 4841, ed. M. Iye, & A. F. M. Moorwood, 1581
Muller, E., Ott, J., Hughes, A., et al. 2010, ApJ, 712, 1248
Payne, J. L., Filipović, M. D., Reid, W., et al. 2004, MNRAS, 355, 44
Payne, J. L., White, G. L., Filipović, M. D., & Pannuti, T. G. 2007, MNRAS, 376, 1793
Porquet, D., Decourchelle, A., & Warwick, R. S. 2003, A&A, 401, 197
Pounds, K. A., Nandra, K., Stewart, G. C., George, I. M., & Fabian, A. C. 1990, Nature, 344, 132
Reynolds, S. P., & Chevalier, R. A. 1981, ApJ, 245, 912
Rosati, P., Tozzi, P., Giacconi, R., et al. 2002, ApJ, 566, 667
Russell, S. C., & Dopita, M. A. 1992, ApJ, 384, 508
Shklovskii, I. S. 1968, Supernovae, 13
Slane, P., Helfand, D. J., van der Swaluw, E., & Murray, S. S. 2004, ApJ, 616, 403
Smith, C., Leiton, R., & Pizarro, S. 2000, in Stars, Gas and Dust in Galaxies: Exploring the Links, ed. D. Alloin, K. Olsen, & G. Galaz, ASP Conf. Ser., 221, 83
Stanimirović, S., Staveley-Smith, L., Dickey, J. M., Sault, R. J., & Snowden, S. L. 1999, MNRAS, 302, 417
Subramanian, S., & Subramaniam, A. 2009, A&A, 496, 399
Turner, T. J., & Pounds, K. A. 1989, MNRAS, 240, 833
Turtle, A. J., Ye, T., Amy, S. W., & Nicholls, J. 1998, PASA, 15, 280
Udalski, A., Szymanski, M., Kubiak, M., et al. 1998, Acta Astron., 48, 147
van der Heyden, K. J., Bleeker, J. A. M., & Kaastra, J. S. 2004, A&A, 421, 1031
Williams, R. M., Chu, Y., Dickel, J. R., et al. 2005, ApJ, 628, 704
Wilms, J., Allen, A., & McCray, R. 2000, ApJ, 542, 914
Zaritsky, D., Harris, J., Thompson, I. B., Grebel, E. K., & Massey, P. 2002, AJ, 123, 855

A.10 Related Paper 10

Wong, G. F., Filipović, M. D., Crawford, E. J., De Horta, A. Y., Galvin, T., Drašković, D., and Payne, J. L. (2011a). New 20-cm Radio-Continuum Study of the Small Magellanic Cloud: Part I - Images. *Serbian Astronomical Journal*, 182:43–52

My contribution was to assist in the data analysis. This is a 20% contribution.

Serb. Astron. J. № 182 (2011), 43 - 52 **UDC 52–13–77 : 524.722.7**
DOI: 10.2298/SAJ1182043W Professional paper

NEW 20-CM RADIO-CONTINUUM STUDY OF THE SMALL MAGELLANIC CLOUD: PART I - IMAGES

G. F. Wong, M. D. Filipović, E. J. Crawford, A. De Horta, T. Galvin, D. Drašković, J. L. Payne

University of Western Sydney, Locked Bag 1797, Penrith South DC, NSW 1797, Australia
E–mail: *m.filipovic@uws.edu.au*

(Received: April 5, 2011; Accepted: April 8, 2011)

SUMMARY: We present and discuss new high-sensitivity and resolution radio-continuum images of the Small Magellanic Cloud (SMC) at λ=20 cm (ν=1.4 GHz). The new images were created by merging 20-cm radio-continuum archival data, from the Australian Telescope Compact Array and the Parkes radio-telescope. Our images span from $\sim 10''$ to $\sim 150''$ in resolution and sensitivity of r.m.s.$\geq$0.5 mJy/beam. These images will be used in future studies of the SMC's intrinsic sources and its overall extended structure.

Key words. Magellanic Clouds – Radio Continuum: galaxies

1. INTRODUCTION

The well established proximity of the Small Magellanic Cloud (SMC; ∼60 kpc; Hilditch et al. 2005) and its location in one of the coldest areas of the radio sky towards South Celestial Pole, allows observation of its radio emissions to be made without the interference of our own galaxy's dust, gas and stars (Galactic Foreground Radiation). This means that, not only the study of its intrinsic properties including its extended emission and polarisation are of great interest, but that it is an ideal location to study other objects such as supernova remnants (SNRs; Filipović et al. 2005, 2008), H II regions and Planetary Nebulae (PNe; Filipović et al. 2009a) which are difficult to study in our own galaxy and other galaxies that are further away.

Over the last 40 years extensive radio-continuum surveys of the Small Magellanic Cloud have been made including interferometric observations made using the Molonglo Synthesis Telescope (MOST; Ye et al. 1995) and Australian Telescope Compact Array (ATCA; Filipović et al. 2002, Payne et al. 2004, Filipović et al. 2009b, Mao et al. 2008, Dickel et al. 2010), and single dish observations from the 64-m Parkes radio-telescope (Filipović et al. 1997, 1998). Most of these surveys, however, suffer from either low resolution, poor sensitivity and/or poor *uv*-coverage.

In this paper, we present and discuss a method of merging various radio-continuum observations of the SMC at λ=20 cm (ν=1.4 GHz) in an attempt to make the best use of the currently available data prior to the next generation of radio-telescope surveys (such as ASKAP, MeerKAT and SKA). By combining a large amount of existing observational data of the SMC and with the latest generation of computer power we can create various new high-resolution and high-sensitivity images.

The newly constructed images are analysed and the difference between the various SMC images created at 20 cm are discussed. In Section 2 we describe the observational data and reduction techni-

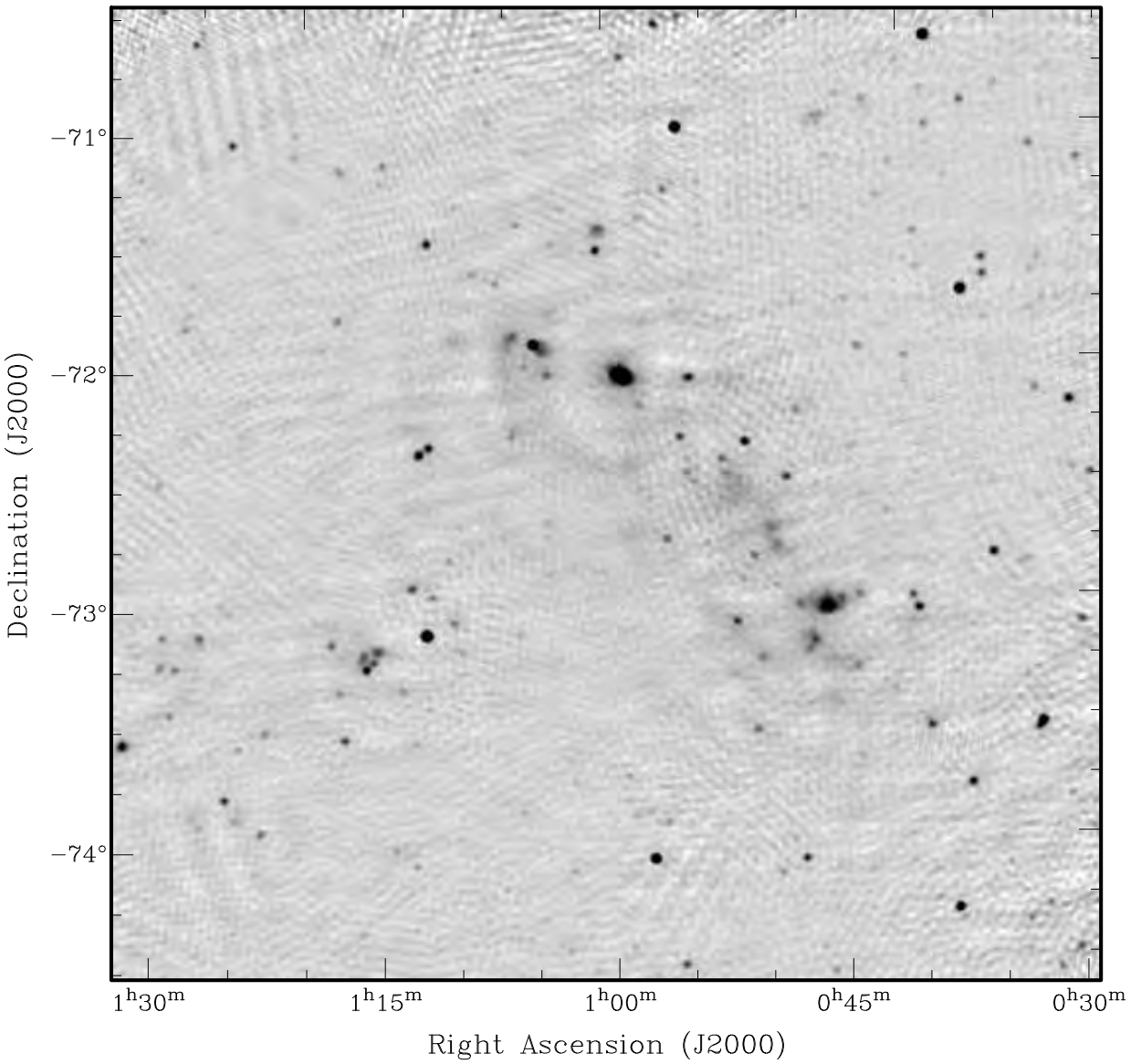

Fig. 1. *ATCA project C159 radio-continuum total intensity image of the SMC merged with Parkes. The synthesised beam is 98″ and the r.m.s=1.5 mJy/beam.*

ques. In Section 3 we present our new maps with a brief discussion and in Section 4 is the conclusion. The astrophysical interpretation of sources found in the surveys will be presented in subsequent papers.

2. OBSERVATIONAL DATA

2.1. Observational Data Details

To create the highest fidelity and resolution image to date of the SMC at 20 cm, we looked for mosaic observations that covered the SMC region. After an extensive search in the Australian Telescope Online Archive[1] (ATOA), we retrieved three projects C159, C1197 and C1288 that observed the whole SMC.

All these three projects taken from the ATOA were ATCA mosaic observations of the SMC. Used as part of a survey of neutral hydrogen emission in the SMC by Staveley-Smith et al. (1997; see paper for observation details), project C159 (Fig. 1) provided the first large scale image using a mosaic mode. The ATCA project C1197 (Fig. 3) contained two sets of observations using different array configurations (H214 and H75). Observations of the H75 array configurations were part of a study into the cool gas in the Magellanic Stream (see Matthews et al. 2009 for observation details). The ATCA project

[1]http://atoa.atnf.csiro.au

C1288 (Fig. 2) was used as part of a study of magnetic fields of the SMC, carrying out radio Faraday rotation and optical starlight polarisation data (see Mao et al. (2008) for observation details). The Parkes data was obtained from a radio-continuum study (Fig. 4) of the SMC (Filipović et al. 1997). The source 1934-638 was used for the primary calibration and the source 0252-712 as the secondary calibrator for all ATCA images. A brief summary of the three ATCA projects can be found in Table 1.

Table 1. ATOA mosaic observational data used in imaging of SMC.

ATCA Project	*Date Observed*	*Array*	*Bandwidth(MHz)*
C159	06-10-1992 to 07-10-1992	375	4
	09-10-1992 to 14-10-1992	375	4
C1288	10-07-2004 to 18-07-2004	6A	128
C1197	20-10-2003 to 01-11-2003	H214	128
	31-07-2005 to 02-08-2005	H75	128
	09-09-2006 to 10-09-2006	H75	128
	12-09-2006 to 15-09-2006	H75	128
	19-09-2006 to 22-09-2006	H75	128

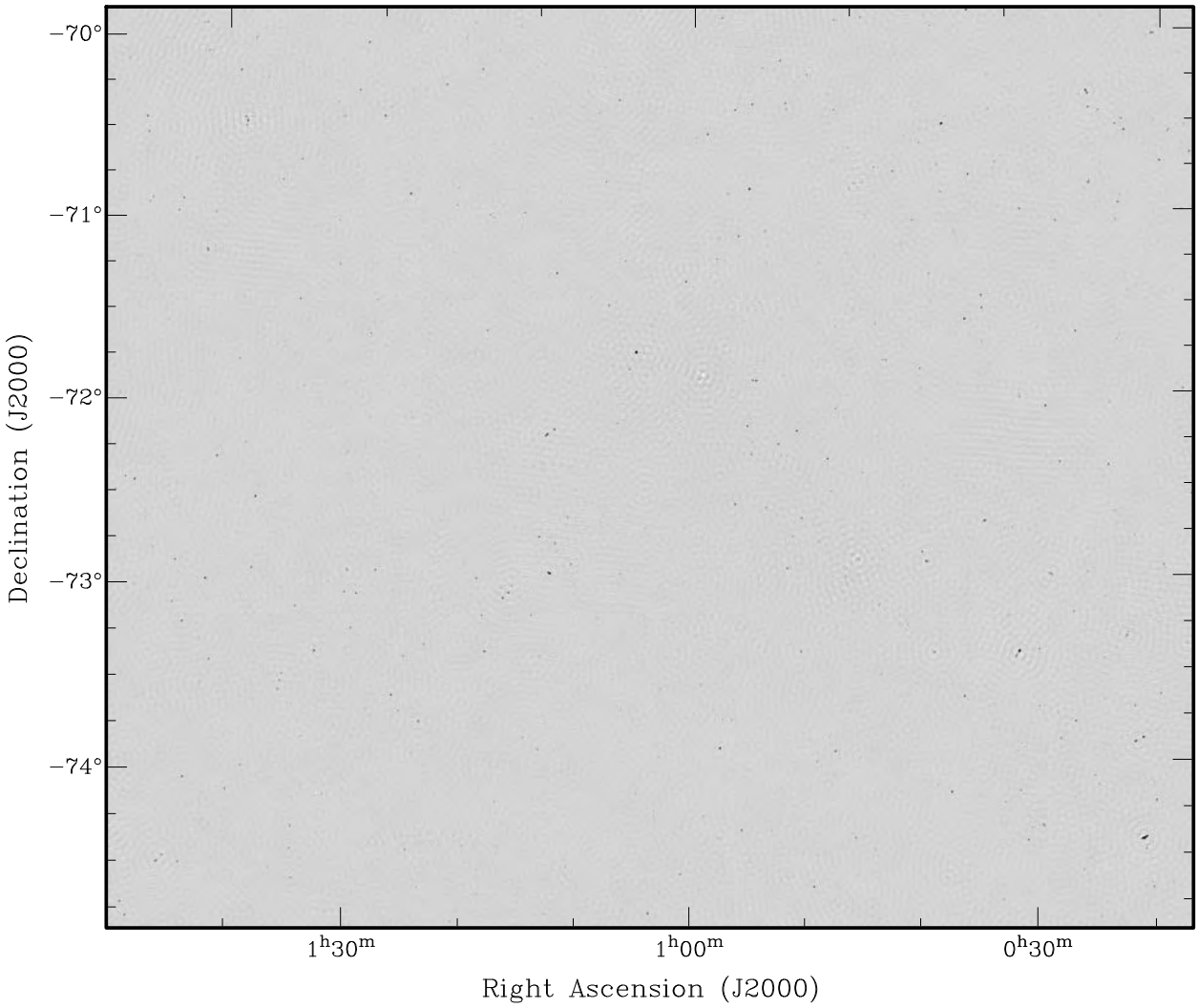

Fig. 2. *ATCA Project C1288 radio-continuum total intensity image of the SMC merged with Parkes. The synthesised beam is 17.8″×12.2″ and the r.m.s=0.7 mJy/beam.*

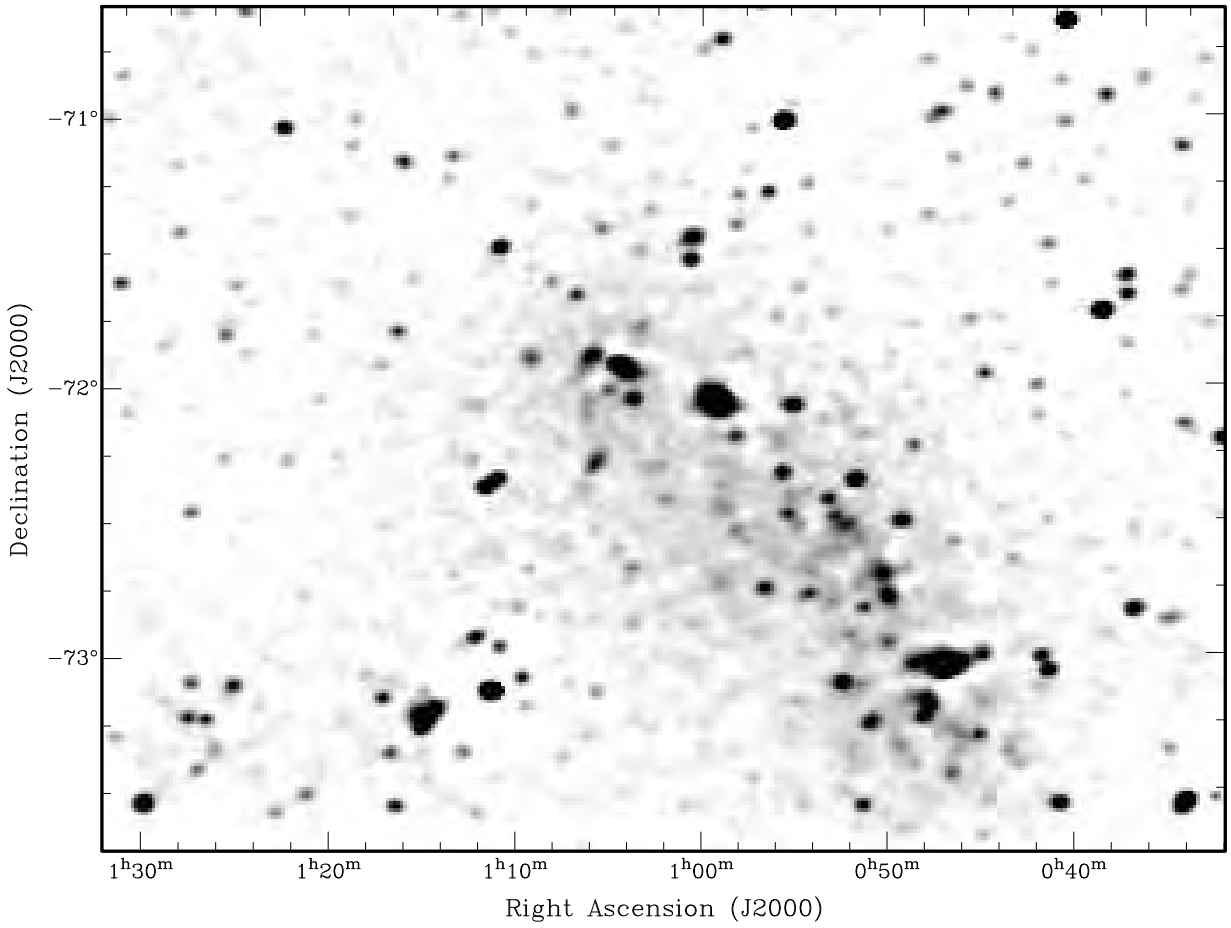

Fig. 3. *ATCA Project C1197 radio-continuum total intensity image of the SMC. The synthesised beam is 158.2″×124.8″ and the r.m.s=1.0 mJy/beam.*

2.2. Image Creation

The software packages MIRIAD (Sault and Killeen 2010) and KARMA (Gooch 2006) were used for the data reduction and analysis. Initial high-resolution images were produced from the full dataset using the MIRIAD multi-frequency synthesis (Sault and Wieringa 1994) with natural weighting.

The joint-deconvolution method (Cornwell 1988) was used in the imaging process to give better *uv*-coverage from the different pointings that were overlapping each other.

The deconvolution process employed MIRIAD tasks MOSSDI and MOSMEM (or combination of both). Ideal for the deconvolution of point source emissions, MOSSDI is an SDI variance of the clean algorithm that is designed for Mosaics (Steer et al. 1984). The map created from ATCA project C1288 (Fig. 2), consisted mostly of point sources due to the long baselines, therefore MOSSDI was used to deconvolve it.

While on the other hand, MOSMEM is a method that uses maximum entropy (Cornwell 1989) and is suited for extended objects. This task was used for ATCA projects C159 (Fig. 1) and C1197 (Fig. 3) where the short baseline was used and extended emission dominates.

The various resolution maps were created by restricting the radial distance in the *uv*-plane of the three ATCA projects. The combined maps with various resolutions (with the exception of the highest resolution map), were created using a combination of both the MIRIAD task MOSSDI and MOSMEM. This method struck the balance between the two deconvolution tasks and its effects on point source emission and extended emission. Using MOSSDI to clean the mosaic with a low number of iterations till the side lobes of strong point sources are no longer present, removed any interference. Then using MOSMEM to complete the deconvolution process allowed the extended emissions from the data of the short baselines to remain.

To create the best possible SMC mosaic image at 20 cm, we examined the radial distance in the *uv*-plane of all three ATCA projects combined (Fig. 5), and identified where significant gaps between baselines existed. The first significant gap was found at 3kλ (see this image in Fig. 6). Using this as a starting point we were able to process and successfully create an image. Subsequently we increased the radial distance from 3kλ to 6kλ (Fig. 7) and later 16kλ (Fig. 8).

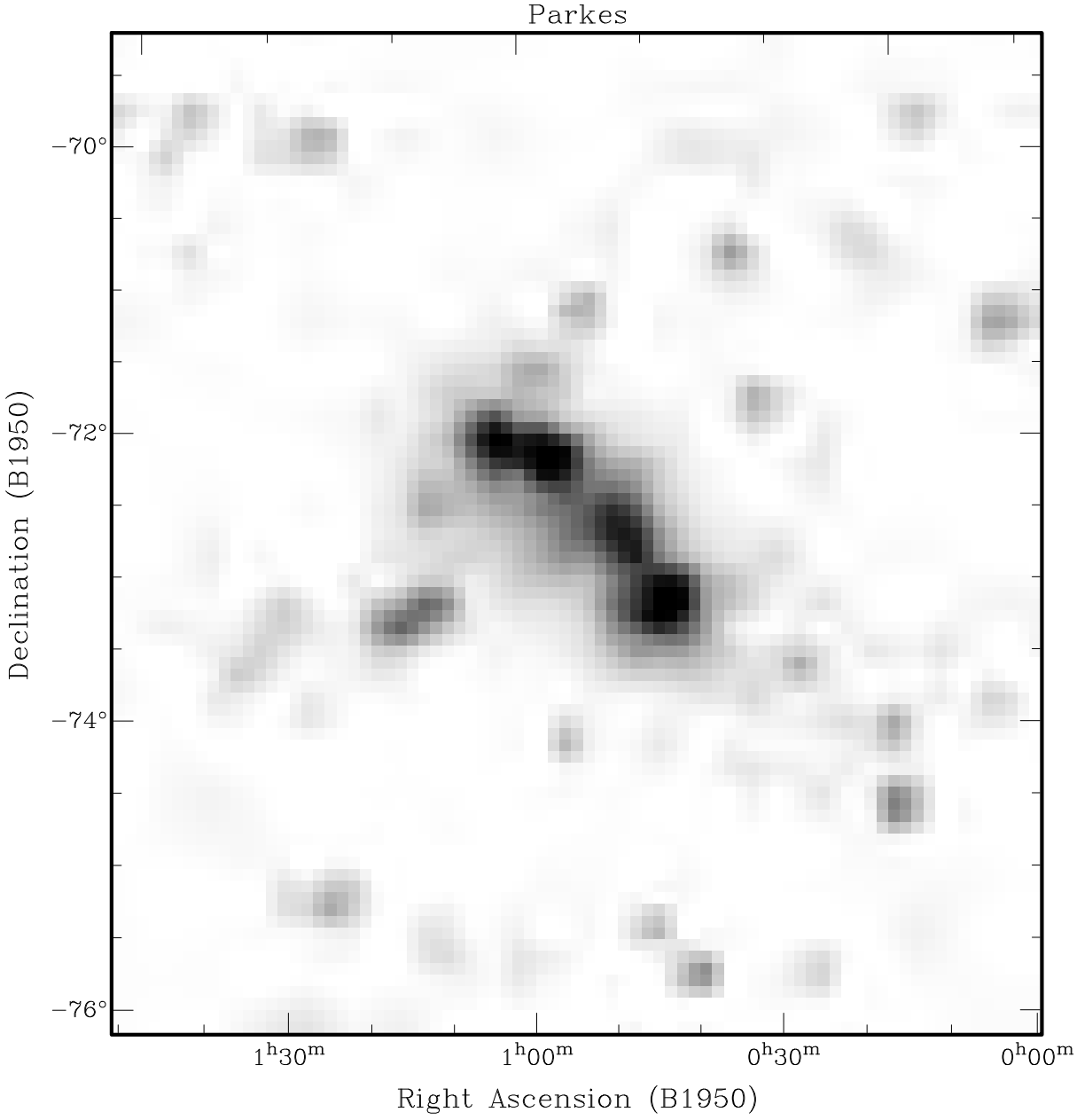

Fig. 4. *A radio-continuum total intensity of SMC taken from Parkes retrieved from Filipović et al. (1997). The synthesised beam is 13.8′ and r.m.s=15 mJy/beam.*

We also merged all mosaics with the Parkes observations to provide the essential and important short spacing data (Stanimirović 2002).

The new images presented in this paper show the individual maps (from all ATCA projects; Table 2) and combined maps that are merged with Parkes data. Table 3. lists the details of the various combined images.

Table 2. The details of ATCA projects of SMC mosaics at 20-cm.

ATCA Project	*Beam Size* (arcsec)	*PA* (degree)	*r.m.s.* (mJy/beam)
C159	98.0×98.0	0	1.5
C1288	17.8×12.2	26	0.7
C1197	158.2×124.8	85	1.0

Table 3. The details of three SMC merged mosaics at 20-cm.

uvdistance (kλ)	*Beam Size* (arcsec)	*PA* (degree)	*r.m.s.* (mJy/beam)
3	48.4 × 33.6	26	0.5
6	30.1 × 20.1	27	0.5
16	16.3 × 9.5	22	0.5

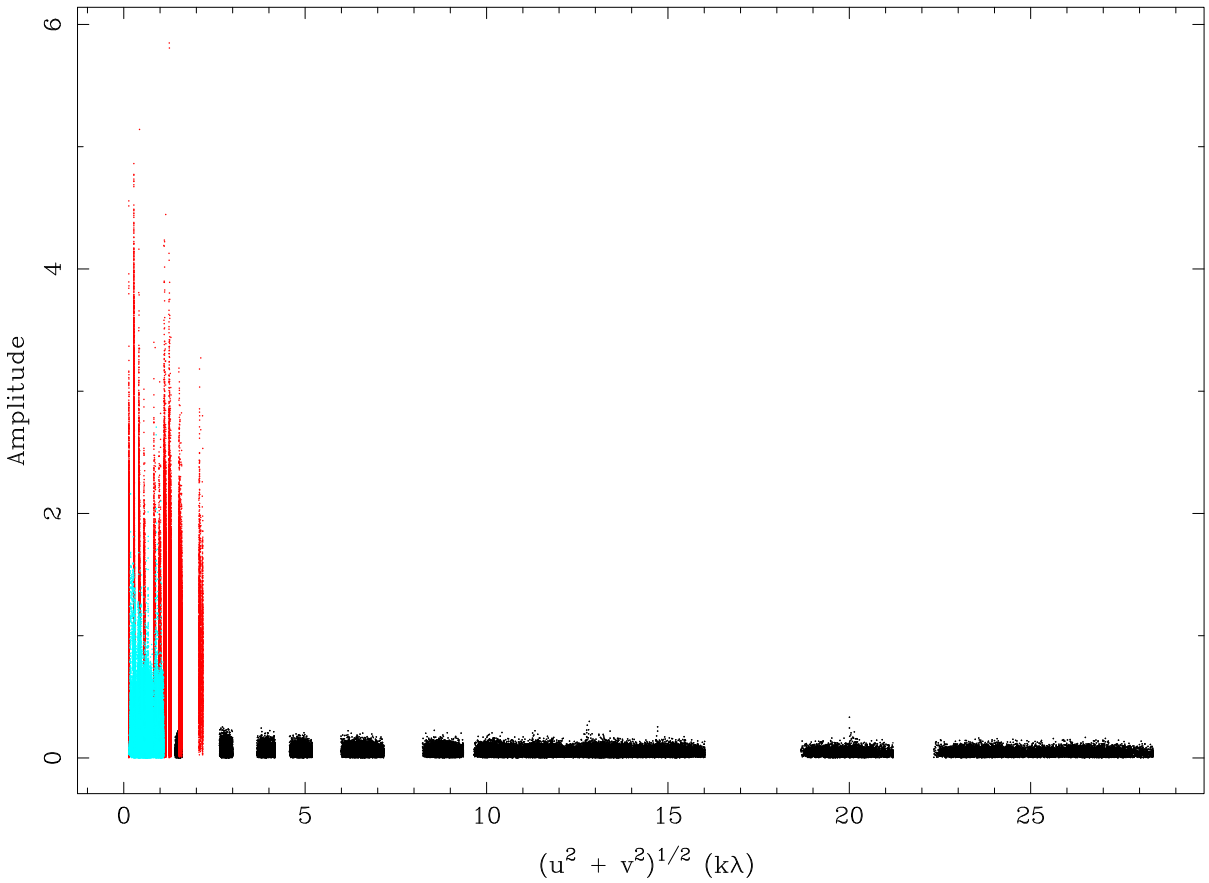

Fig. 5. *Amplitude vs. uv-distance graph of the three projects overlapping with each other. Blue colour represents observational data from ATCA project C1197, red from C159 and black from C1288. (See the electronic edition of the Journal for a color version of this figure).*

3. RESULTS AND DISCUSSION

In Figs. 1 to 3, we show the individual intensity mosaic maps of the SMC from ATCA projects C159, C1288 and C1197 respectively and in Fig. 4 we reproduce the Parkes (single-dish) image from Filipović et al. (1997). The Figs. 6, 7 and 8 are images at *uv* distance of 3, 6 and 16 kλ respectively (Table 3).

All these images can be downloaded from the Astronomy Digital Image Library (ADIL) at http://adil.ncsa.uiuc.edu/.

3.1. Individual SMC Mosaics at λ=20 cm

Comparing the individual images of the SMC at 20 cm created from the ATCA projects, we can see the effects of the different array configurations. While shorter baseline images such as C159 (Fig. 1) and C1197 (Fig. 3) show much intensive extended emission, compared to C1288 image (Fig. 2; 6A array) which contains point sources at higher resolution.

Fig. 1 was imaged from the C159 observations and later merged with the data from Parkes single-dish radio-telescope. It contains a combination of extended emission and point source emission. From the individual images (Figs. 1 to 4), Fig. 1 has a balanced combination of the different types of emission and resolution.

Using an array configuration of 6A, image in Fig. 2 (ATCA project C1288) has the longest baseline and only point sources can be seen. However, Fig. 2 has the highest resolution compared to the other individual images presented in this paper and is dominated by the radio point source population.

Created from ATCA project C1197, in Fig. 3 the most prominent feature is extended emission. Although this image suffers from poor resolution due to the dominance of shorter baselines, which upon closer examination means a lack of detail of individual objects.

In Fig. 4 we show observation taken from single dish telescope (Parkes). As a result, this image has the lowest resolution compared to Figs. 1 to 3 which are observations taken from an array interferometer. The main characteristic of Fig. 4 is the extended emission and the shape of the SMC galaxy.

We note that the area coverage of these three mosaics is different. Therefore, when combining the mosaics we only used the individual observations that overlapped with each other.

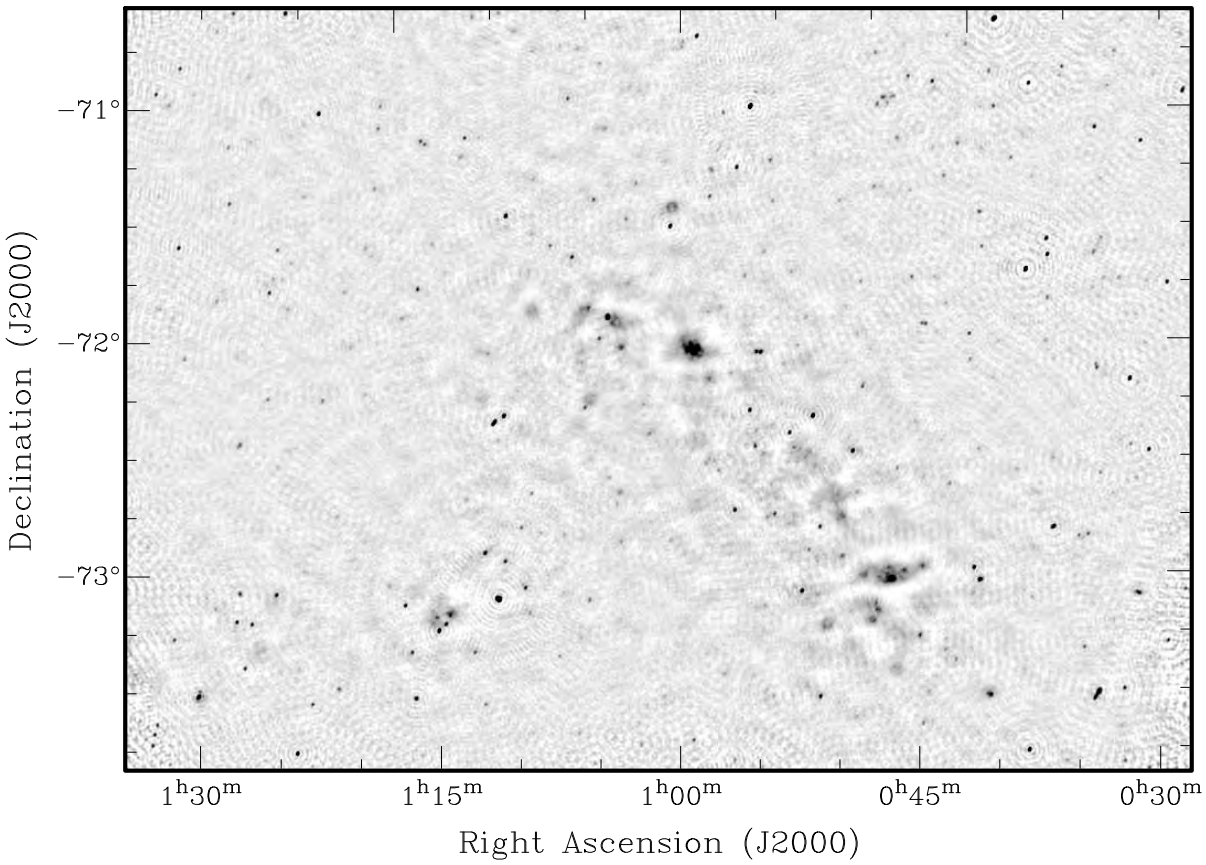

Fig. 6. *A radio-continuum total intensity images of the SMC at 3kλ. The synthesised beam is 48.4″×33.6″ and the r.m.s=0.5 mJy/beam.*

3.2. New Combined SMC Mosaics at λ=20 cm

Figs. 6-8 are combination images with various resolutions, the features of the images have a combination of point source emission and extended emission.

We also point out that some differences between various images can be attributed to slightly different deconvolution techniques and careful flagging of highly noisy observational data. Our new high-resolution and high-sensitive analysis of these images will be presented in future papers.

4. CONCLUSION

In this paper we present and discuss new high-sensitivity and resolution radio-continuum images of the SMC at 20 cm. The new images were created by merging sensitive 20-cm mosaic radio surveys, from the ATOA, and later the data from Parkes 64-m radio-telescope. These images will be used in future studies of the SMC's intrinsic sources and overall structure.

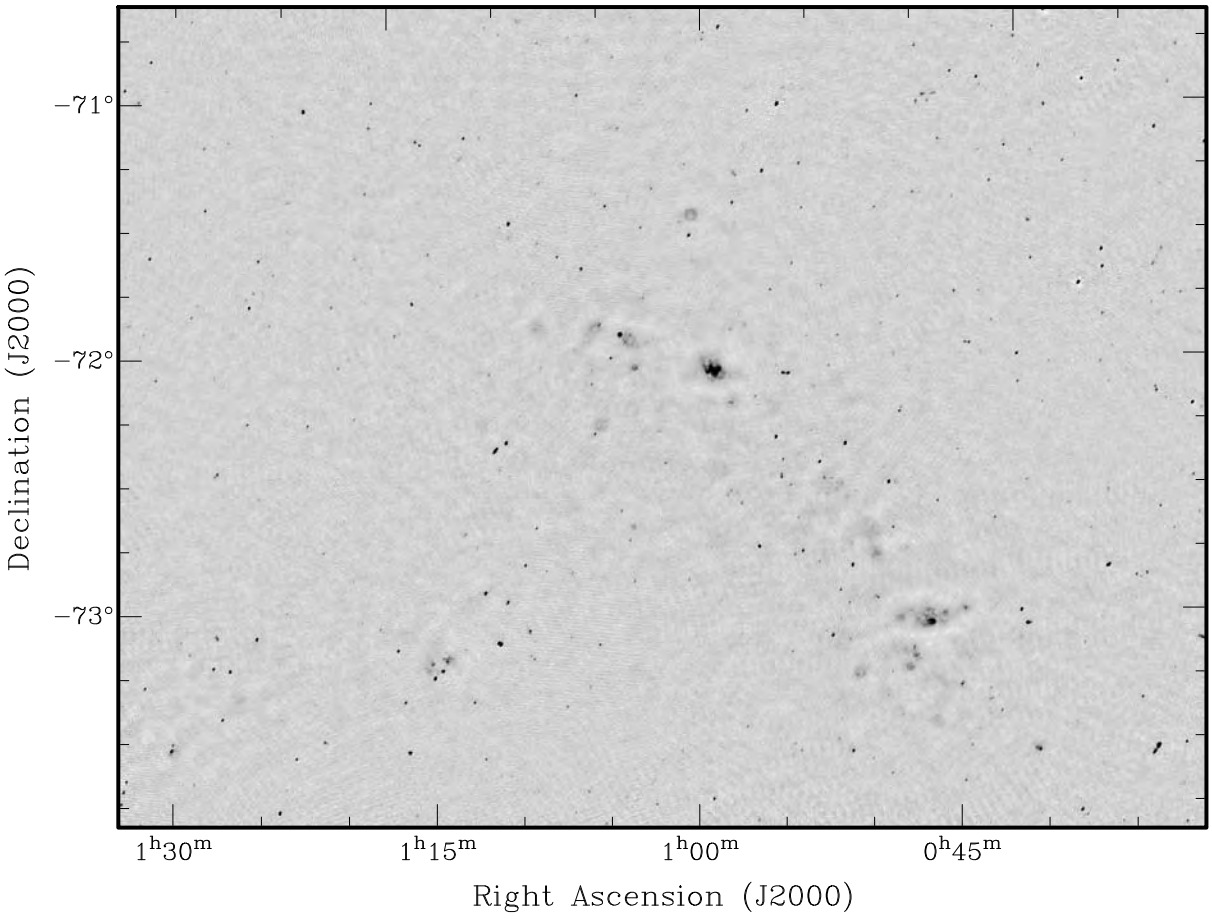

Fig. 7. *A radio-continuum total intensity images of the SMC at 6kλ. The synthesised beam is 30.1″×20.1″ and the r.m.s=0.5 mJy/beam.*

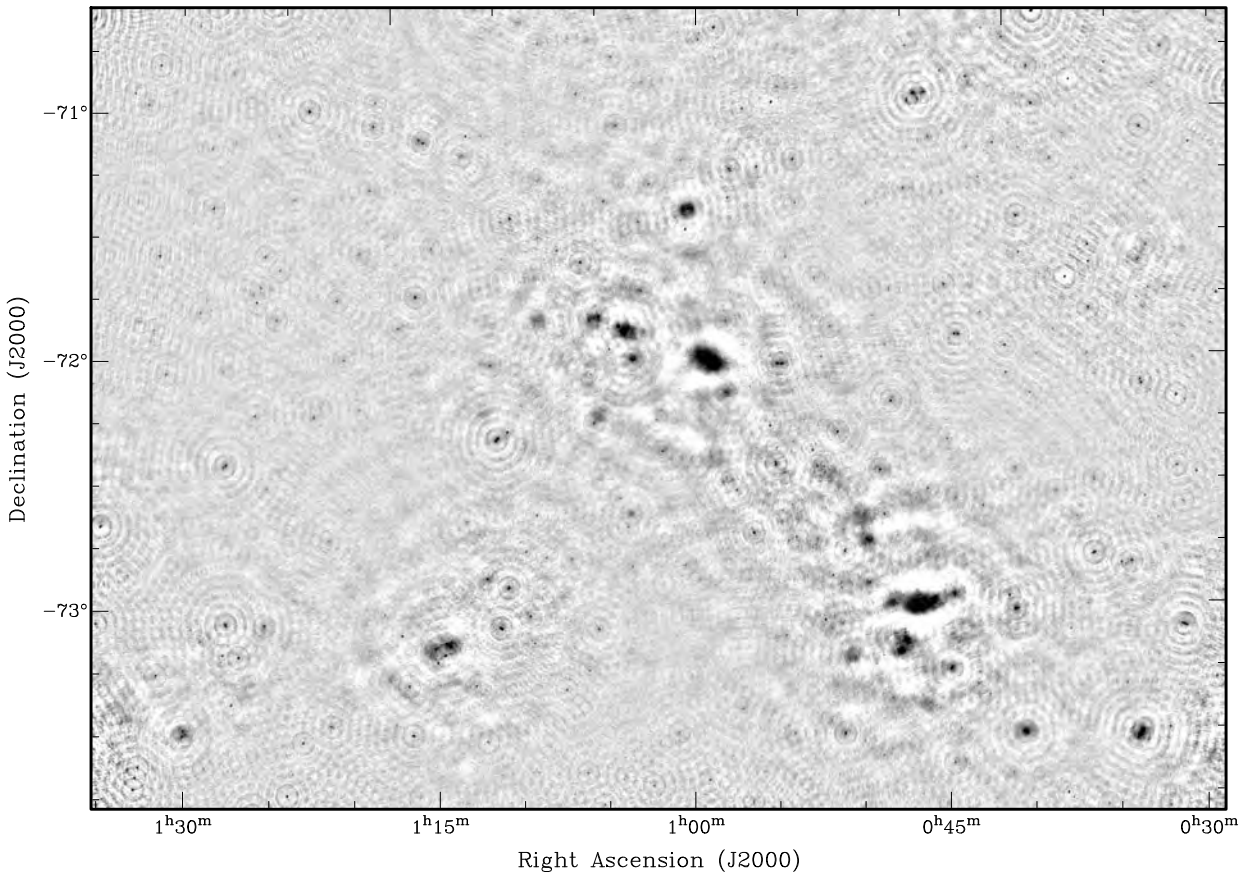

Fig. 8. *A radio-continuum total intensity images of the SMC at 16kλ. The synthesised beam is 16.3″×9.5″ and the r.m.s=0.5 mJy/beam.*

Acknowledgements – The Australia Telescope Compact Array and Parkes radio- telescope is part of the Australia Telescope National Facility which is funded by the Commonwealth of Australia for operation as a National Facility managed by CSIRO. This paper includes archived data obtained through the Australia Telescope Online Archive (http://atoa.atnf.csiro.au).

REFERENCES

Cornwell, T. J.: 1988, *Astron. Astrophys.*, **202**, 316.
Cornwell, T. J.: 1989, *Highlights of Astronomy*, **8**, 547.
Dickel, J. R., Gruendl, R. A., McIntyre, V. J., Shaun W.A.: 2010, *Astron. J.*, **140**, 1511.
Filipović, M. D., Jones, P. A., White, G. L, Haynes, R. F, Klein, U., Wielebinski, R.: 1997, *Astron. Astrophys. Suppl. Series*, **121**, 321.
Filipović, M. D., Haynes, R. F., White, G. L., Jones, P. A.: 1998, *Astron. Astrophys. Suppl. Series*, **130**, 421.
Filipović, M. D., Bohlsen, T., Reid, W., Staveley-Smith, L., Jones, P. A, Nohejl, K., Goldstein, G.: 2002, *Mon. Not. R. Astron. Soc.*, **335**, 1085.
Filipović, M. D., Payne, J. L., Reid, W., Danforth, C. W., Staveley-Smith, L., Jones, P. A., White, G. L.: 2005, *Mon. Not. R. Astron. Soc.*, **364**, 217.
Filipović, M. D., Haberl, F., Winkler, P. F., Pietsch, W., Payne, J. L., Crawford, E. J., de Horta, A. Y., Stootman, F. H., Reaser, B. E.: 2008, *Astron. Astrophys.*, **485**, 63.
Filipović, M. D., Cohen, M., Reid, W. A., Payne, J. L., Parker, Q. A., Crawford, E. J., Bojičić, I. S., de Horta, A. Y., Hughes, A., Dickel, J., Stootman, F.: 2009a, *Mon. Not. R. Astron. Soc.*, **399**, 769.
Filipović, M. D., Crawford E. J., Hughes A., Leverenz H., de Horta A. Y., Payne J. L., Staveley-Smith L., Dickel J. R., Stootman F. H., White G. L.: 2009b, in van Loon J. T., Oliveira J. M., eds, *IAU Symposium Vol. 256 of IAU Symposium*, PDF8.
Gooch, R.: 2008, KARMA Users Manual, ATNF, Sydney.
Hilditch, R. W, Howarth, I. D., Harries, T. J.: 2005, *Mon. Not. R. Astron. Soc.*, **357**, 304.
Mao, S. A., Gaensler, B. M., Stanimirović, S., Haverkorn, M., McClure-Griffiths, N. M., Staveley-Smith, L., Dickey, J. M.: 2008, *Astrophys. J.*, **688**, 1029.
Matthews, D., Staveley-Smith, L., Dyson, P., Muller,

E.: 2009, *Astrophys. J.*, **691**, L115.
Payne, J. L., Filipović, M. D., Reid, W., Jones, P. A., Staveley-Smith, L., White, G. L.: 2004, *Mon. Not. R. Astron. Soc.*, **355**, 44.
Sault, R. J., Killeen, N.: 2010, Miriad Users Guide, ATNF, Sydney.
Sault, R. J., Wieringa, M. H.: 1994, *Astron. Astrophys. Suppl. Series*, **108**, 585.
Stanimirović, S.: 2002, *Astron. Soc. of the Pacific Conf. Ser.*, **278**, 375.
Staveley-Smith, L., Sault, R. J., Hatzidimitriou, D., Kesteven, M. J., McConnell, D.: 1997, *Mon. Not. R. Astron. Soc.*, **289**, 280.
Steer, D. G., Dewdney, P. E., Ito, M. R.: 1984, *Astron. Astrophys.*, **137**, 159.

НОВО ПРОУЧАВАЊЕ МАЛОГ МАГЕЛАНОВОГ ОБЛАКА У РАДИО-КОНТИНУУМУ НА 20 цм: ДЕО I - СНИМЦИ

G. F. Wong, M. D. Filipović, E. J. Crawford, A. De Horta, T. Galvin, D. Drašković, J. L. Payne

School of Computing and Mathematics, University of Western Sydney
Locked Bag 1797, Penrith South DC, NSW 1797, Australia

E–mail: *m.filipovic@uws.edu.au*

УДК 52–13–77 : 524.722.7
Стручни чланак

У овој студији представљамо нове ATCA резултате посматрања високе резолуције и осетљивости у радио-континууму Малог Магелановог Облака (ММО) на λ=20 cm (ν=1.4 GHz). Нове радио-мапе настале су спајањем архивских мозаик посматрања на 20 cm са Аустралија Телескоп Онлајн Архива и података са Паркс радио-телескопа (отвор антене 64 m). Наши нови снимци су резолуције од $\sim$10″ до $\sim$150″ и осетљивости од r.m.s.$\geq$0.5 mJy/beam. Ови снимци ће бити коришћени у будућим истраживањима како објеката тако и укупне структуре ММО-а.

A.11 Related Paper 11

Wong, G. F., Filipović, M. D., Crawford, E. J., Tothill, N. F. H., De Horta, A. Y., Drašković, D., Galvin, T. J., Collier, J. D., and Payne, J. L. (2011b). New 20-cm Radio-Continuum Study of the Small Magellanic Cloud: Part II - Point Sources. *Serbian Astronomical Journal*, 183:103–106

My contribution was to provide some of the data, and assist in the analysis. This is a 20% contribution.

Serb. Astron. J. № 183 (2011), 103 - 106 **UDC 52–13–77 : 524.722.7**
DOI: 10.2298/SAJ1183103W Professional paper

NEW 20-cm RADIO-CONTINUUM STUDY OF THE SMALL MAGELLANIC CLOUD: PART II – POINT SOURCES

G. F. Wong, M. D. Filipović, E. J. Crawford, N. F. H. Tothill, A. Y. De Horta, D. Drašković, T. J. Galvin, J. D. Collier and J. L. Payne

University of Western Sydney, Locked Bag 1797, Penrith South DC, NSW 2751, Australia
E–mail: *m.filipovic@uws.edu.au*

(Received: October 17, 2011; Accepted: October 24, 2011)

SUMMARY: We present a new catalogue of radio-continuum sources in the field of the Small Magellanic Cloud (SMC). This catalogue contains sources previously not found in 2370 MHz (λ=13 cm) with sources found at 1400 MHz (λ=20 cm) and 843 MHz (λ=36 cm). 45 sources have been detected at 13 cm, with 1560 sources at 20 cm created from new high sensitivity and resolution radio-continuum images of the SMC at 20 cm from paper I. We also created a 36 cm catalogue to which we listed 1689 radio-continuum sources.

Key words. Magellanic Clouds – radio continuum: galaxies – catalogs

1. INTRODUCTION

The Small Magellanic Cloud (SMC), with its well established distance (∼60 kpc; Hilditch et al. 2005) and ideal location in the coldest areas of the radio sky towards the South Celestial Pole, allows observation of radio emissions to be made without interference from Galactic foreground radiation. This means that the SMC is an ideal location to study radio sources such as supernova remnants (SNRs; Filipović et al. 2005, 2008), H II regions and Planetary Nebulae (PNe; Filipović et al. 2009a) which may be difficult to study in our own and other more distant galaxies.

Over the last 40 years extensive radio-continuum surveys of the SMC have been made including interferometric observations using the Molonglo Obervatory Synthesis Telescope (MOST; Ye et al. 1995) and Australia Telescope Compact Array (ATCA; Filipović et al. 2002, Payne et al. 2004, Filipović et al. 2009b, Mao et al. 2008, Dickel et al. 2010), and single dish observations from the 64-m Parkes radio-telescope (Filipović et al. 1997, 1998).

Catalogues of radio-continuum point sources towards the SMC have been produced from these surveys, and from wider surveys of the southern sky. The first SMC source catalogue was produced by McGee et al. (1976) using the Parkes radio telescope at 5009 MHz (λ=6 cm); it contained 27 sources, 13 of them were also detected at 8800 MHz (λ=3.4 cm). The resolution of the observations was limited to $4'$ at 6 cm and $2.7'$ at 3.4 cm.

From the mid-1970s to the present, other surveys have been performed, increasing the number of sources detected (see Table 1). We recently published a set of new high-resolution radio-continuum mosaic images of the SMC at 1400 MHz ($\lambda = 20$ cm), created by combining observations from ATCA and Parkes (Wong et al. 2011, hereafter paper I).

We now present a catalogue of radio-continuum sources towards the SMC derived from an 2370 MHz ($\lambda = 13$ cm) mosaic image from Filipović et al. (2002), one of our 20 cm mosaic radio-conti-

Table 1. Summary of previous radio-continuum source catalogues of the SMC.

Telescope	Freq (MHz)	Beam Size (arcmin)	No of Sources Detected	Reference
Molonglo	408	2.62 × 2.86	75	1
Parkes	1400	15.0	21	2
Parkes	2700	7.7	25	3
Parkes	5009	4.0	27	2
Parkes	8800	2.5	13	2
Parkes	1400	15.0	28	4
MOST	843	0.75	450	5
Parkes	1420	13.8	85	6
Parkes	2450	9.0	107	6
Parkes	4750	4.5	99	6
Parkes	4850	4.9	187	6
Parkes	8550	2.7	41	6
ATCA	1420	1.63	534	7
ATCA	2370	0.67	697	7
ATCA	4800	0.5	75	7
ATCA	8640	0.25	54	7

1. Clarke et al. (1976), 2. McGee et al. (1976), 3. PKSCAT-90, 4. Haynes et al.(1986), 5. Turtle et al. (1998), 6. Filipović et al. (1997), 7. Filipović et al. (2002)

nuum images (Fig. 2 in paper I), and from an 843 MHz (λ = 36 cm) MOST image (Turtle et al. 1998). In Section 2 we describe the data used to derive the radio-continuum point sources. In Section 3 we describe our source fitting and detection methods. Section 4 contains our conclusions and the Appendix contains the radio-continuum source catalogue.

2. DATA

The 13 cm radio-continuum catalogue was produced from a SMC mosaic radio survey of 20 square degrees (Filipović et al. 2002). These observations have a beam size of $\sim 40''$ and r.m.s. noise of 0.4 mJy/beam.

The 20 cm mosaic image (Fig. 2 in paper I) was created by combining data from ATCA project C1288 (Mao et al. 2008) with data obtained for a Parkes radio-continuum study of the SMC (Filipović et al. 1997). This image has a beam size of $17\farcs8 \times 12\farcs2$ with r.m.s. noise of 0.7 mJy/beam.

The 36 cm image comes from a radio survey of 36 square degrees containing the SMC (Turtle et al. 1998). These observations have a beam size of $\sim 45''$ and r.m.s. noise of 0.7 mJy/beam — approximately equal to that of the 20 cm image.

Table 2 contains the field size of all the images used to derive the radio-continuum sources contained in this paper (Appendix).

Table 2. Field size of images used.

Image	RA_1	RA_2	DEC_1	DEC_2
13 cm	00°27′	01°35′	-70°30′	-75°15′
20 cm	00°10′	01°43′	-69°16′	-75°40′
36 cm	00°16′	01°40′	-72°30′	-74°38′

3. SOURCE FITTING AND DETECTION

The MIRIAD task IMSAD (Sault and Killeen 2010) was used to detect sources in the 20 cm and 36 cm images, requiring a fitted Gaussian flux density $>5\sigma$ (3.5 mJy). All sources were then visually examined to confirm that they are genuine point sources, excluding extended emission, bright side lobes, etc.

The radio-continuum sources catalogued in Table A1, are extra sources at 13 cm that were not previously identified as part of the 13 cm catalogue taken from Filipović et al (2002). The 13 cm catalogue retrieved from Filipović et al. (2002) was detected with a fitted Gaussian flux density of $>5\sigma$ (2.0 mJy). Sources catalogued in Table A1 were visually found with a σ between 3σ and 5σ.

Table 3. Information on the images and catalogue of radio-continuum sources.

λ (cm)	RMS (mJy/beam)	Number of Sources	Within of the Field of the 13 cm image	Beam Size (arcsec)
13 cm	0.4	743*	743*	45
20 cm	0.7	1560	824	14.8×12.2
36 cm	0.7	1689	1198	40

* Values include the original catalogue retrieved from Filipović et al. (2002)

The catalogue of radio-continuum sources contains positions RA(J2000), Dec(J2000) and integrated flux densities at 13 cm (Table A1), 20 cm (Table A2) and 36 cm (Table A3). Table 3 contains the r.m.s., number of sources detected, number of sources identified within the field of the 13 cm image and beam size for each image.

4. CONCLUSION

We present a new catalogue of radio-continuum sources towards the SMC, containing sources previously not identified at 13 cm and sources found at 20 cm and 36 cm.

The 13 cm catalogue contains 45 sources from a mosaic 13 cm radio survey (Table A1; Filipović et al. 2002). Containing 1560 sources (Table A2) the 20 cm catalogue has been created from new high-sensitivity and resolution radio-continuum images of the SMC at 20 cm from paper I. We also created a 36 cm catalogue to which we listed 1689 radio-continuum sources (Table A3) created from a MOST radio survey of the SMC (Turtle et al. 1998).

Acknowledgements – The Australia Telescope Compact Array and Parkes radio telescope are parts of the Australia Telescope National Facility which is funded by the Commonwealth of Australia for operation as a National Facility managed by CSIRO. This paper includes archived data obtained through the Australia Telescope Online Archive (http://atoa.atnf.csiro.au). We used the KARMA and MIRIAD software package developed by the ATNF.

REFERENCES

Clarke, J. N., Little A. G., Mills B. T.: 1979 *Aust. J. Phys. Astrophys. Suppl.*, **40**, 1.
Dickel, J. R., Gruendl, R. A., McIntyre, V. J., Shaun, W. A.: 2010, *Astron. J.*, **140**, 1511.
Filipović, M. D., Jones, P. A., White, G. L, Haynes, R. F., Klein, U., Wielebinski, R.: 1997, *Astron. Astrophys. Suppl. Series*, **121**, 321.
Filipović, M. D., Haynes, R. F., White, G. L., Jones, P. A.: 1998, *Astron. Astrophys. Suppl. Series*, **130**, 421.
Filipović, M. D., Bohlsen, T., Reid, W, Staveley-Smith, L., Jones, P. A., Nohejl, K., Goldstein, G.: 2002, *Mon. Not. R. Astron. Soc.*, **335**, 1085.
Filipović, M. D., Payne, J. L., Reid, W., Danforth, C. W., Staveley-Smith, L., Jones, P. A., White, G. L.: 2005, *Mon. Not. R. Astron. Soc.*, **364**, 217.
Filipović, M. D., Haberl, F., Winkler, P. F., Pietsch, W., Payne, J. L., Crawford, E. J., de Horta, A. Y., Stootman, F. H., Reaser, B. E.: 2008, *Astron. Astrophys.*, **485**, 63.
Filipović, M. D., Cohen, M., Reid, W. A., Payne, J. L., Parker, Q. A., Crawford, E. J., Bojičić, I. S., de Horta, A. Y., Hughes, A., Dickel, J., Stootman, F.: 2009a, *Mon. Not. R. Astron. Soc.*, **399**, 769.
Filipović, M. D., Crawford E. J., Hughes A., Leverenz H., de Horta A. Y., Payne J. L., Staveley-Smith L., Dickel J. R., Stootman F. H., White G. L.: 2009b, in van Loon J. T., Oliveira J. M., eds, *IAU Symposium*, **256**, PDF8.
Haynes, R. F., Murray, J. D., Klein, U., Wielebinski, R.: 1986, *Astron. Astrophys.*, **159**, 22.
Hilditch, R. W., Howarth, I. D., Harries, T. J.: 2005, *Mon. Not. R. Astron. Soc.*, **357**, 304.
Mao, S. A., Gaensler, B. M., Stanimirović, S., Haverkorn, M., McClure-Griffiths, N. M., Staveley-Smith, L., Dickey, J. M.: 2008, *Astrophys. J.*, **688**, 1029.
McGee, R. X., Newton, L. M., Butler, P. W.: 1976, *Aust. J. of Phys.*, **29**, 329.
Payne, J. L., Filipović, M. D., Reid, W., Jones, P. A., Staveley-Smith, L., White, G. L.: 2004, *Mon. Not. R. Astron. Soc.*, **355**, 44.
Sault, R., Killeen, N.: 2010, Miriad Users Guide, ATNF.
Turtle, A. J., Ye, T., Amy, S. W., Nicholls, J.: 1998, *Publ. Astron. Soc. Aust.*, **15**, 280.
Wong, G. F., Filipović, M. D., Crawford, E. J., de Horta, A. Y., Galvin, T., Drašković, D., Payne, J. L.: 2011, *Serb. Astron. J.*, **182**, 43.
Ye, T. S., Amy, S. W., Wang, Q. D., Ball, L., Dickel, J.: 1995, *Mon. Not. R. Astron. Soc.*, **275**, 1218.

APPENDIX

Tables A1, A2 and A3 in Appendix are available online at
http://saj.matf.bg.ac.rs/183/pdf/Appendix.pdf.

НОВО ПРОУЧАВАЊЕ МАЛОГ МАГЕЛАНОВОГ ОБЛАКА У РАДИО-КОНТИНУУМУ НА 20 cm: ДЕО II - СНИМЦИ

G. F. Wong, M. D. Filipović, E. J. Crawford, N. F. H. Tothill, A. Y. De Horta, D. Drašković, T. J. Galvin, J. D. Collier and J. L. Payne

University of Western Sydney, Locked Bag 1797, Penrith South DC, NSW 2751, Australia
E–mail: *m.filipovic@uws.edu.au*

УДК 52–13–77 : 524.722.7
Стручни чланак

У другом делу ове студије представљамо нове ATCA радио-континуум каталоге тачкастих објеката у пољу Малог Магелановог облака (ММО) на $\lambda = 20$ cm ($\nu = 1400$ MHz) и $\lambda = 36$ cm ($\nu = 843$ MHz). Такође, представљамо и нових 46 објеката као додатак $\lambda = 13$ cm ($\nu = 2300$ MHz) каталогу Filipović et al. (2002). Укупно у овом новом каталогу представљено је 1576 тачкастих објеката детектованих на 20 cm и 1692 на 36 cm. Ови каталози ће бити коришћени у будућим истраживањима природе ових објеката.

APPENDIX

Table A1. 13 cm Catalogue of point sources in the field of the SMC with integrated flux density.

Name ATCA	R.A.$_{2370}$ (J2000)	Dec.$_{2370}$ (J2000)	S_{13} (mJy)
J003414-722655	00:34:14.1	-72:26:55.5	2.51
J003446-733321	00:34:46.0	-73:33:21.0	2.77
J003609-740501	00:36:09.8	-74:05:01.2	2.79
J003850-732947	00:38:50.4	-73:29:47.4	2.57
J003903-735148	00:39:03.6	-73:51:48.8	2.48
J004021-735211	00:40:21.1	-73:52:11.3	2.22
J004351-704250	00:43:51.2	-70:42:50.4	3.21
J004445-733529	00:44:45.2	-73:35:29.6	2.66
J004506-733357	00:45:06.0	-73:33:57.9	2.52
J004604-713151	00:46:04.5	-71:31:51.3	2.48
J005022-712124	00:50:22.2	-71:21:24.2	2.73
J005127-742827	00:51:27.8	-74:28:27.8	1.96
J005620-720417	00:56:20.6	-72:04:17.1	2.78
J005812-713526	00:58:12.5	-71:35:26.0	2.39
J010326-750944	01:03:26.2	-75:09:44.2	2.77
J010356-751845	01:03:56.5	-75:18:45.5	2.60
J010402-750815	01:04:02.8	-75:08:15.6	3.28
J010422-744935	01:04:22.5	-74:49:35.6	2.81
J010740-742208	01:07:40.5	-74:22:08.8	2.13
J011044-750947	01:10:44.2	-75:09:47.4	2.48
J011336-735543	01:13:36.7	-73:55:43.6	2.23
J011439-724905	01:14:39.5	-72:49:05.5	2.45
J011440-723501	01:14:40.2	-72:35:01.6	2.49
J011525-730025	01:15:25.2	-73:00:25.4	2.40
J011553-742822	01:15:53.9	-74:28:22.6	2.80
J011700-724830	01:17:00.2	-72:48:30.2	2.14
J011718-751123	01:17:18.5	-75:11:23.3	2.51
J011748-734441	01:17:48.4	-73:44:41.1	2.24
J011814-750838	01:18:14.0	-75:08:38.3	2.63
J011805-725033	01:18:05.1	-72:50:33.8	2.71
J011805-735033	01:18:05.1	-73:50:33.8	2.71
J011911-724652	01:19:11.2	-72:46:52.4	2.53
J011915-751346	01:19:15.6	-75:13:46.7	2.46
J011921-751144	01:19:21.8	-75:11:44.9	2.41
J011937-750552	01:19:37.4	-75:05:52.3	3.11
J011909-751536	01:19:09.1	-75:15:36.8	2.25
J012014-750348	01:20:14.6	-75:03:48.6	2.56
J012016-750447	01:20:16.2	-75:04:47.5	2.42
J012210-745509	01:22:10.4	-74:55:09.1	2.46
J012515-732257	01:25:15.3	-73:22:57.0	2.71
J012524-732154	01:25:24.6	-73:21:54.0	2.82
J012657-713454	01:26:57.9	-71:34:54.1	2.85
J012701-743700	01:27:01.2	-74:37:00.1	1.80
J012712-705929	01:27:12.0	-70:59:29.1	2.25
J013035-745840	01:30:35.2	-74:58:40.0	3.02

Table A2. 20 cm Catalogue of point sources in the field of the SMC with integrated flux density.

Name ATCA	R.A.$_{1400}$ (J2000)	Dec.$_{1400}$ (J2000)	S_{20} (mJy)
J001013-732120	00:10:13.4	-73:21:20.6	26.97
J001014-753530	00:10:14.5	-75:35:30.8	35.13
J001055-724428	00:10:55.6	-72:44:28.8	12.14
J001008-732111	00:10:08.6	-73:21:11.8	19.75
J001116-745723	00:11:16.2	-74:57:23.1	14.11
J001157-734955	00:11:57.4	-73:49:55.4	107.45
J001106-731155	00:11:06.3	-73:11:55.8	15.00
J001224-752707	00:12:24.5	-75:27:07.8	8.25
J001243-741643	00:12:43.7	-74:16:43.5	49.10
J001246-731250	00:12:46.6	-73:12:50.7	7.65
J001250-734256	00:12:50.8	-73:42:56.7	10.00
J001258-732728	00:12:58.8	-73:27:28.3	8.17
J001320-722934	00:13:20.4	-72:29:34.5	22.99
J001320-741709	00:13:20.5	-74:17:09.5	12.37
J001326-724833	00:13:26.6	-72:48:33.6	98.33
J001356-733635	00:13:56.8	-73:36:35.6	13.95
J001307-722500	00:13:07.7	-72:25:00.8	37.36
J001400-741001	00:14:00.5	-74:10:01.3	11.16
J001424-733908	00:14:24.3	-73:39:08.7	296.22
J001437-734609	00:14:37.4	-73:46:09.6	18.59
J001459-750128	00:14:59.4	-75:01:28.5	10.27
J001510-732408	00:15:10.0	-73:24:08.6	6.68
J001510-724802	00:15:10.1	-72:48:02.5	4.37
J001514-733102	00:15:14.7	-73:31:02.1	7.67
J001521-753136	00:15:21.6	-75:31:36.2	44.01
J001526-744246	00:15:26.4	-74:42:46.7	8.25
J001503-724737	00:15:03.6	-72:47:37.4	25.47
J001545-724200	00:15:45.5	-72:42:00.7	5.89
J001556-744559	00:15:56.9	-74:45:59.9	5.60
J001612-751946	00:16:12.1	-75:19:46.7	8.36
J001612-731354	00:16:12.8	-73:13:54.0	6.37
J001618-723545	00:16:18.6	-72:35:45.1	6.58
J001602-741658	00:16:02.6	-74:16:58.5	5.96
J001622-752815	00:16:22.3	-75:28:15.1	7.78
J001625-723629	00:16:25.9	-72:36:29.7	17.87
J001626-742501	00:16:26.0	-74:25:01.3	10.11
J001638-743354	00:16:38.9	-74:33:54.2	4.38
J001648-730440	00:16:48.4	-73:04:40.5	7.06
J001659-733846	00:16:59.7	-73:38:46.7	4.92
J001718-724304	00:17:18.2	-72:43:04.5	4.24
J001719-723407	00:17:19.7	-72:34:07.8	4.79
J001720-730554	00:17:20.6	-73:05:54.4	109.12
J001707-751418	00:17:07.6	-75:14:18.1	75.51
J001816-741517	00:18:16.8	-74:15:17.5	25.04
J001817-732517	00:18:17.7	-73:25:17.8	8.51
J001818-732518	00:18:18.5	-73:25:18.6	8.94
J001819-730909	00:18:19.7	-73:09:09.1	7.40
J001841-725446	00:18:41.1	-72:54:46.2	4.01
J001841-752809	00:18:41.6	-75:28:09.4	9.66
J001851-734217	00:18:51.7	-73:42:17.8	15.58

Table A2. Continued.

Name ATCA	R.A.$_{1400}$ (J2000)	Dec.$_{1400}$ (J2000)	S_{20} (mJy)
J001852-723705	00:18:52.1	-72:37:05.5	4.30
J001857-734222	00:18:57.8	-73:42:22.8	28.57
J001858-732448	00:18:58.4	-73:24:48.8	25.98
J001807-723922	00:18:07.9	-72:39:22.7	11.97
J001915-742911	00:19:15.4	-74:29:11.1	4.90
J001920-751430	00:19:20.0	-75:14:30.6	4.04
J001903-734116	00:19:03.3	-73:41:16.4	6.43
J001932-723132	00:19:32.2	-72:31:32.5	12.96
J001933-733305	00:19:33.9	-73:33:05.9	5.43
J001936-744430	00:19:36.0	-74:44:30.9	5.39
J001938-723123	00:19:38.4	-72:31:23.0	19.98
J001939-744643	00:19:39.6	-74:46:43.0	5.42
J001907-751843	00:19:07.8	-75:18:43.5	13.56
J001909-744028	00:19:09.3	-74:40:28.8	14.33
J002017-732121	00:20:17.1	-73:21:21.1	12.33
J002019-731850	00:20:19.8	-73:18:50.0	8.07
J002031-724158	00:20:31.4	-72:41:58.3	7.34
J002034-743145	00:20:34.3	-74:31:45.3	4.73
J002043-744309	00:20:43.5	-74:43:09.7	44.92
J002043-732128	00:20:43.9	-73:21:28.0	8.37
J002049-735319	00:20:49.8	-73:53:19.4	5.77
J002051-732137	00:20:51.4	-73:21:37.8	14.41
J002054-734643	00:20:54.9	-73:46:43.3	4.13
J002007-751227	00:20:07.0	-75:12:27.7	27.34
J002007-732749	00:20:07.3	-73:27:49.4	6.50
J002120-725531	00:21:20.3	-72:55:31.3	7.72
J002127-732222	00:21:27.9	-73:22:22.1	8.54
J002132-750125	00:21:32.1	-75:01:25.0	31.98
J002142-742942	00:21:42.4	-74:29:42.6	4.35
J002143-741459	00:21:43.8	-74:14:59.5	116.50
J002145-723548	00:21:45.1	-72:35:48.6	4.90
J002152-743122	00:21:52.3	-74:31:22.5	42.94
J002159-742716	00:21:59.8	-74:27:16.3	104.10
J002215-730833	00:22:15.3	-73:08:33.4	8.37
J002215-742804	00:22:15.5	-74:28:04.8	55.50
J002202-734557	00:22:02.6	-73:45:57.9	6.31
J002223-742825	00:22:23.0	-74:28:25.1	145.10
J002226-715029	00:22:26.5	-71:50:29.3	8.20
J002226-713722	00:22:26.9	-71:37:22.4	11.65
J002227-734134	00:22:27.6	-73:41:34.5	4.73
J002230-743834	00:22:30.5	-74:38:34.0	4.24
J002237-724638	00:22:37.3	-72:46:38.2	6.68
J002238-742714	00:22:38.4	-74:27:14.6	14.55
J002246-710654	00:22:46.9	-71:06:54.3	28.92
J002248-734008	00:22:48.0	-73:40:08.1	48.26
J002253-741135	00:22:53.5	-74:11:35.5	7.11
J002254-741014	00:22:54.4	-74:10:14.2	2.76
J002255-740851	00:22:55.7	-74:08:51.5	3.04
J002256-723305	00:22:56.1	-72:33:05.5	58.39
J002207-740941	00:22:07.0	-74:09:41.2	22.55

Table A2. Continued.

Name ATCA	R.A.$_{1400}$ (J2000)	Dec.$_{1400}$ (J2000)	S_{20} (mJy)
J002209-751354	00:22:09.0	-75:13:54.9	8.75
J002300-722742	00:23:00.3	-72:27:42.7	4.48
J002300-722739	00:23:00.5	-72:27:39.5	4.48
J002314-695212	00:23:14.0	-69:52:12.6	16.66
J002315-744656	00:23:15.5	-74:46:56.0	3.74
J002320-722317	00:23:20.4	-72:23:17.5	3.89
J002325-735513	00:23:25.8	-73:55:13.7	5.63
J002327-722411	00:23:27.5	-72:24:11.5	10.90
J002332-732732	00:23:32.6	-73:27:32.9	3.20
J002335-700827	00:23:35.8	-70:08:27.2	6.03
J002336-735528	00:23:36.2	-73:55:28.1	201.90
J002339-731310	00:23:39.6	-73:13:10.9	4.28
J002350-731703	00:23:50.1	-73:17:03.2	23.12
J002359-723253	00:23:59.7	-72:32:53.4	4.52
J002309-752529	00:23:09.8	-75:25:29.5	6.84
J002400-725905	00:24:00.7	-72:59:05.3	15.69
J002410-714254	00:24:10.7	-71:42:54.4	6.73
J002411-735716	00:24:11.5	-73:57:16.8	149.60
J002417-751823	00:24:17.1	-75:18:23.6	7.17
J002422-714908	00:24:22.1	-71:49:08.6	9.33
J002428-700925	00:24:28.3	-70:09:25.9	82.75
J002430-721225	00:24:30.3	-72:12:25.2	14.69
J002433-700829	00:24:33.0	-70:08:29.2	6.80
J002404-694859	00:24:04.8	-69:48:59.6	15.81
J002440-734540	00:24:40.0	-73:45:40.6	33.03
J002442-741419	00:24:42.5	-74:14:19.2	4.27
J002443-745600	00:24:43.2	-74:56:00.6	18.40
J002446-734614	00:24:46.0	-73:46:14.4	3.90
J002447-715915	00:24:47.1	-71:59:15.1	33.54
J002448-705544	00:24:48.4	-70:55:44.2	100.02
J002409-725804	00:24:09.2	-72:58:04.9	29.53
J002518-735021	00:25:18.1	-73:50:21.9	4.70
J002522-735654	00:25:22.6	-73:56:54.0	6.28
J002529-752416	00:25:29.4	-75:24:16.3	8.38
J002535-723606	00:25:35.7	-72:36:06.0	2.98
J002504-720238	00:25:04.2	-72:02:38.5	5.46
J002541-693752	00:25:41.3	-69:37:52.6	5.79
J002543-740718	00:25:43.0	-74:07:18.4	4.67
J002547-732150	00:25:47.9	-73:21:50.2	5.84
J002553-745457	00:25:53.0	-74:54:57.4	4.99
J002554-732058	00:25:54.8	-73:20:58.2	5.77
J002558-721936	00:25:58.1	-72:19:36.3	4.33
J002507-720238	00:25:07.2	-72:02:38.1	4.41
J002611-732350	00:26:11.0	-73:23:50.9	9.81
J002611-751829	00:26:11.2	-75:18:29.9	5.18
J002613-752600	00:26:13.1	-75:26:00.3	5.72
J002613-744449	00:26:13.7	-74:44:49.2	7.05
J002620-743739	00:26:20.9	-74:37:39.8	11.29
J002622-742259	00:26:22.1	-74:22:59.6	7.11
J002627-693642	00:26:27.7	-69:36:42.7	25.34

Table A2. Continued.

Name ATCA	R.A.$_{1400}$ (J2000)	Dec.$_{1400}$ (J2000)	S_{20} (mJy)
J002628-740019	00:26:28.0	-74:00:19.6	13.84
J002629-723224	00:26:29.6	-72:32:24.0	3.10
J002631-741314	00:26:31.5	-74:13:14.5	21.60
J002631-751857	00:26:31.6	-75:18:57.4	10.00
J002634-751902	00:26:34.4	-75:19:02.7	11.20
J002638-725000	00:26:38.0	-72:50:00.6	16.99
J002604-732153	00:26:04.7	-73:21:53.7	18.25
J002645-744137	00:26:45.3	-74:41:37.2	27.30
J002645-710008	00:26:45.7	-71:00:08.1	25.50
J002646-732734	00:26:46.7	-73:27:34.7	12.68
J002647-704044	00:26:47.1	-70:40:44.8	118.40
J002605-712542	00:26:05.2	-71:25:42.5	4.02
J002605-724940	00:26:05.5	-72:49:40.0	7.54
J002657-741032	00:26:57.4	-74:10:32.5	29.30
J002658-720242	00:26:58.7	-72:02:42.4	8.88
J002606-725007	00:26:06.3	-72:50:07.2	4.74
J002606-732307	00:26:06.9	-73:23:07.7	34.27
J002607-742129	00:26:07.4	-74:21:29.8	8.08
J002702-734458	00:27:02.4	-73:44:58.5	10.50
J002702-692850	00:27:02.7	-69:28:50.5	9.09
J002724-703156	00:27:24.2	-70:31:56.1	20.20
J002724-733651	00:27:24.5	-73:36:51.5	12.35
J002729-711336	00:27:29.3	-71:13:36.2	4.48
J002737-733136	00:27:37.7	-73:31:36.7	15.37
J002744-700104	00:27:44.2	-70:01:04.8	4.24
J002749-753112	00:27:49.9	-75:31:12.6	6.13
J002705-741028	00:27:05.7	-74:10:28.3	7.32
J002750-753146	00:27:50.6	-75:31:46.1	6.73
J002753-695817	00:27:53.1	-69:58:17.6	11.38
J002707-694220	00:27:07.0	-69:42:20.6	6.16
J002814-731135	00:28:14.7	-73:11:35.3	16.19
J002816-741831	00:28:16.2	-74:18:31.6	15.07
J002818-694230	00:28:18.6	-69:42:30.4	68.36
J002820-723156	00:28:20.2	-72:31:56.9	6.74
J002821-733321	00:28:21.0	-73:33:21.5	6.84
J002821-735039	00:28:21.8	-73:50:39.6	6.41
J002823-703419	00:28:23.0	-70:34:19.1	21.43
J002823-724311	00:28:23.8	-72:43:11.8	21.92
J002825-700823	00:28:25.0	-70:08:23.8	10.67
J002826-703501	00:28:26.4	-70:35:01.0	44.49
J002803-694804	00:28:03.9	-69:48:04.1	8.58
J002833-705608	00:28:33.5	-70:56:08.4	8.64
J002835-693340	00:28:35.3	-69:33:40.8	45.90
J002841-704516	00:28:41.6	-70:45:16.0	98.36
J002843-734554	00:28:43.8	-73:45:54.9	4.10
J002853-704440	00:28:53.2	-70:44:40.2	6.98
J002857-732346	00:28:57.4	-73:23:46.1	5.02
J002900-694555	00:29:00.0	-69:45:55.8	14.47
J002910-740907	00:29:10.8	-74:09:07.0	6.54
J002918-722811	00:29:18.9	-72:28:11.3	105.00

Table A2. Continued.

Name ATCA	R.A.$_{1400}$ (J2000)	Dec.$_{1400}$ (J2000)	S_{20} (mJy)
J002919-754019	00:29:19.2	-75:40:19.1	255.29
J002902-751803	00:29:02.4	-75:18:03.2	11.51
J002923-744455	00:29:23.2	-74:44:55.9	6.24
J002926-732342	00:29:26.4	-73:23:42.0	11.16
J002926-693441	00:29:26.8	-69:34:41.8	291.10
J002929-703217	00:29:29.5	-70:32:17.6	14.44
J002929-745926	00:29:29.6	-74:59:26.2	3.71
J002929-731616	00:29:29.9	-73:16:16.5	4.15
J002903-695613	00:29:03.4	-69:56:13.9	5.55
J002903-712731	00:29:03.4	-71:27:31.2	8.42
J002938-712956	00:29:38.8	-71:29:56.7	7.97
J002944-712636	00:29:44.8	-71:26:36.2	4.11
J002945-730419	00:29:45.2	-73:04:19.3	15.94
J002950-720731	00:29:50.9	-72:07:31.6	20.72
J002955-753537	00:29:55.6	-75:35:37.5	7.54
J002956-714637	00:29:56.8	-71:46:37.8	20.56
J002957-735938	00:29:57.4	-73:59:38.1	7.20
J002907-735348	00:29:07.0	-73:53:48.7	83.23
J003001-735940	00:30:01.8	-73:59:40.8	7.90
J003014-700305	00:30:14.0	-70:03:05.9	30.80
J003021-735647	00:30:21.6	-73:56:47.9	4.50
J003022-700319	00:30:22.4	-70:03:19.7	53.90
J003025-731810	00:30:25.8	-73:18:10.6	34.42
J003026-702331	00:30:26.0	-70:23:31.7	4.52
J003030-742926	00:30:30.6	-74:29:26.7	36.91
J003030-731856	00:30:30.9	-73:18:56.8	5.00
J003031-750105	00:30:31.1	-75:01:05.5	4.57
J003037-735149	00:30:37.2	-73:51:49.2	12.80
J003037-742901	00:30:37.7	-74:29:01.7	48.82
J003038-725717	00:30:38.8	-72:57:17.9	8.51
J003047-715451	00:30:47.0	-71:54:51.5	3.79
J003048-694449	00:30:48.3	-69:44:49.7	81.55
J003005-700018	00:30:05.8	-70:00:18.1	11.57
J003052-713440	00:30:52.6	-71:34:40.5	7.33
J003053-743407	00:30:53.8	-74:34:07.1	3.72
J003007-740015	00:30:07.1	-74:00:15.2	30.88
J003101-705838	00:31:01.1	-70:58:38.0	16.22
J003115-714948	00:31:15.9	-71:49:48.4	4.22
J003120-703648	00:31:20.4	-70:36:48.5	131.20
J003120-732303	00:31:20.8	-73:23:03.2	10.04
J003125-701951	00:31:25.1	-70:19:51.1	4.84
J003129-704109	00:31:29.0	-70:41:09.4	4.21
J003103-715513	00:31:03.0	-71:55:13.2	5.77
J003131-743030	00:31:31.7	-74:30:30.7	22.37
J003136-703313	00:31:36.3	-70:33:13.0	53.28
J003140-743447	00:31:40.6	-74:34:47.2	54.25
J003142-711226	00:31:42.7	-71:12:26.2	3.51
J003150-741743	00:31:50.3	-74:17:43.2	3.50
J003158-703514	00:31:58.9	-70:35:14.8	50.37
J003106-710111	00:31:06.7	-71:01:11.5	54.71

Table A2. Continued.

Name ATCA	R.A.$_{1400}$ (J2000)	Dec.$_{1400}$ (J2000)	S_{20} (mJy)
J003107-710657	00:31:07.7	-71:06:57.9	25.83
J003108-724813	00:31:08.1	-72:48:13.5	5.73
J003211-703814	00:32:11.1	-70:38:14.4	4.10
J003215-713551	00:32:15.6	-71:35:51.2	8.67
J003215-693752	00:32:15.8	-69:37:52.0	4.48
J003217-703946	00:32:17.5	-70:39:46.2	12.67
J003224-730657	00:32:24.8	-73:06:57.5	23.40
J003230-710418	00:32:30.1	-71:04:18.8	6.34
J003230-692424	00:32:30.8	-69:24:24.7	154.57
J003231-730646	00:32:31.1	-73:06:46.4	22.50
J003231-703118	00:32:31.8	-70:31:18.8	7.06
J003234-734138	00:32:34.3	-73:41:38.7	5.13
J003234-734633	00:32:34.5	-73:46:33.1	4.02
J003237-704914	00:32:37.0	-70:49:14.6	16.87
J003239-730636	00:32:39.1	-73:06:36.1	10.50
J003204-701821	00:32:04.7	-70:18:21.5	7.95
J003241-711632	00:32:41.7	-71:16:32.6	3.04
J003242-733152	00:32:42.4	-73:31:52.7	44.92
J003249-741856	00:32:49.7	-74:18:56.9	39.59
J003252-722933	00:32:52.5	-72:29:33.6	67.14
J003254-701859	00:32:54.5	-70:18:59.8	6.10
J003255-714545	00:32:55.1	-71:45:45.6	52.40
J003208-735038	00:32:08.8	-73:50:38.2	24.69
J003301-715317	00:33:01.3	-71:53:17.1	5.54
J003310-745518	00:33:10.6	-74:55:18.4	17.46
J003311-740342	00:33:11.6	-74:03:42.5	14.46
J003311-703125	00:33:11.8	-70:31:25.7	32.21
J003312-704847	00:33:12.7	-70:48:47.1	3.71
J003313-705524	00:33:13.5	-70:55:24.9	22.50
J003315-705603	00:33:15.6	-70:56:03.9	39.90
J003315-741838	00:33:15.6	-74:18:38.6	5.36
J003318-703218	00:33:18.0	-70:32:18.3	9.74
J003320-691511	00:33:20.4	-69:15:11.6	11.38
J003326-722348	00:33:26.2	-72:23:48.4	4.95
J003326-723712	00:33:26.2	-72:37:12.1	11.85
J003303-694241	00:33:03.1	-69:42:41.3	6.97
J003333-693444	00:33:33.6	-69:34:44.3	22.20
J003341-743055	00:33:41.3	-74:30:55.9	10.31
J003342-704118	00:33:42.7	-70:41:18.6	9.28
J003343-695930	00:33:43.1	-69:59:30.1	6.71
J003343-692807	00:33:43.9	-69:28:07.4	3.85
J003346-720203	00:33:46.1	-72:02:03.1	4.76
J003348-731440	00:33:48.0	-73:14:40.4	6.31
J003348-743124	00:33:48.6	-74:31:24.2	3.87
J003349-733532	00:33:49.9	-73:35:32.4	8.03
J003305-742127	00:33:05.2	-74:21:27.8	9.66
J003352-703053	00:33:52.2	-70:30:53.3	43.13
J003353-701920	00:33:53.4	-70:19:20.1	4.96
J003355-721234	00:33:55.7	-72:12:34.5	7.16
J003356-722839	00:33:56.9	-72:28:39.8	15.30

Table A2. Continued.

Name ATCA	R.A.$_{1400}$ (J2000)	Dec.$_{1400}$ (J2000)	S_{20} (mJy)
J003357-742322	00:33:57.6	-74:23:22.9	21.90
J003358-703947	00:33:58.5	-70:39:47.8	6.12
J003307-753740	00:33:07.2	-75:37:40.9	6.72
J003401-702627	00:34:01.0	-70:26:27.0	65.00
J003413-733321	00:34:13.3	-73:33:21.2	111.50
J003402-711017	00:34:02.4	-71:10:17.6	4.41
J003420-751957	00:34:20.6	-75:19:57.2	4.56
J003424-721144	00:34:24.5	-72:11:44.4	149.50
J003425-733509	00:34:25.1	-73:35:09.0	24.71
J003425-691925	00:34:25.7	-69:19:25.6	8.92
J003426-715454	00:34:26.5	-71:54:54.2	6.29
J003403-714555	00:34:03.9	-71:45:55.8	8.81
J003431-713312	00:34:31.7	-71:33:12.9	3.30
J003433-692516	00:34:33.8	-69:25:16.2	8.42
J003436-722750	00:34:36.0	-72:27:50.9	4.74
J003440-724141	00:34:40.1	-72:41:41.2	7.74
J003449-733313	00:34:49.5	-73:33:13.1	5.57
J003405-702552	00:34:05.5	-70:25:52.3	25.80
J003453-705230	00:34:53.4	-70:52:30.6	6.59
J003454-733344	00:34:54.2	-73:33:44.0	5.47
J003455-713558	00:34:55.5	-71:35:58.3	3.04
J003409-702521	00:34:09.9	-70:25:21.2	62.00
J003511-710956	00:35:11.2	-71:09:56.0	52.40
J003512-752732	00:35:12.0	-75:27:32.9	3.65
J003517-700840	00:35:17.8	-70:08:40.1	10.91
J003524-732222	00:35:24.3	-73:22:22.3	24.91
J003530-723655	00:35:30.7	-72:36:55.4	20.06
J003531-694119	00:35:31.9	-69:41:19.3	13.67
J003536-714603	00:35:36.9	-71:46:03.8	14.09
J003504-730653	00:35:04.1	-73:06:53.4	4.39
J003544-735208	00:35:44.7	-73:52:08.8	11.86
J003547-721117	00:35:47.5	-72:11:17.5	6.80
J003550-693510	00:35:50.4	-69:35:10.9	3.85
J003552-693129	00:35:52.2	-69:31:29.9	29.86
J003552-725301	00:35:52.3	-72:53:01.8	18.96
J003553-693935	00:35:53.2	-69:39:35.4	3.82
J003509-692253	00:35:09.9	-69:22:53.3	5.09
J003610-725401	00:36:10.2	-72:54:01.8	6.13
J003619-720950	00:36:19.9	-72:09:50.3	24.89
J003624-720852	00:36:24.5	-72:08:52.0	12.83
J003624-725342	00:36:24.6	-72:53:42.6	19.44
J003628-714633	00:36:28.2	-71:46:33.8	10.49
J003635-752546	00:36:35.6	-75:25:46.9	5.14
J003636-715132	00:36:36.2	-71:51:32.5	5.30
J003643-754509	00:36:43.1	-75:45:09.5	57.01
J003647-713601	00:36:47.5	-71:36:01.4	7.90
J003650-703934	00:36:50.6	-70:39:34.0	7.34
J003655-744428	00:36:55.6	-74:44:28.9	4.39
J003659-713810	00:36:59.1	-71:38:10.7	7.95
J003608-742924	00:36:08.6	-74:29:24.8	6.43

Table A2. Continued.

Name ATCA	R.A.$_{1400}$ (J2000)	Dec.$_{1400}$ (J2000)	S_{20} (mJy)
J003608-754436	00:36:08.8	-75:44:36.7	8.82
J003609-740454	00:36:09.6	-74:04:54.5	3.93
J003701-714906	00:37:01.6	-71:49:06.3	7.97
J003712-751417	00:37:12.1	-75:14:17.8	10.80
J003713-705616	00:37:13.0	-70:56:16.0	4.11
J003716-692204	00:37:16.1	-69:22:04.0	7.96
J003716-751412	00:37:16.1	-75:14:12.2	15.80
J003716-705645	00:37:16.8	-70:56:45.5	9.95
J003725-693003	00:37:25.8	-69:30:03.0	3.96
J003726-695246	00:37:26.4	-69:52:46.2	6.98
J003726-741825	00:37:26.5	-74:18:25.3	4.57
J003703-704726	00:37:03.6	-70:47:26.3	11.61
J003738-714102	00:37:38.5	-71:41:02.4	4.76
J003743-710736	00:37:43.5	-71:07:36.6	43.29
J003749-735128	00:37:49.8	-73:51:28.2	12.73
J003705-752759	00:37:05.1	-75:27:59.0	3.89
J003753-694753	00:37:53.4	-69:47:53.9	5.40
J003755-704312	00:37:55.0	-70:43:12.8	4.60
J003755-725157	00:37:55.2	-72:51:57.7	103.70
J003756-694803	00:37:56.8	-69:48:03.4	10.60
J003758-745045	00:37:58.9	-74:50:45.9	4.58
J003708-694716	00:37:08.3	-69:47:16.1	6.31
J003709-712054	00:37:09.3	-71:20:54.7	6.38
J003709-714005	00:37:09.7	-71:40:05.8	11.48
J003800-725211	00:38:00.8	-72:52:11.5	46.70
J003801-730434	00:38:01.9	-73:04:34.1	6.98
J003814-701443	00:38:14.7	-70:14:43.3	3.99
J003817-713145	00:38:17.9	-71:31:45.9	4.05
J003818-692415	00:38:18.3	-69:24:15.4	4.25
J003819-723420	00:38:19.0	-72:34:20.9	4.96
J003820-723400	00:38:20.8	-72:34:00.9	5.42
J003824-742211	00:38:24.4	-74:22:11.9	255.70
J003836-695325	00:38:36.3	-69:53:25.2	16.24
J003850-720848	00:38:50.1	-72:08:48.3	5.96
J003850-720015	00:38:50.3	-72:00:15.5	4.43
J003850-731052	00:38:50.8	-73:10:52.8	13.23
J003851-732951	00:38:51.7	-73:29:51.8	4.87
J003853-702053	00:38:53.7	-70:20:53.8	3.88
J003854-704931	00:38:54.8	-70:49:31.9	3.15
J003857-724850	00:38:57.8	-72:48:50.8	3.92
J003808-745023	00:38:08.7	-74:50:23.2	8.77
J003809-735023	00:38:09.2	-73:50:23.9	132.10
J003809-710721	00:38:09.6	-71:07:21.9	4.80
J003901-725726	00:39:01.0	-72:57:26.4	4.19
J003917-694842	00:39:17.4	-69:48:42.7	72.98
J003917-720345	00:39:17.5	-72:03:45.2	3.89
J003902-752620	00:39:02.2	-75:26:20.0	6.20
J003920-720405	00:39:20.7	-72:04:05.7	9.36
J003924-695552	00:39:24.8	-69:55:52.2	4.23
J003926-713637	00:39:26.6	-71:36:37.1	3.60

Table A2. Continued.

Name ATCA	R.A.$_{1400}$ (J2000)	Dec.$_{1400}$ (J2000)	S_{20} (mJy)
J003926-715242	00:39:26.6	-71:52:42.7	13.37
J003936-742017	00:39:36.4	-74:20:17.3	20.50
J003939-714142	00:39:39.8	-71:41:42.4	84.50
J003904-724337	00:39:04.7	-72:43:37.3	6.69
J003942-735622	00:39:42.4	-73:56:22.3	7.34
J003943-694718	00:39:43.5	-69:47:18.0	4.39
J003944-705248	00:39:44.1	-70:52:48.8	30.33
J003945-695848	00:39:45.3	-69:58:48.5	18.58
J003947-713734	00:39:47.4	-71:37:34.8	83.84
J003950-705505	00:39:50.6	-70:55:05.2	12.30
J003906-734627	00:39:06.6	-73:46:27.5	5.30
J004001-714504	00:40:01.5	-71:45:04.9	5.89
J004022-714511	00:40:22.5	-71:45:11.8	3.98
J004028-714405	00:40:28.7	-71:44:05.7	3.34
J004028-703515	00:40:28.8	-70:35:15.8	24.64
J004033-695126	00:40:33.5	-69:51:26.0	6.18
J004033-751457	00:40:33.7	-75:14:57.3	7.01
J004037-714337	00:40:37.5	-71:43:37.8	3.43
J004040-750358	00:40:40.2	-75:03:58.1	5.59
J004045-702356	00:40:45.8	-70:23:56.5	15.28
J004047-714559	00:40:47.9	-71:45:59.7	409.70
J004048-733701	00:40:48.0	-73:37:01.4	35.58
J004052-712154	00:40:52.3	-71:21:54.4	5.88
J004009-705811	00:40:09.2	-70:58:11.5	4.11
J004112-715859	00:41:12.2	-71:58:59.8	7.65
J004102-714640	00:41:02.7	-71:46:40.4	4.93
J004124-734706	00:41:24.7	-73:47:06.2	4.39
J004125-740706	00:41:25.0	-74:07:06.8	4.15
J004125-705744	00:41:25.4	-70:57:44.0	87.31
J004126-700400	00:41:26.4	-70:04:00.3	4.31
J004133-711103	00:41:33.5	-71:11:03.6	6.12
J004135-730859	00:41:35.8	-73:08:59.3	4.55
J004143-721829	00:41:43.7	-72:18:29.0	3.14
J004152-743339	00:41:52.1	-74:33:39.2	3.89
J004159-720509	00:41:59.2	-72:05:09.3	7.18
J004200-700441	00:42:00.8	-70:04:41.3	7.39
J004201-730727	00:42:01.4	-73:07:27.1	37.60
J004210-721445	00:42:10.0	-72:14:45.4	9.71
J004211-722509	00:42:11.8	-72:25:09.2	5.10
J004213-740835	00:42:13.6	-74:08:35.0	4.18
J004213-695220	00:42:13.8	-69:52:20.9	19.37
J004215-730916	00:42:15.2	-73:09:16.9	3.79
J004215-714708	00:42:15.5	-71:47:08.9	5.11
J004218-731059	00:42:18.4	-73:10:59.1	4.06
J004224-703113	00:42:24.3	-70:31:13.0	8.87
J004224-700244	00:42:24.8	-70:02:44.3	59.90
J004226-730418	00:42:26.2	-73:04:18.0	77.55
J004227-751355	00:42:27.4	-75:13:55.5	18.55
J004228-700257	00:42:28.2	-70:02:57.2	41.60
J004229-693917	00:42:29.8	-69:39:17.6	19.83

Table A2. Continued.

Name ATCA	R.A.$_{1400}$ (J2000)	Dec.$_{1400}$ (J2000)	S_{20} (mJy)
J004229-742847	00:42:29.9	-74:28:47.6	7.43
J004230-745450	00:42:30.6	-74:54:50.7	6.34
J004237-700622	00:42:37.0	-70:06:22.2	5.48
J004239-700133	00:42:39.2	-70:01:33.8	42.10
J004204-711724	00:42:04.8	-71:17:24.0	16.25
J004240-723325	00:42:40.0	-72:33:25.1	10.44
J004241-703328	00:42:41.6	-70:33:28.1	6.63
J004205-730717	00:42:05.0	-73:07:17.4	39.00
J004301-742521	00:43:01.3	-74:25:21.0	3.80
J004311-710425	00:43:11.7	-71:04:25.6	21.44
J004315-700536	00:43:15.8	-70:05:36.4	4.28
J004318-714058	00:43:18.3	-71:40:58.5	23.62
J004319-735515	00:43:19.3	-73:55:15.9	4.39
J004327-704138	00:43:27.9	-70:41:38.8	318.20
J004331-721024	00:43:31.1	-72:10:24.5	18.50
J004334-705513	00:43:34.6	-70:55:13.6	17.85
J004335-713159	00:43:35.2	-71:31:59.3	17.96
J004336-730225	00:43:36.7	-73:02:25.0	5.24
J004339-720346	00:43:39.4	-72:03:46.8	26.70
J004304-752337	00:43:04.8	-75:23:37.4	7.24
J004340-703819	00:43:40.3	-70:38:19.6	3.92
J004340-732550	00:43:40.7	-73:25:50.1	8.80
J004341-711527	00:43:41.5	-71:15:27.1	6.54
J004341-712230	00:43:41.9	-71:22:30.9	4.46
J004342-732923	00:43:42.4	-73:29:23.8	5.39
J004347-732319	00:43:47.1	-73:23:19.3	5.34
J004348-732603	00:43:48.6	-73:26:03.9	10.74
J004306-732827	00:43:06.6	-73:28:27.9	19.67
J004401-695206	00:44:01.6	-69:52:06.3	4.10
J004413-724301	00:44:13.7	-72:43:01.3	18.80
J004414-733311	00:44:14.6	-73:33:11.9	4.65
J004416-702746	00:44:16.9	-70:27:46.7	5.43
J004417-750215	00:44:17.6	-75:02:15.6	9.94
J004419-703259	00:44:19.8	-70:32:59.1	4.82
J004421-744316	00:44:21.1	-74:43:16.0	24.06
J004424-693723	00:44:24.8	-69:37:23.6	5.90
J004431-692707	00:44:31.9	-69:27:07.0	4.51
J004438-733710	00:44:38.7	-73:37:10.9	12.52
J004443-700906	00:44:43.5	-70:09:06.8	21.37
J004446-742514	00:44:46.6	-74:25:14.4	4.41
J004452-691641	00:44:52.0	-69:16:41.0	48.12
J004452-734537	00:44:52.2	-73:45:37.8	18.13
J004452-731851	00:44:52.4	-73:18:51.6	3.80
J004453-704843	00:44:53.4	-70:48:43.4	18.72
J004459-711438	00:44:59.7	-71:14:38.8	25.98
J004459-711330	00:44:59.9	-71:13:30.6	4.19
J004514-704306	00:45:14.2	-70:43:06.7	4.30
J004519-695519	00:45:19.9	-69:55:19.7	15.40
J004502-731638	00:45:02.9	-73:16:38.7	6.38
J004520-704442	00:45:20.4	-70:44:42.7	3.68

Table A2. Continued.

Name ATCA	R.A.$_{1400}$ (J2000)	Dec.$_{1400}$ (J2000)	S_{20} (mJy)
J004522-695509	00:45:22.9	-69:55:09.6	6.60
J004525-732259	00:45:25.7	-73:22:59.1	16.07
J004527-693250	00:45:27.3	-69:32:50.5	5.06
J004529-750135	00:45:29.2	-75:01:35.4	6.33
J004530-745056	00:45:30.1	-74:50:56.2	9.88
J004533-720402	00:45:33.0	-72:04:02.2	5.85
J004537-712316	00:45:37.2	-71:23:16.8	22.35
J004504-715613	00:45:04.5	-71:56:13.6	11.33
J004545-724142	00:45:45.5	-72:41:42.5	6.31
J004546-752906	00:45:46.3	-75:29:06.4	7.29
J004548-714932	00:45:48.7	-71:49:32.2	7.64
J004555-704646	00:45:55.5	-70:46:46.6	16.33
J004557-731331	00:45:57.6	-73:13:31.6	4.59
J004611-741759	00:46:11.1	-74:17:59.9	4.92
J004616-711611	00:46:16.8	-71:16:11.7	5.51
J004602-744004	00:46:02.0	-74:40:04.1	38.22
J004621-720154	00:46:21.5	-72:01:54.0	19.25
J004623-710041	00:46:23.4	-71:00:41.6	7.01
J004623-722724	00:46:23.4	-72:27:24.6	10.88
J004628-731508	00:46:28.7	-73:15:08.4	4.38
J004629-731449	00:46:29.5	-73:14:49.0	3.98
J004603-741328	00:46:03.0	-74:13:28.8	10.81
J004630-722250	00:46:30.9	-72:22:50.5	3.43
J004631-720419	00:46:31.0	-72:04:19.0	3.49
J004632-705856	00:46:32.4	-70:58:56.8	47.17
J004632-742507	00:46:32.4	-74:25:07.0	7.36
J004636-735332	00:46:36.1	-73:53:32.9	5.10
J004639-695712	00:46:39.1	-69:57:12.3	69.70
J004639-693128	00:46:39.6	-69:31:28.8	41.02
J004644-695710	00:46:44.2	-69:57:10.3	52.80
J004646-743405	00:46:46.1	-74:34:05.5	8.84
J004647-695715	00:46:47.7	-69:57:15.3	33.40
J004608-720156	00:46:08.3	-72:01:56.7	24.43
J004700-700347	00:47:00.6	-70:03:47.0	7.11
J004701-701438	00:47:01.7	-70:14:38.0	9.96
J004711-745929	00:47:11.7	-74:59:29.7	9.80
J004719-723947	00:47:19.0	-72:39:47.5	20.74
J004702-710143	00:47:02.0	-71:01:43.1	4.55
J004725-712728	00:47:25.5	-71:27:28.1	11.69
J004703-714957	00:47:03.9	-71:49:57.5	23.07
J004731-711101	00:47:31.2	-71:11:01.2	4.06
J004732-750057	00:47:32.0	-75:00:57.6	9.19
J004736-694327	00:47:36.9	-69:43:27.3	17.50
J004740-753011	00:47:40.9	-75:30:11.1	339.60
J004705-750233	00:47:05.1	-75:02:33.0	6.60
J004750-705756	00:47:50.5	-70:57:56.7	32.88
J004752-703946	00:47:52.3	-70:39:46.1	3.09
J004709-743011	00:47:09.4	-74:30:11.6	3.24
J004801-701820	00:48:01.2	-70:18:20.7	3.84
J004810-711422	00:48:10.8	-71:14:22.9	4.33

Table A2. Continued.

Name ATCA	R.A.$_{1400}$ (J2000)	Dec.$_{1400}$ (J2000)	S_{20} (mJy)
J004815-703645	00:48:15.2	-70:36:45.7	4.08
J004816-711401	00:48:16.7	-71:14:01.6	17.72
J004825-720034	00:48:25.6	-72:00:34.0	3.76
J004803-704911	00:48:03.6	-70:49:11.4	3.87
J004803-741234	00:48:03.9	-74:12:34.5	3.05
J004830-710315	00:48:30.9	-71:03:15.6	7.19
J004832-743310	00:48:32.4	-74:33:10.1	4.80
J004835-734433	00:48:35.6	-73:44:33.5	5.38
J004836-733055	00:48:36.6	-73:30:55.5	8.80
J004837-701223	00:48:37.5	-70:12:23.4	4.36
J004839-753148	00:48:39.8	-75:31:48.2	4.83
J004844-740729	00:48:44.1	-74:07:29.1	13.91
J004805-752345	00:48:05.7	-75:23:45.0	8.71
J004850-725123	00:48:50.0	-72:51:23.4	6.38
J004851-710513	00:48:51.2	-71:05:13.0	9.85
J004856-704116	00:48:56.0	-70:41:16.7	3.65
J004858-752944	00:48:58.2	-75:29:44.0	26.18
J004858-700906	00:48:58.3	-70:09:06.0	6.61
J004806-741959	00:48:06.7	-74:19:59.5	5.19
J004808-731454	00:48:08.4	-73:14:54.2	17.24
J004808-741205	00:48:08.4	-74:12:05.7	109.10
J004808-743303	00:48:08.9	-74:33:03.6	3.71
J004901-734455	00:49:01.6	-73:44:55.3	11.64
J004912-702030	00:49:12.4	-70:20:30.1	3.83
J004912-700815	00:49:12.9	-70:08:15.0	12.20
J004917-732044	00:49:17.3	-73:20:44.4	14.01
J004918-700754	00:49:18.2	-70:07:54.0	22.80
J004918-722000	00:49:18.6	-72:20:00.0	5.33
J004918-745659	00:49:18.9	-74:56:59.0	62.21
J004923-712659	00:49:23.8	-71:26:59.8	15.39
J004924-710518	00:49:24.9	-71:05:18.8	15.04
J004925-710552	00:49:25.0	-71:05:52.1	12.47
J004927-695019	00:49:27.1	-69:50:19.1	11.18
J004929-732633	00:49:29.0	-73:26:33.5	6.45
J004929-721809	00:49:29.4	-72:18:09.7	9.38
J004933-721901	00:49:33.3	-72:19:01.6	25.38
J004935-741543	00:49:35.6	-74:15:43.8	18.07
J004935-724635	00:49:35.9	-72:46:35.7	17.51
J004937-723552	00:49:37.0	-72:35:52.4	3.77
J004937-705212	00:49:37.2	-70:52:12.3	21.58
J004937-700132	00:49:37.7	-70:01:32.8	73.42
J004938-741606	00:49:38.5	-74:16:06.1	11.66
J004942-724844	00:49:42.1	-72:48:44.5	4.90
J004942-741908	00:49:42.4	-74:19:08.7	4.27
J004945-692624	00:49:45.0	-69:26:24.5	7.33
J004948-722212	00:49:48.9	-72:22:12.8	3.04
J004954-715151	00:49:54.0	-71:51:51.4	19.79
J004956-723554	00:49:56.9	-72:35:54.3	98.90
J004958-693326	00:49:58.0	-69:33:26.5	7.90
J004908-710346	00:49:08.0	-71:03:46.4	13.99

Table A2. Continued.

Name ATCA	R.A.$_{1400}$ (J2000)	Dec.$_{1400}$ (J2000)	S_{20} (mJy)
J004908-744621	00:49:08.8	-74:46:21.3	12.41
J005013-732128	00:50:13.9	-73:21:28.6	3.79
J005015-730325	00:50:15.0	-73:03:25.2	20.14
J005021-744151	00:50:21.6	-74:41:51.0	6.17
J005022-712128	00:50:22.4	-71:21:28.3	4.48
J005022-730306	00:50:22.5	-73:03:06.8	9.63
J005027-695832	00:50:27.6	-69:58:32.3	7.17
J005034-704036	00:50:34.8	-70:40:36.2	3.72
J005034-691534	00:50:34.9	-69:15:34.9	13.33
J005038-691543	00:50:38.3	-69:15:43.4	4.46
J005041-703937	00:50:41.6	-70:39:37.6	28.73
J005042-715828	00:50:42.1	-71:58:28.4	6.92
J005042-700912	00:50:42.3	-70:09:12.7	5.32
J005005-694726	00:50:05.8	-69:47:26.7	8.72
J005053-731707	00:50:53.4	-73:17:07.6	3.94
J005056-700921	00:50:56.6	-70:09:21.9	35.58
J005057-731247	00:50:57.3	-73:12:47.8	3.86
J005007-734134	00:50:07.8	-73:41:34.3	7.38
J005101-753248	00:51:01.5	-75:32:48.5	5.67
J005115-713058	00:51:15.8	-71:30:58.0	17.08
J005117-733959	00:51:17.1	-73:39:59.8	48.62
J005117-705608	00:51:17.6	-70:56:08.8	4.41
J005125-753836	00:51:25.7	-75:38:36.5	11.20
J005126-704019	00:51:26.1	-70:40:19.1	4.09
J005126-722439	00:51:26.6	-72:24:39.2	3.30
J005128-742822	00:51:28.3	-74:28:22.0	6.11
J005135-734420	00:51:35.0	-73:44:20.5	3.76
J005135-694632	00:51:35.7	-69:46:32.4	7.34
J005140-731334	00:51:40.5	-73:13:34.4	9.22
J005141-725555	00:51:41.4	-72:55:55.8	33.41
J005147-730452	00:51:47.6	-73:04:52.7	11.03
J005148-725046	00:51:48.0	-72:50:46.7	7.21
J005153-734522	00:51:53.2	-73:45:22.6	3.66
J005153-743532	00:51:53.9	-74:35:32.4	3.94
J005201-733235	00:52:01.3	-73:32:35.0	5.75
J005212-730850	00:52:12.6	-73:08:50.2	7.46
J005213-731441	00:52:13.4	-73:14:41.8	4.15
J005217-730156	00:52:17.6	-73:01:56.5	24.56
J005218-722707	00:52:18.8	-72:27:07.8	179.60
J005222-752543	00:52:22.6	-75:25:43.8	85.58
J005228-735943	00:52:28.9	-73:59:43.6	5.50
J005230-743748	00:52:30.2	-74:37:48.2	6.65
J005231-693001	00:52:31.9	-69:30:01.1	7.01
J005234-702816	00:52:34.6	-70:28:16.8	32.31
J005238-731244	00:52:38.3	-73:12:44.7	98.30
J005241-702635	00:52:41.4	-70:26:35.3	5.58
J005254-720132	00:52:54.2	-72:01:32.8	13.27
J005255-714550	00:52:55.1	-71:45:50.8	4.24
J005256-711420	00:52:56.3	-71:14:20.3	3.83
J005258-723534	00:52:58.6	-72:35:34.7	12.27

Table A2. Continued.

Name ATCA	R.A.$_{1400}$ (J2000)	Dec.$_{1400}$ (J2000)	S_{20} (mJy)
J005259-731147	00:52:59.0	-73:11:47.2	8.96
J005206-733722	00:52:06.7	-73:37:22.1	6.08
J005317-710656	00:53:17.4	-71:06:56.3	3.86
J005318-720857	00:53:18.3	-72:08:57.0	14.71
J005322-723528	00:53:22.5	-72:35:28.3	10.46
J005325-745556	00:53:25.1	-74:55:56.7	5.10
J005328-723009	00:53:28.7	-72:30:09.4	7.33
J005328-725522	00:53:28.8	-72:55:22.8	10.64
J005333-695709	00:53:33.9	-69:57:09.9	4.60
J005335-691718	00:53:35.8	-69:17:18.4	14.82
J005337-723144	00:53:37.8	-72:31:44.1	72.14
J005347-751441	00:53:47.2	-75:14:41.1	8.10
J005347-714959	00:53:47.9	-71:49:59.7	8.90
J005348-704601	00:53:48.2	-70:46:01.4	5.71
J005305-692243	00:53:05.1	-69:22:43.8	23.90
J005350-693147	00:53:50.8	-69:31:47.8	16.86
J005350-693129	00:53:50.9	-69:31:29.0	15.15
J005351-704000	00:53:51.8	-70:40:00.3	23.16
J005356-703804	00:53:56.2	-70:38:04.7	43.44
J005306-702920	00:53:06.8	-70:29:20.3	10.47
J005308-743904	00:53:08.0	-74:39:04.9	13.77
J005309-701633	00:53:09.7	-70:16:33.9	4.18
J005411-734018	00:54:11.7	-73:40:18.4	10.43
J005402-710939	00:54:02.8	-71:09:39.8	3.89
J005422-702353	00:54:22.7	-70:23:53.7	67.41
J005423-701801	00:54:23.5	-70:18:01.1	3.73
J005423-725257	00:54:23.6	-72:52:57.1	36.39
J005426-741722	00:54:26.2	-74:17:22.5	7.18
J005428-694437	00:54:28.9	-69:44:37.3	4.32
J005429-720158	00:54:29.1	-72:01:58.3	8.27
J005429-694224	00:54:29.5	-69:42:24.7	4.11
J005403-721348	00:54:03.5	-72:13:48.9	7.63
J005431-694217	00:54:31.8	-69:42:17.9	6.62
J005433-700112	00:54:33.9	-70:01:12.5	27.54
J005434-733847	00:54:34.5	-73:38:47.5	10.32
J005439-724506	00:54:39.6	-72:45:06.6	11.50
J005441-722952	00:54:41.8	-72:29:52.3	7.16
J005442-702641	00:54:42.6	-70:26:41.7	9.33
J005448-725353	00:54:48.7	-72:53:53.4	14.77
J005449-744936	00:54:49.3	-74:49:36.1	11.41
J005449-731648	00:54:49.6	-73:16:48.4	12.21
J005405-753403	00:54:05.8	-75:34:03.5	58.92
J005450-735859	00:54:50.5	-73:58:59.9	4.67
J005453-713136	00:54:53.1	-71:31:36.7	18.50
J005456-710340	00:54:56.6	-71:03:40.2	7.64
J005408-722421	00:54:08.2	-72:24:21.2	8.11
J005510-702623	00:55:10.8	-70:26:23.8	3.71
J005516-753204	00:55:16.8	-75:32:04.4	19.78
J005518-714450	00:55:18.9	-71:44:50.7	17.19
J005522-721053	00:55:22.7	-72:10:53.0	76.68

Table A2. Continued.

Name ATCA	R.A.$_{1400}$ (J2000)	Dec.$_{1400}$ (J2000)	S_{20} (mJy)
J005524-695113	00:55:24.3	-69:51:13.2	3.88
J005524-693808	00:55:24.9	-69:38:08.0	9.00
J005527-721057	00:55:27.5	-72:10:57.3	13.40
J005529-710239	00:55:29.0	-71:02:39.2	5.00
J005503-712106	00:55:03.9	-71:21:06.0	20.50
J005530-702627	00:55:30.6	-70:26:27.3	25.68
J005531-695859	00:55:31.8	-69:58:59.7	6.58
J005532-723124	00:55:32.9	-72:31:24.0	17.58
J005534-721054	00:55:34.0	-72:10:54.5	21.50
J005536-723534	00:55:36.3	-72:35:34.4	19.94
J005537-723453	00:55:37.3	-72:34:53.9	10.80
J005537-743925	00:55:37.3	-74:39:25.9	86.97
J005539-694024	00:55:39.6	-69:40:24.1	41.84
J005539-721047	00:55:39.6	-72:10:47.8	27.30
J005548-701356	00:55:48.5	-70:13:56.4	5.55
J005553-710322	00:55:53.4	-71:03:22.2	8.03
J005554-742235	00:55:54.4	-74:22:35.9	9.59
J005557-722604	00:55:57.0	-72:26:04.8	96.90
J005506-723718	00:55:06.4	-72:37:18.7	9.42
J005600-720908	00:56:00.7	-72:09:08.8	6.53
J005611-710707	00:56:11.4	-71:07:07.7	608.60
J005622-715111	00:56:22.3	-71:51:11.3	19.85
J005625-710453	00:56:25.1	-71:04:53.4	3.59
J005627-700034	00:56:27.7	-70:00:34.9	4.06
J005633-735707	00:56:33.2	-73:57:07.9	11.63
J005636-740315	00:56:36.8	-74:03:15.8	27.09
J005644-725201	00:56:44.8	-72:52:01.5	45.42
J005652-712300	00:56:52.6	-71:23:00.6	79.17
J005652-731609	00:56:52.8	-73:16:09.2	3.17
J005658-741159	00:56:58.2	-74:11:59.9	3.76
J005658-752915	00:56:58.5	-75:29:15.1	26.90
J005659-702924	00:56:59.2	-70:29:24.1	4.15
J005608-703846	00:56:08.1	-70:38:46.6	89.69
J005714-733450	00:57:14.9	-73:34:50.4	12.74
J005715-704046	00:57:15.7	-70:40:46.4	85.26
J005715-703328	00:57:15.8	-70:33:28.9	7.37
J005702-703653	00:57:02.0	-70:36:53.6	7.27
J005702-733654	00:57:02.8	-73:36:54.4	4.45
J005720-741226	00:57:20.7	-74:12:26.9	4.86
J005722-740315	00:57:22.4	-74:03:15.6	14.73
J005727-751456	00:57:27.6	-75:14:56.5	6.91
J005728-751258	00:57:28.4	-75:12:58.2	5.31
J005729-723223	00:57:29.8	-72:32:23.2	4.55
J005703-721635	00:57:03.3	-72:16:35.9	17.62
J005731-744213	00:57:31.1	-74:42:13.6	20.53
J005732-741243	00:57:32.5	-74:12:43.3	429.50
J005736-731258	00:57:36.9	-73:12:58.5	4.77
J005737-715933	00:57:37.6	-71:59:33.2	5.75
J005738-710847	00:57:38.4	-71:08:47.7	27.74
J005740-752153	00:57:40.6	-75:21:53.8	9.45

Table A2. Continued.

Name ATCA	R.A.$_{1400}$ (J2000)	Dec.$_{1400}$ (J2000)	S_{20} (mJy)
J005741-724155	00:57:41.6	-72:41:55.0	13.29
J005743-715912	00:57:43.1	-71:59:12.9	4.67
J005746-711721	00:57:46.6	-71:17:21.4	5.51
J005746-712005	00:57:46.7	-71:20:05.3	5.39
J005705-704019	00:57:05.5	-70:40:19.0	3.86
J005750-730601	00:57:50.4	-73:06:01.1	4.50
J005750-704554	00:57:50.7	-70:45:54.0	4.75
J005753-711832	00:57:53.5	-71:18:32.3	5.56
J005756-715719	00:57:56.9	-71:57:19.2	2.87
J005757-740218	00:57:57.6	-74:02:18.7	6.51
J005757-715644	00:57:57.7	-71:56:44.3	5.26
J005812-712408	00:58:12.1	-71:24:08.5	9.95
J005812-735949	00:58:12.3	-73:59:49.7	12.12
J005813-700959	00:58:13.2	-70:09:59.6	43.35
J005813-713519	00:58:13.8	-71:35:19.9	6.96
J005816-723852	00:58:16.8	-72:38:52.6	6.08
J005817-712334	00:58:17.8	-71:23:34.4	9.86
J005820-713040	00:58:20.5	-71:30:40.6	32.30
J005821-732934	00:58:21.6	-73:29:34.8	5.45
J005822-720042	00:58:22.9	-72:00:42.3	7.91
J005827-723954	00:58:27.1	-72:39:54.6	7.11
J005831-740149	00:58:31.4	-74:01:49.3	8.99
J005831-711137	00:58:31.9	-71:11:37.9	3.79
J005832-725112	00:58:32.8	-72:51:12.0	4.45
J005837-694450	00:58:37.2	-69:44:50.5	3.70
J005841-701911	00:58:41.3	-70:19:11.3	6.03
J005847-740403	00:58:47.2	-74:04:03.6	3.64
J005847-744654	00:58:47.8	-74:46:54.4	5.19
J005848-743514	00:58:48.8	-74:35:14.1	19.18
J005912-741400	00:59:12.8	-74:14:00.6	3.49
J005918-750559	00:59:18.8	-75:05:59.7	3.72
J005927-751206	00:59:27.6	-75:12:06.6	3.42
J005935-714625	00:59:35.8	-71:46:25.9	3.79
J005904-704901	00:59:04.4	-70:49:01.3	64.34
J005948-742628	00:59:48.4	-74:26:28.0	3.51
J005948-705028	00:59:48.6	-70:50:28.4	17.43
J005905-750642	00:59:05.1	-75:06:42.7	6.27
J005950-705201	00:59:50.9	-70:52:01.0	13.17
J005906-745849	00:59:06.0	-74:58:49.3	14.54
J005906-735204	00:59:06.6	-73:52:04.2	29.42
J005906-745454	00:59:06.7	-74:54:54.4	9.39
J005909-740239	00:59:09.7	-74:02:39.9	5.48
J010011-693717	01:00:11.2	-69:37:17.9	6.30
J010012-704028	01:00:12.6	-70:40:28.1	10.82
J010020-714433	01:00:20.2	-71:44:33.5	3.68
J010029-713826	01:00:29.8	-71:38:26.2	127.70
J010030-730007	01:00:30.6	-73:00:07.3	12.87
J010041-740506	01:00:41.1	-74:05:06.8	13.80
J010043-712137	01:00:43.1	-71:21:37.3	8.99
J010043-695316	01:00:43.9	-69:53:16.4	18.69

Table A2. Continued.

Name ATCA	R.A.$_{1400}$ (J2000)	Dec.$_{1400}$ (J2000)	S_{20} (mJy)
J010046-745417	01:00:46.7	-74:54:17.9	21.70
J010005-693701	01:00:05.8	-69:37:01.1	6.19
J010050-751354	01:00:50.8	-75:13:54.0	4.91
J010053-705020	01:00:53.0	-70:50:20.3	8.34
J010053-734042	01:00:53.8	-73:40:42.0	7.19
J010054-734215	01:00:54.7	-73:42:15.7	4.84
J010058-713529	01:00:58.2	-71:35:29.3	6.83
J010006-732639	01:00:06.5	-73:26:39.0	4.42
J010006-693030	01:00:06.8	-69:30:30.8	6.91
J010112-702418	01:01:12.0	-70:24:18.2	4.19
J010112-744100	01:01:12.5	-74:41:00.3	13.06
J010116-752021	01:01:16.2	-75:20:21.9	4.68
J010132-693915	01:01:32.1	-69:39:15.5	123.50
J010140-725514	01:01:40.7	-72:55:14.2	4.95
J010142-703204	01:01:42.1	-70:32:04.4	6.70
J010143-723226	01:01:43.3	-72:32:26.8	13.20
J010143-742334	01:01:43.4	-74:23:34.7	3.74
J010147-723226	01:01:47.4	-72:32:26.8	7.60
J010152-695639	01:01:52.3	-69:56:39.8	4.19
J010152-720601	01:01:52.6	-72:06:01.4	4.18
J010157-720657	01:01:57.3	-72:06:57.5	4.06
J010157-734248	01:01:57.6	-73:42:48.6	7.85
J010109-725047	01:01:09.8	-72:50:47.2	3.87
J010213-720444	01:02:13.5	-72:04:44.1	4.68
J010216-723707	01:02:16.5	-72:37:07.7	4.60
J010220-735322	01:02:20.9	-73:53:22.3	12.28
J010221-703717	01:02:21.4	-70:37:17.3	3.54
J010222-712721	01:02:22.0	-71:27:21.2	14.32
J010226-742702	01:02:26.6	-74:27:02.0	5.13
J010229-734732	01:02:29.4	-73:47:32.8	5.50
J010229-750021	01:02:29.6	-75:00:21.8	8.21
J010234-695827	01:02:34.0	-69:58:27.9	15.36
J010234-741534	01:02:34.3	-74:15:34.7	18.37
J010234-734817	01:02:34.6	-73:48:17.9	5.69
J010237-725037	01:02:37.7	-72:50:37.3	4.74
J010204-722447	01:02:04.0	-72:24:47.1	9.30
J010204-710323	01:02:04.4	-71:03:23.3	5.10
J010240-710220	01:02:40.2	-71:02:20.7	5.99
J010241-695831	01:02:41.4	-69:58:31.5	4.06
J010248-752212	01:02:48.5	-75:22:12.6	4.91
J010249-715318	01:02:49.0	-71:53:18.3	9.65
J010251-753524	01:02:51.5	-75:35:24.0	64.01
J010255-713631	01:02:55.5	-71:36:31.6	19.68
J010256-743531	01:02:56.9	-74:35:31.2	18.94
J010257-703903	01:02:57.1	-70:39:03.1	8.29
J010257-703952	01:02:57.1	-70:39:52.9	7.99
J010257-703836	01:02:57.3	-70:38:36.4	6.48
J010258-743344	01:02:58.3	-74:33:44.9	11.27
J010319-704648	01:03:19.1	-70:46:48.4	9.49
J010319-700235	01:03:19.8	-70:02:35.2	12.11

Table A2. Continued.

Name ATCA	R.A.$_{1400}$ (J2000)	Dec.$_{1400}$ (J2000)	S_{20} (mJy)
J010321-721343	01:03:21.3	-72:13:43.8	3.87
J010326-730022	01:03:26.9	-73:00:22.8	13.24
J010329-724724	01:03:29.7	-72:47:24.6	3.50
J010330-743431	01:03:30.9	-74:34:31.2	5.08
J010331-700637	01:03:31.7	-70:06:37.0	55.77
J010331-750703	01:03:31.8	-75:07:03.6	53.33
J010332-752745	01:03:32.2	-75:27:45.7	8.27
J010339-725041	01:03:39.3	-72:50:41.8	13.48
J010341-703532	01:03:41.1	-70:35:32.1	3.27
J010344-694052	01:03:44.8	-69:40:52.1	16.40
J010344-695829	01:03:44.8	-69:58:29.8	20.76
J010345-732049	01:03:45.3	-73:20:49.8	2.97
J010345-694924	01:03:45.9	-69:49:24.1	33.23
J010348-712403	01:03:48.8	-71:24:03.7	4.04
J010359-711255	01:03:59.1	-71:12:55.0	9.61
J010410-733808	01:04:10.5	-73:38:08.4	6.04
J010411-705602	01:04:11.8	-70:56:02.1	8.62
J010412-752357	01:04:12.6	-75:23:57.4	8.80
J010402-750833	01:04:02.2	-75:08:33.0	5.42
J010424-711254	01:04:24.6	-71:12:54.6	6.35
J010425-742732	01:04:25.6	-74:27:32.5	15.07
J010403-752754	01:04:03.6	-75:27:54.3	4.11
J010431-720725	01:04:31.3	-72:07:25.2	34.99
J010435-740410	01:04:35.0	-74:04:10.2	3.54
J010436-695822	01:04:36.9	-69:58:22.8	34.81
J010441-713122	01:04:41.2	-71:31:22.7	29.69
J010444-745703	01:04:44.2	-74:57:03.0	3.75
J010405-724343	01:04:05.4	-72:43:43.0	11.32
J010455-752921	01:04:55.5	-75:29:21.4	5.18
J010458-703734	01:04:58.0	-70:37:34.5	52.03
J010406-735127	01:04:06.5	-73:51:27.5	5.22
J010407-711007	01:04:07.2	-71:10:07.1	3.85
J010511-753444	01:05:11.4	-75:34:44.3	26.90
J010514-703258	01:05:14.8	-70:32:58.7	2.93
J010516-735739	01:05:16.3	-73:57:39.7	10.40
J010520-695511	01:05:20.4	-69:55:11.5	11.82
J010521-705154	01:05:21.1	-70:51:54.5	5.24
J010523-753421	01:05:23.9	-75:34:21.4	31.27
J010524-731517	01:05:24.1	-73:15:17.0	17.90
J010525-722523	01:05:25.1	-72:25:23.1	25.31
J010525-732318	01:05:25.4	-73:23:18.9	3.12
J010531-721020	01:05:31.0	-72:10:20.9	2.26
J010532-743330	01:05:32.3	-74:33:30.1	6.69
J010532-721331	01:05:32.9	-72:13:31.1	11.90
J010536-743201	01:05:36.0	-74:32:01.0	8.49
J010536-753339	01:05:36.3	-75:33:39.9	6.72
J010536-740005	01:05:36.7	-74:00:05.7	18.09
J010504-715925	01:05:04.1	-71:59:25.0	9.72
J010543-745326	01:05:43.0	-74:53:26.6	4.64
J010544-750546	01:05:44.0	-75:05:46.7	13.22

Table A2. Continued.

Name ATCA	R.A.$_{1400}$ (J2000)	Dec.$_{1400}$ (J2000)	S_{20} (mJy)
J010549-702623	01:05:49.3	-70:26:23.4	13.58
J010551-703850	01:05:51.8	-70:38:50.9	3.58
J010556-714606	01:05:56.6	-71:46:06.9	36.15
J010557-710457	01:05:57.5	-71:04:57.0	30.13
J010558-732513	01:05:58.8	-73:25:13.6	9.57
J010507-721841	01:05:07.0	-72:18:41.6	3.77
J010507-723858	01:05:07.8	-72:38:58.3	3.83
J010509-712838	01:05:09.6	-71:28:38.7	6.36
J010610-734956	01:06:10.4	-73:49:56.8	4.50
J010610-744116	01:06:10.6	-74:41:16.7	5.13
J010614-744128	01:06:14.7	-74:41:28.1	4.88
J010614-735000	01:06:14.8	-73:50:00.1	8.30
J010619-705113	01:06:19.3	-70:51:13.2	7.02
J010620-704144	01:06:20.9	-70:41:44.5	18.43
J010629-745135	01:06:29.1	-74:51:35.2	4.30
J010633-714807	01:06:33.5	-71:48:07.9	3.77
J010638-695913	01:06:38.2	-69:59:13.6	3.47
J010604-693126	01:06:04.3	-69:31:26.5	13.21
J010642-712003	01:06:42.6	-71:20:03.2	4.96
J010643-703008	01:06:43.6	-70:30:08.0	4.74
J010646-741931	01:06:46.3	-74:19:31.2	5.93
J010647-725814	01:06:47.5	-72:58:14.0	7.03
J010651-752014	01:06:51.0	-75:20:14.4	4.60
J010652-721837	01:06:52.7	-72:18:37.0	7.61
J010653-693928	01:06:53.5	-69:39:28.4	15.32
J010657-731320	01:06:57.8	-73:13:20.6	5.75
J010659-735454	01:06:59.8	-73:54:54.7	7.98
J010607-693207	01:06:07.3	-69:32:07.6	5.87
J010717-732949	01:07:17.4	-73:29:49.2	13.56
J010702-703417	01:07:02.6	-70:34:17.8	9.41
J010704-692013	01:07:04.8	-69:20:13.8	15.44
J010741-715311	01:07:41.3	-71:53:11.7	5.47
J010748-705215	01:07:48.3	-70:52:15.5	9.93
J010749-714505	01:07:49.7	-71:45:05.7	3.90
J010756-712534	01:07:56.3	-71:25:34.0	10.27
J010758-703526	01:07:58.8	-70:35:26.9	3.09
J010759-710822	01:07:59.7	-71:08:22.4	3.75
J010708-714305	01:07:08.5	-71:43:05.9	24.34
J010811-754155	01:08:11.2	-75:41:55.9	21.16
J010811-725738	01:08:11.7	-72:57:38.1	9.73
J010815-692356	01:08:15.0	-69:23:56.1	18.56
J010816-693654	01:08:16.2	-69:36:54.0	2.70
J010817-745520	01:08:17.5	-74:55:20.4	5.91
J010818-692355	01:08:18.5	-69:23:55.5	8.57
J010802-712553	01:08:02.8	-71:25:53.5	3.93
J010821-714924	01:08:21.6	-71:49:24.6	4.72
J010825-700556	01:08:25.9	-70:05:56.3	5.22
J010829-753406	01:08:29.0	-75:34:06.6	3.84
J010836-704701	01:08:36.9	-70:47:01.9	4.62
J010839-724715	01:08:39.1	-72:47:15.4	20.23

Table A2. Continued.

Name ATCA	R.A.$_{1400}$ (J2000)	Dec.$_{1400}$ (J2000)	S_{20} (mJy)
J010846-704653	01:08:46.6	-70:46:53.4	5.23
J010847-752628	01:08:47.6	-75:26:28.2	13.51
J010851-715018	01:08:51.9	-71:50:18.8	4.55
J010855-740522	01:08:55.2	-74:05:22.0	4.46
J010857-721140	01:08:57.3	-72:11:40.6	4.41
J010808-713947	01:08:08.0	-71:39:47.0	9.90
J010809-720913	01:08:09.6	-72:09:13.2	7.21
J010901-731815	01:09:01.3	-73:18:15.1	17.49
J010901-722903	01:09:01.8	-72:29:03.6	3.53
J010912-731728	01:09:12.2	-73:17:28.6	8.00
J010913-731138	01:09:13.0	-73:11:38.7	36.19
J010914-722939	01:09:14.3	-72:29:39.1	5.76
J010919-725600	01:09:19.4	-72:56:00.2	26.82
J010902-713316	01:09:02.1	-71:33:16.6	4.37
J010920-731051	01:09:20.6	-73:10:51.0	3.97
J010928-704207	01:09:28.6	-70:42:07.8	15.69
J010928-740557	01:09:28.9	-74:05:57.5	8.28
J010903-734926	01:09:03.8	-73:49:26.2	4.95
J010930-725245	01:09:30.0	-72:52:45.1	3.64
J010931-713454	01:09:31.2	-71:34:54.5	119.80
J010932-694618	01:09:32.3	-69:46:18.9	6.89
J010934-753646	01:09:34.5	-75:36:46.7	3.67
J010935-713823	01:09:35.4	-71:38:23.5	6.63
J010936-700211	01:09:36.3	-70:02:11.1	3.26
J010937-745702	01:09:37.8	-74:57:02.0	4.33
J010939-705002	01:09:39.8	-70:50:02.7	6.13
J010940-695557	01:09:40.4	-69:55:57.8	29.20
J010940-695624	01:09:40.6	-69:56:24.0	33.10
J010949-702501	01:09:49.9	-70:25:01.4	8.11
J010955-711346	01:09:55.5	-71:13:46.1	3.85
J010958-713544	01:09:58.8	-71:35:44.1	9.16
J011016-713951	01:10:16.6	-71:39:51.6	4.03
J011018-704815	01:10:18.1	-70:48:15.4	6.91
J011020-730425	01:10:20.1	-73:04:25.0	19.20
J011022-702517	01:10:22.9	-70:25:17.5	6.31
J011023-730450	01:10:23.7	-73:04:50.2	12.60
J011025-695503	01:10:25.4	-69:55:03.8	68.30
J011028-745103	01:10:28.1	-74:51:03.9	16.67
J011029-745358	01:10:29.4	-74:53:58.4	7.00
J011030-723309	01:10:30.6	-72:33:09.0	9.36
J011033-700311	01:10:33.3	-70:03:11.5	4.54
J011035-720024	01:10:35.2	-72:00:24.3	6.23
J011036-722810	01:10:36.4	-72:28:10.7	65.43
J011037-701041	01:10:37.0	-70:10:41.4	3.91
J011039-705752	01:10:39.1	-70:57:52.9	3.60
J011041-731454	01:10:41.1	-73:14:54.3	5.57
J011044-750953	01:10:44.4	-75:09:53.0	8.33
J011048-711415	01:10:48.2	-71:14:15.9	8.09
J011049-704953	01:10:49.2	-70:49:53.3	4.22
J011049-731427	01:10:49.9	-73:14:27.8	497.90

Table A2. Continued.

Name ATCA	R.A.$_{1400}$ (J2000)	Dec.$_{1400}$ (J2000)	S_{20} (mJy)
J011005-722647	01:10:05.3	-72:26:47.9	127.90
J011050-721025	01:10:50.2	-72:10:25.7	7.62
J011053-704252	01:10:53.5	-70:42:52.7	13.74
J011056-731408	01:10:56.6	-73:14:08.2	141.70
J011058-744617	01:10:58.5	-74:46:17.0	3.75
J011007-741047	01:10:07.1	-74:10:47.9	3.68
J011101-723533	01:11:01.4	-72:35:33.5	3.61
J011115-715137	01:11:15.4	-71:51:37.1	7.82
J011116-701146	01:11:16.2	-70:11:46.9	21.42
J011127-694654	01:11:27.2	-69:46:54.9	3.98
J011103-720050	01:11:03.8	-72:00:50.4	4.84
J011130-754503	01:11:30.8	-75:45:03.5	64.20
J011132-730209	01:11:32.5	-73:02:09.4	66.96
J011134-753807	01:11:34.1	-75:38:07.9	92.81
J011134-711413	01:11:34.4	-71:14:13.8	37.90
J011136-731023	01:11:36.1	-73:10:23.1	6.95
J011146-703530	01:11:46.0	-70:35:30.7	10.86
J011146-711850	01:11:46.9	-71:18:50.3	6.94
J011153-725119	01:11:53.0	-72:51:19.4	7.61
J011153-711908	01:11:53.7	-71:19:08.3	4.64
J011157-734129	01:11:57.9	-73:41:29.0	19.95
J011158-694908	01:11:58.0	-69:49:08.6	4.03
J011108-692611	01:11:08.3	-69:26:11.6	117.92
J011211-753502	01:12:11.0	-75:35:02.5	3.28
J011222-703926	01:12:22.5	-70:39:26.5	4.62
J011223-741212	01:12:23.2	-74:12:12.3	33.91
J011226-732751	01:12:26.0	-73:27:51.7	27.16
J011226-724801	01:12:26.5	-72:48:01.5	7.11
J011231-750617	01:12:31.4	-75:06:17.8	13.85
J011204-695531	01:12:04.5	-69:55:31.9	10.61
J011246-731522	01:12:46.8	-73:15:22.8	7.25
J011248-701928	01:12:48.0	-70:19:28.6	15.12
J011251-752530	01:12:51.6	-75:25:30.3	12.51
J011256-753504	01:12:56.7	-75:35:04.0	3.79
J011258-700620	01:12:58.5	-70:06:20.9	4.11
J011300-701337	01:13:00.9	-70:13:37.3	8.76
J011301-740711	01:13:01.8	-74:07:11.0	5.37
J011319-743451	01:13:19.1	-74:34:51.9	8.84
J011302-714903	01:13:02.5	-71:49:03.3	5.95
J011321-752550	01:13:21.3	-75:25:50.5	37.62
J011321-752820	01:13:21.4	-75:28:20.3	96.25
J011325-695102	01:13:25.4	-69:51:02.3	4.03
J011303-732107	01:13:03.4	-73:21:07.4	4.95
J011332-693855	01:13:32.5	-69:38:55.4	34.71
J011332-740757	01:13:32.6	-74:07:57.6	29.13
J011338-714119	01:13:38.9	-71:41:19.7	11.96
J011304-701656	01:13:04.2	-70:16:56.9	3.47
J011344-711520	01:13:44.3	-71:15:20.5	21.10
J011349-731801	01:13:49.8	-73:18:01.4	16.21
J011351-753339	01:13:51.2	-75:33:39.0	35.07

Table A2. Continued.

Name ATCA	R.A.$_{1400}$ (J2000)	Dec.$_{1400}$ (J2000)	S_{20} (mJy)
J011357-702530	01:13:57.3	-70:25:30.9	68.65
J011357-742655	01:13:57.3	-74:26:55.3	4.20
J011357-711424	01:13:57.4	-71:14:24.9	27.75
J011306-731728	01:13:06.1	-73:17:28.1	4.26
J011401-702622	01:14:01.4	-70:26:22.6	4.19
J011413-700944	01:14:13.7	-70:09:44.6	16.90
J011417-700951	01:14:17.4	-70:09:51.0	7.20
J011418-731729	01:14:18.6	-73:17:29.7	6.00
J011419-731543	01:14:19.6	-73:15:43.8	5.82
J011427-733313	01:14:27.8	-73:33:13.5	1.97
J011403-732006	01:14:03.7	-73:20:06.4	31.40
J011432-732143	01:14:32.8	-73:21:43.1	132.40
J011434-715259	01:14:34.8	-71:52:59.0	24.30
J011436-715233	01:14:36.9	-71:52:33.1	19.90
J011446-731948	01:14:46.9	-73:19:48.7	5.82
J011454-701434	01:14:54.1	-70:14:34.4	20.67
J011457-700028	01:14:57.1	-70:00:28.1	4.60
J011457-732811	01:14:57.8	-73:28:11.9	4.45
J011407-732005	01:14:07.1	-73:20:05.5	28.50
J011500-703713	01:15:00.2	-70:37:13.7	9.52
J011510-694652	01:15:10.7	-69:46:52.4	3.48
J011515-694403	01:15:15.4	-69:44:03.7	3.29
J011518-704445	01:15:18.0	-70:44:45.3	3.99
J011518-715927	01:15:18.0	-71:59:27.8	3.77
J011518-713725	01:15:18.4	-71:37:25.4	3.03
J011526-730018	01:15:26.1	-73:00:18.3	3.95
J011526-720730	01:15:26.8	-72:07:30.7	4.79
J011529-700101	01:15:29.4	-70:01:01.6	4.50
J011529-741111	01:15:29.8	-74:11:11.1	4.81
J011535-720008	01:15:35.4	-72:00:08.9	14.15
J011543-701843	01:15:43.8	-70:18:43.4	5.72
J011550-713950	01:15:50.4	-71:39:50.6	3.99
J011550-741101	01:15:50.8	-74:11:01.2	5.26
J011551-700418	01:15:51.8	-70:04:18.8	48.09
J011552-723552	01:15:52.3	-72:35:52.2	4.79
J011559-705554	01:15:59.3	-70:55:54.5	4.04
J011559-710441	01:15:59.8	-71:04:41.1	22.68
J011506-743646	01:15:06.6	-74:36:46.8	6.64
J011610-733900	01:16:10.6	-73:39:00.6	54.50
J011611-711028	01:16:11.2	-71:10:28.7	17.03
J011615-733851	01:16:15.7	-73:38:51.8	34.20
J011615-732657	01:16:15.8	-73:26:57.1	35.46
J011622-700641	01:16:22.2	-70:06:41.5	6.62
J011623-702957	01:16:23.0	-70:29:57.2	47.83
J011628-731438	01:16:28.9	-73:14:38.8	66.52
J011603-744325	01:16:03.6	-74:43:25.5	19.56
J011635-712604	01:16:35.7	-71:26:04.0	15.95
J011637-701422	01:16:37.2	-70:14:22.6	3.69
J011604-735354	01:16:04.5	-73:53:54.3	10.09
J011646-743530	01:16:46.0	-74:35:30.9	5.41

Table A2. Continued.

Name ATCA	R.A.$_{1400}$ (J2000)	Dec.$_{1400}$ (J2000)	S_{20} (mJy)
J011605-695849	01:16:05.7	-69:58:49.9	5.55
J011650-695300	01:16:50.6	-69:53:00.1	3.71
J011652-695540	01:16:52.4	-69:55:40.0	4.16
J011606-743210	01:16:06.4	-74:32:10.4	6.52
J011609-742814	01:16:09.9	-74:28:14.2	22.93
J011701-714325	01:17:01.4	-71:43:25.4	4.10
J011718-703432	01:17:18.1	-70:34:32.0	9.68
J011719-714116	01:17:19.6	-71:41:16.1	7.26
J011722-730917	01:17:22.2	-73:09:17.2	12.89
J011724-744706	01:17:24.4	-74:47:06.5	6.28
J011726-695313	01:17:26.4	-69:53:13.5	6.78
J011732-705110	01:17:32.3	-70:51:10.9	3.73
J011732-743338	01:17:32.3	-74:33:38.1	7.69
J011744-745550	01:17:44.4	-74:55:50.5	3.73
J011747-734445	01:17:47.0	-73:44:45.2	3.30
J011705-695306	01:17:05.4	-69:53:06.6	3.85
J011757-721911	01:17:57.9	-72:19:11.5	11.79
J011759-745002	01:17:59.6	-74:50:02.2	13.03
J011816-695147	01:18:16.0	-69:51:47.1	540.50
J011819-730723	01:18:19.8	-73:07:23.8	2.51
J011825-731800	01:18:25.1	-73:18:00.1	3.67
J011829-753402	01:18:29.9	-75:34:02.1	5.72
J011803-720502	01:18:03.9	-72:05:02.5	4.33
J011833-725042	01:18:33.6	-72:50:42.5	3.71
J011834-720647	01:18:34.4	-72:06:47.9	12.15
J011837-725726	01:18:37.6	-72:57:26.6	6.54
J011841-715217	01:18:41.3	-71:52:17.2	9.53
J011844-744439	01:18:44.2	-74:44:39.7	4.14
J011805-745825	01:18:05.8	-74:58:25.3	22.22
J011855-724301	01:18:55.0	-72:43:01.6	6.68
J011856-700310	01:18:56.9	-70:03:10.0	3.64
J011808-694559	01:18:08.5	-69:45:59.6	106.60
J011910-750146	01:19:10.3	-75:01:46.1	7.57
J011910-724647	01:19:10.9	-72:46:47.9	3.50
J011918-710530	01:19:18.5	-71:05:30.7	70.39
J011902-692956	01:19:02.4	-69:29:56.7	21.50
J011927-735122	01:19:27.0	-73:51:22.9	4.90
J011933-725931	01:19:33.4	-72:59:31.8	3.54
J011943-694540	01:19:43.9	-69:45:40.1	4.70
J011958-750314	01:19:58.7	-75:03:14.5	12.82
J011909-744208	01:19:09.2	-74:42:08.1	15.57
J012011-703605	01:20:11.4	-70:36:05.2	18.35
J012012-745554	01:20:12.2	-74:55:54.0	3.95
J012012-721934	01:20:12.9	-72:19:34.7	3.45
J012023-721956	01:20:23.8	-72:19:56.2	19.41
J012024-700538	01:20:24.3	-70:05:38.5	3.75
J012030-712640	01:20:30.3	-71:26:40.3	5.72
J012035-750633	01:20:35.8	-75:06:33.5	22.98
J012036-713330	01:20:36.9	-71:33:30.6	4.26
J012037-703841	01:20:37.9	-70:38:41.2	54.38

Table A2. Continued.

Name ATCA	R.A.$_{1400}$ (J2000)	Dec.$_{1400}$ (J2000)	S_{20} (mJy)
J012048-733513	01:20:48.8	-73:35:13.2	8.48
J012053-734938	01:20:53.6	-73:49:38.7	3.26
J012055-733454	01:20:55.9	-73:34:54.2	27.19
J012059-753819	01:20:59.1	-75:38:19.3	22.23
J012006-725017	01:20:06.8	-72:50:17.5	11.21
J012114-702751	01:21:14.5	-70:27:51.2	4.85
J012116-701341	01:21:16.2	-70:13:41.8	103.60
J012122-695930	01:21:22.8	-69:59:30.4	3.39
J012124-693242	01:21:24.6	-69:32:42.5	23.89
J012128-714335	01:21:28.7	-71:43:35.2	10.67
J012138-694344	01:21:38.4	-69:43:44.4	7.97
J012144-695718	01:21:44.2	-69:57:18.8	86.90
J012145-731658	01:21:45.8	-73:16:58.4	4.70
J012146-703126	01:21:46.1	-70:31:26.7	3.54
J012149-695646	01:21:49.4	-69:56:46.1	101.70
J012150-740005	01:21:50.5	-74:00:05.7	32.68
J012153-711959	01:21:53.8	-71:19:59.6	4.24
J012154-715526	01:21:54.4	-71:55:26.1	9.47
J012156-744640	01:21:56.4	-74:46:40.1	4.61
J012109-693141	01:21:09.5	-69:31:41.7	11.10
J012200-744635	01:22:00.3	-74:46:35.9	4.69
J012210-693402	01:22:10.1	-69:34:02.3	31.13
J012220-751902	01:22:20.5	-75:19:02.4	3.83
J012220-730350	01:22:20.8	-73:03:50.4	5.94
J012233-714724	01:22:33.9	-71:47:24.2	12.68
J012235-733817	01:22:35.9	-73:38:17.0	27.81
J012239-741013	01:22:39.0	-74:10:13.5	14.96
J012244-692957	01:22:44.6	-69:29:57.9	21.28
J012244-694415	01:22:44.8	-69:44:15.1	103.00
J012246-742631	01:22:46.7	-74:26:31.6	8.37
J012205-714735	01:22:05.6	-71:47:35.3	5.81
J012250-715043	01:22:50.6	-71:50:43.2	43.95
J012251-705427	01:22:51.2	-70:54:27.2	9.10
J012255-731429	01:22:55.0	-73:14:29.0	4.12
J012255-700708	01:22:55.1	-70:07:08.4	4.68
J012257-751506	01:22:57.1	-75:15:06.5	580.60
J012258-714842	01:22:58.4	-71:48:42.6	7.58
J012207-744638	01:22:07.1	-74:46:38.1	4.80
J012207-702918	01:22:07.8	-70:29:18.3	51.05
J012209-713954	01:22:09.8	-71:39:54.1	24.49
J012311-745417	01:23:11.1	-74:54:17.4	12.21
J012311-741812	01:23:11.7	-74:18:12.0	8.27
J012311-732843	01:23:11.8	-73:28:43.5	5.67
J012315-750720	01:23:15.4	-75:07:20.0	6.95
J012315-751616	01:23:15.5	-75:16:16.6	3.85
J012317-723605	01:23:17.6	-72:36:05.9	8.23
J012317-703731	01:23:17.8	-70:37:31.6	13.10
J012321-734526	01:23:21.4	-73:45:26.6	6.57
J012321-703740	01:23:21.7	-70:37:40.9	18.30
J012324-735606	01:23:24.0	-73:56:06.4	29.46

Table A2. Continued.

Name ATCA	R.A.$_{1400}$ (J2000)	Dec.$_{1400}$ (J2000)	S_{20} (mJy)
J012324-740243	01:23:24.2	-74:02:43.5	7.90
J012330-721814	01:23:30.9	-72:18:14.5	21.24
J012336-703231	01:23:36.6	-70:32:31.8	16.35
J012349-735038	01:23:49.7	-73:50:38.1	79.55
J012305-735704	01:23:05.6	-73:57:04.9	3.93
J012352-744143	01:23:52.9	-74:41:43.7	28.34
J012354-700039	01:23:54.6	-70:00:39.1	3.54
J012306-711122	01:23:06.4	-71:11:22.3	7.43
J012306-695559	01:23:06.6	-69:55:59.8	42.21
J012308-700211	01:23:08.6	-70:02:11.0	5.36
J012415-704151	01:24:15.9	-70:41:51.9	11.62
J012417-711203	01:24:17.9	-71:12:03.4	17.71
J012424-713138	01:24:24.6	-71:31:38.7	3.76
J012426-703422	01:24:26.5	-70:34:22.6	3.37
J012430-752241	01:24:30.0	-75:22:41.9	61.94
J012433-712644	01:24:33.4	-71:26:44.6	29.79
J012449-692216	01:24:49.1	-69:22:16.9	17.75
J012449-701421	01:24:49.5	-70:14:21.9	3.97
J012458-720627	01:24:58.2	-72:06:27.9	8.10
J012408-730904	01:24:08.0	-73:09:04.1	52.93
J012513-700239	01:25:13.7	-70:02:39.6	8.00
J012520-722915	01:25:20.4	-72:29:15.5	19.43
J012525-714901	01:25:25.1	-71:49:01.6	6.47
J012529-722946	01:25:29.7	-72:29:46.9	8.85
J012530-703610	01:25:30.5	-70:36:10.3	2.48
J012536-735633	01:25:36.0	-73:56:33.1	10.26
J012540-712937	01:25:40.7	-71:29:37.9	4.91
J012546-695210	01:25:46.4	-69:52:10.1	3.54
J012546-731602	01:25:46.9	-73:16:02.6	45.72
J012548-701818	01:25:48.3	-70:18:18.2	6.32
J012548-715134	01:25:48.7	-71:51:34.7	17.62
J012549-705738	01:25:49.2	-70:57:38.5	4.24
J012554-713423	01:25:54.6	-71:34:23.6	3.55
J012506-694216	01:25:06.7	-69:42:16.9	15.89
J012600-735417	01:26:00.2	-73:54:17.8	15.02
J012611-692720	01:26:11.4	-69:27:20.6	10.92
J012615-730804	01:26:15.8	-73:08:04.9	18.20
J012618-701515	01:26:18.1	-70:15:15.1	6.52
J012618-731249	01:26:18.1	-73:12:49.4	5.23
J012619-730737	01:26:19.4	-73:07:37.2	11.90
J012622-693336	01:26:22.2	-69:33:36.3	16.90
J012623-693417	01:26:23.0	-69:34:17.4	12.30
J012625-705024	01:26:25.2	-70:50:24.0	33.16
J012629-732714	01:26:29.3	-73:27:14.6	39.55
J012639-731501	01:26:39.9	-73:15:01.7	55.80
J012604-695210	01:26:04.8	-69:52:10.1	31.21
J012641-741625	01:26:41.4	-74:16:25.8	5.00
J012647-734320	01:26:47.2	-73:43:20.6	7.25
J012650-731632	01:26:50.0	-73:16:32.6	3.93
J012655-751121	01:26:55.5	-75:11:21.8	49.45

Table A2. Continued.

Name ATCA	R.A.$_{1400}$ (J2000)	Dec.$_{1400}$ (J2000)	S_{20} (mJy)
J012714-705937	01:27:14.4	-70:59:37.4	14.77
J012719-693401	01:27:19.1	-69:34:01.4	64.31
J012723-701001	01:27:23.3	-70:10:01.8	7.30
J012726-703240	01:27:26.5	-70:32:40.8	17.02
J012732-695131	01:27:32.5	-69:51:31.3	26.37
J012733-693816	01:27:33.1	-69:38:16.8	60.71
J012733-713639	01:27:33.9	-71:36:39.0	54.68
J012704-700532	01:27:04.1	-70:05:32.0	10.80
J012750-705622	01:27:50.0	-70:56:22.3	38.63
J012752-731103	01:27:52.2	-73:11:03.8	10.79
J012753-691517	01:27:53.1	-69:15:17.4	32.20
J012758-720534	01:27:58.4	-72:05:34.9	19.12
J012815-730759	01:28:15.9	-73:07:59.1	9.74
J012816-751257	01:28:16.9	-75:12:57.2	82.50
J012802-702125	01:28:02.6	-70:21:25.5	17.58
J012820-712251	01:28:20.1	-71:22:51.9	5.13
J012820-715426	01:28:20.7	-71:54:26.7	7.32
J012829-734142	01:28:29.0	-73:41:42.3	9.04
J012832-700805	01:28:32.9	-70:08:05.6	32.23
J012834-715711	01:28:34.9	-71:57:11.2	5.47
J012845-692557	01:28:45.7	-69:25:57.7	6.11
J012846-693616	01:28:46.2	-69:36:16.1	354.70
J012849-731403	01:28:49.2	-73:14:03.2	3.79
J012805-741105	01:28:05.1	-74:11:05.0	6.66
J012808-751249	01:28:08.9	-75:12:49.9	170.40
J012913-692713	01:29:13.4	-69:27:13.8	8.24
J012924-733151	01:29:24.2	-73:31:51.7	15.98
J012924-703417	01:29:24.6	-70:34:17.0	11.48
J012926-752437	01:29:26.5	-75:24:37.1	24.08
J012928-730647	01:29:28.1	-73:06:47.7	5.62
J012903-715202	01:29:03.4	-71:52:02.5	5.44
J012930-733310	01:29:30.2	-73:33:10.3	181.80
J012931-703407	01:29:31.4	-70:34:07.0	9.74
J012932-705353	01:29:32.2	-70:53:53.0	7.99
J012943-692611	01:29:43.2	-69:26:11.8	5.00
J012945-703530	01:29:45.1	-70:35:30.5	53.98
J012945-723234	01:29:45.5	-72:32:34.2	4.57
J012945-703504	01:29:45.6	-70:35:04.1	17.95
J012947-701810	01:29:47.5	-70:18:10.5	49.51
J012951-703648	01:29:51.2	-70:36:48.5	25.28
J012951-721031	01:29:51.3	-72:10:31.8	3.78
J012952-703353	01:29:52.0	-70:33:53.8	18.78
J012955-701525	01:29:55.0	-70:15:25.1	9.94
J012955-692056	01:29:55.3	-69:20:56.0	5.06
J012958-724438	01:29:58.6	-72:44:38.1	4.58
J013012-721822	01:30:12.1	-72:18:22.9	5.19
J013013-703423	01:30:13.5	-70:34:23.7	4.16
J013013-742023	01:30:13.7	-74:20:23.7	25.55
J013016-703553	01:30:16.4	-70:35:53.9	4.80
J013017-742541	01:30:17.3	-74:25:41.0	4.61

Table A2. Continued.

Name ATCA	R.A.$_{1400}$ (J2000)	Dec.$_{1400}$ (J2000)	S_{20} (mJy)
J013019-702643	01:30:19.8	-70:26:43.2	4.28
J013002-700908	01:30:02.4	-70:09:08.9	9.83
J013002-695008	01:30:02.6	-69:50:08.8	6.46
J013002-710642	01:30:02.8	-71:06:42.3	3.29
J013024-692229	01:30:24.1	-69:22:29.6	7.57
J013024-743928	01:30:24.8	-74:39:28.9	7.88
J013027-692514	01:30:27.8	-69:25:14.0	5.08
J013030-714815	01:30:30.7	-71:48:15.3	6.21
J013031-695115	01:30:31.8	-69:51:15.3	244.40
J013032-731740	01:30:32.3	-73:17:40.9	29.12
J013033-745839	01:30:33.2	-74:58:39.7	3.92
J013037-695201	01:30:37.8	-69:52:01.1	3.43
J013041-734630	01:30:41.1	-73:46:30.0	3.66
J013058-700937	01:30:58.5	-70:09:37.5	10.91
J013059-700353	01:30:59.2	-70:03:53.3	10.26
J013008-710933	01:30:08.8	-71:09:33.7	4.31
J013110-715138	01:31:10.3	-71:51:38.5	4.04
J013121-725246	01:31:21.6	-72:52:46.0	8.59
J013124-713341	01:31:24.2	-71:33:41.1	16.92
J013124-740040	01:31:24.3	-74:00:40.5	18.09
J013131-710306	01:31:31.1	-71:03:06.0	5.81
J013134-700042	01:31:34.8	-70:00:42.5	28.26
J013138-713353	01:31:38.6	-71:33:53.9	5.49
J013142-701008	01:31:42.2	-70:10:08.6	35.71
J013147-734942	01:31:47.8	-73:49:42.1	18.04
J013148-700050	01:31:48.3	-70:00:50.0	7.50
J013105-700634	01:31:05.9	-70:06:34.9	3.88
J013150-720516	01:31:50.7	-72:05:16.6	9.91
J013151-700527	01:31:51.7	-70:05:27.2	5.08
J013153-700035	01:31:53.1	-70:00:35.2	8.50
J013154-741735	01:31:54.9	-74:17:35.7	6.59
J013106-745840	01:31:06.4	-74:58:40.6	8.11
J013212-710612	01:32:12.3	-71:06:12.8	8.95
J013214-742000	01:32:14.6	-74:20:00.2	3.61
J013214-733903	01:32:14.8	-73:39:03.3	33.47
J013218-715348	01:32:18.9	-71:53:48.1	29.85
J013223-723949	01:32:23.7	-72:39:49.7	7.10
J013229-734122	01:32:29.1	-73:41:22.6	35.94
J013229-723957	01:32:29.8	-72:39:57.0	219.80
J013236-710415	01:32:36.6	-71:04:15.1	26.63
J013238-722137	01:32:38.4	-72:21:37.9	21.34
J013239-734422	01:32:39.7	-73:44:22.2	11.70
J013243-734412	01:32:43.8	-73:44:12.4	31.20
J013247-711639	01:32:47.4	-71:16:39.2	9.92
J013250-710324	01:32:50.8	-71:03:24.6	2.73
J013206-730804	01:32:06.8	-73:08:04.5	4.16
J013316-731627	01:33:16.1	-73:16:27.4	5.00
J013317-711520	01:33:17.6	-71:15:20.5	3.54
J013323-730324	01:33:23.4	-73:03:24.6	7.13
J013326-705331	01:33:26.5	-70:53:31.0	8.35

Table A2. Continued.

Name ATCA	R.A.$_{1400}$ (J2000)	Dec.$_{1400}$ (J2000)	S_{20} (mJy)
J013328-743632	01:33:28.2	-74:36:32.4	28.90
J013329-730303	01:33:29.8	-73:03:03.9	54.77
J013330-704519	01:33:30.9	-70:45:19.0	10.91
J013331-711629	01:33:31.5	-71:16:29.5	45.61
J013332-711556	01:33:32.6	-71:15:56.1	15.50
J013334-733644	01:33:34.8	-73:36:44.6	9.35
J013337-720219	01:33:37.0	-72:02:19.5	6.21
J013338-692836	01:33:38.6	-69:28:36.6	113.13
J013339-744608	01:33:39.4	-74:46:08.5	22.20
J013339-725057	01:33:39.9	-72:50:57.3	7.22
J013341-693651	01:33:41.8	-69:36:51.7	4.26
J013343-731749	01:33:43.1	-73:17:49.5	7.99
J013344-744613	01:33:44.3	-74:46:13.1	8.80
J013348-692843	01:33:48.8	-69:28:43.8	119.25
J013305-700218	01:33:05.6	-70:02:18.2	4.41
J013350-700419	01:33:50.8	-70:04:19.3	14.16
J013352-693550	01:33:52.4	-69:35:50.2	27.94
J013356-711014	01:33:56.5	-71:10:14.7	12.83
J013306-741931	01:33:06.2	-74:19:31.3	5.64
J013307-693034	01:33:07.1	-69:30:34.1	25.81
J013309-742917	01:33:09.3	-74:29:17.2	36.05
J013401-703421	01:34:01.9	-70:34:21.0	4.74
J013410-753525	01:34:10.9	-75:35:25.9	6.06
J013413-734756	01:34:13.4	-73:47:56.2	3.38
J013421-722717	01:34:21.7	-72:27:17.7	6.97
J013422-731809	01:34:22.9	-73:18:09.2	6.04
J013426-701414	01:34:26.6	-70:14:14.7	4.26
J013403-715118	01:34:03.8	-71:51:18.1	12.11
J013436-752412	01:34:36.4	-75:24:12.8	5.37
J013439-722125	01:34:39.1	-72:21:25.8	10.41
J013404-731122	01:34:04.3	-73:11:22.2	4.00
J013440-721246	01:34:40.0	-72:12:46.6	12.22
J013440-705803	01:34:40.7	-70:58:03.6	80.42
J013441-722432	01:34:41.3	-72:24:32.9	3.92
J013443-705626	01:34:43.9	-70:56:26.0	5.64
J013448-692142	01:34:48.8	-69:21:42.6	23.82
J013450-752359	01:34:50.3	-75:23:59.5	5.98
J013453-722444	01:34:53.5	-72:24:44.2	91.77
J013459-701644	01:34:59.5	-70:16:44.3	3.21
J013500-711258	01:35:00.2	-71:12:58.0	6.66
J013500-702211	01:35:00.5	-70:22:11.4	8.27
J013511-751200	01:35:11.0	-75:12:00.5	7.49
J013527-744137	01:35:27.3	-74:41:37.3	9.60
J013530-704824	01:35:30.0	-70:48:24.1	10.02
J013542-694428	01:35:42.6	-69:44:28.9	5.30
J013545-693029	01:35:45.8	-69:30:29.9	24.64
J013545-733202	01:35:45.9	-73:32:02.6	3.91
J013548-693012	01:35:48.2	-69:30:12.6	16.38
J013551-712603	01:35:51.8	-71:26:03.7	6.25
J013551-742919	01:35:51.8	-74:29:19.1	5.98

Table A2. Continued.

Name ATCA	R.A.$_{1400}$ (J2000)	Dec.$_{1400}$ (J2000)	S_{20} (mJy)
J013556-753905	01:35:56.5	-75:39:05.9	25.30
J013558-741248	01:35:58.9	-74:12:48.0	8.45
J013559-720259	01:35:59.9	-72:02:59.0	10.10
J013506-710155	01:35:06.8	-71:01:55.7	38.45
J013600-715510	01:36:00.9	-71:55:10.7	7.48
J013601-725057	01:36:01.3	-72:50:57.9	5.13
J013618-720723	01:36:18.3	-72:07:23.0	9.63
J013618-702901	01:36:18.9	-70:29:01.8	93.40
J013622-703412	01:36:22.6	-70:34:12.7	56.76
J013623-743250	01:36:23.5	-74:32:50.1	6.28
J013627-691840	01:36:27.7	-69:18:40.2	16.34
J013632-740659	01:36:32.2	-74:06:59.1	30.47
J013634-733653	01:36:34.7	-73:36:53.8	12.66
J013635-744333	01:36:35.0	-74:43:33.2	3.85
J013635-711647	01:36:35.9	-71:16:47.4	3.79
J013644-705608	01:36:44.4	-70:56:08.3	28.65
J013644-752314	01:36:44.8	-75:23:14.1	4.25
J013646-711725	01:36:46.0	-71:17:25.2	3.60
J013652-691643	01:36:52.0	-69:16:43.7	39.47
J013652-693938	01:36:52.2	-69:39:38.3	7.34
J013652-713719	01:36:52.2	-71:37:19.6	14.87
J013653-700836	01:36:53.3	-70:08:36.7	16.67
J013653-692610	01:36:53.4	-69:26:10.3	11.02
J013658-705723	01:36:58.9	-70:57:23.5	29.28
J013710-732735	01:37:10.0	-73:27:35.5	3.32
J013720-700731	01:37:20.8	-70:07:31.8	5.94
J013724-745333	01:37:24.1	-74:53:33.7	12.16
J013724-700658	01:37:24.2	-70:06:58.5	5.41
J013728-730621	01:37:28.3	-73:06:21.3	7.26
J013703-730414	01:37:03.0	-73:04:14.1	121.00
J013737-732802	01:37:37.7	-73:28:02.2	4.72
J013704-692137	01:37:04.3	-69:21:37.9	15.25
J013742-733049	01:37:42.4	-73:30:49.4	53.03
J013757-712240	01:37:57.9	-71:22:40.5	4.53
J013800-741351	01:38:00.4	-74:13:51.1	42.06
J013800-720329	01:38:00.5	-72:03:29.2	8.85
J013811-710308	01:38:11.4	-71:03:08.2	15.93
J013812-704414	01:38:12.2	-70:44:14.2	5.15
J013813-732338	01:38:13.3	-73:23:38.7	14.62
J013817-723549	01:38:17.0	-72:35:49.1	4.24
J013818-711448	01:38:18.0	-71:14:48.2	17.73
J013821-725703	01:38:21.5	-72:57:03.5	7.67
J013823-723652	01:38:23.4	-72:36:52.1	7.05
J013825-744115	01:38:25.1	-74:41:15.6	7.55
J013825-744135	01:38:25.4	-74:41:35.8	4.59
J013803-723202	01:38:03.7	-72:32:02.7	4.89
J013837-691235	01:38:37.6	-69:12:35.9	64.52
J013837-695221	01:38:37.7	-69:52:21.6	4.57
J013842-733750	01:38:42.1	-73:37:50.5	5.79
J013845-715912	01:38:45.3	-71:59:12.6	8.99

Table A2. Continued.

Name ATCA	R.A.$_{1400}$ (J2000)	Dec.$_{1400}$ (J2000)	S_{20} (mJy)
J013846-733806	01:38:46.3	-73:38:06.1	4.79
J013913-750040	01:39:13.4	-75:00:40.7	32.41
J013913-714606	01:39:13.6	-71:46:06.9	6.32
J013915-710445	01:39:15.3	-71:04:45.7	5.95
J013915-695543	01:39:15.6	-69:55:43.2	5.98
J013919-731655	01:39:19.6	-73:16:55.7	41.84
J013924-724144	01:39:24.7	-72:41:44.3	7.11
J013925-745548	01:39:25.2	-74:55:48.4	8.88
J013925-700613	01:39:25.3	-70:06:13.1	8.99
J013930-730955	01:39:30.9	-73:09:55.0	8.23
J013933-703235	01:39:33.6	-70:32:35.6	11.08
J013937-714409	01:39:37.5	-71:44:09.4	6.25
J013941-702051	01:39:41.3	-70:20:51.0	7.26
J013946-693324	01:39:46.7	-69:33:24.4	30.56
J013905-725628	01:39:05.5	-72:56:28.3	66.63
J013905-741639	01:39:05.9	-74:16:39.7	4.02
J013950-731000	01:39:50.6	-73:10:00.2	27.10
J014000-702410	01:40:00.2	-70:24:10.3	5.84
J014010-742249	01:40:10.0	-74:22:49.2	5.35
J014013-742312	01:40:13.1	-74:23:12.7	5.18
J014022-733049	01:40:22.4	-73:30:49.0	4.25
J014023-692830	01:40:23.5	-69:28:30.1	14.22
J014025-705715	01:40:25.0	-70:57:15.9	10.24
J014025-711312	01:40:25.2	-71:13:12.0	8.18
J014027-724812	01:40:27.6	-72:48:12.9	13.74
J014039-725059	01:40:39.6	-72:50:59.2	15.22
J014005-702842	01:40:05.9	-70:28:42.1	4.78
J014050-724059	01:40:50.3	-72:40:59.1	15.89
J014056-704232	01:40:56.0	-70:42:32.5	7.04
J014056-694437	01:40:56.9	-69:44:37.7	40.37
J014058-704245	01:40:58.0	-70:42:45.9	8.02
J014006-692158	01:40:06.0	-69:21:58.2	9.76
J014006-693915	01:40:06.7	-69:39:15.6	43.64
J014008-693846	01:40:08.7	-69:38:46.0	18.58
J014110-714047	01:41:10.0	-71:40:47.0	4.76
J014110-714929	01:41:10.8	-71:49:29.8	6.70
J014114-740731	01:41:14.8	-74:07:31.8	52.58
J014115-701455	01:41:15.2	-70:14:55.2	19.66
J014119-704118	01:41:19.3	-70:41:18.3	34.99
J014126-753047	01:41:26.1	-75:30:47.7	9.52
J014128-701636	01:41:28.9	-70:16:36.4	45.95
J014128-712540	01:41:28.9	-71:25:40.3	5.10
J014136-733117	01:41:36.0	-73:31:17.6	6.20
J014139-712434	01:41:39.2	-71:24:34.6	5.24
J014143-722623	01:41:43.0	-72:26:23.3	40.06
J014105-715828	01:41:05.8	-71:58:28.6	25.09
J014154-701530	01:41:54.1	-70:15:30.6	9.88
J014155-694127	01:41:55.1	-69:41:27.7	498.49
J014106-722750	01:41:06.4	-72:27:50.0	90.41
J014211-700640	01:42:11.3	-70:06:40.4	29.31

Table A2. Continued.

Name ATCA	R.A.$_{1400}$ (J2000)	Dec.$_{1400}$ (J2000)	S_{20} (mJy)
J014223-730214	01:42:23.8	-73:02:14.9	9.02
J014223-721112	01:42:23.9	-72:11:12.9	9.35
J014228-730160	01:42:28.3	-73:01:60.0	14.97
J014232-713841	01:42:32.9	-71:38:41.2	5.30
J014233-733657	01:42:33.0	-73:36:57.1	10.26
J014236-723001	01:42:36.0	-72:30:01.3	36.71
J014204-740756	01:42:04.2	-74:07:56.1	5.68
J014243-711216	01:42:43.0	-71:12:16.5	4.58
J014249-735837	01:42:49.3	-73:58:37.2	19.73
J014249-743444	01:42:49.9	-74:34:44.8	40.57
J014253-743843	01:42:53.6	-74:38:43.0	6.23
J014255-700919	01:42:55.6	-70:09:19.0	8.30
J014311-712932	01:43:11.6	-71:29:32.6	5.99
J014315-733800	01:43:15.5	-73:38:00.1	6.74
J014316-713642	01:43:16.2	-71:36:42.7	14.01
J014318-713628	01:43:18.9	-71:36:28.9	12.85
J014302-701514	01:43:02.4	-70:15:14.0	22.38
J014325-744306	01:43:25.8	-74:43:06.4	3.87
J014339-731848	01:43:39.1	-73:18:48.1	5.59
J014305-731616	01:43:05.1	-73:16:16.7	10.68
J014351-722220	01:43:51.9	-72:22:20.2	18.26
J014358-743132	01:43:58.6	-74:31:32.6	30.75
J014410-703634	01:44:10.0	-70:36:34.0	12.99
J014410-725522	01:44:10.5	-72:55:22.8	4.60
J014416-702746	01:44:16.9	-70:27:46.7	5.43
J014402-714124	01:44:02.5	-71:41:24.9	5.32
J014424-730944	01:44:24.4	-73:09:44.4	6.21
J014436-743312	01:44:36.9	-74:33:12.9	26.26
J014440-701919	01:44:40.0	-70:19:19.2	75.28
J014446-700902	01:44:46.4	-70:09:02.7	10.81
J014406-695556	01:44:06.0	-69:55:56.2	7.79
J014408-750918	01:44:08.9	-75:09:18.2	6.28
J014512-730247	01:45:12.5	-73:02:47.7	30.43
J014514-740449	01:45:14.7	-74:04:49.1	4.28
J014515-704842	01:45:15.8	-70:48:42.8	100.39
J014520-742124	01:45:20.2	-74:21:24.2	6.92
J014523-751758	01:45:23.5	-75:17:58.4	13.45
J014524-730822	01:45:24.9	-73:08:22.0	12.26
J014503-712516	01:45:03.3	-71:25:16.1	15.55
J014541-695357	01:45:41.1	-69:53:57.6	8.82
J014546-751617	01:45:46.7	-75:16:17.8	132.51
J014611-745115	01:46:11.6	-74:51:15.3	6.05
J014637-740428	01:46:37.0	-74:04:28.9	12.49
J014643-724404	01:46:43.9	-72:44:04.3	20.09
J014608-701938	01:46:08.5	-70:19:38.1	16.00
J014609-740817	01:46:09.1	-74:08:17.9	12.81
J014700-725733	01:47:00.0	-73:00:11.0	5.11
J014702-742716	01:47:02.6	-74:27:16.3	8.15
J014740-730300	01:47:40.3	-73:03:00.7	9.17
J014749-744649	01:47:49.7	-74:46:49.1	8.89

Table A2. Continued.

Name ATCA	R.A.$_{1400}$ (J2000)	Dec.$_{1400}$ (J2000)	S_{20} (mJy)
J014754-752535	01:47:54.4	-75:25:35.5	16.79
J014758-744833	01:47:58.7	-74:48:33.4	70.06
J014800-725733	01:48:00.1	-72:57:33.7	37.82
J014810-744344	01:48:10.0	-74:43:44.2	71.07
J014858-750724	01:48:58.8	-75:07:24.7	6.37
J014859-724950	01:48:59.6	-72:49:50.0	27.88
J014918-740111	01:49:18.5	-74:01:11.1	10.26
J014928-730226	01:49:28.2	-73:02:26.1	41.50
J014903-750639	01:49:03.3	-75:06:39.9	14.19
J014906-731253	01:49:06.1	-73:12:53.2	29.47

Table A3. 36 cm Catalogue of point sources in the field of the SMC with integrated flux density.

Name ATCA	R.A.$_{843}$ (J2000)	Dec.$_{843}$ (J2000)	S_{36} (mJy)
J001459-750128	00:14:59.8	-75:01:28.7	14.38
J001526-744248	00:15:26.3	-74:42:48.7	12.61
J001544-744902	00:15:44.4	-74:49:02.9	3.75
J001557-744558	00:15:57.8	-74:45:58.1	10.23
J001601-741658	00:16:01.2	-74:16:58.5	6.92
J001614-741446	00:16:14.0	-74:14:46.5	3.28
J001622-744524	00:16:22.0	-74:45:24.7	8.38
J001626-742501	00:16:26.3	-74:25:01.6	11.70
J001638-743348	00:16:38.9	-74:33:48.2	5.21
J001638-743523	00:16:38.9	-74:35:23.1	3.65
J001608-741541	00:16:08.6	-74:15:41.1	4.14
J001726-735028	00:17:26.0	-73:50:28.1	5.79
J001748-745148	00:17:48.9	-74:51:48.5	4.05
J001755-732758	00:17:55.5	-73:27:58.4	4.16
J001758-732940	00:17:58.8	-73:29:40.8	6.41
J001817-741520	00:18:17.1	-74:15:20.4	38.75
J001818-732517	00:18:18.6	-73:25:17.1	15.34
J001818-730907	00:18:18.9	-73:09:07.1	18.34
J001820-734145	00:18:20.5	-73:41:45.7	3.41
J001846-741159	00:18:46.0	-74:11:59.7	3.14
J001857-734219	00:18:57.5	-73:42:19.4	98.31
J001858-732449	00:18:58.8	-73:24:49.4	52.32
J001860-732254	00:18:60.0	-73:22:54.8	3.77
J001916-742916	00:19:16.9	-74:29:16.3	3.28
J001902-734127	00:19:02.6	-73:41:27.7	28.70
J001934-733308	00:19:34.1	-73:33:08.7	10.79
J001935-734922	00:19:35.6	-73:49:22.3	12.73
J001935-744432	00:19:35.9	-74:44:32.0	5.27
J001938-745803	00:19:38.6	-74:58:03.3	2.91
J001941-744644	00:19:41.2	-74:46:44.7	5.83
J001909-744030	00:19:09.7	-74:40:30.1	25.15
J002001-724439	00:20:01.0	-72:44:39.4	3.82
J002010-744628	00:20:10.8	-74:46:28.6	4.18
J002019-732119	00:20:19.9	-73:21:19.7	86.90
J002020-731854	00:20:20.5	-73:18:54.3	14.92

Table A3. Continued.

Name ATCA	R.A.$_{843}$ (J2000)	Dec.$_{843}$ (J2000)	S_{36} (mJy)
J002024-725722	00:20:24.5	-72:57:22.0	3.93
J002024-745757	00:20:24.6	-74:57:57.0	13.63
J002031-724157	00:20:31.1	-72:41:57.3	15.85
J002033-735042	00:20:33.5	-73:50:42.1	3.05
J002033-733928	00:20:33.8	-73:39:28.5	3.29
J002034-743143	00:20:34.2	-74:31:43.9	7.67
J002044-744310	00:20:44.0	-74:43:10.9	75.39
J002047-732133	00:20:47.6	-73:21:33.5	52.41
J002005-723238	00:20:05.7	-72:32:38.3	7.78
J002050-751359	00:20:50.8	-75:13:59.2	3.37
J002051-735326	00:20:51.8	-73:53:26.8	11.17
J002054-734633	00:20:54.3	-73:46:33.8	7.09
J002007-732748	00:20:07.5	-73:27:48.5	18.88
J002008-751228	00:20:08.1	-75:12:28.7	43.17
J002101-743614	00:21:01.7	-74:36:14.6	4.40
J002113-722307	00:21:13.0	-72:23:07.8	5.74
J002120-725528	00:21:20.5	-72:55:28.0	21.93
J002120-725826	00:21:20.5	-72:58:26.8	3.21
J002125-732217	00:21:25.3	-73:22:17.5	31.70
J002126-745124	00:21:26.6	-74:51:24.2	6.19
J002129-744945	00:21:29.4	-74:49:45.7	5.21
J002129-734828	00:21:29.9	-73:48:28.1	5.38
J002132-750124	00:21:32.7	-75:01:24.8	30.85
J002144-741500	00:21:44.0	-74:15:00.1	166.40
J002145-723543	00:21:45.1	-72:35:43.2	11.47
J002145-745253	00:21:45.9	-74:52:53.4	6.65
J002152-743123	00:21:52.5	-74:31:23.1	41.16
J002154-723810	00:21:54.5	-72:38:10.3	3.17
J002156-722554	00:21:56.1	-72:25:54.4	6.76
J002210-751355	00:22:10.0	-75:13:55.9	12.23
J002215-732601	00:22:15.4	-73:26:01.5	3.39
J002215-730833	00:22:15.8	-73:08:33.8	13.67
J002217-731458	00:22:17.4	-73:14:58.6	3.15
J002217-742813	00:22:17.5	-74:28:13.3	603.10
J002202-734555	00:22:02.5	-73:45:55.6	6.39
J002220-722105	00:22:20.3	-72:21:05.6	7.75
J002225-715026	00:22:25.9	-71:50:26.2	10.84
J002226-713718	00:22:26.7	-71:37:18.9	25.04
J002227-734134	00:22:27.7	-73:41:34.5	11.10
J002228-724455	00:22:28.7	-72:44:55.7	4.05
J002230-715859	00:22:30.8	-71:58:59.9	3.48
J002231-743836	00:22:31.1	-74:38:36.8	5.82
J002237-724638	00:22:37.1	-72:46:38.4	10.61
J002239-744339	00:22:39.3	-74:43:39.8	3.96
J002239-742722	00:22:39.8	-74:27:22.6	27.30
J002248-734008	00:22:48.0	-73:40:08.5	81.93
J002248-714418	00:22:48.8	-71:44:18.7	5.45
J002251-742914	00:22:51.7	-74:29:14.0	3.64
J002253-741136	00:22:53.9	-74:11:36.1	7.95
J002254-744854	00:22:54.5	-74:48:54.8	3.32

Table A3. Continued.

Name ATCA	R.A.$_{843}$ (J2000)	Dec.$_{843}$ (J2000)	S_{36} (mJy)
J002254-740847	00:22:54.9	-74:08:47.6	7.50
J002255-741015	00:22:55.0	-74:10:15.2	6.98
J002256-723307	00:22:56.4	-72:33:07.6	114.10
J002207-740941	00:22:07.2	-74:09:41.6	34.62
J002301-722740	00:23:01.4	-72:27:40.9	10.59
J002315-744700	00:23:15.2	-74:47:00.1	6.33
J002318-720032	00:23:18.5	-72:00:32.4	3.80
J002327-722406	00:23:27.5	-72:24:06.7	15.76
J002303-721722	00:23:03.8	-72:17:22.8	3.82
J002331-722944	00:23:31.1	-72:29:44.4	6.31
J002333-732730	00:23:33.9	-73:27:30.7	7.23
J002336-735528	00:23:36.4	-73:55:28.8	434.60
J002343-750240	00:23:43.3	-75:02:40.8	9.21
J002350-731704	00:23:50.0	-73:17:04.4	32.05
J002357-724746	00:23:57.9	-72:47:46.6	3.32
J002306-734842	00:23:06.0	-73:48:42.7	3.78
J002307-742219	00:23:07.2	-74:22:19.2	3.79
J002309-715920	00:23:09.2	-71:59:20.2	4.50
J002400-723255	00:24:00.0	-72:32:55.3	6.32
J002400-725908	00:24:00.8	-72:59:08.6	33.40
J002410-714251	00:24:10.5	-71:42:51.4	5.85
J002410-735714	00:24:10.9	-73:57:14.8	328.70
J002411-732847	00:24:11.9	-73:28:47.1	3.28
J002415-732127	00:24:15.6	-73:21:27.2	3.85
J002418-751819	00:24:18.0	-75:18:19.8	8.47
J002421-740338	00:24:21.1	-74:03:38.0	7.19
J002422-714908	00:24:22.2	-71:49:08.7	16.89
J002428-703550	00:24:28.3	-70:35:50.0	8.75
J002430-721226	00:24:30.3	-72:12:26.5	21.26
J002437-722533	00:24:37.5	-72:25:33.3	7.63
J002439-730501	00:24:39.7	-73:05:01.5	4.69
J002404-711758	00:24:04.4	-71:17:58.5	3.06
J002440-734537	00:24:40.0	-73:45:37.7	63.10
J002443-741416	00:24:43.1	-74:14:16.5	8.14
J002443-745600	00:24:43.7	-74:56:00.2	27.52
J002444-721525	00:24:44.6	-72:15:25.2	3.51
J002445-724205	00:24:45.9	-72:42:05.9	4.55
J002446-715915	00:24:46.4	-71:59:15.0	79.28
J002448-705544	00:24:48.6	-70:55:44.2	132.60
J002450-704855	00:24:50.6	-70:48:55.0	4.36
J002451-703013	00:24:51.3	-70:30:13.5	3.95
J002459-732416	00:24:59.3	-73:24:16.1	2.77
J002408-731445	00:24:08.8	-73:14:45.7	3.23
J002408-725807	00:24:08.9	-72:58:07.7	71.49
J002409-711505	00:24:09.6	-71:15:05.1	7.95
J002511-721154	00:25:11.1	-72:11:54.6	8.71
J002517-735023	00:25:17.5	-73:50:23.9	9.20
J002521-750049	00:25:21.6	-75:00:49.7	4.42
J002523-735653	00:25:23.0	-73:56:53.6	15.59
J002503-720234	00:25:03.9	-72:02:34.2	14.63

Table A3. Continued.

Name ATCA	R.A.$_{843}$ (J2000)	Dec.$_{843}$ (J2000)	S_{36} (mJy)
J002535-723609	00:25:35.4	-72:36:09.3	11.73
J002537-745730	00:25:37.7	-74:57:30.9	4.48
J002542-740718	00:25:42.5	-74:07:18.4	12.72
J002544-743133	00:25:44.6	-74:31:33.9	33.90
J002548-701440	00:25:48.1	-70:14:40.2	7.21
J002548-732151	00:25:48.3	-73:21:51.4	10.30
J002505-742644	00:25:05.2	-74:26:44.4	3.35
J002551-710024	00:25:51.2	-71:00:24.8	4.77
J002553-745453	00:25:53.3	-74:54:53.2	15.11
J002554-722353	00:25:54.7	-72:23:53.8	3.45
J002555-732057	00:25:55.3	-73:20:57.4	8.80
J002557-731312	00:25:57.8	-73:13:12.9	2.80
J002557-721939	00:25:57.9	-72:19:39.9	4.23
J002506-714024	00:25:06.4	-71:40:24.0	3.79
J002612-713528	00:26:12.8	-71:35:28.0	4.51
J002614-705135	00:26:14.2	-70:51:35.1	10.17
J002614-744449	00:26:14.8	-74:44:49.8	10.84
J002621-743740	00:26:21.2	-74:37:40.6	18.82
J002622-742258	00:26:22.6	-74:22:58.3	9.11
J002624-704922	00:26:24.6	-70:49:22.4	6.62
J002628-740019	00:26:28.1	-74:00:19.8	13.71
J002629-723224	00:26:29.8	-72:32:24.2	6.83
J002603-732149	00:26:03.9	-73:21:49.3	40.30
J002631-741316	00:26:31.7	-74:13:16.2	47.85
J002631-724133	00:26:31.8	-72:41:33.8	9.07
J002637-724959	00:26:37.9	-72:49:59.8	34.96
J002640-711523	00:26:40.8	-71:15:23.3	3.44
J002646-710008	00:26:46.0	-71:00:08.4	47.53
J002646-744137	00:26:46.0	-74:41:37.6	51.30
J002646-732734	00:26:46.9	-73:27:34.9	21.32
J002647-731013	00:26:47.3	-73:10:13.4	2.70
J002648-704041	00:26:48.1	-70:40:41.8	90.64
J002605-712541	00:26:05.3	-71:25:41.4	8.29
J002605-724948	00:26:05.4	-72:49:48.7	22.54
J002605-720400	00:26:05.6	-72:04:00.9	4.96
J002655-740255	00:26:55.9	-74:02:55.2	5.28
J002657-720240	00:26:57.8	-72:02:40.9	15.12
J002658-741031	00:26:58.5	-74:10:31.7	65.36
J002606-732309	00:26:06.9	-73:23:09.7	114.00
J002607-742130	00:26:07.7	-74:21:30.1	12.48
J002608-725933	00:26:08.7	-72:59:33.0	3.15
J002701-734459	00:27:01.7	-73:44:59.9	9.96
J002724-703156	00:27:24.3	-70:31:56.6	32.77
J002724-733651	00:27:24.3	-73:36:51.4	22.11
J002726-710807	00:27:26.9	-71:08:07.0	5.40
J002729-720231	00:27:29.2	-72:02:31.8	6.83
J002703-720348	00:27:03.4	-72:03:48.2	3.66
J002735-733137	00:27:35.6	-73:31:37.9	34.01
J002737-731114	00:27:37.4	-73:11:14.6	3.92
J002738-744530	00:27:38.6	-74:45:30.1	3.16

Table A3. Continued.

Name ATCA	R.A.$_{843}$ (J2000)	Dec.$_{843}$ (J2000)	S_{36} (mJy)
J002742-751252	00:27:42.6	-75:12:52.6	6.50
J002745-722012	00:27:45.8	-72:20:12.4	4.32
J002706-742532	00:27:06.7	-74:25:32.3	2.90
J002800-702941	00:28:00.7	-70:29:41.0	4.01
J002814-731130	00:28:14.6	-73:11:30.9	22.68
J002816-741831	00:28:16.3	-74:18:31.2	21.44
J002816-711421	00:28:16.4	-71:14:21.9	2.95
J002817-741216	00:28:17.7	-74:12:16.1	3.09
J002820-723156	00:28:20.1	-72:31:56.2	10.15
J002820-705344	00:28:20.3	-70:53:44.3	3.97
J002821-733320	00:28:21.0	-73:33:20.5	9.00
J002822-735034	00:28:22.3	-73:50:34.0	7.00
J002823-724311	00:28:23.4	-72:43:11.8	46.55
J002825-703452	00:28:25.9	-70:34:52.3	78.54
J002832-705609	00:28:32.9	-70:56:09.2	13.54
J002837-703629	00:28:37.9	-70:36:29.2	4.29
J002804-711940	00:28:04.4	-71:19:40.2	3.22
J002804-724506	00:28:04.7	-72:45:06.9	6.26
J002840-742012	00:28:40.6	-74:20:12.6	3.11
J002842-704515	00:28:42.0	-70:45:15.8	91.87
J002843-731326	00:28:43.3	-73:13:26.9	4.76
J002856-731352	00:28:56.1	-73:13:52.8	3.65
J002857-713538	00:28:57.1	-71:35:38.0	3.59
J002857-732342	00:28:57.7	-73:23:42.7	10.22
J002808-703433	00:28:08.2	-70:34:33.4	6.05
J002912-740903	00:29:12.0	-74:09:03.8	13.98
J002917-723707	00:29:17.1	-72:37:07.0	3.20
J002918-722810	00:29:18.4	-72:28:10.3	149.70
J002922-711513	00:29:22.5	-71:15:13.9	3.14
J002923-744456	00:29:23.8	-74:44:56.9	13.26
J002925-720027	00:29:25.3	-72:00:27.4	5.28
J002926-732343	00:29:26.4	-73:23:43.4	6.91
J002929-703218	00:29:29.4	-70:32:18.7	32.03
J002929-731624	00:29:29.5	-73:16:24.8	16.81
J002903-712729	00:29:03.2	-71:27:29.1	18.01
J002936-734540	00:29:36.5	-73:45:40.0	6.55
J002936-721920	00:29:36.8	-72:19:20.0	6.11
J002937-722326	00:29:37.2	-72:23:26.0	3.29
J002938-712954	00:29:38.0	-71:29:54.4	13.70
J002944-712633	00:29:44.2	-71:26:33.1	10.09
J002945-730422	00:29:45.5	-73:04:22.1	42.79
J002950-720731	00:29:50.6	-72:07:31.0	41.04
J002951-720002	00:29:51.3	-72:00:02.1	3.90
J002953-730254	00:29:53.9	-73:02:54.3	2.70
J002956-714636	00:29:56.2	-71:46:36.3	38.23
J002957-733714	00:29:57.9	-73:37:14.3	2.90
J002958-740609	00:29:58.1	-74:06:09.3	3.43
J002906-735348	00:29:06.8	-73:53:48.9	132.60
J002908-711626	00:29:08.1	-71:16:26.5	3.52
J003014-744926	00:30:14.4	-74:49:26.8	6.95

Table A3. Continued.

Name ATCA	R.A.$_{843}$ (J2000)	Dec.$_{843}$ (J2000)	S_{36} (mJy)
J003021-735647	00:30:21.2	-73:56:47.7	7.26
J003022-721923	00:30:22.4	-72:19:23.2	2.80
J003022-733629	00:30:22.8	-73:36:29.3	2.40
J003025-702333	00:30:25.3	-70:23:33.5	7.26
J003025-731812	00:30:25.5	-73:18:12.0	63.90
J003035-742911	00:30:35.2	-74:29:11.9	140.10
J003036-735144	00:30:36.4	-73:51:44.7	46.41
J003038-725717	00:30:38.9	-72:57:17.0	16.13
J003042-745933	00:30:42.6	-74:59:33.6	7.18
J003047-715449	00:30:47.2	-71:54:49.8	10.40
J003052-713441	00:30:52.2	-71:34:41.4	10.44
J003052-713738	00:30:52.7	-71:37:38.7	2.90
J003057-722435	00:30:57.8	-72:24:35.6	3.83
J003006-724154	00:30:06.5	-72:41:54.4	4.37
J003006-740011	00:30:06.5	-74:00:11.7	76.24
J003101-705839	00:31:01.1	-70:58:39.3	32.54
J003101-723732	00:31:01.6	-72:37:32.0	3.67
J003101-715511	00:31:01.9	-71:55:11.6	11.42
J003113-714232	00:31:13.4	-71:42:32.8	3.53
J003116-714951	00:31:16.6	-71:49:51.4	12.26
J003119-732301	00:31:19.9	-73:23:01.2	16.77
J003120-703649	00:31:20.4	-70:36:49.4	188.60
J003125-701953	00:31:25.6	-70:19:53.8	9.79
J003127-740544	00:31:27.8	-74:05:44.3	3.27
J003129-704110	00:31:29.2	-70:41:10.3	10.21
J003131-721018	00:31:31.9	-72:10:18.7	3.67
J003132-743031	00:31:32.1	-74:30:31.0	45.61
J003136-703314	00:31:36.3	-70:33:14.2	73.69
J003137-715024	00:31:37.0	-71:50:24.6	4.14
J003140-734746	00:31:40.2	-73:47:46.2	4.35
J003140-735514	00:31:40.8	-73:55:14.1	4.12
J003141-743447	00:31:41.2	-74:34:47.8	85.05
J003141-711224	00:31:41.7	-71:12:24.7	5.00
J003152-723141	00:31:52.3	-72:31:41.5	6.89
J003152-721303	00:31:52.5	-72:13:03.0	3.00
J003157-724835	00:31:57.6	-72:48:35.1	4.33
J003158-703515	00:31:58.8	-70:35:15.6	79.37
J003106-710112	00:31:06.6	-71:01:12.0	92.90
J003107-710659	00:31:07.7	-71:06:59.4	39.50
J003107-724812	00:31:07.7	-72:48:12.0	9.05
J003108-715103	00:31:08.0	-71:51:03.8	4.97
J003211-703814	00:32:11.0	-70:38:14.0	10.34
J003214-723122	00:32:14.5	-72:31:22.7	3.65
J003215-704804	00:32:15.1	-70:48:04.8	4.73
J003215-713550	00:32:15.3	-71:35:50.9	13.24
J003217-703947	00:32:17.4	-70:39:47.0	23.32
J003225-705126	00:32:25.4	-70:51:26.7	7.24
J003229-730650	00:32:29.9	-73:06:50.1	106.60
J003230-703118	00:32:30.2	-70:31:18.7	19.29
J003230-710419	00:32:30.3	-71:04:19.8	9.16

Table A3. Continued.

Name ATCA	R.A.$_{843}$ (J2000)	Dec.$_{843}$ (J2000)	S_{36} (mJy)
J003234-734139	00:32:34.0	-73:41:39.1	7.98
J003237-734449	00:32:37.0	-73:44:49.1	4.72
J003237-704913	00:32:37.1	-70:49:13.5	14.64
J003204-701822	00:32:04.5	-70:18:22.2	14.80
J003242-711636	00:32:42.1	-71:16:36.3	7.64
J003242-733150	00:32:42.1	-73:31:50.5	80.76
J003247-733742	00:32:47.5	-73:37:42.0	2.90
J003249-741856	00:32:49.8	-74:18:56.6	75.42
J003250-735740	00:32:50.4	-73:57:40.6	6.82
J003252-722932	00:32:52.1	-72:29:32.6	55.69
J003253-701901	00:32:53.9	-70:19:01.4	11.67
J003254-714545	00:32:54.7	-71:45:45.0	109.80
J003208-735038	00:32:08.4	-73:50:38.2	43.78
J003300-715315	00:33:00.8	-71:53:15.5	8.83
J003311-745519	00:33:11.4	-74:55:19.4	37.12
J003311-740342	00:33:11.6	-74:03:42.8	19.22
J003311-703127	00:33:11.7	-70:31:27.1	61.71
J003311-704845	00:33:11.9	-70:48:45.5	3.86
J003314-705549	00:33:14.6	-70:55:49.4	124.20
J003315-741840	00:33:15.7	-74:18:40.6	7.22
J003318-703225	00:33:18.3	-70:32:25.6	15.70
J003322-731032	00:33:22.0	-73:10:32.6	3.25
J003325-722346	00:33:25.6	-72:23:46.1	8.63
J003326-723710	00:33:26.0	-72:37:10.7	24.28
J003303-704440	00:33:03.9	-70:44:40.2	3.18
J003331-701331	00:33:31.6	-70:13:31.4	5.66
J003304-715611	00:33:04.8	-71:56:11.8	3.91
J003342-743056	00:33:42.5	-74:30:56.0	17.54
J003342-704119	00:33:42.7	-70:41:19.2	21.48
J003345-732113	00:33:45.4	-73:21:13.0	7.35
J003346-720202	00:33:46.3	-72:02:02.0	11.52
J003347-731439	00:33:47.6	-73:14:39.2	8.79
J003305-742127	00:33:05.3	-74:21:27.6	16.05
J003305-732719	00:33:05.5	-73:27:19.9	3.59
J003352-703053	00:33:52.5	-70:30:53.8	90.75
J003352-721052	00:33:52.8	-72:10:52.9	6.84
J003353-701917	00:33:53.1	-70:19:17.6	9.45
J003353-725959	00:33:53.4	-72:59:59.6	3.55
J003355-721237	00:33:55.0	-72:12:37.2	9.52
J003357-722840	00:33:57.2	-72:28:40.8	36.56
J003357-742323	00:33:57.4	-74:23:23.6	43.59
J003358-700823	00:33:58.0	-70:08:23.9	5.88
J003358-703952	00:33:58.9	-70:39:52.1	16.32
J003401-702626	00:34:01.4	-70:26:26.3	138.50
J003401-703522	00:34:01.6	-70:35:22.2	3.15
J003401-711017	00:34:01.9	-71:10:17.9	5.48
J003413-733326	00:34:13.7	-73:33:26.6	433.60
J003423-731416	00:34:23.5	-73:14:16.6	2.80
J003423-721142	00:34:23.7	-72:11:42.7	255.40
J003425-733510	00:34:25.6	-73:35:10.5	110.40

Table A3. Continued.

Name ATCA	R.A.$_{843}$ (J2000)	Dec.$_{843}$ (J2000)	S_{36} (mJy)
J003426-715452	00:34:26.5	-71:54:52.1	8.92
J003403-714553	00:34:03.6	-71:45:53.7	14.55
J003432-713309	00:34:32.6	-71:33:09.4	4.98
J003435-722751	00:34:35.7	-72:27:51.4	10.14
J003439-724143	00:34:39.9	-72:41:43.7	12.63
J003446-703951	00:34:46.2	-70:39:51.4	6.27
J003447-705132	00:34:47.7	-70:51:32.7	3.89
J003450-742941	00:34:50.0	-74:29:41.6	3.76
J003450-704451	00:34:50.7	-70:44:51.2	3.26
J003452-724610	00:34:52.1	-72:46:10.0	3.65
J003453-705227	00:34:53.2	-70:52:27.9	9.04
J003454-703801	00:34:54.7	-70:38:01.1	3.54
J003454-713602	00:34:54.9	-71:36:02.1	9.32
J003408-702529	00:34:08.8	-70:25:29.0	185.20
J003409-720239	00:34:09.9	-72:02:39.6	4.08
J003511-710956	00:35:11.2	-71:09:56.5	104.10
J003512-701030	00:35:12.8	-70:10:30.0	4.43
J003524-732222	00:35:24.3	-73:22:22.2	40.14
J003525-713749	00:35:25.1	-71:37:49.7	4.33
J003528-720655	00:35:28.5	-72:06:55.1	3.22
J003530-723654	00:35:30.9	-72:36:54.7	13.81
J003536-714603	00:35:36.5	-71:46:03.6	26.22
J003504-730653	00:35:04.2	-73:06:53.8	7.54
J003544-735208	00:35:44.9	-73:52:08.2	19.34
J003547-721115	00:35:47.1	-72:11:15.7	11.19
J003551-725300	00:35:51.8	-72:53:00.7	42.08
J003506-702200	00:35:06.3	-70:22:00.1	6.94
J003610-725401	00:36:10.8	-72:54:01.0	13.10
J003617-735955	00:36:17.7	-73:59:55.8	4.06
J003619-725857	00:36:19.2	-72:58:57.3	5.90
J003619-720942	00:36:19.8	-72:09:42.3	61.13
J003623-720854	00:36:23.7	-72:08:54.6	31.50
J003624-725341	00:36:24.0	-72:53:41.8	15.13
J003626-701514	00:36:26.6	-70:15:14.3	5.51
J003627-714633	00:36:27.8	-71:46:33.4	21.89
J003636-715130	00:36:36.2	-71:51:30.7	8.68
J003642-735423	00:36:42.3	-73:54:23.1	5.40
J003645-705317	00:36:45.2	-70:53:17.0	7.47
J003645-723437	00:36:45.3	-72:34:37.3	3.39
J003647-713610	00:36:47.7	-71:36:10.9	26.03
J003650-703932	00:36:50.6	-70:39:32.3	10.07
J003650-730650	00:36:50.6	-73:06:50.8	4.79
J003655-741351	00:36:55.0	-74:13:51.9	5.96
J003656-744428	00:36:56.6	-74:44:28.0	8.56
J003658-713808	00:36:58.9	-71:38:08.2	10.37
J003659-720209	00:36:59.8	-72:02:09.8	3.23
J003607-751216	00:36:07.5	-75:12:16.1	9.10
J003609-742921	00:36:09.3	-74:29:21.6	7.59
J003700-714903	00:37:00.8	-71:49:03.2	12.61
J003701-743049	00:37:01.7	-74:30:49.1	3.02

Table A3. Continued.

Name ATCA	R.A.$_{843}$ (J2000)	Dec.$_{843}$ (J2000)	S_{36} (mJy)
J003715-751414	00:37:15.4	-75:14:14.1	48.42
J003716-705641	00:37:16.0	-70:56:41.5	12.01
J003703-704724	00:37:03.4	-70:47:24.5	24.05
J003732-704856	00:37:32.0	-70:48:56.2	3.14
J003732-751305	00:37:32.7	-75:13:05.8	4.76
J003738-714101	00:37:38.5	-71:41:01.4	6.18
J003743-710735	00:37:43.5	-71:07:35.6	83.19
J003705-730753	00:37:05.9	-73:07:53.1	3.32
J003751-735129	00:37:51.2	-73:51:29.4	14.70
J003755-704312	00:37:55.1	-70:43:12.3	9.01
J003756-725159	00:37:56.8	-72:51:59.6	255.86
J003757-720551	00:37:57.2	-72:05:51.4	5.55
J003707-713955	00:37:07.7	-71:39:55.8	34.72
J003709-712053	00:37:09.2	-71:20:53.7	13.34
J003814-701445	00:38:14.7	-70:14:45.4	4.85
J003818-713147	00:38:18.3	-71:31:47.2	4.25
J003802-730430	00:38:02.4	-73:04:30.4	8.08
J003820-723409	00:38:20.1	-72:34:09.9	21.10
J003821-743036	00:38:21.2	-74:30:36.6	3.77
J003822-723244	00:38:22.3	-72:32:44.2	5.40
J003824-742211	00:38:24.7	-74:22:11.4	436.40
J003828-740451	00:38:28.3	-74:04:51.1	5.50
J003829-724703	00:38:29.2	-72:47:03.0	4.84
J003846-705607	00:38:46.9	-70:56:07.1	5.68
J003805-745030	00:38:05.3	-74:50:30.8	27.82
J003850-720011	00:38:50.0	-72:00:11.8	5.62
J003850-704210	00:38:50.1	-70:42:10.3	5.96
J003850-720848	00:38:50.1	-72:08:48.0	10.67
J003851-731052	00:38:51.1	-73:10:52.6	13.84
J003852-732950	00:38:52.0	-73:29:50.5	7.23
J003854-702054	00:38:54.2	-70:20:54.8	4.23
J003855-704932	00:38:55.1	-70:49:32.5	6.24
J003857-705923	00:38:57.3	-70:59:23.3	8.17
J003857-724851	00:38:57.7	-72:48:51.8	5.70
J003858-702000	00:38:58.7	-70:20:00.1	3.55
J003808-710719	00:38:08.4	-71:07:19.8	7.46
J003809-735022	00:38:09.1	-73:50:22.4	208.50
J003901-725733	00:39:01.7	-72:57:33.9	12.48
J003918-720355	00:39:18.6	-72:03:55.8	23.07
J003924-724310	00:39:24.0	-72:43:10.6	8.00
J003927-713636	00:39:27.0	-71:36:36.2	6.57
J003927-715248	00:39:27.3	-71:52:48.7	39.31
J003928-701250	00:39:28.7	-70:12:50.8	3.87
J003931-721346	00:39:31.2	-72:13:46.6	3.81
J003934-734827	00:39:34.0	-73:48:27.3	4.18
J003936-742017	00:39:36.6	-74:20:17.1	30.88
J003937-714315	00:39:37.9	-71:43:15.9	13.50
J003939-714143	00:39:39.8	-71:41:43.2	174.00
J003942-735618	00:39:42.4	-73:56:18.0	12.76
J003944-705248	00:39:44.2	-70:52:48.8	49.23

Table A3. Continued.

Name ATCA	R.A.$_{843}$ (J2000)	Dec.$_{843}$ (J2000)	S_{36} (mJy)
J003945-725550	00:39:45.5	-72:55:50.6	3.93
J003947-713734	00:39:47.4	-71:37:34.4	156.00
J003905-724335	00:39:05.6	-72:43:35.6	16.42
J003950-705506	00:39:50.6	-70:55:06.6	25.12
J003954-722243	00:39:54.5	-72:22:43.7	2.10
J003906-735157	00:39:06.8	-73:51:57.9	4.26
J004001-714501	00:40:01.3	-71:45:01.1	10.76
J004018-713821	00:40:18.8	-71:38:21.8	3.92
J004021-722645	00:40:21.7	-72:26:45.4	2.50
J004023-723805	00:40:23.5	-72:38:05.8	15.26
J004023-735202	00:40:23.9	-73:52:02.8	5.19
J004024-742200	00:40:24.0	-74:22:00.8	4.44
J004027-743923	00:40:27.4	-74:39:23.3	3.61
J004029-703514	00:40:29.1	-70:35:14.8	48.08
J004034-751458	00:40:34.4	-75:14:58.4	11.23
J004040-750353	00:40:40.4	-75:03:53.4	8.24
J004044-741221	00:40:44.1	-74:12:21.7	5.39
J004046-702355	00:40:46.0	-70:23:55.5	33.30
J004046-735211	00:40:46.3	-73:52:11.7	5.21
J004048-714559	00:40:48.0	-71:45:59.3	637.80
J004052-712153	00:40:52.6	-71:21:53.4	9.30
J004058-741319	00:40:58.2	-74:13:19.0	7.29
J004006-714142	00:40:06.4	-71:41:42.9	3.82
J004009-705810	00:40:09.6	-70:58:10.9	7.81
J004112-715856	00:41:12.4	-71:58:56.6	11.22
J004123-723923	00:41:23.4	-72:39:23.2	5.44
J004124-740701	00:41:24.1	-74:07:01.1	11.30
J004124-734704	00:41:24.7	-73:47:04.1	8.03
J004125-705743	00:41:25.5	-70:57:43.7	73.55
J004126-700359	00:41:26.2	-70:03:59.4	7.10
J004127-714009	00:41:27.9	-71:40:09.7	3.88
J004128-720625	00:41:28.9	-72:06:25.6	3.80
J004130-750456	00:41:30.8	-75:04:56.8	6.04
J004133-711104	00:41:33.4	-71:11:04.6	12.21
J004135-730854	00:41:35.3	-73:08:54.8	3.00
J004141-733925	00:41:41.2	-73:39:25.6	5.72
J004143-721823	00:41:43.3	-72:18:23.3	5.21
J004144-733342	00:41:44.1	-73:33:42.5	7.56
J004144-714448	00:41:44.2	-71:44:48.8	11.72
J004105-701413	00:41:05.2	-70:14:13.8	7.43
J004150-720722	00:41:50.9	-72:07:22.1	4.96
J004152-743335	00:41:52.0	-74:33:35.9	6.53
J004154-722244	00:41:54.5	-72:22:44.6	4.60
J004154-714618	00:41:54.6	-71:46:18.7	6.00
J004200-700443	00:42:00.8	-70:04:43.5	14.45
J004211-722507	00:42:11.7	-72:25:07.9	5.03
J004212-740322	00:42:12.4	-74:03:22.0	8.29
J004213-740834	00:42:13.9	-74:08:34.8	6.63
J004215-714708	00:42:15.7	-71:47:08.6	7.68
J004216-715200	00:42:16.6	-71:52:00.9	3.23

Table A3. Continued.

Name ATCA	R.A.$_{843}$ (J2000)	Dec.$_{843}$ (J2000)	S_{36} (mJy)
J004202-730718	00:42:02.4	-73:07:18.6	197.40
J004221-731051	00:42:21.5	-73:10:51.1	11.48
J004224-703111	00:42:24.2	-70:31:11.1	10.76
J004225-700246	00:42:25.9	-70:02:46.0	182.00
J004226-751358	00:42:26.4	-75:13:58.2	53.36
J004226-730416	00:42:26.6	-73:04:16.7	138.90
J004230-742845	00:42:30.1	-74:28:45.9	13.34
J004230-745450	00:42:30.9	-74:54:50.4	6.91
J004233-713737	00:42:33.5	-71:37:37.6	5.38
J004235-703651	00:42:35.7	-70:36:51.7	6.36
J004237-700621	00:42:37.3	-70:06:21.5	9.01
J004239-723322	00:42:39.4	-72:33:22.5	12.31
J004239-700137	00:42:39.9	-70:01:37.1	93.45
J004241-703319	00:42:41.2	-70:33:19.2	5.37
J004249-742427	00:42:49.4	-74:24:27.1	5.65
J004205-711723	00:42:05.0	-71:17:23.8	29.60
J004206-733537	00:42:06.6	-73:35:37.1	2.50
J004209-723841	00:42:09.6	-72:38:41.4	5.66
J004209-721444	00:42:09.8	-72:14:44.9	17.81
J004300-715943	00:43:00.3	-71:59:43.2	4.60
J004301-742521	00:43:01.7	-74:25:21.4	7.84
J004310-723623	00:43:10.7	-72:36:23.5	5.49
J004312-710421	00:43:12.1	-71:04:21.5	49.32
J004312-743424	00:43:12.1	-74:34:24.4	3.51
J004318-714057	00:43:18.2	-71:40:57.8	41.28
J004319-735513	00:43:19.0	-73:55:13.3	10.20
J004319-724834	00:43:19.2	-72:48:34.8	2.10
J004329-704140	00:43:29.0	-70:41:40.8	875.30
J004303-733950	00:43:03.0	-73:39:50.1	3.19
J004330-721018	00:43:30.9	-72:10:18.5	24.55
J004334-713201	00:43:34.1	-71:32:01.8	49.75
J004334-705518	00:43:34.3	-70:55:18.1	44.83
J004336-730226	00:43:36.9	-73:02:26.4	6.25
J004339-703816	00:43:39.1	-70:38:16.0	3.43
J004339-720350	00:43:39.8	-72:03:50.3	58.37
J004341-711525	00:43:41.6	-71:15:25.8	13.36
J004342-732921	00:43:42.3	-73:29:21.4	6.50
J004344-740459	00:43:44.2	-74:04:59.6	3.63
J004345-732557	00:43:45.2	-73:25:57.8	27.46
J004347-732318	00:43:47.6	-73:23:18.2	16.91
J004348-730328	00:43:48.6	-73:03:28.0	8.15
J004348-724613	00:43:48.7	-72:46:13.5	2.00
J004352-705744	00:43:52.3	-70:57:44.2	6.02
J004355-710446	00:43:55.4	-71:04:46.7	6.54
J004306-732827	00:43:06.6	-73:28:27.5	29.20
J004307-711328	00:43:07.6	-71:13:28.9	3.12
J004308-742841	00:43:08.6	-74:28:41.1	5.31
J004414-724259	00:44:14.1	-72:42:59.5	30.68
J004415-733315	00:44:15.1	-73:33:15.3	8.41
J004416-702744	00:44:16.4	-70:27:44.6	6.33

Table A3. Continued.

Name ATCA	R.A.$_{843}$ (J2000)	Dec.$_{843}$ (J2000)	S_{36} (mJy)
J004416-750227	00:44:16.4	-75:02:27.4	18.41
J004417-702250	00:44:17.2	-70:22:50.6	5.55
J004420-703257	00:44:20.4	-70:32:57.6	9.04
J004421-744316	00:44:21.1	-74:43:16.2	37.62
J004437-743917	00:44:37.1	-74:39:17.0	4.47
J004439-733710	00:44:39.1	-73:37:10.0	12.20
J004439-742341	00:44:39.9	-74:23:41.9	4.30
J004444-700900	00:44:44.0	-70:09:00.6	39.47
J004446-733533	00:44:46.4	-73:35:33.3	4.21
J004447-742508	00:44:47.0	-74:25:08.0	7.11
J004448-721223	00:44:48.0	-72:12:23.7	3.57
J004450-751323	00:44:50.6	-75:13:23.9	8.24
J004452-723205	00:44:52.1	-72:32:05.2	4.77
J004452-734536	00:44:52.1	-73:45:36.3	33.90
J004453-704842	00:44:53.2	-70:48:42.7	31.45
J004456-731014	00:44:56.6	-73:10:14.8	5.80
J004459-711331	00:44:59.3	-71:13:31.8	8.00
J004459-711438	00:44:59.9	-71:14:38.1	46.19
J004501-710253	00:45:01.0	-71:02:53.0	4.35
J004512-735620	00:45:12.0	-73:56:20.9	3.75
J004515-704246	00:45:15.2	-70:42:46.7	11.88
J004518-731528	00:45:18.5	-73:15:28.6	4.21
J004520-740830	00:45:20.9	-74:08:30.8	4.94
J004524-732247	00:45:24.2	-73:22:47.4	44.30
J004526-745350	00:45:26.9	-74:53:50.4	2.90
J004529-750136	00:45:29.9	-75:01:36.8	6.98
J004503-731639	00:45:03.5	-73:16:39.4	6.56
J004530-745054	00:45:30.1	-74:50:54.7	12.28
J004532-720359	00:45:32.9	-72:03:59.2	12.99
J004537-712315	00:45:37.1	-71:23:15.4	41.31
J004504-715612	00:45:04.9	-71:56:12.0	18.07
J004545-724139	00:45:45.7	-72:41:39.8	8.91
J004548-714931	00:45:48.4	-71:49:31.3	9.28
J004555-704643	00:45:55.6	-70:46:43.7	28.92
J004556-712054	00:45:56.2	-71:20:54.2	3.18
J004558-731331	00:45:58.0	-73:13:31.3	6.35
J004600-703433	00:46:00.3	-70:34:33.0	3.83
J004611-720154	00:46:11.2	-72:01:54.5	65.63
J004611-741800	00:46:11.4	-74:18:00.4	8.93
J004613-730043	00:46:13.0	-73:00:43.2	3.94
J004616-711609	00:46:16.2	-71:16:09.8	13.19
J004602-744005	00:46:02.1	-74:40:05.1	56.34
J004620-732323	00:46:20.7	-73:23:23.3	8.42
J004621-724507	00:46:21.2	-72:45:07.6	4.46
J004621-720152	00:46:21.8	-72:01:52.5	49.05
J004621-740057	00:46:21.8	-74:00:57.7	3.14
J004623-722722	00:46:23.2	-72:27:22.3	15.40
J004623-710040	00:46:23.4	-71:00:40.0	15.92
J004625-722350	00:46:25.0	-72:23:50.8	3.58
J004627-742620	00:46:27.7	-74:26:20.9	3.50

Table A3. Continued.

Name ATCA	R.A.$_{843}$ (J2000)	Dec.$_{843}$ (J2000)	S_{36} (mJy)
J004631-720418	00:46:31.5	-72:04:18.1	4.02
J004631-722246	00:46:31.7	-72:22:46.8	4.88
J004631-742505	00:46:31.9	-74:25:05.5	11.06
J004632-705856	00:46:32.6	-70:58:56.7	55.66
J004633-730148	00:46:33.0	-73:01:48.1	2.20
J004636-735334	00:46:36.2	-73:53:34.1	7.91
J004637-723624	00:46:37.3	-72:36:24.3	2.40
J004604-741337	00:46:04.2	-74:13:37.8	23.44
J004640-732149	00:46:40.1	-73:21:49.4	8.30
J004644-743240	00:46:44.9	-74:32:40.8	3.33
J004646-743405	00:46:46.4	-74:34:05.3	14.44
J004648-704642	00:46:48.8	-70:46:42.9	5.98
J004658-734528	00:46:58.4	-73:45:28.9	5.07
J004659-700345	00:46:59.6	-70:03:45.3	12.14
J004659-711217	00:46:59.9	-71:12:17.5	3.84
J004607-743103	00:46:07.1	-74:31:03.8	2.70
J004609-731235	00:46:09.2	-73:12:35.3	3.85
J004700-711859	00:47:00.4	-71:18:59.0	5.49
J004701-710135	00:47:01.4	-71:01:35.2	2.90
J004712-745931	00:47:12.2	-74:59:31.1	24.12
J004713-745658	00:47:13.4	-74:56:58.0	6.05
J004719-723946	00:47:19.2	-72:39:46.0	6.96
J004702-701436	00:47:02.1	-70:14:36.3	15.82
J004725-732214	00:47:25.0	-73:22:14.8	9.93
J004725-712726	00:47:25.8	-71:27:26.4	7.96
J004728-750332	00:47:28.7	-75:03:32.1	4.50
J004703-714956	00:47:03.8	-71:49:56.5	42.48
J004730-711100	00:47:30.9	-71:11:00.9	8.05
J004732-750057	00:47:32.3	-75:00:57.8	23.64
J004750-705756	00:47:50.7	-70:57:56.0	49.63
J004751-703948	00:47:51.8	-70:39:48.2	7.31
J004759-711544	00:47:59.0	-71:15:44.5	6.98
J004706-743003	00:47:06.4	-74:30:03.6	5.36
J004706-750242	00:47:06.5	-75:02:42.8	17.70
J004814-703639	00:48:14.7	-70:36:39.4	7.54
J004815-711402	00:48:15.8	-71:14:02.4	39.44
J004802-701818	00:48:02.1	-70:18:18.5	8.34
J004825-720032	00:48:25.7	-72:00:32.7	6.24
J004827-742753	00:48:27.0	-74:27:53.9	2.70
J004803-704908	00:48:03.5	-70:49:08.9	6.39
J004832-743311	00:48:32.4	-74:33:11.1	8.48
J004832-720436	00:48:32.5	-72:04:36.2	3.37
J004834-701216	00:48:34.8	-70:12:16.2	8.76
J004835-710319	00:48:35.3	-71:03:19.3	27.10
J004835-734433	00:48:35.8	-73:44:33.8	8.89
J004836-733054	00:48:36.5	-73:30:54.7	13.92
J004836-712844	00:48:36.8	-71:28:44.0	7.55
J004841-735656	00:48:41.3	-73:56:56.2	4.86
J004843-740729	00:48:43.9	-74:07:29.4	19.61
J004850-725124	00:48:50.0	-72:51:24.1	14.86

Table A3. Continued.

Name ATCA	R.A.$_{843}$ (J2000)	Dec.$_{843}$ (J2000)	S_{36} (mJy)
J004852-710507	00:48:52.4	-71:05:07.1	23.70
J004857-700912	00:48:57.7	-70:09:12.3	10.32
J004807-742001	00:48:07.2	-74:20:01.7	6.23
J004808-741205	00:48:08.2	-74:12:05.0	159.60
J004901-734453	00:49:01.8	-73:44:53.6	12.28
J004912-702033	00:49:12.5	-70:20:33.7	8.20
J004912-720921	00:49:12.5	-72:09:21.4	5.64
J004916-720413	00:49:16.2	-72:04:13.6	3.50
J004917-732044	00:49:17.1	-73:20:44.4	22.33
J004917-744707	00:49:17.1	-74:47:07.0	4.30
J004919-745659	00:49:19.0	-74:56:59.0	126.60
J004919-721953	00:49:19.5	-72:19:53.1	8.30
J004923-712658	00:49:23.3	-71:26:58.7	34.54
J004924-710531	00:49:24.8	-71:05:31.3	45.51
J004928-732634	00:49:28.5	-73:26:34.6	11.07
J004928-740125	00:49:28.6	-74:01:25.9	5.04
J004932-721858	00:49:32.8	-72:18:58.5	23.77
J004936-724634	00:49:36.5	-72:46:34.8	33.41
J004936-741552	00:49:36.6	-74:15:52.3	55.25
J004937-723543	00:49:37.1	-72:35:43.3	6.60
J004937-705208	00:49:37.6	-70:52:08.1	14.14
J004941-724840	00:49:41.4	-72:48:40.9	6.87
J004941-741905	00:49:41.4	-74:19:05.9	3.40
J004905-712654	00:49:05.1	-71:26:54.9	4.30
J004905-710343	00:49:05.8	-71:03:43.4	57.94
J004950-722214	00:49:50.4	-72:22:14.5	6.15
J004954-715149	00:49:54.3	-71:51:49.5	24.06
J004956-723552	00:49:56.8	-72:35:52.8	188.60
J004957-720533	00:49:57.7	-72:05:33.8	11.38
J004909-744622	00:49:09.3	-74:46:22.9	23.36
J005001-722231	00:50:01.6	-72:22:31.5	3.80
J005013-732130	00:50:13.4	-73:21:30.1	5.67
J005015-723228	00:50:15.0	-72:32:28.7	4.47
J005016-730320	00:50:16.6	-73:03:20.3	48.30
J005022-745609	00:50:22.3	-74:56:09.5	3.23
J005022-744149	00:50:22.5	-74:41:49.7	9.25
J005025-705302	00:50:25.3	-70:53:02.7	7.43
J005035-732012	00:50:35.8	-73:20:12.6	3.81
J005004-714154	00:50:04.4	-71:41:54.5	3.68
J005041-703937	00:50:41.8	-70:39:37.2	45.71
J005042-715828	00:50:42.4	-71:58:28.3	10.80
J005045-741036	00:50:45.8	-74:10:36.7	3.13
J005052-731704	00:50:52.2	-73:17:04.3	4.27
J005052-720107	00:50:52.6	-72:01:07.9	3.77
J005007-734133	00:50:07.5	-73:41:33.5	12.53
J005115-713057	00:51:15.9	-71:30:57.0	26.35
J005117-734000	00:51:17.4	-73:40:00.4	86.00
J005117-745142	00:51:17.7	-74:51:42.3	4.38
J005117-705600	00:51:17.9	-70:56:00.4	6.18
J005125-712113	00:51:25.2	-71:21:13.8	3.37

Table A3. Continued.

Name ATCA	R.A.$_{843}$ (J2000)	Dec.$_{843}$ (J2000)	S_{36} (mJy)
J005126-722435	00:51:26.7	-72:24:35.9	3.89
J005126-744606	00:51:26.8	-74:46:06.4	2.90
J005130-713618	00:51:30.2	-71:36:18.7	5.65
J005130-734418	00:51:30.9	-73:44:18.9	7.21
J005139-723813	00:51:39.7	-72:38:13.7	6.19
J005140-731336	00:51:40.9	-73:13:36.3	13.96
J005141-725552	00:51:41.4	-72:55:52.9	71.88
J005147-730449	00:51:47.2	-73:04:49.8	20.24
J005147-725043	00:51:47.8	-72:50:43.4	9.63
J005152-734521	00:51:52.3	-73:45:21.6	5.90
J005201-711926	00:52:01.1	-71:19:26.7	4.30
J005212-730849	00:52:12.7	-73:08:49.4	10.37
J005217-730154	00:52:17.5	-73:01:54.3	39.57
J005218-731106	00:52:18.5	-73:11:06.4	3.57
J005218-722706	00:52:18.6	-72:27:06.2	310.30
J005202-745704	00:52:02.0	-74:57:04.5	3.51
J005202-733233	00:52:02.1	-73:32:33.7	10.51
J005224-713209	00:52:24.7	-71:32:09.0	3.55
J005226-711344	00:52:26.7	-71:13:44.5	3.86
J005228-735941	00:52:28.2	-73:59:41.8	3.42
J005230-743747	00:52:30.8	-74:37:47.6	9.95
J005238-731243	00:52:38.1	-73:12:43.8	143.94
J005238-732613	00:52:38.2	-73:26:13.4	4.47
J005239-735343	00:52:39.8	-73:53:43.0	5.92
J005240-711910	00:52:40.3	-71:19:10.7	7.34
J005249-741138	00:52:49.7	-74:11:38.3	6.74
J005253-711524	00:52:53.5	-71:15:24.3	3.75
J005253-720131	00:52:53.9	-72:01:31.4	13.44
J005254-714540	00:52:54.7	-71:45:40.1	2.74
J005257-732956	00:52:57.1	-73:29:56.8	4.66
J005258-711420	00:52:58.3	-71:14:20.1	3.14
J005258-731150	00:52:58.8	-73:11:50.8	15.80
J005206-733722	00:52:06.1	-73:37:22.3	13.85
J005206-714414	00:52:06.2	-71:44:14.5	4.54
J005300-710115	00:53:00.9	-71:01:15.1	3.75
J005315-744237	00:53:15.6	-74:42:37.4	5.54
J005318-720855	00:53:18.0	-72:08:55.2	19.10
J005323-712124	00:53:23.4	-71:21:24.5	3.56
J005325-745556	00:53:25.0	-74:55:56.4	10.53
J005327-723010	00:53:27.3	-72:30:10.5	12.80
J005328-725522	00:53:28.8	-72:55:22.7	18.32
J005337-723142	00:53:37.6	-72:31:42.1	140.30
J005340-731223	00:53:40.0	-73:12:23.7	5.52
J005347-714958	00:53:47.6	-71:49:58.2	16.78
J005347-751443	00:53:47.7	-75:14:43.3	18.50
J005351-715848	00:53:51.1	-71:58:48.8	4.83
J005351-704000	00:53:51.9	-70:40:00.9	42.58
J005356-703804	00:53:56.2	-70:38:04.8	48.70
J005358-724400	00:53:58.0	-72:44:00.7	6.36
J005307-743902	00:53:07.8	-74:39:02.5	2.40

Table A3. Continued.

Name ATCA	R.A.$_{843}$ (J2000)	Dec.$_{843}$ (J2000)	S_{36} (mJy)
J005309-741348	00:53:09.8	-74:13:48.5	2.40
J005411-734017	00:54:11.2	-73:40:17.1	15.03
J005412-750853	00:54:12.0	-75:08:53.6	8.43
J005416-735306	00:54:16.8	-73:53:06.1	4.07
J005423-725255	00:54:23.6	-72:52:55.9	58.73
J005426-741723	00:54:26.4	-74:17:23.0	11.14
J005429-720156	00:54:29.0	-72:01:56.6	10.24
J005403-721350	00:54:03.0	-72:13:50.2	14.82
J005434-733847	00:54:34.7	-73:38:47.2	11.05
J005439-724502	00:54:39.5	-72:45:02.7	17.12
J005441-722951	00:54:41.7	-72:29:51.0	11.46
J005448-725351	00:54:48.5	-72:53:51.3	25.45
J005448-735855	00:54:48.6	-73:58:55.4	12.28
J005449-731646	00:54:49.3	-73:16:46.8	19.90
J005449-744937	00:54:49.3	-74:49:37.8	12.58
J005449-704657	00:54:49.5	-70:46:57.4	3.49
J005453-713136	00:54:53.1	-71:31:36.0	28.93
J005456-710341	00:54:56.8	-71:03:41.0	10.48
J005407-722419	00:54:07.7	-72:24:19.8	12.36
J005518-714449	00:55:18.8	-71:44:49.1	25.92
J005521-731826	00:55:21.9	-73:18:26.1	5.25
J005523-721053	00:55:23.3	-72:10:53.3	242.00
J005503-712102	00:55:03.5	-71:21:02.3	39.83
J005531-702627	00:55:31.3	-70:26:27.3	45.87
J005532-723123	00:55:32.9	-72:31:23.3	29.75
J005535-703946	00:55:35.2	-70:39:46.3	4.10
J005536-723520	00:55:36.4	-72:35:20.2	90.00
J005537-743926	00:55:37.4	-74:39:26.0	197.60
J005538-721047	00:55:38.8	-72:10:47.3	78.56
J005553-741232	00:55:53.8	-74:12:32.9	5.75
J005554-730342	00:55:54.3	-73:03:42.3	4.74
J005554-710318	00:55:54.6	-71:03:18.1	16.74
J005555-742233	00:55:55.0	-74:22:33.7	7.44
J005556-722603	00:55:56.9	-72:26:03.3	111.95
J005557-721954	00:55:57.1	-72:19:54.8	4.75
J005506-723718	00:55:06.4	-72:37:18.1	24.10
J005600-720905	00:56:00.7	-72:09:05.2	10.65
J005611-710706	00:56:11.6	-71:07:06.8	875.03
J005616-721733	00:56:16.1	-72:17:33.3	7.13
J005621-712522	00:56:21.0	-71:25:22.6	4.59
J005622-715109	00:56:22.0	-71:51:09.2	31.88
J005632-735707	00:56:32.6	-73:57:07.0	22.47
J005636-740315	00:56:36.8	-74:03:15.8	22.02
J005604-723450	00:56:04.9	-72:34:50.8	3.24
J005643-725205	00:56:43.8	-72:52:05.3	112.90
J005645-722505	00:56:45.1	-72:25:05.8	4.89
J005652-712300	00:56:52.6	-71:23:00.1	120.56
J005655-745547	00:56:55.1	-74:55:47.2	3.24
J005608-703846	00:56:08.6	-70:38:46.9	150.39
J005712-710209	00:57:12.8	-71:02:09.1	2.97

Table A3. Continued.

Name ATCA	R.A.$_{843}$ (J2000)	Dec.$_{843}$ (J2000)	S_{36} (mJy)
J005714-733450	00:57:14.2	-73:34:50.6	18.38
J005715-703330	00:57:15.8	-70:33:30.9	16.52
J005716-704046	00:57:16.1	-70:40:46.2	81.05
J005702-703651	00:57:02.9	-70:36:51.6	8.91
J005722-740315	00:57:22.3	-74:03:15.2	28.49
J005727-751457	00:57:27.1	-75:14:57.4	6.73
J005727-751258	00:57:27.9	-75:12:58.4	5.28
J005729-723226	00:57:29.2	-72:32:26.4	4.03
J005703-721634	00:57:03.1	-72:16:34.0	28.54
J005703-702737	00:57:03.7	-70:27:37.9	5.11
J005731-744213	00:57:31.1	-74:42:13.4	36.99
J005732-741243	00:57:32.3	-74:12:43.2	837.20
J005732-745748	00:57:32.4	-74:57:48.3	3.32
J005733-703556	00:57:33.8	-70:35:56.0	4.61
J005736-731255	00:57:36.8	-73:12:55.3	3.34
J005738-715928	00:57:38.4	-71:59:28.6	16.55
J005738-710846	00:57:38.7	-71:08:46.4	44.23
J005704-723757	00:57:04.2	-72:37:57.4	4.76
J005740-734614	00:57:40.9	-73:46:14.7	5.13
J005741-724156	00:57:41.7	-72:41:56.5	22.99
J005747-711716	00:57:47.4	-71:17:16.9	8.40
J005749-732546	00:57:49.8	-73:25:46.4	2.62
J005749-723017	00:57:49.9	-72:30:17.0	4.46
J005705-730043	00:57:05.0	-73:00:43.1	6.26
J005750-730602	00:57:50.1	-73:06:02.3	3.06
J005751-704555	00:57:51.2	-70:45:55.2	5.58
J005752-711827	00:57:52.2	-71:18:27.3	13.20
J005755-703459	00:57:55.4	-70:34:59.7	4.13
J005755-723919	00:57:55.6	-72:39:19.7	7.51
J005757-740217	00:57:57.2	-74:02:17.3	7.95
J005757-715651	00:57:57.6	-71:56:51.0	10.04
J005810-723109	00:58:10.8	-72:31:09.5	4.16
J005812-735951	00:58:12.1	-73:59:51.2	19.88
J005814-713520	00:58:14.1	-71:35:20.2	4.67
J005814-712351	00:58:14.7	-71:23:51.6	38.25
J005815-723003	00:58:15.1	-72:30:03.3	6.29
J005815-731612	00:58:15.3	-73:16:12.0	4.66
J005816-723853	00:58:16.4	-72:38:53.5	13.88
J005817-723705	00:58:17.1	-72:37:05.3	3.77
J005820-713036	00:58:20.5	-71:30:36.7	38.46
J005820-732934	00:58:20.6	-73:29:34.2	7.62
J005820-703200	00:58:20.8	-70:32:00.4	7.56
J005822-720038	00:58:22.4	-72:00:38.3	21.77
J005826-723958	00:58:26.5	-72:39:58.4	10.30
J005829-723412	00:58:29.6	-72:34:12.9	6.24
J005831-740147	00:58:31.1	-74:01:47.3	18.77
J005832-725110	00:58:32.9	-72:51:10.4	11.34
J005834-750824	00:58:34.7	-75:08:24.0	5.41
J005842-701907	00:58:42.1	-70:19:07.4	9.22
J005844-750421	00:58:44.2	-75:04:21.5	3.52

Table A3. Continued.

Name ATCA	R.A.$_{843}$ (J2000)	Dec.$_{843}$ (J2000)	S_{36} (mJy)
J005845-744652	00:58:45.9	-74:46:52.6	18.74
J005846-730504	00:58:46.0	-73:05:04.3	5.41
J005848-743513	00:58:48.8	-74:35:13.2	33.29
J005851-720325	00:58:51.9	-72:03:25.4	4.17
J005858-701910	00:58:58.9	-70:19:10.7	5.55
J005901-722949	00:59:01.1	-72:29:49.9	5.85
J005911-722419	00:59:11.5	-72:24:19.0	3.96
J005912-723241	00:59:12.0	-72:32:41.3	6.71
J005913-741359	00:59:13.8	-74:13:59.2	6.22
J005918-733200	00:59:18.4	-73:32:00.4	3.79
J005918-750554	00:59:18.6	-75:05:54.0	4.57
J005926-702947	00:59:26.8	-70:29:47.6	3.58
J005927-751207	00:59:27.1	-75:12:07.2	8.14
J005927-730828	00:59:27.2	-73:08:28.3	2.37
J005904-704859	00:59:04.5	-70:48:59.9	155.70
J005947-750216	00:59:47.1	-75:02:16.2	3.80
J005948-705027	00:59:48.6	-70:50:27.5	18.87
J005948-732154	00:59:48.6	-73:21:54.3	4.14
J005905-750643	00:59:05.1	-75:06:43.4	12.60
J005950-742637	00:59:50.4	-74:26:37.6	3.85
J005951-705159	00:59:51.1	-70:51:59.1	17.00
J005906-745455	00:59:06.2	-74:54:55.5	13.60
J005906-745848	00:59:06.3	-74:58:48.7	24.63
J005906-735203	00:59:06.4	-73:52:03.8	31.76
J005909-740236	00:59:09.7	-74:02:36.1	5.24
J010010-731316	01:00:10.2	-73:13:16.4	2.79
J010012-704027	01:00:12.8	-70:40:27.7	16.61
J010015-742531	01:00:15.3	-74:25:31.9	8.25
J010020-714431	01:00:20.5	-71:44:31.8	8.66
J010027-705156	01:00:27.3	-70:51:56.5	2.58
J010029-713824	01:00:29.6	-71:38:24.8	194.30
J010030-730006	01:00:30.2	-73:00:06.5	19.22
J010042-730616	01:00:42.2	-73:06:16.6	4.25
J010042-712137	01:00:42.8	-71:21:37.0	13.69
J010042-744616	01:00:42.9	-74:46:16.9	3.40
J010044-745414	01:00:44.9	-74:54:14.8	66.37
J010046-731613	01:00:46.6	-73:16:13.4	5.36
J010005-732640	01:00:05.9	-73:26:40.2	7.24
J010050-751355	01:00:50.7	-75:13:55.1	11.53
J010053-705017	01:00:53.4	-70:50:17.1	9.32
J010053-734042	01:00:53.6	-73:40:42.4	10.78
J010054-734214	01:00:54.7	-73:42:14.3	5.89
J010058-713528	01:00:58.1	-71:35:28.6	9.88
J010058-734513	01:00:58.8	-73:45:13.2	3.95
J010008-705228	01:00:08.0	-70:52:28.6	4.77
J010101-744454	01:01:01.0	-74:44:54.4	4.17
J010110-723549	01:01:10.0	-72:35:49.3	4.01
J010112-744100	01:01:12.6	-74:41:00.3	25.43
J010117-733132	01:01:17.7	-73:31:32.0	5.13
J010118-741325	01:01:18.2	-74:13:25.3	2.40

Table A3. Continued.

Name ATCA	R.A.$_{843}$ (J2000)	Dec.$_{843}$ (J2000)	S_{36} (mJy)
J010102-745929	01:01:02.5	-74:59:29.5	3.37
J010132-705717	01:01:32.7	-70:57:17.0	3.44
J010140-725510	01:01:40.6	-72:55:10.6	7.64
J010143-703203	01:01:43.0	-70:32:03.5	6.32
J010143-742334	01:01:43.0	-74:23:34.3	11.33
J010143-723223	01:01:43.9	-72:32:23.6	32.42
J010147-725239	01:01:47.4	-72:52:39.8	4.37
J010105-702253	01:01:05.7	-70:22:53.9	10.35
J010154-744522	01:01:54.1	-74:45:22.4	5.08
J010157-734247	01:01:57.3	-73:42:47.7	15.39
J010107-732842	01:01:07.3	-73:28:42.8	3.72
J010107-713643	01:01:07.6	-71:36:43.5	3.12
J010109-725043	01:01:09.5	-72:50:43.8	6.83
J010213-712015	01:02:13.3	-71:20:15.1	4.76
J010214-702331	01:02:14.7	-70:23:31.4	5.24
J010216-723704	01:02:16.9	-72:37:04.3	7.71
J010221-735319	01:02:21.1	-73:53:19.6	29.43
J010221-743806	01:02:21.1	-74:38:06.2	3.53
J010222-712719	01:02:22.0	-71:27:19.8	13.14
J010223-705710	01:02:23.6	-70:57:10.2	5.13
J010223-703722	01:02:23.9	-70:37:22.8	22.96
J010226-742702	01:02:26.8	-74:27:02.5	9.61
J010227-715605	01:02:27.4	-71:56:35.1	3.05
J010203-701555	01:02:03.3	-70:15:55.2	3.43
J010230-750025	01:02:30.0	-75:00:25.7	13.19
J010230-732316	01:02:30.6	-73:23:16.8	7.86
J010232-734759	01:02:32.3	-73:47:59.2	11.19
J010233-744518	01:02:33.4	-74:45:18.3	4.87
J010234-741535	01:02:34.1	-74:15:35.1	38.75
J010237-702019	01:02:37.1	-70:20:19.9	3.36
J010237-725038	01:02:37.4	-72:50:38.2	5.41
J010204-722446	01:02:04.0	-72:24:46.9	13.77
J010204-710322	01:02:04.5	-71:03:22.2	7.48
J010240-710218	01:02:40.7	-71:02:18.3	8.89
J010244-735010	01:02:44.4	-73:50:10.9	4.50
J010253-724112	01:02:53.1	-72:41:12.9	3.22
J010254-722444	01:02:54.0	-72:24:44.6	3.93
J010254-743739	01:02:54.5	-74:37:39.5	6.77
J010255-713629	01:02:55.2	-71:36:29.6	28.56
J010256-743531	01:02:56.6	-74:35:31.2	35.06
J010257-703936	01:02:57.6	-70:39:36.6	30.63
J010258-743346	01:02:58.2	-74:33:46.1	19.06
J010207-744350	01:02:07.3	-74:43:50.9	6.52
J010315-720948	01:03:15.7	-72:09:48.6	57.17
J010319-704648	01:03:19.7	-70:46:48.6	7.97
J010321-721342	01:03:21.2	-72:13:42.6	15.49
J010322-745321	01:03:22.8	-74:53:21.7	5.02
J010326-730021	01:03:26.8	-73:00:21.3	24.04
J010329-724722	01:03:29.4	-72:47:22.0	25.62
J010303-715331	01:03:03.8	-71:53:31.2	4.21

Table A3. Continued.

Name ATCA	R.A.$_{843}$ (J2000)	Dec.$_{843}$ (J2000)	S_{36} (mJy)
J010331-743429	01:03:31.3	-74:34:29.0	8.32
J010332-750703	01:03:32.3	-75:07:03.0	135.80
J010333-745731	01:03:33.7	-74:57:31.2	4.52
J010335-750200	01:03:35.2	-75:02:00.5	3.18
J010336-703954	01:03:36.1	-70:39:54.3	9.24
J010339-725040	01:03:39.1	-72:50:40.4	16.39
J010341-703533	01:03:41.4	-70:35:33.4	5.50
J010345-732048	01:03:45.2	-73:20:48.4	6.41
J010305-705545	01:03:05.0	-70:55:45.4	5.87
J010305-750158	01:03:05.3	-75:01:58.4	3.21
J010309-731040	01:03:09.7	-73:10:40.5	4.63
J010400-711252	01:04:00.4	-71:12:52.3	21.50
J010410-733812	01:04:10.6	-73:38:12.0	5.13
J010412-705601	01:04:12.5	-70:56:01.0	18.49
J010417-730716	01:04:17.9	-73:07:16.5	3.85
J010420-724241	01:04:20.7	-72:42:41.0	3.19
J010421-702149	01:04:21.8	-70:21:49.4	4.18
J010424-711254	01:04:24.2	-71:12:54.4	10.80
J010425-742733	01:04:25.4	-74:27:33.1	21.27
J010431-720723	01:04:31.0	-72:07:23.6	53.04
J010432-720453	01:04:32.9	-72:04:53.6	7.49
J010435-740409	01:04:35.4	-74:04:09.5	7.23
J010404-750842	01:04:04.2	-75:08:42.2	5.71
J010440-745028	01:04:40.0	-74:50:28.0	4.10
J010440-751241	01:04:40.7	-75:12:41.0	6.04
J010441-713121	01:04:41.1	-71:31:21.7	19.48
J010444-745700	01:04:44.8	-74:57:00.6	4.71
J010405-724343	01:04:05.3	-72:43:43.3	19.37
J010405-735124	01:04:05.5	-73:51:24.6	15.27
J010450-702100	01:04:50.8	-70:21:00.4	7.25
J010457-702240	01:04:57.6	-70:22:40.6	3.08
J010458-703735	01:04:58.4	-70:37:35.6	56.31
J010513-731710	01:05:13.2	-73:17:10.7	3.31
J010515-703300	01:05:15.9	-70:33:00.0	4.30
J010516-735740	01:05:16.2	-73:57:40.3	15.81
J010523-731518	01:05:23.4	-73:15:18.1	43.33
J010523-705203	01:05:23.5	-70:52:03.7	16.88
J010524-732321	01:05:24.7	-73:23:21.4	7.27
J010525-722518	01:05:25.4	-72:25:18.1	47.60
J010503-740655	01:05:03.0	-74:06:55.3	3.28
J010532-743331	01:05:32.1	-74:33:31.1	12.09
J010532-721330	01:05:32.7	-72:13:30.6	10.37
J010536-743201	01:05:36.0	-74:32:01.4	9.38
J010536-740005	01:05:36.8	-74:00:05.2	26.71
J010542-720344	01:05:42.9	-72:03:44.1	7.40
J010543-745332	01:05:43.5	-74:53:32.7	6.56
J010544-750548	01:05:44.8	-75:05:48.3	29.68
J010548-744710	01:05:48.8	-74:47:10.7	5.38
J010549-702621	01:05:49.8	-70:26:21.7	20.12
J010550-725932	01:05:50.4	-72:59:32.2	8.34

Table A3. Continued.

Name ATCA	R.A.$_{843}$ (J2000)	Dec.$_{843}$ (J2000)	S_{36} (mJy)
J010556-714606	01:05:56.5	-71:46:06.8	78.27
J010557-710456	01:05:57.8	-71:04:56.3	47.09
J010558-702132	01:05:58.4	-70:21:32.8	3.21
J010558-732515	01:05:58.5	-73:25:15.5	18.58
J010506-723858	01:05:06.9	-72:38:58.6	5.75
J010509-712838	01:05:09.8	-71:28:38.5	9.36
J010601-710928	01:06:01.1	-71:09:28.1	2.80
J010611-744121	01:06:11.7	-74:41:21.5	15.53
J010612-734956	01:06:12.6	-73:49:56.8	25.91
J010618-710230	01:06:18.0	-71:02:30.6	7.22
J010618-705115	01:06:18.5	-70:51:15.0	15.38
J010619-720528	01:06:19.0	-72:05:28.0	8.48
J010621-704144	01:06:21.3	-70:41:44.5	33.97
J010629-745134	01:06:29.4	-74:51:34.1	8.49
J010630-703126	01:06:30.7	-70:31:26.0	6.73
J010633-714806	01:06:33.3	-71:48:06.2	4.80
J010644-703002	01:06:44.7	-70:30:02.4	10.11
J010645-711950	01:06:45.5	-71:19:50.4	7.22
J010645-741931	01:06:45.5	-74:19:31.8	8.95
J010646-724227	01:06:46.1	-72:42:27.2	4.91
J010647-725808	01:06:47.5	-72:58:08.2	17.74
J010647-723453	01:06:47.7	-72:34:53.8	4.04
J010652-721837	01:06:52.4	-72:18:37.8	12.04
J010652-710956	01:06:52.5	-71:09:56.9	3.95
J010657-731318	01:06:57.8	-73:13:18.8	7.22
J010659-735455	01:06:59.5	-73:54:55.2	13.19
J010717-732947	01:07:17.0	-73:29:47.6	32.09
J010719-711750	01:07:19.3	-71:17:50.1	7.03
J010702-703418	01:07:02.3	-70:34:18.3	16.19
J010702-730202	01:07:02.3	-73:02:02.2	2.70
J010720-744808	01:07:20.2	-74:48:08.3	5.20
J010721-713732	01:07:21.3	-71:37:32.9	5.78
J010724-744148	01:07:24.7	-74:41:48.3	3.63
J010730-712914	01:07:30.4	-71:29:14.0	5.58
J010737-713451	01:07:37.8	-71:34:51.4	4.02
J010740-742210	01:07:40.3	-74:22:10.4	3.49
J010741-715310	01:07:41.1	-71:53:10.4	5.59
J010748-705212	01:07:48.5	-70:52:12.8	15.73
J010749-714505	01:07:49.9	-71:45:05.7	6.22
J010758-712537	01:07:58.4	-71:25:37.8	18.80
J010758-703529	01:07:58.6	-70:35:29.9	7.23
J010708-714305	01:07:08.4	-71:43:05.3	46.10
J010709-730724	01:07:09.5	-73:07:24.4	1.96
J010800-710823	01:08:00.2	-71:08:23.9	6.34
J010801-724953	01:08:01.2	-72:49:53.3	3.59
J010811-725736	01:08:11.7	-72:57:36.8	14.33
J010814-710502	01:08:14.5	-71:05:02.7	3.70
J010817-745520	01:08:17.9	-74:55:20.8	9.99
J010819-711431	01:08:19.1	-71:14:31.0	3.83
J010822-714923	01:08:22.2	-71:49:23.7	7.35

Table A3. Continued.

Name ATCA	R.A.$_{843}$ (J2000)	Dec.$_{843}$ (J2000)	S_{36} (mJy)
J010822-742239	01:08:22.8	-74:22:39.8	3.10
J010831-714724	01:08:31.1	-71:47:24.5	3.16
J010833-704236	01:08:33.1	-70:42:36.0	3.01
J010834-751634	01:08:34.8	-75:16:34.2	5.12
J010839-724714	01:08:39.0	-72:47:14.3	38.73
J010841-712747	01:08:41.2	-71:27:47.8	4.11
J010842-721601	01:08:42.2	-72:16:01.7	4.76
J010842-704656	01:08:42.9	-70:46:56.9	21.56
J010844-712458	01:08:44.5	-71:24:58.8	5.47
J010848-741937	01:08:48.4	-74:19:37.7	11.88
J010805-703856	01:08:05.2	-70:38:56.7	5.56
J010850-731132	01:08:50.5	-73:11:32.4	3.11
J010851-715018	01:08:51.5	-71:50:18.7	6.82
J010856-721138	01:08:56.6	-72:11:38.3	6.29
J010807-713945	01:08:07.8	-71:39:45.2	23.38
J010809-720911	01:08:09.2	-72:09:11.1	12.63
J010901-713310	01:09:01.4	-71:33:10.5	6.97
J010901-731813	01:09:01.4	-73:18:13.2	28.72
J010911-731729	01:09:11.1	-73:17:29.7	9.60
J010912-731136	01:09:12.8	-73:11:36.5	53.77
J010913-722937	01:09:13.8	-72:29:37.1	5.49
J010916-722034	01:09:16.5	-72:20:34.8	12.10
J010917-720516	01:09:17.8	-72:05:16.4	3.10
J010919-725559	01:09:19.2	-72:55:59.2	43.00
J010902-743058	01:09:02.8	-74:30:58.6	4.44
J010925-713731	01:09:25.5	-71:37:31.0	3.87
J010927-722218	01:09:27.2	-72:22:18.2	7.59
J010928-704208	01:09:28.4	-70:42:08.2	25.24
J010928-740557	01:09:28.8	-74:05:57.5	10.92
J010930-725244	01:09:30.6	-72:52:44.8	4.64
J010931-713453	01:09:31.3	-71:34:53.9	250.40
J010935-713824	01:09:35.1	-71:38:24.2	14.09
J010938-745703	01:09:38.3	-74:57:03.2	4.98
J010939-705005	01:09:39.9	-70:50:05.2	9.84
J010904-734926	01:09:04.2	-73:49:26.1	8.59
J010947-745805	01:09:47.9	-74:58:05.2	3.17
J010948-722130	01:09:48.4	-72:21:30.4	5.57
J010951-702501	01:09:51.1	-70:25:01.0	19.32
J010951-725617	01:09:51.2	-72:56:17.3	3.27
J010951-744307	01:09:51.4	-74:43:07.8	3.32
J010954-730201	01:09:54.3	-73:02:01.1	4.54
J010955-711343	01:09:55.4	-71:13:43.4	6.19
J010955-750043	01:09:55.8	-75:00:43.3	2.60
J010958-723440	01:09:58.2	-72:34:40.0	7.65
J010958-713544	01:09:58.4	-71:35:44.8	19.45
J011001-720821	01:10:01.0	-72:08:21.5	5.68
J011012-725523	01:10:12.1	-72:55:23.6	8.33
J011013-744633	01:10:13.5	-74:46:33.1	4.21
J011015-713952	01:10:15.7	-71:39:52.6	4.59
J011018-704816	01:10:18.9	-70:48:16.1	10.09

Table A3. Continued.

Name ATCA	R.A.$_{843}$ (J2000)	Dec.$_{843}$ (J2000)	S_{36} (mJy)
J011018-714718	01:10:18.9	-71:47:18.1	3.87
J011020-730657	01:10:20.8	-73:06:57.6	3.90
J011021-730435	01:10:21.5	-73:04:35.9	60.11
J011023-702521	01:10:23.8	-70:25:21.1	10.49
J011027-745102	01:10:27.9	-74:51:02.8	28.27
J011028-750011	01:10:28.4	-75:00:11.7	3.25
J011030-723309	01:10:30.8	-72:33:09.3	14.59
J011031-745351	01:10:31.0	-74:53:51.4	27.51
J011033-734551	01:10:33.9	-73:45:51.6	7.20
J011035-720022	01:10:35.3	-72:00:22.7	9.08
J011036-701045	01:10:36.6	-70:10:45.4	6.03
J011039-722825	01:10:39.3	-72:28:25.6	346.97
J011043-725329	01:10:43.4	-72:53:29.2	3.83
J011044-750952	01:10:44.2	-75:09:52.3	11.20
J011048-711416	01:10:48.3	-71:14:16.8	15.08
J011049-704956	01:10:49.5	-70:49:56.8	5.53
J011005-722647	01:10:05.3	-72:26:47.0	115.60
J011050-721024	01:10:50.4	-72:10:24.6	16.15
J011051-731423	01:10:51.0	-73:14:23.9	1078.00
J011053-704254	01:10:53.5	-70:42:54.1	33.28
J011057-711906	01:10:57.4	-71:19:06.4	3.36
J011058-744611	01:10:58.6	-74:46:11.7	7.62
J011007-741050	01:10:07.7	-74:10:50.5	5.20
J011008-743731	01:10:08.0	-74:37:31.4	5.19
J011110-744344	01:11:10.1	-74:43:44.2	5.06
J011114-743339	01:11:14.9	-74:33:39.5	8.63
J011115-715135	01:11:15.2	-71:51:35.6	11.98
J011115-701148	01:11:15.9	-70:11:48.7	17.15
J011116-750937	01:11:16.9	-75:09:37.3	5.17
J011117-702156	01:11:17.6	-70:21:56.2	3.21
J011118-722254	01:11:18.5	-72:22:54.1	6.79
J011119-751635	01:11:19.8	-75:16:35.8	4.71
J011102-723533	01:11:02.4	-72:35:33.9	7.90
J011124-740031	01:11:24.3	-74:00:31.0	3.80
J011127-741633	01:11:27.6	-74:16:33.3	2.50
J011128-732935	01:11:28.6	-73:29:35.3	3.53
J011129-750029	01:11:29.0	-75:00:29.7	3.16
J011103-720052	01:11:03.8	-72:00:52.1	5.28
J011130-724623	01:11:30.3	-72:46:23.5	3.56
J011132-730208	01:11:32.3	-73:02:08.1	69.22
J011134-711413	01:11:34.5	-71:14:13.5	62.34
J011137-745114	01:11:37.5	-74:51:14.5	3.23
J011142-730948	01:11:42.0	-73:09:48.9	4.43
J011146-703531	01:11:46.2	-70:35:31.8	16.67
J011149-711902	01:11:49.8	-71:19:02.0	25.73
J011153-725118	01:11:53.0	-72:51:18.7	12.47
J011157-734128	01:11:57.6	-73:41:28.7	34.69
J011106-730031	01:11:06.5	-73:00:31.3	3.76
J011108-723816	01:11:08.5	-72:38:16.5	4.03
J011108-734527	01:11:08.5	-73:45:27.5	5.20

Table A3. Continued.

Name ATCA	R.A.$_{843}$ (J2000)	Dec.$_{843}$ (J2000)	S_{36} (mJy)
J011211-712715	01:12:11.5	-71:27:15.2	3.27
J011217-742301	01:12:17.1	-74:23:01.9	10.46
J011218-730253	01:12:18.6	-73:02:53.6	5.06
J011220-730505	01:12:20.9	-73:05:05.5	3.74
J011222-703927	01:12:22.1	-70:39:27.3	7.55
J011223-741212	01:12:23.0	-74:12:12.0	47.21
J011226-732750	01:12:26.1	-73:27:50.3	51.87
J011227-724801	01:12:27.2	-72:48:01.2	21.39
J011231-750615	01:12:31.3	-75:06:15.6	18.45
J011233-712944	01:12:33.9	-71:29:44.6	4.68
J011234-732702	01:12:34.7	-73:27:02.1	4.96
J011246-724518	01:12:46.8	-72:45:18.4	5.88
J011247-731520	01:12:47.7	-73:15:20.1	15.48
J011248-701930	01:12:48.1	-70:19:30.3	23.79
J011300-701345	01:13:00.6	-70:13:45.1	7.29
J011301-740709	01:13:01.6	-74:07:09.3	8.38
J011301-714858	01:13:01.8	-71:48:58.7	12.74
J011318-743452	01:13:18.7	-74:34:52.1	11.03
J011324-741936	01:13:24.0	-74:19:36.9	2.30
J011332-740757	01:13:32.4	-74:07:57.4	53.22
J011335-704416	01:13:35.7	-70:44:16.1	3.76
J011338-735547	01:13:38.1	-73:55:47.8	5.94
J011338-714118	01:13:38.9	-71:41:18.8	25.16
J011340-713223	01:13:40.7	-71:32:23.1	4.56
J011342-750413	01:13:42.3	-75:04:13.8	5.12
J011344-711514	01:13:44.3	-71:15:14.8	48.00
J011344-732109	01:13:44.6	-73:21:09.9	5.14
J011347-712409	01:13:47.4	-71:24:09.7	5.28
J011354-744210	01:13:54.8	-74:42:10.3	3.31
J011356-724805	01:13:56.5	-72:48:05.3	4.88
J011356-711427	01:13:56.8	-71:14:27.9	55.13
J011357-742653	01:13:57.5	-74:26:53.3	5.30
J011357-702531	01:13:57.7	-70:25:31.2	81.48
J011359-701613	01:13:59.0	-70:16:13.7	4.17
J011359-744451	01:13:59.4	-74:44:51.8	5.39
J011413-740914	01:14:13.8	-74:09:14.1	4.41
J011414-700947	01:14:14.5	-70:09:47.3	30.77
J011414-732703	01:14:14.6	-73:27:03.8	5.27
J011420-731733	01:14:20.2	-73:17:33.7	9.30
J011427-725218	01:14:27.1	-72:52:18.1	2.40
J011427-721710	01:14:27.4	-72:17:10.5	4.66
J011427-733315	01:14:27.9	-73:33:15.2	8.68
J011434-732144	01:14:34.0	-73:21:44.3	169.00
J011434-745227	01:14:34.7	-74:52:27.6	4.68
J011435-715248	01:14:35.8	-71:52:48.4	83.88
J011404-743523	01:14:04.1	-74:35:23.5	4.69
J011440-723504	01:14:40.0	-72:35:04.9	5.89
J011448-705459	01:14:48.5	-70:54:59.1	5.36
J011449-742043	01:14:49.0	-74:20:43.6	4.96
J011449-741815	01:14:49.2	-74:18:15.6	5.87

Table A3. Continued.

Name ATCA	R.A.$_{843}$ (J2000)	Dec.$_{843}$ (J2000)	S_{36} (mJy)
J011405-732005	01:14:05.5	-73:20:05.7	128.02
J011450-715948	01:14:50.4	-71:59:48.6	2.90
J011454-701434	01:14:54.3	-70:14:34.5	35.72
J011457-732810	01:14:57.8	-73:28:10.0	10.60
J011458-745634	01:14:58.4	-74:56:34.5	5.00
J011458-743355	01:14:58.5	-74:33:55.6	6.98
J011407-751758	01:14:07.5	-75:17:58.8	7.56
J011500-703712	01:15:00.4	-70:37:12.7	10.68
J011517-702527	01:15:17.8	-70:25:27.6	4.20
J011518-713726	01:15:18.6	-71:37:26.8	7.05
J011518-704444	01:15:18.7	-70:44:44.1	5.47
J011518-715928	01:15:18.7	-71:59:28.8	8.30
J011522-724117	01:15:22.4	-72:41:17.3	4.37
J011524-715259	01:15:24.8	-71:52:59.8	7.60
J011525-730017	01:15:25.6	-73:00:17.3	2.64
J011526-720729	01:15:26.7	-72:07:29.7	7.39
J011529-741112	01:15:29.5	-74:11:12.8	8.77
J011503-731101	01:15:03.0	-73:11:01.0	1.60
J011534-722636	01:15:34.4	-72:26:36.6	3.48
J011534-712559	01:15:34.9	-71:25:59.2	5.36
J011535-720006	01:15:35.0	-72:00:06.1	30.84
J011540-741719	01:15:40.5	-74:17:19.3	2.80
J011543-735000	01:15:43.3	-73:50:00.3	3.61
J011545-701845	01:15:45.0	-70:18:45.0	7.89
J011546-724648	01:15:46.9	-72:46:48.9	3.87
J011550-741102	01:15:50.6	-74:11:02.5	8.80
J011551-713954	01:15:51.2	-71:39:54.1	8.26
J011551-721149	01:15:51.6	-72:11:49.9	3.59
J011551-723551	01:15:51.8	-72:35:51.8	7.48
J011559-705554	01:15:59.6	-70:55:54.0	7.05
J011559-710441	01:15:59.8	-71:04:41.5	37.99
J011506-743645	01:15:06.9	-74:36:45.1	7.71
J011611-711028	01:16:11.3	-71:10:28.1	37.56
J011612-733856	01:16:12.0	-73:38:56.6	150.80
J011615-732656	01:16:15.7	-73:26:56.2	56.70
J011619-750555	01:16:19.7	-75:05:55.6	6.44
J011622-712623	01:16:22.3	-71:26:23.9	7.20
J011622-702957	01:16:22.9	-70:29:57.1	83.77
J011627-703214	01:16:27.9	-70:32:14.5	5.62
J011628-731437	01:16:28.9	-73:14:37.7	141.30
J011629-731623	01:16:29.5	-73:16:23.2	1.90
J011603-744326	01:16:03.7	-74:43:26.1	36.87
J011632-725803	01:16:32.3	-72:58:03.9	2.10
J011636-712603	01:16:36.0	-71:26:03.7	29.54
J011637-714433	01:16:37.6	-71:44:33.1	4.01
J011638-732000	01:16:38.1	-73:20:00.3	1.80
J011604-735354	01:16:04.3	-73:53:54.0	17.03
J011640-743232	01:16:40.3	-74:32:32.9	3.25
J011645-743533	01:16:45.2	-74:35:33.5	8.81
J011650-725602	01:16:50.4	-72:56:02.8	2.50

Table A3. Continued.

Name ATCA	R.A.$_{843}$ (J2000)	Dec.$_{843}$ (J2000)	S_{36} (mJy)
J011650-734234	01:16:50.6	-73:42:34.1	6.21
J011652-703145	01:16:52.8	-70:31:45.5	3.41
J011658-715140	01:16:58.4	-71:51:40.3	5.51
J011658-731200	01:16:58.4	-73:12:00.1	2.80
J011606-743210	01:16:06.2	-74:32:10.7	10.20
J011608-704114	01:16:08.0	-70:41:14.4	8.68
J011609-742813	01:16:09.2	-74:28:13.4	35.57
J011701-714324	01:17:01.2	-71:43:24.3	6.43
J011701-742724	01:17:01.7	-74:27:24.8	3.30
J011717-710039	01:17:17.4	-71:00:39.7	9.82
J011717-703432	01:17:17.8	-70:34:32.0	15.95
J011721-714113	01:17:21.5	-71:41:13.3	22.73
J011725-744700	01:17:25.3	-74:47:00.6	7.40
J011726-732008	01:17:26.9	-73:20:08.5	2.00
J011732-743337	01:17:32.3	-74:33:37.8	12.21
J011744-710426	01:17:44.3	-71:04:26.3	5.21
J011744-745553	01:17:44.4	-74:55:53.1	6.98
J011746-734442	01:17:46.2	-73:44:42.1	10.53
J011757-732540	01:17:57.2	-73:25:40.8	3.52
J011757-721910	01:17:57.8	-72:19:10.6	18.80
J011759-745004	01:17:59.0	-74:50:04.7	24.65
J011708-731709	01:17:08.6	-73:17:09.2	1.90
J011709-703247	01:17:09.0	-70:32:47.1	3.76
J011709-733630	01:17:09.3	-73:36:30.0	2.97
J011801-712629	01:18:01.6	-71:26:29.1	3.68
J011810-704049	01:18:10.0	-70:40:49.0	5.42
J011816-711746	01:18:16.1	-71:17:46.2	4.26
J011819-730726	01:18:19.7	-73:07:26.5	6.18
J011802-713816	01:18:02.7	-71:38:16.4	6.50
J011826-731755	01:18:26.0	-73:17:55.3	8.42
J011828-732454	01:18:28.3	-73:24:54.1	5.43
J011803-720506	01:18:03.2	-72:05:06.7	5.27
J011803-741626	01:18:03.4	-74:16:26.8	1.90
J011834-720646	01:18:34.5	-72:06:46.5	19.50
J011836-725721	01:18:36.9	-72:57:21.9	9.02
J011840-710306	01:18:40.2	-71:03:06.4	3.42
J011842-715213	01:18:42.7	-71:52:13.9	18.34
J011853-742604	01:18:53.0	-74:26:04.2	8.09
J011855-724301	01:18:55.3	-72:43:01.5	12.31
J011806-745826	01:18:06.0	-74:58:26.3	36.62
J011911-750147	01:19:11.1	-75:01:47.1	12.03
J011911-724646	01:19:11.6	-72:46:46.4	3.99
J011912-710832	01:19:12.6	-71:08:32.6	4.89
J011914-741858	01:19:14.3	-74:18:58.1	2.70
J011916-751352	01:19:16.0	-75:13:52.0	5.86
J011918-702326	01:19:18.3	-70:23:26.7	5.10
J011918-710529	01:19:18.6	-71:05:29.9	179.00
J011925-730158	01:19:25.1	-73:01:58.5	4.47
J011926-735121	01:19:26.8	-73:51:21.8	6.35
J011932-725932	01:19:32.9	-72:59:32.6	5.68

Table A3. Continued.

Name ATCA	R.A.$_{843}$ (J2000)	Dec.$_{843}$ (J2000)	S_{36} (mJy)
J011939-742558	01:19:39.2	-74:25:58.3	2.60
J011942-745537	01:19:42.1	-74:55:37.2	4.25
J011943-743656	01:19:43.1	-74:36:56.3	3.92
J011956-751431	01:19:56.2	-75:14:31.8	3.98
J011959-750314	01:19:59.3	-75:03:14.1	22.54
J011909-744208	01:19:09.1	-74:42:08.4	36.26
J012011-703606	01:20:11.2	-70:36:06.2	42.09
J012011-745550	01:20:11.7	-74:55:50.5	5.09
J012020-703424	01:20:20.9	-70:34:24.8	3.83
J012023-721953	01:20:23.5	-72:19:53.9	33.29
J012028-712642	01:20:28.2	-71:26:42.4	17.44
J012036-713625	01:20:36.1	-71:36:25.0	4.80
J012036-750633	01:20:36.3	-75:06:33.7	22.24
J012036-735650	01:20:36.6	-73:56:50.2	5.07
J012036-713330	01:20:36.7	-71:33:30.0	7.33
J012037-703845	01:20:37.4	-70:38:45.1	125.40
J012054-733457	01:20:54.0	-73:34:57.3	49.08
J012055-711039	01:20:55.2	-71:10:39.6	12.10
J012006-710813	01:20:06.7	-71:08:13.4	6.59
J012006-725017	01:20:06.9	-72:50:17.0	19.83
J012115-702748	01:21:15.0	-70:27:48.5	5.93
J012116-701341	01:21:16.0	-70:13:41.7	156.60
J012120-701013	01:21:20.4	-70:10:13.7	3.41
J012126-710448	01:21:26.9	-71:04:48.3	4.03
J012128-721541	01:21:28.5	-72:15:41.9	4.80
J012128-714334	01:21:28.6	-71:43:34.3	19.56
J012103-714354	01:21:03.3	-71:43:54.7	3.15
J012130-745745	01:21:30.1	-74:57:45.0	3.85
J012140-740930	01:21:40.9	-74:09:30.2	4.81
J012145-731656	01:21:45.6	-73:16:56.2	9.70
J012150-740009	01:21:50.6	-74:00:09.8	96.41
J012152-710304	01:21:52.9	-71:03:04.6	5.62
J012153-712001	01:21:53.2	-71:20:01.2	8.14
J012154-715528	01:21:54.4	-71:55:28.9	19.57
J012200-744639	01:22:00.9	-74:46:39.1	31.35
J012210-713953	01:22:10.0	-71:39:53.6	40.40
J012210-705004	01:22:10.1	-70:50:04.1	5.01
J012218-732945	01:22:18.3	-73:29:45.9	3.66
J012222-713411	01:22:22.6	-71:34:11.2	6.26
J012223-731121	01:22:23.1	-73:11:21.5	3.15
J012231-703916	01:22:31.3	-70:39:16.4	6.04
J012234-714723	01:22:34.0	-71:47:23.7	14.15
J012235-723151	01:22:35.3	-72:31:51.8	9.84
J012235-733817	01:22:35.6	-73:38:17.7	65.41
J012238-741016	01:22:38.4	-74:10:16.5	35.14
J012246-743546	01:22:46.6	-74:35:46.0	8.86
J012246-742630	01:22:46.8	-74:26:30.0	13.41
J012205-714733	01:22:05.6	-71:47:33.9	11.35
J012250-715045	01:22:50.6	-71:50:45.3	63.72
J012251-705426	01:22:51.3	-70:54:26.0	12.37

Table A3. Continued.

Name ATCA	R.A.$_{843}$ (J2000)	Dec.$_{843}$ (J2000)	S_{36} (mJy)
J012254-731427	01:22:54.5	-73:14:27.4	3.86
J012257-751506	01:22:57.5	-75:15:06.7	880.87
J012258-714842	01:22:58.3	-71:48:42.4	10.91
J012258-735359	01:22:58.9	-73:53:59.4	5.28
J012206-750814	01:22:06.5	-75:08:14.9	11.15
J012207-702917	01:22:07.6	-70:29:17.6	83.99
J012209-723119	01:22:09.6	-72:31:19.3	3.65
J012301-704435	01:23:01.3	-70:44:35.9	9.18
J012301-732943	01:23:01.5	-73:29:43.9	4.47
J012311-745417	01:23:11.4	-74:54:17.4	15.69
J012311-741812	01:23:11.5	-74:18:12.2	9.35
J012312-732843	01:23:12.0	-73:28:43.9	5.47
J012313-741943	01:23:13.8	-74:19:43.7	3.66
J012317-723603	01:23:17.3	-72:36:03.1	12.05
J012320-703737	01:23:20.0	-70:37:37.2	49.08
J012322-714724	01:23:22.7	-71:47:24.6	6.40
J012323-703437	01:23:23.6	-70:34:37.1	3.77
J012323-735605	01:23:23.6	-73:56:05.4	26.62
J012324-740242	01:23:24.5	-74:02:42.0	12.44
J012324-742247	01:23:24.9	-74:22:47.6	3.23
J012330-721813	01:23:30.8	-72:18:13.6	31.81
J012336-703231	01:23:36.3	-70:32:31.4	26.87
J012343-703422	01:23:43.6	-70:34:22.9	3.44
J012345-710520	01:23:45.8	-71:05:20.1	3.48
J012345-735449	01:23:45.8	-73:54:49.3	3.20
J012346-732312	01:23:46.1	-73:23:12.7	2.60
J012349-735037	01:23:49.5	-73:50:37.5	190.30
J012305-735705	01:23:05.4	-73:57:05.2	11.42
J012352-744141	01:23:52.8	-74:41:41.0	68.30
J012354-725617	01:23:54.8	-72:56:17.7	2.70
J012359-703449	01:23:59.0	-70:34:49.6	3.07
J012306-711119	01:23:06.1	-71:11:19.5	14.97
J012411-711919	01:24:11.3	-71:19:19.3	3.46
J012415-704152	01:24:15.2	-70:41:52.6	19.16
J012415-734116	01:24:15.5	-73:41:16.6	6.49
J012417-711203	01:24:17.9	-71:12:03.4	27.58
J012424-713139	01:24:24.7	-71:31:39.2	5.71
J012426-703419	01:24:26.5	-70:34:19.1	5.61
J012428-703804	01:24:28.8	-70:38:04.4	3.17
J012433-712644	01:24:33.5	-71:26:44.2	53.05
J012404-705627	01:24:04.8	-70:56:27.8	4.94
J012453-722511	01:24:53.0	-72:25:11.6	2.87
J012458-720627	01:24:58.3	-72:06:27.2	14.22
J012515-750213	01:25:15.9	-75:02:13.6	5.13
J012518-731633	01:25:18.8	-73:16:33.4	4.39
J012521-722918	01:25:21.7	-72:29:18.9	51.23
J012525-714901	01:25:25.3	-71:49:01.2	6.22
J012530-743458	01:25:30.8	-74:34:58.9	6.64
J012531-703610	01:25:31.1	-70:36:10.0	6.00
J012535-735636	01:25:35.0	-73:56:36.5	27.23

Table A3. Continued.

Name ATCA	R.A.$_{843}$ (J2000)	Dec.$_{843}$ (J2000)	S_{36} (mJy)
J012539-732948	01:25:39.0	-73:29:48.4	6.25
J012541-712937	01:25:41.1	-71:29:37.1	9.26
J012542-734349	01:25:42.3	-73:43:49.5	5.41
J012546-731603	01:25:46.5	-73:16:03.3	98.13
J012547-725105	01:25:47.3	-72:51:05.9	3.51
J012548-715134	01:25:48.5	-71:51:34.7	33.13
J012548-701818	01:25:48.8	-70:18:18.6	11.67
J012549-705736	01:25:49.1	-70:57:36.8	5.76
J012550-744022	01:25:50.5	-74:40:22.6	10.02
J012551-743641	01:25:51.1	-74:36:41.7	3.98
J012551-740010	01:25:51.6	-74:00:10.2	13.08
J012555-713424	01:25:55.6	-71:34:24.7	7.53
J012509-725106	01:25:09.6	-72:51:06.0	4.11
J012600-735417	01:26:00.4	-73:54:17.3	32.81
J012611-713601	01:26:11.3	-71:36:01.9	6.40
J012617-730749	01:26:17.4	-73:07:49.5	76.42
J012618-731248	01:26:18.2	-73:12:48.1	11.95
J012625-705023	01:26:25.1	-70:50:23.6	64.18
J012629-732713	01:26:29.1	-73:27:13.9	60.47
J012603-705547	01:26:03.6	-70:55:47.9	4.32
J012634-744859	01:26:34.8	-74:48:59.5	8.39
J012639-731500	01:26:39.7	-73:15:00.9	103.60
J012641-741625	01:26:41.9	-74:16:25.2	8.01
J012645-703029	01:26:45.0	-70:30:29.7	4.03
J012647-734319	01:26:47.4	-73:43:19.0	10.35
J012649-731928	01:26:49.4	-73:19:28.7	4.80
J012649-731630	01:26:49.6	-73:16:30.2	9.64
J012650-740307	01:26:50.2	-74:03:07.1	7.04
J012651-735256	01:26:51.2	-73:52:56.0	4.95
J012655-751121	01:26:55.8	-75:11:21.9	78.85
J012657-711740	01:26:57.0	-71:17:40.1	4.48
J012658-713457	01:26:58.4	-71:34:57.1	3.44
J012606-724826	01:26:06.0	-72:48:26.5	3.45
J012701-715051	01:27:01.2	-71:50:51.2	6.68
J012711-730938	01:27:11.0	-73:09:38.5	5.64
J012714-705936	01:27:14.3	-70:59:36.4	26.18
J012718-741640	01:27:18.6	-74:16:40.3	4.30
J012725-712049	01:27:25.5	-71:20:49.4	3.96
J012726-703241	01:27:26.0	-70:32:41.9	29.76
J012728-724207	01:27:28.0	-72:42:07.7	3.53
J012733-713639	01:27:33.9	-71:36:39.2	93.87
J012744-712507	01:27:44.3	-71:25:07.7	3.80
J012749-705621	01:27:49.7	-70:56:21.8	64.25
J012751-712849	01:27:51.7	-71:28:49.7	4.55
J012752-731100	01:27:52.3	-73:11:00.9	18.58
J012758-720535	01:27:58.5	-72:05:35.1	25.67
J012706-703851	01:27:06.3	-70:38:51.6	3.62
J012811-715303	01:28:11.1	-71:53:03.7	3.77
J012811-751253	01:28:11.4	-75:12:53.2	373.90
J012815-730758	01:28:15.6	-73:07:58.3	15.99

Table A3. Continued.

Name ATCA	R.A.$_{843}$ (J2000)	Dec.$_{843}$ (J2000)	S_{36} (mJy)
J012819-715426	01:28:19.9	-71:54:26.8	17.30
J012802-702126	01:28:02.5	-70:21:26.4	35.09
J012802-705016	01:28:02.8	-70:50:16.4	4.22
J012820-712254	01:28:20.2	-71:22:54.2	14.59
J012823-744129	01:28:23.7	-74:41:29.3	5.41
J012828-734141	01:28:28.9	-73:41:41.8	12.54
J012832-733811	01:28:32.0	-73:38:11.7	4.13
J012835-715711	01:28:35.4	-71:57:11.6	7.68
J012841-742321	01:28:41.7	-74:23:21.3	7.97
J012842-725207	01:28:42.4	-72:52:07.8	5.41
J012848-731405	01:28:48.5	-73:14:05.3	4.95
J012805-741105	01:28:05.2	-74:11:05.5	12.53
J012850-705009	01:28:50.0	-70:50:09.1	4.28
J012851-704837	01:28:51.0	-70:48:37.6	3.12
J012859-712258	01:28:59.7	-71:22:58.6	7.86
J012900-715156	01:29:00.5	-71:51:56.1	20.21
J012900-744302	01:29:00.7	-74:43:02.2	3.46
J012917-723956	01:29:17.1	-72:39:56.4	6.75
J012923-733145	01:29:23.7	-73:31:45.8	31.10
J012927-742821	01:29:27.4	-74:28:21.9	4.74
J012928-743546	01:29:28.0	-74:35:46.2	3.06
J012928-730646	01:29:28.2	-73:06:46.2	10.39
J012928-703405	01:29:28.3	-70:34:05.5	47.30
J012930-733311	01:29:30.0	-73:33:11.0	197.80
J012931-704448	01:29:31.2	-70:44:48.7	3.51
J012931-705352	01:29:31.9	-70:53:52.7	16.75
J012937-701137	01:29:37.0	-70:11:37.4	8.95
J012940-740745	01:29:40.9	-74:07:45.7	5.83
J012943-702749	01:29:43.0	-70:27:49.0	4.03
J012945-703520	01:29:45.2	-70:35:20.9	177.40
J012945-723235	01:29:45.3	-72:32:35.9	7.55
J012947-701809	01:29:47.0	-70:18:09.0	105.10
J012949-743712	01:29:49.6	-74:37:12.7	3.45
J012950-703646	01:29:50.1	-70:36:46.5	43.60
J012950-703403	01:29:50.5	-70:34:03.4	81.00
J012951-721031	01:29:51.1	-72:10:31.5	5.88
J012954-701532	01:29:54.8	-70:15:32.7	17.27
J012958-701257	01:29:58.5	-70:12:57.0	6.80
J012959-724437	01:29:59.3	-72:44:37.0	7.90
J013001-700909	01:30:01.6	-70:09:09.0	15.66
J013012-703755	01:30:12.7	-70:37:55.2	4.44
J013012-721824	01:30:12.7	-72:18:24.8	11.59
J013013-742023	01:30:13.9	-74:20:23.9	26.46
J013017-742549	01:30:17.0	-74:25:49.5	13.07
J013020-702644	01:30:20.2	-70:26:44.0	8.13
J013025-743929	01:30:25.3	-74:39:29.4	7.81
J013026-731126	01:30:26.1	-73:11:26.4	2.70
J013003-710640	01:30:03.4	-71:06:40.5	6.59
J013031-714813	01:30:31.4	-71:48:13.0	12.86
J013032-731740	01:30:32.1	-73:17:40.4	51.98

Table A3. Continued.

Name ATCA	R.A.$_{843}$ (J2000)	Dec.$_{843}$ (J2000)	S_{36} (mJy)
J013035-745837	01:30:35.2	-74:58:37.1	4.23
J013040-723222	01:30:40.0	-72:32:22.0	6.47
J013040-734630	01:30:40.8	-73:46:30.5	3.93
J013041-725050	01:30:41.8	-72:50:50.5	3.50
J013053-723050	01:30:53.6	-72:30:50.7	3.84
J013058-700939	01:30:58.0	-70:09:39.1	16.86
J013006-743555	01:30:06.1	-74:35:55.4	6.80
J013008-710930	01:30:08.9	-71:09:30.2	6.68
J013110-715139	01:31:10.2	-71:51:39.3	6.36
J013112-740715	01:31:12.6	-74:07:15.4	3.77
J013116-730356	01:31:16.5	-73:03:56.7	3.31
J013119-745748	01:31:19.9	-74:57:48.9	7.40
J013121-725244	01:31:21.4	-72:52:44.2	19.10
J013121-711133	01:31:21.6	-71:11:33.4	3.71
J013124-713342	01:31:24.1	-71:33:42.3	25.35
J013124-740040	01:31:24.1	-74:00:40.5	41.80
J013129-705726	01:31:29.6	-70:57:26.3	3.32
J013103-704856	01:31:03.5	-70:48:56.1	7.14
J013130-710306	01:31:30.8	-71:03:06.5	13.23
J013133-750444	01:31:33.9	-75:04:44.5	2.91
J013134-750155	01:31:34.8	-75:01:55.2	3.95
J013138-713359	01:31:38.5	-71:33:59.9	6.40
J013141-701008	01:31:41.9	-70:10:08.5	61.87
J013147-734941	01:31:47.6	-73:49:41.9	34.25
J013150-724452	01:31:50.2	-72:44:52.7	6.18
J013150-720516	01:31:50.8	-72:05:16.7	16.42
J013154-741736	01:31:54.8	-74:17:36.8	8.56
J013107-745844	01:31:07.2	-74:58:44.5	22.59
J013210-750351	01:32:10.9	-75:03:51.5	8.65
J013212-710612	01:32:12.4	-71:06:12.3	15.23
J013212-742010	01:32:12.7	-74:20:10.7	9.02
J013214-733902	01:32:14.8	-73:39:02.3	70.34
J013219-715347	01:32:19.0	-71:53:47.6	47.75
J013219-715518	01:32:19.4	-71:55:18.1	3.26
J013221-713551	01:32:21.8	-71:35:51.7	3.72
J013227-742559	01:32:27.7	-74:25:59.0	3.70
J013228-734121	01:32:28.8	-73:41:21.6	57.17
J013229-723957	01:32:29.6	-72:39:57.3	388.00
J013203-705415	01:32:03.8	-70:54:15.9	3.79
J013230-743020	01:32:30.7	-74:30:20.7	6.69
J013234-710031	01:32:34.1	-71:00:31.2	9.06
J013236-710414	01:32:36.5	-71:04:14.8	44.11
J013238-722137	01:32:38.5	-72:21:37.8	35.75
J013239-741340	01:32:39.5	-74:13:40.8	3.12
J013242-734415	01:32:42.2	-73:44:15.7	76.84
J013246-743348	01:32:46.5	-74:33:48.3	9.27
J013247-711637	01:32:47.3	-71:16:37.8	15.03
J013252-710321	01:32:52.0	-71:03:21.7	5.10
J013256-710851	01:32:56.2	-71:08:51.9	3.18
J013207-730758	01:32:07.0	-73:07:58.8	3.20

Table A3. Continued.

Name ATCA	R.A.$_{843}$ (J2000)	Dec.$_{843}$ (J2000)	S_{36} (mJy)
J013314-731625	01:33:14.5	-73:16:25.0	2.50
J013316-711519	01:33:16.9	-71:15:19.4	7.99
J013326-705330	01:33:26.4	-70:53:30.7	16.02
J013327-701820	01:33:27.9	-70:18:20.1	4.66
J013328-743632	01:33:28.3	-74:36:32.2	46.77
J013329-730304	01:33:29.4	-73:03:04.1	104.50
J013303-730932	01:33:03.7	-73:09:32.2	2.60
J013331-704526	01:33:31.0	-70:45:26.1	32.04
J013332-711616	01:33:32.1	-71:16:16.7	125.70
J013334-733645	01:33:34.8	-73:36:45.0	17.55
J013336-731940	01:33:36.8	-73:19:40.5	3.67
J013337-720218	01:33:37.0	-72:02:18.9	10.31
J013337-703219	01:33:37.9	-70:32:19.1	3.94
J013339-725056	01:33:39.9	-72:50:56.2	12.08
J013341-744611	01:33:41.2	-74:46:11.5	66.76
J013342-731749	01:33:42.1	-73:17:49.2	24.76
J013350-712340	01:33:50.7	-71:23:40.9	3.04
J013356-711014	01:33:56.3	-71:10:14.8	19.05
J013306-743514	01:33:06.4	-74:35:14.9	3.74
J013306-741929	01:33:06.6	-74:19:29.9	11.15
J013307-723006	01:33:07.2	-72:30:06.0	5.69
J013309-742917	01:33:09.3	-74:29:17.4	59.86
J013401-703423	01:34:01.5	-70:34:23.6	8.63
J013411-700813	01:34:11.2	-70:08:13.7	8.79
J013413-734751	01:34:13.1	-73:47:51.9	4.07
J013402-715116	01:34:02.6	-71:51:16.9	15.48
J013421-722018	01:34:21.2	-72:20:18.9	5.05
J013421-722719	01:34:21.5	-72:27:19.8	6.74
J013423-731811	01:34:23.2	-73:18:11.8	12.71
J013426-703940	01:34:26.4	-70:39:40.9	3.70
J013427-701401	01:34:27.6	-70:14:01.6	4.71
J013430-720726	01:34:30.5	-72:07:26.1	3.40
J013431-714018	01:34:31.5	-71:40:18.4	6.26
J013434-723837	01:34:34.5	-72:38:37.1	5.14
J013435-731539	01:34:35.8	-73:15:39.7	9.37
J013436-704738	01:34:36.7	-70:47:38.8	4.11
J013439-722126	01:34:39.5	-72:21:26.7	18.33
J013439-721246	01:34:39.8	-72:12:46.5	24.14
J013404-731121	01:34:04.1	-73:11:21.9	4.49
J013440-705803	01:34:40.6	-70:58:03.7	74.84
J013443-705625	01:34:43.8	-70:56:25.1	4.13
J013446-723640	01:34:46.4	-72:36:40.0	7.25
J013446-732340	01:34:46.9	-73:23:40.7	4.78
J013453-722444	01:34:53.4	-72:24:44.1	160.20
J013455-725457	01:34:55.4	-72:54:57.7	4.02
J013459-701641	01:34:59.5	-70:16:41.2	6.84
J013500-702209	01:35:00.4	-70:22:09.1	15.16
J013500-711257	01:35:00.6	-71:12:57.2	4.22
J013510-721317	01:35:10.2	-72:13:17.8	3.22
J013511-751200	01:35:11.9	-75:12:00.5	12.21

Table A3. Continued.

Name ATCA	R.A.$_{843}$ (J2000)	Dec.$_{843}$ (J2000)	S_{36} (mJy)
J013527-744137	01:35:27.6	-74:41:37.3	21.81
J013529-704823	01:35:29.9	-70:48:23.9	18.85
J013542-740528	01:35:42.6	-74:05:28.9	8.65
J013547-733157	01:35:47.9	-73:31:57.3	12.53
J013547-741332	01:35:47.9	-74:13:32.5	4.90
J013551-712608	01:35:51.3	-71:26:08.5	10.23
J013551-720916	01:35:51.3	-72:09:16.6	3.85
J013551-742921	01:35:51.4	-74:29:21.0	5.44
J013559-741245	01:35:59.6	-74:12:45.1	16.66
J013506-710155	01:35:06.7	-71:01:55.4	53.32
J013600-720257	01:36:00.0	-72:02:57.9	17.84
J013600-715510	01:36:00.7	-71:55:10.5	11.11
J013618-720723	01:36:18.2	-72:07:23.1	15.04
J013602-725057	01:36:02.0	-72:50:57.1	7.14
J013623-743252	01:36:23.5	-74:32:52.1	9.08
J013631-740659	01:36:31.9	-74:06:59.2	60.30
J013634-733653	01:36:34.4	-73:36:53.5	19.04
J013635-744331	01:36:35.5	-74:43:31.6	6.05
J013643-711720	01:36:43.9	-71:17:20.1	9.34
J013644-705604	01:36:44.1	-70:56:04.3	47.63
J013649-721252	01:36:49.4	-72:12:52.3	3.16
J013651-713719	01:36:51.9	-71:37:19.5	21.05
J013658-705723	01:36:58.6	-70:57:23.9	40.88
J013608-713502	01:36:08.5	-71:35:02.8	3.66
J013710-713116	01:37:10.2	-71:31:16.4	7.78
J013715-744404	01:37:15.5	-74:44:04.3	3.78
J013718-720611	01:37:18.8	-72:06:11.8	3.31
J013702-730413	01:37:02.9	-73:04:13.2	258.20
J013724-731655	01:37:24.0	-73:16:55.0	3.52
J013724-745333	01:37:24.2	-74:53:33.2	18.87
J013727-730618	01:37:27.8	-73:06:18.2	10.15
J013703-740258	01:37:03.3	-74:02:58.4	5.10
J013730-713042	01:37:30.6	-71:30:42.8	2.92
J013737-732801	01:37:37.6	-73:28:01.7	6.21
J013704-715939	01:37:04.0	-71:59:39.4	3.11
J013741-720103	01:37:41.7	-72:01:03.3	3.87
J013742-733049	01:37:42.3	-73:30:49.0	73.16
J013754-715604	01:37:54.5	-71:56:04.2	5.47
J013758-732747	01:37:58.6	-73:27:47.1	9.62
J013708-732738	01:37:08.2	-73:27:38.1	14.52
J013800-720327	01:38:00.1	-72:03:27.5	14.97
J013800-741351	01:38:00.2	-74:13:51.0	69.44
J013813-732338	01:38:13.1	-73:23:38.5	27.29
J013813-744328	01:38:13.4	-74:43:28.5	6.96
J013816-723558	01:38:16.1	-72:35:58.2	11.60
J013821-725704	01:38:21.7	-72:57:04.4	12.64
J013823-743013	01:38:23.6	-74:30:13.3	4.98
J013825-723647	01:38:25.1	-72:36:47.0	17.83
J013825-744124	01:38:25.1	-74:41:24.6	17.65
J013803-723202	01:38:03.6	-72:32:02.2	6.34

Table A3. Continued.

Name ATCA	R.A.$_{843}$ (J2000)	Dec.$_{843}$ (J2000)	S_{36} (mJy)
J013835-723654	01:38:35.6	-72:36:54.3	14.40
J013842-733757	01:38:42.9	-73:37:57.9	39.10
J013846-715917	01:38:46.3	-71:59:17.9	18.69
J013805-721434	01:38:05.8	-72:14:34.7	4.80
J013853-743027	01:38:53.8	-74:30:27.9	2.80
J013910-721026	01:39:10.2	-72:10:26.4	4.97
J013913-750041	01:39:13.4	-75:00:41.0	60.22
J013919-731655	01:39:19.3	-73:16:55.9	94.18
J013902-741850	01:39:02.5	-74:18:50.6	3.20
J013923-724144	01:39:23.6	-72:41:44.0	23.33
J013924-745547	01:39:24.4	-74:55:47.8	11.07
J013927-735755	01:39:27.0	-73:57:55.0	8.78
J013929-723829	01:39:29.1	-72:38:29.4	4.64
J013931-730952	01:39:31.5	-73:09:52.8	9.64
J013940-734516	01:39:40.2	-73:45:16.6	14.06
J013905-725628	01:39:05.6	-72:56:28.6	122.00
J013950-731000	01:39:50.7	-73:10:00.4	71.39
J013906-741639	01:39:06.3	-74:16:39.2	3.90
J014001-750041	01:40:01.1	-75:00:41.4	7.35
J014011-742302	01:40:11.8	-74:23:02.2	16.50
J014022-733049	01:40:22.7	-73:30:49.0	5.88
J014023-732557	01:40:23.0	-73:25:57.7	5.76
J014025-743918	01:40:25.0	-74:39:18.7	5.60
J014027-724809	01:40:27.8	-72:48:09.0	16.64
J014039-725100	01:40:39.3	-72:51:00.6	28.38
J014050-735806	01:40:50.0	-73:58:06.6	6.08
J014053-744803	01:40:53.1	-74:48:03.9	4.25
J014058-744905	01:40:58.7	-74:49:05.7	6.11
J014113-744912	01:41:13.3	-74:49:12.9	4.83
J014115-740733	01:41:15.6	-74:07:33.5	109.40
J014121-744015	01:41:21.3	-74:40:15.3	4.18
J014122-732450	01:41:22.8	-73:24:50.0	3.74
J014127-730358	01:41:27.1	-73:03:58.9	9.18
J014131-733807	01:41:31.4	-73:38:07.7	7.53
J014136-733114	01:41:36.6	-73:31:14.2	13.67
J014139-733536	01:41:39.0	-73:35:36.7	7.84
J014202-740755	01:42:02.0	-74:07:55.8	6.47
J014233-733658	01:42:33.1	-73:36:58.1	18.46
J014242-743319	01:42:42.0	-74:33:19.3	4.06
J014249-735837	01:42:49.1	-73:58:37.8	36.44
J014249-743444	01:42:49.9	-74:34:44.9	70.84
J014253-743841	01:42:53.8	-74:38:41.5	17.10
J014310-743432	01:43:10.6	-74:34:32.5	3.58
J014320-742638	01:43:20.2	-74:26:38.4	3.08
J014326-744302	01:43:26.5	-74:43:02.2	5.20
J014303-742634	01:43:03.2	-74:26:34.2	3.54
J014355-744718	01:43:55.9	-74:47:18.4	5.44
J014401-743134	01:44:01.2	-74:31:34.6	76.60
J014433-743110	01:44:33.6	-74:31:10.4	4.63
J014433-743308	01:44:33.7	-74:33:08.3	116.10

Table A3. Continued.

Name ATCA	R.A.$_{843}$ (J2000)	Dec.$_{843}$ (J2000)	S_{36} (mJy)
J014436-750749	01:44:36.1	-75:07:49.6	4.86
J014408-750922	01:44:08.0	-75:09:22.3	12.88
J014611-745116	01:46:11.8	-74:51:16.7	8.23
J014703-751028	01:47:03.9	-75:10:28.8	7.77

A.12 Related Paper 12

Haberl, F., Sturm, R., Filipović, M. D., Pietsch, W., and Crawford, E. J. (2012c). SXP 1062, a young Be X-ray binary pulsar with long spin period. Implications for the neutron star birth spin. *A&A*, 537:L1

My contribution was to assist in the data analysis. This is a 10% contribution.

A&A 537, L1 (2012)
DOI: 10.1051/0004-6361/201118369

Astronomy & Astrophysics

Letter to the Editor

SXP 1062, a young Be X-ray binary pulsar with long spin period⋆

Implications for the neutron star birth spin

F. Haberl[1], R. Sturm[1], M. D. Filipović[2], W. Pietsch[1], and E. J. Crawford[2]

[1] Max-Planck-Institut für extraterrestrische Physik, Giessenbachstraße, 85748 Garching, Germany
e-mail: fwh@mpe.mpg.de
[2] University of Western Sydney, Locked Bag 1797, Penrith South DC, NSW1797, Australia

Received 31 October 2011 / Accepted 1 December 2011

ABSTRACT

Context. The Small Magellanic Cloud (SMC) is ideally suited to investigating the recent star formation history from X-ray source population studies. It harbours a large number of Be/X-ray binaries (Be stars with an accreting neutron star as companion), and the supernova remnants can be easily resolved with imaging X-ray instruments.
Aims. We search for new supernova remnants in the SMC and in particular for composite remnants with a central X-ray source.
Methods. We study the morphology of newly found candidate supernova remnants using radio, optical and X-ray images and investigate their X-ray spectra.
Results. Here we report on the discovery of the new supernova remnant around the recently discovered Be/X-ray binary pulsar CXO J012745.97−733256.5 = SXP 1062 in radio and X-ray images. The Be/X-ray binary system is found near the centre of the supernova remnant, which is located at the outer edge of the eastern wing of the SMC. The remnant is oxygen-rich, indicating that it developed from a type Ib event. From *XMM-Newton* observations we find that the neutron star with a spin period of 1062 s (the second longest known in the SMC) shows a very high average spin-down rate of 0.26 s per day over the observing period of 18 days.
Conclusions. From the currently accepted models, our estimated age of around 10 000−25 000 years for the supernova remnant is not long enough to spin down the neutron star from a few 10 ms to its current value. Assuming an upper limit of 25 000 years for the age of the neutron star and the extreme case that the neutron star was spun down by the accretion torque that we have measured during the *XMM-Newton* observations since its birth, a lower limit of 0.5 s for the birth spin period is inferred. For more realistic, smaller long-term average accretion torques our results suggest that the neutron star was born with a correspondingly longer spin period. This implies that neutron stars in Be/X-ray binaries with long spin periods can be much younger than currently anticipated.

Key words. stars: neutron – X-rays: binaries – Magellanic Clouds – stars: emission-line, Be

1. Introduction

One of the most cataclysmic events in the universe is the explosion of a massive star as a supernova, which can create a neutron star (NS). NSs are thought to be born rapidly spinning with rotation periods of a few 10 ms. Their rotation is first slowed down by magnetic dipole braking and then by the propeller effect when the NS is in a binary star system and mass loss from the companion star begins (for a review see e.g. Bhattacharya & van den Heuvel 1991). When rotating slowly enough, accretion onto the NS sets in (Ghosh & Lamb 1978) and the system can be detected as an X-ray binary. The spin evolution of the NS in a high-mass X-ray binary (HMXB) system depends on the initial magnetic field strength of the NS and on the mass accretion rate (Urpin et al. 1998).

Be/X-ray binary (BeXRB) systems are a subgroup of HMXBs with an NS accreting matter from the circumstellar disk of a Be star (Reig 2011). The Small Magellanic Cloud (SMC) harbours an extraordinarily large number of BeXRBs (Coe et al. 2005; Shtykovskiy & Gilfanov 2005; Haberl et al. 2008). These are believed to have been created during a burst of star formation about 42 million years ago (Antoniou et al. 2010). For more than fifty BeXRBs in the SMC the NS spin period is known from the detection of coherent pulsations in their X-ray flux. The spin periods range from 2.16 s (XTE J0119-731 = SXP 2.16; Corbet et al. 2003) to 1320 s (RX J0103.6-7201 = SXP 1323; Haberl & Pietsch 2005) with a bimodal structure indicated in their distribution (Knigge et al. 2011).

From ROSAT HRI data, Hughes & Smith (1994) proposed two BeXRBs within supernova remnants (SNRs) in the SMC. For one of them, located in the direction of the SNR IKT 21 (van der Heyden et al. 2004), pulsations of 345 s were discovered by Israel et al. (2000, SAX J0103.2-7209). The other – still unconfirmed – candidate BeXRB in the direction of IKT 25 was not detected by *XMM-Newton* or *Chandra*. In both cases it is not clear whether the BeXRB (or candidate) is physically associated with the SNR because they are not located near the centre of the remnant and the high number of BeXRBs in the bar of the SMC make chance coincidences likely. The SNR, which was created by the supernova explosion, is expected to have faded beyond detectability before accretion onto the NS starts. Finding a BeXRB associated to a SNR would therefore suggest a much faster spin-down than predicted by the standard models, or else the NS star was born with slow rotation. Here, we present the discovery of an SNR in radio and X-rays around the BeXRB

⋆ Based on observations with *XMM-Newton*, an ESA Science Mission with instruments and contributions directly funded by ESA Member states and the USA (NASA).

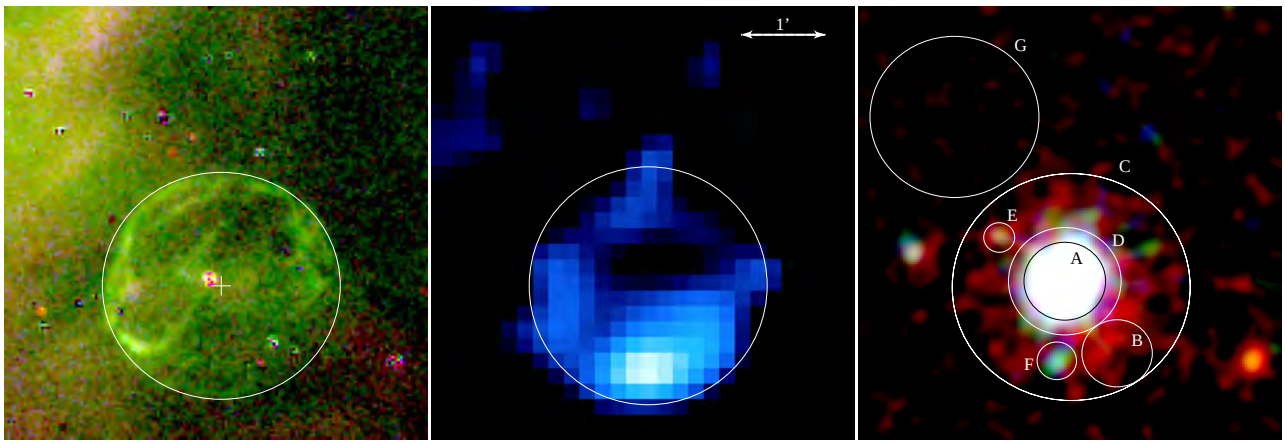

Fig. 1. Images of the region around the BeXRB SXP 1062. *Left*: continuum-subtracted MCELS images. Red, green, and blue correspond to Hα, [O III] and [S II]. The cross marks the centre of the white circle (RA = $01^h27^m44\overset{s}{.}15$, Dec = $-73°33'01\overset{''}{.}6$, J2000), which indicates the estimated size of the SNR in all images. The Be star counterpart of SXP 1062 is visible close to the cross. *Middle*: MOST 36 cm radio image, logarithmically scaled from 0.5 to 3 mJy. *Right*: combined, instrument background-subtracted EPIC-pn and MOS colour image obtained from the *XMM-Newton* observations. Red, green, and blue denote X-ray intensities in the 0.2−1.0, 1.0−2.0, and 2.0−4.5 keV bands. The images from the individual bands were adaptively smoothed with a Gaussian σ of 4″ (at high intensities) to 20″ (low intensities). Circles indicate the extraction regions for the X-ray spectra: Source region for SXP 1062 (A, 29″ radius) and associated background (B, 25″). For the SNR spectrum (C, 84.5″), regions D (40″), E (11″), and F (14″) were excluded and region G (60″) was used to estimate the background. Regions E and F were excluded because they contain possible point sources in the direction of the SNR as found in source detection runs on the EPIC images.

pulsar CXO J012745.97−733256.5 = SXP 1062. The discovery of the new SMC pulsar and its possible association with a shell nebula around it has recently been reported by Henault-Brunet et al. (2011, hereafter HB11).

2. Multi-wavelength observations and data analysis

2.1. Optical

The Magellanic Cloud Emission Line Survey[1] was carried out from the 0.6 m University of Michigan/CTIO Curtis Schmidt telescope, equipped with an SITE 2048 × 2048 CCD. This resulted in a field of 1.35° × 1.35° with a pixel scale of 2.4″ × 2.4″. The Magellanic Clouds were mapped in narrow wavelength bands corresponding to Hα, [O III], and [S II], together with matching red and green continuum bands. All the images were continuum-subtracted, flux-calibrated, and assembled into mosaic images. A composite image in the three bands of the region around SXP 1062 is presented in Fig. 1, revealing a shell-type nebula dominated by the strong [O III] line as also discussed by HB11.

2.2. Radio-continuum

The field of SXP 1062 was observed with the Australia Telescope Compact Array (ATCA) on 2009-01-05 with array configuration 6C, and on 2009-02-05 in array configuration EW352 (ATCA project C1869). The field was observed at wavelengths of 20 cm and 13 cm. Each session was carried out in "snap-shot" mode, totalling ~3.5 h of integration time over a 12 h period. These data were combined with the relevant parts of the data from Wong et al. (2011) and Filipovic et al. (1995) to improve *u*-*v* plane coverage. The 13 cm data proved unusable due to radio frequency interference. The 20 cm data was useful only when long baselines were excluded thus the final image has a resolution of 145″×131″ with an r.m.s. noise of 0.5 mJy/beam. We report an integrated flux density of 6 mJy at 20 cm.

Using the image of Ye & Turtle (1993), we measured an integrated flux density of 9 mJy at 36 cm (see Fig. 1). Combining this measurement with the 20 cm measurement we derive a spectral index ($S_\nu \propto \nu^\alpha$) of $\alpha = -0.8 \pm 0.4$ which is steeper than most SNRs in the Magellanic Clouds (Filipovic et al. 1998). We estimate that the surface brightness of this SNR is 1.6×10^{-22} W m^{-2} Hz^{-1} Sr^{-1} with a luminosity of 3.4×10^{15} W Hz^{-1}, assuming a distance of 60 kpc and diameter of 166″. This makes it the faintest known radio SNR in the SMC (Filipović et al. 2005, 2008; Owen et al. 2011).

2.3. X-rays

Chandra (between 2010-03-31 and 2010-04-29) and *XMM-Newton* (2010-03-25 to 2010-04-12) observed the field around the star-forming region NGC 602 and revealed the new BeXRB SXP 1062 in the eastern wing of the SMC (HB11) with a spin period of 1062 s, the second longest known in the SMC after SXP 1323. Here, we present the analysis of the four *XMM-Newton* observations (observation IDs 0602520401, 0602520201, 0602520301, and 0602520501) with durations of 66.3, 119.0, 91.2, and 55.0 ks and spread over 18 days.

2.3.1. Morphology

Following the analysis of the SMC survey with *XMM-Newton* (Haberl et al., in prep.; Sturm et al., in prep.), we produced X-ray images from the combined EPIC-pn (Strüder et al. 2001) and EPIC-MOS (Turner et al. 2001) data in the energy bands 0.2−1.0 keV, 1.0−2.0 keV, and 2.0−4.5 keV. Our analysis of the EPIC data used the tools from the *XMM-Newton* SAS package version 11.0.1[2]. To optimise the sensitivity for faint diffuse X-ray emission we removed intervals of high background caused by soft protons and subtracted the contribution of the detector particle background from the images. For EPIC-pn also

[1] MCELS: http://www.ctio.noao.edu/~mcels/

[2] Science Analysis Software (SAS), http://xmm.esac.esa.int/sas/

the out-of-time events recorded during CCD readout were subtracted. The final colour image of the region around SXP 1062 is presented in Fig. 1. Although the emission from SXP 1062 dominates the hard energy bands, soft extended emission is clearly seen around the X-ray pulsar. The extent of this emission is similar to the radio and MCELS images. We also checked the *Chandra* images for the soft emission, but the sensitivity at low energies is insufficient for the *Chandra* ACIS-I instrument to allow a significant detection.

2.3.2. Spectral analysis

We extracted EPIC spectra from the X-ray pulsar and the soft emission region, merging the data from all four observations. The extraction regions are indicated in Fig. 1 and described below. No MOS1 data is available because the source was located on CCD 6, which is no longer operative. For the spectra we selected single and double-pixel events (PATTERN 0-4) for pn and single to quadruple events (PATTERN 0-12) for MOS with FLAG = 0 to avoid bad pixels. Applying the same background flare screening as for the images resulted in net exposures for the spectra of 206.8 ks for pn and 236.7 ks for MOS2.

To extract the spectra of SXP 1062 we used a circular region and a very close background region inside the soft emission region to remove the contribution of this component. We fitted the pn and MOS2 simultaneously with a power-law, attenuated by two absorption components. The first accounts for the Galactic foreground absorption with a fixed column density of 6×10^{20} cm^{-2} and solar abundances (Wilms et al. 2000), while the second models the absorption along the line of sight within the SMC and local to the source with free column density and reduced abundances of 0.2 for elements heavier than helium (Russell & Dopita 1992). This resulted in an acceptable fit with reduced χ^2 of 1.12 for 377 degrees of freedom (see Fig. 2). The best-fit value for the column density in the SMC was $1.8 \pm 0.2 \times 10^{21}$ cm^{-2} and the power-law photon index 0.74 ± 0.02, values typical of BeXRBs in the SMC (Haberl et al. 2008). The observed average flux (0.2–10 keV) during the *XMM-Newton* observations was 1.4×10^{-12} erg cm^{-2} s^{-1} (as obtained from the pn spectrum), which corresponds to a source luminosity corrected for absorption of 6.3×10^{35} erg s^{-1} (assuming a distance of 60 kpc). The flux increased after the first observation and finally dropped by 27% in the last observation (1.33×10^{-12} erg cm^{-2} s^{-1}, 1.53×10^{-12} erg cm^{-2} s^{-1}, 1.54×10^{-12} erg cm^{-2} s^{-1} and 1.13×10^{-12} erg cm^{-2} s^{-1} in chronological order), which could indicate that we witnessed a typical type I outburst (Okazaki & Negueruela 2001).

To investigate the soft extended emission, we extracted the EPIC spectra from a ring around the position of SXP 1062. The relatively wide wings in the point spread function of the *XMM-Newton* telescopes means a contribution from the X-ray pulsar to the soft emission cannot be avoided. Therefore, we modelled the spectrum of the diffuse emission with a power-law component in addition to a thermal component. We kept the SMC absorption and photon index for the power-law fixed at the values derived from the spectra of SXP 1062, allowing only a free normalisation. For the thermal component we used the plasma emission model `mekal` (also with SMC abundances as for the absorption) available in XSPEC (Mewe et al. 1985) with SMC absorption (free in the fit and different to that of the power-law component). The resulting best-fit parameters (reduced χ^2 = 1.22 for 16 degrees of freedom) are $7.3^{+8.8}_{-6.8} \times 10^{20}$ cm^{-2} for the SMC absorption and 0.23 ± 0.05 keV for the temperature. The observed flux (0.2–2 keV) of 1.1×10^{-14} erg cm^{-2} s^{-1} makes

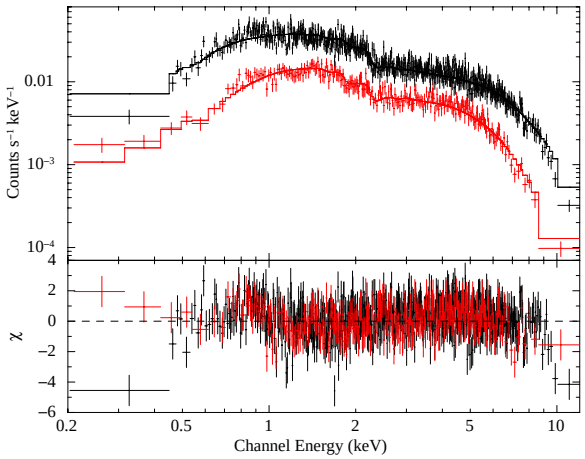

Fig. 2. EPIC-pn (black) and MOS2 (red) spectra of SXP 1062 combining the data from the four *XMM-Newton* observations. The best-fit ower-law model is plotted as histogram, and the lower panel shows the fit residuals.

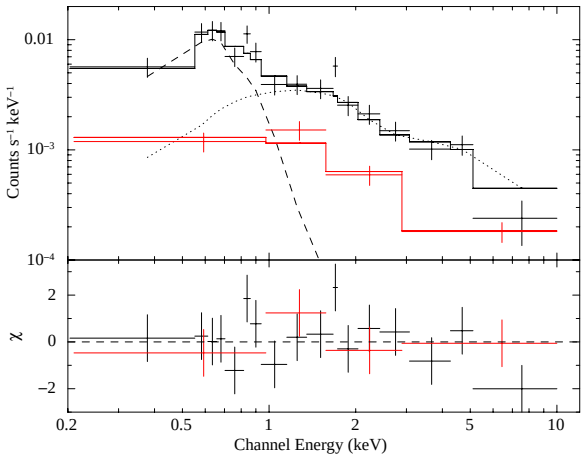

Fig. 3. EPIC spectra as in Fig. 2 extracted from the soft emission region around SXP 1062. The best-fit model is composed of a thermal (dashed line) and a power-law (dotted) component (see text).

it the X-ray faintest SNR known in the SMC (for other faint remnants see Filipović et al. 2008). The spectra with the best-fit model are presented in Fig. 3. Unfortunately, the low-quality statistics of the spectra do not allow a more detailed comparison of different models for the thermal spectral component.

The H I column density of the SMC in the direction of SXP 1062 is measured to 2.1×10^{21} cm^{-2} (Stanimirovic et al. 1999). The absorption inferred from the X-ray spectrum of SXP 1062 is similar, while for the soft emission region we can only place an upper limit of $\sim 1.6 \times 10^{21}$ cm^{-2}. The fact that BeXRBs show source intrinsic absorption and the large uncertainty in the column density of the soft X-ray emission spectrum do not allow deriving any constraints on the radial position of the objects within the SMC. Nevertheless, the two column densities inferred from the X-ray spectra of the BeXRB and the diffuse X-ray emission region (the SNR) are consistent with a location of the BeXRB within the SNR.

2.3.3. Timing analysis of SXP 1062

We performed a timing analysis of the EPIC light curves using the Bayesian approach (Gregory & Loredo 1996) and a Rayleigh

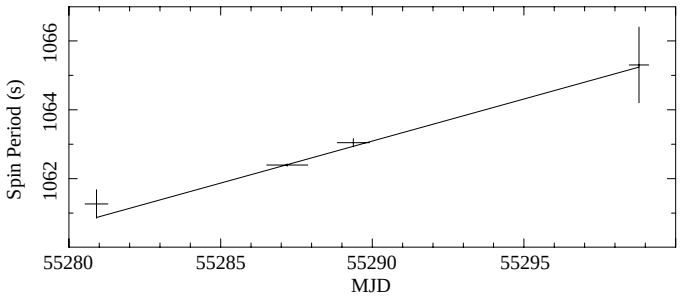

Fig. 4. Evolution of the spin period of SXP 1062 as obtained from the combined EPIC-pn and EPIC-MOS2 data of the four *XMM-Newton* observations. Spin periods and 1-σ errors were derived with the Bayesian odds ratio method.

Z^2 test for one harmonic (Haberl & Zavlin 2002; Buccheri et al. 1983) around the known periodicity of 1062 s. To investigate a possible evolution of the spin period we first analysed each *XMM-Newton* observation separately. The obtained spin periods are plotted versus time in Fig. 4 and show a steady spin-down trend over the observing interval of about 18 days. A linear fit to the spin period evolution (line in Fig. 4) results in a period change $\dot{P}$ of $2.8^{+0.8}_{-0.7} \times 10^{-6}$ s s^{-1} ($0.24^{+0.07}_{-0.06}$ s day^{-1}). This value was used as starting point for a phase-coherent analysis combining the EPIC-pn data of all four observations searching a grid of different values for the spin period P and a constant $\dot{P}$. We used the Z^2 test with one harmonic to account for the first harmonic seen in the FFT power density spectrum. This resulted in a maximum Z^2_1 value of 344.1 for P = 1061.24 s (at an epoch of MJD 55 280.53, the start of the first EPIC-pn exposure) and $\dot{P} = 3.0 \pm 0.5 \times 10^{-6}$ s s^{-1}.

3. Discussion and conclusions

Our multi-wavelength morphological studies of the field around the new BeXRB pulsar SXP 1062 confirm the previously unknown SNR proposed by HB11. Its SNR nature is further supported by its X-ray spectrum obtained from both the *XMM-Newton* EPIC data and its steep radio spectrum. The strong [O III] line emission suggests the SNR as oxygen-rich type (Arbutina & Urošević 2005), which usually comes from a type Ib event, the explosion of a massive O, B, or WR star.

SXP 1062 is detected close to the centre of the SNR. At the outer edge of the eastern wing of the SMC, only very few BeXRBs are detected, and all known SNRs are located in the bar of the SMC (Payne et al. 2007; Filipović et al. 2008). This makes a chance coincidence of SXP 1062 with the SNR very unlikely. However, the ages of SNRs and BeXRBs are expected to be rather different. While SNRs can usually be seen for at most a few 10^5 years in X-rays and radio (for the methods used to estimate SNR ages see e.g. Xu et al. 2005), BeXRBs are expected to become X-ray active much later (see below). Using the relation $t_y = 3.8 \times 10^2 R_{pc} (kT)^{-1/2}_{keV}$ from Xu et al. (2005) of temperature derived from X-ray spectral modelling (0.23 keV) and the size of the SNR (~2.5′ in diameter, corresponding to ~40 pc at a distance of 60 kpc), we estimate the age of the SNR to ~16 ky. If one compares the ages estimated for SNRs in the SMC by van der Heyden et al. (2004) with their sizes as listed in Badenes et al. (2010), one finds ages of at most 25 ky for remnants with diameters around 40–50 pc.

We estimate the distance between the BeXRB and the centre of the SNR to about 9″, which corresponds to $\sim 8 \times 10^{13}$ km at SMC distance. From evolutionary investigations, kick velocities around 100−200 km s^{-1} were invoked for neutron stars in HMXB systems (Portegies Zwart 1995). Using this as maximum space velocities for the binary systems and neglecting a velocity component in radial direction, it would take 13−26 ky for SXP 1062 to move from the SNR centre to its current position, compatible with the SNR age estimates from above, which are also consistent with those of HB11.

Statistical measurements of BeXRBs in the SMC result in lower space velocities: Coe (2005) inferred a lower limit of 30 km s^{-1} from measuring the separation of BeXRBs to nearby young stellar clusters. Similarly Antoniou et al. (2010) argue from the correlation between the number of BeXRBs and the local star formation rate 42 My ago at their current position for a maximum velocity of 15−20 km s^{-1}. Both cases should actually be regarded as minimum velocities as the BeXRB might not have been born in the nearest star cluster. The work of Knigge et al. (2011) might also suggest that BeXRB pulsars with long spin period received stronger kicks. In either case, using lower space velocities (and also components in radial direction) would correspondingly increase the SNR age estimate.

According to the model calculations of Urpin et al. (1998), it seems very unlikely that an NS can be spun down to a period around 1000 s within a few 10^4 years if it was born with a spin period around 10 ms. Of course, such model calculations assume simplified approximations of the conditions in a BeXRB (in particular concerning the highly variable accretion usually observed in such systems), but only for models with extreme conditions (high magnetic field strength for the NS and low accretion rates), spin periods in excess of a few 100 s are reached after more than 10^6 years. If the NS in SXP 1062 is indeed the compact remnant from the supernova explosion, which also created the SNR around it, then either the NS was born with a much longer spin period than 10 ms, or some other effect plays an important role to efficiently decelerate the rotation of the NS.

SXP 1062 was discovered as a transient BeXRB pulsar during *XMM-Newton* and *Chandra* observations in 2010 when its X-ray luminosity was at the level of 6×10^{35} erg s^{-1}. The BeXRB was not active during the ROSAT PSPC observations of the SMC (Haberl et al. 2000). Based on the longest PSPC observation from 1991-10-07 and assuming the spectral shape measured by EPIC, we derive an upper limit of 1.5×10^{-13} erg cm^{-2} s^{-1} (0.2−10 keV), assuming an upper limit of 10 cts and a vignetting-corrected exposure of 9.7 ks at the position of SXP 1062. This is about a factor of 10 lower than the flux during the *XMM-Newton* observations. While BeXRB transients generally exhibit spin-up during intervals of increased accretion (e.g. Bildsten et al. 1997), SXP 1062 is peculiar as it showed a strong spin-down consistent with a constant rate of 0.26 s day^{-1} over 18 days. Coe et al. (2010) investigated RXTE monitoring data covering ~10 years to study the spin period changes of BeXRB pulsars in the SMC over their active periods, which typically last 50−500 days. They find four out of 15 systems with measured short-term spin period changes, which showed spin-down during outburst. In Table 1, we summarise the pulse period changes for some X-ray binary pulsars, which show times of spin-down. We list the frequency derivative $\dot{f} = -\dot{P}/P^2$, which is directly related to the accretion torque exerted on the NS. We include the three SMC BeXRB pulsars with well measured values of $\dot{P}$ and for comparison Cen X-3 (a super-giant HMXB with Roche-lobe overflow) and GX 1+4, a low-mass system with M5 III donor star. SXP 1062 exhibits spin-down about five times larger than the other listed SMC BeXRBs (which have remarkably similar values). It should be noted that the values derived by Coe et al. (2010) are average values over longer periods of time

Table 1. X-ray binary pulsars with periods of spin-down.

Object name	Pulse period [s]	$\dot{f}$ [Hz s^{-1}]	Reference
Cen X-3	4.82	$-(1-5)\times10^{-12}$	Bildsten et al. (1997)
SXP 8.80	8.90	-5.1×10^{-13}	Coe et al. (2010)
GX 1+4	110.2	-2.1×10^{-13}	Makishima et al. (1988)
SXP 144	144.5	-5.9×10^{-13}	Coe et al. (2010)
SXP 1062	1062	-2.6×10^{-12}	this work
SXP 1323	1325	-5.0×10^{-13}	Coe et al. (2010)

and that intermittent intervals of spin-up (as usually seen from accreting pulsars, Bildsten et al. 1997) reduce the longer-term average.

SXP 1062 shows a remarkably large accretion torque, similar in magnitude to that of Cen X-3. In this HMXB intervals of steady spin-up and spin-down alternate, which last typically 10−100 days (Bildsten et al. 1997), but at much higher X-ray luminosities of $\sim10^{38}$ erg s^{-1} (e.g. Nagase et al. 1992). Also GX 1+4 was still observed at 10^{36} erg s^{-1} during its extended lowstate (Makishima et al. 1988), about a factor of 2 brighter than SXP 1062. This demonstrates that the generally accepted model for accretion, where the torque is directly proportional to the mass accretion rate (hence luminosity) is probably too simple, as similar torques can be exerted, although the luminosity is more than a factor of 100 different. The work of Bildsten et al. (1997) suggests that disk-accreting pulsars are subject to instantaneous torques with similar magnitude but opposite sign. Different average long-term spin-up or spin-down values of individual pulsars would then be the result of different time scales for reversals between spin-up and -down.

SXP 1062 most likely also shows intervals of alternating spin-up and spin-down, which would reduce the magnitude of the long-term spin change. Assuming the extreme case that the NS was spun down with -2.6×10^{-12} Hz s^{-1} (-8.4×10^{-5} Hz y^{-1}) over its whole life of 25 ky (the maximum age) an upper limit of 2 Hz for the total spin-down is derived, which corresponds to a lower limit of 0.5 s for the spin period at birth. For a more realistic, smaller long-term average accretion torque a correspondingly longer birth spin period is expected. Therefore, if the NS in SXP 1062 is indeed the compact remnant from the supernova explosion that created the SNR, our results show that the NS was most likely born with a spin period much longer than a few tens of ms as generally adopted for an NS at birth.

We confirm the existence of a new SNR around the BeXRB SXP 1062 in the SMC, independently suggested by Henault-Brunet et al. (2011). The SNR is detected in optical, radio, and X-ray wavelengths and shows a shell-like structure with the BeXRB close to its projected centre. We estimate an age of around 10−25 ky for the remnant. Such a time scale is too short to spin down the neutron star in a BeXRB to ∼1000 s if it was born with a canonical spin period of a few 10 ms. SXP 1062 is remarkable for showing a strong average spin-down rate $\dot{f}$ of -2.6×10^{-12} Hz s^{-1} during the *XMM-Newton* observations distributed over 18 days, while it was detected during high X-ray activity at 6.3×10^{35} erg s^{-1}. Assuming the extreme case that such a high reverse accretion torque was exerted on the neutron star for its whole life, a lower limit of 0.5 s for the birth spin period is inferred. If the neutron star in SXP 1062 is indeed the compact remnant from the supernova explosion that created the SNR, we conclude that the neutron star in SXP 1062 was born with an even longer spin period for more realistic, lower long-term average accretion torques.

Acknowledgements. The *XMM-Newton* project is supported by the Bundesministerium für Wirtschaft und Technologie/Deutsches Zentrum für Luft- und Raumfahrt (BMWI/DLR, FKZ 50 OX 0001) and the Max-Planck Society. The MCELS data are provided by R. C. Smith, P. F. Winkler, and S. D. Points. The MCELS project has been supported in part by NSF grants AST-9540747 and AST-0307613, and through the generous support of the Dean B. McLaughlin Fund at the University of Michigan, a bequest from the family of Dr. Dean B. McLaughlin in memory of his lasting impact on Astronomy. The National Optical Astronomy Observatory is operated by the Association of Universities for Research in Astronomy Inc. (AURA), under a cooperative agreement with the National Science Foundation. We used the KARMA and MIRIAD software package developed by the ATNF. The ATCA is part of the Australia Telescope, which is funded by the Commonwealth of Australia for operation as a National Facility managed by CSIRO. R.S. acknowledges support from the BMWI/DLR grant FKZ 50 OR 0907.

References

Antoniou, V., Zezas, A., Hatzidimitriou, D., & Kalogera, V. 2010, ApJ, 716, L140
Arbutina, B., & Urošević, D. 2005, MNRAS, 360, 76
Badenes, C., Maoz, D., & Draine, B. T. 2010, MNRAS, 407, 1301
Bhattacharya, D., & van den Heuvel, E. P. J. 1991, Phys. Rep., 203, 1
Bildsten, L., Chakrabarty, D., Chiu, J., et al. 1997, ApJS, 113, 367
Buccheri, R., Bennett, K., Bignami, G. F., et al. 1983, A&A, 128, 245
Coe, M. J. 2005, MNRAS, 358, 1379
Coe, M. J., Edge, W. R. T., Galache, J. L., & McBride, V. A. 2005, MNRAS, 356, 502
Coe, M. J., McBride, V. A., & Corbet, R. H. D. 2010, MNRAS, 401, 252
Corbet, R., Markwardt, C. B., Marshall, F. E., et al. 2003, IAU Circ., 8064, 4
Filipovic, M. D., Haynes, R. F., White, G. L., et al. 1995, A&AS, 111, 311
Filipovic, M. D., Haynes, R. F., White, G. L., & Jones, P. A. 1998, A&AS, 130, 421
Filipović, M. D., Payne, J. L., Reid, W., et al. 2005, MNRAS, 364, 217
Filipović, M. D., Haberl, F., Winkler, P. F., et al. 2008, A&A, 485, 63
Ghosh, P., & Lamb, F. K. 1978, ApJ, 223, L83
Gregory, P. C., & Loredo, T. J. 1996, ApJ, 473, 1059
Haberl, F., & Pietsch, W. 2005, A&A, 438, 211
Haberl, F., & Zavlin, V. E. 2002, A&A, 391, 571
Haberl, F., Filipović, M. D., Pietsch, W., & Kahabka, P. 2000, A&AS, 142, 41
Haberl, F., Eger, P., & Pietsch, W. 2008, A&A, 489, 327
Henault-Brunet, V., Oskinova, L. M., Guerrero, M. A., et al. 2011, MNRAS in press [arXiv:1110.6404]
Hughes, J. P., & Smith, R. C. 1994, AJ, 107, 1363
Israel, G. L., Campana, S., Covino, S., et al. 2000, ApJ, 531, L131
Knigge, C., Coe, M., & Podsiadlowski, P. 2011, Nature, 479, 372
Makishima, K., Ohashi, T., Sakao, T., et al. 1988, Nature, 333, 746
Mewe, R., Gronenschild, E. H. B. M., & van den Oord, G. H. J. 1985, A&AS, 62, 197
Nagase, F., Corbet, R. H. D., Day, C. S. R., et al. 1992, ApJ, 396, 147
Okazaki, A. T., & Negueruela, I. 2001, A&A, 377, 161
Owen, R. A., Filipović, M. D., Ballet, J., et al. 2011, A&A, 530, A132
Payne, J. L., White, G. L., Filipović, M. D., & Pannuti, T. G. 2007, MNRAS, 376, 1793
Portegies Zwart, S. F. 1995, A&A, 296, 691
Reig, P. 2011, Ap&SS, 332, 1
Russell, S. C., & Dopita, M. A. 1992, ApJ, 384, 508
Shtykovskiy, P., & Gilfanov, M. 2005, MNRAS, 362, 879
Stanimirovic, S., Staveley-Smith, L., Dickey, J. M., Sault, R. J., & Snowden, S. L. 1999, MNRAS, 302, 417
Strüder, L., Briel, U., Dennerl, K., et al. 2001, A&A, 365, L18
Turner, M. J. L., Abbey, A., Arnaud, M., et al. 2001, A&A, 365, L27
Urpin, V., Konenkov, D., & Geppert, U. 1998, MNRAS, 299, 73
van der Heyden, K. J., Bleeker, J. A. M., & Kaastra, J. S. 2004, A&A, 421, 1031
Wilms, J., Allen, A., & McCray, R. 2000, ApJ, 542, 914
Wong, G. F., Filipovic, M. D., Crawford, E. J., et al. 2011, Serbian Astron. J., 182, 43
Xu, J.-W., Zhang, X.-Z., & Han, J.-L. 2005, Chinese J. Astron. Astrophys., 5, 165
Ye, T., & Turtle, A. J. 1993, in Lecture Notes in Physics (Berlin: Springer Verlag), New Aspects of Magellanic Cloud Research, ed. B. Baschek, G. Klare, & J. Lequeux, 416, 167

A.13 Related Paper 13

Grondin, M.-H., Sasaki, M., Haberl, F., Pietsch, W., Crawford, E. J., Filipović, M. D., Bozzetto, L. M., Points, S., and Smith, R. C. (2012). XMMU J0541.8-6659, a new supernova remnant in the Large Magellanic Cloud. *A&A*, 539:A15

My contribution was to assist in the data analysis. This is a 10% contribution.

A&A 539, A15 (2012)
DOI: 10.1051/0004-6361/201117881

Astronomy & Astrophysics

XMMU J0541.8-6659, a new supernova remnant in the Large Magellanic Cloud⋆

M.-H. Grondin[1], M. Sasaki[1], F. Haberl[2], W. Pietsch[2], E. J. Crawford[3], M. D. Filipović[3], L. M. Bozzetto[3], S. Points[4], and R. C. Smith[4]

[1] Institut für Astronomie und Astrophysik Tübingen, Universität Tübingen, Sand 1, 72076 Tübingen, Germany
e-mail: marie-helene.grondin@mpi-hd.mpg.de
[2] Max-Planck-Institut für extraterrestrische Physik, Giessenbachstrasse, 85748 Garching, Germany
[3] University of Western Sydney, Locked Bag 1797, Penrith South DC, NSW 1797, Australia
[4] Cerro Tololo Inter-American Observatory, Casilla 603, La Serena, Chile

Received 13 August 2011 / Accepted 12 December 2011

ABSTRACT

Context. The high sensitivity of the *XMM-Newton* instrumentation offers the opportunity to study faint and extended sources in the Milky Way and nearby galaxies such as the Large Magellanic Cloud (LMC) in detail. The ROSAT PSPC survey of the LMC has revealed more than 700 X-ray sources, among which there are 46 supernova remnants (SNRs) and candidates.
Aims. We have observed the field around one of the most promising SNR candidates in the ROSAT PSPC catalogue, labelled [HP99] 456 with *XMM-Newton*, to determine its nature.
Methods. We investigated the *XMM-Newton* data along with new radio-continuum, near infrared and optical data. In particular, spectral and morphological studies of the X-ray and radio data were performed.
Results. The X-ray images obtained in different energy bands reveal two different structures. Below 1.0 keV the X-ray emission shows the shell-like morphology of an SNR with a diameter of ∼73 pc, one of the largest known in the LMC. For its thermal spectrum we estimate an electron temperature of (0.49 ± 0.12) keV assuming non-equilibrium ionisation. The X-ray images above 1.0 keV reveal a less extended source within the SNR emission, located 1′ west of the centre of the SNR and coincident with bright point sources detected in radio-continuum. This hard component has an extent of 0.9′ (i.e. ∼13 pc at a distance of ∼50 kpc) and a non-thermal spectrum. The hard source coincides in position with the ROSAT source [HP99] 456 and shows an indication for substructure.
Conclusions. We firmly identify a new SNR in the LMC with a shell-like morphology and a thermal spectrum. Assuming the SNR to be in the Sedov phase yields an age of ∼23 kyr. We explore possible associations of the hard non-thermal emitting component with a pulsar wind nebula (PWN) or background active galactic nucleus (AGN).

Key words. Magellanic Clouds – ISM: supernova remnants

1. Introduction

The study of supernova remnants (SNRs) is crucial for a complete understanding of the chemical composition and evolution of the ISM in a galaxy because of their energy and matter inputs into the interstellar medium (ISM). The sample of SNRs studied in our Galaxy is biased because of the high absorption in the Galactic disk. Therefore, observations of nearby galaxies allow us to perform unbiased population studies and constrain the physical properties of the sources in detail. It is thus also possible to better understand the evolution and structure of the ISM in the Milky Way.

Located at a distance of ∼50 kpc to the Earth (Freedman et al. 2001; Macri et al. 2006), the Large Magellanic Cloud (LMC) offers the ideal laboratory for studying a large sample of different types of objects (such as SNRs) in greater detail than in any other galaxy. Since its first detection in X-rays (Mark et al. 1969), the LMC has been extensively observed, but the major step forward came from more than 200 observations in a $10^\circ \times 10^\circ$ field centred on the LMC, which have been performed with the ROSAT position sensitive proportional counter (PSPC) from 1990 to 1994. For a description of the ROSAT mission and PSPC detectors, see Trümper (1982), Briel & Pfeffermann (1986), and Pfeffermann et al. (1987). This survey revealed 758 sources (Haberl & Pietsch 1999, hereafter labelled HP99), among which 46 sources were classified as firmly identified SNRs or candidates.

Several SNRs in the LMC have been investigated using observations with ROSAT (Filipović et al. 1998; Williams et al. 1999), *Chandra* X-ray Observatory (Hughes et al. 2006; Seward et al. 2010) and *XMM-Newton* (Williams et al. 2004; Klimek et al. 2010; Crawford et al. 2010) satellites, allowing a more detailed view of their morphologies and spectra. Badenes et al. (2010) have studied the size distribution of the SNRs in the Magellanic Clouds (MCs), which has a maximum at ∼40 pc and may extend up to sizes of ∼100 pc. With an extent of over 100 pc, SNR 0450-70.9 and SNR 0506-6542 (DEM L 72) are among the largest SNRs detected in the LMC (Williams et al. 2004; Cajko et al. 2009; Desai et al. 2010; Klimek et al. 2010), which may be highly evolved (age up to 100 kyr). The size distribution of the MC SNRs as well as those in our Galaxy or the neaby spiral galaxy M 33 cannot be explained only by the Sedov expansion model for SNRs, but seems to be largely affected by the ambient

⋆ Based on observations with *XMM-Newton*, an ESA Science Mission with instruments and contributions directly funded by ESA Member states and the USA (NASA).

ISM densities (Bandiera & Petruk 2010; Badenes et al. 2010, and references therein).

Furthermore, multi-frequency observations of several SNR candidates located in the LMC have enabled their firm identification based on morphological and spectral criteria (Bojičić et al. 2007; Crawford et al. 2010) and have revealed a strong correlation between the X-ray sources and the emission observed by the Magellanic Cloud Emission Line Survey (MCELS; Smith et al. 2000). Indeed, an enhancement of the [S] and Hα coincident with the X-ray emission can be observed in most cases. In particular, the ratio [S]/Hα is often higher than 0.4 (Levenson et al. 1995; Williams et al. 2004). However, several SNRs in the MCs such as LMC SNR J0528-6714 or/and SMC SNR J010505-722319 do not have any optical emission.

While the emission of the gas shocked by the shock waves of SNRs is mainly of thermal nature, there can also be a pulsar or a pulsar wind nebula (PWN) in an SNR, which produce non-thermal emission. Pulsars are rapidly rotating neutron stars characterised by short periods (up to a few 10 s) and high surface magnetic fields (Manchester et al. 2005). The dissipation of the rotational energy of pulsars via magnetised particle winds can be at the origin of PWNe (Gaensler & Slane 2006). A high percentage of PWNe known in our Galaxy have been detected in X-rays, and present a power-law spectra with a mean spectral index of $\Gamma = -1.8 \pm 0.6$ (Kargaltsev & Pavlov 2008, 2010). Sensitive X-ray observations have enabled the detection of several PWNe and candidates within the MCs, with similar properties as PWNe in the Milky Way (Gaensler et al. 2003; Williams et al. 2005; Owen et al. 2011).

There are now over 50 well-established SNRs in the LMC (Badenes et al. 2010; Klimek et al. 2010, and references therein) and some additional ~20 SNR candidates (Bozzetto et al., in prep.). This would comprise one of the most complete samples of SNRs in external galaxies. Therefore, it is of prime interest to study LMC SNRs and compare them with SNRs in other galaxies such as M 33 (Long et al. 2010), M 83 (Dopita et al. 2010), the Small Magellanic Cloud (SMC; Filipović et al. 2005; Payne et al. 2007; Filipović et al. 2008) and our Galaxy (Stupar et al. 2008; Green 2009).

The SNR candidates in the ROSAT PSPC catalogue have been classified based on the X-ray spectrum and spatial extent. Additional comparison to radio data taken with the Molonglo Observatory Synthesis Telescope (MOST; $\nu = 843$ MHz; Turtle & Mills 1984) and with optical data of MCELS has shown that there are ROSAT PSPC sources with radio or optical counterparts indicative of an SNR but with a hard X-ray spectrum and therefore no typical SNR characteristics in X-rays. The source [HP99] 456 is one of the most promising new SNR candidates of this kind, with hard emission detected by ROSAT PSPC and a possible radio or optical counterpart. It has been recently re-investigated through new observations with *XMM-Newton* and the Australia Telescope Compact Array (ATCA; Hughes et al. 2007).

In this paper, we report on the results of the analysis of new *XMM-Newton* and ATCA follow-up observations of the source [HP99] 456. Section 2 presents the observations and analysis techniques. Results of the multi-frequency analyses are presented in Sect. 3. Section 4 presents the discussion on the SNR properties and on the different scenarios to explain the non-thermal emission. In particular, we explore a possible association of this second component with a PWN or an Active Galactic Nucleus (AGN). Conclusions are presented in Sect. 5.

2. Observations and data reduction

2.1. X-rays

The *XMM-Newton* satellite is an X-ray observatory operated by the European Space Agency (ESA). The source [HP99] 456 has been proposed for observations with *XMM-Newton* (Obs. Id. 0651880101, P.I.: M. Sasaki). This paper presents results of the X-ray analysis of a 20 ks observation obtained on this source.

The source [HP99] 456 has been observed on 2010 June 06 (from 04:18:56 to 09:52:50 UT) with the European Photon Imaging Camera (EPIC) in full-frame mode and thin filters. Using the EPIC MOS1, MOS2 and pn CCDs, it offers the opportunity to perform sensitive X-ray observations of a field of the sky of diameter of 30′. More detailed technical descriptions of the EPIC cameras are presented by Turner et al. (2001) and Strüder et al. (2001).

The EPIC data were analysed with SAS v10.0.0[1]. The exposure time, after removing periods of high background, is ~11 ks. Pixels flagged as bad were not taken into account and screening on the patterns (from 0 to 12 for MOS; from 0 to 4 for pn), corresponding to the canonical set of valid X-ray events (calibrated on the ground) was applied for the image and spectral analyses. We performed source detection by using the SAS tasks *eboxdetect* and *emldetect*.

2.2. Radio-continuum

The field of [HP99] 456 was observed with the ATCA on 2010 November 29, with an array configuration 6C, at wavelengths of 3 and 6 cm (9000 and 5500 MHz), and a bandwidth of 2 GHz (ATCA project C2367). The observations were carried out in snap-shot mode, totalling about 1 h of integration over a 12 h period. PKS B1934-638 was used for flux and bandpass calibration and PKS 0530-727 was used for phase calibration. Standard calibration, editing and imaging techniques (Sault & Killeen 2011) were used. Large bandwidth multifrequency clean (Sault & Wieringa 1994) was used to deconvolve the image. We point out that interferometers such as the ATCA suffer from missing flux owing to the lack of short spacings, which significantly affects the overall detection of extended emission like that from SNRs.

We also used various other radio observations (see Table 1) including 843 MHz by Mills et al. (1984), 1377 MHz from Hughes et al. (2007) and 4800 MHz and 8640 MHz taken from the mosaic project of Dickel (2005).

2.3. Optical

The Magellanic Cloud Emission Line Survey (MCELS)[2] was carried out from the 0.6 m University of Michigan/CTIO *Curtis* Schmidt telescope, equipped with a SITE 2048 × 2048 CCD, which gave a field of 1.35° at a scale of 2.4″ pixel^{-1} (Smith et al. 2006; Winkler et al., in prep.). Both the LMC and SMC were mapped in narrow bands corresponding to Hα, [O] (λ = 5007 Å), and [S] (λ = 6716, 6731 Å), plus matched red and green continuum bands. All data were continuum subtracted, flux-calibrated and assembled into mosaic images (a small section of which is shown in Fig. 6).

[1] Science Analysis Software: http://xmm.esac.esa.int/sas/
[2] MCELS: http://www.ctio.noao.edu/mcels/

Table 1. Integrated radio flux densities of [HP99] 456.

ν (MHz)	λ (cm)	rms (mJy)	Beam size ($''$)	$S_{\rm Total}$ (mJy)	Reference
843	36	1.5	43.0×43.0	0.045	Mills et al. (1984)
1377	20	1.5	45.0×45.0	0.029	Hughes et al. (2007)
4800	6	0.6	30.0×30.0	0.008	Dickel (2005)
8640	3	0.6	12.0×12.0	0.004	Dickel (2005)
5500	6	0.1	2.8×2.2	–	This work
9000	3	0.1	2.8×2.2	–	This work

Table 2. Morphological details on the two emitting regions.

Emitting region	RA (hh:mm:ss.d)	Dec (°:′:″)	Size ($'$)	Position angle (°)	pn count rate (cts s^{-1})
Soft emission	05:41:51.5	–66:59:02.8	5.0×4.6	–45	$(18 \pm 2) \times 10^{-2}$
Hard emission	05:41:39.4	–66:58:45.8	0.9×0.45	–15	$(2.8 \pm 0.3) \times 10^{-2}$

Notes. The last column lists the count rates estimated from the analysis of EPIC-pn data between 0.3 and 5.0 keV.

3. Data analysis

3.1. X-ray morphology

The morphological analysis was performed in three energy ranges: 0.2–1.0 keV (soft band), 1.0–2.0 keV (medium band), 2.0–4.5 keV (hard band). For each energy interval, exposure-corrected images were obtained using SAS tools using the following method.

First, X-ray data were cleaned using the selection procedure described in the previous section. We computed event images and exposure maps using the filtered dataset. Then we applied a mask to remove bad pixels from the three instruments. We divided each resulting event image by the corresponding exposure map and smoothed the resulting images with a Gaussian filter using *asmooth*. Finally, we added the event images from the different instruments for each energy band.

Figure 1 shows the RGB exposure-corrected image around the unidentified source [HP99] 456 obtained with the EPIC data in the three bands defined above (red: 0.2–1.0 keV; green: 1.0–2.0 keV; blue: 2.0–4.5 keV) after subtraction of the instrumental background (see caption). The emission seen in the hardest band is similar to the medium band. This morphological analysis reveals the existence of two distinct emitting regions:

1. A soft emitting region: below 1.0 keV, the X-ray emission is dominated by a bright thermal (for more details, see Sect. 3.2) component. It presents a shell-like morphology with an extent of $\sim 5.0' \times 4.6'$.
2. A hard emitting region: above 1.0 keV, the X-ray analysis reveals a less extended harder component. Its centre is located $\sim 1'$ west from the centre of the soft shell-like emission and presents an elongated morphology of length $\sim 0.9'$. The position is consistent with the ROSAT position of [HP99] 456.

The presence of the hard emitting region coincident with the ROSAT source suggests that [HP99] 456 is unrelated to the shell-like emission region. Therefore, we designated the soft, shell-like source XMMU J0541.8-6659 according to its approximate central coordinates. Additional details on the positions and extents of both emitting regions are summarised in Table 2. The count rates of the EPIC-pn observations are listed in the last column.

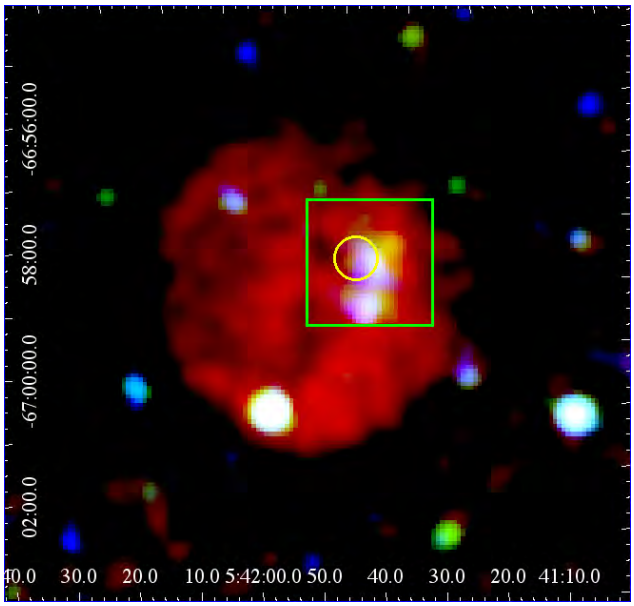

Fig. 1. Smoothed RGB three-colour image of combined exposure-corrected *XMM-Newton* EPIC pn, MOS1 and MOS2 data (red: 0.2–1.0 keV; green: 1.0–2.0 keV; blue: 2.0–4.5 keV, square root scale). The instrumental background was estimated using the method described in Sect. 3.2.1 and subtracted from the images. The renormalisation factor was derived from the shaded detector corners. The field of the radio image presented in Fig. 5 is overlaid for comparison (green square). The position of the ROSAT source [HP99] 456 is represented by a yellow circle.

3.2. X-ray spectral analysis

The following sections present the results of the subsequent spectral analyses of the two spectral components mentioned above. We first describe the method used to estimate the contribution from the intrinsic detector and X-ray background for each emitting region. The spectral analysis was performed using the XSPEC v 12.6.0 package (Arnaud 1996; Dorman & Arnaud 2001).

Point sources that were detected using the method described in Sect. 2.1 were excluded from the spectral analysis. We used data between 0.3 keV and 5.0 keV because no significant emission is detected at higher energies.

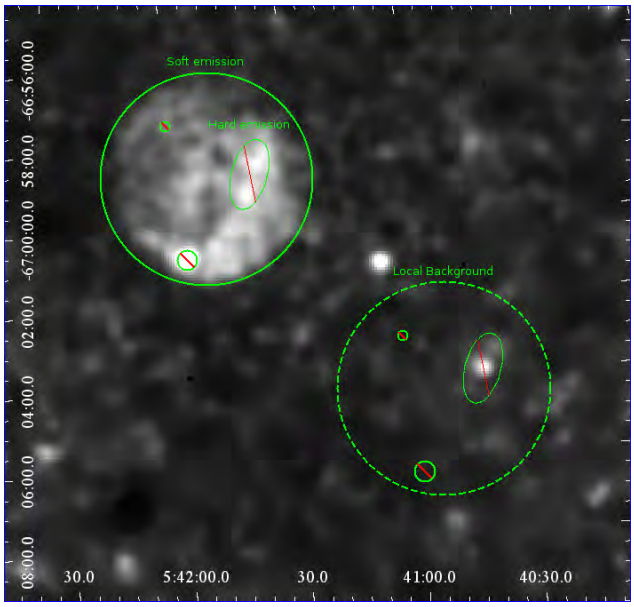

Fig. 2. Smoothed image of exposure-corrected *XMM-Newton* EPIC data in the 0.2–1.0 keV energy range. The dashed circle shows the region considered for the estimation of the local background. The thick circle represents the region used to derive the spectrum of the soft emission from the shell-like structure. Cancelled circles show the position of the bright sources excluded from the spectral analysis.

3.2.1. Estimation of the instrumental background

We estimated the contribution from the intrinsic instrumental background using the filter wheel closed (FWC) data (Freyberg et al. 2001a,b). The intrinsic background is composed of internal electronic noise as well as continuous and fluorescent X-ray emission induced by high-energy particles. This background is measured by operating the EPIC instruments in the "closed" filter wheel position, where no photons from astrophysical sources can be observed. The FWC spectrum needs to be renormalised using the continuum at higher energies.

3.2.2. Estimation of the X-ray background

The contribution of the X-ray local background emission was derived from the same observation as the source itself. We defined a region located close to our source (see Fig. 2), and extracted the spectrum from the observation and the FWC data. We estimated the renormalisation factor of the FWC spectrum with respect to the observed spectrum using the total count rates measured above 5 keV in the corners outside the field of view of the EPIC camera. The value of the renormalisation factor is 1.3.

The spectrum of the diffuse emission after subtracting the instrumental background can be modelled as a sum of the following three components:

– a soft component, modelling the emission from the local bubble with a collisional plasma, non-equilibrium model (NEI; Borkowski et al. 1994, 2001; Hamilton et al. 1983; Liedahl et al. 1995)[3] assuming a low temperature (0.1 keV);
– a hard component modelled with an absorbed NEI model with a temperature of 0.3 keV, which stands for the emission from the Galactic halo;
– an absorbed power-law of spectral index $\Gamma = 1.46$, to describe the extragalactic unresolved emission.

[3] For more details on XSPEC models, please see http://heasarc.nasa.gov/xanadu/xspec/manual/manual.html

Table 3. *XMM-Newton* spectral results of the soft thermal emitting region in the 0.3–5.0 keV energy range.

Parameter	Value
$N_{\rm H}$ ($\times 10^{21}$ cm^{-2}) in the Galaxy	0.6 (fixed)
$N_{\rm H}$ ($\times 10^{21}$ cm^{-2}) in the LMC	0 (fixed)
kT (keV)	0.49 ± 0.12
Ionisation timescale* τ (s cm^{-3})	$(1.5 \pm 0.7) \times 10^{10}$
Absorbed flux (0.3–5.0 keV, erg/cm^2/s)	2.5×10^{-13}
Absorbed luminosity (0.3–5.0 keV, erg/s)	5.1×10^{34}
Unabsorbed luminosity (0.3–5.0 keV, erg/s)	8.9×10^{34}
Reduced χ^2	1.27
Degrees of freedom	86

Notes. Model is VNEI with abundances fixed to 0.5 of the solar abundances. $^{(*)}$ The ionisation timescale $\tau = n_{\rm e}t$, where $n_{\rm e}$ is the electron number density and t is the age of the gas.

The parameters are fixed to values similar to those used by Kuntz & Snowden (2010).

The two last components are convolved with a Tübingen-Boulder ISM absorption model (TBABS). The Galactic foreground hydrogen column density of 0.6×10^{21} cm^{-2} was derived from Stark et al. (1992) and was used for the absorption in the Galaxy.

3.2.3. Soft-emission region

The X-ray emission below 1.0 keV is dominated by a structure presenting a shell-like morphology with a maximal diameter of ∼5.0′ and centred at RA(J2000) = $05^{\rm h}41^{\rm m}51.5^{\rm s}$, Dec(J2000) = –66°59′02.8″. Photons located within the region corresponding to the hard X-ray emitting region, as defined in Table 2, were excluded from the source spectrum to avoid any contamination, as were detected point sources visible in Fig. 1.

The spectrum of the shell-like structure was obtained after the subtraction of the instrumental background. The X-ray background was estimated using a local background spectrum extracted from the same data. The source spectrum and the local background were modelled simultaneously in XSPEC by using a background model consisting of the components as explained in the previous section. All parameters of the three background components were fixed except the normalisations. The normalisations of the background components and the parameters of an additional model component for the shell emission were free fit parameters.

The spectral analysis of the soft circular emitting region reveals a thermal spectrum. It can be modelled with a single-temperature non-equilibrium ionisation collisional plasma model (VNEI; Borkowski et al. 1994, 2001; Hamilton et al. 1983; Liedahl et al. 1995) with a temperature of (0.49 ± 0.12) keV with an absorption of $N_{\rm H} = 0.6 \times 10^{21}$ cm^{-2} for the Galactic foreground (with solar abundances) and a value of $N_{\rm H}$ for the absorption in the LMC. The abundances were fixed to 0.5 of the solar system abundances for the emission and absorption taking place in the LMC. This value is the standard mean value for the LMC (Russell & Dopita 1992). The value of $N_{\rm H}$ for the LMC turned out to tend towards 0 with an 90% C.L. upper limit of 0.4×10^{21} cm^{-2}. This parameter was therefore fixed to 0.

The resulting spectrum is presented in Fig. 3. The corresponding spectral parameters are given in Table 3.

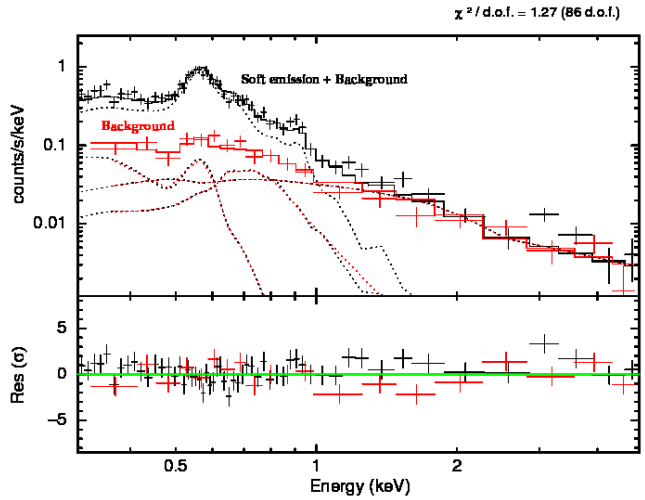

Fig. 3. *XMM-Newton* EPIC-pn spectrum and model of the soft emitting region with a VNEI model fit (black points and solid line). The estimation of the local background spectrum and model (red points and solid line) is described in Sect. 3.2.1. The background spectrum was not subtracted from the source spectrum but was modelled simultaneously and is included in the spectral model of the source spectrum. The different spectral components are shown separately (red and black dotted lines) for the background and source spectra. The bottom panel shows the residuals from the best-fit models.

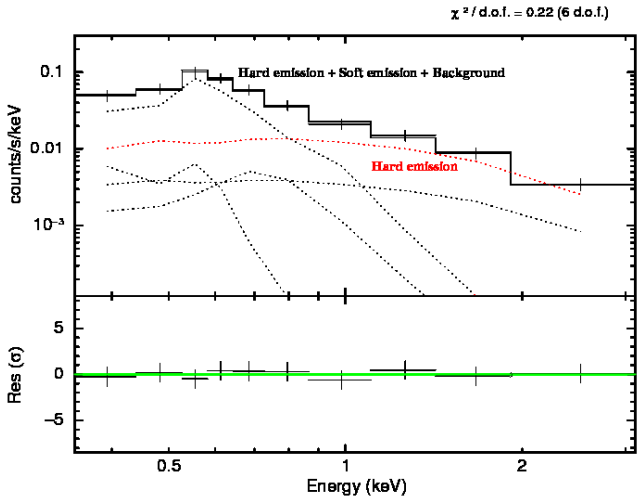

Fig. 4. *XMM-Newton* EPIC-pn spectrum of the hard emitting region with a power-law model fit. The solid line is for the hard emission plus background spectra. Here, the background is the sum of the shell emission and the local emission. The background spectrum and shell spectrum were evaluated as described in Sect. 3.2.4. The background spectrum was not subtracted from the source spectrum but was modelled simultaneously and is included in the spectral model of the source spectrum. The contribution from the hard emitting region is represented in red. The bottom panel shows the residuals from the best-fit model.

3.2.4. Hard-emission region

The X-ray emission above 1.0 keV is dominated by a narrow structure of length ∼0.9′ located ∼1′ to the west of the centroid of the shell-like thermal emission, as seen from Fig. 1. Above 1.0 keV, the hard source has a surface brightness of $\sim 5.8 \times 10^{-3}$ counts/s/arcmin^2, i.e. ∼6 times the background level, which has a surface brightness of $\sim 9.4 \times 10^{-4}$ counts/s/arcmin^2. There is indication for substructure in the X-ray image, which could be caused by multiple sources. The ROSAT source [HP99] 456 coincides with the northern part of the narrow structure.

To analyse the spectrum of this second component again the instrumental background spectrum was subtracted and the X-ray spectrum was modelled simultaneously, this time using the surrounding shell-like emission as the local background. The normalisations of the component corresponding to the X-ray background components were renormalised to the area and were fitted, along with the spectral parameters of the hard emitting region.

The spectrum of the hard emitting region is non-thermal and can be modelled in the 0.3–5.0 keV energy range with an absorbed power-law with a spectral index of $\Gamma = 1.8 \pm 0.3$, with an absorption of $N_{\rm H} = 0.6 \times 10^{21}$ cm^{-2} for the Galactic foreground (fixed, with solar abundances) and a value of $N_{\rm H}$ for the absorption in the LMC of $N_{\rm H} = (0.58 \pm 0.53) \times 10^{21}$ cm^{-2}. This yields an absorbed flux of $\sim 9.5 \times 10^{-14}$ erg/cm^2/s (reduced $\chi^2 = 0.22$ for 6 degrees of freedom). The resulting spectrum is shown in Fig. 4. In particular, the contribution from the hard X-ray emitting region is represented in red.

An alternative technique was used to derive the spectrum of the hard emitting region. Instead of using the FWC data, we extracted a background spectrum from a nearby region located within the shell and subtracted it from the source spectrum. This method yields consistent results for the hard emission.

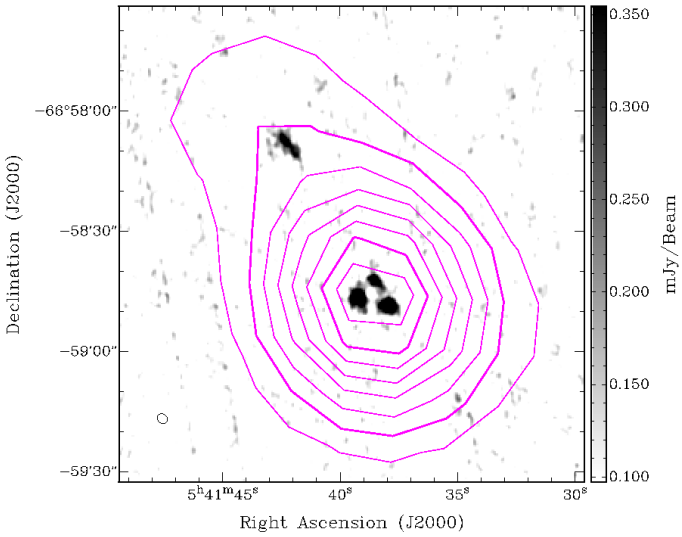

Fig. 5. High-resolution ATCA radio-continuum image at 6 cm (5.5 GHz) overlaid with 20 cm contours (violet) from the low-resolution mosaic image of the immediate surroundings of [HP99] 456. Contours are from 3 to 18 mJy/beam in steps of 1 mJy/beam and 6 cm beam size (2.8″ × 2.2″) is shown in the bottom left corner.

3.3. Radio

New high-resolution (∼2″) radio-continuum observations resolved low-resolution emission into three bright sources within the hard X-ray emitting region (Fig. 5). For comparison, the size of the radio image shown in Fig. 5 is represented in Fig. 1. In particular, three bright sources can be seen coinciding with the central position of this hard non-thermal X-ray emitting region. The brightest source (the most eastern one) has a spectral index of $\alpha = -0.5 \pm 0.1$ with integrated flux densities of (0.85 ± 0.05) mJy at 5.5 GHz and (0.67 ± 0.05) mJy at 9.0 GHz.

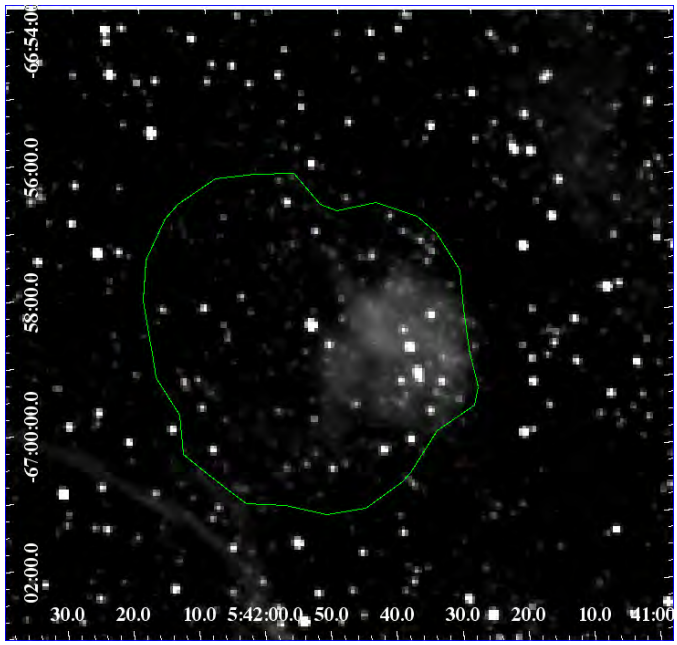

Fig. 6. Hα emission (arbitrary units) derived from the MCELS in the surroundings of [HP99] 456. A contour of the soft thermal emission of XMMU J0541.8-6659 is overlaid in green for comparison.

Our estimate of the SNR overall radio spectral index (excluding central point source; using flux densities from mosaic surveys only and listed in Table 1 i.e. observations from 843, 1377, 4800, 8640 MHz) is $\alpha = -1.0 \pm 0.2$, which is more typical for younger SNRs.

3.4. Optical

The emission from optical lines (Hα and [S]) derived from the MCELS were considered. The Hα emission in the surroundings of [HP99] 456 are presented in Fig. 6. This image shows a possible correlation between the western part of the shell-like X-ray thermal emission observed by *XMM-Newton*, the low-resolution radio-continuum and the Hα emission line, as seen in Figs. 5 and 6. However, we acknowledge that this correlation could be a chance coincidence because the Hα "cloud" could be an unrelated H region.

Low-resolution radio-continuum images at 36, 20, 6 and 3 cm show good alignment with the optical (MCELS) feature and also coincide with the maximum emission from the X-rays.

Supernova remnants can show significant Hα, [S] and [O] line emission if they are in the radiative phase. In this case, the flux ratio [S]/Hα is a crucial parameter to distinguish between SNRs and e.g., H regions (Levenson et al. 1995). However, the [S]/Hα ratio around [HP99] 456 is ~0.3, which is not necessarily indicative of SNR emission.

Hα emission is spatially coincident with the hard emitting region, but additional studies are required to determine if they are associated or not.

4. Discussion

Thanks to the high sensitivity of *XMM-Newton*, a recent observation of the field of [HP99] 456 has revealed the existence of two emitting components. The softer component presents a circular morphology and is firmly identified as a new SNR, designated XMMU J0541.8-6659. The nature of the emitting region with harder spectrum is still unclear, but we examined the possible identification as a PWN or a background AGN.

4.1. Properties of the newly identified SNR XMMU J0541.8-6659

X-ray data reveal a large structure of soft emission close to the ROSAT PSPC source [HP99] 456 in the LMC. Analyses performed in different energy ranges indicate that this source dominates the X-ray emission below 1.0 keV.

The spectrum of the SNR XMMU J0541.8-6659 can be modelled with an absorbed component representing a plasma in non-equilibrium ionisation characterised by a temperature of ~0.49 keV, which is the average of the typical temperature of previously detected SNRs in the LMC. We note that the spectral parameters quoted in Table 3 are consistent with the parameters of the unambiguously identified SNRs in the LMC (Klimek et al. 2010; Levenson et al. 1995; Williams et al. 1999, 2004). It further supports the identification of this thermal emission with an SNR.

The soft emitting region is firmly identified as a new SNR, in view of its morphology and X-ray spectrum. It has a maximum diameter of ~5.0′, which corresponds to a maximum extent of ~73 pc at a distance of ~50 kpc. Therefore, XMMU J0541.8-6659 is one of the largest SNR observed in the LMC (Williams et al. 1999; Klimek et al. 2010).

However, the large extent of the source does not necessarily imply an old age for the SNR. Indeed, assuming the SNR to be in the Sedov phase, the dynamic age of the source can be estimated using the shock temperature as follows:

$$k_{\rm B}T_{\rm s} = 1.8 \times 10^5 \left(\frac{R_{\rm s}}{t}\right)^2 \ {\rm keV}, \quad (1)$$

where $k_{\rm B}$ is the Boltzmann constant, $T_{\rm s}$ is the temperature of the shock, which is comparable here to the plasma temperature estimated in Sect. 3.2.3, $R_{\rm s}$ is the radius of the shock (in pc) and t is the age of the SNR (in yr).

From the spectral fit yielding a plasma temperature of $k_{\rm B}T_{\rm s} \approx 0.49$ keV, we derived an age of ~23 kyr. This value is well below the age of previous largely-extended SNRs detected in the LMC (e.g. Klimek et al. 2010; Williams et al. 2004).

This result means that the large extent of the source is not due to its high age, but rather to an expansion in a probably rarefied ambient medium. This is not surprising knowing the position of XMMU J0541.8-6659 at the north-east part of the LMC, where the gas density is quite low.

As a legacy project of the *Spitzer* Space Telescope, a survey of the MCs has been carried out called "Surveying the Agents of Galaxy Evolution" (SAGE)[4] (Meixner et al. 2006) to obtain images and spectra of the dust emission. A uniform survey of the LMC was performed in a 7° × 7° by the Infrared Array Camera (IRAC, dedicated to near infrared observations at wavelength 3.6, 4.5, 5.8, and 8 μm) and Multiband Imaging Photometer for *Spitzer* (MIPS, mid- and far-infrared observations at wavelengths 24, 70, and 160 μm). The near-infrared emission (at 5.8 μm) in the region surrounding the source [HP99] 456 is presented in Fig. 7. *Spitzer*-SAGE observations (Meixner et al. 2006) reveal dust emission spatially coincident with the eastern half of the shell-like soft emitting region. However, there is no clear indication that this dust emission is associated to the source XMMU J0541.8-6659.

[4] *Spitzer*-SAGE: http://sage.stsci.edu/index.php

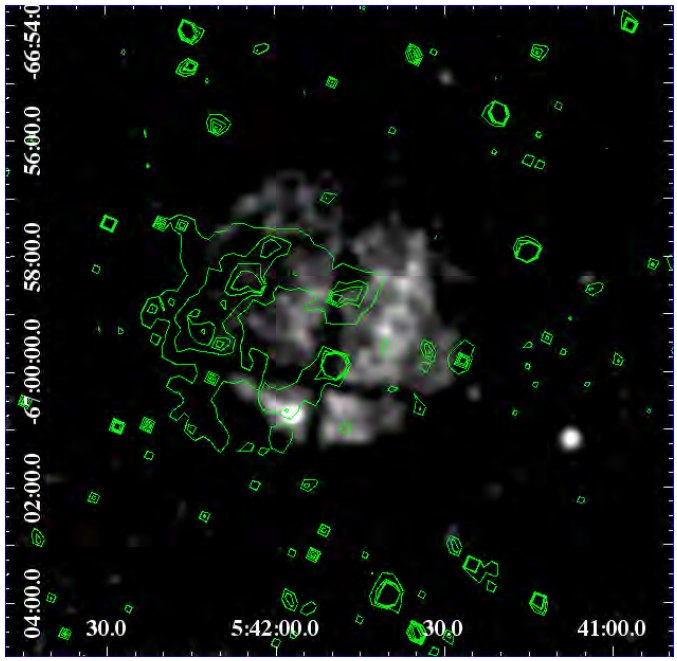

Fig. 7. Soft X-ray emission of XMMU J0541.8-6659. The contours of the near-infrared emission (*Spitzer*, 5.8 μm) are overlaid for comparison.

4.2. Hard-emission region: a PWN or background AGN?

Energy-dependent morphological studies of the X-ray emission in the surroundings of [HP99] 456 have revealed an extended elongated structure located within the SNR, which dominates the X-ray emission above 1.0 keV. Its centre is located ∼1′ from the centre of the SNR. This hard emission region has an apparent extent of ∼0.9′, corresponding to ∼13 pc at a distance of ∼50 kpc and a non-thermal spectrum. However, the angular resolution of *XMM-Newton* does not allow us to clarify if this hard source is indeed extended (with substructure) or if it is a conglomerate of point sources. A careful look at the ROSAT images reveals that the position of [HP99] 456 is consistent with the hard source detected with *XMM-Newton* and in particular with the more northern knot in the hard emission (see Fig. 1). Hence, a possible association between the soft and the hard components and the exact nature of the hard X-ray source remains unclear. The radio observations reveal several point sources at the position of the northern X-ray knot. This may point towards an identification as a pulsar with PWN. However, equivalently, one may argue for an existence of several background sources such as AGN. We investigate the different scenarios below.

Firstly, we examine the possibility that the hard X-ray emitting region is associated to background AGN. With a flux of 5.1×10^{-14} erg cm^{-2} s^{-1} (0.5–2 keV), we expect to see ∼12 AGN per square degree in the sky (Rosati et al. 2002). We have an 8% probability for an AGN inside a 5.0′ × 4.5′ SNR shell. This low probability and the non-detection of any similar morphological (jet-like) structure either in radio, IR or in optical renders an association of the hard X-ray component with an AGN quite unlikely.

It is worth noticing that the different values of absorption obtained during the spectral fit of the hard and soft emitting regions may indicate that they are located at different distances from us. While the absorption of the shell is consistent with the SNR being located in the LMC, the slightly higher absorption of the hard emission suggests that the source might be located behind the SNR.

Secondly, we consider the possible association of the hard X-ray component with a PWN. Three radio sources are embedded in the hard and narrow X-ray component. The brightest radio source presents a spectrum that can be modelled with a power-law of index $\alpha \approx -1.0$ which is consistent with spectra of pulsars. If this radio source is indeed a pulsar, then it might power a PWN that would be seen in the X-ray domain. Timing observations are required to confirm or invalidate this identification. Furthermore, it is worth noticing that with a spectral index of $\Gamma = 1.8 \pm 0.3$, the spectrum of the hard X-ray emitting source is similar to spectra of PWNe in the Milky Way (spectral indices ranging from –2.5 to –1.2; Kargaltsev & Pavlov 2008, 2010) but also typical for AGN.

The multi-frequency observations along with the spectral and morphological results of our X-ray and radio data analyses do not uniquely identify the nature of the hard X-ray emission embedded in the SNR XMMU J0541.8-6659. Deeper X-ray observations with higher angular resolution are required to differentiate between the two scenarios.

5. Conclusions

A recent X-ray observation with *XMM-Newton* of [HP99] 456 previously discovered by ROSAT led to the identification of a new SNR (XMMU J0541.8-6659) in the LMC, which presents a shell-like morphology and a soft thermal spectrum. No clear correlation can be found between the X-ray and optical emission. The physical properties (temperature, size, etc.) of this new SNR are consistent with SNRs previously identified in the LMC by X-ray observations (Levenson et al. 1995; Klimek et al. 2010; Williams et al. 1999, 2004).

Additional analyses of the *XMM-Newton* data have revealed a harder and narrower emitting region within the shell, which may be a PWN or background AGN. This emission is likely the counterpart of the hard source discovered by ROSAT. Follow-up observations with ATCA revealed several radio point sources coincident with the hard emitting region, one of which could be a pulsar. Deeper observations of the hard X-ray emitting region with the *Chandra* X-ray Observatory will help to distinguish between the different scenarios and to unveil its nature.

Acknowledgements. The XMM project is supported by the Bundesministerium für Wirtschaft und Technologie/Deutsches Zentrum für Luft- und Raumfahrt (BMWI/DLR, FKZ 50 OX 0001) and the Max-Planck Society. The Australia Telescope Compact Array is part of the Australia Telescope, which is funded by the Commonwealth of Australia for operation as a National Facility managed by the CSIRO. This work is based in part on observations made with the *Spitzer* Space Telescope, obtained from the NASA/IPAC Infrared Science Archive, both of which are operated by the Jet Propulsion Laboratory, California Institute of Technology under a contract with the National Aeronautics and Space Administration. The Magellanic Clouds Emission Line Survey (MCELS) data are provided by R. C. Smith, P. F. Winkler, and S. D. Points. The MCELS project has been supported in part by NSF grants AST-9540747 and AST-0307613, and through the generous support of the Dean B. McLaughlin Fund at the University of Michigan, a bequest from the family of Dr. Dean B. McLaughlin in memory of his lasting impact on Astronomy. The National Optical Astronomy Observatory is operated by the Association of Universities for Research in Astronomy Inc. (AURA), under a cooperative agreement with the National Science Foundation. M.-H. Grondin is supported by the BMBF/DLR grant #50-0R-1009.

References

Arnaud, K. A. 1996, Astronomical Data Analysis Software and Systems V, ed. G. Jacoby, & J. Barnes, ASP Conf. Ser., 101, 17
Badenes, C., Maoz, D., & Draine, B. T. 2010, MNRAS, 407, 1301
Bandiera, R., & Petruk, O. 2010, A&A, 509, A34

Bojičić, I. S., Filipović, M. D., Parker, Q. A., et al. 2007, MNRAS, 378, 1237
Borkowski, K. J., Sarazin, C. L., & Blondin, J. M. 1994, ApJ, 429, 710
Borkowski, K. J., Lyerly, W. J., & Reynolds, S. P. 2001, ApJ, 548, 820
Briel, U. G., & Pfeffermann, E. 1986, Nuclear Instruments and Methods in Physics Research Section A, 242, 376
Cajko, K. O., Crawford, E. J., & Filipović, M. D. 2009, Serbian Astron. J., 179, 55
Crawford, E. J., Filipović, M. D., Haberl, F., et al. 2010, A&A, 518, A35
Desai, K. M., Chu, Y.-H., Gruendl, R. A., et al. 2010, AJ, 140, 584
Dickel, J. R. 2005, AAS Meeting, 207, 27, 1403
Dopita, M. A., Blair, W. P., Long, K. S., et al., 2010, ApJ, 710, 964
Dorman, B., & Arnaud, K. A. 2001, Astronomical Data Analysis Software and Systems X, ed. F. R. Harnden, Jr., F. A. Primini, & H. E. Payne, 238, 415
Filipović, M. D., Pietsch, W., Haynes, R. F., et al. 1998, A&AS, 127, 119
Filipović, M. D., Payne, J. L., Reid, W., et al. 2005, MNRAS, 364, 217
Filipović, M. D., Haberl, F., Winkler, P. F., et al. 2008, A&A, 485, 63
Freedman, W. L., Madore, B. F., Gibson, B. K., et al. 2001, ApJ, 553, 47
Freyberg, M. J., Pfeffermann, E., & Briel, U. G. 2001a, Proc. Symposium New visions of the X-ray Universe in the *XMM-Newton* and Chandra era, November 2001, ESTEC, The Netherlands
Freyberg, M. J., Briel, U. G., Dennerl, J., et al. 2001b, Proc. Symposium New visions of the X-ray Universe in the XMM-Newton and Chandra era, November, ESTEC, The Netherlands
Gaensler, B. M., & Slane, P. O. 2006, ARA&A, 44, 17
Gaensler, B. M., Hendrick, S. P., Reynolds, S. P., & Borkowski, K. J. 2003, ApJ, 594, L111
Green, D. A. 2009, BASI, 37, 45
Haberl, F., & Pietsch, W., 1999, A&AS, 139, 277
Hamilton, A. J. S., Sarazin, C. L., & Chevalier, R. A. 1983, ApJS, 51, 115
Hughes, J. P., Rafelski, M., Warren, J. S., et al. 2006, ApJ, 645, L117
Hughes, A., Staveley-Smith, L., Kim, S., Wolleben, M., & Filipović, M. 2007, MNRAS, 382, 543
Kargaltsev, O., & Pavlov, G. G. 2008, AIPC, 983, 171
Kargaltsev, O., & Pavlov, G. G. 2010, AIPC, 1248, 25
Klimek M. D., Points, S. D., Smith, R. C., Shelton, R. L., & Williams, R. 2010, ApJ, 725, 2281
Kuntz, K. D., & Snowden, S. L. 2010, ApJS, 188, 46
Long, K. S., Blair, W. P., & Winkler, P. F. 2010, ApJS, 187, 495
Levenson, N. A., Kischner, R. P., Blair, W. P., & Winkler, P. F. 1995, AJ, 110, 739
Liedahl, D. A., Osterheld, A. L., & Goldstein, W. H. 1995, ApJ, 438, L11
Macri, L. M., Stanek, K. Z., Bersier, D., Greenhill, L. J., & Reid, M. J. 2006, ApJ, 652, 1133
Manchester, R. N., Hobbs, G. B., Teoh, A., & Hobbs, M. 2005, AJ, 129, 1993
Mark, H., Price, R., Rodrigues, R., Seward, F. D., & Swift, C. D. 1969, ApJ, 155, L143
Meixner, M., Gordon, K. D., Indebetouw, R., et al. 2006, AJ, 132, 2268
Mills, B. Y., Turtle, A. J., Little, A. G., & Durdin, J. M. 1984, Austr. J. Phys., 37, 321
Owen, R. A., Filipović, M. D., Ballet, J., et al. 2011, A&A, 530, A132
Payne, J. L., White, G. L., Filipović, M. D., & Pannuti, T. G. 2007, MNRAS, 376, 1793
Pfeffermann, E., Briel, U. G., Hippmann, H., et al. 1987, Soft X-ray optics and technology, Proc. Meeting, Berlin, SPIE, 733, 519
Rosati, P., Tozzi, P., Giacconi, R., et al. 2002, ApJ, 566, 667
Russell, S. C., & Dopita, M. A. 1992, ApJ, 384, 508
Sault, B., & Killeen, N. 2011, Users Guide, Australia Telescope National Facility
Sault, R. J., & Wieringa, M. H. 1994, A&AS, 108, 585
Seward, F. D., Williams, R. M., Chu, Y.-H., Gruendl, R. A., & Dickel, J. R. 2010, AJ, 140, 177
Smith, R. C., Leiton, R., & Pizarro, S. 2000, ASP Conf. Proc., 221, 83
Smith, R. C., Points, S., & Winkler, P. F., 2006, NOAO Newsletter, 85, 6
Stark, A. A., Gammie, C. F., Wilson, R. W., et al. 1992, ApJ, 79, 77
Strüder, L., Briel, U., Dennerl, K., et al. 2001, A&A, 365, L18
Stupar, M., Parker, Q. A., & Filipović, M. D. 2008, MNRAS, 390, 1037
Trümper, J. 1982, Adv. Space Res., 2, 241
Turner, M. L. J., Abbey, A., Arnaud, M., et al. 2001, A&A, 365, L27
Turtle, A. J., & Mills, B. Y. 1984, Astronomical Society of Australia, 5, 537
Williams, R. M., Chu, Y.-H., Dickel, J. R., et al. 1999, ApJS, 123, 467
Williams, R. M., Chu, Y.-H., Dickel, J. R., et al. 2004, ApJ, 613, 948
Williams, R. M., Chu, Y., Dickel, J. R., et al. 2005, ApJ, 628, 704

A.14 Related Paper 14

Bozzetto, L. M., Filipović, M. D., Crawford, E. J., Haberl, F., Sasaki, M., Urošević, D., Pietsch, W., Payne, J. L., De Horta, A. Y., Stupar, M., Tothill, N. F. H., Dickel, J., Chu, Y.-H., and Gruendl, R. (2012b). Multifrequency study of the Large Magellanic Cloud supernova remnant J0529-6653 near pulsar B0529-66. *MNRAS*, 420:2588–2595

My contribution was to assist in the data analysis. This is a 10% contribution.

Monthly Notices of the ROYAL ASTRONOMICAL SOCIETY

Mon. Not. R. Astron. Soc. **420,** 2588–2595 (2012) doi:10.1111/j.1365-2966.2011.20231.x

Multifrequency study of the Large Magellanic Cloud supernova remnant J0529−6653 near pulsar B0529–66

L. M. Bozzetto,[1] M. D. Filipović,[1⋆] E. J. Crawford,[1] F. Haberl,[2] M. Sasaki,[3] D. Urošević,[4,5] W. Pietsch,[2] J. L. Payne,[1] A. Y. De Horta,[1] M. Stupar,[6,7] N. F. H. Tothill,[1] J. Dickel,[8] Y.-H. Chu[9] and R. Gruendl[9]

[1]*School of Computing and Mathematics, University of Western Sydney Locked Bag 1797, Penrith South DC, NSW 1797, Australia*
[2]*Max-Planck-Institut für extraterrestrische Physik, Giessenbachstraße, D-85748 Garching, Germany*
[3]*Institut für Astronomie und Astrophysik Tübingen, Sand 1, D-72076 Tübingen, Germany*
[4]*Department of Astronomy, Faculty of Mathematics, University of Belgrade, Studentski trg 16, 11000 Belgrade, Serbia*
[5]*Isaac Newton Institute of Chile, Yugoslavia Branch*
[6]*Department of Physics, Macquarie University, Sydney, NSW 2109, Australia*
[7]*Australian Astronomical Observatory, PO Box 296, Epping, NSW 1710, Australia*
[8]*Physics and Astronomy Department, University of New Mexico, MSC 07-4220, Albuquerque, NM 87131, USA*
[9]*Department of Astronomy, University of Illinois, 1002 West Green Street, Urbana, IL 61801, USA*

Accepted 2011 November 18. Received 2011 November 14; in original form 2011 September 22

ABSTRACT

We report the Australia Telescope Compact Array (ATCA) and *ROSAT* detection of supernova remnant (SNR) J0529−6653 in the Large Magellanic Cloud (LMC) which is positioned in the projected vicinity of the known radio pulsar PSR B0529−66. In the radio continuum frequencies, this LMC object follows a typical SNR structure of a shell morphology with brightened regions in the south-west. It exhibits an almost circular shape of $D = 33 \times 31$ pc (1-pc uncertainty in each direction) and radio spectral index of $\alpha = -0.68 \pm 0.03$ – typical for mid-age SNRs. We also report detection of polarized regions with a peak value of $\sim 17 \pm 7$ per cent at 6 cm. An investigation of *ROSAT* images produced from merged Position Sensitive Proportional Counter (PSPC) data reveals the presence of extended X-ray emission coincident with the radio emission of the SNR. In X-rays, the brightest part is in the north-east. We discuss various scenarios with regard to the SNR–pulsar association with emphasis on the large age difference, lack of a pulsar trail and no prominent point-like radio or X-ray source.

Key words: pulsars: general – ISM: supernova remnants – Magellanic Clouds.

1 INTRODUCTION

The Large Magellanic Cloud (LMC) provides an excellent laboratory to study supernova remnants (SNRs) at a known distance of 50 kpc (di Benedetto 2008). The line of sight to the LMC lies well away from the Galactic plane, minimizing the obscuration and confusion from the foreground gas, dust and stars.

A distinguishing characteristic of SNRs in radio wavelengths is their predominantly non-thermal continuum emission. Generally, SNRs display a radio spectral index of $\alpha \sim -0.5$ (defined by $S \propto \nu^{\alpha}$), although α may vary significantly, as there exists a wide variety of types of SNRs in different environments and stages of evolution (Filipović et al. 1998). For example, younger remnants can have a spectral index of $\alpha \sim -0.8$, while older SNRs and pulsar wind nebulae (PWNs) tend to have flatter radio spectra with $\alpha \sim -0.2$. SNRs have a great impact on the physical properties, structure and evolution of the interstellar medium (ISM). Conversely, the interstellar environments in which SNRs reside will heavily affect the remnants' evolution.

Type II supernovae result from the core collapse of massive stars with initial masses greater than $\gtrsim 8 \pm 1\,M_{\odot}$ (Smartt 2009), and may leave behind compact central objects, such as neutron stars that may be observable as pulsars. However, not many SNRs from Type II supernovae are observed to host pulsars. Among the 51 confirmed and 25 possible candidate SNRs in the LMC (Desai et al. 2010; Klimek et al. 2010; Filipović et al. in preparation), only three (N 49, 30 Dor B and B0540−693) have documented associations with a pulsar (Manchester et al. 2006). There are over 70 well-studied SNRs in the Magellanic Clouds (MCs) as well as 19 detected pulsars. Ridley & Lorimer (2010) modelled the potentially observable radio pulsars in the MCs and predicted some 1.79×10^4

⋆E-mail: m.filipovic@uws.edu.au

pulsars. The Milky Way (MW) has 274 SNRs (Green 2009) and ∼1900 pulsars. Therefore, the observed SNR/PSR ratio in the MCs is much less than in the MW (∼1/20). However, if the pulsar surveys are sensitivity limited, then the expected ratio of the mean distances $\sim(10/50)^2$ would result in the two fractions being similar. This rarity of pulsar–SNR connections may be attributed to the fact that many young neutron stars in SNRs exhibit different properties from the traditional radio pulsars (Gotthelf & Vasisht 2000). Radio pulsars remain detectable well after their SNRs have merged into the ISM; therefore, most pulsars are not in SNRs and their general properties may be different from those young ones in SNRs.

PSR B0529−66 in the LMC was the first extragalactic pulsar discovered. It was found by McCulloch et al. (1983) using the 64-m radio telescope at the Parkes Observatory. The pulsar was studied by Costa, McCulloch & Hamilton (1991) at a frequency of 600 MHz with the intent of using a polarimeter to collect integrated profiles, rotation and dispersion measures. Crawford et al. (2001) used the Parkes telescope at 20 cm and improved the radio positional accuracy to RA (J2000) = $05^{\rm h}29^{\rm m}50\overset{\rm s}{.}92(\pm0\overset{\rm s}{.}13)$ and Dec. (J2000) = $-66^\circ52'38\overset{''}{.}2$ ($\pm0\overset{''}{.}9$). Manchester et al. (2005) then included new and more detailed information on the pulsar in a catalogue along with 1532 other pulsars and in 2006 re-observed the pulsar at Parkes at a wavelength of 20 cm. Filipović et al. (1998) detected the radio source LMC B0530−6655 and suggested it to be an SNR candidate based on its non-thermal spectral index. We note that the SNR J0529−6653 (or LMC B0530−6655) lies just on the north-east edge of the arc of Hα nebulosity DEM L214 (Davies, Elliott & Meaburn 1976). Finally, Haberl & Pietsch (1999, hereafter HP99) detected a nearby *ROSAT* X-ray source ([HP99] 440) at a position of RA (J2000) = $05^{\rm h}29^{\rm m}59\overset{\rm s}{.}3$ and Dec. (J2000) = $-66^\circ53'13''$.

Here, we report on radio continuum, X-ray and optical observations of the candidate LMC SNR J0529−6653 with its possible association with the LMC pulsar PSR B0529−66. Observations, data reduction and imaging techniques are described in Section 2. The astrophysical interpretation of the moderate-resolution total intensity and polarimetric images are discussed in Section 3.

2 OBSERVATIONS AND DATA REDUCTION

2.1 Radio continuum

We used radio observations at four frequencies (Table 1) to study and measure flux densities of SNR J0529−6653. For the 36-cm [Molonglo Synthesis Telescope (MOST)] flux density measurement given in Table 1, we used unpublished images as described by Mills et al. (1984), and for the 20 cm, we used image from Hughes et al. (2007). Two Australia Telescope Compact Array (ATCA) project (C634 and C797; at 6/3 cm) observations were combined with mosaic observations from project C918 (Dickel et al. 2005). Data for project C634 were taken by the ATCA on 1997 August 2, using the array configuration EW375. 4 d of observations were taken from project C797: 1999 May 1–2 (array configuration: 1.5C), 1999 July 21 (array configuration 750D) and 1999 July 31 (array configuration: 1.5D). For the final image (stokes parameter *I*), we exclude baselines created with the sixth ATCA antenna, leaving the remaining five antennas to be arranged in a compact configuration. C634 observations were carried out in 'snap-shot' mode, totalling ∼1 h of integration over a 12-h period. Source PKS B1934−638 was used as the primary calibrator and source PKS B0530−727 was used as the secondary calibrator. The MIRIAD (Sault & Killeen 2006) and KARMA (Gooch 2006) software packages were used for reduction and analysis. The 6- and 3-cm images (Fig. 1) were constructed using MIRIAD multifrequency synthesis (Sault & Wieringa 1994). Deconvolution was achieved with the CLEAN and RESTOR tasks with primary beam correction applied using the LINMOS task. Similar procedures were used for the *U* and *Q* stokes parameters.

Table 1. Integrated flux densities of SNR J0529−6653. The flux density at $\lambda = 36$ cm was estimated using images from Mills et al. (1984) and at $\lambda = 20$ cm from Hughes et al. (2007).

ν (MHz)	λ (cm)	Beam size (arcsec)	rms (mJy)	$S_{\rm Total}$ (mJy)
843	36	43.0 × 43.0	0.50	99
1377	20	40.0 × 40.0	0.50	69
4800	6	17.3 × 14.0	0.11	28
8640	3	17.3 × 14.0	0.06	21

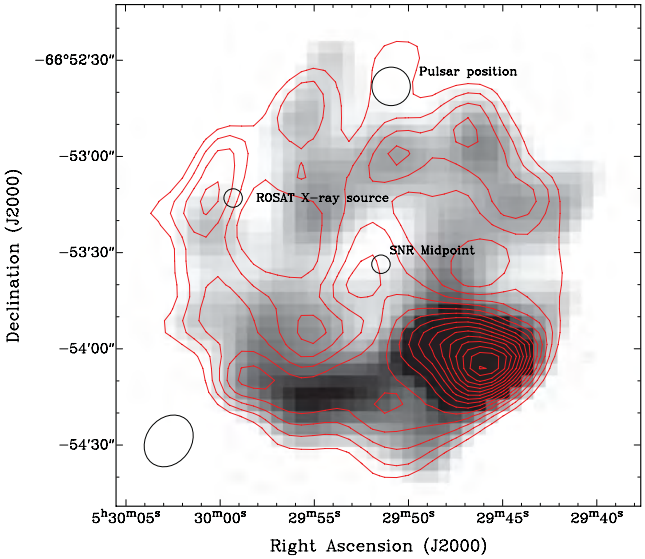

Figure 1. ATCA image of SNR J0529−6653 at 3 cm overlaid with 6-cm contours. The contours are from 3σ until 17σ with spacings of 1σ (0.11 mJy). The black ellipse in the lower-left corner represents the synthesized beamwidth of 17.3 × 14.0 arcsec^2. The circle in the centre marks the mid-point of the SNR. The circle in the east shows the catalogued X-ray location of [HP99] 440 and the circle in the north is the position of the pulsar PSR B0529−66.

2.2 Optical

We have examined images (Fig. 2) from the Magellanic Clouds Emission Line Survey (MCELS) (Smith, Points & Winkler 2006) and higher resolution Hα images (Fig. 3) obtained with the MOSAIC II camera on the Blanco 4-m Telescope at the Cerro Tololo Inter-American Observatory. The extended arc of the H II region DEM L214 is readily seen, but we do not find any optical nebulosity associated with the SNR candidate or PSR B0529−66. Additional long-slit observations were performed on 2010 September 20, using the 1.9-m telescope and Cassegrain spectrograph at the South African Astronomical Observatory (SAAO) in Sutherland. While the observing conditions were good, we did not detect any emission from the SNR candidate.

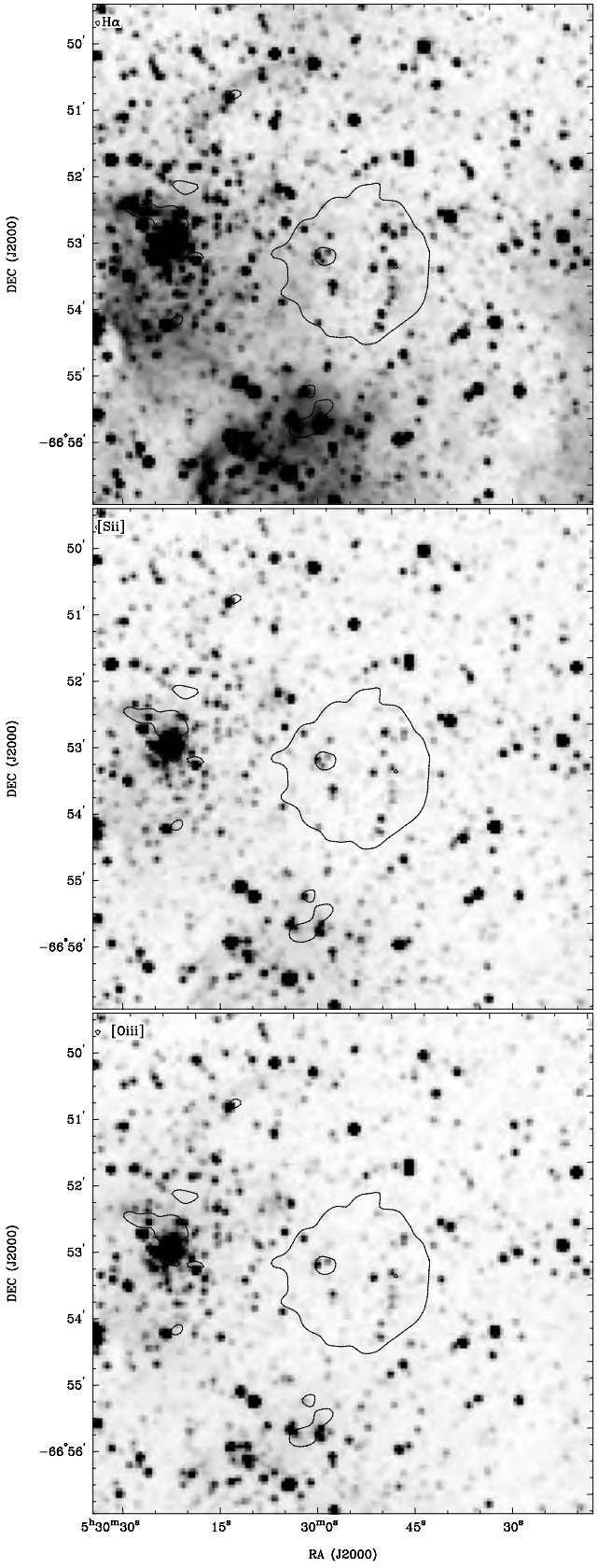

Figure 2. MCELS Hα (top), [S II] (middle) and [O III] (bottom) images of the area around SNR J0529−6653 overlaid with 6-cm 3σ (0.33-mJy) radio continuum contour.

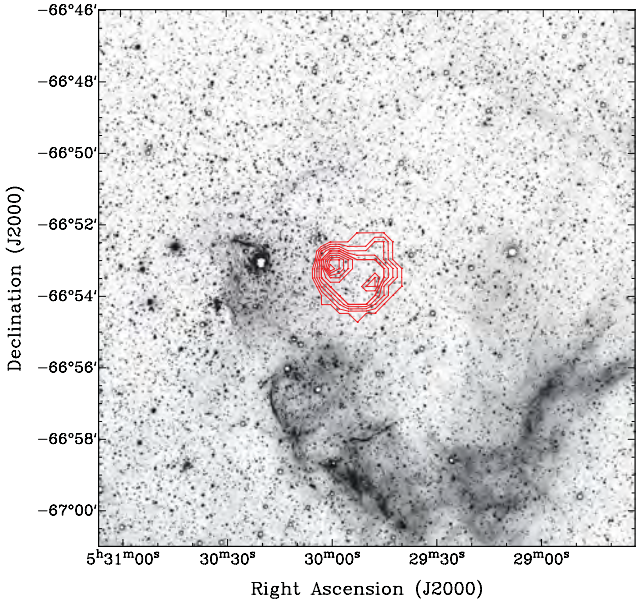

Figure 3. The MCELS-2 Hα image of the area SNR J0529−6653 overlaid with the *ROSAT* PSPC contours from the broad-band (0.1–2.4 keV) image (pixel size: 15 arcsec). Contours are from 3 to 7 count pixel^{-1} with 0.5 count pixel^{-1} spacings.

2.3 X-rays

ROSAT performed a raster of pointed observations with the Position Sensitive Proportional Counter (PSPC) to map the soft X-ray emission from the hot gas in the LMC supergiant shell-4 (SGS LMC-4; Meaburn 1980; Bomans & Dennerl 1999). A number of these observations with typical exposures of 1000 s include SNR J0529−6653 (Figs 3 and 4). The HP99 catalogue includes a very weak detection within the extent of the radio emission from SNR J0529−6653 which does not allow us to derive much about the X-ray properties of the source (the position of [HP99] 440 is shown in Fig. 1). The hardness ratios are undefined and therefore give no information on

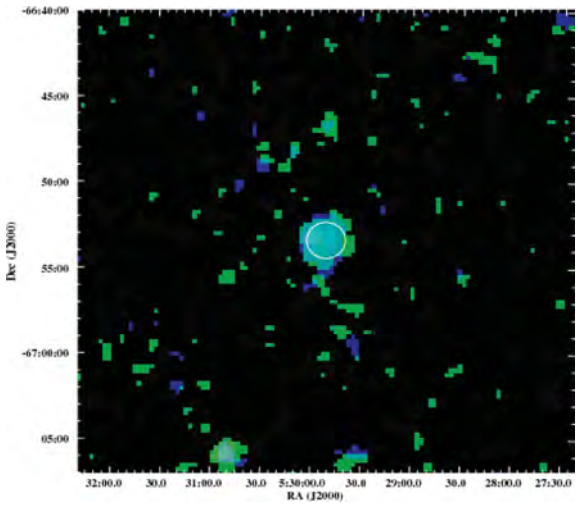

Figure 4. The *ROSAT* PSPC RGB colour image of the area around SNR J0529−6653. The energy bands are red (0.1–0.4 keV), green (0.5–0.9 keV) and blue (0.9–2.0 keV). The image has a pixel size of 15 arcsec and is smoothed with a σ of 1 pixel. A white ellipse is centred on the position of the SNR J0529−6653 with an extent of 137 × 128 arcsec^2 (33 × 31 pc).

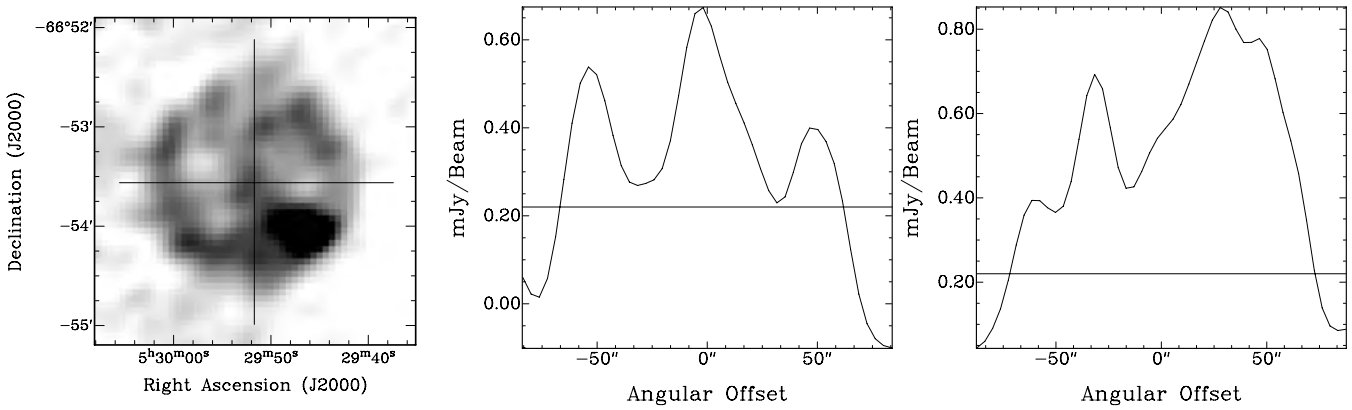

Figure 5. The left-hand image shows the 6-cm image overlaid with the major and minor axis labels. The centre and right-hand images show the *I* profile of the major and minor axes, respectively, with an overlaid black line at 3σ.

the spectrum. The catalogue of HP99 was derived from the individual PSPC observations, not utilizing the combined exposure of overlapping fields. To investigate [HP99] 440 and its possible association with SNR J0529−6653 and PSR B0529−66 in more detail, we selected 13 observations from the SGS LMC-4 raster which covered the SNR/PSR within 24 arcmin of the optical axis (to avoid the degraded point spread function at larger off-axis angles). We produced images in different energy bands (broad: 0.1–2.4 keV, soft: 0.1–0.4 keV, hard1: 0.5–0.9 keV and hard2: 0.9–2.0 keV) from the merged data. A colour image of the area around the SNR with net exposure (vignetting corrected) of 11.0 ks is shown in Fig. 4, with red, green and blue representing the X-ray intensities in the soft, hard1 and hard2 bands. The resolution of the *ROSAT* PSPC varies with energy, but the point spread function is always less than 1 arcmin.

3 RESULTS AND DISCUSSION

The radio continuum remnant SNR J0529−6653 exhibits a ring-like morphology, indicative of a shell structure, with brightened region along the south-west rim (Fig. 1). It is centred at RA (J2000) = $05^{\rm h}29^{\rm m}51\overset{\rm s}{.}0$ and Dec. (J2000) = $-66^\circ53'27\overset{''}{.}1$. We estimate the spatial extent of SNR J0529−6653 (Fig. 5) at the 3σ (Table 1, column 4) level (0.33 mJy) along the major (NS) and minor (EW) axes. Its size at 6 cm is 137 arcsec × 128 arcsec ± 4 arcsec (33 × 31 pc, with 1-pc uncertainty in each direction). We also estimate the SNR J0529−6653 ring thickness to <20 arcsec (5 pc) at 6 cm, about 30 per cent of the SNR's radius.

An extended X-ray source is clearly seen at the location of the SNR with a brighter spot right at the position of [HP99] 440. Our images are based on the combination of data from 13 observations, which had too short exposures to allow an astrometric alignment to a common reference system. Therefore, in order to verify the source extent, we compared the projected profiles of the extended source and other nearby sources, which appear point-like. For the profile, we projected the counts in the 0.1–2.4 keV image within a slice of 220-arcsec width and position angle of 330° (to investigate the profile of the bright spot). We measure a full with at half-maximum of 130 ± 7 arcsec for the extended source and 75 ± 7 arcsec for the source visible at the southern rim of the image in Fig. 4, which exhibits a similar peak intensity. The extended profile shows a peak on top of the broader intensity distribution confirming the brightest part of the X-ray emission in the north-

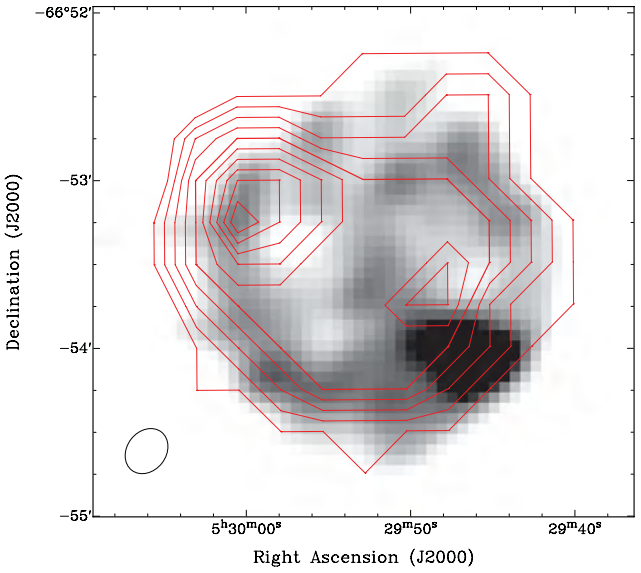

Figure 6. ATCA image of SNR J0529−6653 at 6 cm overlaid with the contours from *ROSAT* PSPC image (0.1–2.4 keV). Contours are as in Fig. 3. The ellipse in the bottom-left corner represents the beam of 17.3 × 14.0 arcsec^2.

east. The presence of extended X-ray emission is coincident with the radio emission of the SNR (Fig. 6).

The latter is also supported from the relation between X-ray luminosity and energy loss for rotation-powered pulsars [$L_{\rm x}$ = (10^{-4} to 10^{-2}) × $\dot{E}$; Becker & Truemper (1997)]. With a value of $\dot{E} = 6.6 \times 10^{32}$ erg s^{-1} (from online ATNF pulsar catalogue[1]) for PSR B0529−66, we expect an X-ray luminosity for the pulsar of well below 10^{31} erg s^{-1}, several orders of magnitude below the detection limit of $\sim 10^{34}$ erg s^{-1} for a 10-ks *ROSAT* PSPC observation. Also, from the estimated spin-down age of $\sim 10^6$ yr (see also below) one would not expect the existence of a PWN.

The net counts of 337 ± 25 count s^{-1} derived from the SNR in the 0.1–2.4 keV band are insufficient for spectral modelling in order to derive temperature and density from which one could estimate the explosion energy. Assuming a thermal emission model (APEC) with a temperature kT = 0.19 keV, typical for faint SNR in the MCs

[1] http://www.atnf.csiro.au/research/pulsar/psrcat/

(Filipović et al. 2008) and a foreground absorption of 6×10^{20} H cm^{-2}, we can roughly estimate the absorption-corrected X-ray luminosity to 5.7×10^{35} erg s^{-1}.

We estimate the radio spectral index $\alpha = -0.68 \pm 0.03$ from the integrated flux densities given in Table 1. This spectral index is consistent with those of known SNRs of mid-age to younger age. SNR J0529−6653 is located at the centre of the SGS LMC-4 (∼3° from 30 Dor) and therefore conceivable that it is expanding in a very low density environment, which causes a slightly steeper spectral index for its age (see Section 3).

Fig. 7 shows a surface brightness–diameter (Σ–D) diagram at 1 GHz with theoretically derived evolutionary tracks (Berezhko & Völk 2004) superposed. SNR J0529−6653 lies at (D, Σ) = (32 pc, 2.3×10^{-21} W m^{-2} Hz^{-1} sr^{-1}) on the diagram. Its position tentatively suggests that it is in the early Sedov phase of evolution – expanding into a very low density environment with the higher initial energy of a supernova explosion (2×10^{51}–3×10^{51} erg) and the age of ∼25 000 yr. We acknowledge that such scenario could not explain for the lack of SNR's optical emission. Alternatively, this SNR could be a bit older (∼70 000 yr; the end of adiabatic phase) and expanding into the medium dense environment with the minimal start-up energy.

A linear polarization image was created for 6-cm wavelength using Q and U parameters (Fig. 8). The mean fractional polarization was calculated using flux density and polarization: $P = \sqrt{S_Q^2 + S_U^2}/S_I$ 100 per cent, where S_Q, S_U and S_I are integrated intensities for the Q, U and I Stokes parameters. Our estimated peak value is 17 ± 7 per cent (3σ) at 6 cm and no reliable detection at 3 cm. Along the southern side of the SNR shell, there is a pocket of uniform polarization (Fig. 8), possibly indicating varied dynamics along the shell. The polarization appear to be uniformly distributed (tangential orientation) coinciding with the SNR total intensity. As the whole SNR is nearly round, the only irregularity is the brightness variations. While the distance from the nearby Hα filament (DEM L214) seems a bit far away, it is most likely that the SNR interacted with some less obvious local clouds, so the radio continuum shape has not yet been disturbed.

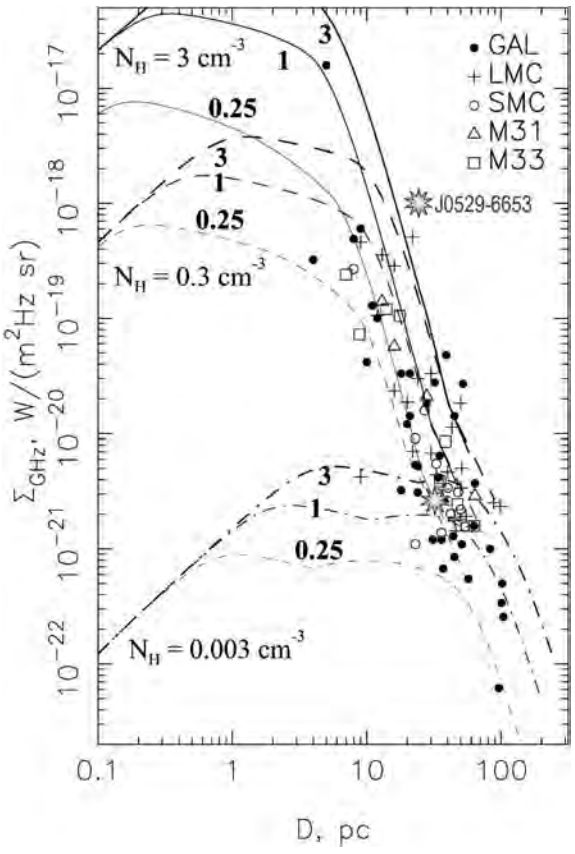

Figure 7. Surface brightness–diameter diagram from Berezhko & Völk (2004), with SNR J0529−6653 added. The evolutionary tracks are for ISM densities of $N_H = 3$, 0.3 and 0.003 cm^{-3} and explosion energies of $E_{SN} = 0.25$, 1 and 3×10^{51} erg.

Without reliable polarization measurements at a second frequency (3 cm), we cannot determine the Faraday rotation and thus cannot deduce the magnetic field strength. However, by using the new equipartition formula for SNRs (Arbutina et al. 2011), we can estimate the magnetic field strength for SNR J0529−6653. The derivation of the new equipartition formula is based on the Bell (1978) diffuse shock acceleration theory. This derivation is purely analytical, accommodated especially for the estimation of magnetic field strength in SNRs. Using this new formula, the calculated magnetic field strengths for SNRs are between those calculated by using classical equipartition (Pacholczyk 1970) and revised equipartition (Beck & Krause 2005). The average equipartition field over the whole shell of SNR J0529−6653 is ∼48 μG (see Arbutina et al. 2011, and the corresponding 'calculator'[2]), corresponding to those of young to middle-aged SNRs where the interstellar magnetic field is compressed and amplified by the strong shocks.

The Parkes pulsar catalogue suggests that the pulsar PSR B0529−66 is $9.97 \pm 0.77 \times 10^5$ yr old. SNRs normally merge into the ISM and become unrecognizable after ∼150 000 yr. We point out that a measured radius of ∼17 pc would imply a mean expansion speed of only about 0.1 km s^{-1} for an age of a million years which is clearly unreasonable. Therefore, this factor of ∼6 in age difference would rule out the possibility that the pulsar and SNR were formed from a common supernova explosion. However, Migliazzo et al. (2002) showed that pulsar age estimates from its 'characteristic age' ($\tau_c = P/2\dot{P}$) could be uncertain when compared to its corresponding SNR age. Also, for nearby Galactic isolated neutron stars, large differences between the characteristic age and the dynamic age estimated from their proper motion and the likely birth place are found (a factor of ∼8 for the case of RX J1856.5−3754; see Tetzlaff et al. 2011). They also argue that the ratio depends on the magnetic field strength and its evolution in the past.

If we assume that SNR J0529−6653 and pulsar PSR B0529−66 are associated and that the pulsar was born near the geometric centre of the SNR, then the pulsar must have moved ∼14 ± 1 pc to its current location (Crawford et al. 2001). Assuming the above 'characteristic pulsar age', the pulsar would be travelling (in the sky plane) at ∼14 km s^{-1}, an absolute minimum kick velocity. If we assume a canonical SNR age of 25 000–50 000 yr, then the pulsar velocity in the sky plane would be in the range 550–275 km s^{-1}, in agreement with the typical pulsar kick velocities (Lyne & Lorimer 1994). The direction of the pulsar's travel is not necessarily in the sky plane, so this is a lower limit. However, unless the direction of the pulsar motion is significantly out of the sky plane, its real velocity will not be much greater. Klinger et al. (2002) found a jet-like structure and that a point X-ray source within the LMC SNR N 206 travels at a speed of 800 km s^{-1}, and Owen et al. (2011) estimated the kick velocity of the pulsar candidate inside SMC PWN

[2] The calculator is available on http://poincare.matf.bg.ac.rs/~arbo/eqp/

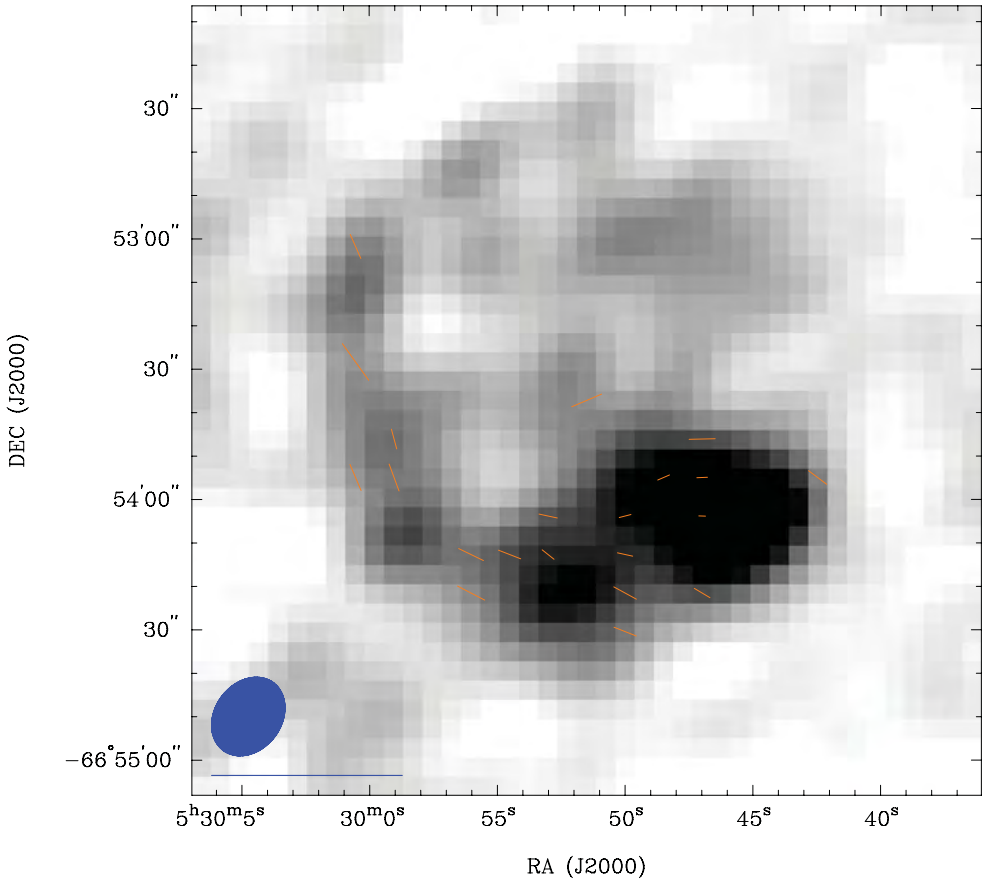

Figure 8. SNR J0529−6653 at 6 cm overlaid with polarization (*E*) vectors that peak at 17 ± 7 per cent. The ellipse in the bottom-left corner represents the beam of 17.3 × 14.0 arcsec^2 and the line under it represents a polarization *E* vector of 100 per cent.

IKT 16 to be approximately 580 km s^{-1}. The possible pulsars have left prominent radio trails in N 206 and IKT 16, but no such trail can be seen in our radio images of SNR J0529−6653. This makes a SNR–pulsar connection less likely. Nevertheless, if PSR B0529−66 is related to the SNR, it is likely to be travelling more slowly and thus any trail would be less prominent. We acknowledge that even if the pulsar is not travelling, there may still be a prominent PWN in the X-rays, although it will not be trailed. Unfortunately, the lack of evidence of PWNs in the *ROSAT* data is purely because of resolution and, therefore, cannot be taken as an evidence of lacking a PWN.

The absence of detectable optical emission (Fig. 2) from this SNR is not unique as other well-studied SNRs, such as LMC SNR J0528–6714 (Crawford et al. 2010) or the Galactic Vela Jr (Stupar et al. 2005), also do not exhibit optical emission. The ISM in the interior of SGS LMC-4 must have very low density and hence the lack of optical emission. We argue that, as with the majority of other SNRs in the MCs, this intriguing SNR is most likely in the adiabatic phase of its evolution (Payne, White & Filipović 2008) simply because of its modest size.

In the MCELS-2 Hα image (Fig. 3), we clearly see the large extent of H II region DEM L214 in the south, south-west and south-east. We also see smaller scale filamentary structures in the north of the remnant which, together with DEM L214 and the Hα emission around the cluster in the east, seem to form a large-scale shell. This and the distribution of the massive stars (see the next paragraph) indicate that some heating must have already taken place where the SNR is located. A shock expanding in a already hot thin medium is not efficient and expands quickly. This may explain the faint X-ray appearance of the remnant SNR J0529−6653.

As massive stars rarely form in isolated environments, core-collapse supernovae are most likely superposed on a stellar population rich in massive stars. We have used the Magellanic Cloud Photometric Survey (MCPS; Zaritsky et al. 2004) data to construct colour–magnitude diagrams (CMDs) and identify blue stars more massive than ∼8 M$_\odot$ within the area of SNR J0529−6653. The CMD in Fig. 9 (left-hand panel) indicates that most of the blue massive stars are main-sequence B stars. Their spatial distribution marked in blue (Fig. 9, right-hand panel) shows higher concentrations towards a cluster to the east and the nebulosity to the south-east of the SNR, but not within the SNR and its immediate vicinity. The progenitor of SNR J0529−6653 could be a B star (core-collapse supernova) or an accreting white dwarf in a binary system (Type Ia supernova). To distinguish between these two possibilities, deep *XMM–Newton* X-ray observations with sufficient counts for spectral analysis of plasma abundances are needed.

4 CONCLUSION

We have carried out the first detailed multifrequency study on a recently detected LMC SNR J0529−6653, which previously had records for a pulsar at this position. We estimated a diameter of 137 arcsec × 128 arcsec ± 4 arcsec (33 × 31 pc with 1-pc uncertainty in each direction), a spectral index of $\alpha = -0.68 \pm 0.03$ and

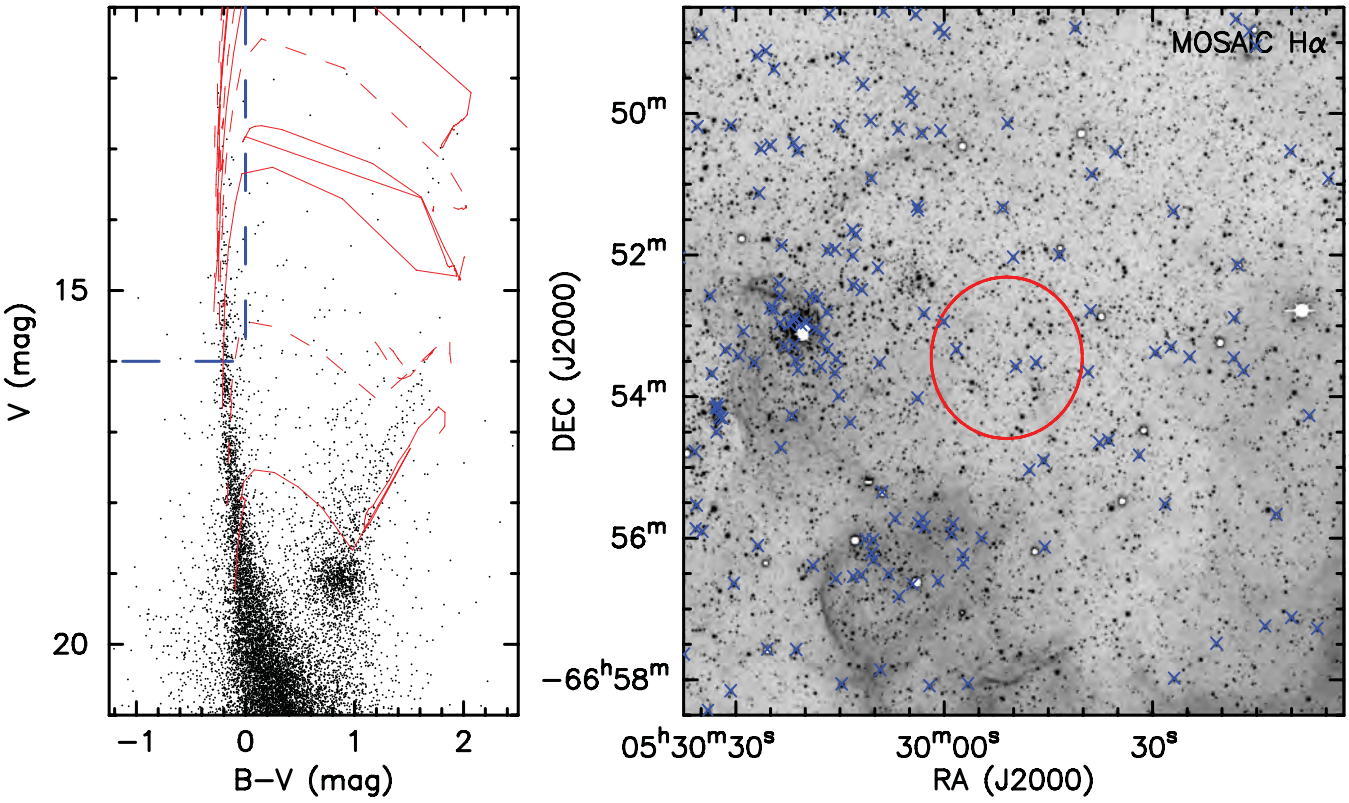

Figure 9. Left-hand panel shows a $B - V$ versus V CMD from the MCPS (Zaritsky et al. 2004). Stellar evolutionary tracks from Lejeune & Schaerer (2001) are shown with solid red lines (5, 15, 25 and 60 $M_{\odot}$) and dashed red lines (3, 9, 20 and 40 $M_{\odot}$). The selection criteria used for probable B star candidates are shown as heavy dashed blue lines. On the right is the MCELS-2 Hα image of the area around SNR J0529−6653 overlaid with probable B star candidates (blue crosses) from the MCPS. A 90-arcsec-radius circle (red) is centred on the position of the SNR.

a peak polarization of $\sim 17 \pm 7$ per cent. We note that even though there is no optical emission (and thus no [S II]/H$\alpha > 0.4$), the presence of the non-thermal radio and the X-rays do satisfy two of the three criteria for calling it an SNR. While there is a positional association between the SNR and PSR, they are not necessarily related as the ages are inconsistent. While assuming that the PSR has the same age as the SNR yields estimated kick velocities that are fairly typical, there is no radio frequency trail of the kind seen in other SNR–pulsar connections.

ACKNOWLEDGMENTS

We used the KARMA software package developed by the ATNF. The ATCA is part of the Australia Telescope which is funded by the Commonwealth of Australia for operation as a National Facility managed by CSIRO. We thank the MCELS team for access to the optical images. Travel to the SAAO was funded by Australian Government AINSTO AMNRF grant number 10/11-O-06. This research is supported by the Ministry of Education and Science of the Republic of Serbia through project No. 176005. We thank the referee for excellent comments that improved this manuscript.

REFERENCES

Arbutina B., Urošević D., Andjelić M., Pavlović M., 2011, Mem. Soc. Astron. Ital, preprint (arXiv:1111.5465)
Beck R., Krause M., 2005, Astron. Nachr., 326, 414
Becker W., Truemper J., 1997, A&A, 326, 682
Bell A. R., 1978, MNRAS, 182, 443
Berezhko E. G., Völk H. J., 2004, A&A, 427, 525
Bomans D. J., Dennerl K., 1999, in Chu Y.-H., Suntzeff N., Hesser J., Bohlender D., eds, Proc. IAU Symp. 190, New Views of the Magellanic Clouds. Kluwer, Dordrecht p. 158
Costa M. E., McCulloch P. M., Hamilton P. A., 1991, MNRAS, 252, 13
Crawford F., Kaspi V. M., Manchester R. N., Lyne A. G., Camilo F., D'Amico N., 2001, ApJ, 553, 367
Crawford E. J., Filipović M. D., Haberl F., Pietsch W., Payne J. L., de Horta A. Y., 2010, A&A, 518, A35
Davies R. D., Elliott K. H., Meaburn J., 1976, Mem. R. Astron. Soc., 81, 89
Desai K. M. et al., 2010, AJ, 140, 584
di Benedetto G. P., 2008, MNRAS, 390, 1762
Dickel J. R., McIntyre V. J., Gruendl R. A., Milne D. K., 2005, AJ, 129, 790
Filipović M. D. et al., 1998, A&AS, 127, 119
Filipović M. D., Jones P. A., White G. L., Haynes R. F., 1998, A&AS, 130, 441
Filipović M. D. et al., 2008, A&A, 485, 63
Gooch R., 2006, Karma Users Manual. Australia Telescope National Facility
Gotthelf E. V., Vasisht G., 2000, in Kramer M., Wex N., Wielebinski R., eds, IAU Colloq. 177, ASP Conf. Ser. Vol. 202, Pulsar Astronomy - 2000 and Beyond. Astron. Soc. Pac., San Francisco, p. 699
Green D. A., 2009, Bull. Astron. Soc. India, 37, 45
Haberl F., Pietsch W., 1999, A&AS, 139, 277 (HP99)
Hughes A., Staveley-Smith L., Kim S., Wolleben M., Filipović M., 2007, MNRAS, 382, 543
Klimek M. D., Points S. D., Smith R. C., Shelton R. L., Williams R., 2010, ApJ, 725, 2281
Klinger R. J., Dickel J. R., Fields B. D., Milne D. K., 2002, AJ, 124, 2135
Lejeune T., Schaerer D., 2001, A&A, 366, 538
Lyne A. G., Lorimer D. R., 1994, Nat, 369, 127

McCulloch P. M., Hamilton P. A., Ables J. G., Hunt A. J., 1983, Nat, 303, 307
Manchester R. N., Fan G., Lyne A. G., Kaspi V. M., Crawford F., 2006, ApJ, 649, 235
Manchester R. N., Hobbs G. B., Teoh A., Hobbs M., 2005, VizieR Online Data Catalog, 7245, 0
Meaburn J., 1980, MNRAS, 192, 365
Migliazzo J. M., Gaensler B. M., Backer D. C., Stappers B. W., van der Swaluw E., Strom R. G., 2002, ApJ, 567, L141
Mills B. Y., Turtle A. J., Little A. G., Durdin J. M., 1984, Australian J. Phys., 37, 321
Owen R. A. et al., 2011, A&A, 530, A132
Pacholczyk A. G., 1970, Radio Astrophysics. Nonthermal Processes in Galactic and Extragalactic Sources. Freeman & Co., San Francisco
Payne J. L., White G. L., Filipović M. D., 2008, MNRAS, 383, 1175
Ridley J. P., Lorimer D. R., 2010, MNRAS, 406, L80
Sault B., Killeen N., 2006, Miriad Users Guide. Australia Telescope National Facility
Sault R. J., Wieringa M. H., 1994, A&AS, 108, 585
Smartt S. J., 2009, ARA&A, 47, 63
Smith C., Points S., Winkler P. F., 2006, NOAO Newslett., 85, 6
Stupar M., Filipović M. D., Jones P. A., Parker Q. A., 2005, Advances Space Res., 35, 1047
Tetzlaff N., Eisenbeiss T., Neuhaeuser R., Hohle M. M., 2011, MNRAS, 417, 617
Zaritsky D., Harris J., Thompson I. B., Grebel E. K., 2004, AJ, 128, 1606

This paper has been typeset from a TEX/LATEX file prepared by the author.

A.15 Related Paper 15

De Horta, A. Y., Filipović, M. D., Bozzetto, L. M., Maggi, P., Haberl, F., Crawford, E. J., Sasaki, M., Urošević, D., Pietsch, W., Gruendl, R., Dickel, J., Tothill, N. F. H., Chu, Y.-H., Payne, J. L., and Collier, J. D. (2012). Multi-frequency study of supernova remnants in the Large Magellanic Cloud. The case of LMC SNR J0530-7007. *A&A*, 540:A25

My contribution was to assist in the data analysis. This is a 10% contribution.

A&A 540, A25 (2012)
DOI: 10.1051/0004-6361/201118694

Astronomy & Astrophysics

Multi-frequency study of supernova remnants in the Large Magellanic Cloud

The case of LMC SNR J0530–7007

A. Y. De Horta[1], M. D. Filipović[1], L. M. Bozzetto[1], P. Maggi[2], F. Haberl[2], E. J. Crawford[1], M. Sasaki[3], D. Urošević[4,5], W. Pietsch[2], R. Gruendl[6], J. Dickel[7], N. F. H. Tothill[1], Y.-H. Chu[6], J. L. Payne[1], and J. D. Collier[1]

[1] School of Computing and Mathematics, University of Western Sydney Locked Bag 1797, Penrith South DC, NSW 1797, Australia
e-mail: a.dehorta@uws.edu.au
[2] Max-Planck-Institut für extraterrestrische Physik, Giessenbachstraße, 85748 Garching, Germany
[3] Institut für Astronomie und Astrophysik Tübingen, Sand 1, 72076 Tübingen, Germany
[4] Department of Astronomy, Faculty of Mathematics, University of Belgrade, Studentski trg 16, 11000 Belgrade, Serbia
[5] Isaac Newton Institute of Chile, Yugoslavia Branch, Belgrade, Serbia
[6] Department of Astronomy, University of Illinois, 1002 West Green Street, Urbana, IL 61801, USA
[7] Physics and Astronomy Department, University of New Mexico, MSC 07-4220, Albuquerque, NM 87131, USA

Received 21 December 2011 / Accepted 8 February 2012

ABSTRACT

Context. The supernova remnants (SNRs) known in the Large Magellanic Cloud (LMC) show a variety of morphological structures in the different wavelength bands. This variety is the product of the conditions in the surrounding medium with which the remnant interacts and the inherent circumstances of the supernova event itself.
Aims. This paper performs a multi-frequency study of the LMC SNR J0530–7007 by combining Australia Telescope Compact Array (ATCA), Molonglo Observatory Synthesis Telescope (MOST), Röntgensatellit (ROSAT) and Magellanic Clouds Emission Line Survey (MCELS) observations.
Methods. We analysed radio-continuum, X-ray and optical data and present a multi-wavelength morphological study of LMC SNR J0530–7007.
Results. We find that this object has a shell-type morphology with a size of 215″ × 180″ (52 pc × 44 pc); a radio spectral index ($\alpha = -0.85 \pm 0.13$); with [S]/H$\alpha > 0.4$ in the optical; and the presence of non-thermal radio and X-ray emission.
Conclusions. We confirmed this object as a bona-fide shell-type SNR which is probably a result of a Type Ia supernova.

Key words. ISM: supernova remnants – Magellanic Clouds – radio continuum: ISM – ISM: individual objects: SNR J0530–7007

1. Introduction

Lying towards the south ecliptic pole, the Large Magellanic Cloud (LMC), is in one of the coldest parts of the radio sky, uncontaminated by Galactic foreground emission (Haynes et al. 1991). The LMC's position and its known distance of 50 kpc (di Benedetto 2008) makes the LMC arguably the best galaxy in which to study supernova remnants (SNRs) in our Local Group of galaxies.

In the radio-continuum, SNR emission is predominantly non-thermal, giving rise to a typical radio spectral index of $\alpha \sim -0.5$ ($S \propto \nu^{\alpha}$). However, the environment in which the SNR evolves i.e. the interstellar medium (ISM) with its ambient magnetic field, will not only affect the radio spectral index observed but also the SNR's morphology, structure and behaviour (Filipović et al. 1998).

In a Hα survey of the LMC, Davies et al. (1976) reported "diffuse filaments" with a size of 10′×9′ at RA(J2000) = $5^{h}30^{m}30\overset{s}{.}35$ and Dec(J2000) = –70°07′51″.5 and named it DEM L218. A radio source designated 0531-701 was identified by Turtle & Mills (1984) at RA(J2000) = $5^{h}30^{m}38\overset{s}{.}19$ and Dec(J2000) = –70°07′33″ and classified as an SNR candidate in a survey with the Molonglo Observatory Synthesis Telescope (MOST). Filipović et al. (1998) detected this source in the Parkes radio surveys of the Magellanic Clouds (MCs; $\lambda = 6$ cm and 3 cm) but due to a rather flat spectrum of $\alpha = -0.17 \pm 0.24$ and the survey's low resolution (Parkes Beam Sizes: 4′.9 at $\lambda = 6$ cm; 2′.7 at $\lambda = 3$ cm), they were unable to classify it as an SNR at that time. Haberl & Pietsch (1999, hereafter HP99) detected a nearby Röntgensatellit (ROSAT) X-ray source ([HP99] 1081) at a position of RA(J2000) = $05^{h}30^{m}51.8^{s}$ and Dec(J2000) = –70°06′44″; however, this object is close to the LMC bar where confusion is significant. The object was rediscovered using the Magellanic Clouds Emission Line Survey (MCELS) (Smith et al. 2004). This study inferred that the object is likely a large, old radiative shell-type SNR with enhanced [S] ([S]/H$\alpha > 0.4$). Blair et al. (2006) also observed the object using the Far Ultraviolet Spectroscopic Explorer (FUSE) satellite, at a position of RA(J2000) = $05^{h}30^{m}37^{s}$, Dec(J2000) = –70°08′40″ with a beamsize of 145″. Weak, yet moderately broad lines of O were detected, in addition to possible, but uncertain C lines. Desai et al. (2010) reported that there are no molecular clouds detected towards this object and that there are no young stellar objects in its vicinity.

In this paper, we report new Australia Telescope Compact Array (ATCA) radio-continuum observations at at $\lambda = 3$ cm and 6 cm. These new radio-continuum observations in conjunction with previous radio-continuum ($\lambda = 20$ cm and 13 cm

Table 1. Integrated flux densities of SNR J0530–7007.

ν (MHz)	λ (cm)	Beam size ($''$)	rms (mJy)	S_{Total} (mJy)
843	36	43.0×43.0	0.5	107[a]
843	36	43.0×43.0	0.5	80
1400	20	40.0×40.0	0.5	62
2400	13	54.1×48.9	0.4	52
5500	6	33.8×33.8	0.05	23
9000	3	22.5×22.5	0.05	10

Notes. [(a)] Integrated flux density from Turtle & Mills (1984).

(ATCA), λ = 36 cm (MOST)), X-ray (ROSAT) and optical (MCELS) observations are used to confirm that the object in the LMC centered at RA(J2000) = $5^h30^m40.4^s$ and Dec(J2000) = –70°07′27.4″ is a bona-fide SNR that, hereafter, we will call SNR J0530–7007. The observations, data reduction and imaging techniques are described in Sect. 2. Astrophysical interpretation of the newly obtained moderate-resolution total intensity images, in combination with existing ROSAT and MCELS images are discussed in Sect. 3.

2. Observations and data reduction

2.1. Radio-continuum

Radio-continuum observations at the five frequencies shown in Table 1 have been used to study and measure the flux densities of SNR J0530–7007. For the 36 cm (MOST) flux density measurement given in Table 1, we used the unpublished image as described by Mills et al. (1984). The 20 cm (ATCA) image used is from Hughes et al. (2007).

Australia Telescope Compact Array (ATCA) observations from 1992 April 29 and 30 (project C195) of SNR J0530–7007 were also used. These observations were made at wavelengths λ = 13 cm and 20 cm (ν = 2400 MHz and 1400 MHz) using the 375 array configuration.

Recently, on 2011 November 15, we observed SNR J0530–7007 (project C634), with the ATCA in the EW352 configuration, at λ = 3/6 cm (9000 and 5500 MHz) and a bandwidth of 2 GHz (ATCA project C634). In addition to this, SNR J0530–7007 was observed using the ATCA on 1995 November 12 with the 6A array (ATCA Project C461; λ = 3/6 cm (ν = 8640 MHz and 4800 MHz)). Both observations were carried out in snap-shot mode, totalling about 1 hr (each) of integration over a 12 h period. These two sets of observations were combined with mosaic observations from project C918 (Dickel et al. 2005).

For all these radio-continuum observations, baselines formed with ATCA antenna 6 were excluded, as the other five antennas were arranged in a compact configuration. Source PKS B1934–638 was used for primary (flux) calibration and source PKS B0530–727 was used for secondary (phase) calibration. More information on the observing procedure and other sources observed under the project C634 can be found in Bojičić et al. (2007); Crawford et al. (2008a,b); Čajko et al. (2009); Crawford et al. (2010); Bozzetto et al. (2010, 2011, 2012). Parkes radio-continuum data from Filipović et al. (1995, 1996) were initially combined with the ATCA data wherever the shortest ATCA baselines were less than the Parkes diameter of 64 m, and the observational frequencies corresponded, in order to provide zero-spacing. However, as the rms noise of the Parkes

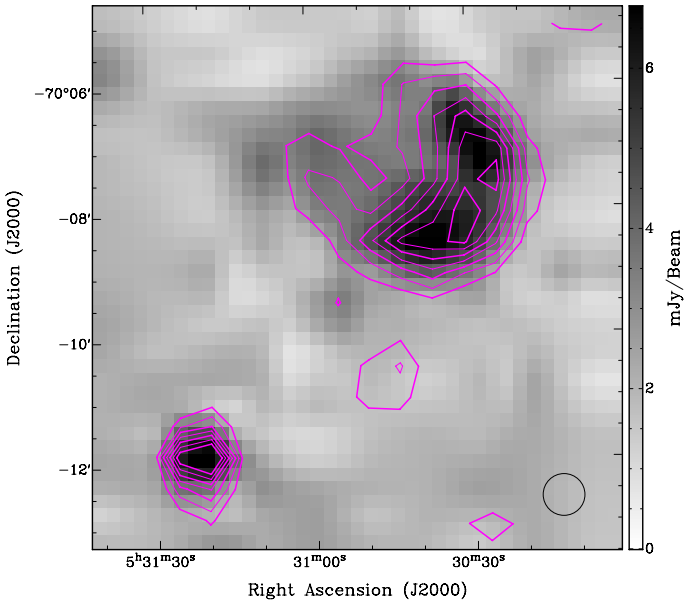

Fig. 1. Combined ATCA observations of SNR J0530–7007 at 20 cm (1400 MHz) overlaid with MOST 36 cm (843 MHz) contours. Contours are from 2 to 8 mJy/beam in steps of 1 mJy/beam. The black circle in the lower right corner represents the synthesised beamwidth (at 20 cm) of 40″.

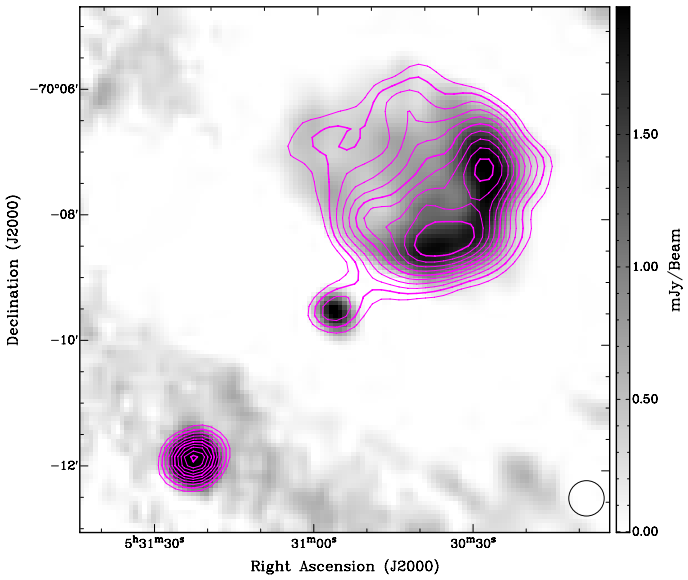

Fig. 2. Combined ATCA observations of SNR J0530–7007 at 6 cm (5500 MHz) overlaid with 13 cm (2400 MHz) contours. Contours are from 1.5 to 6 mJy/beam in steps of 0.5 mJy/beam. The black circle in the lower right corner represents the synthesised beamwidth (at 6 cm) of 33.8″.

observations are significantly higher, especially at 3/6 cm, it was decided not to use these observations in our final analysis.

The total-intensity images in Figs. 1 and 2 were formed using the standard (Sault et al. 1995) tasks employing multi-frequency synthesis using a natural weighting scheme with a correction for the primary beam response applied. A similar procedure was used for both U and Q Stokes parameter maps. However, due to the low dynamic-range (signal to noise ratio between the source flux and 3σ noise level) self-calibration could not be applied.

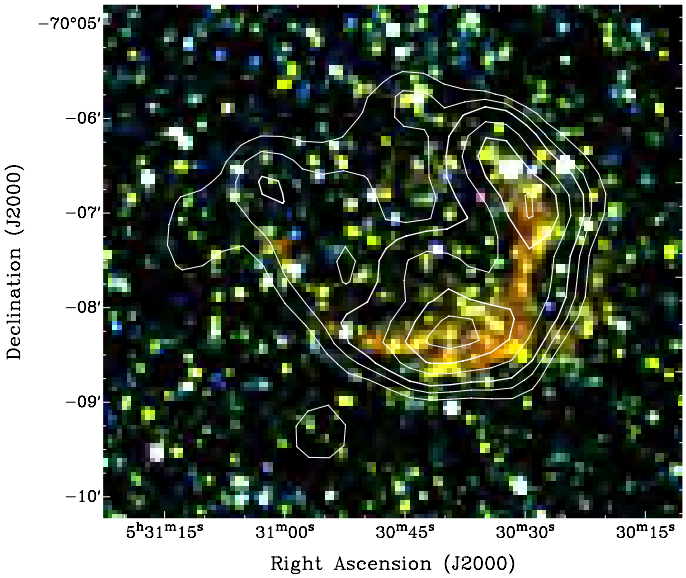

Fig. 3. MCELS composite optical image (RGB = Hα,[S],[O]) of SNR J0530–7007 overlaid with 20 cm radio contours. Contours are 3, 3.5, 4, 5, 6 and 7 mJy/beam.

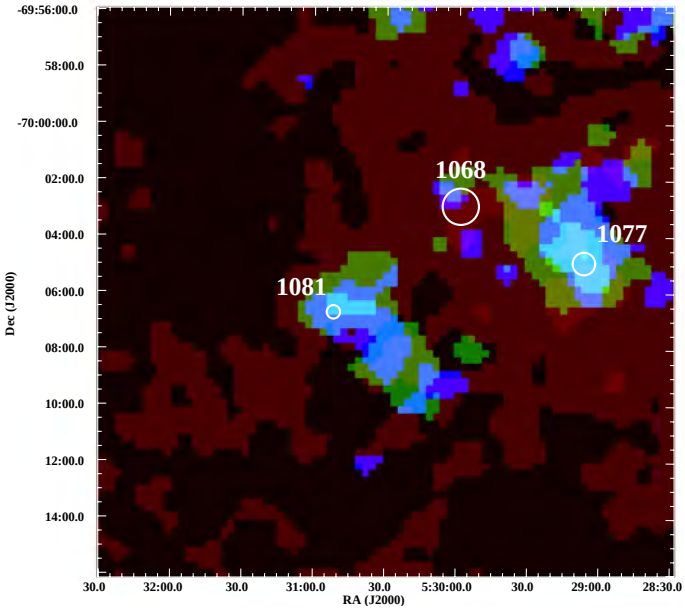

Fig. 4. The ROSAT PSPC RGB colour image of the area around SNR J0530–7007. The energy bands are: red (0.1–0.4 keV), green (0.5–0.9 keV) and blue (0.9–2.0 keV). The image has a pixel size of 15″ and is smoothed with a σ of 1.5 pixel. The annotations denote sources from HP99.

2.2. Optical

The MCELS observations (Smith et al. 2006) were carried out with the 0.6 m University of Michigan/Cerro Tololo Inter-American Observatory (CTIO) Curtis Schmidt telescope, equipped with a SITe 2048 × 2048 CCD, giving a field of 1.35° × 1.35° at a pixel scale of 2.4″ × 2.4″. It mapped both the LMC and SMC in narrow bands covering Hα, [O] (λ = 5007 Å), and [S] (λ = 6716, 6731 Å). Also observed were matched red and green continuum bands, used primarily to subtract the stars from the images to reveal the full extent of the faint diffuse emission. All the data has been flux-calibrated and assembled into mosaic images; a small section of the mosaic is shown in Fig. 3.

The high-resolution Hα image in Fig. 3 was obtained with the MOSAIC II camera on the Blanco 4-m telescope at the CTIO. It confirms a distinctive optical nebulosity associated with the SNR candidate. Here, for the first time, we present optical images of this object in combination with our new ATCA radio-continuum and ROSAT X-ray data.

2.3. X-rays

SNR J0530–7007 lies in the field of view of several pointed observations of ROSAT's Position Sensitive Proportional Counter (PSPC). The HP99 catalogue includes a very weak detection ([HP99] 1081, Fig. 4) within the extent of the radio emission from SNR J0530–7007. However, the X-ray properties of this source are unclear: The hardness ratios are poorly defined (HR1 = 1.00 ± 1.23) or undefined (HR2) and therefore give no meaningful information on the spectrum. The HP99 catalogue was derived from individual PSPC observations, without combining the exposures of overlapping fields. To investigate [HP99] 1081 and its possible association with SNR J0530–7007 in more detail, we selected 9 observations of the LMC which covered the SNR within 24′ of the optical axis (to avoid the degraded point spread function at larger off-axis angles). In Table 2 we give the ROSAT sequence number, target name, exposure time and central coordinates of the selected pointings, as well as the off-axis angle of SNR J0530–7007 in each of them. Images were produced at different energy bands (broad: 0.1–2.4 keV, soft: 0.1–0.4 keV, hard: 0.5–2.0 keV, hard1: 0.5–0.9 keV and hard2: 0.9–2.0 keV) from the merged data. A colour image of the area around the SNR with net exposure (vignetting corrected) of ∼48 ks is shown in Figs. 4 and 5 with red, green and blue representing the X-ray intensities in the soft, hard1 and hard2 bands. The resolution of the ROSAT PSPC varies with energy but the point spread function is always less than 1′.

The HP99 catalogue contains two other sources detected in the neighbourhood of source 1081 (see Fig. 4). [HP99] 1068 is a weak source with an existence likelihood of 11.8, just above the threshold used for the catalogue. No useful information about extent or hardness ratios can be derived. Source [HP99] 1077 is a clear detection (existence likelihood 22.8) with indication for an extent of 31″(likelihood for the extent of 13.3). Therefore, [HP99] 1077 looks like an extended source itself, but no significant radio nor optical emission in the MCELS images is seen at its position. Future X-ray observations are required to investigate the whole region around the three ROSAT sources in more detail.

3. Results and discussion

The remnant has a typical horse-shoe morphology (Figs. 1, 2 and 3), centered at RA(J2000) = $5^h30^m40.4^s$ and Dec(J2000) = –70°07′27.4″. The measured position differs from that of the FUSE observations (Blair et al. 2006), since the FUSE observation was aimed only at the Southern side of the shell and not at the centre of the SNR.

The size of SNR J0530–7007 at λ = 20 cm is 215″±4″ × 180″±4″ (52 ± 1 pc × 44 ± 1 pc). The size was measured by taking line profiles along the major (NE-SW) and minor (SE-NW) axis (PA = 45°) of the remnant using the [1] (Gooch 2006) tool and detemining the distance between the

[1] http://www.atnf.csiro.au/computing/software/karma/

Table 2. ROSAT observations summary of SNR J0530–7007 (sorted by RA).

ROSAT sequence	Target name	Obs. time (s)	RA (J2000)	Dec (J2000)	Off-axis angle[a] (arcmin)
180 287p	NOVA LMC 1995	2531	$05^h26^m50.04^s$	−70°01′11.5″	21.3
400 298p	RX J0527.8–6954	1058	$05^h27^m48.00^s$	−69°54′00.0″	20.2
400 298p-1	RX J0527.8–6954	7502	$05^h27^m48.00^s$	−69°54′00.0″	20.2
400 298p-2	RX J0527.8–6954	7802	$05^h27^m48.00^s$	−69°54′00.0″	20.2
400 148p	RX J0527.8–6954	6064	$05^h27^m48.00^s$	−69°54′00.0″	20.2
180 255p	RX J0527.8–6954	9763	$05^h27^m50.04^s$	−69°54′00.0″	20.0
300 172p	NOVA LMC 1988 a	6272	$05^h32^m28.08^s$	−70°21′36.0″	17.0
300 172p-1	NOVA LMC 1988 a	2993	$05^h32^m28.08^s$	−70°21′36.0″	17.0
300 172p-2	NOVA LMC 1988 a	3880	$05^h32^m28.08^s$	−70°21′36.0″	17.0

Notes. [(a)] Mean angular distance of [HP99] 1081 to the optical axis of the telescope.

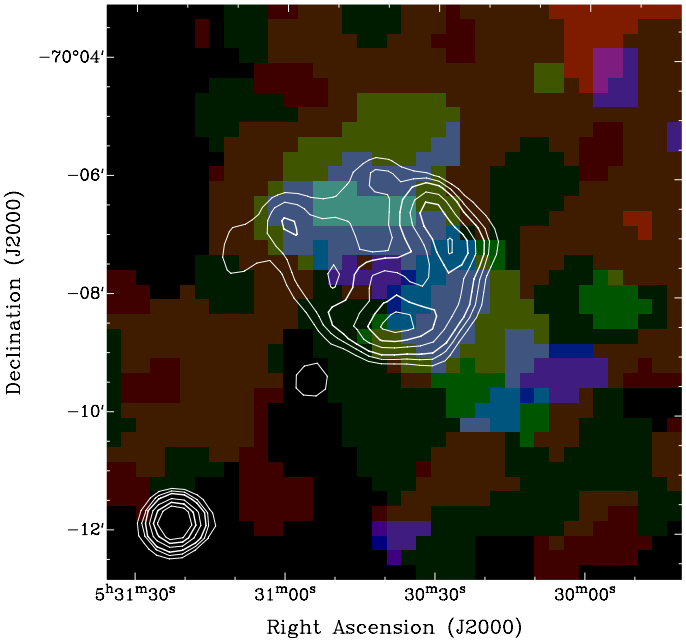

Fig. 5. The ROSAT PSPC RGB colour image of SNR J0530–7007 overlaid with the contours of 20 cm intensity. Contours are 3, 3.5, 4, 5, 6 and 7 mJy/beam.

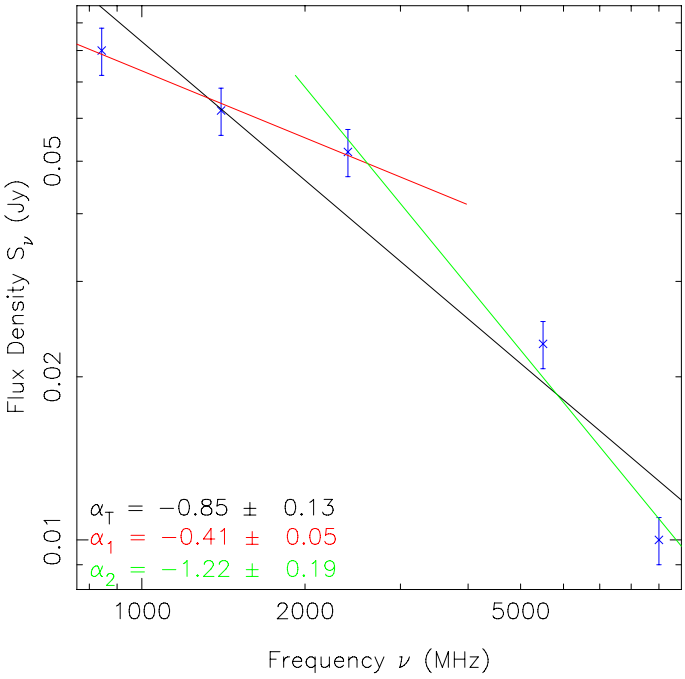

Fig. 6. Radio-continuum spectrum of SNR J0530–7007. The black line (α_T) is the overall radio-continuum spectra, the red line (α_1) between 36 cm and 13 cm, and the green line (α_2) between 13 cm and 3 cm. Note log−log scale.

point when the line profile first rises above 3σ (1.50 mJy) and the point when it finally falls below 3σ. The thickness of the shell is estimated to be <30″ (7 pc) at 6 cm, about 30% of the SNR's radius (ie. a filling factor of 0.64).

The merged ROSAT PSPC images reveal an elongated structure of X-ray emission at the location of the SNR with a brighter spot right at the position of [HP99] 1081. The presence of extended X-ray emission is coincident with the radio emission of the SNR (Fig. 5). In X-rays, the brightest part is in the north-east while the MCELS optical emission closely follows radio-continuum appearance (Fig. 3).

We note that the significant difference in the flux density measurement at 36 cm (107 mJy in Turtle & Mills (1984) vs 80 mJy in this work) may introduce a very large uncertainty in the spectral index measurement ($S \propto \nu^\alpha$). A possible explanation for this discrepancy is that we applied different fitting model then Turtle & Mills (1984). Using all values of integrated flux density estimates (except for 36 cm value from Turtle & Mills (1984); Table 1), a spectral index ($S \propto \nu^\alpha$) distribution is plotted in Fig. 6. The overall radio-continuum spectra (Fig. 6; black line) from SNR J0530–7007 was estimated to be $\alpha_T = -0.85 \pm 0.13$, while the typical SNR spectral index is $\alpha = -0.5 \pm 0.2$ (Filipović et al. 1998). This somewhat steeper spectral index would indicate a younger age despite its (large) size of 52 × 44 pc, suggesting it as an older (more evolved) SNR. We also note that this may indicate that a simple model does not accurately describe the data, and that a higher order model is needed. This is not unusual, given that several other Magellanic Clouds SNR's exhibit this "curved" spectra (Crawford et al. 2008a; Bozzetto et al. 2010, 2011). Noting the breakdown of the power law fit at shorter wavelengths, we decomposed the spectral index estimate into two components, one (α_1) between 36 and 13 cm, and the other (α_2) between 13 and 3 cm. The first component (Fig. 6; red line), $\alpha_1 = -0.41 \pm 0.05$ is a reasonable fit and typical for an evolved SNR, whereas the second (Fig. 6; green line), $\alpha_2 = -1.22 \pm 0.19$, is a poor fit, and indicates that non-thermal emission can be described by different populations of electrons with different energy indices. Although the low flux at

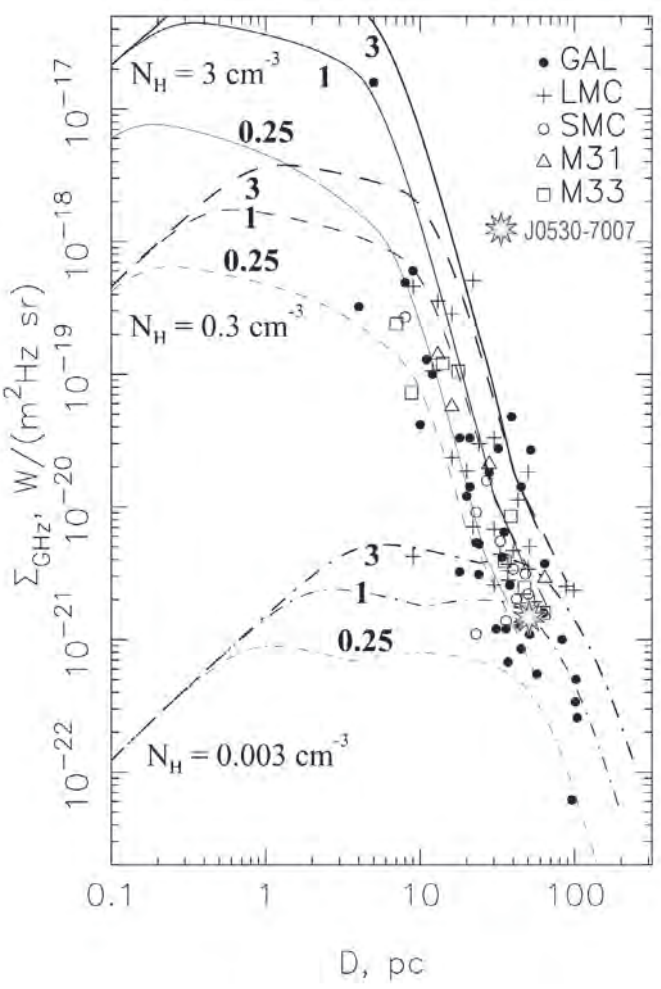

Fig. 7. 1 GHz Surface brightness-to-diameter diagram from Berezhko & Völk (2004), with SNR J0530–7007 added. The evolutionary tracks are for ISM densities of $N_{\rm H}$ = 3, 0.3 and 0.003 cm^{-3} and explosion energies of $E_{\rm SN}$ = 0.25, 1 and 3 × 10^{51} erg.

3 cm (and to a lesser extent at 6 cm) could cause the large deviations, an underestimate of up to ~50% would still lead to a "curved" spectrum.

Without reliable polarisation measurements at any radio-continuum frequency we cannot determine the Faraday rotation and thus cannot deduce the magnetic field strength. However, we can use the new equipartion formula derived by Arbutina et al. (2012) from diffusive shock acceleration (DSA) theory (Bell 1978) to estimate a magnetic field strength: This formula is particularly relevant to magnetic field estimation in SNRs, and yields magnetic field strengths, similar to but more precise than, those given by classical equipartition (Pacholczyk 1970) and the revised equipartition (Beck & Krause 2005) method. The average equipartition field over the whole shell of SNR J0530–7007 is ~53 μG (see Arbutina et al. (2012); and corresponding "calculator"[2]), corresponding those of middle-aged SNRs where the interstellar magnetic field is compressed and moderately amplified by the strong shocks.

Figure 7 shows a surface brightness-diameter ($\Sigma - D$) diagram at 1 GHz with theoretically-derived evolutionary tracks (Berezhko & Völk 2004) superposed. SNR J0530–7007 lies at (D, Σ) = (48 pc, 1.1×10^{-21} W m^{-2} Hz^{-1} Sr^{-1}) on the diagram. Its position tentatively suggests that it is in the early Sedov phase of evolution – expanding into a very low density environment with the canonical initial energy of a supernova explosion (10^{51} erg).

High-mass stars rarely form in isolation, so core-collapse supernovae are expected to be associated with other high-mass stars. We used data from the Magellanic Cloud Photometric Survey (MCPS Zaritsky et al. 2004) to construct colour-magnitude diagrams (CMDs) and identify blue stars more massive than ~8 $M_\odot$ within a 100 pc (396″) radius of SNR J0530–7007. The CMD in Fig. 8 (left) contains only 13 B-star candidates ($V < 16$, $B - V < 0$). The red crosses in Fig. 8 (right) shows where the B-star candidates are with respect to SNR J0530–7007. These criteria would also find stars as late as B2-3 stars. More stringent criteria ($V < 14$, $B - V < 0$), roughly equivalent to searching for OB stars in the Sanduleak (1970) catalog, would find only 1 star.

Comparison of the star formation histories (Harris & Zaritsky 2009) in the vicinity of SNR J0530–7007 and SNR J0529–6654 (Bozzetto et al., in press) yields a significant difference: The star formation rate near SNR J0530–7007 shows an upturn around 50 Myr ago, whereas the vicinity of SNR J0529–6654 has a strong spike in the star formation rate in the last 12–25 Myr. The lack of recent high-mass star formation around SNR J0530–7007 suggests that it is more likely to be the remnant of a Type Ia supernova.

4. Conclusion

We have carried out the first detailed multi-frequency study of the LMC SNR J0530–7007, showing that:

1. SNR J0530–7007 is a relatively large (215″ ± 4″ × 180″ ± 4″ (52 ± 1 pc × 44 ± 1 pc)) shell-type SNR;
2. It has radio spectral index $\alpha = -0.85 \pm 0.13$ between 843 MHz and 9000 MHz, but the spectrum appears to be peaked/curved;
3. SNR J0530–7007 is in the early Sedov phase, expanding into a very low density environment;
4. The average equipartition field over the whole shell of SNR J0530–7007 is ~53 μG;
5. There is a lack of recent local high-mass star formation, suggesting that SNR J0530–7007 is the remnant of a Type Ia supernova.

With strong optical [S] emission ([S]/H$\alpha > 0.4$), the presence of non-thermal radio and X-ray emission, this object satisfies all three criteria for classifying it as an SNR.

Acknowledgements. We used the and software package developed by the ATNF. The ATCA is part of the Australia Telescope which is funded by the Commonwealth of Australia for operation as a National Facility managed by CSIRO. The Magellanic Clouds Emission Line Survey (MCELS) data are provided by R. C. Smith, P. F. Winkler, and S. D. Points. The MCELS project has been supported in part by NSF grants AST-9540747 and AST-0307613, and through the generous support of the Dean B. McLaughlin Fund at the University of Michigan, a bequest from the family of Dr. Dean B. McLaughlin in memory of his lasting impact on Astronomy. The National Optical Astronomy Observatory is operated by the Association of Universities for Research in Astronomy Inc. (AURA), under a cooperative agreement with the National Science Foundation. This research is supported by the Ministry of Education and Science of the Republic of Serbia through project No. 176005. P. Maggi acknowledges support

[2] Calculator available at http://poincare.matf.bg.ac.rs/~arbo/eqp/

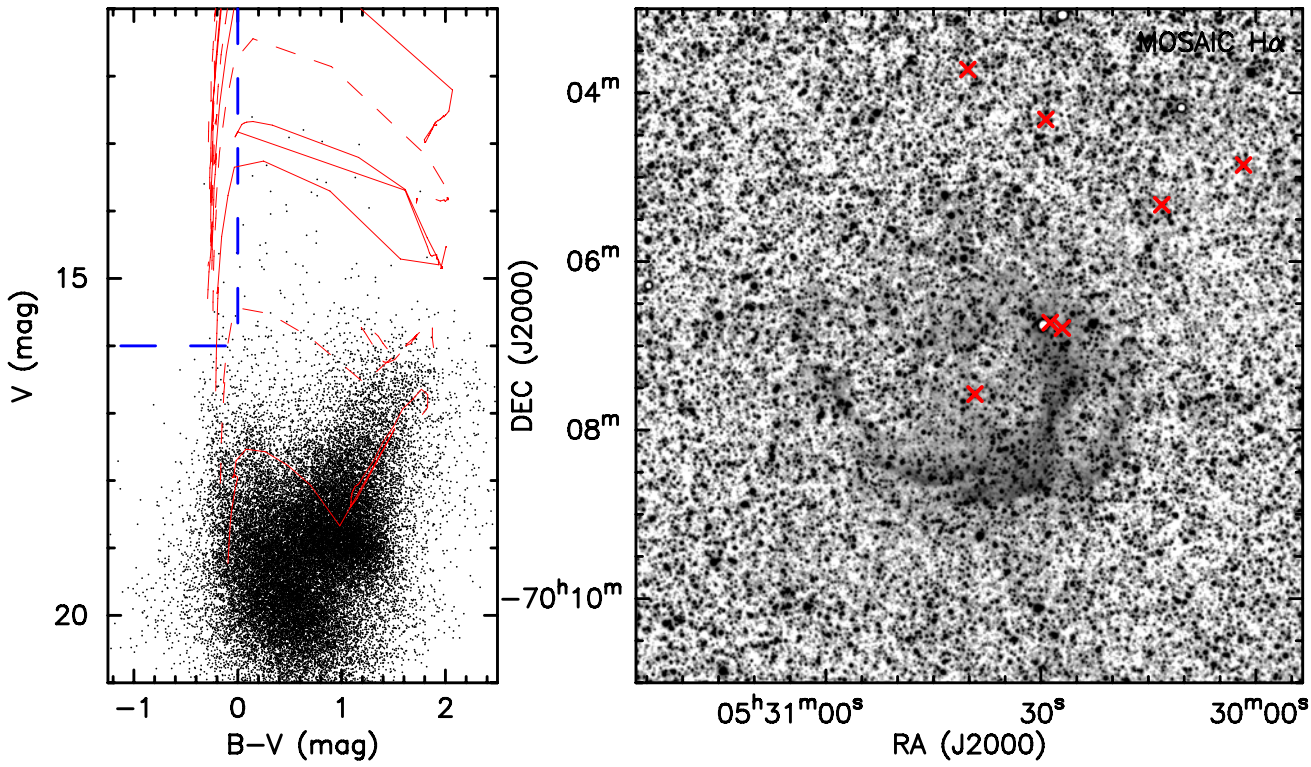

Fig. 8. The *left panel* shows a $B-V$,V colour–magnitude diagram from the MCPS (Zaritsky et al. 2004). Stellar evolutionary tracks from Lejeune & Schaerer (2001) are shown as dashed red lines (*bottom to top*: 5, 15, 25 and 60 $M_{\odot}$) and solid red lines (*bottom to top*: 3, 9, 20 and 40 $M_{\odot}$). Heavy dashed blue lines denote the selection criteria for B-star candidates, which lie in the top left corner of the diagram. The *right panel* shows the MCELS-2 Hα image of the area around SNR J0530–7007. B-star candidates are denoted by overlaid red crosses.

from the Bundesministerium für Wirtschaft und Technologie/Deutsches Zentrum für Luft- und Raumfahrt (BMWI/DLR) grant FKZ 50 OR 1201.

References

Arbutina, B., Urosević, D., Andjelić, M. M., Pavlović, M. Z., & Vukotić, B. 2012, ApJ, 746, 79
Beck, R., & Krause, M. 2005, Astron. Nachr., 326, 414
Bell, A. R. 1978, MNRAS, 182, 443
Berezhko, E. G., & Völk, H. J. 2004, A&A, 427, 525
Blair, W. P., Ghavamian, P., Sankrit, R., & Danforth, C. W. 2006, ApJS, 165, 480
Bojičić, I. S., Filipović, M. D., Parker, Q. A., et al. 2007, MNRAS, 378, 1237
Bozzetto, L. M., Filipović, M. D., Crawford, E. J., et al. 2010, Serbian Astron. J., 181, 43
Bozzetto, L. M., Filipović, M. D., Crawford, E. J., et al. 2011, Rev. Mex. Astron. Astrofis., submitted [arXiv:1109.3945]
Bozzetto, L. M., Filipović, M. D., Crawford, E. J., et al. 2012, MNRAS, 420, 2588
Čajko, K. O., Crawford, E. J., & Filipović, M. D. 2009, Serbian Astron. J., 179, 55
Crawford, E. J., Filipović, M. D., De Horta, A. Y., Stootman, F. H., & Payne, J. L. 2008a, Serbian Astron. J., 177, 61
Crawford, E. J., Filipović, M. D., & Payne, J. L. 2008b, Serbian Astron. J., 176, 59
Crawford, E. J., Filipović, M. D., Haberl, F., et al. 2010, A&A, 518, A35
Davies, R. D., Elliott, K. H., & Meaburn, J. 1976, MmRAS, 81, 89
Desai, K. M., Chu, Y.-H., Gruendl, R. A., et al. 2010, AJ, 140, 584
di Benedetto, G. P. 2008, MNRAS, 390, 1762
Dickel, J. R., McIntyre, V. J., Gruendl, R. A., & Milne, D. K. 2005, AJ, 129, 790
Filipović, M. D., Haynes, R. F., White, G. L., et al. 1995, A&AS, 111, 311
Filipović, M. D., White, G. L., Haynes, R. F., et al. 1996, A&AS, 120, 77
Filipović, M. D., Haynes, R. F., White, G. L., & Jones, P. A. 1998, A&AS, 130, 421
Gooch, R. 2006, Karma Users Manual (Australia Telescope National Facility)
Haberl, F., & Pietsch, W. 1999, A&AS, 139, 277 (HP99)
Harris, J., & Zaritsky, D. 2009, AJ, 138, 1243
Haynes, R. F., Klein, U., Wayte, S. R., et al. 1991, A&A, 252, 475
Hughes, A., Staveley-Smith, L., Kim, S., Wolleben, M., & Filipović, M. 2007, MNRAS, 382, 543
Lejeune, T., & Schaerer, D. 2001, A&A, 366, 538
Mills, B. Y., Turtle, A. J., Little, A. G., & Durdin, J. M. 1984, Aust. J. Phys., 37, 321
Pacholczyk, A. G. 1970, Radio astrophysics. Nonthermal processes in galactic and extragalactic sources, ed. A. G. Pacholczyk (San Francisco: Freeman)
Sanduleak, N. 1970, Contributions from the Cerro Tololo Inter-American Observatory, 89
Sault, R. J., Teuben, P. J., & Wright, M. C. H. 1995, in Astronomical Data Analysis Software and Systems IV, ed. R. A. Shaw, H. E. Payne, & J. J. E. Hayes, ASP Conf. Ser., 77, 433
Smith, R. C., Points, S., Aguilera, C., et al. 2004, BAAS, 36, 101.08
Smith, C., Points, S., & Winkler, P. F. 2006, NOAO Newsletter, 85, 6
Turtle, A. J., & Mills, B. Y. 1984, Proc. Astron. Soc. Australia, 5, 537
Zaritsky, D., Harris, J., Thompson, I. B., & Grebel, E. K. 2004, AJ, 128, 1606

A.16 Related Paper 16

Bozzetto, L. M., Filipović, M. D., Crawford, E. J., Payne, J. L., De Horta, A. Y., and Stupar, M. (2012c). Radio continuum observations of LMC SNR J0550-6823. *Rev. Mexicana Astron. Astrofis.*, 48:41–46

My contribution was to assist in the data analysis. This is a 10% contribution.

Revista Mexicana de Astronomía y Astrofísica, **48**, 41–46 (2012)

RADIO CONTINUUM OBSERVATIONS OF LMC SNR J0550-6823

L. M. Bozzetto,[1] M. D. Filipović,[1] E. J. Crawford,[1] J. L. Payne,[1] A. Y. De Horta,[1] and M. Stupar[2,3]

Received 2011 May 20; accepted 2011 September 14

RESUMEN

Reportamos nuevas observaciones del remanente de supernova J0550-6823 (DEM L328) en la Nube Mayor de Magallanes, realizadas con el Arreglo Compacto de Telescopios de Australia (ATCA). El objeto es un remanente de supernova típico, en forma de herradura, con un diámetro de $373'' \times 282'' \pm 4''$ ($90 \times 68 \pm 1$ pc), el cual lo distingue como uno de los más grandes remanentes de supernova en el Grupo Local. Estimamos un índice espectral en radio relativamente alto, $\alpha = -0.79 \pm 0.27$. Sin embargo, la polarización observada (50% ± 10%) es mayor a la esperada y es atípica para remanentes de supernova viejos y evolucionados. Notamos también una fuerte correlación entre [O III] y las imágenes de radio, lo cual permite clasificar a este remanente como dominado por el oxígeno.

ABSTRACT

We report on new Australia Telescope Compact Array (ATCA) observations of the Large Magellanic Cloud (LMC) supernova remnant (SNR) J0550-6823 (DEM L328). This object is a typical horseshoe SNR with a diameter of $373'' \times 282'' \pm 4''$ ($90 \times 68 \pm 1$ pc), making it one of the largest known SNRs in the Local Group. We estimate a relatively steep radio spectral index of $\alpha = -0.79 \pm 0.27$. However, its stronger than expected polarisation of 50% ± 10% is atypical for older and more evolved SNRs. We also note a strong correlation between [O III] and radio images, classifying this SNR as oxygen dominant.

Key Words: ISM: individual objects (DEM L328, SNR J0550-6823) — ISM: supernova remnants — Magellanic Clouds

1. INTRODUCTION

Located at approximately 50 kpc (di Benedetto 2008), the Large Magellanic Cloud (LMC) is considered to be an ideal laboratory to study Supernova Remnants (SNRs). Furthermore, the LMC is located in the direction of the South Celestial Pole, one of the coldest areas of the radio sky, making it possible to observe radio emissions without interference from galactic foreground radiation. Today's modern instruments make it possible to achieve detailed observations of these objects.

There are over 50 well established SNRs in the LMC (Klimek et al. 2010) with an additional ∼20 SNR candidates (Bozzetto et al., in preparation). This comprises one of the most complete samples of SNRs in external galaxies. Therefore, it is of prime interest to study LMC SNRs and compare them with their cousins in other galaxies such as M 33 (Long et al. 2010), M 38 (Dopita et al. 2010), the SMC (Filipović et al. 2005; Payne et al. 2007; Filipović et al. 2008) and our Galaxy (Stupar, Parker, & Filipović 2008; Green 2009).

Davis, Elliott, & Meaburn (1976) observed an object in the LMC named DEM L328 at Hα wavelengths and reported a nebulosity with a diameter of $25' \times 8'$. Savage (1976) detected this source in the Parkes 2700 MHz survey and reported a radio diameter of $\sim 3'$. Filipović et al. (1998b), using *ROSAT* All Sky Survey (RASS) observations, detected X-ray emission from this source (LMC RASS 309) and then calculated a spectral index from their Parkes data (Filipović et al. 1998a) of $\alpha = -0.37 \pm 0.06$.

Here, we present new medium-resolution observations of LMC SNR 0550-6823. Observations, data reduction and imaging techniques are described in § 2. The astrophysical interpretation of newly obtained moderate-resolution total intensity and polarimetric image is discussed in § 3.

[1]University of Western Sydney, Australia.
[2]Department of Physics, Macquarie University, Sydney, Australia.
[3]Australian Astronomical Observatory, Australia.

TABLE 1

INTEGRATED FLUX DENSITY OF SNR 0550-6823
AND POINT SOURCE ATCA J0550-6820

ν (MHz)	λ (cm)	R.M.S (mJy)	Beam Size (arcsec)	S_{SNR} (mJy)	S_{PS} (mJy)	Reference
0408	73	–	156×156	980	—	Clarke et al. (1976)
0843	36	1.5	43.0×43.0	643	132	This Work
1377	20	1.5	45.0×45.0	593	86	This Work
4800	6	0.15	40.2×35.3	346	24	This Work
8640	3	0.17	40.2×35.3	83	7	This Work

2. OBSERVATIONS

We observed SNR J0550-6823 with the Australia Telescope Compact Array (ATCA) on the 2nd and 5th of October 1997 (project C634), using the array configuration EW375, at wavelengths of 3 and 6 cm (ν = 8640 and 4800 MHz). Baselines formed with the 6th ATCA antenna were removed from the imaging and the remaining five antennas were arranged in a compact configuration. Observations were taken in "snap-shot" mode, totalling ∼1.5 hours of integration over a 12 hour period. Source PKS B1934-638 was used for primary calibration and source PKS B0530-727 provided secondary (phase) calibration. The MIRIAD (Sault & Killeen 2010) and KARMA (Gooch 2006) software packages were used for reduction and analysis. It is well established that interferometers such as the ATCA will suffer from missing flux due to the missing short spacings. To compensate for this short-coming, we combined our new ATCA observations with Parkes observations from Filipović et al. (1995) and ATCA mosaic survey data from Dickel et al. (2005).

In addition to our own observations at 6 cm and 3 cm, we also used 73 cm (ν = 408 MHz) observations from Clarke, Little, & Mills (1976), 36 cm (ν = 843 MHz) observations from Turtle & Mills (1984) taken by the Molonglo Observatory Synthesis Telescope (MOST), and 20 cm (ν = 1400 MHz) observations from the mosaics presented by Hughes et al. (2007) combining observations from ATCA and Parkes (Filipović et al. 1995). We remeasured flux values for the 36 cm and 20 cm observations as shown in Table 1.

Our new images at 6 and 3 cm were initially created using only ATCA observations from project C634 and then processed using MIRIAD multi-frequency synthesis (Sault & Wieringa 1994) and natural weighting. They were deconvolved using the CLEAN and RESTOR algorithms with primary beam correction applied using the LINMOS task. A similar procedure was used for both U and Q Stokes parameter maps. Due to the low dynamic range[4], self-calibration could not be applied. The 6 cm image (Figure 1) has a resolution of $36'' \times 33''$ at PA=0° and an estimated rms noise of 0.15 mJy/beam. This image was used for the polarisation study only. Similarly, we made an image of SNR J0550-6823 at 3 cm, matching the resolution to the 6 cm image (Figure 2).

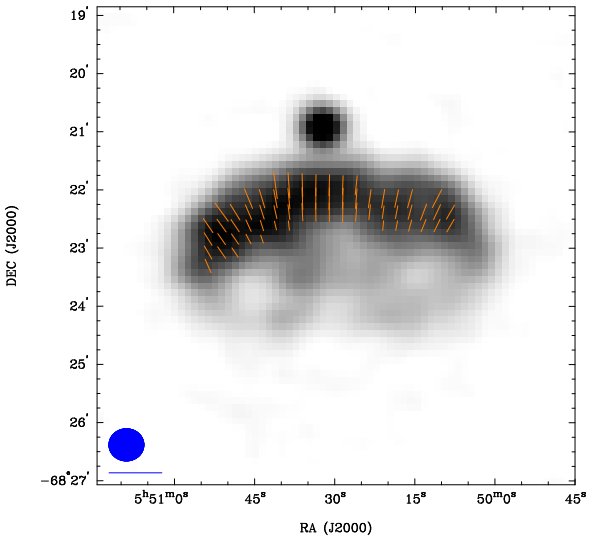

Fig. 1. ATCA "snap-shot" observations (C634 project only) of SNR J0550-6823 at 6 cm (4.8 GHz) overlaid with polarisation vectors. The ellipse in the lower left corner represents the synthesised beam width of $36'' \times 33''$, and the line below the ellipse is a polarisation vector of 100%.

[4]Defined as the ratio between the source flux and noise level.

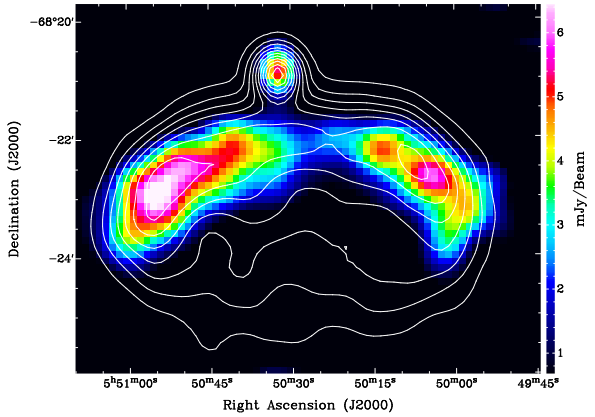

Fig. 2. SNR J0550-6823 at 3 cm (8.6 GHz) overlaid with 6 cm (4.8 GHz) contours. The contours are from 1 to 21 mJy/beam in steps of 2 mJy/beam. The sidebar quantifies the pixel map and its units are mJy/beam.

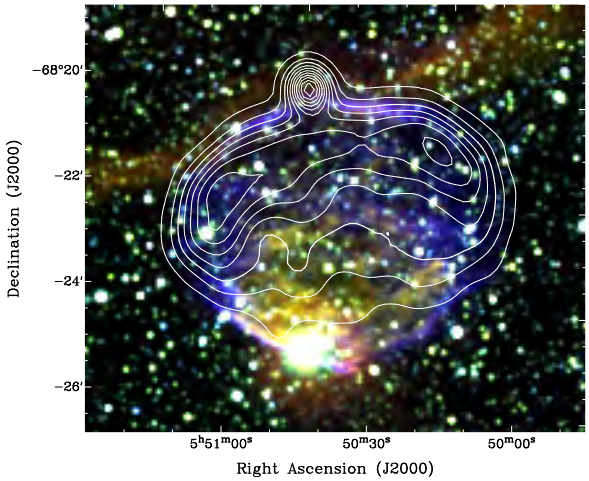

Fig. 3. MCELS composite optical image (RGB=Hα,[SII],[OIII]) of SNR J0550-6823 overlaid with 6 cm contours from our new combined image of all ATCA and Parkes observations. The contours are from 1 to 21 mJy/beam in steps of 2 mJy/beam.

Our analysis also made use of the Magellanic Cloud Emission Line Survey (MCELS) by Smith, Points, & Winkler (2006). This survey was carried out with the 0.6 m University of Michigan/CTIO Curtis Schmidt telescope, equipped with a SITE 2048×2048 CCD having a field of 1.35° at a scale of 2.4″ pixel^{-1}. They mapped both the LMC and SMC in narrow bands corresponding to Hα, [OIII] (λ=5007 Å) and [SII] (λ=6716,6731 Å), matching red and green continuum bands in order to subtract most of the stars from the images to reveal the full extent of the faint diffuse emission. All of the data have been flux-calibrated and assembled into mosaic images, a small section of which is shown in Figure 3. Further details regarding the MCELS are given by Smith et al. (2006) and at `http://www.ctio.noao.edu/mcels`. Here, for the first time, we present optical images of this object in combination with our new radio-continuum data.

3. RESULTS AND DISCUSSION

SNR J0550-6823 exhibits a one sided shell brightened morphology, dissipating in the southern region (Figure 2). We note what is likely an unrelated background point source in its northern region. The remnant is centred at RA(J2000) = $5^h50^m30.7^s$, DEC(J2000) = −68°23′37.0″ with a diameter at 6 cm measuring $373'' \times 282'' \pm 4''$ ($90 \times 68 \pm 1$ pc). We estimate the extent at the 3σ noise level (0.15 mJy) along the major (E-W) and minor (N-S) axis (PA=90°) as presented in Figure 4. However, we notice that at optical wavelengths SNR J0550-6823 extends further south and appears to have a near circular shape with the minor axis of ∼75–80 pc. Also, it appears that this SNR is more prominent in the [OIII] image and therefore is an excellent candidate for an oxygen dominant type of SNR such as N 132D or 1E0102-72. New observations similar to Vogt & Dopita (2011) will confirm the true nature of this object.

Using all values of integrated flux density estimates (except for 73 cm; Table 1), a spectral index ($S \propto \nu^{\alpha}$) distribution is plotted in Figure 5. The overall radio-continuum spectrum (Figure 5; black line) from SNR 0550-6823 was estimated to be $\alpha = -0.79 \pm 0.27$, while the typical SNR spectral index is $\alpha = -0.5 \pm 0.2$ (Filipović et al. 1998a). This somewhat steeper spectral index would indicate a younger age despite its (large) size of $90 \times 68 \pm 1$ pc, suggesting it is an older (more evolved) SNR. We also note that this may indicate that a simple model does not accurately describe the data, and that a higher order model is needed. This is not unusual, given that several other Magellanic Clouds SNR's exhibit "curved" spectra (Crawford et al. 2008a; Bozzetto et al. 2010). Noting the breakdown of the power law fit at shorter wavelengths, we decomposed the spectral index estimate into two components, one (α_1) between 36 and 20 cm, and the other (α_2) between 6 and 3 cm. The first component (Figure 5; red line), $\alpha_1 = -0.16 \pm 0.41$ is a reasonable fit and typical for an evolved SNR, whereas the second (Figure 5; green line), $\alpha_2 = -2.43 \pm 0.34$, is a poor fit, and indicates that non-thermal emission can be described by different populations of electrons with different energy

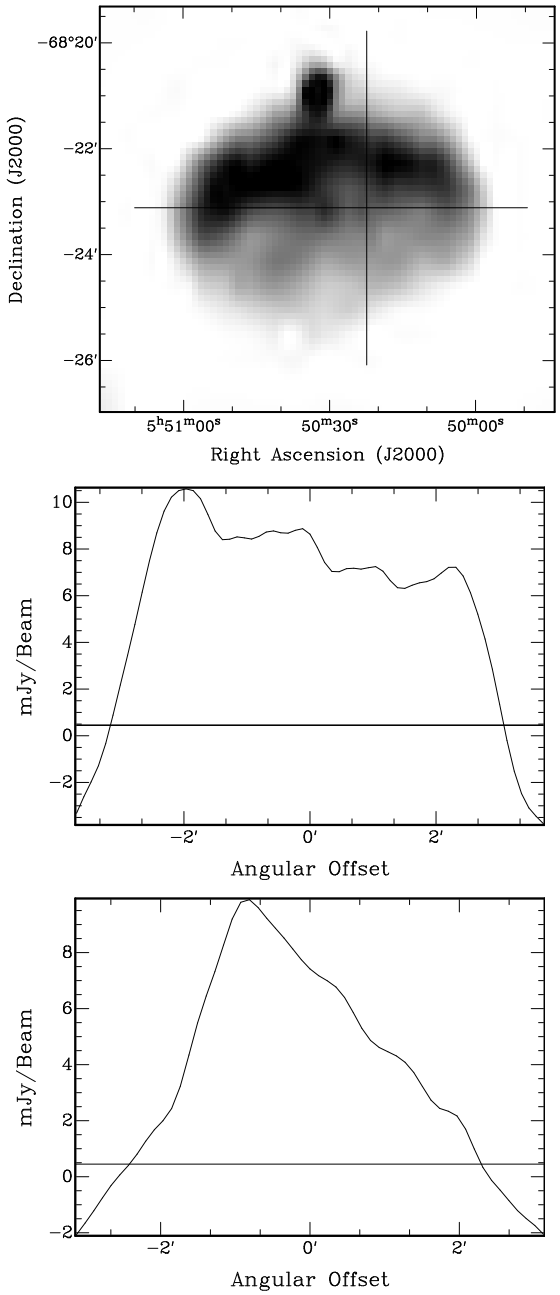

Fig. 4. The top image shows the major and minor axis, with the major axis starting at the E end and the minor axis starting at the N end. The center image shows the I-Profile of the major axis with the 3σ line shown. The bottom image shows the I-Profile of the minor axis with the 3σ line shown.

indices. Although the low flux at 3 cm (and to a lesser extent at 6 cm) could cause the large deviations, an underestimate of up to ∼50% would still lead to a "curved" spectrum.

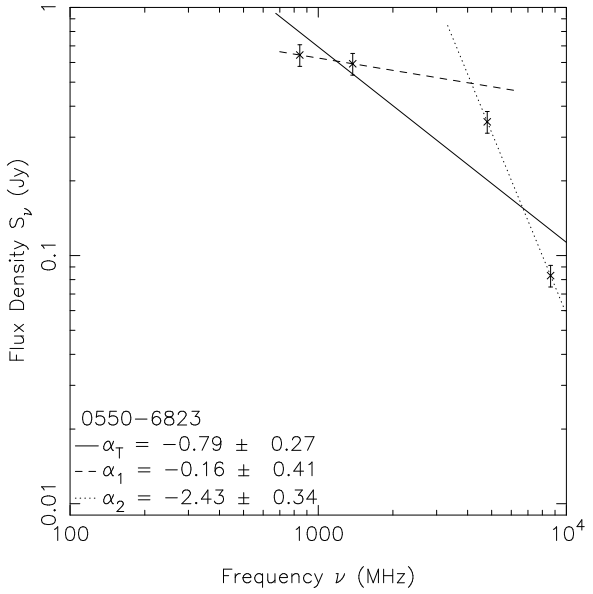

Fig. 5. Radio-continuum spectrum of SNR J0550-6823. The 73 cm (408 MHz) value was disregarded in this estimate due to confusion from the strong point source in the northern region of the SNR.

SNR J0550-6823 is located on the eastern side of the LMC, far away from the main body of this dwarf galaxy. We also point out the dissipating shell in the southern region of the remnant. Therefore, it is reasonable to assume that this SNR is expanding in a very low density environment.

We estimate the spectral index of the point source (ATCA J0550-6820) in the northern region of the SNR to be $\alpha = -1.2 \pm 0.2$ (Table 1). This significantly steeper spectrum adds further evidence that the point source is unrelated to SNR 0550-6823 and is most likely a background AGN. Hence, this background source may "contaminate" correct spectral index estimates of SNR J0550-6823, especially in low-resolution studies such as that of Filipović et al. (1998a) (-0.37 ± 0.06 previous vs. -0.79 ± 0.27 this paper). For this reason we do not include the 73-cm flux density measurements in the new spectral index estimate, as the beam size (resolution) is over $2.5'$.

We also considered this point source to be a runaway pulsar related to SNR 0550-6823. We ruled out this scenario due to a lack of prominent trails (or pulsar wind nebulae) as found in LMC SNR N206 (Klinger et al. 2002) or SMC SNR IKT 16 (Owen et al. 2011).

Linear polarisation images were created for each frequency using the Q and U parameters (Figure 1).

Relatively strong linear polarisation is evident in the 6 cm image and is greater than in many LMC SNRs (Bojičić et al. 2007; Crawford, Filipović, & Payne 2008b; Crawford et al. 2008a; Čajko, Crawford, & Filipović 2009; Crawford et al. 2010) but somewhat weaker than in LMC SNR J0527-6549 (DEM L204) (Bozzetto et al. 2010).

The mean fractional polarisation at 6 cm was calculated using flux density and polarisation:

$$P = \frac{\sqrt{S_Q^2 + S_U^2}}{S_I} \cdot 100\%\,, \qquad (1)$$

where S_Q, S_U and S_I are the integrated intensities for the Q, U and I Stokes parameters. Our estimated peak value at 6 cm is $50\% \pm 10\%$ (Figure 1) while there is no reliable detection at 3 cm. Without reliable polarisation measurements at a second frequency we could not determine the Faraday rotation and thus cannot deduce the magnetic field strength. We also note that the point source in the northern region is not polarised. This is also consistent with it being an unrelated background source.

4. CONCLUSION

We carried out a radio-continuum study of SNR J0550-6823. From this analysis, we found that the SNR followed a one sided shell brightened morphology with a diameter of $373'' \times 282'' \pm 4''$ ($90 \times 68 \pm 1$ pc). It has a relatively flat spectral index ($\alpha = -0.79 \pm 0.27$) and a strong 6 cm polarisation of $\sim$50% $\pm$ 10%. We also note correlations between the optical ([OIII]) and radio observation of this object, with the optical observations accounting for the seemingly "missing" southern emission seen in the images at radio wavelengths. These new observations will further improve our knowledge of this SNR as well as SNRs in general.

We used the KARMA software package developed by the ATNF. The Australia Telescope Compact Array is part of the Australia Telescope which is funded by the Commonwealth of Australia for operation as a National Facility managed by CSIRO. The Magellanic Clouds Emission Line Survey (MCELS) data were provided by R. C. Smith, P. F. Winkler, and S. D. Points. The MCELS project has been supported in part by NSF grants AST-9540747 and AST-0307613, and through the generous support of the Dean B. McLaughlin Fund at the University of Michigan, a bequest from the family of Dr. Dean B. McLaughlin in memory of his lasting impact on Astronomy. The National Optical Astronomy Observatory is operated by the Association of Universities for Research in Astronomy Inc. (AURA), under a cooperative agreement with the National Science Foundation.

REFERENCES

Bojičić, I. S., et al. 2007, MNRAS, 378, 1237
Bozzetto, L. M., et al. 2010, Serb. Astron. J., 181, 43
Čajko, K. O., Crawford, E. J., & Filipović, M. D. 2009, Serb. Astron. J., 179, 55
Clarke, J. N., Little, A. G., & Mills, B. Y. 1976, Aust. J. Phys., Astrophys. Suppl., 40, 1
Crawford, E. J., Filipović, M. D., de Horta, A. Y., Stootman, F. H., & Payne, J. L. 2008a, Serb. Astron. J., 177, 61
Crawford, E. J., Filipović, M. D., Haberl, F., Pietsch, W., Payne, J. L., & de Horta, A. Y. 2010, A&A, 518, A35
Crawford, E. J., Filipović, M. D., & Payne, J. L. 2008b, Serb. Astron. J., 176, 59
Davies, R. D., Elliott, K. H., & Meaburn, J. 1976, MmRAS, 81, 89
di Benedetto, G. P. 2008, MNRAS, 390, 1762
Dickel, J., McIntyre, V., Gruendl, R., & Milne, D. K. 2005, AJ, 129, 790
Dopita, M. A., et al. 2010, ApJ, 710, 964
Filipović, M. D., Haynes, R. F., White, G. L., & Jones, P. A. 1998a, A&AS, 130, 421
Filipović, M. D., Haynes, R. F., White, G. L., Jones, P. A., Klein, U., & Wielebinski, R. 1995, A&AS, 111, 311
Filipović, M. D., Payne, J. L., Reid, W., Danforth, C. W., Staveley-Smith, L., Jones, P. A., & White, G. L. 2005, MNRAS, 364, 217
Filipović, M. D., et al. 1998b, A&AS, 127, 119
Filipović, M. D., et al. 2008, A&A, 485, 63
Gooch, R. 2006, Karma Users Manual (Sydney: ATNF)
Green, D. A. 2009, Bull. Astron. Soc. India, 37, 45
Hughes, A., Staveley-Smith, L., Kim, S., Wolleben, M., & Filipović, M. 2007, MNRAS, 382, 543
Klimek, M. D., Points, S. D., Smith, R. C., Shelton, R. L., & Williams, R. 2010, ApJ, 725, 2281
Klinger, R. J., Dickel, J. R., Fields, B. D., & Milne, D. K. 2002, AJ, 124, 2135
Long, K. S., et al. 2010, ApJS, 187, 495
Owen, R., et al. 2011, A&A, 530, A132
Payne, J. L., White, G. L., Filipović, M. D., & Pannuti, T. G. 2007, MNRAS, 376, 1793
Sault, B., & Killeen, N. 2010, Miriad User Manual (Sidney: ATNF)
Sault, R. J., & Wieringa, M. H. 1994, A&AS, 108, 585
Savage, A. 1976, MNRAS, 174, 259
Smith, C., Points, S., & Winkler, P. F. 2006, NOAO Newsletter, 85, 6

Stupar, M., Parker, Q. A., & Filipović, M. D. 2008, MNRAS, 390, 1037

Turtle, A. J., & Mills, B. Y. 1984, Proc. Astron. Soc. Australia, 5, 537

Vogt, F., & Dopita, M. A. 2011, Ap&SS, 331, 521

L. M. Bozzetto, M. D. Filipović, E. J. Crawford, J. L. Payne and A. Y. De Horta: School of Computing and Mathematics, University of Western Sydney, Locked Bag 1797, Penrith South DC, NSW 1797, Australia (luke.bozzetto@gmail.com).

M. Stupar: Department of Physics, Macquarie University, Sydney 2109, NSW, Australia.

A.17 Related Paper 17

Galvin, T. J., Filipović, M. D., Crawford, E. J., Tothill, N. F. H., Wong, G. F., and De Horta, A. Y. (2012a). 20 cm VLA Radio-Continuum Study of M31 - Images and Point Source Catalogues. *Serbian Astronomical Journal*, 184:41–68

My contribution was to assist in the data analysis. This is a 20% contribution.

Serb. Astron. J. № 184 (2012), 41 - 68 **UDC 52–13–77 : 524.726 M31**
DOI: 10.2298/SAJ1284041G Original scientific paper

20 cm VLA RADIO-CONTINUUM STUDY OF M 31 – IMAGES AND POINT SOURCE CATALOGUES

T. J. Galvin, M. D. Filipović, E. J. Crawford, N. F. H. Tothill, G. F. Wong and A. Y. De Horta

University of Western Sydney, Locked Bag 1797, Penrith South DC, NSW 2751, Australia
E–mail: *m.filipovic@uws.edu.au*

(Received: April 24, 2012; Accepted: April 27, 2012)

SUMMARY: We present a series of new high-sensitivity and high-resolution radio-continuum images of M 31 at λ=20 cm (ν=1.4 GHz). These new images were produced by merging archived 20 cm radio-continuum observations from the Very Large Array (VLA) telescope. Images presented here are sensitive to rms=60 μJy and feature high angular resolution ($<10''$). A complete sample of discrete radio sources have been catalogued and analysed across 17 individual VLA projects. We identified a total of 864 unique discrete radio sources across the field of M 31. One of the most prominent regions in M 31 is the ring feature for which we estimated total integrated flux of 706 mJy at λ=20 cm. We compare here detected sources to those listed in Gelfand et al. (2004) at λ=92 cm and find 118 sources in common to both surveys. The majority (61%) of these sources exhibit a spectral index of $\alpha <-0.6$ indicating that their emission is predominantly non-thermal in nature, that is more typical for background objects.

Key words. techniques: image processing – radio continuum – catalogs

1. INTRODUCTION

A member of the Andromeda constellation, M31, at a distance of ∼778 Kpc (Karachentsev et al. 2004), is the closest spiral galaxy to our own. For this reason, it plays a significant role in galactic and extragalactic studies. A number of previous radio-continuum studies at λ=20 cm (Braun 1990a) focused on general properties of M 31, such as its structure and magnetic fields. Also, Braun (1990b) presented a list of 20-cm sources (534) in the north-east parts of M 31. A number of other studies such as Dickel et al. (1982) estimated flux densities of M 31 supernova remnants (SNRs) and H II regions.

In this paper, we reexamine all available archived radio-continuum observations performed with the Very Large Array (VLA) at λ=20 cm (ν=1.4 GHz) with the intention of merging these observations into a single mosaic radio-continuum image. By combining a large amount of existing data, while using the latest generation of computing power, we can create new images that feature both high angular resolution and improved sensitivity. The newly constructed images are analysed and the differences between the various M 31 images created at 20 cm are discussed.

In Section 2 we describe the observational data and reduction techniques. In Section 3 we present our new maps and a brief discussion. Source catalogues are given in Section 4 and Section 5 is the conclusion.

2. DATA

A collection of existing, archived radio-continuum observations at λ=20 cm with pointings centred on M 31 were obtained from the National Radio Astronomy Observatory (NRAO)[1] online data retrieval system. In total, 15 VLA projects with a variety of array configurations were selected for use in this study, as summarised in Table 1. These projects were observed between the 1^{st} of October 1983 and 27^{th} of September 1997 and are comprised of 28 individual observational runs.

3. IMAGE CREATION

The MIRIAD (Sault et al. 1995) and KARMA (Gooch 1996) software packages were used for data reduction and analysis. Because of the large volume of data, the MIRIAD package was compiled to run on a 16-processor high-performance computer system.

Initially, observations were imported into AIPS using the task FILLM, and then all sources were split with SPLIT. Using the task UVFIX, source coordinates were converted from the B1950 to the J2000 reference frame and the task FITTP was used to export each source to a FITS file.

The MIRIAD package was then used for actual data reduction. The task ATLOD was used to convert ATCA observations into MIRIAD files, while the task FITS was used to import the previous AIPS-produced fits files and convert them to MIRIAD files. Typical calibration and flagging procedures were then carried out (Sault et al. 1995). Using the task INVERT, each project was imaged individually using a natural weighting scheme. Images with a single pointing were cleaned using the task CLEAN, while each mosaic image was cleaned using the task MOSSDI. Each of these cleaning tasks uses a SDI clean algorithm to reduce image artefacts (Steer et al. 1984). To convolve a clean model the task RESTOR was then used on each of the cleaned maps, followed by LINMOS to correct for the primary beam for single pointing observations. For more information on data analysis and image creation see Galvin et al. (2012) and Payne et al. (2004).

The catalogue of radio-continuum sources contains positions RA(J2000), Dec(J2000) and integrated flux densities at 13 cm (Table A1), 20 cm (Table A2) and 36 cm (Table A3). Table 3 contains the r.m.s., number of sources detected, number of sources identified within the field of the 13 cm image and beam size for each image.

4. RESULTS

By comparing the individual maps produced from a variety of observations, the effects of varying array configurations can be seen, as shown in Figs. 1-18. For example, projects AC0101 and AB0551 show a region of extended emission with poorly resolved point sources across all individual images. This can be attributed to the short baselines of the D type configuration used by the VLA to produce each of these images.

As expected, observations conducted with a C and B type array configuration, such as AM0464 and AT0149 respectively, demonstrate a progressive loss of extended emission and improved point source resolution across their field of view. Observations that used an A type configuration, such as AH0139 and AH0221, show a significant loss of extended emission but better point source resolution.

4.1. New Combined M 31 Mosaics at λ=20 cm

Figs. 19 and 20 are the resulting images when all fully polarised VLA observations are merged together. Both images suffer from artefacts around the outer region of the field of view. This can be attributed to the image stacking process, where observations conducted with the use of a compact array configuration get stretched to meet the resolution of the image as a whole.

Fig. 19 shows the resulting radio-continuum image when all fully polarised VLA observations are merged together with a restricted *uv* coverage of 0-5 kλ. This restriction was introduced in order to preserve the intricate structure of the extended emission while partly resolving point sources across the field.

Fig. 20 is the same data-set as Fig. 19 with a restricted *uv* coverage of 0-25 kλ. This restriction was imposed after a trial and error process where we identified the MIRIAD's software limitations. Despite this restriction, point sources are well resolved and there remains a region of extended emission.

Fig. 21 shows a mosaic radio-continuum image of VLA projects AB0396 and AB0999 with a restricted *uv* coverage of 0-35 kλ. Point sources are seen prominently across the field of view with little extended emission. This can be attributed to the larger array configurations, and thus longer baselines, which these observations are constructed of.

Fig. 22 is a mosaic radio-continuum image comprised of all calibrated VLA observations from this study with a restricted *uv* coverage of 0-5 kλ. This restriction was implemented to place greater emphasis on the intrinsic structure of the extended emission throughout the field of view. The majority of observations within VLA projects AB0396 and AB0999 were made with B configuration types. This provided *uv* coverage data that was noticeably absent in other observations. This has significantly improved the overall clarity of the image when compared to Fig. 19. One of the most prominent regions in M 31 is the ring feature for which we estimated total integrated flux of 706$\pm$35 mJy.

In Fig. 23, we show the resulting image when all calibrated VLA observations are merged together with a restricted *uv* coverage of 0-25 kλ. Again, this restricted *uv* coverage was used to overcome the limit of the MIRIAD software imaging capabilities. Point sources are well resolved and there remains a region of extended emission.

[1] https://archive.nrao.edu/archive/e2earchivex.jsp

Table 1. List of VLA projects of M 31 used in this study. RA and DEC represent coordinates of central pointings.

Project ID	RA h m s	DEC ° ′ ″	Array Config	Date	Freq. (MHz)	Bandwidth (MHz)	Time on Source (hrs)	Recorded Polarisation	Primary Calibrator	Secondary Calibrator
AH0139	00:42:44.24	41:16:25.65	A	01/10/1983	1465, 1515	50	1.18	rr,ll,rl,lr	1328+307	0107+562
AH0221	00:43:20.37	41:13:00.17	A	06/04/1986	1465	50	0.61	rr,ll,rl,lr	0137+331	0026+346
AH0221	00:43:44.50	41:17:34.87	A	06/04/1986	1465	50	0.61	rr,ll,rl,lr	0137+331	0026+346
AH0221	00:40:13.76	40:50:06.55	A	06/04/1986	1465	50	0.64	rr,ll,rl,lr	0137+331	0026+346
AH0221	00:45:36.88	41:03:53.32	A	06/04/1986	1465	50	0.62	rr,ll,rl,lr	0137+331	0026+346
AH0221	00:46:00.39	42:06:22.99	A	06/04/1986	1465	50	0.56	rr,ll,rl,lr	0137+331	0026+346
AH0221	00:46:56.73	42:20:27.18	A	06/04/1986	1465	50	0.64	rr,ll,rl,lr	0137+331	0026+346
AH0221	00:48:03.74	41:40:53.21	A	06/04/1986	1465	50	0.65	rr,ll,rl,lr	0137+331	0026+346
AH0221	00:41:30.83	40:58:32.59	A	06/04/1986	1465	50	0.49	rr,ll,rl,lr	0137+331	0026+346
AH0221	00:42:03.74	40:20:31.17	A	06/04/1986	1465	50	0.61	rr,ll,rl,lr	0137+331	0026+346
AH0221	00:42:20.03	40:57:40.96	A	06/04/1986	1465	50	0.63	rr,ll,rl,lr	0137+331	0026+346
AH0221	00:42:30.20	41:19:25.83	A	06/04/1986	1465	50	0.63	rr,ll,rl,lr	0137+331	0026+346
AH0221	00:42:30.14	41:09:25.84	A	06/04/1986	1465	50	0.63	rr,ll,rl,lr	0137+331	0026+346
AH0221	00:42:56.31	41:19:25.49	A	06/04/1986	1465	50	0.61	rr,ll,rl,lr	0137+331	0026+346
AH0221	00:42:56.25	41:09:25.50	A	06/04/1986	1465	50	0.61	rr,ll,rl,lr	0137+331	0026+346
AH0221	00:43:09.17	40:48:03.41	A	06/04/1986	1465	50	0.63	rr,ll,rl,lr	0137+331	0026+346
AT0149	00:42:41.02	41:15:30.69	B	18/04/1993	1385,1465	50	0.06	rr,ll,rl,lr	0137+331	0248+430
AB0679	00:42:46.05	41:16:11.63	C	26/08/1993	1365,1465	50	6.55	rr,ll,rl,lr	0137+331	0038+328
AB0679	00:42:46:05	41:16:11.63	C	29/08/1993	1365,1465	50	14.02	rr,ll,rl,lr	0137+331	0038+328
AH0524	00:41:25.89	41:12:26.66	C	18/12/1994	1365, 1465	50	4.74	rr,ll,rl,lr	0137+331	0026+346
AM0464	00:40:20.00	40:31:30.00	C	01/11/1994	1385, 1415	50	1.07	rr,ll,rl,lr	0137+331	0029+349
AM0464	00:41:05.00	40:46:30.00	C	01/11/1994	1385, 1415	50	1.05	rr,ll,rl,lr	0137+331	0029+349
AM0464	00:41:05.00	41:04:45.00	C	01/11/1994	1385, 1415	50	1.05	rr,ll,rl,lr	0137+331	0029+349
AM0464	00:42:45.00	41:04:25.00	C	01/11/1994	1385, 1415	50	1.06	rr,ll,rl,lr	0137+331	0029+349
AM0464	00:44:00.00	41:34:25.00	C	01/11/1994	1385, 1415	50	1.06	rr,ll,rl,lr	0137+331	0029+349
AM0464	00:44:30.00	41:22:25.00	C	01/11/1994	1385, 1415	50	1.05	rr,ll,rl,lr	0137+331	0029+349
AM0464	00:45:40.00	41:47:09.00	C	01/11/1994	1385, 1415	50	1.06	rr,ll,rl,lr	0137+331	0029+349
AC0496	00:42:35.44	41:57:46.80	C	27/09/1997	1365,1435	50	0.04	rr,ll,rl,lr	0137+331	0102+584
AC0101	00:42:44.54	41:16:28.65	D	13/07/1984	1465, 1515	50	0.10	rr,ll,rl,lr	0137+331	2234+282
AB0551	00:42:46.05	41:16:11.63	D	27/07/1989	1465, 1515	50	4.38	rr,ll,rl,lr	0137+331	0038+328
AB0491	00:42:05.93	40:50:26.15	D	08/09/1988	1465	50	8.66	rr,ll,rl,lr	1328+307	0026+346
AB0647	00:44:49.83	41:26:23.97	D	(25,27)/07/1992	1465,1515	50	3.01, 2.60	rr,ll,rl,lr	0137+331	0038+328
AB0647	00:45:08.07	41:51:23.72	D	(25,27)/07/1992	1465,1515	50	2.99, 2.57	rr,ll,rl,lr	0137+331	0038+328
AB0437	00:43:43.64	40:58:27.19	D	04/04/1987	1465,1515	50	8.86	rr,ll,rl,lr	0137+331	0038+328

Table 1. Continued.

Project ID	RA h m s	DEC ° ′ ″	Array Config	Date	Freq. (MHz)	Bandwidth (MHz)	Time on Source (hrs)	Recorded Polarisation	Primary Calibrator	Secondary Calibrator
AB0437	00:40:13.44	40:46:27.56	D	13/04/1987	1465,1515	50	8.84	rr,ll,rl,lr	0137+331	0038+328
AC0308	00:42:00.00	40:41:42.00	D	08/09/1996	1365, 1435	50	0.01	rr,ll,rl,lr	0521+166	0141+138
AC0308	00:42:00.00	41:13:12.00	D	08/09/1996	1365, 1435	50	0.01	rr,ll,rl,lr	0521+166	0141+138
AC0308	00:43:30.00	40:57:30.00	D	08/09/1996	1365, 1435	50	0.01	rr,ll,rl,lr	0521+166	0141+138
AC0308	00:43:30.00	41:29:06.00	D	08/09/1996	1365, 1435	50	0.01	rr,ll,rl,lr	0521+166	0141+138
AC0308	00:43:30.00	42:01:00.00	D	08/09/1996	1365, 1435	50	0.01	rr,ll,rl,lr	0521+166	0141+138
AC0308	00:45:00.00	41:13:12.00	D	20/09/1996	1365, 1435	50	0.01	rr,ll,rl,lr	0521+166	2202+422
AC0308	00:45:00.00	42:17:00.00	D	20/09/1996	1365, 1435	50	0.01	rr,ll,rl,lr	0521+166	2202+422
AC0308	00:46:30.00	41:29:06.00	D	20/09/1996	1365, 1435	50	0.01	rr,ll,rl,lr	0521+166	2202+422
AC0308	00:46:30.00	42:01:00.00	D	20/09/1996	1365, 1435	50	0.01	rr,ll,rl,lr	0521+166	2202+422
AC0308	00:39:00.00	40:10:24.00	D	24/09/1996	1365, 1435	50	0.01	rr,ll,rl,lr	0521+166	2202+422
AC0308	00:39:00.00	40:41:42.00	D	24/09/1996	1365, 1435	50	0.01	rr,ll,rl,lr	0521+166	2202+422
AC0308	00:40:30.00	40:26:06.00	D	24/09/1996	1365, 1435	50	0.01	rr,ll,rl,lr	0521+166	2202+422
AC0308	00:40:30.00	40:57:30.00	D	24/09/1996	1365, 1435	50	0.01	rr,ll,rl,lr	0521+166	2202+422
AC0308	00:40:30.00	41:29:06.00	D	24/09/1996	1365, 1435	50	0.01	rr,ll,rl,lr	0521+166	2202+422
AB0396	00:42:46.05	41:16:11.62	B	27/07/1986	1465	50	0.97	RCP	1328+307	2352+495
AB0396	00:42:46.05	41:16:11.62	B	(18,29)/08/1986	1465	50	0.94, 0.92	RCP	1328+307	2352+495
AB0396	00:42:46.05	41:16:11.62	B	04/09/1986	1465	50	1.64	RCP	1328+307	2352+495
AB0396	00:43:58.16	41:33:32.67	B	27/07/1986	1465	50	0.97	RCP	1328+307	2352+495
AB0396	00:43:58.16	41:33:32.67	B	(18,29)/08/1986	1465	50	0.94, 0.92	RCP	1328+307	2352+495
AB0396	00:43:58.16	41:33:32.67	B	04/09/1986	1465	50	0.92	RCP	1328+307	2352+495
AB0396	00:45:10.98	41:50:50.67	B	27/07/1986	1465	50	0.96	RCP	1328+307	2352+495
AB0396	00:45:10.98	41:50:50.67	B	(18,29)/08/1986	1465	50	0.93, 0.93	RCP	1328+307	2352+495
AB0396	00:45:10.98	41:50:50.67	B	04/09/1986	1465	50	0.93	RCP	1328+307	2352+495
AB0396	00:46:24.41	42:08:05.64	B	27/07/1986	1465	50	0.80	RCP	1328+307	2352+495
AB0396	00:46:24.41	42:08:05.64	B	(18,29)/081986	1465	50	0.93, 0.92	RCP	1328+307	2352+495
AB0396	00:46:24.41	42:08:05.64	B	04/09/1986	1465	50	0.92	RCP	1328+307	2352+495
AB0396	00:44:08.20	41:18:06.53	B	27/07/1986	1465	50	0.96	RCP	1328+307	2352+495
AB0396	00:44:08.20	41:18:06.53	B	(18,29)/081986	1465	50	0.92, 0.93	RCP	1328+307	2352+495
AB0396	00:44:08.20	41:18:06.53	B	04/09/1986	1465	50	0.91	RCP	1328+307	2352+495
AB0396	00:45:20.82	41:35:23.54	B	27/07/1986	1465	50	0.95	RCP	1328+307	2352+495
AB0396	00:45:20.82	41:35:23.54	B	(18,29)/08/1986	1465	50	0.92, 0.92	RCP	1328+307	2352+495
AB0396	00:45:20.82	41:35:23.54	B	04/09/1986	1465	50	0.93	RCP	1328+307	2352+495
AB0396	00:46:33.94	41:52:38.51	B	27/07/1986	1465	50	0.96	RCP	1328+307	2352+495
AB0396	00:46:33.94	41:52:38.51	B	(18,29)/08/1986	1465	50	0.93, 0.92	RCP	1328+307	2352+495

Table 1. Continued.

Project ID	RA h m s	DEC ° ′ ″	Array Config	Date	Freq. (MHz)	Bandwidth (MHz)	Time on Source (hrs)	Recorded Polarisation	Primary Calibrator	Secondary Calibrator
AB0396	00:46:33.94	41:52:38.51	B	04/09/1986	1465	50	0.93	RCP	1328+307	2352+495
AB0396	00:42:35.70	41:31:37.76	B	27/07/1986	1465	50	0.96	RCP	1328+307	2352+495
AB0396	00:42:35.70	41:31:37.76	B	(18,29)/08/1986	1465	50	0.92, 0.92	RCP	1328+307	2352+495
AB0396	00:42:35.70	41:31:37.76	B	04/09/1986	1465	50	0.93	RCP	1328+307	2352+495
AB0396	00:43:48.11	41:48:58.80	B	27/07/1986	1465	50	0.96	RCP	1328+307	2352+495
AB0396	00:43:48.11	41:48:58.80	B	(18,29)/08/1986	1465	50	0.92, 0.92	RCP	1328+307	2352+495
AB0396	00:43:48.11	41:48:58.80	B	04/09/1986	1465	50	0.93	RCP	1328+307	2352+495
AB0396	00:45:01.14	42:06:17.81	B	27/07/1986	1465	50	0.96	RCP	1328+307	2352+495
AB0396	00:45:01.14	42:06:17.81	B	(18,29)/08/1986	1465	50	0.93, 0.93	RCP	1328+307	2352+495
AB0396	00:45:01.14	42:06:17.81	B	04/09/1986	1465	50	0.93	RCP	1328+307	2352+495
AB0396	00:42:46.05	41:16:11.62	C	14/12/1986	1465	50	0.93	RCP	1328+307	2352+495
AB0396	00:43:58.16	41:33:32.67	C	14/12/1986	1465	50	0.93	RCP	1328+307	2352+495
AB0396	00:45:10.98	41:50:50.67	C	14/12/1986	1465	50	0.92	RCP	1328+307	2352+495
AB0396	00:46:24.41	42:08:05.64	C	14/12/1986	1465	50	0.92	RCP	1328+307	2352+495
AB0396	00:44:08.20	41:18:06.53	C	14/12/1986	1465	50	0.93	RCP	1328+307	2352+495
AB0396	00:45:20.82	41:35:23.54	C	14/12/1986	1465	50	0.94	RCP	1328+307	2352+495
AB0396	00:46:33.94	41:52:38.51	C	14/12/1986	1465	50	0.93	RCP	1328+307	2352+495
AB0396	00:42:35.70	41:31:37.76	C	14/12/1986	1465	50	0.93	RCP	1328+307	2352+495
AB0396	00:43:48.11	41:48:58.80	C	14/12/1986	1465	50	0.93	RCP	1328+307	2352+495
AB0396	00:45:01.14	42:06:17.81	C	14/12/1986	1465	50	0.89	RCP	1328+307	2352+495
AB0396	00:45:10.98	41:50:50.67	D	13/03/1986	1465	50	0.90	RCP	1328+307	2352+495
AB0396	00:46:24.41	42:08:05.64	D	13/03/1986	1465	50	0.85	RCP	1328+307	2352+495
AB0396	00:45:20.82	41:35:23.54	D	13/03/1986	1465	50	0.74	RCP	1328+307	2352+495
AB0396	00:46:33.94	41:52:38.51	D	13/03/1986	1465	50	0.80	RCP	1328+307	2352+495
AB0396	00:43:48.11	41:48:58.80	D	13/03/1986	1465	50	0.89	RCP	1328+307	2352+495
AB0396	00:45:01.14	42:06:17.81	D	13/03/1986	1465	50	0.88	RCP	0137+331	0137+331
AB0999	00:42:46.05	41:16:11.62	D	23/01/1986	1465	50	0.20	RCP	0137+331	0137+331
AB0999	00:43:58.16	41:33:32.67	D	23/01/1986	1465	50	0.26	RCP	0137+331	0137+331
AB0999	00:45:10.98	41:50:50.67	D	23/01/1986	1465	50	0.20	RCP	0137+331	0137+331
AB0999	00:46:24.41	42:08:05.64	D	23/01/1986	1465	50	0.17	RCP	0137+331	0137+331
AB0999	00:44:08.20	41:18:06.53	D	23/01/1986	1465	50	0.27	RCP	0137+331	0137+331
AB0999	00:45:20.82	41:35:23.54	D	23/01/1986	1465	50	0.27	RCP	0137+331	0137+331
AB0999	00:46:33.94	41:52:38.51	D	23/01/1986	1465	50	0.25	RCP	0137+331	0137+331
AB0999	00:42:35.70	41:31:37.76	D	23/01/1986	1465	50	0.27	RCP	0137+331	0137+331
AB0999	00:43:48.11	41:48:58.80	D	23/01/1986	1465	50	0.27	RCP	0137+331	0137+331
AB0999	00:45:01.14	42:06:17.81	D	23/01/1986	1465	50	0.27	RCP	0137+331	0137+331

Table 2. The details of VLA single and merged projects of M 31 mosaics at 20 cm.

VLA Project	Beam Size (arcsec)	r.m.s. (mJy/beam)	Figure
AC0101-a	45.9×43.2	0.49	1
AB0551-a	35.9×32.1	0.12	2
AB0491-a	39.0×33.8	0.12	3
AB0647-a	41.2×37.3	0.24	4
AB0647-b	40.9×35.4	0.24	5
AB0437-a	36.0×31.0	0.10	6
AB0437-b	36.0×31.1	0.19	7
AC0308-a	57.9×49.8	0.72	8
AC0308-b	58.9×48.9	0.54	9
AC0308-c	58.0×50.2	0.60	10
AC0496-a	54.6×14.0	0.08	11
AM0464-a	12.8×12.2	0.13	12
AH0524-a	12.8×12.2	0.07	13
AB0679-a	12.0×11.7	0.07	14
AB0679-b	12.1×11.5	0.08	15
AT0149-a	4.0×3.4	0.08	16
AH0221-a	3.4×3.2	0.22	17
AH0139-a	7.2×6.6	0.16	18
Fully Polarised (5 kλ restricted)	35.73×16.38	0.15	19
Fully Polarised (25 kλ restricted)	6.4×5.4	0.09	20
Mosaic AB0396 and AB0999 (35 kλ restricted)	4.6×3.8	0.08	21
All Calibrated (5 kλ restricted)	32.6×16.4	0.13	22
All Calibrated (25 kλ restricted)	6.1×5.4	0.12	23

5. DISCRETE RADIO-CONTINUUM SOURCES IN THE FIELD OF M 31

For each project imaged, a source catalogue was created. Tables 3-20 list sources found in each individual project that has been imaged in this study. These catalogues contain source's RA and DEC positions (J2000) and integrated flux density. All catalogues have been cross referenced and sources common to multiple projects have been noted in Col. 6 of each table.

Across fifteen individual and three merged projects, a total of 864 unique discrete sources are identified. We compared these discrete sources to those listed in Gelfand et al. (2004) at λ=92 cm and found 118 sources in common to both surveys. Table 21 is an extract of this comparison, where Col. 11 is the estimated spectral index ($S_\nu \propto \nu^\alpha$) of each source. The complete list and all catalogues can be found in on-line archive (http://cds.u-strasbg.fr/).

The average flux density, as listed in Col. 5 of Table 21, was calculated by averaging the flux density from each project where a discrete source was found. A source's error, as listed in Col. 6, was calculated by finding the largest difference between the average flux density of a source, and the flux density from each project it appeared in. In the case where a source was found in multiple projects, its name, project, RA and DEC, as listed in Cols. 1-4, were taken from the highest resolution image.

In Fig. 24, we compare the RA and DEC between our 20 cm catalogue and Gelfand et al. (2004) sources as listed in Table 21. The concentration of points near the centre of graph indicates an accurate model for comparison. We found that the average positional difference in ΔRA and ΔDEC is –0$''$.01 (with a SD of 1$''$.912) and +0$''$.18 (with a SD of 1$''$.543) respectively.

Fig. 25 shows the spectral index distribution of sources listed in Table 21. The majority (61%) of sources exhibit a spectral index of <–0.6 indicating that their emission is predominantly non-thermal in nature. This implies that most of these sources will be background ANGs or Quasars. Some of these background source could qualify as compact steep spectrum sources.

Table 3. Sample list of sources at 20 cm found in Project AB0437-a.

1	2	3	4	5	6
#	Name	RA (J2000)	DEC (J2000)	Flux (mJy)	Notes
1	J003904+410822	00:39:04.30	+41:08:22.20	2.46	
2	J003907+410346	00:39:07.94	+41:03:46.10	20.65	
3	J003908+410338	00:39:08.28	+41:03:38.21	7.59	
4	J003918+410301	00:39:18.15	+41:03:01.10	12.43	
5	J003918+411634	00:39:18.88	+41:16:34.06	5.65	

Table 4. Sample list of sources at 20 cm found in Project AB0437-b.

1	2	3	4	5	6
#	Name	RA (J2000)	DEC (J2000)	Flux (mJy)	Notes
1	J003839+403300	00:38:39.00	+40:33:00.60	4.85	
2	J003908+403007	00:39:08.25	+40:30:07.71	2.88	
3	J003908+410335	00:39:08.39	+41:03:35.80	6.62	
4	J003917+410258	00:39:17.98	+41:02:58.90	9.85	
5	J003927+405425	00:39:27.05	+40:54:25.00	4.61	

Table 5. Sample list of sources at 20 cm found in Project AB0491-a. Column 6 describes the source in additional projects.

1	2	3	4	5	6
#	Name	RA (J2000)	DEC (J2000)	Flux (mJy)	Notes
1	J004013+405005	00:40:13.84	+40:50:05.9	41.99	Table:17 #6
2	J004017+405824	00:40:17.03	+40:58:24.8	21.55	Table:17 #8
3	J004024+410711	00:40:24.78	+41:07:11.3	26.70	Table:19 #24
4	J004036+411910	00:40:36.91	+41:19:10.9	15270.00	
5	J004044+404845	00:40:44.56	+40:48:45.3	13.30	

Table 6. Sample list of sources at 20 cm found in Project AB0551-a. Column 6 describes the source in additional projects.

1	2	3	4	5	6
#	Name	RA (J2000)	DEC (J2000)	Flux (mJy)	Notes
1	J004056+405734	00:40:56.81	+40:57:34.31	13.90	
2	J004100+411358	00:41:00.71	+41:13:58.30	5.53	
3	J004109+412456	00:41:09.61	+41:24:56.80	27.57	
4	J004117+412316	00:41:17.91	+41:23:16.22	2.16	
5	J004120+411044	00:41:20.12	+41:10:44.7	18.97	Table:9 #3, Table:10 #5

Table 7. Sample list of sources at 20 cm found in Project AB0647-a.

1	2	3	4	5	6
#	Name	RA (J2000)	DEC (J2000)	Flux (mJy)	Notes
1	J004132+412429	00:41:32.19	+41:24:29.20	2.13	
2	J004139+414252	00:41:39.59	+41:42:52.90	2.87	
3	J004139+413040	00:41:39.64	+41:30:40.80	5.69	
4	J004155+413720	00:41:55.95	+41:37:20.10	1.93	
5	J004212+414828	00:42:12.82	+41:48:28.00	4.40	

Table 8. Sample list of sources at 20 cm found in Project AB0647-b. Column 6 describes the source in additional projects.

1	2	3	4	5	6
#	Name	RA (J2000)	DEC (J2000)	Flux (mJy)	Notes
1	J004200+415408	00:42:00.51	+41:54:08.4	0.76	
2	J004204+412932	00:42:04.53	+41:29:32.3	2.41	
3	J004218+412930	00:42:18.89	+41:29:30.6	155.90	Table:7 #6
4	J004233+412929	00:42:33.41	+41:29:29.7	2.92	
5	J004235+415743	00:42:35.77	+41:57:43.4	24.40	Table:7 #7

Table 9. Sample list of sources at 20 cm found in Project AB0679-a. Column 6 describes the source in additional projects.

1	2	3	4	5	6
#	Name	RA (J2000)	DEC (J2000)	Flux (mJy)	Notes
1	J004108+412454	00:41:08.11	+41:24:54.7	10.76	Table:10 #1
2	J004112+412458	00:41:12.10	+41:24:58.6	44.01	
3	J004120+411045	00:41:20.18	+41:10:45.3	19.68	Table:6 #5, Table:10 #5
4	J004139+413031	00:41:39.60	+41:30:31.3	32.32	Table:12 #20, Table:6 #7, Table:10 #6
5	J004141+410338	00:41:41.50	+41:03:38.9	45.71	Table:6 #8, Table:10 #8

Table 10. Sample list of sources at 20 cm found in Project AB0679-b. Column 6 describes the source in additional projects.

1	2	3	4	5	6
#	Name	RA (J2000)	DEC (J2000)	Flux (mJy)	Notes
1	J004108+412455	00:41:08.18	+41:24:55.20	13.54	
2	J004112+412458	00:41:12.32	+41:24:58.10	4.45	
3	J004114+412454	00:41:14.03	+41:24:54.40	3.03	
4	J004119+412314	00:41:19.17	+41:23:14.37	1.09	
5	J004120+411045	00:41:20.17	+41:10:45.1	19.05	Table:6 #5

Table 11. Sample list of sources at 20 cm found in Project AC0101-a.

1	2	3	4	5	6
#	Name	RA (J2000)	DEC (J2000)	Flux (mJy)	Notes
1	J004057+412133	00:40:57.97	+41:21:33.30	10.70	
2	J004107+412129	00:41:07.74	+41:21:29.70	6.36	
3	J004108+412444	00:41:08.09	+41:24:44.50	13.49	
4	J004120+411042	00:41:20.00	+41:10:42.30	15.50	
5	J004139+413035	00:41:39.65	+41:30:35.70	27.95	

Table 12. Sample list of sources at 20 cm found in Project AC0308-a.

1	2	3	4	5	6
#	Name	RA (J2000)	DEC (J2000)	Flux (mJy)	Notes
1	J003938+410327	00:39:38.55	+41:03:27.90	5.31	
2	J003957+411138	00:39:57.13	+41:11:38.70	11.93	
3	J004002+412634	00:40:02.34	+41:26:34.40	5.37	
4	J004010+411825	00:40:10.88	+41:18:25.90	3.47	
5	J004014+410841	00:40:14.02	+41:08:41.10	14.23	

Table 13. Sample list of sources at 20 cm found in Project AC0308-b.

1	2	3	4	5	6
#	Name	RA (J2000)	DEC (J2000)	Flux (mJy)	Notes
1	J004257+411643	00:42:57.84	+41:16:43.80	8.25	
2	J004335+421219	00:43:35.23	+42:12:19.90	3.64	
3	J004337+412019	00:43:37.28	+41:20:19.40	8.92	
4	J004341+405435	00:43:41.76	+40:54:35.90	9.40	
5	J004345+412839	00:43:45.22	+41:28:39.90	4.91	

Table 14. Sample list of sources at 20 cm found in Project AC0308-c.

1	2	3	4	5	6
#	Name	RA (J2000)	DEC (J2000)	Flux (mJy)	Notes
1	J003651+404452	00:36:51.36	+40:44:52.40	4.81	
2	J003724+403821	00:37:24.96	+40:38:21.30	2.61	
3	J003730+401239	00:37:30.21	+40:12:39.10	4.95	
4	J003745+402513	00:37:45.61	+40:25:13.50	22.56	
5	J003807+405252	00:38:07.88	+40:52:52.90	3.04	

Table 15. Sample list of sources at 20 cm found in Project AC0496-a.

1	2	3	4	5	6
#	Name	RA (J2000)	DEC (J2000)	Flux (mJy)	Notes
1	J004057+415438	00:40:57.96	+41:54:38.20	1.17	
2	J004105+414451	00:41:05.89	+41:44:51.43	1.28	
3	J004112+415643	00:41:12.36	+41:56:43.10	1.63	
4	J004114+414339	00:41:14.21	+41:43:39.31	1.18	
5	J004129+413536	00:41:29.23	+41:35:36.41	1.02	

Table 16. Sample list of sources at 20 cm found in Project AH0139-a. Column 6 describes the source in additional projects.

1	2	3	4	5	6
#	Name	RA (J2000)	DEC (J2000)	Flux (mJy)	Notes
1	J004141+410343	00:41:41.34	+41:03:43.0	33.45	
2	J004147+411847	00:41:47.93	+41:18:48.0	30.44	Table:17 #20, Table:6 #11, Table:20 #11,Table:11 #7, Table:9 #8, Table:10 #11
3	J004151+411439	00:41:51.14	+41:14:39.4	17.68	Table:6 #12, Table:9 #9, Table:10 #12
4	J004218+412922	00:42:18.63	+41:29:22.6	245.11	
5	J004222+410805	00:42:22.03	+41:08:05.4	2.50	Table:9 #18, Table:10 #20

Table 17. Sample list of sources at 20 cm found in Project AH0221-a.

1	2	3	4	5	6
#	Name	RA (J2000)	DEC (J2000)	Flux (mJy)	Notes
1	J003933+404405	00:39:33.35	+40:44:05.34	4.16	
2	J003949+410421	00:39:49.41	+41:04:21.22	6.32	
3	J004012+410840	00:40:12.28	+41:08:40.73	2.85	
4	J004013+410839	00:40:13.28	+41:08:39.05	5.16	
5	J004013+410836	00:40:13.69	+41:08:36.59	6.31	

Table 18. Sample list of sources at 20 cm found in Project AH0524-a. Column 6 describes the source in additional projects.

1	2	3	4	5	6
#	Name	RA	DEC	Flux	Notes
		(J2000)	(J2000)	(mJy)	
1	J003918+410301	00:39:18.49	+41:03:01.0	9.27	Table:19 #3
2	J003922+411040	00:39:22.15	+41:10:40.9	3.70	
3	J003931+411511	00:39:31.41	+41:15:11.8	2.36	
4	J003932+410440	00:39:32.22	+41:04:40.7	1.17	
5	J003935+411432	00:39:35.96	+41:14:32.7	4.74	Table:14 #37

Table 19. Sample list of sources at 20 cm found in Project AM0464-a.

1	2	3	4	5	6
#	Name	RA	DEC	Flux	Notes
		(J2000)	(J2000)	(mJy)	
1	J003908+403009	00:39:08.78	+40:30:09.99	1.84	
2	J003916+403629	00:39:16.37	+40:36:29.37	0.59	
3	J003918+410300	00:39:18.55	+41:03:00.50	5.41	
4	J003919+402206	00:39:19.50	+40:22:06.08	0.74	
5	J003922+411038	00:39:22.16	+41:10:38.50	3.01	

Table 20. Sample list of sources at 20 cm found in Project AT0149-a.

1	2	3	4	5	6
#	Name	RA	DEC	Flux	Notes
		(J2000)	(J2000)	(mJy)	
1	J004036+412404	00:40:36.79	+41:24:04.70	3.23	
2	J004037+412051	00:40:37.42	+41:20:51.49	3.78	
3	J004046+411637	00:40:46.52	+41:16:37.03	2.26	
4	J004049+411226	00:40:49.05	+41:12:26.92	2.30	
5	J004054+412632	00:40:54.52	+41:26:32.00	3.88	

Table 21. Flux density comparison (sample) between sources in common to λ=20 cm and λ=92 cm surveys of the M 31. Columns 1-4 describe source information from the highest 20-cm resolution project available. Columns 5 and 6 from sources common across projects and integrated flux density (Col. 5) represent an average flux density across the derived various project detections. Columns 7-10 are from Gelfand et al. (2004). Column 11 is the spectral index of Col. 5 and 9.

#	1 Source Name	2 Project #	3 RA (J2000)	4 DEC (J2000)	5 S_{20-cm} (mJy)	6 ΔS_{20-cm} (mJy)	7 RA (J2000)	8 DEC (J2000)	9 S_{92-cm} (mJy)	10 ΔS_{92-cm} (mJy)	11 α
1	J003807+405252	AC0308-c	00:38:07.88	+40:52:52.90	3.04	0.06	00:38:7.90	+40:52:53.75	7.03	0.67	-0.54933
2	J003904+410822	AB0437-a	00:39:04.30	+41:08:22.20	2.46	0.06	00:39:4.34	+41:08:18.21	8.54	0.69	-0.81555
3	J003918+411636	AC0308-c	00:39:18.45	+41:16:36.30	4.08	0.06	00:39:18.23	+41:16:36.85	23.39	1.29	-1.14424
4	J003927+405425	AB0437-b	00:39:27.05	+40:54:25.00	4.49	0.12	00:39:27.03	+40:54:26.57	10.48	0.74	-0.55542
5	J003933+404401	AM0464-a	00:39:33.02	+40:44:01.40	9.84	2.73	00:39:32.79	+40:43:59.63	18.14	2.85	-0.40081
6	J003932+400837	AC0308-c	00:39:32.83	+40:08:37.90	50.17	0.06	00:39:32.82	+40:08:36.74	126.12	8.99	-0.60404
7	J003948+403433	AM0464-a	00:39:48.29	+40:34:33.91	7.99	2.20	00:39:48.25	+40:34:35.00	16.20	5.27	-0.46316
8	J003949+410421	AH0221-a	00:39:49.41	+41:04:21.22	7.80	2.71	00:39:49.41	+41:04:20.91	15.68	0.99	-0.45797
9	J003950+402657	AM0464-a	00:39:50.41	+40:26:57.10	1.80	0.06	00:39:50.24	+40:26:55.81	6.82	0.76	-0.87287
10	J003956+411134	AB0437-b	00:39:56.37	+41:11:34.90	63.62	0.06	00:39:56.14	+41:11:37.89	106.35	7.11	-0.33668
11	J003957+411358	AH0524-a	00:39:57.59	+41:13:58.00	2.33	0.20	00:39:57.38	+41:13:58.60	6.46	0.57	-0.66822
12	J004005+401605	AC0308-c	00:40:05.32	+40:16:05.10	3.21	0.06	00:40:5.09	+40:16:8.15	5.40	0.64	-0.34082
13	J004006+402148	AM0464-a	00:40:06.40	+40:21:48.40	8.49	1.12	00:40:6.32	+40:21:45.83	21.63	1.29	-0.61319
14	J004013+410839	AH0221-a	00:40:13.28	+41:08:39.05	35.05	29.89	00:40:13.29	+41:08:42.35	68.40	4.71	-0.43811
15	J004016+405824	AH0221-a	00:40:16.93	+40:58:24.36	21.58	7.55	00:40:16.79	+40:58:25.32	61.06	4.45	-0.68159
16	J004017+395508	AC0308-c	00:40:17.24	+39:55:08.10	15.54	0.06	00:40:17.13	+39:55:4.17	190.41	9.23	-1.64195
17	J004024+412926	AC0308-c	00:40:24.13	+41:29:26.70	6.09	0.06	00:40:24.11	+41:29:27.98	24.36	1.41	-0.90840
18	J004024+410712	AH0221-a	00:40:24.36	+41:07:12.95	26.96	11.04	00:40:24.51	+41:07:12.58	83.05	5.94	-0.73731
19	J004024+412029	AH0524-a	00:40:24.84	+41:20:29.50	8.82	0.55	00:40:24.65	+41:20:32.44	9.73	0.72	-0.06434
20	J004030+402755	AM0464-a	00:40:30.30	+40:27:55.50	6.18	1.55	00:40:30.29	+40:27:54.50	10.15	0.79	-0.32476
21	J004035+413511	AC0308-c	00:40:35.58	+41:35:11.10	16.02	0.06	00:40:35.75	+41:35:10.89	12.81	0.82	0.14653
22	J004044+404846	AH0221-a	00:40:44.29	+40:48:46.59	12.66	4.15	00:40:44.35	+40:48:45.42	34.27	3.65	-0.65274
23	J004047+405525	AH0221-a	00:40:47.11	+40:55:25.17	2.60	0.43	00:40:47.05	+40:55:24.20	3.69	0.42	-0.22942
24	J004055+405723	AH0221-a	00:40:55.88	+40:57:23.48	28.16	2.61	00:40:55.90	+40:57:23.34	153.25	7.59	-1.11024
25	J004057+415438	AC0496-a	00:40:57.96	+41:54:38.20	1.17	0.06	00:40:58.08	+41:54:37.59	23.45	2.62	-1.96442
26	J004100+411354	AH0524-a	00:41:00.26	+41:13:54.40	5.74	2.83	00:41:0.18	+41:13:54.90	12.79	0.86	-0.52558
27	J004103+410430	AH0524-a	00:41:03.03	+41:04:30.30	2.68	0.21	00:41:2.91	+41:04:27.99	3.36	0.41	-0.14940
28	J004111+402411	AH0221-a	00:41:11.30	+40:24:11.01	11.55	1.02	00:41:11.33	+40:24:10.59	51.26	2.58	-0.97631
29	J004111+403328	AM0464-a	00:41:11.43	+40:33:28.70	5.37	0.49	00:41:11.74	+40:33:28.97	15.67	0.96	-0.70174
30	J004112+412454	AH0524-a	00:41:12.82	+41:24:54.38	9.01	0.06	00:41:12.88	+41:24:57.51	28.65	2.89	-0.75803

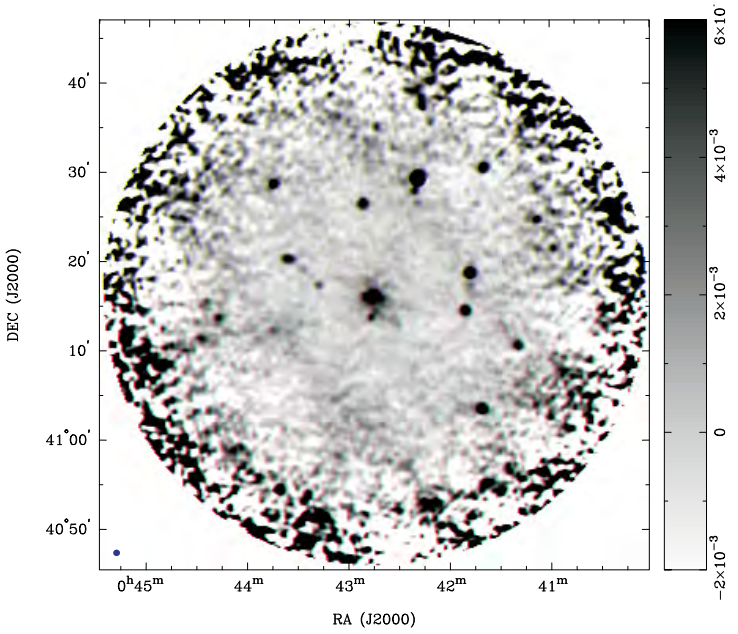

Fig. 1. *VLA Project AC0101 radio-continuum total intensity image of M 31. The synthesised beam, as represented by the blue circle in the lower left hand corner, is* $45\overset{''}{.}9 \times 43\overset{''}{.}2$ *and the r.m.s noise is 0.49 mJy/beam.*

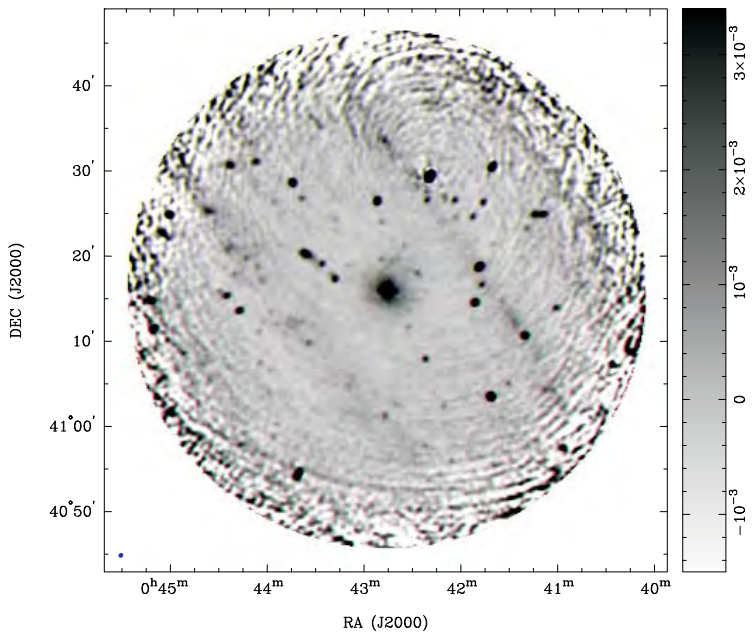

Fig. 2. *VLA Project AB0551 radio-continuum total intensity image of M 31. The synthesised beam, as represented by the blue circle in the lower left hand corner, is* $35\overset{''}{.}9 \times 32\overset{''}{.}1$ *and the r.m.s noise is 0.12 mJy/beam. This image is in terms of Jy/Beam.*

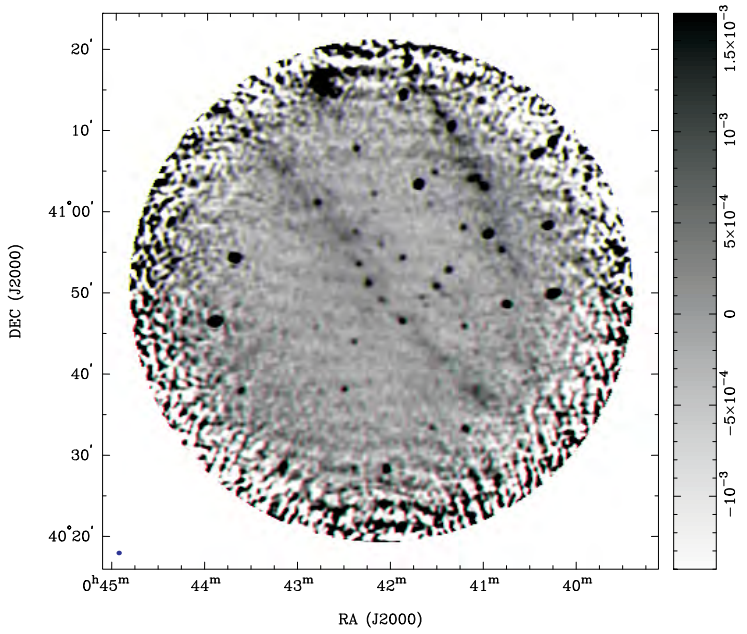

Fig. 3. *VLA Project AB0491 radio-continuum total intensity image of M 31. The synthesised beam, as represented by the blue circle in the lower left hand corner, is* $39\farcs0 \times 33\farcs8$ *and the r.m.s noise is 0.12 mJy/beam. This image is in terms of Jy/Beam.*

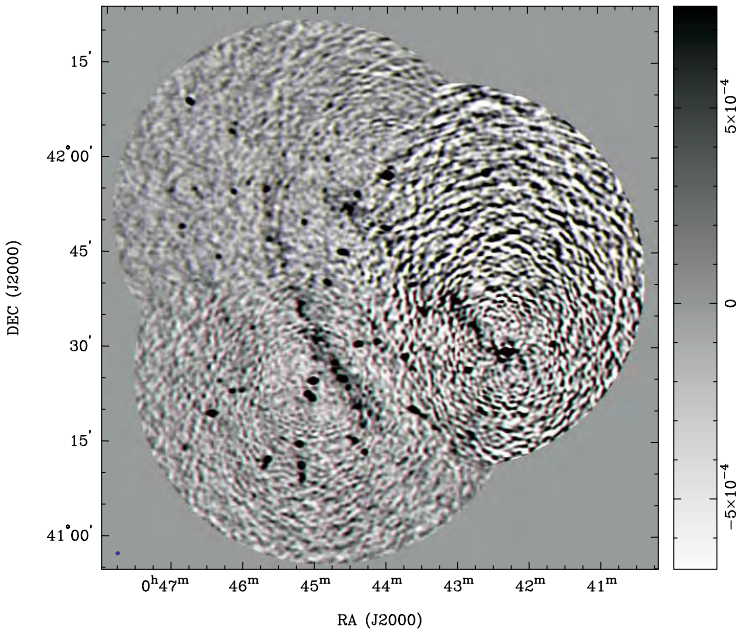

Fig. 4. *VLA Project AB0647, segment a, radio-continuum total intensity image of M 31. The synthesised beam, as represented by the blue circle in the lower left hand corner, is* $41\farcs2 \times 37\farcs3$ *and the r.m.s noise is 0.24 mJy/beam. This image is in terms of Jy/Beam.*

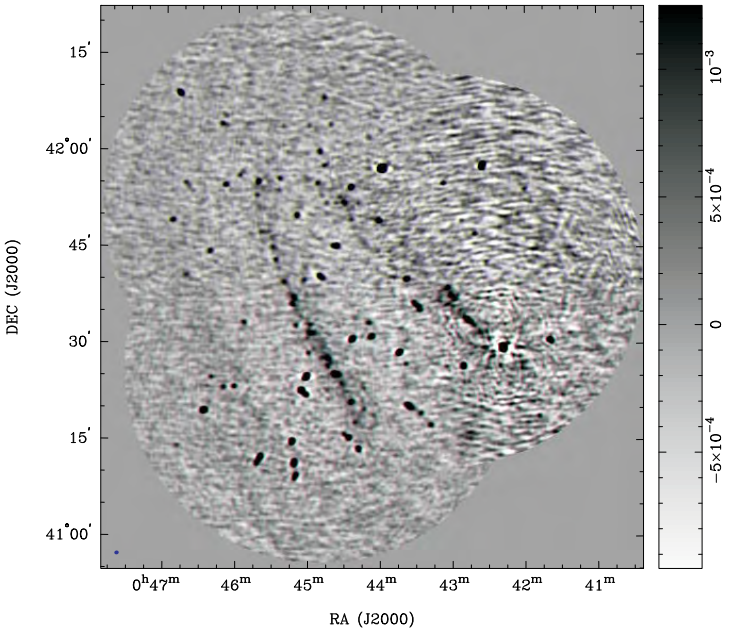

Fig. 5. *VLA Project AB0647, segment b, radio-continuum total intensity image of M 31. The synthesised beam, as represented by the blue circle in the lower left hand corner, is* $40\farcs9 \times 35\farcs4$ *and the r.m.s noise is 0.24 mJy/beam. This image is in terms of Jy/Beam.*

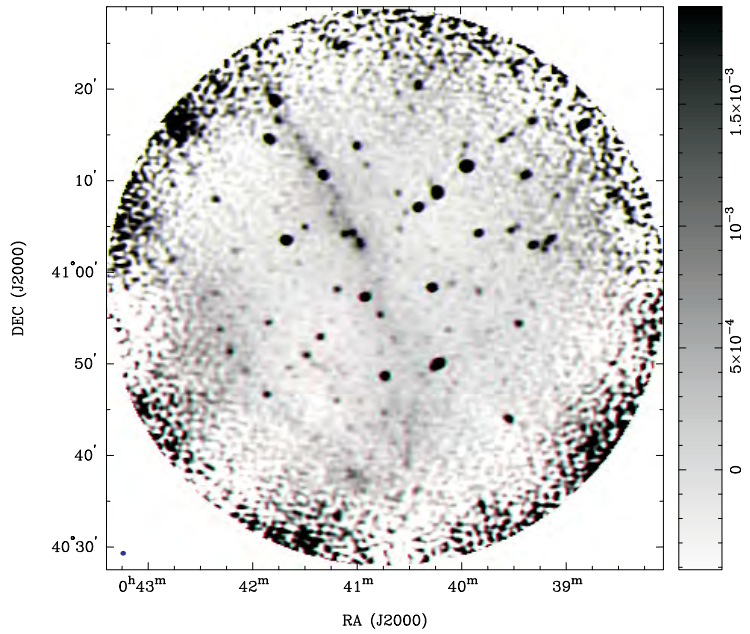

Fig. 6. *VLA Project AB0437, segment a, radio-continuum total intensity image of M 31. The synthesised beam, as represented by the blue circle in the lower left hand corner, is* $36\farcs0 \times 31\farcs0$ *and the r.m.s noise is 0.10 mJy/beam. This image is in terms of Jy/Beam.*

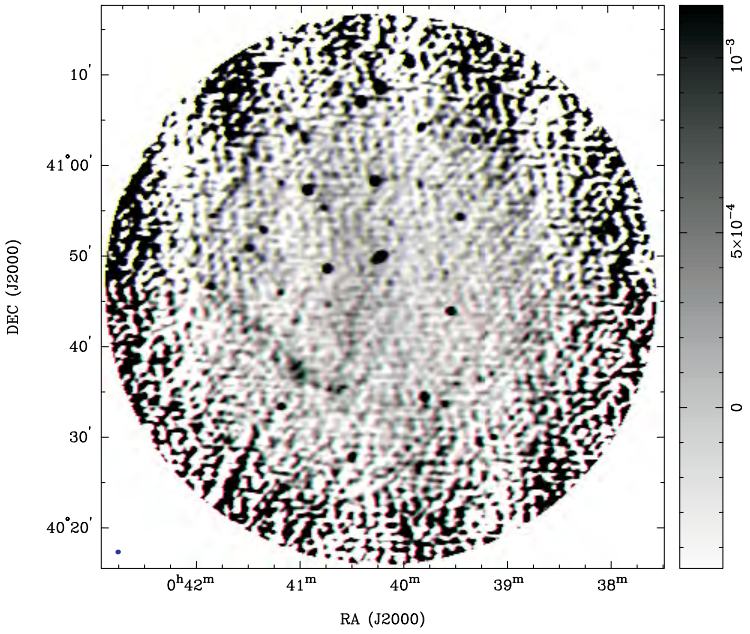

Fig. 7. *VLA Project AB0437, segment b, radio-continuum total intensity image of M 31. The synthesised beam, as represented by the blue circle in the lower left hand corner, is* $36\farcs0 \times 31\farcs1$ *and the r.m.s noise is 0.19 mJy/beam. This image is in terms of Jy/Beam.*

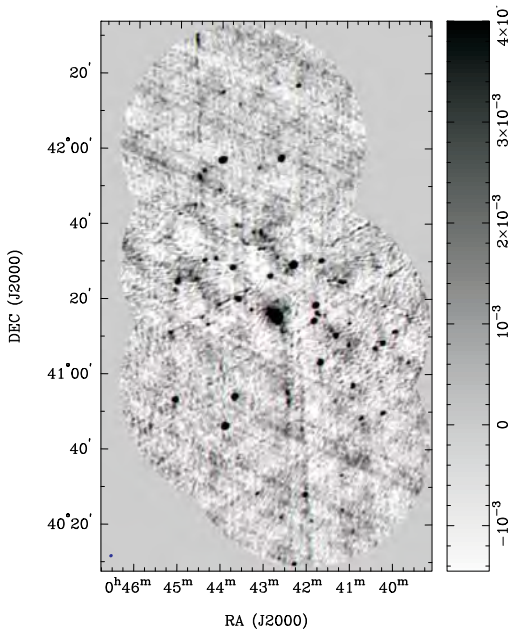

Fig. 8. *VLA Project AC0308, segment a, radio-continuum total intensity image of M 31. The synthesised beam, as represented by the blue circle in the lower left hand corner, is* $57\farcs9 \times 49\farcs8$ *and the r.m.s noise is 0.72 mJy/beam. This image is in terms of Jy/Beam.*

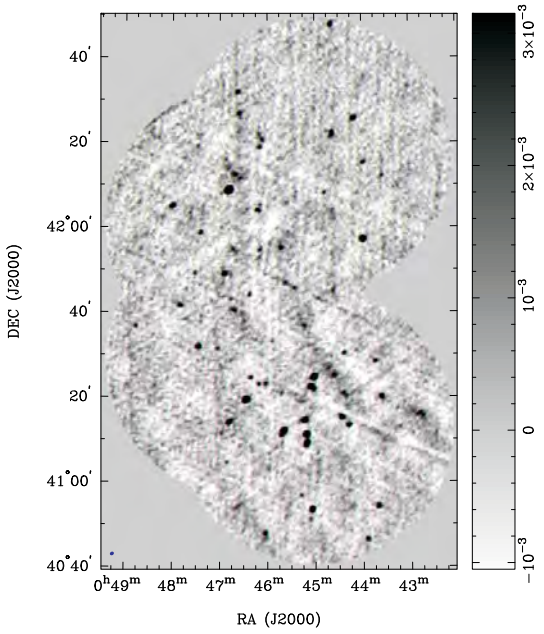

Fig. 9. *VLA Project AC0308, segment b, radio-continuum total intensity image of M 31. The synthesised beam, as represented by the blue circle in the lower left hand corner, is* $58\overset{''}{.}9 \times 48\overset{''}{.}9$ *and the r.m.s noise is 0.54 mJy/beam. This image is in terms of Jy/Beam.*

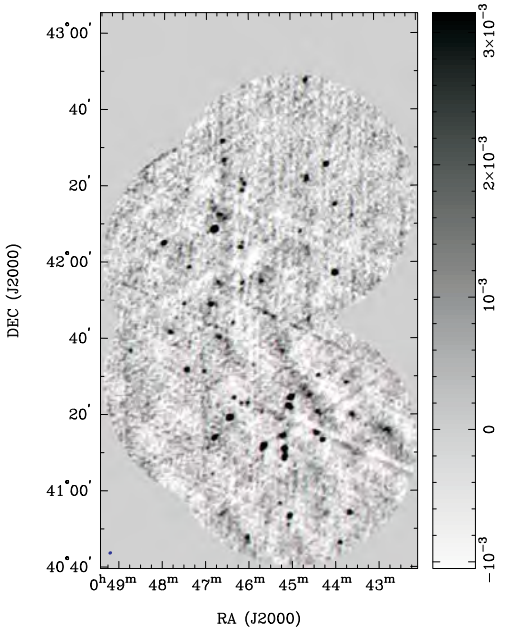

Fig. 10. *VLA Project AC0308, segment c, radio-continuum total intensity image of M 31. The synthesised beam, as represented by the blue circle in the lower left hand corner, is* $58\overset{''}{.}0 \times 50\overset{''}{.}2$ *and the r.m.s noise is 0.60 mJy/beam. This image is in terms of Jy/Beam.*

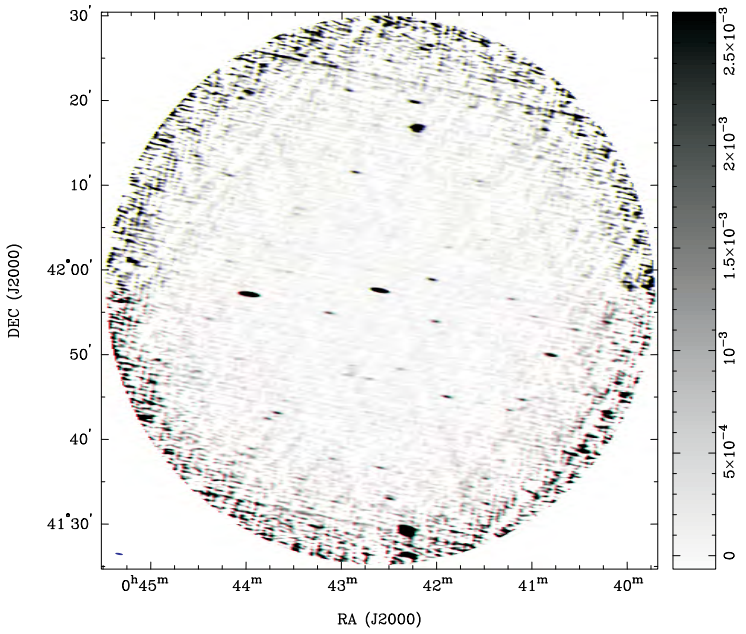

Fig. 11. *VLA Project AC0496 radio-continuum total intensity image of M 31. The synthesised beam, as represented by the blue circle in the lower left hand corner, is* $54\farcs6 \times 14\farcs0$ *and the r.m.s noise is 0.08 mJy/beam. This image is in terms of Jy/Beam.*

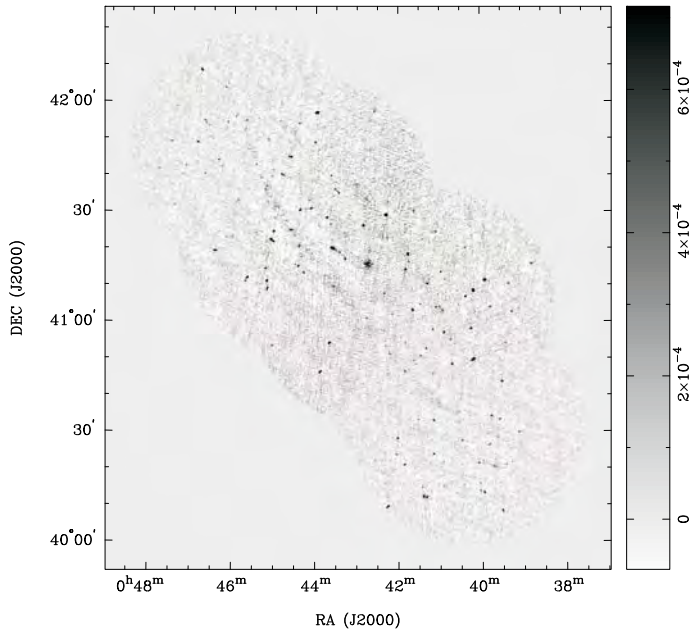

Fig. 12. *VLA Project AM0464 radio-continuum total intensity image of M 31. The synthesised beam is* $12\farcs8 \times 12\farcs2$ *and the r.m.s noise is 0.13 mJy/beam. This image is in terms of Jy/Beam.*

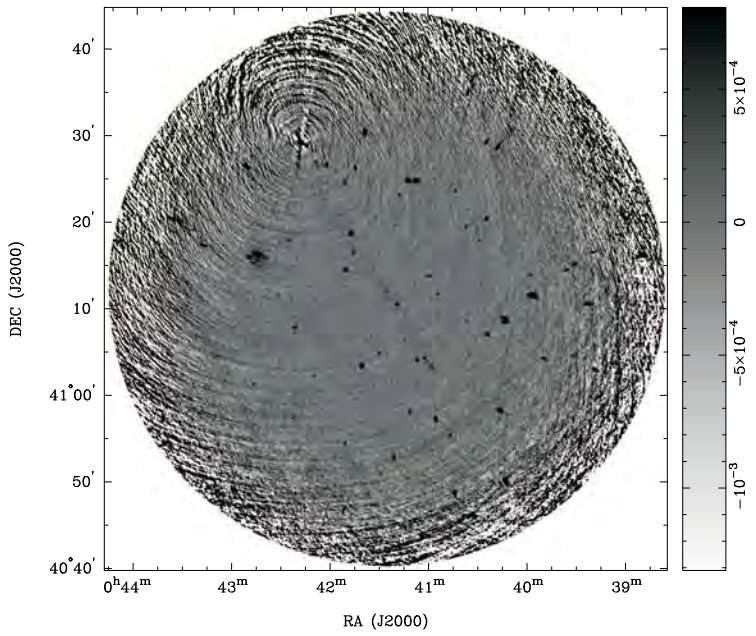

Fig. 13. *VLA Project AH0524 radio-continuum total intensity image of M 31. The synthesised beam is* $12\farcs8 \times 12\farcs2$ *and the r.m.s noise is 0.07 mJy/beam. This image is in terms of Jy/Beam.*

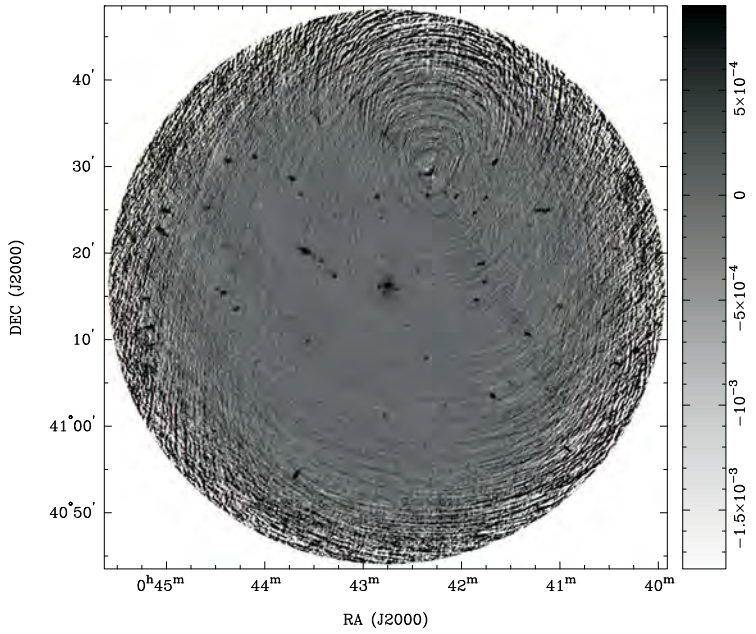

Fig. 14. *VLA Project AB0679, segment a, radio-continuum total intensity image of M 31. The synthesised beam is* $12\farcs0 \times 11\farcs7$ *and the r.m.s noise is 0.07 mJy/beam. This image is in terms of Jy/Beam.*

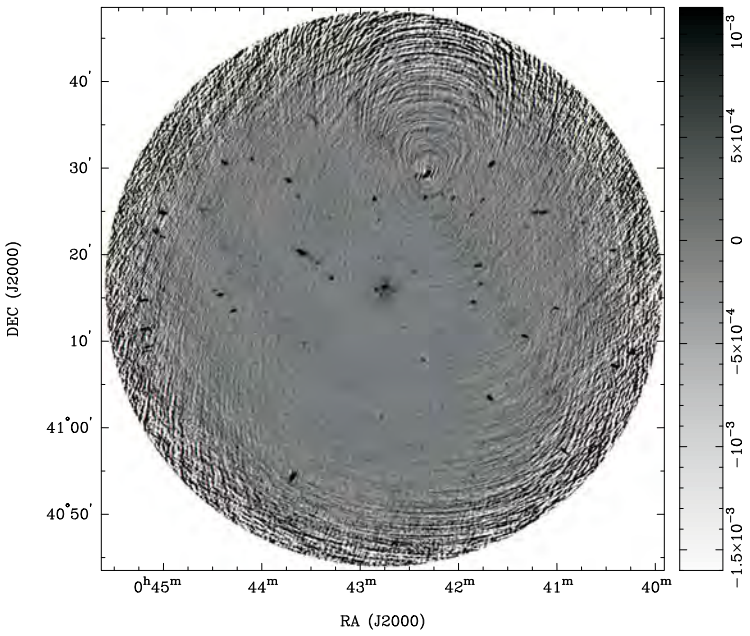

Fig. 15. *VLA Project AB0679, segment b, radio-continuum total intensity image of M 31. The synthesised beam is* $12\farcs1 \times 11\farcs5$ *and the r.m.s noise is 0.08 mJy/beam. This image is in terms of Jy/Beam.*

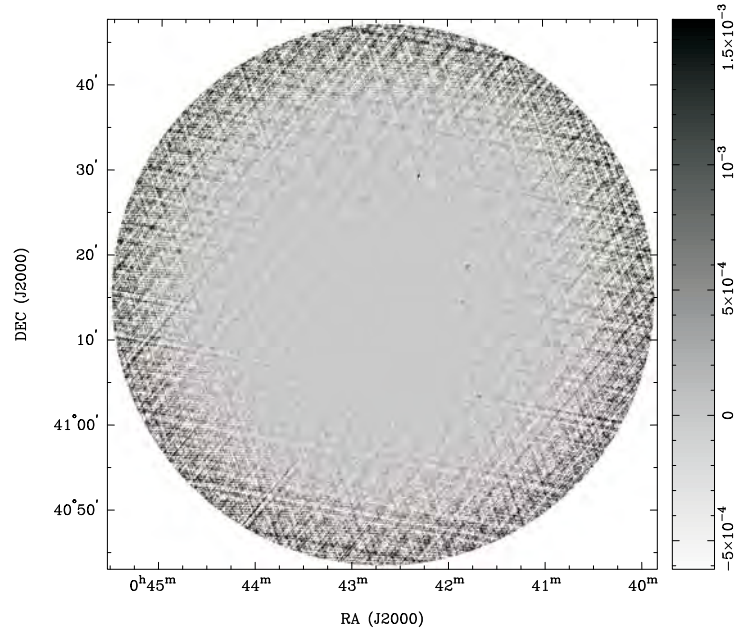

Fig. 16. *VLA Project AT0149 radio-continuum total intensity image of M 31. The synthesised beam is* $4\farcs0 \times 3\farcs4$ *and the r.m.s noise is 0.08 mJy/beam. This image is in terms of Jy/Beam.*

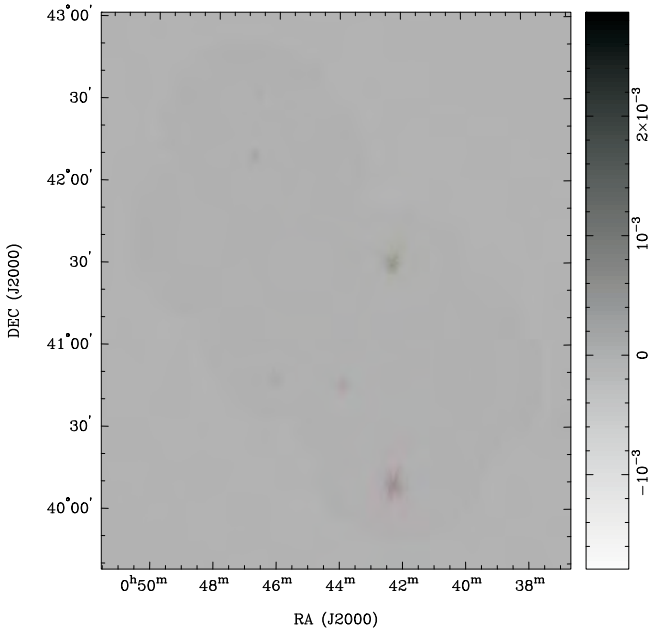

Fig. 17. *VLA Project AH0221 radio-continuum total intensity image of M 31. The synthesised beam is* $3\farcs4 \times 3\farcs2$ *and the r.m.s noise is 0.22 mJy/beam. This image is in terms of Jy/Beam.*

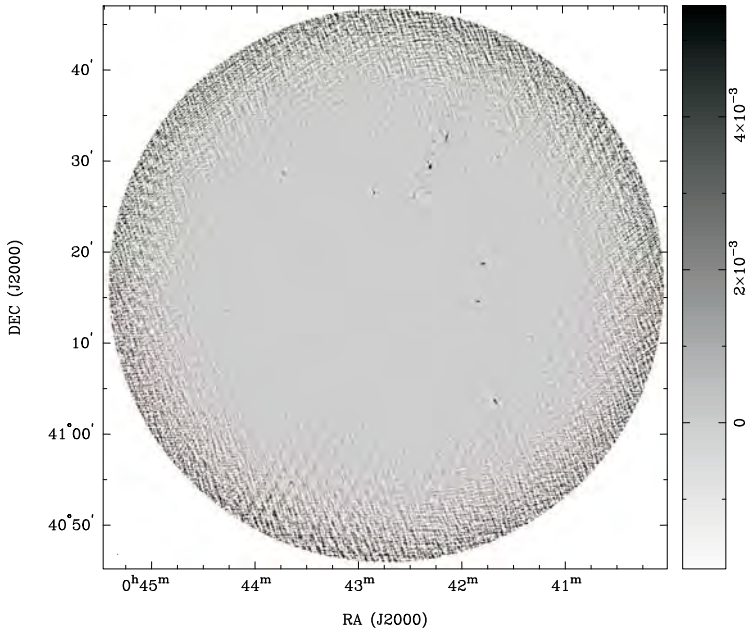

Fig. 18. *VLA Project AH0139 radio-continuum total intensity image of M 31. The synthesised beam is* $7\farcs2 \times 6\farcs6$ *and the r.m.s noise is 0.16 mJy/beam. This image is in terms of Jy/Beam.*

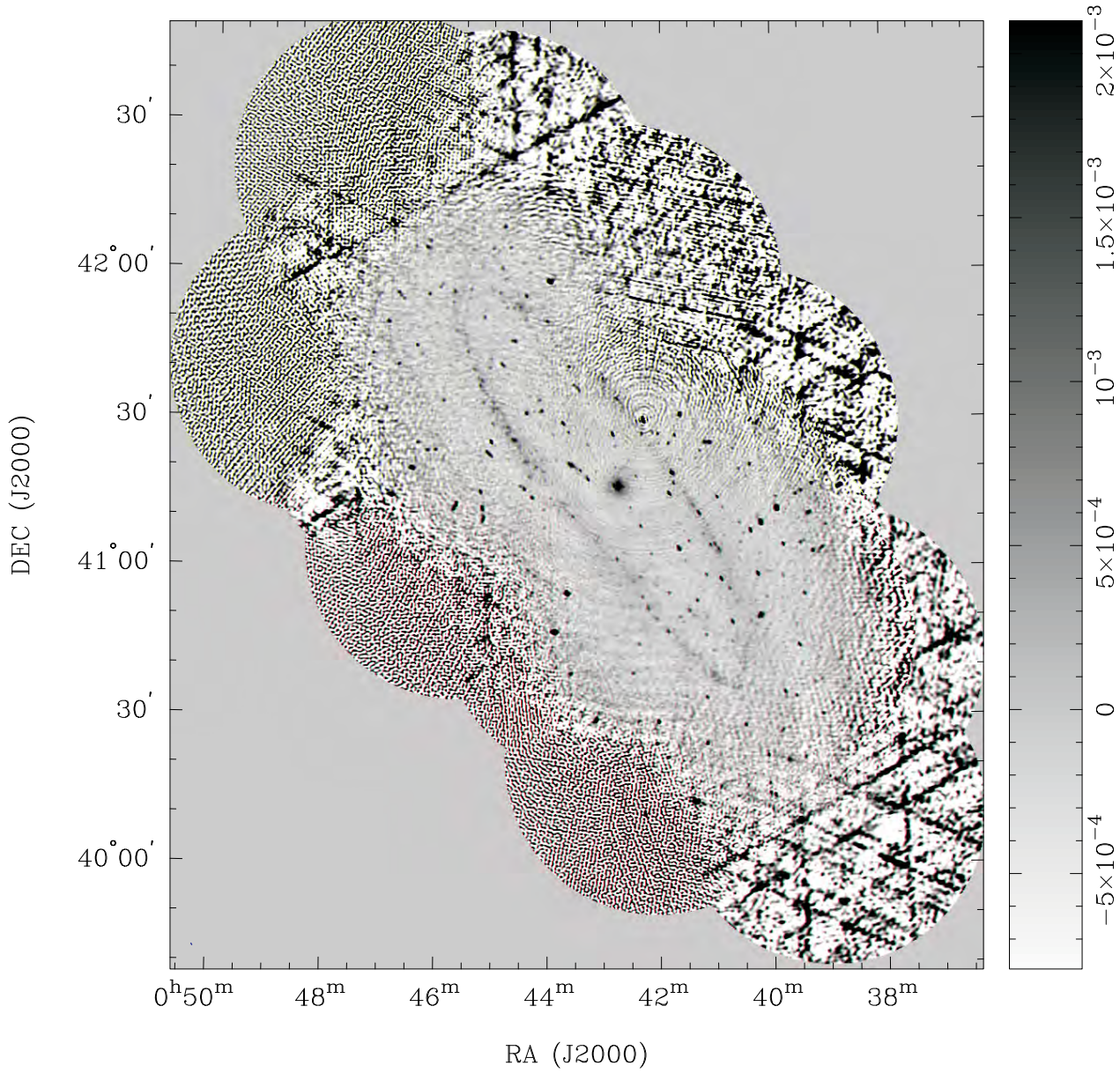

Fig. 19. *A mosiac radio-continuum total intensity image of M 31produced with all fully polarised VLA observations with a uv restriction of 0-5 kλ. The synthesised beam, as represented by the blue circle in the lower left hand corner, is* $35\farcs73 \times 16\farcs38$ *and the r.m.s noise is 0.145 mJy/beam. This image is in Jy/Beam.*

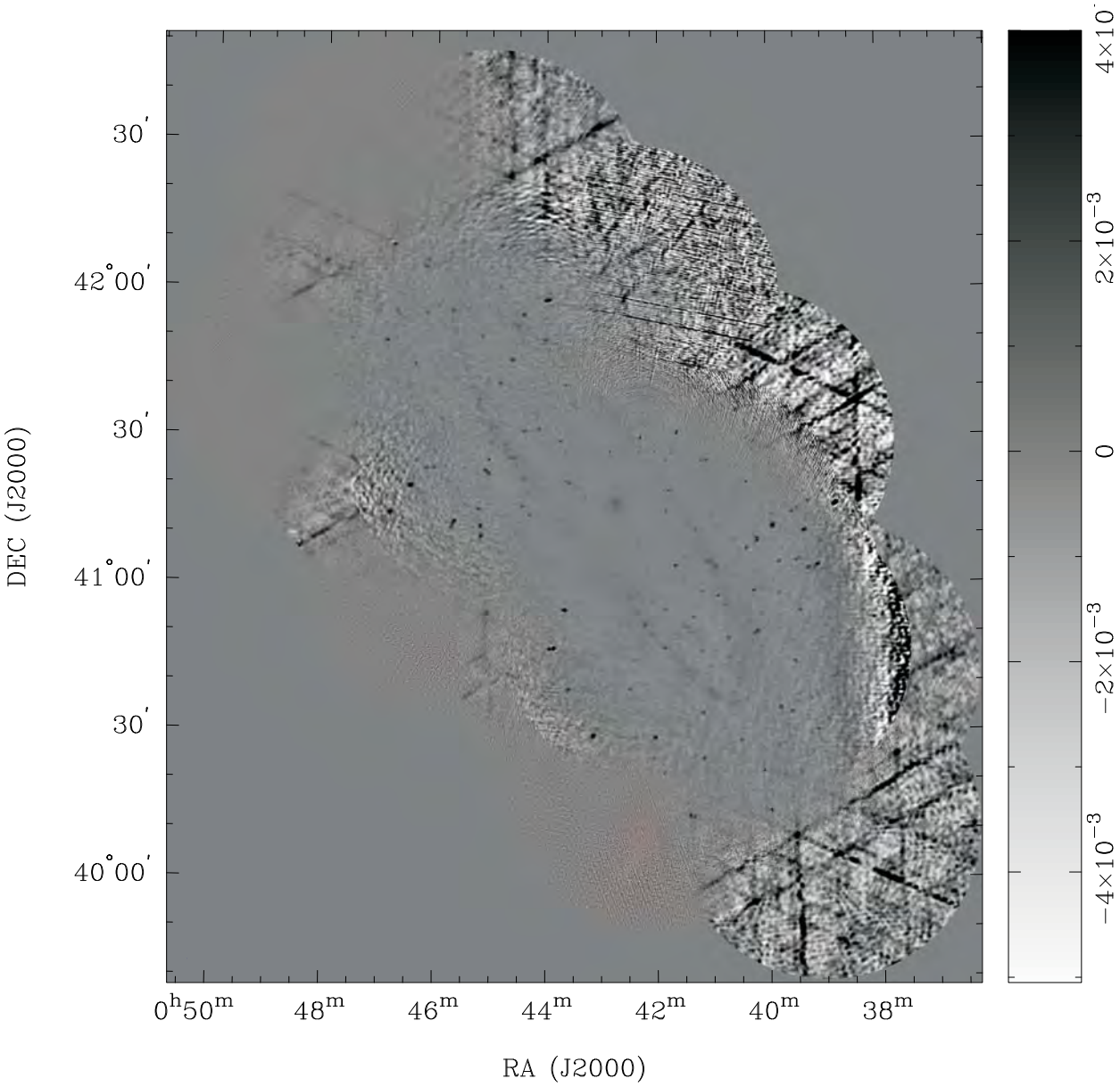

Fig. 20. *A mosiac radio-continuum total intensity image of M 31produced with all fully polarised VLA observations. The synthesised beam is* $6\farcs14 \times 5\farcs35$ *and the r.m.s noise is 0.09 mJy/beam. This image is in Jy/Beam.*

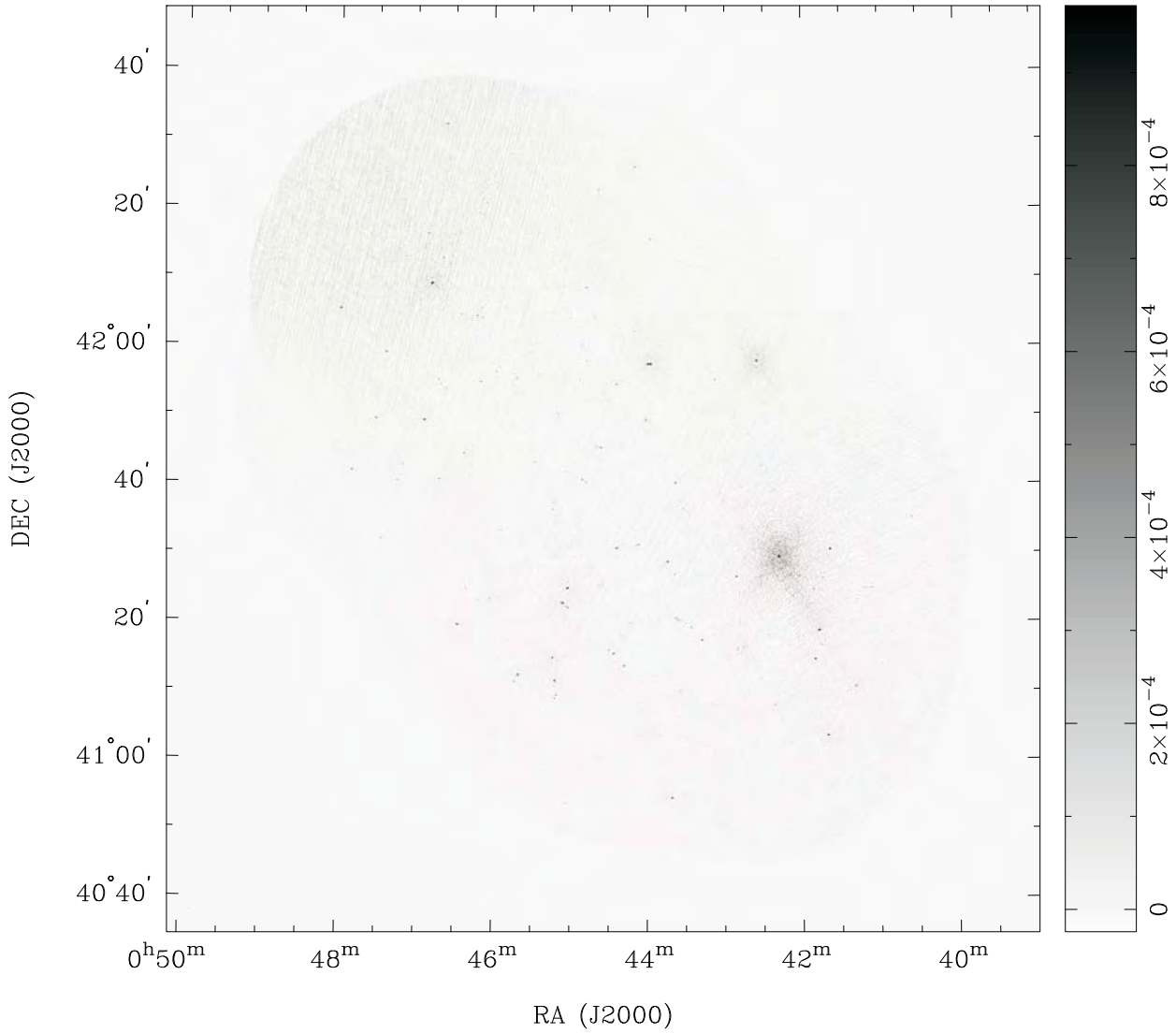

Fig. 21. *A mosiac radio-continuum total intensity image of M 31produced with VLA project AB0396 and AB0999. The synthesised beam is* $4\farcs63 \times 3\farcs78$ *and the r.m.s noise is 0.08 mJy/beam. This image is in terms of Jy/Beam.*

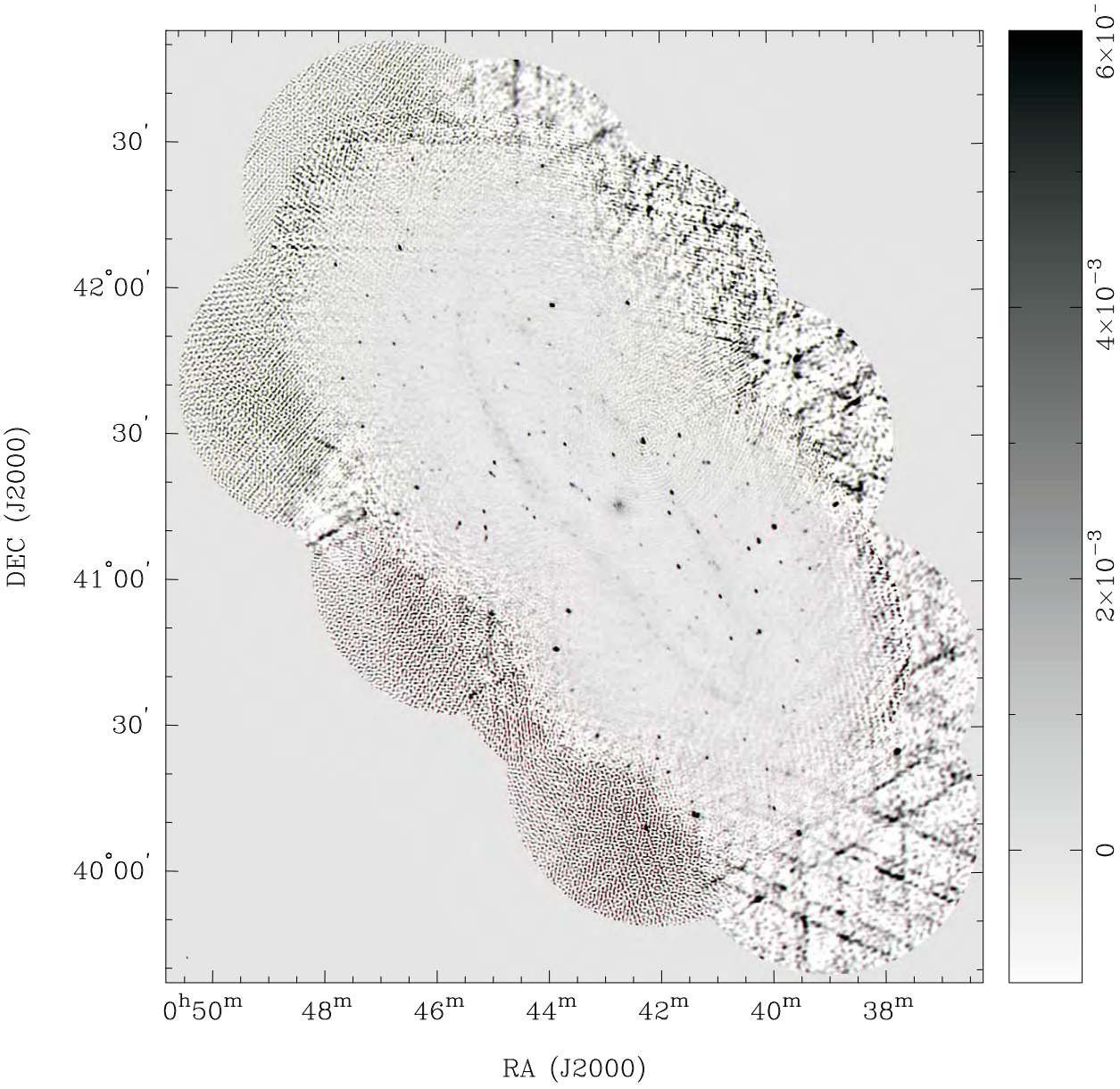

Fig. 22. *A mosiac radio-continuum total intensity image of M 31produced with all calibrated VLA observations. The synthesised beam, as represented by the blue circle in the lower left hand corner, is* $32\farcs61 \times 16\farcs36$ *and the r.m.s noise is 0.13 mJy/beam. This image is in terms of Jy/Beam.*

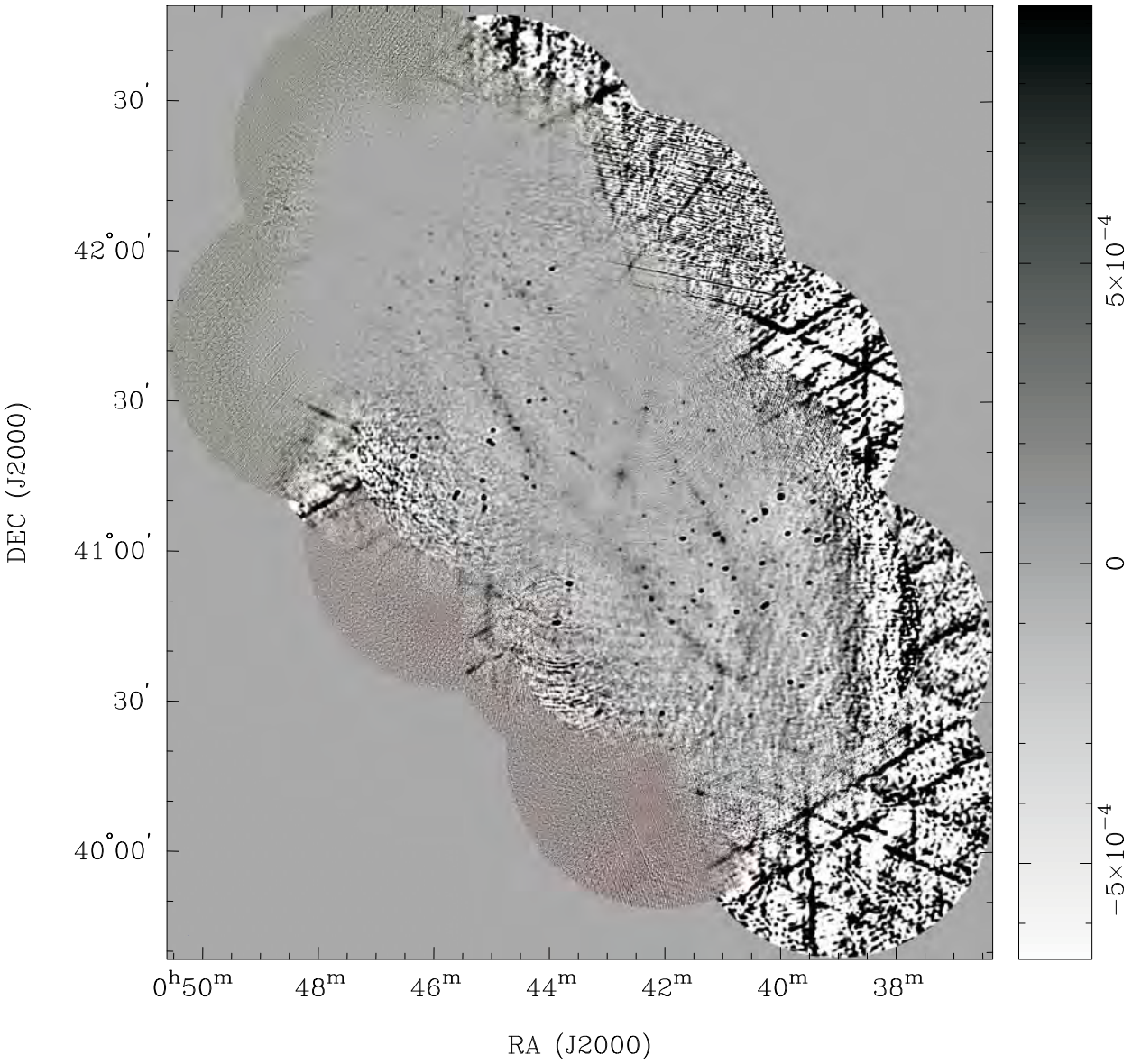

Fig. 23. *A mosiac radio-continuum total intensity image of M 31produced with all calibrated VLA observations. The synthesised beam is* $6\farcs13 \times 5\farcs35$ *and the r.m.s noise is 0.12 mJy/beam. This image is in terms of Jy/Beam.*

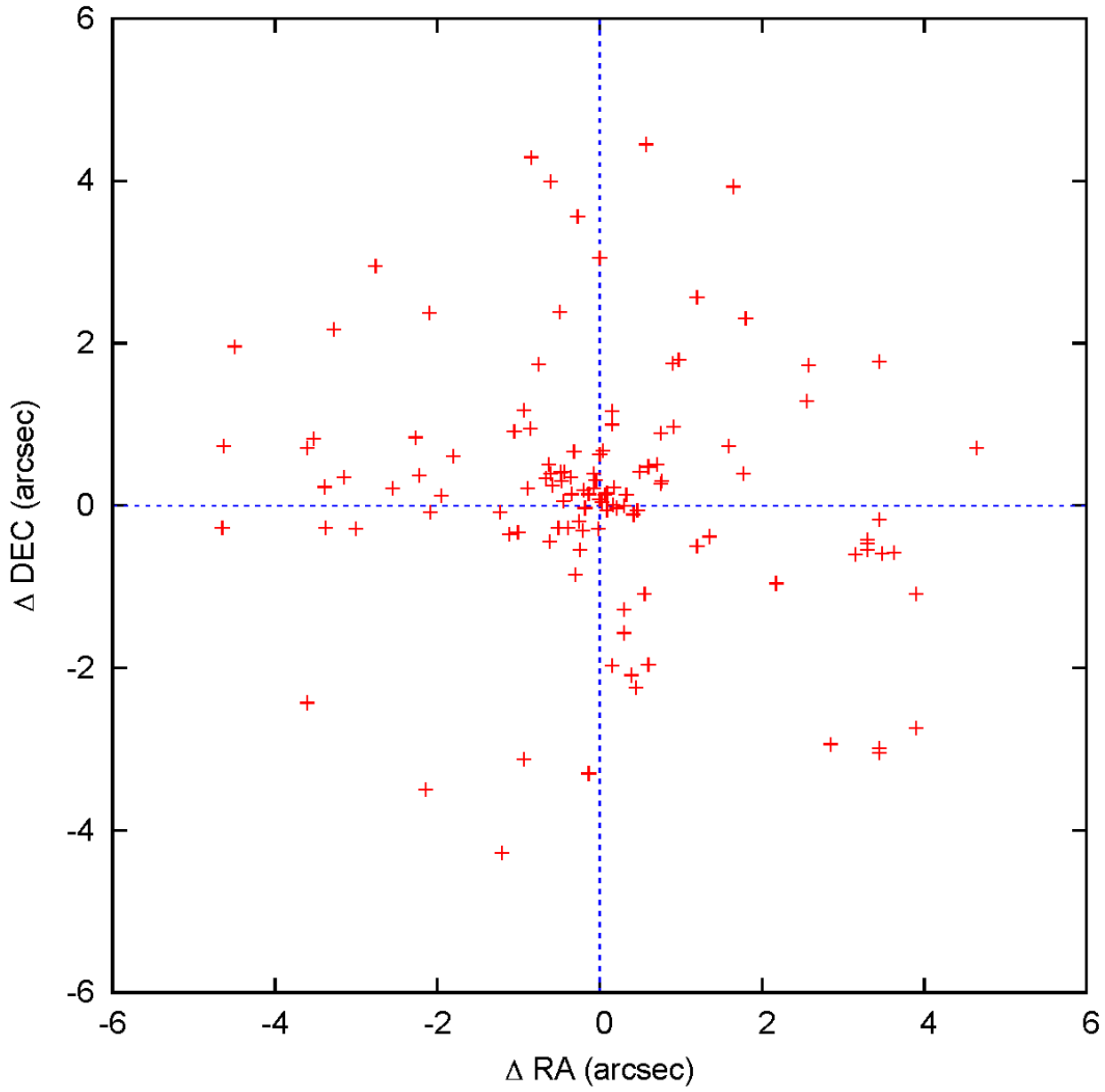

Fig. 24. *Comparison of positional differences (ΔRA and ΔDEC) between our catalogue and Gelfand et al. (2004).*

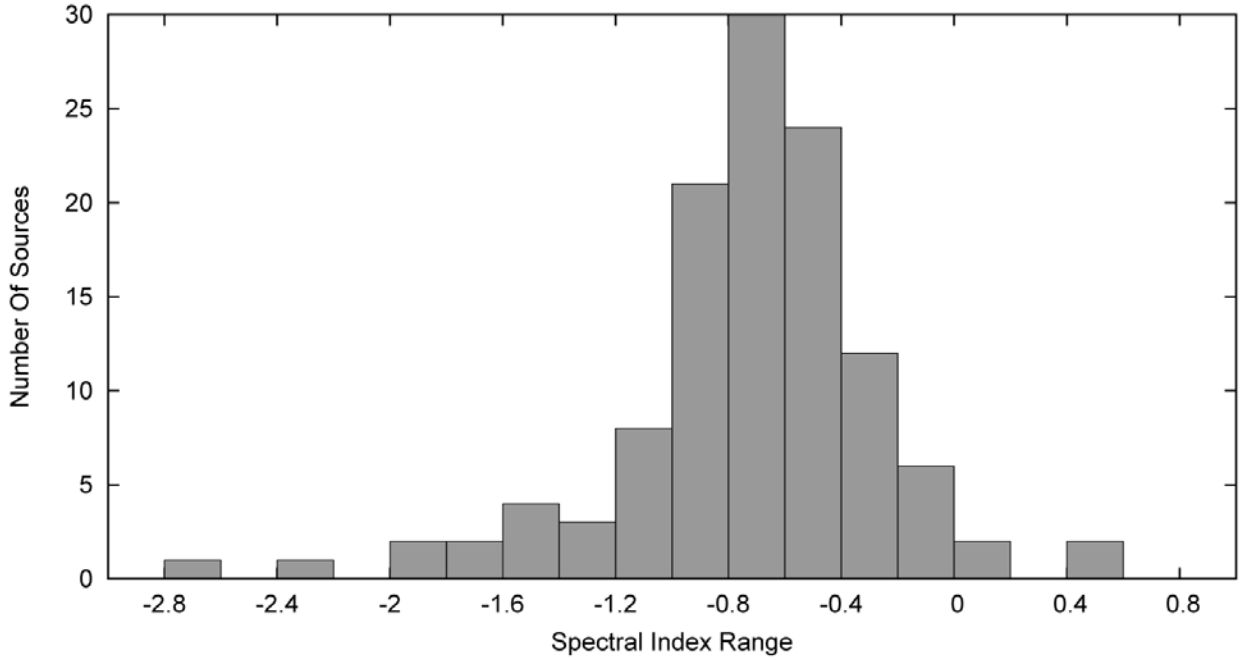

Fig. 25. *Spectral index distribution of point sources in the field of M 31.*

6. CONCLUSIONS

We present new λ=20 cm (ν=1.4 GHz) images of M 31 constructed from archived VLA radio-continuum observations. These new images consist of 17 individual VLA projects which are of high-sensitivity and resolution. Images presented here are sensitive to rms=60 μJy and feature a high angular resolution (<10″). Also, we present a complete sample of 864 unique discrete radio sources across the field of M 31. The most prominent region in M 31 is "the ring feature" for which we estimate a total integrated flux density of 706 mJy at λ=20 cm. From our 20-cm catalogue, we find 118 discrete sources that are in common to those listed in Gelfand et al. (2004) at λ=92 cm. The majority (61%) of these sources exhibit a spectral index of α<–0.6 indicating predominant non-thermal emission which is more typical of background objects.

Acknowledgements – We used the KARMA and MIRIAD software packages developed by the ATNF. The National Radio Astronomy Observatory is a facility of the National Science Foundation operated under cooperative agreement by Associated Universities, Inc.

REFERENCES

Braun, R.: 1990a, *Aust. J. Phys. Astrophys. Suppl.*, **72**, 755.
Braun, R.: 1990b, *Aust. J. Phys. Astrophys. Suppl.*, **72**, 761.
Dickel, J. R., Dodorico, S.: 1984, *Mon. Not. R. Astron. Soc.*, **206**, 351.
Dickel, J. R., Dodorico, S., Felli, M., Dopita, M.: 1982, *Aust. J. of Phys.*, **252**, 582.
Galvin, T. J.: et al., 2012, *Astrophys. Space Sci.*, in press.
Gelfand, J. D., Lazio, T. J. W., Gaensler, B. M., 2004, *Aust. J. Phys. Astrophys. Suppl.*, **155**, 89.
Gooch, R.: 1996, in "Astronomical Society of the Pacific Conference Series, Vol. 101, Astronomical Data Analysis Software and Systems V", G. H. Jacoby and J. Barnes, ed., 80.
Karachentsev, I. D., Karachentseva, V. E., Huchtmeier, W. K., Makarov, D. I.: 2004, *Astron. J.*, **127**, 2031.
Payne, J. L., Filipović, M. D., Pannuti, T. G., Jones, P. A., Duric N., White, G. L., Carpano, S.: 2004, *Astron. Astrophys.*, **425**, 443.
Sault, R. J., Teuben, P. J., Wright, M. C. H.: 1995, in "Astronomical Society of the Pacific Conference Series, Vol. 77, Astronomical Data Analysis Software and Systems IV", R. A. Shaw, H. E. Payne and J. J. E. Hayes, ed., 433.
Steer, D. G., Dewdney, P. E., Ito, M. R.: 1984, *Astron. Astrophys.*, **137**, 159.

НОВО ПРОУЧАВАЊЕ M 31 У РАДИО-КОНТИНУУМУ НА 20 cm – МАПЕ И КАТАЛОЗИ ТАЧКАСТИХ ИЗВОРА

T. J. Galvin, M. D. Filipović, E. J. Crawford, N. F. H. Tothill, G. F. Wong and A. Y. De Horta

University of Western Sydney, Locked Bag 1797, Penrith South DC, NSW 2751, Australia
E–mail: *m.filipovic@uws.edu.au*

УДК 52–13–77 : 524.726 M31
Оригинални научни рад

У овој студији представљамо нове Very Large Array (VLA) радио-континуум мапе и каталоге тачкастих објеката у пољу M 31 на λ=20 cm (ν=1.4 GHz). Нове мапе високе резолуције (<10″) и осетљивости (rms=60 μJy) су направљене спајањем свих 17 архивираних посматрања VLA телескопа. Комплетан каталог свих објеката у пољу M 31 галаксије садржи 864 радио-извора. Ови објекти су упоређени са Gelfand et al. (2004) каталогом на λ=92 cm и нађено је 118 заједничих радио-извора у оба каталога. Већина ових објеката (61%) имају веома стрм радио спектрални индекс (α <–0.6) што је типично за нетермалне изворе који се налазе ван M 31 галаксије. Детектовали смо и једну од најпроминентнијих области у M 31 галаксији – прстен – са укупном густином флукса од 706 mJy на λ=20 cm.

A.18 Related Paper 18

Bozzetto, L. M., Filipović, M. D., Crawford, E. J., De Horta, A. Y., and Stupar, M. (2012a). Multifrequency Radio Observations of SNR J0536-6735 (N 59B) with Associated Pulsar. *Serbian Astronomical Journal*, 184:69–76

My contribution was to assist in the data analysis. This is a 20% contribution.

Serb. Astron. J. № 184 (2012), 69 - 76 **UDC 524.722.3 : 524.354–77**
DOI: 10.2298/SAJ1284069B Original scientific paper

MULTIFREQUENCY RADIO OBSERVATIONS OF SNR J0536–6735 (N 59B) WITH ASSOCIATED PULSAR

L. M. Bozzetto[1], M. D. Filipović[1], E. J. Crawford[1], A. Y. De Horta[1] and M. Stupar[2,3]

[1]*School of Computing and Mathematics, University of Western Sydney Locked Bag 1797, Penrith South DC, NSW 1797, Australia*

[2]*Department of Physics, Macquarie University, Sydney, NSW 2109, Australia*

[3]*Australian Astronomical Observatory, PO Box 296, Epping, NSW 1710, Australia*

E–mail: *m.filipovic@uws.edu.au*

(Received: April 23, 2012; Accepted: April 27, 2012)

SUMMARY: We present a study of new Australian Telescope Compact Array (ATCA) observations of supernova remnant, SNR J0536–6735. This remnant appears to follow a shell morphology with a diameter of D=36×29 pc (with 1 pc uncertainty in each direction). There is an embedded H II region on the northern limb of the remnant which made various analysis and measurements (such as flux density, spectral index and polarisation) difficult. The radio-continuum emission followed the same structure as the optical emission, allowing for extent and flux density estimates at 20 cm. We estimate the surface brightness at 1 GHz of 2.55×10^{-21} Wm^{-2} Hz^{-1} sr^{-1} for the SNR. Also, we detect a distinctive radio-continuum point source which confirms the previous suggestion of this remnant being associated with pulsar wind nebula (PWN). The tail of this remnant is not seen in the radio-continuum images and is only seen in the optical and X-ray images.

Key words. ISM: supernova remnants – Magellanic Clouds – radio continuum: ISM – ISM: individual objects : SNR J0536–6735

1. INTRODUCTION

The Large Magellanic Cloud (LMC) is an irregular dwarf galaxy located at a distance of 50 kpc (Macri et al. 2006). It is considered to be a near ideal galaxy for achieving detailed observations of celestial objects such as supernova remnants (SNRs). The LMC is located in the direction towards the South Pole (one of the coldest areas of the radio sky), minimising interference from galactic foreground radiation. Furthermore, the LMC resides outside the Galactic plane, rendering the influence of dust, gas and stars as negligible.

Predominately non-thermal emission is a well-known characteristic of SNRs in the radio-continuum. SNRs have a typical radio spectral index of $\alpha \sim -0.5$ defined by $S \propto \nu^{\alpha}$. However, this can significantly vary, as there exists a wide variety of SNRs in differing environments (Filipović et al. 1998). The morphology, structure, behaviour and evolution of the ISM can be attributed to SNRs, and, in turn, the ISM heavily impacts the properties of SNRs as their expansion and evolution are heavily dependant on their surrounding environment.

Type II supernova are the result of core collapse SNRs in large stars with an initial mass greater than $8 \pm 1\ M_{\odot}$(Smartt 2009). Depending on how massive the progenitor star is, the explosion may leave behind a compact central object such as a neutron star, or if spinning in our line of sight, a pulsar. There appears to be a lack of pulsar detections in the MC's when compared to the $\sim 1.79 \times 10^4$ predicated pulsars as modelled by Ridley and Lorimer (2010). Out of the 56 confirmed and some 20 candidate LMC SNRs, there are currently only 4 known SNR-pulsar associations (N 49, 30 Dor B, B0540-693 & B0453-68) with an additional two candidates, J0529-6653 (Bozzetto et al. 2012) and J0541.8-6659 (Grondin et al. 2012). In contrast, the Milky Way (MW) contains 274 SNRs (Green 2009) and some ∼1900 pulsars. Globally, this lack of larger SNR–pulsar associations in the LMC and MW can be explained by the fact that radio pulsars live a significantly longer life in comparison to their associated SNRs, resulting in them ejecting energy into the ISM long after their SNR has dissipated into the ambient ISM. Also, it maybe be attributed to the fact that many neutron stars posses properties different to those of conventional radio pulsars (Gotthelp and Vasisht 2000).

Davies et al. (1976) described N 59B region as being very bright with a diameter of $8' \times 8'$ and commented on the appearance of optical knots. Clarke et al. (1976) observed SNR J0536-6735 object as a part of their catalogue of radio sources and recorded a peak intensity of 0.36 Jy (408 MHz) and made note of the extended emission. Mathewson et al. (1985) recorded an optical size of 50 pc, integrated flux density of 0.244 Jy (843 MHz) and used this new flux measurement with the 408 MHz measurement (Clarke et al. 1976) to produce a spectral index of α=–0.6. They recorded a [S II]-to-Hα ratio of 0.6 which supported SNR identification. They also noted the strong HII region at the northern shell of the remnant. This object was also observed by Filipović et al. (1995) in their survey of the Magellanic Clouds, reporting an integrated flux measurement of 0.1096 Jy at 8550 MHz. Haberl and Piestch (1999) measured an X-ray extent of $56\farcs6$ and named this object HP 551. SNR J0536–6735 was not detected with the Far Ultraviolet Spectroscopic Explorer (FUSE) in the Blair et al. (2006) survey of the Magellanic Clouds SNRs. Bamba et al. (2006) observed this object with the XMM-Newton, reporting elongated structure with a compact central source. They suggest that this compact source may be a pulsar wind nebula (PWN) and that the progenitor of this SNR would be a massive star greater than 20 $M_{\odot}$. Payne et al. (2008) measured optical spectra lines and found that canonical [SII]/Hα ratio is 0.4. Desai et al. (2010) reported an extent of $2\farcm4$ with detection of a young stellar object (YSO) and detection in the NANTEN survey. They made note, however, that this SNR is superimposed on an OB association and therefore uncertain whether the YSO is related to this SNR and its progenitor.

Here, we report on new radio-continuum observations of SNR J0536–6735. The observations, data reduction and imaging techniques are described in Section 2. The astrophysical interpretation of newly obtained moderate-resolution total intensity in combination with the existing Magellanic Cloud Emission Line Survey (MCELS) images are discussed in Section 3.

2. OBSERVATIONS

We observed SNR J0536–6735 with the Australia Telescope Compact Array (ATCA) on the 15$^{\rm th}$ and 16$^{\rm th}$ of November 2011, using the new Compact Array Broadband Backend (CABB) with an array configuration of EW367 at wavelengths of 3 and 6 cm (ν=9000 and 5500 MHz). Baselines formed with the 6$^{\rm th}$ ATCA antenna were excluded, as the other five antennas were arranged in a compact configuration. The observations were carried out in the so called "snap-shot" mode, totalling ∼50 minutes of integration over a 14 hour period. Source PKS B1934-638 was used for primary calibration and source PKS B0530-727 was used for secondary (phase) calibration. The MIRIAD (Sault et al. 1995) and KARMA (Gooch 2006) software packages were used for reduction and analysis. More information on the observing procedure and other sources observed in this session/project can be found in Bojičić et al. (2007), Crawford et al. (2008a,b, 2010), Čajko et al. (2009), Bozzetto et al. (2010, 2012a,b) and de Horta et al. (2012).

The 20/13 cm images as well as our 6/3 cm images were formed by using the MIRIAD multi-frequency synthesis (Sault and Wieringa 1994) and natural weighting. They were deconvolved by using the MFCLEAN and RESTOR algorithms with primary beam correction applied by using the LINMOS task. The 6 cm image has a resolution of $46\farcs4 \times 43\farcs0$ at PA=0° and an estimated r.m.s. noise of 0.2 mJy/beam. Our 6/3 cm images encountered a dynamic range problem due to the strong H II region located towards the Northern limb of the remnant, which in turn drowned out the SNR.

Other observations used in this project included a 36 cm unpublished image (Fig. 1) taken by the Molonglo Synthesis Telescope (MOST) as described by Mills et al. (1984). The 20 and 13 cm images (Fig. 1) were created from project C354 which made use of 1.5D, 1.5B & 6C baselines. The 6 & 3 cm (Fig. 1) images were taken from project C918 (Dickel et al. 2005).

Archival observations at X-Ray wavelengths taken by the XMM-Newton were also used in this project. We also used the Magellanic Cloud Emission Line Survey (MCELS) that was carried out with the 0.6 m University of Michigan/CTIO Curtis Schmidt telescope, equipped with a SITE 2048 × 2048 CCD, which gave a field of $1\fdg35$ at a scale of $2\farcs4\,\mathrm{pixel}^{-1}$. Both the LMC and SMC were mapped in narrow bands corresponding to Hα, [O III] (λ=5007 Å), and [S II] (λ=6716, 6731 Å), plus matched red and green continuum bands that are used primarily to subtract

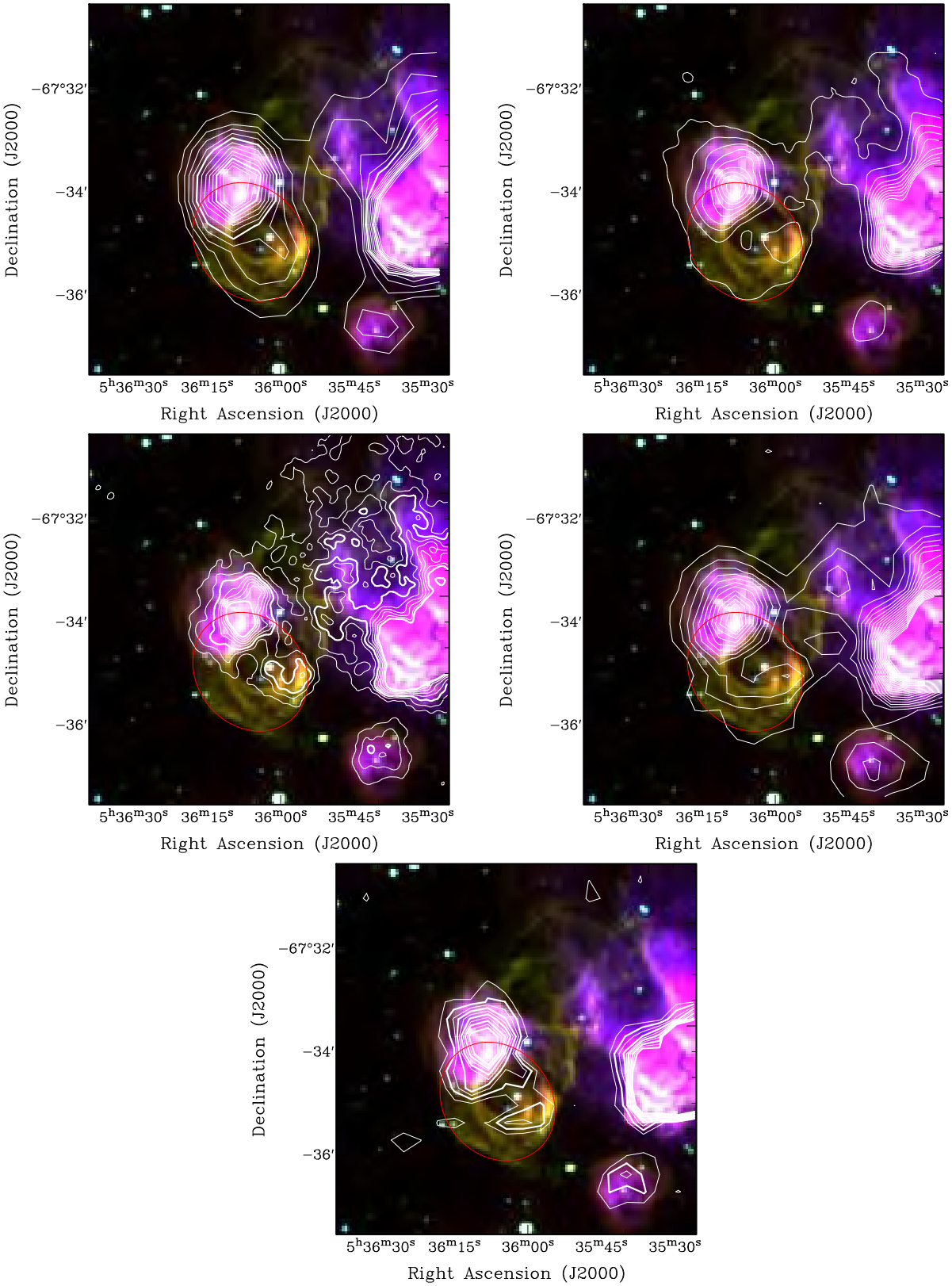

Fig. 1. *MCELS composite optical image (RGB =Hα,[SII],[OIII]) of SNR J0536–6735 overlaid with 36 cm [top left] 20 cm [top right], 13 cm [mid left], 6 cm [mid right] & 3 cm [bottom] contours.*

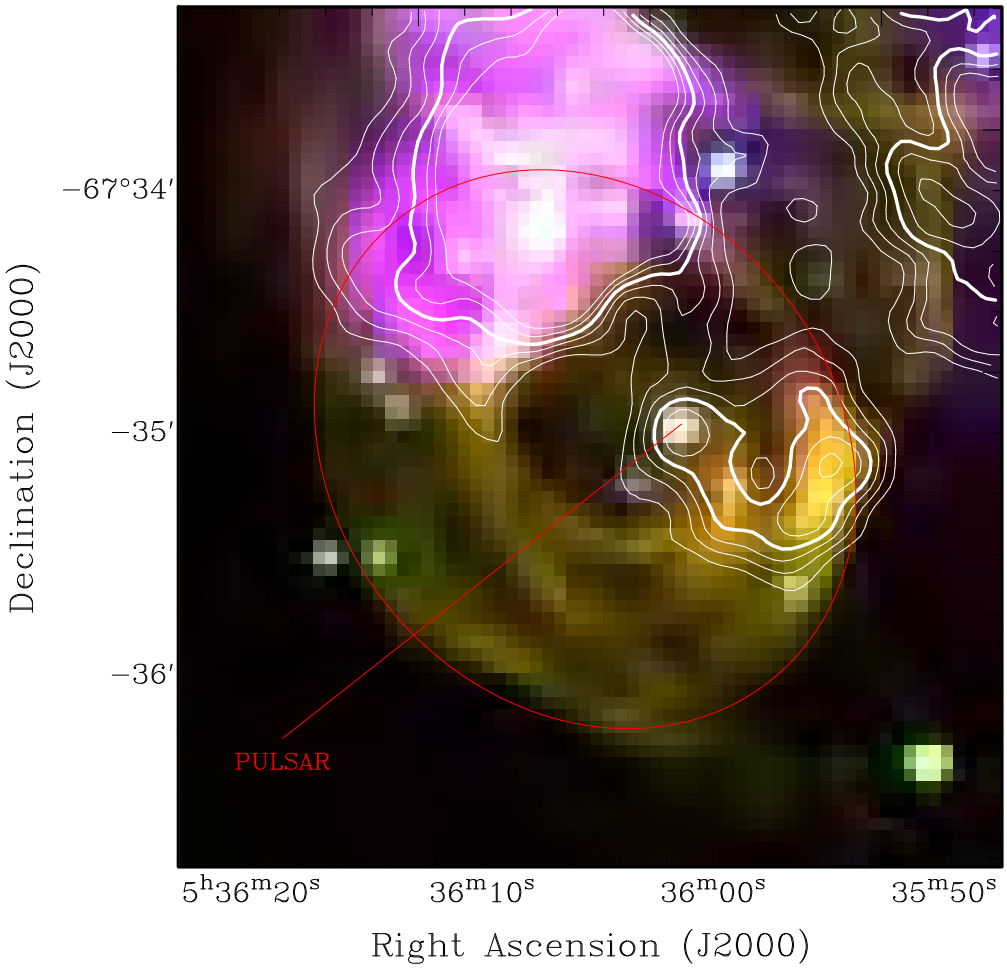

Fig. 2. *Close up MCELS image of SNR J0536–6735 with 13 cm as seen in Fig. 1. An overlaid annotation file has been added to show the position of the pulsar.*

most of the stars from the images to reveal the full extent of the faint diffuse emission. All the data has been flux-calibrated and assembled into mosaic images, a small section of which is shown in Figs. 2 and 3. Further details regarding the MCELS are given by Smith et al. (2006) and at http://www.ctio.noao.edu/mcels. Here, for the first time, we present optical images of this object in combination with our new radio-continuum data.

3. RESULTS AND DISCUSSION

The remnant SNR J0536–6735 displays some distinctive elements of a shell morphology at radio and optical frequencies. While it is difficult to determine where the centre of the SNR is exactly located, instead, we note the position of the strong point-like source at RA(J2000)=$5^{\rm h}36^{\rm m}00\overset{\rm s}{.}0$, DEC(J2000)=–67°35′09″.1. There is an embedded H II region at the northern side of the remnant and an even larger/stronger H II region just outside the western region of the remnant. We estimate a diameter of 148″×120″±4″ (36×29±1 pc) for this remnant based on its optical and X-Ray emission while the radio-continuum emission followed closely other frequencies appearance only around the unimpaired southern region of the SNR.

At lower radio frequencies (843, 1400 & 2400 MHz), SNR J0536–6735 has a clear association with the central point source discovered initially at X-rays (Bamba et al. 2006). We note that on either side of this SNR, there appears to be significantly less emission, which would be expected of an object (like a pulsar) that is injecting high amounts of energy into the surrounding environment, thus clearing a cone-like path within the confines of the remnant. Bamba et al. (2006) inferred that PWN may be associated with this SNR. If this is a valid connection between the central object and the remnant, this would be the 5^{th} confirmed SNR/PWN association in the LMC (after N49, 30 Dor B and B0540–693, B0453–68) with two other candidates J0529-6653 (Bozzetto et al. 2012) and J0541.8-6659 (Grondin et al. 2012).

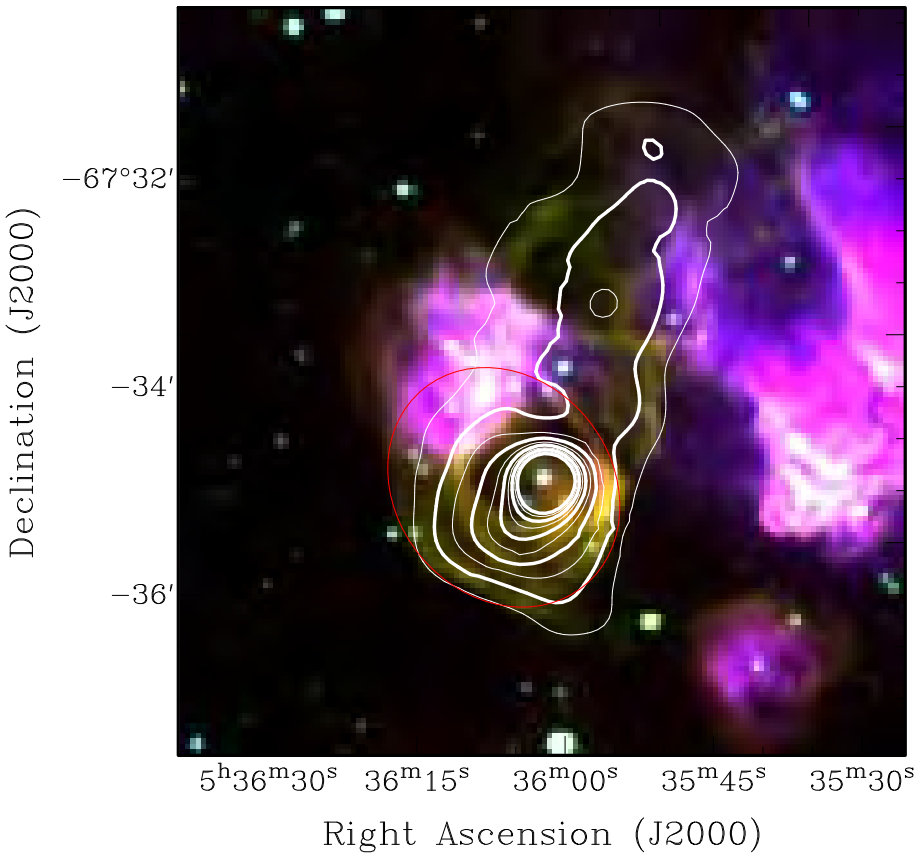

Fig. 3. *MCELS composite optical image (RGB =Hα,[SII],[OIII]) of SNR J0536–6735 overlaid with XMM contours.*

The X-Ray emission for this remnant somewhat differs from the radio and optical appearance. While most of the known SNRs (including SNRs associated with a PWN) exhibit typical shell-like emission, this object has a "tail" like structure emanating out from the North-West of the central remnant source. There is a distinct area of peak emission across the SNR located in the 'head' of the remnant.

The MCELS image (Figs. 1 and 2) also shows the point source that is seen at X-Ray and lower radio frequencies. The remnant appears to be predominately [S II] and Hα dominated with lower levels of [O III] emission. There is a clear distinction between the head and the tail of the emission in which we see the head with significantly stronger emission and the tail dissipating further away from the head it resides. This would infer that the pulsar of SNR J0536–6735 has travelled over a quite substantial distance, especially in comparison to the outer borders of the remnant. Alternatively, this tail may be indicative of emission being blown away from this region, possibly by the PWN.

Measuring the integrated flux density for the remnant was difficult due to the embedded H II region at the northern side of the remnant. Integrated flux density measurements were taken of the point source in this SNR at frequencies of 1400 & 2400 MHz and used to estimate the spectra of this source (Table 1) of α=0.38±0.37 (Fig. 3). These rather inverted/flat spectra are typical of the PWN (Haberl et al. 2012). A spectral map was created, however, the interference from this object influenced the fluxes for the SNR to an extent where measurements were completely unreliable. Because of this, estimating a surface brightness with the current spectra would result in skewed values. Instead, we adopt the typical SNR spectral index of α=–0.55 and use this, coupled with a 20 cm flux estimate, to produce a surface brightness at 1 GHz of 2.55×10^{-21} W m^{-2} Hz^{-1} sr^{-1}. A representation of this surface brightness vs. diameter can be seen in Fig. 4, using the values (D, Σ)=(32.6 pc, 2.55×10^{-21} Wm^{-2} Hz^{-1} sr^{-1}) for this remnant. It's apparent that this estimate of Σ–D falls within the same range of surface brightness-diameter measurements previously taken of LMC SNRs.

Table 1. Flux Density of Pulsar J0536-6735.

ν (MHz)	λ (cm)	R.M.S (mJy)	Beam Size ($''$)	$S_{\rm Total}$ (mJy)
1400	20	0.50	13.9×13.2	4.20
2400	13	0.22	8.2×7.7	5.16

We did not detect any polarisation associated with this object in either the Q or U intensity maps. However, there is a strong source just outside the western field of this SNR as seen in the optical images (Fig. 2) which exhibited strong polarisation. This may have obstructed any polarisation this SNR had, so we can not completely rule out that this source may be significantly polarised.

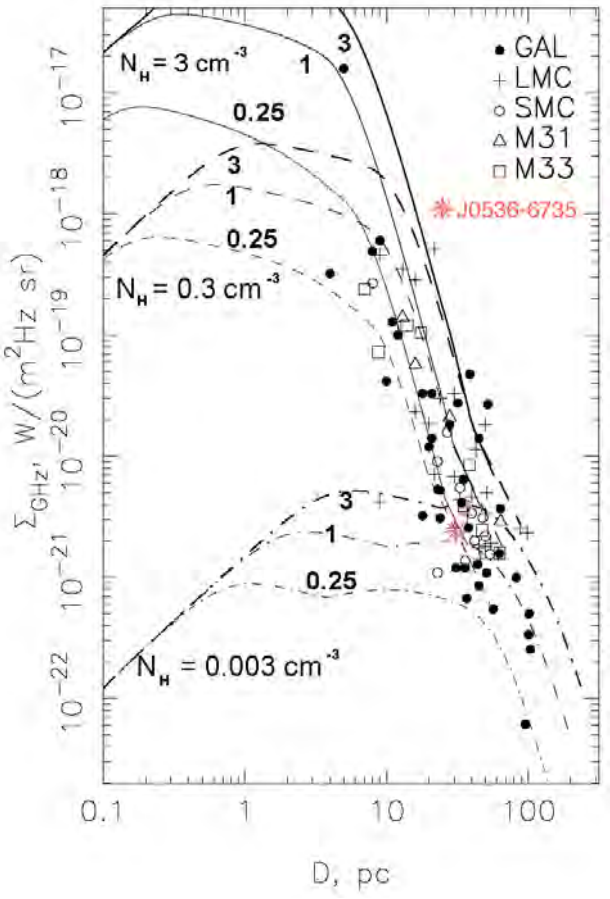

Fig. 4. *Surface brightness-diameter diagram from Berezhko and Volk (2004), with SNR J0536–6735 added. The evolutionary tracks are for ISM densities of N_H = 3, 0.3 and 0.003 cm^{-3} and explosion energies of E_{SN} = 0.25, 1 and 3 × 10^{51} erg.*

4. CONCLUSION

This remnant appears to exhibit a shell morphology with an extent of D=(36×29)±1 pc, a close association between optical and X-Ray images for both the head and tail of the emission, with the radio-continuum images displaying emission from the head of the remnant but none from the tail. Analyses in this paper supports previous suggestions of the point source within the head of the SNR being a PWN associated with this remnant.

Acknowledgements – We used the KARMA and MIRIAD software packages developed by the ATNF. The Australia Telescope Compact Array is part of the Australia Telescope which is funded by the Commonwealth of Australia for operation as a National Facility managed by CSIRO. We thank the Magellanic Clouds Emission Line Survey (MCELS) team for access to the optical images. The MCELS project has been supported in part by NSF grants AST-9540747 and AST-0307613, and through the generous support of the Dean B. McLaughlin Fund at the University of Michigan, a bequest from the family of Dr. Dean B. McLaughlin in memory of his lasting impact on Astronomy.

REFERENCES

Bamba, A., Ueno, M., Nakajima, H., Mori, K., Koyama, K.: 2006, *Astron. Astrophys.*, **450**, 585.
Berezhko E. G., Volk H. J.: 2004, *Astron. Astrophys.*, **427**, 525.
Blair, W. P., Ghavamian, P., Sankrit, R., Danforth, C. W.: 2006, *Astrophys. J. Suppl. Series*, **165**, 480.
Bojičić, I. S., Filipović, M. D., Parker, Q. A., Payne, J. L., Jones, P. A., Reid, W., Kawamura, A., Fukui, Y.: 2007, *Mon. Not. R. Astron. Soc.*, **378**, 1237.
Bozzetto, L. M., Filipović, M. D., Crawford, E. J., Bojičić, I. S., Payne, J. L., Mendik, A., Wardlaw, B. and de Horta, A. Y.: 2010, *Serb. Astron. J.*, **181**, 43.
Bozzetto, L. M., Filipović, M. D., Crawford, E. J., Payne, J. L., De Horta, A. Y. and Stupar, M.: 2012, *Rev. Mex. Astron. Astrofis.*, **48**, 41.
Bozzetto, L. M., Filipović, M. D., Crawford, E. J., Haberl, F., Sasaki, M., Urošević, D., Pietsch, W., Payne, J. L., de Horta, A. Y., Stupar, M., Tothill, N. F. H., Dickel, J., Chu, Y.-H. and Gruendl, R.: 2012, *Mon. Not. R. Astron. Soc.*, **420**, 2588.
Čajko K. O., Crawford E. J., Filipović, M. D.: 2009, *Serb. Astron. J.*, **179**, 55.
Clarke, J. N., Little, A. G., Mills, B. Y.: 1976, *Aust. J. Phys. Astrophys. Suppl.*, **40**, 1.
Crawford, E. J., Filipović, M. D. and Payne, J. L.: 2008a, *Serb. Astron. J.*, **176**, 59.
Crawford, E. J., Filipović, M. D., De Horta, A. Y., Stootman, F. H., Payne J. L.: 2008b, *Serb. Astron. J.*, **177**, 61.

Crawford, E. J., Filipović, M. D., Haberl, F., Pietsch, W., Payne, J. L., De Horta, A. Y.: 2010, *Astron. Astrophys.*, **518**, A35.
Davies, R.D., Elliott, K. H., Meaburn, J.: 1976, *Mon. Mem. Royal Astron. Society*, **81**, 89.
Desai, K. M., Chu, Y.-H., Gruendl, R. A., Dluger, W., Katz, M., Wong, T, Chen, C.-H. R., Looney, L. W., Hughes, A., Muller, E., Ott, J. and Pineda, J. L.: 2010, *Astron. J.*, **140**, 584.
de Horta, A. Y., Filipović, M. D., Bozzetto, L. M., Maggi, P., Haberl, F., Crawford, E. J., Sasaki, M., Urošević, D., Pietsch, W., Gruendl, R., Dickel, J., Tothill, N. F. H., Chu, Y.-H., Payne, J. L., Collier, J. D.: 2012, *Astron. Astrophys.*, **540**, A25.
Dickel, J. R., McIntyre, V. J.; Gruendl, R. A.; Milne, D. K.: 2005, *Astron. J.*, **129**, 790.
Filipović, M. D., Haynes, R. F., White, G. L., Jones, P. A., Klein, U., Wielebinski, R.: 1995, *Astron. Astrophys. Suppl. Series*, **111**, 331.
Filipović, M. D., Haynes, R. F., White, G. L., Jones, P. A.: 1998, *Astron. Astrophys. Suppl. Series*, **130**, 421.
Gooch, R.: 1996, in "Astronomical Society of the Pacific Conference Series, Vol. 101, Astronomical Data Analysis Software and Systems V", G. H. Jacoby and J. Barnes, ed., 80.
Gotthelf E. V., Vasisht G.: 2000, in Kramer M., Wex N., Wielebinski R., eds, IAU Colloq. 177, ASP Conf. Ser. Vol. 202, Pulsar Astronomy - 2000 and Beyond. Astron. Soc. Pac., San Francisco, p. 699.
Green D. A.: 2009, *Bull. Astron. Soc. India*, **37**, 45.
Grondin, M.-H., Sasaki, M., Haberl, F., Pietsch, W., Crawford, E. J., Filipović, M. D., Bozzetto, L. M., Points, S., Smith, R. C.: 2012, *Astron. Astrophys.*, **539**, 15.
Haberl, F., Pietsch, W.: 1999, *Astron. Astrophys. Suppl. Series.* **139**, 277.
Macri, L. M., Stanek, K. Z., Bersier, D., Greenhill, L. J. and Reid, M. J.: 2006, *Astrophys. J.*, **652**, 1133.
Mathewson, D. S., Ford, V. L., Tuohy, I. R., Mills, B. Y., Turtle, A. J., Helfand, D. J.: 1985 *Astrophys. J. Suppl. Series*, **58**, 197.
Mills, B. Y., Turtle, A. J., Little, A. G., Durdin, J. M.: 1984, *Aust. J. Phys.*, **37**, 321.
Payne, J. L., White, G. L., Filipović, M. D.: 2008, *Mon. Not. R. Astron. Soc.*, **383**, 1175.
Ridley J. P., Lorimer D. R.: 2010, *Mon. Not. R. Astron. Soc.*, **406**, L80.
Sault, R. J., Teuben, P. J., Wright, M. C. H.: 1995, in "Astronomical Society of the Pacific Conference Series, Vol. 77, Astronomical Data Analysis Software and Systems IV", R. A. Shaw, H. E. Payne, and J. J. E. Hayes, ed., 433.
Sault, R. J., Wieringa, M. H.: 1994, *Astron. Astrophys. Suppl. Series*, **108**, 585.
Smartt S. J., 2009, *ARA&A*, **47**, 63.
Smith, C., Points, S., Winkler, P. F.: 2006, *NOAO Newsletter*, **85**, 6.

МУЛТИФРЕКВЕНЦИОНА РАДИО-ПОСМАТРАЊА ОСТАТКА СУПЕРНОВЕ У ВЕЛИКОМ МАГЕЛАНОВОМ ОБЛАКУ – SNR J0536–6735(N59B)

L. M. Bozzetto[1], M. D. Filipović[1], E. J. Crawford[1], A. Y. De Horta[1] and M. Stupar[2,3]

[1]*School of Computing and Mathematics, University of Western Sydney*
Locked Bag 1797, Penrith South DC, NSW 1797, Australia

[2]*Department of Physics, Macquarie University, Sydney, NSW 2109, Australia*

[3]*Australian Astronomical Observatory, PO Box 296, Epping, NSW 1710, Australia*

E–mail: *m.filipovic@uws.edu.au*

УДК 524.722.3 : 524.354–77
Оригинални научни рад

У овој студији представљамо нове ATCA резултате посматрања у радио-континууму остатка супернове у Великом Магелановом Облаку – SNR J0536–6735. Овај објекат је типичан остатак супернове са љускастом морфологијом. Измерена вредност дијаметра износи D=(36×29)±1 парсека. На северној страни овог остатка супернове видљив је јак HII регион који додатно отежава прецизно мерење (нпр. густине флукса и поларизације) и даљу детаљнију анализу овог објекта. Емисија у радио-континууму је идентичне структуре као и на осталим фреквенцијама (оптичка и рентгенска) а површински сјај овог остатка на 1 GHz је процењен на 2.55×10^{-21} $\mathrm{Wm^{-2}\ Hz^{-1}\ sr^{-1}}$. Коначно, открили смо и тачкасти објекат у радио-континууму који је највероватније тесно повезан са претходно предложеним пулсаром и PWN. Такозвани "реп" овог остатка није видљив ни на једној од наших радио-мапа иако је веома уочљив и на оптичким и на рентгенским фреквенцијама.

A.19 Related Paper 19

Wong, G. F., Crawford, E. J., Filipović, M. D., De Horta, A. Y., Tothill, N. F. H., Collier, J. D., Drašković, D., Galvin, T. J., and Payne, J. L. (2012a). New 6 and 3-cm Radio-Continuum Maps of the Small Magellanic Cloud: Part II - Point Source Catalogue. *Serbian Astronomical Journal*, 184:93–95

My contribution was to o provide some of the data, and assist in the data analysis. This is a 20% contribution.

Serb. Astron. J. № 184 (2012), 93 - 95 **UDC 52–13–77 : 524.722.7**
DOI: 10.2298/SAJ1284093W Professional paper

NEW 6 AND 3-cm RADIO-CONTINUUM MAPS OF THE SMALL MAGELLANIC CLOUD: PART II – POINT SOURCE CATALOGUE

G. F. Wong, E. J. Crawford, M. D. Filipović, A. Y. De Horta, N. F. H. Tothill, J. D. Collier, D. Drašković, T. J. Galvin and J. L. Payne

University of Western Sydney, Locked Bag 1797, Penrith South DC, NSW 2751, Australia
E–mail: *m.filipovic@uws.edu.au*

(Received: March 8, 2012; Accepted: March 19, 2012)

SUMMARY: We present two new catalogues of radio-continuum sources in the field of the Small Magellanic Cloud (SMC). These catalogues contain sources found at 4800 MHz (λ=6 cm) and 8640 MHz (λ=3 cm). Some 457 sources have been detected at 3 cm with 601 sources at 6 cm created from new high-sensitivity and resolution radio-continuum images of the SMC from Crawford et al. (2011).

Key words. Magellanic Clouds – radio continuum : galaxies – catalogs

1. INTRODUCTION

The Small Magellanic Cloud (SMC), well known for its close proximity (∼60 kpc; Hilditch et al. 2005) and ideal location in one of the coldest areas of the radio sky (also towards the South Celestial Pole), allows observations of radio emission to be made without interference from the Galactic foreground radiation (Haynes et al. 1986). Therefore, the SMC is an ideal location to study radio sources like supernova remnants (SNRs; Filipović et al. 2005, 2008, Payne et al. 2007, Owen et al. 2011, Haberl et al. 2012), H II regions (Reid et al. 2006) and Planetary Nebulae (PNe; Filipović et al. 2009a, Crawford et al. 2012) which may otherwise be difficult to study in our own and other more distant galaxies.

Extensive radio-continuum surveys of the SMC have been made over the last 40 years using various interferometric observations like the Molonglo Obervatory Synesis Telescope (MOST; Ye et al. 1995) and Australia Telescope Compact Array (ATCA; Filipović et al. 2002, Payne et al. 2004, Filipović et al. 2009b, Mao et al. 2008, Dickel et al. 2010), and single dish observations from the 64-m Parkes radio-telescope (Filipović et al. 1997, 1998).

Catalogues of radio-continuum point sources covering the region of the SMC have been created from these surveys, and from wider surveys of the southern sky (see the summary of these catalogues in Wong et al. 2011a,b).

We recently published a set of new high-resolution radio-continuum maps of the SMC at 6 and 3-cm, created by combining observations from ATCA (Crawford et al. 2011, hereafter Paper I). We now present a catalogue of radio-continuum sources in the region of the SMC derived from our 6 and 3 cm radio-continuum maps (Fig. 1 and Fig. 3 in Paper I).

In Section 2 we describe the data used to derive the radio-continuum point sources. In Section 3 we describe our source fitting and detection methods. Section 4 contains our conclusions and the appendix contains the radio-continuum source catalogue.

2. DATA

The 6 and 3 cm maps (Fig. 1 and Fig. 3 in Paper I) were created by combining data from various ATCA projects that covered the SMC (Table 1 in Paper I). The majority of the data used come from ATCA project C1207 (Dickel et al. 2010). The 3 and 6 cm maps have a resolution of 20″ and 30″, and sensitivity of 0.8 and 0.7 mJy/beam, respectively.

Table 1 contains the field size of all the images used to derive the radio-continuum sources contained in this paper (Tables A1 and A2).

Table 1. Field size (in J2000) of images used in this study.

Image	RA_1	RA_2	Dec_1	Dec_2
3 cm	$00^h\ 26^m$	$01^h\ 27^m$	–70°35′	–75°21′
6 cm	$00^h\ 26^m$	$01^h\ 28^m$	–70°29′	–75°29′
13 cm	$00^h\ 27^m$	$01^h\ 35^m$	–70°30′	–75°15′
20 cm	$00^h\ 10^m$	$01^h\ 43^m$	–69°16′	–75°40′
36 cm	$00^h\ 16^m$	$01^h\ 40^m$	–72°30′	–74°38′

3. SOURCE FITTING AND DETECTION

The MIRIAD task IMSAD (Sault et al. 1995) was used to detect sources in the 3 cm and 6 cm images, requiring a fitted Gaussian flux density $>5\sigma$ (3.5 mJy). All sources were then visually examined to confirm that they are genuine point sources, excluding extended emission, bright side lobes, etc.

The catalogue of radio-continuum sources contains positions RA(J2000), Dec(J2000) and integrated flux densities at 3 cm (Table A1) and 6 cm (Table A2). Table 2 provides a summary of the images and resulting catalogues of radio-continuum sources used in this study. In addition, the 13, 20 and 36 cm information from Wong et al. (2011a,b) is repeated for comparison. Table 2 also contains the number of sources identified within the field of the 13 cm image (see Table 1), the smallest of all the survey regions compared.

Table 2. Information on the images and catalogue of radio-continuum sources.

λ (cm)	RMS (mJy/beam)	Number of Sources	Within the Field of the 3 cm image	Beam Size (arcsec)
3	0.8	457	457	20
6	0.7	601	601	30
13	0.4	743*	743*	45
20	0.7	1560	824	14.8×12.2
36	0.7	1689	1198	40

* Values include the original catalogue retrieved from Filipović et al. (2002)

4. CONCLUSION

We present a new catalogue of radio-continuum sources towards the SMC, containing sources found at 3 cm and 6 cm.

The 3 cm and 6 cm catalogue, containing 457 and 601 sources respectively, has been created from new high-sensitivity and resolution radio-continuum maps of the SMC from Paper I.

Acknowledgements – The Australia Telescope Compact Array and Parkes radio telescope are parts of the Australia Telescope National Facility which is funded by the Commonwealth of Australia for operation as a National Facility managed by CSIRO. This paper includes archived data obtained through the Australia Telescope Online Archive (http://atoa.atnf.csiro.au). We used the KARMA and MIRIAD software package developed by the ATNF.

REFERENCES

Crawford, E. J., Filipović, M. D., Bojicić, I. S., Cohen, M., Payne, J. L., De Horta, A. Y., Reid, W.: 2012, *arXiv* 1201.6101

Crawford, E. J., Filipovic, M. D., de Horta, A. Y., Wong, G. F., Tothill, N. F. H., Drašković, D., Collier, J. D., Galvin, T. J.: 2011, *Serb. Astron. J.*, **183**, 95. (Paper I).

Dickel, J. R., Gruendl, R. A., McIntyre, V. J., Shaun W. A.: 2010, *Astron. J.*, **140**, 1511.

Filipović, M. D., Jones, P. A., White, G. L., Haynes, R. F., Klein, U., Wielebinski, R.: 1997, *Astron. Astrophys. Suppl. Series*, **121**, 321.

Filipović, M. D., Haynes, R. F., White, G. L., Jones, P. A.: 1998, *Astron. Astrophys. Suppl. Series*, **130**, 421.

Filipović, M. D., Bohlsen, T., Reid, W., Staveley-Smith, L., Jones, P. A., Nohejl, K., Goldstein, G.: 2002, *Mon. Not. R. Astron. Soc.*, **335**, 1085.

Filipović, M. D., Payne, J. L., Reid, W., Danforth, C. W., Staveley-Smith, L., Jones, P. A., White, G. L.: 2005, *Mon. Not. R. Astron. Soc.*, **364**, 217.

Filipović, M. D., Haberl, F., Winkler, P. F., Pietsch, W., Payne, J. L., Crawford, E. J., de Horta, A. Y., Stootman, F. H., Reaser, B. E.: 2008, *Astron. Astrophys.*, **485**, 63.

Filipović, M. D., Cohen, M., Reid, W. A., Payne, J. L., Parker, Q. A., Crawford, E. J., Bojičić, I. S., de Horta, A. Y., Hughes, A., Dickel, J., Stootman, F.: 2009a, *Mon. Not. R. Astron. Soc.*, **399**, 769.

Filipović, M. D., Crawford E. J., Hughes A., Leverenz H., de Horta A. Y., Payne J. L., Staveley-Smith L., Dickel J. R., Stootman F. H., White G. L.: 2009b, in van Loon J. T., Oliveira J. M., eds, *IAU Symposium Vol. 256*, PDF8.

Haberl, F., Sturm, R., Filipović, M. D., Pietsch, W., Crawford, E. J.: 2012, *Astron. Astrophys.*, **537**, L1.

Haynes, R. F., Murray, J. D., Klein, U., Wielebinski, R.: 1986, *Astron. Astrophys.*, **159**, 22.
Hilditch, R. W., Howarth, I. D., Harries, T. J.: 2005, *Mon. Not. R. Astron. Soc.*, **357**, 304.
Mao, S. A., Gaensler, B. M., Stanimirović, S., Haverkorn, M., McClure-Griffiths, N. M., Staveley-Smith, L., Dickey, J. M.: 2008, *Astrophys. J.*, **688**, 1029.
Owen, R. A., Filipović, M. D., Ballet, J., Haberl, F., Crawford, E. J., Payne, J. L., Sturm, R., Pietsch, W., Mereghetti, S., Ehle, M., Tiengo, A., Coe, M. J., Hatzidimitriou, D., Buckley, D. A. H.: 2011 *Astron. Astrophys.*, **530**, A132.
Payne, J. L., Filipović, M. D., Reid, W., Jones, P. A., Staveley-Smith, L., White, G. L.: 2004, *Mon. Not. R. Astron. Soc.*, **355**, 44.
Payne, J. L., White, G. L., Filipović, M. D., Pannuti, T. G.: 2007, *Mon. Not. R. Astron. Soc.*, **376**, 1793.
Reid, W. A., Payne, J. L., Filipović, M. D., Danforth, C. W., Jones, P. A., White, G. L., Staveley-Smith, L.: 2006, *Mon. Not. R. Astron. Soc.*, **367**, 1379.
Sault, R. J., Teuben, P. J. and Wright, M. C. H.: 1995, *Astronomical Data Analysis Software and Systems IV*, **77**, 433
Wong, G. F., Filipović, M. D., Crawford, E. J., de Horta, A. Y., Galvin, T., Drašković, D., Payne, J. L.: 2011a, *Serb. Astron. J.*, **182**, 43.
Wong, G. F., Filipović, M. D., Crawford, E. J., Tothill, N. F. H., de Horta, A. Y., Drašković, D., Galvin, T., Collier, J. D., Payne, J. L.: 2011b, *Serb. Astron. J.*, **183**, 103.
Ye, T. S., Amy, S. W., Wang, Q. D., Ball, L., Dickel, J.: 1995, *Mon. Not. R. Astron. Soc.*, **275**, 1218.

APPENDIX

Tables A1 and A2 in Appendix are available online at
http://saj.matf.bg.ac.rs/184/pdf/Appendix.pdf.

НОВО ПРОУЧАВАЊЕ МАЛОГ МАГЕЛАНОВОГ ОБЛАКА У РАДИО-КОНТИНУУМУ НА 6 И 3 cm: ДЕО II - КАТАЛОГ ТАЧКАСТИХ ИЗВОРА

G. F. Wong, E. J. Crawford, M. D. Filipović, A. Y. De Horta, N. F. H. Tothill, J. D. Collier, D. Drašković, T. J. Galvin and J. L. Payne

University of Western Sydney, Locked Bag 1797, Penrith South DC, NSW 2751, Australia
E–mail: *m.filipovic@uws.edu.au*

УДК 52–13–77 : 524.722.7
Стручни чланак

У другом делу ове студије представљамо нове ATCA радио-континуум каталоге тачкастих објеката у пољу Малог Магелановог Облака (ММО) на λ=6 cm (ν=4800 MHz) i λ=3 cm (ν=8640 MHz). Укупно, у овом новом каталогу представљено је 457 тачкастих објеката детектованих на 3 cm и 601 на 6 cm.

Table A1. 3 cm Catalogue of point sources in the field of the SMC with integrated flux density.

Name ATCA	R.A.$_{8600}$ (J2000)	Dec.$_{8600}$ (J2000)	S_3 (mJy)
J002815-741832	00:28:15.78	-74:18:32.50	3.79
J002826-744625	00:28:26.37	-74:46:25.40	5.69
J002906-735348	00:29:06.80	-73:53:48.40	20.10
J002909-741131	00:29:09.74	-74:11:31.20	7.58
J002959-735936	00:29:59.29	-73:59:36.40	3.84
J003006-740015	00:30:06.53	-74:00:15.00	18.20
J003007-744859	00:30:07.82	-74:48:59.80	4.01
J003026-731803	00:30:26.57	-73:18:03.30	8.91
J003030-742926	00:30:30.54	-74:29:26.87	3.07
J003036-735148	00:30:36.56	-73:51:48.54	3.46
J003036-742902	00:30:36.86	-74:29:02.87	7.47
J003131-743028	00:31:31.87	-74:30:28.20	6.14
J003140-743447	00:31:40.58	-74:34:47.00	16.90
J003140-734755	00:31:40.79	-73:47:55.00	6.61
J003148-721328	00:31:48.76	-72:13:28.60	4.23
J003152-735613	00:31:52.57	-73:56:13.40	4.89
J003233-730649	00:32:33.34	-73:06:49.80	33.40
J003233-734140	00:32:33.59	-73:41:40.10	8.74
J003243-733159	00:32:43.15	-73:31:59.90	6.91
J003249-741858	00:32:49.18	-74:18:58.00	6.68
J003252-722933	00:32:52.68	-72:29:33.10	55.80
J003255-714545	00:32:55.07	-71:45:45.70	12.00
J003311-740343	00:33:11.04	-74:03:43.21	2.21
J003314-705540	00:33:14.44	-70:55:40.00	34.00
J003314-743907	00:33:14.85	-74:39:07.40	5.36
J003326-741837	00:33:26.45	-74:18:37.20	5.75
J003332-733200	00:33:32.04	-73:32:00.40	8.01
J003342-743055	00:33:42.25	-74:30:55.45	3.05
J003356-722842	00:33:56.18	-72:28:42.00	4.79
J003357-742321	00:33:57.64	-74:23:21.70	12.50
J003402-732249	00:34:02.73	-73:22:49.00	4.65
J003413-733323	00:34:13.38	-73:33:23.80	54.30
J003415-704547	00:34:15.12	-70:45:47.00	4.25
J003415-731828	00:34:15.28	-73:18:28.20	5.94
J003415-733450	00:34:15.52	-73:34:50.30	7.75
J003417-733407	00:34:17.27	-73:34:07.50	6.92
J003424-721143	00:34:24.32	-72:11:43.30	24.10
J003427-733523	00:34:27.66	-73:35:23.32	5.32
J003431-713318	00:34:31.56	-71:33:18.90	4.05
J003436-744242	00:34:36.06	-74:42:42.80	5.74
J003442-743008	00:34:42.44	-74:30:08.10	5.15
J003455-724654	00:34:55.18	-72:46:54.80	5.05
J003513-704729	00:35:13.46	-70:47:29.60	4.37
J003518-733452	00:35:18.59	-73:34:52.90	5.33
J003531-723654	00:35:31.17	-72:36:54.00	19.90

Table A1. Continued.

Name ATCA	R.A.$_{8600}$ (J2000)	Dec.$_{8600}$ (J2000)	S_3 (mJy)
J003553-725301	00:35:53.07	-72:53:01.80	8.82
J003624-725341	00:36:24.95	-72:53:41.20	17.70
J003625-720903	00:36:25.15	-72:09:03.30	4.73
J003628-720322	00:36:28.78	-72:03:22.20	5.70
J003642-713601	00:36:42.76	-71:36:01.70	4.93
J003700-713809	00:37:00.53	-71:38:09.70	8.60
J003701-714903	00:37:01.81	-71:49:03.40	4.83
J003702-704728	00:37:02.55	-70:47:28.00	10.30
J003709-714006	00:37:09.93	-71:40:06.10	4.21
J003714-705644	00:37:14.69	-70:56:44.60	7.44
J003716-751410	00:37:16.22	-75:14:10.70	13.90
J003739-714105	00:37:39.02	-71:41:05.10	4.33
J003742-710737	00:37:42.78	-71:07:37.00	10.20
J003751-710502	00:37:51.95	-71:05:02.50	4.96
J003755-725156	00:37:55.09	-72:51:56.20	19.80
J003809-735023	00:38:09.04	-73:50:23.00	36.30
J003811-745017	00:38:11.68	-74:50:17.90	6.88
J003824-742209	00:38:24.33	-74:22:09.70	37.90
J003851-731051	00:38:51.25	-73:10:51.40	32.70
J003855-720842	00:38:55.58	-72:08:42.10	4.18
J003857-724845	00:38:57.10	-72:48:45.50	5.35
J003917-731842	00:39:17.14	-73:18:42.90	6.55
J003924-720338	00:39:24.12	-72:03:38.20	4.51
J003940-714147	00:39:40.01	-71:41:47.20	18.10
J003940-743453	00:39:40.81	-74:34:53.40	5.24
J003943-705249	00:39:43.36	-70:52:49.50	7.31
J003947-713733	00:39:47.18	-71:37:33.30	14.00
J003948-733414	00:39:48.63	-73:34:14.80	5.06
J003950-705500	00:39:50.32	-70:55:00.10	4.32
J003951-722915	00:39:51.59	-72:29:15.80	6.22
J003959-722611	00:39:59.91	-72:26:11.10	7.52
J004013-714329	00:40:13.10	-71:43:29.10	5.05
J004014-722717	00:40:14.08	-72:27:17.30	5.93
J004021-723802	00:40:21.04	-72:38:02.40	8.92
J004034-751506	00:40:34.88	-75:15:06.70	2.46
J004047-712206	00:40:47.02	-71:22:06.20	5.64
J004047-734818	00:40:47.76	-73:48:18.10	5.06
J004047-714559	00:40:47.89	-71:45:59.20	99.90
J004048-733700	00:40:48.06	-73:37:00.70	36.30
J004056-734321	00:40:56.46	-73:43:21.70	4.49
J004059-733649	00:40:59.27	-73:36:49.60	11.00
J004111-715901	00:41:11.95	-71:59:01.30	6.01
J004125-705744	00:41:25.08	-70:57:44.20	49.50
J004131-720635	00:41:31.08	-72:06:35.90	4.70
J004134-722648	00:41:34.65	-72:26:48.40	5.84

Table A1. Continued.

Name ATCA	R.A.$_{8600}$ (J2000)	Dec.$_{8600}$ (J2000)	S_3 (mJy)
J004143-721824	00:41:43.51	-72:18:24.10	4.21
J004159-720508	00:41:59.41	-72:05:08.00	3.62
J004204-711728	00:42:04.58	-71:17:28.10	5.26
J004207-723416	00:42:07.80	-72:34:16.50	4.79
J004225-751351	00:42:25.14	-75:13:51.40	18.00
J004226-744636	00:42:26.12	-74:46:36.90	8.14
J004230-742851	00:42:30.31	-74:28:51.25	2.04
J004252-725612	00:42:52.54	-72:56:12.40	6.01
J004313-710421	00:43:13.03	-71:04:21.60	11.10
J004318-714056	00:43:18.17	-71:40:56.30	6.38
J004320-734810	00:43:20.71	-73:48:10.10	4.43
J004328-704141	00:43:28.95	-70:41:41.00	130.00
J004335-713200	00:43:35.63	-71:32:00.90	13.40
J004337-730215	00:43:37.71	-73:02:15.90	5.64
J004337-704101	00:43:37.72	-70:41:01.10	4.09
J004340-720347	00:43:40.12	-72:03:47.20	9.02
J004341-711650	00:43:41.74	-71:16:50.20	4.57
J004343-730220	00:43:43.14	-73:02:20.90	6.51
J004348-704159	00:43:48.72	-70:41:59.10	6.73
J004408-735014	00:44:08.48	-73:50:14.30	4.84
J004413-724301	00:44:13.38	-72:43:01.60	2.46
J004415-710949	00:44:15.29	-71:09:49.10	7.48
J004416-750211	00:44:16.92	-75:02:11.40	8.34
J004419-744319	00:44:19.82	-74:43:19.70	5.77
J004426-745423	00:44:26.19	-74:54:23.00	5.54
J004426-734900	00:44:26.69	-73:49:00.00	4.39
J004432-713803	00:44:32.83	-71:38:03.10	5.33
J004437-742320	00:44:37.65	-74:23:20.90	6.45
J004441-750300	00:44:41.91	-75:03:00.70	5.07
J004444-710008	00:44:44.12	-71:00:08.40	4.31
J004447-751305	00:44:47.68	-75:13:05.30	3.59
J004452-734531	00:44:52.81	-73:45:31.60	6.43
J004453-704840	00:44:53.84	-70:48:40.70	6.48
J004459-711440	00:44:59.82	-71:14:40.20	6.49
J004502-715556	00:45:02.19	-71:55:56.60	3.38
J004508-735145	00:45:08.15	-73:51:45.90	6.14
J004517-723514	00:45:17.23	-72:35:14.30	5.26
J004524-732249	00:45:24.58	-73:22:49.50	56.00
J004540-750034	00:45:40.35	-75:00:34.40	5.71
J004548-724107	00:45:48.15	-72:41:07.10	5.29
J004549-714933	00:45:49.15	-71:49:33.50	4.58
J004553-704700	00:45:53.71	-70:47:00.70	4.40
J004559-723201	00:45:59.81	-72:32:01.80	9.08
J004602-744001	00:46:02.13	-74:40:01.70	11.70
J004607-705608	00:46:07.76	-70:56:08.00	17.90

Table A1. Continued.

Name ATCA	R.A.$_{8600}$ (J2000)	Dec.$_{8600}$ (J2000)	S_3 (mJy)
J004608-720158	00:46:08.64	-72:01:58.50	4.63
J004628-742432	00:46:28.60	-74:24:32.70	3.68
J004632-705856	00:46:32.20	-70:58:56.70	23.40
J004635-730557	00:46:35.21	-73:05:57.90	45.20
J004649-731355	00:46:49.11	-73:13:55.90	6.04
J004650-713925	00:46:50.12	-71:39:25.30	13.20
J004652-734323	00:46:52.25	-73:43:23.00	5.51
J004702-715006	00:47:02.76	-71:50:06.50	6.75
J004713-734051	00:47:13.10	-73:40:51.10	6.24
J004718-723946	00:47:18.77	-72:39:46.50	29.90
J004725-712727	00:47:25.53	-71:27:27.80	24.90
J004729-732210	00:47:29.34	-73:22:10.80	4.09
J004733-750058	00:47:33.60	-75:00:58.20	4.38
J004740-733434	00:47:40.90	-73:34:34.20	6.57
J004748-731725	00:47:48.96	-73:17:25.40	5.65
J004749-705757	00:47:49.93	-70:57:57.00	6.28
J004808-741205	00:48:08.13	-74:12:05.70	29.10
J004816-711405	00:48:16.67	-71:14:05.40	6.00
J004816-741158	00:48:16.92	-74:11:58.90	4.83
J004829-710317	00:48:29.90	-71:03:17.40	4.28
J004842-734211	00:48:42.06	-73:42:11.30	5.54
J004850-710507	00:48:50.44	-71:05:07.70	5.97
J004850-725117	00:48:50.83	-72:51:17.00	4.24
J004910-722211	00:49:10.06	-72:22:11.80	5.64
J004917-732049	00:49:17.34	-73:20:49.20	4.72
J004918-723408	00:49:18.37	-72:34:08.20	5.27
J004918-745659	00:49:18.39	-74:56:59.10	16.10
J004918-734317	00:49:18.85	-73:43:17.20	3.44
J004923-712657	00:49:23.79	-71:26:57.60	4.05
J004928-733400	00:49:28.64	-73:34:00.40	6.57
J004928-732628	00:49:28.93	-73:26:28.30	9.02
J004933-721856	00:49:33.35	-72:18:56.60	4.29
J004935-741545	00:49:35.23	-74:15:45.50	9.38
J004935-724635	00:49:35.28	-72:46:35.80	4.17
J004937-705212	00:49:37.15	-70:52:12.30	62.70
J004954-715148	00:49:54.46	-71:51:48.40	3.99
J004956-723552	00:49:56.58	-72:35:52.80	12.80
J005015-730322	00:50:15.34	-73:03:22.40	5.72
J005021-712130	00:50:21.91	-71:21:30.80	3.60
J005022-744144	00:50:22.84	-74:41:44.84	2.81
J005024-735943	00:50:24.36	-73:59:43.20	5.12
J005031-711922	00:50:31.46	-71:19:22.90	5.14
J005040-703934	00:50:40.83	-70:39:34.20	6.17
J005042-715820	00:50:42.28	-71:58:20.90	4.66
J005056-731249	00:50:56.50	-73:12:49.10	2.47

Table A1. Continued.

Name ATCA	R.A.$_{8600}$ (J2000)	Dec.$_{8600}$ (J2000)	S_3 (mJy)
J005111-712030	00:51:11.70	-71:20:30.60	4.60
J005115-713052	00:51:15.42	-71:30:52.90	3.41
J005116-705603	00:51:16.98	-70:56:03.90	5.08
J005117-733959	00:51:17.09	-73:39:59.40	25.10
J005126-712136	00:51:26.57	-71:21:36.90	3.73
J005134-723236	00:51:34.56	-72:32:36.20	6.50
J005141-731336	00:51:41.54	-73:13:36.10	11.10
J005141-725552	00:51:41.58	-72:55:52.60	7.26
J005151-725537	00:51:51.24	-72:55:37.80	4.87
J005156-721651	00:51:56.43	-72:16:51.20	5.67
J005218-730154	00:52:18.23	-73:01:54.20	1.87
J005219-722706	00:52:19.04	-72:27:06.90	31.80
J005226-712924	00:52:26.20	-71:29:24.10	6.97
J005238-731245	00:52:38.47	-73:12:45.80	15.80
J005253-720132	00:52:53.44	-72:01:32.10	7.73
J005306-743902	00:53:06.93	-74:39:02.86	2.44
J005314-721837	00:53:14.20	-72:18:37.80	5.08
J005320-723511	00:53:20.18	-72:35:11.10	11.00
J005336-723146	00:53:36.66	-72:31:46.20	5.92
J005341-723931	00:53:41.32	-72:39:31.20	5.49
J005346-751449	00:53:46.09	-75:14:49.20	5.66
J005352-704001	00:53:52.74	-70:40:01.50	14.70
J005355-703804	00:53:55.55	-70:38:04.00	3.45
J005402-721343	00:54:02.30	-72:13:43.60	4.77
J005423-725256	00:54:23.82	-72:52:56.50	7.29
J005430-714516	00:54:30.78	-71:45:16.20	5.47
J005448-744937	00:54:48.68	-74:49:37.60	5.55
J005449-725346	00:54:49.42	-72:53:46.90	5.75
J005450-731650	00:54:50.07	-73:16:50.60	4.43
J005510-723734	00:55:10.20	-72:37:34.30	5.30
J005525-721053	00:55:25.31	-72:10:53.60	28.90
J005529-710254	00:55:29.01	-71:02:54.30	4.44
J005533-703954	00:55:33.64	-70:39:54.20	8.85
J005536-723514	00:55:36.15	-72:35:14.10	10.54
J005539-743928	00:55:39.06	-74:39:28.50	5.36
J005540-731313	00:55:40.21	-73:13:13.50	4.49
J005540-721047	00:55:40.28	-72:10:47.10	8.62
J005554-742235	00:55:54.47	-74:22:35.30	15.70
J005557-722604	00:55:57.13	-72:26:04.10	33.50
J005606-750307	00:56:06.98	-75:03:07.20	6.62
J005607-703847	00:56:07.81	-70:38:47.30	7.61
J005611-710708	00:56:11.25	-71:07:08.50	114.00
J005617-712536	00:56:17.70	-71:25:36.90	3.56
J005633-735710	00:56:33.27	-73:57:10.70	6.41
J005636-740316	00:56:36.51	-74:03:16.40	18.70

Table A1. Continued.

Name ATCA	R.A.$_{8600}$ (J2000)	Dec.$_{8600}$ (J2000)	S_3 (mJy)
J005644-725205	00:56:44.46	-72:52:05.70	17.40
J005652-712302	00:56:52.55	-71:23:02.00	20.90
J005705-704012	00:57:05.21	-70:40:12.40	9.32
J005714-733454	00:57:14.74	-73:34:54.90	3.65
J005715-704045	00:57:15.52	-70:40:45.90	89.60
J005719-703818	00:57:19.16	-70:38:18.30	4.75
J005721-740315	00:57:21.57	-74:03:15.10	4.88
J005726-751457	00:57:26.03	-75:14:57.80	3.67
J005728-751259	00:57:28.64	-75:12:59.70	5.59
J005731-744213	00:57:31.31	-74:42:13.60	5.85
J005732-741243	00:57:32.30	-74:12:43.40	34.50
J005736-731301	00:57:36.62	-73:13:01.90	4.82
J005737-710850	00:57:37.24	-71:08:50.30	10.30
J005741-724153	00:57:41.65	-72:41:53.50	8.77
J005754-723911	00:57:54.37	-72:39:11.10	5.09
J005811-712409	00:58:11.74	-71:24:09.80	4.23
J005820-713042	00:58:20.25	-71:30:42.30	3.87
J005827-723954	00:58:27.21	-72:39:54.30	11.80
J005830-740149	00:58:30.44	-74:01:49.40	3.20
J005842-722716	00:58:42.89	-72:27:16.60	5.04
J005903-704902	00:59:03.48	-70:49:02.50	11.70
J005906-735206	00:59:06.57	-73:52:06.00	25.10
J005948-715655	00:59:48.50	-71:56:55.50	4.49
J005948-705026	00:59:48.57	-70:50:26.80	19.40
J010001-730555	01:00:01.43	-73:05:55.10	5.72
J010029-713826	01:00:29.55	-71:38:26.70	24.20
J010046-745422	01:00:46.01	-74:54:22.30	3.27
J010058-734201	01:00:58.61	-73:42:01.90	4.19
J010113-744058	01:01:13.21	-74:40:58.40	5.28
J010133-715132	01:01:33.52	-71:51:32.50	5.38
J010204-722443	01:02:04.71	-72:24:43.60	5.43
J010220-735323	01:02:20.69	-73:53:23.28	4.97
J010233-741538	01:02:33.16	-74:15:38.80	6.01
J010234-752116	01:02:34.16	-75:21:16.30	3.92
J010243-715942	01:02:43.57	-71:59:42.40	5.08
J010255-713631	01:02:55.10	-71:36:31.30	5.90
J010256-743436	01:02:56.30	-74:34:36.60	4.75
J010258-722520	01:02:58.49	-72:25:20.20	6.87
J010301-743352	01:03:01.78	-74:33:52.20	3.99
J010331-750706	01:03:31.54	-75:07:06.60	11.20
J010339-725043	01:03:39.77	-72:50:43.00	5.60
J010359-750844	01:03:59.33	-75:08:44.90	4.96
J010429-712446	01:04:29.04	-71:24:46.60	5.59
J010431-720717	01:04:31.44	-72:07:17.30	8.84
J010432-720746	01:04:32.91	-72:07:46.20	4.76

Table A1. Continued.

Name ATCA	R.A.$_{8600}$ (J2000)	Dec.$_{8600}$ (J2000)	S_3 (mJy)
J010440-713121	01:04:40.78	-71:31:21.70	10.70
J010456-703730	01:04:56.96	-70:37:30.90	53.80
J010509-732021	01:05:09.32	-73:20:21.60	3.95
J010519-714302	01:05:19.41	-71:43:02.30	5.48
J010523-731518	01:05:23.17	-73:15:18.60	6.31
J010525-722523	01:05:25.14	-72:25:23.60	6.52
J010532-704444	01:05:32.83	-70:44:44.40	8.24
J010533-721331	01:05:33.10	-72:13:31.40	7.09
J010536-743159	01:05:36.16	-74:31:59.60	18.00
J010536-740004	01:05:36.98	-74:00:04.60	6.78
J010543-750545	01:05:43.88	-75:05:45.60	3.17
J010556-714603	01:05:56.66	-71:46:03.90	12.20
J010557-710455	01:05:57.70	-71:04:55.60	8.57
J010558-745904	01:05:58.85	-74:59:04.00	5.20
J010602-724345	01:06:02.25	-72:43:45.30	6.25
J010614-735008	01:06:14.75	-73:50:08.30	4.65
J010615-725214	01:06:15.08	-72:52:14.70	6.21
J010647-741929	01:06:47.43	-74:19:29.70	5.63
J010725-721636	01:07:25.99	-72:16:36.40	5.74
J010744-751529	01:07:44.77	-75:15:29.80	5.94
J010748-705213	01:07:48.50	-70:52:13.30	5.77
J010759-710824	01:07:59.40	-71:08:24.10	9.96
J010806-703847	01:08:06.04	-70:38:47.20	5.94
J010808-713951	01:08:08.83	-71:39:51.20	5.80
J010817-745521	01:08:17.08	-74:55:21.90	5.10
J010826-742217	01:08:26.21	-74:22:17.20	3.55
J010831-723531	01:08:31.36	-72:35:31.70	5.87
J010858-731121	01:08:58.15	-73:11:21.90	5.40
J010903-734926	01:09:03.00	-73:49:26.00	5.30
J010903-731751	01:09:03.29	-73:17:51.20	8.22
J010912-731732	01:09:12.17	-73:17:32.00	5.30
J010919-725602	01:09:19.40	-72:56:02.00	5.15
J010920-731049	01:09:20.94	-73:10:49.30	3.56
J010922-722051	01:09:22.33	-72:20:51.20	4.34
J010927-731512	01:09:27.52	-73:15:12.20	5.30
J010928-704207	01:09:28.04	-70:42:07.30	4.47
J010928-740608	01:09:28.24	-74:06:08.20	4.95
J010931-713454	01:09:31.30	-71:34:54.40	14.90
J010939-745702	01:09:39.27	-74:57:02.20	4.47
J010939-705008	01:09:39.33	-70:50:08.60	5.33
J010954-720721	01:09:54.66	-72:07:21.90	5.33
J011005-722647	01:10:05.58	-72:26:47.70	41.70
J011022-730441	01:10:22.52	-73:04:41.40	25.40
J011029-745353	01:10:29.39	-74:53:53.30	3.84
J011038-722817	01:10:38.05	-72:28:17.10	70.50

Table A1. Continued.

Name ATCA	R.A.$_{8600}$ (J2000)	Dec.$_{8600}$ (J2000)	S_3 (mJy)
J011039-731257	01:10:39.46	-73:12:57.50	5.79
J011045-722853	01:10:45.36	-72:28:53.91	32.60
J011046-711426	01:10:46.96	-71:14:26.10	5.03
J011049-731427	01:10:49.74	-73:14:27.30	146.00
J011050-721026	01:10:50.98	-72:10:26.20	6.17
J011053-731416	01:10:53.21	-73:14:16.20	139.18
J011111-750938	01:11:11.73	-75:09:38.50	4.53
J011125-730132	01:11:25.94	-73:01:32.40	5.37
J011128-732937	01:11:28.26	-73:29:37.40	9.97
J011132-730208	01:11:32.51	-73:02:08.60	63.20
J011133-745044	01:11:33.55	-74:50:44.90	4.26
J011134-711415	01:11:34.76	-71:14:15.60	12.20
J011158-734126	01:11:58.00	-73:41:26.10	4.48
J011203-705932	01:12:03.63	-70:59:32.00	10.60
J011207-731625	01:12:07.41	-73:16:25.60	4.36
J011211-743512	01:12:11.92	-74:35:12.10	4.70
J011222-741211	01:12:22.98	-74:12:11.90	6.96
J011226-732755	01:12:26.19	-73:27:55.90	6.52
J011230-750619	01:12:30.98	-75:06:19.50	15.90
J011234-720909	01:12:34.73	-72:09:09.10	5.59
J011301-714904	01:13:01.89	-71:49:04.20	4.37
J011318-705109	01:13:18.33	-70:51:09.40	5.48
J011319-743451	01:13:19.19	-74:34:51.50	12.50
J011332-740756	01:13:32.08	-74:07:56.00	5.43
J011334-725548	01:13:34.74	-72:55:48.70	4.83
J011340-714107	01:13:40.83	-71:41:07.00	6.35
J011343-711522	01:13:43.62	-71:15:22.70	8.69
J011349-731802	01:13:49.65	-73:18:02.20	122.00
J011352-742639	01:13:52.05	-74:26:39.40	7.19
J011352-731551	01:13:52.69	-73:15:51.50	5.45
J011356-744251	01:13:56.57	-74:42:51.40	3.91
J011356-711425	01:13:56.84	-71:14:25.00	6.69
J011357-730425	01:13:57.50	-73:04:25.10	4.91
J011405-732007	01:14:05.72	-73:20:07.00	17.30
J011413-721821	01:14:13.57	-72:18:21.10	3.34
J011423-731245	01:14:23.56	-73:12:45.70	5.48
J011430-721716	01:14:30.10	-72:17:16.70	3.89
J011432-732143	01:14:32.73	-73:21:43.70	28.90
J011435-715244	01:14:35.86	-71:52:44.90	11.90
J011438-731825	01:14:38.02	-73:18:25.90	29.30
J011505-732826	01:15:05.20	-73:28:26.10	7.44
J011527-734137	01:15:27.26	-73:41:37.90	4.34
J011600-705603	01:16:00.39	-70:56:03.10	5.19
J011606-744330	01:16:06.61	-74:43:30.50	5.03
J011610-742813	01:16:10.29	-74:28:13.60	7.13

Table A1. Continued.

Name ATCA	R.A.$_{8600}$ (J2000)	Dec.$_{8600}$ (J2000)	S_3 (mJy)
J011611-733858	01:16:11.00	-73:38:58.30	20.10
J011616-732657	01:16:16.03	-73:26:57.70	9.63
J011624-735944	01:16:24.46	-73:59:44.10	5.38
J011627-731439	01:16:27.52	-73:14:39.70	7.11
J011645-743532	01:16:45.65	-74:35:32.20	3.06
J011650-730851	01:16:50.17	-73:08:51.00	5.92
J011706-740454	01:17:06.96	-74:04:54.10	4.11
J011723-744653	01:17:23.70	-74:46:53.90	8.49
J011732-743337	01:17:32.48	-74:33:37.40	9.06
J011757-705931	01:17:57.10	-70:59:31.90	6.31
J011805-735031	01:18:05.25	-73:50:31.40	5.89
J011825-750406	01:18:25.81	-75:04:06.40	4.97
J011830-725710	01:18:30.43	-72:57:10.10	5.26
J011848-742619	01:18:48.51	-74:26:19.20	2.21
J011858-742531	01:18:58.80	-74:25:31.10	4.86
J011911-724642	01:19:11.05	-72:46:42.90	4.17
J011914-733543	01:19:14.80	-73:35:43.10	3.94
J011918-710530	01:19:18.07	-71:05:30.60	22.30
J011919-730436	01:19:19.17	-73:04:36.80	5.23
J011926-732921	01:19:26.98	-73:29:21.20	2.59
J011934-750537	01:19:34.75	-75:05:37.80	3.70
J011943-732844	01:19:43.09	-73:28:44.10	4.75
J011954-750328	01:19:54.56	-75:03:28.80	4.68
J012009-714659	01:20:09.61	-71:46:59.20	4.78
J012023-721956	01:20:23.30	-72:19:56.00	6.28
J012035-750633	01:20:35.45	-75:06:33.50	18.50
J012035-713336	01:20:35.93	-71:33:36.00	3.98
J012037-703843	01:20:37.94	-70:38:43.20	22.50
J012048-733506	01:20:48.90	-73:35:06.80	4.61
J012055-733453	01:20:55.55	-73:34:53.80	19.90
J012059-720423	01:20:59.98	-72:04:23.00	7.16
J012100-733911	01:21:00.96	-73:39:11.90	3.93
J012131-710733	01:21:31.60	-71:07:33.30	4.92
J012148-720923	01:21:48.24	-72:09:23.80	5.26
J012151-740009	01:21:51.43	-74:00:09.30	18.60
J012157-744638	01:21:57.65	-74:46:38.60	9.41
J012201-713242	01:22:01.89	-71:32:42.80	6.36
J012209-713949	01:22:09.96	-71:39:49.60	10.30
J012215-745500	01:22:15.91	-74:55:00.80	4.35
J012230-711421	01:22:30.58	-71:14:21.90	6.56
J012234-714722	01:22:34.05	-71:47:22.00	13.90
J012234-733808	01:22:34.34	-73:38:08.50	4.32
J012239-741010	01:22:39.46	-74:10:10.90	6.45
J012247-751533	01:22:47.85	-75:15:33.90	6.67
J012250-715045	01:22:50.26	-71:50:45.40	8.97

Table A1. Continued.

Name ATCA	R.A.$_{8600}$ (J2000)	Dec.$_{8600}$ (J2000)	S_3 (mJy)
J012257-751505	01:22:57.39	-75:15:05.60	96.70
J012311-741809	01:23:11.90	-74:18:09.40	7.10
J012311-732840	01:23:11.98	-73:28:40.80	4.23
J012312-745411	01:23:12.63	-74:54:11.60	4.87
J012318-751744	01:23:18.47	-75:17:44.60	3.79
J012320-734526	01:23:20.55	-73:45:26.30	6.81
J012324-735607	01:23:24.66	-73:56:07.80	4.38
J012324-740238	01:23:24.75	-74:02:38.87	3.99
J012331-721811	01:23:31.66	-72:18:11.30	5.59
J012347-735444	01:23:47.89	-73:54:44.20	5.11
J012349-735038	01:23:49.79	-73:50:38.00	30.00
J012351-734633	01:23:51.74	-73:46:33.90	3.64
J012353-744139	01:23:53.13	-74:41:39.60	9.77
J012418-711156	01:24:18.07	-71:11:56.80	6.58
J012433-712643	01:24:33.31	-71:26:43.60	7.24
J012450-743642	01:24:50.84	-74:36:42.00	5.13
J012516-731622	01:25:16.19	-73:16:22.10	4.26
J012521-722928	01:25:21.29	-72:29:28.60	16.00
J012525-714901	01:25:25.67	-71:49:01.80	6.51
J012527-741617	01:25:27.33	-74:16:17.40	6.09
J012534-713110	01:25:34.16	-71:31:10.40	5.35
J012534-735625	01:25:34.83	-73:56:25.30	6.18
J012546-731602	01:25:46.30	-73:16:02.40	7.99
J012548-705740	01:25:48.80	-70:57:40.50	4.94
J012555-740125	01:25:55.47	-74:01:25.40	5.63
J012600-735417	01:26:00.10	-73:54:17.02	2.19
J012615-730805	01:26:15.18	-73:08:05.70	5.82
J012625-705022	01:26:25.71	-70:50:22.20	4.29
J012629-732712	01:26:29.74	-73:27:12.00	12.90
J012638-731503	01:26:38.76	-73:15:03.80	12.70
J012639-741624	01:26:39.93	-74:16:24.70	3.96
J012641-713732	01:26:41.23	-71:37:32.30	6.85
J012652-731930	01:26:52.51	-73:19:30.80	4.00
J012655-751119	01:26:55.77	-75:11:19.70	12.20
J012717-734955	01:27:17.15	-73:49:55.20	6.58
J012751-731104	01:27:51.80	-73:11:04.50	7.17
J012809-751249	01:28:09.70	-75:12:49.75	21.08
J012809-751218	01:28:09.97	-75:12:18.00	4.85
J012816-751257	01:28:16.83	-75:12:57.18	7.80
J012828-734143	01:28:28.91	-73:41:43.30	5.22
J012907-733851	01:29:07.05	-73:38:51.80	4.70
J012928-732835	01:29:28.03	-73:28:35.40	4.46
J012930-733310	01:29:30.33	-73:33:10.60	55.90
J013003-751256	01:30:03.61	-75:12:56.90	5.37
J013013-742025	01:30:13.46	-74:20:25.70	24.30

Table A1. Continued.

Name ATCA	R.A.$_{8600}$ (J2000)	Dec.$_{8600}$ (J2000)	S_3 (mJy)
J013020-733234	01:30:20.19	-73:32:34.50	13.40
J013020-733151	01:30:20.86	-73:31:51.20	5.09
J013024-743928	01:30:24.56	-74:39:28.80	8.18
J013032-745833	01:30:32.94	-74:58:33.90	5.74
J013037-734657	01:30:37.35	-73:46:57.30	4.03
J013124-740040	01:31:24.62	-74:00:40.70	6.50
J013214-750339	01:32:14.36	-75:03:39.30	5.83

Table A2. 6 cm Catalogue of point sources in the field of the SMC with integrated flux density.

Name ATCA	R.A.$_{4800}$ (J2000)	Dec.$_{4800}$ (J2000)	S_6 (mJy)
J002815-741829	00:28:15.67	-74:18:29.90	8.20
J002628-740021	00:26:28.07	-74:00:21.21	36.44
J002822-735036	00:28:22.41	-73:50:36.09	1.89
J002850-751115	00:28:50.44	-75:11:15.90	4.27
J002902-751757	00:29:02.73	-75:17:57.20	5.71
J002906-735348	00:29:06.92	-73:53:48.90	33.62
J002909-741129	00:29:09.19	-74:11:29.90	9.27
J002911-740914	00:29:11.89	-74:09:14.22	2.65
J002919-722810	00:29:19.08	-72:28:10.66	31.04
J002921-744507	00:29:21.90	-74:45:07.96	2.88
J002926-732339	00:29:26.76	-73:23:39.00	10.30
J002937-734543	00:29:37.61	-73:45:43.30	3.69
J002949-730418	00:29:49.66	-73:04:18.90	5.75
J002959-735939	00:29:59.73	-73:59:39.73	7.31
J003012-744932	00:30:12.85	-74:49:32.00	3.54
J003026-731814	00:30:26.18	-73:18:14.00	15.58
J003035-742910	00:30:35.73	-74:29:10.70	38.38
J003037-735148	00:30:37.63	-73:51:48.20	8.25
J003007-740015	00:30:07.12	-74:00:15.82	20.78
J003123-732301	00:31:23.50	-73:23:01.70	3.68
J003131-743030	00:31:31.76	-74:30:30.00	8.86
J003140-743447	00:31:40.35	-74:34:47.30	28.21
J003140-734745	00:31:40.99	-73:47:45.10	3.71
J003155-724835	00:31:55.76	-72:48:35.00	3.92
J003106-724827	00:31:06.79	-72:48:27.68	2.99
J003208-735037	00:32:08.72	-73:50:37.10	7.81
J003215-713557	00:32:15.52	-71:35:57.40	4.37
J003231-710419	00:32:31.02	-71:04:19.62	3.77
J003233-730649	00:32:33.15	-73:06:49.80	24.82
J003234-734136	00:32:34.60	-73:41:36.70	9.29
J003236-704915	00:32:36.93	-70:49:15.30	9.35
J003242-733151	00:32:42.37	-73:31:51.30	12.83
J003249-741857	00:32:49.38	-74:18:57.60	15.91
J003252-722932	00:32:52.62	-72:29:32.90	79.10
J003255-714545	00:32:55.21	-71:45:45.00	19.88
J003309-745517	00:33:09.86	-74:55:17.90	7.27
J003301-715320	00:33:01.34	-71:53:20.01	2.79
J003311-740343	00:33:11.68	-74:03:43.90	6.75
J003314-705543	00:33:14.28	-70:55:43.10	40.52
J003326-723708	00:33:26.17	-72:37:08.51	1.68
J003326-722344	00:33:26.40	-72:23:44.76	1.98
J003304-715617	00:33:04.72	-71:56:17.56	2.22
J003341-743054	00:33:41.84	-74:30:54.40	4.90
J003342-704114	00:33:42.33	-70:41:14.70	3.77
J003349-731426	00:33:49.78	-73:14:26.48	1.79

Table A2. Continued.

Name ATCA	R.A.$_{4800}$ (J2000)	Dec.$_{4800}$ (J2000)	S_6 (mJy)
J003305-742123	00:33:05.03	-74:21:23.88	2.01
J003355-721233	00:33:55.95	-72:12:33.60	4.12
J003357-742323	00:33:57.25	-74:23:23.90	10.08
J003358-722842	00:33:58.29	-72:28:42.60	9.80
J003358-703948	00:33:58.61	-70:39:48.30	3.95
J003413-733324	00:34:13.77	-73:33:24.00	83.76
J003424-721144	00:34:24.45	-72:11:44.20	44.85
J003426-733515	00:34:26.11	-73:35:15.47	18.46
J003426-715452	00:34:26.25	-71:54:52.10	3.66
J003438-722751	00:34:38.38	-72:27:51.69	2.16
J003404-714604	00:34:04.86	-71:46:04.42	2.40
J003440-724134	00:34:40.55	-72:41:34.21	2.59
J003446-703952	00:34:46.63	-70:39:52.07	3.86
J003455-713602	00:34:55.31	-71:36:02.20	2.87
J003511-710956	00:35:11.10	-71:09:56.40	10.87
J003524-732221	00:35:24.89	-73:22:21.90	10.39
J003531-723653	00:35:31.03	-72:36:53.20	21.45
J003537-714559	00:35:37.59	-71:45:59.30	4.29
J003544-735207	00:35:44.65	-73:52:07.00	4.18
J003547-721116	00:35:47.43	-72:11:16.60	3.25
J003553-725301	00:35:53.11	-72:53:01.20	12.97
J003611-725405	00:36:11.43	-72:54:05.01	1.08
J003620-720948	00:36:20.13	-72:09:48.40	10.02
J003624-725342	00:36:24.89	-72:53:42.20	19.48
J003625-720855	00:36:25.07	-72:08:55.87	4.15
J003626-714632	00:36:26.15	-71:46:32.88	1.01
J003635-715136	00:36:35.31	-71:51:36.42	1.15
J003647-713604	00:36:47.67	-71:36:04.80	6.11
J003650-703939	00:36:50.09	-70:39:39.79	1.86
J003656-744422	00:36:56.49	-74:44:22.90	3.47
J003659-713809	00:36:59.16	-71:38:09.50	11.91
J003607-742918	00:36:07.35	-74:29:18.73	1.06
J003701-714900	00:37:01.61	-71:49:00.50	5.54
J003703-704724	00:37:03.37	-70:47:24.10	8.59
J003708-714001	00:37:08.03	-71:40:01.90	7.00
J003709-712054	00:37:09.48	-71:20:54.90	4.56
J003715-751412	00:37:15.44	-75:14:12.70	19.76
J003716-705641	00:37:16.31	-70:56:41.80	8.70
J003739-714113	00:37:39.68	-71:41:13.71	1.93
J003743-710736	00:37:43.08	-71:07:36.60	23.13
J003749-735127	00:37:49.11	-73:51:27.40	3.89
J003755-725157	00:37:55.69	-72:51:57.40	50.97
J003806-745028	00:38:06.66	-74:50:28.20	7.38
J003809-735023	00:38:09.10	-73:50:23.40	59.98
J003819-723404	00:38:19.94	-72:34:04.30	4.27

Table A2. Continued.

Name ATCA	R.A.$_{4800}$ (J2000)	Dec.$_{4800}$ (J2000)	S_6 (mJy)
J003824-742211	00:38:24.27	-74:22:11.80	76.80
J003850-720850	00:38:50.89	-72:08:50.60	3.88
J003851-720013	00:38:51.12	-72:00:13.50	2.39
J003851-731051	00:38:51.27	-73:10:51.60	21.91
J003857-724854	00:38:57.40	-72:48:54.20	3.37
J003920-720359	00:39:20.09	-72:03:59.40	4.70
J003927-715246	00:39:27.15	-71:52:46.50	8.57
J003936-742017	00:39:36.17	-74:20:17.50	8.34
J003939-735611	00:39:39.02	-73:56:11.77	2.19
J003940-714141	00:39:40.06	-71:41:41.70	23.12
J003941-714228	00:39:41.23	-71:42:28.90	3.53
J003943-705247	00:39:43.68	-70:52:47.50	11.25
J003947-713734	00:39:47.28	-71:37:34.90	27.83
J003907-724340	00:39:07.53	-72:43:40.61	2.58
J004025-723757	00:40:25.30	-72:37:57.40	4.13
J004029-703511	00:40:29.83	-70:35:11.78	4.09
J004033-751455	00:40:33.88	-75:14:55.96	2.37
J004047-714559	00:40:47.97	-71:45:59.60	175.50
J004048-733659	00:40:48.44	-73:36:59.10	48.13
J004051-712149	00:40:51.67	-71:21:49.69	1.89
J004112-715859	00:41:12.08	-71:58:59.70	4.87
J004125-734704	00:41:25.05	-73:47:04.30	4.42
J004125-705743	00:41:25.27	-70:57:43.30	59.18
J004127-740719	00:41:27.65	-74:07:19.36	2.05
J004143-721826	00:41:43.61	-72:18:26.55	2.71
J004145-714447	00:41:45.05	-71:44:47.40	3.57
J004159-720507	00:41:59.89	-72:05:07.00	9.62
J004202-730722	00:42:02.77	-73:07:22.60	37.55
J004205-711720	00:42:05.31	-71:17:20.40	7.92
J004209-721448	00:42:09.74	-72:14:48.00	3.59
J004211-722509	00:42:11.66	-72:25:09.19	1.75
J004226-730417	00:42:26.20	-73:04:17.90	19.95
J004226-751353	00:42:26.44	-75:13:53.00	14.82
J004228-742850	00:42:28.39	-74:28:50.41	2.38
J004230-745449	00:42:30.22	-74:54:49.60	4.72
J004239-723323	00:42:39.07	-72:33:23.70	5.50
J004306-732827	00:43:06.24	-73:28:27.80	5.46
J004312-710422	00:43:12.26	-71:04:22.50	14.10
J004318-714055	00:43:18.32	-71:40:55.80	8.80
J004320-712717	00:43:20.30	-71:27:17.30	6.21
J004325-703416	00:43:25.55	-70:34:16.29	6.32
J004328-704141	00:43:28.78	-70:41:41.00	182.90
J004331-721023	00:43:31.21	-72:10:23.40	8.44
J004333-705516	00:43:33.96	-70:55:16.10	6.58
J004334-713203	00:43:34.43	-71:32:03.40	12.97

Table A2. Continued.

Name ATCA	R.A.$_{4800}$ (J2000)	Dec.$_{4800}$ (J2000)	S_6 (mJy)
J004336-730223	00:43:36.99	-73:02:23.70	6.00
J004340-720346	00:43:40.23	-72:03:46.00	9.20
J004341-712225	00:43:41.83	-71:22:25.90	3.99
J004346-703808	00:43:46.36	-70:38:08.30	6.73
J004346-732315	00:43:46.88	-73:23:15.30	4.55
J004412-733310	00:44:12.79	-73:33:10.45	2.41
J004413-724301	00:44:13.26	-72:43:01.20	8.42
J004417-750216	00:44:17.50	-75:02:16.50	13.88
J004421-744317	00:44:21.01	-74:43:17.80	8.93
J004438-733709	00:44:38.69	-73:37:09.10	4.84
J004445-750403	00:44:45.42	-75:04:03.40	4.63
J004448-742510	00:44:48.01	-74:25:10.95	2.45
J004451-734537	00:44:51.99	-73:45:37.80	7.78
J004453-704846	00:44:53.79	-70:48:46.60	6.63
J004459-711438	00:44:59.79	-71:14:38.50	11.36
J004504-715611	00:45:04.50	-71:56:11.00	4.80
J004508-735146	00:45:08.37	-73:51:46.30	3.77
J004524-732251	00:45:24.64	-73:22:51.10	30.03
J004529-750136	00:45:29.33	-75:01:36.64	2.86
J004530-745052	00:45:30.04	-74:50:52.30	4.54
J004531-720401	00:45:31.86	-72:04:01.45	2.47
J004537-712319	00:45:37.39	-71:23:19.10	7.63
J004549-714931	00:45:49.45	-71:49:31.70	5.14
J004554-704644	00:45:54.85	-70:46:44.40	6.40
J004601-744003	00:46:01.95	-74:40:03.80	17.19
J004603-741332	00:46:03.61	-74:13:32.20	5.26
J004605-744752	00:46:05.58	-74:47:52.70	4.42
J004609-720153	00:46:09.37	-72:01:53.20	9.65
J004611-741757	00:46:11.79	-74:17:57.40	4.44
J004620-720153	00:46:20.53	-72:01:53.06	2.05
J004623-722720	00:46:23.21	-72:27:20.40	4.43
J004626-710039	00:46:26.10	-71:00:39.80	3.61
J004629-742506	00:46:29.00	-74:25:06.80	3.86
J004632-705856	00:46:32.19	-70:58:56.10	29.50
J004637-735358	00:46:37.95	-73:53:58.20	3.68
J004646-743407	00:46:46.59	-74:34:07.32	2.55
J004650-713921	00:46:50.78	-71:39:21.30	14.54
J004701-710146	00:47:01.38	-71:01:46.80	3.58
J004703-714955	00:47:03.77	-71:49:55.20	8.99
J004706-750237	00:47:06.09	-75:02:37.60	4.41
J004711-745930	00:47:11.94	-74:59:30.20	5.11
J004714-750255	00:47:14.23	-75:02:55.30	4.27
J004718-723947	00:47:18.68	-72:39:47.30	38.72
J004725-712726	00:47:25.31	-71:27:26.60	24.02
J004732-750102	00:47:32.31	-75:01:02.50	5.12

Table A2. Continued.

Name ATCA	R.A.$_{4800}$ (J2000)	Dec.$_{4800}$ (J2000)	S_6 (mJy)
J004750-705755	00:47:50.04	-70:57:55.30	12.72
J004808-741206	00:48:08.24	-74:12:06.00	45.82
J004816-711402	00:48:16.57	-71:14:02.60	7.70
J004825-720033	00:48:25.70	-72:00:33.93	1.92
J004832-743312	00:48:32.15	-74:33:12.87	2.37
J004832-710309	00:48:32.31	-71:03:09.93	5.86
J004837-733057	00:48:37.65	-73:30:57.60	4.70
J004843-740729	00:48:43.69	-74:07:29.40	4.09
J004850-725124	00:48:50.38	-72:51:24.20	5.62
J004851-710509	00:48:51.18	-71:05:09.30	7.18
J004807-741946	00:48:07.33	-74:19:46.95	2.00
J004901-734455	00:49:01.54	-73:44:55.90	5.08
J004907-710347	00:49:07.81	-71:03:47.10	10.52
J004916-732046	00:49:16.99	-73:20:46.30	4.97
J004918-745659	00:49:18.56	-74:56:59.20	27.13
J004918-721958	00:49:18.65	-72:19:58.20	3.56
J004923-712700	00:49:23.39	-71:27:00.70	8.03
J004924-710526	00:49:24.70	-71:05:26.70	6.52
J004930-721812	00:49:30.49	-72:18:12.60	5.36
J004933-721859	00:49:33.18	-72:18:59.90	7.03
J004936-741550	00:49:36.22	-74:15:50.90	11.10
J004936-724637	00:49:36.25	-72:46:37.10	7.29
J004937-705212	00:49:37.10	-70:52:12.00	46.95
J004953-715149	00:49:53.91	-71:51:49.80	8.96
J004956-723554	00:49:56.75	-72:35:54.00	27.65
J004958-720537	00:49:58.48	-72:05:37.10	3.76
J004908-744625	00:49:08.40	-74:46:25.59	2.17
J005015-723232	00:50:15.40	-72:32:32.10	5.25
J005020-712124	00:50:20.89	-71:21:24.00	5.53
J005022-744152	00:50:22.11	-74:41:52.00	3.46
J005024-705258	00:50:24.58	-70:52:58.70	4.71
J005040-715826	00:50:40.74	-71:58:26.02	4.35
J005041-703937	00:50:41.14	-70:39:37.90	12.71
J005057-731248	00:50:57.68	-73:12:48.30	3.57
J005008-734129	00:50:08.85	-73:41:29.82	2.59
J005112-712038	00:51:12.48	-71:20:38.00	3.81
J005115-713056	00:51:15.75	-71:30:56.10	6.46
J005117-705610	00:51:17.35	-70:56:10.10	6.57
J005117-734000	00:51:17.35	-73:40:00.80	29.83
J005140-731335	00:51:40.90	-73:13:35.20	10.00
J005141-725556	00:51:41.61	-72:55:56.30	21.29
J005146-730500	00:51:46.35	-73:05:00.83	2.10
J005201-721708	00:52:01.55	-72:17:08.00	3.90
J005204-721607	00:52:04.25	-72:16:07.70	4.12
J005207-733720	00:52:07.63	-73:37:20.00	3.61

Table A2. Continued.

Name ATCA	R.A.$_{4800}$ (J2000)	Dec.$_{4800}$ (J2000)	S_6 (mJy)
J005212-730852	00:52:12.82	-73:08:52.40	1.97
J005217-730155	00:52:17.47	-73:01:55.40	6.76
J005218-722707	00:52:18.94	-72:27:07.30	60.57
J005222-752544	00:52:22.34	-75:25:44.84	20.41
J005226-723630	00:52:26.03	-72:36:30.20	4.03
J005229-735944	00:52:29.14	-73:59:44.20	4.74
J005230-743754	00:52:30.86	-74:37:54.86	2.21
J005238-731244	00:52:38.18	-73:12:44.70	33.25
J005239-723818	00:52:39.50	-72:38:18.00	3.72
J005253-720133	00:52:53.63	-72:01:33.80	7.10
J005258-731148	00:52:58.47	-73:11:48.60	3.63
J005307-743906	00:53:07.10	-74:39:06.70	2.96
J005318-720857	00:53:18.43	-72:08:57.30	4.63
J005321-723531	00:53:21.89	-72:35:31.00	7.72
J005324-745551	00:53:24.17	-74:55:51.76	2.67
J005328-725523	00:53:28.93	-72:55:23.00	5.39
J005337-723144	00:53:37.81	-72:31:44.30	14.98
J005341-723928	00:53:41.87	-72:39:28.80	3.53
J005346-751443	00:53:46.86	-75:14:43.10	5.30
J005347-714959	00:53:47.50	-71:49:59.40	4.40
J005349-715856	00:53:49.35	-71:58:56.27	3.20
J005351-704000	00:53:51.69	-70:40:00.70	14.24
J005355-703804	00:53:55.75	-70:38:04.30	18.14
J005403-721344	00:54:03.97	-72:13:44.10	5.21
J005407-722423	00:54:07.35	-72:24:23.80	3.83
J005411-734016	00:54:11.72	-73:40:16.50	5.19
J005423-725256	00:54:23.70	-72:52:56.50	14.07
J005425-741729	00:54:25.79	-74:17:29.00	2.43
J005428-720156	00:54:28.80	-72:01:56.50	3.66
J005435-733848	00:54:35.04	-73:38:48.00	4.81
J005440-724504	00:54:40.02	-72:45:04.84	2.30
J005441-722945	00:54:41.92	-72:29:45.86	2.01
J005448-725350	00:54:48.43	-72:53:50.30	9.06
J005449-744935	00:54:49.42	-74:49:35.30	6.88
J005450-731646	00:54:50.01	-73:16:46.10	8.70
J005453-713135	00:54:53.22	-71:31:35.30	6.38
J005456-710342	00:54:56.47	-71:03:42.10	2.68
J005503-712102	00:55:03.57	-71:21:02.20	8.90
J005506-723721	00:55:06.91	-72:37:21.10	6.43
J005518-714449	00:55:18.49	-71:44:49.10	4.57
J005533-723123	00:55:33.51	-72:31:23.60	6.24
J005533-703950	00:55:33.97	-70:39:50.50	8.19
J005536-723523	00:55:36.13	-72:35:23.70	12.92
J005536-743926	00:55:36.99	-74:39:26.10	14.48
J005554-742235	00:55:54.24	-74:22:35.70	14.34

Table A2. Continued.

Name ATCA	R.A.$_{4800}$ (J2000)	Dec.$_{4800}$ (J2000)	S_6 (mJy)
J005555-710320	00:55:55.32	-71:03:20.50	4.55
J005557-722604	00:55:57.07	-72:26:04.00	52.37
J005600-720904	00:56:00.81	-72:09:04.60	3.98
J005607-703845	00:56:07.98	-70:38:45.70	25.61
J005611-710707	00:56:11.39	-71:07:07.20	211.70
J005621-715111	00:56:21.82	-71:51:11.20	5.48
J005632-735705	00:56:32.95	-73:57:05.40	8.17
J005636-740316	00:56:36.62	-74:03:16.50	26.63
J005643-725206	00:56:43.77	-72:52:06.10	23.36
J005652-712259	00:56:52.63	-71:22:59.20	20.94
J005703-721636	00:57:03.77	-72:16:36.10	6.01
J005706-741203	00:57:06.94	-74:12:03.30	3.06
J005715-733453	00:57:15.01	-73:34:53.10	4.97
J005715-704046	00:57:15.60	-70:40:46.20	74.28
J005721-740316	00:57:21.92	-74:03:16.40	8.82
J005727-751456	00:57:27.34	-75:14:56.20	5.47
J005729-723223	00:57:29.86	-72:32:23.50	4.13
J005730-744213	00:57:30.95	-74:42:13.90	8.89
J005732-741243	00:57:32.33	-74:12:43.90	82.71
J005737-731256	00:57:37.66	-73:12:56.70	2.23
J005737-710845	00:57:37.90	-71:08:45.50	11.84
J005742-724155	00:57:42.17	-72:41:55.70	11.04
J005756-723923	00:57:56.59	-72:39:23.10	5.72
J005756-740216	00:57:56.81	-74:02:16.54	2.80
J005808-745633	00:58:08.62	-74:56:33.80	3.85
J005812-735951	00:58:12.90	-73:59:51.80	3.36
J005816-723851	00:58:16.80	-72:38:51.50	10.58
J005816-721807	00:58:16.95	-72:18:07.70	9.13
J005820-713039	00:58:20.39	-71:30:39.10	12.65
J005821-732934	00:58:21.56	-73:29:34.24	2.03
J005823-720042	00:58:23.27	-72:00:42.70	3.56
J005826-723954	00:58:26.65	-72:39:54.00	10.22
J005831-740145	00:58:31.21	-74:01:45.00	5.96
J005833-725111	00:58:33.74	-72:51:11.79	2.26
J005837-743746	00:58:37.39	-74:37:46.20	3.70
J005842-722715	00:58:42.68	-72:27:15.70	4.80
J005845-744654	00:58:45.29	-74:46:54.70	3.86
J005845-730507	00:58:45.78	-73:05:07.30	3.82
J005849-743513	00:58:49.03	-74:35:13.10	6.44
J005904-704900	00:59:04.05	-70:49:00.00	18.85
J005905-745851	00:59:05.88	-74:58:51.00	5.57
J005906-735204	00:59:06.42	-73:52:04.60	23.74
J005906-745450	00:59:06.99	-74:54:50.30	5.30
J005913-722425	00:59:13.91	-72:24:25.71	3.30
J005929-751207	00:59:29.72	-75:12:07.73	2.67

Table A2. Continued.

Name ATCA	R.A.$_{4800}$ (J2000)	Dec.$_{4800}$ (J2000)	S_6 (mJy)
J005948-705027	00:59:48.62	-70:50:27.90	23.35
J005951-705200	00:59:51.22	-70:52:00.40	6.62
J010012-704028	01:00:12.55	-70:40:28.60	5.31
J010029-713826	01:00:29.70	-71:38:26.50	43.50
J010030-730007	01:00:30.63	-73:00:07.20	5.05
J010041-744629	01:00:41.09	-74:46:29.50	4.63
J010043-712137	01:00:43.42	-71:21:37.70	3.78
J010044-745416	01:00:44.53	-74:54:16.20	12.33
J010051-751358	01:00:51.00	-75:13:58.78	2.49
J010053-705016	01:00:53.22	-70:50:16.50	3.90
J010054-734039	01:00:54.42	-73:40:39.10	3.38
J010055-734217	01:00:55.77	-73:42:17.28	3.86
J010059-734515	01:00:59.04	-73:45:15.06	2.50
J010007-732636	01:00:07.63	-73:26:36.72	2.41
J010112-744059	01:01:12.32	-74:40:59.40	5.93
J010116-752027	01:01:16.48	-75:20:27.40	3.90
J010142-725514	01:01:42.00	-72:55:14.94	3.14
J010145-723223	01:01:45.54	-72:32:23.10	4.81
J010157-734251	01:01:57.91	-73:42:51.83	3.35
J010205-722447	01:02:05.25	-72:24:47.50	3.65
J010220-735322	01:02:20.95	-73:53:22.80	6.60
J010221-712722	01:02:21.88	-71:27:22.50	4.94
J010222-703723	01:02:22.02	-70:37:23.91	2.29
J010228-750030	01:02:28.73	-75:00:30.50	3.16
J010230-734734	01:02:30.28	-73:47:34.57	2.00
J010233-741536	01:02:33.77	-74:15:36.50	10.26
J010236-725040	01:02:36.88	-72:50:40.60	3.48
J010238-710211	01:02:38.72	-71:02:11.12	3.69
J010255-713633	01:02:55.41	-71:36:33.10	9.57
J010256-743530	01:02:56.38	-74:35:30.20	10.78
J010256-703852	01:02:56.51	-70:38:52.98	2.34
J010256-703948	01:02:56.88	-70:39:48.79	7.42
J010319-704647	01:03:19.32	-70:46:47.00	7.07
J010326-730021	01:03:26.15	-73:00:21.90	5.36
J010329-724721	01:03:29.55	-72:47:21.60	6.09
J010330-743430	01:03:30.61	-74:34:30.80	7.06
J010331-750704	01:03:31.61	-75:07:04.70	21.50
J010339-725042	01:03:39.23	-72:50:42.30	6.72
J010348-712406	01:03:48.52	-71:24:06.10	3.52
J010305-715334	01:03:05.00	-71:53:34.26	4.04
J010359-711254	01:03:59.11	-71:12:54.50	4.14
J010402-750836	01:04:02.91	-75:08:36.10	3.78
J010405-724342	01:04:05.32	-72:43:42.70	5.24
J010406-735126	01:04:06.28	-73:51:26.70	4.30
J010410-733805	01:04:10.92	-73:38:05.40	5.09

Table A2. Continued.

Name ATCA	R.A.$_{4800}$ (J2000)	Dec.$_{4800}$ (J2000)	S_6 (mJy)
J010412-705559	01:04:12.56	-70:55:59.80	4.25
J010422-744931	01:04:22.85	-74:49:31.10	4.88
J010425-711253	01:04:25.30	-71:12:53.76	2.16
J010425-742733	01:04:25.71	-74:27:33.60	6.38
J010431-720725	01:04:31.34	-72:07:25.10	12.11
J010434-740406	01:04:34.84	-74:04:06.72	1.79
J010441-713121	01:04:41.17	-71:31:21.70	18.38
J010443-745712	01:04:43.01	-74:57:12.50	1.18
J010446-722208	01:04:46.74	-72:22:08.70	5.30
J010457-703734	01:04:57.69	-70:37:34.90	49.31
J010515-735739	01:05:15.82	-73:57:39.60	4.95
J010523-731520	01:05:23.91	-73:15:20.20	7.94
J010525-722521	01:05:25.21	-72:25:21.70	11.87
J010530-721021	01:05:30.46	-72:10:21.80	3.33
J010532-721331	01:05:32.80	-72:13:31.30	9.47
J010536-743200	01:05:36.28	-74:32:00.00	16.55
J010536-740004	01:05:36.84	-74:00:04.50	11.94
J010541-720342	01:05:41.26	-72:03:42.00	4.50
J010544-750547	01:05:44.51	-75:05:47.00	8.74
J010556-714606	01:05:56.50	-71:46:06.10	19.23
J010557-710457	01:05:57.59	-71:04:57.70	12.26
J010558-732517	01:05:58.90	-73:25:17.20	4.93
J010559-745904	01:05:59.41	-74:59:04.30	10.35
J010506-712832	01:05:07.00	-71:28:32.79	2.77
J010507-723855	01:05:07.08	-72:38:55.57	2.56
J010610-744120	01:06:10.53	-74:41:20.16	3.47
J010612-734958	01:06:12.71	-73:49:58.40	5.02
J010618-705112	01:06:18.81	-70:51:12.70	3.62
J010621-704141	01:06:21.11	-70:41:41.30	6.51
J010633-714803	01:06:33.75	-71:48:03.45	1.34
J010643-712005	01:06:43.00	-71:20:05.10	3.45
J010645-741930	01:06:45.88	-74:19:30.70	5.15
J010648-725811	01:06:48.23	-72:58:11.70	4.27
J010653-721842	01:06:53.60	-72:18:42.43	1.17
J010656-731314	01:06:56.94	-73:13:14.32	1.21
J010700-735453	01:07:00.84	-73:54:53.75	2.72
J010708-714305	01:07:08.66	-71:43:05.20	7.46
J010717-732951	01:07:17.42	-73:29:51.40	5.71
J010739-742211	01:07:39.69	-74:22:11.04	1.80
J010742-715309	01:07:42.08	-71:53:09.20	4.61
J010743-751529	01:07:43.07	-75:15:29.10	5.00
J010748-705216	01:07:48.10	-70:52:16.20	5.12
J010749-714514	01:07:49.59	-71:45:14.80	3.47
J010756-712535	01:07:56.31	-71:25:35.40	5.34
J010759-710822	01:07:59.48	-71:08:22.80	8.61

Table A2. Continued.

Name ATCA	R.A.$_{4800}$ (J2000)	Dec.$_{4800}$ (J2000)	S_6 (mJy)
J010804-703902	01:08:04.56	-70:39:02.40	4.30
J010808-713948	01:08:08.13	-71:39:48.40	3.72
J010811-725734	01:08:11.21	-72:57:34.60	4.77
J010818-745517	01:08:18.45	-74:55:17.10	6.70
J010836-704706	01:08:36.79	-70:47:06.64	1.28
J010838-724712	01:08:38.90	-72:47:12.30	5.44
J010848-741930	01:08:48.03	-74:19:30.29	3.61
J010809-720909	01:08:09.31	-72:09:09.61	2.72
J010900-713316	01:09:00.47	-71:33:16.98	2.11
J010901-731812	01:09:01.55	-73:18:12.20	5.54
J010913-731731	01:09:13.09	-73:17:31.90	6.64
J010913-731138	01:09:13.11	-73:11:38.80	47.23
J010915-722946	01:09:15.04	-72:29:46.70	2.29
J010917-722039	01:09:17.25	-72:20:39.50	4.02
J010919-725601	01:09:19.68	-72:56:01.00	10.14
J010927-740554	01:09:27.92	-74:05:54.70	3.49
J010928-704207	01:09:28.30	-70:42:07.90	7.74
J010903-734923	01:09:03.80	-73:49:23.15	2.49
J010931-713453	01:09:31.42	-71:34:53.60	34.83
J010936-713827	01:09:36.59	-71:38:27.23	2.49
J010937-745700	01:09:37.90	-74:57:00.90	3.72
J010940-705001	01:09:40.16	-70:50:01.60	8.42
J010954-720720	01:09:54.61	-72:07:20.80	4.42
J011000-720821	01:10:00.87	-72:08:21.00	1.42
J011005-722648	01:10:05.40	-72:26:48.30	72.59
J011016-713941	01:10:16.59	-71:39:41.14	1.90
J011018-704813	01:10:18.53	-70:48:13.54	3.13
J011021-730435	01:10:21.36	-73:04:35.40	25.47
J011027-745103	01:10:27.79	-74:51:03.60	5.41
J011030-745349	01:10:30.80	-74:53:49.90	4.71
J011035-722810	01:10:35.99	-72:28:10.30	36.80
J011044-750949	01:10:44.38	-75:09:49.30	3.87
J011044-722846	01:10:44.65	-72:28:46.04	74.95
J011048-711418	01:10:48.03	-71:14:18.34	2.43
J011048-704956	01:10:48.92	-70:49:56.20	6.24
J011050-731426	01:10:50.01	-73:14:26.30	273.50
J011050-721025	01:10:50.52	-72:10:25.90	9.46
J011052-704255	01:10:52.64	-70:42:55.80	7.07
J011055-733241	01:10:55.00	-73:32:41.30	3.55
J011115-715137	01:11:15.15	-71:51:37.40	3.58
J011117-730155	01:11:17.10	-73:01:55.50	4.61
J011128-732936	01:11:28.36	-73:29:36.40	9.12
J011132-730208	01:11:32.27	-73:02:08.90	63.25
J011134-711413	01:11:34.18	-71:14:13.30	20.60
J011151-725125	01:11:51.96	-72:51:25.30	4.27

Table A2. Continued.

Name ATCA	R.A.$_{4800}$ (J2000)	Dec.$_{4800}$ (J2000)	S_6 (mJy)
J011157-734130	01:11:57.89	-73:41:30.50	7.26
J011223-703921	01:12:23.33	-70:39:21.20	4.60
J011223-741209	01:12:23.43	-74:12:09.20	13.97
J011226-732750	01:12:26.11	-73:27:50.30	13.60
J011226-724804	01:12:26.23	-72:48:04.50	4.71
J011231-750616	01:12:31.69	-75:06:16.30	16.03
J011251-752531	01:12:51.54	-75:25:31.52	12.28
J011302-714858	01:13:02.06	-71:48:58.90	4.27
J011302-740709	01:13:02.29	-74:07:09.00	3.72
J011319-743452	01:13:19.79	-74:34:52.40	12.10
J011332-740756	01:13:32.69	-74:07:56.90	10.36
J011336-735546	01:13:36.84	-73:55:46.10	3.34
J011339-714119	01:13:39.18	-71:41:19.70	3.96
J011344-711520	01:13:44.81	-71:15:20.10	12.10
J011352-731551	01:13:52.02	-73:15:51.70	4.47
J011357-742653	01:13:57.21	-74:26:53.70	4.49
J011357-711425	01:13:57.25	-71:14:25.60	12.47
J011405-732006	01:14:05.82	-73:20:06.80	30.64
J011413-721817	01:14:13.43	-72:18:17.90	3.82
J011427-733319	01:14:27.67	-73:33:19.70	3.21
J011432-732143	01:14:32.76	-73:21:43.40	54.12
J011435-715247	01:14:35.46	-71:52:47.70	14.57
J011449-705442	01:14:49.77	-70:54:42.04	3.13
J011449-742053	01:14:49.99	-74:20:53.46	3.84
J011459-732809	01:14:59.79	-73:28:09.13	3.41
J011500-703726	01:15:00.70	-70:37:26.40	3.33
J011505-743646	01:15:05.24	-74:36:46.80	3.34
J011518-713732	01:15:18.77	-71:37:32.01	2.66
J011527-723001	01:15:27.07	-72:30:01.50	7.46
J011527-720744	01:15:27.52	-72:07:44.82	2.70
J011534-720005	01:15:34.44	-72:00:05.50	6.40
J011551-741103	01:15:51.26	-74:11:03.68	2.01
J011551-723554	01:15:51.88	-72:35:54.75	2.47
J011552-713950	01:15:52.32	-71:39:50.40	3.50
J011559-705556	01:15:59.38	-70:55:56.57	2.15
J011559-710439	01:15:59.97	-71:04:39.90	6.17
J011603-744323	01:16:03.57	-74:43:23.80	7.16
J011605-735358	01:16:05.19	-73:53:58.00	4.37
J011606-743210	01:16:06.00	-74:32:10.20	3.32
J011609-742813	01:16:09.27	-74:28:13.30	9.93
J011611-733857	01:16:11.25	-73:38:57.80	26.30
J011611-711026	01:16:11.72	-71:10:26.60	7.95
J011615-732657	01:16:15.62	-73:26:57.90	12.40
J011628-731438	01:16:28.48	-73:14:38.30	11.35
J011636-712602	01:16:36.52	-71:26:02.50	3.77

Table A2. Continued.

Name ATCA	R.A.$_{4800}$ (J2000)	Dec.$_{4800}$ (J2000)	S_6 (mJy)
J011646-743531	01:16:46.13	-74:35:31.60	5.23
J011648-734240	01:16:48.58	-73:42:40.80	2.68
J011719-714122	01:17:19.70	-71:41:22.00	4.64
J011721-730918	01:17:21.60	-73:09:18.10	5.10
J011725-744703	01:17:25.17	-74:47:03.30	5.62
J011732-743338	01:17:32.01	-74:33:38.30	12.22
J011743-745545	01:17:43.97	-74:55:45.96	2.77
J011755-721907	01:17:55.63	-72:19:07.51	4.01
J011800-745001	01:18:00.52	-74:50:01.90	6.51
J011805-735032	01:18:05.87	-73:50:32.30	4.32
J011805-745822	01:18:05.88	-74:58:22.20	7.83
J011821-730724	01:18:21.43	-73:07:24.06	2.67
J011834-720645	01:18:34.92	-72:06:45.75	1.77
J011837-725724	01:18:37.23	-72:57:24.50	3.83
J011840-715216	01:18:40.37	-71:52:16.20	6.44
J011843-744435	01:18:43.42	-74:44:35.30	4.60
J011910-744206	01:19:10.23	-74:42:06.50	5.79
J011911-750148	01:19:11.04	-75:01:48.00	3.93
J011913-710827	01:19:13.45	-71:08:27.22	2.25
J011918-710530	01:19:18.63	-71:05:30.70	31.98
J011929-732908	01:19:29.69	-73:29:08.10	4.25
J011933-725931	01:19:33.86	-72:59:31.48	1.29
J011959-750315	01:19:59.28	-75:03:15.90	3.45
J012006-725019	01:20:06.31	-72:50:19.60	5.23
J012011-703601	01:20:11.51	-70:36:01.89	8.07
J012023-721955	01:20:23.84	-72:19:55.30	7.27
J012035-750635	01:20:35.79	-75:06:35.20	12.80
J012036-713336	01:20:36.41	-71:33:36.24	2.66
J012037-703844	01:20:37.60	-70:38:44.90	36.93
J012055-733455	01:20:55.46	-73:34:55.20	22.82
J012128-714338	01:21:28.22	-71:43:38.50	4.10
J012151-740009	01:21:51.24	-74:00:09.60	20.91
J012154-712001	01:21:54.47	-71:20:01.01	2.77
J012154-715529	01:21:54.71	-71:55:29.00	5.68
J012200-744638	01:22:00.76	-74:46:38.50	5.71
J012209-713950	01:22:09.31	-71:39:50.50	9.59
J012224-731120	01:22:24.00	-73:11:20.00	3.85
J012233-714723	01:22:33.78	-71:47:23.90	14.47
J012235-733817	01:22:35.75	-73:38:17.30	10.13
J012238-741016	01:22:38.39	-74:10:16.40	9.34
J012247-742632	01:22:47.08	-74:26:32.70	4.46
J012250-715042	01:22:50.49	-71:50:42.40	18.47
J012251-705427	01:22:51.92	-70:54:27.20	6.54
J012253-731429	01:22:53.43	-73:14:29.70	3.56
J012257-751506	01:22:57.40	-75:15:06.20	192.60

Table A2. Continued.

Name ATCA	R.A.$_{4800}$ (J2000)	Dec.$_{4800}$ (J2000)	S_6 (mJy)
J012311-732845	01:23:11.15	-73:28:45.80	10.96
J012311-745416	01:23:11.47	-74:54:16.60	5.14
J012311-751644	01:23:11.90	-75:16:44.30	4.50
J012312-741811	01:23:12.12	-74:18:11.90	3.61
J012314-741940	01:23:14.90	-74:19:40.10	3.67
J012317-723605	01:23:17.41	-72:36:05.00	4.33
J012317-734555	01:23:17.68	-73:45:55.70	3.93
J012319-703737	01:23:19.97	-70:37:37.40	13.84
J012320-734528	01:23:20.62	-73:45:28.10	5.18
J012323-735605	01:23:23.87	-73:56:05.90	14.79
J012324-740240	01:23:24.03	-74:02:40.10	5.76
J012330-721816	01:23:30.50	-72:18:16.20	8.45
J012349-735037	01:23:49.55	-73:50:37.40	45.90
J012352-744138	01:23:52.56	-74:41:38.70	13.87
J012306-711125	01:23:06.60	-71:11:25.91	2.17
J012415-734115	01:24:15.03	-73:41:15.61	2.17
J012415-704158	01:24:15.34	-70:41:58.10	3.57
J012417-711201	01:24:17.85	-71:12:01.30	7.10
J012430-752239	01:24:30.55	-75:22:39.50	22.38
J012433-712644	01:24:33.22	-71:26:44.40	11.99
J012519-722918	01:25:19.97	-72:29:18.20	10.46
J012525-714902	01:25:25.46	-71:49:02.20	5.17
J012528-722946	01:25:28.87	-72:29:46.70	4.90
J012535-735635	01:25:35.12	-73:56:35.20	4.76
J012539-732946	01:25:39.19	-73:29:46.28	2.87
J012546-731602	01:25:46.18	-73:16:02.60	19.73
J012549-705736	01:25:49.44	-70:57:36.60	7.63
J012549-715136	01:25:49.63	-71:51:36.60	3.79
J012552-740006	01:25:52.62	-74:00:06.80	3.56
J012559-735413	01:25:59.77	-73:54:13.00	6.53
J012616-730753	01:26:16.89	-73:07:53.50	10.94
J012625-705021	01:26:25.86	-70:50:21.60	12.77
J012629-732714	01:26:29.13	-73:27:14.40	19.94
J012639-731501	01:26:39.59	-73:15:01.50	17.19
J012651-731629	01:26:51.92	-73:16:29.58	3.51
J012655-751121	01:26:55.49	-75:11:21.10	22.78
J012714-705934	01:27:14.61	-70:59:34.50	11.79
J012733-713638	01:27:33.95	-71:36:38.40	20.58
J012750-705620	01:27:50.52	-70:56:20.91	8.63
J012750-731106	01:27:50.93	-73:11:06.50	7.62
J012758-720532	01:27:58.99	-72:05:32.32	7.51
J012805-741107	01:28:05.24	-74:11:07.60	4.12
J012811-751254	01:28:11.98	-75:12:54.00	60.55
J012816-730757	01:28:16.43	-73:07:57.10	3.39
J012829-734138	01:28:29.41	-73:41:38.40	6.60

Table A2. Continued.

Name ATCA	R.A.$_{4800}$ (J2000)	Dec.$_{4800}$ (J2000)	S_6 (mJy)
J012924-733147	01:29:24.76	-73:31:47.90	4.82
J012927-752439	01:29:27.15	-75:24:39.37	28.57
J012930-733310	01:29:30.29	-73:33:10.80	119.10
J012945-723243	01:29:45.16	-72:32:43.90	3.47
J013013-742025	01:30:13.38	-74:20:25.00	26.43
J013024-743926	01:30:24.83	-74:39:26.70	13.70
J013031-731744	01:30:31.97	-73:17:44.22	9.89
J013033-745835	01:30:33.58	-74:58:35.90	9.76
J013040-734633	01:30:40.52	-73:46:33.60	4.81
J013049-734621	01:30:49.57	-73:46:21.10	3.92
J013107-745844	01:31:07.02	-74:58:44.70	5.62
J013120-745743	01:31:20.24	-74:57:43.40	3.49
J013124-740038	01:31:24.60	-74:00:38.30	10.57
J013148-734944	01:31:48.05	-73:49:44.50	6.64
J013341-744610	01:33:41.48	-74:46:10.96	9.66
J013309-742914	01:33:09.02	-74:29:14.70	10.81

A.20 Related Paper 20

Haberl, F., Filipović, M. D., Bozzetto, L. M., Crawford, E. J., Points, S. D., Pietsch, W., De Horta, A. Y., Tothill, N., Payne, J. L., and Sasaki, M. (2012a). Multi-frequency observations of SNR J0453-6829 in the LMC. A composite supernova remnant with a pulsar wind nebula. *A&A*, 543:A154

My contribution was to assist in the data analysis. This is a 10% contribution.

A&A 543, A154 (2012)
DOI: 10.1051/0004-6361/201218971

Astronomy & Astrophysics

Multi-frequency observations of SNR J0453–6829 in the LMC

A composite supernova remnant with a pulsar wind nebula

F. Haberl[1], M. D. Filipović[2], L. M. Bozzetto[2], E. J. Crawford[2], S. D. Points[3], W. Pietsch[1], A. Y. De Horta[2], N. Tothill[2], J. L. Payne[2], and M. Sasaki[4]

[1] Max-Planck-Institut für extraterrestrische Physik, Giessenbachstraße, 85748 Garching, Germany
e-mail: fwh@mpe.mpg.de
[2] University of Western Sydney, Locked Bag 1797, Penrith South DC, NSW1797, Australia
[3] Cerro Tololo Inter-American Observatory, National Optical Astronomy Observatory, Cassilla 603, La Serena, Chile
[4] Institut für Astronomie und Astrophysik Tübingen, Sand 1, 72076 Tübingen, Germany

Received 6 February 2012 / Accepted 21 June 2012

ABSTRACT

Context. The Large Magellanic Cloud (LMC) is rich in supernova remnants (SNRs), which can be investigated in detail with radio, optical, and X-ray observations. SNR J0453–6829 is an X-ray and radio-bright remnant in the LMC, within which previous studies revealed the presence of a pulsar wind nebula (PWN), making it one of the most interesting SNRs in the Local Group of galaxies.
Aims. We study the emission of SNR J0453–6829 to improve our understanding of its morphology, spectrum, and thus the emission mechanisms in the shell and the PWN of the remnant.
Methods. We obtained new radio data with the Australia Telescope Compact Array and analysed archival *XMM-Newton* observations of SNR J0453–6829. We studied the morphology of SNR J0453–6829 from radio, optical, and X-ray images and investigated the energy spectra in the different parts of the remnant.
Results. Our radio results confirm that this LMC SNR hosts a typical PWN. The prominent central core of the PWN exhibits a radio spectral index $\alpha_{\rm Core}$ of -0.04 ± 0.04, while in the rest of the SNR shell the spectral slope is somewhat steeper with $\alpha_{\rm Shell} = -0.43 \pm 0.01$. We detect regions with a mean polarisation of $P \cong (12 \pm 4)$% at 6 cm and (9 ± 2)% at 3 cm. The full remnant is of roughly circular shape with dimensions of (31 ± 1) pc $\times$ (29 ± 1) pc. The spectral analysis of the *XMM-Newton* EPIC and RGS spectra allowed us to derive physical parameters for the SNR. Somewhat depending on the spectral model, we obtain for the remnant a shock temperature of around 0.2 keV and estimate the dynamical age to 12 000–15 000 years. Using a Sedov model we further derive an electron density in the X-ray emitting material of 1.56 cm^{-3}, typical for LMC remnants, a large swept-up mass of 830 $M_\odot$, and an explosion energy of 7.6×10^{50} erg. These parameters indicate a well evolved SNR with an X-ray spectrum dominated by emission from the swept-up material.

Key words. ISM: supernova remnants – ISM: individual objects: SNR J0453-6829 – Magellanic Clouds

1. Introduction

The Magellanic Clouds (MCs) are considered to be one of the most ideal environments when it comes to the investigation of various supernova remnant (SNR) types and their different evolutionary stages. While their relatively small distance is very favourable for detailed studies, the MCs are also located in one of the coldest parts of the radio sky, allowing us to detect and investigate radio emission with little disturbing Galactic foreground radiation (Haynes et al. 1991). As they are located outside of the Galactic plane, the influence of dust, gas and stars is small, reducing the absorption of soft X-rays. Particularly, the Large Magellanic Cloud (LMC) at a distance of 50 kpc (di Benedetto 2008), allows for detailed analysis of the energetics of various types of remnants. In the radio-continuum regime SNRs are well-known for their strong and predominantly non-thermal radio emission, which is characterised by a typical spectral index of $\alpha \sim -0.5$ (as defined by $S \propto \nu^{\alpha}$). However, this value shows a significant scatter due to the wide variety of SNR types and this variance can be used as an age indicator for the SNR (Filipović et al. 1998a).

SNRs have a significant influence on the structure of the interstellar medium (ISM). The appearance of spherically symmetric shell-like structures is very often perturbed by interaction with a non-homogeneous structure of the ISM. SNRs influence the behaviour, structure and evolution of the ISM. In turn, the evolution of SNRs is dependent on the environment in which they reside.

Here, we report on new radio-continuum and archival X-ray observations of SNR J0453–6829, one of five SNRs in the LMC (B0540-693, N157B, B0532-710, DEM L241 and SNR J0453–6829) with a known or candidate pulsar wind nebula (PWN) inside. SNR J0453–6829 was initially classified as an SNR based on the *Einstein* X-Ray survey by Long et al. (1981, source 1 in their catalogue) and Wang et al. (1991, their source 2). Mathewson et al. (1983) catalogued this object based on studies of optical and MOlonglo Synthesis Telescope (MOST) survey data, and reported an optical size of $140'' \times 131''$. SNR J0453–6829 is also listed in the 408 MHz MC4 catalogue of Clarke et al. (1976) as a distinctive point-like radio source, for which Mathewson et al. (1983) later re-measured a flux density of 350 mJy. Mills et al. (1984) detected this source with specific MOST pointings and reported a rather flat spectral index of $\alpha = -0.38$. ROSAT detected X-ray emission from SNR J0453–6829 during the all-sky survey (Filipović et al. 1998b) and in deeper pointed observations using the PSPC (source 670 in the catalogue of Haberl & Pietsch 1999) and HRI detector (source 8 in Sasaki et al. 2000).

Filipović et al. (1998a) added further confirmation from radio data over a wide frequency range. Williams et al. (1999) classified it as an SNR with a "diffuse face". Hughes et al. (1998) presented X-ray spectra based on ASCA observations. Their spectral modelling did not take into account the hard X-ray emission of the PWN, which was discovered later, and therefore overestimated its temperature. The most detailed study of SNR J0453–6829 was performed by Gaensler et al. (2003) based on high resolution radio data obtained in 2002 with the Australia Telescope Compact Array (ATCA) and *Chandra* X-ray data from 2001. This lead to the discovery of the PWN inside the SNR and an age estimate of around 13 000 years. Blair et al. (2006) reported no detection at far ultraviolet wavelengths based on data from the FUSE (Far Ultraviolet Spectroscopic Explorer) satellite. Williams et al. (2006) detected this SNR in their *Spitzer* IR surveys as the object with the highest 70 μm to 24 μm flux ratio of any SNR. However, due to high background emission at 70 μm, in particular in the south western region of the remnant, they could only investigate the northern rim of the SNR shell. No radio pulsar within the area of SNR J0453–6829 was found in the systematic search within the LMC performed by Manchester et al. (2006). Also Payne et al. (2008) did not detect SNR J0453–6829 in their optical spectroscopic survey of LMC SNRs. Finally, Lopez et al. (2009) classified this LMC object based on its circular morphology as a core-collapse SNR.

2. Observations and data reduction

2.1. Radio-continuum

We observed SNR J0453–6829 with the ATCA on October 5, 1997, with the array configuration EW375 (ATCA Project C634), at wavelengths of 3 cm and 6 cm (8640 MHz and 4800 MHz). The observations were carried out in the "snapshot" mode, totalling ~1 h of integration time over a 12 h period. Source PKS B1934-638 was used for primary calibration and source PKS B0530-727 for secondary calibration. In addition to our own observations, we included unpublished 3 cm and 6 cm observations from project C1074 (Gaensler et al. 2003) and mosaic data taken from project C918 (Dickel et al. 2010). When combined together, all 3 cm and 6 cm observations of SNR J0453–6829 total ~11 h of integration time. Baselines formed with the 6th ATCA antenna were excluded, as the other five antennas were arranged in a compact configuration.

The MIRIAD (Sault et al. 1995) and KARMA (Gooch 1996) software packages were used for reduction and analysis. More information on the observing procedure and other sources observed in this session can be found in Bojičić et al. (2007), Crawford et al. (2008b,a, 2010), Čajko et al. (2009), and Bozzetto et al. (2010, 2012a,b). Images were constructed using the MIRIAD multi-frequency synthesis package (Sault & Wieringa 1994). Deconvolution was achieved with the CLEAN and RESTOR tasks with primary beam correction applied using the LINMOS task. Similar procedures were used for the *U* and *Q* stokes parameters.

The ATCA 3 cm image is shown in Fig. 1 together with 6 cm contours. We also reanalysed the 20 cm and 13 cm observations from Gaensler et al. (2003, ATCA Project C1074) and, while we achieved slightly better resolution and rms noise, the estimated flux densities stay essentially the same (Fig. 1). We measured the flux density of SNR J0453–6829 at six frequencies, which are summarised in Table 1. For the 36 cm (0.843 MHz, MOST) measurement we used the unpublished image described by Mills et al. (1984) and for 20 cm (1.388 GHz, ATCA project C373) the

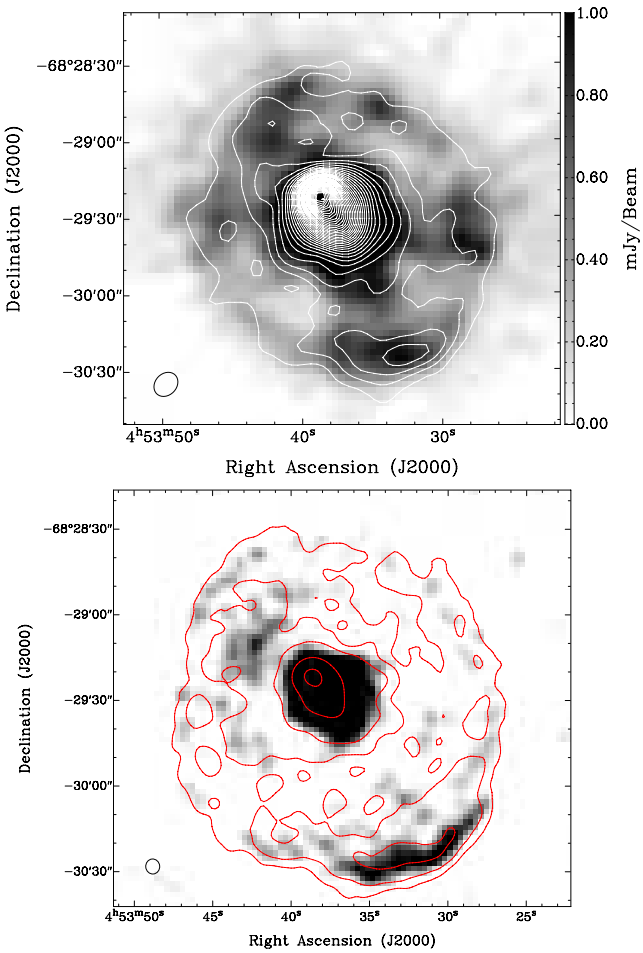

Fig. 1. ATCA observations of SNR J0453–6829. *Top*: 3 cm (8.6 GHz) image overlaid with 6 cm (4.8 GHz) contours. The contours are from 0.3 to 12.0 mJy/beam in steps of 0.3 mJy/beam with a beam size of 10.3″ × 8.4″. *Bottom*: 20 cm (1.4 GHz) image overlaid with 13 cm (2.4 GHz) contours. The contours are 0.12, 0.4, 1, 4 and 8 mJy/beam with the 20 cm image beam size of 5.2″ × 4.9″. Beam sizes are indicated in the bottom left corners.

image from Hughes et al. (2007). We took the 20 cm (1.4 GHz) and 13 cm (2.4 GHz) measurements from Gaensler et al. (2003) and added measurements at 20 cm (1.4 GHz) from the mosaics presented by Filipović et al. (2009) and Hughes et al. (2007). The main source of uncertainty in the measured flux densities is the definition of the area best representing the SNR, which dominates the statistical error. Based on different trials, we estimate that the combined flux density errors from all radio images used in this study (apart from 73 cm where the error is in order of 20%; Mathewson et al. 1983; Clarke et al. 1976), are ~10% at each given frequency. Using the flux densities from Table 1, we estimated spectral indices for the PWN ($\alpha_{\rm Core} = -0.04 \pm 0.04$), the outer SNR shell excluding the core ($\alpha_{\rm Shell} = -0.43 \pm 0.01$), and the whole SNR ($\alpha_{\rm Total} = -0.39 \pm 0.03$); see Fig. 2.

In Fig. 3 we show the spatial distribution of the spectral index for SNR J0453–6829 derived from wavelengths of 20 cm, 13 cm, 6 cm, and 3 cm. This image was formed by reprocessing all observations to a common $u - v$ range, and then fitting $S \propto \nu^{\alpha}$ pixel by pixel using all four images simultaneously. From this image, we can see that the vicinity around the central compact object exhibits relatively flat spectra with indices in the range $-0.2 < \alpha < +0.2$, while the rest of the SNR exhibits spectra with $\alpha \sim -0.35$ to -0.7, typical for a standard SNR.

Table 1. Integrated flux density of SNR J0453–6829.

ν (GHz)	λ (cm)	ATCA Project	rms (mJy)	Beam size ($''$)	$S_{\rm Core}$ (mJy)	$S_{\rm Shell}$ (mJy)	$S_{\rm Total}$ (mJy)	Reference
0.408	73	MOST	50	157.3×171.6	—	—	350	Mathewson et al. (1983)
0.843	36	MOST	0.4	43	57	171	228	This work
1.388	20	C373	1.2	40	45	140	185	This work – MOSAIC
1.400	20	C1074	0.1	7.3×6.7	46	140	186	Gaensler et al. (2003)
1.400	20	C1074, C373	0.05	5.2×4.9	46	140	185	This work
2.400	13	C1074	0.07	9.2×8.4	46	105	151	Gaensler et al. (2003)
2.400	13	C1074	0.04	7.8×7.3	48	105	153	This work
4.790	6	C634, C918, C1074	0.1	10.3×8.4	48	81	129	This work
8.640	3	C634, C918, C1074	0.1	10.3×8.4	46	64	100	This work

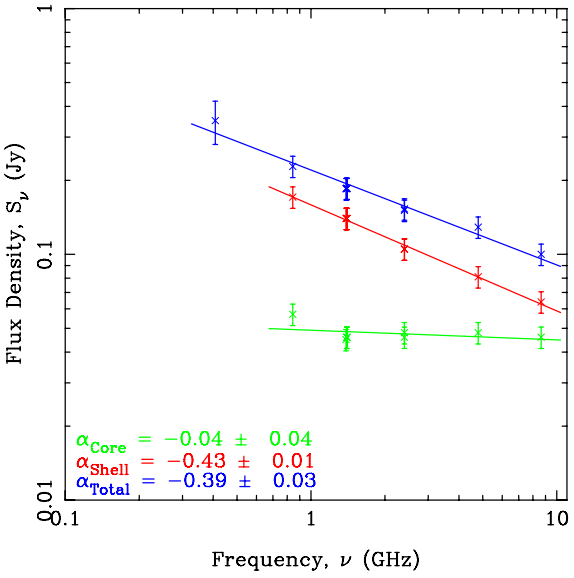

Fig. 2. Radio-continuum spectrum of SNR J0453–6829. The lines represent power-law fits to the flux densities of the core (green), shell (red) and combined core and shell (blue).

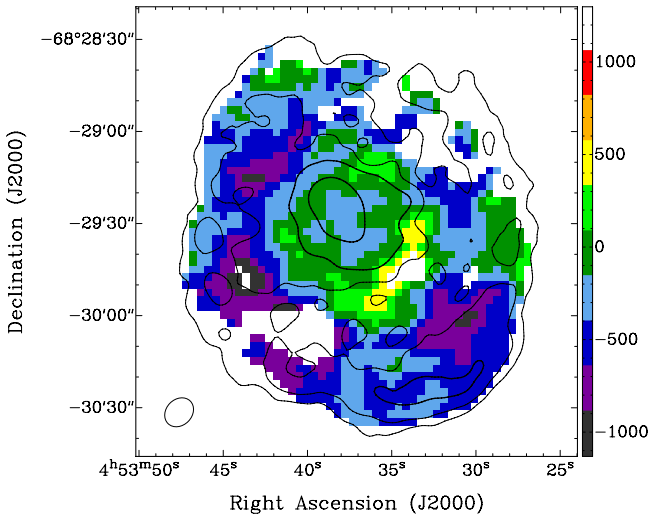

Fig. 3. Spectral index map of SNR J0453–6829 using wavelengths of 3 cm, 6 cm, 13 cm, and 20 cm. The sidebar gives the spectral index scale, e.g. −500 corresponds to $\alpha = -0.5$. Contours (from 13 cm) are 0.12, 0.4, 1 and 4 mJy/beam. The beam size of $10.3'' \times 8.4''$ is indicated in the bottom left corner.

Linear polarisation images of SNR J0453–6829 at 6 cm and 3 cm were created using the *Q* and *U* Stokes parameters and are illustrated in Fig. 4. The fractional polarisation has been evaluated using the the standard MIRIAD task IMPOL. The majority of the polarised emission is seen in the core region. At 6 cm, the SNR core shows a mean fractional polarisation of ∼7% whilst along the shell (at the southern side of the SNR), there is a pocket of quite strong uniform polarisation, with a mean value of ∼32% (Fig. 4, top) which corresponds to the observed total intensity brightening and possibly indicates varied dynamics along the shell. At 3 cm the mean fractional polarisation is ∼9%. Our estimated peak value is $P \cong 44 \pm 12\%$ at 6 cm and $12 \pm 6\%$ at 3 cm.

2.2. X-rays

SNR J0453–6829 was observed with the instruments of the *XMM-Newton* satellite. The observation (Obs. Id. 0062340101) was performed in March 2001 and here we present the results of the analysis of the X-ray data obtained by the European Photon Imaging Cameras (EPIC) and the Reflection Grating Spectrometers (RGS). The EPIC instruments were operated in full imaging modes using the medium optical blocking filters. Using the EPIC MOS1, MOS2 and pn CCDs yields sensitive X-ray observations of a ∼30′ field in the 0.15–10 keV energy band. Technical descriptions of the EPIC cameras can be found in Turner et al. (2001) and Strüder et al. (2001). The two RGS provide high-resolution X-ray spectra in the 0.3−2 keV band (den Herder et al. 2001). A summary of the observations with the instrumental setups is given in Table 2. The *XMM-Newton* data were analysed with SAS v10.0.0[1]. The data were affected by background flaring activity of moderate intensity. To produce images and spectra from the EPIC data we therefore removed intervals of high background while for the RGS the background level was below the recommended threshold (2 cts s^{-1} in CCD number 9 of the instrument) and we used the full exposure time for spectral extraction. The final net exposure times used for spectral analysis are listed in Table 2. For the EPIC spectra we extracted events subject to the canonical set of valid pixel patterns (0 to 12 for MOS; 0 to 4 for pn) and rejecting events from pixels flagged as bad. SNR J0453–6829 is of roughly circular shape with a diameter of about 2′ (Gaensler et al. 2003), which causes a broadening of emission lines in the RGS spectra. This was taken into account when creating the response files with the task RGSRMFGEN by supplying the intensity profile of the remnant in the direction of the dispersion axis. This was created from an EPIC-pn image in the 0.2−2.0 keV

[1] Science Analysis Software (SAS): http://xmm.esac.esa.int/sas/

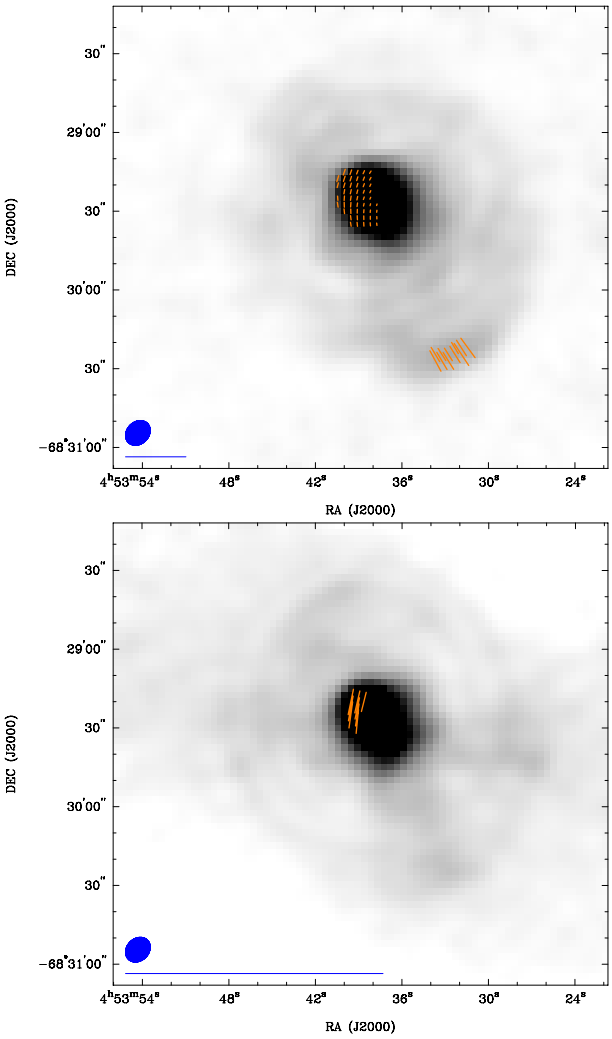

Fig. 4. Radio observations of SNR J0453–6829 at 6 cm (*top*) and 3 cm (*bottom*) matched to the 6 cm resolution. The blue circle in the lower left corner of the images represents the synthesised beam width of $10.3'' \times 8.4''$. The length of the vectors represent the fractional polarised intensity at each position, and the orientation of the vectors indicates the mean position angle of the electric field (averaged over the observing bandwidth not corrected for Faraday rotation). The blue line below each circle represents the length of a polarisation vector of 100%.

Table 2. *XMM-Newton* observation of SNR J0453–6829 on 2001-03-29.

Instrument[a] configuration	Start time (UT)	End time (UT)	Exposure[b] (s)
EPIC MOS1 FF	11:47:15	17:39:19	7366
EPIC MOS2 FF	11:47:15	17:39:19	7370
EPIC pn eFF	13:00:34	17:40:02	3619
RGS1 Spectro	11:40:55	17:41:01	20 820
RGS2 Spectro	11:40:55	17:41:01	20 440

Notes. [(a)] FF: full frame CCD readout mode with 2.6 s for MOS; EFF: pn "extended FF" with 200 ms frame time; [(b)] net exposure time used for spectral analysis after removing intervals of high background.

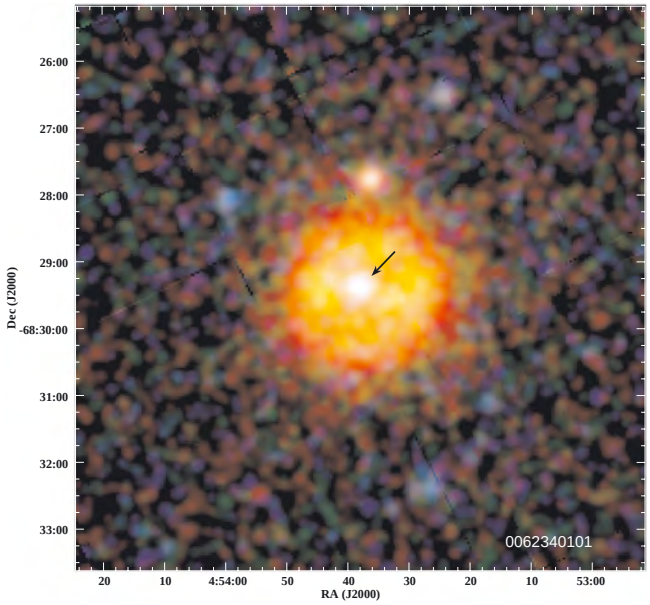

Fig. 5. Combined EPIC colour image of the field around SNR J0453–6829. Red, green, and blue colours denote X-ray intensities in the 0.2–1.0, 1.0–2.0 and 2.0–4.5 keV bands. The strong soft X-ray emission from the SNR shell appears in yellow, while the bright white spot in the centre of the SNR (marked with a black arrow) is caused by the emission from the PWN. Unrelated point sources are seen around the remnant.

band. A colour image produced from the combined EPIC data is shown in Fig. 5. The PWN at the centre of the SNR cannot be resolved by the *XMM-Newton* instruments. Therefore, we extracted X-ray spectra from the full emission region of the remnant, including the PWN, and modelled the emission from the SNR and the PWN with different emission components.

All *XMM-Newton* spectra were modelled simultaneously using XSPEC (Arnaud 1996) version 12.7.0u, only allowing one relative normalisation factor for each instrument (using the EPIC pn spectrum as a reference with the factor fixed at 1.0). We fitted two-component models comprising of a thermal plasma emission and a power-law component, representing the thermal X-ray emission from the SNR and the harder, non-thermal emission from the PWN, respectively. For the plasma emission we used different models available in XSPEC and report here on the results for the fits using either the plane-parallel shock (vpshock) model or the Sedov (vsedov) model (Borkowski et al. 2001). For both cases we used NEI-version 2.0 and allowed some chemical elemental abundances to vary in the fit. For elements which do not contribute strongly to the X-ray spectra, the abundance was fixed to 0.5 solar, as is typical in the LMC (Russell & Dopita 1992). The solar abundance table was taken from Wilms et al. (2000). Both, thermal and non-thermal emission components in the model were attenuated by two absorption components along the line of sight, one accounting for the Galactic foreground absorption with a column density of 6×10^{20} cm^{-2} and solar abundances, and one for the absorption in the LMC with the column density as a free parameter and abundances set to 0.5 solar for all elements heavier than He. For the absorption and emission components in the LMC a radial velocity of 278 km s^{-1} (corresponding to a redshift of 9.27×10^{-4} Richter et al. 1987) was adopted. The slope of the power-law was not well constrained in either model variant and we fixed the photon index at 2.0 (typical values for PWN are between 1.5 and 2.2 Kaspi et al. 2006). For the vpshock model we also fixed the lower parameter τ_l of the ionisation time-scale range $\tau_l < \tau_u$ at 10^8 s cm^{-3}. The mean shock temperature and the electron temperature immediately behind the shock front can both be fitted by the Sedov model. First trial fits resulted in values fully consistent within their errors

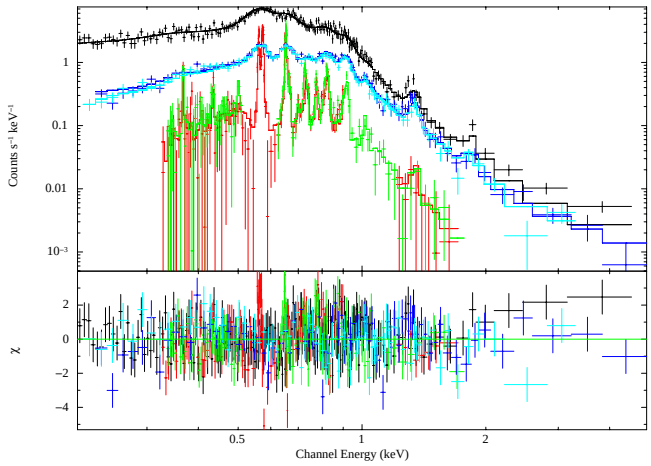

Fig. 6. Combined fit to the EPIC (pn: black, MOS1: blue, MOS2: light blue) and RGS (red: RGS1, green: RGS2) spectra of SNR J0453–6829. The data are denoted by the crosses with error bars and the histograms represent the best-fit model. In the lower panel the residuals are plotted in units of σ. The spectral extraction includes the emission from the SNR shell and the PWN and the model consists of thermal plasma emission (Sedov model) from the shell and a power-law from the PWN.

Table 3. Spectral fits to the *XMM-Newton* spectra of SNR J0453–6829 including its PWN.

Model vpshock (χ^2_r = 1.48 for 574 d.o.f.)		
Component	Parameter	Value[b]
LMC absorption	N_H (10^{21} cm^{-2})	1.52 (1.39–1.69)
shock temperature	kT (eV)	250 (234–269)
abundance[a]	N	0.052 (0.029–0.073)
abundance	O	0.104 (0.094–0.113)
abundance	Ne	0.17 (0.15–0.19)
abundance	Mg	0.31 (0.25–0.36)
abundance	Si	0.85 (0.54–1.18)
abundance	Fe	0.20 (0.18–0.23)
ionisation time scale	τ_u (10^{11} s cm^{-3})	7.0 (5.0–9.0)
Model vsedov (χ^2_r = 1.33 for 574 d.o.f.)		
Component	Parameter	Value
LMC absorption	N_H (10^{21} cm^{-2})	1.05 (0.98–1.17)
shock/electron temp.	kT (eV)	168 (164–173)
abundance	N	0.093 (0.057–0.133)
abundance	O	0.20 (0.17–0.23)
abundance	Ne	0.33 (0.28–0.39)
abundance	Mg	0.52 (0.42–0.62)
abundance	Si	0.81 (0.50–1.14)
abundance	Fe	0.39 (0.34–0.44)
ionisation time scale	τ (10^{13} s cm^{-3})	2.4 (>1.0)

Notes. [a] Elemental abundances are specified relative to solar (Wilms et al. 2000). [b] 90% confidence ranges for one parameter of interest are given in parenthesis.

and in the following fits we forced the two temperatures to be the same.

Both models have the same number of degrees of freedom (d.o.f.) and the Sedov model yields a formally better fit (see Table 3). The *XMM-Newton* spectra, with the best-fit Sedov model, are shown in Fig. 6. The best fit parameters, which were free in the fit, are summarised in Table 3 for both models. The total observed flux in the 0.2–10 keV band is 5.2×10^{-12} erg cm^{-2} s^{-1} with a 12.0% contribution of the power-law (derived from the EPIC-pn spectrum for the Sedov model). This converts to an absorption corrected luminosity of 7.0×10^{37} erg s^{-1}.

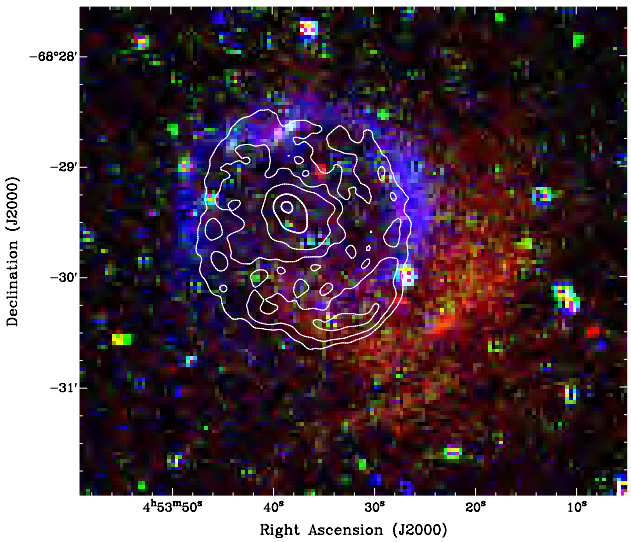

Fig. 7. MCELS composite optical image (RGB = H_α,[S II], [O III]) of SNR J0453–6829 overlaid with 13 cm contours. The contours are 0.12, 0.4, 1, 4 and 8 mJy/beam.

2.3. Optical

The Magellanic Cloud Emission Line Survey (MCELS)[2] was carried out at the 0.6 m University of Michigan/CTIO Curtis Schmidt telescope, equipped with a SITE 2048 × 2048 CCD, which gave a field of 1.35° × 1.35° at a scale of 2.4″ × 2.4″ pixel^{-1} (Smith et al. 2006). Both the LMC and SMC were mapped in narrow bands corresponding to Hα, [O III] (λ = 5007 Å), and [S II] (λ = 6716, 6731 Å), plus matched red and green continuum bands. All the data have been continuum subtracted, flux-calibrated and assembled into mosaic images. The region around SNR J0453–6829 is shown in Fig. 7 which demonstrates that [O III] emission dominates around the outer edge of the SNR. We also note the enhanced H_α emission in the south-west direction adjacent to the SNR.

3. Discussion

The SNR J0453–6829 in the LMC shows a prominent central core in radio and X-ray images, which is interpreted as a PWN (Gaensler et al. 2003). The PWN is surrounded by a slightly elongated shell centred at RA(J2000) = $4^h53^m37^s.2$, Dec(J2000) = –68°29′30″ for which we derive a size of (128″ ± 4″) × (120″ ± 4″) (corresponding to (31 ± 1 pc) × (29 ± 1 pc) at a distance of 50 kpc) from the 13 cm radio data (obtained at position angles of 20° and 110°, running from north to east). The shell radio emission shows brightening along its southern rim. Our size estimate is in agreement with the diameter previously reported from radio data by Gaensler et al. (2003). From the intensity profile of the EPIC data we estimate a size of ∼140″ (roughly in east-west direction, at 10% of maximum intensity), which corresponds to ∼130″ corrected for the angular resolution of the telescope. For a better estimate we re-analysed the *Chandra* data from 2001 presented by (Gaensler et al. 2003). From the *Chandra* image we measure 128″ ± 4″(31±1 pc) as the

[2] MCELS: http://www.ctio.noao.edu/mcels/

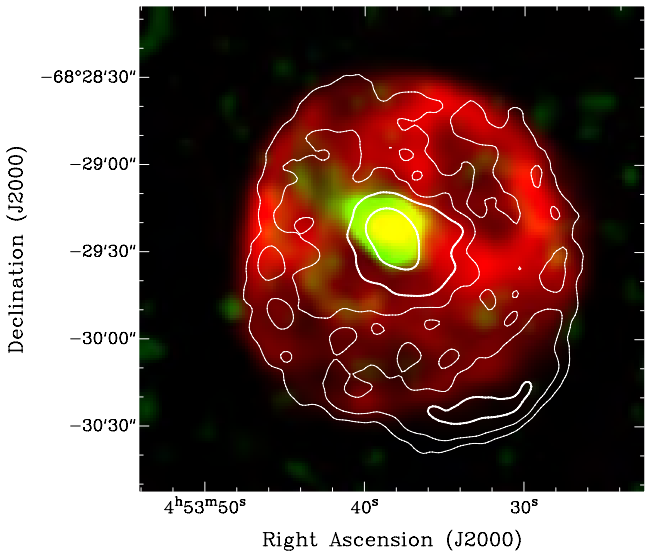

Fig. 8. *Chandra* colour image of SNR J0453–6829 in the 0.3–2.0 keV (red) and 2.0–4.0 keV (green) energy bands overlaid with 13 cm contours. The contours are 0.12, 0.4, 1 and 4 mJy/beam and the *Chandra* image was smoothed to the same resolution as the radio image.

largest extent, which is consistent with the radio extent (Fig. 8). So in the following considerations we assume a radius of 15.5 pc.

To estimate the age of the SNR from the vpshock model we used the relation $t_y = 3.8 \times 10^2 R_{pc}(kT)_{keV}^{-1/2}$ from Xu et al. (2005) and assume the temperature derived from X-ray spectral modelling (0.25 keV) and the radius of the SNR, which results in ∼11.8 kyr, consistent with the age inferred by Gaensler et al. (2003) from a preliminary X-ray spectral modelling. Also using a similar Sedov model and following Owen et al. (2011) who applied it to the spectrum of the SMC SNR IKT 16, we derive – with a shock temperature of 0.17 keV, and the normalisation of the Sedov model fit of 3.74×10^{-2} cm^{-5} – the following physical parameters for SNR J0453–6829: electron density in the X-ray emitting material of 1.56 cm^{-3}, dynamical age of 15.2 kyr, swept-up mass of 830 $M_\odot$ and an explosion energy of 7.6×10^{50} erg. Our estimate for the density is higher than that derived by Hughes et al. (1998) from ASCA observations (without knowledge of the PWN contributing to the X-ray spectrum of the remnant) and consistent with the average value of the other LMC SNRs in that work. This directly reflects the higher density of the ISM in the LMC in comparison to the SMC (van der Heyden et al. 2004).

The shock temperature (and electron temperature in our Sedov modelling) is very low compared to other remnants in the MCs. The whole SMC sample modelled by van der Heyden et al. (2004) and Filipović et al. (2008) in a similar way exhibits temperatures between 0.26 keV and 1.8 keV. The low temperature leads to a relatively high dynamical age for SNR J0453–6829. The high swept-up mass is also consistent with an SNR well evolved into its Sedov phase. As discussed in van der Heyden et al. (2004) the higher ISM density and higher abundances in the LMC compared to the SMC can lead to a faster evolution to the radiative cooling stage.

The abundances derived from our spectral analysis exhibit some model dependences, but are generally consistent or somewhat lower than average abundances in the ISM of the LMC. The only exception is Si which is overabundant with respect to the other elements. This suggests that the X-ray spectrum is dominated by emission from swept-up ISM material, which makes it difficult to draw conclusions on the type of supernova explosion from abundance measurements. In the case of SNR J0453–6829 the association of the PWN with the remnant and its morphology favour a core-collapse supernova (Lopez et al. 2009).

The radio spectral index of $\alpha_{Shell} = -0.43$, confirms the non-thermal nature of the SNR shell emission in the radio band, while the flat spectral index for the core of $\alpha_{Core} = -0.04$ is typical for a PWN. The overall spectral index of $\alpha = -0.39$ is slightly "flatter" in comparison with typical values of −0.5 for SNRs (Mathewson et al. 1985; Filipović et al. 1998a). The radio spectra definitely confirm the PWN nature of the central object. At higher frequencies (Fig. 2) the flux density decreases as expected whereas at lower frequencies non-thermal radiation of the shell dominates. Overall, the radio-continuum properties of SNR J0453–6829 are very similar to SNR B0540–693, the most prominent SNR with a PWN in the LMC (Manchester et al. 1993).

Mathewson et al. (1983) found distinctive optical connections to X-ray and radio features of this SNR. As can be seen in the MCELS images (Fig. 7), the [O III] emission dominates in the outer parts of the remnant. This could indicate an oxygen-rich type of SNR and suggests a type Ib SN event – the explosion of a massive O, B, or WR star (Arbutina & Urošević 2005). We also note that prominent Hα emission is visible in the south-west, which might suggest that higher density ISM material is causing the brightening in the radio shell emission at the outer rim of the SNR in this direction. While no molecular clouds are reported in this region (Fukui et al. 2008; Kawamura et al. 2009), we do note that SNR J0453–6829 lies in a region of low H I column density with the rim density highest in the south west (Kim et al. 1998, 1999). The radio spectral index (Fig. 3) in this south-west region indicates non-thermal emission ($\alpha \sim -0.4$). Careful comparison (after correcting for the rotated presentation) of the 24 and 70 μm infra-red data shows no correspondence between the enhanced background reported by Williams et al. (2006) and SNR J0453–6829. In contrast however, the *Chandra* image reveals only weak X-ray emission at the location of the bright radio feature. This could be explained by the higher density material being located in front of the rim of the SNR, suppressing the X-rays, or, together with the high polarisation of the 6 cm radio emission in this area, might favour a locally increased magnetic field strength enhancing the non-thermal radio emission. Future spatially resolved X-ray spectroscopy should be able to resolve this question.

Acknowledgements. This publication is partly based on observations with *XMM-Newton*, an ESA Science Mission with instruments and contributions directly funded by ESA Member states and the USA (NASA). The *XMM-Newton* project is supported by the Bundesministerium für Wirtschaft und Technologie/Deutsches Zentrum für Luft- und Raumfahrt (BMWI/DLR, FKZ 50 OX 0001) and the Max-Planck Society. We used the KARMA software package developed by the ATNF. The Australia Telescope Compact Array is part of the Australia Telescope which is funded by the Commonwealth of Australia for operation as a National Facility managed by CSIRO. The Magellanic Clouds Emission Line Survey (MCELS) data are provided by R. C. Smith, P. F. Winkler, and S. D. Points. The MCELS project has been supported in part by NSF grants AST-9540747 and AST-0307613, and through the generous support of the Dean B. McLaughlin Fund at the University of Michigan, a bequest from the family of Dr. Dean B. McLaughlin in memory of his lasting impact on Astronomy. The National Optical Astronomy Observatory is operated by the Association of Universities for Research in Astronomy Inc. (AURA), under a cooperative agreement with the National Science Foundation.

References

Arbutina, B., & Urošević, D. 2005, MNRAS, 360, 76
Arnaud, K. A. 1996, in Astronomical Data Analysis Software and Systems V, ASP Conf. Ser., 101, 17

Blair, W. P., Ghavamian, P., Sankrit, R., & Danforth, C. W. 2006, ApJS, 165, 480
Bojičić, I. S., Filipović, M. D., Parker, Q. A., et al. 2007, MNRAS, 378, 1237
Borkowski, K. J., Lyerly, W. J., & Reynolds, S. P. 2001, ApJ, 548, 820
Bozzetto, L. M., Filipović, M. D., Crawford, E. J., et al. 2010, Serbian Astron. J., 181, 43
Bozzetto, L. M., Filipović, M. D., Crawford, E. J., et al. 2012a, MNRAS, 420, 2588
Bozzetto, L. M., Filipovic, M. D., Crawford, E. J., et al. 2012b, Rev. Mex. Astron. Astrofis., 48, 41
Čajko, K. O., Crawford, E. J., & Filipović, M. D. 2009, Serbian Astron. J., 179, 55
Clarke, J. N., Little, A. G., & Mills, B. Y. 1976, Aust. J. Phys. Astrophys. Suppl., 40, 1
Crawford, E. J., Filipović, M. D., de Horta, A. Y., Stootman, F. H., & Payne, J. L. 2008a, Serbian Astron. J., 177, 61
Crawford, E. J., Filipovic, M. D., & Payne, J. L. 2008b, Serbian Astron. J., 176, 59
Crawford, E. J., Filipović, M. D., Haberl, F., et al. 2010, A&A, 518, A35
den Herder, J. W., Brinkman, A. C., Kahn, S. M., et al. 2001, A&A, 365, L7
di Benedetto, G. P. 2008, MNRAS, 390, 1762
Dickel, J. R., Gruendl, R. A., McIntyre, V. J., & Amy, S. W. 2010, AJ, 140, 1511
Filipović, M. D., Haynes, R. F., White, G. L., & Jones, P. A. 1998a, A&AS, 130, 421
Filipović, M. D., Pietsch, W., Haynes, R. F., et al. 1998b, A&AS, 127, 119
Filipović, M. D., Haberl, F., Winkler, P. F., et al. 2008, A&A, 485, 63
Filipović, M. D., Crawford, E. J., Hughes, A., et al. 2009, in IAU Symp. 256, eds. J. T. van Loon, & J. M. Oliveira, 8
Fukui, Y., Kawamura, A., Minamidani, T., et al. 2008, ApJS, 178, 56
Gaensler, B. M., Hendrick, S. P., Reynolds, S. P., & Borkowski, K. J. 2003, ApJ, 594, L111
Gooch, R. 1996, in Astronomical Data Analysis Software and Systems V, eds. G. H. Jacoby, & J. Barnes, ASP Conf. Ser., 101, 80
Haberl, F., & Pietsch, W. 1999, A&AS, 139, 277
Haynes, R. F., Klein, U., Wayte, S. R., et al. 1991, A&A, 252, 475
Hughes, J. P., Hayashi, I., & Koyama, K. 1998, ApJ, 505, 732
Hughes, A., Staveley-Smith, L., Kim, S., Wolleben, M., & Filipović, M. 2007, MNRAS, 382, 543
Kaspi, V. M., Roberts, M. S. E., & Harding, A. K. 2006, Isolated neutron stars, eds. W. H. G. Lewin, & M. van der Klis, 279
Kawamura, A., Mizuno, Y., Minamidani, T., et al. 2009, ApJS, 184, 1
Kim, S., Staveley-Smith, L., Dopita, M. A., et al. 1998, ApJ, 503, 674
Kim, S., Dopita, M. A., Staveley-Smith, L., & Bessell, M. S. 1999, AJ, 118, 2797
Long, K. S., Helfand, D. J., & Grabelsky, D. A. 1981, ApJ, 248, 925
Lopez, L. A., Ramirez-Ruiz, E., Badenes, C., et al. 2009, ApJ, 706, L106
Manchester, R. N., Staveley-Smith, L., & Kesteven, M. J. 1993, ApJ, 411, 756
Manchester, R. N., Fan, G., Lyne, A. G., Kaspi, V. M., & Crawford, F. 2006, ApJ, 649, 235
Mathewson, D. S., Ford, V. L., Dopita, M. A., et al. 1983, ApJS, 51, 345
Mathewson, D. S., Ford, V. L., Tuohy, I. R., et al. 1985, ApJS, 58, 197
Mills, B. Y., Turtle, A. J., Little, A. G., & Durdin, J. M. 1984, Aust. J. Phys., 37, 321
Owen, R. A., Filipović, M. D., Ballet, J., et al. 2011, A&A, 530, A132
Payne, J. L., White, G. L., & Filipović, M. D. 2008, MNRAS, 383, 1175
Richter, O.-G., Tammann, G. A., & Huchtmeier, W. K. 1987, A&A, 171, 33
Russell, S. C., & Dopita, M. A. 1992, ApJ, 384, 508
Sasaki, M., Haberl, F., & Pietsch, W. 2000, A&AS, 143, 391
Sault, R. J., & Wieringa, M. H. 1994, A&AS, 108, 585
Sault, R. J., Teuben, P. J., & Wright, M. C. H. 1995, in Astronomical Data Analysis Software and Systems IV, eds. R. A. Shaw, H. E. Payne, & J. J. E. Hayes, ASP Conf. Ser., 77, 433
Smith, C., Points, S., & Winkler, P. F. 2006, NOAO Newsletter, 85, 6
Strüder, L., Briel, U., Dennerl, K., et al. 2001, A&A, 365, L18
Turner, M. J. L., Abbey, A., Arnaud, M., et al. 2001, A&A, 365, L27
van der Heyden, K. J., Bleeker, J. A. M., & Kaastra, J. S. 2004, A&A, 421, 1031
Wang, Q., Hamilton, T., Helfand, D. J., & Wu, X. 1991, ApJ, 374, 475
Williams, R. M., Chu, Y.-H., Dickel, J. R., et al. 1999, ApJS, 123, 467
Williams, B. J., Borkowski, K. J., Reynolds, S. P., et al. 2006, ApJ, 652, L33
Wilms, J., Allen, A., & McCray, R. 2000, ApJ, 542, 914
Xu, J.-W., Zhang, X.-Z., & Han, J.-L. 2005, Chin. J. Astron. Astrophys., 5, 165

A.21 Related Paper 21

Galvin, T. J., Filipović, M. D., Crawford, E. J., Wong, G., Payne, J. L., De Horta, A., White, G. L., Tothill, N., Drašković, D., Pannuti, T. G., Grimes, C. K., Cahall, B. J., Millar, W. C., and Laine, S. (2012b). Radio-continuum study of the Nearby sculptor group galaxies. Part 1: NGC 300 at λ=20 cm. *Ap&SS*, 340:133–142

My contribution was to assist in the data analysis. This is a 10% contribution.

Astrophys Space Sci (2012) 340:133–142
DOI 10.1007/s10509-012-1044-3

ORIGINAL ARTICLE

Radio-continuum study of the Nearby sculptor group galaxies. Part 1: NGC 300 at λ = 20 cm

Timothy J. Galvin · Miroslav D. Filipović · Evan J. Crawford · Graeme Wong · Jeff L. Payne · Ain De Horta · Graeme L. White · Nick Tothill · Danica Drašković · Thomas G. Pannuti · Caleb K. Grimes · Benjamin J. Cahall · William C. Millar · Seppo Laine

Received: 31 August 2011 / Accepted: 1 March 2012 / Published online: 24 March 2012

Abstract A series of new radio-continuum (λ = 20 cm) mosaic images focused on the NGC 300 galactic system were produced using archived observational data from the VLA and/or ATCA. These new images are both very sensitive (rms = 60 μJy) and feature high angular resolution (<10″). The most prominent new feature is the galaxy's extended radio-continuum emission, which does not match its optical appearance. Using these newly created images a number of previously unidentified discrete sources have been discovered. Furthermore, we demonstrate that a joint deconvolution approach to imaging this complete data-set is inferior when compared to an IMMERGE approach.

T.J. Galvin (✉) · M.D. Filipović · E.J. Crawford · G. Wong · J.L. Payne · A. De Horta · G.L. White · N. Tothill · D. Drašković
University of Western Sydney, Locked Bag 1797, Penrith South DC, NSW 1797, Australia
e-mail: t.galvin@bigpond.com

G.L. White
School of Dentistry, Charles Sturt University, Wagga Wagga, NSW, Australia

T.G. Pannuti · C.K. Grimes · B.J. Cahall
Department of Earth and Space Sciences, Space Science Center, Morehead State University, 235 Martindale Drive, Morehead, KY 40351, USA

W.C. Millar
Centre for Astronomy, James Cook University, Townsville, Queensland 4811, Australia

W.C. Millar
Grand Rapids Community College, 143 Bostwick N.E., Grand Rapids, MI 49503, USA

S. Laine
Spitzer Science Center, California Institute of Technology, MS 220-6, Pasadena, CA 91125, USA

Keywords Galaxies: general · Galaxies: NGC 300 · Radio continuum: galaxies

1 Introduction

At ∼1.9 Mpc away (Rizzi et al. 2006), NGC 300 is the closest spiral galaxy of the nearby Sculptor Group. This proximity is an advantage because it allows for this galaxy to be examined in great detail. Previous radio-continuum and optical studies of NGC 300 (Pannuti et al. 2000; Payne et al. 2004; Millar et al. 2011) utilised either the Australia Telescope Compact Array (ATCA) or the Very Large Array (VLA) as their primary instrument. However, these past studies suffer from either low resolution, poor sensitivity or both.

Until the next generation radio telescopes, such as the Australian Square Kilometre Array Pathfinder (ASKAP), Karoo Array Telescope (KAT & MeerKAT) and Square Kilometre Array (SKA), become operational we are restricted to consolidating a selection of NGC 300 radio observations. In this paper, we reexamine all available archived radio-continuum observations performed at ATCA and VLA at λ = 20 cm (ν = 1.4 GHz) with the intention of merging these observations into a single radio-continuum image. By combining a large amount of existing data using the latest generation of computer power we can create new images that feature both high angular resolution and excellent sensitivity. The newly constructed images are analysed and the difference between the various NGC 300 images created at 20 cm are discussed.

In Sect. 2 we describe the observational data and reduction techniques. In Sect. 3 we present our new maps, a brief discussion is given in Sects. 4, and Sect. 5 is the conclusion.

Table 1 List of VLA and ATCA observations of NGC 300 used in this study. RA and DEC represent coordinates of central pointings

Project code	RA (J2000) (h m s)	Dec (J2000) (° ′ ″)	Dates	Instrument	Array type	ν (MHz)	$\Delta\nu$ (MHz)	Duration (hours)	Primary calibrator	Secondary calibrator
AL445	00 54 53.20	−37 40 57.00	13/06/1998	VLA	AB	1435, 1465	15, 15	1	0134+329	0022-423
AC101	00 54 52.72	−37 41 09.02	13/07/1984	VLA	CD	1465, 1515	50, 50	0.1	0134+329	0023-263
AC308	00 55 30.00	−37 51 54.00	09/10/1993	VLA	CD	1365, 1435	50, 50	0.01	0521+166	0116-208
C828	00 54 53.47	−37 41 00.00	27–28/02/2000	ATCA	6A	1384	128	10.50	1934-638	0823-500
C1757	00 54 11.81	−37 32 49.00	20/11/2007	ATCA	EW367	1384	128	1.04	1934-638	0008-421
C1757	00 54 11.81	−37 32 49.00	02/02/2008	ATCA	EW367	1384	128	1.15	1934-638	0008-421
C1757	00 55 35.19	−37 49 19.00	03/02/2008	ATCA	EW367	1384	128	1.14	1934-638	0008-421
C1757	00 55 35.19	−37 32 49.00	23/05/2008	ATCA	EW367	1384	128	1.22	1934-638	0008-421
C1757	00 54 11.81	−37 49 19.00	24/05/2008	ATCA	EW367	1384	128	1.33	1934-638	0008-421
C1757	00 55 35.19	−37 49 19.00	13/11/2008	ATCA	EW367	1384	128	1.17	1934-638	0008-421
C1757	00 55 35.19	−37 32 49.00	17/11/2008	ATCA	EW367	1384	128	1.28	1934-638	0008-421
C1757	00 54 11.81	−37 49 19.00	19/11/2008	ATCA	EW367	1384	128	1.23	1934-638	0008-421

2 Observational data

2.1 Observational data

To create a high-resolution and sensitive radio-continuum image a number (5) of observations from the ATCA and VLA were used. These observations were selected from the Australian Telescope Online Archive (ATOA) and the National Radio Astronomy Observatory (NRAO) Science Data Archive. The observations which were selected and used here are summarised in Table 1. Because NGC 300 is far south, the VLA could only record data for short durations (see Table 1) and therefore over limited hour angle ranges.

ATCA project C1757 was conducted in mosaic mode with a total of eight pointings being observed over eight days. This project mapped the neutral hydrogen emission of NGC 300 (Westmeier et al. 2011), which extends significantly beyond the galaxy's optical emission. We used only the four innermost pointings which were directly centred on NGC 300. Other VLA and ATCA observations used in this study consist of single pointings of NGC 300. All images are primary beam corrected.

For both ATCA projects, the source **PKS** 1934-638 was used as the primary calibrator. The sources **PKS** 0008-421 and **PKS** 0823-500 were used as secondary calibrators for ATCA projects C1757 and C828 respectively. VLA observations AC101 and AL445 used source 0134+329 **(IAU J0137+3309)** as their primary calibrator, while sources 0023-263 **(IAU J0025-2602)** and 0022-423 **(IAU J0024-4202)** were used as the secondary calibrator, respectively. Project AC308 used 0521+166 **(PKS J0521+1638)** as its primary calibrator and source 0116-208 **(PKS J0116-2052)** as its secondary calibrator.

2.2 Image creation

To create the best possible NGC 300 mosaic image at 20 cm, we examined the radial distance in the *uv*-plane of all observations combined (Fig. 1) and found that the *uv*-plane is densely sampled up to ∼30 kλ, but quite sparsely sampled at longer baselines. Thus we restricted our imaging to the 0–30 kλ range and discarded longer baselines in VLA observations.

The MIRIAD (Sault and Killeen 2006), AIPS (Greisen 2010) and KARMA (Gooch 2006) software packages were used for data reduction and analysis. Because of the large volume of data, the MIRIAD package was compiled to run on a 16-processor high-performance computer system.

Initially, observations which were performed using the VLA were imported into AIPS using the task FILLM, and then all sources were split with SPLIT. Using the task UVFIX, source coordinates were converted from the B1950 to the J2000 reference frame and the task FITTP was used to export each source to a FITS file.

The MIRIAD package was then used for actual data reduction. The task ATLOD was used to convert ATCA observations into MIRIAD files, while the task FITS was used to import the previous AIPS-produced fits files and convert them to MIRIAD files.

Typical calibration and flagging procedures were then carried out (Sault and Killeen 2006). Using the task INVERT, two mosaic images (one based on ATCA data and the other on VLA data) were created using a natural weighting scheme. Each mosaic image was then cleaned using the task MOSSDI. The MOSSDI task is a SDI clean algorithm designed for mosaic images (Steer et al. 1984). To convolve a clean model the task RESTOR was then used on each of the cleaned maps.

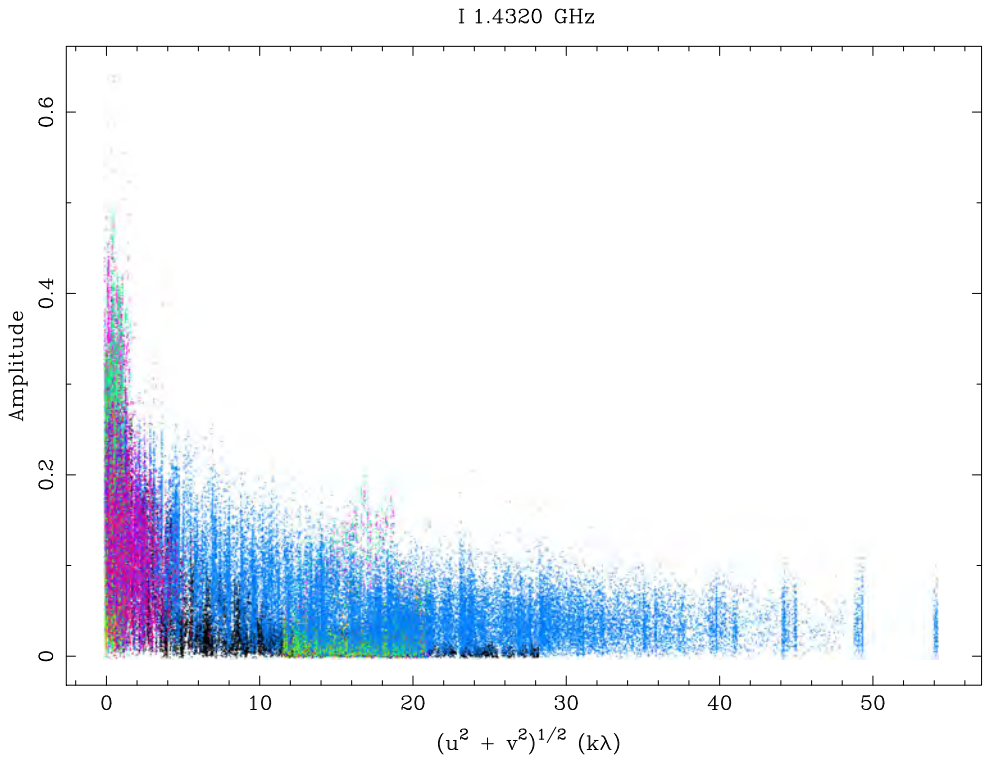

Fig. 1 Graph showing the unrestricted amplitude vs *uv*-distance of all ATCA/VLA projects used in this work. Each project is represented as different colour in this graph. Here, project C828 is *dark blue*, project C1757 is *green*, project AL445 is *light blue*, project AC308 is *pink* and project AC101 is *purple*

The restored mosaic images were then merged together using the task IMMERGE. This task uses a linear approach to merge images of a different resolution, where the low resolution image is assumed to better represent short spacing, and the higher resolution image to better represent the fine structure. IMMERGE changes the weighting by the normalisation process in the overlapping region.

We also created a single mosaic image which was comprised of all selected ATCA and VLA projects using the task INVERT. The dirty map was then cleaned with MOSSDI before being convolved with RESTOR.

The difference between the two approaches to data combination is that the single image (in which all *uv*-data are inverted simultaneously) contains all calibration uncertainties and weightings from each data set, while the image produced by merging individual images normalises the different calibrations in regions of *uv* overlap.

The ATCA bandpass comprises 13 channels, one of which is contaminated by H I emission. From the H I results of Westmeier et al. (2011), the H I contamination can be seen to be restricted to channel 4, which was flagged out and does not contribute to our images.

3 Results

When comparing individual maps created from each observation, the different effects of varying array configurations can be seen. The mosaic image produced from C1757

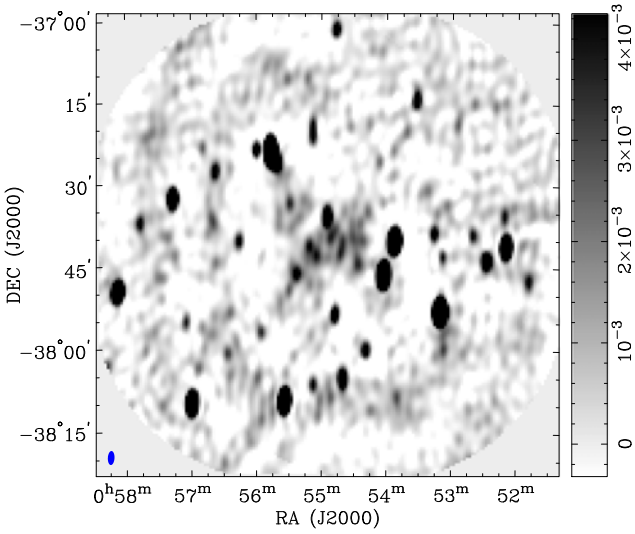

Fig. 2 ATCA Project C1757 mosaic radio-continuum total intensity image of NGC 300. The synthesised beam, as represented by the *blue ellipse* in the *lower left hand corner*, is 153.1″ × 72.5″ and the r.m.s. noise is 0.30 mJy/beam. This image is in terms of Jy/Beam

(Fig. 2) showed a much better defined region of extended emission. However, it lacked the high resolution of project C828 (Fig. 3), due to the shorter baselines of the C1757 project.

VLA observation AL445 (Fig. 4) was performed using the longest baseline, giving this image the highest resolution among all the individual images presented in this paper.

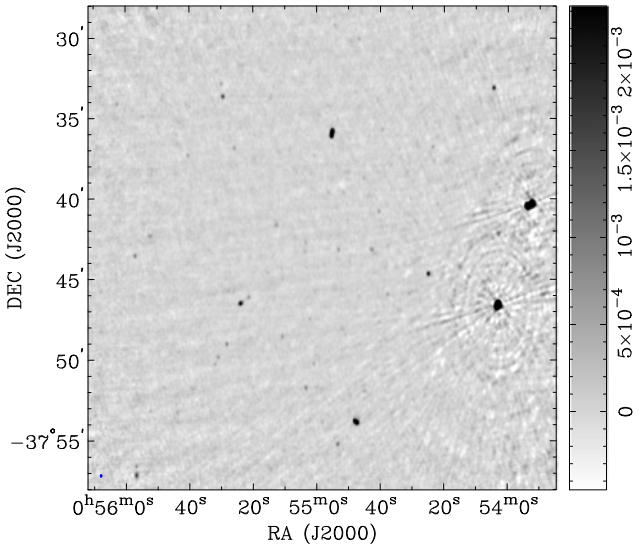

Fig. 3 ATCA Project C828 radio-continuum total intensity image of NGC 300. The synthesised beam, as represented by the *blue ellipse* in the *lower left hand corner*, is $13.8'' \times 10.1''$ and the r.m.s. noise is 0.07 mJy/beam. This image is in terms of Jy/beam

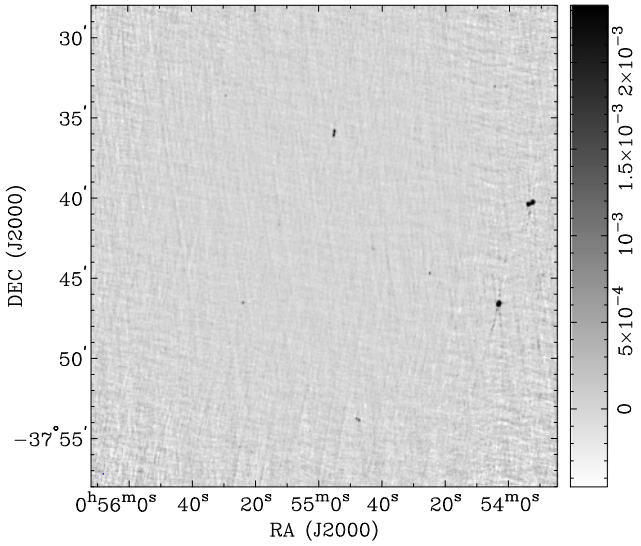

Fig. 4 VLA Project AL0445 radio-continuum total intensity image of NGC 300. The synthesised beam, as represented by the *blue ellipse* in the *lower left hand corner*, is $7.0'' \times 4.5''$ and the r.m.s. noise is 0.15 mJy/beam. This image is in terms of Jy/beam

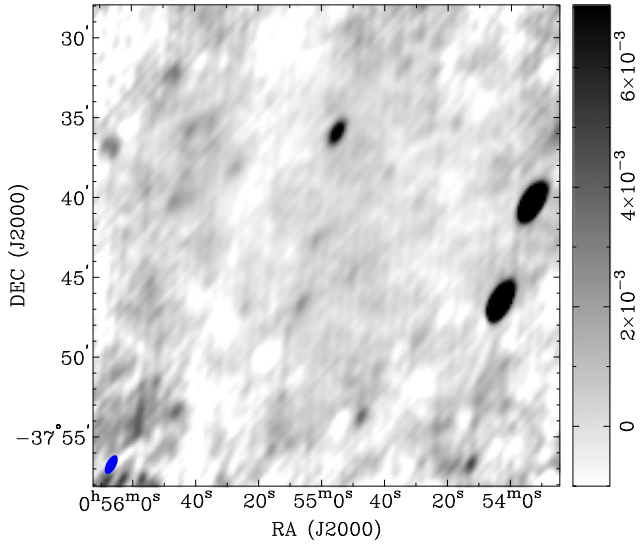

Fig. 5 VLA Project AC0101 radio-continuum total intensity image of NGC 300. The synthesised beam, as represented by the *blue ellipse* in the l*ower left hand corner*, is $77.9'' \times 36.7''$ and the r.m.s. noise is 0.30 mJy/beam. This image is in terms of Jy/beam

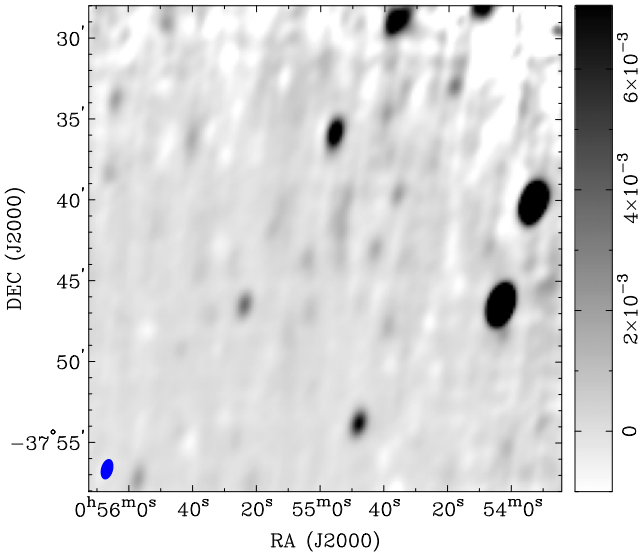

Fig. 6 VLA Project AC0308 radio-continuum total intensity image of NGC 300. The synthesised beam, as represented by the *blue ellipse* in the *lower left hand corner*, is $77.8'' \times 44.7''$ and the r.m.s. noise is 0.50 mJy/beam. This image is in terms of Jy/beam

As expected, point sources dominate this field. The other VLA observations, AC101 (Fig. 5) and AC308 (Fig. 6), were taken with much smaller array configurations, resulting in lower-resolution images with significant extended emission. Both of these observations have short integration times. AC308 had only 36 seconds integration, leading to a very shallow image.

Figure 7 is a mosaic image containing both ATCA observations C1757 and C828. It shows a well-defined region of extended emission with a number of definitive point sources.

We also created a mosaic image comprised of VLA observations AL445, AC308 and AC101 (Fig. 8). Although there is no obvious extended emission in this image, there are a number of resolved point sources.

In Fig. 9 we show the mosaic image produced with all five observations. Although there is a clear region of extended emission and a number of resolved point sources, this image suffers from significant side-lobe distortion. Finally, in Fig. 10 we present the result of merging together

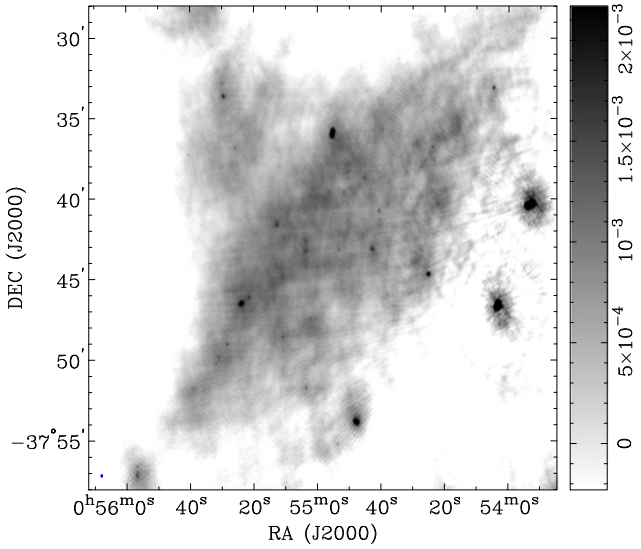

Fig. 7 Combined ATCA projects C1757 and C828 mosaic radio–continuum total intensity image of NGC 300. The synthesised beam, as represented by the *blue ellipse* in the *lower left hand corner*, is $13.8'' \times 10.1''$ and the r.m.s. noise is 0.07 mJy/beam. This image is in terms of Jy/beam

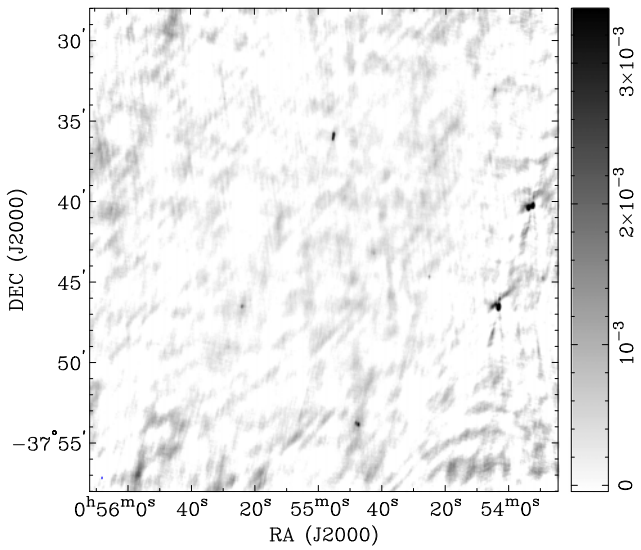

Fig. 8 Combined VLA projects AL445, AC101 and AC308 mosaic radio-continuum total intensity image of NGC 300. The synthesised beam, as represented by the *blue ellipse* in the *lower left hand corner*, is $10.9'' \times 4.8''$ and the r.m.s. noise is 0.09 mJy/beam. This image is in terms of Jy/beam

each mosaic image. We note a well-defined region of extended emission in this image, with a total integrated flux density estimated to be 4.62 ± 0.01 Jy at 20 cm. The details of all new images presented here, including the various combined images, are summarised in Table 2. Images were also produced using a uniform weighing scheme, but were disregarded because of the absence of the extended emission structure.

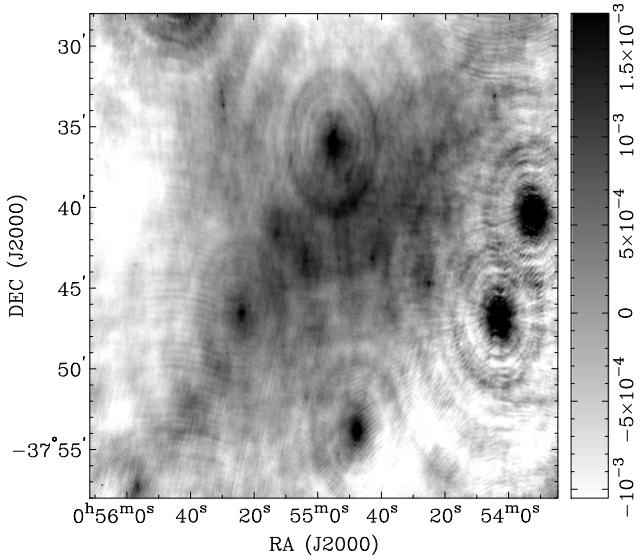

Fig. 9 All ATCA and VLA projects radio-continuum total intensity image of NGC 300. The synthesised beam, as represented by the *blue ellipse* in the *lower left hand corner*, is $11.8'' \times 5.0''$ and the r.m.s. noise is 0.13 mJy/beam. This image is in terms of Jy/beam

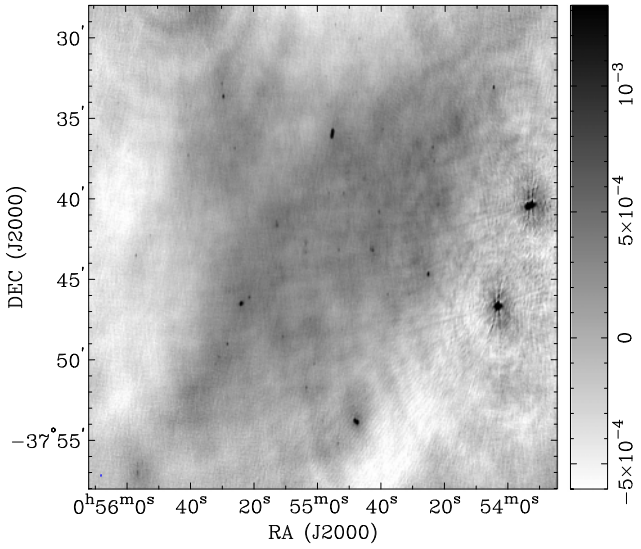

Fig. 10 All ATCA and VLA projects radio-continuum total intensity image of NGC 300 produced using the MIRIAD task IMMERGE. The synthesised beam, as represented by the *blue ellipse* in the *lower left hand corner*, is $10.8'' \times 4.8''$ and the r.m.s. noise is 0.06 mJy/beam. This image is in terms of Jy/beam

4 Discussion

4.1 Discrete sources within the field of NGC 300

Our most sensitive and highest-resolution image is shown in Fig. 10. Using this image, a total of 72 radio sources above 3σ (0.18 mJy/beam) were identified within the area defined by Payne et al. (2004) (Table 3). All sources identified in this study were (Gaussian) fitted without subtract-

Table 2 The details of ATCA/VLA single and merged projects of NGC 300 mosaics at 20 cm

ATCA/VLA project	*Beam size* (arcsec)	*r.m.s.* (mJy/beam)	*Figure*
C1757	153.1 × 72.5	0.30	2
C828	13.8 × 10.1	0.07	3
AL445	7.0 × 4.5	0.15	4
AC101	77.9 × 36.7	0.30	5
AC308	77.8 × 44.7	0.50	6
All ATCA	13.8 × 10.1	0.07	7
All VLA	10.9 × 4.8	0.09	8
All (invert)	11.8 × 5.0	0.13	9
All (merged)	10.8 × 4.8	0.06	10

ing the background which changes across the field. While the uncertainty is dependent on the flux density of a source (with larger uncertainties for weaker sources) we estimate that the overall uncertainty in source flux density is less than 10 % (see Sect. 4.2).

A previous radio-continuum study of NGC 300 was able to identify a total of 47 sources at the wavelength of 20 cm (Payne et al. 2004; combined Columns 5 and 6 from Table 4). These sources were found by combining two independent observations by the ATCA and the VLA. Eleven of these 47 sources could not be identified in our final image. This difference can be attributed to the method of identifying sources which the previous study adopted. For a source to be considered real, it only had to appear in one of the two radio-continuum images. Of the eleven sources which were found not to be in our final image, none could be identified in both 20 cm images which were produced in the previous studies. This potentially indicates that these eleven sources are not real as they can only be found in a single 20 cm radio-continuum image. Alternatively, they may represent some sort of transient or variable sources (e.g. QSOs) with very low flux densities of around 3σ. Indeed, we found some seven sources (Table 3; difference between the new flux densities (Column 4) and previous (Columns 5 or 6)) with very different flux densities (>20 %) indicating a small but significant population of variable sources.

We also compared our radio-continuum catalogue with a list of 28 well-established optically identified H II regions in NGC 300 (Bresolin et al. 2009). We note that 11 of our radio sources (sources # 2, 11, 18, 21, 25, 28, 34, 39, 51, 52 and 54) coincide (to within 5″) with H II regions from this list. Our source # 39 (ATCA J005451.7-373940) was previously classified as a SNR in Payne et al. (2004).

In Fig. 11 we show the flux density distribution of all radio-continuum sources found in this study (Table 3; Column 3). As expected, the majority of sources (85 %) are within 10σ flux density level.

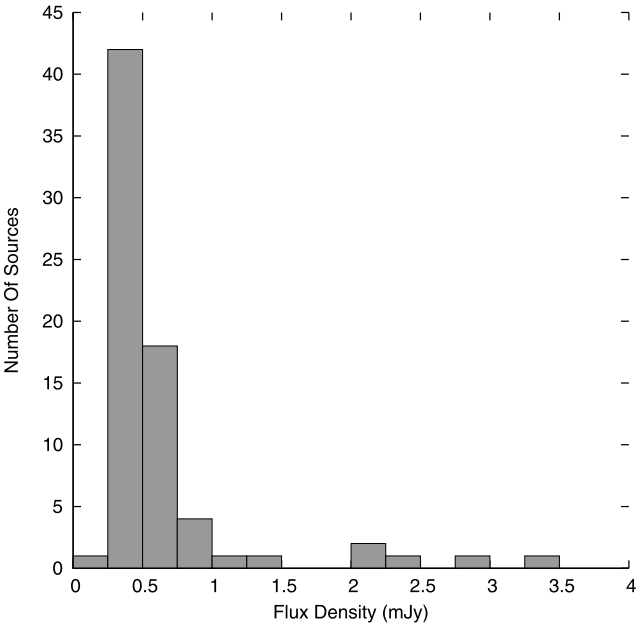

Fig. 11 A histogram of source flux density distribution within the field of NGC 300. Source No. 42 from Table 3 is excluded from this graph

4.2 Comparison of discrete source flux densities

While our flux densities are highly-correlated with those of Payne et al. (2004), they are systematically higher. Assuming no systematic offset between the two sets of flux densities, we find that our flux densities (Column 4 of Table 3) are about 20 % greater than those reported by Payne et al. (2004) (ATCA observations in Column 5 and VLA in Column 6). The ATCA and VLA flux densities of Payne et al. (2004) (Columns 5 and 6) are in good internal agreement with ATCA/VLA= 1.07 ± 0.06 (standard error of mean for 33 sources in common). However, our new determinations of flux densities are higher than those of Payne et al. (2004) by 19±5 %: For the 8 sources from our study (Column 4) which are stronger than 1 mJy, four sources (# 9, 24, 42 and 62) had corresponding flux densities listed by Payne et al. (2004) (Columns 5 and 6). We found that from these four sources our flux densities are 23±9 % higher than the average of the ATCA and VLA observations; for all 35 sources in common with the ATCA observations (Column 5), our flux densities are higher by 18±6 %; for the 33 sources in common with VLA observations (Column 6), our flux densities are higher by 19±7 %.

The discrepancy between the flux density measurements is likely to be due to the extended continuum emission discussed below. In the earlier study, this component was resolved out of the images, and therefore not measured in the point-source flux densities, whereas our image includes this emission, and our point-source flux densities also include it.

Table 3 List of sources at 20 cm within the field of NGC 300. *Columns* 1, 2, 3 and 4 are from this work. *Columns* 5 and 6 are partially extracted from Payne et al. (2004). *Columns* 7 and 8 correspond to the DSS2 (optical) and Spitzer (IR) identification

	1 Identifier GFC2012	2 RA (J2000) (h m s)	3 Dec (J2000) (° ′ ″)	4 S_I (mJy)	5 ATCA (mJy)	6 VLA (mJy)	7 Opt. ID	8 IR ID	9 Identifier PFP2004	10 Source type
1	J005404.9-373305	00:54:04.89	−37:33:05.02	2.34						
2	J005416.6-373500	00:54:16.58	−37:35:00.14	0.42			y	Y		H II
3	J005419.2-374322	00:54:19.23	−37:43:22.58	0.36						
4	J005421.2-373606	00:54:21.17	−37:36:06.20	0.41						
5	J005422.3-374022	00:54:22.25	−37:40:22.49	0.38			y			H II
6	J005422.4-373613	00:54:22.43	−37:36:13.62	0.78	1.37±0.04				J005422.5-373615	
7	J005423.5-373741	00:54:23.47	−37:37:41.59	0.55	0.41±0.02	0.38±0.06		Y	J005423.4-373741	H II
8	J005423.9-373649	00:54:23.91	−37:36:49.47	0.68	0.64±0.02	0.58±0.06			J005423.8-373648	SNR
9	J005425.2-374441	00:54:25.25	−37:44:41.28	2.96	2.44±0.10	2.55±0.10		Y	J005425.2-374441	BKG
10	J005427.3-374320	00:54:27.31	−37:43:20.70	3.29			y			H II
11	J005428.8-374134	00:54:28.80	−37:41:34.16	0.30			y	Y		H II
12	J005428.8-374351	00:54:28.80	−37:43:51.31	0.39						
13	J005430.7-374004	00:54:30.71	−37:40:04.27	0.27				Y		H II
14	J005431.2-374556	00:54:31.23	−37:45:56.95	0.51	0.41±0.03	0.33±0.04		Y	J005431.2-374554	H II
15	J005433.7-374158	00:54:33.69	−37:41:58.04	0.17						
16	J005434.0-373549	00:54:34.02	−37:35:49.95	0.25				Y		H II
17	J005438.0-374557	00:54:37.96	−37:45:57.65	0.66	0.65±0.03	0.66±0.06			J005437.9-374559	BKG
18	J005438.4-374147	00:54:38.35	−37:41:47.51	0.30	0.27±0.02	0.34±0.06	Y	Y	J005438.1-374144	H II
19	J005438.4-374257	00:54:38.36	−37:42:57.18	0.30		0.33±0.02			J005438.4-374240	SNR/H II
20	J005439.6-373541	00:54:39.57	−37:35:41.55	0.46	0.42±0.02	0.43±0.10		Y	J005439.6-373543	SNR
21	J005440.7-374049	00:54:40.66	−37:40:49.21	0.47	0.56±0.03	0.30±0.05	Y	Y	J005440.6-374049	H II
22	J005441.2-373349	00:54:41.19	−37:33:49.77	0.34	0.29±0.02	0.33±0.05		Y	J005441.0-373348	SNR
23	J005442.3-374329	00:54:42.26	−37:43:29.58	0.40						
24	J005442.7-374313	00:54:42.66	−37:43:13.09	1.07	0.63±0.07	0.69±0.06	Y	Y	J005442.7-374313	SNR/H II
25	J005443.4-374309	00:54:43.38	−37:43:09.45	0.88	0.59±0.08	0.75±0.05	Y	Y	J005442.7-374313	H II
26	J005443.8-373949	00:54:43.75	−37:39:49.75	0.36						
27	J005444.8-375226	00:54:44.79	−37:52:26.04	0.39						
28	J005445.1-373846	00:54:45.13	−37:38:46.09	0.60	0.30±0.03		Y	Y	J005445.3-373847	H II
29	J005445.1-375155	00:54:45.14	−37:51:55.68	0.34						
30	J005447.8-373324	00:54:47.83	−37:33:24.06	0.29	0.31±0.03	0.37±0.07		Y	J005448.0-373323	H II
31	J005448.0-375352	00:54:47.97	−37:53:52.24	2.02						
32	J005448.8-375254	00:54:48.80	−37:52:54.21	0.37						
33	J005450.0-373616	00:54:49.99	−37:36:16.96	0.37						
34	J005450.2-373822	00:54:50.19	−37:38:22.43	0.61	0.36±0.05	0.23±0.01	Y	Y	J005450.3-373822	H II
35	J005450.3-373849	00:54:50.26	−37:38:49.74	0.55	0.24±0.02		Y	Y	J005450.3-373850	xrb
36	J005450.3-375212	00:54:50.27	−37:52:12.34	0.41				Y		H II
37	J005450.5-374129	00:54:50.52	−37:41:29.11	0.33	0.28±0.02	0.30±0.03			J005450.5-374123	BKG
38	J005451.0-373823	00:54:51.01	−37:38:23.41	0.34	0.95±0.05	0.33±0.01	Y	Y	J005451.1-373826	SNR/H II
39	J005451.8-373940	00:54:51.76	−37:39:40.55	0.53	0.35±0.03	0.46±0.03	Y	Y	J005451.7-373939	H II

Table 3 (*Continued*)

	1 Identifier GFC2012	2 RA (J2000) (h m s)	3 Dec (J2000) (° ′ ″)	4 S_I (mJy)	5 ATCA (mJy)	6 VLA (mJy)	7 Opt. ID	8 IR ID	9 Identifier PFP2004	10 Source type
40	J005453.3-374312	00:54:53.29	−37:43:12.57	0.62	0.69±0.04	0.66±0.06	Y	Y	J005453.3-374311	SNR/H II
41	J005453.5-375512	00:54:53.53	−37:55:12.43	0.89				Y		
42	J005455.3-373556	00:54:55.26	−37:35:56.15	19.90	17.88±1.31	16.78±1.06		Y	J005455.3-373557	BKG; Double
43	J005456.4-373939	00:54:56.41	−37:39:39.75	0.31	0.39±0.06	0.68±0.06	Y	Y	J005456.3-373940	H II
44	J005456.8-373412	00:54:56.77	−37:34:12.18	0.30	0.28±0.03	0.31±0.06			J005456.7-373413	BKG
45	J005458.4-375347	00:54:58.35	−37:53:47.66	0.48				Y		H II
46	J005458.4-375147	00:54:58.40	−37:51:47.18	0.42						
47	J005500.9-373721	00:55:00.85	−37:37:21.34	0.30	0.22±0.01	0.29±0.04			J005500.9-373720	BKG
48	J005501.1-375016	00:55:01.00	−37:50:16.79	0.47				Y		H II
49	J005502.3-374731	00:55:02.27	−37:47:31.30	0.37	0.36±0.03	0.26±0.02			J005502.2-374731	BKG
50	J005503.5-375144	00:55:03.54	−37:51:44.38	0.82				Y		H II
51	J005503.6-374248	00:55:03.56	−37:42:48.17	0.46	0.34±0.02	0.41±0.03	Y	Y	J005503.5-374246	H II
52	J005503.7-374320	00:55:03.70	−37:43:20.89	0.43	0.33±0.03	0.32±0.04	Y	Y	J005503.6-374320	H II
53	J005510.9-374834	00:55:10.85	−37:48:34.24	0.62	0.52±0.04	0.30±0.05	Y	Y	J005510.8-374835	SNR/H II
54	J005512.7-374134	00:55:12.68	−37:41:34.80	0.62	0.49±0.04	0.55±0.01	Y	Y	J005512.7-374140	H II
55	J005512.8-374130	00:55:12.79	−37:41:30.14	0.36			y	Y		H II
56	J005513.0-374417	00:55:13.02	−37:44:17.28	0.28			y			H II
57	J005513.8-373305	00:55:13.83	−37:33:05.01	0.41						
58	J005515.3-374438	00:55:15.33	−37:44:38.68	0.31	0.20±0.01	0.22±0.02	Y	Y	J005515.4-374439	SNR/H II
59	J005519.5-373605	00:55:19.54	−37:36:05.00	0.25				Y		H II
60	J005521.3-374608	00:55:21.33	−37:46:08.91	0.60	0.67±0.03	0.76±0.06			J005521.3-374609	BKG
61	J005522.0-373635	00:55:22.00	−37:36:35.10	0.45						
62	J005524.0-374632	00:55:23.95	−37:46:32.48	2.05	2.23±0.17	2.10±0.29			J005523.9-374632	BKG
63	J005525.8-373652	00:55:25.82	−37:36:52.57	0.61	0.63±0.05	0.55±0.05			J005525.8-373653	BKG
64	J005527.6-374546	00:55:27.60	−37:45:46.76	0.37	0.36±0.03	0.30±0.01			J005527.6-374546	BKG
65	J005528.2-374902	00:55:28.23	−37:49:02.18	0.75	0.96±0.05	0.77±0.06			J005528.2-374903	SNR
66	J005529.4-373339	00:55:29.36	−37:33:39.25	1.37						
67	J005529.8-373252	00:55:29.81	−37:32:52.58	0.67						
68	J005530.8-374951	00:55:30.80	−37:49:51.05	0.53			y	Y		H II
69	J005531.9-375016	00:55:31.92	−37:50:16.83	0.42				Y		H II
70	J005540.4-373718	00:55:40.36	−37:37:18.24	0.57			y	Y		H II
71	J005552.2-374217	00:55:52.23	−37:42:17.13	0.39						
72	J005556.8-374331	00:55:56.76	−37:43:31.14	0.73						

4.3 Extended radio-continuum emission from NGC 300

Figure 12 shows a DSS2 optical image of NGC 300 overlaid with our final radio-continuum contours from Fig. 10. The structure of the radio emission from NGC 300 is significantly different from that of its optical emission.

Although the radio overlay aligns with a number of sources found in the optical image, there is a clear region of radio-continuum emission continuing past the apparent optical boundaries of NGC 300 and at a different position angle. The radio-continuum contours are consistent with the existence and positioning of the H I outer disc spanning more than 1° (equivalent to about 35 kpc) across the sky (Westmeier et al. 2011). They suggested that there is a substantial change in the position angle between the inner and the outer disc, resulting in a twisted appearance of NGC 300 which is particularly obvious in the velocity field. One possible scenario for this twist is that the distortion and warping of the outer disc of NGC 300 was caused by tidal forces during a

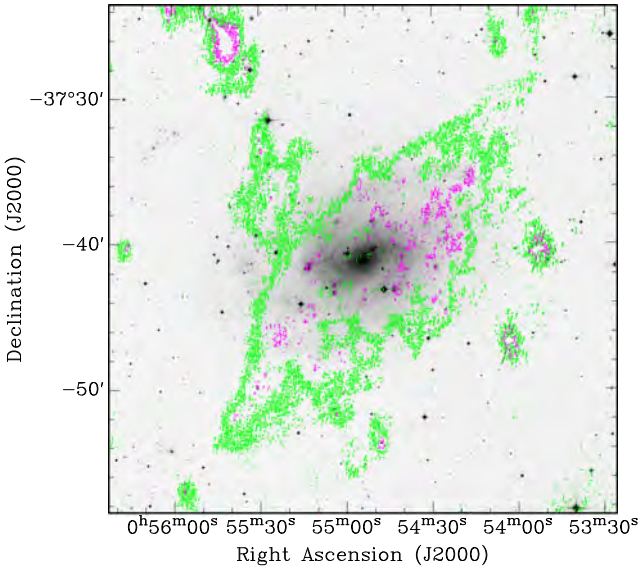

Fig. 12 An optical image of NGC 300 overlaid with our final radio–continuum image from Fig. 10. The overlaid contours are 0.21 (3σ; green) and 0.49 mJy/beam (magenta)

recent encounter with another galaxy, with nearby NGC 45 as a potential candidate for a close encounter.

While it is very difficult to precisely estimate the total flux density of NGC 300 extended radio-continuum emission at 20 cm we selected a tight region around 3σ contour seen in Fig. 12 and we summed all intensity inside this region to an integrated flux density of 4.687 ± 0.005 Jy. This includes the extended emission to the north-east of the main disk.The total flux density of all point sources detected within this region is 0.067 ± 0.005 Jy, so we estimate the flux density of the extended emission to be 4.62 ± 0.01 Jy.

4.4 Source classification

Thirty-five radio-continuum sources previously classified by Payne et al. (2004) were detected in our study. These sources are classified into three groups: background sources (such as AGN), Supernova Remnants (SNRs) and H II regions. To determine the true nature of the newly discovered sources from this survey, we used the previous classification scheme in addition to comparison with the available optical images such as DSS2.

We found 8 new sources (marked as lower case *y* in Table 3; Column 7) that are in common with optical and radio images making a total of 24 sources in common between optical and radio surveys. These 8 newly detected optical sources are most likely to originate in NGC 300 as either SNRs or H II regions. Because of their prominent optical extended emission, two sources (Table 3; Nos. 40 and 53) which were previously classified as background AGN's are more likely to be intrinsic to NGC 300. We also compared our new radio catalogue with existing NGC 300 IR Spitzer images (Helou et al. 2004) at all frequencies (3.6, 4.5, 5.8, 8.0 24, 70 and 150 μm). We found 37 sources in common between radio and various IR frequencies. In total, 21 sources are common to all three surveys. Combining previous work and the new radio maps we classify 51 objects. From these 51 sources some 29 are most likely to be H II regions, four are SNRs and one is an X-ray binary. We classify eleven sources as background sources (Table 3; Nos. 9, 17, 37, 42, 44, 47, 49, 60, 62, 63 and 64 where 42 is a double source) and six sources being within NGC 300 (SNRs or H II). Finally, the remaining 21 radio-continuum sources are still not classified.

We estimated the flux density of a bright Galactic SNR (such as Cas A) at a distance of 1.9 Mpc, and compared this to our radio point source catalogue; we find that there are no Cas A analogues in NGC 300. The luminous radio SNR source # 62 (at about 2 mJy) is twice that of a Crab Nebula analogue (which would be about a 1 mJy source in NGC 300). These results are similar to those in Pannuti et al. (2000).

5 Conclusion

We present and discuss our new high-sensitivity and high-resolution radio-continuum images of NGC 300 at 20 cm. The new images were created from merging sensitive 20-cm mosaic radio surveys from ATCA, and from the VLA synthesis radio-telescope. We were able to dramatically improve both the sensitivity and resolution of the final radio-continuum image when compared to previous studies. This resulted in the identification of a number of previously unknown sources bringing the number of known radio sources within the area of NGC 300 to 72. We also detected a previously unseen region of NGC 300's extended radio-continuum emission estimated to have an integrated flux density of 4.62 ± 0.01 Jy. It was also demonstrated that a joint deconvolved image produced by both ATCA and VLA observations (Fig. 9) was inferior to an image produced with an IMMERGE (Fig. 10) approach. We believe that this difference is attributed to MIRIAD's inability to produce an accurate beam representation when datasets from multiple telescopes are jointly inverted. Existing sidelobes are exaggerated when cleaning the resulting dirty map because of the inaccurate beam.

Acknowledgements The National Radio Astronomy Observatory is a facility of the National Science Foundation operated under cooperative agreement by Associated Universities, Inc. The Australia Telescope Compact Array is part of the Australia Telescope National Facility which is funded by the Commonwealth of Australia for operation as a National Facility managed by CSIRO. This paper includes archived data obtained through the Australia Telescope Online Archive (http://atoa.atnf.csiro.au) and VLA.

We would also like to thank the anonymous referee, whose feedback greatly improved this paper.

References

Bresolin, F., Gieren, W., Kudritzki, R.-P., Pietrzyński, G., Urbaneja, M.A., Carraro, G.: Astrophys. J. **700**, 309 (2009). doi:10.1088/0004-637X/700/1/309

Gooch, R.: Karma Users Guide. ATNF, Sydney (2006)

Greisen, E. (ed.): Aips Cookbook. The National Radio Astronomy Observatory, Charlottesville (2010)

Helou, G., Roussel, H., Appleton, P., Frayer, D., Stolovy, S., Storrie-Lombardi, L., Hurt, R., Lowrance, P., Makovoz, D., Masci, F., Surace, J., Gordon, K.D., Alonso-Herrero, A., Engelbracht, C.W., Misselt, K., Rieke, G., Rieke, M., Willner, S.P., Pahre, M., Ashby, M.L.N., Fazio, G.G., Smith, H.A.: Astrophys. J. Suppl. Ser. **154**, 253 (2004). doi:10.1086/422640

Millar, W.C., White, G.L., Filipović, M.D., Payne, J.L., Crawford, E.J., Pannuti, T.G., Staggs, W.D.: Astrophys. Space Sci. **332**, 221 (2011). doi:10.1007/s10509-010-0556-y

Pannuti, T.G., Duric, N., Lacey, C.K., Goss, W.M., Hoopes, C.G., Walterbos, R.A.M., Magnor, M.A.: Astrophys. J. **544**, 780 (2000). doi:10.1086/317238

Payne, J.L., Filipović, M.D., Pannuti, T.G., Jones, P.A., Duric, N., White, G.L., Carpano, S.: Astron. Astrophys. **425**, 443 (2004). doi:10.1051/0004-6361:20041058

Rizzi, L., Bresolin, F., Kudritzki, R., Gieren, W., Pietrzyński, G.: Astrophys. J. **638**, 766 (2006). doi:10.1086/498705

Sault, R., Killeen, N.: Miriad Users Guide. ATNF, Sydney (2006)

Steer, D.G., Dewdney, P.E., Ito, M.R.: Astron. Astrophys. **137**, 159 (1984)

Westmeier, T., Braun, R., Koribalski, B.S.: Mon. Not. R. Astron. Soc. **410**, 2217 (2011). doi:10.1111/j.1365-2966.2010.17596.x

A.22 Related Paper 22

Maggi, P., Haberl, F., Bozzetto, L. M., Filipović, M. D., Points, S. D., Chu, Y.-H., Sasaki, M., Pietsch, W., Gruendl, R. A., Dickel, J., Smith, R. C., Sturm, R., Crawford, E. J., and De Horta, A. Y. (2012). Multi-frequency study of supernova remnants in the Large Magellanic Cloud. Confirmation of the supernova remnant status of DEM L205. *A&A*, 546:A109

My contribution was to assist in the data analysis. This is a 10% contribution.

A&A 546, A109 (2012)
DOI: 10.1051/0004-6361/201219708

Astronomy & Astrophysics

Multi-frequency study of supernova remnants in the Large Magellanic Cloud⋆

Confirmation of the supernova remnant status of DEM L205

P. Maggi[1], F. Haberl[1], L. M. Bozzetto[2], M. D. Filipović[2], S. D. Points[3], Y.-H. Chu[4], M. Sasaki[5], W. Pietsch[1], R. A. Gruendl[4], J. Dickel[6], R. C. Smith[3], R. Sturm[1], E. J. Crawford[2], and A. Y. De Horta[2]

[1] Max-Planck-Institut für extraterrestrische Physik, Postfach 1312, Giessenbachstr., 85741 Garching, Germany
e-mail: pmaggi@mpe.mpg.de
[2] University of Western Sydney, Locked Bag 1797, Penrith South DC, NSW 1797, Australia
[3] Cerro Tololo Inter-American Observatory, National Optical Astronomy Observatory, Cassilla 603 La Serena, Chile
[4] Astronomy Department, University of Illinois, 1002 West Green Street, Urbana, IL 61801, USA
[5] Institut für Astronomie und Astrophysik Tübingen, Universität Tübingen, Sand 1, 72076 Tübingen, Germany
[6] Physics and Astronomy Department, University of New Mexico, MSC 07-4220, Albuquerque, NM 87131, USA

Received 29 May 2012 / Accepted 23 July 2012

ABSTRACT

Context. The Large Magellanic Cloud (LMC) is an ideal target for the study of an unbiased and complete sample of supernova remnants (SNRs). We started an X-ray survey of the LMC with *XMM-Newton*, which, in combination with observations at other wavelengths, will allow us to discover and study remnants that are either even fainter or more evolved (or both) than previously known.
Aims. We present new X-ray and radio data of the LMC SNR candidate DEM L205, obtained by *XMM-Newton* and ATCA, along with archival optical and infrared observations.
Methods. We use data at various wavelengths to study this object and its complex neighbourhood, in particular in the context of the star formation activity, past and present, around the source. We analyse the X-ray spectrum to derive some remnant's properties, such as age and explosion energy.
Results. Supernova remnant features are detected at all observed wavelengths : soft and extended X-ray emission is observed, arising from a thermal plasma with a temperature kT between 0.2 keV and 0.3 keV. Optical line emission is characterised by an enhanced [S]-to-Hα ratio and a shell-like morphology, correlating with the X-ray emission. The source is not or only tentatively detected at near-infrared wavelengths (shorter than 10 μm), but there is a detection of arc-like emission at mid and far-infrared wavelengths (24 and 70 μm) that can be unambiguously associated with the remnant. We suggest that thermal emission from dust heated by stellar radiation and shock waves is the main contributor to the infrared emission. Finally, an extended and faint non-thermal radio emission correlates with the remnant at other wavelengths and we find a radio spectral index between −0.7 and −0.9, within the range for SNRs. The size of the remnant is ∼79 × 64 pc and we estimate a dynamical age of about 35 000 years.
Conclusions. We definitely confirm DEM L205 as a new SNR. This object ranks amongst the largest remnants known in the LMC. The numerous massive stars and the recent outburst in star formation around the source strongly suggest that a core-collapse supernova is the progenitor of this remnant.

Key words. Magellanic Clouds – ISM: supernova remnants – ISM: individual objects: MCSNR J0528-6727 – X-rays: ISM

1. Introduction

Supernova remnants (SNRs) are an important class of objects, as they contribute to the energy balance and chemical enrichment and mixing of the interstellar medium (ISM). However, in our own Galaxy, distance uncertainties and high absorption inhibit the construction of a complete and unbiased sample of SNRs. On the other hand, the Large Magellanic Cloud (LMC) offers a target with a low foreground absorption at a relatively small distance of ∼50 kpc (di Benedetto 2008).

Furthermore, the broad multi-frequency coverage of the LMC, from radio to X-rays, allows for easier detection and classification of SNRs, which is most usually done using three signatures: thermal X-ray emission in the (0.2–2 keV) band, optical line emission with enhanced [S] to Hα ratio ($\gtrsim$0.4, Mathewson & Clarke 1973), and non-thermal (synchrotron) radio-continuum emission, with a typical spectral index of $\alpha \sim -0.5$ (using $S \propto \nu^{\alpha}$, where S is the flux density and ν the frequency), although α can have a wide range of values (Filipovic et al. 1998). Nevertheless, the interstellar environment in which the supernova (SN) exploded strongly affects the subsequent evolution of the remnant, so that some SNRs do not exhibit all three conventional signatures simultaneously (Chu 1997).

In this paper, we present new X-ray and radio-continuum observations (with *XMM-Newton* and ATCA) of the LMC SNR candidate DEM L205. Archival optical and infrared (IR) observations are analysed as well. The source lies in a very complex environment, at the eastern side of the H complex LHA 120-N 51 (in the nebular notation of Henize 1956). It was

⋆ Based on observations obtained with *XMM-Newton*, an ESA science mission with instruments and contributions directly funded by ESA Member States and NASA.

Table 1. Details of the *XMM-Newton* observations

ObsId	Obs. start date	Central coordinates (J2000) RA	Dec	Filter[a] pn/MOS1/MOS2	Total/filtered exposure time (ks)[b] pn	MOS1	MOS2	Off-axis angle[c]
0671010101	2011 Dec. 19	$05^h29^m55.7^s$	$-67°26'14''$	T/M/M	25.0/20.1	26.6/21.7	26.6/21.7	8.8
0071940101	2001 Oct. 31	$05^h26^m04.9^s$	$-67°27'21''$	T/T/T	27.6/26.8	31.9/31.2	31.9/31.2	13.7

Notes. [(a)] T: Thin; M: Medium. [(b)] Performed duration (total) and useful (filtered) exposure times, after removal of high background intervals. [(c)] Angle in arcmin between the centre of the pn detector and the centre of the X-ray source (as defined in Sect. 3.1.1).

classified as a "possible SNR" by Davies et al. (1976) (from which the identifier "DEM" is taken) based on its optical shell-like morphology. In X-rays, the catalogue of *ROSAT*'s PSPC sources in the LMC (Haberl & Pietsch 1999) includes [HP99] 534, located within the extent of DEM L205. However, the short exposure and large off-axis position prevented any classification of the X-ray source. Dunne et al. (2001) classified DEM L205 as a superbubble (SB) with an excess of X-ray emission.

In our new and archival observations, we detected the object at all wavelengths. The subsequent analyses allowed us to confirm the SNR nature of the source and estimate some of its parameters. The paper is organised as follows: in Sect. 2, we present our new X-ray and radio-continuum observations, and archival optical and IR data. The X-ray, radio, and IR data analyses are detailed in Sect. 3. We discuss the implications of our multi-frequency study in Sect. 4, and we give our conclusions in Sect. 5.

2. Observations and data reduction

2.1. X-rays

DEM L205 was in the field of view of the European Photon Imaging Camera (EPIC) X-ray instrument, comprising a pn CCD imaging camera (Strüder et al. 2001) and two MOS CCD imaging cameras (Turner et al. 2001), during the first pointing of our recently started LMC survey with *XMM-Newton*. The 28 ks observation (ObsId 0671010101) was carried out on 19 December 2011. The EPIC cameras operating in full-frame mode were used as the prime instruments. We used the XMM SAS[1] version 11.0.1 for the data reduction. After the screening of high background-activity intervals, the useful exposure times for pn and MOS detectors were ~20 and 22 ks, respectively.

An archival *XMM-Newton* observation (ObsId 0071940101, pointing at the LMC SB N 51D) includes the remnant in the field of view, at a larger off-axis angle. None of the EPIC cameras covered the remnant to its full extent. We used data from this observation only for the purpose of imaging but not spectrometry. This gives us a longer exposure time, particularly in the western part of the remnant, which is covered by all cameras in both observations. In Table 1 we list the details of the observations.

Images and exposure maps were extracted in the standard *XMM-Newton* energy bands (see Table 3 in Watson et al. 2009) for all three cameras. Single and double-pixel events (`PATTERN` = 0 to 4) from the pn detector were used. In the softest band (0.2–0.5 keV), only single-pixel events were selected to avoid the higher detector noise contribution from the double-pixel events. All single to quadruple-pixel (`PATTERN` = 0 to 12) events from the MOS detectors were used. We performed a simultaneous source detection on images in all five energy bands of all three instruments, using the SAS task *edetectchain*.

[1] Science Analysis Software, `http://xmm.esac.esa.int/sas/`

We then subtracted the detector background taken from filter wheel closed data, scaled by a factor estimated from the count rates in the corner of the images not exposed to the sky. MOS and pn data were merged and we applied a mask to remove bad pixels. Images from the two observations were merged and adaptively smoothed, using Gaussian kernels with a minimum full width at half maximum (FWHM) of 10″. Kernel sizes were computed at each position in order to reach a typical signal-to-noise ratio of five. Finally, we divided the smoothed images by the vignetted exposure maps.

2.2. Radio

We observed DEM L205 with the Australia Telescope Compact Array (ATCA) on the 15 and 16 November 2011 at wavelengths of 3 cm and 6 cm (9000 MHz and 5500 MHz), using the array configuration EW367. We excluded baselines formed with the sixth antenna, leaving the remaining five antennae to be arranged in a compact configuration. More information about this observation and the data reduction can be found in de Horta et al. (2012). Our 6 cm observations were merged with those from Dickel et al. (2005, 2010). In addition, we made use of the 36 cm Molonglo Synthesis Telescope (MOST) unpublished mosaic image as described by Mills et al. (1984) and an unpublished 20 cm mosaic image from Hughes et al. (2007). Beam sizes were $46.4'' \times 43.0''$ for the 36 and 20 cm images. Our 6 cm image beam size was $41.8'' \times 28.5''$, with a position angle of 49.6°.

2.3. Optical

We used data from the Magellanic Clouds Emission Line Survey (MCELS, e.g. Smith et al. 2000). A $8° \times 8°$ region centred on the LMC was observed with the 0.6 m *Curtis Schmidt* telescope from the University of Michigan/Cerro Tololo Inter-American Observatory (CTIO), using the three narrow-band filters [S]$\lambda\lambda$6716, 6731 Å, Hα, and [O]λ5007 Å and matching red and green continuum filters. We flux-calibrated and combined all MCELS data covering the SNR, with a pixel size of $2'' \times 2''$. The [S] and Hα images were stellar continuum-subtracted to produce a map of [S]/Hα, which is an efficient criterion for distinguishing SNRs from H regions, where the ratio is typically >0.4 and ≲0.1, respectively (Fesen et al. 1985). The X-ray composite image and [S]/Hα contours from these data are shown in Fig. 2. In addition, we present an unpublished higher-resolution Hα image in Fig. 6 (pixel size of $1'' \times 1''$), which was obtained as part of the ongoing MCELS2 program with the MOSAIC camera on the Blanco 4-m telescope at the CTIO.

2.4. Infrared

During the SAGE survey (Meixner et al. 2006), the *Spitzer* Space Telescope observed a $7° \times 7°$ area in the LMC with the Infrared Array Camera (IRAC; Fazio et al. 2004) in its 3.6, 4.5, 5.8, and 8 μm bands, and with the Multiband Imaging Photometer

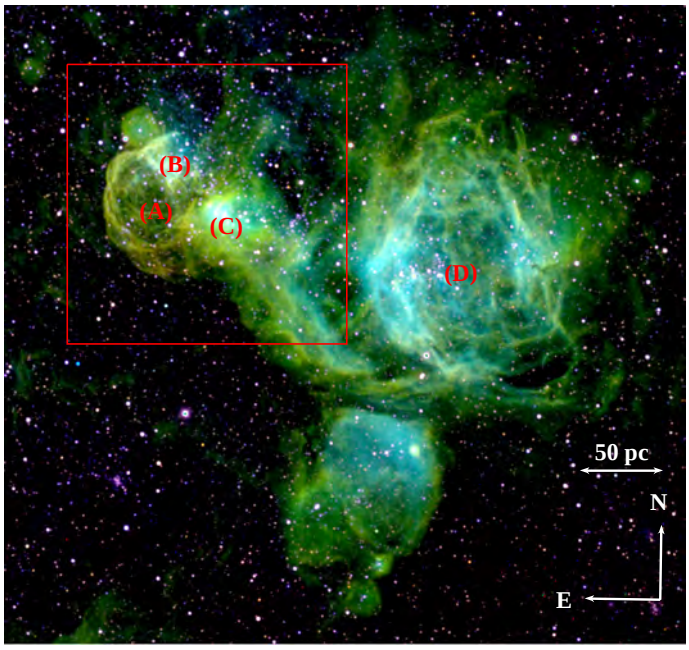

Fig. 1. The giant H complex LHA 120-N 51 in the light of [S] (red), Hα (green), and [O] (blue), all data from MCELS (see Sect. 2.3). The red box delineates the area shown in Fig. 2. Noticeable substructures are : DEM L205 (A), the SNR candidate analysed in this paper; N51A (B) and N51C (C, also named DEM L201), two H regions also seen in the radio and the IR; the SB N51D, or DEM L192, in (D).

(MIPS; Rieke et al. 2004) in its 24, 70, and 160 μm bands. To study the IR emission of the source and its environment, we retrieved the IRAC and MIPS mosaiced, flux-calibrated (in units of MJy sr^{-1}) images processed by the SAGE team. The pixel sizes are 0.6″ for all IRAC wavelengths and 2.49″ and 4.8″ for 24 μm and 70 μm MIPS data, respectively.

3. Data analysis and results

3.1. X-rays

3.1.1. Imaging

We created composite images, using the energy ranges 0.2−1 keV for the red component, 1−2 keV for the green, 2−4.5 keV for the blue. The X-ray image is shown in Fig. 2. In addition to soft diffuse emission and many point sources, an extended soft source is clearly seen. This source correlates with the positions of [HP99] 534 and DEM L205. The images alone already show that the source has hardly any emission above 1 keV.

The X-ray emission can be clearly delineated by an ellipse centred at RA = $05^h28^m05^s$ and Dec = −67°27′20″, with a position angle of 30° (with respect to the north and towards the east, see Fig. 2). The major and minor axes have sizes of 5.4′ and 4.4′, respectively. At a distance of 50 kpc, this corresponds to an extent of ∼79 × 64 pc. We note that the eastern and southern boundaries of the X-ray emission are more clearly defined than the western and northern ones. We discuss this issue in Sect. 4.3.

3.1.2. Spectral fitting

We created a vignetting-weighted event list to take into account the effective area variation across the source extent. The spectrum was extracted from a circular region with a radius of 3′ and the same centre as the ellipse defined in Sect. 3.1.1. A nearby region of the same size, free of diffuse emission, was used to extract a background spectrum. Point sources were excluded from the extraction regions. Spectra were rebinned with a minimum of 30 counts per bin to allow the use of the χ^2-statistic. The spectral-fitting package XSPEC (Arnaud 1996) version 12.7.0u was used to perform the spectral analysis.

Because of the low surface brightness of the source, the spectrum of the source region (background + source) contains a relatively low number of counts. Constraining the parameters of the source model was therefore challenging. The spectra were extracted from different regions of the detector (even from different CCD chips) that have different responses. Simply subtracting the background spectrum would have led to a further loss in the statistical quality of the source spectrum, hindering the spectral fitting of the source emission. A way to prevent this was to estimate the background using a physically motivated model (although any model fitting the data could in principle be used), and then fit the spectra of the source and background regions simultaneously.

For the X-ray background, we used a three-component model, as in Kuntz & Snowden (2010), which consists of *i)* an unabsorbed thermal component for the Local Hot Bubble (LHB), *ii)* an absorbed thermal component to model the Galactic halo emission, and *iii)* an absorbed power-law to account for non-thermal, unresolved extragalactic background. The spectral index was fixed to 1.46 (Chen et al. 1997). We used photoelectric absorption with the cross-sections taken from Balucinska-Church & McCammon (1992) and assumed the elemental abundances of Wilms et al. (2000).

In addition to this X-ray background model, an instrumental fluorescent line of Al Kα, with E = 1.49 keV, and a soft proton contamination (SPC) term were also included. The SPC was modelled by a power-law *not* convolved with the instrumental response, which is appropriate for photons but not for protons (Kuntz & Snowden 2008).

Three models were used for the emission of the remnant : a thermal plasma, using the Astrophysical Plasma Emission Code (APEC), a plane-parallel shock, and a Sedov model (Borkowski et al. 2001), called vapec, vpshock, and vsedov in XSPEC (where the prefix "v" indicates that abundances can vary). The vsedov model computes the X-ray spectrum of an SNR in the Sedov-Taylor stage of its evolution. The parameters of the Sedov model are the mean shock temperature T_s, the postshock electron temperature T_{es} and the ionisation timescale τ_0, defined as the product of the electron density behind the shock front and the remnant's age. As Borkowski et al. emphasised, in the case of older and cooler SNRs, only T_s can be determined from spatially integrated X-ray observations with modest spectral resolution. We indeed found little or no variations in the best-fit parameters and the χ^2 when constraining $\beta = T_{es}/T_s$ between 0 (by taking T_{es} = 0.01 keV, the minimal value in the Sedov model implemented in XSPEC) and 1. As a consequence, we constrained the mean shock and postshock electron temperature to be the same. This is a reasonable assumption, since old remnants should be close to ion-electron temperature equilibrium.

The vpshock model parameters are the shock temperature and the upper limit to the linear distribution of ionisation timescales τ_{up}. This model has been shown to approximate the Sedov model better than the commonly used non-equilibrium ionisation (NEI) model (Borkowski et al. 2001). There are deviations between vpshock and vsedov models for low-temperature shocks, but these occur predominantly above 2 keV.

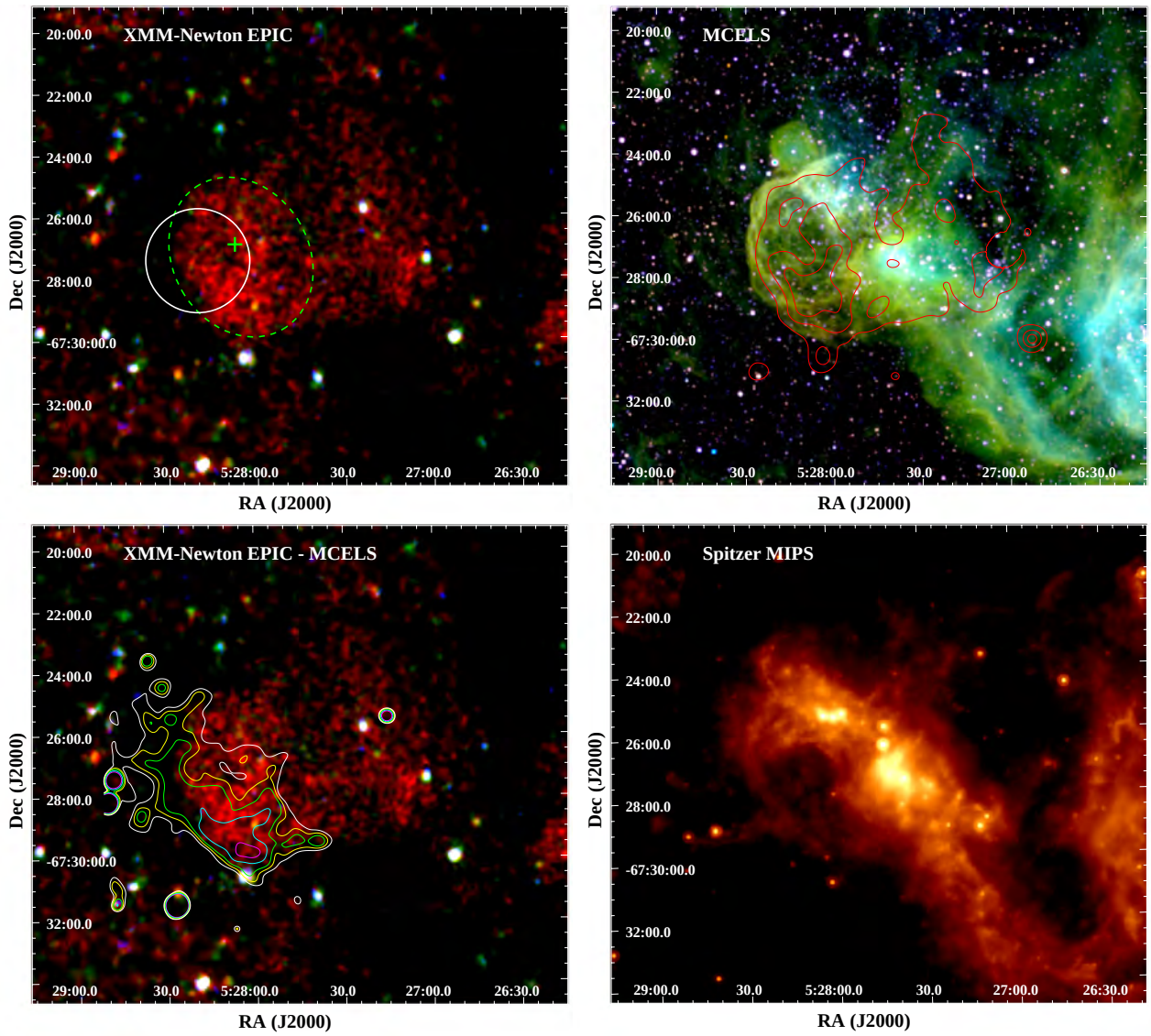

Fig. 2. A multicolour view of DEM L205. *Top left*: X-ray colour image of the remnant, combining all EPIC cameras. Data from two overlapping observations are combined and smoothed (see Sect. 3.1.1 for details). The red, green, and blue components are soft, medium, and hard X-rays, as defined in the text. The white circle is the 90% confidence error of the [HP99] 534 position and the green cross is the central position of DEM L205. The green dashed ellipse (defined in Sect. 3.1.1) encompasses the X-ray emission and is used to define the nominal centre and extent of the remnant. *Top right*: the same region of the sky in the light of [S] (red), Hα (green), and [O] (blue), where all data are from the MCELS. The soft X-ray contours from the top left image are overlaid. *Bottom left*: same EPIC image as above but with [S]-to-Hα ratio contours from MCELS data. Levels are (inwards) 0.4, 0.45, 0.5, 0.6, and 0.7. *Bottom right*: the remnant as seen at 24 μm by *Spitzer* MIPS. Optical and IR images are displayed logarithmically.

When fitted to the source region spectrum, the normalisations of the X-ray background components were allowed to vary, but their *ratios* were constrained to be the same as in the background region. We found 5 % or smaller variations between the normalisations of the background components of the two regions (which are shown by the dashed lines in Fig. 3). Because the background spectrum was extracted from the same observation (that is, at the same time period) and at a similar position and off-axis angle as the source spectrum, the SPC contribution was not expected to vary much (Kuntz & Snowden 2008). The validity of this assumption was checked a posteriori by looking at our data above 3 keV. We therefore used the same SPC parameters for the background and source spectra.

To account for the absorption of the source emission, we included two photoelectric absorption components, one with a column density $N_{\rm H\ Gal}$ for the Galactic absorption and another one with $N_{\rm H\ LMC}$ for the LMC. Except for O and Fe, which were allowed to vary, the metal abundances for the source emission models were fixed to the average metallicity in the LMC (i.e., half the solar values, Russell & Dopita 1992), because the observations were not deep enough to permit abundance measurements and because high-resolution spectroscopic data were unavailable.

3.1.3. Spectral results

We fitted the data between 0.2 keV and 7 keV. We extended the fit down to low energies to constrain the parameters of the LHB component, which had a low plasma temperature ($kT \lesssim$ 0.1 keV). The data above 2 keV, where the Galactic components hardly contribute, were necessary to constrain the non-thermal extragalactic emission and the SPC (Kuntz & Snowden 2010).

The quality of our data statistics was too low to place strong constraints on the foreground hydrogen absorption column. The

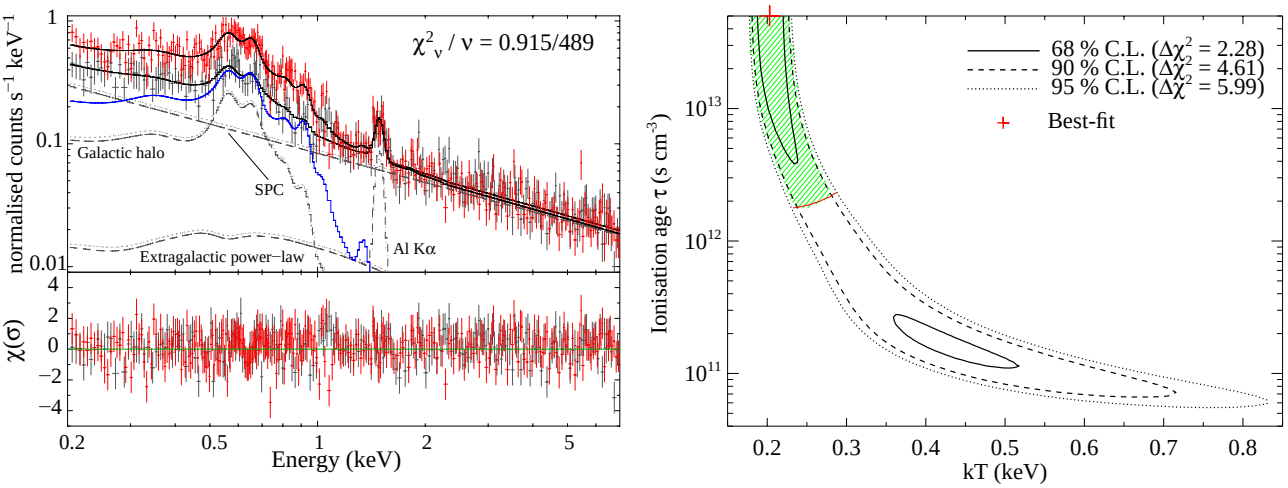

Fig. 3. *Left*: EPIC-pn spectrum of DEM L205. The spectra in the background and source regions (grey and red data points, respectively) are modelled simultaneously. The background model components are shown by the dashed lines and labelled. The Sedov model used for the remnant is shown by the blue solid line. Residuals are shown in the lower panel in terms of σ. *Right*: the $kT - \tau$ parameter plane for the Sedov model. The 68, 90, and 95% CL contours are shown by the solid, dashed, and dotted black lines, respectively. The formal best-fit, occurring at the upper limit of the ionisation ages of the XSPEC model (5×10^{13} s cm^{-3}) is marked by the red plus sign. The red line shows the 99% CL lower contour of emission measure obtained with the APEC model. The green hatching indicates the region where $\Delta\chi^2 < 4.61$ and EM is in the 99% CL range of the APEC model (see Sect. 3.1.3).

best fit value for $N_{\rm H\ Gal}$ was 5.3×10^{20} cm^{-2} (using the APEC component), with a 90% confidence interval from 3 to 10×10^{20} cm^{-2}. We therefore fixed it at 5.9×10^{20} cm^{-2} (based on the H measurement of Dickey & Lockman 1990). We found that the best-fit intrinsic LMC column density value tended to 0, with a 90% confidence upper limit of 3.9×10^{20} cm^{-2} (using the APEC component), and then fixed $N_{\rm H\ LMC}$ to 0. We note that even though the best-fit temperature of the Local Hot Bubble we derived (85 eV) agrees well with the results of Henley & Shelton (2008), the errors are large because this component contributes only to a small number of energy bins. The significance of the LHB component was less than 10% (using a standard F-test), and we removed this component from our final analysis. The power-law component was also faint but more than 99.99% significant.

We achieved good fits and obtained significant constraints on the source parameters. The reduced χ^2 were between 0.91 and 0.92. The plasma temperatures (kT between 0.2 keV and 0.3 keV) are consistent for all models. They are similar to temperatures found in other extensive SNRs (e.g. Williams et al. 2004; Klimek et al. 2010). The unabsorbed X-ray luminosity of the Sedov model is 1.43×10^{35} erg s^{-1} in the range 0.2−5 keV, whilst the other models yield similar values. More than 90% of the energy is released below 0.9 keV.

The best-fit values with 90% confidence levels (CL) errors are listed in Table 2. The spectrum fitted by the best-fit Sedov model is shown in Fig. 3. The ionisation timescales were large (more than 10^{12} s cm^{-3}), which indicates quasi-equilibrium. In this regime, kT and τ are degenerate, because the spectra hardly change when increasing kT and decreasing τ. This effect is shown in Fig. 3. However, the emission measure (EM), which is a function of the volume of emitting plasma and densities, *does not* depend on the model used, provided the column density is the same. With the help of the 99% CL range of EM obtained using the APEC model ($16.0–25.4 \times 10^{57}$ cm^{-3}), which does not have the $kT - \tau$ degeneracy problem, we obtained additional constraints on kT and τ.

The O and Fe abundances are (about 0.2 dex) lower than those in Russell & Dopita (1992) but consistent with the results found by Hughes et al. (1998) in other LMC SNRs. The abundances found for DEM L205 match well those reported in the nearby (13′ or ∼190 pc in projection) LMC SB N 51D (Yamaguchi et al. 2010).

3.2. Radio

3.2.1. Morphology

To assess the morphology of the source, we overlaid the radio contours on the *XMM-Newton* image. Weak, extended ring-like emission correlates with the eastern side of the X-ray remnant and is most prominent, as expected, at 36 cm, but only marginally detected at higher frequencies (Fig. 4, top). It is difficult to classify the morphology of this SNR at radio wavelengths because it lies in a crowded field. The surrounding radio emission is dominated in the north by LHA 120-N 51A, which is classified as an H region (Filipovic et al. 1998) and also correlates with the small molecular cloud [FKM2008] LMC N J0528−6726 (Fukui et al. 2008), and in the west by the H region LHA 120-N 51C.

If we assumed that the analysable region of the 36 cm image (Fig. 4, top left) is typical of the rest of the remnant's structure, the SNR would have a typical ring morphology. Nevertheless, with the present resolution, one cannot easily estimate the total flux density of this SNR at any radio frequency. However, we note the steep drop (across the eastern side of the ring) in flux density at higher frequencies, which results in a nearly completely dissipated remnant as seen at 6 cm (Fig. 4, top right).

3.2.2. Radio-continuum spectral energy distribution

We were unable to compile a global spectral index for the remnant because a large portion of DEM L205 cannot be analysed at radio wavelengths (as described in Sect. 3.2.1). However, a spectral index map (Fig. 5) shows the change in flux density from 36 cm to 6 cm. The map was formed by reprocessing all observations to a common $u-v$ range, and then fitting $S \propto \nu^{\alpha}$ pixel by pixel using all three images simultaneously. The areas of the SNR that are uncontaminated by strong sources have spectral indices between −0.7 and −0.9, which is steeper but close to

Table 2. X-ray spectral results for DEM L205.

Background model best-fit parameters							
Model	$N_{\rm H\ Gal}$[a] (10^{20} cm^{-2})	$kT_{\rm Halo}$ (eV)	$\rm EM_{Halo}$[b] (10^{57} cm^{-3})	$\Gamma_{\rm XRB}$[a, c]	$A_{\rm XRB}$	$\Gamma_{\rm SPC}$	$A_{\rm SPC}$
vapec	5.9	201^{+20}_{-9}	$5.2^{+0.8}_{-0.8}$	1.46	$2.68^{+1.4}_{-1.3} \times 10^{-5}$	$0.78^{+0.05}_{-0.06}$	$8.48^{+0.9}_{-0.9} \times 10^{-2}$
vpshock	5.9	203^{+15}_{-12}	$5.1^{+0.7}_{-0.8}$	1.46	$2.39^{+1.1}_{-1.5} \times 10^{-5}$	$0.79^{+0.05}_{-0.06}$	$8.69^{+1.0}_{-1.0} \times 10^{-2}$
vsedov	5.9	205^{+13}_{-12}	$5.0^{+0.6}_{-0.5}$	1.46	$2.02^{+1.4}_{-0.7} \times 10^{-5}$	$0.79^{+0.03}_{-0.02}$	$8.93^{+0.4}_{-.04} \times 10^{-2}$
Source models best-fit parameters							
Model	$N_{\rm H\ LMC}$[a] (10^{20} cm^{-2})	kT (eV)	τ (10^{12} s cm^{-3})	EM (10^{57} cm^{-3})	12 + log(O/H)	12 + log(Fe/H)	χ^2/d.o.f.
vapec	0	251^{+18}_{-18}	—	$20.6^{+3.0}_{-3.0}$	$8.22^{+0.10}_{-0.11}$	$6.57^{+0.25}_{-0.33}$	452.96/490
vpshock	0	257^{+60}_{-33}	4.21 (>1.02)	22.0	$8.10^{+0.11}_{-0.11}$	$6.86^{+0.27}_{-0.31}$	446.09/489
vsedov	0	203^{+72}_{-20}	50.0 (>1.90)	24.5	$8.16^{+0.12}_{-0.10}$	$6.84^{+0.25}_{-0.30}$	447.44/489

Notes. The top panel lists the best-fit parameters of the background model and the bottom panel shows the parameters of the source models (details are in Sect. 3.1.2). Errors are given at the 90% confidence level. We required the emission measures of the vpshock and vsedov models to be in the 99% CL range of EM obtained with the vapec model (see Sect. 3.1.3), and this gave us the range of errors for kT and τ of the vpshock and vsedov models. The χ^2 and associated degrees of freedom (d.o.f.) are also listed. [(a)] Fixed parameter (see text for details). [(b)] Emission measure $\int n_{\rm e} n_{\rm H} {\rm d}V$. [(c)] Γ_i and A_i are the spectral indices and normalisations of the power-law component i, where i is either the X-ray background (XRB) or soft proton contamination (SPC). A_i are given in photons keV^{-1} cm^{-2} s^{-1} at 1 keV.

the typical SNR radio-continuum spectral index of $\alpha \sim -0.5$. We note that uncertainties in the determination of the background emission are likely to cause a bias toward steeper spectral indices. We also point out that the bright point source seen in the north-east (mainly at 36 cm) is most likely a background galaxy or an active galactic nucleus (AGN).

3.3. Infrared flux measurement

The IR data suffer from the same crowding issues as the radio-continuum data. The IR emission in the SNR region (see Fig. 4, bottom) is dominated by the two H regions seen in radio, whose positions are shown in the 8 μm images (Fig. 4, bottom left). However, at 24 μm, an arc of shell-like emission is seen in the eastern and south-eastern regions of the remnant (outlined in Fig. 4, bottom middle) at the same position of the 36 cm emission. We used the optical and X-ray emission contours to constrain the region at 24 μm that can be truly associated with the SNR and found that this arc tightly follows the Hα and X-ray morphologies. We integrated the 24 μm surface brightness in this region (in white in Fig. 4, bottom middle) and found a flux density of $F_{24} = 660$ mJy.

To calibrate our method of flux density measurement and estimate the uncertainties, we derived the 24 μm flux densities of the LMC SNRs N132D, N23, N49B, B0453–68.5, and DEM L71, and compared them to the values published in Borkowski et al. (2006) and Williams et al. (2006). We were able to reproduce these authors' values, but with rather large error ranges (~30%), chiefly because of uncertainties in the definition of the integration region. The two aforementioned studies integrated the flux density only in limited areas of the SNRs, and the integration regions are not explicitly defined in their papers. In the case of DEM L205 it is also difficult to define the area of IR emission from the SNR only, so we believe these 30% error ranges are a reasonable estimate of the error in the flux density measurement. The systematic uncertainties in the flux calibration of the *Spitzer* images are small in comparison and can be neglected. In particular, given that the thickness of our region in the plane of the sky is 20″–25″, only a small aperture correction would be needed (at least at 24 μm).

The 70 μm image (Fig. 4, bottom right) shows that DEM L205 has the same morphology as at 24 μm, but with lower resolution, hence the confusion is even higher. Simply using the same region as for F_{24}, we found a flux density of $F_{70} = 3.4$ Jy, with similarly large errors. We discuss the origin of the IR emission in Sect. 4.1.

In the IRAC wavebands, no significant shell-like emission is detected. We tentatively identified two arcs at 8 μm (marked in cyan in Fig. 4, bottom left) that could originate from the interaction of the shock with higher densities towards the H regions. The two arcs are also present at 5.8 μm (not shown) but neither at 4.5 μm nor 3.6 μm, where only point sources are seen.

4. Discussion

Since the source exhibits all the classical SNR signatures, we can confirm DEM L205 as a *new supernova remnant*. This brings the total number of SNRs in the LMC to 56, using the list of 54 remnants assembled by Badenes et al. (2010) and the new SNR identified by Grondin et al. (2012). For the naming of SNRs in the Magellanic Clouds, we advocate the use of the acronym "MCSNR", which was pre-registered to the International Astronomical Union by Williams et al., who maintain the Magellanic Cloud Supernova Remnants online database[2]. This should ensure that there is a more consistent and general naming system for future studies using the whole sample of SNRs in the LMC. On the basis of the J2000 X-ray position, DEM L205 would thus be called MCSNR J0528−6727.

In the following sections, we take advantage of the multi-wavelength observations of the remnant and discuss the origin of the IR emission (Sect. 4.1), derive some physical properties of the remnant (Sect. 4.2), compare the morphology at all observed wavelengths and discuss the environment in which the SN exploded (Sect. 4.3), and analyse the star formation activity around the SNR (Sect. 4.4).

[2] http://www.mcsnr.org/Default.aspx

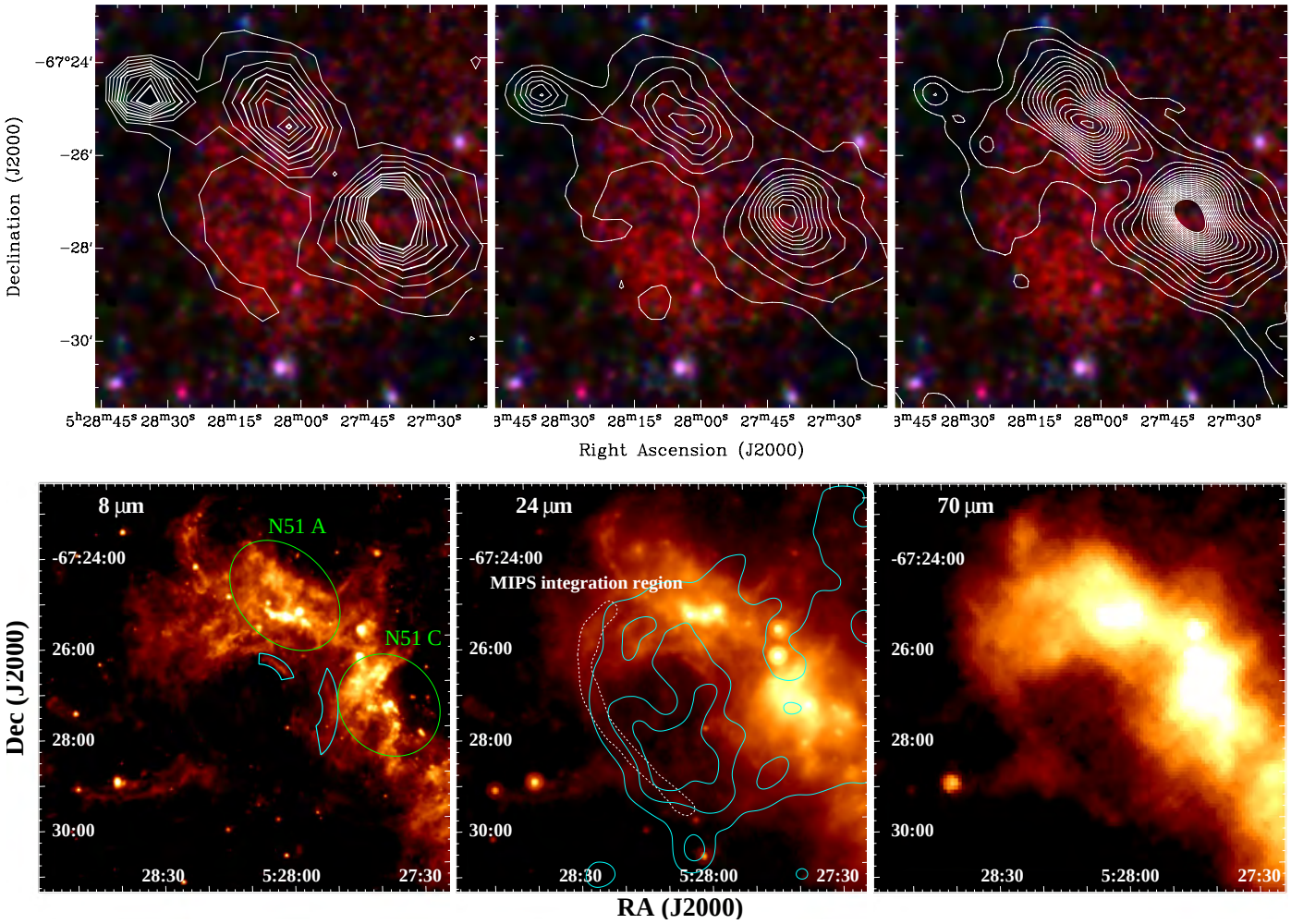

Fig. 4. *Top row*: radio contours of DEM L205 overlaid on the X-ray image. *Left*: 36 cm contours from 5 to 50σ with 5σ steps (σ = 0.4 mJy/beam). *Middle*: 20 cm contours from 3 to 23σ with 2σ steps (σ = 1.3 mJy/beam). *Right*: 6 cm contours from 3 to 200σ with 9σ steps (σ = 0.1 mJy/beam). Beam sizes are 40″ × 40″ for the 36 and 20 cm images, and 41.8″ × 28.5″ at 6 cm. Note that the portion of the sky shown is smaller than in Fig. 2. *Bottow row*: *Spitzer* images of DEM L205 at 8, 24, and 70 μm (from left to right). All images show a similar portion of the sky as the radio images and are displayed logarithmically. The green ellipses on the 8 μm image show the positions of the two H regions seen in the 36 cm image (*top left*), and the cyan arcs indicate the 8 μm emission possibly associated with the SNR. The white dashed line shown in the 24 μm image marks the region where we measured the flux densities at 24 μm and 70 μm (Sect. 3.3). Soft X-ray contours are overlaid in cyan.

4.1. Origin of the IR emission

Supernova remnants emit IR light chiefly in forbidden lines, rotational/vibrational lines of molecular hydrogen, emission in polycyclic aromatic hydrocarbon (PAH) bands, and thermal continuum emission from dust collisionally heated by shock waves (e.g. Koo et al. 2007) and/or by stellar-radiation reprocessing. Infrared synchrotron emission is only expected in pulsar wind nebulae, for instance in the Crab (Temim et al. 2006). Polycyclic aromatic hydrocarbons are thought to be destroyed by shocks with velocities higher than 100 km s^{-1} and should not survive for more than a thousand years in a tenuous hot gas (Micelotta et al. 2010a,b). However, PAH features have been detected in Galactic SNRs (Andersen et al. 2011), where shock velocities are rather low owing to interactions with a molecular cloud environment, and even in the strong shocks of the young LMC remnant N132D (Tappe et al. 2006).

No significant emission from DEM L205 was detected in the IRAC wavebands (which have been chosen to include the main PAH features), with the possible exception of the two 8 and 5.8 μm arcs (Fig. 4, bottom left) in the direction of the neighbouring H regions (in the north and west). This means that PAHs have been efficiently destroyed. The absence of IR spectroscopic observations precludes further interpretation.

The presence of Hα emission shows that hydrogen is not in the molecular phase, hence rotational/vibrational line contribution is negligible. The emission in the 24 and 70 μm wavebands should then be dominated either by dust or ionic forbidden lines. Ionic lines in the 24 μm filter bandpass are [S] 25.2 μm, [Fe] 24.50 and 25.99 μm, [Fe] 22.95 μm, and [O] 25.91 μm. [S] emission is not expected because of the prominent [S] optical emission, showing that S^+ is the primary ionisation stage of sulphur. The morphological similarities between the MIR and X-ray emission lead us to the interpretation that we mainly observe the thermal continuum of dust. The correlation with 70 μm supports this scenario, and the 70-to-24 μm ratio (~5.2) is consistent with a dust temperature of 50–80 K (Williams et al. 2006). We note, however, that in the northern part of the arc of 24 μm emission (encompassed by the white dashed line in Fig. 4, bottom middle), the MIR emission is slightly ahead of the shock (delineated by the X-ray emission), whereas it correlates tightly with the shock in the rest of the arc. This morphology and the presence of the OB association LH 63 (see Fig. 6, right) indicates that stellar radiation dominates

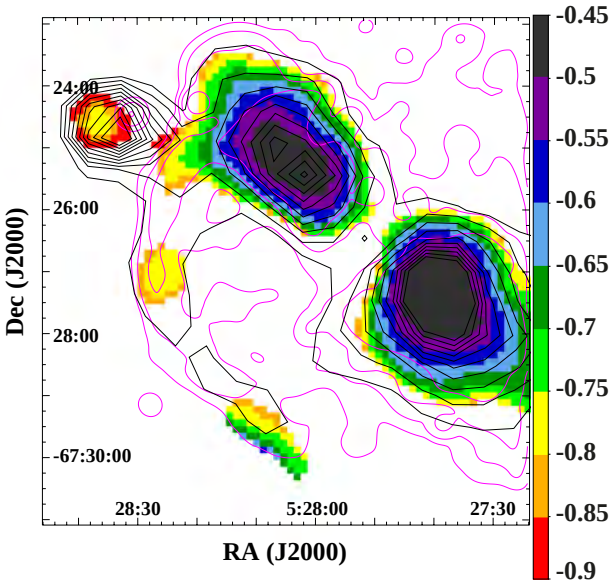

Fig. 5. Spectral index map of DEM L205 between wavelength of 36, 20, and 6 cm, covering the same field as Fig. 4. The sidebar gives the spectral index α, as defined in the introduction. The 36 cm contours (black) are overlaid, with the same levels as in Fig. 4. The Hα structures (Figs. 1 and 2) are sketched by the magenta contours.

the heating of the dust in the north. In the southern part, shock waves could play a more significant role in heating the dust.

The lack of spectroscopic data prevent us from establishing the precise contribution of dust vs. O and Fe lines. Because of these limitations and the confusion with the background, and because only part of the SNR is detected at IR wavelengths, we did not attempt to derive a dust mass. Consequently, no dust-to-gas ratio (using the swept-up gas mass estimate from X-ray observations) and dust destruction percentage can be given.

4.2. Properties of DEM L205 derived from the X-ray observations

From the X-ray spectral analysis, we can derive several physical properties of the remnant: electron and hydrogen densities n_e and n_H, dynamical and ionisation ages t_{dyn} and t_i, swept-up mass M, and initial explosion energy E_0. We used a system of equations adapted from van der Heyden et al. (2004), given by

$$n_e = \frac{1}{f}\sqrt{r_e \frac{EM}{V}} \quad \left(\mathrm{cm}^{-3}\right) \tag{1}$$

$$n_H = n_e / r_e \quad \left(\mathrm{cm}^{-3}\right) \tag{2}$$

$$t_{dyn} = 1.3 \times 10^{-16} \frac{R}{\sqrt{kT_s}} \quad (\mathrm{yr}) \tag{3}$$

$$t_i = 3.17 \times 10^{-8} \frac{\tau}{n_e} \quad (\mathrm{yr}) \tag{4}$$

$$M = 5 \times 10^{-34}\, m_p\, r_m\, n_e\, f^2\, V \quad (M_\odot) \tag{5}$$

$$E_0 = 2.64 \times 10^{-8}\, kT_s\, R^3\, n_H \quad (\mathrm{erg})\,, \tag{6}$$

where EM is the emission measure ($=n_e n_H V$) in cm^{-3}, kT_s is the shock temperature in keV, and τ is the ionisation timescale in s cm^{-3}. These parameters are determined by the spectral fitting. In addition, R is the radius of the X-ray remnant in cm (using the semi-major axis of 39.5 pc, see Sect. 3.1.1), V is the volume ($4\pi/3 \times R^3$) assuming spherical symmetry (as discussed below), m_p is the proton mass in g, r_m is the total number of baryons per hydrogen atom ($=n_m/n_H$), and r_e is the number of electrons per hydrogen atom ($=n_e/n_H$). Assuming a plasma with 0.5 solar metal abundances, as done in the spectral fitting, we have $r_m \approx 1.40$ and $r_e \approx 1.20$ (for full ionisation). Finally, f is a filling factor to correct for any departure from spherical symmetry, as inferred from the X-ray morphology. f is defined as $\sqrt{V_t/V}$, where V_t is the true X-ray emitting (ellipsoidal) volume. Adopting the semi-minor axis of the X-ray emitting ellipse (32 pc) as the second semi-principal axis, f is in the range 0.81–0.90, with the third semi-principal axis being between 32 pc and 39.5 pc. The properties are listed in Table 3, using f in this range and EM in the range defined in Sect. 3.1.3.

Table 3. Physical properties of DEM L205.

n_e	n_H	t_{dyn}	M	E_0
$\left(10^{-2}\ \mathrm{cm}^{-3}\right)$		$(10^3\ \mathrm{yr})$	$(M_\odot)$	$(10^{51}\ \mathrm{erg})$
5.6–7.8	4.7–6.5	35^{+2}_{-5}	400–460	0.52–0.77

The large amount (from 400 $M_\odot$ to 460 $M_\odot$) of swept-up gas justifies a posteriori that the SNR is indeed well-established in the Sedov phase. Because the remnant is old, the plasma is close to or in collisional ionisation equilibrium, as indicated by either the acceptable fit of the APEC model or the large ionisation timescale τ, for which only a lower limit is found. Thus, the spectrum changes very slowly with time and τ is no longer a sensitive age indicator (van der Heyden et al. 2004). This explains why t_i is unrealistically long (>770 kyr, from Eqs. (1) and (4)) and unreliable.

4.3. Multi-wavelength morphology

In Fig. 2, we see an X-ray remnant with a slightly elongated shape and a maximal extent of 79 pc. Therefore, DEM L205 ranks amongst the largest known in the LMC (compared e.g. to SNRs described in Cajko et al. 2009; Klimek et al. 2010; Grondin et al. 2012). The optical emission-line images (Figs. 2 and 6) show the shell-like structure of DEM L205 coinciding with the boundary of the X-ray emission from the remnant. Dunne et al. (2001) classified the shell as a SB, interpreting the morphology of DEM L205 as a blister blown by the OB association LH 63 (see Sect. 4.4 and Fig. 6, right). They measured a mild expansion velocity of ~70 km s^{-1} for the Hα shell, which is typical of SBs. Supernova remnants exhibit higher expansion velocities ($\gtrsim$100 km s^{-1}), although this is not a necessary condition (Chu 1997).

On the basis of the low densities (<0.1 cm^{-3}) derived from the X-ray spectral analysis, we conclude that the supernova exploded inside the blister, producing the bright X-ray emission in the interior of the SB. The SNR shocks reaching the inner edge of the bubble might then have produced non-thermal radio emission, and the observed morphology at 36 cm is consistent with this picture.

The remnant is located in a complex environment. In the north and west, we detected two H regions and a strip of dust and gas extending down towards the south-west. The H regions also show bright IR emission, mainly from dust heated by stellar radiation, and bright (thermal) radio-continuum emission (Fig. 4). The [S]-to-Hα ratio is higher in the south of the remnant, indicating that the diffuse optical emission there is caused by the SNR shocks. In addition, the lower ratio in the north and west parts of the remnant is most likely due to photoionisation by the massive stars (bringing sulphur to ionisation stages higher

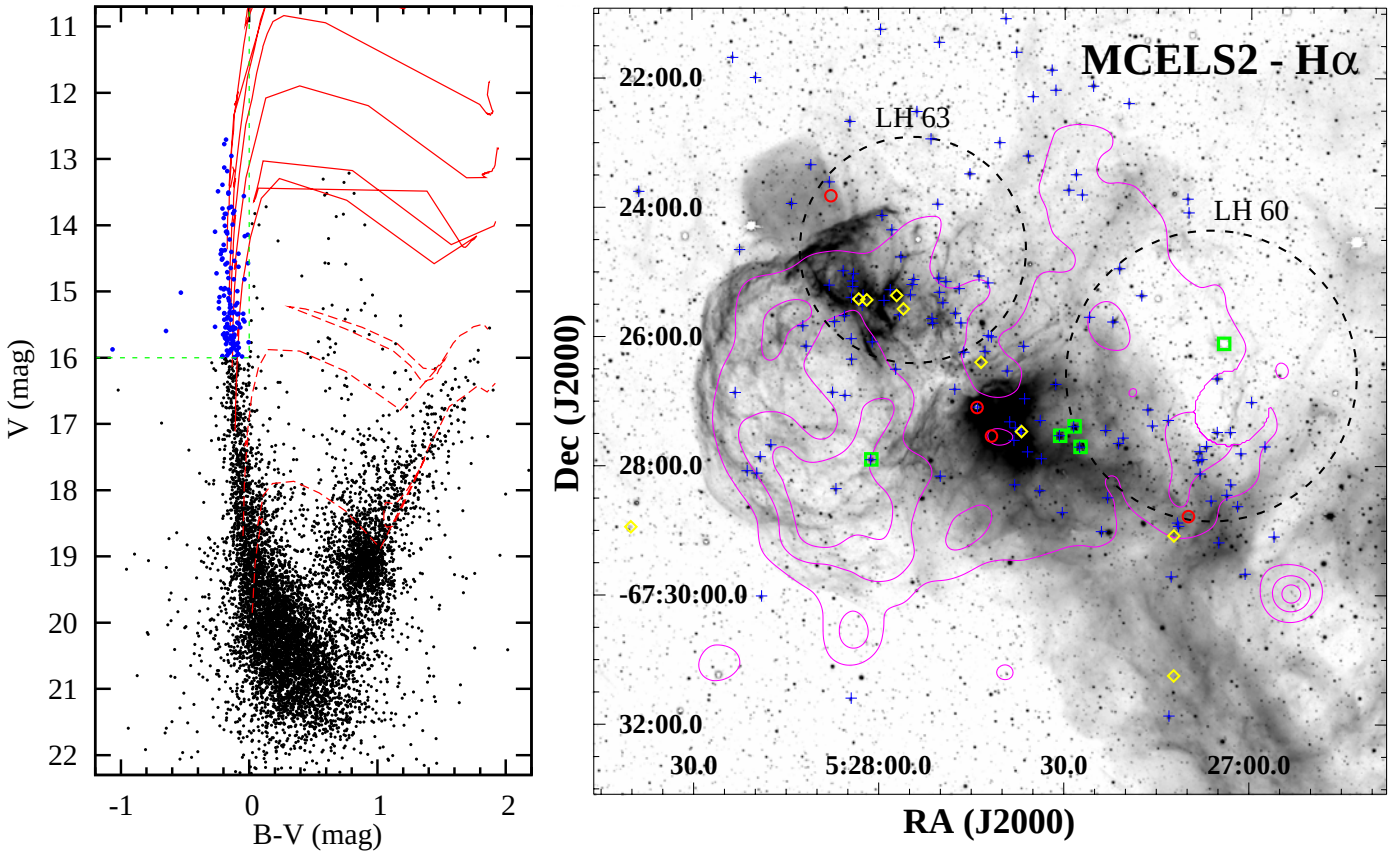

Fig. 6. *Left*: colour–magnitude diagram (CMD) of the MCPS stars (Zaritsky et al. 2004) within 100 pc (~6.9′) of the central position of DEM L205. Geneva stellar evolution tracks (Lejeune & Schaerer 2001) are shown as red lines, for metallicity of 0.4 $Z_{\odot}$ and initial masses of 3, 5 $M_{\odot}$ (dashed lines) and 10, 15, 20, 25, and 40 $M_{\odot}$ (solid lines), from bottom to top. The green dashed line shows the criteria used to identify the OB stars ($V < 16$ and $B - V < 0$). Stars satisfying these criteria are shown as blue dots. *Right*: MCELS2 Hα image of the SNR, with the soft X-ray contours in magenta. The blue plus signs show the positions of the OB candidates identified in the CMD and green squares identify Sanduleak OB stars. The black dashed circles encompass the nearby OB associations 60 and 63 from Lucke & Hodge (1970). Positions of definite (yellow diamond) and probable (red circle) YSOs from Gruendl & Chu (2009) are also shown.

than S^+) from the same OB associations that power the H regions and produced the SB in which the supernova exploded. We therefore propose that the SNR and the H regions are physically connected.

Furthermore, whilst the X-ray surface brightness falls abruptly across the eastern and southern boundaries of the remnant, much weaker emission is detected in the north and west, right at the positions of the H regions seen at all other wavelengths (Figs. 2 and 4). This indicates that the remnant is *behind* the H regions. The absorption column density is higher in the north and west, suppressing the X-ray emission and giving rise to the observed asymmetrical, irregular shape in these regions. The ellipse defined in Sect. 3.1.1 is probably an oversimplification of the actual morphology of the X-ray emitting region. The remnant may have a more spherical shape, with some parts masked by the H regions.

We also detected soft and faint diffuse X-ray emission on the other side of the dust/gas strip. The diffuse X-ray emission is enclosed by very sharp and faint Hα filaments (Figs. 2 and 6). The presence of the OB association (LH 60) suggests that we observed another stellar-wind-blown SB in which a SN had exploded. The faintness of the X-ray and optical emission precludes further analysis. We note here that the [S]-to-Hα ratio is <0.4. However, it cannot be used in that case because of the presence of massive stars from the OB association.

4.4. Past and present star formation activity around the SNR

The star formation history (SFH) and high-mass-star content of the local environment of DEM L205 can help us to determine whether the remnant's supernova progenitor type is either thermonuclear (type Ia) or core-collapse (CC). The latter originates from massive stars that rarely form in isolation. Therefore, the combination of a recent peak in the star formation rate and the presence of many early-type stars is expected in the case of CC SNe, whereas the contrary would be more consistent with a type Ia SN.

To investigate the star content around the remnant, we used the Magellanic Clouds Photometric Survey (MCPS) catalogue of Zaritsky et al. (2004) and constructed the colour-magnitude diagram (CMD) of the ~20 000 stars lying within 100 pc (6.9′) of the remnant's centre. The CMD (Fig. 6, left) shows a prominent upper main-sequence branch. We added stellar evolutionary tracks of Lejeune & Schaerer (2001), for $Z = 0.4\ Z_{\odot}$ and initial masses from 3 $M_{\odot}$ to 40 $M_{\odot}$, assuming a distance modulus of 18.49 and extinction $A_V = 0.5$ (the average extinction for "hot" stars, Zaritsky et al. 2004). We used the criteria of $V < 16$ and $B - V < 0$ to identify OB stars, and found 142 of them in our sample (shown in a Hα image in Fig. 6, right). Using $V < 15$ or 14 instead of 16 would give 86 and 20 stars, respectively.

We also looked for nearby OB associations in Lucke & Hodge (1970) and OB stars in the catalogue of Sanduleak (1970). Contamination by Galactic stars was monitored by performing a cross-correlation with Tycho-2 stars (Høg et al. 2000). Five Sanduleak stars are in this region, four of them having a match in the MCPS catalogue, with our selection criteria. The "missed" Sanduleak star is a VV Cepheid (a binary with a red component), which thus possibly explains why our criteria were not satisfied. Two OB associations (LH 60 and 63) lie close to the remnant (~6′ and 3′, respectively), and their extent indeed contain many OB stars from the MCPS catalogue.

Harris & Zaritsky (2008) performed a spatially resolved analysis of the SFH of the "Constellation III" region, and DEM L205 was included in their study (the "E00" cell in their Fig. 2). They identified that a very strong peak in the star formation rate occurred in the region of the remnant 10 Myr ago, and that little star formation activity had occurred prior to this burst.

The rich content of high-mass stars and the recent peak in SFH around the remnant strongly suggest that a core-collapse supernova has formed DEM L205. It is however impossible to completely rule out a type Ia event. Considering at face value that most of the stars were formed in the SFR peak 10 Myr ago, we estimated a lower limit for the mass of the SN progenitor of 20 $M_{\odot}$, because less massive stars have a lifetime longer than 10 Myr (Meynet et al. 1994). We cannot estimate an upper limit, because the progenitor might have formed more recently (the region is still actively forming stars, see below).

We searched for nearby young stellar objects (YSOs) to assess the possibility of SNR-triggered star formation, as in Desai et al. (2010). Using the YSOs from the catalogue of Gruendl & Chu (2009), we report an SNR – molecular cloud – YSOs association around DEM L205: the positions of young stars are shown in our Hα image (Fig. 6, right). Four YSOs lie in the H region/molecular cloud in the north, and are closely aligned with the X-ray emission rim. In addition, four YSOs lie in the western H region, significantly beyond the remnant's emission but correlated with the diffuse X-ray emission from the SB around LH 60 (see Sect. 4.3). Two additional YSOs are aligned with the south-western edge of the SB.

Given the contraction timescale for the intermediate to massive YSOs (10^6 yr to 10^5 yr, Bernasconi & Maeder 1996), the shocks from the remnant cannot have triggered the formation of the YSOs already present. These YSOs are more likely to have formed by interactions with winds and ionisation fronts from the local massive stars, as illustrated by the alignment of young stars along the rim of the adjacent SB. The remnant will be able to trigger star formation in the future, when the shocks have slowed down to below 45 km s^{-1} (Vanhala & Cameron 1998). By this time, however, the neighbouring massive stars will also have triggered further star formation. It is therefore difficult to assess the exact triggering agent of star formation, as Desai et al. (2010) pointed out, in particular in such a complex environment.

5. Conclusions

The first observation of our LMC survey with *XMM-Newton* included the SNR candidate DEM L205 in the field of view. In combination with unpublished radio-continuum data and archival optical and IR observations, we have found all classical SNR signatures, namely:

- Extended X-ray emission.
- Optical emission with a shell-like morphology and an enhanced [S]-to-Hα ratio.
- Non-thermal and extended radio-continuum emission.

The source is also detected in the IR where we predominantly observe thermal emission from dust. We can therefore definitely confirm this object as a supernova remnant. A core-collapse supernova origin is favored, in light of the recent burst of star formation and the presence of many massive stars in the close vicinity of the remnant. The SN exploded in a SB, thus expanding in a low density medium. With a size of ~79 × 64 pc, DEM L205 is one of the largest SNR known in the LMC. Given the low plasma temperature ($kT \sim 0.2-0.3$ keV), we derived a dynamical age of about 35 kyr. Whilst completing our survey, we can expect to find other similarly evolved remnants, thereby refining the faint end of the size and luminosity distributions of SNRs in the LMC.

Acknowledgements. The *XMM-Newton* project is supported by the Bundesministerium für Wirtschaft und Technologie/Deutsches Zentrum für Luft- und Raumfahrt (BMWi/DLR, FKZ 50 OX 0001) and the Max-Planck Society. Cerro Tololo Inter-American Observatory (CTIO) is operated by the Association of Universities for Research in Astronomy Inc. (AURA), under a cooperative agreement with the National Science Foundation (NSF) as part of the National Optical Astronomy Observatories (NOAO). We gratefully acknowledge the support of CTIO and all the assistance which has been provided in upgrading the *Curtis Schmidt* telescope. The MCELS is funded through the support of the Dean B. McLaughlin fund at the University of Michigan and through NSF grant 9540747. The Australia Telescope Compact Array is part of the Australia Telescope which is funded by the Commonwealth of Australia for operation as a National Facility managed by CSIRO. We used the software package developed by the ATNF. This research has made use of Aladin, SIMBAD and VizieR, operated at CDS, Strasbourg, France. Pierre Maggi thanks Philipp Lang for helpful discussions regarding IR data analysis. P.M. and R.S. acknowledge support from the BMWi/DLR grants FKZ 50 OR 1201 and FKZ OR 0907, respectively. R.A.G. was partially supported by the NSF grant AST 08-07323.

References

Andersen, M., Rho, J., Reach, W. T., Hewitt, J. W., & Bernard, J. P. 2011, ApJ, 742, 7
Arnaud, K. A. 1996, in Astronomical Data Analysis Software and Systems V, eds. G. H. Jacoby, & J. Barnes, ASP Conf. Ser., 101, 17
Badenes, C., Maoz, D., & Draine, B. T. 2010, MNRAS, 407, 1301
Balucinska-Church, M., & McCammon, D. 1992, ApJ, 400, 699
Bernasconi, P. A., & Maeder, A. 1996, A&A, 307, 829
Borkowski, K. J., Lyerly, W. J., & Reynolds, S. P. 2001, ApJ, 548, 820
Borkowski, K. J., Williams, B. J., Reynolds, S. P., et al. 2006, ApJ, 642, L141
Cajko, K. O., Crawford, E. J., & Filipovic, M. D. 2009, Serb. Astron. J, 179, 55
Chen, L.-W., Fabian, A. C., & Gendreau, K. C. 1997, MNRAS, 285, 449
Chu, Y.-H. 1997, AJ, 113, 1815
Davies, R. D., Elliott, K. H., & Meaburn, J. 1976, MmRAS, 81, 89
de Horta, A. Y., Filipović, M. D., Bozzetto, L. M., et al. 2012, A&A, 540, A25
Desai, K. M., Chu, Y.-H., Gruendl, R. A., et al. 2010, AJ, 140, 584
di Benedetto, G. P. 2008, MNRAS, 390, 1762
Dickel, J. R., McIntyre, V. J., Gruendl, R. A., & Milne, D. K. 2005, AJ, 129, 790
Dickel, J. R., McIntyre, V. J., Gruendl, R. A., & Milne, D. K. 2010, AJ, 140, 1567
Dickey, J. M., & Lockman, F. J. 1990, ARA&A, 28, 215
Dunne, B. C., Points, S. D., & Chu, Y.-H. 2001, ApJS, 136, 119
Fazio, G. G., Hora, J. L., Allen, L. E., et al. 2004, ApJS, 154, 10
Fesen, R. A., Blair, W. P., & Kirshner, R. P. 1985, ApJ, 292, 29
Filipovic, M. D., Haynes, R. F., White, G. L., & Jones, P. A. 1998, A&AS, 130, 421
Fukui, Y., Kawamura, A., Minamidani, T., et al. 2008, ApJS, 178, 56
Grondin, M.-H., Sasaki, M., Haberl, F., et al. 2012, A&A, 539, A15
Gruendl, R. A., & Chu, Y.-H. 2009, ApJS, 184, 172
Haberl, F., & Pietsch, W. 1999, A&AS, 139, 277
Harris, J., & Zaritsky, D. 2008, PASA, 25, 116
Henize, K. G. 1956, ApJS, 2, 315
Henley, D. B., & Shelton, R. L. 2008, ApJ, 676, 335
Høg, E., Fabricius, C., Makarov, V. V., et al. 2000, A&A, 355, L27
Hughes, J. P., Hayashi, I., & Koyama, K. 1998, ApJ, 505, 732
Hughes, A., Staveley-Smith, L., Kim, S., Wolleben, M., & Filipović, M. 2007, MNRAS, 382, 543
Klimek, M. D., Points, S. D., Smith, R. C., Shelton, R. L., & Williams, R. 2010, ApJ, 725, 2281
Koo, B.-C., Lee, H.-G., Moon, D.-S., et al. 2007, PASJ, 59, 455

Kuntz, K. D., & Snowden, S. L. 2008, A&A, 478, 575
Kuntz, K. D., & Snowden, S. L. 2010, ApJS, 188, 46
Lejeune, T., & Schaerer, D. 2001, A&A, 366, 538
Lucke, P. B., & Hodge, P. W. 1970, AJ, 75, 171
Mathewson, D. S., & Clarke, J. N. 1973, ApJ, 180, 725
Meixner, M., Gordon, K. D., Indebetouw, R., et al. 2006, AJ, 132, 2268
Meynet, G., Maeder, A., Schaller, G., Schaerer, D., & Charbonnel, C. 1994, A&AS, 103, 97
Micelotta, E. R., Jones, A. P., & Tielens, A. G. G. M. 2010a, A&A, 510, A37
Micelotta, E. R., Jones, A. P., & Tielens, A. G. G. M. 2010b, A&A, 510, A36
Mills, B. Y., Turtle, A. J., Little, A. G., & Durdin, J. M. 1984, Austr. J. Phys., 37, 321
Rieke, G. H., Young, E. T., Engelbracht, C. W., et al. 2004, ApJS, 154, 25
Russell, S. C., & Dopita, M. A. 1992, ApJ, 384, 508
Sanduleak, N. 1970, Contributions from the Cerro Tololo Inter-American Observatory, 89
Smith, C., Leiton, R., & Pizarro, S. 2000, in Stars, Gas and Dust in Galaxies: Exploring the Links, eds. D. Alloin, K. Olsen, & G. Galaz, ASP Conf. Ser., 221, 83
Strüder, L., Briel, U., Dennerl, K., et al. 2001, A&A, 365, L18
Tappe, A., Rho, J., & Reach, W. T. 2006, ApJ, 653, 267
Temim, T., Gehrz, R. D., Woodward, C. E., et al. 2006, AJ, 132, 1610
Turner, M. J. L., Abbey, A., Arnaud, M., et al. 2001, A&A, 365, L27
van der Heyden, K. J., Bleeker, J. A. M., & Kaastra, J. S. 2004, A&A, 421, 1031
Vanhala, H. A. T., & Cameron, A. G. W. 1998, ApJ, 508, 291
Watson, M. G., Schröder, A. C., Fyfe, D., et al. 2009, A&A, 493, 339
Williams, R. M., Chu, Y.-H., Dickel, J. R., et al. 2004, ApJ, 613, 948
Williams, B. J., Borkowski, K. J., Reynolds, S. P., et al. 2006, ApJ, 652, L33
Wilms, J., Allen, A., & McCray, R. 2000, ApJ, 542, 914
Yamaguchi, H., Sawada, M., & Bamba, A. 2010, ApJ, 715, 412
Zaritsky, D., Harris, J., Thompson, I. B., & Grebel, E. K. 2004, AJ, 128, 1606

A.23 Related Paper 23

Bozzetto, L. M., Filipović, M. D., Urošević, D., and Crawford, E. J. (2012d). Radio-Continuum Observations of Small, Radially Polarised Supernova Remnant J0519-6902 in the Large Magellanic Cloud. *Serbian Astronomical Journal*, 185:25–33

My contribution was to assist in the data analysis. This is a 20% contribution.

Serb. Astron. J. № 185 (2012), 25 - 33 **UDC 524.722.3 : 524.354–77**
DOI: 10.2298/SAJ1285025B Original scientific paper

RADIO-CONTINUUM OBSERVATIONS OF SMALL, RADIALLY POLARISED SUPERNOVA REMNANT J0519–6902 IN THE LARGE MAGELLANIC CLOUD

L. M. Bozzetto[1], M. D. Filipović[1], D. Urošević[2] and E. J. Crawford[1]

[1]*University of Western Sydney, Locked Bag 1797, Penrith South DC, NSW 1797, Australia*

[2]*Department of Astronomy, Faculty of Mathematics, University of Belgrade, Studentski trg 16, 11000 Belgrade, Serbia*

E–mail: *m.filipovic@uws.edu.au*

(Received: November 4, 2012; Accepted: November 15, 2012)

SUMMARY: We report on new Australian Telescope Compact Array (ATCA) observations of SNR J0519–6902. The Supernova Remnant (SNR) is small in size (∼8 pc) and exhibits a typical SNR spectrum with $\alpha = -0.53 \pm 0.07$, with steeper spectral indices towards the northern limb of the remnant. SNR J0519–6902 contains a low level of radially orientated polarisation at wavelengths of 3 and 6 cm, which is typical of younger SNRs. A fairly strong magnetic field was estimated to ∼171 μG. The remnant appears to be the result of a typical Type Ia supernova, sharing many properties with another small and young Type Ia LMC SNR, J0509–6731.

Key words. ISM: supernova remnants – Magellanic Clouds – radio continuum: ISM – ISM: individual objects – SNR J0519–6902

1. INTRODUCTION

Supernova Remnants (SNRs) play an essential role in the ecology of the universe, enriching the interstellar medium (ISM) as well as having a significant impact on the ISM structure and physical properties. The study of SNRs in our own galaxy isn't ideal due to the high level of absorption, in addition to difficulties in achieving accurate distance measurements. Instead, we look to the small dwarf galaxy, the Large Magellanic Cloud (LMC), for our study, which is located at a distance of 50 kpc (Macri et al. 2006). This proximity to us is still far enough that we can assume all objects within the galaxy to be located at the same distance, making measurements of extent and surface brightness more reliable. LMC also offers us an environment that is outside of the galactic plane at an angle of 35° (van der Marel and Cioni 2001) and, as a result, a low foreground absorption.

One of the signatures of SNRs is their predominately non-thermal radio-continuum emission, typically exhibiting a spectrum with $\alpha \sim -0.5$ (defined by $S \propto \nu^{\alpha}$). However, this value can vary as there is a wide variety of SNRs in different stages of evolution (Filipović et al. 1998, Payne et al. 2008)

SNR J0519–6902 was observed by Tuohy et al. (1982) who recorded an integrated flux density measurement at 408 MHz of 150±30 mJy and 33±5 mJy at 5000 MHz. They make note that the SNR is Balmer dominated with a broad Hα compo-

nent and reported an X-ray extent of $\sim 30''$ and an optical extent of $28''$. They estimate a shock velocity of 2900±400 km s^{-1} and an age of ∼500 years. It is also mentioned that the remnant is expanding into a low density region composed of neutral hydrogen, inferring Type I supernovae, and they estimate the progenitor mass to be between 1.2 and 4 solar masses. Mathewson et al. (1983) recorded a spectral index of –0.6. Mills et al. (1984) record a 843 MHz flux density measurement of 145 mJy, updating the spectrum of the remnant to –0.65. Chu and Kennicutt (1988) associated this SNR with the nearby (200 pc) OB – LH41 and classified it as population II. Smith et al. (1991) estimated an age between 500 – 1500 years, noting that this makes the remnant one of the youngest in the LMC. Dickel and Milne (1994) state that this SNR is similar to Tycho or Kepler SNR in the Milky Way. Dickel and Milne (1995) then observed this remnant at wavelengths of 20 and 13 cm, obtaining integrated flux densities of 100 mJy and 70 mJy, respectively. They also estimate the mean fractional polarisation across the remnant of 1.5±0.6% (20 cm) and 4.1±0.6% (13 cm), and make note of the radial magnetic field and similarities to other young galactic SNRs. Filipović et al. (1995) measured an integrated flux density measurement of 57 mJy at 3 cm. Filipović et al. (1998) reobserved this SNR with the Parkes radio-telescope at 6 cm, estimating an integrated flux density of 72 mJy. Haberl and Piestch (1999) observed this SNR with the ROSAT and gave the association [HP] 789. Borkowski et al. (2006) place the age of SNR at 600 years with a 30% error. Vukotić et al. (2007) estimated the magnetic field of this SNR using the classical equipartition formula (186 μG) as well as a revised equipartition formula (270 μG). Desai et al. (2010) found no young stellar object (YSO) associated with this SNR. Kosenko et al. (2010) used Chandra and the XMM Newton telescopes to estimate an age of 450±200 for this remnant. Most recently, Edwards et al. (2012) state that based on their current models, this SNR could have only been the result of a supersoft source or a double degenerate system mimicking a Type I SN event.

In this paper we present new radio-continuum measurements and polarimetric analysis of SNR J0519–6902. The observations, data reduction and imaging techniques are described in Section 2. The astrophysical interpretation of newly obtained moderate-resolution total intensity images are discussed in Section 3.

2. OBSERVATIONS

We observed SNR J0519–6902 on November 15 and 16, 2011 with the Australian Telescope Compact Array (ATCA) using the new Compact Array Broadband Backend (CABB) receiver at the array configuration EW367 at and wavelengths of 3 and 6 cm (ν=9000 and 5500 MHz). Baselines formed with the 6$^{\rm th}$ ATCA antenna were omitted while the other five antennas were arranged in a compact configuration. The observations were carried out in the so called "snap-shot" mode, totaling ∼50 minutes of integration over a 14 hour period. The source PKS B1934-638 was used for primary calibration and source PKS B0530-727 was used for secondary (phase) calibration. The MIRIAD (Sault et al. 1995) and KARMA (Gooch 1995) software packages were used for reduction and analysis. More information on the observing procedure and other sources observed in this session/project can be found in Bojičić et al. (2007), Crawford et al. (2008a,b, 2010), Čajko et al. (2009), De Horta et al. (2012), Grondin et al. (2012), Maggi et al. (2012) and Bozzetto et al. (2010, 2012a,b,c,d).

Images were formed using the MIRIAD multi-frequency synthesis (Sault and Wieringa 1994) and natural weighting. They were deconvolved using the MFCLEAN and RESTOR algorithms with primary beam correction applied using the LINMOS task. A similar procedure was used for both U and Q Stokes parameter maps.

In addition to our own observations, we made use of two ATCA projects (C354 and C149) at wavelengths of 13 and 20 cm. Observations from project C354 were taken on September 18 (array 1.5B), 22 and 23 (array 1.5D), 1994. Observations from project C149 were taken on March 22 (array 6A) and April 2 (array 6C).

3. RESULTS AND DISCUSSION

SNR J0519–6902 exhibits a ring-like shell morphology with three brightened regions towards the northern, southern and eastern limb of the remnant (Fig. 1). The SNR is centred at RA(J2000)=$5^h19^m34.9^s$, DEC(J2000)=–69°02′07.9″. We estimate the spatial extent of SNR J0519–6902 at the 3σ (Table 1; Col. 2) level (0.9 mJy) along the major (N-S) and minor (E-W) axes. Its size at 13 cm is $34''\times34''\pm4''$ (8×8 pc with 1 pc uncertainty in each direction). We also estimate the ring thickness of the remnant to $\sim 7.3''$ (1.8 pc) at 13 cm, about 43% of the SNR's radius.

We use the integrated flux density measurements from Table 1 to estimate the non weighted radio spectral index of this remnant (α=−0.53±0.07). The 408 MHz value has an error of 20%, while we assume a 10% error for the remaining values. The spectrum of this remnant (Fig. 2) is steeper than that of –0.44 measured by Dickel and Milne (1995). However, they make note that there was uncertainty in this measurement. The flux density at 408 MHz is slightly lower than expected for a linear fit. While it is most likely that this is due to the large error and missing short spacings, we can not rule out whether the absorption is responsible for this slight flattening of the spectrum. To see the change in flux across the remnant, we created a spectral map image (Fig. 3) between 20 and 13 cm wavelengths. The map was produced by reprocessing both 20 and 13 cm images to a common $u - v$ range and then fitting $S \propto \nu^{\alpha}$ pixel by pixel in both images simultaneously. The

emission falls predominately between –0.5 and –0.8, which is what we would generally expect of a younger SNR and is consistent with the overall spectrum of this image (–0.53). The white centre in this image is formed due to the SNRs ring morphology, where the emission towards the core of the remnant was less than the 3σ cutoff level.

Table 1. Flux Density of SNR J0519-6902.

λ (cm)	ν MHz	R.M.S (mJy)	Beam Size ($''$)	$S_{\rm Total}$ (mJy)
73	408	–	157×172	150.0
36	843	0.5	46×43	145.0
20	1376	0.3	20×19	121.8
13	2378	0.3	6×5	78.5
6	5500	0.3	38×24	46.5
3	9000	0.3	23×16	33.0

Linear polarisation images were created at 6 and 3 cm using Q and U stoke parameters (Figs. 4 and 5). The mean fractional polarisation was calculated using flux density and polarisation:

$$\mathrm{P}=\frac{\sqrt{S_Q^2+S_U^2}}{S_I}\cdot 100\%$$

where S_Q, S_U and S_I are integrated intensities for the Q, U and I Stokes parameters. Our estimated peak value is 8.1%±2.2% (7σ) at 6 cm and 9.3%±4.8% (6σ) at 3 cm. The polarisation from the remnant appears radial at both wavelengths. We estimate a mean polarisation across the remnant of ∼2.2% at 6 cm and ∼3.2% at 3 cm.

This radial polarisation is expected of smaller, younger, SNRs and is comparable to similarly small SNRs in our own galaxy (Tycho's SNR – Dickel et al. 1991) and SNRs in the LMC (SNR 0509-6731 – Bozzetto et al. in prep). The remnant's low level of radial polarisation is consistent with previous polarisation studies of SNR J0519–6902 at wavelengths of 20 and 13 cm by Dickel et al. (1995), who also found this radially orientated polarisation, with a mean fractional polarisation of 1.5±0.6% (20 cm) and 4.1±0.6% (13 cm) across the remnant.

The polarisation position angles from these 6 and 3 cm observations were used to estimate the Faraday rotation across the remnant (Fig. 6). Filled squares represent positive rotation measure, and open boxes negative rotation measure. Average rotation measure across the entire remnant was estimated at ∼10 rad m^{-2}. However, as there was a significant amount of both positive and negative rotation measure across the remnant, we have broken down the remnant into three regions and performed separate analysis on each. Field 01 (North-East region) – This region is dominated by negative rotation measure with an average value of –272 rad m^{-2}, and a peak of – 431 rad m^{-2}. Field 02 (North-West region) – In contrast, this region is dominated by positive rotation measure, with an average value of 462 rad m^{-2} and a peak of 624 rad m^{-2}. Field 03 (Southern region) – Similarly, this region is also dominated by positive rotation measure, with an average value of 697 rad m^{-2} and a peak of 784 rad m^{-2}. The two southernmost rotation measure pixels in this image were omitted from analysis as they were towards the edge of the remnant, where the polarised intensity is too weak to measure accurate rotation measure.

We used modified equipartition formula for SNRs (Arbutina et al. 2012) to estimate the magnetic field strength for the SNR J0519–6902. The derivation of the new equipartition formula is based on the Bell (1978) diffuse shock acceleration (DSA) theory. This derivation is purely analytical, accommodated especially for the estimation of magnetic field strength in SNRs. The average equipartition field over the whole shell of SNR J0519–6902 is ∼171 μG with an estimate of $\mathrm{E}_{min} = 1.82\times10^{49}$ ergs (see Arbutina et al. (2012); and corresponding "calculator"[1]). This value is typical of young SNRs with a strongly amplified magnetic field.

The surface brightness–diameter ($\Sigma - D$) relationship for this SNR can be seen in Fig. 7 at 1 GHz with theoretically-derived evolutionary tracks (Berezhko and Völk 2004) superposed. SNR J0519–6902 is positioned at $(\Sigma, D) = (5.5\times\ 10^{-20}$ W m^{-2} Hz^{-1} Sr^{-1}, 8.2 pc) on the diagram. The location on the diagram shows that this is a young SNR in the early Sedov phase of evolution. Also, this object evolves in a low density environment and the initial energy of explosion was low.

[1]The calculator is available on http://poincare.matf.bg.ac.rs/~arbo/eqp/

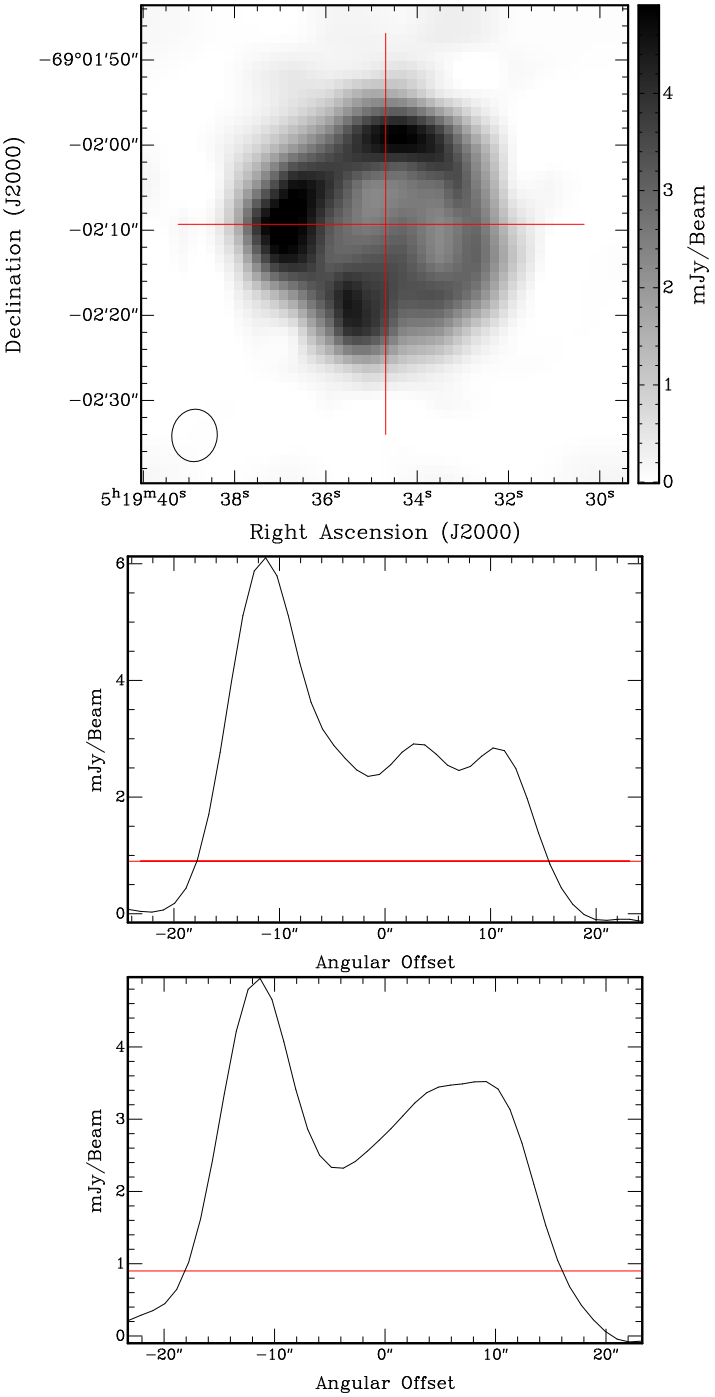

Fig. 1. *The top image is an ATCA image of SNR J0519–6902 overlaid with major (EW) and minor (NS) axis. The middle and lower image show the flux emission at the major and minor axis respectively, with an overlaid line at 3σ.*

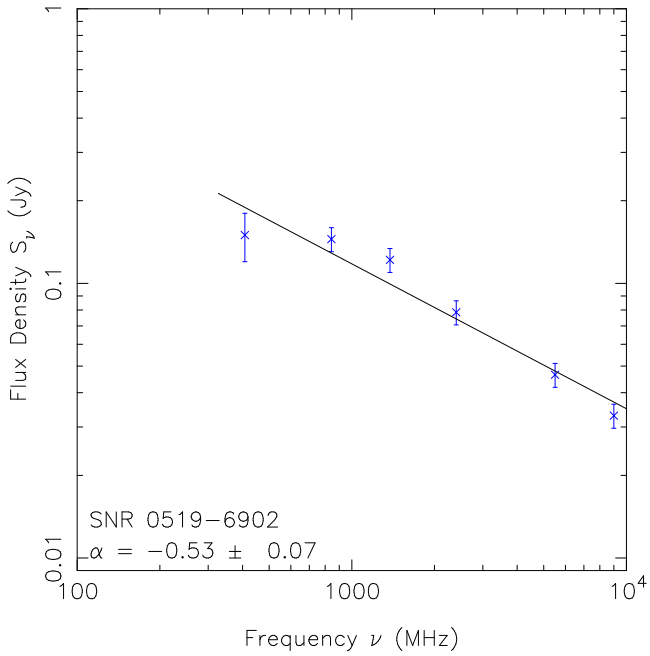

Fig. 2. *Radio-continuum spectrum of SNR J0519–6902.*

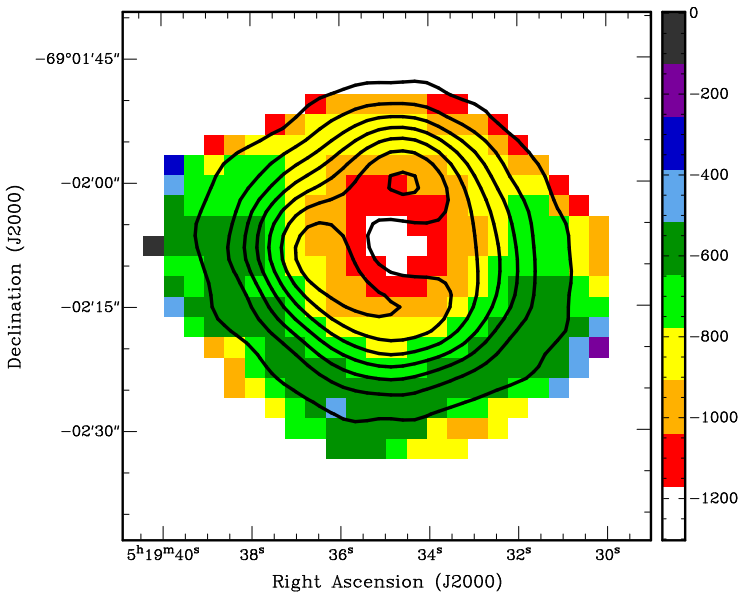

Fig. 3. *Spectral map of SNR J0519–6902 between 20 and 13 cm with overlaid contours at 13 cm of 3, 9, 15, 21, 27, 33 and 39σ. The sidebar quantities indicate the change in spectral index. For example: -200 represents α=–0.2.*

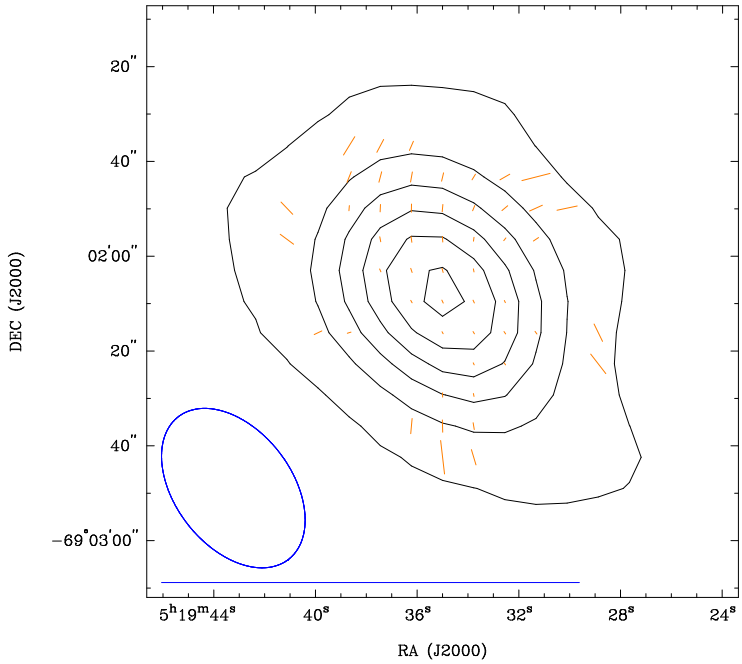

Fig. 4. *Polarisation vectors overlaid on 6 cm ATCA observations of SNR J0519–6902. The contours used are 3, 23, 43, 63, 83 and 103σ. The ellipse in the lower left corner represents the synthesised beamwidth of 23.1″×16.1″ and the line below the ellipse represents a polarisation vector of 100%.*

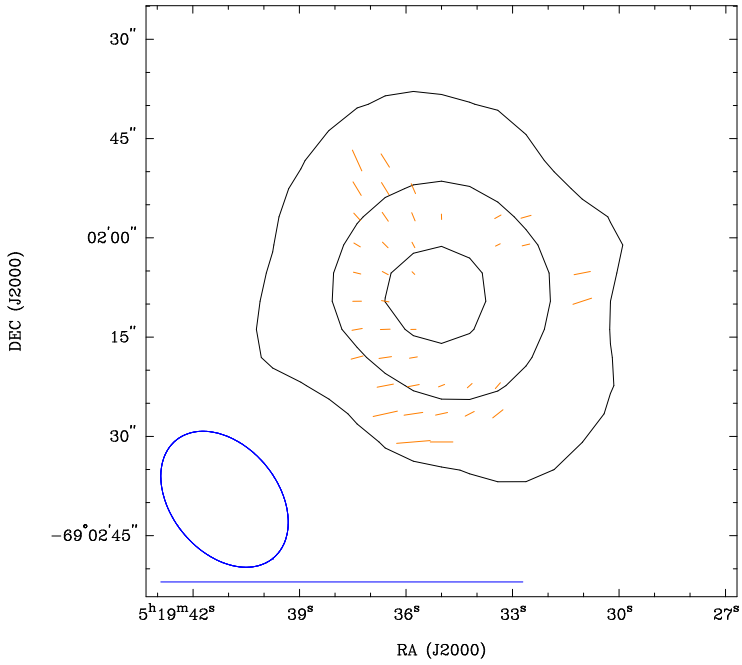

Fig. 5. *Polarisation vectors overlaid on 3 cm ATCA observations of SNR J0519–6902. The contours used are 3, 23 and 43σ. The ellipse in the lower left corner represents the synthesised beamwidth of 38.0″×24.6″ and the line below the ellipse represents a polarisation vector of 100%.*

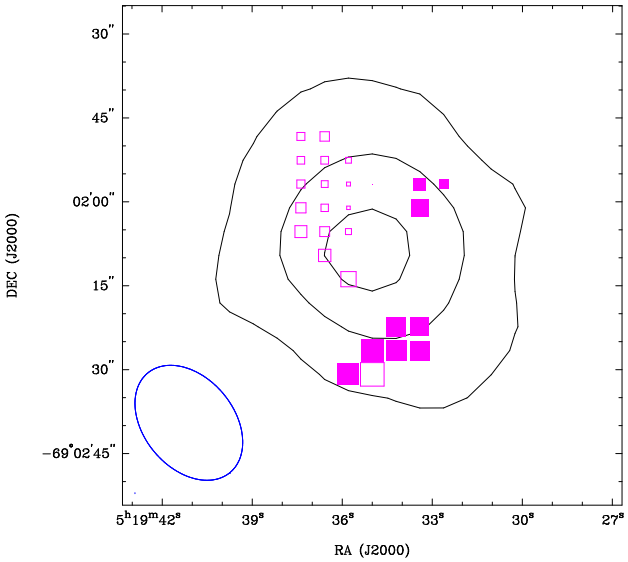

Fig. 6. *Faraday rotation measure of SNR J0519–6902 overlaid on 3 cm image contours. The contours used are 3, 23 and 43σ. Filled squares represent positive rotation measure while open squares represent negative rotation measure. The ellipse in the lower left represents the synthesised beamwidth of 38.0″×24.6″.*

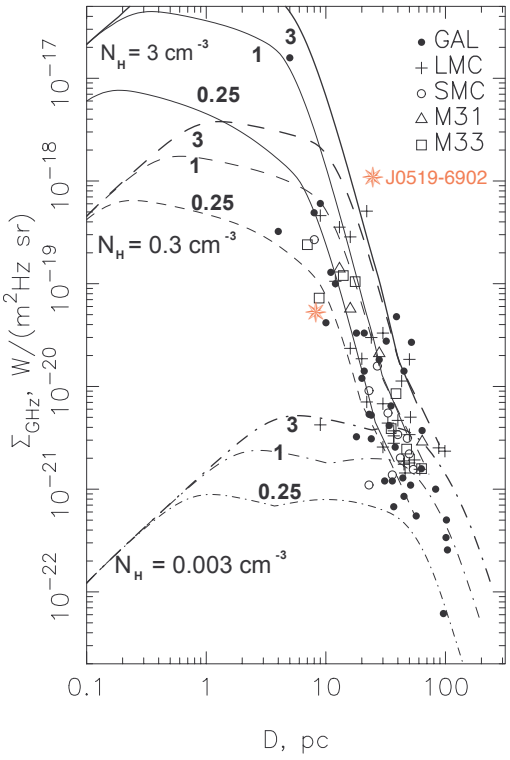

Fig. 7. *Surface brightness-to-diameter diagram from Berezhko and Völk (2004), with SNR J0519–6902 added. The evolutionary tracks are for ISM densities of N_H= 3, 0.3 and 0.003 cm^{-3} and explosion energies of E_{SN} = 0.25, 1 and 3×10^{51} erg.*

4. CONCLUSION

This remnant appears to exhibit a ring-like shell morphology with an extent of D=(8×8)±1 pc, radial polarisation at 6 and 3 cm with a mean integrated polarisation of ∼2.2% and ∼3.2% respectively, a typical spectrum of α = –0.53±0.07, areas of positive (mean = 544 rad m^{-2}) and negative (mean = –290 rad m^{-2}) rotation measure. The estimated value of the magnetic field and location in the $\Sigma - D$ diagram show that this SNR is young, in the early Sedov phase of evolution. It expands in a less dense environment and the initial energy of probably Type Ia explosion was low.

Acknowledgements – We used the KARMA software package developed by the ATNF. The Australia Telescope Compact Array is part of the Australia Telescope which is funded by the Commonwealth of Australia for operation as a National Facility managed by CSIRO. This research is supported by the Ministry of Education and Science of the Republic of Serbia through project No. 176005.

REFERENCES

Arbutina, B., Urošević, D., Andjelić, M. M., Pavlović, M. Z. and Vukotić, B.: 2012, *Astrophys. J.*, **746**, 79.

Bell A. R.: 1978, *Mon. Not. R. Astron. Soc.*, **182**, 443.

Berezhko, E. G. and Völk, H. J.: 2004, *Astron. Astrophys.*, **427**, 525.

Bojičić, I. S., Filipović, M. D., Parker, Q. A., Payne, J. L., Jones, P. A., Reid, W., Kawamura, A., Fukui, Y.: 2007, *Mon. Not. R. Astron. Soc.*, **378**, 1237.

Borkowski, K. J., Hendrick, S. P. and Reynolds, S. P.: 2006, *Astrophys. J.*, 652, 1259.

Bozzetto, L. M., Filipović, M. D., Crawford, E. J., Bojičić, I. S., Payne, J. L., Mendik, A., Wardlaw, B. and de Horta, A. Y.: 2010, *Serb. Astron. J.*, **181**, 43

Bozzetto, L. M., Filipović, M. D., Crawford, E. J., Payne, J. L., De Horta, A. Y. and Stupar, M.: 2012, *Rev. Mex. Astron. Astrofis.*, **48**, 41.

Bozzetto, L. M., Filipović, M. D., Crawford, E. J., Haberl, F., Sasaki, M., Urošević, D., Pietsch, W., Payne, J. L., de Horta, A. Y., Stupar, M., Tothill, N. F. H., Dickel, J., Chu, Y.-H. and Gruendl, R.: 2012, *Mon. Not. R. Astron. Soc.*, 420, 2588.

Bozzetto, L. M., Filipović, M. D., Crawford, E. J., De Horta, A. Y. and Stupar, M.: 2012, *Serb. Astron. J.*, **184**, 69.

Bozzetto, L. M., Filipović, M. D., Crawford, E. J., De Horta, A. Y., Kothes, R., Urošević, D.: 2013, in preperation.

Čajko K. O., Crawford E. J., Filipović, M. D.: 2009, *Serb. Astron. J.*, **179**, 55.

Chu, Y-H., and Kennicutt, R. C.: 1988, *Astron. J.*, **96**, 1874.

Crawford, E. J., Filipović, M. D. and Payne, J. L.: 2008a, *Serb. Astron. J.*, **176**, 59.

Crawford, E. J., Filipović, M. D., De Horta, A. Y., Stootman, F. H., Payne J. L.: 2008b, *Serb. Astron. J.*, **177**, 61.

Crawford, E. J., Filipović, M. D., Haberl, F., Pietsch, W., Payne, J. L., De Horta, A. Y.: 2010, *Astron. Astrophys.*, **518**, A35.

De Horta, A. Y., Filipović, M. D., Bozzetto, L. M., Maggi, P., Haberl, F., Crawford, E. J., Sasaki, M., Urosević, D., Pietsch, W., Gruendl, R., Dickel, J., Tothill, N. F. H., Chu, Y.-H., Payne, J. L. and Collier, J. D.: 2012, *Astron. Astrophys.*, 540, A25.

Dickel, J. R. and Milne, D. K.: 1994, *Publ. Astron. Soc. Aust.*, **11**, 99.

Dickel, J. R. and Milne, D. K.: 1995, *Astron. J.*, **109**, 200.

Desai, K. M., Chu, Y.-H., Gruendl, R. A., Dluger, W., Katz, M., Wong, T, Chen, C.-H. R., Looney, L. W., Hughes, A., Muller, E., Ott, J. and Pineda, J. L.: 2010, *Astron. J.*, **140**, 584.

Edwards, Z. I., Pagnotta, A. and Schaefer, B. E.: 2012, *Astrophys. J. Letters*, **747**, L19.

Filipovic, M. D., Haynes, R. F., White, G. L., Jones, P. A., Klein, U. and Wielebinski, R.: 1995, *Astron. Astrophys. Suppl. Series*, **111**, 311.

Filipović, M. D., Pietsch, W., Haynes, R. F., White, G. L., Jones, P. A., Wielebinski, R., Klein, U., Dennerl, K., Kahabka, P., Lazendić, J. S.: 1998, *Astron. Astrophys. Suppl. Series*, **127**, 119.

Gooch, R.: 1995, *Publ. Astron. Soc. Pac. Conf. Series*, **77**, 144.

Grondin, M.-H., Sasaki, M., Haberl, F., Pietsch, W., Crawford, E. J., Filipović, M. D., Bozzetto, L. M., Points, S., Smith, R. C.: 2012, *Astron. Astrophys.*, **539**, 15.

Haberl, F., Pietsch, W.: 1999, *Astron. Astrophys. Suppl. Series*, **139**, 277.

Kosenko, D., Helder, E. A. and Vink, J.: 2010, *Astron. Astrophys.*, **519**, A11.

Macri, L. M., Stanek, K. Z., Bersier, D., Greenhill, L. J. and Reid, M. J.: 2006, *Astrophys. J.*, **652**, 1133.

Maggi, P., Haberl, F., Bozzetto, L. M., Filipović, M. D., Points, S. D., Chu, Y.-H., Sasaki, M., Pietsch, W., Gruendl, R. A., Dickel, J., Smith, R. C., Sturm, R., Crawford, E. J., De Horta, A. Y.: 2012, *Astron. Astrophys.*, **546**, 109.

Mathewson, D. S., Ford, V. L., Dopita, M. A., Tuohy, I. R., Long, K. S., Helfand, D. J.: 1983, *Astrophys. J. Suppl. Series*, **51**, 345.

Mills, B. Y., Turtle, A. J., Little, A. G., Durdin, J. M.: 1984, *Aust. J. Phys.*, **37**, 321.

Payne, J. L., White, G. L., Filipović, M. D.: 2008, *Mon. Not. R. Astron. Soc.*, **383**, 1175.

Sault, R. J., Teuben, P. J. and Wright, M. C. H.: 1995, *Publ. Astron. Soc. Pac. Conf. Ser.*, **77**, 433.

Sault, R. J., Wieringa, M. H.: 1994, *Astron. Astrophys. Suppl. Series*, **108**, 585.

Smith, R. C., Kirshner, R. P., Blair, W. P. and Winkler, P. F.: 1991, *Astrophys. J.*, **375**, 652.

Tuohy, I. R., Dopita, M. A., Mathewson, D. S., Long, K. S. and Helfand, D. J.: 1982, *Astrophys. J.*, **261**, 473.

Vukotic, B., Arbutina, B. and Urosevic, D.: 2007, *Rev. Mex. Astron. Astrofis.*, **43**, 33.

МУЛТИФРЕКВЕНЦИОНА ПОСМАТРАЊА ОСТАТАКА СУПЕРНОВИХ У ВЕЛИКОМ МАГЕЛАНОВОМ ОБЛАКУ – СЛУЧАЈ SNR J0519–6902

L. M. Bozzetto[1], M. D. Filipović[1], D. Urošević[2] and E. J. Crawford[1]

[1]*University of Western Sydney,*
Locked Bag 1797, Penrith South DC, NSW 1797, Australia

[2]*Department of Astronomy, Faculty of Mathematics, University of Belgrade,*
Studentski trg 16, 11000 Belgrade, Serbia

E–mail: *m.filipovic@uws.edu.au*

УДК 524.722.3 : 524.354–77
Оригинални научни рад

Представљамо нова ATCA посматрања остатка супернове (ОС) у Великом Магелановом Облаку – SNR J0519–6902. Овај ОС је малих димензија (∼8 pc) и има типичан спектар са спектралним индексом α =–0.53±0.07, као и са стрмијим спектралним индексом на северној ивици остатка.

SNR J0519–6902 емитује низак ниво радијално оријентисаног поларизованог зрачења на таласним дужинама од 3 и 6 cm, карактеристичног за млађе ОС. Процењено је да има прилично јако магнетно поље у вредности од 171 μG. Овај остатак је типичан резултат експлозије супернове типа Ia, који има више заједничких особина са исто тако младим и у својим димензијама малим ОС типа Ia, LMC SNR J0509-6731.

A.24 Related Paper 24

Wong, G. F., Filipović, M. D., Crawford, E. J., Tothill, N. F. H., De Horta, A. Y., and Galvin, T. J. (2012b). New 20-cm Radio-Continuum Study of the Small Magellanic Cloud: Part III - Compact HII Regions. *Serbian Astronomical Journal*, 185:53–64

My contribution was to assist in the data analysis. This is a 10% contribution.

Serb. Astron. J. № 185 (2012), 53 - 64 **UDC 524.722.7–77 : 524.523**
DOI: 10.2298/SAJ1285053W Professional paper

NEW 20-cm RADIO-CONTINUUM STUDY OF THE SMALL MAGELLANIC CLOUD: PART III – COMPACT H II REGIONS

G. F. Wong, M. D. Filipović, E. J. Crawford, N. F. H. Tothill, A. Y. De Horta and T. J. Galvin

University of Western Sydney, Locked Bag 1797, Penrith South DC, NSW 2751, Australia
E–mail: *m.filipovic@uws.edu.au*

(Received: October 29, 2012; Accepted: November 6, 2012)

SUMMARY: We present and discuss a new catalogue of 48 compact H II regions in the Small Magellanic Cloud (SMC) and a newly created deep 1420 MHz (λ=20 cm) radio-continuum image of the N 19 region located in the southwestern part of the SMC. The new images were created by merging 1420 MHz radio-continuum archival data from the Australian Telescope Compact Array. The majority of these detected radio compact H II regions have rather flat spectral indices which indicates, as expected, that the dominant emission mechanism is of thermal nature.

Key words. Magellanic Clouds – radio continuum: ISM – catalogs

1. INTRODUCTION

The Small Magellanic Cloud (SMC), with its well established distance (∼60 kpc; Hilditch et al. 2005) and ideal position in the sky - towards the coldest areas near the South Celestial Pole, allows observation of radio sources to be conducted without significant interference from Galactic foreground radiation. The SMC is an ideal location to study celestial objects like compact H II regions (Mezger et al. 1967), which may be difficult to study in our own and other distant galaxies.

The SMC has been surveyed at multiple radio frequencies using archival data (Crawford et al. 2011, Wong et al. 2011a, hereafter Paper I). Deep observations of SMC young stellar objects, compact H II regions, Supernova Remnants (SNRs) and Planetary Nebulae (PNe) were presented in Oliveira et al. (2012), Indebetouw et al. (2004), Filipović et al. (2005), Filipović et al. (2008) and Filipović et al. (2009), respectively. A catalogue of radio-continuum point sources (Wong et al. 2012) towards the SMC was derived from images taken from Crawford et al. (2011).

This is the third paper in this series; Paper I presented newly developed high sensitivity and resolution images of the SMC. The second instalment (Wong et al. 2011b, hereafter Paper II) presented a point source catalogue created from the images in paper I. In this paper, we present newly constructed images of the N 19 region covering the southwestern part of the SMC, at ν=1.4 GHz (λ=20 cm). We also present a catalogue of compact H II regions sources towards the SMC. The catalogue is derived from images at 4800 MHz (λ=6 cm) and 8600 MHz (λ=3 cm) from Crawford et al. (2011), a 2370 MHz ($\lambda = 13$ cm) mosaic image from Filipović et al. (2002), one of our SMC 20 cm mosaic radio-continuum images (Fig. 2 in Paper I), the N 19 images presented in this paper and an 843 MHz (λ=36 cm) MOST image (Turtle et al. 1998).

In Section 2 we describe the data used to create the N 19 images and identify the compact H II region. In Section 3 we describe our source fitting and detection methods. In Section 4 we present our new maps with a brief discussion, Section 5 contains our conclusions, and the Appendix contains the catalogue of compact H II regions.

2. DATA

2.1. SMC Mosaic Radio-continuum Images

The 3 and 6 cm images (Fig. 3 and Fig. 1 in Crawford et al. 2011) were created by combining data from various ATCA projects that covered the SMC (Table 1 in Crawford et al. 2011). The 3 and 6 cm maps have resolutions of $\sim$20″ and $\sim$30″ and r.m.s. noise of 0.8 and 0.7 mJy/beam, respectively. The 13 cm radio-continuum catalogue was produced from a SMC mosaic radio survey of 20 square degrees (Filipović et al. 2002). These observations have a beam size of $\sim$40″ and r.m.s. noise of 0.4 mJy/beam. The 20 cm mosaic image (Fig. 2 in Paper I) was created by combining data from ATCA project C1288 (Mao et al. 2008) with data obtained for a Parkes radio-continuum study of the SMC (Filipović et al. 1997). This image has a beam size of 17.″8 × 12.″2 with r.m.s. noise of 0.7 mJy/beam.

The 36 cm image comes from the MOST radio survey of 36 square degrees containing the SMC field (Turtle et al. 1998). These observations have a beam size of $\sim$45″ and r.m.s. noise of 0.7 mJy/beam — equal to that of the 20 cm image.

Table 1 gives the field size and central position of all images used to derive the compact H II region catalogue contained in this paper.

Table 1. Field size and central position of SMC images used.

Image	RA	Dec	Field Size
3 cm	01:00:00	-73:00:00	5°× 5°
6 cm	01:00:00	-73:00:00	5°× 5°
13 cm	01:00:00	-72:50:00	5°× 4°
20 cm	01:00:00	-72:00:30	7°× 9°
36 cm	01:00:00	-72:30:30	6°× 6°

2.2. The SMC N 77 region

Observations were conducted with ATCA (project C281) over two 12 hour sessions on August 25, 1993 and February 10, 1994. Two array configurations at 20 and 13 cm (ν=1377/2377 MHz) were used – 1.5B and 6B. More details about these observations can be found in Ye et al. (1995) and Bojičić et al. (2010).

2.3. The SMC N 19 region

2.3.1. Image Creation

In order to create high-fidelity and high-resolution radio-continuum images of the SMC N 19 region, we searched the Australia Telescope Online Archive[1] (ATOA), identifying three complementary ATCA observations that covered N 19: projects C468, C882 and C1607. The source 1934-638 was used as the primary calibrator and 0252-712 as the secondary calibrator for all ATCA SMC observations. A brief summary of the three ATCA projects is shown in Table 2.

The software packages MIRIAD (Sault and Killeen 2010) and KARMA (Gooch 2006) were used for the data reduction and analysis. Initial high-resolution images were produced from the full dataset using the MIRIAD multi-frequency synthesis (Sault and Wieringa 1994) with natural weighting. The deconvolution process used MIRIAD tasks MOSSDI, an SDI variant of the clean algorithm designed for mosaics (Steer et al. 1984).

Figs. 1-3 show maps from individual ATCA projects (Table 2), Figs. 4 and 5 show maps derived from combining multiple observations.

Table 2. ATOA data used to image N 19.

ATCA Project	Date Observed	Array
C468	1997 Aug 06–07	375
	1995 Oct 26–27	1.5D
	1997 Nov 22	6C
C882	2000 Jun 20–17	6B
C1607	2006 Dec 02–12	6B
	2006 Dec 12–18	750A

2.3.2. Images

Comparing individual maps of N 19 (Figs. 1–3), we can see the effects of different array configurations. Fig. 1 is created from project C468, containing a combination of extended and point source emission, as a result of three different array configurations. Fig. 2 (project C882) only contains a long-baseline observation (array configuration 6B), so the map is dominated by point sources. Fig. 3 has extended and point source emission, derived from short and long-baseline array configurations 750A and 6B respectively. Table 3 lists the details of the individual maps.

Table 3. Details of N 19 mosaics at 20-cm.

ATCA Project	Beam Size (arcsec)	Position Angle	r.m.s. noise (mJy/beam)
C468	5.3×5.1	2.°7	0.1
C882	6.6×6.2	-1.°3	0.1
C1607	6.9×5.5	-2.°8	0.1

[1] http://atoa.atnf.csiro.au

Figs. 4 and 5 show images created from a combination of observations (Table 2): Fig. 4 was created from ATCA projects C468 and C1607 while Fig. 5 contains observations C468, C882 and C1607. The images contain a combination of point sources and extended emission.

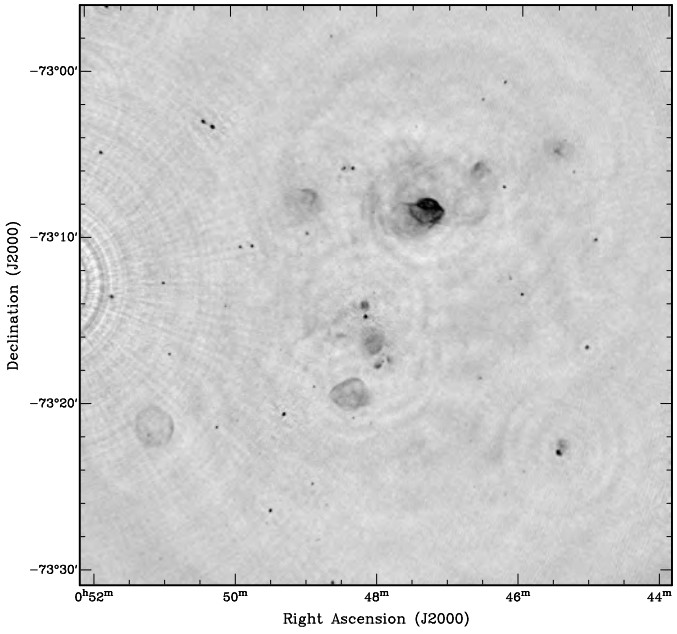

Fig. 1. *ATCA project C468 radio-continuum total intensity image of N 19. The synthesised beam is 5″.3×5″.1 and the r.m.s. noise is ∼0.1 mJy/beam.*

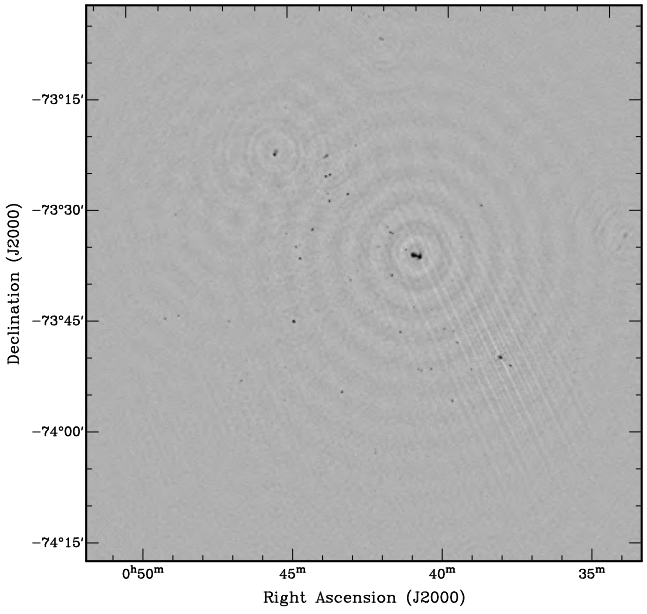

Fig. 2. *ATCA project C882 radio-continuum total intensity image of N 19. The synthesised beam is 6″.6×6″.2 and the r.m.s. noise is ∼0.1 mJy/beam.*

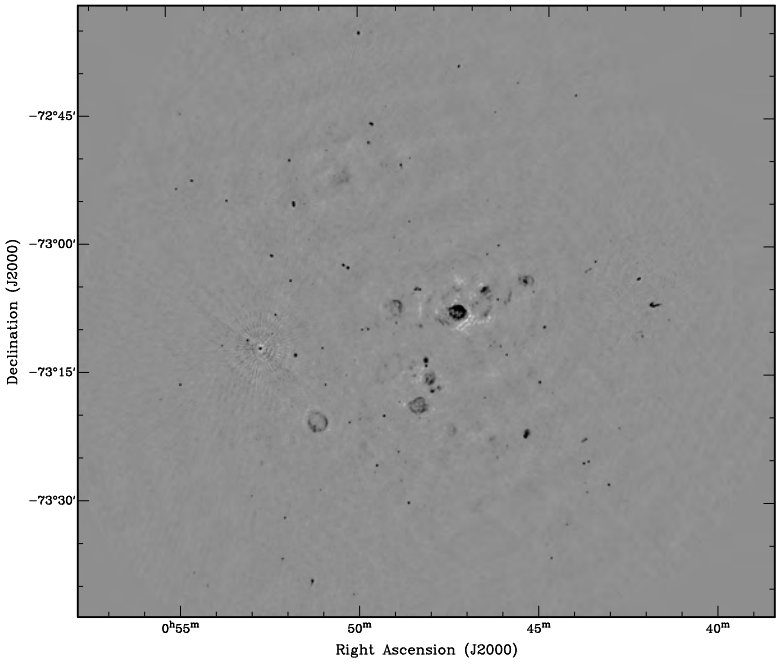

Fig. 3. *ATCA project C1607 radio-continuum total intensity image of N 19. The synthesised beam is 6″.9×5″.5 and the r.m.s. noise is ∼0.1 mJy/beam.*

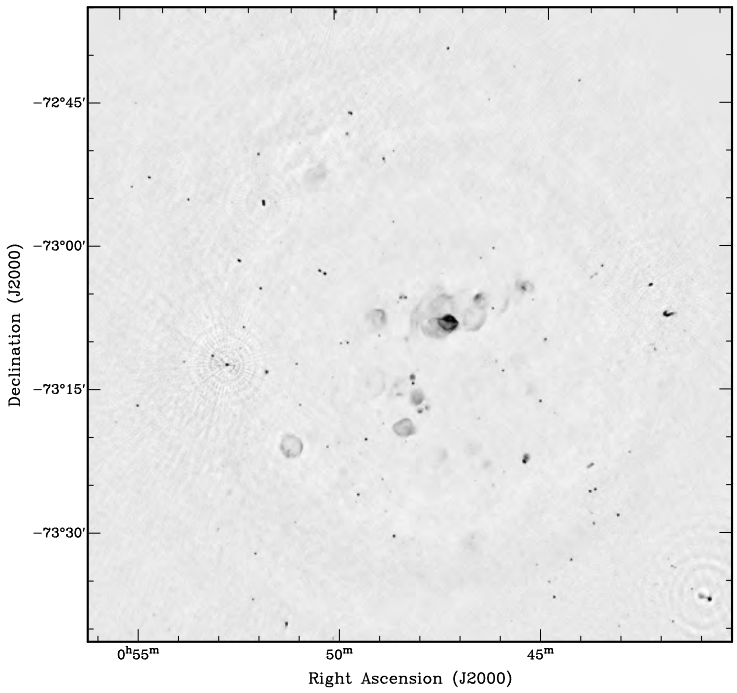

Fig. 4. *Combined ATCA projects C468 and C1607 radio-continuum total intensity image of N 19. The synthesised beam is 5″.3×5″.0 and the r.m.s. noise is ∼0.1 mJy/beam.*

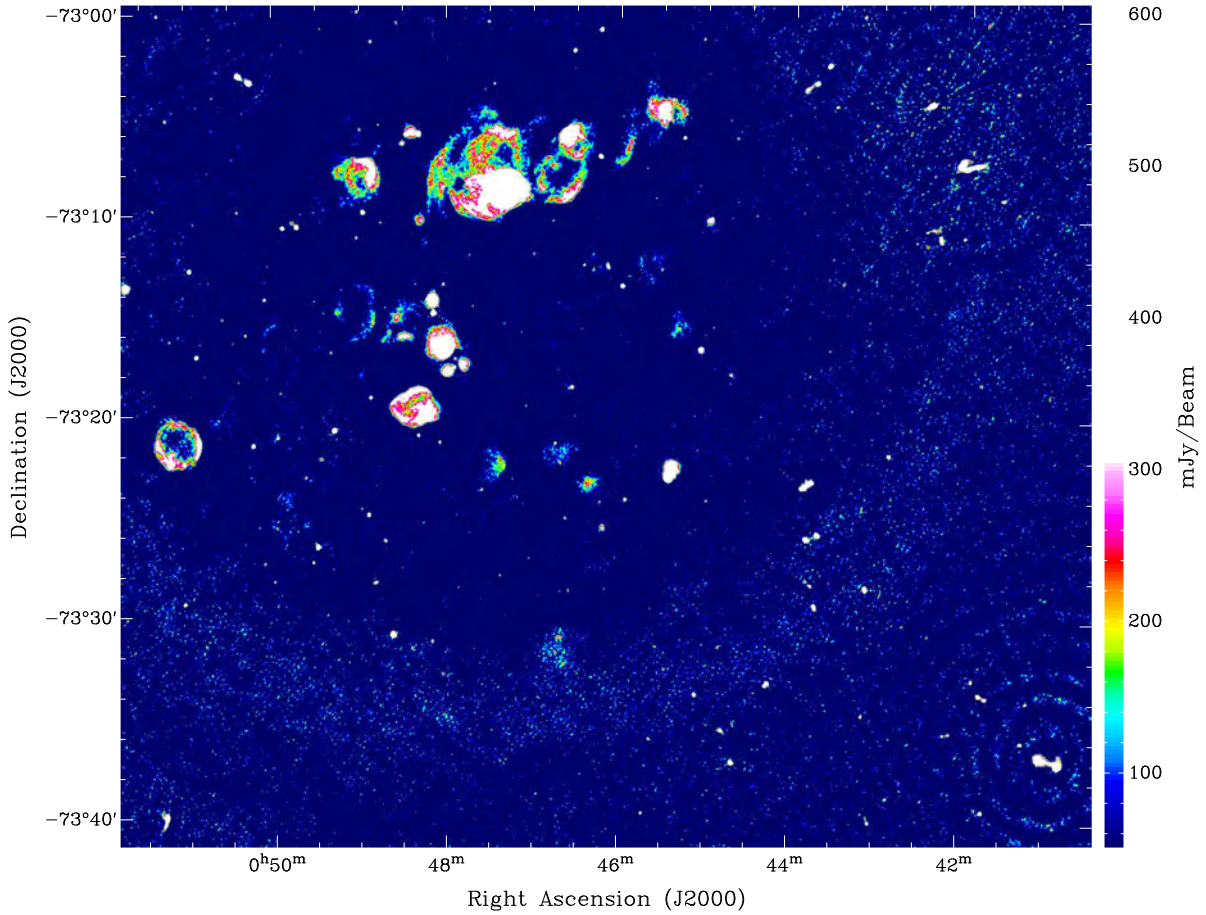

Fig. 5. *20 cm total intensity continuum image of N 19, derived from ATCA projects C468, C882 and C1607. The synthesised beam is 5.″3×5.″0 and the r.m.s. noise is ∼0.1 mJy/beam.*

3. THE SMC COMPACT H II REGIONS: SOURCE FITTING AND DETECTION

Compact H II regions were identified by comparing our list of radio-continuum point sources (Paper II and Wong et al. 2012) to an Hα observation from the Magellanic Cloud Emission Line Survey (MCELS; Smith et al. 1999). Sources were examined visually to confirm that matched Hα sources were point or point-like in Hα and within ∼5″of the radio point source detection.

The list of candidate compact H II regions was narrowed down by cross-checking with catalogues of known objects like supernova remnants (Filipović et al. 2008) and planetary nebulae (Filipović et al. 2009, Crawford et al. 2012, Bojičić et al. 2010).

Table A1 gives the names, positions (J2000, derived from the 1420 MHz image of the whole SMC) and the integrated flux values at various frequencies for the compact H II regions. The integrated fluxes in columns 5–12 are: flux density values taken from the MOST image; 1420 MHz flux density measurements from SMC (high resolution Fig. 2, Paper I) and new N 19 (Fig. 5) mosaic images; flux measurements retrieved from the N 77 20 and 13 cm images (Ye et al. 1995); flux values from an SMC 2370 MHz mosaic image (Filipović et al. 2002); 4800 and 8640 MHz flux values from Crawford et al. (2011; Figs. 1 and 3).

4. RESULTS AND DISCUSSION

Figs. 1–3 show the individual intensity mosaic maps of the N 19 region derived from projects C468, C882 and C1607, respectively, while Figs. 4 and 5 are images created by combining different observations. All these images can be downloaded from: space-science.uws.edu.au/mc/smc/N19/. A sample of 48 compact H II regions was selected; table A1 lists the compact H II regions with integrated flux values at various frequencies. These flux values are derived from gaussians fitted to the images described in Section 2.

30 of the 48 catalogue sources were detected at more than one wavelength. Spectral indices α ($S_\nu \propto \nu^\alpha$), with errors, were estimated for all of these sources, fitted to all available flux measurements. Integrated fluxes at 1 GHz were also derived from these fits. Integrating the fitted spectra from 10 MHz to 100 GHz yielded fluxes (in $10^{-26}\,\mathrm{W\,m^{-2}}$) which were then converted into radio luminosities using the known distance to the SMC. Table A2 lists all compact H II regions: The estimated flux density at 1 GHz; spectral index with errors; and the radio luminosity (i.e. the luminosity of the compact H II region over the radio spectrum) in units of 10^{26} W and in solar luminosities.

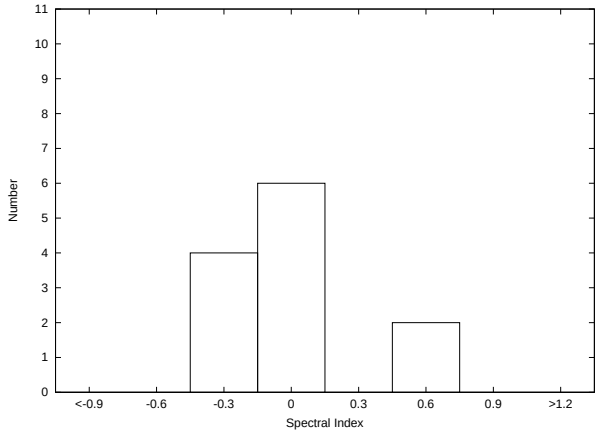

Fig. 6. *Spectral Index distribution of compact H II regions in N 19.*

Figs. 6–8 contain spectral index distributions of the compact H II regions in the N 19 region in the SMC (without N 19) and the combination of the two. We expect compact H II regions to have flat radio spectra ($\alpha \approx -0.1$), turning into $\alpha \approx 2$ below the cutoff frequency (which depends on the individual region); the spectral index distributions are indeed peaked around small values of α. While the spectral index distribution of SMC sources has a broad peak with several sources having quite large α, the distribution of N 19 sources is much more sharply peaked near $\alpha = 0$. The maps of N 19 have better resolution and sensitivity than the maps of the rest of the SMC, so the N 19 sources might be expected to have more accurate fluxes and hence more accurate spectral indices. Overall, ∼60% of the sources have spectral index within the expected range of $-0.3 < \alpha < 0.3$. Higher spectral indices may be explained by the cutoff frequency lying within the frequency range of our observations (see notes on individual sources below). There are also a few sources with significantly negative spectral indices, which is not consistent with thermal emission — these may be contaminating non-H II region sources.

The radio luminosity distribution (Fig. 9) peaks around $\sim 0.3\,\mathrm{L_\odot}$: It falls off towards higher luminosities as there are fewer sufficiently bright stars to power compact H II regions at such high luminosities; it falls off towards lower luminosities due to the lack of completeness of our catalogue. Our catalogue is likely to be quite complete down to a limiting radio luminosity of $\sim 0.3\,\mathrm{L_\odot}$.

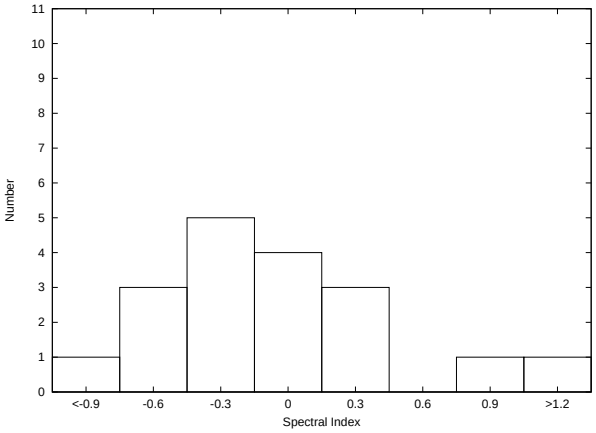

Fig. 7. *Spectral Index distribution of SMC compact H II regions (excluding N 19 sources).*

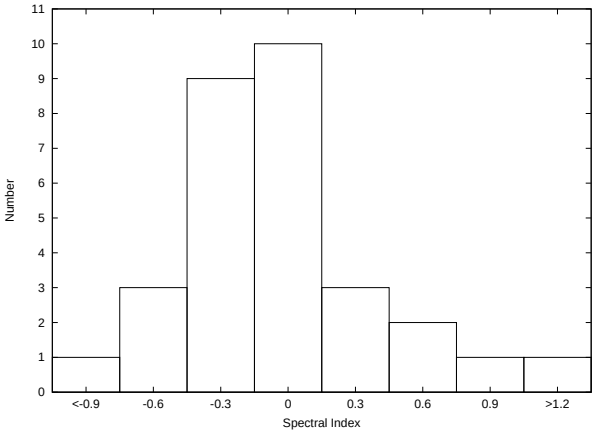

Fig. 8. *Spectral Index distribution of compact H II regions in SMC (including N 19 sources).*

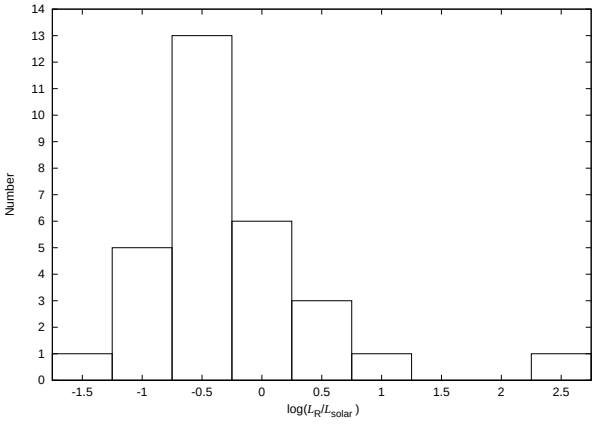

Fig. 9. *Radio luminosity distribution of SMC compact H II regions from all maps.*

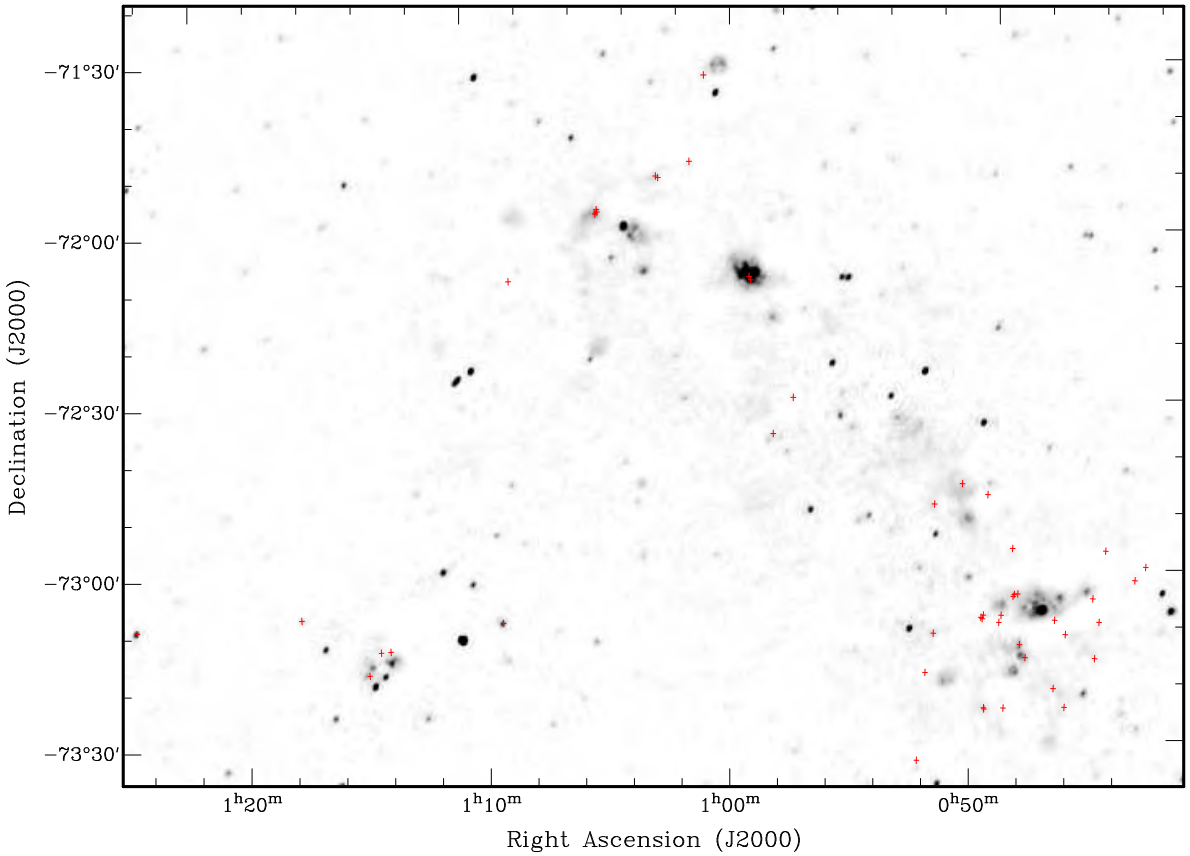

Fig. 10. *Location of compact H II regions overlaid on a continuum map of the SMC (Fig 6, Paper I).*

4.1. Notes on individual sources

4.1.1. J005914-721103 (Source 33)

This compact H II region candidate is the extreme positive outlier in Figs. 7 and 8, with a spectral index of $+2.0 \pm 0.4$; it is only detected in the 13 cm and 20 cm N 77 images, so the spectral index is defined purely by these fluxes. It is possible that this is a compact H II region with a very high-frequency spectral break, so that it has a spectral index of 2 even in the higher-frequency maps. However, in the 13 cm image, the source is located at the edge of the primary beam, so that the 13 cm flux is rather unreliable, and so this spectral index may not be accurate. It is also possible that this source could be a variable background galaxy that flared during the N 77 observations, and is otherwise undetected. The very high estimated luminosity is largely due to the extreme spectral index, and is unlikely to be accurate — if the source is indeed a compact H II region with a very high cutoff frequency, the high luminosity is due to extrapolation of the low-frequency spectral index to the whole radio region.

4.1.2. J010132-715042 (Source 36)

This is the other source with a highly positive spectral index ($+1.0 \pm 0.4$), and could only be detected in the 20 cm and 36 cm images. It is likely that this is a compact H II region whose spectral break lies between 36 cm and 20 cm. Fitting a single power-law to these data then gives an average spectral index of about 1. This will also lead to a large overestimate in the luminosity.

4.1.3. J012408-730904 (Source 48)

This compact H II region candidate has a very high radio luminosity of 23.5 $L_{\odot}$; this estimate comes from a combination of a positive estimated spectral index (which implies rising flux through the GHz spectrum, and hence a large luminosity) and very high fluxes in all images. The source is detected at 36 cm, and the higher-frequency data yield a spectral index of $\sim -0.2 \pm 0.1$. This is quite consistent with the source being a compact H II region with a cutoff

frequency between 843 MHz and 1.4 GHz. Although the luminosity may be overestimated, this is clearly a very luminous radio source. If it is a compact H II region, it is likely to be powered by a cluster of young high-mass stars, which can supply such a large luminosity.

5. CONCLUSION

In this paper we present a new catalogue of 48 candidate compact H II regions within the SMC. This catalogue is derived from previously-presented datasets, and from a new set of high-sensitivity and high-resolution radio-continuum images of the N 19 region at 1420 MHz (λ=20 cm), created from archival ATCA data. We have collected flux measurements at as many wavelengths as possible for all sources, and used these fluxes to fit a power-law radio spectrum, which, in turn, yields estimates of the flux at 1 GHz and the spectral index. The distribution of spectral indices is consistent with a population of sources dominated by compact H II regions, i.e. peaked around $\alpha \approx 0$, with better data yielding sharper peaks, and a few sources with significantly positive spectral indices — consistent with compact H II regions whose cutoff frequencies lie within our frequency range. We have also estimated the radio luminosity of the sources: The distribution of radio luminosities is strongly peaked around a presumed threshold luminosity, but includes some very luminous regions, such as J012408-730904, whose very high radio luminosity suggests that it is powered by a cluster of young high-mass stars.

Acknowledgements – The Australia Telescope Compact Array is part of the Australia Telescope National Facility which is funded by the Commonwealth of Australia for operation as a National Facility managed by CSIRO. This paper includes archived data obtained through the Australia Telescope Online Archive (http://atoa.atnf.csiro.au). We used the KARMA and MIRIAD software packages developed by ATNF. We thank the anonymous referee and Richard Sturm for their valuable comments, which have led to an improved paper.

REFERENCES

Bojičić, I. S., Filipović, M. D., Crawford, E. J.: 2010, *Serb. Astron. J.*, **181**, 63.

Dickel, J. R., Gruendl, R. A., McIntyre, V. J., Shaun, W. A.: 2010, *Astron. J.*, **140**, 1511.

Crawford, E. J., Filipović, M. D., de Horta, A. Y., Wong, G. F., Tothill, N. F. H., Drašković,, D., Collier, J. D., Galvin, T. J.: 2011, *Serb. Astron. J.*, **183**, 95.

Crawford, E. J., Filipović, M. D., Bojičić, I. S., Cohen, M., Payne, J. L., De Horta, A. Y., Reid, W.: 2012, *IAU Symposium Vol. 283 of IAU Symposium.*

Filipović, M. D., Jones, P. A., White, G. L, Haynes, R. F, Klein, U., Wielebinski, R.: 1997, *Astron. Astrophys. Suppl. Series*, **121**, 321.

Filipović, M. D., Haynes, R. F., White, G. L., Jones, P. A.: 1998, *Astron. Astrophys. Suppl. Series*, **130**, 421.

Filipović, M. D., Bohlsen, T., Reid, W, Staveley-Smith, L., Jones, P. A, Nohejl, K., Goldstein, G.: 2002, *Mon. Not. R. Astron. Soc.*, **335**, 1085.

Filipović, M. D., Payne, J. L., Reid, W., Danforth, C. W., Staveley-Smith, L., Jones, P. A., White, G. L.: 2005, *Mon. Not. R. Astron. Soc.*, **364**, 217.

Filipović, M. D., Haberl, F., Winkler, P. F., Pietsch, W., Payne, J. L., Crawford, E. J., de Horta, A. Y., Stootman, F. H., Reaser, B. E.: 2008, *Astron. Astrophys.*, **485**, 63.

Filipović, M. D., Cohen, M., Reid, W. A., Payne, J. L., Parker, Q. A., Crawford, E. J., Bojičić, I. S., de Horta, A. Y., Hughes, A., Dickel, J., Stootman, F.: 2009, *Mon. Not. R. Astron. Soc.*, **399**, 769.

Gooch, R.: 2008, KARMA Users Manual, ATNF, Sydney.

Hilditch, R. W., Howarth, I. D., Harries, T. J.: 2005, *Mon. Not. R. Astron. Soc.*, **357**, 304.

Indebetouw, R., Johnson, K. E., Conti, P.: 2004, *Astron. J.*, **128**, 2206.

Mao, S. A., Gaensler, B. M., Stanimirović, S., Haverkorn, M., McClure-Griffiths, N. M., Staveley-Smith, L., Dickey, J. M.: 2008, *Astrophys. J.*, **688**, 1029.

Mezger, P. G., Altenhoff, W., Schraml, J., Burke, B. F., Reifenstein, E. C., III, Wilson, T. L.: 1967, *Astron. J.*, **150**, L157.

Oliveira, J. M., Th. van Loon, J., Sloan, G. C., Sewilo, M., Kraemer, K.E.,Wood, P. R., Indebetouw, R., Filipović, M. D., Crawford, E. J., Wong, G. F., Hora, J. L., Meixner M., Robitaille, T. P., Shiao, B. Simon, J. D.: 2012, *Mon. Not. R. Astron. Soc.*, (in press).

Sault, R., Killeen, N.: 2010, Miriad Users Guide, ATNF.

Sault, R. J., Wieringa, M. H.: 1994, *Astron. Astrophys. Suppl. Series*, **108**, 585.

Smith,R. C. and MCELS Team: 1999, *IAU Symposium Vol. 190 of IAU Symposium.*

Steer, D. G., Dewdney, P. E., Ito, M. R.: 1984, *Astron. Astrophys.*, **137**, 159.

Turtle, A. J., Ye, T., Amy, S. W., Nicholls, J.: 1998, *Publ. Astron. Soc. Aust.*, **15**, 280.

Wong, G. F., Filipović, M. D., Crawford, E. J., de Horta, A. Y., Galvin, T., Drašković, D., Payne, J. L.: 2011a, *Serb. Astron. J.*, **182**, 43.

Wong, G. F., Filipović, M. D., Crawford, E. J., Tothill, N. F. H., de Horta, A. Y., Drašković, D., Galvin, T. J., Collier, J. D., Payne, J. L.: 2011b, *Serb. Astron. J.*, **183**, 103.

Wong, G. F., Crawford, E. J., Filipović, M. D., De Horta, A. Y., Tothill, N. F. H., Collier, J. D., Drašković, D., Galvin, T. J., Payne, J. L.: 2012, *Serb. Astron. J.*, **184**, 93.

Ye, T. S., Amy, S. W., Wang, Q. D., Ball, L., Dickel, J.: 1995, *Mon. Not. R. Astron. Soc.*, **275**, 1218.

APPENDIX

Table A1. Compact H II regions and their fluxes.

(1) No	(2) Name	(3) RA (J2000)	(4) Dec (J2000)	(5) S_{843} (mJy)	(6) S_{1420} (SMC) (mJy)	(7) S_{1420} (N 19) (mJy)	(8) S_{1377} (N77) (mJy)	(9) S_{2377} (N77) (mJy)	(10) S_{2370} (SMC) (mJy)	(11) S_{4800} (mJy)	(12) S_{8640} (mJy)
1	J004312-725958	00:43:12.6	-72:59:58	—	—	0.55	—	—	—	—	—
2	J004336-730227	00:43:36.4	-73:02:27	5.9	5.0	2.44	—	—	5.2	5.8	4.8
3	J004451-725734	00:44:51.6	-72:57:34	—	2.3	0.20	—	—	—	—	—
4	J004457-731012	00:44:57.1	-73:10:12	5.7	3.0	2.66	—	—	4.6	5.2	3.5
5	J004502-731639	00:45:02.6	-73:16:39	6.3	6.4	2.61	—	—	5.4	4.4	4.5
6	J004515-730607	00:45:15.7	-73:06:07	—	—	1.54	—	—	—	—	—
7	J004610-732534	00:46:10.7	-73:25:34	—	—	0.40	—	—	—	—	—
8	J004617-731243	00:46:17.7	-73:12:43	—	—	0.23	—	—	—	—	—
9	J004640-732221	00:46:40.3	-73:22:21	—	—	0.31	—	—	—	—	—
10	J004645-731017	00:46:45.9	-73:10:17	—	—	0.19	—	—	—	—	—
11	J004753-731709	00:47:53.5	-73:17:09	—	6.7	0.38	—	—	—	—	—
12	J004808-731454	00:48:08.6	-73:14:54	19.8	15.6	12.47	—	—	11.2	16.2	18.3
13	J004818-730558	00:48:18.7	-73:05:58	—	4.9	2.15	—	—	—	—	—
14	J004826-730606	00:48:27.0	-73:06:06	—	4.9	1.93	—	—	—	—	—
15	J004829-730626	00:48:29.9	-73:06:26	—	4.4	0.42	—	—	—	—	—
16	J004836-725759	00:48:36.4	-72:57:59	—	2.8	1.59	—	—	—	2.2	—
17	J004841-732614	00:48:41.8	-73:26:14	—	—	0.58	—	—	—	—	—
18	J004857-730952	00:48:57.1	-73:09:52	—	1.6	0.91	—	—	—	—	—
19	J004901-731109	00:49:01.8	-73:11:09	—	—	0.45	—	—	—	—	1.6
20	J004929-732633	00:49:29.2	-73:26:33	9.7	7.2	5.53	—	—	4.1	5.9	5.6
21	J004930-732621	00:49:30.4	-73:26:21	—	—	0.23	—	—	—	—	—
22	J004940-730958	00:49:40.4	-73:09:58	—	—	0.15	—	—	—	—	—
23	J004941-724840	00:49:41.5	-72:48:40	6.6	2.8	1.42	—	—	3.4	5.7	5.5
24	J004942-731037	00:49:42.7	-73:10:37	7.3	3.6	3.25	—	—	—	5.2	3.5
25	J004946-731024	00:49:46.1	-73:10:24	—	—	0.25	—	—	—	—	—
26	J005043-724655	00:50:43.4	-72:46:55	—	7.1	0.53	—	—	—	—	—
27	J005141-731331	00:51:41.2	-73:13:31	12.5	7.7	2.88	—	—	5.7	10.8	8.0
28	J005148-725041	00:51:48.3	-72:50:41	9.2	7.2	2.27	—	—	5.1	5.9	6.6
29	J005158-732030	00:51:58.3	-73:20:30	—	—	0.32	—	—	—	—	—
30	J005212-733604	00:52:12.6	-73:36:04	—	1.4	0.20	—	—	—	1.3	—

Table A1. Continued.

(1) No	(2) Name	(3) RA (J2000)	(4) Dec (J2000)	(5) S_{843} (mJy)	(6) S_{1420} (SMC) (mJy)	(7) S_{1420} (N 19) (mJy)	(8) S_{1377} (N77) (mJy)	(9) S_{2377} (N77) (mJy)	(10) S_{2370} (SMC) (mJy)	(11) S_{4800} (mJy)	(12) S_{8640} (mJy)
31	J005729-723223	00:57:29.9	-72:32:23	4.0	4.4	—	—	—	1.4	3.3	3.3
32	J005816-723849	00:58:16.5	-72:38:49	12.7	5.1	—	—	—	5.0	14.8	9.5
33	J005914-721103	00:59:14.9	-72:11:03	—	—	—	2.2	5.9	—	—	—
34	J005911-721140	00:59:11.0	-72:11:40	—	—	—	—	—	—	7.0∗	5.0∗
35	J010058-713527	01:00:58.5	-71:35:27	9.3	6.7	—	—	—	4.7	7.5	7.5
36	J010132-715042	01:01:32.2	-71:50:42	1.5	2.4	—	—	—	—	—	—
37	J010243-715331	01:02:43.6	-71:53:31	8.1	2.5	—	0.4	—	—	2.6	1.6
38	J010248-715314	01:02:48.7	-71:53:14	13.9	9.1	—	5.9	6.9	5.3	8.9	12.1
39	J010503-715926	01:05:03.8	-71:59:26	—	14.5	—	5.8	12.5	—	24.5	17.4
40	J010504-715900	01:05:05.0	-71:59:00	—	5.9	—	2.5	3.0	—	10.5	4.7
41	J010508-715946	01:05:08.4	-71:59:46	—	7.9	—	3.1	—	—	10.3	6.2
42	J010832-721119	01:08:32.4	-72:11:19	—	—	—	—	—	—	0.8∗	0.6∗
43	J010912-731138	01:09:13.0	-73:11:38	50.0	33.1	—	—	—	60.1	35.7	37.5
44	J011352-731546	01:13:52.1	-73:15:46	8.7	3.5	—	—	—	—	4.7	4.8
45	J011415-731550	01:14:15.8	-73:15:50	9.5	4.3	—	—	—	5.9	7.2	8.2
46	J011447-731946	01:14:47.1	-73:19:46	15.0	8.0	—	—	—	3.4	4.0	5.2
47	J011724-730917	01:17:25.0	-73:09:17	20.1	12.5	—	—	—	7.4	4.3	4.7
48	J012408-730904	01:24:08.1	-73:09:04	39.6	51.4	—	—	—	115.3	92.8	94.2

∗ Values taken from Indebetouw et al. 2004

Table A2. Compact H II regions and their properties.

(1) No	(2) Name	(3) RA (J2000)	(4) Dec (J2000)	(5) S_{1000} (mJy)	(6) Spectral Index	(7) Luminosity $\times 10^{26}$ W/Hz	(8) Luminosity in $L_\odot$
1	J004312-725958	00:43:12.6	-72:59:58	—	—	—	—
2	J004336-730227	00:43:36.4	-73:02:27	4.4	0.1 ± 0.2	2.5	0.6
3	J004451-725734	00:44:51.6	-72:57:34	—	—	—	—
4	J004457-731012	00:44:57.1	-73:10:12	4.0	0.0 ± 0.2	1.7	0.5
5	J004502-731639	00:45:02.6	-73:16:39	5.0	-0.1 ± 0.2	1.7	0.4
6	J004515-730607	00:45:15.7	-73:06:07	—	—	—	—
7	J004610-732534	00:46:10.7	-73:25:34	—	—	—	—
8	J004617-731243	00:46:17.7	-73:12:43	—	—	—	—
9	J004640-732221	00:46:40.3	-73:22:21	—	—	—	—
10	J004645-731017	00:46:45.9	-73:10:17	—	—	—	—
11	J004753-731709	00:47:53.5	-73:17:09	—	—	—	—
12	J004808-731454	00:48:08.6	-73:14:54	14.9	0.0 ± 0.1	7.1	1.9
13	J004818-730558	00:48:18.7	-73:05:58	—	—	—	—
14	J004826-730606	00:48:27.0	-73:06:06	—	—	—	—
15	J004829-730626	00:48:29.9	-73:06:26	—	—	—	—
16	J004836-725759	00:48:36.4	-72:57:59	2.1	0.1 ± 0.4	1.1	0.3
17	J004841-732614	00:48:41.8	-73:26:14	—	—	—	—
18	J004857-730952	00:48:57.1	-73:09:52	—	—	—	—
19	J004901-731109	00:49:01.8	-73:11:09	0.3	0.7 ± 0.1	2.2	0.6
20	J004929-732633	00:49:29.2	-73:26:33	7.0	-0.2 ± 0.1	1.7	0.4
21	J004930-732621	00:49:30.4	-73:26:21	—	—	—	—
22	J004940-730958	00:49:40.4	-73:09:58	—	—	—	—
23	J004941-724840	00:49:41.5	-72:48:40	3.1	0.2 ± 0.3	3.1	0.8
24	J004942-731037	00:49:42.7	-73:10:37	4.8	-0.1 ± 0.2	1.4	0.4
25	J004946-731024	00:49:46.1	-73:10:24	—	—	—	—
26	J005043-724655	00:50:43.4	-72:46:55	—	—	—	—
27	J005141-731331	00:51:41.2	-73:13:31	6.7	0.1 ± 0.3	3.9	1.0
28	J005148-725041	00:51:48.3	-72:50:41	5.5	0.0 ± 0.3	2.6	0.7
29	J005158-732030	00:51:58.3	-73:20:30	—	—	—	—
30	J005212-733604	00:52:12.6	-73:36:04	0.4	0.7 ± 1.4	2.8	0.7
31	J005729-723223	00:57:29.9	-72:32:23	3.3	-0.1 ± 0.3	1.1	0.3
32	J005816-723849	00:58:16.5	-72:38:49	7.7	0.1 ± 0.3	5.1	1.3
33	J005911-721140	00:59:11.0	-72:11:40	17.3	-0.6 ± 0.3	1.2	0.3
34	J005914-721103	00:59:14.9	-72:11:03	1.1	2.0 ± 0.4	1363.6	355.2
35	J010058-713527	01:00:58.5	-71:35:27	7.2	-0.0 ± 0.1	2.7	0.7
36	J010132-715042	01:01:32.2	-71:50:42	1.7	1.0 ± 0.4	35.4	9.2
37	J010243-715331	01:02:43.6	-71:53:31	2.4	-0.2 ± 0.7	0.5	0.1
38	J010248-715314	01:02:48.7	-71:53:14	8.1	0.0 ± 0.2	4.1	1.1
39	J010503-715926	01:05:03.8	-71:59:26	8.4	0.5 ± 0.3	20.2	5.3
40	J010504-715900	01:05:05.0	-71:59:00	3.4	0.3 ± 0.4	4.7	1.2
41	J010508-715946	01:05:08.4	-71:59:46	4.9	0.2 ± 0.4	5.0	1.3
42	J010832-721119	01:08:32.4	-72:11:19	1.7	-0.5 ± 0.3	0.1	0.0
43	J010912-731138	01:09:13.0	-73:11:38	46.1	-0.1 ± 0.1	14.2	3.7
44	J011352-731546	01:13:52.1	-73:15:46	5.9	-0.1 ± 0.2	1.5	0.4
45	J011415-731550	01:14:15.8	-73:15:50	6.5	0.1 ± 0.2	3.3	0.9
46	J011447-731946	01:14:47.1	-73:19:46	9.3	-0.5 ± 0.3	0.9	0.2
47	J011724-730917	01:17:25.0	-73:09:17	15.5	-0.7 ± 0.1	0.9	0.2
48	J012408-730904	01:24:08.1	-73:09:04	51.2	0.4 ± 0.2	90.0	23.4

НОВО ПРОУЧАВАЊЕ МАЛОГ МАГЕЛАНОВОГ ОБЛАКА У РАДИО-КОНТИНУУМУ НА 20 cm: ДЕО III - КОМПАКТНИ H II РЕГИОНИ

G. F. Wong, M. D. Filipović, E. J. Crawford, N. F. H. Tothill, A. Y. De Horta and T. J. Galvin

University of Western Sydney, Locked Bag 1797, Penrith South DC, NSW 2751, Australia

E–mail: *m.filipovic@uws.edu.au*

УДК 524.722.7–77 : 524.523

Стручни чланак

Представљамо нови каталог од 48 компактних H II региона у Малом Магелановом Облаку (ММО). Такође, представљамо и нове радио-континуум слике N19 региона који се налази у југозападном делу ММО. Нове слике су креиране спајањем свих расположивих 20 cm посматрања са ATCA телескопа (Australian Telescope Compact Array). Већина детектованих комапктних H II региона има типичан "раван" спектар што указује да је доминантни емисиони механизам термалне природе.

A.25 Related Paper 25

Kavanagh, P. J., Sasaki, M., Points, S. D., Filipović, M. D., Maggi, P., Bozzetto, L. M., Crawford, E. J., Haberl, F., and Pietsch, W. (2013). Multiwavelength study of the newly confirmed supernova remnant MCSNR J0527-7104 in the Large Magellanic Cloud. *A&A*, 549:A99

My contribution was to assist in the data analysis. This is a 10% contribution.

A&A 549, A99 (2013)
DOI: 10.1051/0004-6361/201220431

Astronomy & Astrophysics

Multiwavelength study of the newly confirmed supernova remnant MCSNR J0527−7104 in the Large Magellanic Cloud

P. J. Kavanagh[1], M. Sasaki[1], S. D. Points[2], M. D. Filipović[3], P. Maggi[4], L. M. Bozzetto[3], E. J. Crawford[3], F. Haberl[4], and W. Pietsch[4]

[1] Institut für Astronomie und Astrophysik, Kepler Center for Astro and Particle Physics, Eberhard Karls Universität, 72076 Tübingen, Germany
e-mail: kavanagh@astro.uni-tuebingen.de
[2] Cerro Tololo Inter-American Observatory, 603 Casilla, La Serena, Chile
[3] University of Western Sydney, Locked Bag 1797, Penrith NSW 2751, Australia
[4] Max-Planck-Institut für extraterrestrische Physik, Giessenbachstraße, 85748 Garching, Germany

Received 23 September 2012 / Accepted 20 November 2012

ABSTRACT

Context. The Large Magellanic Cloud (LMC) hosts a rich and varied population of supernova remnants (SNRs). Optical, X-ray, and radio observations are required to identify these SNRs, as well as to ascertain the various processes responsible for the large array of physical characteristics observed.
Aims. In this paper we attempted to confirm the candidate SNR [HP99] 1234, identified in X-rays with ROSAT, as a true SNR by supplementing these X-ray data with optical and radio observations.
Methods. Optical data from the Magellanic Cloud Emission Line Survey (MCELS) and new radio data from the Molonglo Observatory Synthesis Telescope (MOST), in addition to the ROSAT X-ray data, were used to perform a multiwavelength morphological analysis of this candidate SNR.
Results. An approximately ellipsoidal shell of enhanced [S] emission, typical of an SNR ([S]/Hα > 0.4), was detected in the optical. This enhancement is positionally coincident with faint radio emission at λ = 36 cm. Using the available data we estimated the size of the remnant to be ∼5.1′ × 4.0′ (∼75 pc × 59 pc). However, the measurement along the major-axis was somewhat uncertain due to a lack of optical and radio emission at its extremities and the poor resolution of the X-ray data. Assuming this SNR is in the Sedov phase and adopting the ambient mass density of 1.2×10^{-25} g cm^{-3} measured in a nearby H region, an age estimate of ∼25 kyr was calculated for a canonical initial explosion energy of 10^{51} erg. However, this age estimate should be treated cautiously due to uncertainties on the adopted parameters. Analysis of the local stellar population suggested a type Ia event as a precursor to this SNR, however, a core-collapse mechanism could not be ruled out due to the possibility of the progenitor being a runaway massive star.
Conclusions. With the detection of X-ray, radio and significant optical line emission with enhanced [S], this object was confirmed as an SNR to which we assign the identifier MCSNR J0527−7104.

Key words. ISM: supernova remnants – Magellanic Clouds – ISM: individual objects: MCSNR J0527-7104

1. Introduction

Supernova remnants (SNRs) are of vital importance to the physical and chemical evolution of the interstellar medium (ISM). The expanding shells of the remnants impart kinetic energy to the surrounding ISM, as well as enriching it with the metals synthesized in the cores of their progenitor stars. Thus, an understanding of these objects is crucial to the understanding of star formation and matter recycling in galaxies. Unfortunately, due to SNRs being located primarily in the Galactic disk, studies of these objects in the Galaxy are hindered by high foreground absorption. Hence, we must look to nearby galaxies to perform unbiased studies of SNRs and SNR populations.

The Large Magellanic Cloud (LMC) is, for a variety of reasons, the best galaxy in the Local Group for the study of SNRs. At a distance of 50 kpc (di Benedetto 2008) it is sufficiently close that its stellar population and diffuse structure is resolved in most wavelength regimes. In addition, the LMC is almost face-on (inclination angle of ∼30°−40°, van der Marel & Cioni 2001; Nikolaev et al. 2004) making the entire population of SNRs available for study. The modest extinction in the line of sight (average Galactic foreground $N_{\rm H} \approx 7 \times 10^{20}$ cm^{-2}) means optical and X-ray observations of SNRs are only slightly affected by foreground absorption, whereas its location in one of the coldest parts of the radio sky (Haynes et al. 1991) allows for improved radio observations without interference from Galactic emission. There are over 50 confirmed SNRs in the LMC (Badenes et al. 2010; Klimek et al. 2010) with a further ∼20 SNR candidates (Payne et al. 2008). However, continuing studies with new and archival optical, radio, and X-ray observations strive to add to the number of these SNRs and candidate SNRs. In addition, ever improving multiwavelength observational data allows the characterisation of the physical processes responsible for this rich and varied population. Recent works in this area include Maggi et al. (2012); Grondin et al. (2012).

Various SNR classification criteria exist in the literature. In this paper we adopt the criteria of the Magellanic Cloud Supernova Remnant (MCSNR) Database[1]. In this classification system, an SNR must satisfy at least two of the following three observational criteria: significant Hα, [S], and/or [O] line

[1] See http://www.mcsnr.org/about.aspx

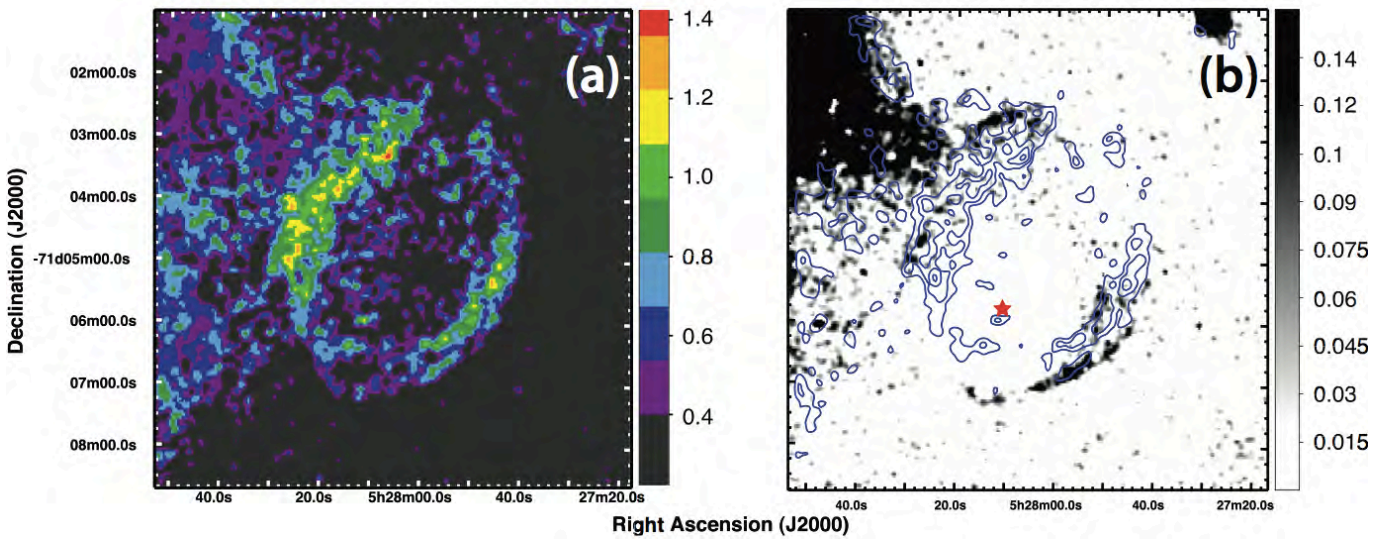

Fig. 1. MCELS derived images of MCSNR J0527−7104. **a)** [S]/Hα ratio map with the colour scale adjusted so only regions of enhanced [S] are visible. The SNR is clearly seen with two prominent arcs of enhanced [S] located NE and SW of the centre. The emission to the east of the SNR is due to the N 206 H complex. **b)** Continuum subtracted [O] image of MCSNR J0527−7104. [S]/Hα contours are overlaid, emphasising regions where the ratio is clearly enhanced, ranging from 0.67 to the maximal value with intermediate levels of 25, 50, and 75% of the maximum. The grayscale is in units of 10^{-15} erg cm^{-2} s^{-1}. The location of the bright foreground source HD 36877, which was masked for the continuum subtraction, is indicated by the red star. Each image has been smoothed using a 3 × 3 pixel Gaussian filter.

emission with an [S]/Hα flux ratio >0.4 (Mathewson & Clarke 1973; Fesen et al. 1985); extended non-thermal radio emission; and extended thermal X-ray emission. The ROSAT PSPC catalogue of X-ray sources in the LMC (Haberl & Pietsch 1999, hereafter HP99) contains [HP99] 1234 at a J2000 position of RA = $05^{h}27^{m}57.2^{s}$ and Dec = $-71^{d}04^{m}30^{s}$. It was classified as a candidate SNR in HP99 based on its X-ray hardness ratios and extent. However, without optical or radio detections to supplement the X-ray identification, this source has remained mired in the "candidate SNR" category.

In this paper we report the identification of enhanced [S] emission typical of an SNR in the vicinity of [HP99] 1234 using data from the Magellanic Cloud Emission Line Survey (MCELS). In addition, we detected faint radio emission positionally coincident with the [S] enhancement using observations by the Molonglo Synthesis Telescope (MOST) at λ = 36 cm. Hence, [HP99] 1234 appears to satisfy all three criteria for SNR classification and is, thus, confirmed as such. We will hereafter refer to this source as MCSNR J0527−7104 (adopting the MCSNR Database nomenclature). The optical, radio and X-ray observations and data reduction are described in Sect. 2. We discuss the interpretation of the observational data in Sect. 3 before offering our conclusions in Sect. 4.

2. Observations and data reduction

2.1. Optical

The MCELS observations (Smith et al. 2006) were taken with the 0.6 m University of Michigan/Cerro Tololo Inter-American Observatory (CTIO) *Curtis* Schmidt Telescope equipped with a SITE 2048 × 2048 CCD, producing individual images of 1.35° × 1.35° at a scale of 2.3″ pixel^{-1}. The survey mapped both the LMC (8° × 8°) and the SMC (3.5° × 4.5°) in narrow bands covering [O]λ5007 Å, Hα, and [S]λ6716, 6731 Å, in addition to matched green and red continuum bands. The survey data were flux calibrated and combined to produce mosaicked images. We extracted cutouts centred on MCSNR J0527−7104 from the MCELS mosaics. Our SNR falls across two regions of differing exposure times in each of the MCELS mosaic's exposure maps. The exposure times of these regions were 2.4 ks and 2.7 ks in the green continuum, red continuum, and Hα images, and 4.8 ks and 5.4 ks in the [O] and [S] images. We subtracted the continuum images from the corresponding emission line images, thereby removing the stellar continuum and revealing the full extent of the faint diffuse emission. The continuum subtracted [S] and Hα images were used to produce the [S]/Hα ratio map shown in Fig. 1a, the colour bar of which has been adjusted to only show regions of enhanced [S] ([S]/Hα > 0.4). MCSNR J0527−7104 is clearly seen, manifest as two bright arcs propagating into the northeast (NE) and southwest (SW) directions. The [S] enhancement to the east of the SNR is related to the N 206 H complex (Henize 1956) and is discussed in a separate paper (Kavanagh et al. 2012). In Fig. 1b we show the continuum subtracted [O] image of MCSNR J0527−7104 with [S]/Hα contours overlaid, emphasising regions where the ratio is clearly enhanced ([S]/Hα > 0.67, Fesen et al. 1985). However, due to the green continuum image being heavily contaminated by the foreground star HD 36877 (V = 9.36), the continuum subtraction in this region was somewhat unreliable. To account for this we completely excised the source from the [O] and green continuum images before performing the continuum subtraction. Very faint [O] emission was seen at the leading edges of the enhanced [S] emission regions, notably in the southwestern arc. This provides further evidence for the SNR classification as [O] emission is expected from the cooling zone closest to the SNR shock front.

2.2. Radio-continuum

We used a mosaic image taken from 36 cm MOST observations (as described in Mills et al. 1984) to investigate a radio association with this SNR (Fig. 2). There were two distinct regions evident in the radio image, located in the northeastern and southwestern areas. This radio morphology is consistent

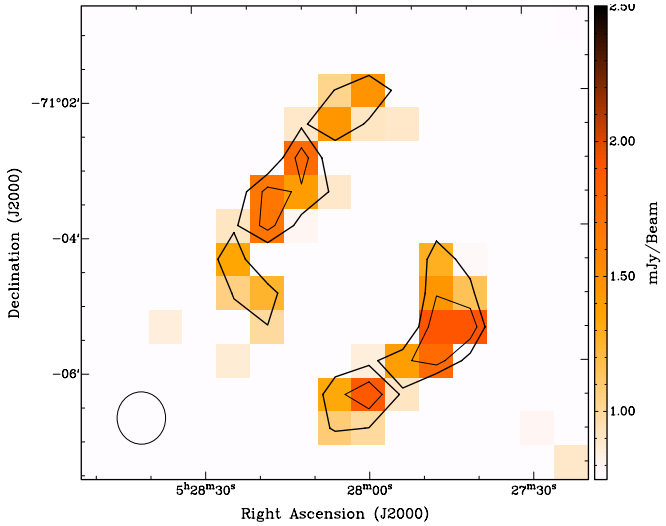

Fig. 2. 36 cm radio map of MCSNR J0527−7104. Contours are at the 3σ and 4σ levels (σ = 0.25 mJy/beam). The circle in the lower left corner indicates the beamwidth of 43″.

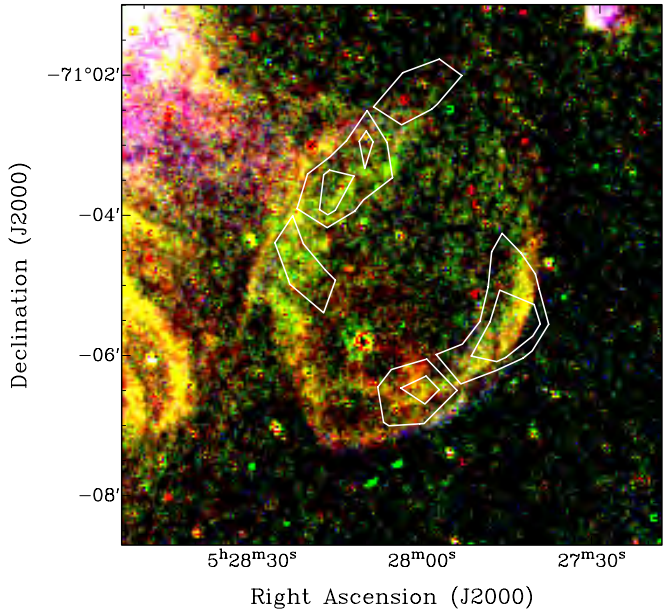

Fig. 3. MCELS composite optical image (RGB = Hα, [S], [O]) of MCSNR J0527−7104 overlaid with 36 cm radio contours determined as in Fig. 2.

with the long known "bilateral" class of SNRs, characterised by a clear axis of symmetry with low levels of emission along the axis and bright limb emission (see Gardner & Milne 1965; Kesteven & Caswell 1987; Gaensler 1998, for examples and descriptions of this morphological class). At all other radio frequencies, this SNR was well below the detection limit making it one of the weakest SNRs ever detected in the radio. For this reason, polarisation, spectral index and magnetic field studies of MCSNR J0527−7104 were beyond our grasp. In Fig. 3 we plot the radio contours shown in Fig. 2 over the MCELS RGB image, which clearly demonstrates the association of the radio emission with the optical shell of MCSNR J0527−7104.

2.3. X-rays

The HP99 catalogue was derived from individual PSPC observations, not taking advantage of overlapping exposures. To

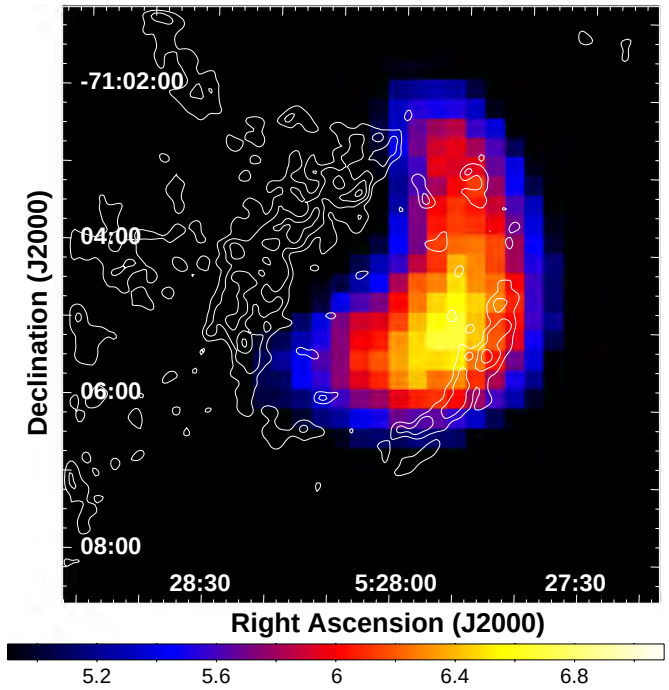

Fig. 4. ROSAT PSPC broad band (0.5−2 keV) count rate map of MCSNR J0527−7104. The image has a pixel size of 15″ and is smoothed with a 2′ kernel. The colour bar is in units of 10^{-5} counts pixel^{-1} s^{-1}. [S]/Hα contours are overlaid, ranging from 0.67 to the maximal value with intermediate levels of 25, 50, and 75% of the maximum.

examine the relation between X-rays, radio, and optical data, we searched all observations in the ROSAT archive covering MCSNR J0527−7104. Unfortunately, we found only two such observations with identifiers ROR rp300335 and ROR rp300172. The ROSAT observation with ROR rp300335 was used for the HP99 entry. Both observations were short at 11.3 ks and 13.2 ks, respectively. However, observation rp300172 was split in three parts and the source is seen at an even larger off-axis angle (∼50′) than in observation rp300335 (∼44′). Given the low exposure times of each part of observation rp300172 (∼3 ks, vignetting corrected), the large off-axis angle and corresponding PSF (∼3′, as opposed to ∼2′ for observation rp300335), we decided to exclude data from observation rp300335 from our analysis as their inclusion would serve to decrease the quality of our results. We produced an exposure corrected image with a pixel size of 15″ from observation rp30033. Due to the limited number of counts (∼55) from the source we did not split the data into different energy bands. Instead, we produced a broad band (0.5−2 keV) count rate map of MCSNR J0527−7104, shown in Fig. 4. Taking into account the degraded angular resolution of ROSAT at large off-axis angle, we smoothed the image with a Gaussian kernel of 2′. For an easier comparison of X-rays and optical data, we overlaid [S]/Hα line ratio contours derived from Fig. 1a. HP99 determined the extent of this SNR to be ∼39″ but with a very low likelihood for the extent of 0.2. Due to the low number of counts for the SNR in our analysis of observation rp300335 we were prohibited from performing a comparison of the source morphology to the ROSAT PSF at the large off-axis angle to confirm the extended nature of the source.

3. Discussion

Shell-like optical line emission follows an ellipsoidal morphology, elongated toward a southeast-northwest (SE-NW) axis. Two

arcs of enhanced [S]/Hα were seen parallel to the major axis, which correlate with faint radio emission at 36 cm. We identified X-ray emission from the west of the SNR in the ROSAT PSPC data. However, we stress that the remnant was only observed at a large off-axis angle during a shallow observation with ROSAT (see Sect. 2.3) and, thus, had very limited resolution and sensitivity. Because of this we were prevented from performing a more detailed analysis and the apparent extent of the X-ray emission should be treated cautiously.

The quality of the radio and X-ray data for this SNR prohibited size determinations in these wavebands. Hence, we determined the dimensions of this SNR from the MCELS data, specifically from the [S] enhanced regions. Given that there is a significant background in the east owing to the N 206 H region, we considered only the regions with clearly enhanced [S] ([S]/H$\alpha > 0.67$), namely the arcs indicated by the contours in Fig. 1b. The size along the NE-SW axis was measured as the distance between the leading edges of the arcs. We determined a size of 4.0′, or ∼59 pc at the LMC distance, for this axis. The size of the orthogonal SE-NW axis was somewhat less straightforward given the absence of an optical shell at its extremities. Since the leading edges of the arcs of enhanced [S]/Hα were approximately ellipsoidal in shape, we fitted an ellipse to these edges with the minor axis size set to 4.0′, as determined above. We measured a major axis size of ∼5.1′, or ∼75 pc at the LMC distance, using this method. However, we emphasise that this estimate is subject to much uncertainty given that we cannot definitively state that this SNR is fully ellipsoidal in shape. We already see some evidence to the contrary if we consider the radio image. In some regions, notably in the north, the arcs of radio emission extend slightly beyond the ellipse representing MCSNR J0527−7104. Thus, our estimate of ∼5.1′ (∼75 pc) in the SE-NW direction is likely lower than the actual SNR dimension. However, without further information a conclusive measurement remains beyond our grasp. Observations by *Chandra* or *XMM-Newton* would allow the true dimensions of the SNR to be determined, given that the X-ray emitting regions could be traced to much smaller spatial scales. The determined dimensions of MCSNR J0527−7104 of ∼5.1′ × 4.0′ (∼75 pc × 59 pc), make it comparable in size to large SNRs such as XMMU J0541.8−6659 (Grondin et al. 2012). However, the MCSNR J0527−7104 is still smaller than the largest confirmed SNRs in the LMC such as SNR 0450−70.9 (Mathewson et al. 1985; Williams et al. 2004; Cajko et al. 2009), LMC SNR J0550−6823 (Davies et al. 1976; Filipovic et al. 1998; Bozzetto et al. 2012) and SNR0506-6542 (Klimek et al. 2010).

If we assume that MCSNR J0527−7104 is in the Sedov phase of its evolution, we can estimate an age from the relation $r(t) = 1.17(E_0/\rho_0)^{1/5}t^{2/5}$ (Woltjer 1972), where $r(t)$ is the radius of the SNR at time t, E_0 is the initial explosion energy, and ρ_0 is the mass density of the ambient ISM. Williams et al. (2005) estimated the ISM mass density surrounding the other known SNR in the N 206 H region, SNR B0532-71.0, to be $\sim 1.2 \times 10^{-25}$ g cm^{-3}, derived from the determined density of the hot gas behind the SNR shock. SNR B0532-71.0 is also located on the outskirts of N 206, but some ∼19′ (∼214 pc) from MCSNR J0527−7104. Gorjian et al. (2004) reported on *Spitzer* observations of the N 206 region, highlighting the dust distribution using 24 μm, 70 μm, and 160 μm images. These images suggested that the ISM around SNR B0532-71.0 is slightly denser than the ISM around MCSNR J0527−7104. It is not ideal to adopt the ambient ISM mass density of SNR B0532-71.0 for that of MCSNR J0527−7104, especially given the calculations are quite sensitive to this parameter. However, it allows us to at least suggest an age for our SNR. For a canonical initial input energy of 10^{51} erg, we determined an age of ∼25 kyr for MCSNR J0527−7104 using the Sedov relation. We again stress that this age determination is very sensitive to the adopted ambient density, as well as the initial explosion energy. Using these parameters and our age estimate, we can rearrange the Sedov relation (setting the units as the input parameter values of $\rho_0 = 1.2 \times 10^{-25}$ g cm^{-3} and $E_0 = 10^{51}$) to highlight the dependence of the SNR age on the ambient mass density and initial explosion energy as

$$t \approx 25 \left(\frac{E_0}{10^{51}\ \mathrm{erg}}\right)^{-\frac{1}{2}} \left(\frac{\rho_0}{1.2 \times 10^{-25}\ \mathrm{g\ cm^{-3}}}\right)^{\frac{1}{2}} \mathrm{kyr}. \quad (1)$$

So, for example, an increase in the ambient mass density to double our adopted value results in an increase of ∼10 kyr in age to ∼35 kyr. A similar increase in age is seen if the initial explosion energy is halved. A combination of both of these examples leads to a doubling of the age estimate to ∼50 kyr. Hence, our determined age should be treated with the utmost caution.

Using the adopted ambient density and explosion energy we can also estimate the time at which this SNR will enter the radiative phase (t_{rad}) using the relation of Vink (2012),

$$t_{\mathrm{rad}} = 1.5 \times 10^{-13} \left(\frac{\xi E_0}{\rho_0}\right)^{\frac{1}{3}}, \quad (2)$$

where ξ is a dimensionless constant depending on the adiabatic index, which is 2.026 for a monatomic gas with $\gamma = 5/3$. We determine that MCSNR J0527−7104 will enter the radiative phase at ∼122 kyr. While this estimate seems to verify our original assumption that MCSNR J0527−7104 is indeed in the Sedov phase of its evolution, we again stress the dependence on our assumed ambient mass density and initial explosion energy values and the resulting uncertainty in age and t_{rad}. To obtain a more robust age estimate would require more observational data than is currently available. High quality X-ray data from *XMM-Newton* and/or *Chandra* would certainly be beneficial. By determining the physical characteristics of the hot gas in the SNR from X-ray spectral analysis, the age of the SNR could be inferred (see Maggi et al. 2012, for example). Alternatively, optical echelle data could provide a measurement of the expansion velocity of the SNR shell, from which an age could be determined (see Williams et al. 2004, for example).

Given the propensity of high-mass stars to form in clusters, we can assess the likely supernova (SN) mechanism that produced MCSNR J0527−7104 based on the surrounding high-mass stellar population, or lack thereof. We used data from the Magellanic Cloud Photometric Survey (MCPS, Zaritsky et al. 2004) to produce a colour–magnitude diagram (CMD) for the survey entries within 100 pc (6.6′) of MCSNR J0527−7104 (Fig. 5 left panel). Candidate blue stars more massive than $\sim 8\,M_{\odot}$ were identified using the appropriate photometric selection criteria ($V < 16, B - V < 0$), yielding 5 candidate main sequence B-stars. Interestingly, four of the five candidates were located to the east of MCSNR J0527−7104 toward the N 206 H region. There was, however, no candidate in the immediate vicinity of the SNR. N 206 is known to harbour several high-mass stellar associations (Massey et al. 1995; Bica et al. 1999) with ages <10 Myr (Gorjian et al. 2004; Kavanagh et al. 2012), the closest of which is ∼150 pc from our SNR. In addition, the region is known to be actively forming stars (Romita et al. 2010), a picture that is echoed by the analysis

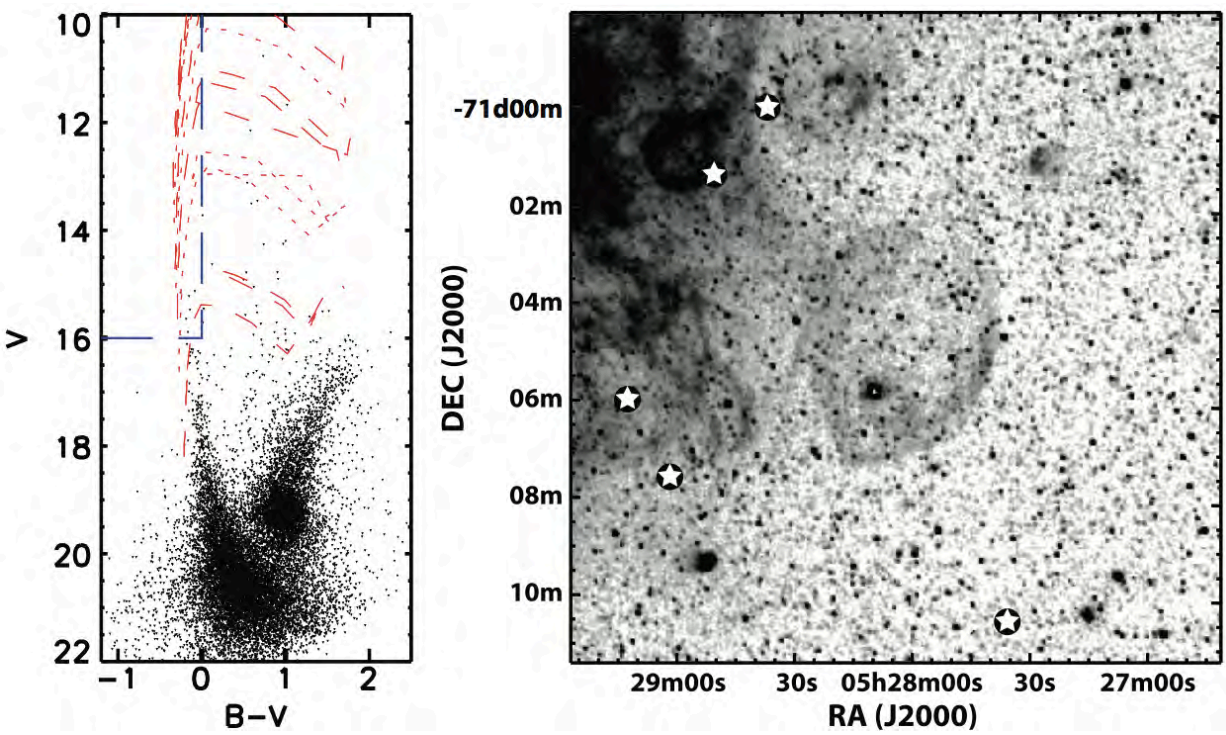

Fig. 5. Photometric identification and location of candidate blue high-mass stars within 100 pc of MCSNR J0527−7104. *Left panel*: $B - V$, V colour–magnitude diagram of stars within 100 pc of MCSNR J0527−7104, taken from the Magellanic Cloud Photometric Survey (Zaritsky et al. 2004). Also shown are stellar evolutionary tracks from Lejeune & Schaerer (2001) with, from bottom to top, the long dashed red lines showing the 5 $M_\odot$, 15 $M_\odot$, 25 $M_\odot$, and 60 $M_\odot$ tracks, and the short dashed red lines showing the 10 $M_\odot$, 20 $M_\odot$, and 40 $M_\odot$ tracks. The selection criteria for identification of blue high-mass stars is indicated by the dashed blue lines. *Right panel*: location of the candidate blue high-mass stars in relation to MCSNR J0527−7104 marked on the MCELS Hα image.

of Harris & Zaritsky (2009), who reconstructed the spatially resolved star formation history (SFH) of the LMC. The star formation rate of N206 has been relatively high for ∼50 Myr, with a notable surge in the last ∼12.5 Myr. MCSNR J0527−7104 was at the centre of four 12′ × 12′ cells in the SFH map of Harris & Zaritsky (2009). The average SFH from these cells is shown in Fig. 6. The peak at 12.5 Myr reflects the higher recent star formation activity seen only in the northeastern cell, in N 206. Another episode of star formation was seen ∼630 Myr ago, about the timescale for a "delayed" SN Ia to go off. However, as stressed by Badenes et al. (2009), care should be taken in regions with inhomogeneous stellar populations on short scale. If, due to dynamical ejection or SN kick processes, a runaway star with a modest ejection/kick velocity of ∼30 km s^{-1} (Perets & Šubr 2012, and references therein) was ejected from the N 206 stellar associations, it could travel ∼150 pc in <5 Myr. In an SN kick scenario, this travel time in addition to the time until a binary companion >20 $M_\odot$ undergoes an SN event is well within the lifetime of the lowest mass core-collapse SN progenitors. Thus, even though the old local stellar population favours a type Ia event, the possibility of a core-collapse SN by a runaway massive star remains plausible. Only high quality X-ray spectra with sufficient counts to determine plasma abundances will resolve this issue provided X-ray emission from SN ejecta can be detected and separated from swept-up ISM emission.

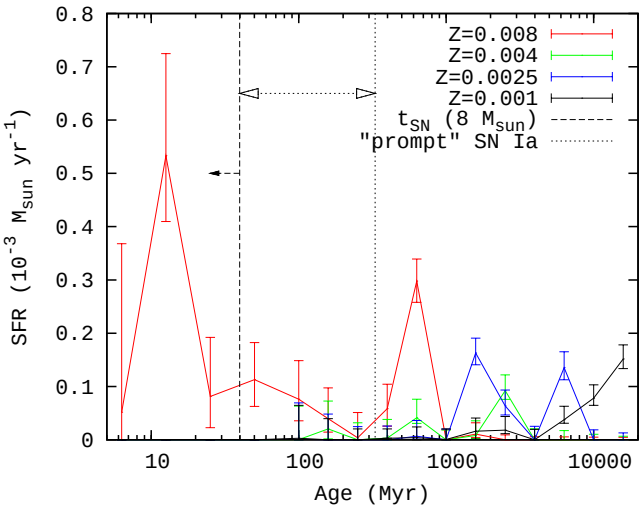

Fig. 6. Average SFH of the 12′ × 12′ cells, centred on MCSNR J0527−7104, from the data of Harris & Zaritsky (2009). The SFH is broken into four metallicity bins as indicated in the plot key. Also shown are the time ranges from which we expect either core collapse (indicated by the dashed arrow) or "prompt" type Ia (indicated by the dotted double sided arrow) progenitors to be formed. The peak at 12.5 Myr reflects the higher recent star formation activity seen only in the northeastern cell which contains N 206. Another episode of star formation is seen ∼630 Myr ago.

4. Conclusions

We have detected significant Hα, [S], and [O] optical line emission, characteristic of an optical SNR, in the region of the X-ray identified candidate SNR [HP99] 1234. In addition, very faint radio emission at 36 cm is detected coincident to the optical line emission which is consistent with a "bilateral" SNR morphology. At all other radio frequencies this SNR was well below the detection limit making it one of the weakest SNRs ever detected in the radio. The enhanced [S] and faint radio emission were found to be shell-like with an ellipsoidal morphology. In contrast, the X-ray emission was concentrated towards

the west of the SNR. However, due to its location at a large off-axis angle in a shallow ROSAT observation, the extent of the X-ray emission should be treated cautiously. The dimensions of the SNR, determined from the higher quality optical data, were found to be $\sim 5.1' \times 4.0'$ ($\sim$75 pc $\times$ 59 pc). However, the size estimate along the major axis was somewhat uncertain due to an absence of optical and radio emission at its extremities and the sensitivity and resolution of the X-ray data being too poor to perform a reliable measurement. We assumed the SNR to be in the Sedov phase of its evolution and determined an age estimate of $\sim$25 kyr for a canonical initial explosion energy of 10^{51} erg and an ambient mass density of 1.2×10^{-25} g cm^{-3}, measured for another SNR in the N 206 region. Additionally, we determined that for the adopted parameters, MCSNR J0527−7104 will enter the radiative phase of its evolution after $\sim$122 kyr, validating our initial assumption that the SNR is in the Sedov phase. However, we stress the sensitivity of the age and radiative time estimates to the assumed explosion energy and ambient mass density. We assessed the SN explosion mechanism responsible for our SNR based on the nearby stellar population, showing that both core-collapse and Type Ia scenarios are possible.

With the detection of radio emission, X-ray emission and significant Hα, [S], and [O] line emission with a [S]/Hα flux ratio >0.4, this SNR satisfied all the criteria for SNR classification and we assign it the identifier of MCSNR J0527−7104. However, issues such as the uncertain age and size of the SNR, the true explosion mechanism for the SNR and the explanation for the very faint radio emission persist. High quality X-ray images and spectra obtained with *XMM-Newton* and/or *Chandra* would provide answers to these outstanding questions.

Acknowledgements. We wish to thank the anonymous referee for their constructive suggestions to improve the paper. P.K. and P.M. are funded through the BMWI/DLR grants FKZ 50 OR 1009 and 50 OR 1201, respectively. M.S. acknowledges support by the Deutsche Forschungsgemeinschaft through the Emmy Noether Research Grant SA 2131/1. The MCELS data are kindly provided by R. C. Smith, P. F. Winkler, and S. D. Points. The MCELS project has been supported in part by NSF grants AST-9540747 and AST-0307613, and through the generous support of the Dean B. McLaughlin Fund at the University of Michigan. The National Optical Astronomy Observatory is operated by the Association of Universities for Research in Astronomy Inc. (AURA), under a cooperative agreement with the National Science Foundation. This research has made use of the SIMBAD database operated at CDS, Strasbourg, France.

References

Badenes, C., Harris, J., Zaritsky, D., & Prieto, J. L. 2009, ApJ, 700, 727
Badenes, C., Maoz, D., & Draine, B. T. 2010, MNRAS, 407, 1301
Bica, E. L. D., Schmitt, H. R., Dutra, C. M., & Oliveira, H. L. 1999, AJ, 117, 238
Bozzetto, L. M., Filipovic, M. D., Crawford, E. J., et al. 2012, Rev. Mex. Astron. Astrofis., 48, 41
Cajko, K. O., Crawford, E. J., & Filipovic, M. D. 2009, Serbian Astron. J., 179, 55
Chu, Y.-H., Chang, H.-W., Su, Y.-L., & Mac Low, M.-M. 1995, ApJ, 450, 157
Davies, R. D., Elliott, K. H., & Meaburn, J. 1976, MmRAS, 81, 89
di Benedetto, G. P. 2008, MNRAS, 390, 1762
Dunne, B. C., Points, S. D., & Chu, Y.-H. 2001, ApJS, 136, 119
Fesen, R. A., Blair, W. P., & Kirshner, R. P. 1985, ApJ, 292, 29
Filipovic, M. D., Pietsch, W., Haynes, R. F., et al. 1998, A&AS, 127, 119
Gaensler, B. M. 1998, ApJ, 493, 781
Gardner, F. F., & Milne, D. K. 1965, AJ, 70, 754
Gorjian, V., Werner, M. W., Mould, J. R., et al. 2004, ApJS, 154, 275
Grondin, M.-H., Sasaki, M., Haberl, F., et al. 2012, A&A, 539, A15
Haberl, F., & Pietsch, W. 1999, A&AS, 139, 277
Harris, J., & Zaritsky, D. 2009, AJ, 138, 1243
Haynes, R. F., Klein, U., Wayte, S. R., et al. 1991, A&A, 252, 475
Henize, K. G. 1956, ApJS, 2, 315
Kavanagh, P. J., Sasaki, M., & Points, S. D. 2012, A&A, 547, A19
Kennicutt, Jr., R. C., & Hodge, P. W. 1986, ApJ, 306, 130
Kesteven, M. J., & Caswell, J. L. 1987, A&A, 183, 118
Klimek, M. D., Points, S. D., Smith, R. C., Shelton, R. L., & Williams, R. 2010, ApJ, 725, 2281
Lejeune, T., & Schaerer, D. 2001, A&A, 366, 538
Maggi, P., Haberl, F., Bozzetto, L. M., et al. 2012, A&A, 546, A109
Massey, P., Lang, C. C., Degioia-Eastwood, K., & Garmany, C. D. 1995, ApJ, 438, 188
Mathewson, D. S., & Clarke, J. N. 1973, ApJ, 179, 89
Mathewson, D. S., Ford, V. L., Tuohy, I. R., et al. 1985, ApJS, 58, 197
Mills, B. Y., Turtle, A. J., Little, A. G., & Durdin, J. M. 1984, Aust. J. Phys., 37, 321
Nikolaev, S., Drake, A. J., Keller, S. C., et al. 2004, ApJ, 601, 260
Payne, J. L., White, G. L., & Filipović, M. D. 2008, MNRAS, 383, 1175
Perets, H. B., & Šubr, L. 2012, ApJ, 751, 133
Romita, K. A., Carlson, L. R., Meixner, M., et al. 2010, ApJ, 721, 357
Smith, R. C., Points, S. D., & Winkler, F. 2006, NOAO Newsletter, 85, 6
van der Marel, R. P., & Cioni, M.-R. L. 2001, AJ, 122, 1807
Vink, J. 2012, A&ARv, 20, 49
Weaver, R., McCray, R., Castor, J., Shapiro, P., & Moore, R. 1977, ApJ, 218, 377
Williams, R. M., Chu, Y.-H., Dickel, J. R., et al. 2004, ApJ, 613, 948
Williams, R. M., Chu, Y.-H., Dickel, J. R., et al. 2005, ApJ, 628, 704
Woltjer, L. 1972, ARA&A, 10, 129
Zaritsky, D., Harris, J., Thompson, I. B., & Grebel, E. K. 2004, AJ, 128, 1606

A.26 Related Paper 26

De Horta, A. Y., Collier, J. D., Filipović, M. D., Crawford, E. J., Urošević, D., Stootman, F. H., and Tothill, N. F. H. (2013). Radio confirmation of Galactic supernova remnant G308.3-1.4. *MNRAS*, 428:1980–1985

My contribution was to assist in the data analysis. This is a 10% contribution.

Monthly Notices
of the
ROYAL ASTRONOMICAL SOCIETY

MNRAS **428,** 1980–1985 (2013) doi:10.1093/mnras/sts168

Radio confirmation of Galactic supernova remnant G308.3−1.4

A. Y. De Horta,[1⋆] J. D. Collier,[1] M. D. Filipović,[1] E. J. Crawford,[1] D. Urošević,[2,3] F. H. Stootman[1] and N. F. H. Tothill[1]

[1]*University of Western Sydney, Locked Bag 1797, Penrith South, DC, NSW 1797, Australia*
[2]*Department of Astronomy, Faculty of Mathematics, University of Belgrade, Studentski trg 16, 11000 Belgrade, Serbia*
[3]*Isaac Newton Institute of Chile, Yugoslavia Branch, Volgina 7, 11060 Belgrade Serbia*

Accepted 2012 October 6. Received 2012 October 1; in original form 2011 December 14

ABSTRACT

We present radio-continuum observations of the Galactic supernova remnant (SNR) candidate, G308.3−1.4, made with the Australia Telescope Compact Array, Molonglo Observatory Synthesis Telescope and the Parkes radio telescope. Our results combined with *Chandra* X-ray images confirm that G308.3−1.4 is a bona fide SNR with a shell morphology. The SNR has average diameter of $D = 34 \pm 19$ pc, radio spectral index of $\alpha = -0.68 \pm 0.16$ and linear polarization of 10 ± 1 per cent. We estimate the SNR to have a magnetic field of $B \approx 29\,\mu$G. Employing a Σ–D relation, we estimate a distance to G308.3−1.4 of $d = 19 \pm 11$ kpc. The radio morphology, although complex, suggests a smaller size for the SNR than previously implied in an X-ray study. These results imply that G308.3−1.4 is a young to middle-aged SNR in the early adiabatic phase of evolution.

Key words: supernovae: general – ISM: individual objects: G308.3−1.4 – ISM: supernova remnants – radio continuum: general.

1 INTRODUCTION

The chemical and physical state of the interstellar medium (ISM) is significantly influenced by supernovae (SNe) and their resulting supernova remnants (SNRs). SNe and SNRs are important drivers of Galactic evolution (Tammann, Loeffler & Schroeder 1994; Nomoto et al. 2006) as they can induce star formation by accelerating cosmic rays, heating and compressing nearby clouds and injecting heavy elements into the ISM. According to the continuously updated, online catalogue created by Green (2009), some 274 SNRs are identified in our Galaxy. Understanding the SNR population and its effects on the structure of our Galaxy requires as complete a sample of confirmed SNRs as possible.

G308.3−1.4 was initially classified as an SNR candidate amongst ∼350 others by Busser (1998), when conducting a search for extended and unidentified X-ray sources in the *ROSAT* All-Sky Survey (RASS) data base. Schaudel et al. (2002) narrowed these to 14 likely SNR candidates, of which G308.3−1.4 was one. They noted that G308.3−1.4 exhibited a complex radio morphology but that it coincided with the RASS Position Sensitive Proportional Counter hard X-ray data, suggesting more strongly the SNR status of G308.3−1.4.

G308.3−1.4 appears in the source catalogue (Wright et al. 1994) of the Parkes–MIT–NRAO (PMN) survey at RA (J2000) = $13^{\rm h}41^{\rm m}03\overset{\rm s}{.}7$, Dec. (J2000) = $-63^\circ40'58\overset{''}{.}0$ with a flux density of 89 ± 8 mJy. It also appears[1] in the Molonglo Observatory Synthesis Telescope (MOST) SNR catalogue (MSC; Whiteoak & Green 1996) with a flux density of $S_\nu = 800$ mJy, dimensions 14×4 arcmin and surface brightness 1.3×10^{-21} W m^{-2} Hz^{-1} sr^{-1}. The MSC comments on the possible SNR having several arcs, suggesting a double-ring morphology.

Here, we present a new analysis of unpublished archival radio-continuum observations of the SNR candidate G308.3−1.4 made with the Parkes radio telescope, the Australia Telescope Compact Array (ATCA) and the MOST at wavelengths $\lambda = 6$, 13, 20 and 36 cm. Our work confirms the status of G308.3−1.4 as a bona fide SNR and suggests a different interpretation of its morphology from that of Hui et al. (2012) that also identifies G308.3−1.4 as an SNR from an analysis of the X-ray emission. We make the first estimate of its distance and its integrated flux density. In addition we measured its polarization and spectral index.

2 OBSERVATIONS AND DATA REDUCTION

2.1 Australia Telescope Compact Array

From the Australia Telescope Online Archive[2] (ATOA) we extracted ATCA observational data of G308.3−1.4 (Project C992; PI: W. Becker). These radio data are rereduced and published here for

⋆ E-mail: a.dehorta@uws.edu.au

[1] Incorrectly listed as G308.4−1.4.
[2] http://atoa.atnf.csiro.au

the first time. G308.3−1.4 was observed at 13 and 20 cm in 128-MHz continuum mode: 32 full-polarization 4-MHz channels are spread over 128-MHz intervals centred on 2496 and 1384 MHz. The first observation took 4.26 h on 2001 September 1–2 in the 6B configuration (baselines from 214 to 5969 m), but these data were adversely affected by storms and covered only a narrow range of parallactic angle. The second observation took place on 2002 January 11. The source was observed for 9.18 h over a total of 11.36 h in the 750A configuration (baselines from 77 to 3750 m). In both cases, PKS 1934−638 was observed for flux density and bandpass calibration and PKS 1329−665 for phase calibration.

The MIRIAD (Sault, Teuben & Wright 1995) and KARMA (Gooch 2006) software packages were used for data reduction and analysis. The 6B data were not used. Combining them with the 750A data yielded no improvement of the final image, due to their poor parallactic angle coverage and contamination by severe interference. The images were constructed using a natural weighting scheme, and the sixth antenna was removed to obtain the best signal-to-noise ratio, since the array was in a compact arrangement. The final 20-cm image (Fig. 1) has an estimated rms noise level of 0.70 mJy beam^{-1}, and the final 13-cm image (Fig. 2) has an estimated rms noise of 0.22 mJy beam^{-1}. These images suffer from missing short spacings and incomplete hour angle coverage, resulting in the highly negative regions seen enclosing the SNR emission. However, they are the highest resolution images of this object currently available in the radio continuum.

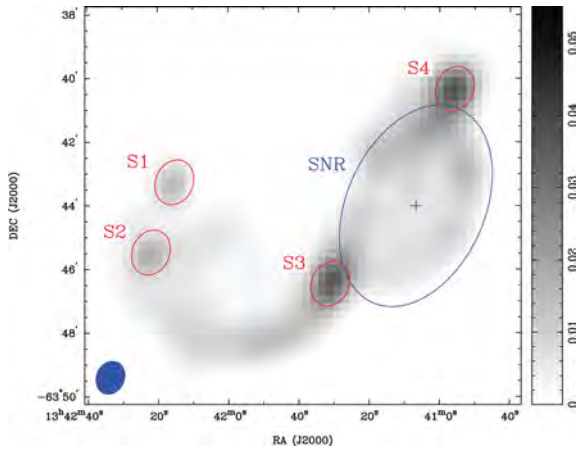

Figure 1. 20-cm ATCA image of Galactic SNR G308.3−1.4. The ellipse in the lower-left corner represents the synthesized beam of 65.25 × 53.91 arcsec^2 at PA = −24.°1. Grey-scale units are Jy beam^{-1}.

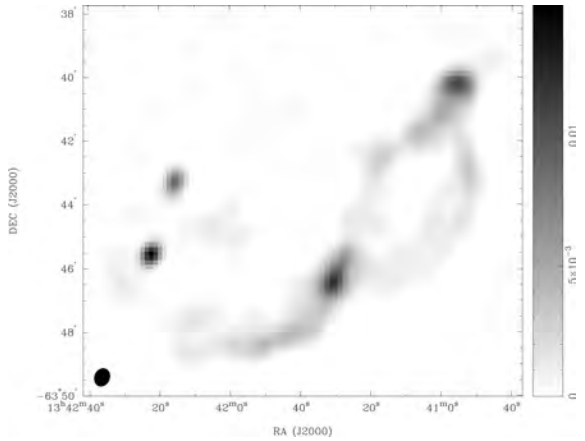

Figure 2. 13-cm ATCA image of Galactic SNR G308.3−1.4. The ellipse in the lower-left corner represents the synthesized beam of 35.32 × 28.98 arcsec^2 at PA=−23.°5. Grey-scale units are Jy beam^{-1}.

2.2 Ancillary data

The MOST image we used was obtained from the Sydney University Molonglo Sky Survey (SUMSS) Postage Stamp Server (release 0.2).[3] SUMSS is a deep radio survey of the sky south of $\delta = -30°$, covering ∼3400 deg^2. The catalogue (Mauch et al. 2003) contains ∼100 000 sources down to a flux density limit of 10 mJy beam^{-1} (∼5σ). Each observation is a 12-h synthesis, with a synthesized beam shape of 45 × 45 csc δ arcsec^2 at position angle (PA) 0°.

The Parkes image of G308.3−1.4 used in this project was obtained from the PMN 4850-MHz survey, downloaded from the ATNF data base.[4] This survey, which was conducted in 1990 June and November, detected 36 640 sources (see Griffith & Wright 1993, for the data reduction details). The final images have a 5-arcmin beam.

The *Chandra* satellite (Weisskopf, O'dell & van Speybroeck 1996) observed G308.3−1.4 on 2010 June 26 for 17 ks (observation ID 11249), and we extracted these data products from the *Chandra* Data Archive (CDA).[5]

3 RESULTS

3.1 Morphology

Fig. 1 shows the elliptical region that we contend corresponds to SNR G308.3−1.4. We define the SNR centre to be RA (J2000) = 13^{h}41^{m}06.^{s}72, Dec. (J2000) = −63°44′01.″2 (indicated by the cross symbol in Fig. 1), which corresponds to the mid-point of this elliptical region.

In considering the complex radio-continuum emission shown in Fig. 1 we need to determine how likely the point-like emission is associated with the extended emission. The emission will be either intrinsic to G308.3−1.4 or from unassociated foreground or background sources.

The bright regions on the north-west and south-east edges of this ellipse (S4 and S3 in Figs 1 and 3), in addition to the two sources seen east of the remnant (S1 and S2 in Figs 1, 3 and 4), do not have X-ray counterparts. We argue that these sources are not likely to be associated with the SNR in any way, and are most likely to be background sources [radio galaxy or active galactic nucleus (AGN)] or unresolved foreground sources. To confirm this we created a 20-cm image (Fig. 3) including all baselines, i.e. with the sixth antenna included, and with the Brigg's visibility weighting robustness parameter set to 0.5 in order to achieve the best balance between sidelobe suppression and signal-to-noise ratio. In this image, S1 and S2 appear clearly as point sources, elongated at the PA of the beam and with similar dimensions. Furthermore, S2 has an infrared counterpart given in the *InfraRed Astronomy Satellite* (*IRAS*) Point Source Catalogue as IRAS 13388−6330. The source labelled S3 is a point-like source with what appears to be radio jets coming out of either side of the centre to the north-west and south-east. To further test the point-like properties of these sources

[3] http://www.astrop.physics.usyd.edu.au/cgi-bin/postage.pl
[4] http://www.parkes.atnf.csiro.au/observing/databases/pmn/pmn.html
[5] http://cxc.harvard.edu/cda/

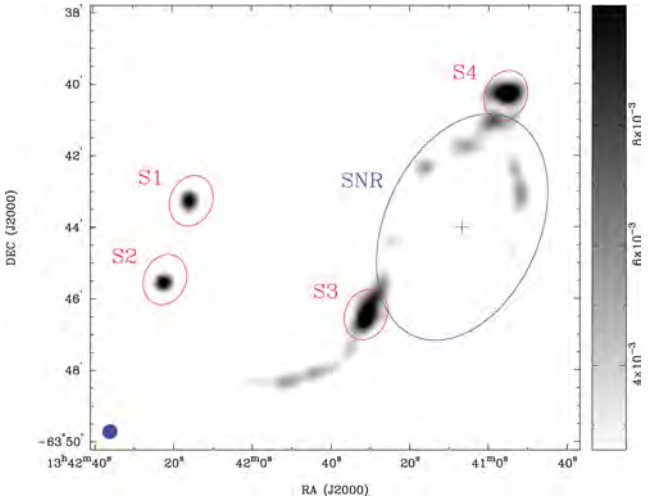

Figure 3. 20-cm ATCA image of Galactic SNR G308.3−1.4 with the sixth antenna included and clipped below 10σ. The ellipse in the lower-left corner represents the synthesized beam of 25.02×23.82 arcsec^2 at PA $= -65\overset{\circ}{.}08$. $\sigma = 25.9$ mJy beam^{-1}. Grey-scale units are Jy beam^{-1}.

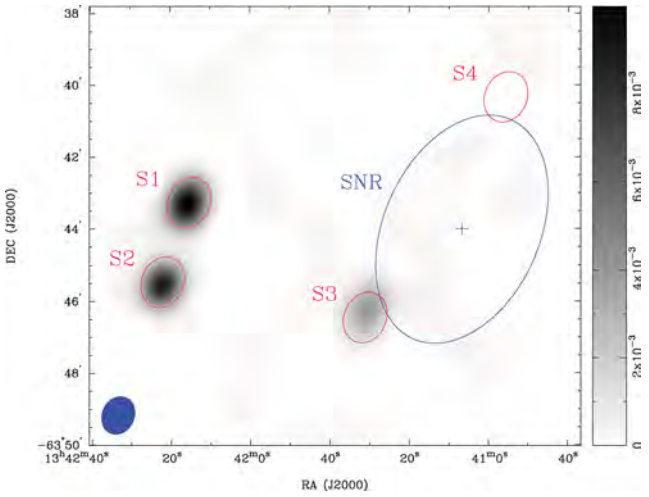

Figure 4. 20-cm ATCA image of Galactic SNR G308.3−1.4 using only the sixth antenna, smoothed to the beam size and shape of Fig. 1. The ellipse in the lower-left corner represents the synthesized beam of 65.25×53.91 arcsec^2 at PA $= -24\overset{\circ}{.}1$. $\sigma = 10.04$ mJy beam^{-1}. Grey-scale units are Jy beam^{-1}.

another 20-cm image (Fig. 4) was created using only the longest baselines, i.e. those from antenna 6 to the other elements. S1, S2 and S3 retain their point-like appearance, which further strengthens the case for them being background sources and not part of the SNR. We calculated three-point spectral indices, α,[6] at wavelengths $\lambda = 36$, 20 and 13 cm for sources S1–S4 to be, respectively, $\alpha = -0.85 \pm 0.50$, -0.06 ± 0.36, -1.47 ± 0.02 and -0.99 ± 0.17. The flat spectral index of S2 might indicate that it is a Galactic or foreground source, such as a compact H II region. However, we do not believe it to be associated with G308.3−1.4, as it is well outside the shock fronts. Although source S4 and the SNR are resolved out in Fig. 4 (using the 5969 m ATCA baseline), S4 is still likely to be a radio galaxy or possibly an AGN, because of its localized flux density (Fig. 3) and steep spectral index.

[6] Spectral index defined as $S \propto \nu^{\alpha}$.

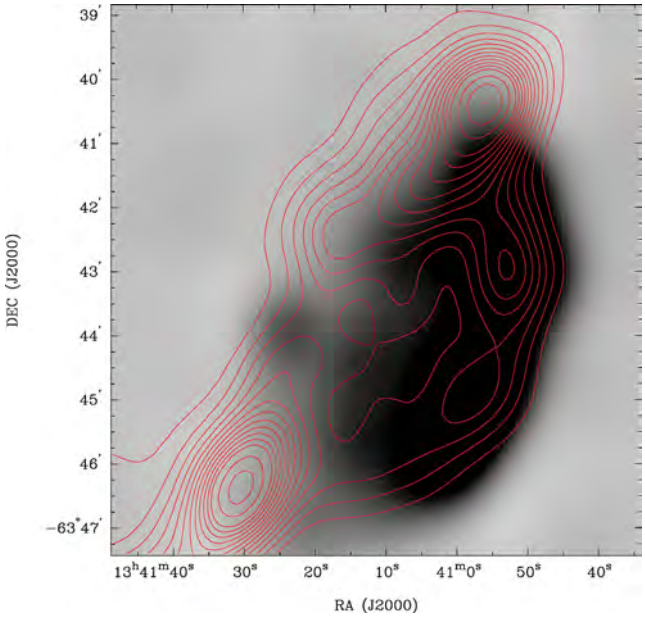

Figure 5. *Chandra* X-ray image (maximum positional error $\delta\alpha = 3.08$ arcsec, $\delta\delta = 1.46$ arcsec) smoothed to match 20-cm beam overlaid with 20-cm contours. Contours at the following multiples of $3\sigma = 2.1$ mJy: 1, 2, 3,...,12, 14, 16, 18, 20).

The *Chandra* image (Fig. 5) shows a strong correlation with the western side of the proposed SNR region. Such a one-sided, asymmetric morphology suggests a Type II, Ib or Ic SN progenitor. If this were the case, then the eastern side of the 'shell' seen in the image might be a radio jet emitting out of the opposite side of S3. However, despite there appearing to be no shock front X-ray emission on the eastern side of the SNR shell, the centre of the remnant still contains emission, appearing relatively brighter than the background noise. Additionally, no evidence can be found for an associated pulsar wind nebula or neutron star that would be expected from a Type II, Ib or Ic SN progenitor. Prinz & Becker (in preparation) consider the possibility of the X-ray emission originating from a galaxy cluster, but conclude that its X-ray spectral properties strongly favour an SNR nature. Given all this, and taking into account the likelihood of the different SNR morphologies (Gaensler 1999), we determine that this object is a shell SNR, slightly elongated in the north–south direction.

3.1.1 Angular diameter

Profile plots of intensity against position, for the minor and major axes of the object (shown in Fig. 6) are shown in Fig. 7. From these, we determine the angular size of the SNR to be $4 \times 8 \pm 0.5$ arcmin and the shell thickness (width of the peaks above 3σ) to be 1.00 ± 0.25 arcmin. This gives a volume-filling factor $V_{\rm Shell}/V_{\rm SNR}$ of 0.41 ± 0.05.

3.2 Integrated flux density

Table 1 lists the estimated integrated flux density S_ν at the different frequencies. The integrated flux densities were estimated by including all the flux measurements corresponding to the remnant (i.e. within our SNR region as seen in Fig. 1), which was determined by a contour at the 3σ level. The Parkes image suffers from confusion and the flux density measured includes the background sources.

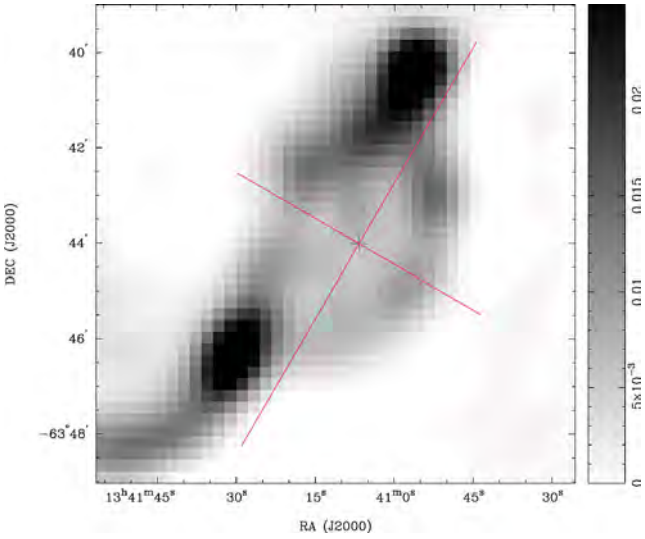

Figure 6. 20-cm image of G308.3−1.4 showing lines along which the line profiles in Fig. 7 are made.

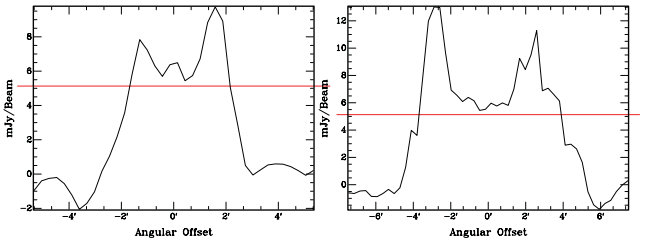

Figure 7. Line profiles of the minor axis (left) and major axis (right). Red line indicates the 3σ noise level.

Table 1 Integrated flux densities of G308.3−1.4.

Radio Telescope	ν (MHz)	λ (cm)	σ (mJy beam^{-1})	Beam size (arcsec)	S_ν (mJy)
MOST	843	36	1.5	45 × 50	257
ATCA	1384	20	0.7	65 × 54	215
ATCA	2496	13	0.5	41 × 34	124
Parkes	4850	6	15.0	295 × 295	84

Additionally, it should be noted that the flux density at 13 cm was calculated based on an image constructed with a *uv*-range up to 4 kλ. We estimate that the error in flux densities is no more than $\pm$10 per cent.

3.3 Spectral index

By fitting a power law to the measured integrated flux densities at wavelengths $\lambda = 36$, 20 and 13 cm we created a three-point spectral index plot (Fig. 8). The estimated spectral index is $\alpha = -0.68 \pm 0.16$, indicating that the radio emission from G308.3−1.4 is mostly non-thermal synchrotron radiation. This spectral index is consistent with a typical SNR spectrum, with $-0.8 < \alpha < -0.2$ (Filipović et al. 1998). Given this trend for the integrated flux density as a function of frequency, we estimate the flux density at 1 GHz to be $S_{1\mathrm{GHz}} \approx 242$ mJy.

In a similar fashion, we constructed the three-point spectral distribution map (36, 20 and 13 cm) shown in Fig. 9. The map shows the region corresponding to the SNR having a spectral index primarily

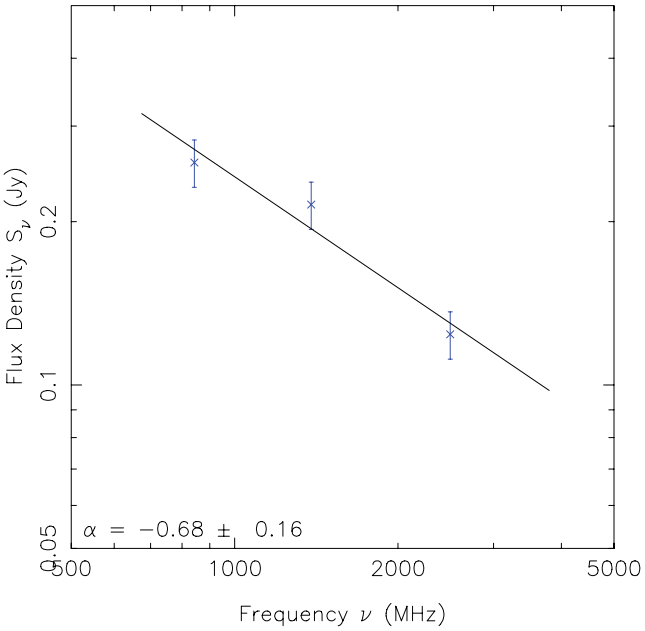

Figure 8. Radio-continuum spectrum of G308.3−1.4 between 36, 20 and 13 cm.

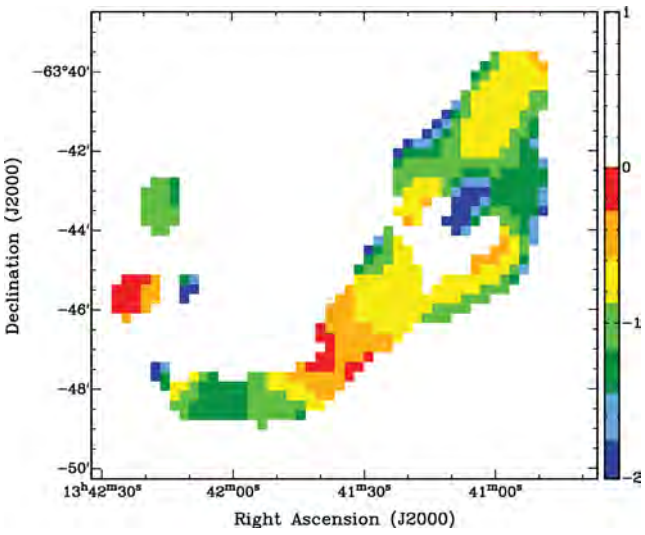

Figure 9. Three-point spectral distribution map: synthesized beam of 65.25 × 53.91 arcsec^2 at PA $=-24.^\circ1$.

in the range $-0.5 < \alpha < -1.5$. The spectral index is quite steep at the edge of the shell of the SNR but becomes shallower towards the centre of the remnant. This distribution would be expected from a young to middle-aged SNR which accelerates particles efficiently at the strong shock front, producing strong synchrotron radiation.

3.4 Distance estimate

Although controversial, the Σ–D relation (Shklovsky 1960; Case & Bhattacharya 1998; Arbutina et al. 2004; Urošević et al. 2005, 2010) is the only method that can be used to estimate a distance from our data. It states that the surface brightness Σ is related to the diameter D by $\Sigma_\nu = AD^{-\beta}$, where A is a constant dependent on the characteristics of the SN's initial explosion and the surrounding ISM, while β is almost entirely independent of these. The theory surrounding

the Σ–D relation has evolved greatly since it was originally proposed, now incorporating many SNR cases, including that of bremsstrahlung radiation (Urošević & Pannuti 2005). G308.3−1.4 exhibits features typical of an SNR in the adiabatic stage, such as bright X-ray emission, a negative spectral index and significant linear polarization. Since precise details about the local environment of G308.3−1.4 are unknown, we estimated a distance to the SNR using the new Galactic Σ–D relation (Pavlović et al. 2012) which is calibrated with 50 Galactic shell-like SNRs with independently determined distances using the orthogonal fitting procedure.

We estimate the surface brightness at 1 GHz to be $\Sigma_{1\,\mathrm{GHz}} = 1.1 \times 10^{-21}$ W m^{-2} Hz^{-1} sr^{-1} which gives an average diameter of $D = 34 \pm 19$ pc and thus an average distance of $d = 19 \pm 11$ kpc, which would indicate that G308.3−1.4 is on the far side of the Galaxy. This average distance comes from the average of the major and minor axes, while the uncertainties arise from the upper and lower limits for A. At this distance, G308.3−1.4 would lie ∼500 pc above the Galactic plane, with linear dimensions of $23 \times 45 \pm 3$ pc and shell thickness ∼5.5 pc.

Placing G308.3−1.4 on the Berezhko & Völk (2004) surface brightness–diameter diagram (at 1 GHz) suggests that G308.3−1.4 is in the early adiabatic phase of evolution, expanding into an extremely low density environment with an initial energy somewhat lower than the canonical SN energy of 10^{51} erg. The suggested low-density environment is consistent with our estimated position of the SNR, 0.5 kpc out of the Galactic plane.

3.5 Polarimetry

Since the ATCA observations recorded Stokes parameters Q, U and V, in addition to total intensity I, we were able to determine the polarization of the SNR at 20 cm. Fig. 10 shows the regions polarized above a level of 3σ. The electric field vectors are parallel with the shell of the SNR around most of the circumference of the SNR, particularly along its western side. This arrangement is expected as the SNR particles are experiencing the greatest acceleration and most efficiently producing synchrotron radiation. The maximum fractional polarization is estimated to be $P = 10 \pm 1$ per cent. The polarization vectors overlaying background source S4 are probably unreliable, due to possible confusion between the SNR and background source. No reliable polarization was detected at 13 cm. This might indicate significant depolarization in the remnant, but the polarimetric response of the ATCA is poor at 13 cm.

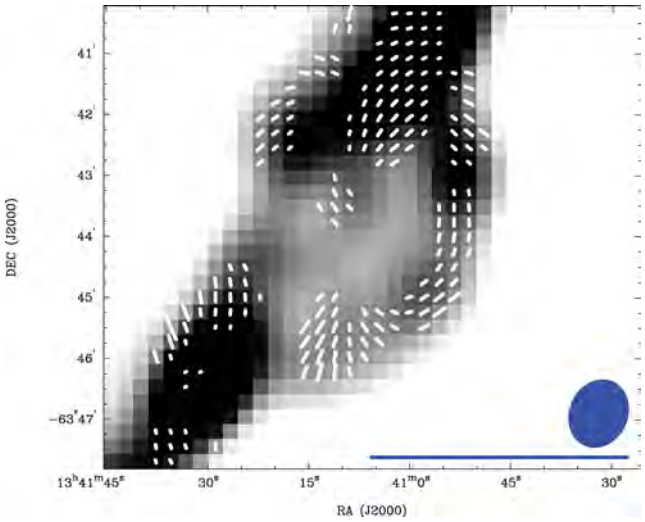

Figure 10. 20-cm ATCA observations of G308.3−1.4. The ellipse in the lower-right corner of the image represents the synthesized beam width of 65.25×53.91 arcsec^2 at PA $= -24.^\circ1$. The length of the vectors represent the fractional polarized intensity at each pixel position, and their orientations indicate the mean PA of the electric field (averaged over the observing bandwidth, not corrected for any Faraday rotation). The blue line below the beam ellipse represents the length of a fractional polarization vector of 100 per cent. The maximum fractional polarization is 10 ± 1 per cent.

We used the new equipartition formula derived by Arbutina et al. (2012) based on the diffusive shock acceleration (DSA) theory of Bell (1978) to estimate a magnetic field strength. This formula is particularly relevant to magnetic field estimation in SNRs and yields magnetic field strengths between those given by the classical equipartition (Pacholczyk 1970) and revised equipartition (Beck & Krause 2005) methods. We estimate the magnetic field strength, $B \approx 29\,\mu$G, and the minimum total energy of the synchrotron radiation, $E_{\min} \approx 2 \times 10^{49}$ erg (see Arbutina et al. 2012, and corresponding online 'calculator[7]').

The value of 29 μG indicates that this SNR's magnetic field is not only influenced by the compression of the ISM magnetic field (∼1 μG in a low-density environment), but is also (moderately) amplified by DSA effects (see Bell 2004). The relatively young estimated age of this SNR, somewhat steep spectral index (Bell, Schure & Reville 2011) and moderately amplified magnetic field constitute the standard description of an SNR in the early Sedov phase of evolution.

4 CONCLUSIONS

Analysis of our new radio-continuum images of the galactic radio source G308.3−1.4, produced from $\lambda = 20$ and 13 cm ATCA archival data, confirms that the object is indeed a bona fide SNR. The overall spectral index of G308.3−1.4 is $\alpha = -0.68 \pm 0.16$, with the emission 10 ± 1 per cent linearly polarized. These properties indicate that it is likely to be young to middle aged, with the majority of its radio emission being non-thermal, due to the strong shock wave driving the shell and accelerating particles creating synchrotron radiation. We suggest G308.3−1.4 is in the early adiabatic expansion stage, due to its significant X-ray brightness, steep non-thermal spectral index and linear polarization. We estimate the magnetic field strength, $B \approx 29\,\mu$G, which is consistent with the SNR being at this evolutionary stage.

Taking these new ATCA radio-continuum images in conjunction with the high-resolution *Chandra* X-ray image, we find that G308.3−1.4 is likely to be of an elongated shell-like morphology, with the X-ray emission appearing stronger on the western side of the shell. No evidence for an associated compact central object was found.

We have used the new Galactic Σ–D relation of Pavlović et al. (2012) to estimate the dimensions of the source and thus its distance: G308.3−1.4 was found to have an average diameter of 34 ± 19 pc and a distance of 19 ± 11 kpc.

Our radio images could be greatly improved by further ATCA observations with better parallactic angle coverage and higher resolution. Additional X-ray spectral observations with the *XMM–Newton* satellite would also yield new insights into the elemental abundances and energies of G308.3−1.4.

[7] http://poincare.matf.bg.ac.rs/~arbo/eqp/

ACKNOWLEDGMENTS

We used the KARMA software package developed by the Australia Telescope National Facility (ATNF). The Australia Telescope Compact Array and Parkes radio telescope are part of the ATNF which is funded by the Commonwealth of Australia for operation as a National Facility managed by CSIRO. This paper includes archived data obtained through the Australia Telescope Online Archive (http://atoa.atnf.csiro.au). This research is supported by the Ministry of Education and Science of the Republic of Serbia through project no. 176005.

REFERENCES

Arbutina B., Urošević D., Stanković M., Tešić Lj., 2004, MNRAS, 350, 346
Arbutina B., Urošević D., Andjelić M. M., Pavlović M. Z., Vukotić B., 2012, ApJ, 746, 79
Beck R., Krause M., 2005, Astron. Nachr., 326, 414
Bell A. R., 1978, MNRAS, 182, 443
Bell A. R., 2004, MNRAS, 353, 550
Bell A. R., Schure K. M., Reville B., 2011, MNRAS, 418, 1208
Berezhko E. G., Völk H. J., 2004, A&A, 427, 525
Busser J.-U., 1998, PhD thesis, Munich
Case G. L., Bhattacharya D., 1998, ApJ, 504, 761
Filipović M. D., Haynes R. F., White G. L., Jones P. A., 1998, A&AS, 130, 421
Gaensler B. M., 1999, PhD thesis, Univ. Sydney
Gooch R., 2006, Karma Users Manual. Australia Telescope National Facility
Green D. A., 2009, Bull. Astron. Soc. India, 37, 45
Griffith M. R., Wright A. E., 1993, AJ, 105, 1666
Hui C. Y., Seo K. A., Huang R. H. H., Trepl L., Woo Y. J., Lu T.-N., Kong A. K. H., Walter F. M., 2012, ApJ, 750, 7
Mauch T., Murphy T., Buttery H. J., Curran J., Hunstead R. W., Piestrzynski B., Robertson J. G., Sadler E. M., 2003, MNRAS, 342, 1117
Nomoto K., Tominaga N., Umeda H., Kobayashi C., Maeda K., 2006, Nuclear Phys. A, 777, 424
Pacholczyk A. G., 1970, inPacholczyk A. G., ed., Radio Astrophysics. Nonthermal Processes in Galactic and Extragalactic Sources. Freeman & Co., San Francisco
Pavlović M., Urošević D., Vukotić B., Arbutina B., Göker Ü., 2012, ApJS, in press (arXiv:1210.4602)
Sault R. J., Teuben P. J., Wright M. C. H., 1995, in Shaw R. A., Payne H. E., Hayes J. J. E., eds, ASP Conf. Ser. Vol. 77, Astronomical Data Analysis Software and Systems IV. Astron. Soc. Pac., San Francisco. p. 433
Schaudel D., Becker W., Voges W., Aschenbach B., Reich W., Weisskopf M., 2002, in Slane P. O., Gaensler B. M., eds, ASP Conf. Ser. Vol. 271, Neutron Stars in Supernova Remnants. Astron. Soc. Pac., San Francisco. p. 391
Shklovsky I., 1960, Astron. Zh., 37, 369
Tammann G. A., Loeffler W., Schroeder A., 1994, ApJS, 92, 487
Urošević D., Pannuti T. G., 2005, Astropart. Phys., 23, 577
Urošević D., Pannuti T. G., Duric N., Theodorou A., 2005, A&A, 435, 437
Urošević D., Vukotić B., Arbutina B., Sarevska M., 2010, ApJ, 719, 950
Weisskopf M. C., O'dell S. L., van Speybroeck L. P., 1996, in Hoover R. B., Walker A. B., eds, Society of Photo-Optical Instrumentation Engineers (SPIE) Conference Series, Vol. 2805, Multilayer and Grazing Incidence X-Ray/EUV Optics III. SPIE, p. 2.
Whiteoak J. B. Z., Green A. J., 1996, A&AS, 118, 329
Wright A. E., Griffith M. R., Burke B. F., Ekers R. D., 1994, ApJS, 91, 111

This paper has been typeset from a TEX/LATEX file prepared by the author.

A.27 Related Paper 27

Oliveira, J. M., van Loon, J. T., Sloan, G. C., Sewiło, M., Kraemer, K. E., Wood, P. R., Indebetouw, R., Filipović, M. D., Crawford, E. J., Wong, G. F., Hora, J. L., Meixner, M., Robitaille, T. P., Shiao, B., and Simon, J. D. (2013). Early-stage young stellar objects in the Small Magellanic Cloud. *MNRAS*, 428:3001–3033

My contribution was to assist in the data analysis. This is a 10% contribution.

Monthly Notices of the ROYAL ASTRONOMICAL SOCIETY

MNRAS **428,** 3001–3033 (2013) doi:10.1093/mnras/sts250

Early-stage young stellar objects in the Small Magellanic Cloud

J. M. Oliveira,[1⋆] J. Th. van Loon,[1] G. C. Sloan,[2] M. Sewiło,[3] K. E. Kraemer,[4] P. R. Wood,[5] R. Indebetouw,[6,7] M. D. Filipović,[8] E. J. Crawford,[8] G. F. Wong,[8] J. L. Hora,[9] M. Meixner,[10] T. P. Robitaille,[11] B. Shiao[10] and J. D. Simon[12]

[1]*School of Physical and Geographical Sciences, Lennard-Jones Laboratories, Keele University, Staffordshire ST5 5BG*
[2]*Department of Astronomy, Cornell University, Ithaca, NY 14853, USA*
[3]*Department of Physics and Astronomy, The Johns Hopkins University, 3400 N. Charles Street, Baltimore, MD 21218, USA*
[4]*Boston College, Institute for Scientific Research, 140 Commonwealth Avenue, Chestnut Hill, MA 02467, USA*
[5]*Research School of Astronomy and Astrophysics, Australian National University, Cotter Road, Weston Creek, ACT 2611, Australia*
[6]*Department of Astronomy, University of Virginia, PO Box 3818, Charlottesville, VA 22903, USA*
[7]*National Radio Astronomical Observatory, Charlottesville, VA 22904, USA*
[8]*University of Western Sydney, Locked Bag 1797, Penrith South DC, NSW 1797, Australia*
[9]*Harvard-Smithsonian Center for Astrophysics, 60 Garden Street, MS-65, Cambridge, MA 02138-1516, USA*
[10]*Space Telescope Science Institute, 3700 San Martin Drive, Baltimore, MD 21218, USA*
[11]*Max-Planck-Institut für Astronomie, Königstuhl 17, D-69117 Heidelberg, Germany*
[12]*Observatories of the Carnegie Institution of Washington, 813 Santa Barbara St., Pasadena, CA 91101, USA*

Accepted 2012 October 18. Received 2012 October 18; in original form 2012 September 18

ABSTRACT

We present new observations of 34 young stellar object (YSO) candidates in the Small Magellanic Cloud (SMC). The photometric selection required sources to be bright at 24 and 70 μm (to exclude evolved stars and galaxies). The anchor of the analysis is a set of *Spitzer* Infrared Spectrograph (IRS) spectra, supplemented by ground-based 3–5 μm spectra, *Spitzer* Infrared Array Camera and Multiband Imaging Photometer for *Spitzer* photometry, near-infrared (IR) imaging and photometry, optical spectroscopy and radio data. The sources' spectral energy distributions and spectral indices are consistent with embedded YSOs; prominent silicate absorption is observed in the spectra of at least 10 sources, silicate emission is observed towards four sources. Polycyclic aromatic hydrocarbon (PAH) emission is detected towards all but two sources. Based on band ratios (in particular the strength of the 11.3-μm and the weakness of the 8.6-μm bands) PAH emission towards SMC YSOs is dominated by predominantly small neutral grains. Ice absorption is observed towards 14 sources in the SMC. The comparison of H_2O and CO_2 ice column densities for SMC, Large Magellanic Cloud and Galactic samples suggests that there is a significant H_2O column density threshold for the detection of CO_2 ice. This supports the scenario proposed by Oliveira et al., where the reduced shielding in metal-poor environments depletes the H_2O column density in the outer regions of the YSO envelopes. No CO ice is detected towards the SMC sources. Emission due to pure rotational 0–0 transitions of molecular hydrogen is detected towards the majority of SMC sources, allowing us to estimate rotational temperatures and H_2 column densities. All but one source are spectroscopically confirmed as SMC YSOs. Based on the presence of ice absorption, silicate emission or absorption and PAH emission, the sources are classified and placed in an evolutionary sequence. Of the 33 YSOs identified in the SMC, 30 sources populate different stages of massive stellar evolution. The presence of ice- and/or silicate-absorption features indicates sources in the early embedded stages; as a source evolves, a compact H II region starts to emerge, and at the later stages the source's IR spectrum is completely dominated by PAH and fine-structure emission. The remaining three sources are classified as intermediate-mass

⋆E-mail: j.oliveira@keele.ac.uk

YSOs with a thick dusty disc and a tenuous envelope still present. We propose one of the SMC sources is a D-type symbiotic system, based on the presence of Raman, H and He emission lines in the optical spectrum, and silicate emission in the IRS spectrum. This would be the first dust-rich symbiotic system identified in the SMC.

Key words: astrochemistry – circumstellar matter – stars: formation – stars: protostars – galaxies: individual: SMC – Magellanic Clouds.

1 INTRODUCTION

Star formation is a complex interplay of various chemophysical processes. During the onset of gravitational collapse of a dense cloud, dense cores can only develop if heat can be dissipated. The most efficient cooling mechanisms are via radiation through fine-structure lines of carbon and oxygen, and rotational transitions in abundant molecules such as water (e.g. van Dishoeck 2004). These cooling agents all contain at least one metallic atom. Furthermore, dust grains are crucial in driving molecular cloud chemistry, as dust opacity shields cores from radiation, and grain surfaces enable chemical reactions to occur that would not happen in the gas phase. These facts suggest that metallicity is an important parameter to explore in understanding star formation. However, most of what is known about the physics of star formation is deduced from observations in solar metallicity Galactic star-forming regions (SFRs). The nearest templates for the detailed study of star formation under metal-poor conditions are the Magellanic Clouds (MCs), with interstellar medium (ISM) metallicities of $Z_{\rm SMC} \sim 0.2\,{\rm Z}_{\odot}$ and $Z_{\rm LMC} \sim 0.4\,{\rm Z}_{\odot}$, respectively, for the Small Magellanic Cloud (SMC) and Large Magellanic Cloud (LMC; e.g. Russell & Dopita 1992). Even over the metallicity range covered by the Galaxy and the MCs, cooling and chemistry rates, and star formation time-scales could be affected (Banerji et al. 2009). The low metallicity of the SMC in particular is typical of galaxies during the early phases of their assembly, and studies of star formation in the SMC provide a stepping stone to understanding star formation at high redshift where these processes cannot be directly observed.

The *Spitzer Space Telescope* (*Spitzer*; Werner et al. 2004) finally allowed the identification of sizable samples of young stellar objects (YSOs) in the MCs. The *Spitzer* Legacy Programs (SAGE, Meixner et al. 2006; SAGE-SMC, Gordon et al. 2011a) have identified thousands of previously unknown YSOs, both in the LMC and the SMC (Whitney et al. 2008; Gruendl & Chu 2009; Sewiło et al., in preparation). Follow-up spectroscopic programmes have provided unique insight into the abundances of ices in Magellanic YSOs, revealing differences in the composition of circumstellar material at lower metallicity (Oliveira et al. 2009, 2011; Shimonishi et al. 2010; Seale et al. 2011).

In this paper we present a sample of 34 photometrically selected YSO candidates in the SMC, observed with *Spitzer* Infrared Spectrograph (IRS; Houck et al. 2004). Based on the properties of their IRS spectra and a variety of multiwavelength diagnostics, we classify 33 sources as YSOs in the SMC (27 previously unknown) and one source as a symbiotic system. This paper is organized as follows. After describing the sample selection and the different observations, the spectral properties of the SMC sources are analysed in detail in Section 4, with the aim of assessing the sources' evolutionary stage. We describe the spectral energy distribution (SED) properties and modelling, dust and ice absorption, polycyclic aromatic hydrocarbon (PAH), ionic fine structure and H_2 emission and the properties of optical counterparts to the infrared (IR) sources. The source classification and their evolutionary status are then discussed in Section 5. Section 6 describes the process that allowed us to identify one of the sources as the first D-type symbiotic system in the SMC.

2 DEFINING THE YSO SAMPLE

The *Spitzer* Survey of the Small Magellanic Cloud (S3MC; Bolatto et al. 2007) imaged the main body of the SMC (central 3 deg^2) in all seven *Spitzer* photometric bands, using the Infrared Array Camera (IRAC; Fazio et al. 2004) and the Multiband Imaging Photometer for *Spitzer* (MIPS; Rieke et al. 2004). The resulting photometric catalogue was used to select the present YSO sample as described below.

The near- and mid-IR colours of evolved stars can be as red as embedded YSOs (especially carbon stars, which are common in the SMC). This makes the 70 μm photometry critical in identifying YSOs with cold dust (as opposed to the warm dust surrounding evolved stars). Thus, we selected targets with detections in all IRAC bands and at 24 and 70 μm. We also imposed a 10 mJy lower limit to the 8 and 24 μm fluxes so that the sources are suitable for *Spitzer* spectroscopy. From the 160 objects with 70 μm detections, we were left with 46 candidates. By cross-correlating their positions with the SIMBAD data base and the *Spitzer* Reserved Object Catalog, we rejected 15 objects which might be (or are near to) evolved stars or planetary nebulae. The 31 remaining targets have colours [3.6]–[5.8] > 1.35 and [8]–[24] > 2.75 mag, typical for embedded YSOs (Rho et al. 2006). Background galaxies can also have colours similar to those of YSOs (Eisenhardt, Stern & Brodwin 2004). However, the selected YSO candidates are bright, sit well above the bulk of background galaxy contamination (Jørgensen et al. 2006; Lee et al. 2006), and most are located in active regions of star formation (Fig. 1). Thus they are likely genuine YSOs and not more uniformly distributed evolved stars or background galaxies. YSO candidates separate better from the bulk SMC population in colour–magnitude diagrams, rather than colour–colour diagrams (Whitney et al. 2008; Sewiło et al., in preparation), as demonstrated in Fig. 2. Our selection criteria imply the final sample is composed of massive YSOs ($M \gtrsim 10\,{\rm M}_{\odot}$). The sample is obviously not complete but it is ideally designed to identify massive YSOs that can be the subjects of a *detailed* spectroscopic analysis.

Our strategy has proved very successful, with all but one of the 31 candidates confirmed as an embedded YSO or compact H II region (Section 4). We add to the SMC sample the three YSOs identified by van Loon et al. (2008), MSX SMC 79, IRAS 01039−7305 and IRAS 01042−7215, based on the appearance of their 3–4 μm spectra(Section 3.3). The locations of these 34 YSO candidates superposed on a 70-μm MIPS image of the SMC are shown in Fig. 1. Fig. 2 shows [3.6]–[8.0] versus [8.0]–[24] colour–colour and [8.0] versus [8.0]–[24] colour–magnitude diagrams for the 34 YSO candidates, together with the field SMC population (Gordon et al. 2011a).

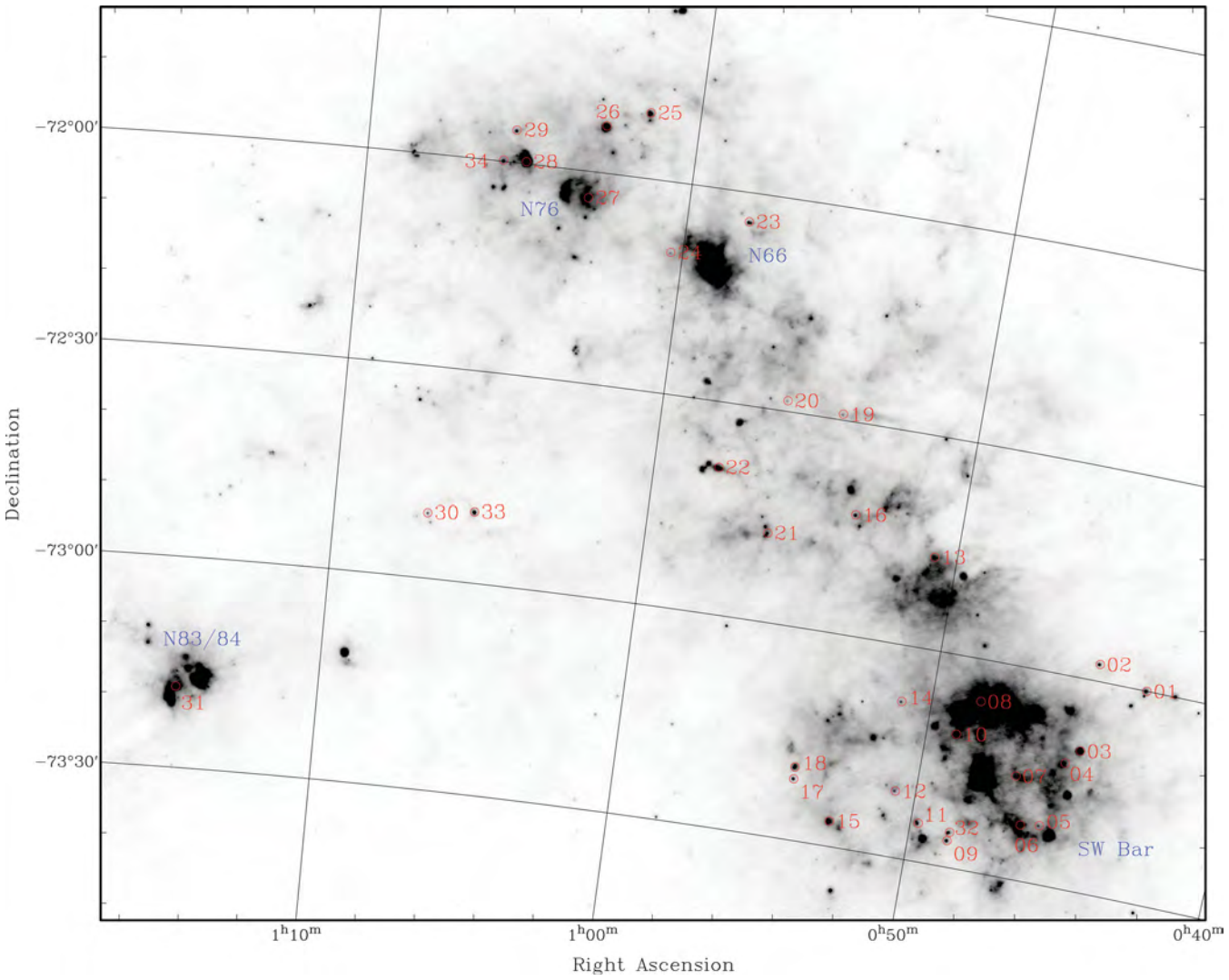

Figure 1. SAGE-SMC MIPS 70-μm image showing the location of the 34 YSO candidates (red circles and labels); sources #01 to 31 were first identified in this survey (see also van Loon et al. 2010; Oliveira et al. 2011), while sources #32 (MSX SMC 79), #33 (IRAS 01039−7305) and #34 (IRAS 01042−7215) were identified by van Loon et al. (2008). The SFRs discussed in Section 4.3 are labelled in blue.

3 OBSERVATIONS AND CATALOGUES

3.1 *Spitzer*-IRS and MIPS-SED spectroscopy

The mid-IR, low-resolution spectra of the 31 candidate YSOs were obtained using the *Spitzer*-IRS and the spectral energy distribution (SED) mode of MIPS (Rieke et al. 2004) on board *Spitzer*, taken as part of the SMC-Spec programme (PID: 50240, P.I.: G. C. Sloan). This Guaranteed Time Observations (GTO) programme aimed at providing a comprehensive spectroscopic survey of the SMC. Scientifically its goals were to study dust in nearly every stage of its life cycle in the SMC in order to assess how the interactions of dust and its host galaxy differ from more metal-rich systems like the Galaxy and the LMC. The programme was designed to provide the SMC counterpart of the LMC SAGE-Spec programme (Kemper et al. 2010), albeit at a smaller scale. The SMC observations targeted important classes generally under-represented in the *Spitzer* archive of SMC sources, such as YSOs and compact H II regions, objects in transition to and from the asymptotic giant branch, and supergiants. The aforementioned three additional objects from van Loon et al. (2008) were initially thought to be evolved stars; their *Spitzer*-IRS spectra were obtained as part of a cycle 1 GTO programme (PID: 3277, P.I.: M. Egan).

The IRS observations of the point sources in SMC-Spec were performed in staring mode, using the Short-Low and Long-Low modules (SL and LL, respectively). The 8- and 24-μm fluxes were used to set exposure times, aiming at signal-to-noise ratios of ∼60 in SL and ∼30 in LL. The archival spectra mentioned previously were also obtained in the SL and LL staring modes. All spectra were reduced following standard reduction techniques. Flat-fielded images from the standard *Spitzer* reduction pipeline (version S18.18) were background subtracted and cleaned of 'rogue' pixels and artefacts. Spectra were extracted individually for each data collection event (DCE) and co-added to produce one spectrum per nod position. Individual spectra are extracted both using optimal and tapered extraction; optimal extraction uses supersampled point spread function (PSF) profiles to weight the pixels from the spatial profiles, while tapered column extraction integrates the flux in a spectral window that expands with wavelength (Lebouteiller et al. 2010). For each extraction, the nods were then combined to produce a single

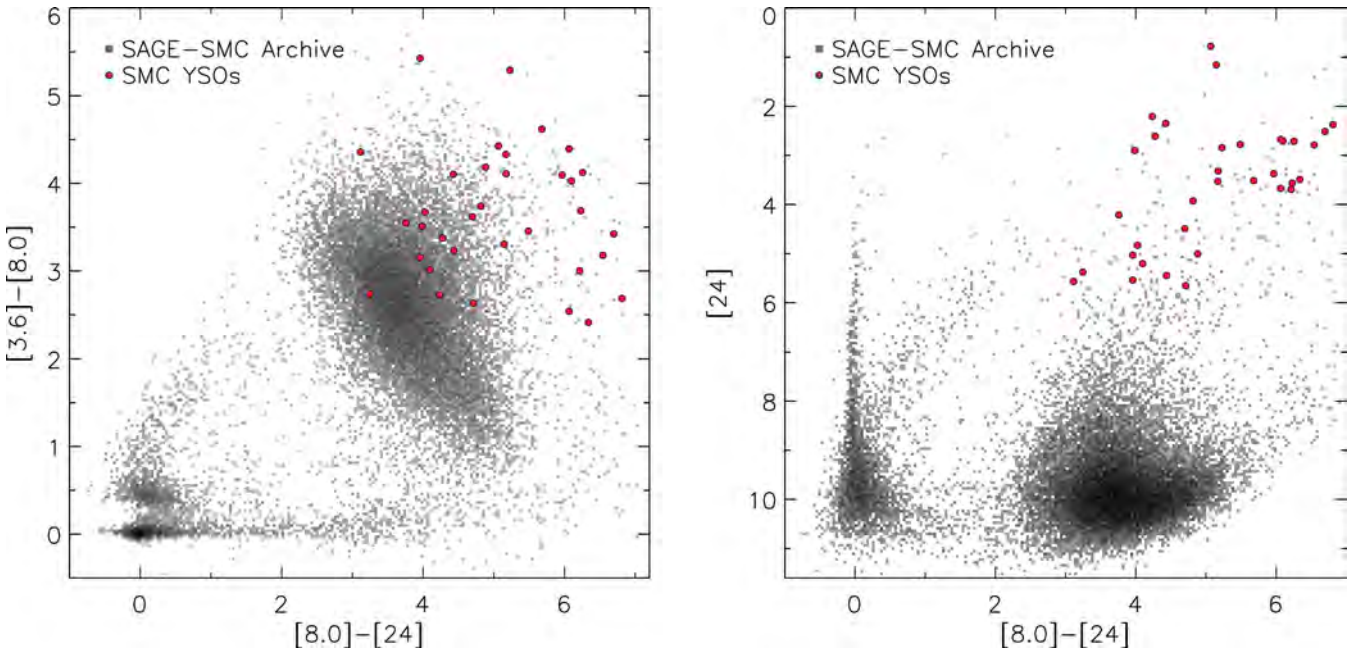

Figure 2. Colour–colour and colour–magnitude diagrams for the YSO candidates (filled red circles), as well as the field SMC population (grey-scale).

spectrum per order, rejecting 'spikes' that appear in only one of the nod positions. Finally, the spectra of all the segments were combined including the two bonus orders that are useful in correcting for discontinuities between the orders.

While for point sources optimal extraction produces the best signal-to-noise ratio, tapered extraction performs better if the source is extended (Lebouteiller et al. 2010). Some of the sources in our sample could be marginally extended; we opt to use optimal extracted spectra but check the veracity and strength of the spectral features against the tapered extraction spectra. The strength of relevant emission features (Sections 4.3 and 4.4) is measured by first fitting a series of line segments to the continua on either side of feature and then integrating in F_λ space.

For 10 objects in the sample (see Table A1) we also have MIPS-SED spectra, covering the wavelength range 52–90 μm, as described in van Loon et al. (2010). The IRS and MIPS-SED *Spitzer* spectra are shown in Fig. 3 (selected examples) and Appendix B (complete sample).

3.2 SAGE-SMC photometric data

The SAGE-SMC (Surveying the Agents of Galaxy Evolution in the Tidally Stripped, Low Metallicity Small Magellanic Cloud) *Spitzer* Legacy programme (PID: 40245, P.I.: K. Gordon) mapped almost the entire SMC using IRAC and MIPS. Gordon et al. (2011a) provide a full discussion of the observations, data reduction and catalogue generation; we highlight here only the more relevant details.

In the overlap region, the SAGE-SMC and (reprocessed) S3MC images were combined to produce mosaic images from which photometric catalogues were created (we use the 'Single Frame + Mosaic Photometry' catalogue). There is a systematic offset between the IRAC photometry in the SAGE-SMC and S3MC catalogues (Gordon et al. 2011a); since there is an excellent agreement between the SAGE-SMC fluxes and those predicted from the IRAC calibration stars we adopt the IRAC SAGE-SMC catalogue fluxes. Because of updated processing and improved calibrations, the S3MC and SAGE-SMC MIPS fluxes are also different (see Gordon et al. 2011a, for full details); we also adopt the MIPS SAGE-SMC catalogue fluxes. Catalogue fluxes are listed in Table 1.

Because of the complexity of the multiple data sets, the SAGE-SMC catalogue relies on a stringent set of rules to create the final catalogues, designed to maximize reliability rather than completeness (Gordon et al. 2011b). Therefore, the SAGE-SMC catalogues do not provide fluxes for all the IR sources in our target list: even though the images clearly show a point source, a few sources are missing the shortest or all IRAC band fluxes for a variety of reasons. Some YSOs sit in regions where there is a complex structure of extended emission (characteristic of star-forming environments), and may be also marginally extended. Other issues can arise during the source extraction and band merging processes causing a particular source not to make it into the final IRAC photometric catalogue, for instance variability and source confusion. As part of their paper on SMC YSOs identified using SAGE-SMC images and catalogues, Sewiło et al. (in preparation) visually inspected all the images of the 34 YSO candidates in this sample, and performed aperture photometry on the mosaic images. When SAGE-SMC catalogue fluxes are unavailable, Table 1 lists extracted aperture fluxes (identified by $*$). The adopted aperture sizes are 5 arcsec for the IRAC bands, and 8 and 15 arcsec, respectively, for MIPS 24 and 70 μm.

3.3 Thermal-infrared ground-based spectroscopy

L-band (2.8–4.1 μm) spectra of 11 bright sources in the SMC sample (Table A1) were obtained with the Infrared Spectrometer And Array Camera (ISAAC) at the European Southern Observatory (ESO) Very Large Telescope (VLT) at Paranal, on the nights of 2006 October 28 and 29 (ESO Programme 078.C-0338, P.I.: J. M. Oliveira) to search for H_2O ice absorption at 3 μm. The standard IR technique of chopping and nodding was employed to cancel the high background. The resolving power was $\lambda/\Delta\lambda \approx 500$. Exposure times varied between 60 and 105 min. The hydrogen lines in the standard stars left remnants of at most a few per cent of the continuum level. Telluric lines were used to calibrate the wavelength scale to an accuracy of $\Delta\lambda \approx 0.002$ μm.

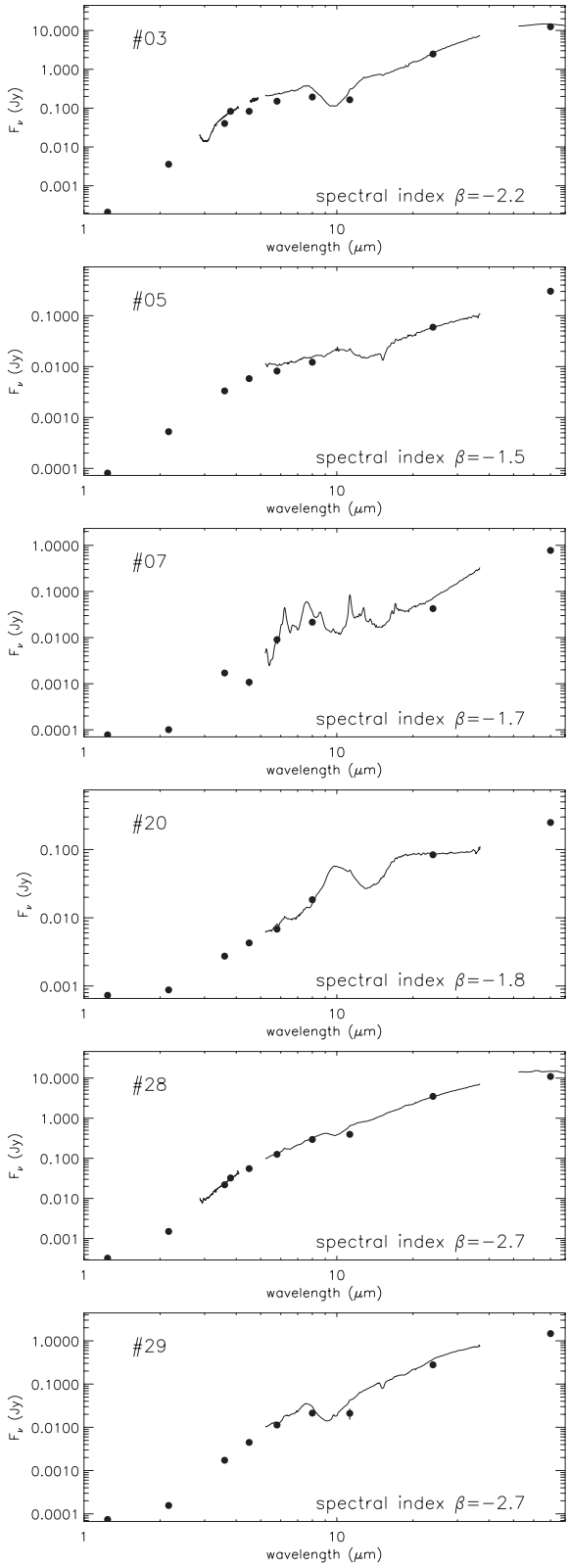

Figure 3. Selected examples of SEDs of YSO candidates in the SMC. Spectral indices calculated in the range 3.6–24 μm are given in each panel. The SEDs of all objects in the sample are provided in Appendix B.

M-band spectra of five bright SMC objects (Table A1) were also obtained with ISAAC at the VLT, on the nights of 2009 November 4 and 5 (ESO Programme 084.C-0955, P.I.: J. M. Oliveira) to search for the CO ice feature at 4.67 μm. Exposure times varied between 45 and 90 min. The *M*-band spectra were obtained and reduced in the same way as the *L*-band spectra. Telluric lines were used to calibrate the wavelength scale to an accuracy of $\Delta\lambda \approx 0.003$ μm.

Acquisition for the *L*-band spectroscopy was done using high spatial resolution L'-band images ($\lambda = 3.8$ μm). Magnitudes were obtained using aperture photometry on the targets and spectral standard stars observed at regular intervals during each night. Magnitudes were converted to fluxes using the following conversion: a 16-mag star has a flux of 9.414×10^{-5} Jy. These resulting fluxes (Table 1) were used to flux calibrate the *L*-band spectra.

Some of these spectra have been published previously; van Loon et al. (2008) first identified MSX SMC 79 (source #32), IRAS 01039−7305 (#33) and IRAS 01042−7215 (#34) as YSOs based on their *L*-band spectra; Oliveira et al. (2011) discussed the ice features of sources #03, 17, 18 and 34; they did not discuss the spectra of source #33 since the ice detections are uncertain (see also Table 2).

3.4 Near- and mid-infrared ground-based imaging

The near-IR imaging observations were performed with the Son of ISAAC (SOFI) imager at the New Technology Telescope (NTT) at ESO La Silla, between 2006 October 1 and 2006 November 10 in service mode (ESO Programme 078.C-0319, P.I.: J. Th. van Loon). Images were obtained with the J_s and K_s filters using the 0.288 arcsec pixel^{-1} plate scale, with a total integration time of 11 min filter^{-1}. The total integration time was split into jittered 1 min exposures to allow for efficient sky removal. For each filter, the jittered images were reduced and combined using standard IR reduction steps implemented within ESO's data reduction pipelines: detector cross-talk correction, flat-field correction, sky subtraction and shift addition of jittered frames. Photometric calibration was done using dedicated standard star observations; these were observed several times per night in order to estimate magnitude zero-points. Since zero-points were well behaved, we adopted a single value to calibrate all observations: $z_{J_s} = 23.09 \pm 0.02$ mag and $z_{K_s} = 22.37 \pm 0.04$ mag. PSF photometry was performed using the DAOPHOT package (Stetson 1987) within IRAF. Typical full width at half-maximum (FWHM) of the stellar profiles were 3.8 and 3.6 pixels, corresponding to, respectively, 1.1 and 1.0 arcsec in the J_s and K_s bands. Aperture correction was performed using bright PSF stars. Magnitudes were converted to fluxes using the following conversion: a 16-mag star has fluxes of 6.112×10^{-4} and 2.584×10^{-4} Jy, respectively, in J_s and K_s. Fluxes are listed in Table 1. In Appendix C, J_sK_s colour composite images are shown for each target (Fig. C1), together with *Spitzer*/IRAC [3.6]–[5.8]–[8] colour composites. Some sources sit in complex cluster-like environments; we carefully investigated each image to identify the redder source as the counterpart for the mid-IR sources (these identifications were usually very obvious).

SOFI imaging was obtained only for the original 31 objects, not for the additional objects identified by van Loon et al. (2008). However, source #32 is in the SOFI field-of-view of source #09 and J_s and K_s fluxes were also measured. For the remaining two sources (#33 and 34) we use JHK_s fluxes and images from the IR Survey Facility (IRSF; Kato et al. 2007).

The 21 brightest mid-IR objects were imaged with the VLT Imager and Spectrograph for the IR (VISIR) at ESO, Paranal, in

Table 1. Infrared fluxes (in mJy) for the SMC YSO candidates. *Spitzer* photometry is from the SAGE-SMC catalogue (Gordon et al. 2011a); when catalogue photometry is unavailable, aperture photometry fluxes are used (indicated by $*$). Listed J_sK_s fluxes are from this work, except for fluxes of sources #32 and 33 that are from the IRSF catalogue (Kato et al. 2007). Source IDs are from the S3MC catalogue, unless stated otherwise. S3MC objects were identified by Bolatto et al. (2007). Some sources were identified spectroscopically using IRS and MIPS-SED spectra by 1 – van Loon et al. (2008); 2 – van Loon et al. (2010); 3 – Oliveira et al. (2011); 4 – Martayan et al. (2007) identified source #20 as a candidate Herbig B[e] star. Source classification is discussed in Sections 5 and 6.

#	RA and Dec. (J2000)	J_s	K_s	L'	$F_{3.6}$	$F_{4.5}$	$F_{5.8}$	F_8	$F_{11.3}$	F_{24}	F_{70}	Source ID	Ref.
01	00 43 12.86 −72 59 58.3	0.339 ± 0.029	0.341 ± 0.030		*2.56 ± 0.30	*1.98 ± 0.27	*10.35 ± 0.62	*25.74 ± 0.98	<6	337.6 ± 1.7	3316 ± 21	004312.85−725958.30 IRAS 00413−7316	
02	00 44 51.87 −72 57 34.2	0.258 ± 0.016	0.937 ± 0.047	7.76 ± 0.75	5.76 ± 0.17	9.92 ± 0.23	15.73 ± 0.36	31.69 ± 0.45	33 ± 4	555.4 ± 4.9	1620 ± 18	IRAS 00429−7313	2
03	00 44 56.30 −73 10 11.8	0.210 ± 0.030	3.583 ± 0.171	82.75 ± 7.98	40.27 ± 0.66	*82.85 ± 1.00	150.60 ± 1.60	193.10 ± 2.46	164 ± 10	2470.0 ± 12.4	12440 ± 60	IRAS 00430−7326	2, 3
04	00 45 21.26 −73 12 18.7	0.977 ± 0.028	1.010 ± 0.051		1.78 ± 0.18	2.17 ± 0.06	2.92 ± 0.19	4.59 ± 0.63		39.3 ± 0.4	917 ± 11	004521.26−731218.68	
05	00 45 47.51 −73 21 42.4	0.081 ± 0.004	0.527 ± 0.024		3.33 ± 0.08	5.81 ± 0.07	8.18 ± 0.14	12.20 ± 0.24		59.4 ± 0.5	281 ± 6		
06	00 46 24.45 −73 22 07.1	0.077 ± 0.006	0.363 ± 0.024	3.89 ± 0.38	2.85 ± 0.14	8.82 ± 0.17	14.40 ± 0.31	20.40 ± 0.48	<6	192.5 ± 0.9	2154 ± 20	004624.46−732207.30	2
07	00 46 51.72 −73 15 25.3	0.078 ± 0.008	0.101 ± 0.012		*1.71 ± 0.25	*1.08 ± 0.20	*9.04 ± 0.58	*21.60 ± 1.00		42.5 ± 0.4	776 ± 11	004651.71−731525.34	
08	00 48 25.83 −73 05 57.3	0.166 ± 0.014	0.316 ± 0.023		2.07 ± 0.08	3.25 ± 0.06	8.76 ± 0.16	19.30 ± 0.44	19 ± 2	592.8 ± 5.2	7779 ± 55	004825.83−730557.29	
09	00 48 41.78 −73 26 15.3	0.141 ± 0.015	0.146 ± 0.028		*1.93 ± 0.26	0.98 ± 0.04	3.01 ± 0.10	7.00 ± 0.43	<6	239.4 ± 1.0	1875 ± 18	004841.77−732615.25	
10	00 49 01.64 −73 11 09.6	0.086 ± 0.008	0.163 ± 0.016		*2.49 ± 0.30	0.80 ± 0.13	5.06 ± 0.27	13.30 ± 0.95	<6	708.7 ± 4.0	3109 ± 25	004901.63−731109.60	
11	00 49 44.57 −73 24 32.8	0.121 ± 0.009	0.166 ± 0.015		*1.59 ± 0.24	0.52 ± 0.03	3.39 ± 0.17	7.13 ± 0.46		47.5 ± 0.5	*900 ± 73	004944.57−732432.75	
12	00 50 40.25 −73 20 37.0	0.090 ± 0.007	0.124 ± 0.011		0.66 ± 0.03	0.46 ± 0.01	3.02 ± 0.07	7.11 ± 0.19		71.3 ± 0.5	452 ± 6	005040.24−732036.99	
13	00 50 43.24 −72 46 56.2	0.252 ± 0.021	0.336 ± 0.024		1.63 ± 0.27	1.27 ± 0.05	5.89 ± 0.18	16.60 ± 0.54	8 ± 1	589.2 ± 3.6	2762 ± 28	005043.23−724656.24	
14	00 50 58.09 −73 07 56.8	0.391 ± 0.019	0.817 ± 0.048		2.11 ± 0.04	2.42 ± 0.03	4.95 ± 0.07	13.50 ± 0.19		114.3 ± 1.1	461 ± 6	005058.09−730756.78	
15	00 52 38.84 −73 26 23.9	0.227 ± 0.013	0.246 ± 0.020		1.57 ± 0.20	1.04 ± 0.06	6.98 ± 0.22	20.50 ± 0.51	14 ± 6	610.7 ± 3.4	2695 ± 19	005238.84−732623.92 IRAS 00509−7342	
16	00 53 25.36 −72 42 53.2	0.364 ± 0.022	0.369 ± 0.025		0.84 ± 0.10	0.67 ± 0.02	4.03 ± 0.19	13.50 ± 0.57	19 ± 4	282.0 ± 1.5	1226 ± 14	005325.36−724253.20 IRAS 00516−7259	
17	00 54 02.31 −73 21 18.6	0.357 ± 0.022	2.244 ± 0.120	26.41 ± 2.55	19.50 ± 0.25	46.30 ± 0.66	78.40 ± 0.71	113.00 ± 0.91	69 ± 10	496.5 ± 3.5	1669 ± 14	005402.30−732118.70	2, 3
18	00 54 03.36 −73 19 38.4	0.247 ± 0.022	1.104 ± 0.060	18.61 ± 1.80	12.50 ± 0.18	38.60 ± 0.37	84.20 ± 0.78	125.00 ± 1.02	91 ± 7	824.6 ± 5.6	3987 ± 25	005403.36−731938.30	2, 3
19	00 54 19.16 −72 29 09.6	0.249 ± 0.009	0.287 ± 0.012		1.27 ± 0.03	3.72 ± 0.05	10.80 ± 0.15	37.90 ± 0.34	76 ± 3	522.6 ± 3.1	319 ± 5	005419.16−722909.63	
20	00 56 06.38 −72 28 28.1	0.731 ± 0.048	0.877 ± 0.045		2.74 ± 0.06	4.28 ± 0.07	6.81 ± 0.11	18.40 ± 0.20		83.8 ± 0.7	221 ± 3	005606.37−722828.05	4
21	00 56 06.50 −72 47 22.7	0.075 ± 0.013	0.167 ± 0.021		1.14 ± 0.05	1.15 ± 0.02	3.75 ± 0.11	7.77 ± 0.27	<6	269.3 ± 1.8	1081 ± 13	005606.49−724722.66	
22	00 57 57.11 −72 39 15.4	0.330 ± 0.021	0.655 ± 0.048	2.77 ± 0.27	3.46 ± 0.63	3.80 ± 0.12	6.04 ± 0.23	8.19 ± 0.66	<6	243.8 ± 1.6	3276 ± 29	005757.10−723915.40 IRAS 00562−7255	
23	00 58 06.41 −72 04 07.3	0.347 ± 0.015	0.385 ± 0.020		1.19 ± 0.14	0.86 ± 0.03	4.89 ± 0.17	11.80 ± 0.67	<6	321.1 ± 2.5	1442 ± 17	005806.41−720407.32 IRAS 00563−7220	
24	01 00 22.32 −72 09 58.1	0.072 ± 0.003	0.469 ± 0.023		2.45 ± 0.05	4.04 ± 0.06	5.90 ± 0.08	10.20 ± 0.13		43.6 ± 0.5	202 ± 4		
25	01 01 31.70 −71 50 40.3	0.348 ± 0.027	0.386 ± 0.047		*2.79 ± 0.32	0.91 ± 0.17	4.55 ± 0.26	11.90 ± 1.39	<6	550.7 ± 2.3	3875 ± 19	010131.69−715040.30	
26	01 02 48.54 −71 53 18.0	0.167 ± 0.011	0.482 ± 0.028		*3.57 ± 0.36	*4.58 ± 0.41	5.07 ± 0.24	7.52 ± 0.64	<6	288.2 ± 2.1	5616 ± 30	010248.54−715317.98	
27	01 03 06.14 −72 03 44.0	0.073 ± 0.005	0.154 ± 0.009		0.48 ± 0.09	0.37 ± 0.01	2.01 ± 0.12	*16.26 ± 1.00		69.6 ± 0.6	1123 ± 11	010306.13−720343.95	
28	01 05 07.26 −71 59 42.7	0.325 ± 0.022	1.503 ± 0.082	32.34 ± 3.12	21.90 ± 0.37	55.40 ± 0.85	126.00 ± 1.31	295.00 ± 3.46	396 ± 22	3507.0 ± 22.8	10960 ± 67	010507.25−715942.70	2
29	01 05 30.71 −71 55 21.3	0.074 ± 0.005	0.156 ± 0.023		1.73 ± 0.07	4.48 ± 0.06	11.30 ± 0.16	21.30 ± 0.20	21 ± 6	278.3 ± 2.2	1467 ± 14	010530.71−715521.25	
30	01 06 59.67 −72 50 43.1	0.699 ± 0.020	2.282 ± 0.101	8.75 ± 0.84	8.03 ± 0.13	10.90 ± 0.12	16.30 ± 0.18	22.80 ± 0.22		50.6 ± 0.6	536 ± 5	010659.66−725043.10	2
31	01 14 39.38 −73 18 29.3	0.137 ± 0.015	0.310 ± 0.023		*5.02 ± 0.42	2.96 ± 0.14	5.71 ± 0.43	13.60 ± 2.56	12 ± 3	*805.9 ± 14.9	9351 ± 66	011439.38−731829.26	2
32	00 48 39.64 −73 25 01.0	0.282 ± 0.008	1.010 ± 0.017	11.11 ± 1.02	6.94 ± 0.08	12.80 ± 0.13	23.40 ± 0.24	41.60 ± 0.34		148.1 ± 1.7	*1271 ± 45	MSX SMC 79 004839.63−732500.98	1
33	01 05 30.22 −72 49 53.9	1.064 ± 0.049	11.063 ± 0.214	88.26 ± 8.13	60.40 ± 1.92	93.90 ± 2.65	122.00 ± 1.21	170.00 ± 3.71		939.1 ± 4.9	3208 ± 17	IRAS 01039−7305	1, 2
34	01 05 49.29 −71 59 48.8	0.344 ± 0.013	2.578 ± 0.071	47.62 ± 4.39	22.10 ± 0.28	48.30 ± 0.65	80.10 ± 0.81	113.00 ± 0.88		648.0 ± 3.4	1998 ± 18	IRAS 01042−7215	1, 2, 3

service mode over the period 2006 September 4 to October 3 (ESO Programme 078.C-0319, P.I.: J. Th. van Loon). Images were obtained through the narrow-band PAH2 filter (centred at $\lambda = 11.25\,\mu$m, half-band width $\Delta\lambda = 0.59\,\mu$m). Eight standard stars with flux densities in the range 5–11 Jy were observed for photometric calibration. The plate scale was 0.075 arcsec, providing a field-of-view of 19×19 arcsec^2. The standard IR technique of chopping and nodding was employed to cancel the high background. Integration times were 24 min, split in 16 exposures of 23 chop cycles each. The individual exposures were combined and corrected for instrumental effects using version 1.5.0 of the VISIR pipeline. Photometry was performed by collecting the counts within a circular aperture centred on the zero-order maximum of the diffraction pattern, avoiding the first Airy ring; if the source was not detected upper limits were calculated. Table 1 lists the fluxes.

3.5 Ancillary multiwavelength data

3.5.1 Optical spectroscopy

Our optical spectroscopy was obtained using the Double-Beam Spectrograph (DBS) mounted on the Nasmyth focus of the Australian National University 2.3-m telescope at Siding Spring Observatory. More information on the instrument can be found in Rodgers, Conroy & Bloxham (1988). Standard IRAF routines were used for the data reduction (bias subtraction, flat-fielding, wavelength calibration). The blue and red spectra were joined in the interval 6160–6300 Å; the joined spectra cover the wavelength range 3600–9500 Å. Spectral standard stars, observed with the same instrumental set-up as the programme objects, were used to provide a relative flux calibration for each object. Telluric features were removed by observing white dwarf standards with few intrinsic spectral features. The final spectra have an effective resolution of ∼4.5 Å.

Optical spectra were obtained for 32 objects (Appendix D, Fig. D1). At the position of the IR source, source #24 shows no point source at optical wavelengths, only extended emission. There is clearly a point source in the J_s band (Fig. C1) but it is the faintest object in the sample (Table 1); thus it was too faint to obtain an optical spectrum. The position of IR source #31 sits between two bright optical sources; in Fig. C1 it is clear that this region is very complex with many bright sources at short wavelengths as well as bright IR sources. Thus no optical spectrum was obtained for this source.

For sources #05, 06 and 29 the optical spectra exhibit only Balmer absorption lines, i.e. the spectra are typical of more evolved stars. Since these objects are also very faint in the J_s band (Table 1) it is unlikely the obtained optical spectra are associated with the IR source. For sources #02, 10, 11, 14, 16, 17, 18, 23 and 34 the spectra only show Hα emission thus we perform no further analysis of their optical spectra. For the remaining 20 sources we analyse the optical spectra in detail (Section 4.5).

3.5.2 Radio data

Radio free–free emission from (ultra-)compact H II regions is a common signpost of massive star formation.[1] Using all available archival data from the Australia Telescope Compact Array (ATCA) and the Parkes radio telescope, Wong et al. (2011a) and Crawford et al. (2011) created new high-sensitivity, high-resolution radio-continuum images of the SMC at 1.42, 2.37, 4.80 and 8.64 GHz (wavelengths, respectively, 20, 13, 6 and 3 cm), as well as point source catalogues (Wong et al. 2011b, 2012). Of the 34 objects in the sample, 11 sources have radio-continuum detections at least two frequencies. Of these, eight are radio point sources found within 4 arcsec of the IR source (the positional accuracy at 20 and 13 cm). Sources #08 and 31 are in complex and extended H II regions and therefore the source position is less certain; there is no point source at the position of source #15 but we clearly see an extended radio-continuum object. Radio spectral indices ($S_\nu \propto \nu^\alpha$) for these sources are $\alpha \gtrsim -0.3$, consistent with their classification as compact H II regions (e.g. Filipović et al. 1998) – background galaxies are dominated by synchrotron emission with a steeper spectral index. The sources detected at radio wavelengths are the most luminous in our sample (Section 4.1).

[1] By (ultra-)compact H II region we mean a H II region associated with the early stages of massive star formation, without making any statement about the degree of compactness or physical properties (Hoare et al. 2007); this is to distinguish these objects from 'classical' evolved H II regions.

3.6 Resolving YSOs at the distance of the SMC

The *Spitzer* photometry has a spatial resolution of 2, 6, 18 arcsec, respectively, for the IRAC bands and at 24 and 70 μm, while the resolution of the IRS spectra varies between 2.5 and 10 arcsec. At the distance of the SMC (60 pc; Szewczyk et al. 2009), this corresponds to ∼0.6–5 pc for the photometry and ∼0.8–3 pc for the spectra. For comparison the Trapezium core of the Orion nebula cluster extends ∼0.5 pc. Using the near-IR photometry (FWHM typically 1 arcsec or ∼0.3 pc) we show that the *Spitzer* fluxes are dominated by the contribution of a single bright IR source. However, it is likely that some IR sources encase a massive binary or a dominant massive star surrounded by low-mass siblings that we are unable to resolve. Most of our analysis focuses on the YSO chemistry and other envelope properties therefore the detailed luminosity distribution within the YSO source is less important. Another important issue to bear in mind is that the different data sets sample physically distinct spatial scales due to their different spatial resolutions (see discussion in Section 5.1).

4 SPECTRAL PROPERTIES

The spectra of YSOs are characterized by a cold dust continuum, and often exhibit strong silicate features at 10 and 18 μm. Silicate absorption superimposed on a very red continuum is indicative of embedded protostellar objects (e.g. Furlan et al. 2008). Ice absorption features are another common feature in spectra of embedded YSOs. These objects are traditionally classified as Class I sources (based on their IR spectral index; Lada 1987), or as Stage I sources (based on their modelled SEDs; Robitaille et al. 2006). As the nascent massive star becomes hotter and excites its environment (i.e. it develops a compact H II region), emission features attributed to PAHs, and atomic fine-structure and H_2 emission lines also become common. Thus the infrared spectra of YSOs can show a superposition of ice, dust and PAH features that can be difficult to disentangle, in particular in extragalactic sources (e.g. Oliveira et al. 2009).

For intermediate-mass YSOs in the later stages the dust cocoons dissipate and become hotter, and eventually IR emission from a circumstellar disc dominates, with prominent silicate emission. Such objects are usually classified as Class II or Stage II objects. Amongst such objects are Herbig Ae/Be (HAeBe) stars, that are often hot enough to excite PAH emission (e.g. Keller et al. 2008).

Figs 3 and B1 show all available IR photometry and spectroscopy for the 34 YSO candidates. In this section we discuss the main spectral features and their properties and in the next section we discuss object classification.

4.1 Spectral energy distribution and dust features

The spectral index in frequency space defined as $F_\nu \propto \nu^\beta$ corresponds to $\beta = -\alpha - 1$, where α is the spectral index defined in wavelength space: $\alpha = \frac{\mathrm{d}\log(\lambda F_\lambda)}{\mathrm{d}\log\lambda}$ (André & Montmerle 1994). As determined using *Spitzer* photometry of Galactic YSO samples, Class I objects have $\alpha \gtrsim -0.5$, Class II YSOs have $-0.5 \gtrsim \alpha \gtrsim -1.8$ and Class III (discless YSOs) have $\alpha \lesssim -1.8$ (e.g. Muench et al. 2007). This corresponds to $\beta \lesssim -0.5$ (Class I), $-0.5 \lesssim \beta \lesssim 0.8$ (Class II) and finally $\beta \gtrsim 0.8$ (Class III) sources. These classes are more commonly used to describe the early stages of intermediate- and low-mass stellar evolution.

We calculate the spectral indices of the objects in the sample between 3.6 and 24 μm. All objects have steep spectra with $\beta < -1.0$, consistent with a Class I classification. Closer inspection of the SEDs (Fig. B1) reveals that for #19 and 20 the SED flattens considerably above 20 μm, with, respectively, $\beta \sim -0.6$ and $\sim -$ 0.2 between 20 and 32 μm. This suggests the presence of only moderate amounts of cold dust.

As part of their survey of photometric YSO candidates, Sewiło et al. (in preparation) have fitted the SEDs of all the sources in our sample, using the grid of models and fitting tool developed by Robitaille et al. (2006, 2007). Based on model parameters (mass accretion rate, stellar mass and disc mass) the fitting tool classifies objects as Stage I, II and III. The SED models do not include the contribution from PAH emission. Good SED fits are achieved for the majority of objects, and all objects are classified as Stage I sources. Integrated SED luminosities and stellar masses are in the ranges 1.5×10^3–1.4×10^5 $L_\odot$ and 8.2–30 $M_\odot$; sources #20 and 28 are the least and most luminous, respectively. We should point out that this grid of models assumes that a single YSO source is responsible for the fluxes measured at different wavelengths. As discussed in Section 3.6, some of the SMC sources may be binaries or small unresolved clusters; we assume that the central source can be represented by the equivalent of a single luminous object.

Prominent silicate absorption is observed in the IRS spectra of at least 10 YSOs (indicated by ✓ in the relevant column of Table 3). A further two objects have tentative detections of silicate absorption (✓? in Table 3): source #30 shows strong PAH emission while the spectrum of source #24 shows only weak features. As discussed by Oliveira et al. (2009), without detailed modelling of *all* the spectral features in the spectrum it is often difficult to distinguish weak silicate absorption from PAH emission complexes between 7 and 12 μm. Indeed, silicate absorption is conclusively identified only in objects where PAH emission is relatively weak or non-existent. The red wing of the silicate absorption band can be deformed by the presence of the 13-μm libration mode of H_2O ice. This might explain the particularly extended red wing of the silicate feature for source #06, the source with strongest H_2O and CO_2 ice in our sample (see Section 4.2). Recent modelling work (Robinson, Smith & Maldoni 2012) suggests that constraining envelope optical depth and dust properties are crucial in asserting whether the libration mode is present in a spectrum. The 18-μm silicate absorption feature seems to be present in the spectrum of some sources, namely #03, 17, 18, 30, and maybe #29 as well.

The shape of the silicate emission features is a reflection of the composition of the dust grains. Amorphous olivine grains create a typical sawtooth-shaped profile peaking at 9.8 μm, characteristic of small interstellar dust grains. The presence of processed (crystalline) grains is revealed by a shift in the feature's peak to longer wavelengths, and a significant population of larger grains broadens the profile (e.g. Kessler-Silacci et al. 2006). However, as pointed out by Sargent et al. (2009), the presence of a population of large grains is difficult to identify unambiguously.

Four objects in the sample exhibit silicates in emission (indicated by ⋀ in Table 3). None of the spectra exhibits crystalline features. The profile of source #19 is narrow with a sharp 9.8-μm peak, indicating unprocessed small dust grains. This object is not an YSO, as detailed in Section 6. Sources #05, 14 and 20 exhibit broader profiles that could suggest larger grains or mixed grain populations. The spectra of these three objects also show PAH emission at 11.3 μm that, in particular for source #14, masks the underlying profile shape. Sources #05 and 14 exhibit a red underlying continuum while the SED of #20 is essentially flat at wavelengths longer than 20 μm (see above). These objects are discussed in more detail in Section 5.3.

4.2 Ice absorption bands

In cold molecular clouds, layers of ice form on the surface of dust grains. H_2O is by far the most abundant ice (typically 10^{-5}–10^{-4} with respect to H_2), followed by CO_2 and CO, with a combined abundance of 10–30 per cent with respect to H_2O ice (e.g. van Dishoeck 2004). Understanding ice chemistry is crucial to understanding the gas-phase chemistry and to probing the physical conditions within molecular clouds. Surface chemistry and ultraviolet (UV) and cosmic ray processing of the ice mantles are thought to play an important role not only in the formation of more complex ice species but also H_2O, O_2 and gas-phase organic molecules. Prominent ice features in the IRS spectral range are found between 5 and 7 μm (attributed to a mixture of H_2O, NH_3, CH_3OH, HCOOH and H_2CO ices; e.g. Boogert et al. 2008), and at 15.2 μm (attributed to CO_2 ice; e.g. Gerakines et al. 1999; Pontoppidan et al. 2008). The ice complex at 5–7 μm can be difficult to identify due to the superposition of numerous PAH emission features (Spoon et al. 2002). At shorter wavelengths, ice features of H_2O and CO are found in the 3–5 μm range (e.g. Oliveira et al. 2011). Circumstellar ices have been detected in massive YSO environments in the Galaxy (e.g. Gerakines et al. 1999; Gibb et al. 2004) and the LMC (van Loon et al. 2005, 2008; Oliveira et al. 2009, 2011; Shimonishi et al. 2010; Seale et al. 2011).

In the SMC, H_2O and CO_2 ices (at 3 and 15.2 μm, respectively) have been detected in the environments of sources #03, 17, 18, 32 and 34 (van Loon et al. 2008; Oliveira et al. 2011). Even though CO ice at 4.67 μm is detected towards YSOs in the Galaxy and the LMC (Gibb et al. 2004; Oliveira et al. 2011), no CO ice is detected towards sources #03, 17, 18, 33 and 34 (the only SMC sources observed at relevant wavelengths). Oliveira et al. (2011) interpreted this as a metallicity effect. Sources #03, 06 and 17 exhibit a broad feature between 60 and 70 μm in the MIPS-SED spectrum, attributed to crystalline H_2O ice (van Loon et al. 2010b).

In this work we newly identify ice features towards a number of SMC YSO candidates. We detect H_2O and CO_2 ice absorption in the environments of sources #02, 05, 06, 22 and 29 (Figs 4–6). For sources #05 and 29 we do not have 3–4 μm spectra to probe the strongest 3-μm H_2O band, but we detect the 6-μm H_2O band – also identified in sources #03, 06, 17 and 18 (Fig. 6). Additionally we detect only CO_2 ice towards sources #08, 13 and 21 (Fig. 5); no

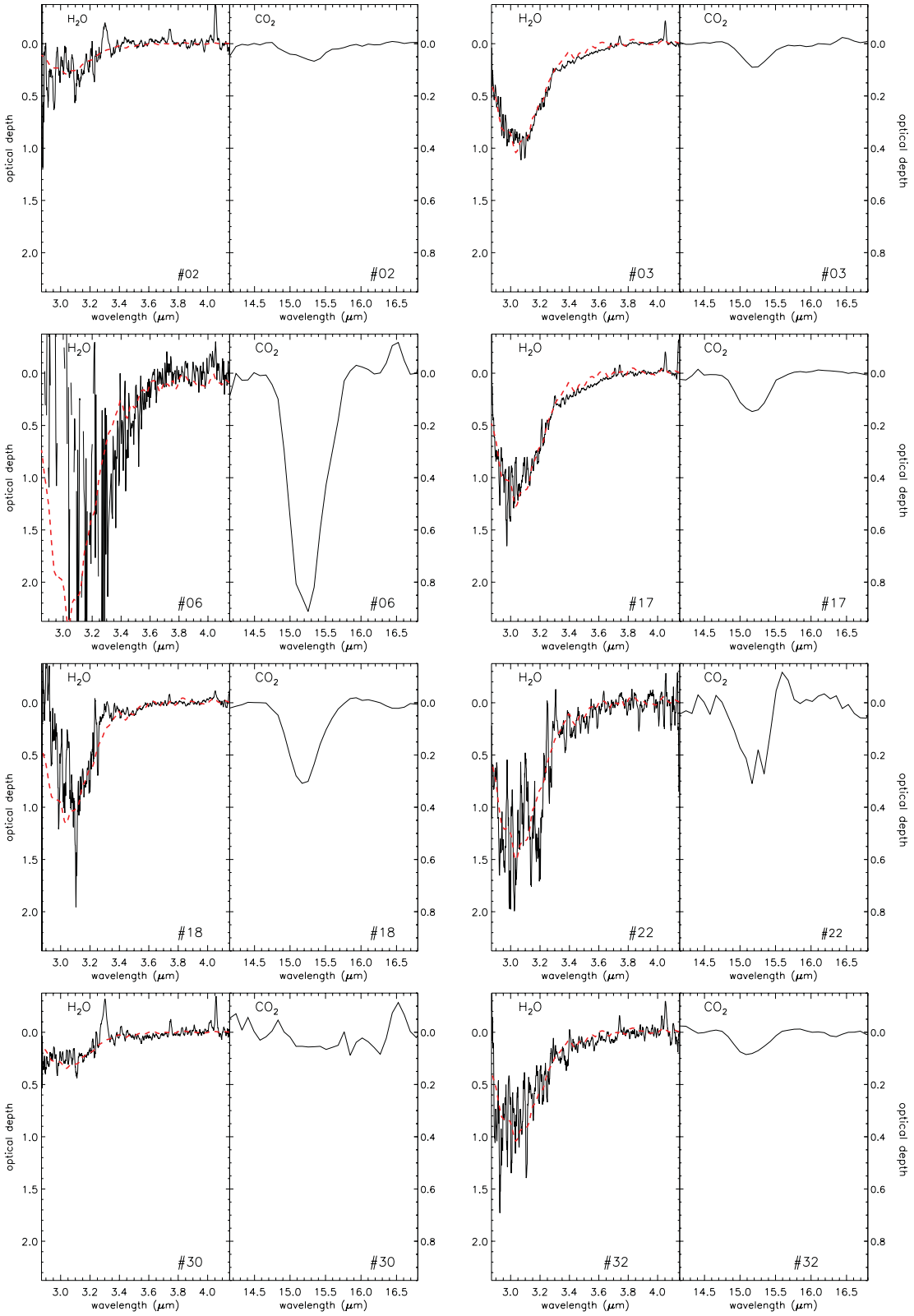

Figure 4. SMC sources with H_2O ice (left) and CO_2 ice (right) detections. Dashed (red) lines show a low-resolution *AKARI* spectrum of a LMC YSO (Shimonishi et al. 2010) to help constrain the blue wing of the H_2O ice feature. Source #30 shows H_2O ice but not CO_2 ice. Many sources show hydrogen emission at 3.74 μm (Pfγ) and 4.05 μm (Brα); sources #02 and 30 exhibit PAH emission at 3.3 μm, and #06 and 30 at 16.45 μm. Source #22 shows [Ne III] emission at 15.6 μm. H_2O ice detection for source #33 is marginal. The CO_2 ice detection for source #34 is weak but significant.

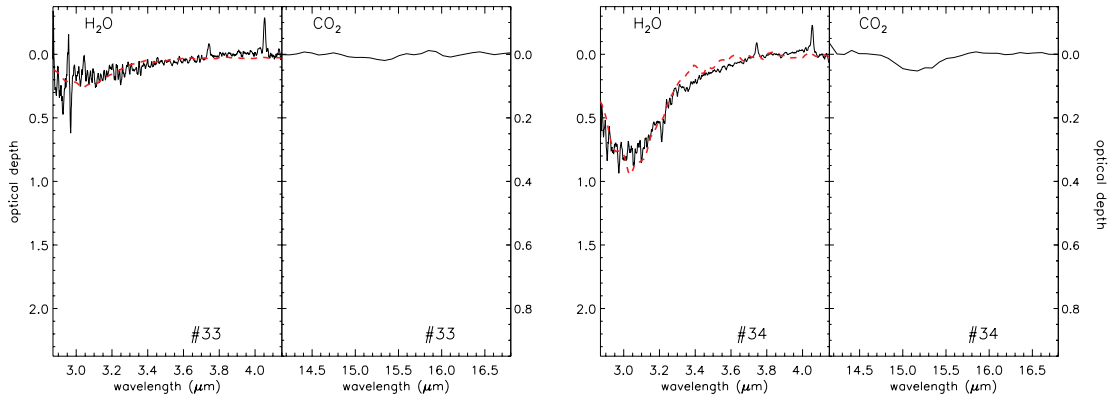

Figure 4 – *continued*

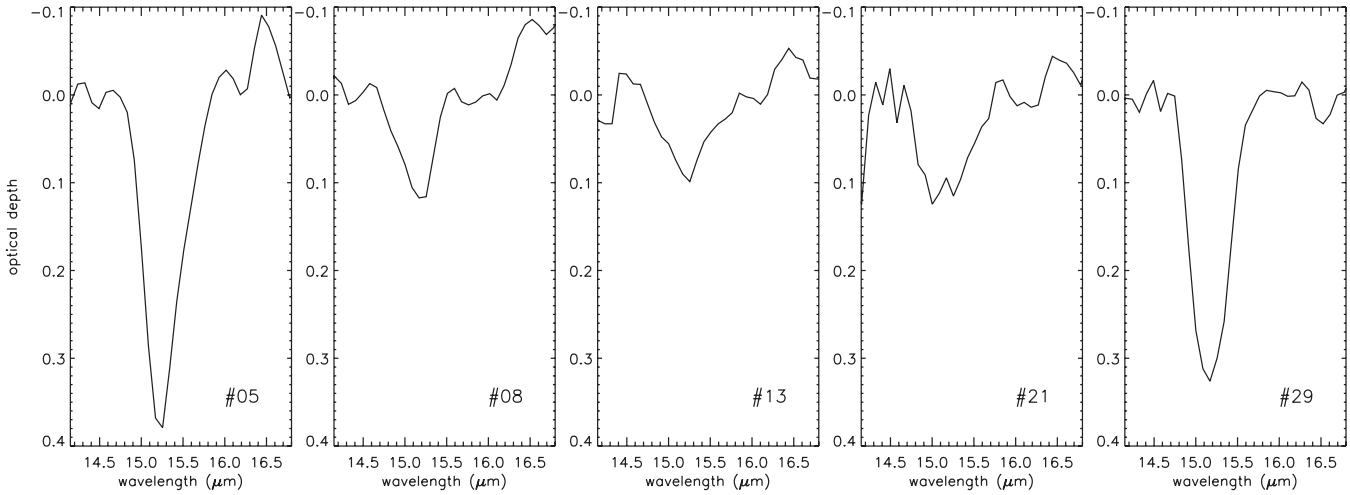

Figure 5. Additional SMC sources with CO_2 ice detections. No 3–4 μm spectrum is available for these sources. The CO_2 ice profile of source #21 is distorted by a couple of pixels with large errors, shifting the peak position.

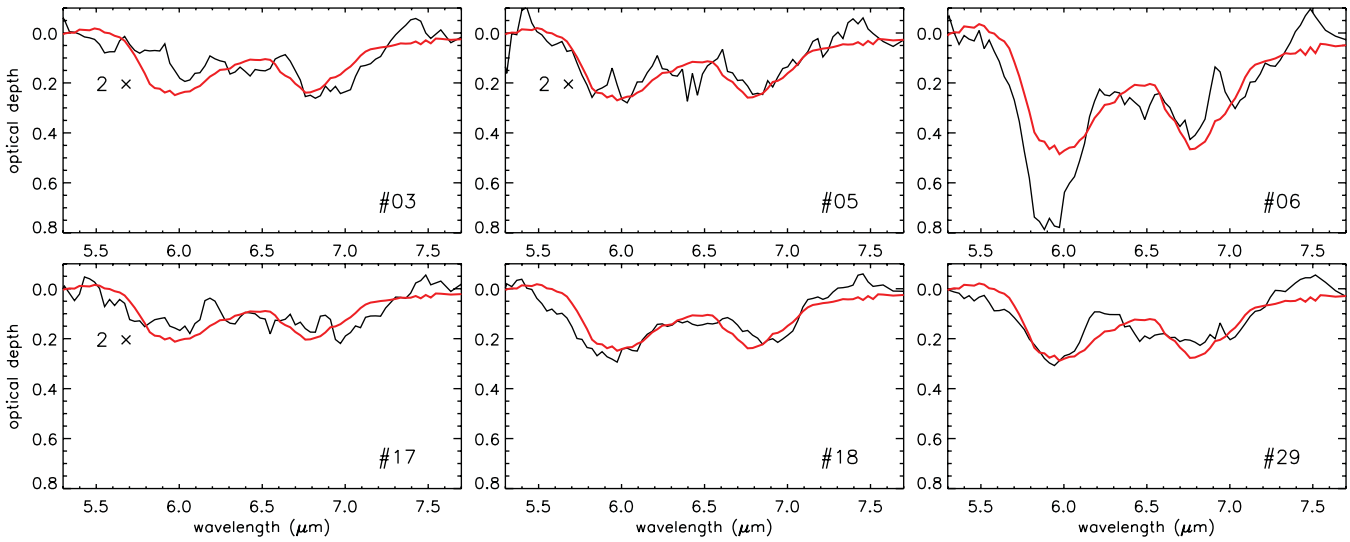

Figure 6. SMC sources with ice detections in the 5–7 μm range. This band is attributed to H_2O ice at 6 μm with smaller contributions from more complex molecules (HCOOH, H_2CO and NH_3), and ammonium (NH_4^+) with a small contribution from methanol (CH_3OH) at 6.85 μm (Boogert et al. 2008). This ice complex can only be clearly identified when the 6.22-μm PAH feature is weak or absent. Some optical depth spectra are multiplied by a factor of 2 (as indicated) to improve feature visibility. The red line is an optical depth spectrum of a Galactic YSO for comparison (Zasowski et al. 2009).

Table 2. Column density measurements (in 10^{17} molecules cm^{-2}) for H_2O and CO_2 ices in SMC YSO candidates. For source #06 the H_2O column density measurement (indicated by asterisk '*') was performed by scaling a better quality spectrum (see text). For sources #05 and 29 H_2O column densities (indicated by double asterisk '**') are estimated from the 6-μm feature, rather than the 3-μm feature (see text).

Source #	$N(H_2O)$	$N(CO_2)$
02	7.2 ± 2.2	1.6 ± 0.2
03	17.7 ± 0.7	1.7 ± 0.1
05	$^{**}19 \pm 5$	7.3 ± 0.9
06	$^{*}46.3 \pm 7$	19.2 ± 0.5
08		2.3 ± 0.2
13		2.2 ± 0.2
17	21.6 ± 0.8	2.8 ± 0.1
18	22.3 ± 1.2	6.0 ± 0.2
21		3.0 ± 0.3
22	27.7 ± 3.3	6.0 ± 1.0
29	$^{**}32 \pm 5$	6.7 ± 0.1
30	4.9 ± 1.0	$\lesssim 2$
32	18.8 ± 1.5	1.5 ± 0.2
33	3.9 ± 1.0	$\lesssim 0.3$
34	16.6 ± 0.7	1.0 ± 0.2

3-μm spectra are available and no ice is detected at 5–7 μm due to the presence of strong PAH emission (Table 3).

The blue edge of the 3-μm H_2O ice feature is set by the Earth's atmospheric cut-off. Therefore we use the sources' K_s-band magnitudes to help constrain the continuum bluewards of the feature; the red continuum is constrained avoiding hydrogen emission at 3.74 μm (Pfγ) and 4.05 μm (Brα). For the CO_2 ice we use a narrow wavelength interval surrounding the feature to constrain the continuum. Optical depth spectra are determined by subtracting a polynomial fitted to this local pseudo-continuum from each spectrum.

The *L*-band spectrum of source #06 is very red and the signal-to-noise ratio in the blue wing of the 3-μm H_2O feature is poor. Therefore we do not measure the column density directly from the ISAAC spectrum. Instead we scaled a low-resolution *AKARI* spectrum of a LMC YSO (SSTISAGE1C J051449.41−671221.5; Shimonishi et al. 2010) to match the red wing of the feature in #06 (as shown in Fig. 4), and measure the column density of the scaled spectrum. This measurement is indicated by asterisk '*' in Table 2. We validate this technique by checking that for the other sources the two methods provide consistent column density measurements. The H_2O column density measurements for sources #02 and 30 are uncertain, since the detection is weak and PAH emission at 3.3 μm fills-in the red wing of the feature. For source #33 the H_2O ice detection is very tentative (4σ detection); we do not consider it any further.

The 6-μm H_2O ice feature is very complex; the contributions from other ice species can lead to overestimates of the H_2O column density (see discussion in Oliveira et al. 2009, and references therein). Therefore we do not measure the H_2O ice column density directly from the 6-μm feature. Since the peak optical depth τ_6 correlates with the column density, we use the τ_6 measurements and the column densities derived from the 3-μm feature for sources #03, 06, 17 and 18 to estimate the H_2O column densities for sources #05 and 29 (assuming a simple linear correlation). These measurements are indicated by double asterisk '**' in Table 2.

The red wing of the CO_2 ice feature for sources #08 and 22 is affected by weak [Ne III] emission at 15.6 μm (see next subsection). Weak H_2O ice is detected towards source #30 but no CO_2 ice is identified (an upper limit is listed in Table 2). The CO_2 ice detection towards source #34 is weak but significant, since clear H_2O ice is detected. For source #33 no CO_2 ice is detected.

Calculated ice column densities are listed in Table 2. The adopted band strengths are 2.0×10^{16} and 1.1×10^{17} cm^2 per molecule, respectively, for H_2O and CO_2 (Gerakines et al. 1995). The quoted uncertainties for measurements in Table 2 do not reflect uncertainties in continuum determination. We have re-calculated CO_2 column densities for sources #03, 17, 18 and 34 using optimally extracted IRS spectra (Oliveira et al. 2011 used tapered-column extraction spectra; the optimal spectra provide better feature contrast due to improved signal-to-noise ratio). Sources with stronger ice absorption tend to be the most embedded (as measured by the spectral index), as observed also in Galactic samples (see for instance Forbrich et al. 2010). However, a steep spectral index does not imply the presence of ice absorption. There is weak anticorrelation between ice column density and the source luminosity.

Oliveira et al. (2011) compared the column densities for H_2O and CO_2 ices for Galactic and LMC samples. They found $N(CO_2)/N(H_2O)$ ratios for the LMC and the Galaxy ∼0.32 and ∼0.2, respectively, consistent with previous determinations. For the SMC, rather than a constant ratio, Fig. 7 suggests that there is a H_2O column density threshold for the detection of CO_2 ice, something not observed in either the LMC or the Galaxy. Source #02 is the only SMC source with $N(H_2O) < 1 \times 10^{18}$ cm^{-2} and a CO_2 ice detection, and as explained above $N(H_2O)$ may be underestimated for this source. We perform linear fits to the SMC data, of the form $N(CO_2) = m\,N(H_2O) + N_0(H_2O)$, where m is the slope and $N_0(H_2O)$

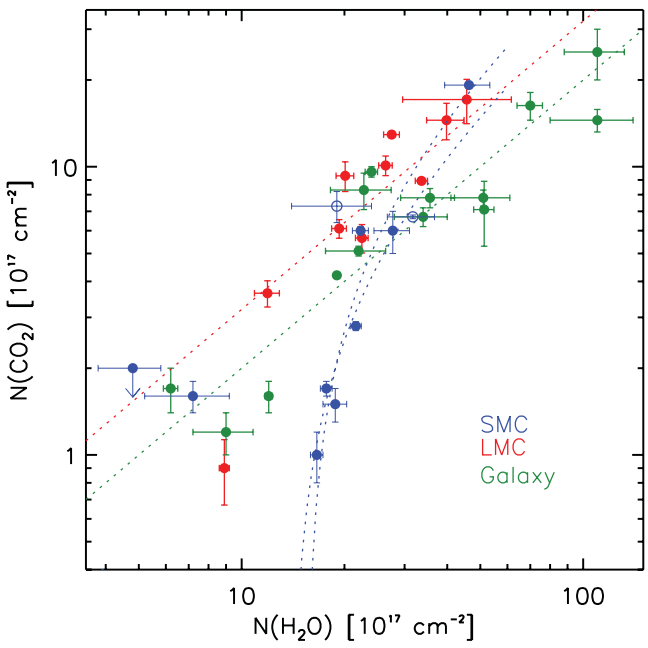

Figure 7. Column densities for H_2O and CO_2 ices. Red and green filled circles represent, respectively, LMC and Galactic YSOs; the dashed red and green lines represent the estimated $N(CO_2)/N(H_2O)$ ratios, respectively, 0.32 and 0.2 (Oliveira et al. 2011, and references therein). SMC measurements are represented by blue circles. Two fits to the SMC data, of the type $N(CO_2) = m\,N(H_2O) + N_0(H_2O)$ (m is the slope and $N_0(H_2O)$ is the H_2O column density threshold), are shown (blue dashed lines), including and excluding the 6-μm H_2O measurements (open blue circles).

is the H_2O ice column density threshold for the detection of CO_2 ice. Excluding sources #02 (see above) and #30 (upper limit), the fitted slope is ∼0.4–0.6 and $N_0(H_2O)$ ∼1.4–1.55 × 10^{18} cm^{-2} (depending on whether the 6-μm H_2O measurements are included, open blue circles in Fig. 7).

In the LMC, CO_2 ice column densities are enhanced with respect to H_2O ice, while the relative CO-to-CO_2 abundances are unchanged. CO_2 production could be increased due to the stronger UV field and/or higher dust temperatures in the LMC. However such harsher conditions would also destroy CO ice (the most volatile ice species), something that is not observed. Instead Oliveira et al. (2011) suggest that H_2O ice is depleted due to the combined effects of a lower gas-to-dust ratio and stronger UV radiation field. This would push the onset of water ice freeze-out deeper into the YSO envelope therefore reducing the observed column density (see their fig. 3). Forming deeper in the YSO envelope, CO_2 ice would remain unaffected.

In the Galaxy, the A_V thresholds for the detection of H_2O and CO_2 ices are statistically indistinguishable (see Oliveira et al. 2011, and references therein), suggesting that the two ices species are co-spatial in YSO envelopes. However, in the SMC the present observations suggest a column density threshold $N_0(H_2O) \sim 1.5 \times 10^{18}$ cm^{-2} for the detection of CO_2 ice; even the LMC measurements are consistent with a small threshold $N_0(H_2O) \sim 3 \times 10^{17}$ cm^{-2}. This suggests that in metal-poor environments part of the envelope may have H_2O ice but not CO_2 ice, supporting the scenario proposed by Oliveira et al. (2011). The role of reduced shielding in regulating the ice chemistry mentioned above is also supported by the non-detection (with high confidence) of CO ice absorption in the spectra of five SMC sources (the only sources observed at 4.67 μm).

4.3 PAH and fine-structure emission

Numerous emission features originate from the C–C and C–H stretching and bending modes of PAH molecules, excited by UV radiation. The best studied emission bands are at 6.2, 7.7, 8.6, 11.3 and 12.7 μm, ubiquitous in the spectra of compact H II regions and planetary nebulae. Many sources also exhibit a PAH emission complex at 17 μm. Often these emission bands are accompanied by fine-structure emission lines such as [S IV] at 10.5 μm, [Ne II] at 12.8 μm, [Ne III] at 15.6 μm, [Si II] at 34.8 μm and [S III] at 18.7 and 33.5 μm. These lines (unresolved in the low-resolution IRS modes) originate from ionized gas. The presence of both PAH and fine-structure line emission clearly suggests the presence of an ionizing source of UV radiation.

In the sample of 34 objects, all but two exhibit PAH emission. Even when other PAH bands are weak, the relatively isolated 11.3-μm band can be easily identified. Thus we use the relative peak strength of this feature to assess how dominant PAH emission is in shaping the IRS spectrum. We fit a local continuum using spectral points to the left and right of the feature, and measure the peak strength of the feature with respect to the underlying continuum, $F_{11.3}/F_c$. Sources with $F_{11.3}/F_c \leq 1.05$ essentially show no PAH emission; this is the case of sources #18 and 19. For sources with $1.05 < F_{11.3}/F_c \leq 1.30$ only the 11.3-μm band can be easily identified, other bands are not clearly visible (typical examples are sources #03 and 20). Sources with $F_{11.3}/F_c > 1.3$ clearly exhibit the complete zoo of PAH features (e.g. #08), and for some sources the spectra are completely dominated by PAH emission ($F_{11.3}/F_c >$ 3, e.g. #07). The different PAH groups are listed in Table 3 as ✗, ✓, ✓, ✓✓ from absent to very strong, and are used in the source classification in Section 5.

Recently, Sandstrom et al. (2012) analysed the properties of PAH emission observed towards a sample of six diverse SFRs in the SMC, namely N76 and N66 in the north-east SMC bar, three regions in the south-west bar including N22, and N83/84 in the SMC Wing. Our sample comprises sources in the *same six regions*, and further extends the spatial coverage by sampling for instance the region in the SMC body that connects N 66 to the south-west bar (see Fig. 1). Fig. 8 summarizes PAH properties in the SMC. On the left we show intensity ratios for the YSO candidates (black filled circles) and the averages for the aforementioned SMC SFRs (red filled circles). On the right we show the intensity of each main band normalized to total PAH intensity. In our sample the 11.3-μm band is strong compared to the 7.7- and 6.2-μm bands, and the 8.6-μm band is very weak compared to total PAH strength, consistent with the Sandstrom et al. (2012) results. Our analysis does not reveal changes to PAH emission properties that would be evidence for the YSO's irradiation of its environment. Thus the PAH emission observed towards at least some YSO candidates may have an important environmental contribution. Nevertheless, for sources with strong emission, total PAH intensity correlates with the luminosity of the source.

Model PAH band ratios (adapted from Draine & Li 2001, as described by Sandstrom et al. 2012) show the regions of the ratio diagram occupied by neutral and ionized PAHs, indicating also the effect of decreasing grain size. The strength of the radiation field also has a slight effect on PAH ratios. As proposed by Sandstrom et al. (2012), the comparison with these models suggests that SMC PAHs are predominantly small and neutral.

By comparing PAH properties in the SMC and the high-metallicity SINGS galaxies (Smith et al. 2007), Sandstrom et al. (2012) explain the observed differences as a metallicity effect: they speculate that, in the metal-poor SMC, PAHs *form* preferably in smaller grains and mostly neutral PAHs *survive* in the ISM. To further investigate whether the observed PAH ratios are directly related to metallicity we extend the comparison to also include the measurements compiled by Galliano et al. (2008) for a diverse sample of galaxies and individual SFRs of a range of metallicities. These data are show in Fig. 8 (left): the SINGS and Galliano samples are represented by open blue and green circles, respectively, and the symbol size reflects each region's gas-phase oxygen abundances, in the intervals $12 + \log(O/H) = 7.7$–8.2, 8.2–8.7 and 8.7–9.2. We adopt $12 + \log(O/H) = 8.0$ for the SMC. Both the SINGS and Galliano samples cover a similar metallicity range, with the majority of objects in each sample above 8.3 and 8.8 dex, respectively. However, these two samples occupy different regions in the PAH ratio diagram (with some overlap) despite their similar metallicities. The SMC measurements sit in a similar region to the Galliano sample, despite its lower metallicity. In summary our analysis supports the suggestion that PAHs throughout the whole SMC are indeed predominantly small and neutral; however, the sample comparisons we describe do not support a simple metallicity explanation; other global environmental parameters should also play a role (e.g. Haynes et al. 2010).

Fine-structure emission from atomic ions can be intrinsic to YSO sources but it can also be a result of contamination from the diffuse gas or nearby H II regions. Furthermore, at this resolution, it is difficult to separate from PAH emission, particularly for the 12.8-μm [Ne II] line. While the IRS spectra of eight objects exhibit the 18.7- and 33.5-μm [S III] emission lines (Table 3), only sources #26 and 31 show strong 8.99-μm [Ar III], 10.5-μm [S IV] and 15.6-μm [Ne III] emission lines, also present but weaker in the spectra of #08 and 22. Spectral contamination from the environment is likely given

Table 3. Detailed properties of SMC YSO candidates. We use the IRS spectra to investigate PAH, fine-structure and H_2 emission and silicate absorption/emission, and calculate the spectral index between 3.6 and 24 μm. The presence or absence of a feature is indicated by ✓ and ✗, ? indicating doubt (see discussion in the text). For PAH emission the contrast of the 11.3-μm feature with respect to the continuum is analysed in more detail: ✓✓, ✓ and ✓ indicate very strong, strong and weak emission, respectively (see text). Four objects with silicate emission are identified with ⋀. For H_2 emission, ✓? indicates objects for which only two emission lines were detected, rather than three to five. Ice species investigated are H_2O (at 3.1, 6 and 60 μm), CO (4.67 μm) and CO_2 (15.2 μm). The optical ionization classes are defined according to the emission lines present in the spectrum: Type I objects exhibit Balmer, Paschen and O I, Type II objects show hydrogen, O I, [N II], [O II] and [S II] emission, Type III objects show the same lines plus [O III], Type IV objects further add [S III] and finally Type V objects show all these lines plus He I emission. Some objects exhibit a stellar absorption spectrum and others only Hα in emission (see text for discussion). Objects that exhibit Hα emission broader than 300 km s^{-1} are also indicated. The next column indicates whether the object has been detected at radio wavelengths; asterisk '*' signals an extended source. The sources are classified using features in their IRS spectrum, according to two classification schemes previously applied to samples of LMC YSOs (Seale et al. 2009; Woods et al. 2011). The last column provides the luminosities determined from the SED fits. All sources are classified as YSOs (Section 5), except for source #19 that is a D-type symbiotic system (Section 6).

#	PAH emission	Silicate	H_2 emission	Fine struct. emission	β 3.6–24 μm	H_2O ice 3 μm	H_2O ice 6 μm	H_2O ice 60 μm	CO ice 4.67 μm	CO_2 ice 15.2 μm	Optical type	Broad Hα	Radio source	YSO class. S09	YSO class. W11	L (10^3 $L_\odot$)
01	✓	✗	✓	✓	−2.6		✗			✗	IV/V	N	Y	PE	G3	16
02	✓	✓	✓	✗	−2.4	✓	✗	✗		✓	Only Hα emission	Y	Y	S	G1	19
03	✓	✓	✓?	✗	−2.2	✓	✓	✓	✗	✓	V	N	Y	S	G1	61
04	✓	✗	✓	✗	−1.6		✗			✗	II	Y	N	P	G3	2.3
05	✓	⋀	✓	✗	−1.5		✓			✓	Absorption lines		N	O	G1	1.6
06	✓	✓	✓	✗	−2.2	✓	✓	✓		✓	Absorption lines		N	S	G1	5.8
07	✓✓	✗	✓	✗	−1.7		✗			✗	II	N	N	P	G3	4.2
08	✓	✗	✓	✓	−3.0		✗			✓	V	N	Y*	PE	G1	1.9
09	✓	✗	✓	✓	−2.5		✗			✗	IV/V	N	Y	PE	G3	7.9
10	✓	✗	✓	✗	−3.0		✗			✗	Only Hα emission	Y	Y	P	G3	33
11	✓✓	✗	✓	✗	−1.8		✗			✗	Only Hα emission	Y	N	P	G3	2.2
12	✓✓	✗	✓	✗	−2.5		✗			✗	III	N	N	P	G3	2.3
13	✓	✗	✓	✓	−3.1		✗			✓	IV	N	N	PE	G1	22
14	✓	⋀	✓?	✗	−2.1		✗			✗	Only Hα emission	Y	N	O	G4	1.8
15	✓	✗	✓	✓	−3.1		✗			✗	V	N	Y*	PE	G3	21
16	✓	✗	✓	✗	−3.1		✗			✗	Only Hα emission	Y	N	P	G3	12
17	✓	✓	✓?	✗	−1.7	✓	✓	✓	✗	✓	Only Hα emission	Y	N	S	G1	22
18	✗	✓	✗	✗	−2.2	✓	✓	✗	✗	✓	Only Hα emission	Y	N	S	G1	28
19	✗	⋀	✗	✗	−3.2		✗			✗	III-V	Y	N	Not a YSO		34
20	✓	⋀	✓?	✗	−1.8		✗			✗	I	Y	N	O	G4	1.5
21	✓	✗	✓	✗	−2.9		✗			✓	II	N	N	P	G1	11
22	✓	✗	✓	✓	−2.2	✓	✗			✓	IV/V	Y	N	PE	G1	9.1
23	✓✓	✗	✓	✗	−2.9		✗			✗	Only Hα emission	N	N	P	G3	14
24	✓	✓?	✓	✗	−1.5		✗			✗	No spectrum		N	P	G2/G3	4.5
25	✓	✗	✓	✗	−2.8		✗			✗	IV	N	Y	P	G3	17
26	✓	✗	✓	✓	−2.3		✗			✗	V	N	Y	PE	G3	12
27	✓✓	✗	✓	✗	−2.6		✗			✗	II	N	N	P	G3	3.3
28	✓	✓	✓?	✗	−2.7	✗	✗	✗		✗	IV/V	N	Y	S	G2	140
29	✓	✓	✓	✗	−2.7		✓			✓	Absorption lines		N	S	G1	10
30	✓	✓?	✓	✗	−1.0	✓	✗	✗		✗	I	Y	N	P	G1	7.9
31	✓	✗	✓?	✓	−2.7		✗	✗		✗	No spectrum		Y*	PE	G3	6.7
32	✓	✓	✓	✗	−1.6	✓	✗			✓	I/II	Y	N	S	G1	3.5
33	✓	✓	✓?	✗	−1.4	?	✗	✗	✗	✗	I/II	Y	N	S	G2	26
34	✓	✓	✓?	✗	−1.8	✓	✗	✗	✗	✓	Only Hα emission	Y	N	S	G1	23

the location of many targets in the vicinity of known H II regions (Fig. 1 and further discussion in Section 5.1).

4.4 H_2 emission

H_2 emission is expected to be ubiquitous in YSO environments. However, only when the molecular gas is heated to a few hundred K is H_2 emission observable. Both UV radiation (released by the accretion process, the emerging star itself or from nearby environment) and shocks (created as outflows interact with the quiescent molecular cloud) can produce warm H_2 gas (for a review see Habart et al. 2005). Extinction-corrected excitation diagrams can be used to diagnose the gas conditions and constrain the excitation mechanism of massive YSOs (e.g. van den Ancker, Tielens & Wesselius 2000).

Several emission lines due to molecular hydrogen are included in the IRS range. In particular pure rotational 0–0 transitions occur at 5.51 S(7), 6.10 S(6), 6.91 S(5), 8.03 S(4), 9.66 S(3), 12.28 S(2), 17.03 S(1) and 28.22 μm S(0). The S(6) and S(4) transitions are difficult to disentangle from the PAH emission, the S(5) line can be contaminated by [Ar III] at 6.99 μm, and the S/N ratio in the region of the S(7) line is sometimes low. Nevertheless we have identified H_2 emission in the spectra of the majority of objects in our sample: for 24 sources three or more unblended emission lines are measured (✓ in Table 3), while for eight sources only two weak lines are identified (✓? in Table 3). There are two sources with no detectable H_2 emission lines (✗ in Table 3).

Since the lines discussed here are optically thin (Parmar, Lacy & Achtermann 1991), the measured line intensities can be used to derive the total number of molecules and the rotational temperature. For excited H_2 gas in local thermodynamic equilibrium (LTE) at a single temperature, the density $N(H_2)$ and temperature T_{rot} are described by the Boltzmann distribution (in logarithmic form):

$$\ln\left(\frac{N(J)}{g_J}\right) = -\frac{E(J)}{k_B T_{rot}} + \ln\left(N(H_2)\frac{hcB}{2k_B T_{rot}}\right), \quad (1)$$

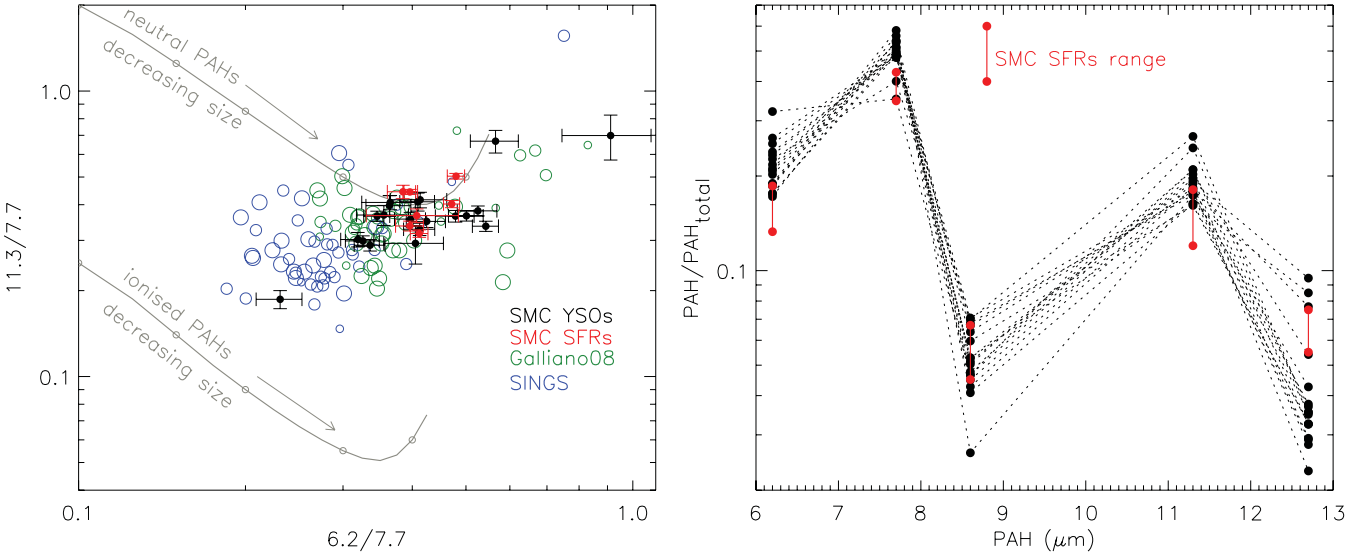

Figure 8. PAH properties towards SMC sources. Left: 11.3/7.7 intensity ratio against 6.2/7.7 ratio. The different samples are SMC YSO candidates (this work, filled black circles), SMC SFRs (Sandstrom et al. 2012, filled red circles), a sample of galaxies and individual SFRs (Galliano et al. 2008, green circles) and finally the SINGS galaxies (Smith et al. 2007, blue circles). Symbol sizes represent three metallicity ranges: 12 + log(O/H) = 7.7–8.2, 8.2–8.7 and 8.7–9.2 dex. Solid grey lines indicate model trends for neutral and ionized PAHs of varying grain sizes adapted from Draine & Li (2001). Right: PAH intensity carried in each band normalized to total PAH intensity.

where g_J, $E(J)$ and $N(J)$ are, respectively, the statistical weight, energy and column density of the upper J level,[2] $B = 59.33$ cm^{-1} is the H_2 molecular constant. The statistical weight is given by $g_J = g_S(2J + 1)$, where the nuclear spin weight $g_S = 3$ for *ortho*-states (odd J) and $g_S = 1$ for *para*-states (even J) – we assume an equilibrium *ortho*-to-*para* ratio opr = 3, appropriate for gas with $T > 300$ K (e.g. Sternberg & Neufeld 1999). The column density $N(J)$ is derived from the measured extinction-corrected line intensities $I(J)$ as follows:

$$N(J) = 4\pi \frac{\lambda}{hc} \frac{I(J)}{A_J \Omega}, \quad (2)$$

where A_J are the transition probabilities and Ω is the beam size in steradian. More details on the method and values of relevant constants and energies can be found in the literature (e.g. Parmar et al. 1991; Bernard-Salas & Tielens 2005; Barsony et al. 2010).

To estimate the beam size Ω we multiply the FWHM of the PSF by the slit width. Slit widths are 3.6 and 10.6 arcsec, respectively, for SL and LL. The FWHM is measured from the two-dimensional PSF as a function of wavelength, ranging from 1.9 arcsec at 5.51 μm to 7 arcsec at 28.2 μm. The PSFs are those used for the optimal extraction of the spectra (Section 3.1 and Lebouteiller et al. 2010). We choose to have a beam size that increases with wavelength since some objects are marginally resolved, and in such complex environments at these large distances, the IRS spectra do sample different sized emission regions.

To estimate the extinction, we use PAHFIT (Smith et al. 2007) since it disentangles the contributions from the dust and PAH emission; the code returns fully mixed relative extinctions that can be used to correct the observed line intensities. The extinction corrections are largest for the S(3) 9.66-μm line, but still usually small for the targets in the present sample.

[2] In the notation 0–0 S(J'), J' indicates the lower rotational state.

Fig. 9 shows examples of H_2 excitation diagrams for several SMC sources, open and full circles represent, respectively, uncorrected and extinction-corrected measurements. For each object with more than two H_2 emission line measurements a straight line can be fitted to the data points, allowing the determination of the temperature and column density, using equation (1). It can be seen from the examples in Fig. 9 that the weighted column density for S(0) is always high compared to the measurements for other lines. This is to be expected since S(0) has the lowest energy, therefore it probes the reservoir of H_2 that is too cool to excite any other transitions. We discuss S(0) emission later.

Whenever possible we perform two fits: the first makes use of all good measurements available except S(0), the second makes use only of S(1), S(2) and S(3) (red and green lines in Fig. 9, respectively). The reason to perform the second fit to the three transitions closest in energy level is to investigate possible deviations from the simple single temperature scenario, as it could be expected if a smaller column of hotter H_2 is also present (van den Ancker et al. 2000). In general, a single-temperature Boltzmann distribution provides good fits to the weighted column densities within the measurement uncertainties. First, this validates the adopted wavelength-dependent beam sizes, rather than a single beam size. Furthermore, the column density of the S(2) line, the only *para*-state we are able to measure, does not deviate from those of the *ortho*-states, suggesting that the adopted LTE value of opr = 3 is adequate. The two fits described above (see examples in Fig. 9) result in temperatures that agree within 1.5σ for all objects except for source #06 (5σ difference). This again shows that a single temperature fit is appropriate to describe the molecular gas responsible for most of the emission. The exception is source #06, for which the excitation diagram and fitted temperatures suggest the presence of a hotter H_2 contribution (top left-hand panel in Fig. 9).

For the fits to four or five data points the median temperature is $T_{rot} = 594 \pm 99$ K (range 439–812 K), while for the three-measurement fits the median temperature is $T_{rot} = 562 \pm 100$ K

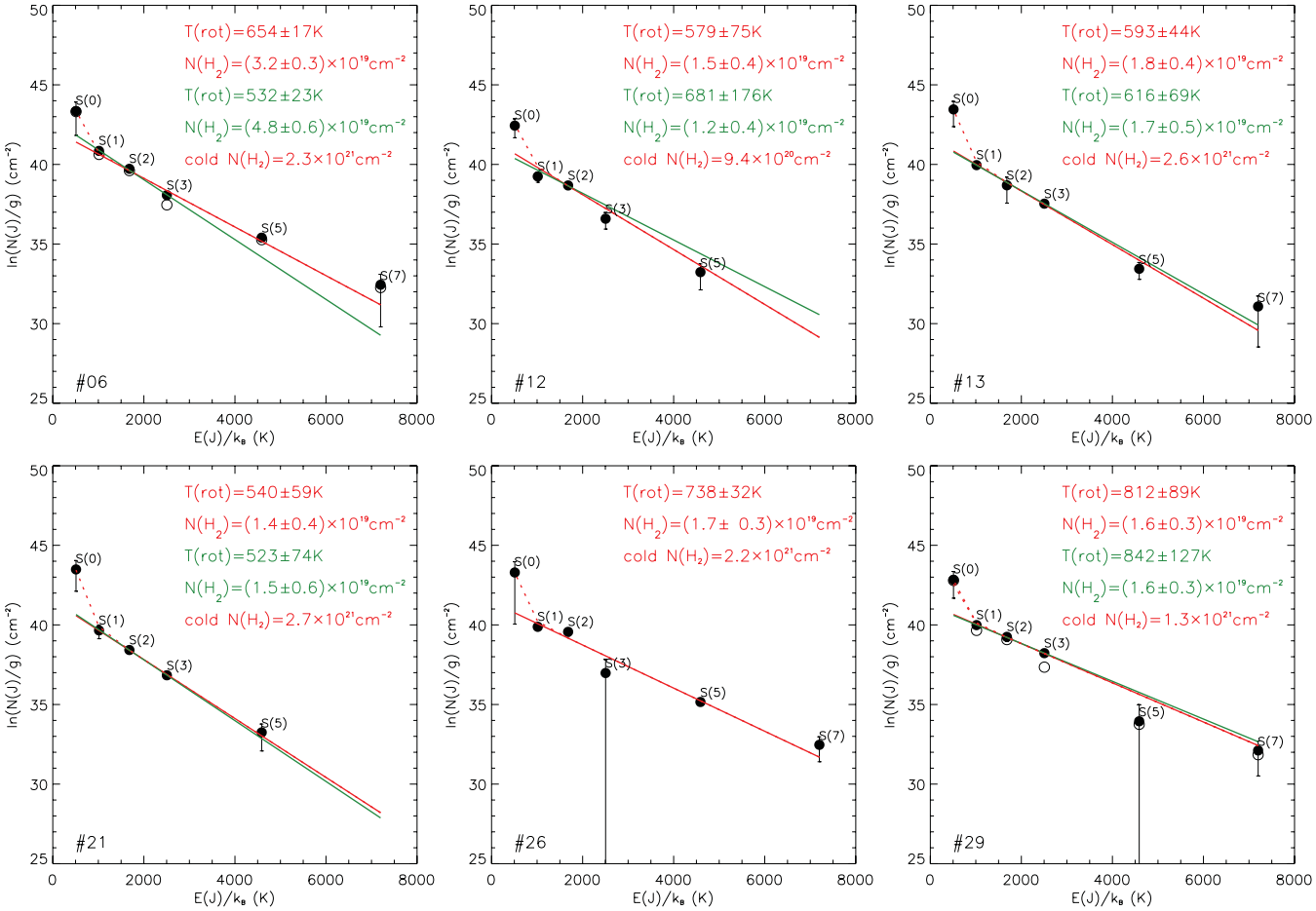

Figure 9. H_2 excitation diagrams for selected SMC YSO candidates. For sources #06 and 29, the line intensities are corrected for extinction (see text for details). The results of two fits are displayed when available: a fit to all measured lines (red), or a fit to only S(1) to S(3) (green). For each fit, the derived rotational temperature $T_{\rm rot}$ and column density $N(H_2)$ are indicated. The dashed red line shows the contribution of a cold H_2 component, with fixed temperature $T_{\rm rot} = 100$ K.

(range 439–843 K). The median densities are, respectively, $N(H_2) = 1.8 \pm 0.9 \times 10^{19}$ cm^{-2} (range 0.6–3.8 $\times$ 10^{19} cm^{-2}) and $N(H_2) = 1.6 \pm 1.5 \times 10^{19}$ cm^{-2} (range 0.7–4.8 $\times$ 10^{19} cm^{-2}). When compared to a sample of Galactic YSOs (van den Ancker 1999) covering the same luminosity range, the rotational temperatures are similar. However, the column densities for the SMC YSO candidates tend to be smaller by a factor of 3, typically $\sim$1.7 $\times$ 10^{19} cm^{-2} rather than $\sim$5 $\times$ 10^{19} cm^{-2}.

Neither H_2 temperature or column density seem correlated with source luminosity for the SMC and Galactic samples. For sources with strong PAH emission, H_2 intensity (using S(3) as a proxy) is largest for sources with the largest total PAH intensity. However, there is no distinction between the derived H_2 properties for sources with ice and silicate absorption, and PAH emission. Since, as discussed in the next section, these features trace the YSO evolution, this implies that H_2 emission does not seem to correlate with evolutionary stage, neither in SMC nor Galactic samples (see also Forbrich et al. 2010).

As already mentioned, the weighted column density for S(0) is too large when compared to the other transitions, suggesting a reservoir of quiescent cold gas. Since this cold component is poorly constrained, we opt to fix its temperature at 100 K (e.g. Lahuis et al. 2010) and simply adjust the column density to match the observed $N(0)/g(0)$. We do not constrain opr, expected to be $\sim$1.6 for this temperature (Sternberg & Neufeld 1999). The contribution of this cold component, added to the main warm component, is shown in Fig. 9 (dashed red line). The fitted column densities are in the range $N(H_2) = 0.4$–3.8×10^{21} cm^{-2} (median density 2.3 $\times$ 10^{21} cm^{-2}). Therefore the contribution of the cold molecular gas reservoir is substantial, even though its signature is only observed in the S(0) emission.

On their own the column densities and temperatures derived in this way cannot constrain the excitation mechanism: there is significant overlap in the parameter range predicted for shocked and photodissociated gas (Bernard-Salas & Tielens 2005; Habart et al. 2005), even though higher temperatures are suggestive of shocked gas. Other diagnostics are available: PAH emission suggests photodissociated gas while [S I] emission at 25.25 μm indicates shocked gas. As already discussed, the majority of the sources in the sample exhibit PAH emission. We do not detect the [S I] line in any of the spectra. Even though it is likely that both mechanisms contribute to H_2 excitation, the available evidence suggests that radiation is the dominant excitation mechanism in these SMC sources. Since H_2 emission is also excited in photodissociation regions (PDRs; e.g. Habart et al. 2005), it is possible that there is an environmental contribution to emission observed towards the YSO candidates.

This may be true in particular for the warmer component, the cool component originating from the denser more shielded regions.

4.5 Optical spectra

In this section we discuss the optical emission-line spectra of 20 SMC sources – for the remaining 14 sources either no optical spectrum could be obtained, the spectrum is not associated with the IR source, or only Hα emission is detected (Section 3.5.1). In H II regions and their precursors surrounding young massive stars, common optical emission lines are due to permitted hydrogen (Balmer and Paschen) and O I emission (8446 Å) and numerous forbidden emission lines: [O I] (6300 Å), [O II] (3727, 7322, 7332 Å), [N II] (6548, 6583 Å), [S II] (6717, 6731 Å), as well as [O III] (4363, 4959, 5007 Å) and [S III] (9068, 9530 Å). If the object is massive enough (early O-type source) an appreciable He^+ ionization zone develops (e.g. Draine 2011) and He I recombination emission is detected (at 3888, 4471, 5875, 6678, 7065 Å). Hydrogen emission in YSOs originates both from the accretion columns and outflows. Forbidden line emission can also originate in the relatively low-density environments of outflowing jets or winds (e.g. White & Hillenbrand 2004) but it is also observed in PDR-like environments (Störzer & Hollenbach 2000). Velocity information can distinguish between the two excitation scenarios (e.g. Störzer & Hollenbach 2000) but our spectra have insufficient velocity resolution (e.g. $\sim$205 km s^{-1} at the position of Hα).

Fig. D1 shows the optical spectra of the 32 SMC sources; the last panel shows the rich spectrum of source #26 with the emission lines identified. We implement a classification scheme that relies on the detection of progressively higher excitation energy emission lines. Thus the classification reflects the harshness of the near-YSO environment. Type I objects exhibit emission from the Balmer and Paschen series and O I, Type II objects add collisionally excited lines of [O II], [N II] and [S II]. Type III objects exhibit also [O III] emission, Type IV objects add [S III], and finally Type V objects show prominent He I recombination emission. The type breakdown of the sample of 20 sources is as follows: two Type I, two Type I/II (only Hα and [S II] emission, see below), four Type II, one Type III, two Type IV, four Type IV/V (a single He I line identified) and four Type V; the optical spectrum of source #19 is discussed in Section 5.

Of the 10 sources classified as Type IV or V, all sources exhibit PAH emission and seven show IR fine-structure emission. Most are also detected at radio wavelengths (see Table 3). Conversely, all the objects that show IR fine-structure emission, and for which we have an optical spectrum, are classified as Type IV–V. These 10 sources have the highest luminosities ($L \gtrsim 10^4\,L_\odot$), as determined from SED fits (Table 3). This builds a consistent picture of these objects representing more evolved YSO candidates, i.e. ultracompact H II regions. However, four of these sources do exhibit ice features in their IRS spectrum (see next section), suggesting deeply embedded objects.

As mentioned above the optical spectra do not have enough resolution to investigate the origin of the emission features. However, we have looked for broadening of the line profiles that would indicate infall and/or outflow activity. In fact, a number of sources show evidence of broadened Hα profiles: 13 sources (indicated in Table 3) have FWHM in the range 300–440 km s^{-1}. Furthermore, two sources (#32 and 33) exhibit extremely broad profiles (FWHM $>$ 600 km s^{-1}) with line centroids shifted to $\sim-$ 200 km s^{-1}. These two sources are classified as Type I/II, since besides Hα only [S II] emission is detected (equally broad). The profiles clearly suggest an origin in optically thick winds in the environments of these two YSO candidates.

5 SOURCE CLASSIFICATION

All but one of the sources in the SMC sample are YSOs, based on the IR spectral properties analysed in the previous section: ice absorption, silicate absorption or emission, PAH and H_2 emission, red continuum and SED fitting. Boyer et al. (2011) tentatively proposed that nine of these sources are very dusty evolved stars, based on *Spitzer* photometric criteria. Seven of those sources show ice absorption and two others show silicate absorption, and are thus clearly SMC YSOs. The only non-YSO source in our sample (#19) is discussed in Section 6.

Two YSO spectral classification schemes have been recently developed and applied to YSO samples in the LMC. Seale et al. (2009) performed an automated spectral classification of YSOs using principal component analysis to identify the spectral features that dominate the spectra; the following classes are relevant for the SMC sample: S objects show spectra dominated by silicate absorption, P and PE objects show PAH emission and IR fine-structure emission and O objects show silicate emission. There is an evolutionary sequence associated with this classification in the sense that objects with S spectra are more embedded while P and PE spectra are associated with more evolved compact H II regions. We have classified the objects in the YSO sample using this classification scheme (Table 3).

The other classification scheme was introduced by Woods et al. (2011): objects are classified in groups depending on spectral features present in the spectrum, from G1 (ice absorption), G2 (silicate absorption), G3 (PAH emission) and G4 (silicate emission). The main difference from the Seale classification is the usage of ice absorption as a clear indicator of a very cool envelope, identifying the earliest embedded sources. Thus we discuss the classification of the SMC YSOs using this method in more detail (Table 3).

5.1 Embedded YSOs

There are 14 SMC sources classified as belonging to group G1, i.e. exhibiting ice absorption. Most G1 sources (eight) also exhibit silicate absorption, but this is not always the case: source #05 shows a silicate emission feature (see Section 5.3), while sources #08, 13, 21, 22 and 30 show strong PAH emission that could mask weak silicate absorption – we suspect this to be the case particularly for #30. Of the aforementioned 14 sources, 10 show definite H_2 emission, three have weak H_2 emission and one source shows no H_2 emission. Eight G1 sources have weak or no PAH emission features while six sources show strong emission (three of which also show fine-structure emission). Of the 14 G1 sources, three have no optical spectra and seven exhibit either only Hα or low-excitation emission lines. Another four G1 sources, namely #03, 08, 13 and 22 are classified as Type IV–V based on the counterpart optical spectrum; except for #03, these sources also show strong PAH and fine-structure emission.

As already mentioned the presence of ice and silicate absorption features indicates the presence of an embedded YSO while PAH, and forbidden and fine-structure emission hint at a compact H II region. However, many sources exhibit both ice absorption and emission features. Galactic YSOs can exhibit both PAH and fine structure emission and ice absorption (e.g. W3 IRS5 and MonR2 IRS2; Gibb et al. 2004), and many LMC YSOs with CO_2 ice signatures also exhibit PAH emission (Oliveira et al. 2009; Seale et al. 2011). The

same is true for the SMC sample, with half the sources exhibiting mixed property spectra. Dust and ice features originate from the cooler regions of the embedded YSO envelope. On the other hand PAH and fine-structure emission can be excited not only by the emerging YSO itself but also by neighbouring massive stars, and more generally in the larger H II complexes in which many YSOs reside. At the LMC and SMC distances (respectively ∼50 and 60 kpc; Ngeow & Kanbur 2008; Szewczyk et al. 2009), it becomes impossible to disentangle the contributions of the different physical environments. The spatial resolution of a IRS spectrum varies typically from 3 to 10 arcsec, corresponding to 1 to 3 pc in the SMC, implying that very different spatial scales are sampled at different wavelengths. This makes it difficult to use spectral features to unequivocally constrain the evolutionary stage of the object.

Nevertheless the six G1 YSOs with ice and silicate absorption, weak or absent PAH emission, no fine-structure emission and quiescent optical spectra are the more embedded, earliest YSOs (sources #02, 17, 18, 29, 32 and 34). Sources #28 and 33 (the two G2 sources) and #24 (G2/G3 source) are still relatively embedded (silicate is seen in absorption) but no ice absorption is detected, suggesting warmer envelopes. At these early stages the YSO has little influence on the physical conditions in its envelope. The remaining G1 YSOs (sources #03, 06, 08, 13, 21, 22 and 30) show both ice absorption and PAH emission in their spectra. These objects are likely more evolved since the PAH and fine-structure emission indicates that the YSO is able to emit copious amounts of UV radiation, while still retaining enough of its cold envelope responsible for the absorption features (with the possible caveat that #06, 08 and 13 sit in particularly complex environments, see Fig. 1). At this stage a (ultra-)compact H II region is emerging.

5.2 PAH-dominated YSOs

There are 14 sources in the sample that we classify as G3, indicating that PAH emission is the noticeable feature in their steep IRS spectra. Five of the sources have fine-structure emission as well. In terms of counterpart optical spectra, there does not seem to be a strong relation between PAH emission and optical type (Section 4.5), since four sources only exhibit Hα emission, three sources are Type II, one source is Type III and five sources are Type IV–V (for one further source we have no spectrum).

These 14 G3 sources are the most evolved in the sample, with the IR spectral features clearly indicating the presence of a well developed compact H II region, in the process of clearing out the remnant dusty envelope.

5.3 Intermediate-mass YSOs

In this subsection we discuss the three YSOs that exhibit silicates in emission in their IRS spectrum, classified as G4 (sources #14 and 20) and source #05 that also shows ice absorption. The SED of #20 is steep but flattens considerably above 20 μm. In fact, its IRS spectrum is very similar to that of the Galactic HAeBe star IRAS 04101+3103 (Furlan et al. 2006), including the weak PAH emission. A spectrum and photometry of the optical counterpart have been analysed by Martayan et al. (2007, identified as SMC5_037102); they suggest that this source is a Herbig B[e] star, based on the presence of numerous Fe II and [Fe II] emission lines and accretion signatures in the Balmer lines. We cannot detect the iron lines in our low-resolution optical spectrum, but we confirm that Hα is broad. The fact that the continuum flux rises from the J_s band to 70 μm suggests that a tenuous dusty envelope remains.

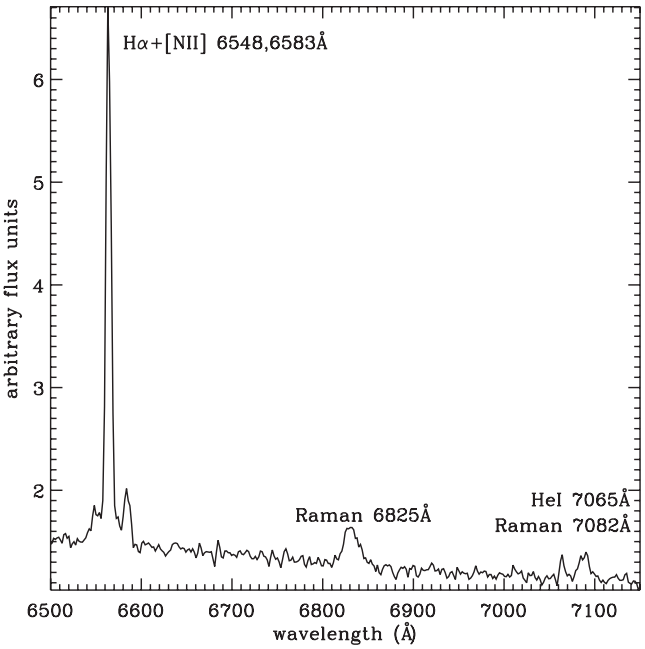

Figure 10. Detail of the optical spectrum of #19, showing the prominent Raman emission lines.

The SEDs of sources #05 and 14 both have silicate emission and steep IRS spectra throughout. Source #14 shows strong PAH emission, while #05 shows weak PAH and H_2 emission as well as H_2O and CO_2 ice absorption. Furlan et al. (2008) describe a number of Galactic objects that they classify as evolved Class I YSOs; these objects still retain a low-density envelope, tenuous enough to reveal the thick accretion disc and the central star. The observed properties of sources #05, 14 and 20 suggest the same classification, with #20 the more evolved of the three sources. Note that the evolutionary scenario discussed in the previous subsection refers to massive star formation, while the present discussion addresses the evolution of intermediate-mass stars.

6 A D-TYPE SYMBIOTIC STAR IN THE SMC

Source #19 is a clear oddity since its optical spectrum (Figs 10 and D1) shows a blue continuum with broad emission lines at 6825 and 7082 Å, as well as Hα, [N II] and [O III] emission, with weak He I emission at 5875 and 7065 Å, and a tentative detection of He II emission at 4686 Å. Fig. C1 shows that next to the IR source there is a bright blue star. By looking at the 2D spectrum (before extraction) we see that the continuum and emission line contributions are offset by about 2 arcsec, in the sense that the continuum originates from the bright blue source, while the emission lines originate from the IR-bright source.

The emission features at 6825 and 7082 Å are identified as Raman scattering of the O VI resonance photons at 1032 and 1038 Å by neutral hydrogen; these lines are usually observed in the spectra of symbiotic binary systems (e.g. Schmid 1989). Symbiotic objects are interacting binaries, in which an evolved giant transfers material to a much hotter, compact companion; according to the classification criteria of Belczyński et al. (2000), the presence of the Raman scattering lines and optical emission lines is enough to identify a symbiotic system, even if no features of the cool giant are found. Recently it has been proposed that massive luminous B[e] stars may also exhibit Raman scattering lines (Torres et al. 2012).

Source #19 has a steep SED from 2 to 20 μm (Fig. 3). Above 20 μm the IRS spectrum flattens considerably and the source becomes fainter at 70 μm. This indicates the presence of a significant amount of (not very cold) dust. It shows a prominent silicate emission feature, suggestive of unprocessed dust, and no PAH emission. This is consistent with this object being a dusty (D-type) symbiotic star (Angeloni et al. 2007). The optical spectrum shows no molecular TiO bands that would indicate the presence of the red giant. This is another common feature of D-type symbiotic stars: the reddened asymptotic giant branch star is not detected at optical wavelengths but it reveals itself at IR wavelengths (e.g. Corradi et al. 2010). In terms of photometry, source #19 has a colour $J_s - K_s \sim 1.1$ mag, and it has not been identified as variable. Given the presence of Raman scattering and H and He emission, its brightness at 70 μm and the properties of its IRS spectrum, we propose that #19 is a D-type symbiotic system in the SMC. This adds to the six S-type (dustless) symbiotic systems already confirmed in the SMC (Mikołajewska 2004).

7 SUMMARY

We present a multiwavelength characterization of 34 YSO candidates in the SMC. The target objects are bright in the 70-μm MIPS band, and the selection strategy aims at excluding both evolved star and bright galaxy interlopers. The basis of the analysis described here are low-resolution IR spectra obtained with *Spitzer*-IRS, supported by *Spitzer* photometry (IRAC and MIPS), near-IR photometry, 3–5 μm spectroscopy, low-resolution optical spectroscopy and radio data. The objective is to confirm the YSO nature of these SMC sources and characterize them. We summarize here our most important results.

(i) Of the 34 sources 33 are spectroscopically identified as YSOs in the SMC. This now sizable sample adds to the SMC YSOs previously identified by van Loon et al. (2008, 2010) and Oliveira et al. (2011).

(ii) One object (source #19) is identified as a D-type symbiotic system, based on the presence of Raman emission at 6825 and 7082 Å and nebular emission lines, as well as prominent silicate emission. This is the first D-type symbiotic identified in the SMC.

(iii) 14 YSOs exhibit ice absorption in their spectra. We analyse H_2O and CO_2 ice column densities; we suggest the presence of a significant H_2O column density threshold for the detection of CO_2 ice in the SMC. The observed differences between Galactic, LMC and SMC samples can be explained as due to metallicity.

(iv) We analyse PAH emission, which is ubiquitous in the sample. We confirm previous results from Sandstrom et al. (2012) who propose that the grains responsible for PAH emission in the SMC are mostly small and neutral. Based on the comparison of different published samples, the observed PAH properties cannot be solely determined by metallicity.

(v) Many objects show narrow emission lines in the IRS spectra attributed to molecular hydrogen. Excitation diagrams constrain the rotational temperature and H_2 column density of the bulk of the gas responsible to the emission. When compared to Galactic sources (van den Ancker 1999) the rotational temperatures are similar, but the H_2 column densities in the SMC are generally smaller. Photodissociation is the dominant excitation mechanism. There does not seem to be a clear correlation between the detection of H_2 emission and its derived properties and the evolutionary stage of the YSO. For most sources there is also a significant reservoir of colder molecular gas ($T_{rot} \sim 100$ K).

(vi) Of the 33 YSOs in our sample, 30 cover the main stages of massive YSO evolution. Based on the presence of ice and silicate absorption and weak/absent PAH emission, six YSOs are still deeply embedded. Three other embedded sources have envelopes already too warm for significant amount of ice to survive on the dust grains. A further seven sources, while still embedded (i.e. showing IR molecular absorption features), already present evidence of an emerging H II region. Finally, 14 sources exhibit spectra with the hallmarks of compact H II regions (strong PAH and fine-structure emission). Three other sources exhibit silicate emission (one shows ice absorption as well); these sources are probably sources in transition between Class I and Class II, i.e. precursors to intermediate-mass HAeBe stars that still retain a tenuous envelope.

Scheduled ground-based observations will target more YSOs with ice signatures; column density measurements and modelling of the ice profiles will help constrain the reason for the observed differences in ice properties for samples of subsolar metallicity. Some of the SMC YSOs are targets of an ongoing *Herschel* spectroscopy program that aims to constrain the role of the main cooling agents (gas-phase CO and water, OH, [C II] and [O I]) and obtain an inventory of the species present both in gas and solid phases.

ACKNOWLEDGMENTS

We thank the staff at ESO's Paranal and La Silla Observatories for their support during the observations. This work is based on observations made with the *Spitzer Space Telescope*, which is operated by the Jet Propulsion Laboratory, California Institute of Technology under contract with NASA. This research has made use of the SIMBAD data base, operated at CDS, Strasbourg, France. We thank the referee for helpful comments.

REFERENCES

André P., Montmerle T., 1994, ApJ, 420, 837
Angeloni R., Contini M., Ciroi S., Rafanelli P., 2007, AJ, 134, 205
Banerji M., Viti S., Williams D. A., Rawlings J. M. C., 2009, ApJ, 692, 283
Barsony M., Wolf-Chase G. A., Ciardi D. R., O'Linger J., 2010, ApJ, 720, 64
Belczyński K., Mikołajewska J., Munari U., Ivison R. J., Friedjung M., 2000, A&AS, 146, 407
Bernard-Salas J., Tielens A. G. G. M., 2005, A&A, 431, 523
Bolatto A. D. et al., 2007, ApJ, 655, 212
Boogert A. C. A. et al., 2008, ApJ, 678, 985
Boyer M. L. et al., 2011, AJ, 142, 103
Corradi R. L. M. et al., 2010, A&A, 509, 41
Crawford E. J., Filipović M. D., de Horta A. Y., Wong G. F., Tothill N. F. H., Drasković D., Collier J. D., Galvin T. J., 2011, Serbian Astron. J., 183, 95
Draine B. T., 2011, Physics of the Interstellar and Intergalactic Medium. Princeton Univ. Press, Princeton, NJ
Draine B. T., Li A., 2001, ApJ, 551, 807
Eisenhardt P. R., Stern D., Brodwin M., 2004, ApJS, 154, 48
Fazio G. G. et al., 2004, ApJS, 154, 10
Filipović M. D., Haynes R. F., White G. L., Jones P. A., 1998, A&AS, 130, 421
Forbrich J., Tappe A., Robitaille T. P., Muench A. A., Teixeira P. S., Lada E., Stolte A., Lada C. J., 2010, ApJ, 716, 1453
Furlan E. et al., 2006, ApJS, 165, 568
Furlan E. et al., 2008, ApJS, 176, 184
Galliano F., Madden S. C., Tielens A. G. G. M., Peeters E., Jones A. P., 2008, ApJ, 679, 310
Gerakines P. A., Schutte W. A., Greenberg J. M., van Dishoeck E. F., 1995, A&A, 296, 810
Gerakines P. A. et al., 1999, ApJ, 522, 357

Gibb E. L., Whittet D. C. B., Boogert A. C. A., Tielens A. G. G. M., 2004, ApJS, 151, 35
Gordon K. et al., 2011a, AJ, 142, 102
Gordon K. et al., 2011b, http://data.spitzer.caltech.edu/popular/sage-smc/20110429_enhanced/documentation/sage-smc_delivery_apr11.pdf
Gruendl R. A., Chu Y.-H., 2009, ApJS, 184, 172
Habart E., Walmsley M., Verstraete L., Cazaux S., Maiolino R., Cox P., Boulanger F., Pineau des Forêts G., 2005, Space Sci. Rev., 119, 71
Haynes K., Cannon J. M., Skillman E. D., Jackson D. C., Gehrz R., 2010, ApJ, 724, 215
Hoare M. G., Kurtz S. E., Lizano S., Keto E., Hofner P., 2007, in Reipurth B., Jewitt D., Keil K., eds, Protostars and Planets V. University of Arizona Press, Tucson, p. 181
Houck J. R. et al., 2004, ApJS, 154, 18
Jørgensen J. K. et al., 2006, ApJ, 645, 1246
Kato D. et al., 2007, PASJ, 59, 615
Keller L. D. et al., 2008, ApJ, 684, 411
Kemper F. et al., 2010, PASP, 122, 683
Kessler-Silacci J. et al., 2006, ApJ, 639, 275
Lada C. J., 1987, in Peimbert M., Jugaku J., eds, Proc. IAU Symp. 115, Star Forming Regions. Reidel, Dordrecht, p. 1
Lahuis F., van Dishoeck E. F., Jørgensen J. K., Blake G. A., Evans N. J., 2010, A&A, 519, 3
Lebouteiller V., Bernard-Salas J., Sloan G. C., Barry D. J., 2010, PASP, 122, 231
Lee J.-E. et al., 2006, ApJ, 648, 491
Martayan C., Floquet M., Hubert A. M., Gutierrez-Soto J., Fabregat J., Neiner C., Mekkas M., 2007, A&A, 472, 577
Meixner M. et al., 2006, AJ, 132, 2268
Mikołajewska J., 2004, Rev. Mex. Astron. Astrofis. Ser. Conf., 20, 33
Muench A. A., Lada C. J., Luhman K. L., Muzerolle J., Young E., 2007, AJ, 134, 411
Ngeow C., Kanbur S. M., 2008, ApJ, 679, 76
Oliveira J. M. et al., 2009, ApJ, 707, 1269
Oliveira J. M. et al., 2011, MNRAS, 411, L36
Parmar P. S., Lacy J. H., Achtermann J. M., 1991, ApJ, 372, 25
Pontoppidan K. M. et al., 2008, ApJ, 678, 1005
Rho J., Reach W. T., Lefloch B., Fazio G. G., 2006, ApJ, 643, 965
Rieke G. H. et al., 2004, ApJS, 154, 25
Robinson G., Smith R. G., Maldoni M. M., 2012, MNRAS, 424, 1530
Robitaille T. P., Whitney B. A., Indebetouw R., Wood K., Denzmore P., 2006, ApJS, 167, 256
Robitaille T. P., Whitney B. A., Indebetouw R., Wood K., 2007, ApJS, 169, 328
Rodgers A. W., Conroy P., Bloxham G., 1988, PASP, 100, 626
Russell S. C., Dopita M. A., 1992, ApJ, 384, 508
Sandstrom K. M. et al., 2012, ApJ, 744, 20
Sargent B. A. et al., 2009, ApJS, 182, 477
Schmid H. M., 1989, A&A, 211, 31
Seale J. P., Looney L. W., Chu Y.-H., Gruendl R. A., Brandl B., Chen R. C.-H., Brandner W., Blake G. A., 2009, ApJ, 699, 150
Seale J. P., Looney L. W., Chen C.-H. R., Chu Y.-H., Gruendl R. A., 2011, ApJ, 727, 36
Shimonishi T., Onaka T., Kato D., Sakon I., Ita Y., Kawamura A., Kaneda H., 2010, A&A, 514, 12
Smith J. D. T. et al., 2007, ApJ, 656, 770
Spoon H. W. W., Keane J. V., Tielens A. G. G. M., Lutz D., Moorwood A. F. M., Laurent O., 2002, A&A, 385, 1022
Sternberg A., Neufeld D. A., 1999, ApJ, 516, 371
Stetson P. B., 1987, PASP, 99, 191
Störzer H., Hollenbach D., 2000, ApJ, 539, 751
Szewczyk O., Pietrzyński G., Gieren W., Ciechanowska A., Bresolin F., Kudritzki R.-P., 2009, AJ, 138, 1661
Torres A. F., Kraus M., Cidale L. S., Barbá R., Borges Fernandes M., Brandi E., 2012, MNRAS, in press (arXiv:1209.2397)
van den Ancker M. E., 1999, PhD thesis, Univ. Amsterdam
van den Ancker M. E., Tielens A. G. G. M., Wesselius P. R., 2000, A&A, 358, 1035
van Dishoeck E. F., 2004, ARA&A, 42, 119
van Loon J. Th. et al., 2005, MNRAS, 364, 71
van Loon J. Th., Cohen M., Oliveira J. M., Matsuura M., McDonald I., Sloan G. C., Wood P. R., Zijlstra A. A., 2008, AJ, 487, 1055
van Loon J. Th., Oliveira J. M., Gordon K. D., Sloan G. C., Engelbracht C. W., 2010, AJ, 139, 68
Werner M. W. et al., 2004, ApJS, 154, 1
White R. J., Hillenbrand L. A., 2004, ApJ, 616, 998
Whitney B. A. et al., 2008, AJ, 136, 18
Wong G. F., Filipović M. D., Crawford E. J., de Horta A. Y., Galvin T., Drasković D., Payne J. L., 2011a, Serbian Astron. J., 182, 43
Wong G. F. et al., 2011b, Serbian Astron. J., 183, 103
Wong G. F. et al., 2012, Serbian Astron. J., 184, 93
Woods Paul M. et al., 2011, MNRAS, 411, 1597
Zasowski G., Kemper F., Watson D. M., Furlan E., Bohac C. J., Hull C., Green J. D., 2009, ApJ, 694, 459

APPENDIX A: SUMMARY OF SPECTROSCOPIC OBSERVATIONS

Table A1 lists the spectroscopic observations available for each target. The details of the observations are described in Section 3.

APPENDIX B: SPECTRAL ENERGY DISTRIBUTIONS

In this appendix we show the SEDs of the 34 sources in the SMC sample (Fig. B1). The photometric data are compiled in Table 1,

Table A1. Summary of spectroscopic observations available for the SMC sources.

#	Optical	3–4 μm	4–5 μm	IRS	MIPS-SED
01	✓	✗	✗	✓	✗
02	✓	✓	✗	✓	✓
03	✓	✓	✓	✓	✓
04	✓	✗	✗	✓	✗
05	✗	✗	✗	✓	✗
06	✗	✓	✗	✓	✓
07	✓	✗	✗	✓	✗
08	✓	✗	✗	✓	✗
09	✓	✗	✗	✓	✗
10	✓	✗	✗	✓	✗
11	✓	✗	✗	✓	✗
12	✓	✗	✗	✓	✗
13	✓	✗	✗	✓	✗
14	✓	✗	✗	✓	✗
15	✓	✗	✗	✓	✗
16	✓	✗	✗	✓	✗
17	✓	✓	✓	✓	✓
18	✓	✓	✓	✓	✓
19	✓	✗	✗	✓	✗
20	✓	✗	✗	✓	✗
21	✓	✗	✗	✓	✗
22	✓	✓	✗	✓	✗
23	✓	✗	✗	✓	✗
24	✗	✗	✗	✓	✗
25	✓	✗	✗	✓	✗
26	✓	✗	✗	✓	✗
27	✓	✗	✗	✓	✗
28	✓	✓	✗	✓	✓
29	✗	✗	✗	✓	✗
30	✓	✓	✗	✓	✓
31	✗	✗	✗	✓	✓
32	✓	✓	✗	✓	✗
33	✓	✓	✓	✓	✓
34	✓	✓	✓	✓	✓

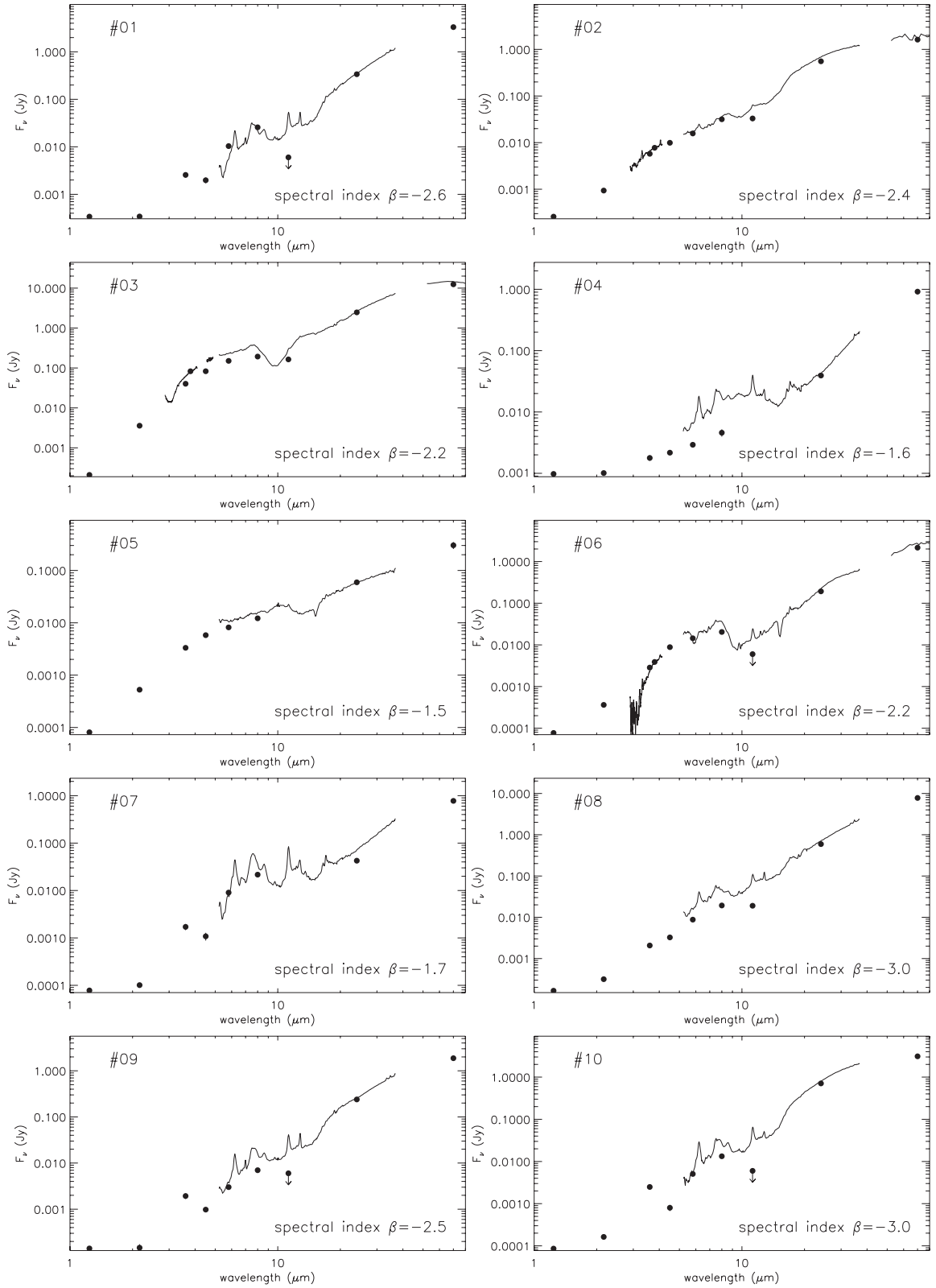

Figure B1. SEDs of the 34 SMC sources analysed in this work, showing all available IR photometry and spectroscopy. Spectral indices calculated in the range 3.6–24 μm are provided.

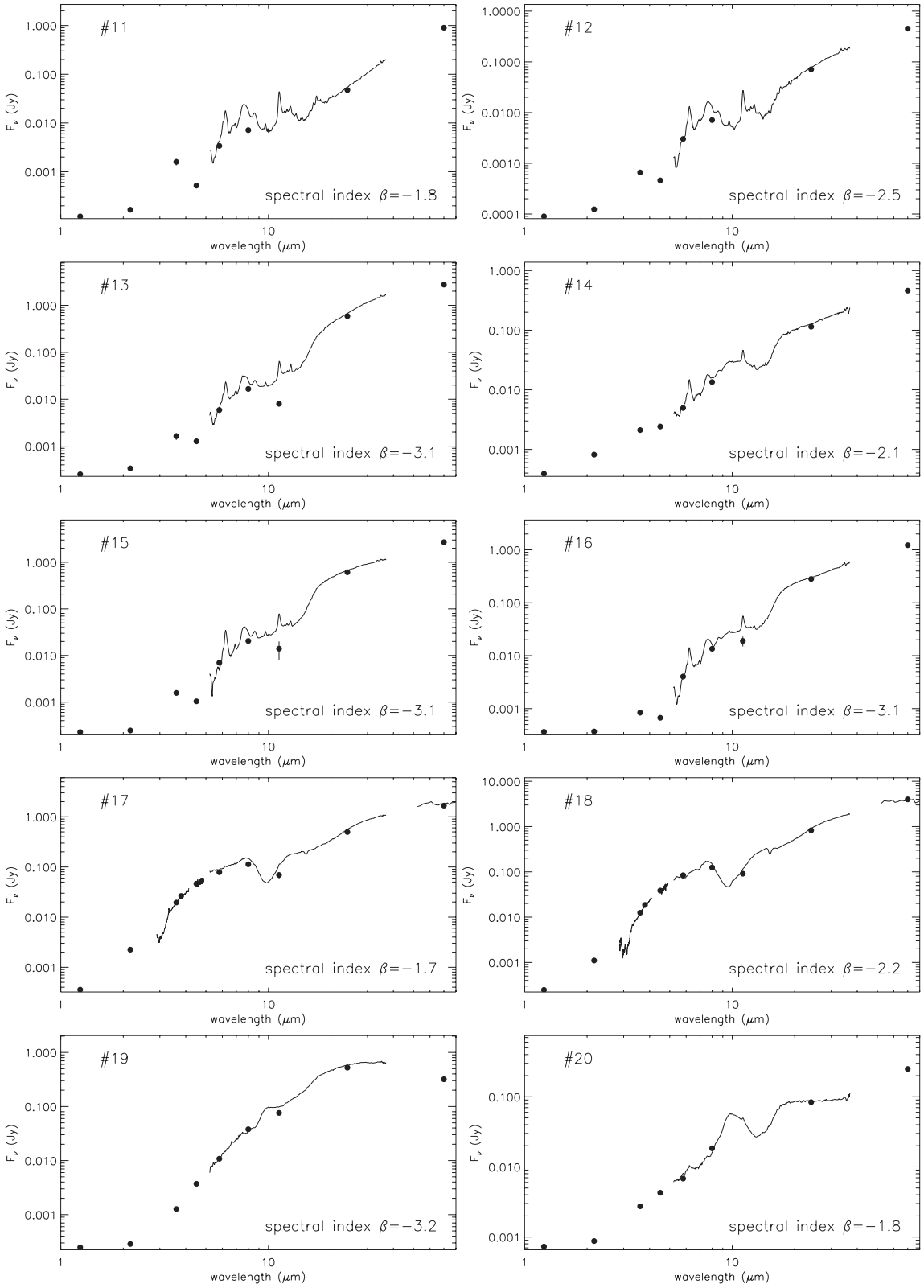

Figure B1 – *continued*

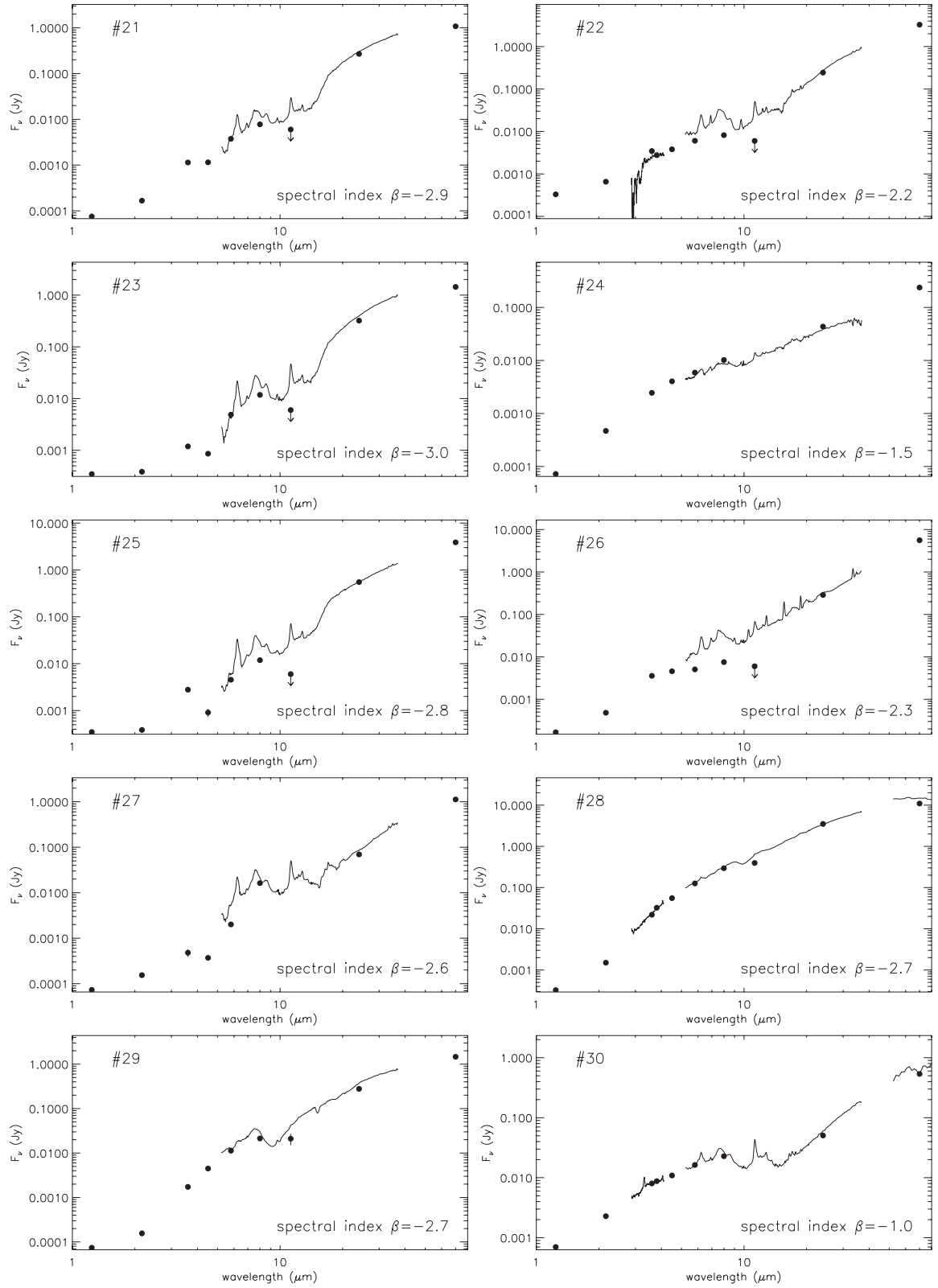

Figure B1 – *continued*

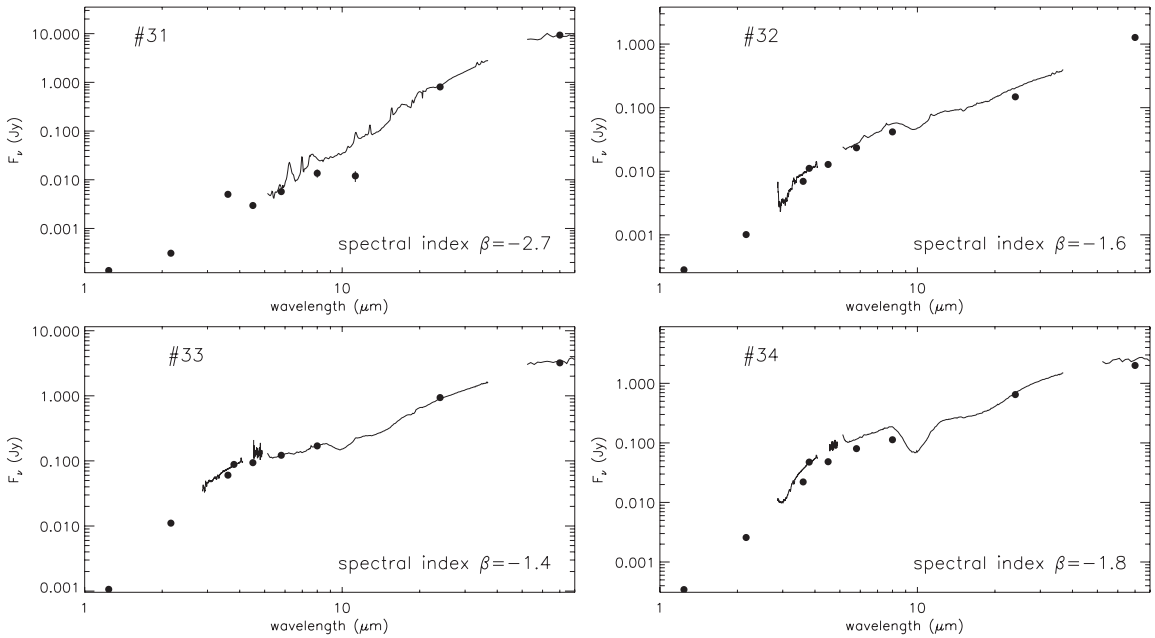

Figure B1 – *continued*

and spectra were obtained at the VLT (3–5 μm) and with *Spitzer*-IRS and MIPS-SED (Table A1). The derived spectral indices β are indicated in each panel.

APPENDIX C: NIR THUMBNAIL IMAGES

In this appendix we show thumbnail images for all sources in the SMC sample (Fig. C1). For sources #01–32, the J_sK_s composite is shown on the left and the *Spitzer* [3.6]–[5.8]–[8] composite is shown on the right – see Section 3 for details on these observations. For sources #33 and 34 we show a *JHK* colour composite, constructed using IRSF images (Kato et al. 2007). These images provide evidence of the complexity of some of the YSO candidate environments.

APPENDIX D: OPTICAL SPECTRA

In this appendix we show all the optical spectra obtained as possible counterparts of the 34 IR sources in the SMC. As described in Section 3.5.1, the observed optical source is not always the correct counterpart for the IR source. No optical counterparts were found for sources #05, 06, 24, 29 and 31. The spectra form the basis of our optical classification scheme, using several emission lines. The last panel of Fig. D1 shows the identifications of the lines discussed in this work for source #26.

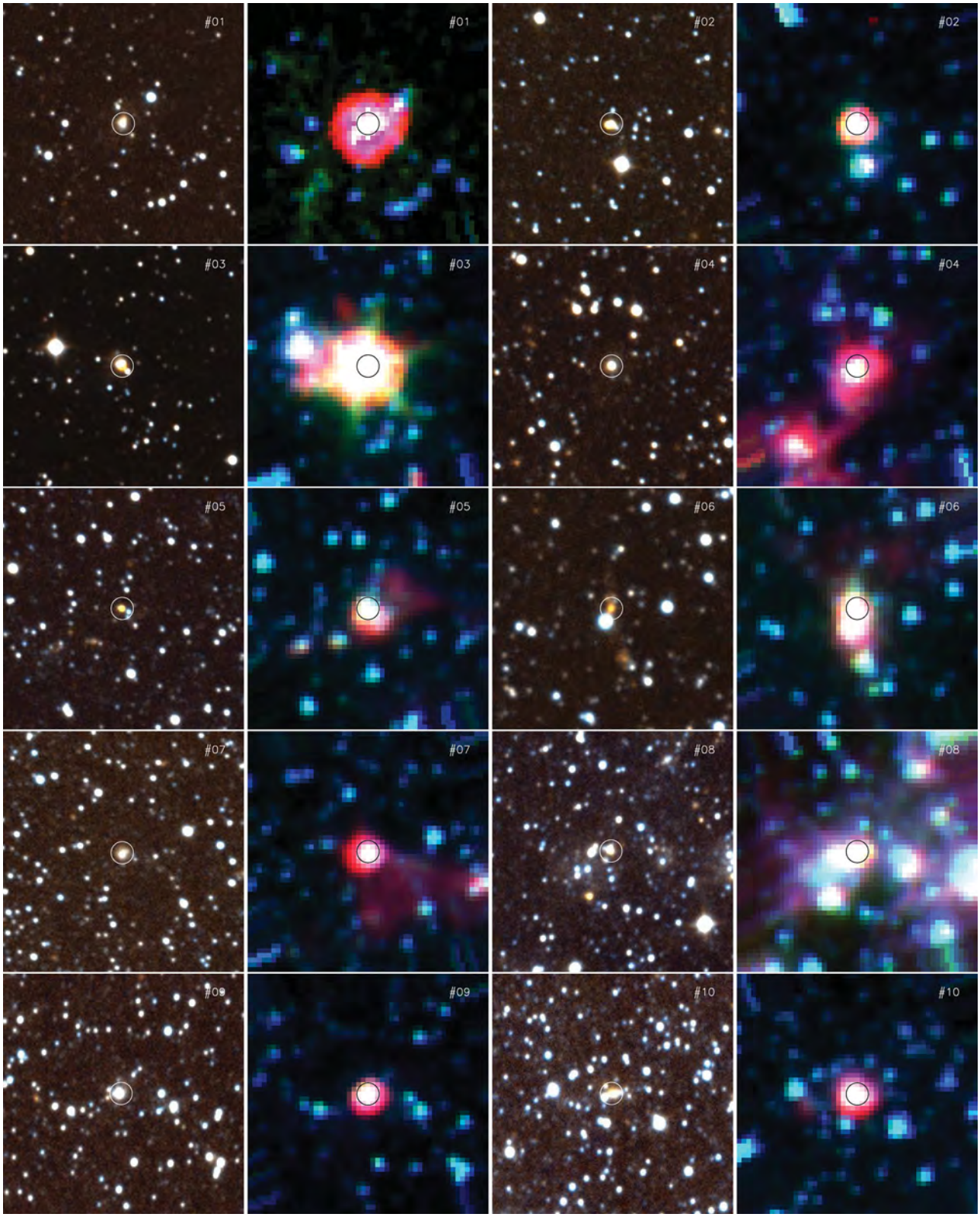

Figure C1. Colour-composite images for the YSO candidates in the SMC. For each object J_sK_s (blue/red) and *Spitzer* [3.6]–[5.8]–[8] images (blue/green/red) are shown. Each image is 1×1 arcmin^2 across and north is to the top and east to the left. For the last two objects we used IRSF images and show the *JHK* colour composite.

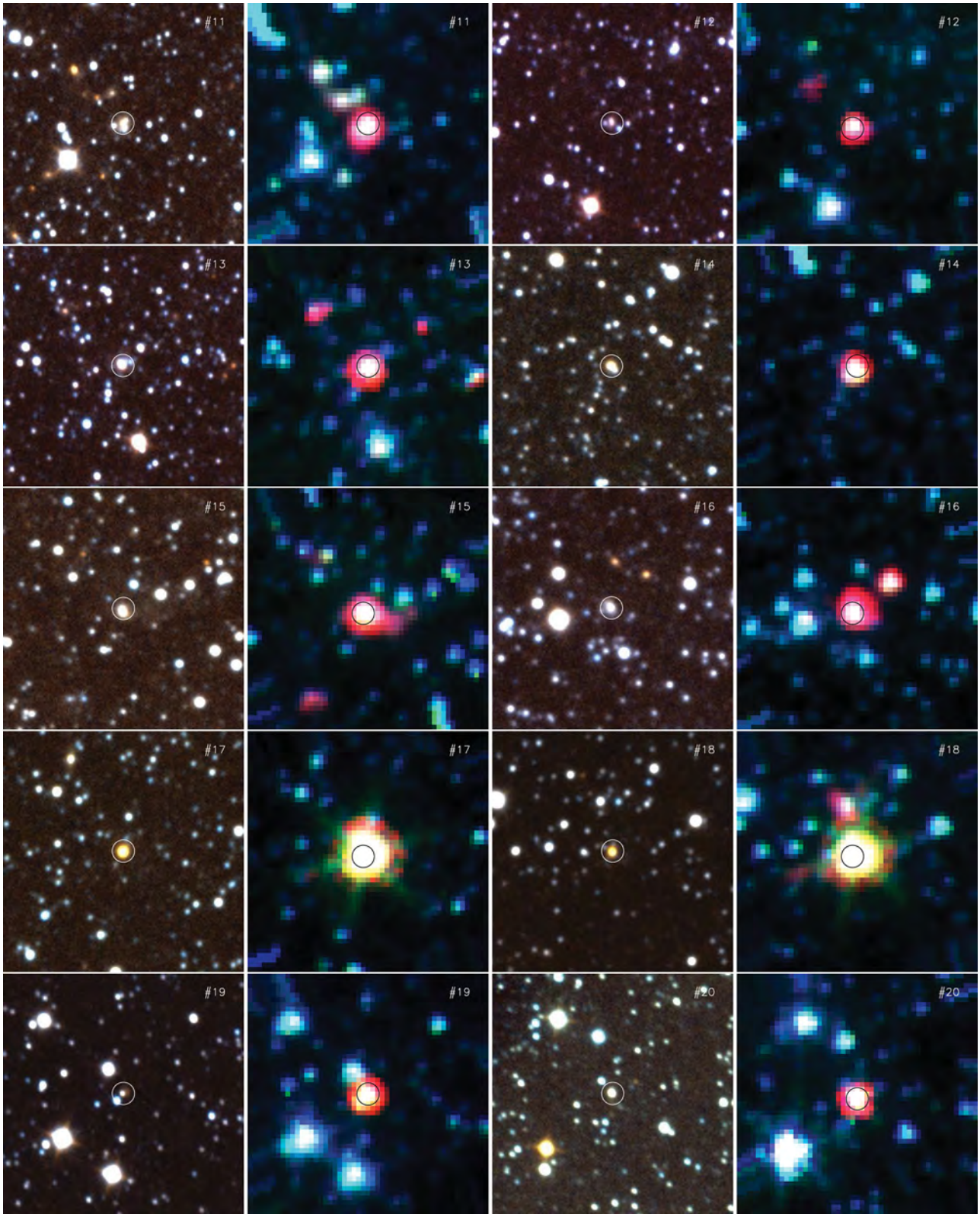

Figure C1 – *continued*

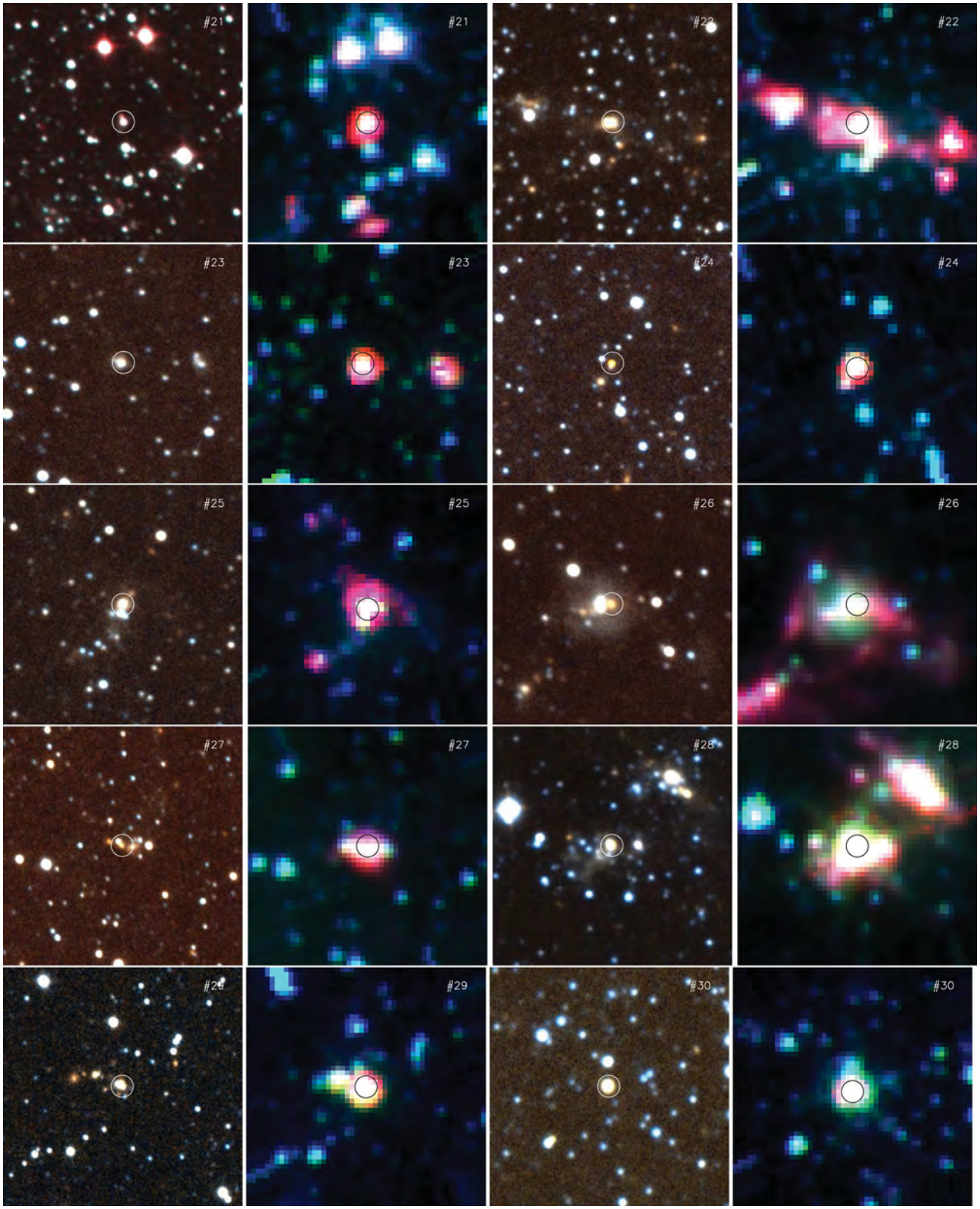

Figure C1 – *continued*

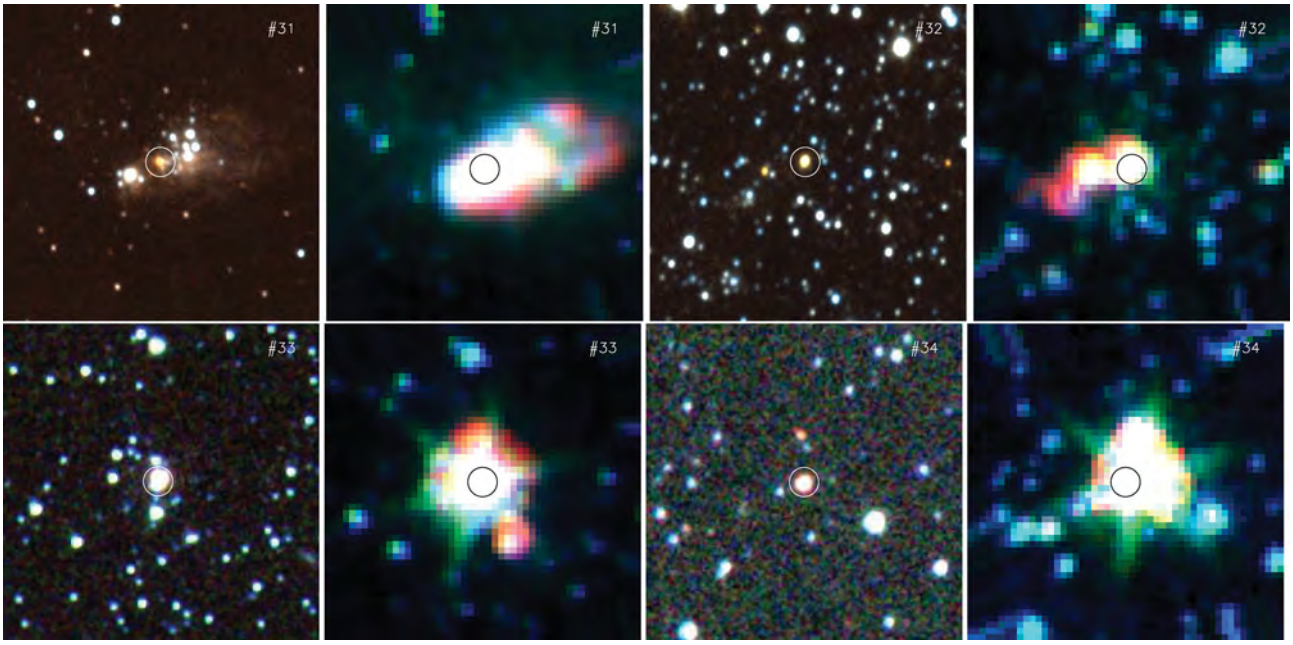

Figure C1 – *continued*

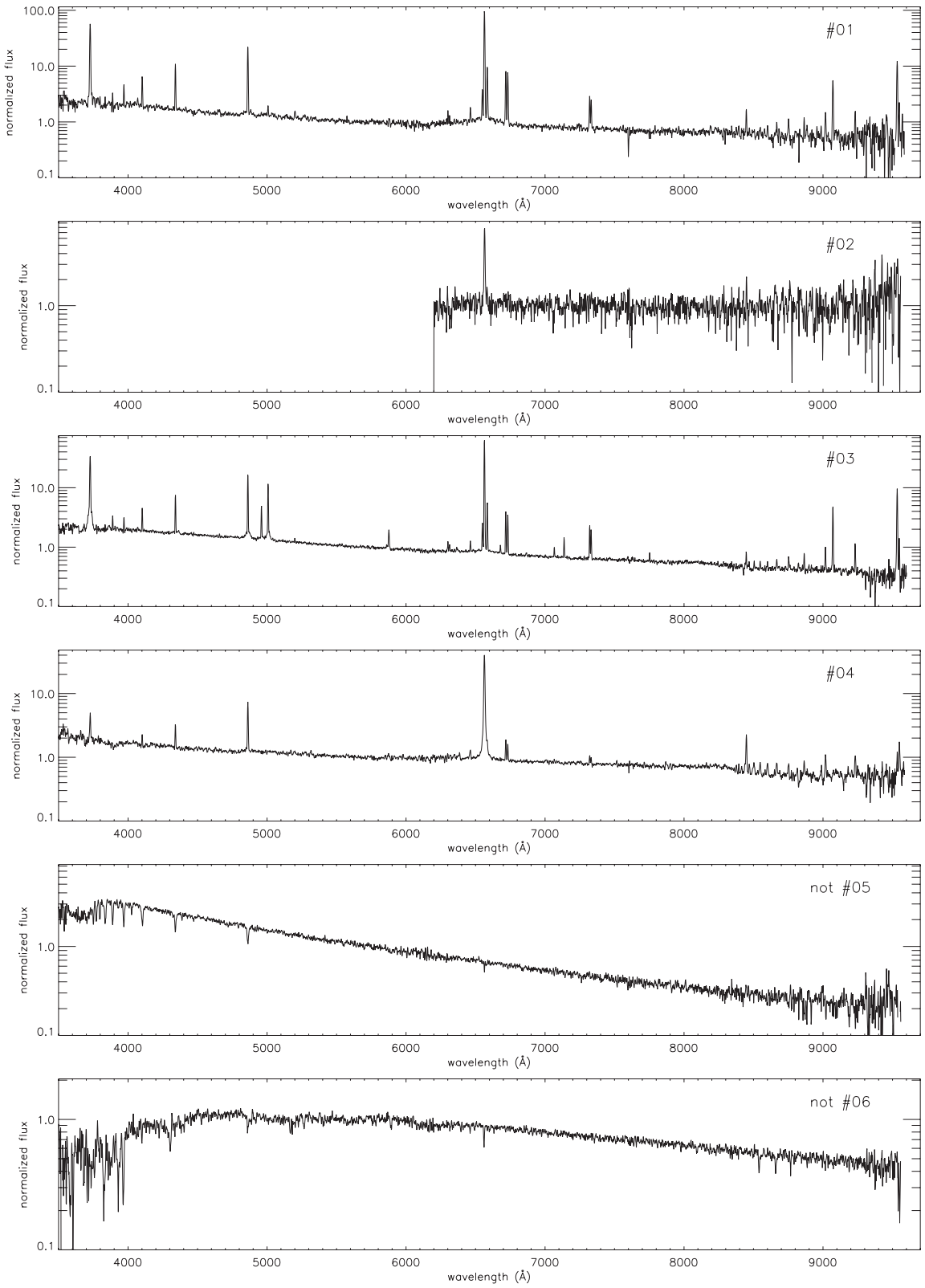

Figure D1. Optical spectra of possible optical counterparts for the IR sources in the SMC. No spectra were obtained for sources #24 and 31, and for sources #05, 06 and 29 the optical spectra are not associated with the IR sources. The most conspicuous spectral features are labelled in the last panel for source #26.

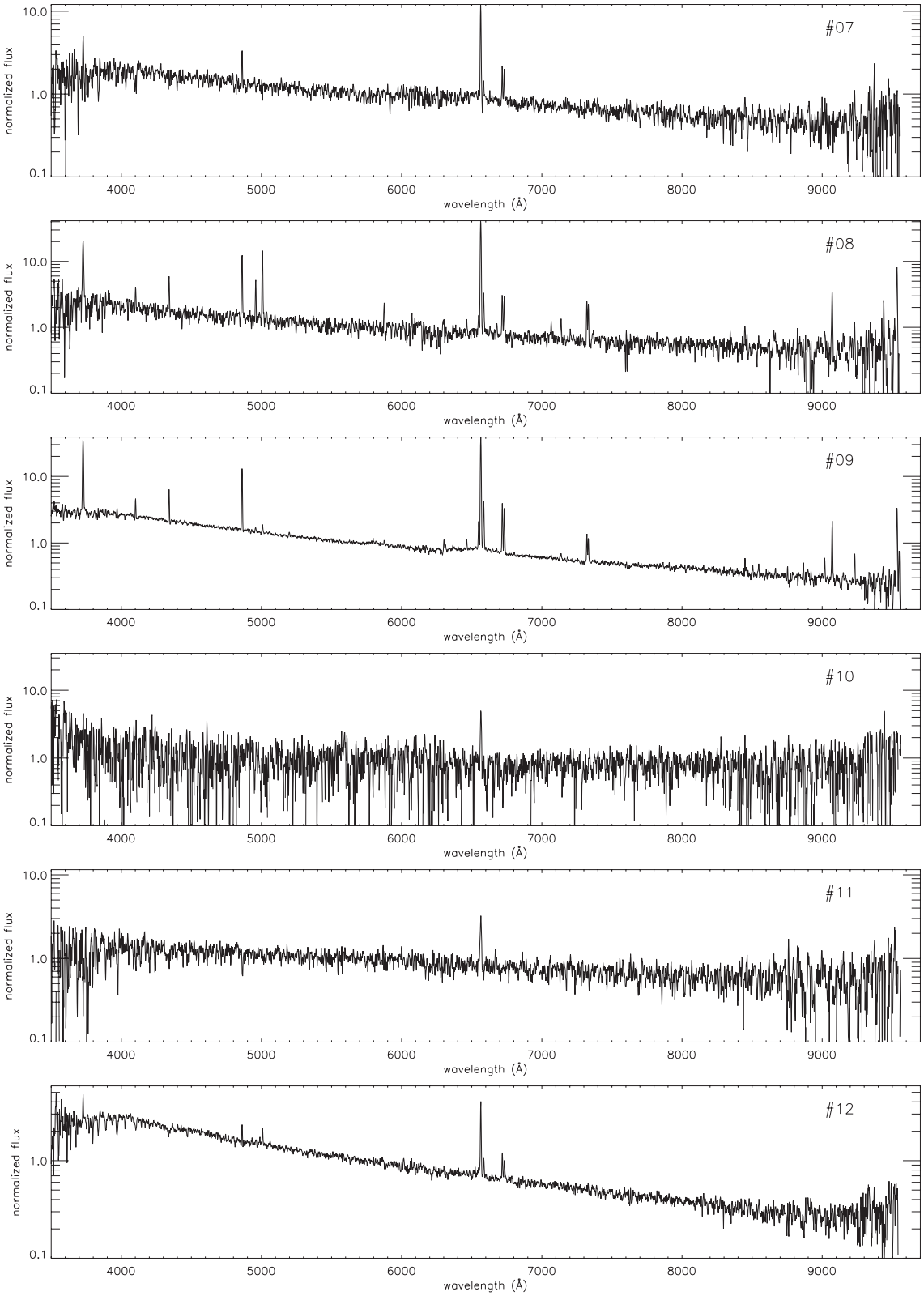

Figure D1 – *continued*

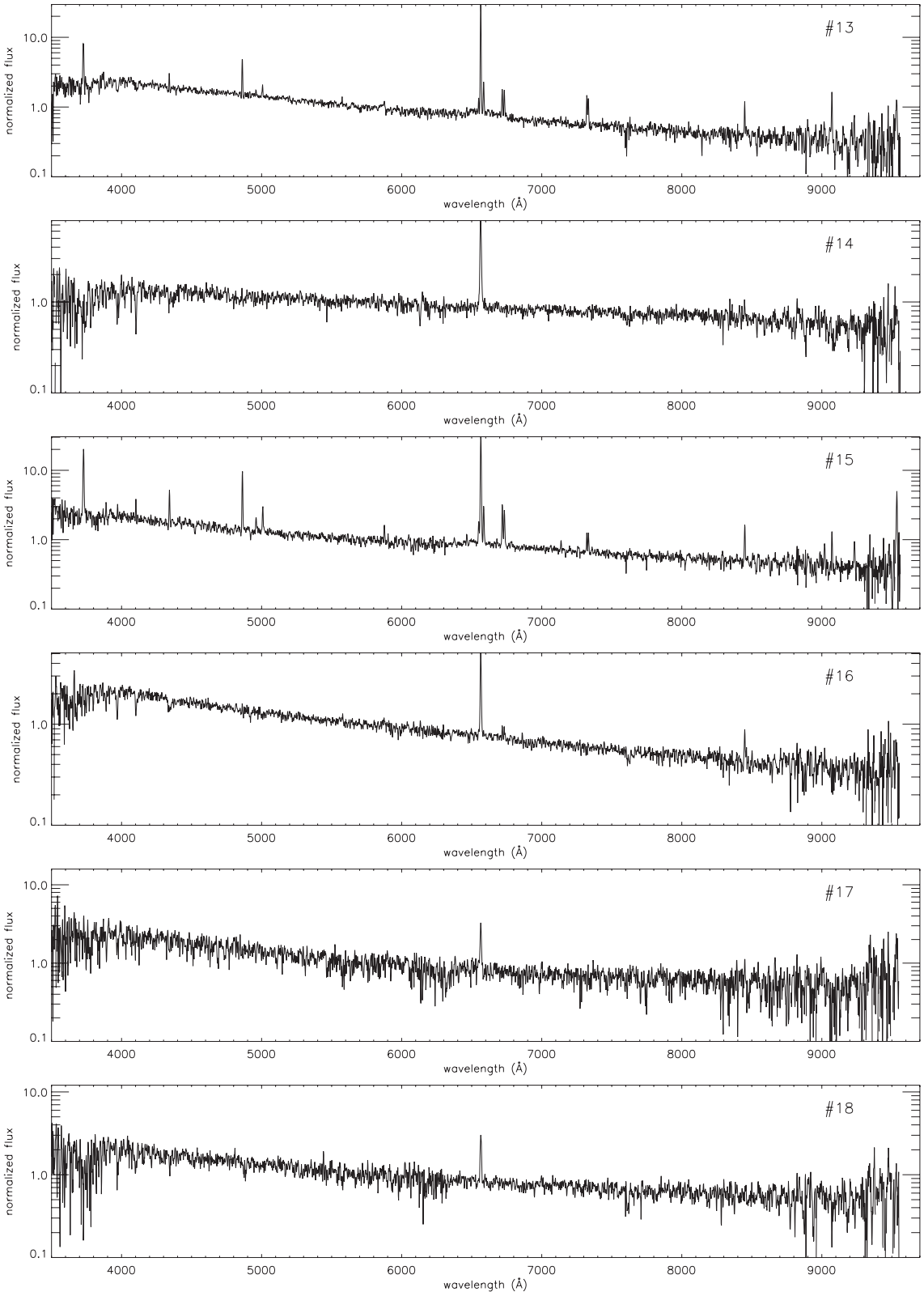

Figure D1 – *continued*

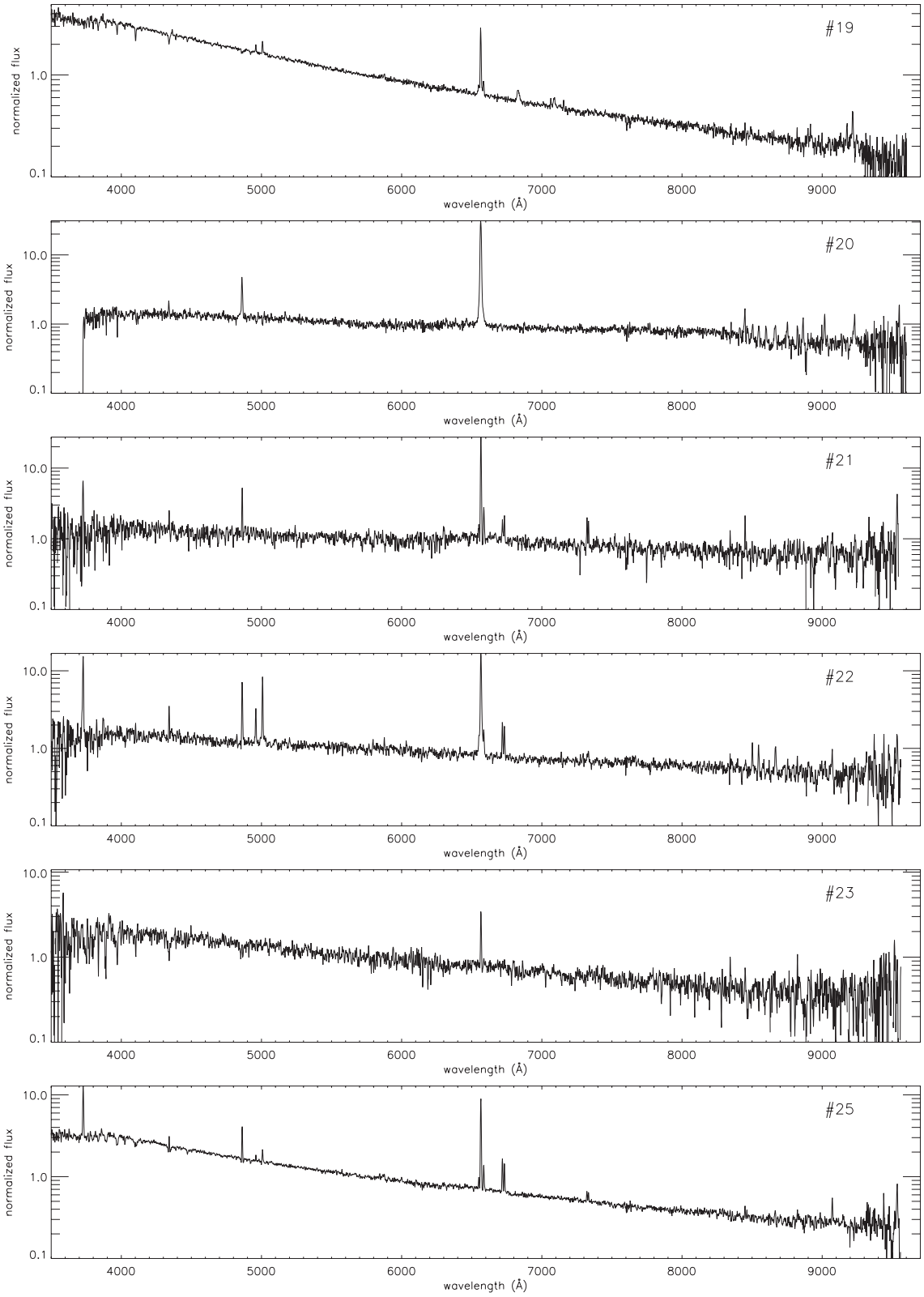

Figure D1 – *continued*

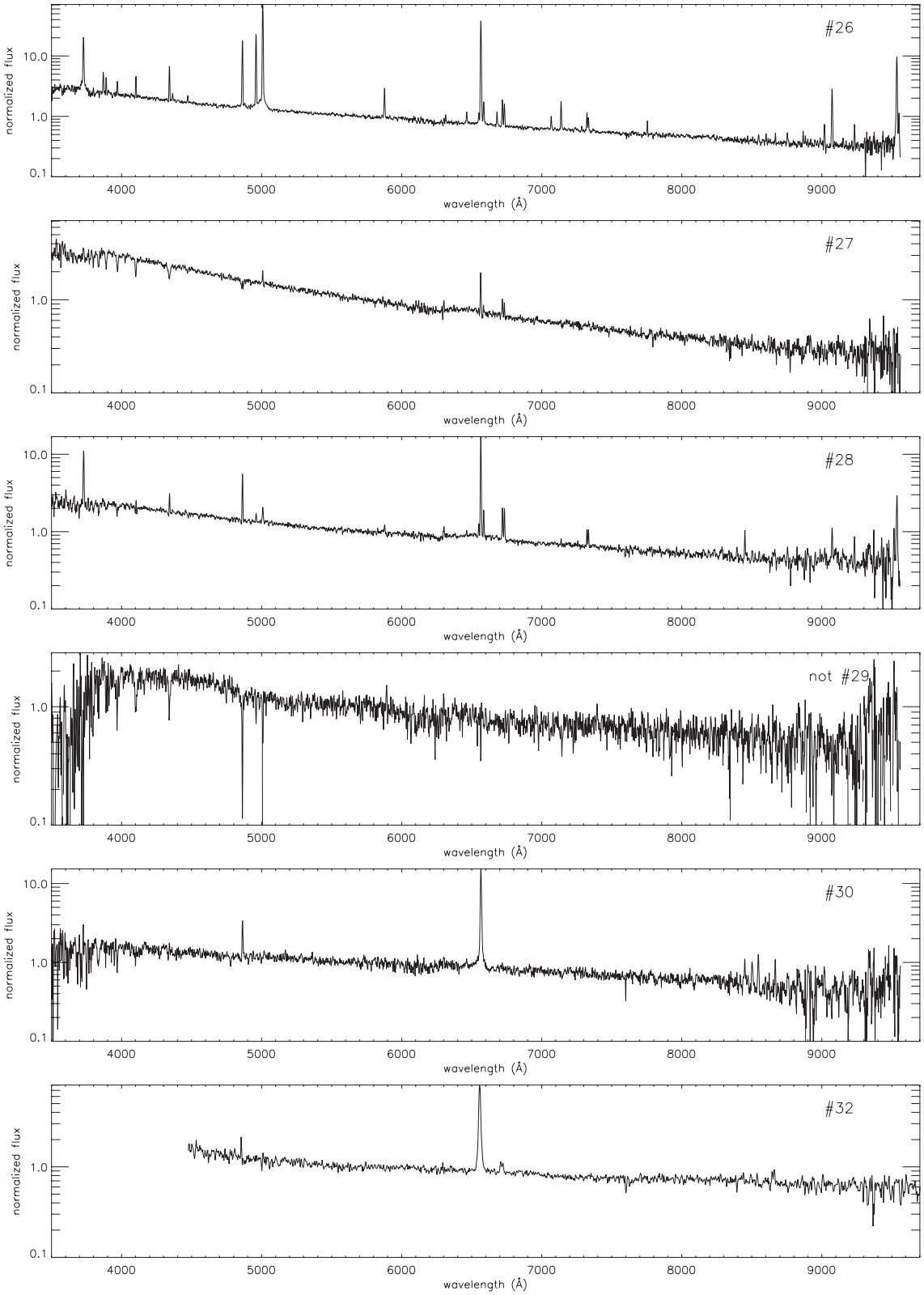

Figure D1 – *continued*

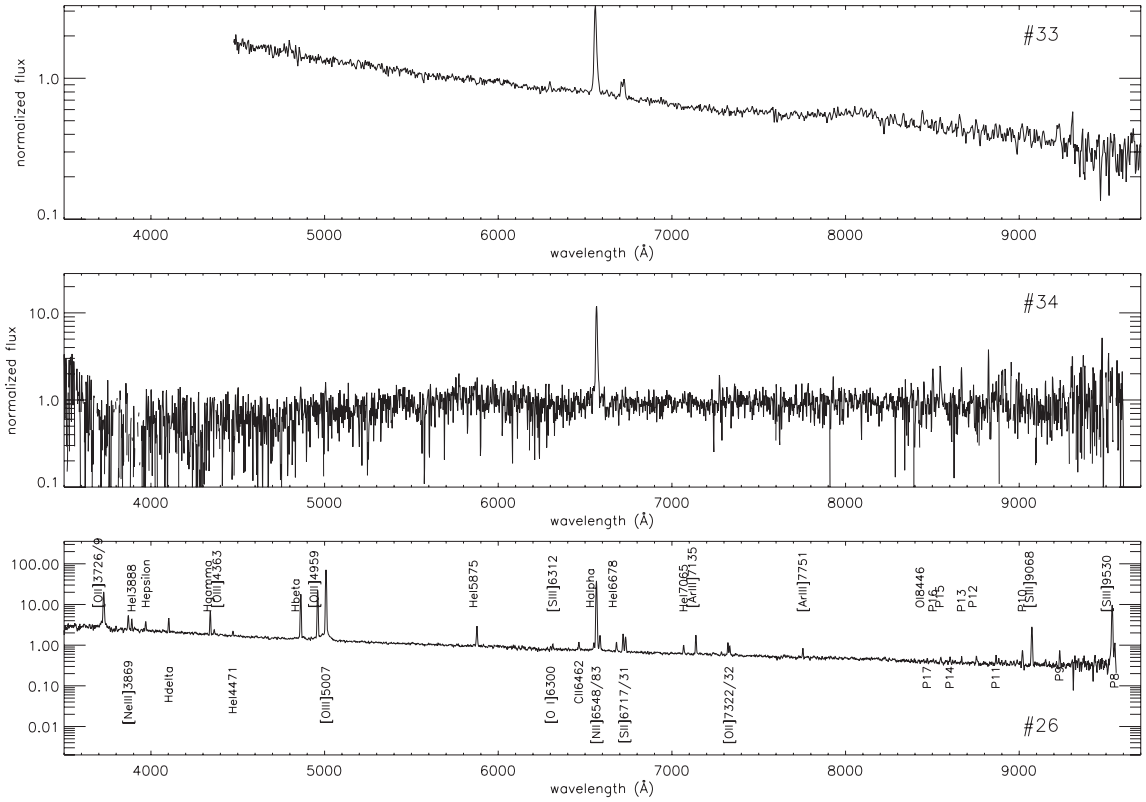

Figure D1 – *continued* The most conspicuous spectral features are labelled for source #26.

This paper has been typeset from a TEX/LATEX file prepared by the author.

A.28 Related Paper 28

Bozzetto, L. M., Filipović, M. D., Crawford, E. J., Sasaki, M., Maggi, P., Haberl, F., Urošević, D., Payne, J. L., De Horta, A. Y., Stupar, M., Gruendl, R., and Dickel, J. (2013). Multifrequency study of SNR J0533-7202, a new supernova remnant in the LMC. *MNRAS*, 432:2177–2181

My contribution was to assist in the data analysis. This is a 10% contribution.

Monthly Notices of the ROYAL ASTRONOMICAL SOCIETY

MNRAS **432,** 2177–2181 (2013) doi:10.1093/mnras/stt568
Advance Access publication 2013 May 9

Multifrequency study of SNR J0533−7202, a new supernova remnant in the LMC

L. M. Bozzetto,[1⋆] M. D. Filipović,[1] E. J. Crawford,[1] M. Sasaki,[2] P. Maggi,[3] F. Haberl,[3] D. Urošević,[4,5] J. L. Payne,[1] A. Y. De Horta,[1] M. Stupar,[6,7] R. Gruendl[8] and J. Dickel[9]

[1]*School of Computing and Mathematics, University of Western Sydney Locked Bag 1797, Penrith South DC, NSW 1797, Australia*
[2]*Institut für Astronomie und Astrophysik Tübingen, Sand 1, D-72076 Tübingen, Germany*
[3]*Max-Planck-Institut für extraterrestrische Physik, Giessenbachstraße, D-85748 Garching, Germany*
[4]*Department of Astronomy, Faculty of Mathematics, University of Belgrade, Studentski trg 16, 11000 Belgrade, Serbia*
[5]*Isaac Newton Institute of Chile, Yugoslavia Branch*
[6]*Department of Physics, Macquarie University, Sydney, NSW 2109, Australia*
[7]*Australian Astronomical Observatory, PO Box 296, Epping, NSW 1710, Australia*
[8]*Department of Astronomy, University of Illinois, 1002 West Green Street, Urbana, IL 61801, USA*
[9]*Physics and Astronomy Department, University of New Mexico, MSC 07-4220, Albuquerque, NM 87131, USA*

Accepted 2013 March 28. Received 2013 March 27; in original form 2013 February 7

ABSTRACT

We present a detailed study of Australia Telescope Compact Array observations of a newly discovered Large Magellanic Cloud supernova remnant (SNR), SNR J0533−7202. This object follows a horseshoe morphology, with a size of 37 pc × 28 pc (1 pc uncertainty in each direction). It exhibits a radio spectrum with the intrinsic synchrotron spectral index of $\alpha = -0.47 \pm 0.06$ between 73 and 6 cm. We report detections of regions showing moderately high fractional polarization at 6 cm, with a peak value of 36 ± 6 per cent and a mean fractional polarization of 12 ± 7 per cent. We also estimate an average rotation measure across the remnant of −591 rad m^{-2}. The current lack of deep X-ray observation precludes any conclusion about high-energy emission from the remnant. The association with an old stellar population favours a thermonuclear supernova origin of the remnant.

Key words: polarization – ISM: supernova remnants – Magellanic Clouds – radio continuum: ISM – X-rays: ISM.

1 INTRODUCTION

Supernova remnants (SNRs) are responsible for the distribution of heavy elements in the Universe, influencing the chemical composition of the next generation of stars. SNRs have a significant effect on their environment, heating up the surrounding gas and dust as the shock waves of the supernova explosion pass through. In turn, however, SNRs are heavily impacted by their environment, as their evolution, structure and expansion is greatly affected by the density of the surrounding interstellar medium. In the radio continuum, SNR emission is predominately non-thermal and will typically display a radio spectral index of $\alpha \sim -0.5$ (defined by $S \propto \nu^{\alpha}$). However, this may significantly vary due to environmental factors, different stages of evolution and various types of SNRs.

The Large Magellanic Cloud (LMC) is an irregular dwarf galaxy in close proximity to our own Milky Way Galaxy at a distance of 50 kpc (Macri et al. 2006). As a result of this relatively close distance, objects in the LMC can be observed with significantly better spatial resolution and sensitivity than those in other galaxies. However, it is far away enough that we are able to assume all objects that lie within the galaxy are at very similar distances, therefore making estimates for various analysis methodologies such as extent and surface brightness more accurate, as these values depend on accurate distances to the object. In contrast, objects in the Milky Way can be difficult to find accurate distances for and therefore leads to imprecise measurements. The LMC is also a desirable environment for various astronomical studies as it contains some of the most active star-forming regions in our Local Group of galaxies as well as residing outside of the Galactic plane, at a moderate inclination angle of 35° (van der Marel & Cioni 2001), which greatly minimizes the interference from stars, gas and dust within the LMC.

In this paper, we report on a newly discovered LMC SNR, SNR J0533−7202. Radio observations of this object were also taken by Filipovic et al. (1995, 1998a,b) in their surveys of the Magellanic Clouds; however, they did not classify this object. The new observations, data reduction and imaging techniques are described in Section 2. The astrophysical interpretation of newly obtained moderate-resolution total intensity and polarimetric images in combination with the existing Magellanic Cloud Emission Line Survey (MCELS) images are discussed in Section 3.

⋆E-mail: luke.bozzetto@gmail.com

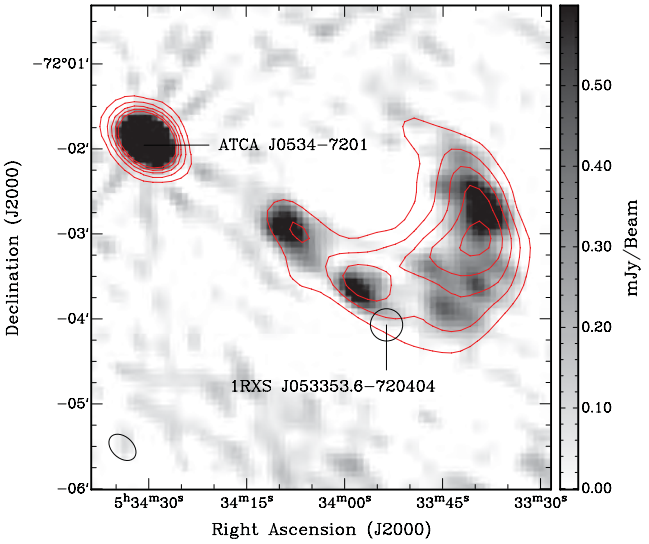

Figure 1. ATCA observations of SNR J0533−7202 at 3 cm (9000 MHz) overlaid with 6 cm (5500 MHz) contours. The contours are 3, 6, 9, 12 and 15σ. The ellipse in the lower-left corner represents the synthesized beamwidth (at 6 cm) of 34.1 arcsec × 26.1 arcsec. The sidebar quantifies the pixel map. The overlaid circle shows the position of a weak X-ray source seen by *ROSAT*.

2 OBSERVATIONS AND DATA REDUCTION

We observed SNR J0533−7202 with the Australia Telescope Compact Array (ATCA) on 2011 November 15 and 16, using the new Compact Array Broad-band Backend (CABB) at array configuration EW367 and at wavelengths of 3 and 6 cm (ν = 9000 and 5500 MHz). Baselines formed with the sixth ATCA antenna were excluded, as the other five antennas were arranged in a compact configuration. The observations were carried out in the so-called 'snap-shot' mode, totalling ∼50 min of integration over a 14 h period. PKS B1934−638 was used for flux density calibration[1] and PKS B0530−727 was used for secondary (phase) calibration. The phase calibrator was observed twice every hour for a total 78 min over the whole observing session. The MIRIAD[2] (Sault, Teuben & Wright 1995) and KARMA (Gooch 1995) software packages were used for reduction and analysis. More information on the observing procedure and other sources observed in this project can be found in Bozzetto et al. (2012a,b) and de Horta et al. (2012).

The CABB 2 GHz bandwidth is a 16 times improvement from the previous 128 MHz, and with the new higher data sampling has increased the sensitivity of the ATCA by a factor of 4. The 2 GHz bandwidth not only aids in high-sensitivity observations, but also allows data to be split into channels which can then be used for measuring Faraday rotation across the entire bandwidth, at frequencies close enough that the $n \times 180^\circ$ ambiguities prevalent when making an estimate between distant frequencies are no longer an issue.

Images were formed using MIRIAD multifrequency synthesis (Sault & Wieringa 1994) and natural weighting. They were deconvolved with primary beam correction applied. The same procedure was used for both *U* and *Q* Stokes parameter maps.

The 3 cm image (Fig. 1) has a resolution [full width half-maximum (FWHM)] of 21.6 arcsec × 15.0 arcsec (position angle, PA = 47.°2). Similarly, we made an image of SNR J0533−7202 at 6 cm (seen as contours in Fig. 1) which has an FWHM of 34.1 arcsec × 26.1 arcsec at PA = 45.°5 and an estimated rms noise of 0.3 mJy beam^{-1} .

[1] Flux densities were assumed to be 5.098 Jy at 6 cm and 2.736 Jy at 3 cm.
[2] http://www.atnf.csiro.au/computing/software/miriad/

3 RESULTS AND DISCUSSION

This new LMC remnant exhibits a horseshoe morphology (Fig. 1), centred at RA (J2000) = $5^h33^m46\overset{s}{.}5$, Dec. (J2000) = −72° 02′ 59″. We selected a one-dimensional intensity profile across the approximate major (NW–SE) and minor (NE–SW) axis (PA = 45°) (Fig. 2) at the 3σ noise level (0.9 mJy) to estimate the spatial extent of SNR J0533−7202. Its size at 6 cm is 152 arcsec × 115 arcsec with a 4 arcsec uncertainty in each direction (37 × 28 pc with a 1 pc uncertainty in each direction). We did not detect any [O III]

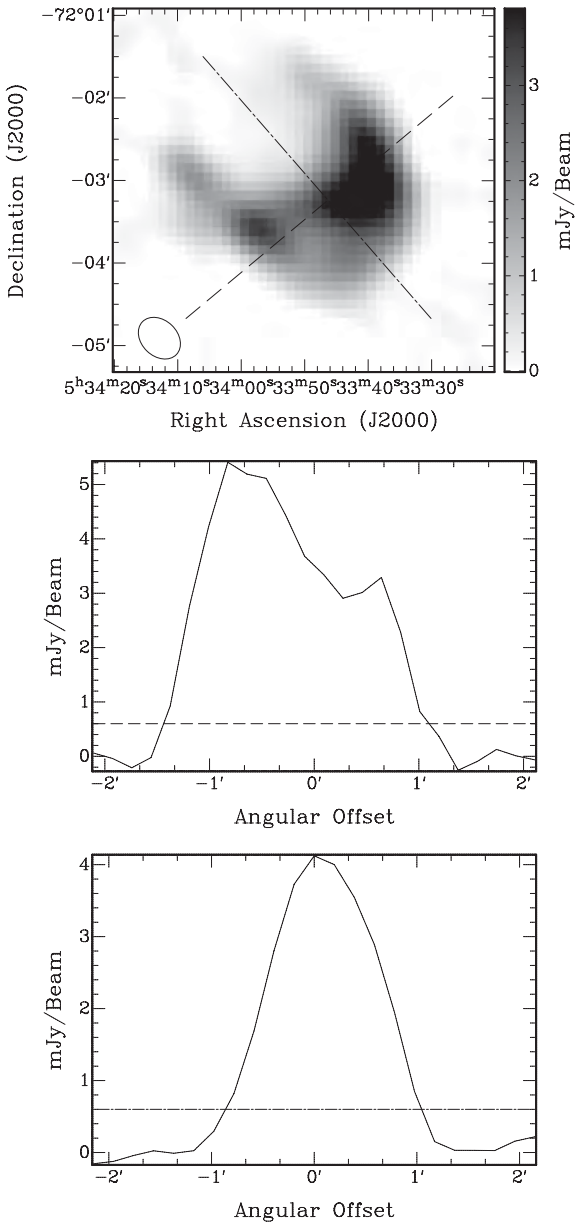

Figure 2. The top image shows the 6 cm intensity image of overlaid with the approximate major (NW–SE) and minor (NE–SW) axis. The middle and lower images show the one-dimensional cross-section along the overlaid lines in the top image, with a superimposed line at 3σ.

Table 1. Integrated flux densities of SNR J0533−7202 and the point source ATCA J0534−7201.

ν (MHz)	λ (cm)	rms (mJy)	Beam size (arcsec)	S_{PS} (mJy)	ΔS_{PS} (mJy)	S_{SNR} (mJy)	ΔS_{SNR} (mJy)	Reference
73	408	40	157.2 × 171.6	–	–	220	22	Clarke et al. (1976)
36[a]	843	0.8	46.4 × 43.0	34	3	153	15	This work
36[b]	843	1.0	46.4 × 43.0	39	4	117	12	This work
20	1384	0.6	40.0 × 40.0	31	3	120	12	This work
6	4800	0.7	35.0 × 35.0	24	2	72	7	This work
6	5500	0.3	34.1 × 26.1	20	2	54	5	This work
3[c]	8640	0.7	22.0 × 22.0	19	2	23	2	This work
3[c]	9000	0.3	21.6 × 15.0	17	2	22	2	This work

[a]Uses the MOST mosaic image.
[b]Uses the SUMMS mosaic image.
[c]Due to short spacing, these 3 cm flux-density estimates are omitted from the SNR SED estimate.

or [S II] emission in the MCELS (Smith, Points & Winkler 2006) images. However, there is some tentative and very faint Hα emission possibly associated with this SNR which was not evident anywhere else in the field surrounding the remnant. Although, more sensitive observations are needed.

An X-ray source at the rim of the SNR was detected in the course of the *ROSAT* all-sky survey and was given the identifier 1RXS J053353.6−720404 (Voges et al. 1999). However, the likelihood of existence[3] in these observations was only 7, meaning only a 3.3σ detection, and therefore not much could be done with respect to the X-ray analysis, apart from plotting the *ROSAT* position (Fig. 1). This *ROSAT* position is slightly south–west of one of the radio-bright regions of the remnant. Low statistics preclude any classification between an extended or compact source.

This SNR did not appear in the *Spitzer* mosaic images of the LMC (Meixner et al. 2006), neither at the 3.6, 4.5, 5.8 and 8 μm wavelengths of the Infrared Array Camera (IRAC) instrument (Fazio et al. 2004), nor in the 24, 70 and 160 μm bands of the Multiband Imaging Photometer for *Spitzer* (MIPS) instrument (Rieke et al. 2004), suggesting that there is no association with mid- or near-infrared wavelengths. There are no OB star candidates in the Magellanic Clouds Photometric Survey catalogue (Zaritsky et al. 2004) within a 100 pc radius around the centre of the remnant, and the star formation history map of the LMC (Harris & Zaritsky 2009) shows no recent episode of star formation activity in the neighbourhood. The association of SNR J0533−7202 with an old stellar population favours a thermonuclear supernova origin of the remnant.

We based the spectral energy distribution (SED) on our own integrated flux estimates, coupled with the 73 cm measurement by Clarke, Little & Mills (1976). These values are shown in Table 1 and then used to produce a spectral index graph (Fig. 3). The point source (ATCA J0534−7201; see Fig. 1) to the east of SNR J0533−7202 was unresolved from the SNR in the 73 cm survey [Molonglo radio source catalogue 4 (MC4; Clarke et al. 1976)]. We estimate 36 cm flux-density measurements from the Molonglo Synthesis Telescope (MOST) mosaic image (as described in Mills et al. 1984) and a 36 cm Sydney University Molonglo Sky Survey (SUMMS) mosaic image (Mauch et al. 2008). We point out that these values differ by some 25 per cent, which is most likely due to the higher sensitivity of the MOST image and its greater UV coverage. The 20 cm flux density was measured from a mosaic image published by Hughes et al. (2007). Two different sets of images were used to estimate integrated flux densities at wavelengths of 6 and 3 cm. The first set (5500 and 9000 MHz) contains our CABB observations merged with the mosaic visibility files from Dickel et al. (2005). These observations use the EW 367 array, which has a shortest baseline of 46 m and as a result, has missing flux from the lack of short spacings. The second set of images (4800 and 8640 MHz) is from the mosaic images published by Dickel et al. (2010), which used EW 367 and EW 352 arrays at both frequencies as well as Parkes at 4800 MHz but not at 8640 MHz, as the Parkes survey at 3 cm did not extend that far south. This survey data had more spatial frequency coverage, particularly for the extended emission, but less sensitivity. We can see the detrimental effect of missing short spacings in the 3 cm flux-density measurements, where they fall well below the trend of the SED at higher wavelengths (Fig. 3). Due to the significant impact of the missing shorter spacings (and as a result, missing flux), we omit the 3 cm measurements from the calculation, leaving all the frequencies up to 6 cm (5500 MHz), and thus a spectral index of $\alpha = -0.47 \pm 0.06$.

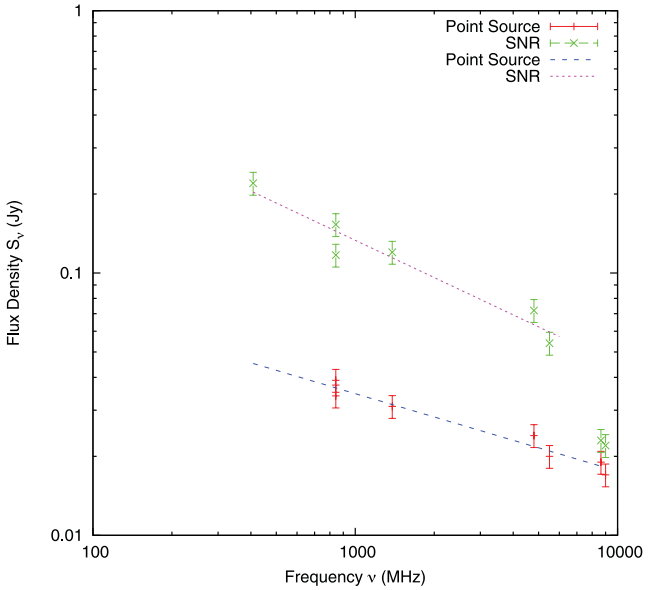

Figure 3. Radio continuum spectrum of SNR J0533−7202 and the point source ATCA J0534−7201. The pink dotted line represents the spectral index of the SNR and the blue dashed line represents the spectrum of the point source.

Fractional polarization (P) was calculated at 6 cm using

$$P = \frac{\sqrt{S_Q^2 + S_U^2}}{S_I}, \quad (1)$$

[3] In the *ROSAT* source detection, a likelihood L is associated with a probability of a detected source being real P by $P = 1 - \exp(-L)$.

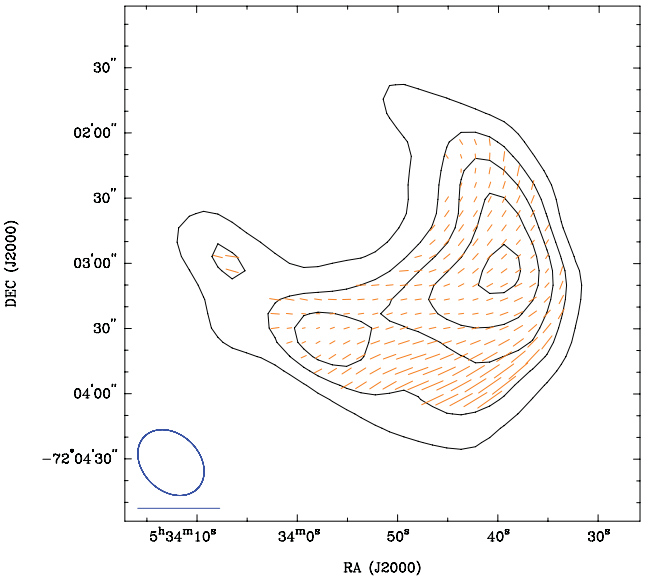

Figure 4. Magnetic-field vectors overlaid on 6 cm contours (3, 6, 9, 12 and 15σ) of SNR J0533−7202 from ATCA observations. The ellipse in the lower-left corner represents the synthesized beamwidth of 34.3 arcsec × 26.0 arcsec and the line below the ellipse shows a polarization vector of 100 per cent.

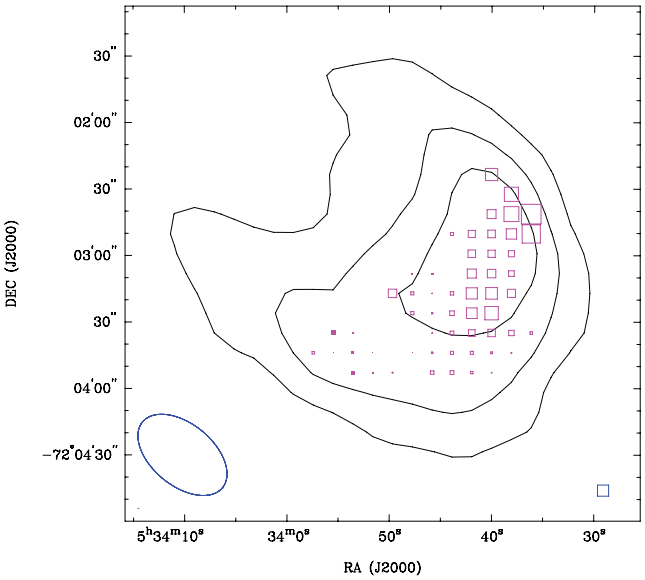

Figure 5. Faraday rotation measure of SNR J0533−7202 overlaid on 6 cm (128 MHz bandwidth) ATCA contours (3, 8 and 13σ). The filled squares represent positive rotation measure while the open squares represent negative rotation measure. The ellipse in the lower-left corner represents the synthesized beamwidth of 46.7 arcsec × 27.9 arcsec and the box in the lower right represents a rotation measure of 1000 rad m^{-2}. The width of the boxes scale with rotation measure.

where S_Q, S_U and S_I are integrated intensities for Q, U and I Stokes parameters (Fig. 4). Our estimated peak value is 36 ± 6 per cent with a mean fractional polarization of 12 ± 7 per cent. This level of fractional polarization is relatively high when compared to various other SNRs in the LMC (Cajko, Crawford & Filipovic 2009; Crawford et al. 2010; Bozzetto et al. 2012a) and would be (theoretically) expected for an SNR with a radio spectrum of around or less than −0.5 (Rolfs & Wilson 2003). This may indicate varied dynamics along the shell.

Polarization position angles were taken from across the 2 GHz bandwidth (at 5500 MHz split into 128 MHz channels) and used to estimate the Faraday rotation for this SNR. The result of this can be seen in Fig. 5, with the open boxes representing negative values of rotation measure and the filled in boxes representing positive rotation measure. The rotation measure varies quite significantly along the SNR with the most change being negative rotation measure near the peak intensity in the western region of the remnant. The average rotation measure across the SNR was −591 rad m^{-2}. This value is nearly double that of the plerion in SNR G326.3−1.8 (Dickel, Milne & Strom 2000) and significantly exceeds what is typical of 'large' values in the LMC and Milky Way of ±250 rad m^{-2} (Dickel & Milne 1995). It would be best to treat this value with some level of caution, as at higher radio frequencies – such as our 6 cm observations – the amount of rotation measure expected from an SNR is within the same range as the expected error. To mitigate this error and achieve a more reliable value of rotation measure, additional observations would need to be taken, preferably at lower radio frequencies where we would expect a higher level of rotation measure.

We were also able to estimate the magnetic field strength for this SNR based on the equipartition formula as given in Arbutina et al. (2012). This formula is based on the Bell (1978) diffuse shock acceleration theory. By using the spectral index value $\alpha = -0.5$, we get an equipartition value for SNR J0533−7202 of ∼45 μG with an estimated minimum energy of $E_{\rm min} = 9.4 \times 10^{49}$ erg.

From the position of SNR J0533−7202 at the surface brightness to diameter (Σ–D) diagram [(D, Σ) = (32.5 pc, 6.2 × 10^{-21} W m^{-2} Hz^{-1} sr^{-1})] by Berezhko & Völk (2004), we can estimate that SNR J0533−7202 is likely to be an SNR in the late energy-conserving phase, with an explosion energy between 0.25 and 1 × 10^{51} erg, which evolves in an environment of density ∼1 cm^{-3}.

4 CONCLUSION

We have added a new SNR to the LMC SNR population through conducting a high-resolution radio continuum study of SNR J0533−7202. We report a relatively large SNR with an extent of ∼152 arcsec × 115 arcsec (∼37 × 28 pc), and a radio spectral index with $\alpha = -0.47$ between 73 and 6 cm. We estimate fractional polarization of the remnant at 6 cm with a peak of 36 ± 6 per cent and a mean integrated value of 12 ± 7 per cent. The lack of recent star formation activity around the remnant makes a thermonuclear supernova origin more likely.

ACKNOWLEDGEMENTS

The Australia Telescope Compact Array is part of the Australia Telescope which is funded by the Commonwealth of Australia for operation as a National Facility managed by CSIRO. We thank the Magellanic Clouds Emission Line Survey (MCELS) team for access to the optical images. This research is supported by the Ministry of Education and Science of the Republic of Serbia through project No. 176005. PM acknowledges support from the Bundesministerium für Wirtschaft und Technologie/Deutsches Zentrum für Luft- und Raumfahrt (BMWi/DLR) grant FKZ 50 OR 1201.

REFERENCES

Arbutina B., Urošević D., Andjelić M. M., Pavlović M. Z., Vukotić B., 2012, ApJ, 746, 79
Bell A. R., 1978, MNRAS, 182, 443

Berezhko E. G., Völk H. J., 2004, A&A, 427, 525
Bozzetto L. M. et al., 2012a, MNRAS, 420, 2588
Bozzetto L. M., Filipovic M. D., Crawford E. J., Payne J. L., de Horta A. Y., Stupar M., 2012b, Rev. Mex. Astron. Astrofis., 48, 41
Cajko K. O., Crawford E. J., Filipovic M. D., 2009, Serb. Astron. J., 179, 55
Clarke J. N., Little A. G., Mills B. Y., 1976, Aust. J. Phys. Astrophys. Suppl., 40, 1
Crawford E. J., Filipović M. D., Haberl F., Pietsch W., Payne J. L., de Horta A. Y., 2010, A&A, 518, A35
de Horta A. Y. et al., 2012, A&A, 540, A25
Dickel J. R., Milne D. K., 1995, AJ, 109, 200
Dickel J. R., Milne D. K., Strom R. G., 2000, ApJ, 543, 840
Dickel J. R., McIntyre V. J., Gruendl R. A., Milne D. K., 2005, AJ, 129, 790
Dickel J. R., McIntyre V. J., Gruendl R. A., Milne D. K., 2010, AJ, 140, 1567
Fazio G. G. et al., 2004, ApJS, 154, 10
Filipovic M. D., Haynes R. F., White G. L., Jones P. A., Klein U., Wielebinski R., 1995, A&AS, 111, 311
Filipovic M. D., Haynes R. F., White G. L., Jones P. A., 1998a, A&AS, 130, 421
Filipovic M. D. et al., 1998b, A&AS, 127, 119
Gooch R., 1995, in Shaw R. A., Payne H. E., Hayes J. J. E., eds, ASP Conf. Ser. Vol. 77, Space and the Spaceball. Astron. Soc. Pac., San Francisco, p. 144
Harris J., Zaritsky D., 2009, AJ, 138, 1243
Hughes A., Staveley-Smith L., Kim S., Wolleben M., Filipović M., 2007, MNRAS, 382, 543
Macri L. M., Stanek K. Z., Bersier D., Greenhill L. J., Reid M. J., 2006, ApJ, 652, 1133
Mauch T., Murphy T., Buttery H. J., Curran J., Hunstead R. W., Piestrzynski B., Ropbertson J. G., Sadler E. M., 2008, VizieR Online Data Catalog, 8081, 0
Meixner M. et al., 2006, AJ, 132, 2268
Mills B. Y., Turtle A. J., Little A. G., Durdin J. M., 1984, Aust. J. Phys., 37, 321
Rieke G. H. et al., 2004, ApJS, 154, 25
Rolfs K., Wilson T., 2003, Tools of Radio Astronomy, 4th edn. Springer, Berlin
Sault R. J., Wieringa M. H., 1994, A&AS, 108, 585
Sault R. J., Teuben P. J., Wright M. C. H., 1995, in Shaw R. A., Payne H. E., Hayes J. J. E., eds, ASP Conf. Ser. Vol. 77, A Retrospective View of MIRIAD. Astron. Soc. Pac., San Francisco, p. 433
Smith C., Points S., Winkler P. F., 2006, NOAO Newslet., 85, 6
van der Marel R. P., Cioni M.-R. L., 2001, AJ, 122, 1807
Voges W. et al., 1999, A&A, 349, 389
Zaritsky D., Harris J., Thompson I. B., Grebel E. K., 2004, AJ, 128, 1606

This paper has been typeset from a TEX/LATEX file prepared by the author.

A.29 Related Paper 29

O'Brien, A. N., Filipović, M. D., Crawford, E. J., Tothill, N. F. H., Collier, J. D., De Horta, A. Y., Wong, G. F., Drašković, D., Payne, J. L., Pannuti, T. G., Napier, J. P., Griffith, S. A., Staggs, W. D., and Kotuš, S. (2013). Radio-continuum study of the nearby Sculptor group Galaxies. Part 2: NGC 55 at λ=20, 13, 6 and 3 cm. *Ap&SS*, 347:159–168

My contribution was to assist in the data analysis. This is a 10% contribution.

Astrophys Space Sci (2013) 347:159–168
DOI 10.1007/s10509-013-1489-z

ORIGINAL ARTICLE

Radio-continuum study of the nearby Sculptor group Galaxies. Part 2: NGC 55 at λ = 20, 13, 6 and 3 cm

Andrew N. O'Brien · Miroslav D. Filipović · Evan J. Crawford · Nicholas F.H. Tothill · Jordan D. Collier · Ain Y. De Horta · Graeme F. Wong · Danica Drašković · Jeff L. Payne · Thomas G. Pannuti · Jared P. Napier · Stephen A. Griffith · Wayne D. Staggs · Srdjan Kotuš

Received: 18 April 2013 / Accepted: 10 May 2013 / Published online: 29 May 2013

Abstract A series of new radio-continuum (λ = 20, 13, 6 and 3 cm) mosaic images focused on the NGC 55 galactic system were produced using archived observational data from the Australia Telescope Compact Array. These new images are both very sensitive (down to rms = 33 μJy) and feature high angular resolution (down to $<4''$). Using these newly created images, 66 previously unidentified discrete sources are identified. Of these sources, 46 were classified as background sources, 11 as H II regions and 6 as supernova remnant candidates. This relatively low number of SNR candidates detected coupled with the low number of large H II regions is consistent with the estimated low star formation rate of the galaxy at 0.06 $M_{\odot}\,\mathrm{year}^{-1}$. Our spectral index map shows that the core of galaxy appears to have a shallow spectral index between $\alpha = -0.2$ and -0.4. This indicates that the core of the galaxy is a region of high thermal radiation output.

Keywords Galaxies: general · Galaxies: NGC 55 · Radio continuum: galaxies

A.N. O'Brien (✉) · M.D. Filipović · E.J. Crawford · N.F.H. Tothill · J.D. Collier · A.Y. De Horta · G.F. Wong · D. Drašković · J.L. Payne
University of Western Sydney, Locked Bag 1797, Penrith, NSW 2751, Australia
e-mail: andrew.obrien@uws.edu.au

T.G. Pannuti · J.P. Napier · S.A. Griffith · W.D. Staggs
Department of Earth and Space Sciences, Space Science Center, Morehead State University, 235 Martindale Drive, Morehead, KY 40351, USA

S. Kotuš
Department of Physics, University of Novi Sad, Trg Dositeja Obradovića 4, 21000 Novi Sad, Serbia

1 Introduction

At ∼2.08 Mpc (scale of ∼10 pc/″) away (Dalcanton et al. 2009), NGC 55 is situated between our own Local Group of galaxies and the nearby Sculptor Group (Karachentsev et al. 2003). The proximity is an advantage as it allows for NGC 55 to be examined in great detail. Previous radio-continuum studies of NGC 55 (Condon et al. 1996; Puche et al. 1991) utilised the Karl G. Jansky Very Large Array (VLA) in compact array configurations as their primary instrument and thus suffer from low resolution. As a result, these studies did not provide source lists of objects within the NGC 55 field.

Until the next generation of radio telescopes such as the Australian Square Kilometre Array Pathfinder (ASKAP), Karoo Array Telescope (KAT & MeerKAT) and the Square Kilometre Array (SKA) become operational, we are restricted to consolidating a selection of NGC 55 radio observations. Part 1 of this paper (Galvin et al. (2012), Paper 1 hereafter) published a new set of highly sensitive and high-resolution radio-continuum images of the NGC 300 field at λ = 20 cm, created by combining data from the Australia Telescope Compact Array (ATCA) and the VLA (also see Payne et al. 2004). In this paper, we examine all available archived radio-continuum observations of NGC 55 conducted with the ATCA and the VLA at λ = 20, 13, 6 and 3 cm (ν = 1.4, 2.3, 5.5, 9.0 GHz) with the intention of merging these observations to create a single radio-continuum image following a similar methodology as presented in Paper 1. By combining a large amount of existing data using the latest generation of computing power we can create new images that feature both high angular resolution and excellent sensitivity. The newly constructed images are analysed and the differences between each map of NGC 55 created at the observed wavelengths are discussed.

Table 1 Summary of VLA and ATCA observations of NGC 55 at $\lambda = 20$ cm used in this study

Instrument	Project code	Dates	Array	ν (MHz)	$\Delta\nu$ (MHz)	Primary calibrator	Secondary calibrator	Integration time (h)	Included in image
VLA	AJ0107:A	23 Mar 1984	BC	1465, 1515	50, 50	0134+329	0008-421	0.68	N
VLA	AC0101:A	13 Jul 1984	CD	1465, 1515	50, 50	0134+329	0025-263	0.12	N
VLA	AS0199:A	29 Aug 1984	D	1465, 1515	50, 50	0134+329	0022-423	0.23	N
VLA	AB0342:A	03 Nov 1985	CD	1465, 1515	50, 50	0134+329	0023-263	0.15	N
VLA	AB0646:A	03 Jul 1992	CD	1465, 1515	50, 50	0134+329	0008-421	2.51	N
VLA	AB0646:B	05 Jul 1992	CD	1465, 1515	50, 50	0134+329	0008-421	2.93	N
ATCA	C1757	18–19 Feb 2009	EW352	1384	128	1934-638	0008-421	61.62	Y
ATCA	C1757	14–21 Nov 2008	EW367	1384	128	1934-638	0008-421	188.00	Y
ATCA	C1757	31 May–01 Jun 2008	EW352	1384	128	1934-638	0008-421	65.57	Y
ATCA	C1612	02–09 Oct 2006	H75	1384	128	0407-658	0008-421	184.10	Y
ATCA	C1341	07–08 Oct 2005	EW214	1384	128	1934-638	0008-421	62.95	Y
ATCA	C1341	18 Jul 2005	H75	1384	128	1934-638	0008-421	21.32	Y
ATCA	C287	25–26 Oct 1995	1.5D	1344	128	1934-638	0008-421	65.07	Y
ATCA	C287	12–13 Jan 1995	375	1380	128	1934-638	0008-421	63.40	Y
ATCA	C287	01–02 Apr 1994	375	1380	128	1934-638	0008-421	54.13	Y
ATCA	C287	01–02 Aug 1993	750D	1380	128	1934-638	0008-421	61.29	Y
ATCA	C295	24 Jun 1994	6C	1380	128	1934-638	0023-263	0.99	N

Table 2 Summary of VLA and ATCA observations of NGC 55 at $\lambda = 13$ cm used in this study

Instrument	Project code	Dates	Array	ν (MHz)	$\Delta\nu$ (MHz)	Primary calibrator	Secondary calibrator	Integration time (h)	Included in image
ATCA	C287	25–26 Oct 1995	1.5D	2378	128	1934-638	0008-421	65.07	Y
ATCA	C287	12–13 Jan 1995	375	2378	128	1934-638	0008-421	63.40	Y
ATCA	C287	01–02 Apr 1994	375	2378	128	1934-638	0008-421	54.13	Y
ATCA	C287	01–02 Aug 1993	750D	2378	128	1934-638	0008-421	61.29	Y

In Sect. 2 we describe the observational data and reduction techniques. In Sect. 3 we present our new maps, a brief discussion and source list is given in Sect. 4, and Sect. 5 is the conclusion.

2 Data and data reduction

2.1 Observational data

In order to create a high-resolution and sensitive radio-continuum image, 29 observations from the ATCA and VLA were considered. These observations were selected from the Australian Telescope Online Archive (ATOA) and the National Radio Astronomy Observatory (NRAO) Science Data Archive. The observations which were selected and considered are summarised in Tables 1, 2, 3 and 4.

All ATCA projects, excluding C295, were conducted in mosaic mode with multiple pointings observed. All VLA observations and ATCA project C295 consisted of single pointings of NGC 55. All images are primary beam corrected.

2.2 Data reduction and image creation

To create the best possible NGC 55 mosaic images, we included data from the fixed-position 6th antenna for all ATCA observations, as the large gaps in the *uv*-plane that dominate compact array configurations were filled mainly with data from observations in other array configurations. The inclusion of these long baselines resulted in images of high resolution with good *uv*-plane coverage.

The MIRIAD (Sault and Killeen 2006), AIPS (Greisen 2010) and KARMA (Gooch 2006) software packages were used for data reduction and analysis. Because of the large volume of data, the MIRIAD package was compiled to run on a 16-processor high-performance computer system.

MIRIAD was used for all data reduction and imaging, however pre-processing in AIPS was required for the VLA

Table 3 Summary of ATCA CABB observations of NGC 55 at $\lambda = 6$ cm used in this study

Instrument	Project code	Dates	Array	ν (MHz)	$\Delta\nu$ (MHz)	Primary calibrator	Secondary calibrator	Integration time (h)	Included in image
ATCA	C2421	15 Mar 2011	1.5A	5500	2048	1934-638	0010-401	27.28	Y
ATCA	C2421	20 Feb 2011	EW352	5500	2048	1934-638	0010-401	26.91	Y
ATCA	C2421	09–10 Nov 2010	750A	5500	2048	1934-638	0010-401	31.04	Y
ATCA	C1974	28 Mar 2010	H168	5600	2048	1934-638	0008-421	136.80	Y
ATCA	C1757	09–10 May 2009	H168	5500	2048	1934-638	0022-423	370.00	Y

Table 4 Summary of ATCA CABB observations of NGC 55 at $\lambda = 3$ cm used in this study

Instrument	Project code	Dates	Array	ν (MHz)	$\Delta\nu$ (MHz)	Primary calibrator	Secondary calibrator	Integration time (h)	Included in image
ATCA	C2421	15 Mar 2011	1.5A	9000	2048	1934-638	0010-401	27.28	Y
ATCA	C2421	20 Feb 2011	EW352	9000	2048	1934-638	0010-401	26.91	Y
ATCA	C2421	09–10 Nov 2010	750A	9000	2048	1934-638	0010-401	31.04	Y

data. This process consisted of importing the data into AIPS using the task FILLM, and then splitting the sources into separate datasets with SPLIT. Using the task UVFIX, source coordinates were converted from the B1950 to the J2000 reference frame. The task FITTP was then used to export each source to a FITS file. The MIRIAD task FITS was then used to import these fits files and convert them to MIRIAD files. For the ATCA data, the task ATLOD was used to convert the raw observation files into MIRIAD files.

Typical calibration and flagging procedures were then carried out (Sault and Killeen 2006), including the use of the guided automatic flagging task PGFLAG. Using the task INVERT with a robust weighting scheme, images were created for each ATCA and VLA project separately. Each image was then cleaned using the task MOSSDI. The MOSSDI task is a SDI clean algorithm designed for mosaic images (Steer et al. 1984). To convolve a clean model the task RESTOR was then used on each of the cleaned maps. These images were created and visually inspected to assess the data quality.

Once the images had been verified to be free of errors, data observed at the same wavelength were combined in the *uv*-plane as mosaics by using the INVERT and providing the datasets of all observations as the input. This produced 4 dirty maps of all calibrated data of NGC 55 at 20, 13, 6 and 3 cm wavelengths, respectively. These dirty maps were then deconvolved using a more directed approach by providing MOSSDI with boxed regions around each visible source. This method produced superior images which were then restored to produce the combined images. The images were then cropped using IMSUB for analysis so that all images covered the same area of sky ($\sim 0.63^\circ \times 0.41^\circ$) centred at approximately 0h 15m 09s, $-39^\circ\ 12'\ 30''$ (J2000).

3 Results

When visually inspecting the images produced from different observations, the effects of the different array configurations is apparent. As mentioned previously, compact arrays produce low resolution images with greater *uv*-coverage whereas larger arrays produce higher resolution images with less *uv*-coverage. While point sources are resolved to be much larger at lower resolutions, the advantage of the lower resolution is that they display extended emission throughout the field. This extended emission is lost in the high resolution images. The difference between an image produced using data from a compact array and an image produced using a larger configuration is obvious as can be seen in Figs. 1 and 2. Ideal images are those which have high resolution but also contain extended emission data, which is where the technique of combining observations is advantageous.

After the initial inspection, it was determined that the data from the ATCA project C295 contained very poor *uv*-coverage and very limited hour angle coverage (0.99 hours). As a consequence, the final image contained several errors. Normally, these errors would disappear or lessen significantly when combined with other data observed in varying array configurations, as the majority of the gaps in the *uv*-coverage would be filled by the combined data. Since C295 was observed in one of the largest configurations (6C) and was the only observation at this configuration, there was insufficient data to fill the missing *uv*-coverage. Therefore, the data from C295 was excluded from the final image. Similarly, projects C1974 and C1757 were not included in the final 6 cm image because of their low resolution. As all of the 6 cm observations were conducted with the upgraded

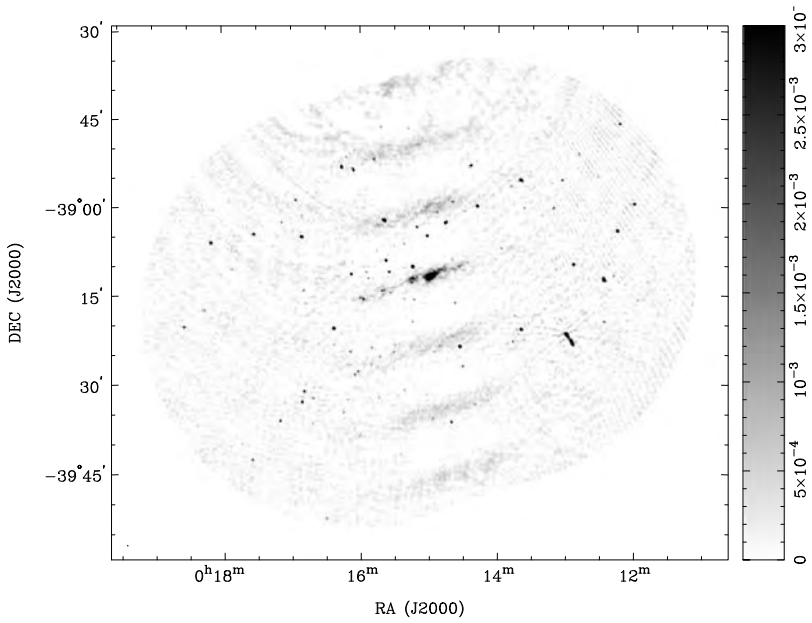

Fig. 1 ATCA Project C287 radio-continuum mosaic of NGC 55 at $\lambda = 20$ cm in Jy/beam. This image illustrates the high resolution produced by observations using a sparse array with long baselines. The synthesised beam is $7.93'' \times 4.99''$ and the r.m.s. noise is 0.09 mJy/beam

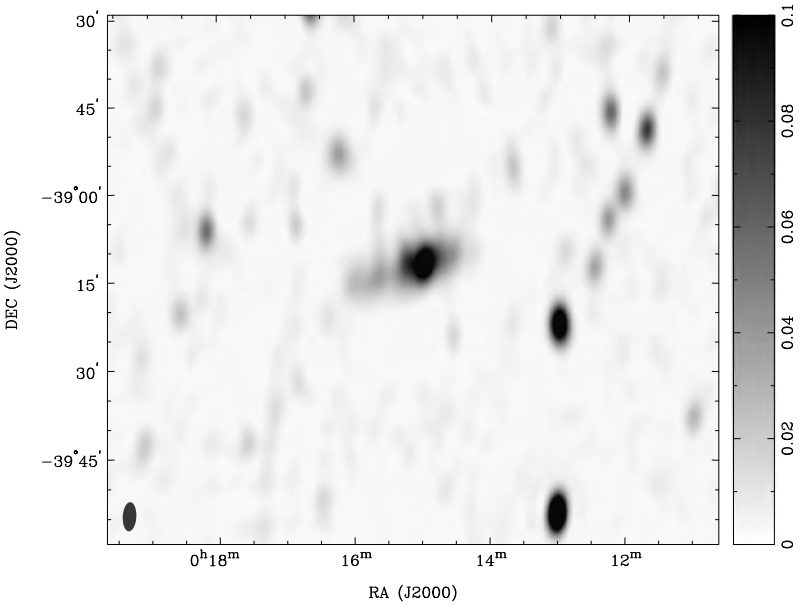

Fig. 2 ATCA Project C1341 radio-continuum mosaic of NGC 55 at $\lambda = 20$ cm in Jy/beam. This image illustrates the low resolution produced by observations using a compact array with short baselines. The synthesised beam is $281.93'' \times 188.82''$ and the r.m.s. noise is 2.13 mJy/beam

ATCA Compact Array Broadband Backend (CABB) and, at present, there exists no wide-bandwidth deconvolution algorithm for mosaics in MIRIAD, we had to merge the images in the image plane using IMMERGE. We found that when using this method, the low resolution data appeared to be weighted incorrectly and much of the high resolution data was overwhelmed by the low resolution data. Thus, these data were not used to create the final 6 cm image.

In addition, the VLA observations were also excluded from the final 20 cm image (Fig. 3) as the inclusion of this data overpowered the extended emission from the ATCA observations. Excluding this data was of little consequence as the main advantage of VLA data is the higher resolution, however the largest VLA array configuration used to observe NGC 55 was a single observation in the BC array which has a maximum baseline separation of approximately 7.6 km. This is relatively close to that of the 6 km maximum baseline at ATCA and so we decided the preservation of the extended emission data was worth more than the slight increase in resolution that would be gained by including the VLA data. Information on the final images used in this paper is given in Table 5.

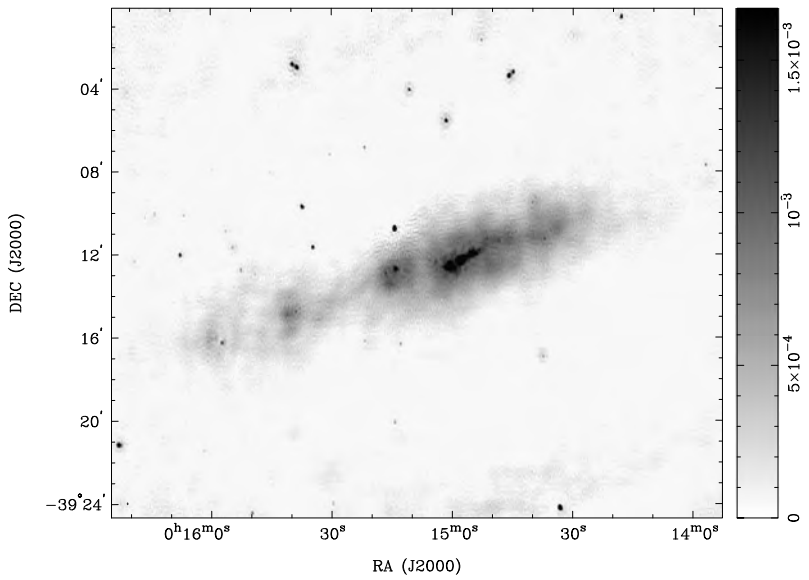

Fig. 3 Cropped total intensity image of all ATCA data (excluding C295) of NGC 55 at $\lambda = 20$ cm in Jy/beam. The synthesised beam is $7.94'' \times 4.99''$ and the r.m.s. noise is 0.12 mJy/beam

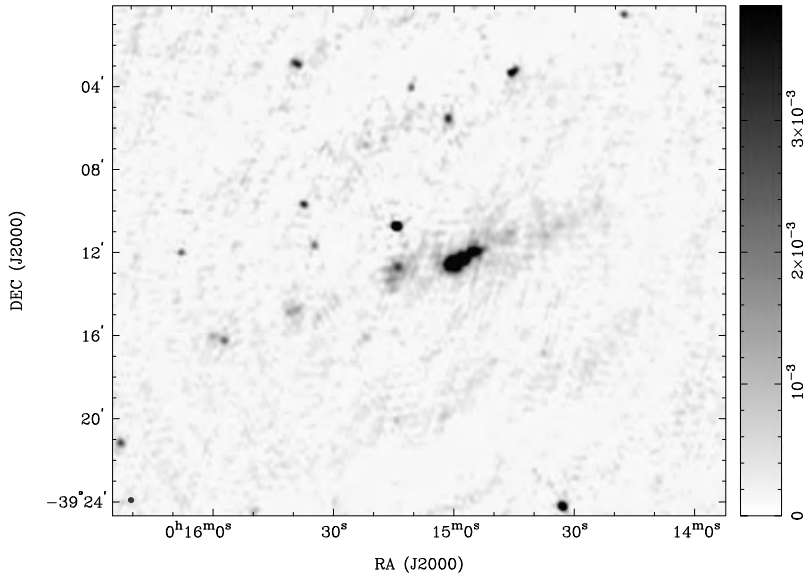

Fig. 4 Cropped total intensity image of all ATCA data of NGC 55 at $\lambda = 13$ cm in Jy/beam. The synthesised beam is $18.29'' \times 16.96''$ and the r.m.s. noise is 0.09 mJy/beam

Table 5 Image details of ATCA single and merged projects of NGC 55 mosaics at 20, 13, 6 and 3 cm that were used to produce the merged images used for the measurements given in this paper. Merged images were created using joint-deconvolution of all projects

ATCA Project	Centre ν (MHz)	Synthesised Beam FWHM ($''$)	r.m.s (mJy/beam)	Figure
C287	1362	7.93×4.99	0.09	1
C1341	1384	281.93×188.82	2.13	2
C1612	1384	426.14×279.93	1.08	–
C1757	1384	29.29×24.04	0.99	–
Merged 20 cm	1366	7.94×4.99	0.09	3
C287	2378	18.29×16.96	0.18	4
C2421	5500	5.43×4.68	0.03	5
C2421	9000	5.26×3.62	0.05	6

Table 6 List of point sources in the NGC 55 field at $\lambda = 20$, 13, 6 and 3 cm. RA (3) and Dec (4) are in J2000 coordinates. Column 9 is the best fit spectral index for all flux measurements of a source. Blank cells indicate no measurement was detected. Asterisks (*) indicate no coverage was available. Daggers (†) indicate sources that were resolved as a single source at $\lambda = 13$ cm but as multiple sources at other wavelengths. These sources were therefore not included in the estimation of α

1 Index	2 Source name	3 RA (h m s)	4 Dec (° ′ ″)	5 S_{20cm} (mJy)	6 S_{13cm} (mJy)	7 S_{6cm} (mJy)	8 S_{3cm} (mJy)	9 α	10 Optical ID	11 IR ID	12 X-Ray ID	13 Source class
1	J001357-390742	00:13:57	−39:07:42	1.05		0.40		-0.69 ± 0.14	*	Y		BKG
2	J001358-390409	00:13:58	−39:04:09			0.41	0.31	-0.55 ± 0.40	*			BKG
3	J001418-390034	00:14:18	−39:00:34	5.47	3.07	0.89		-1.32 ± 0.12	*	Y		BKG (CSS)
4	J001420-390531	00:14:20	−39:05:31			0.21						BKG
5	J001427-391012	00:14:27	−39:10:12			0.15			Y	Y		H II
6	J001430-390129	00:14:30	−39:01:29	0.50					*	Y		BKG
7	J001431-391829	00:14:31	−39:18:29			0.19			Y			BKG
8	J001433-392415	00:14:33	−39:24:15	11.84	10.77			-0.17 ± 0.36	*			BKG
9	J001437-391118	00:14:37	−39:11:18	1.89	1.25	0.37	0.25	-1.13 ± 0.10	Y		Y	SNR
10	J001437-391659	00:14:37	−39:16:59	0.81								BKG
11	J001440-390934	00:14:40	−39:09:34	1.15					Y			H II
12	J001445-390315	00:14:45	−39:03:15	2.96	6.77†	0.73		-1.01 ± 0.14	*		Y	BKG (CSS)
13	J001446-390327	00:14:46	−39:03:27	6.16	6.77†	1.82		-0.88 ± 0.14	*			BKG (CSS)
14	J001446-391104	00:14:46	−39:11:04			0.43			Y	Y		H II
15	J001447-391114	00:14:47	−39:11:14		1.96				Y		Y	SNR
16	J001447-391133	00:14:47	−39:11:33			0.20			Y	Y		H II
17	J001448-391123	00:14:48	−39:11:23			0.25			Y			H II
18	J001451-391118	00:14:51	−39:11:18			0.42			Y			H II
19	J001452-391152	00:14:52	−39:11:52			0.32			Y	Y		H II
20	J001453-390142	00:14:53	−39:01:42	0.97					*	Y		BKG
21	J001457-390556	00:14:57	−39:05:56			0.33						BKG
22	J001457-390559	00:14:57	−39:05:59			0.18						BKG
23	J001502-390537	00:15:02	−39:05:37	3.65	4.37	1.88		-0.52 ± 0.36	Y	Y	Y	BKG
24	J001511-390403	00:15:11	−39:04:03	2.19	2.46	0.18		-1.92 ± 0.92	*			BKG (CSS)
25	J001513-391624	00:15:13	−39:16:24	1.10		0.24		-1.09 ± 0.14		Y		BKG (CSS)
26	J001514-391049	00:15:14	−39:10:49	23.31	20.26	13.68	8.80	-0.51 ± 0.08				BKG
27	J001514-391246	00:15:14	−39:12:46	3.51	4.67	1.62	0.89	-0.81 ± 0.27	Y	Y	Y	SNR
28	J001514-392009	00:15:14	−39:20:09	0.88		0.54		-0.35 ± 0.14	*			BKG
29	J001516-391308	00:15:16	−39:13:08	1.38					Y	Y		H II
30	J001518-390736	00:15:18	−39:07:36			0.12			Y			BKG
31	J001522-390655	00:15:22	−39:06:55	0.98	1.25	0.72		-0.26 ± 0.30				BKG
32	J001522-391613	00:15:22	−39:16:13	0.81	1.05	1.14	0.97	0.10 ± 0.10			Y	BKG
33	J001530-390715	00:15:30	−39:07:15	0.58		0.58		-0.01 ± 0.14	Y	Y	Y	BKG
34	J001530-392403	00:15:30	−39:24:03	0.63					*			BKG
35	J001533-391511	00:15:33	−39:15:11	1.00		0.67	0.42	-0.42 ± 0.13	*	Y	Y	SNR
36	J001535-391143	00:15:35	−39:11:43	3.05	2.38	1.02	0.42	-1.04 ± 0.17	*	Y		BKG (CSS)
37	J001537-390946	00:15:37	−39:09:46	4.53	3.88	1.94	0.87	-0.86 ± 0.17	*	Y	Y	BKG (CSS)
38	J001538-390301	00:15:38	−39:03:01	6.32					*			BKG
39	J001538-391437	00:15:38	−39:14:37	1.08		0.22		-1.13 ± 0.14	*			INTR
40	J001539-390258	00:15:39	−39:02:58		4.67				*			BKG

Table 6 (*Continued*)

1 Index	2 Source name	3 RA (h m s)	4 Dec (° ′ ″)	5 S_{20cm} (mJy)	6 S_{13cm} (mJy)	7 S_{6cm} (mJy)	8 S_{3cm} (mJy)	9 α	10 Optical ID	11 IR ID	12 X-Ray ID	13 Source class
41	J001539-391448	00:15:39	−39:14:48	1.69	2.16†	0.74	0.43	-0.69 ± 0.10	*	Y		INTR
42	J001539-391533	00:15:39	−39:15:33			0.24			*	Y		H II
43	J001540-390252	00:15:40	−39:02:52	4.97					*	Y		BKG
44	J001540-391452	00:15:40	−39:14:52		2.16				*	Y		H II
45	J001541-391457	00:15:41	−39:14:57	2.03	2.16†	0.84	0.46	-0.76 ± 0.12	*	Y	Y	SNR
46	J001545-390807	00:15:45	−39:08:07	0.44					*	Y		BKG
47	J001549-391259	00:15:49	−39:12:59	0.59					*	Y		BKG
48	J001550-392429	00:15:50	−39:24:29	1.32	1.21	0.32		-1.07 ± 0.39	*			BKG (CSS)
49	J001552-391248	00:15:52	−39:12:48	1.00		0.51		-0.48 ± 0.14	*	Y	Y	BKG
50	J001552-392029	00:15:52	−39:20:29			0.18			*			BKG
51	J001552-392042	00:15:52	−39:20:42			0.19			*			BKG
52	J001555-391143	00:15:55	−39:11:43	0.67					*			BKG
53	J001556-391057	00:15:56	−39:10:57	0.50					*			BKG
54	J001557-391618	00:15:57	−39:16:18	1.76	2.86	1.43	0.83	-0.46 ± 0.28	*	Y		H II
55	J001558-391650	00:15:58	−39:16:50			0.55	0.33	-1.02 ± 0.40	*	Y		INTR
56	J001600-390758	00:16:00	−39:07:58	0.23					*	Y		BKG
57	J001600-391605	00:16:00	−39:16:05		1.58	0.74	0.27	-1.29 ± 0.30	*	Y	Y	SNR
58	J001602-392128	00:16:02	−39:21:28	0.30		0.22		-0.22 ± 0.14	*	Y	Y	BKG
59	J001607-391009	00:16:07	−39:10:09	0.66		0.28		-0.63 ± 0.14	*		Y	BKG
60	J001608-391203	00:16:08	−39:12:03	3.23	2.63	1.51	0.86	-0.69 ± 0.10	*			BKG
61	J001609-391420	00:16:09	−39:14:20			0.46	0.25	-1.27 ± 0.40	*			BKG (CSS)
62	J001614-391005	00:16:14	−39:10:05	0.73					*			BKG
63	J001616-391014	00:16:16	−39:10:14	0.40					*			BKG
64	J001619-391221	00:16:19	−39:12:21	0.43		0.24		-0.44 ± 0.14	*			BKG
65	J001622-392111	00:16:22	−39:21:11	6.34	3.40	0.63		-1.69 ± 0.24	*			BKG (CSS)
66	J001624-390151	00:16:24	−39:01:51	0.55					*			BKG

4 Discussion

4.1 Discrete sources within the field of NGC 55

A total of 66 sources above 5σ (0.45, 0.92, 0.15, 0.25 mJy/beam at wavelengths of 20, 13, 6 and 3 cm, respectively) were identified within the field of NGC 55. These sources were catalogued by position and flux density. 33 of these sources were detected at more than one of the observed wavelengths and consequently their spectral index, α, was estimated using the equation $S \propto \nu^{\alpha}$. Simple linear regression was then performed to determine the best-fit value for α between the measured frequencies. This catalogue was then compared to optical (Royal Observatory, Edinburgh et al. 1977), infrared (Dale et al. 2009; Jarrett et al. 2003) and X-ray images (Pannuti et al. 2013; Stobbart et al. 2006) of the NGC 55 field. Source coincidences were accepted for sources within 1 beam of the highest resolution radio image being compared.

Based on their location and comparison with the images at other frequency bands, the sources were classified as either background (BKG) sources, supernova remnants (SNR), or ionised hydrogen regions (H II). Sources outside of the extended emission boundary seen in Fig. 3 were classified as background sources. Sources inside the boundary were classified as intrinsic (INTR) sources which are further classified as either SNRs or H II regions. If X-ray radiation was detected from the intrinsic source, then it was classified as a SNR candidate since the violent explosions and shockwaves produced by a supernova are known to emit strong X-rays. Also, SNRs usually exhibit steeper spectral index of about $\alpha < -0.5$ (Filipovic et al. 1998). Sources emitting

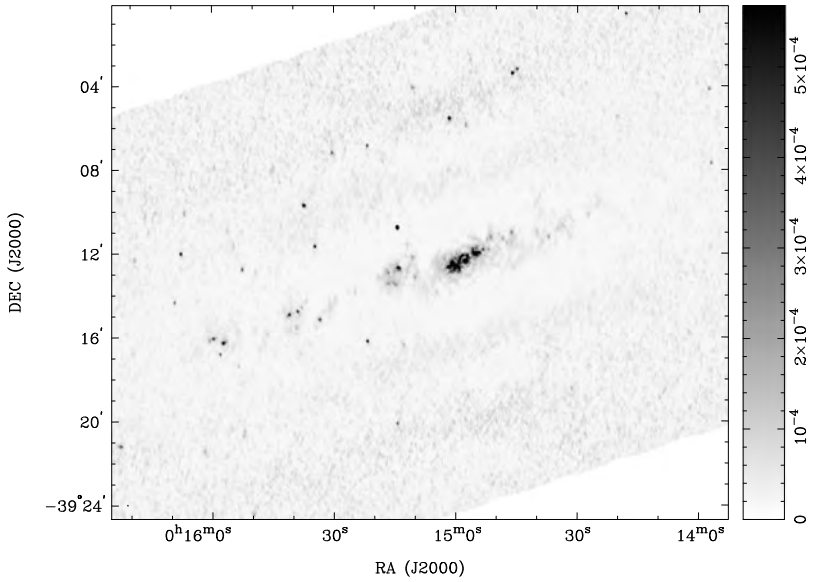

Fig. 5 Cropped total intensity image of all ATCA data of NGC 55 at $\lambda = 6$ cm in Jy/beam. The synthesised beam is $5.43'' \times 4.68''$ and the r.m.s. noise is 0.03 mJy/beam

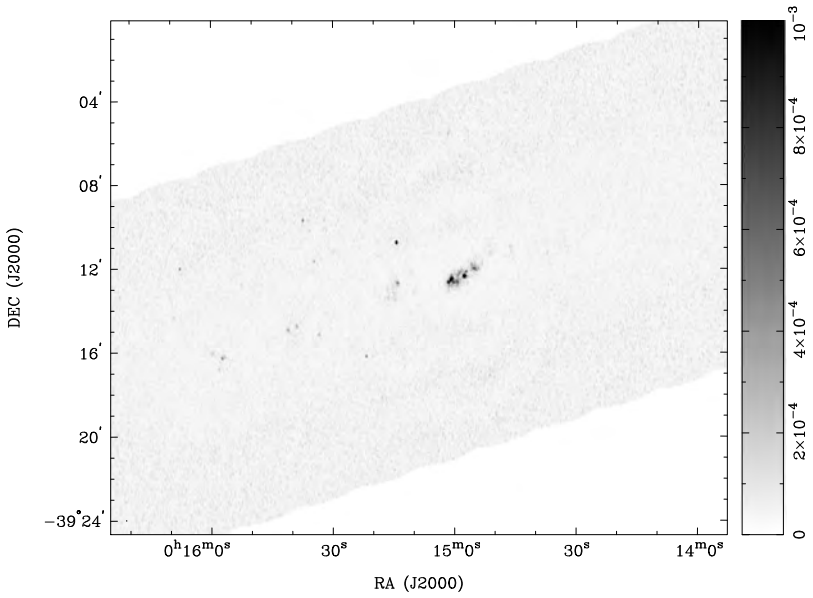

Fig. 6 Cropped total intensity image of all ATCA data of NGC 55 at $\lambda = 3$ cm in Jy/beam. The synthesised beam is $5.26'' \times 3.62''$ and the r.m.s. noise is 0.05 mJy/beam

infrared radiation but no detectable X-rays were classified as H II regions. Of the 66 detected radio-continuum sources, 46 were classified as background sources, 11 as H II regions, and 6 as SNR candidates. The full list of sources with positions, flux densities, spectral index and classifications can be found in Table 6.

The low number of detected SNR candidates suggests that the star formation rate for NGC 55 is relatively low. To estimate the high mass star formation rate, we used the relation described by Kennicutt (1983). We adjusted the estimated Hα luminosity of NGC 55 given by Hoopes et al. (1996) to 4.08×10^{40} ergs s^{-1} to reflect our adopted distance of 2.08 Mpc. The relation provided estimated high mass star formation rate of 0.06 $M_{\odot}$ year^{-1}. Compared to the star formation rates of other galaxies in the Sculptor Group (the highest being NGC 253 at 0.20 $M_{\odot}$ year^{-1}, and the lowest being NGC 45 at 0.01 $M_{\odot}$ year^{-1}), the star formation rate of NGC 55 is comparatively low.

In Fig. 7 we show the spectral index distribution of all radio-continuum sources found in this study (Table 6; Col. 9). Here, we note that the spectral index alone cannot successfully distinguish between various type of sources. Of the 66 sources reported here, 10 have an estimated spectral index of steeper than −0.85, classifying them as can-

didates for compact steep spectrum (CSS) sources (Table 6; Col. 13).

4.2 Spectral index map

We show in Fig. 8 an image where each pixel represents the spectral index calculated across all 4 observed frequencies. This image was created based on measurements from Figs. 3, 4, 5 and 6 after convolving the images to the largest beam size. Pixels below the noise level are ignored.

The core of galaxy is shown to have a shallow spectral index of between −0.2 and −0.4 (shown as red pixels). This indicates that the core of the galaxy is a region of high thermal radiation output. The most likely reason for this is that the core of the galaxy is a dense star forming region. The spectral index becomes steeper moving further away from the centre of NGC 55, indicating a dominance of non-thermal radiation which could be caused by either synchrotron or inverse-Compton radiative mechanisms. Objects which radiate using this mechanism include SNRs and energetic jets.

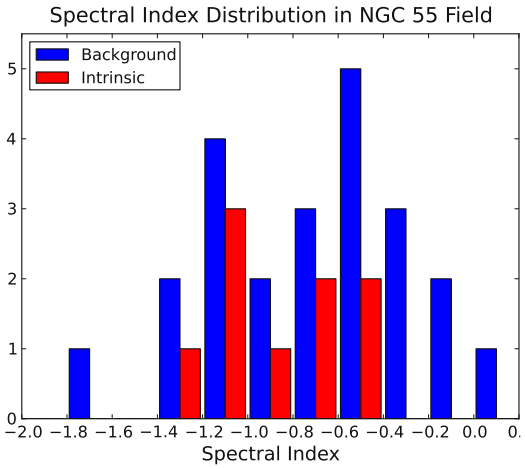

Fig. 7 Histogram of the spectral index distribution of sources in the NGC 55 field with bin widths of 0.2. Sources with high spectral index uncertainties ($> \pm 0.4$) were excluded

5 Conclusion

We present and discuss a series of new highly sensitive, high resolution radio-continuum images of NGC 55 at wavelengths 20, 13, 6 and 3 cm. These images were created by combining data collected from observations using the ATCA radio interferometer telescope. As a result of combining the data, the final images had dramatically reduced levels of noise with higher angular resolution when compared with previous studies. From the new images, a total of 66 radio sources were detected within the field of NGC 55, 33 of which were detected over multiple wavelengths. Of these 66 sources, 46 have been classified as background sources, 11 as H II regions, and 6 as SNR candidates. Spectral indices were also calculated for these multi-wavelength sources. A spectral index map was produced for the galaxy, revealing a high level of thermal radiation emission from the core of the galaxy. Several concentrations of high non-thermal radiation emission were also detected within the plane of the galaxy.

Acknowledgements The National Radio Astronomy Observatory is a facility of the National Science Foundation operated under cooperative agreement by Associated Universities, Inc. The Australia Telescope Compact Array is part of the Australia Telescope National Fa-

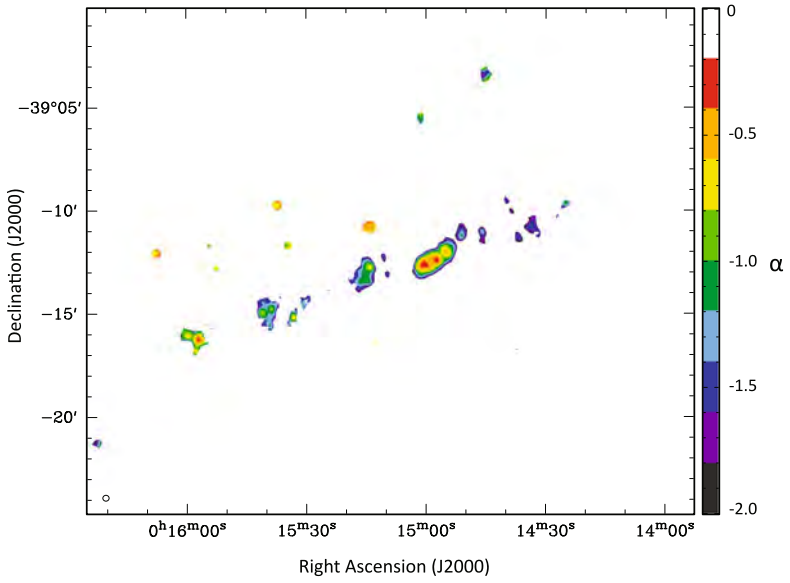

Fig. 8 Spectral index pixel map of NGC 55. Image is in terms of spectral index α. The *colour bar* on the right reflects the spectral index value multiplied by 1000. The synthesised beam is $18.29'' \times 16.96''$

cility which is funded by the Commonwealth of Australia for operation as a National Facility managed by CSIRO. This paper includes archived data obtained through the Australia Telescope Online Archive (http://atoa.atnf.csiro.au) and the NRAO Science Data Archive (http://archive.nrao.edu).

References

Condon, J.J., Helou, G., Sanders, D.B., Soifer, B.T.: Astrophys. J. Suppl. Ser. **103**, 81 (1996)

Dalcanton, J.J., Williams, B.F., Seth, A.C., Dolphin, A., Holtzman, J., Rosema, K., Skillman, E.D., Cole, A., Girardi, L., Gogarten, S.M., Karachentsev, I.D., Olsen, K., Weisz, D., Christensen, C., Freeman, K., Gilbert, K., Gallart, C., Harris, J., Hodge, P., de Jong, R.S., Karachentseva, V., Mateo, M., Stetson, P.B., Tavarez, M., Zaritsky, D., Governato, F., Quinn, T.: Astrophys. J. Suppl. Ser. **183**, 67 (2009)

Dale, D.A., Cohen, S.A., Johnson, L.C., Schuster, M.D., Calzetti, D., Engelbracht, C.W., Gil de Paz, A., Kennicutt, R.C., Lee, J.C., Begum, A., Block, M., Dalcanton, J.J., Funes, J.G., Gordon, K.D., Johnson, B.D., Marble, A.R., Sakai, S., Skillman, E.D., van Zee, L., Walter, F., Weisz, D.R., Williams, B., Wu, S.-Y., Wu, Y.: Astrophys. J. **703**, 517 (2009)

Filipovic, M.D., Haynes, R.F., White, G.L., Jones, P.A.: Astron. Astrophys. Suppl. Ser. **130**, 421 (1998)

Galvin, T.J., Filipović, M.D., Crawford, E.J., Wong, G., Payne, J.L., De Horta, A., White, G.L., Tothill, N., Drašković, D., Pannuti, T.G., Grimes, C.K., Cahall, B.J., Millar, W.C., Laine, S.: Astrophys. Space Sci. **340**, 133 (2012)

Gooch, R.: Karma Users Guide. ATNF, Sydney (2006)

Greisen, E. (ed.): AIPS Cookbook. The National Radio Astronomy Observatory, Charlottesville (2010)

Hoopes, C.G., Walterbos, R.A.M., Greenwalt, B.E.: Astron. J. **112**, 1429 (1996). doi:10.1086/118111

Jarrett, T.H., Chester, T., Cutri, R., Schneider, S.E., Huchra, J.P.: Astron. J. **125**, 525 (2003)

Karachentsev, I.D., Grebel, E.K., Sharina, M.E., Dolphin, A.E., Geisler, D., Guhathakurta, P., Hodge, P.W., Karachentseva, V.E., Sarajedini, A., Seitzer, P.: Astron. Astrophys. **404**, 93 (2003)

Kennicutt, R.C. Jr.: Astrophys. J. **272**, 54 (1983). doi:10.1086/161261

Pannuti, T., Napier, J.P., Schlegel, E.M., Laine, S.J., Filipovic, M.D., Griffith, S.A., Staggs, W.D.: In: American Astronomical Society Meeting Abstracts, vol. 221, p. 249 (2013)

Payne, J.L., Filipović, M.D., Pannuti, T.G., Jones, P.A., Duric, N., White, G.L., Carpano, S.: Astron. Astrophys. **425**, 443 (2004)

Puche, D., Carignan, C., Wainscoat, R.J.: Astron. J. **101**, 447 (1991)

Royal Observatory, Edinburgh, European Southern Observatory, Science Research Council (Great Britain): ESO/SRC Atlas of the Southern Sky. ESO Sky Atlas Laboratory, Geneva (1977)

Sault, R., Killeen, N.: Miriad Users Guide. ATNF, Sydney (2006)

Steer, D.G., Dewdney, P.E., Ito, M.R.: Astron. Astrophys. **137**, 159 (1984)

Stobbart, A.-M., Roberts, T.P., Warwick, R.S.: Mon. Not. R. Astron. Soc. **370**, 25 (2006)

A.30 Related Paper 30

Sturm, R., Drašković, D., Filipović, M. D., Haberl, F., Collier, J., Crawford, E. J., Ehle, M., De Horta, A., Pietsch, W., Tothill, N. F. H., and Wong, G. (2013a). Active galactic nuclei behind the SMC selected from radio and X-ray surveys. *A&A*, 558:A101

My contribution was to assist in the data analysis. This is a 10% contribution.

A&A 558, A101 (2013)
DOI: 10.1051/0004-6361/201220564

Astronomy & Astrophysics

Active galactic nuclei behind the SMC selected from radio and X-ray surveys⋆

R. Sturm[1], D. Drašković[2], M. D. Filipović[2], F. Haberl[1], J. Collier[2], E. J. Crawford[2], M. Ehle[3], A. De Horta[2], W. Pietsch[1], N. F. H. Tothill[2], and G. Wong[2]

[1] Max-Planck-Institut für extraterrestrische Physik, Giessenbachstraße, 85748 Garching, Germany
e-mail: rsturm@mpe.mpg.de
[2] University of Western Sydney, Locked Bag 1797, Penrith South DC, NSW1797 Sydney, Australia
[3] XMM-Newton Science Operations Centre, ESAC, ESA, PO Box 78, 28691 Villanueva de la Cañada, Madrid, Spain

Received 15 October 2012 / Accepted 20 July 2013

ABSTRACT

Context. The *XMM-Newton* survey of the Small Magellanic Cloud (SMC) revealed 3053 X-ray sources with the majority expected to be active galactic nuclei (AGN) behind the SMC. However, the high stellar density in this field often does not allow assigning unique optical counterparts and hinders source classification. On the other hand, the association of X-ray point sources with radio emission can be used to select background AGN with high confidence, and to constrain other object classes like pulsar wind nebula.
Aims. To classify X-ray and radio sources, we use clear correlations of X-ray sources found in the *XMM-Newton* survey with radio-continuum sources detected with ATCA and MOST.
Methods. Deep radio-continuum images were searched for correlations with X-ray sources of the *XMM-Newton* SMC-survey point-source catalogue as well as galaxy clusters seen with extended X-ray emission.
Results. Eighty eight discrete radio sources were found in common with the X-ray point-source catalogue in addition to six correlations with extended X-ray sources. One source is identified as a Galactic star and eight as galaxies. Eight radio sources likely originate in AGN that are associated with clusters of galaxies seen in X-rays. One source is a pulsar wind nebula candidate. We obtain 43 new candidates for background sources located behind the SMC. A total of 24 X-ray sources show jet-like radio structures.

Key words. Magellanic Clouds – radio continuum: general – X-rays: general – catalogs

1. Introduction

Searching for background sources in fields with high stellar density like the Small Magellanic Cloud (SMC) can be intricate. Once background sources behind the SMC are identified, they constitute a valuable sample of sources. Besides studying these sources (e.g. Kelly et al. 2009), when multi-wavelength data from several epochs are available, they provide an ideal reference frame for astrometry as soon as their positions are known precisely. This is important for proper-motion studies of the SMC (e.g. Piatek et al. 2008), but also to reduce systematic uncertainties in the position of X-ray sources (e.g. Watson et al. 2009). Further, the interstellar medium of the SMC may be studied with the help of absorption lines in the spectra of illuminators in the background.

The first two quasars behind the SMC were reported by Mills et al. (1982) and Wilkes et al. (1983). Later on, Tinney et al. (1997) used optical spectroscopy to confirm additional eight candidates, selected from ROSAT X-ray sources. Dobrzycki et al. (2003a,b) added five X-ray selected candidates and five candidates chosen from their optical variability by Eyer (2002). Kozłowski & Kochanek (2009) selected 657 quasar candidates using *Spitzer* infrared and near-infrared photometry. Including also candidates selected from optical variability, Kozłowski et al. (2011, 2013) were able to confirm 193 of 766 observed candidates with followup spectroscopy, raising the number of confirmed background quasars to ∼200.

In this study, we search for sources with common X-ray and radio emission and classify them. The *XMM-Newton* survey of the SMC (Haberl et al. 2012b), provides for the first time a complete coverage of the SMC main body with imaging X-ray optics up to photon energies of 12 keV and with a source-detection sensitivity of $\sim 2 \times 10^{-14}$ erg s^{-1} cm^{-2}. Compared to previous surveys with ROSAT in the (0.1−2.0) keV band (Haberl et al. 2000; Sasaki et al. 2000), the sensitivity of *XMM-Newton* at harder X-rays results in the detection of more background sources. The higher position accuracy allows a more unique correlation with radio counterparts. To identify X-ray and radio sources, we compare our X-ray point-source catalogue with deep merged Australia Telescope radio images of the SMC, having unprecedented sensitivity compared to earlier studies (e.g. Filipović et al. 1997, 1998, 2002; Payne et al. 2004). Except for a few Galactic stars (such as young stellar objects (YSO) or binary stars) and rare SMC objects like pulsar wind nebulae (PWNe), the bulk of discrete sources emitting radio and X-rays are expected to originate in background objects. Active galactic nuclei (AGN) produce hard X-ray emission and relativistic jets visible in radio. In some cases emission can originate in nearby normal galaxies, with little or no contribution of an AGN. Also the AGN host galaxy can be part of a cluster of galaxies (ClG), where X-rays originate in the hot intracluster medium and radio-continuum emission from the AGN. Supernova remnants (SNRs) in the SMC also can show radio and X-ray emission.

⋆ Based on observations obtained with *XMM-Newton*, an ESA science mission with instruments and contributions directly funded by ESA Member States and NASA.

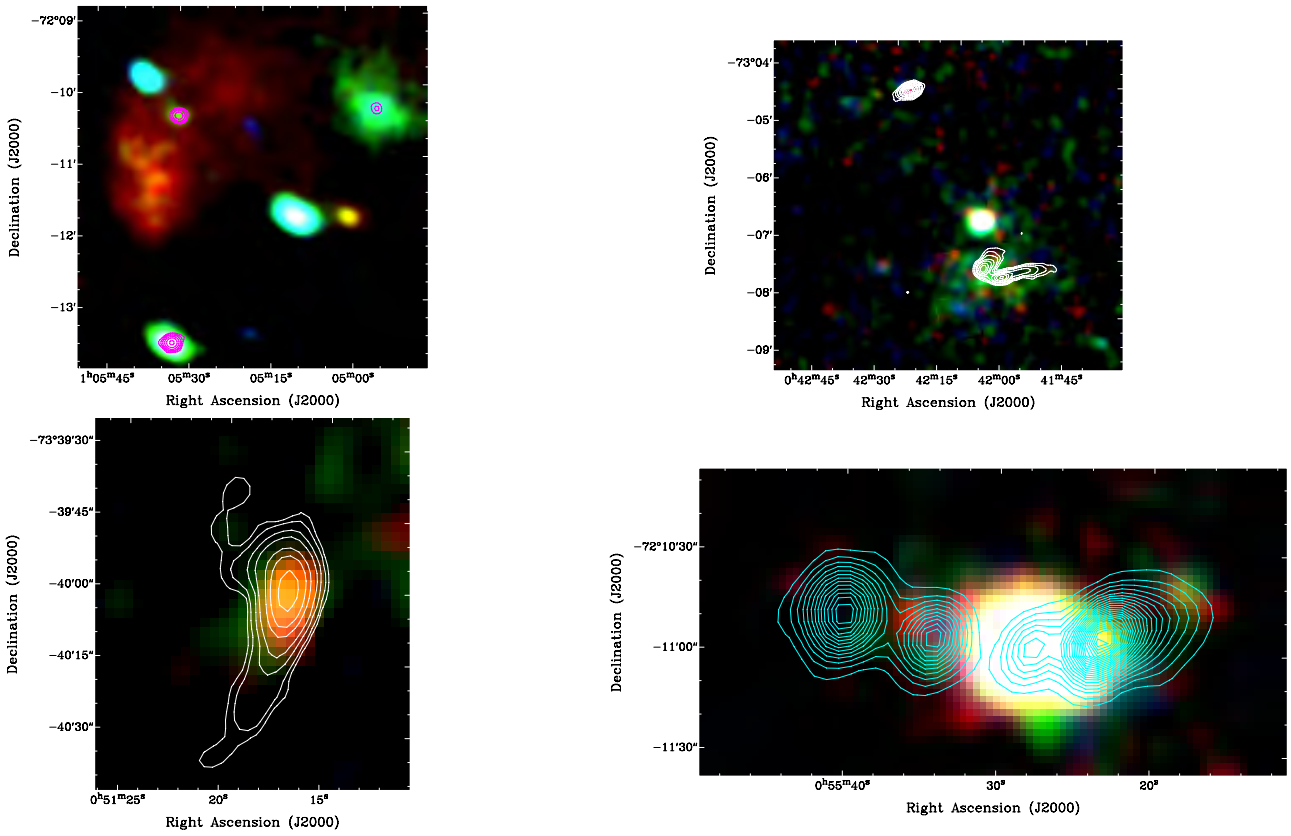

Fig. 1. EPIC X-ray colour images with overlaid radio contours. Red/green/blue corresponds to intensities in the (0.2–1.0) keV, (1.0–2.0) keV and (2.0–4.5) keV band, respectively. *Upper left*: three radio sources in the north-east of the SMC are presented in this image. Source No 14 is seen along SNR DEM S128 (the red structure). In the lower left of the image, source No 8 demonstrates an X-ray and radio point source. In the upper right, a ClG is visible in X-rays, containing a radio source in the centre. Contours are: 0.3, 0.6, 1.2, 2.5, 5, and 10 mJy beam^{-1}, beam = 7.″05 × 6.″63, λ = 20 cm. *Upper right*: the upper radio source correlates with X-ray emission from source No 65. The lower source is a ClG and not included in our X-ray catalogue, due to the extended emission (Haberl et al. 2012b). Two radio jets are visible from one or possibly two AGN, presumably in the ClG. Contours are: 0.3, 0.6, 1, 2, 3, 5, 7, 10, 15, and 20 mJy beam^{-1}, beam = 6.″56 × 6.″16, λ = 20 cm. *Lower left*: source No 27 is a galaxy candidate showing soft X-ray emission and an extended radio structure. Contours are: 0.18, 0.3, 0.6, 1, 2, 3, 5 mJy beam^{-1}, beam = 6.″56 × 6.″16, λ = 20 cm. *Lower right*: source No 3 is a bright X-ray source in the centre of two radio lobes. Contours are: 2 to 50 mJy beam^{-1} in steps of 2 mJy beam^{-1}, beam = 17.″8 × 12.″2, λ = 20 cm.

These sources have a significant extent at the distance of the SMC (10′ translates to ∼3 pc) and can easily be excluded. They are not part of this study as these sources will be reviewed in a subsequent paper. Other X-ray and radio emitting sources like planetary nebulae are unlikely to be detected at SMC distance (Payne et al. 2004).

2. Observations and data reduction

2.1. The XMM-Newton survey of the SMC

The observatory *XMM-Newton* (Jansen et al. 2001) is equipped with three X-ray telescopes (Aschenbach 2002), with EPIC CCD detectors (Strüder et al. 2001; Turner et al. 2001) in their focal planes. *XMM-Newton* performed a survey of the SMC (Haberl et al. 2012b), completely covering the main body with a field size of 5.58 deg^2 and a limiting sensitivity of $\sim 2 \times 10^{-14}$ erg cm^{-2} s^{-1} in the (0.2–12.0) keV band. For each *XMM-Newton* observation, a maximum-likelihood source detection was performed on X-ray images of various energy bands simultaneously, i.e. a similar method as used for the *XMM-Newton* serendipitous source catalogue (Watson et al. 2009). This resulted in a catalogue of 3053 X-ray sources and includes additional outer fields, leading to a total area of 6.32 deg^2. For the list of used observations and a detailed description of the X-ray point-source catalogue, see Sturm et al. (2013). Extended X-ray sources can be found in Haberl et al. (2012b).

2.2. Radio observations of the SMC

Radio-continuum images used in this study (Table 1) were created by combining data from the Australia Telescope Compact Array (ATCA) with data obtained from Parkes radio studies (Filipović et al. 2002; Crawford et al. 2011; Wong et al. 2011a,b, 2012a). We also used high-resolution images from Bojicic et al. (2010) and newly created images of the N 19 region (Wong et al. 2012b). To complement our study we included an image at 36 cm, which was obtained from the MOST survey (Ye & Turtle 1993).

2.3. Correlation

Radio-continuum emission of background sources can show spatial structures caused by jets emitted from the AGN. Examples from this work are shown in Fig. 1. In some cases, the X-ray source, which marks the position of the AGN candidate, is placed in between two radio jets. To find all such sources,

Table 1. Details of radio-continuum data and surveys used in this study.

Column Table 2	λ (cm)	ν (MHz)	Beam size (arcsec)	rms (mJy/beam)	Reference
(9)	36	843	45×45	1.5	Ye & Turtle (1993)
(10)	20	1420	17.8×12.2	1.5	Filipović et al. (2002); Wong et al. (2011a,b)
(11)	20	1420	7.0×6.6	0.1	Ye et al. (1995); Dickel et al. (2001); Bojicic et al. (2010); Wong et al. (2012b)
(12)	13	2370	40×40	1.5	Filipović et al. (2002); Wong et al. (2011b)
(13)	13	2370	7.0×6.6	0.1	Ye et al. (1995); Dickel et al. (2001); Bojicic et al. (2010); Wong et al. (2012b)
(14)	6	4800	30×30	0.5	Crawford et al. (2011); Wong et al. (2012a)
(15)	3	8640	20×20	0.5	Crawford et al. (2011); Wong et al. (2012a)

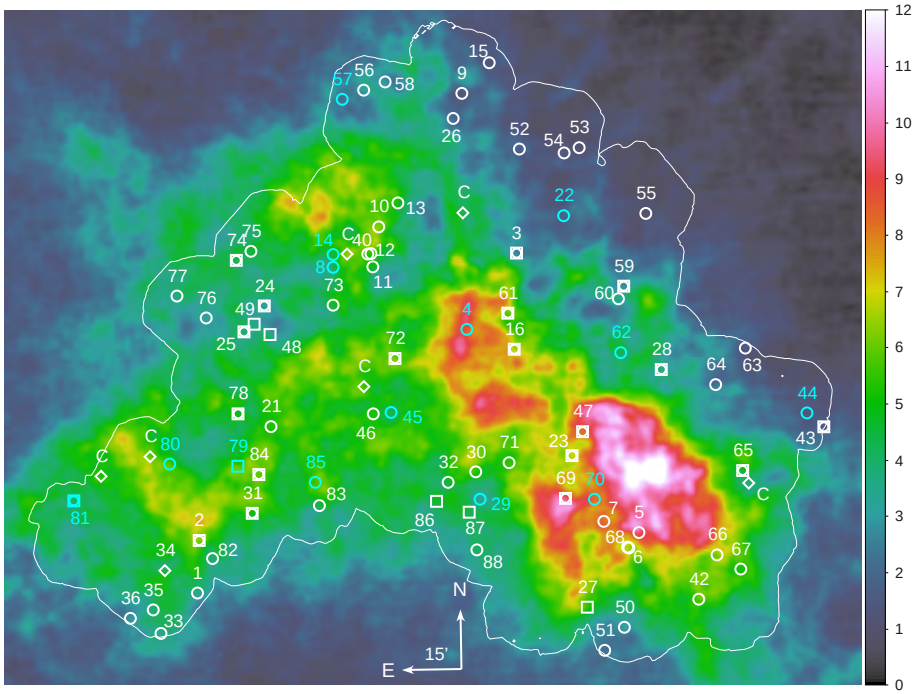

Fig. 2. Spatial distribution of the X-ray sources with radio associations in the main field overplotted on the H map of Stanimirovic et al. (1999). The colour scale indicates the column density in units of 10^{21} cm^{-2}. The white line marks the *XMM-Newton* main field of the SMC survey. Seven additional sources are located in outer fields, not shown here. Labels give the source number (Col. 1 in Table 2). Radio sources in X-ray clusters of galaxies (Table 3) are labelled with C. X-ray radio correlations are shown by circles. If the source shows a jet-like structure in radio, it is shown by a boxed circle. Sources that are classified as galaxies are shown by boxes. Sources that are within ClGs are marked with diamonds. Radio sources with $-0.3 < \alpha < 0$ are plotted in cyan, others in white.

we visually inspected the radio images for counterparts of X-ray sources. We found 88 out of the 3053 sources from the X-ray point-source catalogue with a counterpart visible in at least one radio image. In Table 2, we list the radio sources with an X-ray match. The columns give the following parameters:

(1) running number, No, of the sources in this study;
(2) source number from the *XMM-Newton* SMC point-source catalogue (Sturm et al. 2013);
(3) X-ray flux in the (0.2–4.5) keV band in 10^{-14} erg cm^{-2} s^{-1};
(4) hardness ratio $HR_2 = (R_3 - R_2)/(R_3 + R_2)$ with R_2 and R_3 being the X-ray count rates in the (0.5−1.0) and (1.0−2.0) keV band;
(5−6) sexagesimal J2000 coordinates as derived from radio. For point-like sources a Gaussian fit was used to determine the position, whereas for complex jet-like structures, the position of the peak flux is given. In the case of two radio detections obviously comprising two jets of the same source we list the apparent centre of the perceived origin of the jets;
(7) estimated position uncertainty for the radio position in arcsec based on image resolution;
(8−14) integrated flux densities S_ν in mJy at various radio frequencies ν from the data described in Table 1;
(15) radio spectral index α according to $S_\nu \sim \nu^\alpha$ and uncertainty following Payne et al. (2004);
(16) source classification from this work;
(17) comments on individual sources and references to other catalogues. Jet-like radio structures are noted.

3. Results and discussion

The *XMM-Newton* survey of the SMC provides a continuous coverage of the bar and eastern wing of the SMC and allowed the creation of the most comprehensive X-ray point-source catalogue. At the same time, deeper radio images reveal fainter sources in an even larger area. From the correlation of both datasets we derived a list of 88 discrete sources with X-ray and radio emission. In Fig. 2, we mark all X-ray sources with radio counterparts within the main field (5.58 deg^2) of the *XMM-Newton* survey on an SMC H image from Stanimirovic et al. (1999). The *XMM-Newton* main field is indicated with a white contour. For a description of additional fields disconnected from the main field see Sturm et al. (2013). We do not see a particular correlation of the source density with the SMC H intensity, which is consistent with the sources being mainly background objects. This is also evident when comparing the relative line-of-sight H column density of our sources with the H distribution in the *XMM-Newton* field (Fig. 3). As expected, both show a similar distribution, i.e. we do not find more sources in

Table 2. X-ray to radio-continuum correlations in the SMC field.

(1) No	(2) ID_X	(3) F_X	(4) HR_2	(5) RA_r	(6) Dec_r	(7) ePos	(8) $S_{0.843}$	(9) $S_{1.42}$	(10) $S_{1.42}$	(11) $S_{2.37}$	(12) $S_{2.37}$	(13) $S_{4.8}$	(14) $S_{8.64}$	(15) α	(16) class	(17) comment[a]
1	26	1.1 ± 0.2	0.24 ± 0.13	01 14 27.85	−73 33 12.7	1.5	8.68	1.97	–	2.60	–	3.21	–	−0 .42 ± 0.15	AGN	
2	32	7.7 ± 0.3	0.56 ± 0.03	01 14 05.16	−73 20 06.9	1.5	128.02	78.44	–	51.93	–	30.64	17.34	−0 .84 ± 0.05	AGN	jet, P04, H00, K09
3	59	25.9 ± 0.5	0.19 ± 0.02	00 55 23.16	−72 10 55.8	1.5	242.21	76.68	–	67.44	–	46.78	28.90	−0 .79 ± 0.05	AGN	jet, H00
4	85	2.0 ± 0.2	0.76 ± 0.16	00 58 15.42	−72 30 07.5	1.5	–	2.30	–	–	–	2.25	–	−0 .02 ± 0.25	AGN	H00, K09
5	117	5.4 ± 0.3	0.53 ± 0.17	00 48 18.79	−73 21 00.0	1.0	–	–	0.87	–	0.45	–	–	−1 .33 ± 0.25	AGN/HMXB?	K11, S05, K09
6	118	5.3 ± 0.3	0.31 ± 0.40	00 48 54.42	−73 24 57.2	1.0	1.45	–	1.65	–	0.97	–	–	−0 .40 ± 0.20	AGN	
7	135	0.6 ± 0.1	0.23 ± 0.49	00 50 23.69	−73 18 20.8	1.0	–	–	0.23	–	–	–	–	–	AGN	
8	186	4.0 ± 0.1	0.20 ± 0.03	01 05 32.93	−72 13 30.6	1.0	10.37	11.90	11.76	5.56	13.11	9.47	6.52	−0 .21 ± 0.05	AGN	H00, P04
9	217	3.3 ± 0.3	0.49 ± 0.20	00 58 20.53	−71 30 40.9	1.5	38.46	32.30	–	12.27	–	12.65	3.87	−0 .93 ± 0.07	AGN	P04
10	236	2.7 ± 0.1	0.81 ± 0.16	01 02 58.90	−72 03 47.8	1.0	–	–	5.60	–	4.00	–	–	−0 .68 ± 0.25	AGN	K09
11	299	1.0 ± 0.1	0.61 ± 0.28	01 03 21.24	−72 13 44.5	1.0	–	3.87	9.12	1.75	5.66	1.93	–	−0 .96 ± 0.17	AGN	
12	302	0.4 ± 0.1	0.37 ± 0.16	01 03 27.18	−72 10 22.0	1.0	–	–	0.42	–	–	–	–	–	AGN	
13	306	0.3 ± 0.1	0.96 ± 0.22	01 01 53.07	−71 57 57.8	1.0	2.45	1.27	2.58	–	2.47	0.98	–	−0 .44 ± 0.18	AGN	
14	316	0.5 ± 0.2	−0 .58 ± 0.20	01 05 30.91	−72 10 21.0	1.0	–	2.26	4.53	4.02	4.01	3.33	2.04	−0 .21 ± 0.12	AGN/PWN?	along SNR DEM S128
15	329	2.0 ± 0.2	0.13 ± 0.10	00 56 52.60	−71 23 00.3	1.5	120.56	79.17	–	48.71	–	20.94	8.92	−1 .12 ± 0.05	AGN	P04
16	341	1.8 ± 0.2	0.67 ± 0.09	00 55 36.15	−72 35 14.1	1.5	90.00	19.94	–	21.53	–	12.92	10.54	−0 .87 ± 0.05	AGN	jet, H00
17	365	72.9 ± 1.2	0.32 ± 0.04	00 53 56.23	−70 38 04.8	1.5	48.70	40.72	–	11.35	–	–	3.45	−1 .20 ± 0.07	AGN/galaxy	Seyfert 2 galaxy, J09, S06
18	376	2.2 ± 0.2	−0 .59 ± 0.08	00 52 34.56	−70 28 16.8	1.5	31.90	31.86	–	–	–	–	–	0.00 ± 0.20	galaxy	J09, S06
19	381	1.5 ± 0.3	0.09 ± 0.15	00 56 08.11	−70 38 47.0	1.5	150.39	93.74	–	30.56	–	–	7.61	−1 .32 ± 0.08	AGN	P04
20	400	0.8 ± 0.2	−0 .56 ± 0.24	00 53 47.98	−70 46 01.3	1.5	–	4.26	–	–	–	–	–	–	AGN	
21	402	8.4 ± 0.3	0.89 ± 0.04	01 09 29.90	−72 52 46.1	1.5	4.64	1.98	–	–	–	–	–	−1 .68 ± 0.03	AGN	K09
22	449	2.0 ± 0.2	0.22 ± 0.08	00 52 54.23	−72 01 32.4	1.5	13.44	10.14	–	9.73	–	7.10	7.73	−0 .25 ± 0.13	AGN	P04
23	603	1.8 ± 0.1	0.54 ± 0.09	00 52 17.51	−73 01 56.4	1.0	39.57	20.52	25.73	11.02	–	6.76	1.87	−1 .25 ± 0.08	AGN	jet, P04, H00
24	645	1.0 ± 0.1	−0 .06 ± 0.11	01 09 28.34	−72 22 19.5	1.5	7.59	2.21	–	2.82	–	–	–	−0 .99 ± 0.10	galaxy	jet, P04, S06, J09
25	647	0.7 ± 0.1	−0 .03 ± 0.23	01 10 40.59	−72 28 32.2	1.5	346.97	138.28	–	147.02	–	74.95	32.60	−0 .91 ± 0.05	AGN	jet
26	691	1.8 ± 0.2	0.57 ± 0.14	00 58 50.27	−71 36 55.9	5.0	2.10	–	–	–	–	2.79	2.00	0.16 ± 0.20	AGN	
27	709	0.8 ± 0.1	−0 .13 ± 0.11	00 51 17.18	−73 39 59.6	1.0	86.00	55.24	14.38	52.28	–	29.83	25.16	−0 .33 ± 0.06	galaxy	P04, H00
28	746	8.6 ± 0.3	0.34 ± 0.03	00 47 19.15	−72 39 48.1	1.0	6.96	16.27	10.61	18.15	–	38.72	29.94	0.66 ± 0.05	AGN	jet, H00
29	783	2.2 ± 0.1	0.09 ± 0.05	00 57 36.97	−73 12 58.4	1.5	3.34	2.13	–	2.64	–	2.23	–	−0 .17 ± 0.14	AGN	H00, P04
30	787	2.6 ± 0.3	0.07 ± 0.53	00 57 50.22	−73 05 59.8	1.5	3.06	2.24	–	3.20	–	–	–	0.04 ± 0.25	AGN	P04
31	878	0.9 ± 0.1	0.19 ± 0.43	01 10 53.21	−73 14 16.2	1.5	1244.5	575.78	–	555.33	–	273.56	139.18	−0 .87 ± 0.05	AGN	jet
32	898	1.0 ± 0.2	0.51 ± 0.15	00 59 27.28	−73 08 38.2	5.0	2.37	–	–	–	–	–	–	–	AGN	
33	914	4.7 ± 0.5	0.43 ± 0.12	01 16 49.13	−73 42 38.8	1.5	5.44	2.36	–	–	–	2.68	–	−0 .31 ± 0.15	AGN	P04, H00
34	916	2.8 ± 0.3	0.45 ± 0.08	01 16 15.86	−73 26 57.2	1.5	56.70	36.70	–	31.74	–	12.40	9.63	−0 .80 ± 0.06	ClG	P04, H00
35	946	0.4 ± 0.1	0.39 ± 0.33	01 17 09.47	−73 36 31.7	1.5	2.97	1.29	–	–	–	–	–	−1 .64 ± 0.25	AGN	
36	955	0.5 ± 0.2	−0 .30 ± 0.28	01 18 33.17	−73 38 02.5	1.5	–	–	–	–	–	–	2.07	–	AGN	
37	1041	752.9 ± 1.8	−0 .17 ± 0.00	00 53 07.97	−74 39 05.2	3.0	2.40	10.79	–	20.90	–	2.96	1.43	−0 .47 ± 0.20	star	CF Tuc, P04, H00
38	1046	4.9 ± 0.3	0.08 ± 0.06	00 55 28.33	−74 44 20.5	1.5	1.62	1.35	–	–	–	0.88	–	−0 .35 ± 0.20	AGN	
39	1047	3.1 ± 0.2	0.72 ± 0.08	00 51 54.01	−74 35 32.2	1.5	–	2.24	–	–	–	1.16	–	−0 .53 ± 0.25	AGN	H00
40	1145	0.3 ± 0.1	0.36 ± 0.34	01 03 36.32	−72 10 31.6	1.0	–	–	0.43	–	–	–	–	–	AGN	
41	1267	2.7 ± 0.3	0.01 ± 0.09	00 59 27.59	−75 12 06.6	1.5	8.14	2.54	–	–	–	2.68	–	−0 .51 ± 0.20	AGN	
42	1490	1.4 ± 0.2	0.25 ± 0.17	00 44 38.68	−73 37 10.5	1.0	12.20	11.03	10.48	7.37	–	4.84	–	−0 .57 ± 0.17	AGN	H00

Notes. For a description of the Table, see Sect. 2.3. [a] Comments on individual sources. For details see text. Identifications with sources from other catalogues are marked as follows.

References. (P04) Payne et al. (2004); (H00) Haberl et al. (2000); (J09) Jones et al. (2009); (S06) Skrutskie et al. (2006); (S05) Shtykovskiy & Gilfanov (2005); (K09) Kozłowski & Kochanek (2009).

Table 2. continued.

(1) No	(2) ID_X	(3) F_X	(4) HR_2	(5) RA_r	(6) Dec_r	(7) ePos	(8) $S_{0.843}$	(9) $S_{1.42}$	(10) $S_{1.42}$	(11) $S_{2.37}$	(12) $S_{2.37}$	(13) $S_{4.8}$	(14) $S_{8.64}$	(15) α	(16) class	(17) comment[a]
43	1533	2.5 ± 0.5	0.55 ± 0.21	00 37 57.61	−72 52 02.6	1.5	255.86	155.12	–	94.44	–	50.97	19.82	−1 .06 ± 0.05	AGN	jet
44	1540	0.8 ± 0.2	0.22 ± 0.24	00 38 57.81	−72 48 50.8	1.5	5.70	3.50	–	–	–	3.37	–	−0 .25 ± 0.12	AGN	P04
45	1595	1.1 ± 0.2	0.36 ± 0.14	01 02 37.43	−72 50 38.5	1.5	–	4.12	–	–	–	3.48	–	−0 .14 ± 0.25	AGN	
46	1607	0.8 ± 0.2	0.42 ± 0.37	01 03 39.35	−72 50 41.4	1.5	16.39	10.29	–	6.73	–	6.72	5.60	−0 .42 ± 0.10	AGN	P04
47	1688	0.5 ± 0.1	0.24 ± 0.16	00 51 41.47	−72 55 57.7	1.0	71.88	58.23	58.34	37.53	–	21.29	7.26	−0 .97 ± 0.05	AGN	jet, P04
48	1726	1.2 ± 0.2	−0 .01 ± 0.15	01 09 14.47	−72 29 38.5	1.5	5.49	4.65	–	1.29	–	–	–	−1 .44 ± 0.12	galaxy	J09, S06, P04
49	1739	0.6 ± 0.2	0.75 ± 0.45	01 10 05.35	−72 26 47.9	1.5	115.60	132.46	–	135.10	–	72.59	41.79	−0 .47 ± 0.05	AGN	jet, P04
50	1864	1.3 ± 0.2	0.48 ± 0.14	00 49 01.75	−73 44 55.5	1.0	12.28	6.98	2.06	6.89	–	5.08	0.93	−0 .75 ± 0.09	AGN	P04
51	1870	1.1 ± 0.2	0.34 ± 0.16	00 50 11.08	−73 50 53.0	3.0	–	–	–	–	–	–	2.16	–	AGN	
52	1910	10.4 ± 0.4	0.39 ± 0.05	00 55 18.82	−71 44 51.0	1.5	25.92	13.40	–	9.74	–	4.57	–	−0 .97 ± 0.11	AGN	P04
53	1936	0.9 ± 0.1	0.15 ± 0.19	00 52 06.60	−71 44 15.1	5.0	4.54	–	–	–	–	1.90	–	−0 .50 ± 0.20	AGN	
54	1961	0.3 ± 0.1	−0 .25 ± 0.22	00 52 55.27	−71 45 39.1	5.0	2.74	–	–	–	–	–	–	–	AGN/star?	
55	1990	1.0 ± 0.2	0.69 ± 0.17	00 48 25.77	−72 00 33.7	1.5	–	3.16	–	–	–	0.92	–	−1 .00 ± 0.25	AGN	
56	2055	1.3 ± 0.2	0.28 ± 0.13	01 03 31.90	−71 29 10.8	3.0	–	–	–	3.36	–	–	–	–	AGN	H00
57	2078	0.4 ± 0.1	−0 .04 ± 0.20	01 04 41.29	−71 31 23.1	1.5	19.48	24.61	–	26.69	–	18.38	10.79	−0 .27 ± 0.08	AGN	P04
58	2127	0.6 ± 0.2	0.88 ± 0.25	01 02 22.01	−71 27 20.7	1.5	13.14	11.15	–	10.07	–	4.94	–	−0 .55 ± 0.07	AGN	P04
59	2250	0.6 ± 0.1	1.00 ± 0.26	00 49 33.41	−72 19 01.5	1.5	23.77	20.23	–	18.31	–	7.03	4.29	−0 .78 ± 0.05	AGN	jet, P04
60	2270	0.2 ± 0.1	−0 .41 ± 0.67	00 49 48.88	−72 22 12.8	1.5	6.15	3.01	–	–	–	–	–	−1 .41 ± 0.25	AGN	
61	2302	0.4 ± 0.1	0.39 ± 0.17	00 55 57.07	−72 26 04.7	1.5	111.95	98.53	–	80.32	–	52.37	33.53	−0 .52 ± 0.05	AGN	jet
62	2368	0.3 ± 0.1	0.52 ± 0.35	00 49 36.96	−72 35 52.4	1.5	–	2.25	–	2.36	–	–	1.54	−0 .23 ± 0.15	AGN	
63	2381	5.9 ± 0.6	0.16 ± 0.09	00 42 39.85	−72 33 24.5	1.5	12.31	10.55	–	8.91	–	3.79	–	−0 .67 ± 0.14	AGN	P04
64	2396	0.6 ± 0.1	0.51 ± 0.18	00 44 13.84	−72 43 00.9	1.0	18.37	15.15	3.16	19.56	–	8.42	2.46	−0 .58 ± 0.06	AGN	P04, K09
65	2439	0.5 ± 0.1	−0 .13 ± 0.23	00 42 26.22	−73 04 17.8	1.0	138.90	85.61	49.56	–	–	19.95	9.65	−1 .09 ± 0.05	AGN	jet, P04
66	2496	0.1 ± 0.1	0.46 ± 0.33	00 43 40.76	−73 25 48.6	1.0	–	7.10	6.02	–	–	–	–	–	AGN	
67	2505	0.4 ± 0.1	−0 .14 ± 0.32	00 42 15.25	−73 29 08.8	2.0	–	1.69	–	–	–	–	–	–	AGN	
68	2556	0.3 ± 0.1	−0 .40 ± 0.73	00 48 58.33	−73 24 39.5	1.0	–	–	0.22	–	–	–	–	–	AGN	
69	2568	1.0 ± 0.2	0.74 ± 0.17	00 52 38.31	−73 12 45.0	1.0	143.94	98.95	105.37	72.18	–	33.25	15.85	−0 .95 ± 0.05	AGN	jet, P04
70	2575	0.6 ± 0.1	0.76 ± 0.21	00 50 57.54	−73 12 48.0	1.0	2.06	2.93	4.08	–	4.10	3.57	2.47	−0 .01 ± 0.09	AGN	
71	2609	0.4 ± 0.1	0.55 ± 0.19	00 55 54.47	−73 03 43.9	2.0	4.74	2.46	–	–	–	–	–	−1 .29 ± 0.25	AGN	
72	2695	3.2 ± 0.4	0.38 ± 0.11	01 02 16.60	−72 37 04.6	1.0	–	–	3.26	–	–	–	–	–	ClG	jet
73	2712	0.8 ± 0.2	1.00 ± 0.15	01 05 38.47	−72 23 02.1	1.0	–	–	1.39	–	1.09	2.35	–	0.43 ± 0.30	AGN	P04
74	2738	4.9 ± 0.3	0.41 ± 0.07	01 10 50.08	−72 10 26.7	1.5	16.15	5.63	–	7.52	–	8.25	4.03	−0 .39 ± 0.08	AGN	jet, P04
75	2776	0.5 ± 0.1	−0 .50 ± 0.39	01 10 00.34	−72 08 24.5	1.5	3.16	2.53	–	–	–	1.42	1.18	−0 .43 ± 0.09	AGN	
76	2795	2.0 ± 0.2	0.42 ± 0.08	01 12 44.48	−72 24 21.3	3.0	–	–	–	–	–	–	3.29	–	AGN	
77	2834	0.4 ± 0.1	0.86 ± 0.21	01 14 13.77	−72 18 19.0	3.0	–	–	–	–	–	2.32	1.78	−0 .45 ± 0.25	AGN	
78	2853	0.5 ± 0.1	0.43 ± 0.16	01 11 19.53	−72 49 01.9	3.5	–	–	–	–	–	–	2.59	–	AGN	jet
79	2905	6.3 ± 0.4	0.19 ± 0.06	01 11 32.47	−73 02 09.6	1.5	69.22	70.02	–	74.88	–	63.25	62.74	−0 .05 ± 0.05	galaxy	jet, J09, S06, P04, H00
80	2978	0.2 ± 0.1	0.42 ± 0.41	01 15 26.14	−73 00 18.3	2.0	2.64	2.35	–	–	–	–	–	−0 .23 ± 0.25	AGN	
81	2987	3.7 ± 0.3	0.39 ± 0.07	01 21 07.26	−73 07 06.8	2.0	2.20	2.10	–	–	–	–	–	−0 .09 ± 0.25	AGN	jet, H00
82	3053	1.3 ± 0.1	0.31 ± 0.10	01 13 22.87	−73 24 53.5	3.5	–	–	–	–	–	–	3.11	–	AGN	K09
83	3117	1.1 ± 0.1	0.35 ± 0.09	01 06 58.03	−73 13 20.9	2.0	7.22	2.65	–	–	–	0.93	–	−1 .12 ± 0.20	AGN	
84	3150	0.7 ± 0.2	−0 .26 ± 0.19	01 10 21.91	−73 04 39.4	1.5	70.11	48.71	–	37.29	–	25.47	12.81	−0 .69 ± 0.05	AGN	jet, P04
85	3163	0.3 ± 0.1	0.95 ± 0.35	01 07 08.37	−73 07 19.7	2.0	1.96	1.49	–	1.51	–	–	–	−0 .26 ± 0.16	AGN	
86	3177	0.5 ± 0.2	−0 .63 ± 0.40	01 00 09.87	−73 13 12.4	2.0	2.79	1.73	–	–	–	–	–	−0 .94 ± 0.25	galaxy	S06
87	3208	0.9 ± 0.2	0.07 ± 0.32	00 58 15.56	−73 16 14.1	5.0	4.66	–	–	–	–	–	–	–	galaxy	J09, S06
88	3209	0.1 ± 0.1	−0 .03 ± 0.27	00 57 49.36	−73 25 44.9	5.0	2.62	–	–	–	–	–	–	–	AGN	

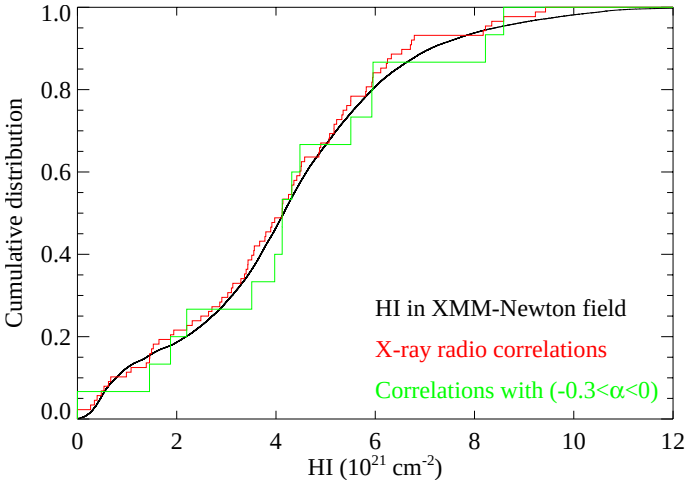

Fig. 3. Cumulative distribution of H column density in the *XMM-Newton* field (black) and of the line-of-sight column densities of our X-ray radio correlations (red). Correlations with $-0.3 < \alpha < 0$ are plotted in green.

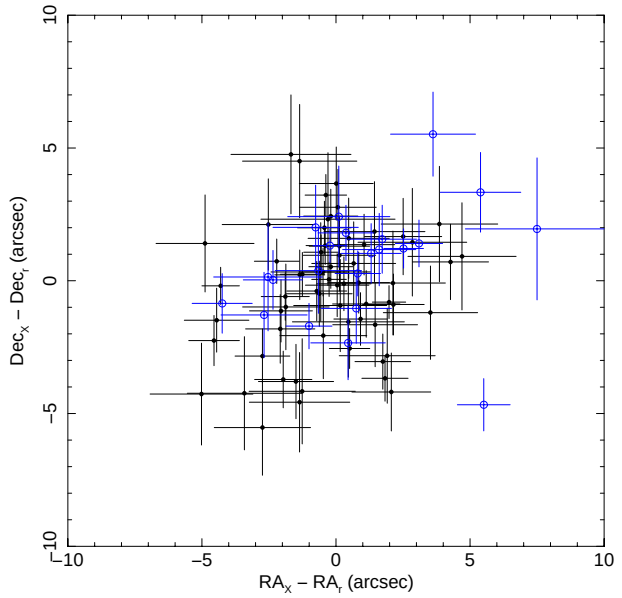

Fig. 4. Separation of X-ray and radio positions. Sources, which have some extent or jets in X-ray or radio are plotted with blue open circles, other sources with black filled circles. Error bars mark 1σ confidence.

regions with higher (or lower) H as it would be the case for a correlation (or anti-correlation). Forty-five of our sources are located behind dense SMC regions with an H column density of $N_{\rm H}^{\rm SMC} > 4{\times}10^{21}$ cm^{-2}, six sources have a $N_{\rm H}^{\rm SMC} > 8{\times}10^{21}$ cm^{-2}. Also no structure according to the bar of the SMC is seen, where sources of star-forming regions are found (e.g. compare compact H regions of Wong et al. 2012b, their Fig. 10, and YSO of Oliveira et al. 2013, their Fig. 1).

3.1. Correlation statistics

We show the angular separation between radio and X-ray positions in Fig. 4. Eighty-four of our 88 correlations have an angular separation of $d \le 5 \times (\sigma_{\rm r}^2 + \sigma_{\rm X}^2)^{1/2}$, where $\sigma_{\rm r}$ and $\sigma_{\rm X}$ are the position uncertainties of the radio and X-ray source. In some cases (e.g. source No 3, Fig. 1 lower right), the small errors and the radio extent cause larger separations as in these cases, the position of the central radio source had to be estimated. The error-weighted average offset for point sources is ΔRA = 0.″14 and ΔDec = −0.″07 with an uncertainty of 0.″18. We do not see systematic deviations.

Since the source correlation was done manually, the determination of the fraction of chance coincidences is not straight forward. However, we can compare our result with the result of a simple angular-separation-based cross matching. We merged the radio catalogues of Wong et al. (2011b, λ = 13, 20, 36 cm) and Wong et al. (2012a, λ = 3, 6 cm), as well as the 13 cm sources of Filipović et al. (2002). These catalogues are based on the same radio data, but omit the deep images and therefore contain only 60 of our 89 radio sources. Also, some sources with long jets were rejected for the radio point-source catalogues. We find 58 of our X-ray radio associations within $d \le 3.439 \times (\sigma_{\rm r}^2 + \sigma_{\rm X}^2)^{1/2}$. Additional 6 correlations were not selected in our manual correlation, as these were regarded as too uncertain, e.g. if a jet-like structure is not pointing towards the X-ray source. To check for chance coincidences, we shifted the coordinates of one catalogue by $\gtrsim$50″ in different directions. This resulted in 2.5 ± 1.6 correlations indicating a chance coincidence rate of ∼5%.

3.2. Spectral characteristics

The spectral index α of radio background sources covers a wide range, but is on average steeper for background sources than for SNRs or the thermal radio emission from H regions (cf. Filipović et al. 1998). For other rare source types, see the following sections. Because the possible α values of AGN, SNRs, and H regions are overlapping, the classification of radio sources based only on α is ambiguous, but with the detection of X-rays strongly points to a background object. The distribution of the spectral index α as estimated from the radio images is shown in Fig. 5. As expected we find a relatively wide distribution in our sample. 60% of the 70 sources with determined spectral index have a steep spectrum ($\alpha < -0.45$ with $S_\nu \sim \nu^\alpha$) and 16% show a flat spectrum ($\alpha > -0.2$). Compared to an unbiased radio sample of background sources (Payne et al. 2004), we find more sources with flat spectrum due to the X-ray selection of our sample (Neumann et al. 1994).

Twenty-five sources (36%) have a very steep spectral index of $\alpha < -0.8$ and are excellent candidates for compact steep spectrum (CSS) sources (O'Dea 1998; Fanti 2009). CSS sources are believed to bridge the evolutionary phase between the early gigahertz peaked-spectrum (GPS) sources and later and larger Fanaro-Riley Type I and II (FR I/II) galaxies. Sources No 57 and 70 are perfect candidates for GPS sources, due to their curved spectral index.

Radio sources with a rather flat radio spectrum and no indication of a radio jet or extended structure in X-rays are good candidates for BL Lac objects. The nearly featureless spectrum of these sources makes them ideal background emitters to measure absorption effects of the interstellar medium in the SMC. We find 22 compact radio sources that have an $\alpha > -0.5$ and are not classified as foreground object. These sources are good candidates for BL Lac objects.

The inverse spectral index ($\alpha > 0$) of source No 28 can be explained by radio variability due to non-simultaneous measurements, as seen from the different flux densities measured at 20 cm. This can also be the case for sources No 26, 30, and 73.

In Fig. 6, we show the distribution of HR_2, defined by $(R_3 - R_2)/(R_3 + R_2)$, where R_2 and R_3 is the X-ray count rate

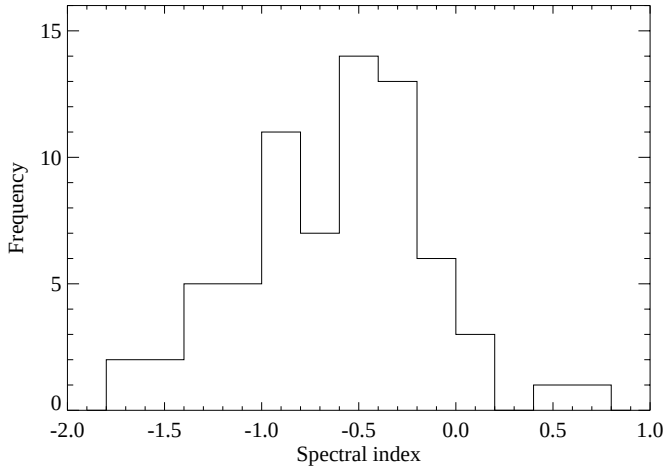

Fig. 5. Histogram of all sources with determined radio spectral index α. The bin width is 0.2.

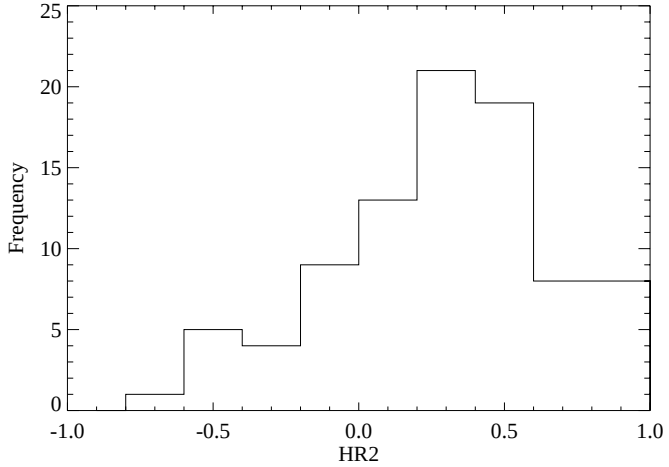

Fig. 6. Histogram of the X-ray hardness ratio HR_2 distribution. The bin width is 0.2.

in the (0.5−1.0) keV and (1.0−2.0) keV band, respectively. Hard X-ray sources, such as AGN or X-ray binaries, show higher HR_2 values than soft X-ray sources such as Galactic stars or SNRs. For AGN, typical values are $HR_2 > 0$, whereas most foreground stars are found with $HR_2 < 0$ (e.g. Stiele et al. 2011). Normal galaxies can show soft and hard X-ray emission, depending on the contribution from X-ray binaries, hot interstellar medium and SNRs. As expected for background sources, the X-ray to radio correlations mainly show hard X-ray emission.

3.3. Galaxies

Six of our sources (No 17, 18, 24, 48, 79, and 87) have a counterpart in the 6dF galaxy survey with determined redshifts (Jones et al. 2009). Remarkably, all of the 6dF correlations with the 3053 X-ray sources show radio emission. No 17 is a known Seyfert 2 galaxy. All these sources have an entry in the 2MASS extended source catalogue (2MASX, Skrutskie et al. 2006). In addition we find 2MASX counterparts for sources No 27 and 86, pointing to a galaxy nature of these sources. The galaxy nature is further supported by a 2MASX galaxy score of 1.0 and a $HR_2 < 0$. Source No 27 is shown in Fig. 1, lower left.

3.4. Galactic stars

Galactic stars can show X-ray and radio emission. The correlation No 37 is identified with the Galactic star CF Tuc. This is an active RS CVn-type binary with known X-ray and radio emission (Kuerster & Schmitt 1996; Gunn et al. 1997). In addition to soft X-ray emission from coronal plasma, a bright ($\log(F_X/F_{opt}) < -1$) optical counterpart is expected for a foreground star (Maccacaro et al. 1988).

Eight of our sources show soft X-ray emission, compatible with the hardness-ratio criteria for stars of Pietsch et al. (2004) or Sturm et al. (2013) and have an appropriate optical counterpart in the Magellanic Cloud Photometric Survey (MCPS, Zaritsky et al. 2002). Five of these can be rejected as stars, because of a 2MASX counterpart (see Sect. 3.3). No 14 is along the SNR DEM S128, which causes a softer HR_2. However, in the X-ray image, a hard X-ray source is clearly seen. Because we are looking out of the Galactic plane we expect a low contribution of young Galactic stars and the jet-like structure of No 47 is more likely caused by a background AGN than by outflows of protostellar jets of a Galactic source. Source No 54 cannot be excluded as possible foreground star. All other sources show hard X-ray emission that is not expected from coronal stellar X-ray emission.

We do not expect a contribution of SMC stars in the X-ray sample, because the moderate X-ray emission of normal stars even during flares ($L_X \lesssim 10^{33}$ erg s^{-1}, Güdel & Nazé 2009; Favata 2002) is below the detection limit of the *XMM-Newton* survey. Further, only the brightest YSOs are detected in the radio observations (Oliveira et al. 2013).

3.5. Cluster of galaxies

Often, clusters of galaxies (ClGs), seen in X-rays, contain radio-continuum sources (e.g. Mittal et al. 2009, and references therein). In these cases, the X-ray emission is caused by the hot intracluster medium, whereas the radio-continuum emission originates in an AGN in or in the direction of the ClG. The sources No 34 and 72 were fitted with a significant extent in X-rays (11.″9 ± 1.″1 and 12.″6 ± 1.″6) and show hard X-ray emission, which points to a ClG nature of these sources. We found also strong radio jets in other cluster candidates, which have a larger extent and were therefore not included in the X-ray point-source catalogue. These cluster candidates can be found in Haberl et al. (2012b). The radio counterparts are listed in Table 3. Examples are given in both upper images of Fig. 1.

3.6. X-ray binaries

Because of the relatively small stellar mass of the SMC, only a few low-mass X-ray binaries (LMXBs) are expected and none is known to date (Coe et al. 2010). In the case of LMXBs, we would not expect to find an optical counterpart. Also no ultra-luminous X-ray source (ULX) in the SMC is known and the measured X-ray luminosities are well below the ULX definition (>10^{39} erg s^{-1}). Therefore, the presence of a microquasar in our sample is unlikely, but cannot be ruled out. Redshift measurements of AGN candidates are needed, to further reduce the possibility of a microquasar in the SMC, that otherwise might only be recognised during a bright outburst.

The SMC hosts around one hundred known high-mass X-ray binaries (HMXB). Only one source in our sample has a proper optical counterpart in the MCPS that is compatible with an early-type star of a HMXB. This source, No 5 = [SG2005] SMC 34,

Table 3. Radio sources in X-ray selected clusters of galaxies from Haberl et al. (2012b).

RA_r	Dec_r	ePos	$S_{0.843}$	$S_{1.42}$	$S_{2.37}$	$S_{4.8}$	$S_{8.64}$	α	Comment
00 42 03.3	−73 07 23	1.2	197.4	139.23	92.0	37.6	25.2	−0.92 ± 0.07	H00, P04, jet
00 58 22.6	−72 00 45	0.6	21.2	18.8	9.9	5.2	–	−0.83 ± 0.07	H00, P04, jet
01 04 07.0	−72 43 51	1.1	19.3	11.3	8.6	3.6	2.2	−0.93 ± 0.07	H00, P04
01 04 45.6	−72 10 19	0.5	–	0.65 (HR)	–	–	–	–	H00
01 16 31.3	−72 58 02	1.5	2.1	2.2	1.9	–	–	−0.10 ± 0.10	
01 19 26.0	−73 01 46	1.9	4.5	2.9	1.9	–	–	−0.79 ± 0.05	jet

Notes. Values and references analogous to Table 2.

was classified as "HMXB candidate" from *XMM-Newton* and optical data by Shtykovskiy & Gilfanov (2005, their source 34) and as "new HMXB" from *Chandra* observations by Antoniou et al. (2009, source 4_4). Antoniou et al. (2009) also found additional possible optical counterparts from OGLE (Udalski et al. 1998) in agreement with the X-ray position. Kozłowski et al. (2011, see their Fig. 2) spectroscopically identified one of the fainter counterparts as a quasar with emission lines at redshift of $z = 0.108$. The *Chandra* source of Antoniou et al. (2009) has a similar angular separation to both OGLE sources, the star (SMC-SC 159896, 0.54″) and the quasar (SMC-SC 159964, 0.53″). Our radio source has an angular separation of 0.60″ and 0.58″, respectively, with a position uncertainty of 1″. From a spectral analysis of the *XMM-Newton* spectrum we could derive rough parameters for an absorbed power-law model. The photon index is between $\Gamma = (0.99–1.97)$ and the source is highly absorbed with $N_H = (1.7–3.9) \times 10^{23}$ cm^{-2}. This is compatible with both AGN and HMXB, which have typical photon indices of 1.75 (Tozzi et al. 2006) and 1.0 (Haberl & Pietsch 2004), respectively, and can show high intrinsic absorption. Therefore, the radio emission is likely caused by the quasar and the X-ray emission can be caused by both, however a background object is more likely.

3.7. Pulsar wind nebulae

A rare but interesting source class are PWNe (e.g. Gaensler & Slane 2006). PWN candidates in the SMC are X-ray and radio emitting sources that are found within thermal SNR shells, like the central sources of HFPK 334 (Filipović et al. 2008) and of IKT 16 (Owen et al. 2011). In the Large Magellanic Cloud (LMC), five candidates for such composite SNRs are known (B0540-693, N157B, B0532-710, DEM L241, and SNR J04536829, see Haberl et al. 2012a, and references therein). However, also PWNe without a thermal SNR shell, like the Crab Nebula or the PWN around the pulsar PSR B0540-69 in the LMC, are possible. The fact, that we do not know such a system in the SMC might be a selection effect.

The expected X-ray spectra of PWNe ($\Gamma \sim 2$) will result in similar hardness ratios as for AGN ($\Gamma \sim 1.75$) and hamper an X-ray-based classification. Typical spectral radio indices of PWNe are $-0.3 < \alpha < 0$, where we find 15 sources in our sample. These sources might be taken as a flux limited sample of candidates for PWNe. However, the source distribution (plotted in cyan in Fig. 2 and green in Fig. 3) is not correlating with star-forming regions in the SMC, i.e. the bar of the SMC where we see most of the SNRs. Therefore, we expect that most of these sources are background objects and that there is no significant contribution of PWNe given the sensitivity of our observations.

A special case is source No 14, which is found along the SNR DEM S128 (upper left of Fig. 1) with a spectral index of $\alpha = -0.21 \pm 0.12$, which is steeper than for the surrounding SNR ($\alpha = -0.48 \pm 0.06$, Filipović et al. 2000). The type-Ia classification of the SNR (van der Heyden et al. 2004) and the offset of its X-ray bright centre from the point source suggest that both sources are not connected with each other. In the SAGE survey (Gordon et al. 2011) we find a mid-infrared *Spitzer*/IRAC counterpart (SSTISAGEMA J010530.69-721021.3) with colours that might be consistent with an AGN. However, in the deep X-ray images, the emission from DEM S128 clearly extends further towards the north-west (compare also Haberl et al. 2012b, Fig. 6.1). Therefore, we cannot exclude No 14 as a candidate for a PWN. DEM S128 will be discussed in more detail by Roper et al. (in prep.).

We can also roughly estimate the probability of finding a radio X-ray association within an SNR using our source list that contains 2.4 sources deg^{-2} with $-0.3 < \alpha < 0$. According to Haberl et al. (2012b), the area covered by known SNRs is ∼0.044 deg^{-2}. For a Poisson distribution, we would expect to find one source along an SNR with a likelihood of 9.4% and more than one source with a likelihood of 0.5%. So the DEM S128 correlation might still be by chance, but this is unlikely to be the case for all PWN candidates in the SMC (HFPK 334 and IKT 16, not included in this study).

3.8. Comparison with previous studies

For 17 of our sources, we find a counterpart in the ROSAT PSPC catalogue (Haberl et al. 2000). These are commented with H00 in Table 2. Twelve of these sources were already associated with radio sources at $\lambda = 13$ cm in that work. In addition, the ROSAT catalogue lists 39 sources with radio association. Of these, nine are outside the *XMM-Newton* field ([HFP2000] 52, 124, 138, 347, 357, 522, 685, 687, and 692), four are now resolved as ClGs ([HFP2000] 101, 147, 317, and 410) and 18 are SNRs ([HFP2000] 45, 107, 125, 145, 148, 194, 217, 281, 285, 334, 401, 413, 414, 419, 437, 454, 461, and 530), where [HFP2000] 281 was probably detected as part of a bubble connected to the SNR DEM S68 (Filipović et al. 2008). [HFP2000] 88 was not detected with *XMM-Newton*. For [HFP2000] 49, 206, 249, 380, 440, 448, and 668, the improved X-ray positions with respect to ROSAT make an X-ray radio association unlikely.

Since the gain of the radio data is rather in sensitivity than in resolution, the comparison with Payne et al. (2004) is somewhat more straight forward. We find 32 of our sources in Payne et al. (2004), marked with P04 in Table 2. All sources but one were classified as background objects by these authors, but only 3 sources are noted as X-ray association. Only source No 22 ([FBR2002] J005254-720132) was classified as

background object or H region. The X-ray emission points to a background source in this case. Further, there are 37 sources for which Payne et al. (2004) give an X-ray luminosity or an X-ray comment. Of these, 13 were identified as SNRs, three are in ClGs, and 14 were classified as H regions where we do not find X-ray sources in our study, confirming the classification. From the remaining sources one is classified as "XRB" (microquasar candidate), correlating with [HFP2000] 295. This X-ray radio association was rejected above. The other sources are candidate background objects, but we do not find X-ray counterparts in the *XMM-Newton* catalogue ([FBR2002] J004552-731339, J004836-733056, J005218-722708, J005602-720908, J005610-721833, and J010525-722525).

4. Conclusions

We inspect the positions of X-ray sources from the *XMM-Newton* SMC survey in the corresponding deep radio-continuum images and found 88 X-ray sources associated with a unique radio counterpart. One source is identified with a foreground star, one is a confirmed quasar probably confused with a HMXB candidate, eight are identified or classified as galaxies, two radio sources are within clusters of galaxies, and one might be a PWN. The remaining 75 X-ray sources associated with a unique radio counterpart are classified as AGN behind the SMC. Due to the precise X-ray positions of our X-ray catalogue (∼1.5″) and the low density of radio sources in the SMC field, chance correlations are unlikely and we derive a high purity for our sample. We expect the contribution of stars to our sample to be ≤2. From background source candidates, seven are infra-red-selected candidates of Kozłowski & Kochanek (2009), 31 were classified as background radio sources by Payne et al. (2004), and 11 as AGN candidates by Haberl et al. (2000). 40 associations are newly classified background objects behind the SMC, for the others, the X-ray radio association affirms the previous background-object classification. For a total of 21 X-ray point sources, we find a jet like structure in radio, which points to the AGN character of the source. In addition, we list six radio sources inside ClGs with high X-ray extent, where three radio sources show a jet.

Acknowledgements. The *XMM-Newton* project is supported by the Bundesministerium für Wirtschaft und Technologie/Deutsches Zentrum für Luft- und Raumfahrt (BMWI/DLR, FKZ 50 OX 0001) and the Max-Planck Society. The ATCA is part of the Australia Telescope which is funded by the Commonwealth of Australia for operation as a National Facility managed by CSIRO. We used the and software package developed by the ATNF. R.S. acknowledges support from the BMWI/DLR grant FKZ 50 OR 0907.

References

Antoniou, V., Zezas, A., Hatzidimitriou, D., & McDowell, J. C. 2009, ApJ, 697, 1695
Aschenbach, B. 2002, in SPIE Conf. Ser. 4496, eds. P. Gorenstein, & R. B. Hoover, 8
Bojicic, I. S., Filipović, M. D., & Crawford, E. J. 2010, Serb. Astron. J., 181, 63
Coe, M., Corbets, R. H. D., McGowan, K. E., & McBride , V. A. 2010, in High Energy Phenomena in Massive Stars, eds. J. Martí, P. L. Luque-Escamilla, & J. A. Combi, ASP Conf. Ser., 422, 224
Crawford, E. J., Filipović, M. D., de Horta, A. Y., et al. 2011, Serb. Astron. J., 183, 95
Dickel, J. R., Williams, R. M., Carter, L. M., et al. 2001, AJ, 122, 849
Dobrzycki, A., Macri, L. M., Stanek, K. Z., & Groot, P. J. 2003a, AJ, 125, 1330
Dobrzycki, A., Stanek, K. Z., Macri, L. M., & Groot, P. J. 2003b, AJ, 126, 734
Eyer, L. 2002, Acta Astron., 52, 241
Fanti, C. 2009, Astron. Nachr., 330, 120
Favata, F. 2002, in Stellar Coronae in the Chandra and XMM-Newton Era, eds. F. Favata, & J. J. Drake, ASP Conf. Ser., 277, 115
Filipović, M. D., Jones, P. A., White, G. L., et al. 1997, A&AS, 121, 321
Filipović, M. D., Haynes, R. F., White, G. L., & Jones, P. A. 1998, A&AS, 130, 421
Filipović, M. D., Haberl, F., Pietsch, W., & Morgan, D. H. 2000, A&A, 353, 129
Filipović, M. D., Bohlsen, T., Reid, W., et al. 2002, MNRAS, 335, 1085
Filipović, M. D., Haberl, F., Winkler, P. F., et al. 2008, A&A, 485, 63
Gaensler, B. M., & Slane, P. O. 2006, ARA&A, 44, 17
Gordon, K. D., Meixner, M., Meade, M. R., et al. 2011, AJ, 142, 102
Güdel, M., & Nazé, Y. 2009, A&ARv, 17, 309
Gunn, A. G., Migenes, V., Doyle, J. G., Spencer, R. . E., & Mathioudakis, M. 1997, MNRAS, 287, 199
Haberl, F., & Pietsch, W. 2004, A&A, 414, 667
Haberl, F., Filipović, M. D., Pietsch, W., & Kahabka, P. 2000, A&AS, 142, 41
Haberl, F., Filipović, M. D., Bozzetto, L. M., et al. 2012a, A&A, 543, A154
Haberl, F., Sturm, R., Ballet, J., et al. 2012b, A&A, 545, A128
Jansen, F., Lumb, D., Altieri, B., et al. 2001, A&A, 365, L1
Jones, D. H., Read, M. A., Saunders, W., et al. 2009, MNRAS, 399, 683
Kelly, B. C., Bechtold, J., & Siemiginowska, A. 2009, ApJ, 698, 895
Kozłowski, S., & Kochanek, C. S. 2009, ApJ, 701, 508
Kozłowski, S., Kochanek, C. S., & Udalski, A. 2011, ApJS, 194, 22
Kozłowski, S., Onken, C. A., Kochanek, C. S., et al. 2013, ApJ, 775, 92
Kuerster, M., & Schmitt, J. H. M. M. 1996, A&A, 311, 211
Maccacaro, T., Gioia, I. M., Wolter, A., Zamorani, G., & Stocke, J. T. 1988, ApJ, 326, 680
Mills, B. Y., Little, A. G., Durdin, J. M., & Kesteve n, M. J. 1982, MNRAS, 200, 1007
Mittal, R., Hudson, D. S., Reiprich, T. H., & Clarke, T. 2009, A&A, 501, 835
Neumann, M., Reich, W., Fuerst, E., et al. 1994, A&AS, 106, 303
O'Dea, C. P. 1998, PASP, 110, 493
Oliveira, J. M., van Loon, J. T., Sloan, G. C., et al. 2013, MNRAS, 428, 3001
Owen, R. A., Filipović, M. D., Ballet, J., et al. 2011, A&A, 530, A132
Payne, J. L., Filipović, M. D., Reid, W., et al. 2004, MNRAS, 355, 44
Pietsch, W., Misanovic, Z., Haberl, F., et al. 2004, A&A, 426, 11
Piatek, S., Pryor, C., & Olszewski, E. W. 2008, AJ, 135, 1024
Sasaki, M., Haberl, F., & Pietsch, W. 2000, A&AS, 147, 75
Shtykovskiy, P., & Gilfanov, M. 2005, MNRAS, 362, 879
Skrutskie, M. F., Cutri, R. M., Stiening, R., et al. 2006, AJ, 131, 1163
Stanimirovic, S., Staveley-Smith, L., Dickey, J. M., Sault, R. J., & Snowden, S. L. 1999, MNRAS, 302, 417
Stiele, H., Pietsch, W., Haberl, F., et al. 2011, A&A, 534, A55
Strüder, L., Briel, U., Dennerl, K., et al. 2001, A&A, 365, L18
Sturm, R., Haberl, F., Pietsch, W., et al. 2013, A&A, 558, A3
Tinney, C. G., Da Costa, G. S., & Zinnecker, H. 1997, MNRAS, 285, 111
Tozzi, P., Gilli, R., Mainieri, V., et al. 2006, A&A, 451, 457
Turner, M. J. L., Abbey, A., Arnaud, M., et al. 2001, A&A, 365, L27
Udalski, A., Szymanski, M., Kubiak, M., et al. 1998, Acta Astron., 48, 147
van der Heyden, K. J., Bleeker, J. A. M., & Kaastra, J. S. . 2004, A&A, 421, 1031
Watson, M. G., Schröder, A. C., Fyfe, D., et al. 2009, A&A, 493, 339
Wilkes, B. J., Wright, A. E., Jauncey, D. L., & Peterson, B. A. 1983, PASA, 5, 2
Wong, G. F., Filipović, M. D., Crawford, E. J., et al. 2011a, Serb. Astron. J., 182, 43
Wong, G. F., Filipović, M. D., Crawford, E. J., et al. 2011b, Serb. Astron. J., 183, 103
Wong, G. F., Crawford, E. J., Filipović, M. D., et al. 2012a, Serb. Astron. J., 184, 93
Wong, G. F., Filipović, M. D., Crawford, E. J., et al. 2012b, Serb. Astron. J., 185, 53
Ye, T., & Turtle, A. J. 1993, Lect. Notes Phys., 416, 167
Ye, T. S., Amy, S. W., Wang, Q. D., Ball, L., & Dickel, J. 1995, MNRAS, 275, 1218
Zaritsky, D., Harris, J., Thompson, I. B., Grebel, E. K., & Massey, P. 2002, AJ, 123, 855

A.31 Related Paper 31

Filipović, M. D., Horner, J., Crawford, E. J., Tothill, N. F. H., and White, G. L. (2013). Mass Extinction and the Structure of the Milky Way. *Serbian Astronomical Journal*, 187:43–52

My contribution was to assist in the data analysis. This is a 20% contribution.

Serb. Astron. J. № 187 (2013), 43 - 52 **UDC 52–37**
DOI: 10.2298/SAJ130819005F Original scientific paper

MASS EXTINCTION AND THE STRUCTURE OF THE MILKY WAY

M. D. Filipović[1], J. Horner[2,3], E. J. Crawford[1], N. F. H. Tothill[1] and G. L. White[1]

[1]*University of Western Sydney, Locked Bag 1797, Penrith South DC, NSW 1797, Australia*
E–mail: *m.filipovic@uws.edu.au, e.crawford@uws.edu.au, n.tothill@uws.edu.au*

[2]*School of Physics, University of New South Wales, Sydney 2052, Australia*

[3]*Australian Centre for Astrobiology, University of New South Wales, Sydney 2052, Australia*
E–mail: *j.a.horner@unsw.edu.au*

(Received: August 19, 2013; Accepted: September 18, 2013)

SUMMARY: We use the most up-to-date Milky Way model and solar orbit data in order to test the hypothesis that the Sun's galactic spiral arm crossings cause mass extinction events on Earth. To do this, we created a new model of the Milky Way's spiral arms by combining a large quantity of data from several surveys. We then combined this model with a recently derived solution for the solar orbit to determine the timing of the Sun's historical passages through the Galaxy's spiral arms. Our new model was designed with a symmetrical appearance, with the major alteration being the addition of a spur at the far side of the Galaxy. A correlation was found between the times at which the Sun crosses the spiral arms and six known mass extinction events. Furthermore, we identify five additional historical mass extinction events that might be explained by the motion of the Sun around our Galaxy. These five additional significant drops in marine genera that we find include significant reductions in diversity at 415, 322, 300, 145 and 33 Myr ago. Our simulations indicate that the Sun has spent ∼60% of its time passing through our Galaxy's various spiral arms. Also, we briefly discuss and combine previous work on the Galactic Habitable Zone with the new Milky Way model.

Key words. galaxy: structure – astrobiology – solar neighbourhood

1. INTRODUCTION

Mass extinctions have the effect of wiping the biological slate clean, freeing up ecological niches and thus producing explosions in biodiversity (e.g. McElwain and Punyasena 2007, Alroy 2008). In the past, several explanations have been proposed to resolve ancient mass extinctions, including vast outpourings of flood basalt (such as the Deccan and Siberian Traps; e.g. Wignall 2001), periods of global glaciation (Mayhew et al. 2008) and the impact of large asteroids and comets upon the Earth (e.g. Alvarez et al. 1980, Bottke et al. 2007). Of these, extreme geological and climate phenomena such as flood basalt outpouring and "snowball Earth" glaciations appear to be very rare and randomly-occurring events in the Earth's history. Overholt et al. (2009) investigate Earth's climate as a function of location in the Galaxy, however, no obvious correlation could be drawn. On the other hand, it is well established that the Earth has been continually pummelled by asteroidal and cometary impactors throughout its history, a process that will continue well into the fu-

ture. Given the damage that would be caused by the impact of a cometary or asteroidal body several kilometres in diameter (an event expected to reoccur on timescales of millions or tens of millions of years), it seems likely that the majority of mass extinctions could be caused by such impact events. Thus, impact theories are strong contenders to explain mass extinctions.

In addition to the extinction risk due to impactors, there is also the possibility that nearby supernovae could also cause mass extinctions. In this case, one would expect the nearby supernova flux to be higher whilst the Sun is traversing the Galaxy's spiral arms than when it is between them (Svensmark 2012). However, given the low frequency of supernovae, the likelihood of one occurring sufficiently close to the Earth to trigger a mass extinction is thought to be relatively low, even during spiral arm crossings (Beech 2011). As such, here, we assume that collisions with comets and asteroids are the dominant cause of exogenous mass extinctions (i.e. those extinctions whose cause is external to the Earth).

The hypothesis of mass extinction driven by cometary or asteroidal impact is part of the burgeoning modern interdisciplinary study of astrobiology – a field in which researchers from the breadth of all the natural sciences come together to try to understand the origin, diversity and history of life on Earth and the prospects for life beyond our Solar system (e.g. Horner and Jones 2010). When considering life on Earth, biologists and geologists have long reported evidence for mass extinctions throughout the history of our planet (e.g. Horner et al. 2009), but have found it difficult to find explanations for those extinctions. Astronomical studies not only inform biologists on the conditions that would have been experienced by the earliest life on the planet, and of the origins of the water considered so vital for life to develop and thrive (e.g. Horner et al. 2011), but can also be used to attempt to explain those mass extinctions for which a terrestrial cause remains elusive.

One of the most intriguing suggestions related to the mass extinctions on Earth is that those extinction events are not randomly distributed through time. Instead, a number of authors have suggested that there is a periodic signal within the mass extinction record, with both the historical major mass extinctions and a number of more minor extinction events following a periodic pattern. In recent years, a number of studies (Rohde and Muller 2005, Melott and Bambach 2011, 2013, Feng and Bailer-Jones 2013, Bailer-Jones and Feng 2013) have discussed and analysed a proposed ∼62 Myr period.

1.1. Impacts on the Earth

The meteors which can be observed on any clear night represent the small, non-threatening end of a spectrum of regular impacts. The largest and most devastating impacts are the least frequent, whilst the smallest (meteors) are so frequent that millions occur across our planet every day. The Earth Impact Database[1] currently lists a total of 182 confirmed large impact structures across our planet's surface. These structures are the scars left behind as a result of collisions between the Earth and asteroidal or cometary objects, and represent just a tiny fraction of the true impact history of our planet. The majority of impacts occur in the Earth's oceans (which make up ∼70% of the planet's surface area) and therefore, despite likely causing devastation at the time, rarely create scars which would survive to the current day to be analysed. Indeed, studies show that a layer of water can significantly reduce the ability of an impactor to leave an impact crater on the ocean floor (e.g. Baldwin et al. 2007, Milner et al. 2008). Since the average depth of the oceans is ∼6 km, it is clear that the great majority of impacts will fail to leave any recognisable scar on the ocean bottom. Furthermore, the ocean floor is recycled on timescales far shorter than the age of our planet, effectively erasing any evidence of ancient impact scars. Even for those impacts which occur on land, erosion and weathering remove the scars from all but the largest impacts on astronomically short timescales. A true idea of the ongoing impact regime experienced by the Earth is therefore best obtained by looking at our nearest neighbour, the Moon, or by examining the surface of Mars (where the effects of weathering and erosion are far less effective at removing the scars left behind by impacts of all scales). Both the Moon and Mars are far more heavily scarred than the Earth – and both display evidence that impacts are certainly a current, rather than historical, concern. The repeated impacts that have been observed on the giant planet Jupiter over the last twenty years add further weight to this argument – both the large Shoemaker-Levy 9 impacts in 1994 (Hammel et al. 1995), and the smaller impacts observed in the last few years (e.g. Sánchez-Lavega et al. 2010).

Over the years, there have been many suggestions that the impact flux of such asteroids and comets upon the Earth has varied significantly as a function of time. The rate of the smallest impacts (i.e. meteors) appears to vary periodically throughout the course of the year, as the Earth encounters streams of debris left behind by passing asteroids and comets[2]. For the larger, more threatening impacts, too, there are suggestions of periodicity (e.g. Raup and Sepkoski 1986, Rampino and Stothers 1984, Rampino 1997, Chang and Moon 2005) – although it is hard to uncover a clear result because of

[1] http://www.passc.net/EarthImpactDatabase/index.html

[2] A simple illustration of this variation can be found in the annual Meteor Shower Calendar hosted by the International Meteor Organisation – http://www.imo.net/calendar/2013

the small number statistics involved in the study of such events. The most widely-accepted hypothesis of time-variation in the record of massive impacts is that of the "Late Heavy Bombardment".

1.2. The Late Heavy Bombardment

The most widely discussed example of temporal variation in the Earth's impact flux is the Late Heavy Bombardment. This hypothesis suggests that, early in the history of the Solar System, the Earth and Moon were subjected to so many massive impacts as to make the Earth entirely uninhabitable (e.g. Oberbeck and Fogleman 1989, Grieve and Pesonen 1992, Gogarten-Boekels et al. 1995, Wells et al. 2003), due to the repeated sterilisation of the planet. The proposed bombardment, thought to have continued until around 800 million years after the Earth's formation, is thought to have been linked to the creation of the "seas" on the Moon.

Current ideas of the Late Heavy Bombardment (e.g. Gomes et al. 2005, Levison et al. 2008) suggest that it was a side-effect of the migration of the giant planets (Jupiter, Saturn, Uranus, Neptune) in the early Solar system. In their models, the initial architecture of the orbits of the giant planets was significantly more compact than that we observe today, with a large amount of material located just beyond the orbit of the outermost planet. As Jupiter and Saturn migrated, they eventually reached a regime where their orbits were strongly mutually interacting, which resulted in the chaotic evolution of the orbits of all four giant planets. In the models presented by those authors, this resulted in the outward scattering of Uranus and Neptune into the massive disk of planetesimals that lay beyond, dispersing that disk (and circularising the orbits of those planets), and in the process flinging vast amounts of cometary and asteroidal material towards the terrestrial planets. The result was a short but remarkably intense period of cataclysmic impacts on the terrestrial planets – the Late Heavy Bombardment, following which the Solar System would have relaxed to its current relatively quiescent state. However, Norman (2009) strongly questioned the cataclysm hypothesis, pointing out a string of inconsistencies in establishing absolute ages of ancient impact basins and the sources for the impactors.

There are other theories that relate the rate of impacts on Earth to the dynamics of our Solar system, many of them focusing on the possible presence of a companion body to the Sun, which perturbs the orbits of comets and planetary debris enough to put them on a collision course with the Earth (e.g. Davis et al. 1984, Whitmire and Jackson 1984, Matese et al. 1995, 1999, Horner and Evans 2002, Matese and Whitmire 2011, Sumi et al. 2011).

Whilst the idea of the Late Heavy Bombardment is still heavily debated (e.g. Haskin et al. 1998, Chapman et al. 2007, Ćuk 2012), the hypothesis clearly demonstrates the importance of understanding astrobiological events and their consequent impact on the biological development of life – hence the field of astrobiology. Theories of planetary migration (themselves inspired both by our study of extrasolar planetary systems and studies of the small bodies in our Solar system (e.g. Lykawka et al. 2009, Malhotra 1995, Nesvorný et al. 2013, Minton and Malhotra 2011)) are used to explain how such a phenomenon could come about, and we come to understand that the planetary environment in which we arose is intimately connected with the detailed dynamical history of the Solar system.

1.3. Impact History and the Structure of Our Galaxy

An interesting alternative explanation for the potential periodicity observed in the Earth's impact and extinction history is that the variation is the direct result of the periodic passage of our Solar system through the spiral arms of the Galaxy (see Fig. 1). Our Solar system lies at significant distance (∼8 kpc) from the centre of a large spiral galaxy, the Milky Way. The Galaxy consists of a central bulge (far interior to the orbit of the Sun about its centre) surrounded by a number of spiral arms. The arms themselves contain large quantities of gas and dust, from which new generations of stars are continually being formed. The most massive stars, which are also the most short-lived, are heavily concentrated within the spiral arms, whilst the spaces between the arms are significantly less densely populated, being relatively free of gas, dust, and massive stars. Because the most massive stars have the shortest lives, supernovae (the cataclysmic explosions of the most massive stars) are also concentrated in spiral arms whose thickness may be up to ∼1-2 kpc (McClure-Grifths et al. 2004).

The motion of the spiral arms around the centre of the Galaxy is somewhat slower than that of the stars that make up the galaxy, which means that, as the Sun orbits the centre of the Galaxy, it follows a path that takes it through the spiral arms every few tens of millions of years. In the spiral arm environment, the Solar System is exposed to a far more hazardous and busy regime than in the inter-arm regions (our current location). The Earth could be relatively close to a star when its life comes to an end in a supernova explosion – which could certainly pose problems for life, although such supernovae are relatively rare, and the odds of the Earth being sufficiently close to one for life to be exterminated entirely are low, even within a spiral arm (Beech 2011). At the same time, close encounters between the Sun and neighbouring stars become more frequent, as do encounters between the Sun and giant gas clouds (see Fig. 2). Such encounters would not pose a direct hazard to life on Earth by changing the orbit of the Earth around the Sun, but could pose a hazard by disturbing the Oort Cloud (Porto de Mello et al. 2009), a vast cloud of comets (Oort 1950) which stretches to a distance of at least 100 000 AU from the Sun. The Oort Cloud is thought to contain trillions of cometary nuclei, left over from the formation of the Solar system, which are only tenuously gravitationally bound to the Sun (the outer members of

the cloud are around halfway to the nearest star). An encounter with a passing star or distant molecular cloud can be enough to deflect an Oort cloud comet, throwing it onto a new orbit that will bring it into the inner Solar system – where it can pose a threat to the Earth. The closer the star approaches to the Sun, or the more massive it is (or both), the more comets it will scatter inwards, and therefore the more likely it will be that one of those in-falling comets will hit the Earth.

Such comet showers are not merely hypothetical – the catalogue of observed long period comets (which come from the Oort cloud) contains a relatively weak, but still statistically significant, sign of a comet shower which is thought to have peaked a few million years ago. This shower (the Biermann shower) was first identified some thirty years ago, and illustrates how even relatively distant encounters between the Sun and passing stars can influence impacts on the Earth (Biermann et al. 1983).

Here, we test the idea that the Sun's orbit around the centre of the Milky Way has a significant influence on the impact regime experienced by the Earth. Using the latest results on the structure of our Galaxy, we construct a detailed and accurate timeline of the Sun's motion through spiral arms, and compare it to the latest knowledge of the history of biodiversity on Earth over time and the vastly improved dataset of global impacts that has become available over the last few years. Correlations between spiral arm crossings and mass extinctions suggest that the history of life on Earth is intimately connected with our place in the Universe.

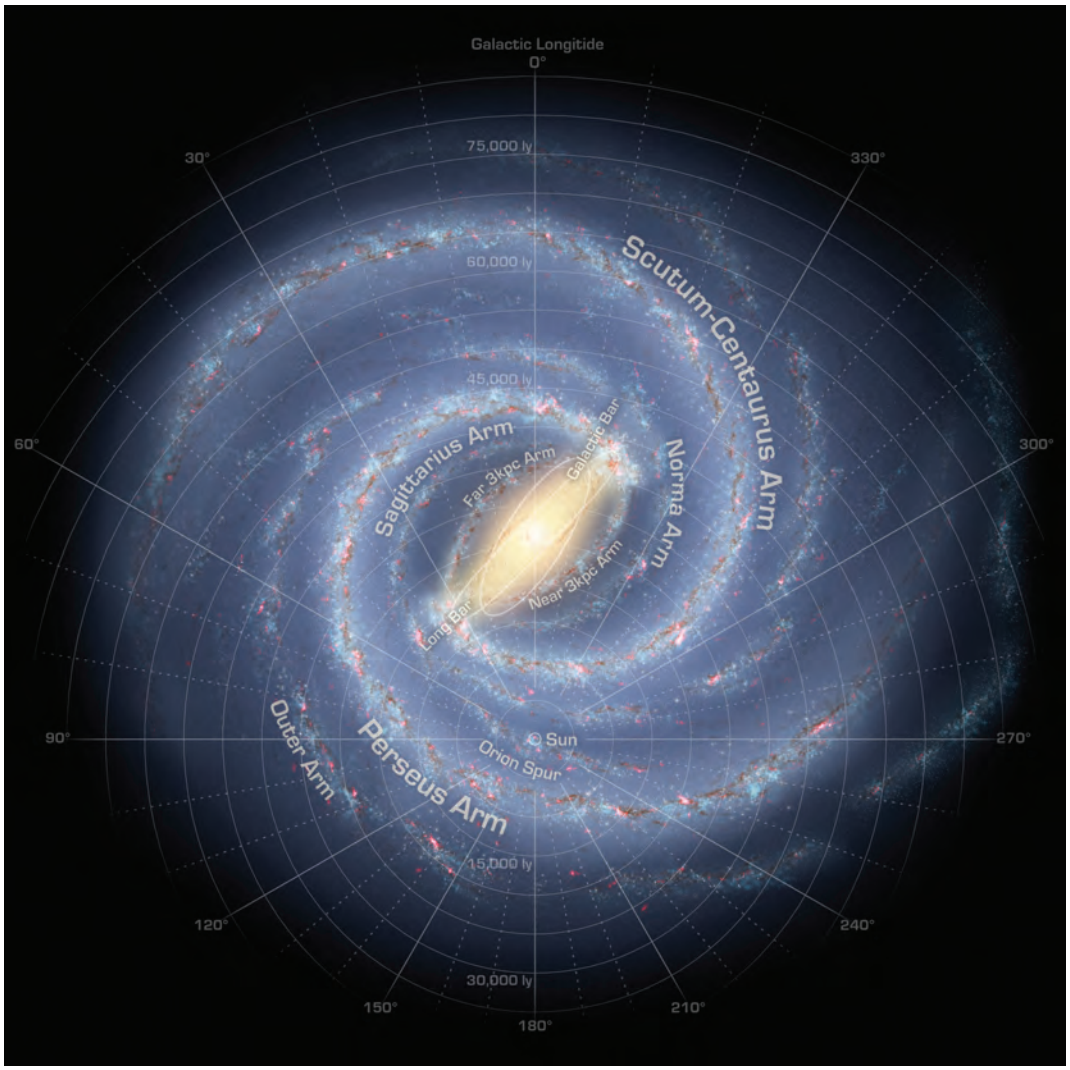

Fig. 1. *The face-on view of the Milky Way (Churchwell et al. 2009). The location of the Sun is indicated, along with the names and locations of the spiral arms and spur.*

2. DATA AND MODELLING

We make use of the major international impact databases to acquire the largest possible database of impact dates and sizes over the past billion years or so. We combine this with the latest understanding of the history of life on Earth, using the results of recent studies of the biodiversity of our oceans as a function of time to determine whether there is any correlation between that biodiversity and the flux of impacts on the Earth. Whilst it is true that any correlation between the two will be somewhat masked (by endogenous causes of mass extinctions, such as snowball Earth epochs, flood basalt outpourings, etc.), there are enough data to definitively determine whether the history of life on Earth has periodically been truncated by asteroid and cometary impactors. However, the further back we look, the more evidence is likely missing, lost to the ages past (i.e. as we go further back, there is less of a fossil record, so smaller mass extinctions could be missed/overlooked).

2.1. Models of the Sun's Trajectory through the Milky Way

In recent years, our understanding of the structure of our Galaxy has improved dramatically. As a result of a number of highly detailed surveys, a new picture is emerging which reveals our Galaxy's structure in far more detail than has ever been shown before. With that model, it is possible to accurately estimate the timing of the Sun's last orbit through the Galaxy's spiral arms – yielding timings that we can compare to the observed impact cratering record and extinction records to determine whether any correlation can be seen.

The kinematic parameters of the Milky Way used in this work are based on previous estimates (Gies and Helsel 2005), with the angular velocity of the Sun set at 26.3 km s^{-1} kpc^{-1} and the difference between the velocity of the Sun's motion and that of the spiral arms being 11.9 km s^{-1} kpc^{-1} (Overholt et al. 2009), which means that the Sun moves at a significantly greater velocity than the spiral arms. According to these values, during the last 500 Myr, the Sun has almost completely circumnavigated the entire spiral arm pattern, crossing two major and two minor arms, and one or two interarm spurs. Svensmark (2006) estimated that the last two spiral arm crossings happened approximately 31 Myr and 142 Myr ago. He also estimated that the spiral arm/interarm density ratio is in the range 1.5–1.8.

Historically, it has been assumed that the Sun's crossing of the Galaxy's spiral arms is a relatively simple, periodic event. However, the new model of our Galaxy's structure (Figs. 1 and 2) reveals the truth to be significantly more complicated. The spiral arms are not evenly spaced, and a number of smaller sub-arms are dotted between them. The result is that encounters between the Sun and the spiral arms will be both more frequent and more randomly distributed in time. By using this new model of galactic structure, we are able to take account of this irregular behaviour for the very first time, enabling us to carry out the first fair study of the influence of the Galaxy's structure on the impact flux at Earth.

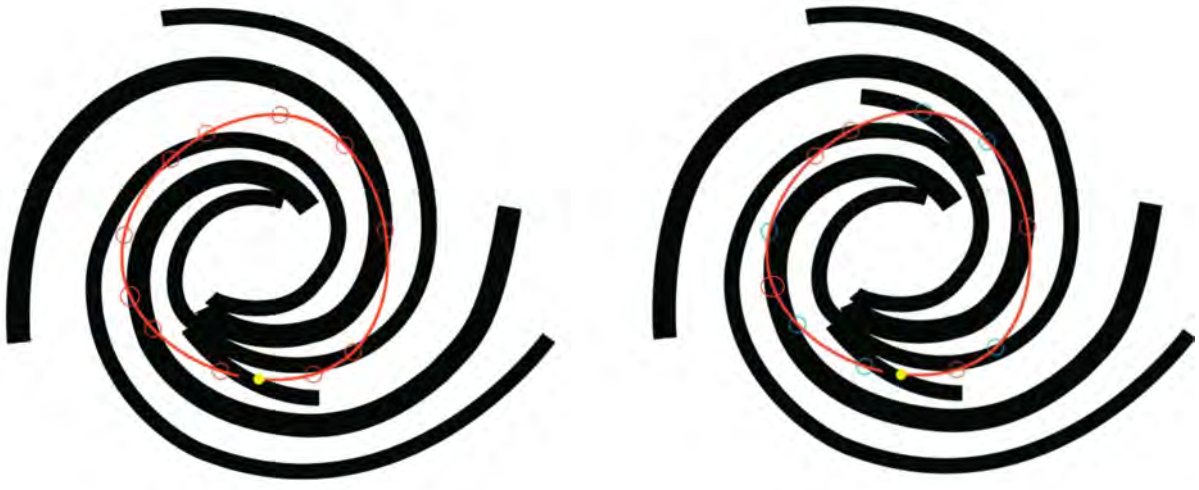

Fig. 2. *The Milky Way model (left), based on Churchwell et al. (2009) and our new weighted symmetrical model (right) of the Galaxy with the Sun's orbital path over 500 Myr. The Sun's current position is indicated with a yellow dot. Eleven extinction events are shown along the path by circles. The six blue circles in the new Galaxy model represent the known mass extinctions as marked in Fig. 3, whilst the orange circles represent the five additional events we propose here. The thickness of two major arms is set to 1.5 kpc and minor arms (as well as spurs) to 1 kpc.*

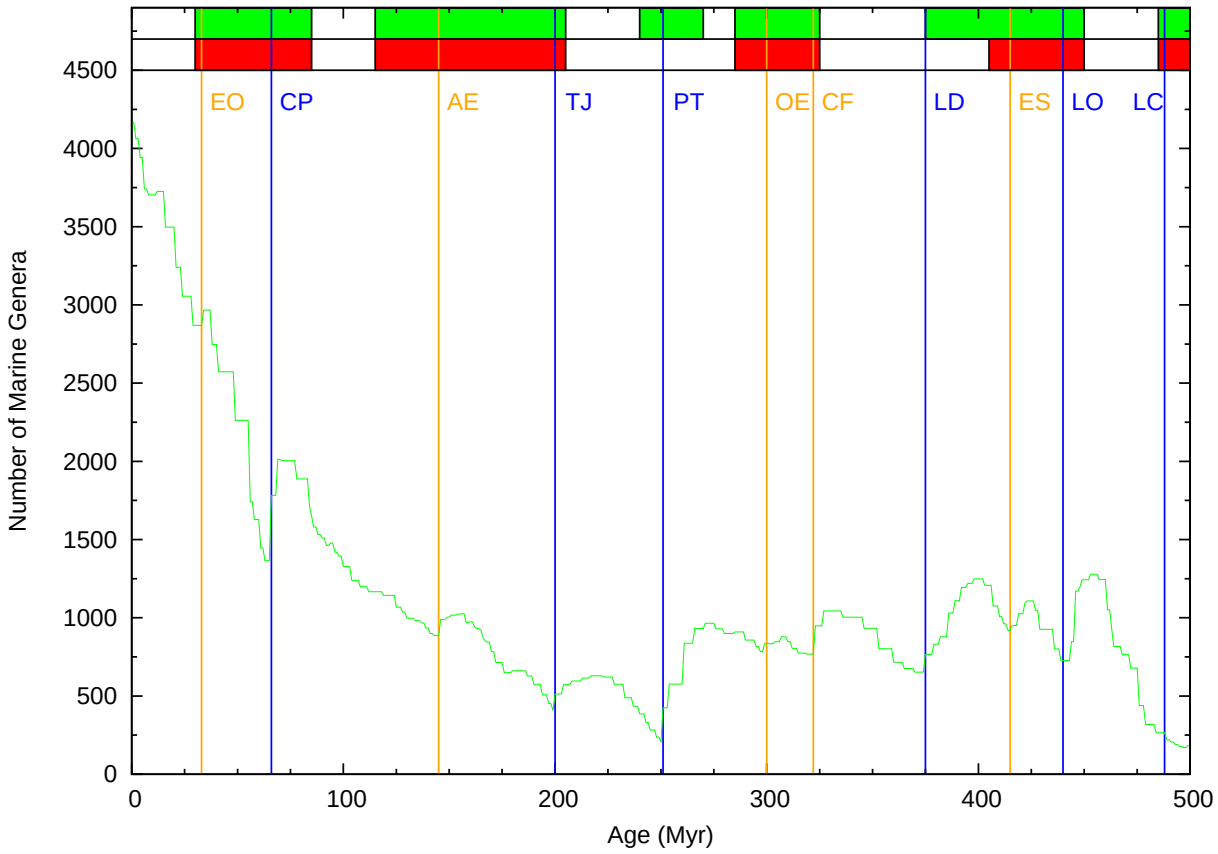

Fig. 3. *The number of marine genera over geological time/age (in Myr). The major mass extinction events are indicated by blue lines; Cretaceous-Paleogene (CP; 66 Myr), Triassic-Jurassic (TJ; 200 Myr), Permian-Triassic (PT; 251 Myr), Late Devonian (LD; 375 Myr), Late Ordovician (LO; 445 Myr) and Late Cambrian (LC; 488 Myr). Five proposed new extinction events are indicated by orange lines; Eocene-Oligocene (EO; 33.9 Myr), Aptian Extinction (AE; 145 Myr), Olson's Extinction (OE; 300 Myr), Carboniferous Rainforest Collapse (CF; 322 Myr) and End-Silurian (ES; 415 Myr). The vertical lines correspond with the orange/blue circles in Fig. 2. The green shaded area on the top represent Sun's passage through the Milky way in the new model while in red we indicate passage in the older model. Figure adapted from Rohde and Muller (2005).*

The model of the Sun's path through the Milky Way can be used as the basis for a model of the impact rate. Such a model would take account of the infall time for new comets (typically of order 500 kyr to 1 Myr), and feature gradual ramping up and slowing down of the impact flux at Earth, as the Solar system transitions between the low-flux state (whilst it lies between the spiral arms) to the high-flux state (whilst passing through the arms) and back to the low-flux state (as it returns to the space between the arms). During the time that the Solar system is located between the spiral arms of the Galaxy, encounters (whether with passing stars or giant molecular clouds) that might perturb the Oort cloud, causing a comet shower and an elevated impact flux will clearly be far less frequent than during the Sun's passage through the crowded spiral arms.

We also note that the model we are using and that of Gies and Helsel (2005) are similar in appearance, but that any differences would result in different gravitational potentials and thus slightly different trajectory shapes. We superimposed the Solar orbit from Gies and Helsel (2005) onto the Milky Way model based on Churchwell et al. (2009) (see Figs. 1 and 2). In Fig. 2, we mark the approximate locations of the known mass extinctions as a function of the Sun's orbit around the centre of the Galaxy, as described in the following section.

Also, we include approximate observational limits on the location of those events that result from obscuration by material in the Galactic centre. This is mainly because of the observational constraints placed on our knowledge of the structure of the far side of our Galaxy.

2.2. Extinctions in Biodiversity

The six largest mass extinction events of the last 500 Myr resulted in significant reductions to the biodiversity of the planet. These six extinction events are: Cretaceous-Paleogene (C-P) (also known as the Cretaceous-Tertiary or K-T, however the Tertiary period is not currently recognised by the International Commission on Stratigraphy) at 66 Myr ago; Triassic-Jurassic (T-J) at 200 Myr ago; Permian-Triassic (P-T) at 251 Myr ago; Late Devonian (LD) at 375 Myr ago; Late Ordovician (LO) at 445 Myr ago; Late Cambrian (LC) at 488 Myr ago. In Fig. 3 we display (blue vertical lines) the position of these mass extinction events along the geological timeline and the global marine genera number distribution over the last 500 Myr (Rohde and Muller 2005).

There is extensive coverage of these mass extinction events in the literature, therefore, we emphasise their position in time rather than their effect on ancient biodiversity. Our study is based on Sepkoski's definition[3] of a mass extinction event (Sepkoski 2002), which is a sharp decrease in marine genera along the diversity curve.

In addition to these mass extinctions, there are five other significant drops in marine genera that we find indicated in the data (they are also known in the literature as "lesser extinctions"). These somewhat smaller reductions in marine genera diversity occur 415, 322, 300, 145 and 33 Myr ago (Fig. 3; orange vertical lines). Not all mass extinctions would be the result of spiral arm crossings. While other events could also contribute (the background impact flux due to the planetary system, and extinctions due to climate and geological reasons), we suggest that the probable cause for these reductions in marine genera is also connected to spiral arm crossings.

Although extinction events have consistently, and some would argue periodically, eroded away life on this planet, they have also likely driven the evolutionary radiation of the species. With the widespread loss of species, surviving species may fill new niches and physically adapt accordingly to new habitats. Without the mechanisms that brought about mass extinction events, the complexity of life as we know it today may not exist. If these mechanisms are of extraterrestrial origin, they may prove to be an essential ingredient, rather than a barrier, to complex life in the Galaxy.

As well as the addition of new extinctions we identify in the data, we also see a pattern in the marine genera data over the last 500 Myr. There is rapid growth beginning at 500 Myr, followed by a general decline in genera, then a prolonged growth leading to the present time. Because marine genera data, and for that matter data on land flora and fauna, are based on fossil evidence, these trends in the data may be due to the efficiency of fossilisation and possibly other unknown factors rather than actual genera populations over time (Bailer-Jones 2009). Bailer-Jones (2009) argues that there is no significant evidence for intrinsic periodicities in biodiversity, impact cratering or climate on timescales of tens to hundreds of Myr; therefore it seems likely that more than one mechanism has contributed to biodiversity variations over the past 500 Myr.

3. NEW MILKY WAY MODEL

With a differential speed of 11.9 km s^{-1} kpc^{-1}, the Sun orbits the centre of the Milky Way galaxy, passing through four spiral arms and a spur, and almost completing one full circuit of the entire spiral arm pattern (last 500 Myr; see Fig. 2 (left)). The thickness of the major arms is set to 1.5 kpc and minor arms, as well as spurs, to 1 kpc.

We have identified eleven significant spikes in the extinction intensity data that we marked on the Sun's orbital path. If we were to contend that all eleven extinctions discussed herein were the result of our passage through the Galaxy's spiral arms, then it is clearly possible to modify our Galaxy model to account for those extinctions. Whilst this is a purely hypothetical exercise, it is not necessarily unreasonable. As can be seen in the right-hand panel of Fig. 2, only a small modification to the Milky Way model put forth by Churchwell et al. (2009) is required in order to ensure that all eleven mass extinctions occur within one or other of the spiral arms. This region of the Galaxy is far less known (observationally) and that significant level of symmetry does exist in other galaxies.

In the original Milky Way model (Fig. 2 (left)), we observe that nine of the extinctions studied happened during the Sun's passage throughout the spiral arms. However, in our modified symmetrical model all eleven events are positioned in the spiral arms. Four (TJ, PT, OE and CF event) of these extinctions lie on a part of the Sun's orbit where our view of the Milky Way's structure is obscured by the Galactic centre. Therefore, this gives some freedom for speculation on a spur, similar to the Orion spur, existing on the other side of the Galaxy. If we were to assume that the extinctions are solely caused by impacts induced by our passage through spiral arms, then this would clearly allow us to constrain their locations independent of astronomical observations – an interesting test for the current model of galactic structure.

However, as we noted earlier, there are a number of endogenous factors that could also cause mass extinctions, and so it seems plausible to assume that those extinctions that fall outside of periods when the Sun is crossing a spiral arm could have an endogenic rather than an exogenic origin. Equally, as we also noted earlier on, being outside of a spiral arm does not preclude close encounters between the Sun and other stars, and so we would expect at least some impact induced extinctions to occur whilst the Sun is between crossings, albeit at a much reduced rate.

[3]Sepkoski's online database can be accessed at http://strata.geology.wisc.edu/jack/

Summed over the entirety of its orbital path over the last 500 Myr, based on the new weighted symmetrical model, we find that the Sun has spent ∼60% of its time in the spiral arms (see the green shaded areas at the top of Fig. 3). By comparison, for the case of the old non-symmetrical model, the Sun would have spent ∼ 50% of the same period in the spiral arms (red shaded areas in Fig. 3).

Given the incompleteness of the available data any claims on mass extinctions' temporal distribution are naturally highly speculative. We therefore employ a simple statistical prediction (null hypothesis) of exactly how many of the extinctions could occur randomly during spiral arm crossings, and estimate the likelihood of that occurring by chance.

The null hypothesis is that no mass extinction has been caused by spiral arm crossings, and therefore all eleven mass extinctions occur within the spiral arms purely by chance. The probability of this is 0.36% (0.6^{11}). The hypothesis that six out of eleven randomly occurring events fall inside spiral arms by pure chance has fairly high probability – 20-25% – which is not negligible. However, the probability that all eleven random events fall within the spiral arms is low (0.36%).

A simple numerical test also produces similar results. We generated a series of data sets in which eleven extinction events were randomly distributed through the last 500 Myr, and then counted the frequency with which all eleven occurred during spiral arm crossings. Our results again support the hypothesis that it is highly unlikely for all of the studied mass extinctions to coincidentally fall during spiral arm crossings, suggesting that their timings are not simply a matter of chance.

Our results suggest that the proposed 62 Myr periodicity (Rohde and Muller 2005) in mass extinctions could be directly related to the Sun's passage through the spiral arms of the Milky Way. However, we stress that significant controversy about 62 Myr periodicity still exists among the scientific community (for detailed analysis see Feng and Bailer-Jones (2013), Melott and Bambach (2013) as well as Bailer-Jones and Feng (2013).

4. CONCLUSIONS AND FUTURE WORK

We created a new model of the Sun's orbit around the centre of the Milky Way, in order to accommodate the influence of spiral arm crossings on the cometary flux through the inner Solar system. Our model reveals the periods when the Earth has suffered the highest risk of cometary impacts – periods that will likely span several million years, and be separated by periods of several tens of millions of years.

We have combined marine genera data, an orbital model of the Sun's path around the Milky Way with two face-on Galactic models. The first Galactic model is based on an artistic rendition of the Milky Way, by Churchwell et al. (2009). The second is an alteration of the first model, which accommodates all the extinctions within the spiral arms and displays a more symmetrical structure. Extinction data were then added to the new model and the existing orbital path of the Sun. In doing so all extinctions fall within the spiral arms.

Our new Galactic model, if correct, would support the idea that spiral arm crossings cause mass extinctions. Although a cyclic occurrence of large scale, global extinction is very likely to have an extraterrestrial origin, complex interactions at the Earth's surface cannot be completely discounted. It becomes harder to argue extinctions are caused by celestial events when they are not cyclic, which is still a controversial topic.

However, reconsidering the possibility that spiral arms do cause extinctions on Earth, we can consider the ramifications of this to possible complex life elsewhere in the Galaxy. If we also consider that extinctions accelerate rather than impede the evolution of complex life, we may better constrain ideas on the Galactic Habitable Zone (Lineweaver et al. 2004). It may be the case that habitable planets orbiting stars further from the Galactic centre do not retain a high enough organic turn over rate due to more infrequent spiral arm crossings, or that closer in the extinction rate exceeds the ability for life to recover. Consideration could also be given to the possibility that habitable planet-hosting stars may have highly eccentric orbits around the Galaxy.

Further statistical work and data on the structure of the Milky Way, kinematics, and the Solar orbit would refine our work and assist in continuing to test the spiral-arm/extinction hypothesis. Our future work will consist of two main threads – the first being the consolidation of the archives of the Earth's impact history, extinction history, and the galactic architecture; the second being the construction of a detailed model that will allow us to test whether the Galactic structure is the dominant factor in defining the rate of Oort cloud comets (and hence impacts) at Earth.

This also lends itself to a prediction – as our knowledge of the ancient Earth improves, if the hypothesis presented here is correct, then the periodicity should become clearer as more extinctions are found going further back. Is it reasonable to assume that the morphology of the Galaxy will have remained unchanged over the last four billion years. If so, then we could possibly argue that the periodic spiral arm crossings will have been happening all the way back – albeit perhaps with some modulation on period and exact timings as a result of the evolution and disruption of the spiral arms and changes in the Sun's orbit around the galactic centre.

Acknowledgements – We thank Scott Williams and Ivan Bojičić for valuable discussion on this topic. We thank the referee for numerous helpful comments that have greatly improved the quality of this paper.

REFERENCES

Alroy, J.: 2008, *Proc. Natl. Acad. Sci. U.S.A.*, **105**, 11536.

Alvarez, L. W., Alvarez, W., Asaro, F. and Michel H. V.: 1980, *Science*, **208**, 1095.

Bailer-Jones, C. A. L.: 2009, *Int. J. Astrobiology*, **8**, 213.

Bailer-Jones, C. A. L. and Feng, F.: 2013, arXiv:1307.4266.

Baldwin, E. C., Milner, D. J., Burchell, M. J. and Crawford, I. A.: 2007, *Meteoritics Planet. Sci.*, **42**, 1905.

Beech, M.: 2011, *Astrophys. Space Sci.*, **336**, 287.

Bottke, W. F., Vokrouhlický, D. and Nesvorný, D.: 2007, *Nature*, **449**, 48.

Chang, H.-Y. and Moon, H.-K.: 2005, *Publ. Astron. Soc. Jpn.*, **57**, 487.

Chapman, C. R., Cohen, B. A. and Grinspoon, D. H.: 2007, *Icarus*, **189**, 233.

Churchwell, E., Babler, B. L., Meade, M. R., Whitney, B. A., Benjamin, R., Indebetouw, R., Cyganowski, C., Robitaille, T. P., Povich, M., Watson, C. and Bracker, S.: 2009, *Publ. Astron. Soc. Pac.*, **121**, 213.

Ćuk, M.: 2012, *Icarus*, **218**, 65.

Davis, M., Hut, P. and Muller, R. A.: 1984, *Nature*, **308**, 715.

Feng, F. and Bailer-Jones, C. A. L.: 2013, *Astrophys. J.*, **768**, 152.

Gies, D. R. and Helsel, J. W.: 2005, *Astrophys. J.*, **626**, 844.

Grieve, R. A. F. and Pesonen, L. J.: 1992, *Tectonophysics*, **216**, 1.

Gogarten-Boekels, M., Hilario, E. and Gogarten, J. P.: 1995, *Orig. Life Evol. Biosph.*, **25**, 251.

Gomes, R., Levison, H. F., Tsiganis, K. and Morbidelli, A.: 2005, *Nature*, **435**, 466.

Hammel, H. B., Beebe, R. F., Ingersoll, A. P., Orton, G. S., Mills, J. R., Simon, A. A., Chodas, P., Clarke, J. T., de Jong, E., Dowling, T. E., Harrington, J., Huber, L. F., Karkoschka, E., Santori, C. M., Toigo, A., Yeomans, D. and West, R. A.: 1995, *Science*, **267**, 1288.

Haskin, L. A., Korotev, R. L., Rocklow, K. M. and Jolliff, B. L.: 1998, *Meteoritics Planet. Sci.*, **33**, 959.

Horner, J. and Evans, N. W.: 2002, *Mon. Not. R. Astron. Soc.*, **335**, 641.

Horner, J. and Jones, B. W.: 2010, *Special issue Papers from the Astrobiology Society of Britain*, **9**, 273.

Horner, J., Mousis, O., Petit, J.-M. and Jones, B. W.: 2009, *Planet. Space Sci.*, **57**, 338.

Horner, J. and Jones, B. W.: 2011, *Astron. Geophys.*, **52**, 1.16.

Levison, H. F., Morbidelli, A., Vanlaerhoven, C., Gomes, R. and Tsiganis, K.: 2008, *Icarus*, **196**, 258.

Lineweaver, C. H., Fenner, Y. and Gibson, B. K.: 2004, *Science*, **303**, 59.

Lykawka, P. S., Horner, J., Jones, B. W. and Mukai, T.: 2009, *Mon. Not. R. Astron. Soc.*, **398**, 1715.

Malhotra, R.: 1995, *Astron. J.*, **110**, 420.

Matese, J. J., Whitman, P. G., Innanen, K. A. and Valtonen, M. J.: 1995, *Icarus*, **116**, 255.

Matese, J. J., Whitman, P. G. and Whitmire, D. P.: 1999, *Icarus*, **141**, 354.

Matese, J. J. and Whitmire, D. P.: 2011, *Icarus*, **211**, 926.

Mayhew, P. J., Jenkins, G. B. and Benton, T. G.: 2008, *Proc. of the Roy. Soc. B.*, **275**, 1630.

McElwain, J. C. and Punyasena, S. W.: 2007, *Trends in Ecology and Evolution*, **22**, 548.

McClure-Grifths, N. M., Dickey, J. M., Gaensler, B. M. and A. J. Green: 2004, *Astrophys. J.*, **607**, L127.

Melott, A. L. and Bambach, R. L.: 2011, *Paleobiology*, **37**, 92.

Melott, A. L. and Bambach, R. L.: 2013, *Astrophys. J.*, **773**, 6.

Milner, D. J., Baldwin, E. C. and Burchell, M. J.: 2008, *Meteoritics Planet. Sci.*, **43**, 2015.

Minton, D. A. and Malhotra, R.: 2011, *Astrophys. J.*, **732**, 53.

Nesvorný, D., Vokrouhlický, D. and Morbidelli, A.: 2013, *Astrophys. J.*, **768**, 45.

Norman, M.: 2009, in: The lunar cataclysm: Reality or "Mythconception"?, Elements, **5**, 23.

Oberbeck, V. R. and Fogleman, G.: 1989, *Nature*, **339**, 434.

Oort, J. H.: 1950, *Bull. Astron. Inst. Neth.*, **11**, 91.

Overholt, A. C., Melott, A. L. and Pohl, M.: 2009, *Astrophys. J.*, **705**, L101.

Porto de Mello, G. F., Lépine, J. R. and da Silva Dias, W.: 2009, *Publ. Astron. Soc. Pac.*, **420**, 349.

Rampino, M. R. and Stothers, R. B.: 1984, *Nature*, **308**, 709.

Rampino, M. R.: 1997, *Celest. Mech. Dyn. Astron.*, **69**, 49.

Raup, D. M. and Sepkoski, J. J.: 1986, *Science*, **231**, 833.

Rohde, R. A. and Muller, R. A.: 2005, *Nature*, **434**, 208.

Sánchez-Lavega, A., Wesley, A., Orton, G., Hueso, R., Perez-Hoyos, S., Fletcher, L. N., Yanamandra-Fisher, P., Legarreta, J., de Pater, I., Hammel, H., Simon-Miller, A., Gomez-Forrellad, J. M., Ortiz, J. L., Garca-Melendo, E., Puetter, R. C. and Chodas, P.: 2010, *Astrophys. J.*, **715**, L155.

Sepkoski, J. J.: 2002, *Bulletins of American Paleontology*, **363**, 560.

Svensmark, H.: 2006, *Astron. Nachr.*, **327**, 866.

Svensmark, H.: 2012, *Mon. Not. R. Astron. Soc.*, **423**, 1234.

Sumi, T., et al.: 2011, *Nature*, **473**, 349.

Wells, L. E., Armstrong, J. C. and Gonzalez, G.: 2003, *Icarus*, **162**, 38.

Whitmire, D. P. and Jackson, A. A.: 1984, *Nature*, **308**, 713.

Wignall, P. D.: 2001, *Earth-Science Reviews*, **53**, 1.

МАСОВНА ИЗУМИРАЊА И СТРУКТУРА МЛЕЧНОГ ПУТА

M. D. Filipović[1], J. Horner[2,3], E. J. Crawford[1], N. F. H. Tothill[1] and G. L. White[1]

[1]*University of Western Sydney, Locked Bag 1797, Penrith South DC, NSW 1797, Australia*
E–mail: *m.filipovic@uws.edu.au, e.crawford@uws.edu.au, n.tothill@uws.edu.au*

[2]*School of Physics, University of New South Wales, Sydney 2052, Australia*
[3]*Australian Centre for Astrobiology, University of New South Wales, Sydney 2052, Australia*
E–mail: *j.a.horner@unsw.edu.au*

УДК 52–37
Оригинални научни рад

Користећи најновији модел Млечног пута и орбите Сунца тестирали смо хипотезу да сваки пролазак Сунца кроз спиралну грану проузрокује масовна изумирања свих живих организама на Земљи. Овде представљамо нови модел Млечног пута који је базиран на мањим модификацијама даљег и теже видљивог дела наше галаксије. Такође, наш нови модел смо прилагодили на до сада познатих и историјски потврђених шест (6) масовних изумирања. Уз ових познатих шест, предложили смо још пет нових која су прорачуната на основу значајне редукције морских живих организама у периодима од пре 415, 322, 300, 145 и 33 милиона година. Наше симулације показују да је Сунце провело најмање 60% времена свог постојања у спиралним гранама што додатно потврђује повезаност масовних изумирања са пролазом Сунца кроз спиралне гране Млечног пута. Такође, разматрамо и утицај овде представљеног новог модела наше Галаксије на стабилност Галактичке настањиве зоне.

A.32 Related Paper 32

Pavan, L., Bordas, P., Pühlhofer, G., Filipović, M. D., De Horta, A., O'Brien, A., Balbo, M., Walter, R., Bozzo, E., Ferrigno, C., Crawford, E., and Stella, L. (2014a). The long helical jet of the Lighthouse nebula, IGR J11014-6103. *A&A*, 562:A122

My contribution was to assist in the data analysis. This is a 5% contribution.

A&A 562, A122 (2014)
DOI: 10.1051/0004-6361/201322588

Astronomy & Astrophysics

The long helical jet of the Lighthouse nebula, IGR J11014-6103

L. Pavan[1], P. Bordas[1,2], G. Pühlhofer[2], M. D. Filipović[3], A. De Horta[3], A. O' Brien[3], M. Balbo[1], R. Walter[1], E. Bozzo[1], C. Ferrigno[1], E. Crawford[3], and L. Stella[4]

[1] ISDC Data Center for Astrophysics, Université de Genève, 16 chemin d'Ecogia, 1290 Versoix, Switzerland
e-mail: Lucia.Pavan@unige.ch
[2] Institut für Astronomie und Astrophysik, Universität Tübingen, Sand 1, 72076 Tübingen, Germany
[3] Computational Astrophysics, Imaging & Simulation School of Computing & Mathematics, University of Western Sydney, 2006 Sydney, Australia
[4] INAF − Osservatorio astronomico di Roma, via di Frascati 33, 00040 Monte Porzio Catone, Roma, Italy

Received 2 September 2013 / Accepted 12 January 2014

ABSTRACT

Context. Jets from rotation-powered pulsars so far have only been observed in systems moving subsonically through their ambient medium and/or embedded in their progenitor supernova remnant (SNR). Supersonic runaway pulsars are also expected to produce jets, but they have not been confirmed to so far.
Aims. We investigated the nature of the jet-like structure associated with the INTEGRAL source IGR J11014-6103 (the "Lighthouse nebula"). The source is a neutron star escaping its parent SNR MSH 11-61A supersonically at a velocity exceeding 1000 km s^{-1}.
Methods. We observed the Lighthouse nebula and its jet-like X-ray structure through dedicated high spatial resolution observations in X-rays (with *Chandra*) and in the radio band (with ATCA).
Results. Our results show that the feature is a true pulsar's jet. It extends highly collimated over $\gtrsim$11pc, displays a clear precession-like modulation, and propagates nearly perpendicular to the system direction of motion, implying that the neutron star's spin axis in IGR J11014-6103 is almost perpendicular to the direction of the kick received during the supernova explosion.
Conclusions. Our findings suggest that jets are common to rotation-powered pulsars, and demonstrate that supernovae can impart high kick velocities to misaligned spinning neutron stars, possibly through distinct, exotic, core-collapse mechanisms.

Key words. X-rays: individuals: IGR J11014-6103 – stars: jets – stars: neutron – supernovae: individual: MSH 11-61A – ISM: jets and outflows – ISM: supernova remnants

1. Introduction

Pulsar wind nebulae (PWNe) powered by pulsars that are still embedded in their progenitor supernova remnant (SNR) are typically seen as extended cocoons, in some cases accompanied by two collimated jets (Weisskopf et al. 2000; Gaensler & Slane 2006; Kargaltsev & Pavlov 2008; Durant et al. 2013). As of yet, jets have not been clearly identified from runaway pulsars that are traveling supersonically through the interstellar medium, which show otherwise cometary-like features formed by the confinement of their winds by a bow-shock (Gaensler & Slane 2006). Deep statistical studies have proved that pulsar's spin axes (and hence jets, when present) are generally aligned with their proper motion (Weisskopf et al. 2000; Johnston et al. 2007; Durant et al. 2013), a relation that has been explained by numerous theoretical models of asymmetric supernova mechanisms (Spruit & Phinney 1998; Lai et al. 2001; Janka 2012). Jets in runaway systems could therefore be either disrupted by the system motion or aligned with (and hidden by) the bow-shocked PWN (Kargaltsev & Pavlov 2008), making their detection difficult.

In a few cases only, puzzling jet-like X-ray features extending over parsec-scales have been observed in association with high velocity pulsars, e.g., in the Guitar nebula (powered by pulsar PSR B2224+65; Hui et al. 2012) and in Morla (powered by PSR J0357+3205; De Luca et al. 2013). In the latter case, the jet-like feature is aligned with the pulsar proper motion, and may correspond to a trail of thermal emission from the shocked ambient medium (Marelli et al. 2013). In the Guitar nebula, in contrast, the collimated X-ray outflow is inclined by ∼118° with respect to the backwards PWN, which is seen in the optical band as a bright H-α nebula (Cordes et al. 1993). Although observations performed at different epochs confirmed the link between this extended X-ray feature and the pulsar (Johnson & Wang 2010), its nature is still under discussion, and different scenarios, including a truly ballistic jet (Johnson & Wang 2010; Hui et al. 2012) or a flow of high-energy electrons diffusing into the ambient magnetic field (Bandiera 2008), have been proposed.

The INTEGRAL source IGR J11014-6103, which we call the Lighthouse nebula, located 11′ southwest of the SNR MSH 11-61A (estimated distance 7±1 kpc, Reynoso et al. 2006), is a complex system that, in X-rays, displays a point source, an elongated cometary tail, and perpendicular to this, a prominent jet-like feature (see Pavan et al. 2011, hereafter Paper I; and Tomsick et al. 2012, T12 in the following). While the previous studies already suggested a PWN scenario for the cometary tail in IGR J11014-6103, the jet-like feature remained as yet uninterpreted due to the poor statistics of the available data. To unveil its real nature, we obtained high spatial resolution observations of the Lighthouse nebula with the *Chandra* X-ray Observatory and in the radio band with the Australia Telescope Compact Array (ATCA).

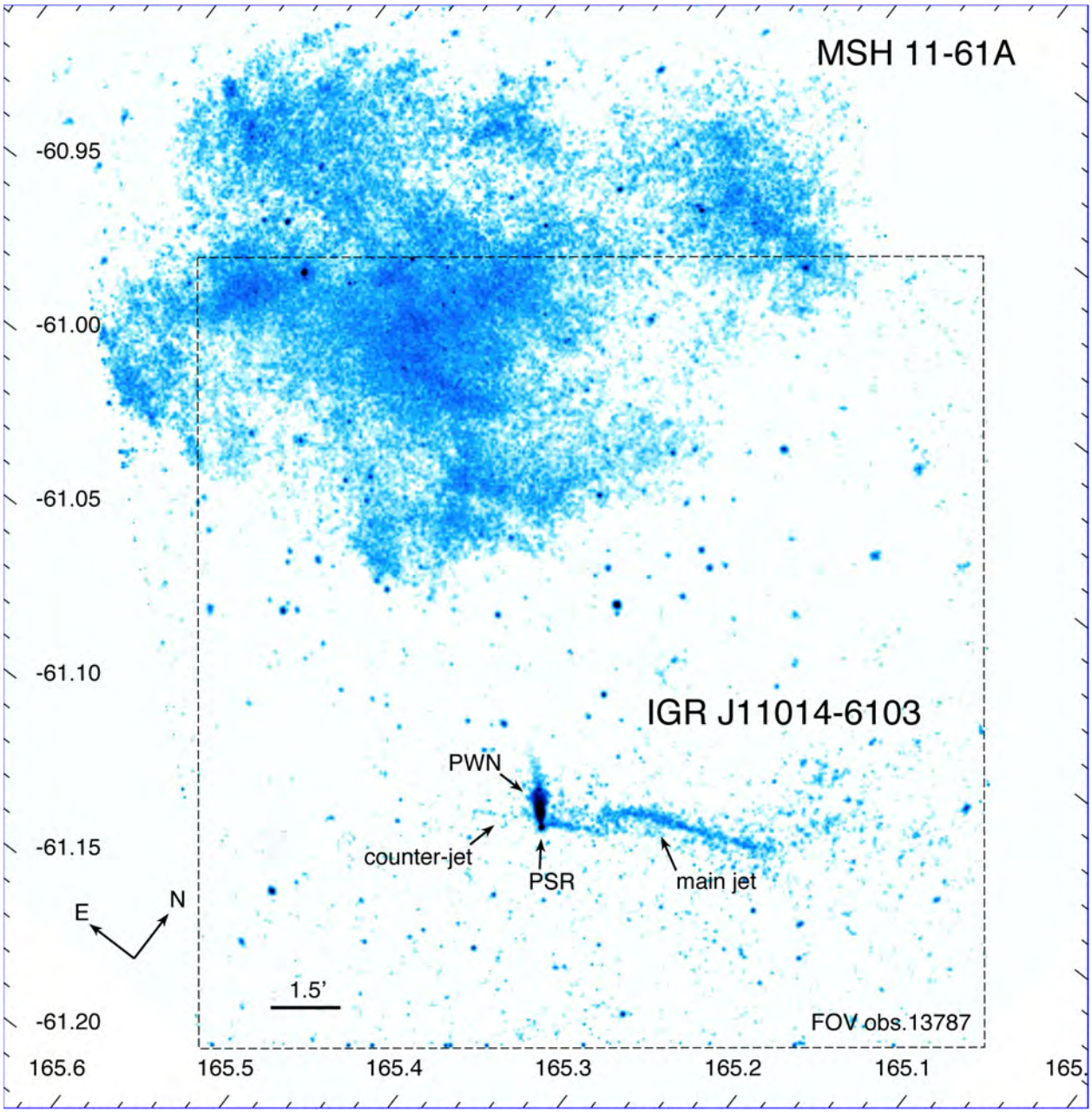

Fig. 1. Lighthouse nebula (IGR J11014-6103) as viewed by *Chandra* during our observation (obs.ID 13787, with the field of view indicated by the dashed box). The image also includes archival observations of SNR MSH 11-61A. The two objects have likely been produced by the same supernova explosion 10−20 kyr ago. The image is adaptively smoothed with a gaussian kernel, rotated by 37.5°, and normalized by the exposure to recover gaps between the chips. Labels indicate the terms used throughout the text for the different components of the Lighthouse nebula.

2. Observations and data analysis

2.1. Chandra X-ray observation

We observed the Lighthouse nebula with *Chandra* for 50 ks on October 11, 2012 (obs.ID 13787). The data have been analyzed with the *Chandra* Interactive Analysis of Observations package (`CIAO` version 4.5; Fruscione et al. 2006) and reprocessed with standard tools using the most recently available calibration, as recommended by the *Chandra* team. We applied standard filters to the event file, on grade, status, and good time intervals. The observation was not affected by strong background flares, resulting in a final net exposure of 49.4 ks.

We performed the observation with the Advanced CCD Imaging Spectrometer (ACIS-I) detector pointing at source 2XMM J110145.0-610140 ("PSR" hereafter, see Fig. 1), with a moderate offset of 0.8′ with respect to the nominal aim point, to optimize the results for the imaging of the PSR itself, the cometary PWN, and jet structures. All components of the Lighthouse nebula and a large portion of the nearby SNR MSH 11-61A are included in the total ACIS field of view (FOV, see dashed box in Fig. 1).

2.1.1. Imaging

Chandra observations in imaging mode are performed with a dithering technique that enables coverage of the gaps between CCDs, though these are characterized by a reduced net exposure. To recover these sections, we computed a fluxed image, by

Table 1. Best fit spectral parameters for the Lighthouse nebula components.

	N_H (10^{22} cm^{-2})	Γ	$F_{2-10\,keV}$ (10^{-13} erg cm^{-2} s^{-1})	$\tilde{\chi}^2$/d.o.f.
PSR	1.0 ± 0.2	1.1 ± 0.2	6.1 ± 0.6	1.09/70
PWN	0.8 ± 0.1	1.9 ± 0.1	6.7 ± 0.5	0.82/76
Main jet	0.8 ± 0.2	1.6 ± 0.2	5.4 ± 0.5	1.08/65

Notes. All spectra were fit using an absorbed power-law model (photon index Γ). Uncertainties are at 90% c.l. on the spectral parameters and 68% c.l. on the fluxes.

normalizing the count map with the local net exposure. The exposure map takes the *Chandra* effective area into account, and is therefore energy-dependent. We thus computed the instrument and exposure maps, weighting them for the spectral distribution observed from the PSR source (see Sect. 2.1.3 and Table 1), through the standard CIAO tools `make_instmap_weights` and `mkinstmap`. We verified that different, reasonable weights for the instrument map did not significantly affect the resulting corrected image (Fig. 1). We detected X-ray extended emission up to 3 keV from the SNR MSH 11-61A in agreement with what has been previously reported by García et al. (2012). The three components of the Lighthouse nebula were clearly visible in our *Chandra* observation. We detected PSR at RA 11:01:44.915, Dec −61:01:38.66 (J2000, associated uncertainty 0.64″) in agreement with the position previously reported by T12. The PWN is detected up to 1.2′ from PSR. The main jet is clearly detected up to ∼5.5′ from PSR in a northwest direction, forming an angle of ∼104° with the PWN axis. The *Chandra* data also revealed for the first time that the long jet is highly collimated and displays a strikingly well-defined corkscrew modulation. In the corrected image, the jet shows a remarkable change of orientation at about 1.4′ from PSR. We did not attempt a more refined analysis and interpretation of this region as it lies in a gap between two CCDs, and thus is characterized by a much lower net exposure time with respect to the surroundings.

In addition to these three components, our observation has revealed a fainter linear region opposite the jet, in a southeast direction (see Fig. 1). This extended region is clearly detected with the Voronoi Tessellation and Percolation source detection (`CIAO/vtpdetect`) algorithm up to 1.5′ from PSR, with a detection significance of 3.7σ. The orientation and position of this linear feature is readily interpreted as a counterjet.

The counterjet is well aligned with the direction of the main jet within the first arcminute from PSR. Both features intersect the PWN at 7.4″ from the point source. Within 30″ from the PSR, however, the jet bends directly toward the point source and is smoothly connected to it (see Fig. 1). The alignment between the jet and counterjet, together with the change of brightness at the PSR location and their smooth connection to PSR, rule out any chance coincidence between these structures.

2.1.2. Point-like source PSR

To verify the point-like nature of PSR, we extracted the radial intensity profile of the source (background subtracted) and compared it to the corresponding instrumental point-spread function (PSF). The PSF was obtained by simulations performed with `ChaRT` (Carter et al. 2003), assuming the spectral profile of the PSR source (see Table 1) and reprojected with `MARX` v.5

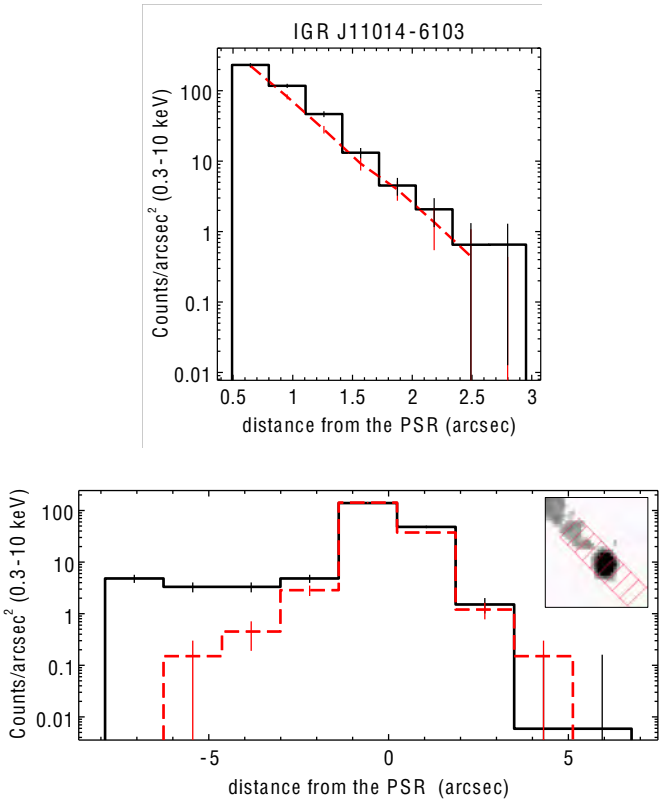

Fig. 2. *Top panel*: radial profile within 3″ from the source PSR (histogram in black) compared to the PSF (dashed red line) simulated with the ChaRT tool at the PSR position and with the measured energy spectrum. *Bottom panel*: same plot as above, but for the regions marked in the *inset picture*. Positive radial distances are in front of the source, in the SW direction, negative are backwards in the NE direction (i.e. in the direction of the PWN).

(Davis et al. 2012) to the observed source position on the ACIS-I3 chip. The observed and simulated profiles, extracted within a region of 3″ around PSR, are displayed in the upper panel of Fig. 2. We verified that there are no variations on the profile between the front and rear regions. Similarly, we extracted the intensity profile along the axis of the PWN from a rectangular region centered on the source and extending up to 7″ (Fig. 2, lower panel). The comparison with the simulated PSF shows that there is no detectable extension in front of the source, and that the PWN is smoothly connected to the point source, emerging 3″ away from it already.

The relatively poor timing resolution of the *Chandra* data in timed exposure mode (3.2 s) did not permit us to analyze the timing periodicity of the point source. Previous searches with *XMM-Newton* (Paper I) and Parkes (T12) did not reveal any significant coherent periodicity. We note, however, that in almost one-third of the known PWN systems there is no clear pulsating signal from the neutron star (see, e.g., Roberts 2004). This can be due to geometrical phenomena, when the beam of light from the pulsar is oriented in a direction not intercepting Earth, as well as physical phenomena, if the presence of a dense region surrounding the pulsar prevent the direct observation of the neutron star surface and its pulsations (Kargaltsev & Pavlov 2008).

2.1.3. Spectra

We extracted background-corrected spectra of the different components of the Lighthouse nebula with the standard

CIAO/specextract tool, and analyzed them with xspec (v.12.7.1; Arnaud 1996).

All the extended components and PSR were comprised in the FOV of ACIS I3. The main jet, which was comprised in ACIS I2, was the only exception. Therefore, the background regions were chosen from source free areas in ACIS chips I2 and I3. We verified that different reasonable choices of the background did not significantly affect our spectral results.

We extracted the spectrum of PSR from a circular region of 2.3″ centered on the source to avoid contamination from the PWN and the jets. We created the corresponding response matrix file (RMF) and energy-corrected ancillary response file (ARF) with the CIAO standard tools. The spectrum was grouped to have at least 15 counts per energy bin. For the jet and PWN, we followed standard CIAO spectral extraction procedure for extended sources. We used specextract to compute weighted RMFs and ARFs for each component.

All spectra could be fit with a simple absorbed power-law model, with best-fit parameters reported in Table 1. We did not attempt any spectral extraction for the counterjet, given the low number of counts. In addition to the previous jet analysis, we extracted spectra from different rectangular regions along the jet, to search for possible spectral variations. The data, however, did not reveal any spectral variation between the various regions, within the uncertainties. The source PSR showed a power-law photon index of $\Gamma = 1.1 \pm 0.2$, which is compatible with that expected from young energetic pulsars surrounded by their wind nebulae (Gotthelf & Halpern 2008). A softer spectrum is obtained for the main jet and the PWN, with $\Gamma = 1.6 \pm 0.2$ and 1.9 ± 0.1, respectively. For the PWN, such a relatively soft spectrum is expected (see, e.g., Gotthelf 2004; and Fig. 8 in Li et al. 2008).

We also tentatively fitted a pure thermal emission model (vmekal model in xspec) to the jet spectrum (see, e.g., the adiabatic expansion scenario for the precessing jets of SS 433, Migliari et al. 2002). This model provides a good fit to the data, ($\tilde{\chi}^2 = 1.09/65$ d.o.f., similar to that obtained with the power-law model), with best fit parameters $N_{\rm H} = (0.8 \pm 0.2) \times 10^{22}$ cm^{-2} and $kT = 11^{+17}_{-5}$ keV. Although line emission should be expected at such temperatures, in particular around 6−7 keV, the relatively low count statistics of the jet spectrum prevents us from probing the existence of such lines. Our fit results, therefore, cannot clearly distinguish between a pure thermal and a power-law model (a fit using both components provides a slightly worse $\tilde{\chi}^2$ and is unable to constrain neither the plasma temperature nor the value of $N_{\rm H}$). We note, however, that in a thermal scenario the plasma is expected to cool down on length-scales much shorter than the ∼11 pc displayed by the main jet, and, therefore, a continuous reheating of the emitting material would be required to explain the observed lack of spectral changes along the jet. In addition, pulsar jets are supposed to have a magnetohydrodynamical origin (see, e.g., Bogovalov & Tsinganos 1999), and therefore a power-law component from synchrotron emission should in any case be expected (see, e.g., Pavlov et al. 2003; Johnson & Wang 2010; De Luca et al. 2011; Hui et al. 2012). We conclude that the thermal model is disfavored with respect to the power-law model, and a synchrotron scenario is assumed in the following.

The jet feature and the counterjet together provide almost 1/3 of the total X-ray flux (∼2×10^{-12} erg cm^{-2} s^{-1}) of the Lighthouse nebula.

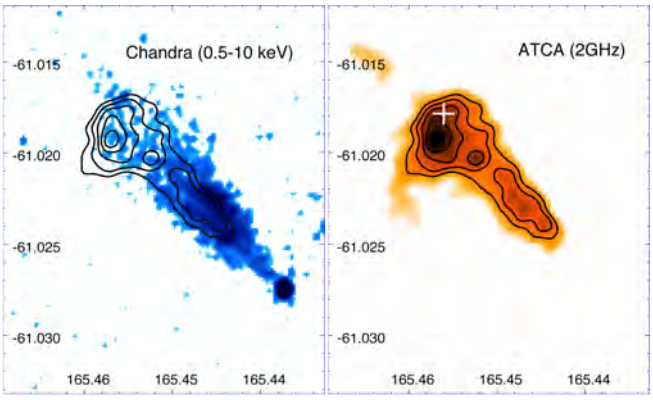

Fig. 3. *Chandra* (*left*) and ATCA 2GHz (*right*) images of the PWN. The ATCA contours are overplotted on both images. On the *right panel*, a cross marks the position of the radio source as reported in the MGPS-2 survey (see text for details).

2.2. ATCA radio observations

We observed the Lighthouse nebula region on January 11, 2013 and February 22, 2013 with ATCA (project C2651), using the new Compact Array Broadband Backend (CABB) receiver at array configurations of EW352 and 6A, and wavelengths of 20, 6, and 3 cm (ν = 2, 5.5 and 9 GHz), with bandwidths of 2 GHz. The observations were carried out in "change-frequency" mode, totaling ∼24 h of integration over the two observing periods. The sources PKS B1934-638 and PKS 1059-63 were used for primary and secondary (phase) calibration, respectively.

We used the miriad (Sault et al. 1995) and karma (Gooch 1996) software packages for reduction and analysis. Images were formed using miriad multifrequency synthesis (Sault et al. 1995) and natural weighting. They were deconvolved using the mfclean and restor algorithms with primary beam correction applied using the linmos task. We used a similar procedure for both U and Q Stokes parameter maps. Because of the good dynamic range (signal-to-noise ratio between the source flux and 3σ noise level), we applied self-calibration, which resulted in our best total intensity image (see Fig. 3). While our shortest baseline was 46 m (at EW352 array), we still suffered from the missing flux from the lack of short (zero) spacings. This effect was far more pronounced at the higher frequencies: at ν = 5.5 and 9 GHz, the observations were significantly affected by this "missing short spacing" and, therefore, were excluded from the analysis, which was then performed only in the 2 GHz band.

The candidate radio counterpart MGPS J110149-610104 (Paper I) was clearly detected in our 2 GHz image as an extended source (the image resolution is 5.177″× 4.146″ at PA = −8.5828° with an estimated rms noise of 0.15 mJy beam^{-1}). Its extension and position coincide well with the X-ray contours of the PWN (Fig. 3), the source extends up to 80″ from PSR (Fig. 4). Its total integrated flux density is 23 ± 2 mJy at 2 GHz. There was no reliable detection in the Q and U intensity parameters at any observed frequency that could be associated with this object. Without these detections, the Faraday rotation and consequently the magnetic field properties could not be determined.

The PSR and the jets were not detected in the 2 GHz image, providing an upper limit of 0.45 mJy beam^{-1} at a 3σ confidence level. For the jet, this translates into a total flux, integrated over the region used for the X-ray spectral extraction (a boxed region of size 228.6′ × 40.5′), lower than ∼4×10^{-15} erg cm^{-2} s^{-1}.

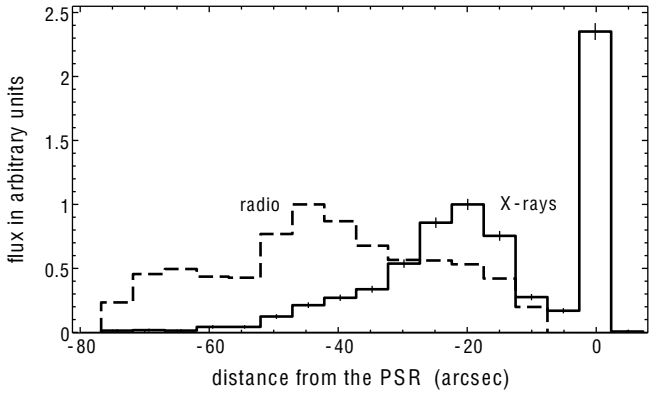

Fig. 4. Intensity profiles along the PWN, at 2 GHz (dashed line) and 0.5−10 keV (solid line), as a function of the distance from PSR. The radio and X-ray profiles peak at different positions, separated by 22″. This can be explained by the cooling of the emitting particles. The shape of the PWN at both wavebands and its alignment are in favor of a high pulsar velocity (>1000 km s^{-1}).

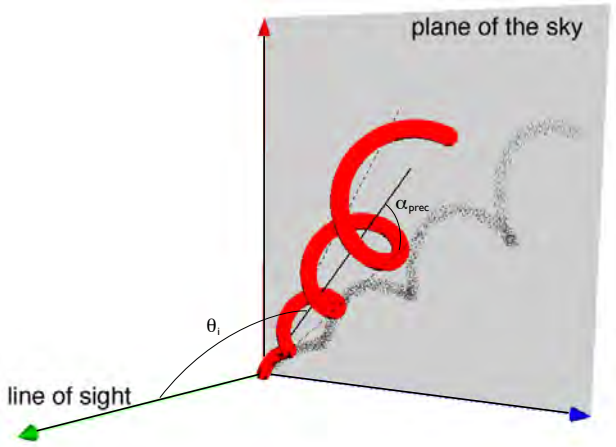

Fig. 5. Sketch of the precession model. The semi-aperture angle of the precession cone is marked as α_{prec}. The angle between the jet axis and the line of sight θ_i is also shown. The projection of the 3D helix on the plane of the sky (shown here in grey) is used to fit the *Chandra* image after being corrected for the Doppler factors of each particle.

2.3. Simplified precession model

Our *Chandra* observation shows the presence of a jet and a counterjet, both well collimated, with different brightness and elongation. This might be interpreted as due to the different orientation with respect to the line of sight under the assumption that the jet and counterjet are intrinsically identical in terms of luminosity and extension. The data also revealed a clear corkscrew modulation of the main jet, reminiscent of that seen in other galactic jets (see, e.g., Stirling et al. 2002; Durant et al. 2013), which can be interpreted either as precession of the neutron star or as kink instabilities in a ballistic jet (see in Sect. 3).

To further investigate this scenario, we used a simplified precession model, which describes the large-scale structure of the jet. We considered particles moving linearly away from the central position, each of them launched toward a direction lying on the precession cone surface (see Fig. 5). In the absence of any external effect, the interpolation of all particles forms a conical helix. We let the semi-aperture angle of the cone, the period of precession, the phase angle of the helix, and the velocity of the particles moving along the helix, as free parameters. In this model, all particles move at the same velocity, equal to the bulk velocity of the jet. The section of the helix has a 2D gaussian profile to simulate the degree of collimation of the jet. The width of this gaussian is another free parameter.

All of the model parameters are strongly dependent on the particles' velocity βc (where c is the speed of light), therefore, we kept this parameter frozen and performed simulations for different values of β. The velocity vector of each particle is used to determine the Doppler boosting factor of the emitted radiation $\delta = \gamma^{-1}\,(1 - \beta\cos\theta_i)^{-1}$ (where $\gamma = (1-\beta^2)^{-1/2}$ is the Lorentz factor of the particle and θ_i is the angle to the observer).

We fixed the position of the jet base in image coordinates to match the observed launching point of the jet. The 3D direction of the precession axis is constrained by the ratio $L_{\rm counterjet}/L_{\rm jet} \sim 0.05$ observed between jet and counterjet apparent luminosities. In this scenario, the $L_{\rm counterjet}/L_{\rm jet}$ ratio is due to the different orientation of the two jets, and to the relativistic beaming effects due to the bulk motion of the emitting particles. Following the same Doppler boosting prescription as above, at each bulk velocity β we find the corresponding angle between the jet axis and the line of sight θ_i needed to reproduce the observed ratio $L_{\rm counterjet}/L_{\rm jet}$. We then derive a lower limit for the velocity of the particles along the jet axis $v_{\rm jet,\parallel} \gtrsim 0.52\ c\ (\sin\theta_i)^{-1}$. The projection of the helix on the plane of the sky, corrected for the Doppler boosting factor of each particle, is then fit to the data with the Sherpa package (Freeman et al. 2001), using the Nelder-Mead Simplex optimization method with Cash statistics (see Fig. 6). We explored several values of the bulk velocity in the permitted range $\beta = v_{\rm jet,\parallel}/c \geq 0.52$.

After the 2D spatial fit is performed, we compare the brightness modulation observed in our *Chandra* data along the jet (see inset in Fig. 6) to the modulation obtained from the model, which is given by approaching/receding relativistic beaming effects, and therefore, provides three-dimensional information of the jet morphology.

The minimum bulk velocity $\beta = 0.52$, which corresponds to a face-on jet with $\theta_i = 0$, is excluded by the observed elongation of the jet and the presence of the counterjet in the *Chandra* data. The fit also provides a more stringent limit $\beta \gtrsim 0.7$, since an inclination angle $\theta_i \gtrsim 40°$ is required to match the jet morphology and the Doppler boosting effects on the brightness profile. Within this refined range, a value $\beta \sim 0.8$ is favored (see Fig. 6), resulting in a jet inclined by $\theta_i \sim 50°$ to the line of sight (with an intrinsic length of the main jet of ∼15 pc), a semi-aperture angle of the precessing cone of 4.5° and a precession period of nearly 66 yr. The relatively low signal to noise ratio of the image did not permit us to estimate the corresponding uncertainties.

3. Discussion

Besides the pulsar, the PWN, and the perpendicular jet-like feature described in earlier works, our *Chandra* observation has revealed the presence of a counterjet extending in the opposite direction from that of the main jet for about 1.5′. The *Chandra* data also showed for the first time that the long jet is highly collimated and displays a strikingly well-defined and continuous corkscrew modulation, with a length of ∼5.5′. The column density estimated in X-rays for the different components of the Lighthouse nebula ($N_{\rm H} = [0.8 \pm 0.2] \times 10^{22}$ cm^{-2}, see Table 1) is in good agreement with that found in various regions of the neighboring SNR MSH 11-61A ([0.4–0.7] × 10^{22} cm^{-2};

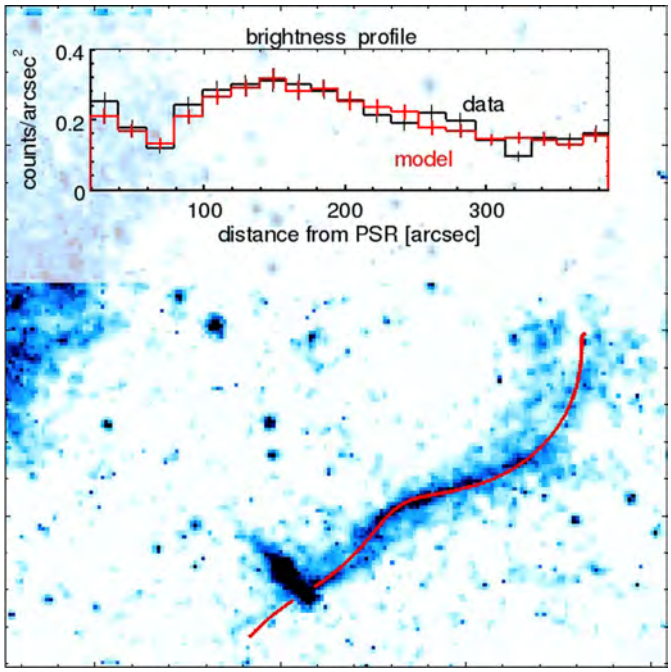

Fig. 6. Best-fit model of a precessing jet (solid red line) overplotted on top of the *Chandra* image of the Lighthouse nebula. The plot (and the inset) is relative to particles with bulk velocity $\beta = 0.8$ (see text for details). The *inset* shows the brightness profile measured along the jet (in black), and the brightness profile obtained from the model (in red in the online version).

García et al. 2012), proving the distance of the Lighthouse nebula to be ∼7 kpc (d_7).

The radio source MGPS J110149-610104, previously identified as a possible counterpart of the Lighthouse nebula (Paper I), is clearly detected in our ATCA observation. Its morphology closely matches the X-ray PWN (see Fig. 3). The flux density measured at 2 GHz (23 ± 2 mJy) is compatible with the flux density reported at 843 MHz in the MGPS-2 archive (24 ± 5 mJy; see Paper I). This indicates that the tail has a flat radio spectrum, i.e., with radio spectral index $\alpha \sim 0$, as typically observed in PWNe (Gaensler & Slane 2006). The neutron star and jet structures are not detected in radio (upper limit at 45 mJy beam^{-1}), which is a common feature amongst many high-energy emitting pulsars (Abdo et al. 2010) and pulsar jets (Dodson et al. 2003; Bietenholz et al. 2004). The source PSR in IGR J11014-6103 shows standard properties of rotation powered pulsars and their associated PWNe (Possenti et al. 2002; Gotthelf 2004; Li et al. 2008), in terms of X-ray luminosity, power-law photon index, and stability over at least 30 yr (Paper I), even if pulsations have not been detected so far (see Sect. 2.1.2; Paper I; T12). The similar luminosities inferred for the PSR and PWN are also in agreement with several observed PWN systems, and with the estimated system age of $1-2\times10^4$ yr (Li et al. 2008). Furthermore, the pulsar spin-down power $\dot{E}_{\rm PSR}$ can be inferred from the total observed X-ray luminosity of the system (see, e.g., Li et al. 2008), $L_{\rm X} \approx 1.2 \times 10^{34}\ d_7^2$ erg s^{-1}. This results in a rather high spin-down power $\dot{E}_{\rm PSR} \sim 10^{37}$ erg s^{-1} for the PSR in IGR J11014-6103, in agreement with the observation of a bright PWN (Gaensler & Slane 2006; Li et al. 2008). For a system with this spin-down power, the presence of the parent SNR should also be expected (Gaensler & Slane 2006).

The PWN in the Lighthouse nebula displays a clear symmetry axis that defines the direction of motion of the system, pointing toward the center of the nearby SNR MSH 11-61A (see Fig. 1). This alignment, together with the similar distance derived from our $N_{\rm H}$ measure, further support the proposed association between the two objects (T12), and imply a pulsar speed[1] $v_{\rm PSR} \sim (1100-2200)\ d_7$ km s^{-1}. This kick velocity makes IGR J11014-6103 one of the most extreme runaway pulsars known so far. Further support for this high velocity comes from the observed geometry of the PWN. Following the analytical description of bow-shock wind confinements proposed by Wilkin (2000), a velocity of $\gtrsim$1000 km s^{-1} is required to match the PWN morphology, where the following parameters were adopted: $\dot{E}_{\rm PSR} \sim 10^{37}$ erg s^{-1}, an external medium particle density of $n_{\rm ISM} = 0.1$ cm^{-3}, and an inclination $i = 0°$ of the velocity vector of the pulsar *(not the inclination of the jet axis)* with respect to the plane of the sky.

The observed shift between the X-ray and radio maxima ($\theta_{\rm peaks} \sim 22''$, see Fig. 3) can be used to estimate the PWN magnetic field. Taking a minimum PWN backflow velocity equal to the pulsar's speed $v_{\rm PSR} \approx 1000$ km s^{-1}, it takes a time $t_{\rm peaks} \sim \theta_{\rm peaks}\, d/v_{\rm PSR}$ for particles to travel from the X-ray peak to the radio peak (d is the distance to IGR J11014-6103). If the same particle population is responsible for the emission at both energies, the synchrotron loss timescale is constrained to be $t_{\rm peaks} \gtrsim t_{\rm sync}(E_{\rm e^-}, B_{\rm PWN}) \approx 422\, E_{\rm e^-}^{-1}\, B_{\rm PWN}^{-2}$ s, where $E_{\rm e^-}$ is the energy of the emitting electrons and $B_{\rm PWN}$ is the magnetic field in the nebula. Synchrotron emission at frequencies $h\nu_{\rm c} = 5$ keV requires, on the other hand, that $h\nu_{\rm 5keV} \approx 5.2\, B_{\rm PWN}\, E_{\rm e^-}^2$. Putting these constraints together, a minimum value $B_{\rm PWN} \approx 10-20\ \mu$G is required, in good agreement with known PWN magnetic fields (Gaensler & Slane 2006).

The PWN X-ray and radio spectra obtained in Sect. 2 imply the existence of a break frequency in between the two energy bands. Extrapolating the radio and X-ray power-law-like spectra, such a break should fall at $\nu_{\rm br} \sim 5 \times 10^{11}$ Hz. This break frequency could be used, in principle, to further constrain the emitting electron distribution and/or the PWN magnetic field. However, the spectral break $\Delta\alpha \sim 0.92$, is much larger than the expected value of 0.5 in a single-population synchrotron-emission scenario. A similar situation is observed in several PWN systems in which additional (still unclear) processes may need to be considered for an accurate derivation of the properties of the electron distribution and the nebular magnetic field (Gaensler & Slane 2006; see also Reynolds 2009).

The distance $d \approx 7$ kpc derived for the Lighthouse nebula implies an intrinsic length of the main jet $l_{\rm jet} \geq 11$ pc, making it the longest X-ray jet detected so far in our Galaxy (accounting for projection further increases this estimate by a factor $(\sin\theta)^{-1}$, where $\theta \in [0, \pi/2]$ is the jet angle to the line of sight, with a most likely value $\theta \sim 50°$, see Sect. 2.3). The observed precession-like helical modulation, similar to that seen, e.g., in other galactic jets (Stirling et al. 2002; Durant et al. 2013), promptly suggests a ballistic jet origin for this structure. The different X-ray brightness and elongation of the jet and counterjet can also be easily reconciled in this scenario, owing to their different orientation with respect to the observer. To further characterize the ballistic pulsar jet scenario, we used a simplified helical model describing the large-scale structure of the jet. The model describes the data well, both in terms of the spatial modulation and the jet brightness profile (see Fig. 6), thus confirming the three-dimensional helical structure and consequently the

[1] The velocity derived here for IGR J11014-6103 differs from the one reported in T12, as we adopted the refined distance of 7 kpc for SNR MSH 11-61A reported in García et al. (2012).

truly ballistic jet nature of the feature. An interpretation in a diffusion scenario of particles in the interstellar medium (Bandiera 2008) can be excluded, as it would require an underlying helical structure for the interstellar medium's magnetic field, which is instead known to be dominated by its turbulent component at scales below ∼100 pc (Gaensler et al. 2011; Giacinti et al. 2012).

The helical pattern seen along the jet could be explained either by free precession of the pulsar (with a period of ∼66 yr; see Sect. 2.3) or by the development of kink instabilities (see, e.g., Lyubarskii 1999). In this latter case, the period observed in the helical model would be associated with the timescale at which successive kinks appear. However, a low level of periodicity should be expected in this scenario, unless the instability is triggered by precession (Durant et al. 2013). Since our data reveal only approximately 1.5 helical steps along the main jet, such periodicity level in the trigger of the kink instabilities is difficult to assess. Periodic modulation has, on the other hand, been tentatively interpreted in some systems as free precession of the pulsar (see, e.g., Akgün et al. 2006; Jones 2012; Durant et al. 2013, and references therein), with periods up to several years (see, e.g. Weisberg et al. 2010). We note, however, that periods as long as several tens of years could hardly be detected in systems which do not show an extended jet, as in these systems the periodic modulation must be inferred by variations of the pulsar properties (e.g., spectral and timing properties, or of the linear polarization angle), based on monitoring of the source typically over timescales of a few years.

A free pulsar precession could be explained assuming a given value for the oblateness (ϵ) of the rotating neutron star (see e.g. Jones 2012), which can be estimated from the pulsar's spin and the precession period as $\epsilon = (I_3 - I_1)/I_1 = P_{\rm spin}/P_{\rm prec}$ (where I_1 and I_3 are principal moments of inertia; see, e.g., Haberl et al. 2006). For comparison with the values inferred for several likely precessing isolated pulsars, in the range $\epsilon \approx 10^{-4}$ to 10^{-10} (Jones & Andersson 2001; Jones 2012; Durant et al. 2013), we compute here the oblateness of IGR J11014-6103. A rough estimate for the spin period of PSR is obtained considering the pulsar age (10−20 kyr) and spin-down energy estimated above, $\dot{E}_{\rm PSR} \sim 10^{37}$ erg s^{-1}, which provides $P_{\rm spin}$ of the order of 0.1 s. A low value of the oblateness parameter is, therefore, obtained for the pulsar in the Lighthouse nebula, $\epsilon \sim 0.5 \times 10^{-10}$, which is close to values found in other cases (see above).

In our simulations, we did not consider any bending of the precessing axis, since it is not apparent in our *Chandra* images. The lack of bending implies that the curvature radius of the jet has to be large, $R_{\rm curv} \gtrsim l_{\rm jet}$. Since $R_{\rm curv} \propto \dot{E}_{\rm jet} R_{\rm jet}^{-2} \rho_{\rm ISM}^{-1} v_{\rm PSR}^{-2}$, where $\dot{E}_{\rm jet}$ is the jet power, $R_{\rm jet}$ its radius, and $\rho_{\rm ISM}$ is the medium mass density (see, e.g., Soker & Bisker 2006, and references therein), it follows that the jet has to be rather powerful and/or collimated. A high jet power is indeed supported by the relative distribution of the total X-ray luminosity of the system. The jet contribution is similar to that of the pulsar and the PWN, suggesting that a sizable fraction of $\dot{E}_{\rm PSR}$ is channeled through the jets.

The jet X-ray spectrum suggests a synchrotron origin for its emission (see Sect. 2), with a relatively hard photon index $\Gamma = 1.6$. Assuming that the radio and X-ray emission are produced by a single electron population, a straight extension of the X-ray spectrum would yield a flux $\sim 10^{-16}$ erg cm^{-2} s^{-1} at 2 GHz, for a bandwidth of 2 GHz. This estimate, being lower than the upper limit $\sim 4 \times 10^{-15}$ erg cm^{-2} s^{-1} obtained with ATCA at the same frequency, can naturally explain the radio nondetection of the jet.

The absence of breaks in the X-ray spectrum all along the jet implies that no significant cooling of the X-ray emitting electrons is taking place. We use the condition $h\nu_{\rm sync}/5$ keV $\equiv h\nu_{5\ {\rm keV}} \approx 5.2\, B_{\rm jet}\, E_{\rm e^-}^2$ again, require that the synchrotron timescale $t_{\rm sync}$ is at least equal to the time taken by electrons to travel up to the jet tip, $\sim l_{\rm jet}/v_{\rm jet}$, and thereby obtain a maximum value for the jet magnetic field $B_{\rm jet} \lesssim 65\, (h\nu_{\rm 5keV})^{-1/3}\, (l_{\rm jet}/15\ {\rm pc})^{-2/3}\, (v_{\rm jet}/0.8c)^{2/3}\ \mu$G. A further constraint on $B_{\rm jet}$ is derived from the requirement that electrons are confined within the jet so that their Larmor radius $r_{\rm L} \approx 1.75 \times 10^{25}\, E_{\rm e^-}\, B_{\rm jet}^{-1}$ cm is at most equal to $R_{\rm jet} \sim 2.3 \times 10^{17}\, d_7$ cm. Putting these constraints together, the jet magnetic field is found to be $B_{\rm jet} \sim 10{-}65\ \mu$G. Assuming instead near-equipartition between particles and magnetic fields (see, e.g., Pacholczyk 1970), we find $B_{\rm jet}^{\rm equip} \approx 15\ \mu$G, implying a minimum jet power $\dot{E}_{\rm jet}^{\rm equip} \approx 2 \times 10^{35}$ erg s^{-1}. This estimate does not account, however, for the presence of relativistic protons, if any, and/or thermal material in the jet, which would make the total jet kinetic luminosity higher, in line with the high relative contribution (nearly 1/3) of the jets to the total system's luminosity and with the absence of any noticeable jet bending.

Although jet-launching mechanisms in pulsars are not yet fully understood, they likely have a magneto-hydrodynamical origin (Komissarov & Lyubarsky 2004). The ultrarelativistic speed and the anisotropy of the pulsar wind (Bogovalov & Khangoulian 2002) suggest that the jets are formed by magnetic hoop stresses onto the wind material downstream of the termination shock (Lyubarsky 2002). This termination shock, for the same conditions of the external medium, is located much closer to the neutron star in a high-velocity pulsar as compared to slow-moving systems (Gaensler & Slane 2006). This could explain the relatively high jet power and collimation degree in the Lighthouse nebula, compared, e.g., to those from the Crab (Weisskopf et al. 2000) and Vela pulsars (Pavlov et al. 2003).

4. Concluding remarks

The Lighthouse nebula is the first case in which a jet from a hyperfast runaway pulsar can be clearly identified. The associated SNR MSH 11-61A is the remnant of a core-collapse explosion from a massive star (García et al. 2012). These types of supernovae are expected to produce in some cases neutron stars with natal kick velocities up to or exceeding 1000 km s^{-1} (Wang et al. 2007; Janka 2012). Simulations of core-collapse mechanisms however have difficulties in predicting orthogonal alignment between the pulsar spin-axis and the direction of motion for the highest-velocity systems, as observed in IGR J11014-6103 (Wang et al. 2007). Alternative models accounting for this misalignment have been suggested (see, e.g., Colpi & Wasserman 2002; Davies et al. 2002), but these require an extreme rotation of the iron core of the presupernova star, not commonly accepted to be achievable (Fryer & Warren 2004).

We remark that for the Guitar nebula (Hui et al. 2012), the pulsar's jet nature of the X-ray linear feature is not proven yet, and the originating SNR is not known so far. Nevertheless, if the feature will be confirmed as a true pulsar's jet, the supernova responsible for the system could already constitute the second example for such an unusual core-collapse episode, similar to the one originating the Lighthouse nebula.

Core-collapse supernovae are also expected to produce bipolar outflows during or right after the explosion (Davies et al. 2002; Paragi et al. 2010; Janka 2012). These events can, under certain circumstances, even lead to the formation of

long-duration gamma-ray bursts (Davies et al. 2002; Paragi et al. 2010; Soderberg et al. 2010). The SNR MSH 11-61A shows a clear bipolar asymmetry along the NW-SE direction (García et al. 2012), which could be the imprint of the past outflow activity during the supernova explosion (Paragi et al. 2010; Janka 2012). The high kick velocity of IGR J11014-6103 and the rough alignment of its jets with the direction of the bipolar asymmetries in SNR MSH 11-61A could then be the echoes of a quenched long-duration gamma-ray burst.

Acknowledgements. This paper is based on *Chandra* and ATCA observations. We thanks prof. D. Lai for useful discussion, and the *Chandra* Uplink Support team, in particular Dr. J. Connelly, for the support in preparing the observation. L.P. thanks the Société Académique de Genève and the Swiss Society for Astrophysics and Astronomy for travel grants sustaining the ongoing collaboration between the ISDC and the ATCA team.

References

Abdo, A. A., Ackermann, M., Ajello, M., et al. 2010, ApJS, 187, 460
Akgün, T., Link, B., & Wasserman, I. 2006, MNRAS, 365, 653
Arnaud, K., A. 1996, in ASP Conf. Ser. 101, eds. G. Jacoby, & J. Barnes, 17
Bandiera, R. 2008, A&A, 490, L3
Bietenholz, M. F., Hester, J. J., Frail, D. A., & Bartel, N. 2004, ApJ, 615, 794
Bogovalov, S. V., & Khangoulian, D. V. 2002, MNRAS, 336, L53
Bogovalov, S., & Tsinganos, K. 1999, MNRAS, 305, 211
Carter, C., Karovska, M., Jerius, D., Glotfelty, K., & Beikman, S. 2003, in Astronomical Data Analysis Software and Systems XII, eds. H. E. Payne, R. I. Jedrzejewski, & R. N. Hook, ASP Conf. Ser., 295, 477
Colpi, M., & Wasserman, I. 2002, ApJ, 581, 1271
Cordes, J. M., Romani, R. W., & Lundgren, S. C. 1993, Nature, 362, 133
Davies, M. B., King, A., Rosswog, S., & Wynn, G. 2002, ApJ, 579, L63
Davis, J. E., Bautz, M. W., Dewey, D., et al. 2012, in Proc. SPIE, 8443, 1A
De Luca, A., Marelli, M., Mignani, R., et al. 2011, ApJ, 733, 104
De Luca, A., Mignani, R. P., Marelli, M., et al. 2013, ApJ, 765, L19
Dodson, R., Lewis, D., McConnell, D., & Deshpande, A. A. 2003, MNRAS, 343, 116
Durant, M., Kargaltsev, O., Pavlov, G. G., Kropotina, J., & Levenfish, K. 2013, ApJ, 763, 72
Freeman, P., Doe, S., & Siemiginowska, A. 2001, in Proc. SPIE 4477, eds. J.-L. Starck, & F. D. Murtagh, 76
Fruscione, A., McDowell, J. C., Allen, G. E., et al. 2006, in Proc. SPIE, 6270, 1V
Fryer, C. L., & Warren, M. S. 2004, ApJ, 601, 391
Gaensler, B., & Slane, P. 2006, ARA&A, 44, 17
Gaensler, B. M., Haverkorn, M., Burkhart, B., et al. 2011, Nature, 478, 214
García, F., Combi, J. A., Albacete-Colombo, J. F., et al. 2012, A&A, 546, A91
Giacinti, G., Kachelrieß, M., & Semikoz, D. V. 2012, Phys. Rev. Lett., 108, 1101
Gooch, R. 1996, in Astronomical Data Analysis Software and Systems V, eds. G. H. Jacoby, & J. Barnes, ASP Conf. Ser., 101, 80
Gotthelf, E. V. 2004, in Young Neutron Stars and Their Environments, eds. F. Camilo, & B. M. Gaensler, IAU Symp., 218, 225
Gotthelf, E. V., & Halpern, J. P. 2008, ApJ, 681, 515
Haberl, F., Turolla, R., de Vries, C. P., et al. 2006, A&A, 451, L17
Hui, C. Y., Huang, R. H. H., Trepl, L., et al. 2012, ApJ, 747, 74
Janka, H.-T. 2012, Ann. Rev. Nucl. Part. Sci., 62, 407
Johnson, S. P., & Wang, Q. D. 2010, MNRAS, 408, 1216
Johnston, S., Kramer, M., Karastergiou, A., et al. 2007, MNRAS, 381, 1625
Jones, D. I. 2012, MNRAS, 420, 2325
Jones, D. I., & Andersson, N. 2001, MNRAS, 324, 811
Kargaltsev, O., & Pavlov, G. G. 2008, AIP Conf. Proc., 983, 171
Komissarov, S. S., & Lyubarsky, Y. E. 2004, MNRAS, 349, 779
Lai, D., Chernoff, D. F., & Cordes, J. M. 2001, ApJ, 549, 1111
Li, X.-H., Lu, F.-J., & Li, Z. 2008, ApJ, 682, 1166
Lyubarskii, Y. E. 1999, MNRAS, 308, 1006
Lyubarsky, Y. E. 2002, MNRAS, 329, 34
Marelli, M., De Luca, A., Salvetti, D., et al. 2013, ApJ, 765, 36
Migliari, S., Fender, R., & Méndez, M. 2002, Science, 297, 1673
Pacholczyk, A. G. 1970, Radio astrophysics. Nonthermal processes in galactic and extragalactic sources (San Francisco: Freeman)
Paragi, Z., Taylor, G. B., Kouveliotou, C., et al. 2010, Nature, 463, 516
Pavan, L., Bozzo, E., Pühlhofer, G., et al. 2011, A&A, 533, A74 (Paper I)
Pavlov, G. G., Teter, M. A., Kargaltsev, O., & Sanwal, D. 2003, ApJ, 591, 1157
Possenti, A., Cerutti, R., Colpi, M., & Mereghetti, S. 2002, A&A, 387, 993
Reynolds, S. P. 2009, ApJ, 703, 662
Reynoso, E. M., Johnston, S., Green, A. J., & Koribalski, B. S. 2006, MNRAS, 369, 416
Roberts, M. S. E. 2004, The Pulsar Wind Nebula Catalog (March 2005 version), McGill University, Montreal, Quebec, Canada, available at http://www.physics.mcgill.ca/~pulsar/pwncat.html
Sault, R., Teuben, P., & Wright, M. 1995, ASP Conf. Ser., 77, 433
Soderberg, A. M., Chakraborti, S., Pignata, G., et al. 2010, Nature, 463, 513
Soker, N., & Bisker, G. 2006, MNRAS, 369, 1115
Spruit, H., & Phinney, E. S. 1998, Nature, 393, 139
Stirling, A. M., Jowett, F. H., Spencer, R. E., et al. 2002, MNRAS, 337, 657
Tomsick, J. A., Bodaghee, A., Rodriguez, J., et al. 2012, ApJ, 750, L39 (T12)
Wang, C., Lai, D., & Han, J. L. 2007, ApJ, 656, 399
Weisberg, J. M., Everett, J. E., Cordess, J. M., Morgan, J. J., & Brisbin, D. G. 2010, ApJ, 721, 1044
Weisskopf, M. C., Hester, J., Tennat, A. F., et al. 2000, ApJ, 536, L81
Wilkin, F. P. 2000, ApJ, 532, 400

A.33 Related Paper 33

Pavan, L., Bordas, P., Pühlhofer, G., Filipović, M. D., De Horta, A., O'Brien, A., Crawford, E., Balbo, M., Walter, R., Bozzo, E., Ferrigno, C., and Stella, L. (2014b). The Puzzling Jet and Pulsar Wind Nebula of Igr J11014-6103. *International Journal of Modern Physics Conference Series*, 28:60172

My contribution was to assist in the data analysis. This is a 5% contribution.

High Energy Phenomena in Relativistic Outflows (HEPRO IV)
International Journal of Modern Physics: Conference Series
Vol. 28 (2014) 1460172 (7 pages)

DOI: 10.1142/S2010194514601720

THE PUZZLING JET AND PULSAR WIND NEBULA OF IGR J11014-6103*

LUCIA PAVAN

ISDC-Department of Astronomy, Université de Genève,
16 chemin d'Ecogia, Versoix, CH-1290, Switzerland
Lucia.Pavan@unige.ch

POL BORDAS† and GERD PÜHLHOFER‡

Institut für Astronomie und Astrophysik, Universität Tübingen,
Sand 1, Tübingen, D-72076, Germany
†*Pol.Bordas@unige.ch*
‡*Gerd.Puehlhofer@astro.uni-tuebingen.de*

MIROSLAV D. FILIPOVIC§, AIN DE HORTA¶, ANDREW O' BRIEN‖
and EVAN CRAWFORD**

Computational Astrophysics, Imaging & Simulation School of Computing & Mathematics,
University of Western Sydney, Locked Bag 1797
Penrith, NSW 2751, Australia
§*m.filipovic@uws.edu.au*
¶*A.DeHorta@uws.edu.au*
‖*andrew.obrien@uws.edu.au*
**E.Crawford@uws.edu.au*

MATTEO BALBO††, ROLAND WALTER‡‡, ENRICO BOZZO§§
and CARLO FERRIGNO¶¶

ISDC-Department of Astronomy, Université de Genève,
16 chemin d'Ecogia, Versoix, CH-1290, Switzerland
††*Matteo.Balbo@unige.ch*
‡‡*Roland.Walter@unige.ch*
§§*Enrico.Bozzo@unige.ch*
¶¶*Carlo.Ferrigno@unige.ch*

LUIGI STELLA

INAF — Osservatorio astronomico di Roma, via di Frascati 33,
Monte Porzio Catone, 00040, Italy
luigi.stella@oa-roma.inaf.it

Received 31 October 2013
Revised 2 December 2013
Published 21 March 2014

IGR J11014-6103 is a hard X-ray source discovered by INTEGRAL. Follow-up X-ray and radio observations revealed an elongated pulsar wind nebula formed by a neutron star escaping supersonically its parent supernova remnant SNR MSH 11-61A. The pulsar also emits highly collimated jets extending perpendicularly to the direction of motion. The jet has a continuous helical structure extending up to more than 10 parsecs. IGR J11014-6103 is a laboratory to study jet ejection in the wind of a pulsar and to constrain the core collapse supernova mechanism responsible for the observed pulsar kick velocity in excess of 1000 km/s.

Keywords: Pulsar jets; pulsar wind nebulae; core collapse mechanisms; objects: individual: IGR J11014-6103, SNR MSH 11-61A.

PACS Numbers: 98.62.Nx, 97.60.Gb, 97.60.Bw, 98.38.Mz

1. Introduction

While the majority of astrophysical jets are produced by accretion-powered systems (e.g. microquasars and active galactic nuclei[1,2]), also isolated rotationally-powered pulsars can produce jets, as the well known cases of Crab and Vela pulsars demonstrate.[3,4] The most common outflow emission from pulsars is however in the form of pulsar wind nebulae (PWNe). Depending on properties both of the pulsar and of the surrounding medium, PWNe develop in a large variety of morphologies. The kick velocity received by the pulsar during the supernova explosion is one of the elements that strongly affect the properties of the PWN. Pulsar three-dimensional velocities are in the range from 60-1000 km/s, with the mean velocity being around 400 km/s.[5] PWNe formed by pulsars travelling at low velocities (e.g. 140 and 80 km/s for Crab and Vela respectively) are typically seen as extended cocoons, and can be in some cases accompanied by two collimated jets.[6,7] At odd with this, runaway pulsars that received a strong kick at birth, produce PWNe confined by the front bow-shock due to the supersonic movement of the pulsar through the interstellar medium. These PWNe have a cometary shape elongated backwards along the direction of motion, and no jets have been identified so far from these systems[7] (but see also the Guitar nebula[8]).

Deep statistical studies have proved that pulsar's spin axis (and hence jets, when present) are generally aligned with their proper motion,[9,3,4] a relation that have been explained by numerous theoretical models of supernovae asymmetric mechanisms.[10–12] Jets in runaway systems could therefore be either disrupted by the system motion or aligned with (and hidden by) the bow-shocked PWN,[7] making their detection difficult.

We present the results from our X-ray and radio observations of IGR J11014-6103, a hyper-fast pulsar which is accompanied in the X-rays by a bow-shock PWN and a prominent jet-like structure. The detailed data analysis

and extended discussion can be found in our publication Pavan *et al.* 2013 *arXiv 1309.6792*, to appear in A&A.

2. IGR J11014-6103

IGR J11014-6103 is a hard X-ray source detected with *INTEGRAL* satellite.[13] The source is located 11 arcmin south-west of the SNR MSH 11-61A, which has a distance[14] of 7 ± 1 kpc. The analysis of all available archival data on IGR J11014-6103 (Pavan *et al.* 2011, hereafter Paper I) and of a short subsequent *Chandra* observation (Tomsick *et al.* 2012, T12 in the following) showed that this source is a complex system that displays in the X-rays the presence of a point source, a 1.2 arcmin cometary tail and, nearly perpendicular to this, a prominent jet-like feature extending over more than 4 arcmin. While these studies already suggested a PWN scenario for the cometary tail in IGR J11014-6103, the jet-like feature remained so-far uninterpreted due to the poor statistics of the available data (Paper I, T12). In order to better investigate the nature of this source, we obtained dedicated high-resolution observations of IGR J11014-6103 in X-rays with *Chandra* (50ks, ACIS-I), and in radio band with the Australia Telescope Compact Array ATCA (two observations totaling together $\sim$24 hours of integration time).[15]

3. Results

All components of IGR J11014-6103 and a large portion of the nearby SNR MSH 11-61A are included in the ACIS field of view of our observation (see Fig. 1). The data have been analysed with `CIAO` package v. 4.5. Besides the pulsar, the PWN, and the perpendicular jet-like feature described above, our *Chandra* observation show the presence of a "counter-jet" extending in a direction opposite to that of the main jet for about 1.5 arcmin. The observation also revealed for the first time that the long jet is highly collimated and displays a strikingly well-defined corkscrew modulation over about 5.5 arcmin. We analysed back-ground subtracted spectra of all the components of IGR J11014-6103. All spectra could be well fit by a simple absorbed power-law model, providing power-law indexes $\Gamma_{PWN} = 1.92 \pm 0.14$, $\Gamma_{PSR} = 1.1 \pm 0.2$ and $\Gamma_{jet} = 1.6 \pm 0.2$. The column density towards IGR J11014-6103 was of $N_{\rm H} = [0.8 \pm 0.2] \times 10^{22}$ cm^{-2}. This value is in good agreement with that found towards the neighboring SNR MSH 11-61A[16] ($[0.4 - 0.7] \times 10^{22}$ cm^{-2}), proving the distance of IGR J11014-6103 to be similar to that of the SNR ($\sim$ 7 kpc). The physical elongation of the jet feature results then in 11 pc (without accounting for the inclination θ with respect to the line, which would increase the length by a factor $1/\sin(\theta)$), the largest X-ray jet detected so far in our Galaxy.

The ATCA observations were conducted simultaneously over the 20, 6 and 3 cm frequencies in "change-frequency" mode. The data were analysed with MIRIAD software. The lower frequencies had missing flux due the lack of short spacings, and were therefore not used in the subsequent analysis. In the 20 cm map we could clearly detect the extended emission from the PWN, whereas the pulsar and

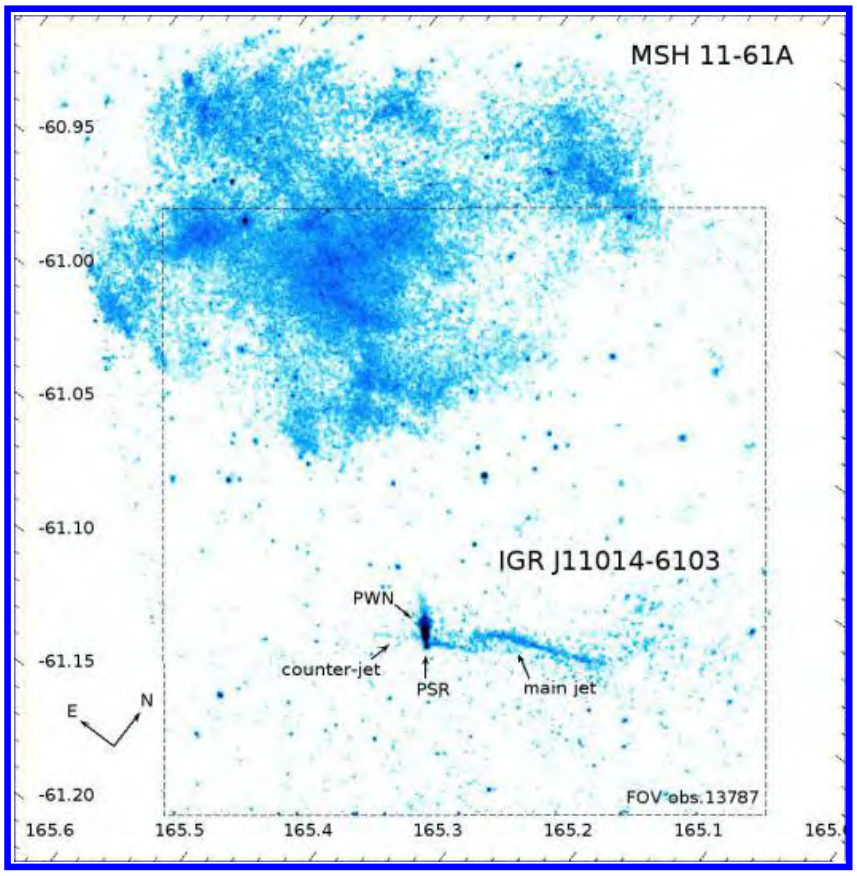

Fig. 1. IGR J11014-6103 as viewed by *Chandra* during our observation (obs.ID 13787). The image also includes archival observations of SNR MSH 11-61A. The two objects have likely been produced by the same supernova explosion 10 – 20 kyr ago. The image is adaptively smoothed and rotated by 37.5°.

the jet remained undetected, with an upper limit of 0.45 μJy/beam at 2 GHz (3σ confidence level). This translates into an upper limit for the total jet flux of 4×10^{-15} erg cm^{-2} s^{-1}, integrated over the region used for the X-ray spectral extraction. The expected radio synchrotron emission, as inferred from the X-ray jet spectrum, is lower than the derived upper limit. The non-detection can therefore be explained by the relatively low luminosity of the jet. The PWN flux density measured at 2 GHz (23 ± 2 mJy) is comparable to the one reported at 843 MHz in the MGPS-2 archive (24 ± 5 mJy, see Paper I), providing a spectral index $\alpha\sim0$, as typically observed in radio PWNe.[6]

The PSR in IGR J11014-6103 shows otherwise standard properties of rotation powered pulsars and their associated PWNe,[18,19] in terms of X-ray luminosity, power-law photon index and flux stability over at least 30 yr. The pulsar spin down power $\dot{E}_{\rm PSR}$ can be inferred from the total observed X-ray luminosity of the system[18] ($L_{\rm X}\approx1.2\times10^{34}$ erg s^{-1}), yielding for IGR J11014-6103 a rather high value $\dot{E}_{\rm PSR}\sim7.5\times10^{36}$ erg s^{-1}, in agreement with the observation of a bright PWN.[6] The alignment between SNR MSH 11-61A and IGR J11014-6103, and their similar distance, strengthen the proposed association between the two objects,[20] and imply a pulsar speed $v_{\rm psr}\sim(1100-2200)$ km/s. This kick velocity makes IGR J11014-6103

one of the most extreme run-away pulsars known so far. The spatial modulation observed along the jet, and the different jet/counter-jet brightness and elongation, suggest a truly pulsar's jet nature for the feature in IGR J11014-6103. Under this hypothesis the orientation with respect to the observer is responsible for the different appearance of the two jets, assumed to be intrinsically identical. The spatial modulation is reminiscent of that seen in other galactic jets[4,21] and could indicate either precession of the pulsar or kink instabilities.[4] Both these effects can produce an helical structure along the jet. To further investigate this scenario we used a simplified helical model to describe the large-scale structure of the jet and produced a bi-dimensional fit to the *Chandra* data. We also compared the brightness modulation observed along the jet, which in this scenario is given by approaching/receding relativistic beaming effects. The brightness and spatial modulations provide together a three-dimensional information of the jet morphology. The model describes well the data, both in terms of spatial modulation and of jet brightness profile (see Fig. 2), thus confirming the three-dimensional helical structure and consequently the truly pulsar's jet nature for the feature in IGR J11014-6103. In our simulations we did not consider any bending along the jet, since it is not apparent in our *Chandra* images. The lack of bending implies that the curvature radius of the jet has to be large, and consequently the jet has to be rather powerful and/or collimated (see Pavan *et al.* 2013 for details). A high jet power is indeed supported by the X-ray jet luminosity which contributes to nearly one third of the total X-ray luminosity

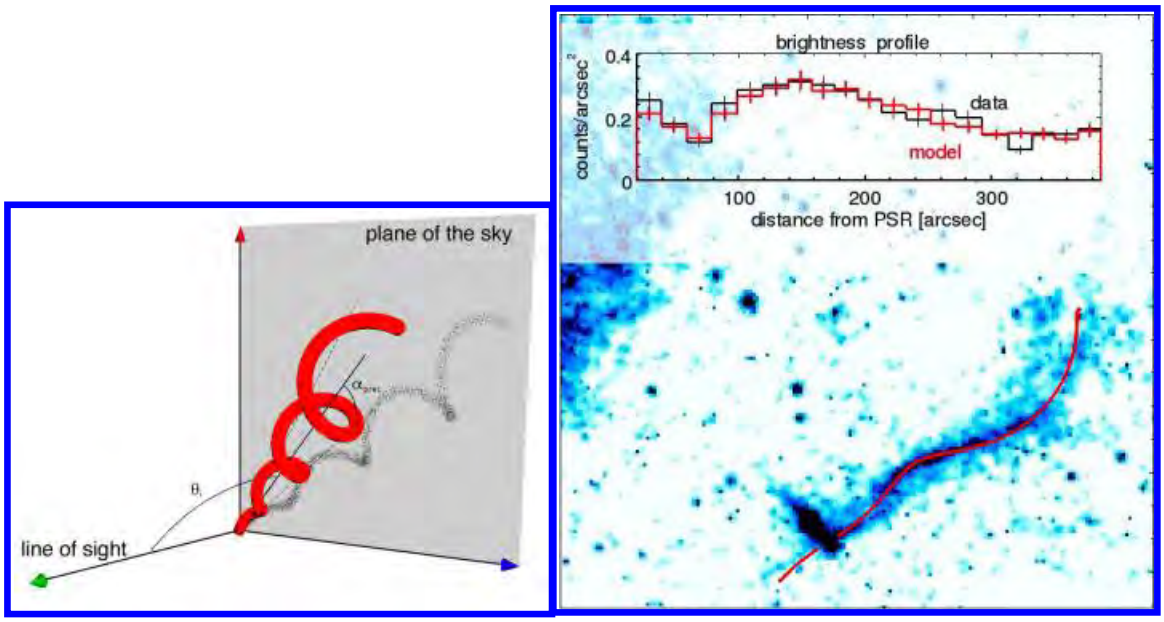

Fig. 2. *L*eft Panel: Sketch of the helical model used to describe the jet. *R*ight Panel: Best fit of the helical jet model (solid red line) overplot on top of the *Chandra* image of IGR J11014-6103. The plot (and the inset) is relative to particles with bulk velocity $\beta = 0.8$ (see Pavan *et al.* 2013 for details). The inset show the brightness profile measured along the jet (in black), and the one obtained from the model (in red).

of the system, suggesting that a sizable fraction of $\dot{E}_{\rm PSR}$ is channeled through the jets.

Although jet-launching mechanisms in pulsars are not yet fully understood, they likely have a magneto-hydrodynamical origin.[22] The ultra-relativistic speed and the anisotropy of the pulsar wind[23] suggest that the jets are formed by magnetic hoop stresses of the wind material downstream of the termination shock.[24] This termination shock, for the same conditions of the external medium, is located much closer to the neutron star in a high-velocity pulsar[6] as compared to slow-moving systems like the Crab[3] and Vela.[4] This could explain the high jet power and collimation degree seen in IGR J11014-6103.

The associated SNR MSH 11-61A is the remnant of a core-collapse explosion from a massive star.[16] Simulations of core-collapse mechanisms however have difficulties in predicting the formation of pulsars with kick velocity exceeding 1000 km/s ejected perpendicularly to their own spin axis,[25] as observed in IGR J11014-6103. Alternative models accounting simultaneously for the misalignment and high velocity have been suggested.[26,27] These models are based on an extreme rotation rate of the iron core of the massive pre-supernova star, ultimately causing its fragmentation. Numerical three-dimensional simulations showed nevertheless that such extreme rotation rates are hardly achieved by the massive stars,[28] disfavoring these core-collapse models. The question of which supernova mechanism could explain the properties of IGR J11014-6103 remains therefore still open.

Acknowledgments

This paper is based on *Chandra* and *ATCA* observations. We thanks D.Lai for useful discussion, and the Chandra Uplink Support team for the support in preparing the observation.

References

1. I. F. Mirabel and L. F. Rodríguez, *Nature* **371**, 46 (1994).
2. D. E. Harris and H. Krawczynski, *ARA&A* **44**, 463 (2006).
3. M. C. Weisskopf, *et al.*, *ApJ* **536**, L81 (2000).
4. M. Durant, *et al.*, *ApJ* **763**, 72 (2013).
5. G. Hobbs, *et al.*, *MNRAS* **360**, 974 (2005).
6. B. Gaensler and P. Slane, *ARA&A* **44**, 17 (2006).
7. O. Kargaltsev and G. G. Pavlov, *AIPC* **983**, 171 (2008).
8. C. Y. Hui, *et al.*, *ApJ* **747**, 74 (2012).
9. S. Johnston, *et al.*, *MNRAS* **381**, 1625 (2007).
10. H. Spruit and E. S. Phinney, *Nature* **393**, 139 (1998).
11. D. Lai, D. F. Chernoff and J. M. Cordes, *ApJ* **549**, 1111 (2001).
12. H.-T. Janka, *ARNPS* **62**, 407 (2012).
13. A. J. Bird, *et al.*, *ApJS* **186**, 1 (2010).
14. E. M. Reynoso, *et al.*, *MNRAS* **369**, 416 (2006).
15. L. Pavan, *et al.*, *arXiv-1309.6792* (2013), to appear in *A& A*.
16. F. García, *et al.*, *A&A* **546**, 91 (2012).

17. L. Pavan, *et al.*, *A&A* **533A**, 74 (2011).
18. A. Possenti, *et al.*, *A&A* **387**, 993 (2002).
19. E. V. Gotthelf, IAU Symposium, **218**, 225 (2004).
20. J. A. Tomsick, *et al.*, *ApJ* **750L**, 39 (2012).
21. A. M. Stirling, *et al.*, *MNRAS* **337**, 657 (2002).
22. S. S. Komissarov and Y. E. Lyubarsky, *MNRAS* **349**, 779 (2004).
23. S. V. Bogovalov and D. V. Khangoulian, *MNRAS* **336**, L53 (2002).
24. Y. E. Lyubarsky, *MNRAS* **329**, 34 (2002).
25. C. Wang, D. Lai and J. L. Han, *ApJ* **656**, 399 (2007).
26. M. Colpi and I. Wasserman, *ApJ* **581**, 1271 (2002).
27. M. B. Davies, *et al.*, *ApJ* **579**, L63 (2002).
28. C. L. Fryer and M. S. Warren, *ApJ* **601**, 391 (2004).

A.34 Related Paper 34

Bozzetto, L. M., Kavanagh, P. J., Maggi, P., Filipović, M. D., Stupar, M., Parker, Q. A., Reid, W. A., Sasaki, M., Haberl, F., Urošević, D., Dickel, J., Sturm, R., Williams, R., Ehle, M., Gruendl, R., Chu, Y.-H., Points, S., and Crawford, E. J. (2014b). Multifrequency study of a new Fe-rich supernova remnant in the Large Magellanic Cloud, MCSNR J0508-6902. *MNRAS*, 439:1110–1124

My contribution was to assist in the data analysis. This is a 5% contribution.

Monthly Notices
of the
ROYAL ASTRONOMICAL SOCIETY

MNRAS **439,** 1110–1124 (2014) doi:10.1093/mnras/stu051
Advance Access publication 2014 February 5

Multifrequency study of a new Fe-rich supernova remnant in the Large Magellanic Cloud, MCSNR J0508−6902

L. M. Bozzetto,[1⋆] P. J. Kavanagh,[2] P. Maggi,[3] M. D. Filipović,[1] M. Stupar,[4,5] Q. A. Parker,[4,5,6] W. A. Reid,[4,5] M. Sasaki,[2] F. Haberl,[3] D. Urošević,[7,8] J. Dickel,[9] R. Sturm,[3] R. Williams,[10] M. Ehle,[11] R. Gruendl,[12] Y.-H. Chu,[12] S. Points[13] and E. J. Crawford[1]

[1]*University of Western Sydney, Locked Bag 1797, Penrith South DC, NSW 1797, Australia*
[2]*Institut für Astronomie und Astrophysik Tübingen, Universität Tübingen, Sand 1, D-72076 Tübingen, Germany*
[3]*Max-Planck-Institut für extraterrestrische Physik, Giessenbachstraße, D-85748 Garching, Germany*
[4]*Department of Physics, Macquarie University, Sydney, NSW 2109, Australia*
[5]*Australian Astronomical Observatory, PO Box 296, Epping, NSW 1710, Australia*
[6]*Research Centre for Astronomy, Astrophysics and Astrophotonics, Macquarie University, Sydney, NSW 2109, Australia*
[7]*Department of Astronomy, Faculty of Mathematics, University of Belgrade, Studentski trg 16, 11000 Belgrade, Serbia*
[8]*Isaac Newton Institute of Chile, Yugoslavia Branch*
[9]*Physics and Astronomy Department, University of New Mexico, MSC 07-4220, Albuquerque, NM 87131, USA*
[10]*Coca-Cola Space Science Center, 701 Front Avenue, Columbus, GA 31901, USA*
[11]*XMM-Newton Science Operations Centre, ESAC, ESA, PO Box 78, E-28691 Villanueva de la Cañada, Madrid, Spain*
[12]*Department of Astronomy, University of Illinois, 1002 West Green Street, Urbana, IL 61801, USA*
[13]*Cerro Tololo Inter-American Observatory, Casilla 603, La Serena, Chile*

Accepted 2014 January 8. Received 2014 January 7; in original form 2013 July 21

ABSTRACT

We present a detailed radio, X-ray and optical study of a newly discovered Large Magellanic Cloud (LMC) supernova remnant (SNR) which we denote as MCSNR J0508−6902. Observations from the Australia Telescope Compact Array (ATCA) and the *XMM–Newton* X-ray observatory are complemented by deep Hα images and Anglo-Australian Telescope AAOmega spectroscopic data to study the SNR shell and its shock ionization. Archival data at other wavelengths are also examined. The remnant follows a filled-in shell-type morphology in the radio continuum and has a size of ∼74 pc × 57 pc at the LMC distance. The X-ray emission exhibits a faint soft shell morphology with Fe-rich gas in its interior – indicative of a Type Ia origin. The remnant appears to be mostly dissipated at higher radio-continuum frequencies leaving only the south-eastern limb fully detectable while in the optical it is the western side of the SNR shell that is clearly detected. The best-fitting temperature to the shell X-ray emission ($kT = 0.41^{+0.05}_{-0.06}$ keV) is consistent with other large LMC SNRs. We determined an O/Fe ratio of <21 and an Fe mass of 0.5–1.8 $M_\odot$ in the interior of the remnant, both of which are consistent with the Type Ia scenario. We find an equipartition magnetic field for the remnant of ∼28 μG, a value typical of older SNRs and consistent with other analyses which also infer an older remnant.

Key words: ISM: supernova remnants – Magellanic Clouds – radio continuum: ISM – X-rays: ISM.

1 INTRODUCTION

The study of supernova remnants (SNRs) is an imperative part in our understanding of the Universe, as they have a profound effect on their surrounding environment. SNRs distribute heavy elements throughout the galaxy, with thermonuclear (Type Ia) explosions contributing a significant amount of iron into the surrounding medium, whilst core-collapse (CC) supernovae (SNe) inject large amounts of oxygen and other α elements (Matteucci & Greggio 1986). Type Ia SNe are thought to arise when a C–O white dwarf (in a binary system) approaches the Chandrasekhar limit. This occurs either through accretion from the binary companion or by a merger with a white dwarf companion, and is currently actively debated (see

⋆ E-mail: luke.bozzetto@gmail.com

e.g. Maoz 2008 and references therein). CC SNe are believed to be the result of a progenitor star (with a main-sequence mass above 8 $M_{\odot}$) being drained of its nuclear fuel and therefore not being able to hold up against its own gravity through the release of nuclear energy.

The Large Magellanic Cloud (LMC) is an irregular dwarf galaxy located in close proximity (50 kpc; di Benedetto 2008) to our own Galaxy, allowing modern instruments to reach high sensitivity levels with sufficient angular resolution, from radio to X-ray wavelengths. At this distance, and because of its moderate inclination angle of 35° (van der Marel & Cioni 2001), we are able to assume that objects which lie within it are all at a similar distance. This allows us to analyse the surface brightness and spatial extent of an object accurately, which is often difficult in our own Galaxy due to uncertainties in distance, foreground absorption and background confusion. Furthermore, the LMC is considered an almost ideal environment for the study of a wide range of celestial objects due to the presence of active star-forming regions and its location outside of the Galactic plane, where absorption by gas and dust is reasonably low.

Several multiwavelength SNR selection criteria exist in the literature (e.g. Fesen, Blair & Kirshner 1985) as well as the powerful, newly evaluated emission-line diagnostic criteria reported by Frew & Parker (2010) and updated in Sabin et al. (2013). These are based on the well-known Sabbadin, Minello & Bianchini (1977) Hα/[N II] versus Hα/[S II] diagnostic diagram and the Baldwin, Phillips & Terlevich (1981) [O III]5007/Hβ versus [S II]/Hαdiagnostic diagrams. In this paper, we adopt the criteria used by the Magellanic Cloud Supernova Remnant (MCSNR) Database[1] which are effectively compatible with these publications. In this classification system, an SNR must satisfy at least two of the following three observational criteria: significant Hα, [S II]and/or [O III] optical line emission with an observed [S II]/Hα flux ratio of >0.4 (Mathewson & Clarke 1973), extended non-thermal radio emission indicative of synchrotron radiation (Filipovic et al. 1998) and extended thermal X-ray emission.

The *ROSAT* position sensitive proportional counter (PSPC) catalogue of X-ray sources in the LMC (Haberl & Pietsch 1999) contains the object [HP99] 791. While this source was confirmed as extended, its large off-axis angle prevented a reliable classification at that time. In this paper, we present new radio-continuum and X-ray observations of [HP99] 791, from the Australia Telescope Compact Array (ATCA) and *XMM–Newton*, respectively. We also present for the first time the clear identification of an unambiguous complete optical shell for the remnant from a deep arcsecond-resolution Hα image, a multi-exposure stack of the central 25 square degrees of the LMC (Reid & Parker 2006a). The shell can also be seen at lower resolution in the Magellanic Cloud Emission Line Survey (MCELS) data. Finally, we present new optical spectra from several components on the enhanced western side of the optical shell taken by the AAOmega spectrograph on the Anglo-Australian Telescope (AAT; Saunders et al. 2004; Sharp et al. 2006) which confirm a strong signature of shock excitation as expected for an SNR. This new discovery clearly satisfies all three criteria for identification as a bona fide SNR and so we assign to the source the identifier MCSNR J0508−6902 following the MCSNR Database nomenclature.

The observations used in this project are described in Section 2, followed by the data analysis in Section 3. The results from these observations are explained in Section 4 and then discussed in Section 5.

[1] See http://www.mcsnr.org/about.aspx. Database maintained by R. Williams et al.

2 OBSERVATIONS

2.1 Radio

The ATCA is a radio interferometer located in northern New South Wales, Australia. Its new 2 GHz bandwidth and improved sensitivity have made it possible to obtain observations of a previously poorly studied group of SNRs, the older and more evolved SNRs that were not detected so far. We observed MCSNR J0508−6902 on 2011 November 15 and 16 with the ATCA, using the new compact array broadband backend receiver in the array configuration EW367, at wavelengths of 3 and 6 cm (ν = 9000 and 5500 MHz). Baselines formed with the sixth ATCA antenna were omitted, as the other five antennas were arranged in a compact configuration. The observations were carried out in the so-called snap-shot mode, totalling ∼50 min of integration over a 14 h period. The source PKS B1934−638 was used for primary (flux) calibration and the source PKS B0530−727 was used for secondary (phase) calibration. The phase calibrator was observed for a period of 2 min every half hour during the observations.

In addition to our own observations, we made use of a 36 cm (843 MHz) Molonglo Observatory Synthesis Telescope (MOST) mosaic image (as described in Mills et al. 1984), a 20 cm (1400 MHz) mosaic image (Hughes et al. 2007) as well as 6 cm (4800 MHz) and 3 cm (8640 MHz) mosaic images from project C918 (Dickel et al. 2005).

2.2 X-ray

Haberl & Pietsch (1999) detected this source in their compilation of *ROSAT* PSPC observations, recording an X-ray position of RA(J2000) = $05^{h}\,08^{m}\,36\overset{s}{.}7$, Dec.(J2000) = $-69^{\circ}\,02'\,54''$, and an extent of $43\overset{''}{.}6$. It is listed as [HP99] 791. However, due to the large off-axis angle of the source, a classification was not possible.

We observed MCSNR J0508−6902 with *XMM–Newton* on two occasions: in 2010 May (Obs. ID 0651880201, PI: M. Sasaki), and, more recently, in 2012 September (Obs. ID 0690752001, PI: F. Haberl) as part of the LMC survey. The European Photon imaging Camera (EPIC) on board *XMM–Newton* (Jansen et al. 2001) consists of a pn CCD (Strüder et al. 2001) and two metal oxide semiconductor (MOS) CCD imaging spectrometers (Turner et al. 2001). The observational data were reduced using the standard reduction tasks of SAS[2] version 12.0.1, filtering for periods of high particle background. Unfortunately, Obs. ID 0651880201 was blighted by very high background, resulting in only ∼9 ks of the exposure being useful. However, in the case of Obs. ID 0690752001, there was virtually no background contamination with almost all data (∼25 ks) available for further analysis.

2.3 Optical: imaging and spectroscopy

We have used deep, arcsecond-resolution, narrow-band optical Hα images created from a median stack of a dozen 2 h exposures on the central 25 square degrees of the LMC as described in detail by Reid & Parker (2006a). These data have been used as the basis for unprecedented new discoveries of emission-line sources in general and planetary nebulae (PN) in particular across the central LMC (e.g. Reid & Parker 2006a,b, 2012). The survey filter, detector and other parameters are described by Parker et al. (2005) but in essence the LMC multiple exposures were taken with fine-grained Kodak Tech-Pan films on the UK Schmidt Telescope using

[2] Science Analysis Software, see http://xmm.esac.esa.int/sas/

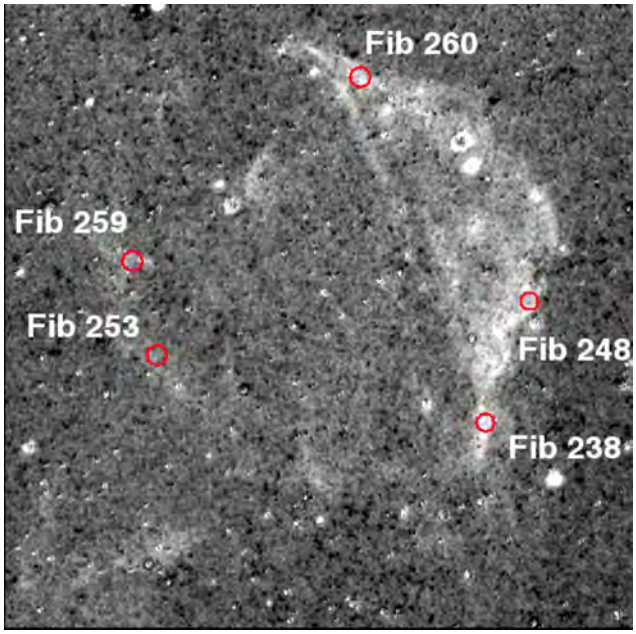

Figure 1. Hα quotient image of the new SNR MCSNR J0508−6902 taken from the data of Reid & Parker (2006a) revealing the complete optical oval shell for the first time but with enhanced emission on the western side. The positions of the 2dF fibres for the optical spectroscopy are indicated. The image is ∼6 arcmin × 6 arcmin on a side and north-east is to the top left.

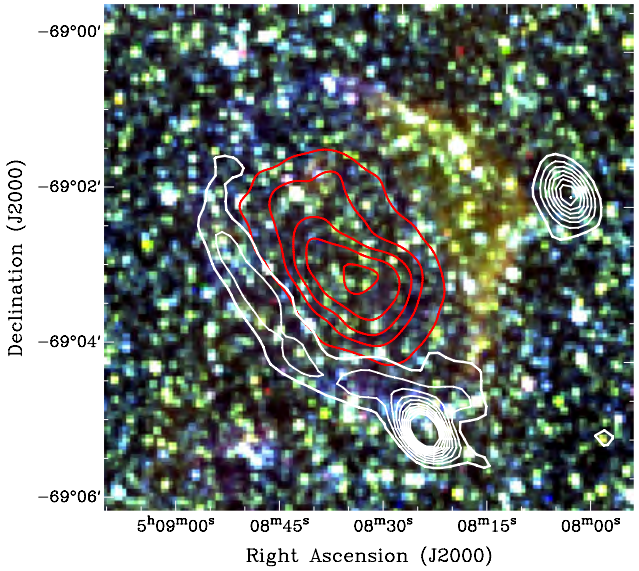

Figure 2. MCELS composite optical image (RGB = Hα,[S II],[O III]) of MCSNR J0508−6902 overlaid with *XMM–Newton* contours (0.7–1.1 keV; red) of 7, 14, 21, 28 and 35 × 10^{-6} counts s^{-1} and ATCA (5500 MHz; white) contours from 3σ to 30σ in steps of 3σ.

a monolithic interference filter of exceptional quality (e.g. Parker & Bland-Hawthorn 1998). These exposures were scanned with the SuperCOSMOS measuring machine (Hambly, Irwin & MacGillivray 2001), [included with an in-built accurate world coordinate system (WCS)] transformed into electronic form and then median stacked to reach depths of $R_{\rm equiv} \sim 22$ for Hα (4.5×10^{-17} erg cm^{-2} s^{-1} Å^{-1}). We extracted Hα and matching SR (short 'broad-band' red) fit images over a 6 arcmin × 6 arcmin area centred on the SNR with 10 μm (0.67 arcsec) pixels from the median-stacked images to create a quotient image (Hα divided by the SR), as shown in Fig. 1, reproduced to clip to the inner 98 per cent of intensity values. North-east is to the top left. A complete oval shell can be seen in Hα but with the western side being enhanced. The centroid of this oval shell and hence the best estimate for the optical centre of the remnant is RA(J2000) = $05^{\rm h}\,08^{\rm m}\,33\overset{\rm s}{.}7$ and Dec.(J2000) = $-69^\circ02'\,33''$. The major axis is 4.5 arcmin in extent and the minor axis only 4 arcmin. The positions of the two-degree field (2dF) spectral samples obtained are also indicated in the figure (see below for further details).

We also checked for detection of the SNR in the MCELS that was carried out with the 0.6 m University of Michigan/Cerro Tololo Inter-American Observatory (CTIO) Curtis Schmidt telescope, equipped with a SITE 2048 × 2048 CCD, which gave a field of $1\overset{\circ}{.}35$ at a scale of 2.3 arcsec $pixel^{-1}$ (∼5 arcsec resolution). Both the LMC and Small Magellanic Cloud (SMC) were mapped in narrow bands corresponding to Hα, [O III] (λ = 5007 Å) and [S II] (λ = 6716, 6731 Å). All the data have been flux calibrated and assembled into mosaic images, a small section of which is shown in Fig. 2. Further details regarding the MCELS are given by Smith, Points & Winkler (2006) and at http://www.ctio.noao.edu/mcels. The MCELS data also reveal the SNR though at the poorer angular resolution it is difficult to discern the full oval optical shell. However, MCELS does have the added advantage of the [O III] and [S II] filters providing additional diagnostic capabilities. The composite RGB image with (R = Hα, G = [S II] and B = [O III]) centred on the new SNR is shown in Fig. 2 with the *XMM–Newton* contours in red (0.7–1.1 keV) and ATCA 5500 MHz radio data contours in white. Interestingly, the strongest radio signature corresponds to the weakest optical emission to the south-east while the X-ray emission occupies the centre of the shell.

2.3.1 *AAT AAOmega spectroscopy*

As part of an AAOmega 2dF service night on the AAT on 2013 May 1, 2 × 900 s exposures were taken on an LMC 2dF centred at RA(J2000) = $05^{\rm h}\,13^{\rm m}\,15\overset{\rm s}{.}7$ and Dec.(J2000) = $-69^\circ29'\,51''$ for the LMC PN project of Reid and Parker (e.g. Reid & Parker 2006a,b, 2013). AAOmega is a powerful double-beam spectrograph (Sharp et al. 2006) that is coupled to the 2dF multi-object fibre spectroscopy system on the AAT (Lewis et al. 2002). Due to the 400 available 2dF fibres, it was possible to sacrifice five 2 arcsec diameter fibres to allocate to the new SNR candidate that happened to be in the field of view (FOV) of one of the Reid–Parker LMC PN fields. The individual SNR fibres were placed at carefully located positions on the western and eastern edges of the SNR shell as indicated in Fig. 1 with their accurate positions listed in Table 1.

Both the 580*V* and 1000*R* gratings were simultaneously employed for the general LMC PN spectroscopic observations with the 1000*R* red grating centred at 6850 Å and giving coverage from 6300 to 7425 Å. This is ideal for medium-resolution coverage of the diagnostic Hα, [N II] and [S II] nebular emission lines common to both PN and SNRs and also provides for more accurate radial velocity estimates. The lower resolution 580*V* blue grating was centred at 4800 Å giving coverage from 3700 to 5850Å. The blue data suffered from the effects of extinction and low signal-to-noise ratio (S/N) and were of limited use for the SNR observations.

The AAOmega data were reduced with the standard 2df data reduction (2DFDR) pipeline (e.g. Croom, Saunders & Heald 2004). Note that the optical fibres sample both target and superposed sky. Hence, it is standard practice to allocate a certain fraction of the 400 2dF fibres to blank sky. This is normally ∼20 fibres as was

Table 1. AAOmega fibre ID and fibre positions and line ratios for the spectral samples taken across the SNR as labelled in Fig. 1. All line intensities are relative, and extinction across the limited wavelength range of these emission lines is ignored. Errors in relative flux for observed lines are ∼10 per cent.

2dF fibre ID	RA (J2000) (^{h} ^{m} ^{s})	Dec. (J2000) (° ′ ″)	[S II]/Hα	Hα	[S II]6717	[S II]6731	[S II]6717/6731	Comments
Fib 238	05 08 16.2	−69 03 34	0.62	938	372	209	1.8	Low-density limit
Fib 248	05 08 13.0	−69 02 41	0.76	1241	638	301	2.2	Low-density limit
Fib 260	05 08 32.0	−69 00 46	0.99	1248	640	594	1.2	$N_e = 240$
Fib 253	05 08 50.8	−69 03 25	0.68	573	283	107	2.6	Low-density limit, low S/N
Fib 259	05 08 53.9	−69 02 33	1.29	363	242	226	1.1	$N_e = 395$ low S/N

the case for these observations. However, because the LMC field is of very high stellar density, it was important to carefully manually select decent and representative sky positions across the 2dF to avoid stellar or nebula contamination. An average of these sky spectra is then automatically subtracted from the individual target spectra as part of the 2DFDR data reduction process to provide the sky-subtracted spectra. The resultant 1D fibre spectra taken at the various points labelled in Fig. 1 are shown in Fig. 3. The measured line ratios are provided in Table 1. All line intensities are relative but the observed line ratios, because they are so close in wavelength, will not be affected by the lack of a proper flux calibration (difficult for fibres) and so extinction across the limited wavelength range of these emission lines can also be safely ignored.

It is a commonly adopted diagnostic (see Fesen et al. 1985) that an [S II]/Hα ratio >0.5 can separate SNRs from PN and H II regions as seen and expected in SNRs (e.g. Stupar & Parker 2012). It is clear from Table 1 that the observed [S II]/Hα ratio which ranges from 0.6 to 1.29 is strongly in the shocked regime for all fibres, particularly for 2dF fibres 260 and 259 which also happen to be on opposing sides of the optical shell. These ratios all fall well within the SNR domain following the updated diagnostic emission-line plots presented by Frew & Parker (2010). Furthermore, the observed [S II]6717/6731 Å line ratios also indicate that the electron density is close to or in the low-density limit as might be expected for such an evolved SNR. Nominal, unphysical, high values (>1.6) for the [S II]6717/6731 Å line ratios are observed in the lowest S/N spectra due to the associated larger measurement errors which are also indicated in Table 1.

The line intensities provided in Table 1 were measured using the IRAF *splot* package. Gaussian profiles were fitted to individual lines, providing the central wavelength, the integrated line flux/intensity, equivalent width and full width at half-maximum (FWHM). The IRAF *emsao* package (Mink & Wyatt 1995) was used to determine the radial velocities for each object as presented in Table 2, clearly showing that the object lies within the LMC. A small 2.5 km s^{-1} heliocentric velocity correction has been applied to the measurements. Errors in overall velocities are returned by *emsao* after it estimates weighted averages for all lines measured. These can be seen to increase as the S/N decreases, particularly affecting fibres 259 and 253, whose combined spectra are shown in Fig. 3.

3 DATA ANALYSIS

3.1 Radio

The MIRIAD (Sault, Teuben & Wright 1995) and KARMA (Gooch 1995) software packages were used for reduction and analysis. More information on the observing procedure and other sources observed in this session/project can be found in Bozzetto et al. (2012a,b,c, 2013) and de Horta et al. (2012).

Images were formed using MIRIAD multifrequency synthesis (Sault & Wieringa 1994) and natural weighting. They were deconvolved using the MFCLEAN and RESTOR algorithms with primary beam correction applied using the *linmos* task. The 6 cm (5500 MHz) ATCA image together with 20 cm (1337 MHz) and 36 cm (843 MHz) mosaic images of MCSNR J0508−6902 is shown in Fig. 4. The resolution of the 6 cm image is 37.7 arcsec × 25.1 arcsec.

3.2 X-rays

3.2.1 Imaging

We extracted images and exposure maps in three energy bands suited to the analysis of SNRs, whose X-ray emission is mostly thermal: a soft band (0.3–0.7 keV) including strong lines from oxygen; a medium band (0.7–1.1 keV), which includes Fe L-shell lines, as well as the Heα and Lyα lines of Neon; and a hard band (1.1–4.2 keV) comprising lines from Mg, Si, S, Ca, Ar and, if present, non-thermal continuum.

From the pn detector, we selected single- and double-pixel events (`PATTERN` = 0 to 4). Below 0.5 keV, only single-pixel events were selected to avoid the higher detector noise contribution from the double-pixel events. All single- to quadruple-pixel (`PATTERN` = 0 to 12) events from the MOS detectors were used. Bad pixels were masked. The detector background (see Section 3.2.3) was taken from filter wheel closed (FWC) data.[3] Before it was subtracted from the raw images, we scaled it by a factor estimated from the count rates in the corners of the detectors not exposed to the sky.

We merged MOS and pn data, and combined images from the two *XMM–Newton* observations. We then adaptively smoothed the images, computing Gaussian kernels at each position in order to reach an approximate S/N of 5. The minimum size for the kernels was set to an FWHM of 20 arcsec. Smoothed images were finally divided by the vignetted exposure maps.

Combining the final images, we show in Fig. 5 the *XMM–Newton* 'true-colour' image of MCSNR J0508−6902, which reveals a striking morphology. A bright central region, dominated by X-rays in the medium band, is surrounded by a fainter and softer shell. The brightness of the interior emission in the 0.7–1.1 keV band, which includes the Fe L-shell lines, suggests that MCSNR J0508−6902 falls into the class of SNRs with central Fe enhancements. Examples of these objects include 0548−70.4 and 0534−69.9 (Hendrick, Borkowski & Reynolds 2003), DEM L238 and DEM L249 (Borkowski, Hendrick & Reynolds 2006) and SNR 0104−72.3 (Lee et al. 2011; Roper et al., in preparation). Spectral differences between the central region and the shell are analysed in Section 4.3. There is little emission from the object above 1.1 keV. Several point sources are

[3] See http://xmm2.esac.esa.int/external/xmm_sw_cal/background/filter_closed/index.shtml

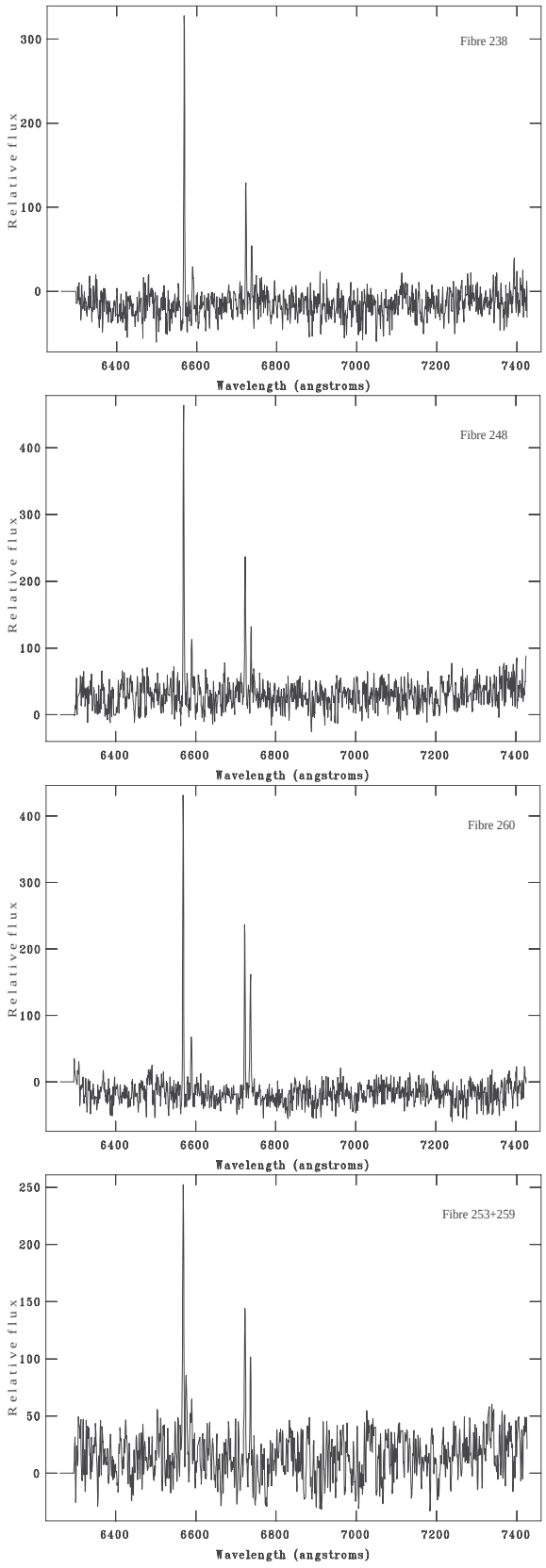

Figure 3. 1000*R* red grating 1D 2dF spectra for fibres 238, 248 and 260 taken on the enhanced western edge and a combined 1D spectrum from fibres 253 and 259 taken on the lower surface brightness eastern edge as indicated in Fig. 1.

Table 2. Heliocentric radial velocities estimated from the reduced 1D 1000*R* red individual AAOmega fibre spectra as provided by the IRAF *emsao* package.

2dF fibre ID	Radial velocity (km s^{-1})	Error (km s^{-1})	Comments
Fib 238	287.8	6.4	for 2/5 lines
Fib 248	323.0	14.4	for 5/5 lines
Fib 260	275.0	15.1	for 3/5 lines
Fib 253	263.5	13.7	for 3/6 lines
Fib 259	267.8	21.3	for 5/6 lines

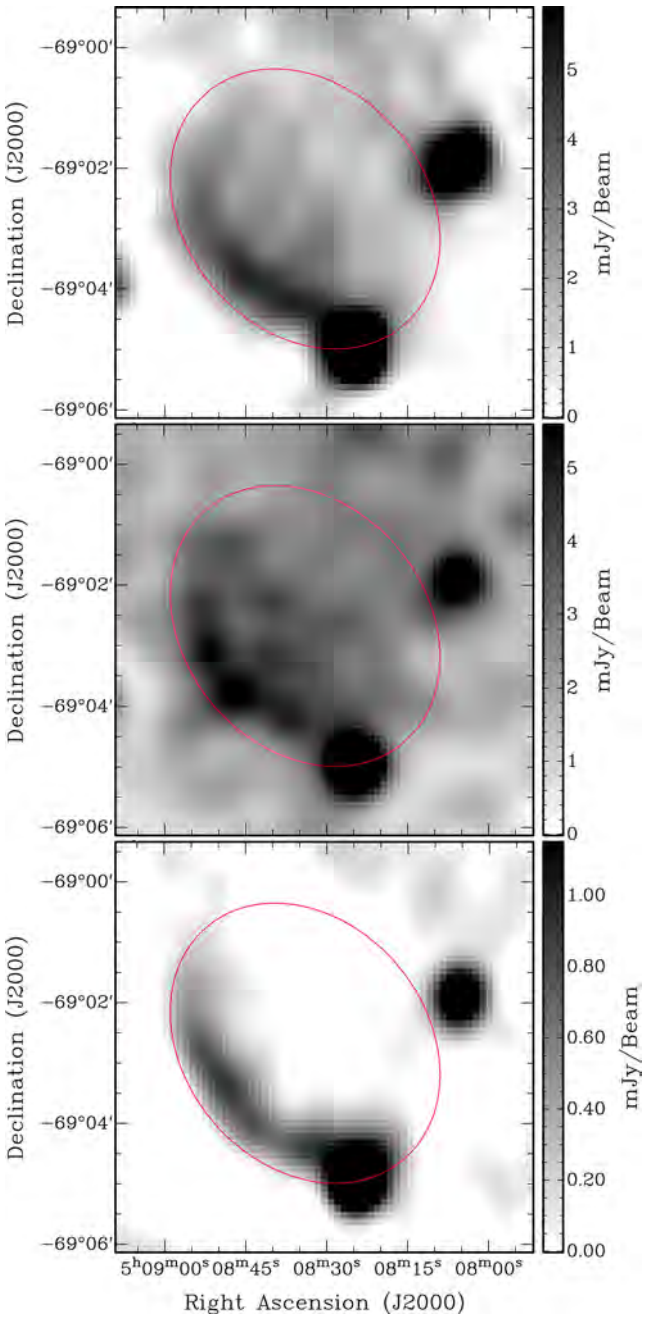

Figure 4. 843 MHz (top), 1400 MHz (middle) and 5500 MHz (bottom) radio-continuum images of MCSNR J0508−6902 with an overlaid ellipse indicating the approximate optical association for this SNR. The side bar quantifies the total intensity in mJy per beam).

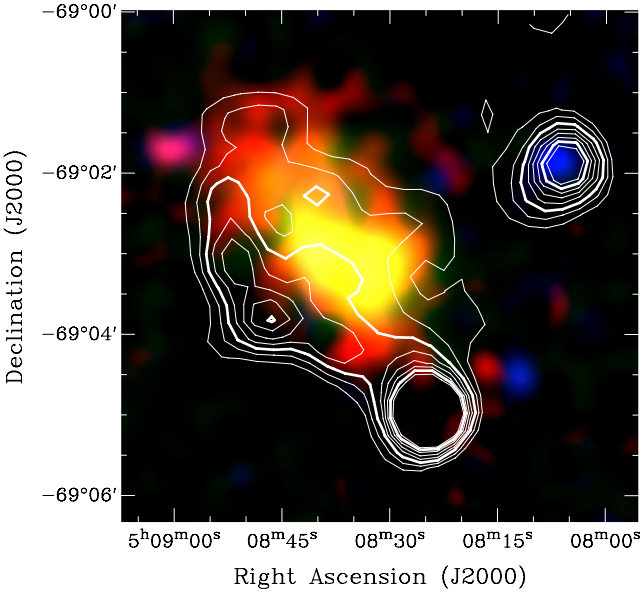

Figure 5. *XMM–Newton* three colour composite (red: 0.3–0.7 keV, green: 0.7–1.1 keV, blue: 1.1–4.2 keV) of MCSNR J0508−6902 smoothed with a Gaussian width of 20 arcsec, and overlaid with 1400 MHz radio contours. The contours are from 3σ to 6.5σ in steps of 0.5σ.

detected outside the boundary of the remnant, which are most likely background objects behind the LMC.

3.2.2 *X-ray spectral analysis*

We consider only Obs. ID 0690752001 for our spectral analysis. The ∼9 ks of data from Obs. ID 0651880201 can add little to our analysis, as e.g. the faint shell of the remnant is not detected in images from this observation only. Furthermore, using the diagnostic devised by De Luca, Molendi, & Leccardi (2004),[4] we found that the flare-filtered event lists were still heavily contaminated by soft protons (SPs).

In addition, only EPIC-pn spectra are considered as the SNR shell is extremely faint in the EPIC-MOS images. Before proceeding with the spectral extraction, we generated a vignetting-weighted event list to correct for the effective area variation across our extended source using the SAS task *evigweight*. Only single- and double-pixel events (PATTERN = 0 to 4) are considered. The extraction area of the central region was defined by enclosing the 0.7–1.1 keV band contours (see Fig. 2) with an ellipse (∼2.8 arcmin × 1.6 arcmin). The shell spectrum was extracted from an ∼5 arcmin diameter region (as determined in Section 4.2), excluding the central extraction region. Backgrounds should ideally be chosen from nearby positions on the detector. However, since the SNR was located close to on-axis and nearby suitable regions were comparatively source- and chip-gap heavy, this was not possible. As such, backgrounds were extracted from a source and diffuse emission-free region immediately to the north-west of the remnant, further off-axis than the source. This introduces important effects which must be considered in the spectral modelling of the particle-induced background, which is discussed in the forthcoming text. All spectra were rebinned using the FTOOL *grppha*[5] so that each bin contained a minimum of 30 counts. All fits were performed using XSPEC (Arnaud 1996) version 12.7.1 with abundance tables set to those of Wilms, Allen & McCray (2000), and photoelectric absorption cross-sections set to those of Balucinska-Church & McCammon (1992).

3.2.3 *X-ray background*

Spectral analysis of extended X-ray sources is complicated by the contributions of the X-ray background, comprising particle-induced and astrophysical components. Often, a subtraction of a nearby background region is inappropriate due to the spectral and/or spatial variation of these background components. While the consideration of the X-ray background for bright extended sources may not be so significant, in the case of faint emission (as is the case with the shell of MCSNR J0508−6902 in particular), the background must be carefully accounted for in order to extract the purest possible information from the source. A commonly used method (see Maggi et al. 2012 for a recent example) is to extract a nearby background spectrum, define a physical model for the background and simultaneously fit this model to the source and background spectra. We adopt this method for our analysis of MCSNR J0508−6902. A detailed description of our background treatment is given in Appendix A.

3.2.4 *MCSNR J0508−6902 emission*

Line-of-sight absorption to MCSNR J0508−6902 consists of a Galactic component ($N_{\rm H\,Gal}$, fixed at 7×10^{20} cm^{-2} as described in Appendix A3) and a foreground LMC component ($N_{\rm H\,LMC,fg}$). These were modelled using photoelectric absorption components with Galactic and LMC abundances, respectively.

Shell emission. We modelled the shell emission using various thermal plasma models appropriate for SNRs. We report here on the results using the standard Sedov model (Borkowski, Lyerly & Reynolds 2001), implemented in XSPEC as *vsedov*. Given the large size of the remnant, the assumption that it is in the Sedov phase is justified. The free parameters of the *vsedov* model are the mean shock temperature ($kT_{\rm s}$), post-shock electron temperature ($kT_{\rm e}$), metal abundances, ionization time-scale (τ_0, the electron density immediately behind the shock front multiplied by the age of the remnant). Due to the relatively poor count statistics, metal abundances for the model were fixed at the average LMC values (0.5 solar; Russell & Dopita 1992). In the case of MCSNR J0508−6902, fixing the metal abundances at 0.5 solar is quite reasonable as we expect the shell to be dominated by swept-up interstellar medium (ISM).

Interior emission. Fits of the central spectrum are complicated by the fact that we must consider both the interior Fe-rich gas and the emission from the shell overlapping this region. To account for the shell emission, we included a *vsedov* component in the fits to the central spectrum with the shell $kT_{\rm s}$ ($= kT_{\rm e}$) and τ_0 fixed to the best-fitting values determined from fits to the shell spectrum (see above). For the interior emission itself, we considered several thermal plasma models, which are discussed in detail in Section 4.3.2.

[4] See http://xmm2.esac.esa.int/external/xmm_sw_cal/background/epic_scripts.shtml

[5] See http://heasarc.nasa.gov/lheasoft/ftools/fhelp/grppha.txt

Table 3. Integrated flux densities of MCSNR J0508−6902 measured in this study.

λ (cm)	ν (MHz)	rms (mJy)	Beam size (arcsec)	$S_{\rm Total}$ (mJy)	$\Delta S_{\rm Total}$ (mJy)
20	1377	0.7	40.0 × 40.0	88	15
6	4800	1.0	35.0 × 35.0	41	10
36	843	0.4	46.4 × 43.0	59	6
20	1377	0.7	40.0 × 40.0	51	5
6	4800	–	33.0 × 33.0	19	2

The top two flux density measurements include a zero-spacing measurement, whereas the lower three measurements do not.

4 RESULTS

4.1 Radio

This remnant exhibits a filled-in shell morphology (at 20 cm) centred at RA(J2000) = $05^{\rm h}\,08^{\rm m}\,33\overset{\rm s}{.}7$ and Dec.(J2000) = $-69^\circ02'\,33''$. There are two unrelated background sources in the field, one in the south [RA(J2000) = $05^{\rm h}\,07^{\rm m}\,57\overset{\rm s}{.}7$, Dec.(J2000) = $-69^\circ03'\,59''.49$], and the other to the west [RA(J2000) = $05^{\rm h}\,08^{\rm m}\,06''.94$, Dec.(J2000) = $-69^\circ01'\,51''.2$] (Fig. 4). At lower radio frequencies in this study (843 and 1400 MHz), the emission of the SNR is fairly uniform across the remnant with significant limb brightening in the south-east. As we move to higher frequencies (≥5500 MHz), the remnant maintains this south-eastern limb but loses the shell emission of the remnant until we get to 9000 MHz, at which point all emission from the SNR is lost.

The large extent of MCSNR J0508−6902 made a spectral energy distribution (SED) estimate difficult, as observations using an interferometer suffer from missing zero-spacings (which are responsible for large-scale, extended emission), and therefore, missing flux. Because of this, we take two different sets of flux density measurements to estimate the SED. The first set of measurements came from mosaic images (20 cm from Hughes et al. 2007 and 6 cm from Dickel et al. 2010) which include a zero-spacing observation. The second set (which do not use a zero-spacing observation) include the two aforementioned mosaics before the zero-spacing (Parkes) observations were added, in addition to a 36 cm measurement from the MOST mosaic image (as described in Mills et al. 1984). The values of these flux density measurements are reported in Table 3, and then used to produce a spectral index graph (Fig. 6). The spectral indices for both the zero-spacing inclusive ($\alpha = -0.62 \pm 0.34$) and the non-inclusive ($\alpha = 0.69 \pm 0.12$) are quite similar. We note however that, as u–v coverage is a function of distance and frequency, the 6 cm measurement without the short spacing is missing more extended emission than those at lower frequencies. Therefore, we would expect a flatter spectral index than we see from these measurements (and potentially closer to what we see in the zero-spacing measurements).

There was no reliable detection in the Q or U intensity parameters associated with this object, implying a lack of polarization at higher radio frequencies (5500 and 9000 MHz). Without these detections, we were unable to determine the Faraday rotation and therefore cannot deduce the magnetic field strength. As an alternative however, we were able to estimate the magnetic field strength for this SNR based on the equipartition formula as given in Arbutina et al. (2012). This formula is based on the Bell (1978) diffuse shock acceleration theory. We use the spectral index which is inclusive of zero-spacing measurements ($\alpha = -0.62$) for this equipartition measurement. We find the average equipartition field over the whole shell of SNR MCSNR J0508−6902 to be ∼28 μG (this value is typical for the compressed interstellar magnetic field by the strong shock wave of an older SNR), and an estimated minimum SN explosion energy of $E_{\rm min} = 1.6 \times 10^{50}$ erg (see Arbutina et al. 2012, and corresponding calculator[6]).

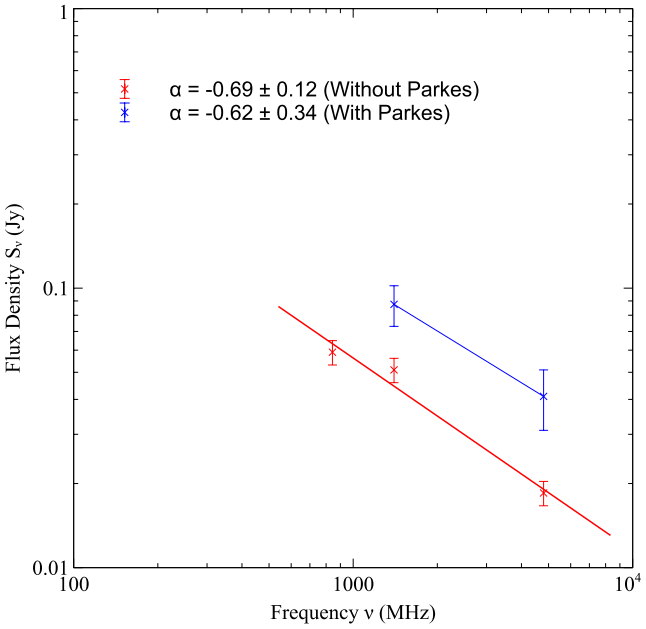

Figure 6. Radio-continuum spectrum of MCSNR J0508−6902.

From the position of MCSNR J0508−6902 at the surface brightness to diameter (Σ–D) diagram [(D, Σ) = (65.5 pc, 1.4×10^{-21} W m^{-2} Hz^{-1} sr^{-1})] by Berezhko & Völk (2004), we can estimate that MCSNR J0508−6902 is likely to be an older SNR probably in the transition phase between Sedov and radiative phases of evolution.

4.2 Multifrequency morphology

The morphology of the soft X-ray emission (0.3–0.7 keV) of MCSNR J0508−6902 is similar to that of the 20 cm radio-continuum emission (Fig. 5), filling out the shell of the remnant. X-ray emission in the medium band (0.7–1.1 keV) appears to be encased within the radio and optical emission, making the central location of this emission evident.

In the MCELS combined RGB Hα, [O III] and [S II] optical image, we can see an association between the [O III] emission and radio emission (Fig. 2) where the [O III] emission perfectly fits within the confines of the radio emission along the south-eastern limb of the remnant and then extending in the northern region to further complete the ellipse ring structure of the remnant. On the other hand, the Hα and [S II] emission located in the north-western regions of the remnant shows no association with the radio-continuum emission at any frequency, or with the X-ray emission (Fig. 2). The Hα and [S II] emission in the north-west is significantly stronger when compared to the faint [O III] emission. Strangely enough, they almost perfectly complement the [O III] emission in creating an ellipse ring morphology. This morphology is similar to that of LMC SNR J0453−6829 (Haberl et al. 2012).

Due to the higher resolution of Hα images from the deep Hα survey of the central 25 square degrees of the LMC by Reid &

[6] The calculator is available at http://poincare.matf.bg.ac.rs/ arbo/eqp/

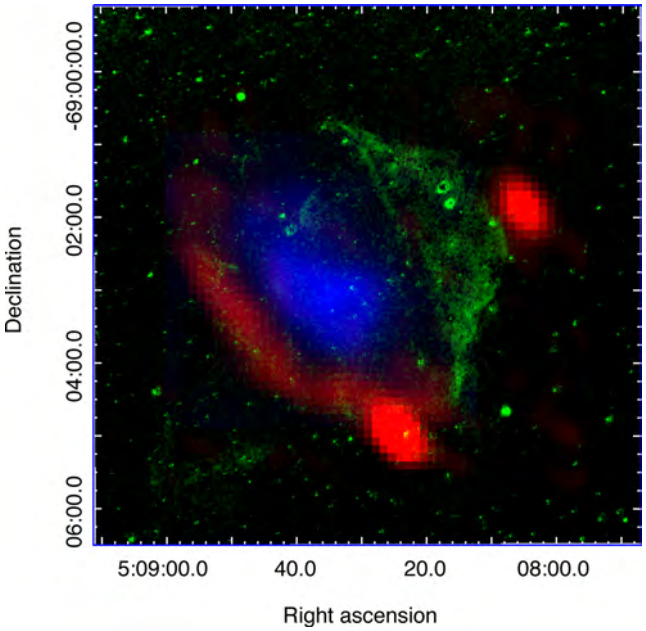

Figure 7. Radio (5500 MHz) (red), Optical (Hα) (green) and X-ray (0.7–1.1 keV) (blue) emission of MCSNR J0508−6902.

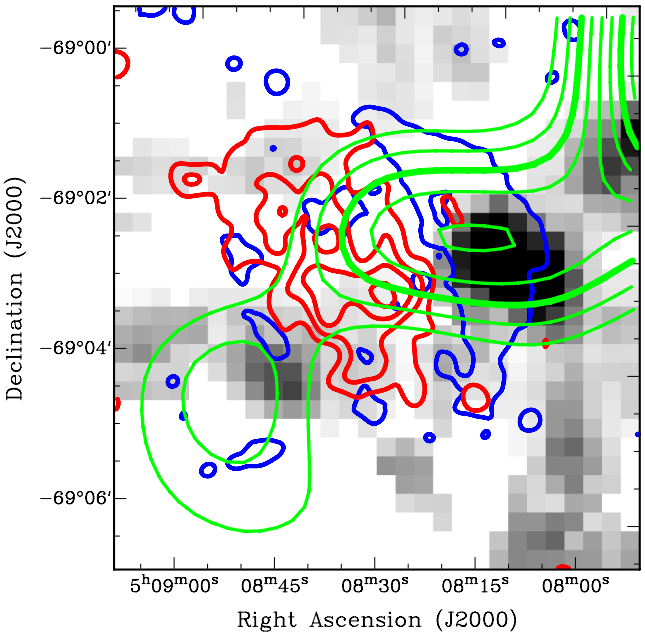

Figure 8. *XMM–Newton* (0.3–0.7 keV; red) and Hα (blue) contours of MCSNR J0508−6902 overlaid on NANTEN molecular cloud contours (green) and MAGMA molecular cloud grey-scale intensity image, showing the association between the denser environment and the emission from the remnant.

Parker (2006a) (Figs 1 and 7), we are able to see a complete optical shell which perfectly follows the radio emission in the south-east. The enhanced optical emission seen in this image towards the north-west suggests propagation of the shock front into the slightly higher density ISM, compared with somewhat lower density ISM on the south-east side. Separate fragmented Hα filaments inside the shell are common in optical observations (as well as in radio), as Hα emission is dominant where the blast propagates into dense, cooler regions.

X-ray, radio and optical images were combined to estimate the extent of this object. To do so, we created an annotation file which comprised of an ellipse that followed the outer emission from these combined images. We deduce an extent of 304 arcsec × 234 arcsec ± 4 arcsec (74 × 57 ± 1 pc), which places this remnant amongst the 20 per cent largest SNRs in the LMC (Badenes, Maoz & Draine 2010).

To gain an understanding of the environment in which the remnant resides, we use an image from the NANTEN molecular cloud survey by Kawamura et al. (2009), and another from the higher resolution Magellanic Mopra Assessment (MAGMA) survey by Wong et al. (2011). From these images (Fig. 8), it appears that the remnant is confined within the CO emission, elongated and stretching into the less dense region towards the north-east. However, this may be a projection effect as there is no reason to believe that the SNR is at the same distance as the molecular cloud. If it is though, perhaps the expansion could have been stopped by the cloud but some of it got broken up and ionized by the radiation from the explosion, giving rise to the asymmetry. MCSNR J0508−6902 was also found to be located at the rim of the supergiant H I shell SGS 5, identified by Kim et al. (1999). We recreated their H I channel maps of SGS 5 (their fig. 5e) at the position of MCSNR J0508−6902 using ATCA–Parkes 21 cm observations from the H I Magellanic Cloud Survey,[7] shown in Fig. 9. The ATCA and Parkes observations are outlined in Kim et al. (1998) and Kim et al. (2003), respectively.

[7] Available at http://www.atnf.csiro.au/research/HI/mc/

By definition, H I supergiant shells have radii that exceed the neutral gas scaleheight of the LMC (∼180 pc) and, thus, have blown out both sides of the disc, effectively creating a cylindrical wall of H I gas. Indeed, the molecular cloud shown in Fig. 8 is most likely located, and may have been formed in SGS 5 (Dawson et al. 2013). The extent of SGS 5 through the LMC disc increases the likelihood of an interaction with MCSNR J0508−6902 and can provide the density gradient required to explain the asymmetric optical and radio emission.

Because of the bright interior X-ray emission, this remnant could be suggested to be a member of the mixed-morphology SNR (MMSNR; Rho & Petre 1998; Lazendic & Slane 2006). These remnants show indications for interactions with molecular clouds and often show associated OH maser emission. These features led some authors to conclude to a CC origin for these type of SNRs (e.g. Miceli 2011). In the case of MCSNR J0508−6902, although there is some evidence of interaction with a molecular cloud, we clearly favour a Type Ia SN progenitor (see Section 4.3.2). We note that other Type Ia SNRs have been found in a molecular cloud/star forming environment (e.g. Lewis et al. 2003; Lee et al. 2011). In addition, overionized (i.e. recombining) plasmas have been found recently in several Galactic MMSNRs (Yamaguchi et al. 2009; Ohnishi et al. 2011; Yamauchi et al. 2013), while this feature is absent in the spectrum of MCSNR J0508−6902. Finally, we note that this classification has only been applied to Galactic remnants and not to the (usually Fe-rich) 'centrally peaked in X-rays' SNRs in the Magellanic Clouds (see Section 5 and references therein).

4.3 X-ray emission of MCSNR J0508−6902

4.3.1 Shell emission

As stated in Section 3.2.4, we modelled $N_{\rm H\,LMC,fg}$ using a photoelectric absorption model with LMC abundances. However, $N_{\rm H\,LMC,fg}$ consistently tended to zero, with upper 90 per cent confidence

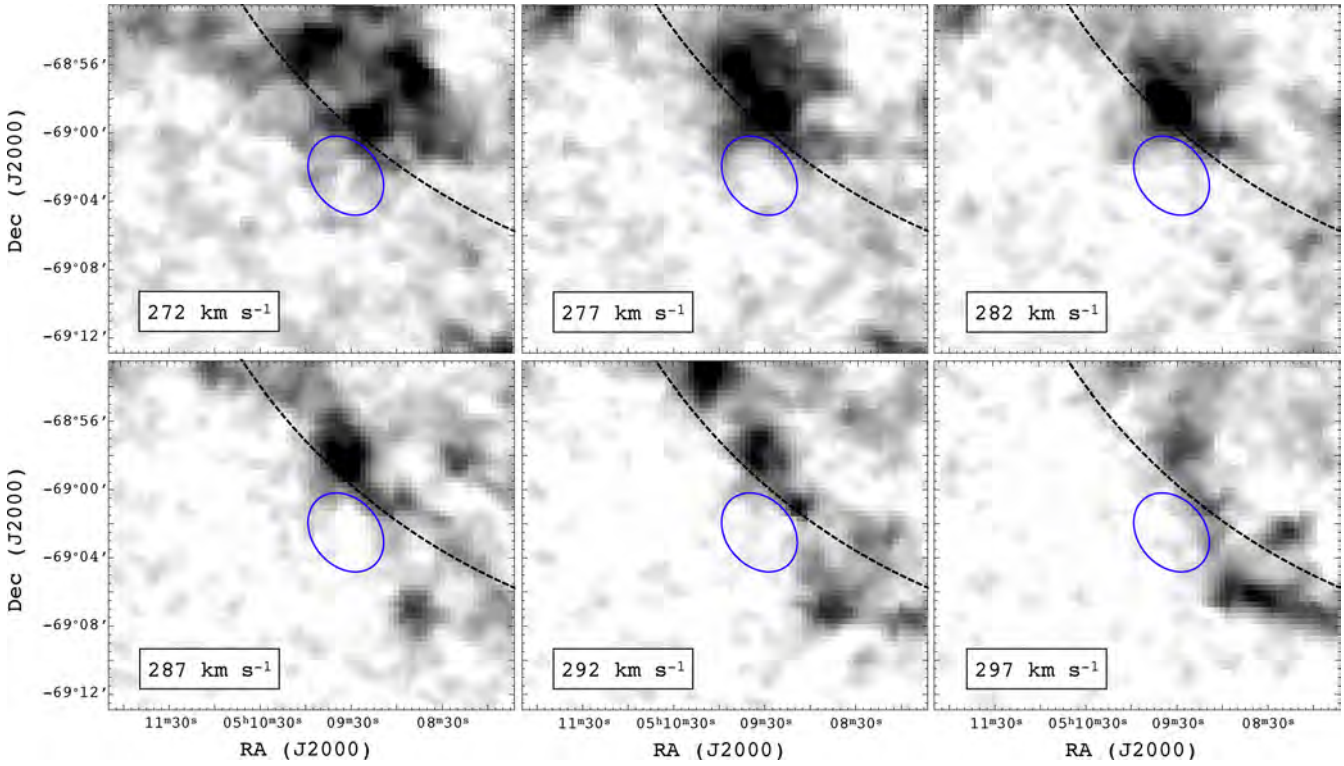

Figure 9. H I channel maps of SGS 5 in the region of MCSNR J0508−6902. The dimensions of the SNR are shown by the blue ellipses. The black dashed lines mark the approximate SGS 5 dimensions as determined by Kim et al. (1999). The heliocentric velocities are also indicated. A density gradient across MCSNR J0508−6902 due to SGS 5 is evident in each channel.

intervals for this parameter of $\sim 8 \times 10^{20}$ cm^{-2} for all fits. Thus, we fixed $N_{\mathrm{H\,LMC,fg}}$ at 0. Initial shell fits with the *vsedov* model resulted in best-fitting values for kT_{s} and kT_{e} to be equal within their 90 per cent confidence intervals and, thus, kT_{s} and kT_{e} were constrained to be the same. Indeed, we should expect that evolved SNRs are close to ion–electron temperature equilibrium (Borkowski et al. 2001).

The results of the spectral fits to the shell and central regions of MCSNR J0508−6902 are given in Table 4, with the spectra and best-fit models plotted in Fig. 10. The *vsedov* model provides an acceptable fit to the shell spectrum with a reduced χ^2 of 1.21. The best-fitting temperature to the shell emission of $kT_{\mathrm{s}} = kT_{\mathrm{e}} = 0.41(^{+0.05}_{-0.06})$ keV is consistent with other large LMC SNRs (see Williams et al. 2004; Grondin et al. 2012, for example), as well as DEM L238 and DEM L249 from Borkowski et al. (2006). The high value of τ_0 ($\sim 10^{12}$ s cm^{-3}) indicates that the plasma is in ionization equilibrium. From the shell component in the fits to the central spectra, we determined that 13–28 per cent of the *total* shell emission is contributing to the central spectrum. The absorption-corrected X-ray luminosity (L_{X}) of the shell in the 0.2–10 keV range was found to be $\sim 5 \times 10^{34}$ erg s^{-1}.

Using our fit results we can further estimate physical parameters of the SNR using the Sedov dynamical model (see Sasaki et al. 2004, for example). We know that MCSNR J0508−6902 is not spherically symmetric since the semi-major and semi-minor axes are 37 pc and 28.5 pc, respectively. Taking these semi-major and semi-minor axes as the first and second semi-principal axes of an ellipsoid describing MCSNR J0508−6902, and assuming that the third semi-principal axis is in the range 28.5–37 pc, we determined the volume (V) limits for the remnant and their corresponding effective radii (R_{eff}) to be $(3.7-4.8) \times 10^{60}$ cm^3 and 31.1–33.9 pc, respectively. In the following calculations, we evaluate the physical parameters of the remnant at these volume and effective radius limits, and determine the resulting range for each parameter.

Table 4. Results of the spectral fits. For the *vsedov* model, the post-shock mean temperature and post-shock electron temperature were set to be the same ($kT_{\mathrm{s}} = kT_{\mathrm{e}} = kT$) and the abundance is set to that of the LMC (0.5 solar). The EM and $L_{\mathrm{X,0.2-10\ keV}}$ values for the shell were calculated for the *total* shell (i.e. central and shell region). The ranges in parentheses represent the 90 per cent confidence intervals on the parameters.

Fit parameter/result	Value
Shell emission: *vsedov* model	
kT (keV)	0.41 (0.35–0.46)
τ (10^{12} s cm^{-3})	2.70 (1.73–6.92)
χ^2/ν	267.08/219
EM (10^{57} cm^{-3})	4.75 (2.54–7.22)
$L_{\mathrm{X,0.2-10\ keV}}$ (10^{34} erg s^{-1})	5.1
Interior emission: pure heavy-element *vapec* models	
$kT_{\mathrm{Fe,O}}$ (keV)	0.78 (0.75–0.81)
χ^2/ν	66.49/64
$n_{\mathrm{e}}n_{\mathrm{Fe}}V$ (10^{53} cm^{-3})	0.58 (0.54–0.61)
$n_{\mathrm{e}}n_{\mathrm{O}}V$ (10^{53} cm^{-3})	2.99 (0–9.96)
$L_{\mathrm{X,0.2-10\ keV}}$ (10^{34} erg s^{-1})	2.8

The X-ray temperature corresponds to a shock velocity

$$v_{\mathrm{s}} = \left(\frac{16kT_s}{3\mu}\right)^{0.5}, \quad (1)$$

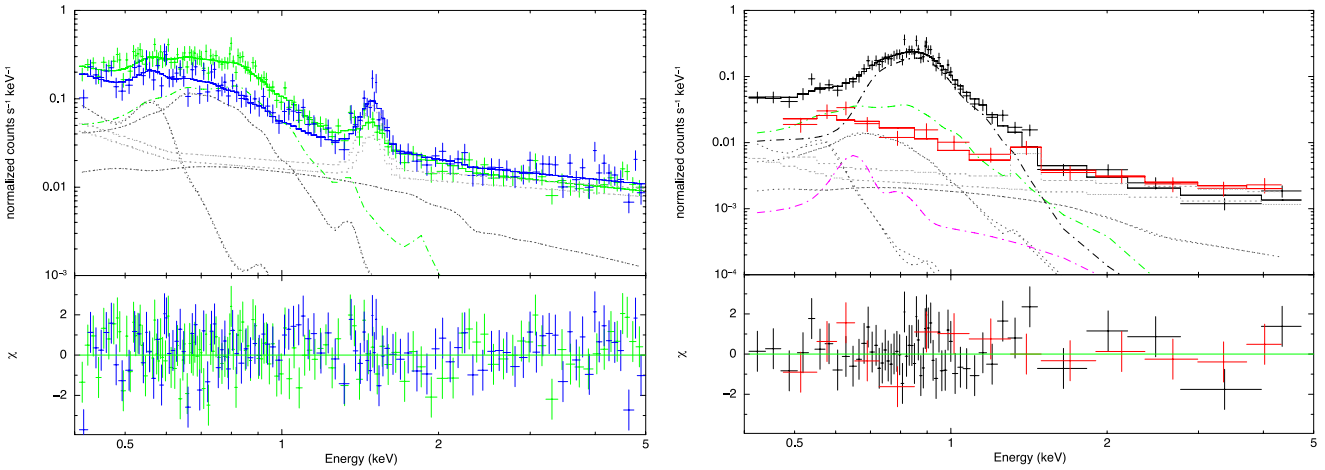

Figure 10. *XMM–Newton* spectral fits to MCSNR J0508−6902 shell (left) and central spectra (right) and associated backgrounds. The shell spectrum is shown in green, the shell background in blue, the central spectrum in black and the central background in red, with the best-fitting model to each represented by the solid lines of matching colour. The astrophysical background components are indicated by the dark grey dotted lines in each plot. The particle-induced background components are indicated by the light grey dotted lines. The green dash–dotted line in each spectrum represents emission from the shell. The black and magenta dash–dotted lines in the central spectrum show the pure Fe component and the pure O component, respectively.

where kT_s is the post-shock temperature and μ is the mean mass per free particle. For a fully ionized plasma with LMC abundances, $\mu = 0.61$, resulting in a shock velocity of $v_s = 572(\pm 36)$ km s^{-1}. The age of the remnant can now be determined from the similarity solution:

$$v_s = \frac{2R}{5t}, \tag{2}$$

where $R = R_{\rm eff}$ and t is the age of the remnant. This gives an age range of 20−25 kyr. The pre-shock H density ($n_{\rm H,0}$) in front of the blast wave can be determined from the emission measure (EM, see Table 4). Evaluating the emission integral over the Sedov solution using the approximation for the radial density distribution of Kahn (1975) gives

$$\int n_e n_H {\rm d}V = {\rm EM} = 2.07 \left(\frac{n_e}{n_H}\right) n_{\rm H,0}^2 V, \tag{3}$$

where n_e and n_H are electron and hydrogen densities, respectively, and V is the volume (e.g. Hamilton, Sarazin & Chevalier 1983). Taking $n_e/n_H = 1.21$ and the determined range of volumes, this equation yields $n_{\rm H,0} = (1.5{-}2.8) \times 10^{-2}$ cm^{-3}. Since the pre-shock density of nuclei is given as $n_0 \sim 1.1 n_{\rm H,0}$, it follows that $n_0 = (1.7{-}3.1) \times 10^{-2}$ cm^{-3}. Hence, the SNR is expanding into a fairly rarefied environment. The initial explosion energy (E_0) can be determined from the equation:

$$R = \left(\frac{2.02 E_0 t^2}{\mu_n n_0}\right)^{1/5}, \tag{4}$$

where μ_n is the mean mass per nucleus ($=1.4 m_p$). This results in an initial explosion energy in the range (0.37–0.75) $\times$ 10^{51} erg which is less than the canonical value of 10^{51} erg but consistent with several Type Ia SNRs in the LMC (see Hendrick et al. 2003, for example). The swept-up mass contained in the shell is given simply by $M = V \mu_n n_0$, which is evaluated to be (32–62) M$_\odot$. This large amount of swept-up material supports our original assumption that MCSNR J0508−6902 is into the Sedov phase of its evolution. All the derived parameters of MCSNR J0508−6902 are summarized in Table 5. Using the determined values of t and n_0, we estimated the expected ionization age for the remnant, given as $4.8 n_{\rm H,0} t$, to be in the range (5.3–9.2) $\times$ 10^{10} cm^{-3} s. This is significantly less than the ionization age determined from the spectral fits with the Sedov model. Given this inconsistency, it is likely that the Sedov model may not be strictly applicable to MCSNR J0508−6902. Several other remnants exhibit a similar discrepancy between measured and expected ionization time-scales. Hughes, Hayashi & Koyama (1998) and van der Heyden et al. (2003) observed this for candidate CC SNRs in the LMC and SMC, respectively. Hughes et al. (1998) suggest the explanation to be that the remnants initially expand into a low-density cavity in the ISM, likely due to the massive stellar wind. The remnant rapidly reaches the wall of the cavity where it meets the denser material, slows down and emits X-rays. This scenario represents a deviation from the standard Sedov model of a remnant expanding into a uniform ambient medium and can account for the discrepancy in the measured and expected ionization ages. The problem with this scenario as an explanation for MCSNR J0508−6902 is that a high-mass stellar wind is required to alter the ambient ISM in such a manner which is likely not the case for MCSNR J0508−6902. Borkowski et al. (2006) also observe such a discrepancy for DEM L238, a Type Ia remnant. They suggest that their derived ambient ISM density may be underestimated resulting in the ionization parameter discrepancy. The reason for the observed discrepancy in MCSNR J0508−6902 is unclear; however, it is most likely the case that it is due to some density variation in the ambient ISM causing a deviation from the standard Sedov picture. The optical and radio morphologies discussed in Section 4.2 suggest that MCSNR J0508−6902 is evolving into a denser medium in the west. The higher $n_{\rm H,0}$ value in the west of the remnant will result in an increased ionization age in the west as compared to the east. This may explain the observed ionization parameter discrepancy. However, in such a picture we would expect variation of the X-ray emission in this direction. Unfortunately, given the already

Table 5. Physical properties of MCSNR J0508−6902 derived from the Sedov model.

n_0 (10^{-2} cm^{-3})	v_s km s^{-1}	t (kyr)	M (M$_\odot$)	E_0 (10^{51} erg)
1.7–3.1	536–608	20–25	32–62	0.37–0.75

low count statistics, an analysis of spatio-spectral variation is not really feasible. In any case, because of the discrepancy between the measured and expected ionization parameters, the SNR properties derived from the Sedov dynamical model are somewhat uncertain.

4.3.2 Interior emission

We initially fitted the interior emission with a *vapec* model at LMC abundances. However, this resulted in a very poor fit (red. $\chi^2 > 2$) with large residuals at ∼0.9 keV due to the Fe L-shell emission lines. Thus, we freed the Fe abundance and re-performed the fit, resulting in a substantially improved fit with $kT = 0.76(0.73–0.79)$ keV, $Z_{\rm Fe} > 2.01\ Z/Z_{\odot}$ and red. $\chi^2 = 1.08$. The lower limit for the Fe abundance is approximately four times higher than the average LMC value, clearly indicating an overabundance of Fe in the central region, most likely due to Fe-rich ejecta being heated by the reverse shock. Allowing other metal abundances to vary (e.g. O) did not improve the fits and were very poorly constrained.

A more realistic model can be applied assuming that the interior gas consists of ejecta only. Hence, we applied thermal plasma models, representative of pure heavy-element plasmas (see Kosenko, Helder & Vink 2010, for example). We performed trial fits with collisional ionization equilibrium (CIE) models and non-equilibrium ionization (NEI) models representing the pure metal plasmas and found that, in both cases, an Fe plasma was required to fit the spectrum of the interior emission with a minimal pure O contribution. The CIE models provided acceptable fits to the spectra (reduced $\chi^2 \approx 1$). Similar quality fits were achieved with NEI models with the formal best-fitting ionization time-scales determined as $\sim 10^{13}$ s cm^{-3}, suggestive of a plasma in CIE. However, no constraints could be placed on these values. Given the quality of the trial fits with the CIE models, the interior plasma is suggested to be close to or in CIE. Hence, we model this emission using the *vapec* model in XSPEC. Initial fits showed that the temperature of the O component was not well constrained. Hence, as in Hughes et al. (2003), we simplified the model by assuming the O and Fe to be co-spatial and constrained their temperatures to be the same. This yielded a best-fitting $kT = 0.78^{+0.03}_{-0.03}$ keV. In our spectral fits, we found that Fe dominates the interior emission with O having little or no contribution to the spectrum. Indeed, the normalization of the O component was pegged at zero, demonstrating that it is formally not required. However, we keep the component in the spectral model as the upper limit to the O contribution can allow us to at least determine the maximal O/Fe ratio (see below). We reiterate that the interior plasma is likely in or close to CIE due to the quality of the *vapec* model fit (reduced $\chi^2 \approx 1$, see Table 4). The $L_{\rm X}$ of the interior gas in the 0.2–10 keV range was found to be $\sim 2.8 \times 10^{34}$ erg s^{-1}.

It is possible to identify the likely SN mechanism responsible for MCSNR J0508−6902 by assessing the O/Fe ratio of the interior region. From the SN nucleosynthesis yields of Iwamoto et al. (1999), the O/Fe ratio is expected to be 0.3–0.7 by number for Type Ia events and ∼70 for CC events. We estimated the maximum allowed O/Fe ratio for MCSNR J0508−6902 using a χ^2 contour plot produced for the Fe and O normalization parameters. This yielded a maximum ratio of <21 at the 90 per cent confidence level, slightly higher than the LMC value of 13.2 (Russell & Dopita 1992). We stress that this upper limit is based on the rather poorly constrained, formally not required O component in the spectral fits. However, it does rule out a CC scenario, indicating that MCSNR J0508−6902 likely resulted from a Type Ia explosion. Another diagnostic for the SN type is the mass of Fe produced. This can be estimated using equation 2 of Kosenko et al. (2010), adapted for Fe. We split this equation into terms which are easily determined from the fit results, given as

$$M_{\rm Fe} = (V_{\rm Fe} EM_{\rm Fe})^{0.5} (n_{\rm e}/n_{\rm Fe})^{-0.5} m_{\rm U} A_{\rm Fe}, \quad (5)$$

where $V_{\rm Fe}$ is the volume occupied by the Fe, $EM_{\rm Fe} = n_{\rm e} n_{\rm Fe} V$ is the EM of the Fe gas, $n_{\rm e}/n_{\rm Fe}$ is the electron-to-Fe-ion ratio, $m_{\rm U}$ is the atomic mass unit and $A_{\rm Fe}$ is the atomic mass of Fe. $V_{\rm Fe}$ is determined from the dimensions of the central region (1.4 arcmin × 0.8 arcmin) and assuming an ellipsoidal morphology with a third semi-axis equal to the mean of the semi-major and semi-minor axes (1.1 arcmin). If the actual morphology is oblate or prolate, the volume would be 13 per cent higher or lower, respectively. $EM_{\rm Fe}$ is obtained from the normalization of the Fe component and is listed in Table 4. We must estimate the $n_{\rm e}/n_{\rm Fe}$ ratio. As discussed in Hughes et al. (2003), there are two plausible scenarios for the number of electrons per Fe ion, depending on the level of admixture of H in the ejecta. If there is no H, then the number of free electrons per Fe ion only depends on the average ionization state of the each metal contributing electrons. We do not consider the contribution of electrons by the minimal O content of the interior region. For a plasma in CIE at $kT = 0.78$ keV ($\log T = 6.95$), the average ionization is 18.3 for Fe (Shull & van Steenberg 1982). Then, from equation (5), the Fe mass is in the range 1.6–1.8 $M_{\odot}$ for the pure heavy-element scenario. The second case proposed by Hughes et al. (2003) is that a similar mass of H is mixed into the metal-rich ejecta. Therefore, the number density of Fe over H is 1/56, and the average number of electrons per Fe ion is 74.3. Thus, from equation (5) we have an Fe mass range of 0.8–0.9 $M_{\odot}$ if there is a comparable mass of H to Fe in the ejecta. The former case gives a value somewhat too high for the explosion of a white dwarf, the latter value being typical of a Type Ia yield. However, the ejecta might be clumpy, with a filling factor of ∼0.4 (see Kosenko et al. 2010, and references therein), in which case the Fe content reduces by a factor of $\sqrt{0.4} \approx 0.63$ giving 1.0–1.1 and 0.5–0.6 $M_{\odot}$ for the pure Fe and Fe+H mixture cases, respectively. The large mass of Fe present in the interior further supports a Type Ia progenitor for MCSNR J0508−6902.

5 DISCUSSION

The X-ray emission from MCSNR J0508−6902 is notable due to the Fe-rich gas in the interior of the remnant, which is typically indicative of a Type Ia origin (Vink 2012, and references therein). MCSNR J0508−6902 is not the only SNR to exhibit such a feature, with a number of SNRs also characterized by central Fe enhancements in both the LMC: 0454−67.2 (Seward et al. 2006); 0548−70.4 and 0534−69.9 (Hendrick et al. 2003); DEM L316A (Nishiuchi et al. 2001; Williams & Chu 2005); DEM L238 and DEM L249 (Borkowski et al. 2006); and the SMC: DEM S128, IKT 5 and IKT 25 (Filipović et al. 2000, 2008; van der Heyden, Bleeker & Kaastra 2004); SNR 0104−72.3 (Lee et al. 2011). Of these, DEM L316A, DEM L238 and DEM L239 are most similar to MCSNR J0508−6902, as not only is a faint shell detected surrounding the interior Fe-rich gas, but also the Fe-rich gas is in CIE. However, as argued by Borkowski et al. (2006), it is likely that many more SNRs fall into this category, and only their shells are so faint as to be undetectable by *XMM–Newton*. DEM S128 (Filipović et al. 2000) and IKT 5 (Roper et al., in preparation) are examples of such SNRs with an Fe-rich gas in CIE but no detected shell. The X-ray structure of such SNRs presents a problem for standard Type Ia models (Dwarkadas & Chevalier 1998; Badenes et al. 2003, 2006; Badenes, Borkowski & Bravo 2005). Assuming that the SN ejecta have

expanded in a uniform ambient ISM, and we know from the X-ray analysis that the ambient density is quite low ($\sim 10^{-2}$ cm^{-3}), then, under the standard Type Ia models, the central Fe-rich gas should be of low density and the ionization times are short, which are not observed. Borkowski et al. (2006) demonstrate these scenarios using 1D hydrodynamic simulations using the model of Dwarkadas & Chevalier (1998) and find consistency with the results of Badenes et al. (2003, 2005, 2006).

To explain the X-ray properties of DEM L238 and DEM L249, Borkowski et al. (2006) argue that, rather than the SNR expanding into an ideal environment of uniform density, the structure of the ejecta and/or the uniformity of the ambient ISM deviates from the standard Type Ia models. The best candidates for such a scenario are the 'prompt' Type Ia explosions (Mannucci, Della Valle & Panagia 2006; Sullivan et al. 2006; Aubourg et al. 2008). These 'prompt' events are produced by relatively massive stars ($\sim$3.5–8 M$_\odot$; Aubourg et al. 2008) and are capable of increasing the circumstellar medium (CSM) density via ejection of their stellar envelope prior to the SN event. Alternatively, the SN ejecta themselves could have stripped the companion of its envelope (Marietta, Burrows & Fryxell 2000). As stated by Borkowski et al. (2006), at late stages of SNR evolution, the Fe-contaminated envelope would be evident as dense Fe-rich gas close to the centre of the SNR. Ultimately, this is simply a plausible scenario to explain the observed X-ray morphologies and spectra of MCSNR J0508−6902 and similar remnants. However, it is clear that the standard Type Ia model fails to explain the properties of these SNRs and some mechanism for a pre-explosion increase in the CSM density is essential. Secondary evidence to support the 'prompt' explosion scenario can be found in the stellar content and star formation history (SFH) of the region, further supporting the scenario described above.

To understand the type of stellar environment the progenitor of this SNR came from, we make use of data from the Magellanic Cloud Photometric Survey (Zaritsky et al. 2004) to construct colour–magnitude diagrams and identify blue stars more massive than $\sim$8 M$_\odot$ within a 100 pc ($\sim$6.9 arcmin) radius of MCSNR J0508−6902. This allows us to see the prevalence of early-type stars close to the remnant. In the case of MCSNR J0508−6902, there are not many early-type stars close to the remnant (16), which are far fewer than around DEM L205 (Maggi et al. 2012), where we found 142 stars and concluded to a CC-SN origin, and more similar to SNRs such as SNR J0530−7007 (de Horta et al. 2012) with 13 early-type stars or J0527−7104 (Kavanagh et al. 2013) with 5 such stars.

Studying the SFH in the neighbourhood of MCSNR J0508−6902 (see Fig. 11) as derived from the map of Harris & Zaritsky (2009), we see modest levels of star formation ($\sim 10^{-3}$ M$_\odot$ yr^{-1}) peaking 12 Myr ago (accounting for the presence of several early-type stars as described in the previous paragraph), 100 Myr ago, and extending back from 250 Myr to 1 Gyr. The peak at a look-back time of 100 Myr is consistent with a relatively young progenitor able to produce dense CSM, but we cannot rule out an older progenitor. A 'delayed' progenitor older than $\sim$2.4 Gyr (e.g. Maoz et al. 2011) is however less likely.

Borkowski et al. (2006) discussed the possibility of the iron-rich DEM L238 and DEM L249 remnants to be those of sub-luminous SN2002cx-like Type Ia SNe. Recent studies of this peculiar class of SNe (Jordan et al. 2012; Foley et al. 2013; Kromer et al. 2013) interpret these SNe as failed detonations of a white dwarf, which leads to relatively low initial kinetic energies ($\sim 0.13 \times 10^{51}$ erg) and ejecta masses ($\lesssim$0.5 M$_\odot$). Our estimates of E_0 and $M_{\rm Fe}$ are at odds with these properties, suggesting that MCSNR J0508−6902 is likely not the remnant of a failed-detonation SN. Further studies of centrally iron-rich SNRs and discovery of new members of that class are highly desirable to address the questions of what are the progenitors of these objects, and if and how they differ from the remnants of 'standard' Type Ia SNe.

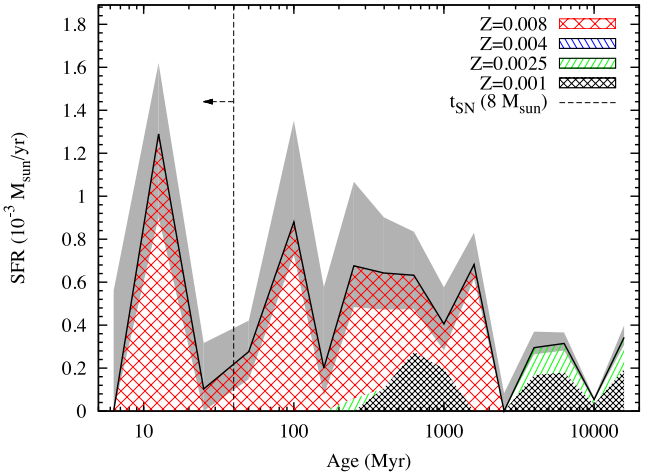

Figure 11. SFH around MCSNR J0508−6902. We show the star formation rate (SFR) as a function of look-back time for different metallicity bins, using the map of Harris & Zaritsky (2009). The grey shading denotes the uncertainties on the total SFR. The time-scale for a CC SN ($\lesssim$40 Myr) to explode is indicated by the dashed line.

6 SUMMARY

We have undertaken a detailed multiwavelength study of a new LMC SNR candidate, MCSNR J0508−6902, using radio, X-ray and optical data (both imaging and spectroscopy) that confirm we have uncovered a new LMC SNR. With this analysis we infer that MCSNR J0508−6902 is an evolved remnant, with a large size of $\sim 74 \times 57$ pc. We estimate the magnetic field strength to be $\sim$28 μG and an age of $\sim$20−25 kyr. Based on the determined O/Fe ratio of the interior gas and the mass of Fe ejecta, we conclude that this remnant is of a thermonuclear SN. It is most likely that this remnant was the result of a 'prompt' Type Ia event, sharing similar properties to various other prompt Ia LMC SNRs.

ACKNOWLEDGEMENTS

We used the KARMA and MIRIAD software packages developed by the ATNF. The Australia Telescope Compact Array is part of the Australia Telescope which is funded by the Commonwealth of Australia for operation as a National Facility managed by CSIRO. We thank the Magellanic Cloud Emission Line Survey (MCELS) team for access to the optical images. We also thank Dr David Frew at Macquarie University for useful discussions. This research is supported by the Ministry of Education and Science of the Republic of Serbia through project No. 176005. MS acknowledges support by the Deutsche Forschungsgemeinschaft through the Emmy Noether Research Grant SA 2131/1. PM and PK acknowledge support from the BMWi/DLR grants FKZ 50 OR 1201 and 50 OR 1209, respectively.

REFERENCES

Arbutina B., Urošević D., Andjelić M. M., Pavlović M. Z., Vukotić B., 2012, ApJ, 746, 79

Arnaud K. A., 1996, in Jacoby G. H., Barnes J., eds, ASP Conf. Ser. Vol. 101, Astronomical Data Analysis Software and Systems V. Astron. Soc. Pac., San Francisco, p. 17
Aubourg É., Tojeiro R., Jimenez R., Heavens A., Strauss M. A., Spergel D. N., 2008, A&A, 492, 631
Badenes C., Bravo E., Borkowski K. J., Domínguez I., 2003, ApJ, 593, 358
Badenes C., Borkowski K. J., Bravo E., 2005, ApJ, 624, 198
Badenes C., Borkowski K. J., Hughes J. P., Hwang U., Bravo E., 2006, ApJ, 645, 1373
Badenes C., Maoz D., Draine B. T., 2010, MNRAS, 407, 1301
Baldwin J. A., Phillips M. M., Terlevich R., 1981, PASP, 93, 5
Balucinska-Church M., McCammon D., 1992, ApJ, 400, 699
Bell A. R., 1978, MNRAS, 182, 443
Berezhko E. G., Völk H. J., 2004, A&A, 427, 525
Borkowski K. J., Lyerly W. J., Reynolds S. P., 2001, ApJ, 548, 820
Borkowski K. J., Hendrick S. P., Reynolds S. P., 2006, ApJ, 652, 1259
Bozzetto L. M., Filipovic M. D., Crawford E. J., Payne J. L., de Horta A. Y., Stupar M., 2012a, Rev. Mex. Astron. Astrofis., 48, 41
Bozzetto L. M., Filipovic M. D., Urosevic D., Crawford E. J., 2012b, Serb. Astron. J., 185, 25
Bozzetto L. M. et al., 2012c, MNRAS, 420, 2588
Bozzetto L. M. et al., 2013, MNRAS, 432, 2177
Chen L.-W., Fabian A. C., Gendreau K. C., 1997, MNRAS, 285, 449
Croom S., Saunders W., Heald R., 2004, Anglo-Australian Observatory Epping Newsletter, 106, 12
Dawson J. R., McClure-Griffiths N. M., Wong T., Dickey J. M., Hughes A., Fukui Y., Kawamura A., 2013, ApJ, 763, 56
de Horta A. Y. et al., 2012, A&A, 540, A25
De Luca A., Molendi S., 2004, A&A, 419, 837
di Benedetto G. P., 2008, MNRAS, 390, 1762
Dickel J. R., McIntyre V. J., Gruendl R. A., Milne D. K., 2005, AJ, 129, 790
Dickel J. R., McIntyre V. J., Gruendl R. A., Milne D. K., 2010, AJ, 140, 1567
Dickey J. M., Lockman F. J., 1990, ARA&A, 28, 215
Dwarkadas V. V., Chevalier R. A., 1998, ApJ, 497, 807
Fesen R. A., Blair W. P., Kirshner R. P., 1985, ApJ, 292, 29
Filipovic M. D., Haynes R. F., White G. L., Jones P. A., 1998, A&AS, 130, 421
Filipović M. D., Haberl F., Pietsch W., Morgan D. H., 2000, A&A, 353, 129
Filipović M. D. et al., 2008, A&A, 485, 63
Foley R. J. et al., 2013, ApJ, 767, 57
Frew D. J., Parker Q. A., 2010, Publ. Astron. Soc. Aust., 27, 129
Freyberg M. J. et al., 2004, in Flanagan K. A., Siegmund O. H. W., eds, Proc. SPIE Conf. Ser. Vol. 5165, EPIC pn-CCD Detector Aboard XMM-Newton: Status of the Background Calibration. SPIE, Bellingham, p. 112
Gooch R., 1995, in Shaw R. A., Payne H. E., Hayes J. J. E., eds, ASP Conf. Ser. Vol. 77, Astronomical Data Analysis Software and Systems IV. Astron. Soc. Pac., San Francisco, p. 144
Grondin M.-H. et al., 2012, A&A, 539, A15
Haberl F., Pietsch W., 1999, A&AS, 139, 277
Haberl F. et al., 2012, A&A, 543, A154
Hambly N. C., Irwin M. J., MacGillivray H. T., 2001, MNRAS, 326, 1295
Hamilton A. J. S., Sarazin C. L., Chevalier R. A., 1983, ApJS, 51, 115
Harris J., Zaritsky D., 2009, AJ, 138, 1243
Hendrick S. P., Borkowski K. J., Reynolds S. P., 2003, ApJ, 593, 370
Hughes J. P., Hayashi I., Koyama K., 1998, ApJ, 505, 732
Hughes J. P., Ghavamian P., Rakowski C. E., Slane P. O., 2003, ApJ, 582, L95
Hughes A., Staveley-Smith L., Kim S., Wolleben M., Filipović M., 2007, MNRAS, 382, 543
Iwamoto K., Brachwitz F., Nomoto K., Kishimoto N., Umeda H., Hix W. R., Thielemann F.-K., 1999, ApJS, 125, 439
Jansen F. et al., 2001, A&A, 365, L1
Jordan G. C., Perets H. B., Fisher R. T., van Rossum D. R., 2012, ApJ, 761, L23
Kahn F. D., 1975, in Pinkau K. et al., eds, Proc. 14th International Cosmic Ray Conference, Munich, Vol. 11, Supernova Remnants. Max-Planck-Inst. extraterrestrische Phys., Garching, p. 3566
Katayama H., Takahashi I., Ikebe Y., Matsushita K., Freyberg M. J., 2004, A&A, 414, 767
Kavanagh P. J. et al., 2013, A&A, 549, A99
Kawamura A. et al., 2009, ApJS, 184, 1
Kim S., Staveley-Smith L., Dopita M. A., Freeman K. C., Sault R. J., Kesteven M. J., McConnell D., 1998, ApJ, 503, 674
Kim S., Dopita M. A., Staveley-Smith L., Bessell M. S., 1999, AJ, 118, 2797
Kim S., Staveley-Smith L., Dopita M. A., Sault R. J., Freeman K. C., Lee Y., Chu Y.-H., 2003, ApJS, 148, 473
Kosenko D., Helder E. A., Vink J., 2010, A&A, 519, A11
Kromer M. et al., 2013, MNRAS, 429, 2287
Kuntz K. D., Snowden S. L., 2008, A&A, 478, 575
Kuntz K. D., Snowden S. L., 2010, ApJS, 188, 46
Lazendic J. S., Slane P. O., 2006, ApJ, 647, 350
Lee J.-J., Park S., Hughes J. P., Slane P. O., Burrows D. N., 2011, ApJ, 731, L8
Lewis I. J. et al., 2002, MNRAS, 333, 279
Lewis K. T., Burrows D. N., Hughes J. P., Slane P. O., Garmire G. P., Nousek J. A., 2003, ApJ, 582, 770
Lumb D. H., Warwick R. S., Page M., De Luca A., 2002, A&A, 389, 93
Maggi P. et al., 2012, A&A, 546, A109
Mannucci F., Della Valle M., Panagia N., 2006, MNRAS, 370, 773
Maoz D., 2008, MNRAS, 384, 267
Maoz D., Mannucci F., Li W., Filippenko A. V., Della Valle M., Panagia N., 2011, MNRAS, 412, 1508
Marietta E., Burrows A., Fryxell B., 2000, ApJS, 128, 615
Mathewson D. S., Clarke J. N., 1973, ApJ, 180, 725
Matteucci F., Greggio L., 1986, A&A, 154, 279
Miceli M., 2011, Mem. Soc. Astron. Ital., 82, 709
Mills B. Y., Turtle A. J., Little A. G., Durdin J. M., 1984, Aust. J. Phys., 37, 321
Mink D. J., Wyatt W. F., 1995, in Shaw R. A., Payne H. E., Hayes J. J. E., eds, ASP Conf. Ser. Vol. 77, Astronomical Data Analysis Software and Systems IV. Astron. Soc. Pac., San Francisco, p. 496
Nevalainen J., Markevitch M., Lumb D., 2005, ApJ, 629, 172
Nishiuchi M., Yokogawa J., Koyama K., Hughes J. P., 2001, PASJ, 53, 99
Ohnishi T., Koyama K., Tsuru T. G., Masai K., Yamaguchi H., Ozawa M., 2011, PASJ, 63, 527
Parker Q. A., Bland-Hawthorn J., 1998, Publ. Astron. Soc. Aust., 15, 33
Parker Q. A. et al., 2005, MNRAS, 362, 689
Read A. M., Ponman T. J., 2003, A&A, 409, 395
Reid W. A., Parker Q. A., 2006a, MNRAS, 365, 401
Reid W. A., Parker Q. A., 2006b, MNRAS, 373, 521
Reid W. A., Parker Q. A., 2012, MNRAS, 425, 355
Reid W. A., Parker Q. A., 2013, MNRAS, 436, 604
Rho J., Petre R., 1998, ApJ, 503, L167
Russell S. C., Dopita M. A., 1992, ApJ, 384, 508
Sabbadin F., Minello S., Bianchini A., 1977, A&A, 60, 147
Sabin L. et al., 2013, MNRAS, 431, 279
Sasaki M., Plucinsky P. P., Gaetz T. J., Smith R. K., Edgar R. J., Slane P. O., 2004, ApJ, 617, 322
Sault R. J., Wieringa M. H., 1994, A&AS, 108, 585
Sault R. J., Teuben P. J., Wright M. C. H., 1995, in Shaw R. A., Payne H. E., Hayes J. J. E., eds, ASP Conf. Ser. Vol. 77, Astronomical Data Analysis Software and Systems IV. Astron. Soc. Pac., San Francisco, p. 433
Saunders W. et al., 2004, in Moorwood A. F. M., Iye M., eds, Proc. SPIE Conf. Ser. Vol. 5492, AAOmega: A Scientific and Optical Overview. SPIE, Bellingham, p. 389
Seward F. D., Williams R. M., Chu Y.-H., Dickel J. R., Smith R. C., Points S. D., 2006, ApJ, 640, 327
Sharp R. et al., 2006, in McLean I. S., Iye M., eds, Proc. SPIE Conf. Ser. Vol. 6269, Performance of AAOmega: The AAT Multi-purpose Fiber-Fed Spectrograph. SPIE, Bellingham, p. 62690G
Shull J. M., van Steenberg M., 1982, ApJS, 48, 95
Smith C., Points S., Winkler P. F., 2006, NOAO Newsletter, 85, 6
Snowden S. L., Mushotzky R. F., Kuntz K. D., Davis D. S., 2008, A&A, 478, 615

Strüder L. et al., 2001, A&A, 365, L18
Stupar M., Parker Q. A., 2012, MNRAS, 419, 1413
Sullivan M. et al., 2006, ApJ, 648, 868
Turner M. J. L. et al., 2001, A&A, 365, L27
van der Heyden K. J., Bleeker J. A. M., Kaastra J. S., Vink J., 2003, A&A, 406, 141
van der Heyden K. J., Bleeker J. A. M., Kaastra J. S., 2004, A&A, 421, 1031
van der Marel R. P., Cioni M.-R. L., 2001, AJ, 122, 1807
Vink J., 2012, A&AR, 20, 49
Williams R. M., Chu Y.-H., 2005, ApJ, 635, 1077
Williams R. M., Chu Y.-H., Dickel J. R., Gruendl R. A., Shelton R., Points S. D., Smith R. C., 2004, ApJ, 613, 948
Wilms J., Allen A., McCray R., 2000, ApJ, 542, 914
Wong T. et al., 2011, ApJS, 197, 16
Yamaguchi H., Ozawa M., Koyama K., Masai K., Hiraga J. S., Ozaki M., Yonetoku D., 2009, ApJ, 705, L6
Yamauchi S., Nobukawa M., Koyama K., Yonemori M., 2013, PASJ, 65, 6
Zaritsky D., Harris J., Thompson I. B., Grebel E. K., 2004, AJ, 128, 1606
Zhang Y.-Y., Reiprich T. H., Finoguenov A., Hudson D. S., Sarazin C. L., 2009, ApJ, 699, 1178

APPENDIX A: X-RAY BACKGROUND

In the case of single- and double-pixel events, the X-ray background comprises particle-induced and astrophysical components, as well as electronic read-out noise. The particle-induced background of the EPIC consists of three components. The first of these is the quiescent particle background (QPB), a continuum component produced by the direct interaction of penetrating high-energy particles with the detector. Depending on the energy range considered, this can be modelled by a power law not folded through the instrumental response (see Freyberg et al. 2004; Nevalainen, Markevitch & Lumb 2005; Zhang et al. 2009, for example). The second component consists of the instrumental fluorescence lines, which are due to the interaction of high-energy particles with the material surrounding the detector (Lumb et al. 2002; Read & Ponman 2003). Below 5 keV, only the Al Kα instrumental fluorescence line at 1.49 keV contributes to the EPIC-pn particle-induced background. Finally, we have residual SP contamination, which is due to SPs travelling through the telescope system to the detector. This component is quite variable with periods of high SP background filtered out of an observation event list during a standard reduction. However, there will always remain some residual SP contamination which escapes the filtering criteria and must be considered. The spectrum of these residual SPs can be described by a power law not convolved with the instrumental response (Kuntz & Snowden 2008), and can vary in both magnitude and slope. The electronic read-out noise is very significant at the lowest energies, increasing dramatically below ∼0.7 keV. Since we limit our spectral analysis to the 0.4–5 keV energy range, we avoid the most affected energy range; however, some increase in the background is expected just above 0.4 keV.

A1 QPB, instrumental fluorescence lines and electronic read-out noise

To model the QPB, instrumental fluorescence lines and the electronic read-out noise, we make use of the *XMM–Newton* FWC data, which were collected with the detector shielded from the astrophysical and SP backgrounds. A full discussion on the FWC data of the EPIC-pn is given in Freyberg et al. (2004). The FWC data were screened using the same event filtering criteria as for the observational data, and were also vignetting corrected using the SAS task *evigweight*. Although the QPB is not subject to vignetting, it is necessary to apply the same correction as to the observational data. For the purposes of spectral fitting, ancillary response files are generated for a flat detector map as the effective area correction has already been applied to the event list.

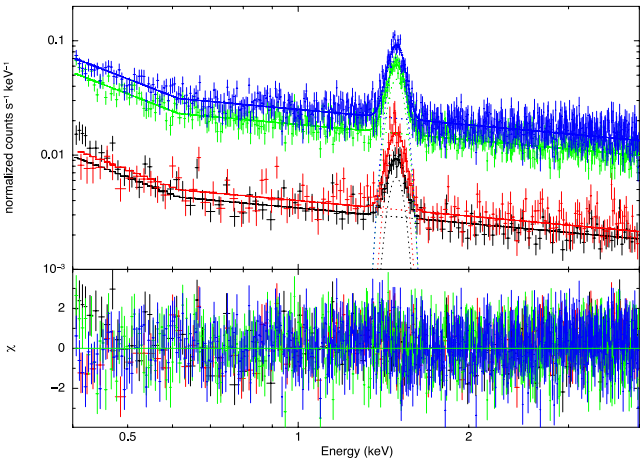

Figure A1. FWC spectra extracted from the same source and background regions defined for the X-ray spectral analysis of MCSNR J0508−6902. The black, red, green and blue data points correspond to the SNR centre, centre background, SNR shell and shell background, respectively. The best-fitting broken power law plus Gaussian line (*bknpower+gauss* in XSPEC) model is indicated by the solid lines ($\Gamma_1 = 1.91$, $\Gamma_2 = 0.45$ and $E_{\rm break} = 0.62$ keV). The difference in normalizations between the corresponding source and background spectra is due to the vignetting-correction process (see the text).

To characterize the FWC spectra, and to assess the likely contribution of the QPB to our observational data, we extract spectra from the FWC data from the same regions of the detector as our SNR source and background spectra. However, these spectra must be scaled to account for differences in the integrated QPB count rates of the observational and FWC data. To perform this scaling, we considered the 10–13 keV count rates for the entire FOV of both data sets and determined a scaling factor. Unless a very bright and hard source is present in the observational FOV, the QPB continuum should dominate both data sets at these high energies. Scaling the FWC data using lower energy range count rates is not safe as there is potentially an astrophysical contribution in the observational data. We selected the energy range 10–13 keV for the scaling as Katayama et al. (2004) showed a good correlation between the 2–7 keV count rate and the 10–13 keV count rate in the FWC observations. Thus, the 10–13 keV count rates can be used to reliably scale the lower energy QPB continuum. The scaled FWC spectra are shown in Fig. A1. As previously mentioned, the background spectra were extracted from regions further off-axis than those of the SNR. The fact that these were obtained from a vignetting-corrected FWC data set has important effects on the normalizations of the QPB components. The vignetting-correction process operates on every event in the data, regardless of photon or particle origin, according to its position on the detector to account for the variation in effective area of the instrument. However, this correction is photon specific and the particle background is not subject to the same effects. This is clearly evident from Fig. A1, with the background spectra having a larger normalization than their corresponding source spectra due to the higher vignetting correction applied to events further off-axis.

We chose not to subtract these FWC spectra from the observational spectra because, as pointed out by Kuntz & Snowden (2008) and Snowden et al. (2008), the fluorescence lines of the EPIC instruments are sufficiently strong that small gain variations and

differences in environment between FWC and filter wheel open positions can produce significant differences in the lines and correspondingly large residuals after subtraction. Hence, we chose instead to explicitly model the background in our spectral fits, using the FWC spectra shown in Fig. A1 as a basis. We fit models to the FWC spectra simultaneously, allowing only normalizations to vary, and found that the QPB continuum and electronic read-out noise components in the 0.4–4 keV range were best fitted using a broken power law (*bknpower* in XSPEC) not folded through the instrument response, with the energy break ($E_{\rm break}$) = 0.62 keV, the photon index for $E < E_{\rm break}$ (Γ_1) = 1.91, the photon index for $E > E_{\rm break}$ (Γ_2) = 0.45 and reduced χ^2 = 1.02 for 1363 d.o.f. Here, Γ_1 represents the electronic read-out noise and Γ_2 the QPB. While at lower energies the electronic read-out noise component requires a more complicated model, in the 0.4–5 keV energy range we consider, a power law is sufficient. A Gaussian line was also included to account for the Al Kα instrumental fluorescence line at 1.49 keV. The fits to the FWC spectra are indicated in Fig. A1 as the solid lines. Above 4–5 keV, the defined model no longer applies as the QPB 'flattens'. However, this is unimportant in our analysis as we can easily constrain the QPB model given that this component dominates the emission above 1.5–2 keV. In our spectral analysis of MCSNR J0508−6902, the ratios of the normalizations of the source and background QPB components were fixed to the values determined from the QPB spectra.

A2 SP contamination

To account for the residual SP contamination in our spectra, we included the appropriate power-law model not convolved with the instrument response. However, the fits would consistently return a zero normalization for the SP component, suggesting that the SP contamination is not significant. This could be expected given the fact that there were no SP flares during the observation. However, we note that a lack of SP flares does not necessarily mean no significant SP contamination. Thus, we ran the diagnostic algorithm of De Luca & Molendi (2004)[8] which suggested little or no contamination by SPs. A further indication that SP contamination is minimal is that the shell spectrum above 2 keV, where we expect the SP contamination to be most noticeable, can be accounted for by the QPB component, with the normalization of the QPB components in all our fits agreeing with those of the FWC spectra within their 90 per cent confidence intervals. For these reasons, we conclude that residual SPs have no significant effect on our spectra and we ignore their contribution in our analysis.

A3 Astrophysical background

The astrophysical background can usually be modelled with four or fewer components (Snowden et al. 2008; Kuntz & Snowden 2010). These are the unabsorbed thermal emission from the local hot bubble (LHB, $kT \sim 0.1$ keV), absorbed cool ($kT \sim 0.1$ keV) and warm ($kT \sim 0.25$ keV) thermal emission from the Galactic halo, and an absorbed power law representing unresolved background cosmological sources ($\Gamma \sim 1.46$; Chen, Fabian & Gendreau 1997). The cool Galactic halo component likely does not contribute to the astrophysical background in this case as it is absorbed by the foreground Galactic absorbing column and, thus, we do not consider it in our background models. During our analysis, we allowed the LHB and warm Galactic halo temperatures to vary, with the spectral index of the unresolved background power law fixed at 1.46. Additionally, it was assumed that the temperature of the thermal components and the surface brightness of the thermal and non-thermal components did not vary significantly between the source and background regions. Thus, the appropriate temperature and normalization parameters were linked. To model the absorption of the Galactic halo and cosmological background sources, we used a photoelectric absorption model in XSPEC. The Galactic halo emission is subject to foreground Galactic absorption ($N_{\rm H\,Gal}$), which was fixed at 7×10^{20} cm^{-2} based on the H I maps of Dickey & Lockman (1990). The unresolved cosmological background component is not only subject to this Galactic absorption, but also absorption by material in the LMC ($N_{\rm H\,LMC}$). This LMC absorption component was incorporated into the fits using a *vphabs* model with abundance at 0.5 solar as appropriate for the LMC (Russell & Dopita 1992). However, the formal best-fitting value of $N_{\rm H\,LMC}$ invariably tended to zero and was ultimately fixed as so. The astrophysical background was sufficiently accounted for by our defined model, the best-fitting parameters of which were consistent in all of our fits. The temperature of the LHB and warm Galactic halo components were (0.08–0.11) and (0.28–0.33) keV, respectively, which are compatible the expected values from Snowden et al. (2008) and Kuntz & Snowden (2010).

[8] See http://xmm2.esac.esa.int/external/xmm_sw_cal/background/epic_scripts.shtml

This paper has been typeset from a TEX/LATEX file prepared by the author.

A.35 Related Paper 35

De Horta, A. Y., Sommer, E. R., Filipović, M. D., O'Brien, A., Bozzetto, L. M., Collier, J. D., Wong, G. F., Crawford, E. J., Tothill, N. F. H., Maggi, P., and Haberl, F. (2014b). Multi-frequency Observations of a Superbubble in the LMC: The Case of LHA 120-N 70. *AJ*, 147:162

My contribution was to assist in the data analysis. This is a 10% contribution.

The Astronomical Journal, 147:162 (8pp), 2014 June doi:10.1088/0004-6256/147/6/162

MULTI-FREQUENCY OBSERVATIONS OF A SUPERBUBBLE IN THE LMC: THE CASE OF LHA 120–N 70

A. Y. De Horta[1], E. R. Sommer[1], M. D. Filipović[1], A. O'Brien[1], L. M. Bozzetto[1], J. D. Collier[1], G. F. Wong[1], E. J. Crawford[1], N. F. H. Tothill[1], P. Maggi[2], and F. Haberl[2]
[1] University of Western Sydney, Locked Bag 1797, Penrith South DC, NSW 1797, Australia; a.dehorta@uws.edu.au
[2] Max-Planck-Institut für extraterrestrische Physik, Giessenbachstrasse, D-85741 Garching, Germany
Received 2013 November 18; accepted 2014 March 28; published 2014 May 14

ABSTRACT

We present a detailed study of new Australia Telescope Compact Array and *XMM-Newton* observations of LHA 120–N 70 (hereafter N 70), a spherically shaped object in the Large Magellanic Cloud, classified as a superbubble. Both archival and new observations were used to produce high quality radio continuum, X-ray, and optical images. The radio spectral index of N 70 is estimated to be $\alpha = -0.12 \pm 0.06$, indicating that while a supernova (SN) or supernovae have occurred in the region at some time in the distant past, N 70 is not the remnant of a single specific SN. N 70 exhibits limited polarization with a maximum fractional polarization of 9% in a small area of the northwest limb. We estimate the size of N 70 to have a diameter of 104 pc (±1 pc). The morphology of N 70 in X-rays closely follows that in radio and optical, with most X-ray emission confined within the bright shell seen at longer wavelengths. Purely thermal models adequately fit the soft X-ray spectrum which lacks harder emission (above 1 keV). We also examine the pressure output of N 70 where the values for the hot ($P_{\rm X}$) and warm ($P_{\rm H\,II}$) phases are consistent with other studied H II regions. However, the dust-processed radiation pressure ($P_{\rm IR}$) is significantly smaller than in any other object studied in Lopez et al. N 70 is a very complex region that is likely to have had multiple factors contributing to both the origin and evolution of the entire region.

Key words: galaxies: individual (LMC) – ISM: bubbles – ISM: individual objects (SBN70) – ISM: supernova remnants – radio continuum: ISM – X-rays: ISM

Online-only material: color figures

1. INTRODUCTION

The Large Magellanic Cloud (LMC), located at a distance of 50 kpc (Pietrzyński et al. 2013), is one of the best galaxies in which to study objects such as (super)bubbles, H II regions and supernova remnants (SNRs), due to its favorable position in the direction toward the South Ecliptic Pole. As well as its viewing position, the LMC is located in one of the coldest areas of the radio sky, which allows us to observe radio emission without the interruption from Galactic foreground radiation. In addition to this, the LMC resides outside of the Galactic plane and therefore the influence of dust, gas, and stars is negligible.

A well-known characteristic of SNRs in the radio continuum is the predominance of non-thermal emission. Although SNRs have a typical radio spectral index of $\alpha \sim -0.5$ (defined by $S \propto \nu^{\alpha}$), indicating a non-thermal emission, this can significantly change due to the environment in which the SNR evolves (Filipović et al. 1998a).

A bubble structure can be created by the stellar wind emanating from a massive O- or B-type star. This stellar wind collides with the surrounding interstellar medium (ISM) producing a hollowed out structure with a shock front, leading to a shell-like nebula (Weaver et al. 1977). This bubble may become bigger and more complex with the combined stellar wind from multiple stars in a cluster. As the most massive of these stars begin to explode as supernovae (SNe), the combined effect produces a (super)bubble. The effects from stellar winds and SNe become even more complex when taking place within H I or H II regions and where the ISM is heterogeneous (Oey 1996a; Oey & García-Segura 2004).

These luminous superbubbles (SBs), measuring up to 100 pc, blown by winds from hot massive stars and SN explosions, with their interior filled with hot expanding gas offer us a chance to explore the crucial connection between the life-cycles of stars and the evolution of galaxies.

Here, we report on new radio continuum, X-ray, and optical observations of the LMC SB called LHA 120–N 70 (hereafter, N 70). The observations, data reduction, and imaging techniques are described in Section 2. The astrophysical interpretation of newly obtained moderate-resolution total intensity and polarimetric images in combination with the existing Magellanic Cloud Emission Line Survey (MCELS) and X-ray *XMM-Newton* images are discussed in Section 3.

1.1. Previous Studies of N 70

1.1.1. Optical

N 70 was first cataloged as an emission nebula in the Magellanic Clouds by Henize (1956) while Davies et al. (1976) listed this complex region DEM L301 which also encompasses the OB association LH 114 (Lucke & Hodge 1970). This stellar association (LH 114) is positioned about 1′ west of the geometric center of N 70 and in the line of sight of a known molecular cloud (Kawamura et al. 2009). It contains six O stars with an O3If the most massive of these (Zhang et al. 2014, in preparation). The first optical spectroscopy study by Danziger & Dennefeld (1976) found strong [S II] lines relative to Hα indicative of an SNR, though the electron density appeared low. Rosado et al. (1981) and Georgelin et al. (1983) measured the expansion velocity of N 70 to be 60–70 km s^{-1} and concluded that this would fit a shock model. They also suggested that N 70 is most likely an ancient SNR, approximately 2.4 $\times 10^5$ yr old, in the adiabatic or radiative phase of expansion and although the central stars are contributing to the ionization, they are not the origin of the shock. Dopita et al. (1981) found that the spectrophotometry of N 70 is inconsistent with the emission from an ionizing

shock, yet the [S II] lines were moderately strong compared to ordinary H II regions, suggesting enhanced ionization due to compression from stellar wind. Inglis & Kitchin (1990) used a number of criteria such as a central star, nature of nebulosity, and filament structure to define N 70 as a possible Wolf–Rayet stellar wind bubble. Oey (1996a, 1996b) describe N 70 as a high-velocity SB—an H II region with OB association stars found within, creating a bubble from a combination of stellar wind and SNe. Oey & Kennicutt (1997) conclude N 70 is an H II region with OB association stars and that the H II region is density bounded rather than ionization bounded. Danforth & Blair (2006) detected [O VI] in *Far Ultraviolet Spectroscopic Explorer* observations of four large stars in N 70, possibly from thermal conduction at the interface between the hot, X-ray emitting gas from inside the bubble and the photoionized material of the outer shell seen in Hα.

1.1.2. Radio

Milne et al. (1980) performed initial radio observations of N 70 at 5 GHz and 14.7 GHz and estimated a spectral index of $\alpha = -0.3$. Dopita et al. (1981) found that unlike previous studies declaring N 70 a non-thermal source, the radio emissions from N 70 are predominantly thermal in origin. They also found that although N 70 exhibits several features that could be explained in terms of an SNR or a mass-loss bubble, the only model that is consistent with all observations is that of a mass-loss bubble confined by the ram pressure of a massive, collapsing, cloud of neutral hydrogen. However, Mills et al. (1984) declared that N 70 was likely a fossil SNR, while Filipović et al. (1998b) list N 70 as an H II region based on Parkes radio observations. Oey et al. (2002) investigated the H I environment of N 70 and found that it shows some evidence of shock activity; however, no correspondence at all was found between the optical nebula and H I emission.

1.1.3. X-ray

Chu & Mac Low (1990; also see Wang & Helfand 1991 and Chu 1997) measured the diffuse X-ray emission of bubbles and SBs and concluded that N 70 was an SNR within a wind-blown bubble. Slater et al. (2011) describe N 70 as an SB but found no difference between H II regions and SBs in IR emission from dust. Rodríguez-González et al. (2011) carried out a simulation exploring the morphology, dynamics, and thermal X-ray emission of SBs and concluded that the structure of N 70 can be explained with both stellar driven wind and an SN. Reyes-Iturbide et al. (2011) discuss the *XMM-Newton* observations and the soft X-ray emission detected within N 70 but also present an image showing some peripheral hard X-ray emission. Most recently Zhang et al. (2014, in preparation), on top of their *XMM-Newton* analysis, obtained high-dispersion long-slit echelle spectroscopic observations. They found that although N 70 has a modest expansion velocity, its diffuse X-ray emission of $\sim 6.1 \times 10^{35}$ erg s^{-1} is higher than the luminosity from a quiescent SB with N 70s density, size, and expansion velocity.

2. OBSERVATIONAL DATA

2.1. Radio Continuum Observations

The data used in this study to produce the radio images of N 70 were gathered from the radio interferometer Australia Telescope Compact Array (ATCA). We observed N 70 on 2011 November 15 and 16 with the ATCA, using the new Compact Array Broadband Backend receiver with the EW367 array configuration at wavelengths of 3 and 6 cm ($\nu = 9000$ and 5500 MHz). Baselines formed with the sixth ATCA antenna were omitted, as the other five antennas were arranged in a compact configuration. The observations were carried out in the so-called snap-shot mode, totaling $\sim$70 minutes of integration over a 14 hr period. PKS B1934-638 was used for primary calibration and PKS B0530-727 was used for secondary (phase) calibration. The MIRIAD (Sault & Killeen 2006) and KARMA (Gooch 1996) software packages were used for reduction and analysis. More information on the observing procedure and other sources observed in this session/project can be found in Bojičić et al. (2007), Crawford et al. (2008a, 2008b, 2010), Čajko et al. (2009), De Horta et al. (2012), Grondin et al. (2012), Maggi et al. (2012), and Bozzetto et al. (2010, 2012a, 2012b, 2012c, 2013).

In addition, during our own observations, we made use of two other ATCA projects (C354 and C149) at wavelengths of 13 and 20 cm. Observations from project C354 were taken on 1994 September 18 (array 1.5B), 22, and 23 (array 1.5D). Observations from project C149 were taken on 1992 March 22 (array 6A) and 1992 April 2 (array 6C).

Tables 1 and 2 summarize the data used for imaging in this paper. Table 1 includes archival observations from 1997 as well as our new observations made in 2011. In Table 2, we list archival data that were retrieved in the raw, uncalibrated form and were calibrated and used to produce the 20 cm images.

Images were formed using MIRIADS multi-frequency synthesis algorithm (Sault & Wieringa 1994) and natural weighting. They were deconvolved using the MFCLEAN and RESTOR algorithms with the primary beam correction applied using the LINMOS task. A similar procedure was used for both *U* and *Q* Stokes parameter maps. Because of the low dynamic range, self-calibration was not attempted. The 6 cm image (Figure 1, left) has a resolution of $39'' \times 25''$ at P.A. $= 48^\circ$ with an estimated rms noise of 0.12 mJy beam^{-1}. Similarly, we made an image of N 70 at 20 cm (Figure 1 right) with a resolution of $40'' \times 40''$ at P.A. $= 0^\circ$ with an estimated rms noise of 0.85 mJy beam^{-1}.

2.2. XMM-Newton Observations

We make use of the only existing *XMM-Newton* observation of N 70 (ObsID: 0503680201, PI: Rosa Williams). The 39 ks long observation was performed on 2008 January 26, with N 70 at the focus point of the European Photon Imaging Camera (EPIC). The EPIC instrument comprises a pn CCD imaging camera (Strüder et al. 2001) and two MOS CCD imaging cameras (Turner et al. 2001). The "thin" optical filter was used for all three cameras, which were operated in full-frame mode. We used the *XMM-Newton* SAS[3] version 12.0.1 to process the data. Periods of high background activity were screened out from the imaging and spectral analysis. We did so by applying a threshold of 8 and 2.5 counts ks^{-1} arcmin^{-2} on pn and MOS background light curves in the 7–15 keV energy band. We were left with a useful exposure time of $\sim$22 ks.

We created adaptively smoothed, vignetting-corrected, and detector-background-subtracted images using the same method as described in Bozzetto et al. (2013). In Figure 2, we combine *XMM-Newton* images in three energy bands (a soft band (0.3–0.7 keV), a medium band (0.7–1.1 keV) and a hard band (1.1–4.2 keV)) into composite and overlay radio (20 cm) contours.

[3] Science Analysis Software, http://xmm.esac.esa.int/sas/

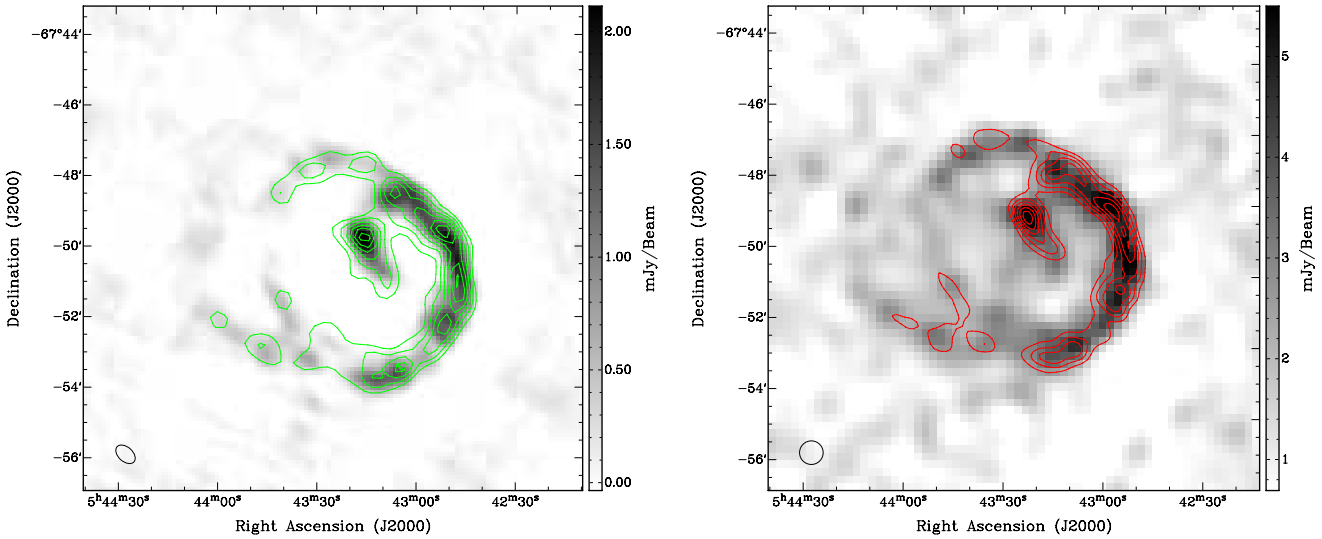

Figure 1. Left: ATCA observations of N 70 at 6 cm (5.5 GHz) overlaid with 20 cm (1.4 GHz) contours at 3σ, 4σ, 5σ, 6σ, and 7σ ($\sigma = 0.85$ mJy beam^{-1}). The black circle in the lower left corner represents the synthesized beamwidth (at 6 cm) of $39'' \times 25''$ at P.A. $= 48°$. Right: ATCA observations of N 70 at 20 cm (1.4 GHz) overlaid with 6 cm (5.5 GHz) contours. The contours are 3σ, 6σ, 9σ, 12σ, 15σ, and 18σ ($\sigma = 0.12$ mJy beam^{-1}). The black circle in the lower left corner represents the synthesized beamwidth (at 20 cm) of $40'' \times 40''$. The sidebar quantifies the pixel map and its units are mJy beam^{-1}.
(A color version of this figure is available in the online journal.)

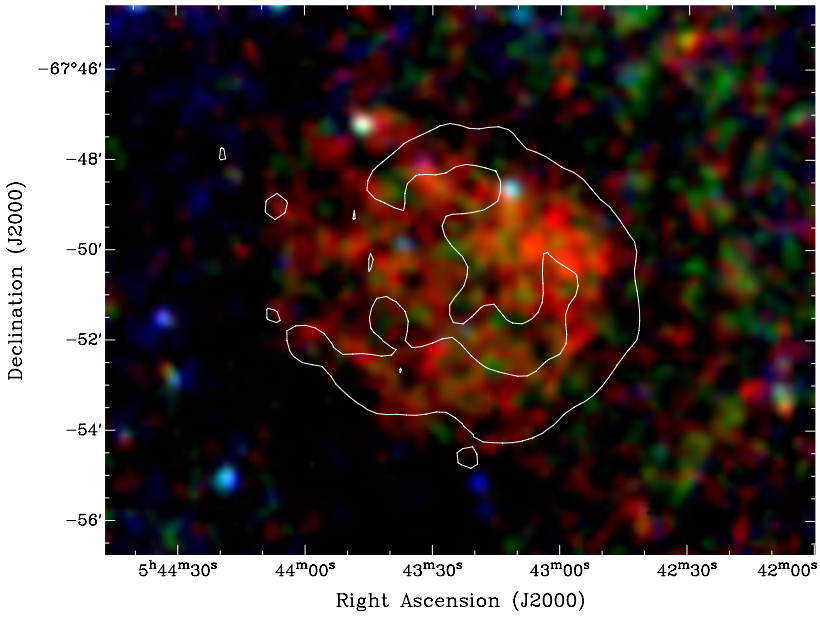

Figure 2. *XMM-Newton* X-ray (R = soft (0.3–0.7 keV), G = medium (0.7–1.1 keV), B = hard 1.1–4.2 keV)) image with 20 cm contour at 2.1 mJy beam^{-1}.
(A color version of this figure is available in the online journal.)

Table 1
Summary of Australia Telescope Online Archive (ATOA) Observations from Project C634 Used in Imaging N 70

Date	Scan Time (minutes)	R.A. (J2000)	Decl. (J2000)	Array	Frequencies (MHz)	Bandwidth (MHz)	Number of Channels
2011 Nov 16	44.6	$5^h43^m25\overset{s}{.}00$	$-67°50'57\overset{''}{.}20$	EW367	5500, 9000	2048.0	2049
2011 Nov 15	24.5	$5^h43^m25\overset{s}{.}00$	$-67°50'57\overset{''}{.}20$	EW367	5500, 9000	2048.0	2049
1997 Oct 6	10.0	$5^h43^m14\overset{s}{.}46$	$-67°51'23\overset{''}{.}75$	375	4790, 8640	128.0	33
1997 Oct 5	10.0	$5^h43^m14\overset{s}{.}46$	$-67°51'23\overset{''}{.}75$	375	4790, 8640	128.0	33
1997 Oct 2	80.0	$5^h43^m14\overset{s}{.}46$	$-67°51'23\overset{''}{.}75$	375	4800, 8640	128.0	33

Table 2
Summary of ATOA Observations from Project C587 Used in Imaging N 70

Date	Scan Time (minutes)	Array
1997 Sep 4	138.3	1.5C
1997 Sep 3	34.0	1.5C
1997 Mar 31	20.8	1.5D
1997 Mar 27	37.0	1.5D
1997 Mar 26	175.0	1.5D
1997 Jan 8	2.3	750D
1997 Jan 7	126.9	750D
1997 Jan 6	98.2	750D
1997 Jan 5	143.8	750D
1996 Nov 28	129.3	750A
1996 Nov 27	112.3	750A

Notes. All projects were observed at a frequency of 1380 MHz and a bandwidth of 128 MHz across 33 channels. All observations were centered at R.A.(J2000) = $5^h43^m39\overset{s}{.}10$ decl.(J2000) = $-67°50'6\overset{''}{.}80$.

For spectral analysis, we utilized pn data only, as this camera has a higher throughput than MOS cameras. We extracted energy spectra from a vignetting-weighted event list. The spectrum of N 70 ("source spectrum") was taken from a circle, whose center and radius were as measured in radio (at 6 cm; Section 3). A background spectrum was extracted from a region of similar area located at the southeast of N 70 excluding point sources detected in this region. Spectral fitting was performed with XSPEC (Arnaud 1996) version 12.8.0. Instead of subtracting the background spectrum from the source spectrum, we modeled the background and simultaneously fit both spectra. For a description of this method, as well as a detailed presentation of the instrumental and astrophysical components of the background, we refer the reader to Bozzetto et al. (2013).

2.3. MCELS

The MCELS is a survey of the two nearest galaxies, the Small Magellanic Cloud, and the LMC. The goal of the project is to trace the ionized gas in the Magellanic Clouds using narrow-band filters (hydrogen (Hα 6563 Å), sulfur ([S II] 6724 Å), and oxygen ([O III] 5007 Å)). The survey is a joint project of the Cerro Tololo Inter-American Observatory (Chile) and the University of Michigan using the CTIO Curtis/Schmidt Telescope. The detector used was a thinned, back-side illuminated Tek 2048×2048 CCD with 24 μm pixels, giving a $1\overset{\circ}{.}35$ field of view at a scale of $2\overset{''}{.}4$ pixel^{-1} with a resulting angular resolution of approximately $4\overset{''}{.}6$. Two slightly offset images were obtained through each filter to allow for cosmic-ray rejection and bad-pixel replacement. The total integration times were 1200 s in the [O III] and [S II] images and 600 s in the Hα images per field. The data were reduced using a modified version of the Esence/SuperMaCHO pipeline for overscan correction, bias subtraction, and flat-field correction. Final astrometric solutions were derived using the IRAF software "ccfind" and "ccmap" using the UCAC catalog. At this time, the images were resampled to have $2'' \times 2''$ pixels with an rms error of approximately 0.1 pixel ($0\overset{''}{.}2$). The individual frames for each field were then aligned using the astrometric solutions and multiple exposures in each filter were combined using a median filter. Further details regarding the MCELS are given by Smith et al. (2000), Pellegrini et al. (2012), and at http://www.ctio.noao.edu/mcels. Here, for the first time, we present optical images (Figures 3 and 4) of this object in combination with our new radio continuum and X-ray data.

Figure 3. Giant SB complex N 70 in the light of Hα (red), [S II] (green), and [O III] (blue); all data from MCELS (see Section 2.3).
(A color version of this figure is available in the online journal.)

3. RESULTS AND DISCUSSION

3.1. Radio Continuum

N 70 has a roughly circular morphology centered at R.A.(J2000) = $5^h43^m22\overset{s}{.}9$, decl.(J2000) = $-67°50'57''$ with a measured diameter at 6 cm of 104 ± 1 pc. The diameter was determined using the KARMA tool KPVSLICE to estimate the extension of N 70 at 6 cm at the 3σ noise level (∼1 mJy). Overall, the optical and radio continuum emissions follow each other.

In order to estimate the radio spectral energy distribution for this object, we used our new integrated flux density measurements at various radio frequencies along with the 408 MHz measurement from Dopita et al. (1981), as well as various *Parkes* and other ATCA estimates (Filipović et al. 1995, 1996, 1998a, 2009; Hughes et al. 2006, 2007). We list these flux density measurements at various frequencies in Table 3 and then plot the N 70 spectral index α in Figure 5. The overall radio continuum spectral index of N 70 is flat ($\alpha = -0.12 \pm 0.06$).

The linear polarization images for each frequency were created using Q and U parameters. The 6 cm image reveals some moderate linear polarization with a mean fractional polarization of 8.8% ± 1.1% (no reliable detection could be made at 3 cm) in a small area of the northwest limb (Figure 6). This linear polarization and the moderate X-ray emission enhancement in the vicinity is indicative of an SN having occurred close to the SB shell within 10^4 yr (Chu & Mac Low 1990). This SN would certainly have provided chemical enrichment of the nebulous material. It would also contribute, in some way, to the overall energy that has shaped this area, but the exact influence of the SN on current N 70 structure is difficult to establish. N 70 exhibits properties of an H II region but the [S II] to Hα ratio on the eastern side is higher than would be expected for a classic H II region (Figures 3 and 4). The young stellar objects found in the cluster of stars within N 70 are not massive enough to be wholly

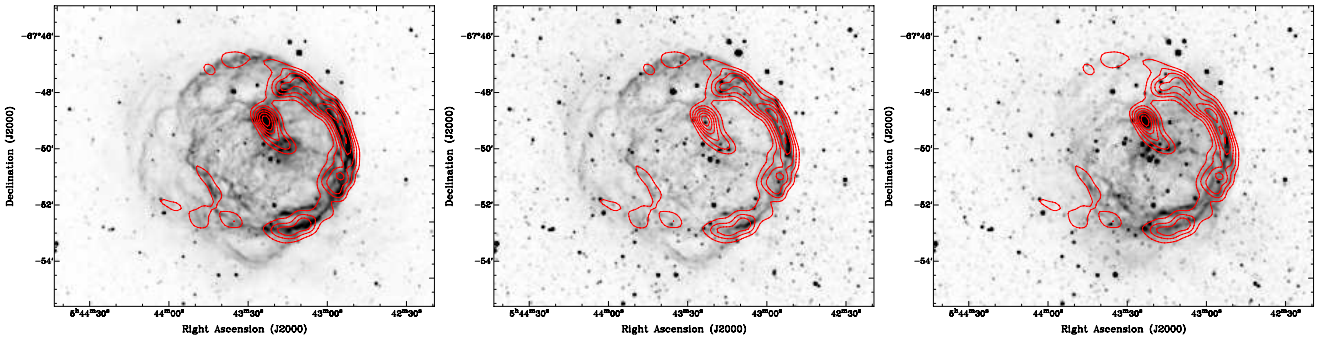

Figure 4. MCELS optical images (Hα (left), [S II] (middle), and [O III] (right)) of N 70 overlaid with 6 cm contours at 3σ, 6σ, 9σ, 12σ, 15σ, and 18σ ($\sigma = 0.12$ mJy beam^{-1}).

(A color version of this figure is available in the online journal.)

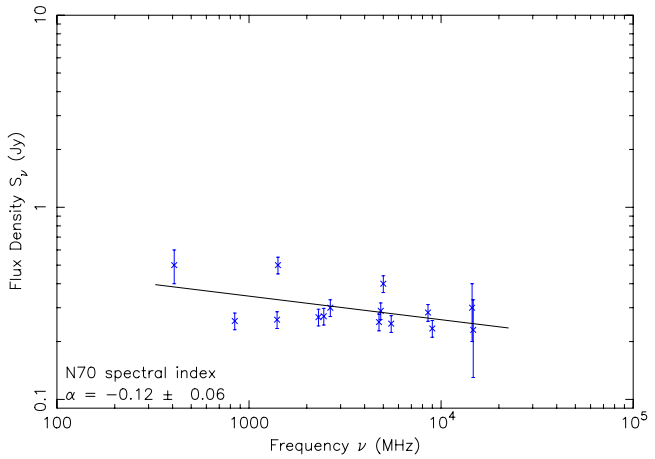

Figure 5. Radio continuum spectrum of N 70. The integrated flux densities at corresponding radio frequencies are listed in Table 3.

(A color version of this figure is available in the online journal.)

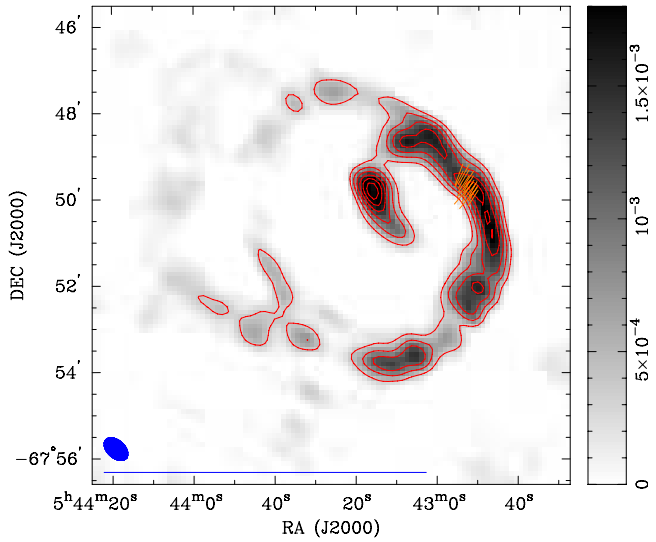

Figure 6. 6 cm (5.5 GHz) ATCA observations of N 70. The blue ellipse in the lower left corner represents the synthesized beam width of $39'' \times 25''$ at P.A. $= 48^\circ$. The length of the vectors represents the fractional polarized intensity at each pixel position, and their orientations indicate the mean P.A. of the electric field (averaged over the observing bandwidth, not corrected for any Faraday rotation). The blue line below the beam ellipse represents the length of a polarization vector of 100%. The sidebar quantifies the pixel map and its units are Jy beam^{-1}. The maximum fractional polarization is 9% ± 1%. Contours at 3σ, 6σ, 9σ, 12σ, 15σ, and 18σ ($\sigma = 0.12$ mJy beam^{-1}).

(A color version of this figure is available in the online journal.)

responsible for the bubble-like structure, even though they are certainly contributing to the energy within the structure (Zhang et al. 2014, in preparation).

3.2. X-ray

The majority of the X-ray emission appears to be in the softest (0.3–0.7 keV) energy band (Figure 7). To search for harder

Table 3
Measured Integrated Flux Density of N 70

ν (MHz)	λ (cm)	Telescope	Beam Size ($''$)	$S_{\rm Total}$ (mJy)	Reference
408	73	Molonglo	174 × 204	500	Dopita et al. (1981)
843	36	MOST	43 × 43	256	This work
1400	21	ATCA	40 × 40	260	This work
1415	21	Fleurs S.T.	174 × 204	500	Dopita et al. (1981)
2300	13	Parkes	540 × 540	268	Filipović et al. (1998a)
2450	12	Parkes	540 × 540	271	Filipović et al. (1998a)
2650	11	Parkes	450 × 450	300	Dopita et al. (1981)
4750	6	Parkes	294 × 294	253	Filipović et al. (1998a)
4850	6	Parkes/PMN	294 × 294	289	Filipović et al. (1998a)
5000	6	Parkes	264 × 264	400	Dopita et al. (1981)
5500	6	ATCA	2.7 × 2.1	248	This work
8550	3	Parkes	162 × 162	283	Filipović et al. (1998a)
9000	3	ATCA	2.7 × 2.1	234	This work
14500	2	Parkes	132 × 132	300	Dopita et al. (1981)

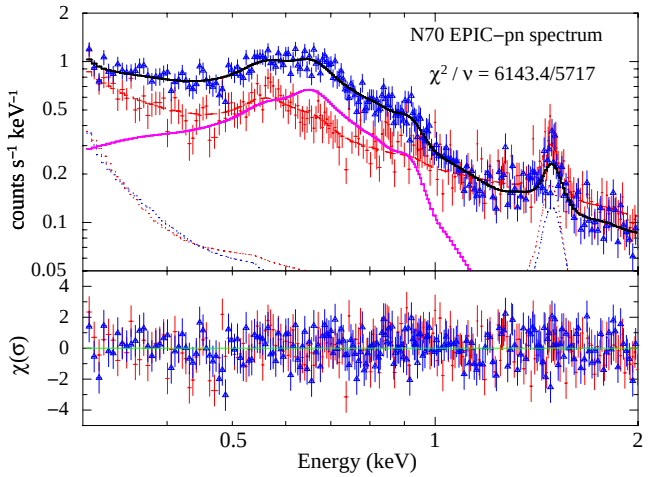

Figure 7. EPIC-pn spectrum of N 70. Data extracted from the source region are shown by blue data points, with the total (source+background) model as the solid black line. The red and blue dash-dotted lines show the instrumental background model measured in the background and source extraction regions, respectively. The X-ray plus instrumental background data and model are shown by the red points and dashed line. The thick magenta line shows the source emission component. The residuals are shown in terms of σ in the bottom panel, where blue and red points are for the source and background spectra, respectively.

(A color version of this figure is available in the online journal.)

X-ray emission associated with N 70 we created images in the 2–12 keV band, subtracted detector background, and applied vignetting corrections as for the softer bands. In particular, subtraction of detector background is important as it dominates at high energies. We carefully inspected our images but find no evidence for diffuse emission above 2 keV as implied in Reyes-Iturbide et al. (2011). The morphology in X-rays closely follows that in radio and optical, with most X-ray emission confined within the bright shell seen at longer wavelengths. A small deviation from circular morphology is observed toward the east of the SB, with fainter X-ray emission extending beyond the (broken) radio shell. There, it also correlates with fainter Hα emission. We note that this is reminiscent of the "blister" morphological classification examined in detail by Pellegrini et al. (2012). They use ionization-parameter mapping, looking at the [S II]/[O III] ratio obtained from MCELS data to estimate the optical depth of H II regions. They found a region optically thick to the east and thin to the west. This points to different conditions between the two directions. We also note that the impact of the hot gas leakage and blisters development on the shell dynamics has been recently discussed by Pittard (2013).

In addition, the X-ray surface brightness is slightly enhanced to the west, where the optical emission inside the shell is also increased. Radio emission at this position, correlating with the small molecular cloud seen in *Nanten* CO (1−0) emission (Fukui et al. 2008; Kawamura et al. 2009) (Figure 8), indicates interaction with higher densities, probably explaining the X-ray enhancement.

The X-ray spectrum of N 70 is shown in Figure 7, on top of the modeled background. To fit the source spectrum, we used a single-temperature model assuming collisional ionization equilibrium. This utilizes the Astrophysical Plasma Emission Code (APEC) in its most recent version available (v2.0.2), which includes updated atomic data (Foster et al. 2012). Possible effects of non-equilibrium ionization were also investigated by trying a plane-parallel shock model (Borkowski et al. 2001, *vpshock* in XSPEC).

We accounted for Galactic foreground absorption toward N 70 by a photoelectric absorption model (*phabs* in XSPEC) at solar metallicity, with cross-sections taken from Balucinska-Church & McCammon (1992). The foreground column density was fixed at $N_H = 6.3 \times 10^{20}$ cm^{-2} (based on the H I measurement of Dickey & Lockman 1990). An additional absorption column to model absorption by atomic gas in the LMC was included, with a half-solar metallicity (Russell & Dopita 1992). Various abundance patterns were tried, such as scaling the solar values (by number, from the table of Wilms et al. 2000) by a single fraction, fixing them at the abundances measured by Russell & Dopita (1992), or leaving the abundances of oxygen and iron free to vary.

Purely thermal models adequately fit the soft spectrum, and the lack of harder emission (above 1 keV) is confirmed by the spectral analysis. We list the best-fit parameters in Table 4. Plasma temperatures found are $kT \sim 0.25$ keV. The temperature and $N_{H\rm LMC}$ are correlated: equally acceptable fits are allowed both for a lower temperature (0.22 keV) with higher $N_{H\rm LMC}$ (1.2×10^{21} cm^{-2}) or for a higher temperature of 0.28 keV and a more moderate absorption (0.3×10^{21} cm^{-2}). We take this as an indication that the LMC-intrinsic absorption column is poorly constrained by the X-ray data alone. The ionization age ($\tau = n_e t$) is large (more than 10^{12} s cm^{-3}), suggesting that NIE effects are small or negligible. We find no evidence for abundances markedly different from LMC values, as the fits are consistent with a metallicity of 0.3–0.5. In particular, the only abundance ratio that we have access in our data (O/Fe) is consistent, within the uncertainties, with that found in the LMC ISM. With the range of absorption column densities obtained from our spectral fitting, we measure an absorption-corrected X-ray luminosity (0.2–5 keV) between 2.3×10^{35} erg s^{-1} and 2.8×10^{35} erg s^{-1}. As Chu & Mac Low (1990) already found, this is one order of magnitude more than expected from a bubble model.

3.3. Analysis of the Pressure Budget of N 70

At present, there are debates (e.g., Lopez et al. 2013; Silich & Tenorio-Tagle 2013) concerning the impact that radiation pressure has on the dynamics of the gas around young stellar clusters. Here, we estimate the pressure contributions by hot and warm gas and by dust-processed radiation.

The density of the X-ray phase can be derived from the spectral fits, using the emission measure $\mathrm{EM} = n_{\rm X,e} n_H f V$, with the electron density $n_{\rm X,e} \sim 1.2$ times the hydrogen density $n_{\rm H}$. As for the volume, V, we use a sphere of 50 pc radius. Given the morphology seen in X-ray, it is likely that this volume is an upper limit (and consequently the derived density is a lower limit). From the result of the APEC model, we have $n_{\rm H} = 0.05\ f^{-1/2}$ cm^{-3}. For the thermal pressure, we take an ideal gas law $P_{\rm X} = 1.9\ n_{\rm X} k T_{\rm X}$ (Lopez et al. 2013, Section 3.4) and then the estimated pressure is $4.56 \times 10^{-11} f^{-1/2}$ dyn cm^{-2} (where f is the filling factor for which we assume a value of one). We compare this to the values of other H II regions in Lopez et al. (2013, Figure 8 and Table 7) and find that it aligns well with the rest of the LMC sample.

We also estimate the warm gas pressure using (Lopez et al. 2013; Section 3.3), as $P_{\rm H\,II} \sim 2 n_{\rm H\,II,e} k T_{\rm H\,II}$ with $T_{\rm H\,II} = 10{,}000$ K. The electron density of the warm phase was estimated from spectroscopy (Rosado et al. 1981) to be $n_{\rm H\,II,e} = 2.5$ cm^{-3}. We point out that $n_{{\rm H\,II},e}$ is at least in the low density limit of <100 cm^{-3}. The $n_{\rm H\,II,e}$ could be better determined using the 3 cm emission assuming it is dominated by free–free emission.

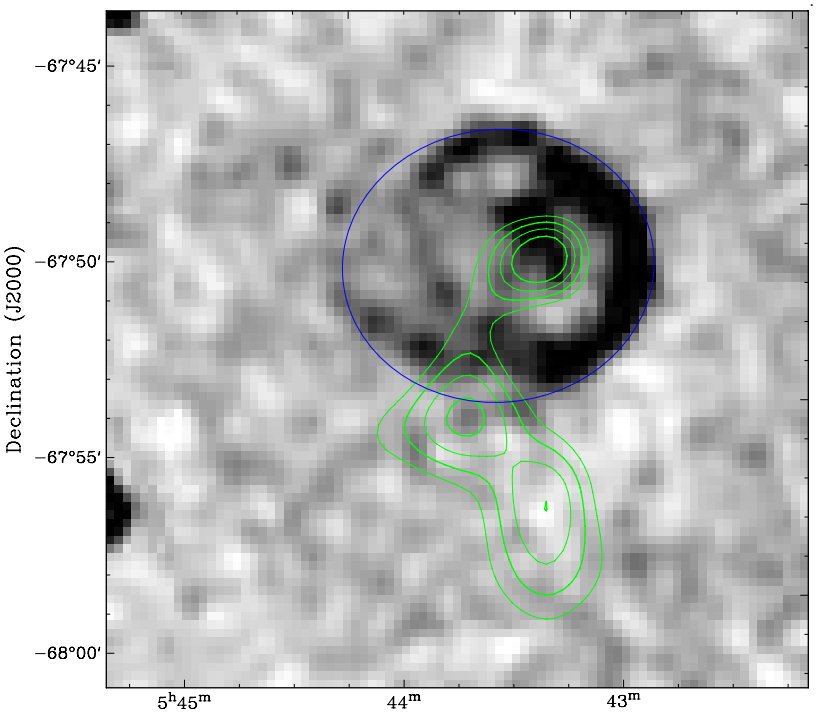

Figure 8. N 70 at 20 cm, overlaid with the velocity-integrated intensity of the CO (10) line obtained by *Nanten* (green) at 0.75, 1, 1.25, and 1.5 K km s^{-1}, showing the association between the denser environment and the emission from the SB. The blue circle indicates the measured extent of the SB.
(A color version of this figure is available in the online journal.)

Table 4
X-ray Spectral Results

Model	$N_{H\,\mathrm{LMC}}$ (10^{20} cm^{-2})	kT (eV)	τ (10^{12} s cm^{-3})	EM[a] (10^{58} cm^{-3})	O/H	Fe/H	χ^2/dof	L_X[b] (10^{35} erg s^{-1})
apec	1.4 (<5.4)	255 ± 9	···	$3.92^{+2.58}_{-1.58}$	$Z = 0.27^{+0.10}_{-0.08} Z_\odot$		6140.0/5718	2.2
vapec	$5.0^{+1.3}_{-3.0}$	248^{+16}_{-12}	···	5.5 ± 0.5	$0.20^{+0.05}_{-0.02}$	$0.21^{+0.04}_{-0.05}$	6145.1/5717	2.7
vpshock	0	256^{+18}_{-6}	47.5 (> 4.3)	$2.34^{+1.18}_{-0.35}$	0.46	0.63	6160.2/5719	1.8

Notes. All errors are given at the 90 % confidence level. Parameters without errors were fixed in the fit.
[a] Emission measure $\int n_e n_H dV$.
[b] Unabsorbed X-ray luminosity in the 0.2–5 keV range.

However, we emphasize that at least a fraction of the flux is non-thermal and estimates could be misleading. Nevertheless, taking $n_{\mathrm{H\,II,e}}$ of 2.5–100 cm^{-3}, we estimate that $P_{\mathrm{H\,II}}$ ranges from 0.69 to 27.6×10^{-11} dyn cm^{-2}. Comparing with P_{X} of 4.56×10^{-11} dyn cm^{-2}, we find that the thermal pressure is slightly higher/lower than $P_{\mathrm{H\,II}}$, as found in Lopez et al. (2013). As $P_{\mathrm{X}}/P_{\mathrm{H\,II}}$ is not $\ll 1$, we determine that there is probably no significant hot gas leakage.

Stephens et al. (2014) estimated the infrared fluxes of N 70. They found that the interstellar radiation field of N 70 has relatively little variation with an average of $U = 6.825$ (where the U is the dimensionless scale factor of energy density defined in Lopez et al. (2013; Section 3.2). This translates as a dust-processed radiation pressure of $P_{\mathrm{IR}} \sim 0.2 \times 10^{-11}$ dyn cm^{-2}. This result is significantly smaller than any other H II region analyzed by Lopez et al. (2013; Table 7, Column 3) as the dust emission for N 70 is likely driven by the shell and not the central region as suggested in Stephens et al. (2014).

Lopez et al. (2013, Section 3.1) implied that the direct radiation pressure (P_{dir}) is generally small (more than an order of magnitude below $P_{\mathrm{H\,II}}$ or P_{X}). We note that the output of the most massive stars in N 70 would not significantly differ from other H II regions in the LMC apart from 30 Dor.

4. CONCLUSION

We present a multi-frequency study of the LMC SB N 70. With a diameter of 104 pc, N 70 is one of the most prominent objects in the entire LMC. The morphology of N 70 in X-rays closely follows that in radio and optical, with most X-ray emission confined within the bright shell. The majority of the X-ray emission appears to be in the softest (0.3–0.7 keV) energy band. We do not detect any harder non-thermal X-ray emission.

We estimate the radio spectral index of N 70 to be $\alpha = -0.12 \pm 0.06$, which is typical for non-SNR objects. However, we also detect limited polarization with a maximum fractional polarization of 9% in a small area of the northwest limb indicative of an SN in the last 10^4 yr (Chu & Mac Low 1990). We report an absorption-corrected X-ray luminosity (0.2–5 keV)

between 2.3×10^{35} erg s^{-1} and 2.8×10^{35} erg s^{-1}. Finally, we examine the pressure output and find that the hot (P_X) and warm ($P_{H\,II}$) phase are consistent with other studied H II regions while the dust-processed radiation pressure (P_{IR}) is significantly smaller than in any other object studied in Lopez et al. (2013).

The ATCA is part of the Australia Telescope National Facility which is funded by the Commonwealth of Australia for operation as a National Facility managed by CSIRO. Based on observations obtained with *XMM-Newton*, an ESA science mission with instruments and contributions directly funded by ESA Member States and NASA. The *XMM-Newton* project is supported by the Bundesministerium für Wirtschaft und Technologie/Deutsches Zentrum für Luft- und Raumfahrt (BMWi/DLR, FKZ 50 OX 0001) and the Max-Planck Society. Cerro Tololo Inter-American Observatory (CTIO) is operated by the Association of Universities for Research in Astronomy Inc. (AURA), under a cooperative agreement with the National Science Foundation (NSF) as part of the National Optical Astronomy Observatories (NOAO). We gratefully acknowledge the support of CTIO and all the assistance which has been provided in upgrading the Curtis Schmidt telescope. The MCELS is funded through the support of the Dean B. McLaughlin fund at the University of Michigan and through NSF grant 9540747. P.M. acknowledges support from the BMWi/DLR grant FKZ 50 OR 1201. This research has made use of Aladin, SIMBAD and VizieR, operated at the CDS, Strasbourg, France. We used the KARMA software package developed by the ATNF. We thank the referee for numerous helpful comments that have greatly improved the quality of this paper.

Facilities: ATCA, *XMM-Newton*, *CTIO*, *Nanten*.

REFERENCES

Arnaud, K. A. 1996, in ASP Conf. Ser. 101, Astronomical Data Analysis Software and Systems V, ed. G. H. Jacoby & J. Barnes (San Francisco, CA: ASP), 17
Balucinska-Church, M., & McCammon, D. 1992, ApJ, 400, 699
Bojičić, I. S., Filipović, M. D., Parker, Q. A., et al. 2007, MNRAS, 378, 1237
Borkowski, K. J., Lyerly, W. J., & Reynolds, S. P. 2001, ApJ, 548, 820
Bozzetto, L. M., Filipovic, M. D., Crawford, E. J., De Horta, A. Y., & Stupar, M. 2012a, SerAJ, 184, 69
Bozzetto, L. M., Filipovic, M. D., Crawford, E. J., et al. 2010, SerAJ, 181, 43
Bozzetto, L. M., Filipovic, M. D., Crawford, E. J., et al. 2012b, RMxAA, 48, 41
Bozzetto, L. M., Filipović, M. D., Crawford, E. J., et al. 2012c, MNRAS, 420, 2588
Bozzetto, L. M., Filipović, M. D., Crawford, E. J., et al. 2013, MNRAS, 432, 2177
Čajko, K. O., Crawford, E. J., & Filipovic, M. D. 2009, SerAJ, 179, 55
Chu, Y.-H. 1997, AJ, 113, 1815
Chu, Y.-H., & Mac Low, M.-M. 1990, ApJ, 365, 510
Crawford, E. J., Filipovic, M. D., De Horta, A. Y., Stootman, F. H., & Payne, J. L. 2008a, SerAJ, 177, 61
Crawford, E. J., Filipović, M. D., Haberl, F., et al. 2010, A&A, 518, A35
Crawford, E. J., Filipovic, M. D., & Payne, J. L. 2008b, SerAJ, 176, 59
Danforth, C. W., & Blair, W. P. 2006, ApJ, 646, 205
Danziger, I. J., & Dennefeld, M. 1976, PASP, 88, 44
Davies, R. D., Elliott, K. H., & Meaburn, J. 1976, MmRAS, 81, 89
De Horta, A. Y., Filipović, M. D., Bozzetto, L. M., et al. 2012, A&A, 540, A25
Dickey, J. M., & Lockman, F. J. 1990, ARA&A, 28, 215
Dopita, M. A., Ford, V. L., McGregor, P. J., Mathewson, D. S., & Wilson, I. R. 1981, ApJ, 250, 103
Filipović, M. D., Cohen, M., Reid, W. A., et al. 2009, MNRAS, 399, 769
Filipović, M. D., Haynes, R. F., White, G. L., & Jones, P. A. 1998a, A&AS, 130, 421
Filipović, M. D., Haynes, R. F., White, G. L., et al. 1995, A&AS, 111, 311
Filipović, M. D., Jones, P. A., White, G. L., & Haynes, R. F. 1998b, PASA, 15, 128
Filipović, M. D., White, G. L., Haynes, R. F., et al. 1996, A&AS, 120, 77
Foster, A. R., Ji, L., Smith, R. K., & Brickhouse, N. S. 2012, ApJ, 756, 128
Fukui, Y., Kawamura, A., Minamidani, T., et al. 2008, ApJS, 178, 56
Georgelin, Y. M., Georgelin, Y. P., Laval, A., Monnet, G., & Rosado, M. 1983, A&AS, 54, 459
Gooch, R. 1996, in ASP Conf. Ser. 101, Astronomical Data Analysis Software and Systems V, ed. G. H. Jacoby & J. Barnes (San Francisco, CA: ASP), 80
Grondin, M.-H., Sasaki, M., Haberl, F., et al. 2012, A&A, 539, A15
Henize, K. G. 1956, ApJS, 2, 315
Hughes, A., Staveley-Smith, L., Kim, S., Wolleben, M., & Filipović, M. 2007, MNRAS, 382, 543
Hughes, A., Wong, T., Ekers, R., et al. 2006, MNRAS, 370, 363
Inglis, M. D., & Kitchin, C. R. 1990, MNRAS, 246, 358
Kawamura, A., Mizuno, Y., Minamidani, T., et al. 2009, ApJS, 184, 1
Lopez, L. A., Krumholz, M. R., Bolatto, A. D., et al. 2013, arXiv:1309.5421
Lucke, P. B., & Hodge, P. W. 1970, AJ, 75, 171
Maggi, P., Haberl, F., Bozzetto, L. M., et al. 2012, A&A, 546, A109
Mills, B. Y., Turtle, A. J., Little, A. G., & Durdin, J. M. 1984, AuJPh, 37, 321
Milne, D. K., Caswell, J. L., & Haynes, R. F. 1980, MNRAS, 191, 469
Oey, M. S. 1996a, ApJ, 467, 666
Oey, M. S. 1996b, ApJS, 104, 71
Oey, M. S., & García-Segura, G. 2004, ApJ, 613, 302
Oey, M. S., Groves, B., Staveley-Smith, L., & Smith, R. C. 2002, AJ, 123, 255
Oey, M. S., & Kennicutt, R. C., Jr. 1997, MNRAS, 291, 827
Pellegrini, E. W., Oey, M. S., Winkler, P. F., et al. 2012, ApJ, 755, 40
Pietrzyński, G., Graczyk, D., Gieren, W., et al. 2013, Natur, 495, 76
Pittard, J. M. 2013, MNRAS, 435, 3600
Reyes-Iturbide, J., Rosado, M., Rodríguez-González, A., Velázquez, P. F., & Ambrocio-Cruz, P. 2011, RMxAA, 40, 199
Rodríguez-González, A., Velázquez, P. F., Rosado, M., et al. 2011, ApJ, 733, 34
Rosado, M., Georgelin, Y. P., Georgelin, Y. M., Laval, A., & Monnet, G. 1981, A&A, 97, 342
Russell, S. C., & Dopita, M. A. 1992, ApJ, 384, 508
Sault, B., & Killeen, N. 2006, Miriad Users Guide (Epping: Australia Telescope National Facility)
Sault, R. J., & Wieringa, M. H. 1994, A&AS, 108, 585
Silich, S., & Tenorio-Tagle, G. 2013, ApJ, 765, 43
Slater, C. T., Oey, M. S., Li, A., et al. 2011, ApJ, 732, 98
Smith, C., Leiton, R., & Pizarro, S. 2000, in ASP Conf. Ser. 221, Stars, Gas and Dust in Galaxies: Exploring the Links, ed. D. Alloin, K. Olsen, & G. Galaz (San Francisco, CA: ASP), 83
Stephens, I. W., Evans, J. M., Xue, R., et al. 2014, ApJ, 784, 147
Strüder, L., Briel, U., Dennerl, K., et al. 2001, A&A, 365, L18
Turner, M. J. L., Abbey, A., Arnaud, M., et al. 2001, A&A, 365, L27
Wang, Q., & Helfand, D. J. 1991, ApJ, 373, 497
Weaver, R., McCray, R., Castor, J., Shapiro, P., & Moore, R. 1977, ApJ, 218, 377
Wilms, J., Allen, A., & McCray, R. 2000, ApJ, 542, 914

A.36 Related Paper 36

Bozzetto, L. M., Filipović, M. D., Urošević, D., Kothes, R., and Crawford, E. J. (2014a). Radio-continuum study of Large Magellanic Cloud supernova remnant J0509-6731. *MNRAS*, 440:3220–3225

My contribution was to assist in the data analysis. This is a 10% contribution.

Monthly Notices of the ROYAL ASTRONOMICAL SOCIETY

MNRAS **440,** 3220–3225 (2014) doi:10.1093/mnras/stu499

Radio-continuum study of Large Magellanic Cloud supernova remnant J0509−6731

L. M. Bozzetto,[1⋆] M. D. Filipović,[1] D. Urošević,[2,3] R. Kothes[4] and E. J. Crawford[1]

[1]*School of Computing and Mathematics, University of Western Sydney Locked Bag 1797, Penrith South DC, NSW 1797, Australia*
[2]*Department of Astronomy, Faculty of Mathematics, University of Belgrade, Studentski trg 16, 11000 Belgrade, Serbia*
[3]*Isaac Newton Institute of Chile, Yugoslavia Branch*
[4]*Dominion Radio Astrophysical Observatory, National Research Council Canada, Herzberg Institute of Astrophysics, PO Box 248, Penticton, BBC V2A 6J9, Canada*

Accepted 2014 March 10. Received 2014 March 6; in original form 2013 August 5

ABSTRACT

We present a detailed study of Australia Telescope Compact Array observations ($\lambda = 20$, 13, 6 and 3 cm) of supernova remnant (SNR) J0509−6731 in the Large Magellanic Cloud. The remnant has a ring morphology with brightened regions towards the south-western limb. We also find a second brightened inner ring which is only seen in the radio continuum. The SNR is almost circular, with a diameter ranging from 7 to 8 pc, and a steep radio spectral index between 36 and 3 cm of $\alpha = -0.73 \pm 0.02$, which is characteristic of younger SNRs. We also report detection of radially orientated polarization across the remnant at 6 cm, with a mean fractional polarization level of $P \cong (26 \pm 13)$ per cent. We find the magnetic field (∼168 μG) and $\Sigma-D$ ($\Sigma = 1.1 \times 10^{-19}$ W m^{-2} Hz^{-1} sr^{-1}, $D = 7.35$ pc) to be consistent with other young remnants.

Key words: polarization – ISM: supernova remnants – Magellanic Clouds – radio continuum: ISM.

1 INTRODUCTION

Supernova remnants (SNRs) play a vital role in the Universe, enriching the interstellar medium (ISM) and significantly influences the ISMs evolution, structure and physical properties. The study of SNRs in our own Galaxy is not ideal due to difficulties in estimating accurate distances (which inhibits accurate analysis such as extent and surface brightness) and the high level of absorption in the direction of the Galactic plane. As an alternative, the Large Magellanic Cloud (LMC) at a proximity of 50 kpc (Macri et al. 2006) is a near-ideal galaxy for the study of SNRs due to its high active star-forming regions (such as 30 Dor) and location outside of the Galactic plane at an angle of 35° (van der Marel & Cioni 2001). Its distance from earth allows us to assume that objects located within are at approximately the same distance, aiding in various analysis methodologies.

In the radio continuum, SNRs predominately emit non-thermal continuum emission and generally exhibit a spectrum of $\alpha \sim -0.5$ (defined by $S \propto \nu^{\alpha}$). Although this can vary as there exists a wide variety of SNRs in different stages of evolution and expanding in different environments (Filipovic et al. 1998).

In this paper, we present new radio-continuum observations of SNR J0509−6731, along with archival radio continuum, X-ray & optical observations. This source was originally classified by Long, Helfand & Grabelsky (1981) as an SNR in their X-ray survey using the *Einstein Observatory*, recording a position of RA (B1950) = $05^{h}09^{m}28^{s}$ and Dec. (B1950) = $-67°34'55''$. Tuohy et al. (1982) estimate an X-ray size of ∼25 arcsec, an optical size of 25 arcsec and estimated a shock velocity of >3600 km s^{-1}. No object was found at this position in the 408 MHz image by Clark, Little & Mills (1976). However, reanalysis of the 408 MHz survey data by Tuohy et al. (1982), found weak emission at this point finding a flux density measurement of 95 ± 15 mJy. Tuohy et al. (1982) also observed this object at 5 GHz and measured a flux density of 30 ± 3 mJy. They note that on a surface brightness to diameter ($\Sigma-D$) diagram, SNR J0509−6731 fell below the mean line by a factor of 13, which is comparable to young Galactic SNRs. They comment that this low $\Sigma-D$ might be a result of differences in the electron acceleration process in Balmer dominated remnants. The remnant is described as a Balmer dominated SNR expanding into a region with a relatively low density ($n_{\rm H} \leq 0.02^{-3}$) of neutral hydrogen and argue for a Type Ia supernova (SN). Mathewson et al. (1983) measure an X-ray size of 27 arcsec and a radio spectrum of $\alpha = -0.46$. Fusco-Femiano & Preite-Martinez (1984) estimate a shock temperature of 3.1 KeV, an age of 900 yr, total swept up mass of 26 $M_{\odot}$ and a shock velocity of 1600 km s^{-1}, which is well below that proposed by Tuohy et al. (1982) of >3600. Mills et al. (1984) record a 843 MHz flux density of 82 mJy, updating the spectral index to −0.48 and also record a surface brightness of $>6.4 \times 10^{20}$ W m^{-2} Hz^{-1} sr^{-1}. van den Bergh (1988) also argues for a younger remnant, commenting that the small diameter indicates an age of ≤1000 yr. Chu & Kennicutt (1988) give this SNR OB association 400 pc to LH38 and class this remnant as Population II. Smith et al. (1991) record

⋆ E-mail: luke.bozzetto@gmail.com

Table 1. Summary of ATCA observations reduced and used in this study.

Date	Scan time (min)	Right Ascension	Declination	Array	Frequencies (MHz)	BWidth (MHz)	Chan	Project
2011-Nov-16	49.7	$5^h9^m31^s.00$	$-67°31'16''.20$	EW367	5500, 9000	2048.0	2049	C634[a]
2011-Nov-15	15.0	$5^h9^m31^s.00$	$-67°31'16''.20$	EW367	5500, 9000	2048.0	2049	C634[a]
2010-Nov-29	98.0	$5^h9^m30^s.00$	$-67°30'60''.00$	6A	5500, 9000	2048.0	2049	C2367
2010-Nov-28	50.3	$5^h9^m30^s.00$	$-67°30'60''.00$	6A	5500, 9000	2048.0	2049	C2367
2005-Jun-24	819.7	$5^h9^m51^s.48$	$-67°16'22''.17$	6B	1384, 1472	128.0	33	C1395
2005-Apr-18	819.8	$5^h9^m51^s.48$	$-67°16'22''.17$	1.5A	1384, 1472	128.0	33	C1395
1997-Aug-11	643.7	$5^h9^m30^s.00$	$-67°30'60''.00$	750B	4800, 4928	128.0	33	C479
1994-Sep-23	57.0	$5^h9^m31^s.00$	$-67°31'15''.00$	1.5D	1380, 2378	128.0	33	C354
1994-Sep-22	482.3	$5^h9^m31^s.00$	$-67°31'15''.00$	1.5D	1380, 2378	128.0	33	C354
1994-Sep-17	260.7	$5^h9^m31^s.00$	$-67°31'15''.00$	1.5B	1380, 2378	128.0	33	C354

[a]The observing procedure in this project is described in the text.

Table 2. Integrated flux densities of SNR J0509−6731.

λ (cm)	ν (MHz)	ATCA Project	rms (mJy)	Beam size (arcsec)	$S_{\rm Total}$ (mJy)	$\Delta S_{\rm Total}$ (mJy)	Reference
73	408	*MOST*	40	157.3 × 171.6	95	15	Tuohy et al. (1982)
36	843	*MOST*[a]	0.4	46.4 × 43.0	111	11	This work
36	843	SUMMS[b]	1.5	48.5 × 45.0	109	11	This work
20	1373	C354	0.3	21.2 × 17.3	73	7	This work
20	1377	C373[c]	0.7	40.0 × 40.0	80	8	This work
20	1381	C1395	0.7	13.0 × 12.2	79	8	This work
13	2377	C354	0.3	12.3 × 10.1	51	5	This work
6	4800	Multiple[d]	1.0	35.0 × 35.0	30	3	This work
6	4800	C479	0.3	28.6 × 11.8	30	3	This work
6	5000	Parkes	–	300 × 300	30	3	Tuohy et al. (1982)
6	5500	C634, C2367	0.1	2.6 × 2.3	31	3	This work
3	8640	Multiple[d]	1.0	22.0 × 22.0	19	2	This work
3	9000	C634	0.2	22.7 × 16.0	20	2	This work

[a]From the image described in Mills et al. (1984).
[b]From the image described in Mauch et al. (2008).
[c]From the image described in Hughes et al. (2007).
[d]From the image described in Dickel et al. (2010).

a shock velocity >2000 km s^{-1} and is in agreement with an age of ≤1000 yr. Hughes et al. (1995) note that there is strong emission of elements from silicon to neon and argues for Type Ia SN. Haberl & Pietsch (1999) record an extent of 9.1arcsec and give this SNR the association [HP99] 542. Warren & Hughes (2004) confirmed that the SN ejecta had an abundance distribution consistent with Type Ia SN explosion models. They also found that the reverse shock is propagating back into the Fe-rich ejecta and suggests that the brightening in the south-west is due to enhanced density in or a deeper penetration of the reverse shock into a portion of the ejecta shell and may be caused by enhanced ambient density or intrinsic asymmetry in the explosion itself. Rest et al. (2005) confirmed the Type Ia classification using light echo spectra and also established it as an SN1991T-type energetic event. Additionally, light echo apparent motion was used to estimate the age of the SNR to be 400 ± 120 yr. Arbutina & Urošević (2005) used a 1 GHz flux density of 70 mJy to estimate a surface brightness–diameter of $(\Sigma-D) = (4.2 \times 10^{-20}$ W m^{-2} Hz^{-1} sr^{-1}, 7 pc). Ghavamian et al. (2007) estimate an age of 295–585 yr, a shock velocity of $V_{\rm s} \geq 4000$ km s^{-1}, they detect broad Lyβ emission and classify this object as a non-radiative (adiabatic) of Type Ia. Badenes et al. (2008) found an age of ∼400 yr, kinetic energy of 1.4×10^{51} erg and concluded that the X-ray properties of SNR J0509−6731 were consistent with models of an energetic 91T-type SN Ia explosion. Seok et al. (2008) state SNR J0509−6731 is thought to be dominated by thermal dust continuum with T(dust) 94 ± 3 K and a dust mass of $8.7 \pm 2.5 \times 10^{-5}$ solar masses. Kosenko et al. (2008) also find that the reverse shock has recently reach the iron layers of the ejecta and are in agreement with previous studies regarding the brightening in the south-west resulting from an asymmetric explosion or density enhancement in the ISM. Models in this study were in good agreement with the observations with circumstellar density of 3×10^{-25} g cm^{-3}, age of ∼400 yr and velocity of ∼5000 km s^{-1}. Desai et al. (2010) found no association between this remnant and a young stellar object (YSO), nor the molecular clouds. Schaefer & Pagnotta (2012) found no ex-companion star to a visual magnitude limit of 26.9 within a radius of 1.43 arcsec, which they state would infer a double-degenerate SN system. Di Stefano & Kilic (2012) and Wheeler (2012) discuss the possibility of this SNR still being the result of a single-degenerate explosion.

The observations, data reduction and imaging techniques are described in Section 2. The astrophysical interpretation of newly obtained moderate-resolution total intensity and polarimetric images in combination with archival *Chandra* X-ray and *Hubble Space Telescope* (*HST*) Hα observations are discussed in Section 3.

2 OBSERVATIONS AND DATA REDUCTION

Five Australia Telescope Compact Array (ATCA) projects (C1395, C354, C479, C634 and C2367; at wavelengths of 20, 20/13, 6, 6/3

and 6/3 cm, respectively) were reduced and analysed in this study. A summary of these projects can be seen in Table 1. Project C634 contain our observations of this SNR, which were taken on 2011 November 15 and 16. These observations were taken by the ATCA using the Compact Array Broadband Backend (CABB) receiver with the array configuration EW367, at wavelengths of 3 and 6 cm ($\nu = 9000$ and 5500 MHz). The observations were carried out in the so called 'snap-shot' mode, totalling ∼50 min of integration over a 14 h period. Source PKS B1934-638 was used for primary (flux density) calibration and source PKS B0530-727 was used for secondary (phase) calibration. At 6 cm, the shorter baselines from the EW367 observations were complemented by observations taken from project C2367, which uses a longer baseline array configuration (6A; Table 1), allowing for a higher resolution image. However, we were unable to make use of the 3 cm data from ATCA project C2367 due to strong interference. This lack of data meant we lost the longer baselines and as a result, no high-resolution image is available at this wavelength.

The MIRIAD[1] (Sault, Teuben & Wright 1995) and KARMA[2] (Gooch 1995) software packages were used for reduction and analysis. More information on the observing procedure and other sources observed in this project can be found in Bozzetto et al. (2012a,b,c, 2013) and de Horta et al. (2012).

Images were formed using MIRIAD multifrequency synthesis (Sault & Wieringa 1994) and natural weighting. They were deconvolved with primary beam correction applied. The same procedure was used for both *U* and *Q* Stokes parameter maps.

We measured the flux density of SNR J0509−6731 from 11 separate images between 36 and 3 cm, which are summarized in Table 2. We obtain five of these flux density measurements from available mosaics; at 36 cm from the *Molonglo Synthesis Telescope* (*MOST*) mosaic image (as described in Mills et al. 1984) and from the SUMMS mosaic image (Mauch et al. 2008), 20 cm from the mosaic by Hughes et al. (2007). We also used 6 and 3 cm mosaics published by Dickel et al. (2010). The remaining six measurements were taken from the data reduced and analysed in this study using the projects listed in Table 1. Errors in flux density measurements predominately arose from uncertainties in defining the 'edge' of the remnant. However, we estimate these errors to be <10 per cent (with the exception of the 73 cm measurement, where the associated error is given by Tuohy et al. 1982). Using the flux density measurements in Table 2 (73–3 cm), we estimate a spectral index of $\alpha = -0.59$. However, it can be seen that the spectrum breaks at 73 cm, where the recorded flux density is at a level well below that which is expected (by ∼50 per cent). Low-frequency absorption can result in this 'break', either through synchrotron self absorption or thermal absorption. A low-frequency turnover assumed to be from free–free absorption was found for seven SNRs in M82 (Wills et al. 1997) at levels comparable to our 408 MHz turnover for SNR J0509−6731. However, M82 has an environment significantly denser than the relatively rarefied environment of SNR J0509−6731, and therefore, the turnover is expected to occur at higher frequencies in this denser environment. The more probable explanation for this break is observational effects or an issue with the measurement. Omitting this outlying value from our calculation results in a steeper spectral index with a value of $\alpha = -0.73 \pm 0.02$.

[1] http://www.atnf.csiro.au/computing/software/miriad/
[2] http://www.atnf.csiro.au/computing/software/karma/

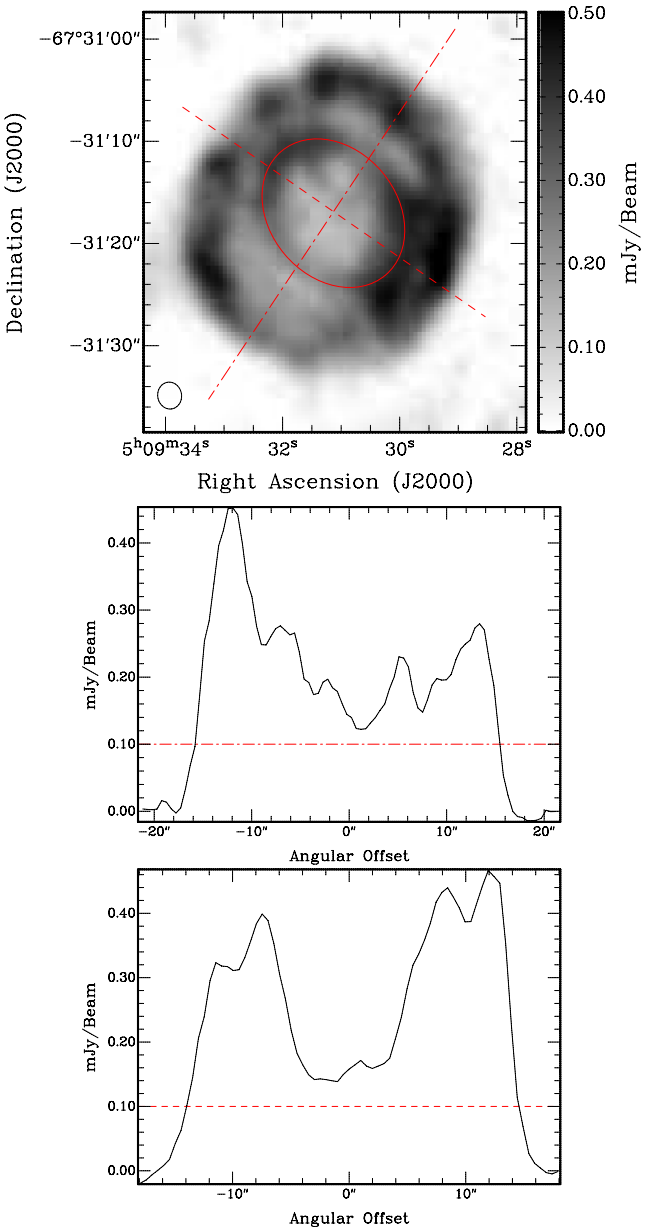

Figure 1. The top image shows the 6 cm intensity image of SNR J0509−6731 overlaid with the approximate major (NW–SE) and minor (NE–SW) axis. The middle and lower images show the one-dimensional cross-section along the overlaid lines in the top image, with a superimposed line at 3σ.

3 RESULTS AND DISCUSSION

SNR J0509−6731 exhibits a ring-like morphology (Fig. 1), centred at RA (J2000) = $05^{h}09^{m}31\overset{s}{.}0$, Dec. (J2000) = $-67^{\circ}31'16\overset{''}{.}4$. We estimate the spatial extent of SNR J0509−6731 (Fig. 1) at the 3σ (Table 2; Col. 4) level (0.1 mJy) along the major (NW–SE) and minor (NE–SW) axes (PA = −34°). Its size at 6 cm (5500 MHz) is 31 arcsec × 29 arcsec ± 1 arcsec (8 × 7 pc with 0.25 pc uncertainty in each direction). We estimate the ring thickness of SNR J0509−6731 to ∼6 arcsec at 6 cm, about 40 per cent of the SNR's radius.

We find a centrally brightening ring in the interior of this remnant (Fig. 1), something that is not common among SNRs. We estimate

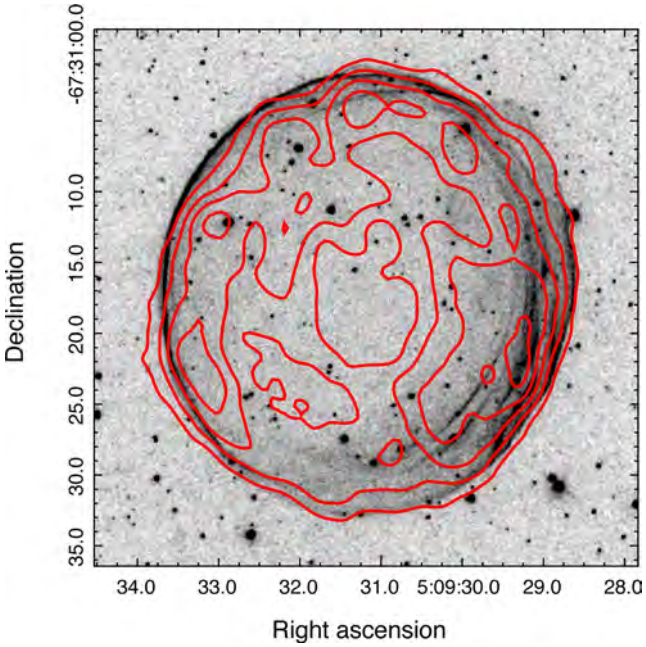

Figure 2. *HST* Hα image of SNR J0509−6731 overlaid with 6 cm ATCA contours. The contours are 3, 6, 9, 12 and 15σ (where $\sigma = 33$ μJy).

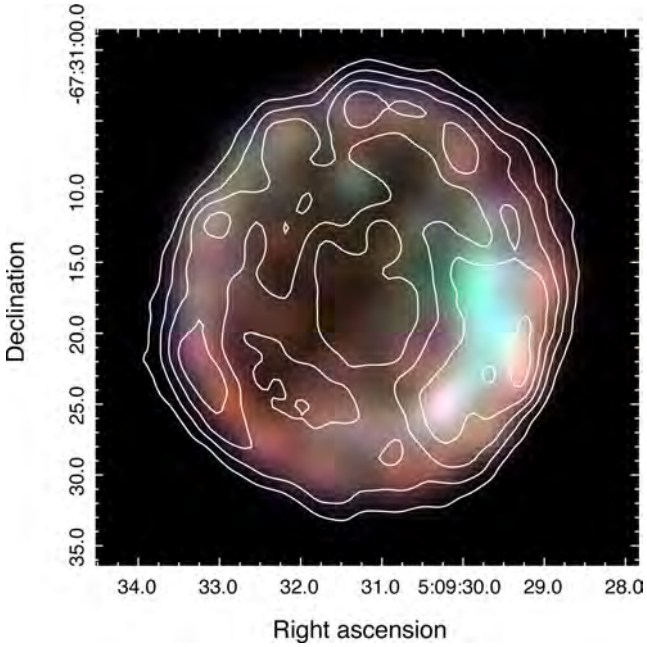

Figure 3. *Chandra* X-ray colour composite image of SNR J0509−6731 at energy levels 0.3–0.6 keV (red) 0.6–0.95 keV (green) and 0.95–7.0 keV (blue). The image has been smoothed using a Gaussian filter ($\sigma = 2$ pixels). ATCA radio contours (at 6 cm) have been overlaid at levels of 3, 6, 9, 12 & 15σ (where $\sigma = 33$ μJy).

the size of this ring at 6 cm to be 16 arcsec × 12 arcsec ± 1 arcsec (4 × 3 pc with 0.25 pc uncertainty in each direction) at PA = 50°.

There is evident correlation between our 6 cm (5500 MHz) radio-continuum emission and the optical Hα emission (*HST*; PropID 11015) for this remnant (Fig. 2). This is particularly evident towards the south-western limb of the SNR (where radio emission is the strongest), where we can see the radio 3σ contour closely following the edge of the optical Hα emission. The astrometry involved in aligning all images in this paper is within 1 arcsec.

We also find similarities between our 6 cm (5500 MHz) radio-continuum emission and 0.3–7.0 keV X-ray emission (*Chandra*; observation ID [ObsID] 776[3]) as seen in Fig. 3.

The optical Hα emission shows highly compressed filaments, denoting at high angular resolution the location of the forward shock moving into the ISM, outlying the ellipsoidal shell region interior to which the smooth, low compressed radio and X-ray emission comes.

The non-thermal nature of this remnant in the radio continuum is confirmed in the spectral energy distribution, shown in Fig. 4, where $\alpha_2 = -0.73 \pm 0.02$. This value is steeper in comparison with typical values of $\alpha = -0.5$ for LMC SNRs (Filipovic et al. 1998) and is more consistent with young SNRs, shown in Table 3. This is in agreement with current estimation of the remnants age, which places it at ∼400 yr (Rest et al. 2005; Ghavamian et al. 2007; Badenes et al. 2008; Kosenko et al. 2008).

A spectral index map was created between 13 and 6 cm (Fig. 5) to show the spatial spectral variations in the remnant. This was achieved by convolving and re-gridding the 6 cm image with the tasks `regrid` and `convol`, to match the size and resolution of the 13 cm image, which had the poorest resolution and thus allowing no oversampling to occur. A spectral index map was then created using these maps from both observed frequencies. This was done

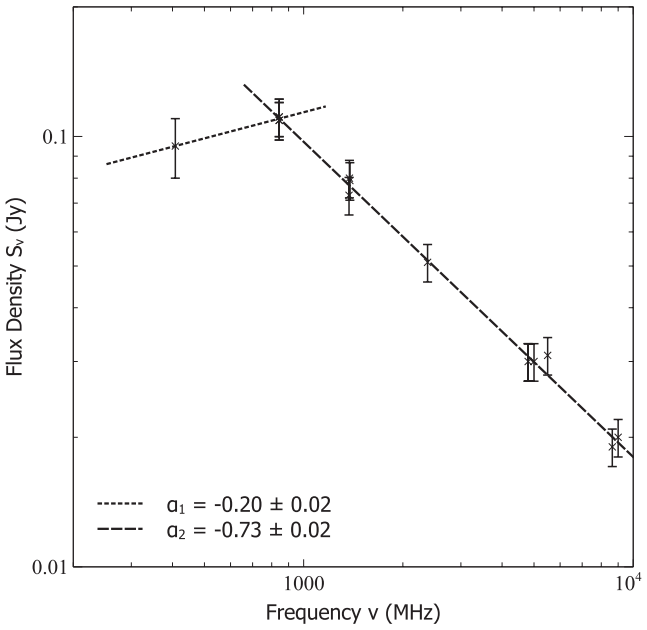

Figure 4. Radio-continuum spectrum of SNR J0509−6731. The markers represent error margins of 10 per cent.

using the MIRIAD task `maths`, which calculated the spectral index[4] (α) of each pixel above a level of 3σ. Pixels below this level were blanked in the spectral index map. We note to two distinctive and opposite regions of somewhat steeper spectra (∼$\alpha = -0.7$) marked in yellow around northern and southern regions of the SNR.

[3] Taken from http://hea-www.harvard.edu/ChandraSNR/snrcat_lmc.html, which is maintained by Fred Seward (SAO).

[4] spectral index α is defined by $S_\nu = \nu^\alpha$, where S_ν is the integrated flux density and ν is the frequency.

Table 3. Comparison of SNR J0509−6731 to similar remnants.

Name	Age (yr)	α^*	P (%)	P_λ (cm)	Reference
0509−67.5	∼400	−0.73	26 ± 13	6	This work
Cassiopeia A	–	−0.77	8–10	6	Anderson, Keohane & Rudnick (1995)
Tycho	∼441	−0.65	20-30[a]	6	Dickel, van Breugel & Strom (1991)
Kepler	∼409	−0.64	6	6	DeLaney et al. (2002)
SN 1006	∼1000	−0.6	17[d]	20	Reynoso, Hughes & Moffett (2013)
N132D	∼2500[b]	−0.70	4	6	Dickel & Milne (1995)
0519−6902	∼600[c]	−0.53	2	6	Bozzetto et al. (2012b)

*Galactic spectral indices came from the catalogue by Green (2009).
[a]Based on the mean polarization found for the brightened limbs.
[b]Vogt & Dopita (2011).
[c]Borkowski et al. (2006).
[d]Higher polarization (near the theoretical limit of ∼70 per cent) was found in regions of weaker radio emission.

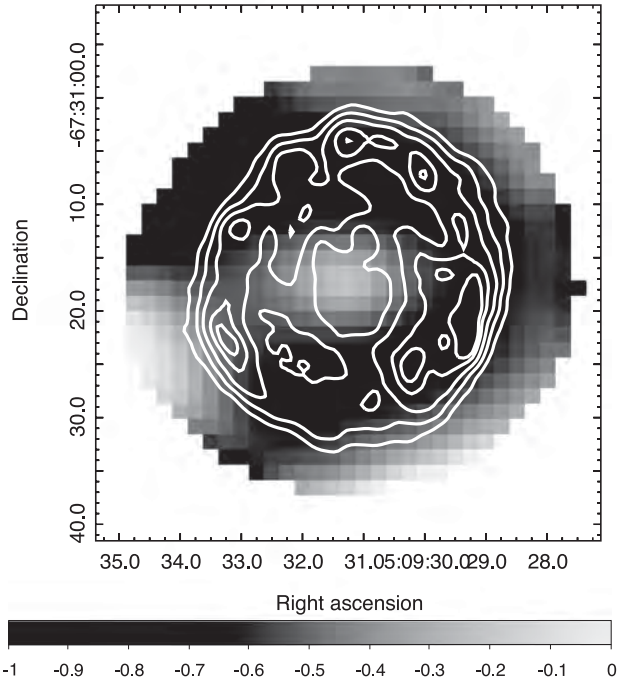

Figure 5. Radio-continuum spectrum map of SNR J0509−6731 between 13 and 6 cm. The sidebar quantifies the spectral index scale. ATCA radio contours (at 6 cm) have been overlaid at 3, 6, 9, 12 and 15σ (where σ = 33 μJy).

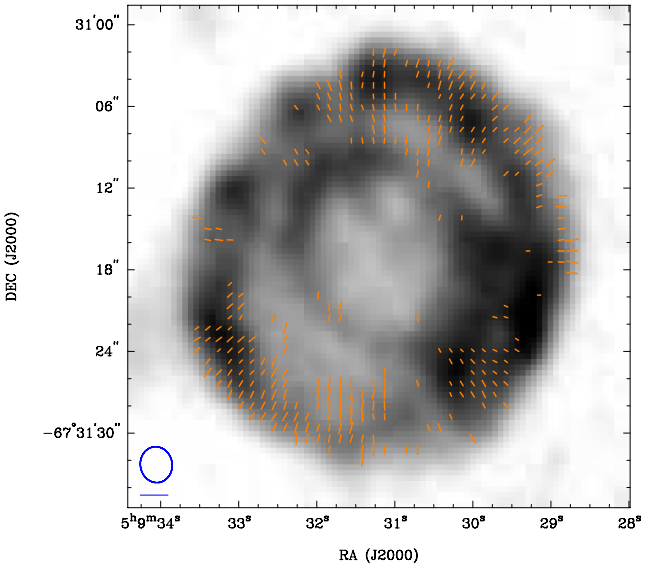

Figure 6. *B*-field polarization vectors overlaid on 6 cm ATCA image of SNR J0509−6731. The blue ellipse in the lower-left corner represents the synthesized beamwidth of 2.6 arcsec × 2.3 arcsec and the blue line below the ellipse represents a polarization vector of 100 per cent.

A fractional polarization image was created at 6 cm using Q and U parameters (Fig. 6). A signal-to-noise cut-off of 2σ was used for the Q and U images, while a level of 6σ was used for the intensity image. Values that fall below these cut-off levels are blanked in the output image. The length of the vectors has been reduced by 50 per cent and placed every 1.5 pixels for display purposes. The mean fractional polarization was calculated using flux density and polarization:

$$P = \frac{\sqrt{S_Q^2 + S_U^2}}{S_I},$$

where S_Q, S_U and S_I are integrated intensities for the Q, U and I Stokes parameters. We estimate a mean fractional polarization value of $P = 26 \pm 13$ per cent at 6 cm. The magnetic field of the remnant at 6 cm appears to be radially oriented, which is to be expected from Rayleigh–Taylor instabilities in the decelerating remnant (Gull 1975; Chevalier 1976). This is consistent with similarly young SNRs in our own Galaxy, as well as in the LMC (for e.g. those listed in Table 3).

Without reliable polarization measurements at a second frequency, we cannot determine the Faraday rotation and thus cannot deduce the magnetic field strength. However, we make use of the equipartition formula as given by Arbutina et al. (2012) to estimate the magnetic field strength of this SNR. This formula is based on the Bell (1978) diffuse shock acceleration theory. This derivation is purely analytical, accommodated especially for the estimation of magnetic field strength in SNRs. The average equipartition field over the whole shell of SNR J0509−6731 is ∼168 μG with an estimated minimum energy of $E_{\rm min} = 1.2 \times 10^{49}$ erg (see Arbutina et al. 2012; and corresponding 'calculator[5]). This value is typical of young SNRs with a strongly amplified magnetic field.

[5] The calculator is available at http://poincare.matf.bg.ac.rs/~arbo/eqp/.

The position of SNR J0509−6731 at the surface brightness to diameter ($\Sigma-D$) diagram ($\Sigma = 1.1 \times 10^{-19}$ W m^{-2} Hz^{-1} sr^{-1}, $D = 7.35$ pc) by Berezhko & Völk (2004), suggests that this remnant is in the transition phase between late free expansion and early Sedov phase, with an explosion energy of $\sim 0.25 \times 10^{51}$, which evolves in an environment with a density of ~ 0.3 cm^{-3}. This estimate of minimum explosion energy is lower than that found by Badenes et al. (2008) who found a value of 1.40×10^{51}, a result of using different models. Our estimate of surface brightness is comparable to values found for galactic remnants in rarified environments, such as Tycho's SNR ($\Sigma = 1.32 \times 10^{-19}$ W m^{-2} Hz^{-1} sr^{-1}, $D = 9.3$ pc) and *Kepler*'s SNR ($\Sigma = 3.18 \times 10^{-19}$ W m^{-2} Hz^{-1} sr^{-1}, $D = 5.2$ pc; Pavlović et al. 2013).

4 CONCLUSION

We have used observations taken by the ATCA to carry out a detailed radio-continuum study on SNR J0509−6731. With a size of only $D \cong 8 \times 7$ pc, SNR J0509−6731 is one of the smallest remnants currently known in the LMC. We find a relatively steep spectrum of ($\alpha = -0.73 \pm 0.02$) and relatively strong magnetic field of 168 μG, which is characteristic of a young remnant (e.g. Jiang, Zhang & Fang 2013). Its small size also sets this SNR apart from typical $\Sigma-D$ values of SNRs at $\Sigma = 1.1 \times 10^{-19}$ W m^{-2} Hz^{-1} sr^{-1}, $D = 7.35$ pc, though, still in close proximity to another Balmer-dominated LMC SNR, SNR J0519−6902. This SNR shares the same radially orientated polarization as other young Type Ia remnants, with a mean fractional polarization level of $P = (26 \pm 13)$ per cent.

ACKNOWLEDGEMENTS

The Australia Telescope Compact Array is part of the Australia Telescope which is funded by the Commonwealth of Australia for operation as a National Facility managed by CSIRO. This research is supported by the Ministry of Education and Science of the Republic of Serbia through project no. 176005.

REFERENCES

Anderson M. C., Keohane J. W., Rudnick L., 1995, ApJ, 441, 300
Arbutina B., Urošević D., 2005, MNRAS, 360, 76
Arbutina B., Urošević D., Andjelić M. M., Pavlović M. Z., Vukotić B., 2012, ApJ, 746, 79
Badenes C., Hughes J. P., Cassam-Chenaï G., Bravo E., 2008, ApJ, 680, 1149
Bell A. R., 1978, MNRAS, 182, 443
Berezhko E. G., Völk H. J., 2004, A&A, 427, 525
Borkowski K. J. et al., 2006, ApJ, 642, L141
Bozzetto L. M., Filipovic M. D., Crawford E. J., Payne J. L., de Horta A. Y., Stupar M., 2012a, Rev. Mex. Astron. Astrofis., 48, 41
Bozzetto L. M., Filipovic M. D., Urosevic D., Crawford E. J., 2012b, Serb. Astron. J., 185, 25
Bozzetto L. M. et al., 2012c, MNRAS, 420, 2588
Bozzetto L. M. et al., 2013, MNRAS, 432, 2177
Chevalier R. A., 1976, ApJ, 207, 872
Chu Y.-H., Kennicutt R. C., Jr, 1988, AJ, 96, 1874
Clarke J. N., Little A. G., Mills B. Y., 1976, Aust. J. Phys. Astrophys. Suppl., 40, 1
de Horta A. Y. et al., 2012, A&A, 540, A25
DeLaney T., Koralesky B., Rudnick L., Dickel J. R., 2002, ApJ, 580, 914
Desai K. M. et al., 2010, AJ, 140, 584
Di Stefano R., Kilic M., 2012, ApJ, 759, 56
Dickel J. R., Milne D. K., 1995, AJ, 109, 200
Dickel J. R., van Breugel W. J. M., Strom R. G., 1991, AJ, 101, 2151
Dickel J. R., McIntyre V. J., Gruendl R. A., Milne D. K., 2010, AJ, 140, 1567
Filipovic M. D. et al., 1998, A&AS, 127, 119
Fusco-Femiano R., Preite-Martinez A., 1984, ApJ, 281, 593
Ghavamian P., Blair W. P., Sankrit R., Raymond J. C., Hughes J. P., 2007, ApJ, 664, 304
Gooch R., 1995, in Shaw R. A., Payne H. E., Hayes J. J. E., eds, ASP Conf. Ser. Vol. 77, Astronomical Data Analysis Software and Systems IV. Astron. Soc. Pac., San Francisco, p. 144
Green D. A., 2009, Bull. Astron. Soc. India, 37, 45
Gull S. F., 1975, MNRAS, 171, 263
Haberl F., Pietsch W., 1999, A&AS, 139, 277
Hughes J. P. et al., 1995, ApJ, 444, L81
Hughes A., Staveley-Smith L., Kim S., Wolleben M., Filipović M., 2007, MNRAS, 382, 543
Jiang Z. J., Zhang L., Fang J., 2013, MNRAS, 433, 1271
Kosenko D., Vink J., Blinnikov S., Rasmussen A., 2008, A&A, 490, 223
Long K. S., Helfand D. J., Grabelsky D. A., 1981, ApJ, 248, 925
Macri L. M., Stanek K. Z., Bersier D., Greenhill L. J., Reid M. J., 2006, ApJ, 652, 1133
Mathewson D. S., Ford V. L., Dopita M. A., Tuohy I. R., Long K. S., Helfand D. J., 1983, ApJS, 51, 345
Mauch T., Murphy T., Buttery H. J., Curran J., Hunstead R. W., Piestrzynski B., Ropbertson J. G., Sadler E. M., 2008, VizieR Online Data Catalog, 8081, 0
Mills B. Y., Turtle A. J., Little A. G., Durdin J. M., 1984, Aust. J. Phys., 37, 321
Pavlović M. Z., Urošević D., Vukotić B., Arbutina B., Göker Ü. D., 2013, ApJS, 204, 4
Rest A. et al., 2005, Nature, 438, 1132
Reynoso E. M., Hughes J. P., Moffett D. A., 2013, AJ, 145, 104
Sault R. J., Wieringa M. H., 1994, A&AS, 108, 585
Sault R. J., Teuben P. J., Wright M. C. H., 1995, in Shaw R. A., Payne H. E., Hayes J. J. E., eds, ASP Conf. Ser. Vol. 77, Astronomical Data Analysis Software and Systems IV. Astron. Soc. Pac., San Francisco, p. 433
Schaefer B. E., Pagnotta A., 2012, Nature, 481, 164
Seok J. Y. et al., 2008, PASJ, 60, 453
Smith R. C., Kirshner R. P., Blair W. P., Winkler P. F., 1991, ApJ, 375, 652
Tuohy I. R., Dopita M. A., Mathewson D. S., Long K. S., Helfand D. J., 1982, ApJ, 261, 473
van den Bergh S., 1988, ApJ, 327, 156
van der Marel R. P., Cioni M.-R. L., 2001, AJ, 122, 1807
Vogt F., Dopita M. A., 2011, Ap&SS, 331, 521
Warren J. S., Hughes J. P., 2004, ApJ, 608, 261
Wheeler J. C., 2012, ApJ, 758, 123
Wills K. A., Pedlar A., Muxlow T. W. B., Wilkinson P. N., 1997, MNRAS, 291, 517

This paper has been typeset from a TEX/LATEX file prepared by the author.

A.37 Related Paper 37

Galvin, T. J., Filipović, M. D., Tothill, N. F. H., Crawford, E. J., O'Brien, A. N., Seymour, N., Pannuti, T. G., Kosakowski, A. R., and Sharma, B. (2014). Radio-continuum study of the nearby sculptor group galaxies. Part 3: NGC 7793 at λ=12.2, 6 and 3 cm. *Ap&SS*, 353:603–611

My contribution was to assist in the data analysis. This is a 10% contribution.

Astrophys Space Sci (2014) 353:603–611
DOI 10.1007/s10509-014-2051-3

ORIGINAL ARTICLE

Radio-continuum study of the nearby sculptor group galaxies. Part 3: NGC 7793 at λ = 12.2, 6 and 3 cm

Timothy J. Galvin · Miroslav D. Filipović · Nicholas F.H. Tothill · Evan J. Crawford · Andrew N. O'Brien · Nicholas Seymour · Thomas G. Pannuti · Alekzander R. Kosakowski · Biswas Sharma

Received: 15 January 2014 / Accepted: 8 July 2014 / Published online: 19 July 2014

Abstract We re-examine a series of archived centimetre radio-continuum observations ($\lambda = 16$, 6 and 3 cm) focusing on NGC 7793 using the Australia Telescope Compact Array. These new images are both very sensitive ($\sigma = 0.011$ mJy/beam) and feature reasonably high angular resolution (down to $<3''$). Using these images, a total of 76 discrete radio sources are identified, of which 57 have been classified. We also studied the radio component of the micro-quasar NGC7793-S26 which shows two distinct regions of somewhat steep spectral index (α) between -0.3 and -0.7.

Keywords Galaxies: general · Galaxies: NGC 7793 · Radio continuum: galaxies

1 Introduction

As part of the Sculptor group galaxies, NGC 7793 is at an approximate distance of 3.91 Mpc (Karachentsev et al. 2003) and has been intimately examined throughout a number of multifrequency studies. Of particular interest is the source NGC7793-S26, initially discovered by Blair and Long (1997). Subsequent X-ray and Very Large Array (VLA) radio observations by Read and Pietsch (1999) and Pannuti et al. (2002) note extended emission associated with a bright point source, designated S26. Further studies by Pakull and Grisé (2008), Pakull et al. (2010), Pannuti et al. (2011), and Dopita et al. (2012) examine this source in greater detail and suggest that it is micro-quasar in nature.

The Australia Telescope Compact Array (ATCA), having been upgraded with the Compact Array Broadband Backend (CABB) (Wilson et al. 2011), was used by Soria et al. (2010) to resolve S26's radio lobe structure and map its spectral index. As a part of our study of nearby Sculptor Group galaxies, we re-examine this data with an additional focus of discrete sources within NGC 7793's field.

Part 1 of this series of papers (Galvin et al. 2012) created a new set of highly sensitive and highly resolved mosaics of NGC 300—another Sculptor Group galaxy—at $\lambda = 20$ cm by combining ATCA and VLA data. Part 2, by O'Brien et al. (2013), re-examines ATCA and VLA data of the NGC 55—yet another Sculptor Group galaxy—field at $\lambda = 20$, 13, 6 and 3 cm. In this paper we re-examine archived centimetre radio-continuum observations ($\lambda = 12.2$, 6 and 3 cm) focusing on NGC 7793 using the ATCA with an additional focus on discrete sources. In Sect. 2 we describe the observational data and reduction techniques. We present and discuss our results in Sect. 3 and conclusion in Sect. 4.

2 Data and data reduction

2.1 Observational data

The data used in this study was obtained from the Australia Telescope Online Archive (ATOA).[1] Project C2096

T.J. Galvin ( ) · M.D. Filipović · N.F.H. Tothill · E.J. Crawford · A.N. O'Brien
University of Western Sydney, Locked Bag 1797, Penrith, NSW 2751, Australia
e-mail: t.galvin@bigpond.com

N. Seymour
CSIRO Astronomy and Space Science, P.O. Box 76, Epping, NSW 1710, Australia

T.G. Pannuti · A.R. Kosakowski · B. Sharma
Space Science Center, Department of Earth and Space Sciences, Morehead State University, 235 Martindale Drive, Morehead, KY 40351, USA

[1] http://atoa.atnf.csiro.au/.

was conducted over 5 non-consecutive days using the ATCA and CABB, which provided a 2 GHz spectral window for each of the observations. The observations used in this study are summarised in Table 1.

2.2 Image creation

In project C2096 we used PKS1934-638 and PKS2357-318 as its primary (flux and bandpass) and secondary (phase) calibrators, respectively. All observations used in this study were centred at RA (J2000) = $23^h57^m59.94^s$ and DEC (J2000) = $-32°33'30.8''$.

The MIRIAD (Sault et al. 2011) and KARMA (Gooch 2011) software packages were used for data reduction and analysis. Typical MIRIAD calibration and flagging procedures were then carried out, including the use of the guided automatic flagging task PGFLAG.

Each observation was then imaged in order to verify its integrity. The task INVERT was used to produce a dirty map and beam. We found that supplying a Briggs robust parameter of 0.5 was the most effective in reducing the areas of sidelobe distortion. As we imaged the full spectral window provided by CABB, MFCLEAN (Sault and Wieringa 1994) was used to deconvolve the multi-frequency synthesised dirty map. Finally, RESTOR and LINMOS were used to convolve and correct for primary beam attenuation.

Table 1 ATCA CABB C2096 observations used in this study. The bandwidth of all observations is 2 GHz

Observation Date	Array	Central Frequency (GHz)	Time on source (hours)
6/08/2009	6D	5.5, 9	6.7
7/08/2009	6D	5.5, 9	6.2
27/06/2010	6C	5.5, 9	10.2
28/06/2010	6C	5.5, 9	9.8
29/06/2010	6C	2.45	9.9

Once we verified that sufficient data flagging and calibration had been carried out for each individual observation, a single image was created by combining datasets from all epochs for each particular frequency.

3 Results and discussion

The final images produced in this study are presented in Figs. 1, 2 and 3. Each image was produced using the collective dataset for that particular frequency. We summarise the details and parameters of each image in Table 2.

Upon inspecting the final images we find that $\lambda = 12.2$ cm (Fig. 1) had a significantly higher RMS noise level ($1\sigma = 0.30$ mJy/beam) than $\lambda = 6$ and 3 cm ($1\sigma = 0.011$ and 0.015 mJy/beam in Figs. 2 and 3 respectively). This was expected as NGC 7793 at $\lambda = 12.2$ cm was only observed for ∼10 hours, where as $\lambda = 6/3$ cm was observed for ∼33 hours. As noise increased towards the edge of the primary beam, the adopted RMS values represent the upper limit in terms of local noise for each image. In the case of Fig. 3, approximately one third of the field of interest was ignored due to the increased confusion at the edge of the primary beam.

3.1 Discrete sources within the field of NGC7793

We initially searched for sources in each image using the automated MIRIAD task SFIND. Using the returned results as a

Table 2 The image details of ATCA project C2096

ν (GHz)	Beam Size (arcsec)	PA °	RMS (σ) (mJy/beam)	Figure #
2.4	7.6×3.8	2.4	0.030	1
5.5	3.6×1.8	1.0	0.011	2
9.0	2.2×1.1	−1.1	0.015	3

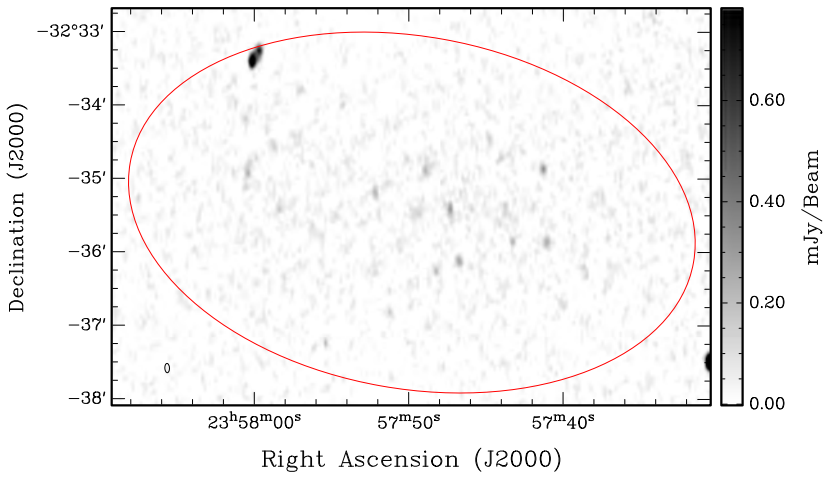

Fig. 1 Project C2096 at $\lambda = 12.2$ cm in mJy/beam. The *red ellipse* highlights the area that was examined for sources. The beam is $7.6'' \times 3.8''$, as represented by the *blue ellipse* in the bottom left corner. The primary beam was blanked after 23′

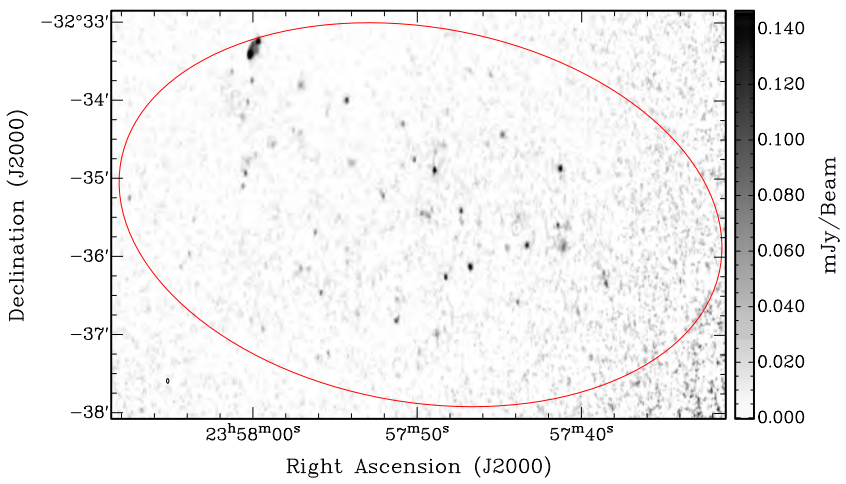

Fig. 2 Project C2096 at $\lambda = 6$ cm in mJy/beam. The *red ellipse* highlights the area that was examined for sources. The beam is $3.6'' \times 1.8''$, as represented by the *blue ellipse* in the bottom left corner. The primary beam was blanked after $9.08'$

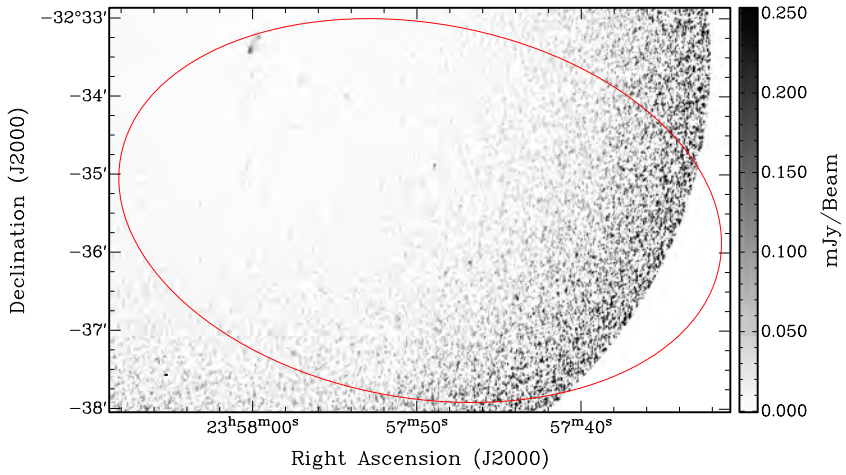

Fig. 3 Project C2096 at $\lambda = 3$ cm in mJy/beam. The *red ellipse* highlights the area that was examined for sources. The beam is $2.2'' \times 1.1''$, as represented by the *blue ellipse* in the bottom left corner. The primary beam was blanked after $5.86'$

starting point list, we then reviewed each listed source in the field to evaluate its reliability. A number of proposed sources from SFIND were discounted as they were either artefacts of side-lobes around particularly strong points or were outside the field of NGC 7793. After removing such sources, we then manually examined each image to identify any remaining sources which were not found by SFIND. The red ellipse in Figs. 1, 2, 3 and 4 highlights the field which was searched for sources and was constructed to tightly cover the centre of NGC 7793 as seen from the Digital Sky Survey[2] (DSS) optical image. The size of the major and minor axis of this ellipse is approximately $7.78''$ by $4.90''$ at a position angle of 280°.

A total of 76 discrete sources above 3σ (0.090, 0.033 and 0.045 mJy/beam at wavelengths 12.2, 6 and 3 cm (Table 3; Column 5, 6 and 7 respectively) were identified within the field of NGC 7793. Using a $5''$ search radius, a value adopt because of the beam size of Fig. 1, a total of 39 sources were found at more than one wavelength. In such cases we estimated sources spectral index, α, defined as $S \propto \nu^{\alpha}$ (Table 3; Column 12). When calculating this spectral index value we assumed a error in flux density of 10 % for each measurement. Position, integrated flux densities and spectral indices of these catalogued sources are presented in Table 3. The positions listed in Table 3 refer to the location of each source from the highest frequency image from which it was found. Due to the smaller primary beam at $\lambda = 3$ cm (Fig. 3), approximately one third of the search ellipse is too noisy for source detection. The 28 sources within this flagged area have been marked in Table 3 with †.

Our new catalogue of 76 discrete radio-continuum sources in NGC 7793 was then compared to the Infrared (Kennicutt et al. 2003), Ultra-violet (Dale et al. 2009), Optical (DSS) and X-ray (Pannuti et al. 2011) catalogues and any source coincidences that were found using a search radius of $5''$ were noted in Table 3 (Columns 8, 9, 10 and 11 respectively).

In Fig. 5 we show the distribution of integrated flux densities of detected sources at $\lambda = 12.2$, 6 and 3 cm as described in Table 3 (Columns 5, 6 and 7 (excluding NGC7793-S26) (Table 3; Index 61)). We note that the majority of sources

[2] http://archive.stsci.edu/cgi-bin/dss_form.

Table 3 List of point sources in the NGC 7793 field at λ = 12.2, 6 and 3 cm. RA (3) and Dec (4) are in J2000 coordinates and are taken from the image with the highest resolution that a source was found in. Column 8 is the best fit spectral index for all flux measurements of a sources. When calculating this spectral index value we assumed a error in flux density of 10 % for each measurement. Blank cells indicate no measurements were detect. The Infrared ID (8), Ultra-Violent ID (9), Optical ID (10) and X-ray ID (11) are from Kennicutt et al. (2003), Dale et al. (2009), Digital Sky Survey and Pannuti et al. (2011) respectively. † represents a point that could not be distinguished from noise as it was outside the sensitive area of the primary beam. Sources which are a strong candidate for their respective classification are presented in upper case, while less robust sources are presented in lower case. The notes 'optically selected SNR' and 'radio selected SNR' denotes SNR candidates and their method of identification as listed by Pannuti et al. (2002), while 'H69' denotes sources classified as HII by Hodge (1969)

1 Index	2 Source name	3 RA (J2000) (h m s)	4 Dec (J2000) (° ′ ″)	5 $S_{16\ cm}$ (mJy)	6 $S_{6\ cm}$ (mJy)	7 $S_{3\ cm}$ (mJy)	8 IR ID	9 UV ID	10 Optical ID	11 X-ray ID	12 Spectral Index α	13 Type	14 Notes
1	J235737-323547	23:57:37.0	−32:35:47.56	0.109		†							
2	J235737-323512	23:57:37.5	−32:35:12.80	0.100		†							
3	J235737-323511	23:57:37.8	−32:35:11.85	0.096		†							
4	J235738-323619	23:57:38.5	−32:36:19.31	0.120	0.120	†	Y	Y	Y		0.00 ± 0.25	HII	H69
5	J235738-323611	23:57:38.6	−32:36:11.73	0.140	0.088	†	Y	Y	Y		-0.57 ± 0.25	snr	H69
6	J235739-323459	23:57:39.5	−32:34:59.35	0.095		†							
7	J235741-323552	23:57:41.0	−32:35:52.80	0.244	0.270	†	Y	Y	Y		0.13 ± 0.25	HII	H69
8	J235741-323451	23:57:41.3	−32:34:51.21	0.336	0.260	†	Y	Y	Y		-0.32 ± 0.25	hII	H69
9	J235741-323534	23:57:41.4	−32:35:34.74	0.093	0.127	†	Y	Y	Y		0.39 ± 0.25	HII	
10	J235743-323550	23:57:43.3	−32:35:50.20	0.214	0.180	†	Y	Y	Y		-0.21 ± 0.25	hII	H69
11	J235743-323521	23:57:43.7	−32:35:21.70	0.160		†	Y						
12	J235743-323528	23:57:43.8	−32:35:28.47		0.047	†							
13	J235743-323634	23:57:43.8	−32:36:34.04		0.098	0.316	Y	Y	Y	Y	2.34 ± 0.41		
14	J235743-323532	23:57:44.0	−32:35:32.52		0.043	†							
15	J235743-323442	23:57:44.0	−32:34:42.14	0.144		†	Y					hII	
16	J235744-323553	23:57:44.5	−32:35:53.03		0.090	†	Y	Y	Y			hII	H69
17	J235744-323425	23:57:44.8	−32:34:25.36	0.140	0.150	†	Y	Y			0.09 ± 0.25	hII	
18	J235744-323531	23:57:44.8	−32:35:31.33		0.038	†	Y		Y				
19	J235745-323339	23:57:45.5	−32:33:39.84		0.058	0.065	Y	Y	Y		0.23 ± 0.41	HII	
20	J235745-323432	23:57:45.8	−32:34:32.41		0.034	†	Y	Y				hII	
21	J235745-323524	23:57:45.9	−32:35:24.66	0.117		†			Y				
22	J235746-323533	23:57:46.2	−32:35:33.37		0.038	†	Y	Y	Y			hII	
23	J235746-323550	23:57:46.2	−32:35:50.21		0.039	†	Y	Y				hII	
24	J235746-323459	23:57:46.5	−32:34:59.56		0.034		Y		Y			hII	
25	J235746-323511	23:57:46.6	−32:35:11.15	0.104					Y				
26	J235746-323606	23:57:46.7	−32:36:06.98	0.269	0.370	0.270	Y	Y	Y	Y	0.04 ± 0.26	snr	radio selected SNR
27	J235746-323336	23:57:46.7	−32:33:36.24		0.043		Y	Y	Y			hII	
28	J235747-323533	23:57:47.2	−32:35:33.00		0.042		Y	Y	Y			hII	
29	J235747-323523	23:57:47.3	−32:35:23.94	0.371	0.175		Y		Y	Y	-0.93 ± 0.25	SNR	optically selected SNR
30	J235748-323614	23:57:48.2	−32:36:14.74	0.196	0.194	0.111	Y	Y	Y		-0.40 ± 0.30	snr	radio selected SNR; H69
31	J235748-323654	23:57:48.3	−32:36:54.78		0.045	†							optically selected SNR
32	J235748-323658	23:57:48.8	−32:36:58.79		0.061	†	Y	Y	Y			hII	
33	J235748-323452	23:57:48.9	−32:34:52.72	0.210	0.310	0.214	Y	Y	Y		0.06 ± 0.33	HII	
34	J235749-323523	23:57:49.1	−32:35:23.01		0.054		Y	Y	Y			hII	
35	J235749-323528	23:57:49.2	−32:35:28.23	0.126	0.065	0.053	Y	Y	Y		-0.68 ± 0.11	snr	

Table 3 (*Continued*)

1 Index	2 Source name	3 RA (J2000) (h m s)	4 Dec (J2000) (° ′ ″)	5 $S_{16\ cm}$ (mJy)	6 $S_{6\ cm}$ (mJy)	7 $S_{3\ cm}$ (mJy)	8 IR ID	9 UV ID	10 Optical ID	11 X-ray ID	12 Spectral Index α	13 Type	14 Notes
36	J235749-323525	23:57:49.7	−32:35:25.90	0.363	0.100		Y	Y	Y		-1.59 ± 0.25	snr	
37	J235749-323712	23:57:49.8	−32:37:12.03		0.048	†	Y	Y				hII	
38	J235749-323723	23:57:49.9	−32:37:23.65		0.036	†							
39	J235750-323444	23:57:50.1	−32:34:44.60	0.109	0.093	0.095			Y		-0.11 ± 0.06	bckg/snr	
40	J235750-323600	23:57:50.6	−32:36:00.72		0.036		Y	Y	Y			hII	
41	J235750-323417	23:57:50.8	−32:34:17.33	0.091	0.096	0.061	Y	Y	Y		-0.27 ± 0.26	HII	H69
42	J235751-323648	23:57:51.2	−32:36:48.03	0.140	0.160	†	Y	Y	Y		0.17 ± 0.25	hII	
43	J235752-323511	23:57:52.0	−32:35:11.94	0.217	0.152	0.090	Y	Y	Y		-0.65 ± 0.17	snr	H69
44	J235752-323614	23:57:52.1	−32:36:14.94	0.098	0.034				Y		-1.31 ± 0.25	bckg/snr	
45	J235753-323446	23:57:54.0	−32:34:46.49	0.097	0.150		Y	Y	Y		0.54 ± 0.25	hII	H69
46	J235754-323359	23:57:54.2	−32:33:59.10	0.132	0.203	0.114	Y	Y	Y		-0.05 ± 0.45	HII	H69
47	J235754-323603	23:57:54.2	−32:36:03.97		0.038		Y	Y	Y			hII	
48	J235754-323553	23:57:54.3	−32:35:53.15		0.034		Y	Y	Y			hII	
49	J235755-323713	23:57:55.3	−32:37:13.28	0.198	0.074	†					-1.22 ± 0.25	bckg/snr	
50	J235755-323408	23:57:55.4	−32:34:08.47		0.034								
51	J235755-323626	23:57:55.8	−32:36:26.96		0.110	0.122	Y				0.21 ± 0.41	HII	
52	J235755-323716	23:57:56.0	−32:37:16.51		0.056	†	Y	Y	Y			hII	
53	J235756-323540	23:57:56.1	−32:35:40.42	0.105	0.073	0.055	Y		Y		-0.49 ± 0.03	HII	
54	J235757-323607	23:57:57.0	−32:36:07.97		0.087		Y	Y	Y			hII	H69
55	J235757-323347	23:57:57.0	−32:33:47.70	0.126	0.120	0.049	Y	Y	Y		-0.66 ± 0.47	snr	H69
56	J235757-323424	23:57:57.0	−32:34:24.11		0.044		Y	Y	Y			hII	
57	J235757-323422	23:57:57.5	−32:34:22.26		0.044								
58	J235758-323523	23:57:58.3	−32:35:23.88	0.156					Y			snr	optically selected SNR
59	J235758-323433	23:57:58.7	−32:34:33.58	0.130	0.085	0.051	Y	Y	Y		-0.70 ± 0.13	snr	
60	J235759-323654	23:57:59.3	−32:36:54.52		0.049	0.049	Y	Y			0.00 ± 0.41	hII	
61	J235759-323317	23:58:00.0	−32:33:17.20	109.000	94.300	74.210					-0.28 ± 0.08	MQ	NGC7793-S26; S26; Double source; H69
62	J235759-323343	23:58:00.0	−32:33:43.80		0.080	0.090	Y	Y	Y		0.24 ± 0.41	hII	H69
63	J235800-323447	23:58:00.2	−32:34:47.31	0.140	0.060		Y	Y	Y		-1.05 ± 0.25	snr	
64	J235800-323359	23:58:00.3	−32:33:59.79		0.060	0.055	Y	Y	Y		-0.18 ± 0.41	hII	
65	J235800-323455	23:58:00.4	−32:34:55.45	0.228	0.120	0.074	Y	Y	Y	Y	-0.86 ± 0.05	SNR	
66	J235800-323505	23:58:00.6	−32:35:05.21	0.119	0.067	0.063	Y	Y			-0.51 ± 0.16	snr	
67	J235800-323411	23:58:00.6	−32:34:11.74	0.131	0.105		Y	Y	Y		-0.27 ± 0.25	snr	
68	J235801-323337	23:58:01.2	−32:33:37.02	0.094	0.075		Y	Y	Y		-0.28 ± 0.25		
69	J235748-323433	23:57:48.4	−32:34:33.27		0.040			Y	Y			hII	
70	J235748-323439	23:57:48.9	−32:34:39.30		0.040		Y	Y	Y			hII	H69
71	J235751-323632	23:57:51.4	−32:36:32.79	0.094	0.050			Y	Y		-0.78 ± 0.25	bckg/snr	
72	J235753-323643	23:57:53.6	−32:36:43.24		0.043		Y	Y	Y			hII	H69
73	J235807-323514	23:58:07.4	−32:35:14.64	0.122	0.069	0.045					-0.76 ± 0.04	bckg	
74	J235804-323607	23:58:04.3	−32:36:07.19		0.049								
75	J235803-323556	23:58:03.8	−32:35:56.19		0.051								
76	J235803-323531	23:58:03.5	−32:35:31.52	0.096	0.041						-1.05 ± 0.25		

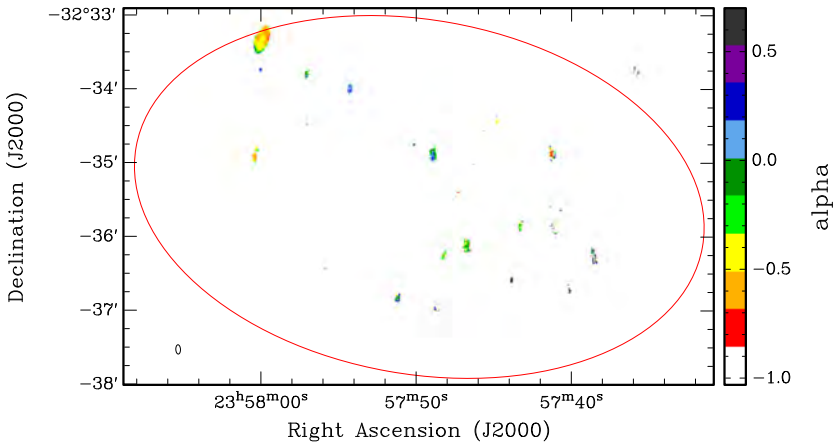

Fig. 4 Spectral index pixel map of NGC 7793 as calculated from $\lambda = 12.2$, 6 and 3 cm data. The image is in terms of spectral index α, where α is defined as $S \propto \nu^{\alpha}$. The *red ellipse* highlights the area that was examined for sources and the colour bar on the right reflects the spectral index value. The synthesised beam, represented by the *blue ellipse* in the lower left hand corner, is $7.56'' \times 3.80''$

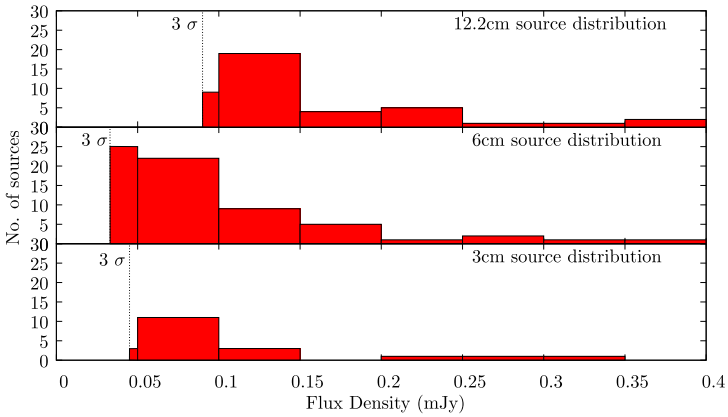

Fig. 5 A histogram showing the distribution of flux densities of sources detected at $\lambda = 12.2$, 6 and 3 cm (Table 3; Columns 5, 6 and 7). All sources have been binned in 0.05 mJy increments. Due to its significant flux density when compared to other discrete sources in this study, NGC7793-S26 (Table 3; Index 61) is excluded from this graph. The *dotted line* represents the 3σ level

(85 %) have an integrated flux density that is below 10σ flux density levels. Figure 6 shows the distribution (in terms of spectral index (Table 3; Column 12) and classification (Table 3; Column 13)) of 38 out of the 76 sources identified in this study. J235743–323634 (Table 3; Index 13) is excluded from this graph. We note two distinctive source groups; one peaking at $\alpha = -0.6$ and second at $\alpha = -0.2$. Out of 39 sources with an estimated spectral index, 24 (61.5 %) can be classified as having a flat or inverted spectrum with an α between 0.7 and -0.5. The remaining 15 sources (38.5 %) have a steeper α between -0.5 to -1.7.

3.2 Source classification

Seventy-six (76) radio-continuum sources were detected in our study. These sources have been classified into three main groups: background sources, Supernova Remnants (SNRs) and HII regions. Combining previous work and our new radio-continuum maps we classify a total of 57 sources. From these 57 sources, 37 are most likely to be HII regions, 14 to be SNRs, 1 to be a micro-quasar (see Pakull and Grisé 2008; Pakull et al. 2010; Pannuti et al. 2011 and Dopita et al. 2012), 1 to be a background galaxy (or AGN) and 4 which could be either an SNR or a background galaxy (or AGN). The remaining 19 radio-continuum sources still have no classification. We list each sources classification, where appropriate, in Table 3; Column 13. Strong candidates are listed as either HII, SNR, MQ (micro-quasar) or BCKG (background galaxy/AGN), while weaker candidates are listed as hII, snr and bckg. Figure 6 shows the distribution of these source classifications.

A source was classified as a strong candidate SNR if it had both a steep negative spectral index and an X-ray counterpart. If a source only had one of these properties it was classified as a weak candidate snr or bckg/snr. Likewise, if a source had a flat spectral index and an Infrared counterpart it was classified as a HII region candidate. If it only had one such property, it was classified as a weak HII region candidate. Each source was also visually inspected to determine if there was any intrinsic structure that would help in its identification. Three sources (Table 3; Index #26, #39 and #67) have been classified as being weak candidate snrs or bckg/snr while having a shallow spectral index. These sources were classified as either weak candidate snrs or snr/bckg based on how many counterparts were seen at additional frequency bands, the lack of extended emission or structure of the source, and the uncertainty associated with borderline steep spectral index values.

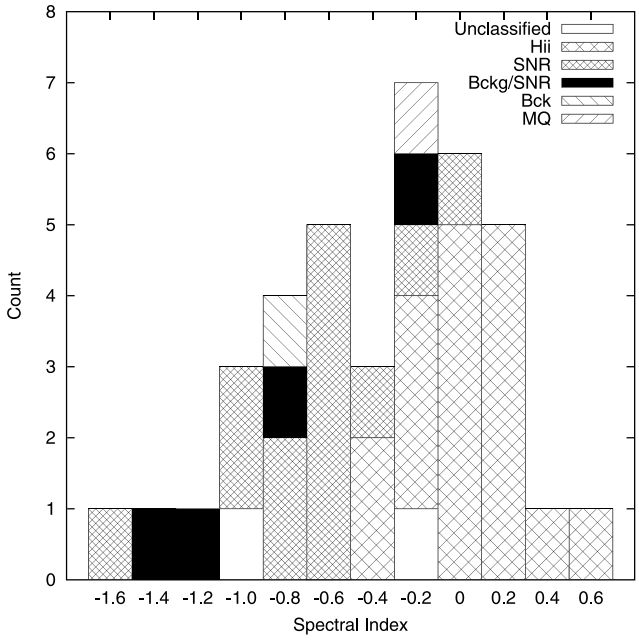

Fig. 6 A histogram showing both the distribution of spectral indexes and classification of sources presented in Table 3; Columns 12 and 13. J235743-323634 (Table 3; Index. 13) is excluded from this graph

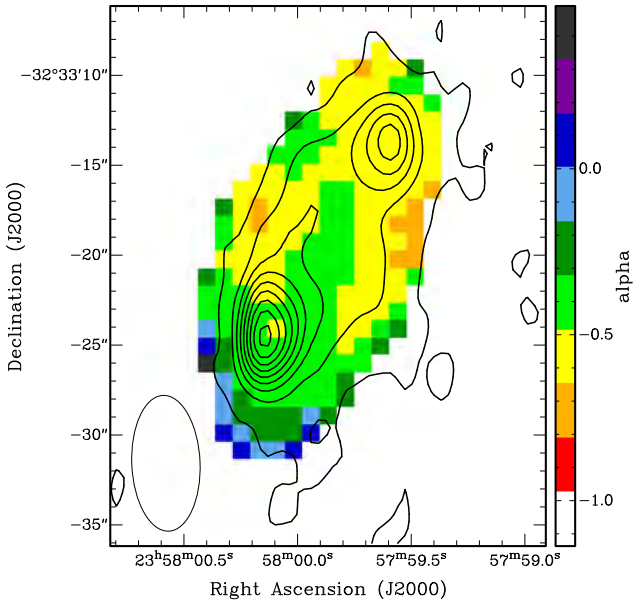

Fig. 7 Spectral index pixel map of NGC7793-S26 as calculated from $\lambda = 12.2$, 6 and 3 cm data. The image is in terms of spectral index α, where α is defined as $S \propto \nu^{\alpha}$. The *colour bar on the right* reflects the spectral index value. The synthesised beam, represented by the *blue ellipse* in the lower left hand corner, is $7.56'' \times 3.80''$. The *contour levels* are 0.01 mJy to 0.80 mJy with 0.05 mJy increments and are representative of the 6 cm data (Fig. 2)

After classifying our sources we then compared them to two additional catalogues. The first catalogue, from Pannuti et al. (2002), listed a total of 33 radio and optically selected SNR candidates. A total of 5 sources were found to be common between both studies, of which we had classified 4 as SNRs and 1 which was not classified. The second catalogue, from Hodge (1969), listed HII regions. When compared to our own we find a total of 17 source matches to be common. Of these 17 sources, we had classified 12 as HII regions and 4 as SNRs. The remaining source was the micro-quasar NGC7793-S26. Hodge (1969) used two photographs, a yellow image and a yellow subtracted H_{α} image, to identify HII regions. This explains why 5 sources were classified differently when compared to Hodge (1969), as these sources would have similar optical emission. These sources are noted in Table 3.

If a source has an X-ray counterpart when compared with Pannuti et al. (2011) (Table 3; Column 11) or was listed as an SNR candidate in Pannuti et al. (2002) (as noted in Table 3; Column 14), we compared the listed positions from both catalogues. We find that the average positional difference in Δ RA and Δ DEC is $-0.13''$ (with a SD of $1.19''$) and $-0.08''$ (with a SD of $0.61''$) respectively.

We find 57 sources in common between radio (Figs. 1, 2 and 3) and at least one additional frequency band (Infrared, Ultra-violet, Optical and X-ray). Of these 5 frequency bands, there were 3 sources which were seen in all five, 38 in four, 11 in three and 3 in two.

3.3 Spectral map

Figure 4 shows a three point spectral map of NGC7793. Each pixel represents the spectral index as measured across Figs. 1, 2 and 3 after convolving the images to the largest beam size (12.2 cm). Pixels below the 3 sigma RMS noise level for each image were ignored.

The compact sources within this study exhibit a shallow (flatish) spectral index of between $-0.2 > \alpha > -0.4$. This indicates dominance of regions with high thermal radiation caused by dense star formation. We can also see occasional steeper areas where $\alpha < -0.4$, implying a dominance of non-thermal radiation possibly caused by either synchrotron or inverse-Compton radiative mechanisms. Objects which radiate using this mechanism include SNRs and energetic jets.

3.3.1 Micro-quasar S26

Pakull et al. (2010) suggest that NGC 7793-S26 (Table 3; Index 61) is powered by a black hole expelling relativistic jets of matter. Through the interactions with the surrounding interstellar medium (ISM), two bubbles have formed either side of the central black hole.

Figure 7 shows NGC7793-S26 from the spectral map (as discussed above) overlaid with contours from Fig. 2 ($\lambda = 6$ cm). When overlaid with contours, the two ISM

bubbles can be clearly seen. The north most bubble (J2000 RA $= 23^h57^m59.7^s$, DEC $= -32°33'13.00''$) has an average spectral index of approximately $\alpha \sim -0.54$ and range of -0.74 to -0.24, while the south most bubble (J2000 RA $= 23^h58^m00.1^s$, DEC $= -32°33'25.00''$) has a slightly flatter average spectral index of $\alpha \sim -0.43$ with a range of -0.65 to -0.04. We also note a slightly positive index (approximately $0 < \alpha < 0.2$) on the outskirts of the southern lobe.

The peak flux intensity of the southern lobe is measured at 1.28 mJy/beam, 0.42 mJy/beam and 0.23 mJy/beam at 12.2, 6 and 3 cm respectively. The northern lobe is somewhat weaker with a peak flux intensity of 0.67 mJy/beam at 12.2 cm, 0.24 mJy/beam at 6 cm and 0.14 mJy/beam at 3 cm.

4 Conclusion

Using archived centimetre radio-continuum observations ($\lambda = 12.2$, 5.5 and 3 cm) of NGC 7793 we catalogue a total of 76 discrete radio sources. Of these 76 sources, we classified a total of 37 sources as HII regions, 14 as SNRs, 1 as a micro-quasar, 1 as a background galaxy and 4 as either background galaxies or SNRs. A spectral index map of NGC 7793 was created which exhibited a mostly shallow spectral index value, indicating dominance of regions with high thermal radiation caused by dense star formation. We also studied the radio component of the micro-quasar NGC7793-S26, and showed that on average it has a somewhat steep spectral index of between -0.3 and -0.7.

Acknowledgements The Australia Telescope Compact Array is part of the Australia Telescope National Facility which is funded by the Commonwealth of Australia for operation as a National Facility managed by CSIRO. This paper includes archived data obtained through the Australia Telescope Online Archive (http://atoa.atnf.csiro.au). The Digitized Sky Surveys were produced at the Space Telescope Science Institute under U.S. Government grant NAG W-2166. The images of these surveys are based on photographic data obtained using the Oschin Schmidt Telescope on Palomar Mountain and the UK Schmidt Telescope. The plates were processed into the present compressed digital form with the permission of these institutions. This research has made use of Aladin, SIMBAD and VizieR, operated at the CDS, Strasbourg, France. We used the KARMA software package developed by the ATNF. Nicholas Seymour is the recipient of an ARC Future Fellowship. We would also like to thank the anonymous referee whose feedback greatly improved the quality of this paper.

References

Blair, W.P., Long, K.S.: Identification of supernova remnants in the sculptor group galaxies NGC 300 and NGC 7793. Astrophys. J. Suppl. Ser. **108**, 261 (1997). doi:10.1086/312958

Dale, D.A., Cohen, S.A., Johnson, L.C., Schuster, M.D., Calzetti, D., Engelbracht, C.W., Gil de Paz, A., Kennicutt, R.C., Lee, J.C., Begum, A., Block, M., Dalcanton, J.J., Funes, J.G., Gordon, K.D., Johnson, B.D., Marble, A.R., Sakai, S., Skillman, E.D., van Zee, L., Walter, F., Weisz, D.R., Williams, B., Wu, S.-Y., Wu, Y.: The Spitzer local volume legacy: survey description and infrared photometry. Astrophys. J. **703**, 517–556 (2009). doi:10.1088/0004-637X/703/1/517

Dopita, M.A., Payne, J.L., Filipović, M.D., Pannuti, T.G.: The physical parameters of the microquasar S26 in the Sculptor Group galaxy NGC 7793. Mon. Not. R. Astron. Soc. **427**, 956–967 (2012). doi:10.1111/j.1365-2966.2012.21947.x

Galvin, T.J., Filipović, M.D., Crawford, E.J., Wong, G., Payne, J.L., De Horta, A., White, G.L., Tothill, N., Drašković, D., Pannuti, T.G., Grimes, C.K., Cahall, B.J., Millar, W.C., Laine, S.: Radio-continuum study of the Nearby sculptor group galaxies. Part 1: NGC 300 at $\lambda = 20$ cm. Astrophys. Space Sci. **340**, 133–142 (2012). doi:10.1007/s10509-012-1044-3

Gooch, R.: Karma: Visualisation Test-Bed Toolkit, February 2011. Astrophysics Source Code Library

Hodge, P.W.: H II regions in twenty nearby galaxies. Astrophys. J. Suppl. Ser. **18**, 73 (1969). doi:10.1086/190185

Karachentsev, I.D., Grebel, E.K., Sharina, M.E., Dolphin, A.E., Geisler, D., Guhathakurta, P., Hodge, P.W., Karachentseva, V.E., Sarajedini, A., Seitzer, P.: Distances to nearby galaxies in Sculptor. Astron. Astrophys. **404**, 93–111 (2003). doi:10.1051/0004-6361:20030170

Kennicutt, R.C., Bendo, G., Engelbracht, C., Gordon, K., Li, A., Rieke, G.H., Rieke, M.J., Smith, J.D., Armus, L., Helou, G., Jarrett, T.H., Roussel, H., Calzetti, D., Leitherer, C., Malhotra, S., Meyer, M., Regan, M.W., Dale, D.A., Draine, B., Grauer, A.D., Hollenbach, D.J., Kewley, L.J., Murphy, E., Thornley, M.D., Walter, F.: SINGS: The SIRTF nearby galaxies survey. In: American Astronomical Society Meeting Abstracts. Bulletin of the American Astronomical Society, vol. 35, p. 1351 (2003)

O'Brien, A.N., Filipović, M.D., Crawford, E.J., Tothill, N.F.H., Collier, J.D., De Horta, A.Y., Wong, G.F., Drašković, D., Payne, J.L., Pannuti, T.G., Napier, J.P., Griffith, S.A., Staggs, W.D., Kotuš, S.: Radio-continuum study of the nearby Sculptor group Galaxies. Part 2: NGC 55 at $\lambda = 20$, 13, 6 and 3 cm. Astrophys. Space Sci. **347**, 159–168 (2013). doi:10.1007/s10509-013-1489-z

Pakull, M.W., Grisé, F.: Ultraluminous X-ray sources: beambags and optical counterparts. In: Bandyopadhyay, R.M., Wachter, S., Gelino, D., Gelino, C.R. (eds.) A Population Explosion: The Nature & Evolution of X-ray Binaries in Diverse Environments. American Institute of Physics Conference Series, vol. 1010, pp. 303–307 (2008). doi:10.1063/1.2945062

Pakull, M.W., Soria, R., Motch, C.: A 300-parsec-long jet-inflated bubble around a powerful microquasar in the galaxy NGC 7793. Nature **466**, 209–212 (2010). doi:10.1038/nature09168

Pannuti, T.G., Duric, N., Lacey, C.K., Ferguson, A.M.N., Magnor, M.A., Mendelowitz, C.: An X-Ray, Optical, and radio search for supernova remnants in the nearby Sculptor group Sd Galaxy NGC 7793. Astrophys. J. **565**, 966–981 (2002). doi:10.1086/337918

Pannuti, T.G., Schlegel, E.M., Filipović, M.D., Payne, J.L., Petre, R., Harrus, I.M., Staggs, W.D., Lacey, C.K.: A Chandra Observation of the nearby sculptor group Sd galaxy NGC 7793. Astron. J. **142**, 20 (2011). doi:10.1088/0004-6256/142/1/20

Read, A.M., Pietsch, W.: ROSAT observations of the Sculptor galaxy NGC 7793. Astron. Astrophys. **341**, 8–22 (1999)

Sault, R.J., Wieringa, M.H.: Multi-frequency synthesis techniques in radio interferometric imaging. Astron. Astrophys. Suppl. Ser. **108**, 585–594 (1994)

Sault, R.J., Teuben, P.J., Wright, M.C.H.: MIRIAD: Multi-channel image reconstruction, image analysis, and display. Astrophysics Source Code Library (2011)

Soria, R., Broderick, J., Corbel, S., Pakull, M., Motch, C.: The newly-discovered radio/optical/X-ray microquasar in NGC 7793. ATNF Proposal, p. 3023 (2010)

Wilson, W.E., Ferris, R.H., Axtens, P., Brown, A., Davis, E., Hampson, G., Leach, M., Roberts, P., Saunders, S., Koribalski, B.S., Caswell, J.L., Lenc, E., Stevens, J., Voronkov, M.A., Wieringa, M.H., Brooks, K., Edwards, P.G., Ekers, R.D., Emonts, B., Hindson, L., Johnston, S., Maddison, S.T., Mahony, E.K., Malu, S.S., Massardi, M., Mao, M.Y., McConnell, D., Norris, R.P., Schnitzeler, D., Subrahmanyan, R., Urquhart, J.S., Thompson, M.A., Wark, R.M.: The Australia telescope compact array broadband backend: description and first results. Mon. Not. R. Astron. Soc. **416**, 832–856 (2011). doi:10.1111/j.1365-2966.2011.19054.x

A.38 Related Paper 38

De Horta, A. Y., Filipovic, M. D., Crawford, E. J., Stootman, F. H., Pannuti, T. G., Bozzetto, L. M., Collier, J. D., Sommer, E. R., and Kosakowski, A. R. (2014a). Radio-Continuum Emission from the Young Galactic Supernova Remnant G1.9+0.3. *Serbian Astronomical Journal*, 189:41–51

My contribution was to assist in the observations and data analysis. This is a 10% contribution.

Serb. Astron. J. № 189 (2014), 41 - 51 **UDC 524.354–77**
DOI: 10.2298/SAJ140605001H Original scientific paper

RADIO-CONTINUUM EMISSION FROM THE YOUNG GALACTIC SUPERNOVA REMNANT G1.9+0.3

A. Y. De Horta[1], M. D. Filipović[1], E. J. Crawford[1], F. H. Stootman[1], T. G. Pannuti[2], L. M. Bozzetto[1], J. D. Collier[1], E. R. Sommer[1] and A. R. Kosakowski[2]

[1] *University of Western Sydney, Locked Bag 1797, Penrith South, DC, NSW 1797, Australia*
E–mail: *a.dehorta@uws.edu.au, m.filipovic@uws.edu.au, e.crawford@uws.edu.au*

[2] *Space Science Center, Department of Earth and Space Sciences, Morehead State University, 235 Martindale Drive, Morehead, KY 40351 USA*
E–mail: *t.pannuti@moreheadstate.edu*

(Received: June 5, 2014; Accepted: June 18, 2014)

SUMMARY: We present an analysis of a new Australia Telescope Compact Array (ATCA) radio-continuum observation of supernova remnant (SNR) G1.9+0.3, which at an age of ∼181±25 years is the youngest known in the Galaxy. We analysed all available radio-continuum observations at 6-cm from the ATCA and Very Large Array. Using this data we estimate an expansion rate for G1.9+0.3 of 0.563%±0.078% per year between 1984 and 2009. We note that in the 1980's G1.9+0.3 expanded somewhat slower (0.484% per year) than more recently (0.641% per year). We estimate that the average spectral index between 20-cm and 6-cm, across the entire SNR is α=–0.72±0.26 which is typical for younger SNRs. At 6-cm, we detect an average of 6% fractionally polarised radio emission with a peak of 17%±3%. The polarised emission follows the contours of the strongest of X-ray emission. Using the new equipartition formula we estimate a magnetic field strength of B≈273 μG, which to date, is one of the highest magnetic field strength found for any SNR and consistent with G1.9+0.3 being a very young remnant.

Key words. ISM: individual objects: G1.9+0.3 – ISM: supernova remnants – radio continuum: ISM – supernovae: general

1. INTRODUCTION

It is widely accepted that current catalogues have a distinct deficit of young Galactic supernova remnants (SNRs), that is, SNRs <2000 years old, with only ∼10 confirmed out of a predicted ∼50 (van den Bergh and Tammann 1991, Cappellaro 2003). Of these confirmed SNRs, G1.9+0.3 is of particular interest as it is believed to be the youngest in the Milky Way (MW), i.e. ∼ 150 years old (Reynolds et al. 2008, Green et al. 2008, Reynolds et al. 2009, Carlton et al. 2011a,b).

Originally identified as a probable SNR by Green and Gull (1984) at 4.9 GHz using the Karl G. Jansky Very Large Array (VLA), G1.9+0.3 was described as a shell source with an approximate brightness slightly less than that of the Tycho and Kepler

SNRs with a spectral index of $\alpha \sim -0.7$[1]. Using the Molonglo Observatory Synthesis Telescope (MOST) Galactic Survey data, Gray (1994) confirmed the classification of G1.9+0.3 as an SNR: the source was described as featuring a shell-like morphology in the radio with an estimated diameter of 1′.2. Later, LaRosa et al. (2000) produced a 90-cm image of G1.9+0.3 using observations from the VLA. They estimated the 20/90-cm spectral index of the SNR to be $\alpha = -0.93 \pm 0.25$ and the angular diameter to be 1′.1. Nord et al. (2004) revisited the data collected by LaRosa et al. (2000) and – through the application of superior data reduction techniques – measured the diameter of G1.9+0.3 to be $<1'$ and placed it at a distance of <7.8 kpc. Green (2004) estimates the diameter of G1.9+0.3 based on 1.49 GHz VLA observations made in 1985 to be 1′.2. Most recently, Roy and Pal (2014) measured the H I absorption distance using known anomalous velocity features near the Galactic Centre (GC) and found a lower limit on G1.9+0.3 distance from Sun as 10 kpc, some 2 kpc further away from the GC. Therefore, multiple radio observations have confirmed that G1.9+0.3 has the smallest angular diameter for a known Galactic SNR, indicative of its young age.

Green et al. (2008) re-observed G1.9+0.3 at 4.86 GHz using the VLA after Reynolds et al. (2008) used 2007 *Chandra* images to show G1.9+0.3 had expanded significantly since 1985 and its X-ray emission appeared to be predominantly synchrotron in nature. By comparing these new VLA observations with the 1985 VLA observations made at 1.49 GHz, Green et al. (2008) determined that G1.9+0.3 had expanded by 15% ± 2% over 23 years (∼0.65% per year). Using the same VLA observations from 1985 and 1989, Gómez and Rodríguez (2009) derived an expansion rate of 0.46%±0.11% and an age of $220\pm^{70}_{45}$ years. By comparing 2007 and 2009 *Chandra* X-ray images and utilising a simple uniform-expansion model, Carlton et al. (2011a,b) find an expansion rate of 0.642% ± 0.049% yr^{-1} and a flux increase of 1.7% ± 1.0% yr^{-1}, ageing the remnant at 156 ± 11 yr assuming no deceleration. Murphy, Gaensler and Chatterjee (2008) found that G1.9+0.3's flux density at 843 MHz increased by $1.22\pm^{0.24}_{0.16}$ % per year over the last two decades.

Borkowski et al. (2013) suggest that G1.9+0.3 was likely a Type Ia SNe with the shell of its remnant in free expansion with a velocity ∼18 000 km s^{-1}. The ejecta shows spatial asymmetry with prominent Fe-group elements in the northern rim. Also, we point out that Abramowski et al. (2014) report no γ-ray signal from G1.9+0.3 using observations from the H.E.S.S. (High Energy Stereoscopic System) Cherenkov telescope array.

The presence of polarised emission and spatial spectral variations are identified by Farnes (2012), with flatter spectra identified in the NW and SE of the remnant.

In this paper, we present the results of our Australia Telescope Compact Array (ATCA) radio-continuum observations of G1.9+0.3 made at 20, 13 and 6 cm in 2009. A comprehensive expansion study is conducted by comparing the new 6-cm observations with a previously unpublished 6-cm ATCA radio-continuum observation, made in 1993, and three 6-cm VLA observations made in 2008, 1989 and 1984 respectively. We also report on the radio-continuum spectral energy distribution and polarisation properties of this young SNR.

2. OBSERVATIONAL DATA

G1.9+0.3 was observed at 20, 13 and 6 cm wavelengths on four days in 2009 (Project C1952). Two of those days being in January 2009 with the remainder in February 2009. The 20-cm and 13-cm observations, taken on the 2nd and 3rd day, were carried out simultaneously as they make use of a common feed-horn. The 6-cm observations taken on the 1st and 4th day, used four different frequencies (two per day) to improve multi-frequency synthesis (MFS). For this purpose, the MIRIAD (Sault and Killeen 2008) task MFPLAN was used to select the most appropriate frequencies. Over the four days G1.9+0.3 was observed with two separate antenna configurations for a total of 29 independent baselines covering a range of spacings from 31 to 6 000 m. See Table 1 for complete observational details.

Table 1. 2009 ATCA observations of G1.9+0.3.

	Day 1	Day 2	Day 3	Day 4
Date	03 Jan	04 Jan	06 Feb	07 Feb
ATCA Array	6C	6C	EW352	EW352
Frequency 1	4.672 GHz	1.384 GHz	1.384 GHz	4.544 GHz
Frequency 2	5.440 GHz	2.368 GHz	2.368 GHz	5.184 GHz
Bandwidth	128 MHz	128 MHz	128 MHz	128 MHz
Time on source	332 min	458 min	509 min	1033 min
Primary Calibrator	J1934-638	J1934-638	J1934-638	J1934-638
Secondary Calibrator	J1741-312	J1751-253	J1751-253	J1741-312

[1]Spectral index defined as $S \propto \nu^{\alpha}$

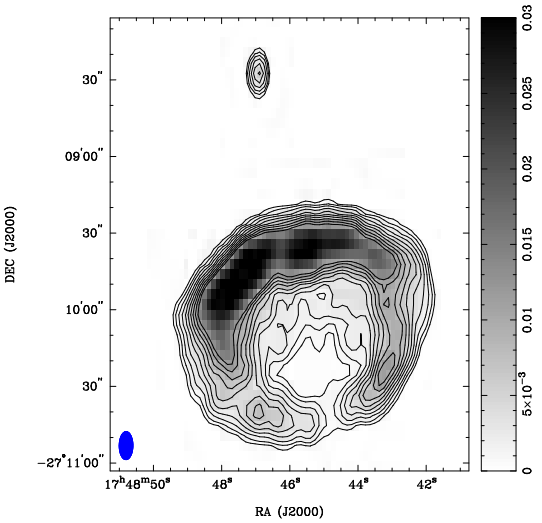

Fig. 1. *ATCA 20-cm image of Galactic SNR G1.9+0.3. The blue ellipse in the lower left corner represents the synthesised beam of* 10.″9 × 5.″4 *at PA=–0.°5. Contours are drawn at* 3σ, 5σ, 8σ, 12σ, 17σ, 23σ, 30σ, 38σ 47σ *and* 57σ *(*σ = 0.22 *mJy/beam).*

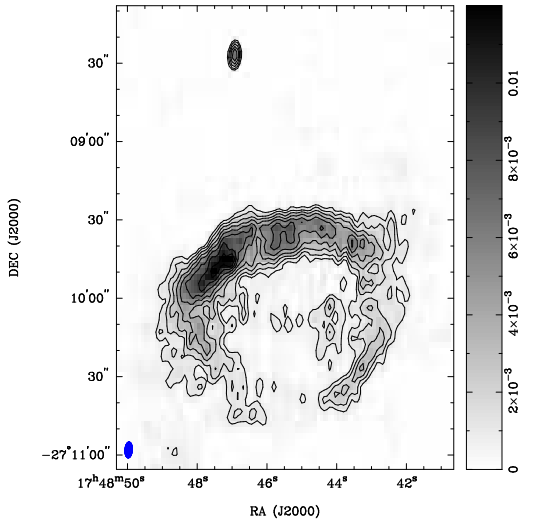

Fig. 2. *ATCA 13-cm image of Galactic SNR G1.9+0.3. The blue ellipse in the lower left corner represents the synthesised beam of* 6.″1 × 2.″9 *at PA=–0.°5. Contours are drawn at* 3σ, 5σ, 8σ, 12σ, 17σ, 23σ, 30σ, 38σ 47σ *and* 57σ *(*σ = 0.32 *mJy/beam).*

In Figs. 1 through 3 we show our new ATCA 2009 images of G1.9+0.3 at 20-cm, 13-cm and 6-cm respectively. All these images were formed using MFS with uniform weighting and were deconvolved using the MIRIAD (Sault and Killeen 2008) CLEAN and RESTOR tasks, with self calibration being applied to the 6-cm image only. We note that our corresponding ATCA flux density measurements are significantly smaller (∼50%) than the VLA estimates of Green et al. (2008). We can attribute this large difference to missing short spacings and poorer *uv* coverage of the ATCA images.

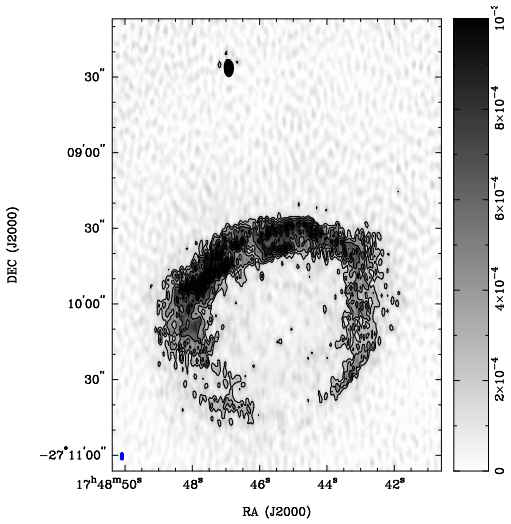

Fig. 3. *ATCA 6-cm image of Galactic SNR G1.9+0.3. The blue ellipse in the lower left corner represents the synthesised beam of* 2.″8 × 1.″2 *at PA=–0.°5. Contours are drawn at* 3σ, 5σ, 8σ, 12σ, 17σ, 23σ, 30σ, 38σ 47σ *and* 57σ *(*σ = 0.07 *mJy/beam).*

3. RESULTS

3.1. G1.9+0.3 Expansion and Age

A simple way to determine the age (in years) of a young SNR is to compare two images of the SNR taken at different epochs and to measure the percentage expansion the SNR has undergone over the time between the observations. Since we know that the SNR will have expanded by 100% in the intervening period between the SN explosion and the later observation, we can apply the simple formula, Age = 100%/ER, where ER is the percentage expansion the SNR has undergone over the time between the observations (in years).

Ideally, to most accurately determine the expansion rate of an SNR, one should compare images from similar observations i.e, at the same wavelength and having similar, if not identical, *uv*-coverage, resolution and *rms* noise.

In the case of G1.9+0.3 the first observations were made in 1984 using the VLA, with the best image produced from the 6 cm data (Fig. 4, bottom left). With this in mind, ATCA and VLA archives

Table 2. VLA observations of G1.9+0.3.

	1984 obs.	1989 obs.	2008 obs.
Date	26 May 1984	23 June 1989	12 March 2008
VLA Array	C	BC	C
Frequency	4.89 GHz	4.89 GHz	4.89 GHz
Bandwidth	50 MHz	50 MHz	50 MHz
Time on source	∼10 min	∼10 min	∼30 min
Primary Calibrator	3C286	3C286	3C286
Secondary Calibrator	J1832-105	J1751-253	J1751-253

were searched for all available radio-continuum data of G1.9+0.3 made at this same wavelength of 6 cm.

For the expansion study carried out in this paper, one ATCA and three VLA observations made at 6-cm were found at different epochs from the original 1984 to 2008.

The archival ATCA observation was taken on the 10^{th} June 1993 (Project C034; P.I.: A. Gray). This observation was made in the 6-cm band centred at 4672 and 5440 MHz with a bandwidth (BW) of 128 MHz and the telescope in 6A configuration[2]. Source 1934-638 was used for primary calibration and source 1748-253 was used for secondary calibration. The observations were done in the so-called "snap-shot" mode, totalling ∼1 hour of integration spread equally over a 12 hour period. With very few short baselines and poor *uv*-coverage, resulting *rms* of 0.2 mJy beam^{-1} is the highest amongst all the analysed observations. Consequently, the data for this observation are of very poor quality and, while the results are still presented here, we exclude measurements from this image in our determination of expansion rates and age. The archival VLA observations were from the 1984 (Project AG0146), 1989 (Project AB0544) and 2008 (project AG0793), see Table 2 for details.

All these observations of G1.9+0.3 were reduced and analysed with the MIRIAD (Sault, Teuben and Wright 1995) and KARMA (Gooch 1995) software packages.

As the resolutions of the produced images varied (due to the various array configuration, observational periods and therefore resultant *uv*-coverage), the resolutions of all the images were smoothed/convolved to match the image with the lowest resolution ($9'' \times 4''$ at a PA of 0°), see Fig. 4.

Since the *rms* noise of the resultant images also varied (see Table 3), it was decided not to try to determine the expansion by looking at how the shock front moved between epochs, but by looking at how the radially averaged shell profile peak moved from epoch to epoch.

Using RA=$17^{\rm h}48^{\rm m}45\overset{\rm s}{.}4$, Dec=$-27°10'06''$ as the centre of G1.9+0.3 we produced normalised shell profiles (Fig. 5), averaged over all angles, for each of the images shown in Fig. 4.

Table 3. G1.9+0.3 *rms* noise (1σ) of 6 cm images shown in Fig. 4. All five images shown in Fig. 4 have matched resolution of $9''\times4''$ at a PA of 0°.

Telescope	Date	Image *rms* (mJy/beam)
VLA	1984	0.09
VLA	1989	0.09
ATCA	1993	0.20
VLA	2008	0.06
ATCA	2009	0.06

From the shell profiles in Fig. 5 we have determined the expansion rate in arc-seconds per year, percentage expansion per year, the averaged expansion velocity in km s^{-1} (assuming a distance of 8.5 kpc[3]), and age in years. These results are summarised in Tables 4 though 7, respectively.

Table 4. Expansion rate of G1.9+0.3 in arc-seconds per year of radially averaged radio-continuum emission peak.

	1984	1989	2008	2009
1984	0			
1989	0.148	0		
2008	0.189	0.200	0	
2009	0.182	0.191	0	0

Table 5. % Expansion of G1.9+0.3 per year of radially averaged radio-continuum emission peak.

	1984	1989	2008	2009
1984	0			
1989	0.484	0		
2008	0.620	0.641	0	
2009	0.598	0.612	0	0

[2]We combined these two frequencies into a single 1 GHz band, see the image shown in Fig. 4 (middle left).

[3]Distance estimates to G1.9+0.3 vary between ∼7.8 kpc (Nord et al. 2004) and 10 kpc (Roy and Pal 2014). We use 8.5 kpc as the most likely distance – suggested by Reynolds et al. (2008).

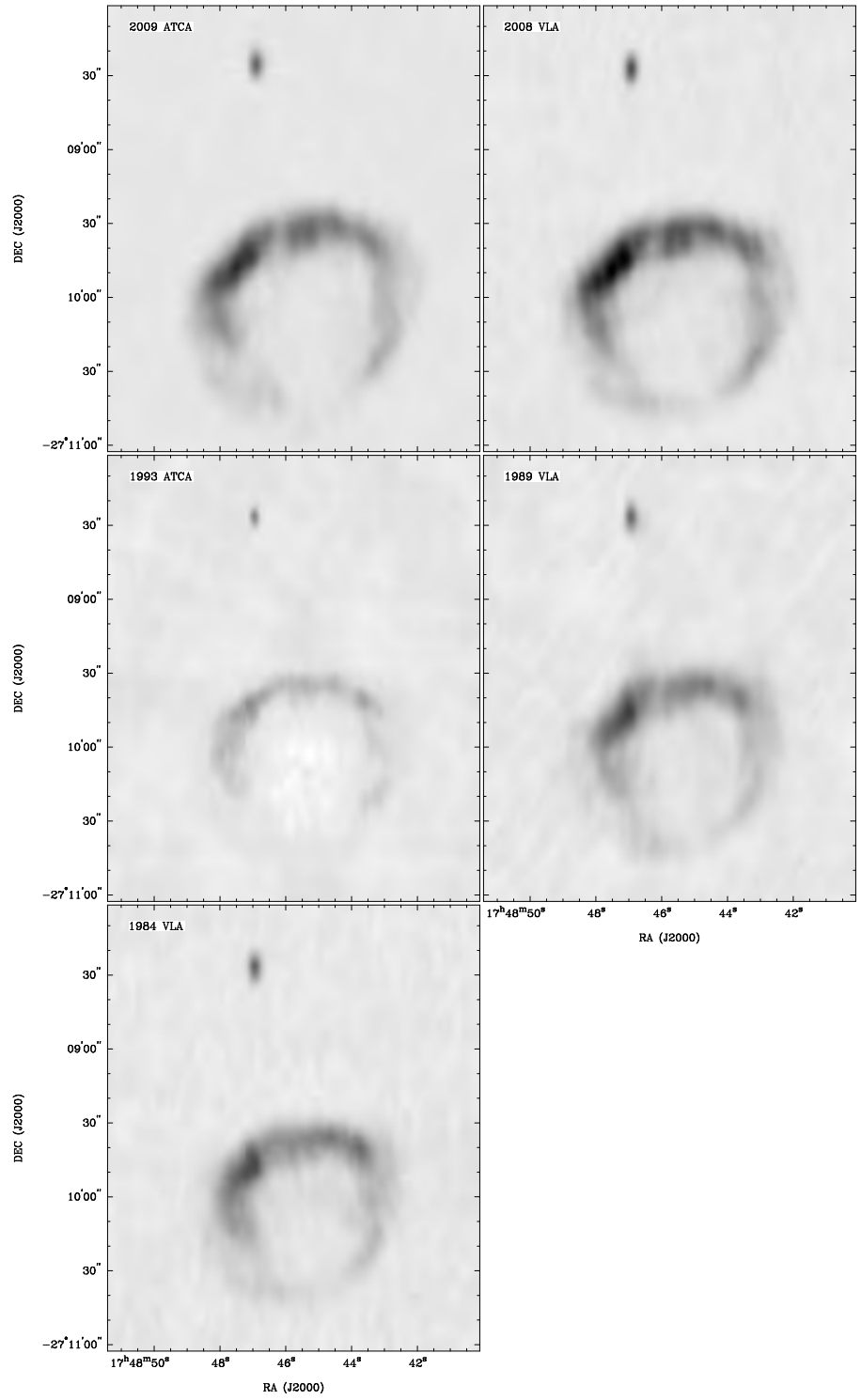

Fig. 4. *Matched resolution ($9'' \times 4''$ at a PA of $0°$) 6-cm images of Galactic SNR G1.9+0.3 (centred at RA(J2000)=$17^{\rm h}48^{\rm m}45\overset{\rm s}{.}4$, Dec(J2000)=$-27°10'06''$) at multiple epochs. Left to right, top to bottom, 2009 ATCA, 2008 VLA, 1993 ATCA, 1989 VLA and 1984 VLA.*

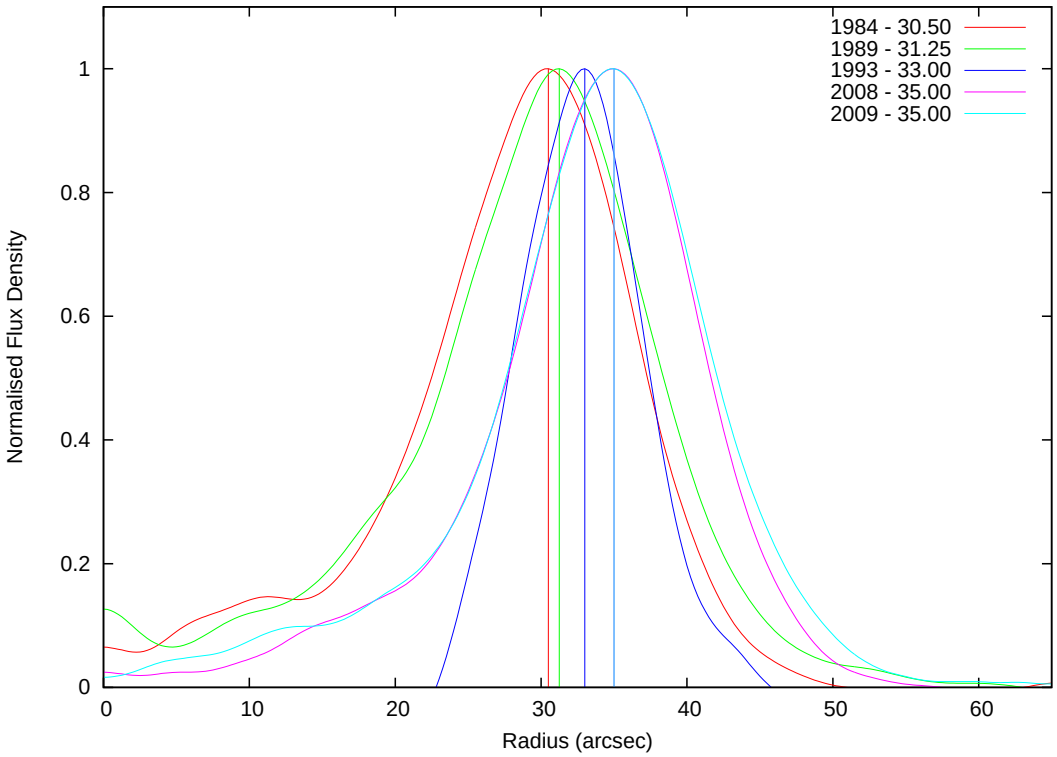

Fig. 5. *Normalised shell profiles averaged over all angles for each image of G1.9+0.3 in Fig. 4.*

Table 6. Estimated age of G1.9+0.3 in years.

	1984	1989	2008	2009
1984	0			
1989	206	0		
2008	161	156	0	
2009	167	163	0	0

Table 7. Speed of radially averaged radio-continuum emission peak in km s^{-1} of G1.9+0.3.

	1984	1989	2008	2009
1984	0			
1989	5 950	0		
2008	7 620	8 070	0	
2009	7 350	7 710	0	0

In Tables 4 and 5 we show the expansion of G1.9+0.3 over the period between 1984 and 2009. The mid range expansion over this period (excluding the 1993 observations) is 0.563%±0.078% yr^{-1} or 0.174±0.026 arcsec yr^{-1}. However, we note that between 1984 and 1989, G1.9+0.3 expanded at a somewhat slower rate (0.484% yr^{-1}) which was also estimated by Gómez and Rodríguez (2009) at 0.46% ± 0.11% based on 20-cm VLA data from the same period. Since 1989, G1.9+0.3 appears to expand at a faster rate of up to 0.641% per year which is in excellent agreement with the X-ray estimates of Carlton et al. (2011a,b) of 0.642%±0.049% and Green et al. (2008) using VLA observations. This may be an indication that perhaps the shock has "broken through" to a region of lower density and thus accelerated. The mid range expansion rate derived here, yields an upper age limit of 181±25 years (Table 6) assuming a constant expansion rate since the SN event. This dates the SN event back to the year 1828 (±25).

Similarly, the speed at which the radially averaged radio-continuum emission peak is moving (assuming a distance to G1.9+0.3 of 8.5 kpc) is somewhat slower in the 1980's (∼6 000 km sec^{-1}) than later, when it speeds up to ∼8 000 km sec^{-1} (Table 7). The speed of radially averaged radio-continuum emission peak should not be confused with the expansion velocity of the SNR shock front, which has been estimated at ∼18 000 km sec^{-1} by Borkowski et al. (2013).

As our determination of the radially averaged radio-continuum emission peak speed is dependent on the distance to the SNR we estimate that at the lower end (between 1984 and 1989) the speed varies between 5 500 km sec^{-1} (at a distance of 7.8 kpc) and 7 000 km sec^{-1} (at a distance of 10 kpc). More recently (between 1989 and 2009), the speed varies between 7 400 km sec^{-1} (at a distance of 7.8 kpc) and 9 500 km sec^{-1} (at a distance of 10 kpc).

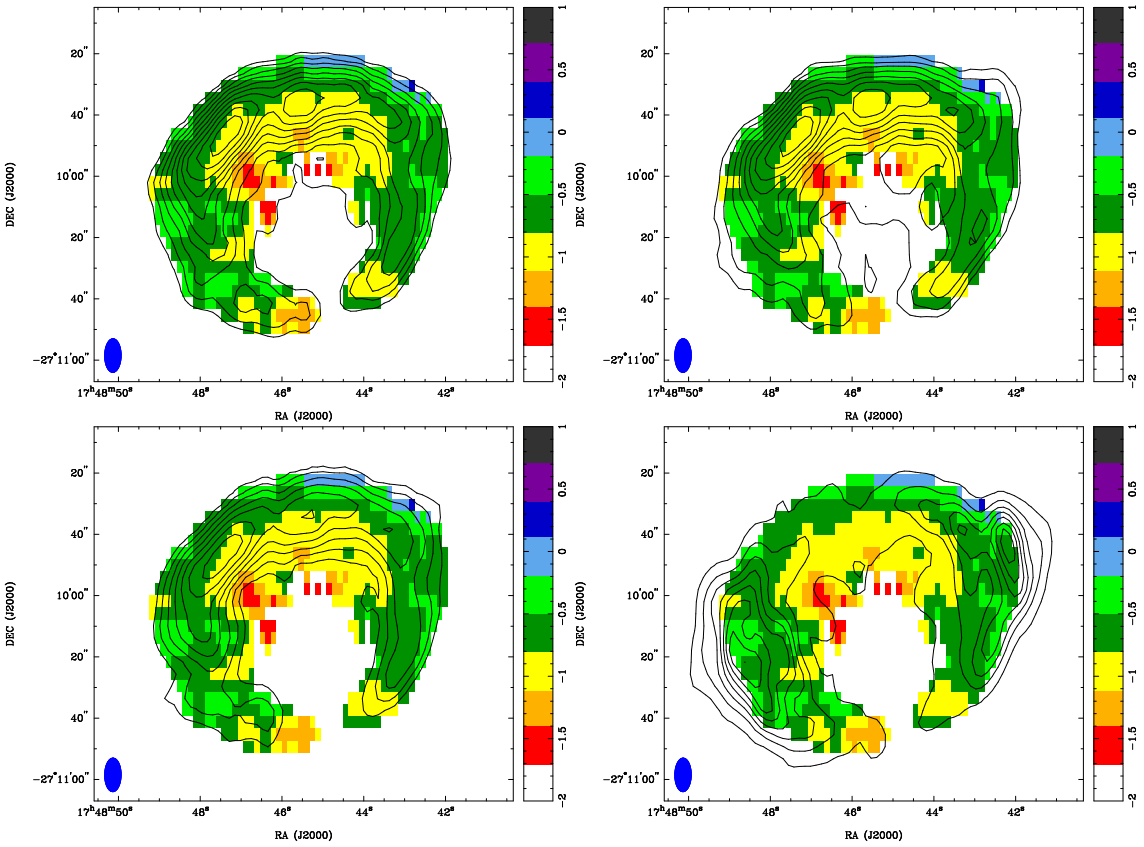

Fig. 6. *The Spectral Index map of G1.9+0.3 overlaid with 20-cm contours (top left; contours are: 3, 5, 8, 12, 12, 17, 23, 30, 38, 47, 57 × 7.5 × 10^{-4} Jy/beam), 13-cm contours (top right; contours are: 3, 5, 8, 12, 17, 23, 30, 38, 47, 57 × 6.0 × 10^{-4} Jy/beam), 6-cm contours (bottom left; contours are: 3, 5, 8, 12, 17, 23, 30 × 5.0 × 10^{-4} Jy/beam) and 2007 Chandra X-ray contours (bottom right; contours are: 33.57, 67.14, 100.7, 134.3, 167.9, 201.4, 235, 268.6 cts/s).*

3.2. G1.9+0.3 Spectral Energy Distribution

By matching the resolutions of our 2009 ATCA images at 6-cm and 13-cm to that of the 20-cm image (10.″9 × 5.″4 at PA=–0.°5), a three point spectral index map was created, allowing for the examination of the spatial spectral variations in the remnant (see Fig. 6). In this map, the colour of each pixel represents the spectral index α across the three observational frequencies.

From this map we can see that the radio-continuum spectral energy distribution across the NW and SE regions is flatter ($\alpha \sim -0.5$) which is also following the contours of the strongest of X-ray emission (so called "X-ray ears" of G1.9+0.3; see Fig. 6 – bottom right). This SED flattening in the NW and SE is also confirmed by Farnes (2012) in his VLA observations. The steeper ($\alpha \sim -1$) radio spectra is dominant in the Northern region of G1.9+0.3 corresponding to where the radio emission is the strongest and therefore indicating the synchrotron radio-continuum emission. We also note that a somewhat steeper spectral index ($\alpha < -1.0$) is dominating the inside part of the SNR, while flatter spectra is at the edges.

We estimate that the average spectral index across the entire SNR is $\alpha = -0.72 \pm 0.26$ which is flatter than LaRosa et al. (2000) ($\alpha = -0.93 \pm 0.25$), however, their estimates are based on 20/90 cm flux density measurements. This may indicate that the synchrotron emission may be even more dominant at higher wavelengths (92 cm). Using Green et al. (2008) flux density estimates at 20 and 6 cm from their 2008 VLA observations, we estimate the spectral index $\alpha = -0.62 \pm 0.08$ which is in good agreement with our ATCA estimates from approximately one year later. This steeper spectral index is expected for younger SNRs (Bell et al. 2011), and further confirms its young age.

3.3. Polarisation of G1.9+0.3

Since the ATCA observations recorded Stokes parameters Q, U and V, in addition to total intensity I, we were able to determine the polarisation of G1.9+0.3. In our 6-cm image (Fig. 7) we show the regions of polarised emission for G1.9+0.3. The electric field vectors follow the shell of the SNR around most of the circumference of the SNR, particularly along its eastern side.

The maximum fractional polarisation is estimated to be $P = 17 \pm 3\%$ with a mean of 6%. No reliable polarisation was detected at 20 or 13 cm. This might indicate a significant depolarisation in the remnant, however the polarimetric response of the ATCA is known to be poor at 13-cm.

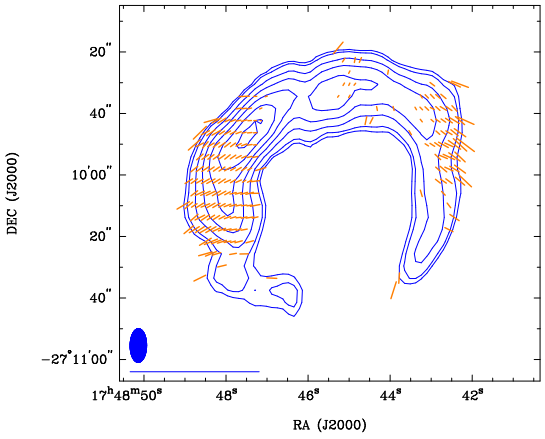

Fig. 7. *6-cm ATCA observations of G1.9+0.3. The blue ellipse in the lower-left corner represents the synthesised beam width of* $10\farcs940 \times 5\farcs384$ *at* $PA = -0\fdg5$. *The length of the vectors represents the fractional polarised intensity at each pixel position, and their orientations indicate the mean PA of the electric field (averaged over the observing bandwidth, not corrected for any Faraday rotation). The blue line below the beam ellipse represents the length of a polarisation vector of* 100%. *The maximum fractional polarisation is* $17\% \pm 3\%$ *with a mean of* 6%. *Contours at 2.2, 2.8, 4.4, 6.6, 9.4, 13, 17, 21, 26 and 32 mJy beam*$^{-1}$*).*

Typically, young type Ia SNRs exhibit a radially oriented magnetic field (tangentially oriented electric field), which is to be expected from Rayleigh-Taylor instabilities in a decelerating remnant (Gull 1975, Chevalier 1976). This is consistent with similarly young Galactic SNRs, as well as in the LMC (e.g. Table 3 in Bozzetto et al. (2014)). As we have plotted electric field vectors, we would expect them to be tangential to the circumference of the remnant. We can see in Fig. 7, the orientation of the electric field vectors roughly follow this arrangement, however, it can be seen that this pattern is not strictly followed around the entire remnant. Given the location of G1.9+0.3, towards the Galactic centre, this is most likely due to Faraday depolarisation.

Farnes (2012) also detected the presence of polarised emission. Our ATCA polarimetric results also suggest that the above observed variation is most consistent with an ambient B field perpendicular to the axis of bilateral symmetry indicated by Farnes (2012). Moreover, Farnes (2012) argues that the increased ordering of the B field in the NW as the strong Faraday depolarisation must also be present.

Farnes (2012) also argues that an intrinsically radially-oriented field could be provided by a systematic gradient in Rotation Measure (RM) of 140 rad m^{-2} from N to S and can also explain the depolarisation that we observe in our ATCA images.

3.4. Magnetic Field of G1.9+0.3

We used the new equipartition formulae derived by Arbutina et al. (2012, 2013) based on the diffusive shock acceleration (DSA) theory of Bell (1978) to estimate a magnetic field strength. These formulae are particularly relevant to magnetic field estimation in SNRs, and yield magnetic field strengths between those given by the classical equipartition (Pacholczyk 1970) and revised equipartition (Beck and Krause, 2005) methods. We estimate the magnetic field strength of G1.9+0.3 to be B $\approx$ 273 μG and the minimum total energy of the synchrotron radiation to be $E_{min} \approx 1.8 \times 10^{48}$ ergs (see Arbutina et al. 2012, 2013); and corresponding online calculator[4]). For this estimate, we used a spectral index value of $\alpha = -0.72$, integrated flux density $S_{1.425}$=0.935 Jy at ν=1.425 GHz (Green et al. 2008), distance D=8.5 kpc, SNR radius of r=46″ and filling factor of 0.33. However, if we additionally assume a shock velocity of 18 000 km s^{-1} (as suggested by Borkowski et al. (2013)) than the magnetic field strength of G1.9+0.3 becomes somewhat lower (B $\approx$ 180 μG) and the minimum total energy of the synchrotron radiation is $E_{min} \approx 7.6 \times 10^{47}$ ergs. These estimates are very similar to Arbutina et al. (2012) estimates of B $\approx$ 228 μG and $E_{min} \approx 9.3 \times 10^{47}$ ergs.

A large magnetic field strength such as this (273 μG) is expected for a young SNR (Bell 2004). Indeed, this makes G1.9+0.3 a remnant with one of the highest estimated magnetic field strengths known to date. For example, other young Galactic SNRs (Beck and Krause 2005, Arbutinal et al. 2012 (see their Table 1)), such as Cas A (B$\approx$ 1250 μG), Kepler (B$\approx$ 414 μG), G349.7+0.2 (B$\approx$ 523 μG) and Tycho (B$\approx$ 285 μG), are known remnants with the strongest magnetic fields. Also, in a Large Magellanic Cloud (LMC) SNR, J0509-6731 (also remnant from a Type Ia SN explosion) at about 400 yrs age has magnetic field strength of 168 μG (Bozzetto et al.

[4]http://poincare.matf.bg.ac.rs/∼arbo/eqp/

2014), while the magnetic field of LMC SNR J0519–6902 is 171 μG (Bozzetto et al. 2012). The Small Magellanic Cloud SNR HFPK 443 (Crawford et al. 2014, in press) has a field strength of 90 μG with numerous other older remnants falling below these values. It is most likely that G1.9+0.3 is going through an evolutionary stage where the magnetic field has been amplified (added to simple compression by the shocks), which may explain such a high magnetic field value (Telezhinsky et al. 2012). The amplification of magnetic field is a process driven by very fast shocks of young SNRs. Because of the strong amplification of magnetic field, a spectral index of $\alpha = -0.72$, and the location in the surface brightness-diameter diagram, this SNR is of younger age, in free expansion stage, and expanding in a low density environment.

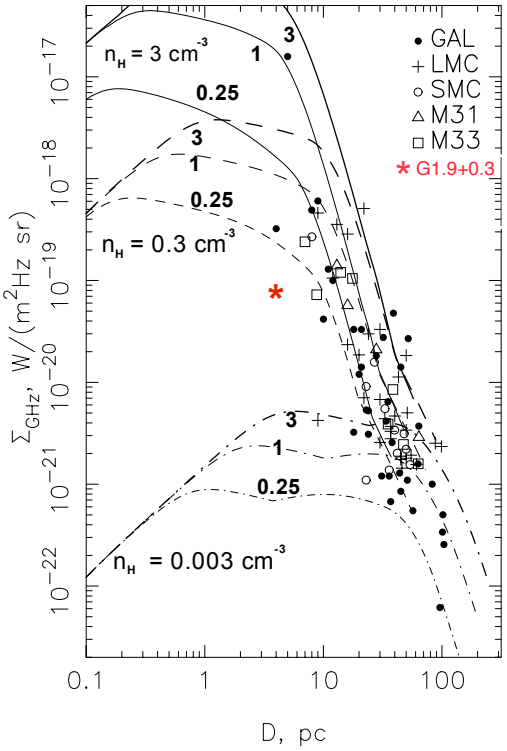

Fig. 8. *1 GHz surface brightness-to-diameter diagram from Berezhko and Völk (2004), with G1.9+0.3 added. The evolutionary tracks are for ISM densities of $N_{\rm H}$= 3, 0.3 and 0.003 cm^{-3} and explosion energies of $E_{\rm SN}$ = 0.25, 1 and 3×10^{51} erg.*

In Fig. 8 we show a surface brightness–diameter ($\Sigma - D$) diagram at 1 GHz with theoretically-derived evolutionary tracks (Berezhko and Völk 2004) superposed. G1.9+0.3 lies at (D, Σ) = (3.8 pc, 7.5×10^{-20} W m^{-2} Hz^{-1} Sr^{-1}) in the diagram. Its position on the diagram tentatively suggests that it is in the mid-to-late free expansion phase of evolution — expanding into a low density environment ($n_{\rm H} \lesssim 0.3$cm^{-3}).

4. CONCLUSIONS

Here, we have presented new 6-cm, 13-cm and 20-cm ATCA observations of Galactic SNR G1.9+0.3 made in 2009. Using the new 6-cm data and archival 6-cm data we observe that there are indications that the expansion of G1.9+0.3 accelerated after 1989. Our results are in a broad agreement with the estimates of expansion made by Reynolds et al. (2008), Green et al. (2008), Gómez and Rodríguez (2009) and Carlton et al. (2011a,b). We find that at $\sim$ 181 yrs, G1.9+0.3 is indeed very young and most likely the youngest SNR in the Milky Way. This very young age is also reinforced by the magnetic field arrangement and strength we estimate.

We make the following findings:

- Expansion rate of 0.484% per year between 1984 and 1989;
- Expansion rate of 0.641% per year between 1989 and 2009;
- Expansion rate of 0.563%±0.078% per year between 1984 and 2009;
- Age of 181 yrs±25 yrs;
- Average spectral index between 20-cm and 6-cm, across the entire SNR is α=–0.72±0.26;
- 6% fractionally polarised radio emission with a peak of 17%±3%;
- Magnetic field strength B≈273 μG;

Acknowledgements – We used the KARMA and MIRIAD software package developed by the ATNF. The Australia Telescope Compact Array is part of the Australia Telescope which is funded by the Commonwealth of Australia for operation as a National Facility managed by CSIRO. The Karl G. Jansky Very Large Array (VLA). The National Radio Astronomy Observatory is a facility of the National Science Foundation operated under cooperative agreement by Associated Universities, Inc.

REFERENCES

Abramowski, A. and H. E. S. S. Collaboration et al.: 2014, *Mon. Not. R. Astron. Soc.*, **441**, 790.
Arbutina B., Urošević D., Andjelić M. M., Pavlović, M. Z. and Vukotić B.: 2012, *Astrophys. J.*, **746**, 79.
Arbutina B., Urošević D., Vučetić M. M., Pavlović, M. Z. and Vukotić B.: 2013, *Astrophys. J.*, **777**, 31.
Beck, R. and Krause, M.: 2005, *Astron. Nachr.*, **326**, 414.
Bell, A. R.: 1978, *Mon. Not. R. Astron. Soc.*, **182**, 443.
Bell, A. R.: 2004, *Mon. Not. R. Astron. Soc.*, **353**, 550.
Bell, A. R., Schure K. M. and Reville B.: 2011, *Mon. Not. R. Astron. Soc.*, **418**, 1208.
Berezhko, E. G. and Völk, H. J.: 2004, *Astron. Astrophys.*, **427**, 525.

Borkowski, K. J., Reynolds, S. P., Hwang, U., Green, D. A., Petre, R., Krishnamurthy, K. and Willett, R.: 2013, *Astrophys. J.*, **771**, L9.

Bozzetto, L. M., Filipović, M. D., Urošević, D. and Crawford, E. J.: 2012, *Serb. Astron. J.*, **185**, 25.

Bozzetto, L. M., Filipović, M. D., Urošević, D., Kothes, R. and Crawford, E. J.: 2014, *Mon. Not. R. Astron. Soc.*, **440**, 3220.

Cappellaro, E.: 2003, in "Supernovae and Gamma-Ray Bursters", ed. Weiler K., Lecture Notes in Physics, Berlin Springer Verlag, Vol. **598**, 37.

Carlton, A. K., Borkowski, K. J., Reynolds, S. P., Willett, R., Krishnamurthy, K., Green, D. A. and Petre, R.: 2011a, in American Astronomical Society Meeting Abstracts 217. p. 256.12.

Carlton, A. K., Borkowski, K. J., Reynolds, S. P., Hwang, U., Petre, R., Green, D. A., Krishnamurthy, K. and Willett, R.: 2011b, *Astrophys. J.*, **737**, L22.

Chevalier, R. A.: 1976, *Astrophys. J.*, **207**, 872.

Farnes, J.: 2012, PhD thesis, University of Cambridge.

Gooch, R. E.: 1995, in Astronomical Data Analysis Software and Systems IV, ASP Conf. Series ed. Shaw, R. A., Payne, H. E. and Hayes, J. J. E., **77**, 144.

Gray, A. D.: 1994, *Mon. Not. R. Astron. Soc.*, **270**, 835.

Green, D. A. and Gull, S. F.: 1984, *Nature*, **312**, 527.

Green, D. A.: 2004, *Bull. Astr. Soc. India*, **32**, 335.

Green, D. A., Reynolds, S. P., Borkowski, K. J., Hwang, U., Harrus, I. and Petre, R.: 2008, *Mon. Not. R. Astron. Soc.*, **387**, L54.

Gómez, Y. and Rodríguez, L. F.: 2009, *Rev. Mex. Astron. Astrofis.*, **45**, 91.

Gull, S. F: 1975, *Mon. Not. R. Astron. Soc.*, **171**, 263.

LaRosa, T. N., Kassim, N. E., Lazio, T. J. W. and Hyman, S. D.: 2000, *Astron. J.*, **119**, 207.

Murphy, T., Gaensler, B. M. and Chatterjee, S.: 2008, *Mon. Not. R. Astron. Soc.*, **389**, L23.

Nord, M. E., Lazio, T. J. W., Kassim, N. E., Hyman, S. D., LaRosa, T. N., Brogan, C. L. and Duric, N.: 2004, *Astron. J.*, **128**, 1646.

Pacholczyk, A. G.: 1970, in "Radio astrophysics. Nonthermal processes in galactic and extragalactic sources", ed. A. G. Pacholczyk (San Francisco: Freeman).

Reynolds, S. P., Borkowski, K. J., Green, D. A., Hwang, U., Harrus, I. and Petre, R.: 2008, *Astrophys. J.*, **680**, L41.

Reynolds, S. P., Borkowski, K. J., Green, D. A., Hwang, U., Harrus, I. and Petre, R.: 2009, *Astrophys. J.*, **695**, L149.

Roy, S. and Pal, S.: 2014, in "Supernova environmental impacts", eds. Ray A. and McCray R. A., IAU Symposium Vol. **296**, 197.

Sault, B. and Killeen, N.: 2008, Miriad Users Guide. Australia Telescope National Facility.

Sault, R. J., Teuben, P. J. and Wright, M. C. H.: 1995, in "Astronomical Data Analysis Software and Systems IV ASP Conference Series", eds. Shaw, R. A., Payne, H. E. and Hayes, J. J. E., **77**, 433.

Telezhinsky, I., Dwarkadas, V. V. and Pohl, M.: 2012, *Astropart. Phys.*, **35**, 300.

van den Bergh, S. and Tammann, G. A.: 1991, *Annu. Rev. Astron. Astrophys.*, **29**, 363.

РАДИО-КОНТИНУУМ ЕМИСИЈА МЛАДОГ ГАЛАКТИЧКОГ ОСТАТКА СУПЕРНОВЕ G1.9+0.3

A. Y. De Horta[1], M. D. Filipović[1], E. J. Crawford[1], F. H. Stootman[1], T. G. Pannuti[2], L. M. Bozzetto[1], J. D. Collier[1], E. R. Sommer[1] and A. R. Kosakowski[2]

[1] *University of Western Sydney, Locked Bag 1797, Penrith South, DC, NSW 1797, Australia*

E–mail: *a.dehorta@uws.edu.au, m.filipovic@uws.edu.au, e.crawford@uws.edu.au*

[2] *Space Science Center, Department of Earth and Space Sciences, Morehead State University, 235 Martindale Drive, Morehead, KY 40351 USA*

E–mail: *t.pannuti@moreheadstate.edu*

УДК 524.354–77

Оригинални научни рад

У овој студији представљамо нова радио-континуум посматрања телескопом ATCA на 6 cm најмлађег остатка супернових (ОС) у нашој Галаксији. Анализирана су и сва доступна ATCA и VLA посматрања на овој фреквенцији. Остатак G1.9+0.3 је ∼181±25 година стар и годишња стопа раста му је 0.563%±0.078% у периоду између 1984. и 1989. Приметили смо да се између 1984. и 1989. остатак ширио нешто спорије (0.484% годишње) него после 1989., када је експанзија достигла ниво од 0.641% годишње. G1.9+0.3 има типичан радио-спектар за младе остатке са $\alpha = -0.72 \pm 0.26$. G1.9+0.3 емитује просечно 6% поларизованог зрачења на таласној дужини од 6 cm, са максималним интензитетом 17%±3%. Ова поларизациона емисија такође тесно прати рендгенско зрачење. Процењено је прилично јако магнетно поље у вредности од 273 μG што представља једно од најснажнијих магнетних поља у до сада посматраним ОС.

A.39 Related Paper 39

Roper, Q., McEntaffer, R. L., DeRoo, C., Filipovic, M., Wong, G. F., and Crawford, E. J. (2015). X-ray Spectroscopy of Potential Small Magellanic Cloud Type Ia Supernova Remnants and Their Environments. *ApJ*, 803:106

My contribution was to assist in the data analysis. This is a 10% contribution.

The Astrophysical Journal, 803:106 (14pp), 2015 April 20 doi:10.1088/0004-637X/803/2/106

X-RAY SPECTROSCOPY OF POTENTIAL SMALL MAGELLANIC CLOUD TYPE Ia SUPERNOVA REMNANTS AND THEIR ENVIRONMENTS

Q. Roper[1], R. L. McEntaffer[1], C. DeRoo[1], M. Filipovic[2], G. F. Wong[2], and E. J. Crawford[2]
[1] Department of Physics and Astronomy, University of Iowa, Van Allen Hall, Iowa City, IA 52242, USA; quentin-roper@uiowa.edu
[2] University of Western Sydney, Locked Bag 1797, Penrith South DC, NSW 1797, Australia
Received 2014 March 3; accepted 2015 February 12; published 2015 April 22

ABSTRACT

We examine three supernova remnants in the SMC, IKT 5 (supernova remnant (SNR) 0047-73.5), IKT 25 (SNR 0104-72.3), and DEM S 128 (SNR 0103-72.4), which are designated as Type Ia in the literature due to their spectra and morphology. This is troublesome because of their asymmetry, a trait not usually associated with young Type Ia remnants. We present *Chandra X-ray Observatory* data on these three remnants and perform a maximum likelihood analysis on their spectra. We find that the X-ray emission is dominated by interactions with the interstellar medium. In spite of this, we find a significant Fe overabundance in all three remnants. Through examination of radio, optical, and infrared data, we conclude that these three remnants are likely not Type Ia SNRs. We detect potential point sources that may be members of the progenitor systems of both DEM S 128 and IKT 5, which could suggest these could be Fe-rich core-collapse remnants.

Key words: ISM: individual objects (IKT 25, IKT 5, DEM S 128) – ISM: supernova remnants – methods: statistical

1. INTRODUCTION

Although much work has been produced in the *Chandra* and *XMM-Newton* era on the supernova remnant (SNR) population of the SMC, there is a subset of these remnants that are relatively understudied in the X-ray regime. This is at least in part due to their relative dimness in X-rays. van der Heyden et al. (2004) performed a detailed study of 13 SNRs using *XMM-Newton* and typed these objects based on morphology and spectral properties. In particular, they grouped three remnants, IKT 25, DEM S 128, and IKT 5 as probable Type Ia candidates, the result of thermonuclear detonation of a white dwarf. Their spectra are dominated by a single broad peak around 1 keV, with little else in the way of line emission. This broad peak could be associated with Fe-L shell emission arising from shock-heated ejecta, thus leading to the Type Ia designations. In addition, they are markedly different from other SMC SNRs in morphology, being very asymmetric in the soft X-ray band, as opposed to other, more symmetric core-collapse (CC) SNRs. SNR 0102-72.3 is a well-studied CC remnant (Flanagan et al. 2004), yet is highly symmetric both circularly and bilaterally. Other CC remnants in van der Heyden et al. (2004) also show high degrees of symmetry, such as IKT 6 (SNR 0049-73.6) and IKT 23 (SNR 0103-72.6).

In recent years, there has been a number of studies that attempt to characterize SNRs by their morphology. Previous studies have shown a link between soft X-ray morphology and progenitor type. Lopez et al. (2011) performed a survey of the young line-dominated LMC and galactic SNRs by analyzing the two-dimensional multipole moments of counts in the soft X-ray regime. When examining the quadrupole versus octupole moments, this population of SNRs was divided into two groups, with Type Ia SNRs having lower quadrupole and octupole moments, thus being more symmetrical in shape, both circularly and bilaterally, than their CC cousins. However, if the typing of SMC SNRs in van der Heyden et al. (2004) is correct, the Lopez et al. (2011) trend appears to be in stark contradiction to the SMC remnants. The previously mentioned SMC CC remnants appear to be relatively symmetric, both circularly and bilaterally. On the other hand, the three previously mentioned Type Ia candidates are highly asymmetric, thus displaying a morphological dichotomy in the SMC that is opposite to that found in the LMC or Milky Way. We present here a study aimed at providing further clarity to this apparent contradiction through spectral and spatial analysis of *Chandra* data for these Type Ia candidates, IKT 25, DEM S 128, and IKT 5. Detailed spectral analysis will either provide new insight into these objects and challenge their classification or confirm the *XMM-Newton* study, thus solidifying the curious difference between the SMC and its closest neighbors.

IKT 25 is the brightest of these three remnants in the X-ray band. Hughes & Smith (1994) presented *ROSAT* observations alongside CTIO Hα images and concluded that an unresolved point source in the X-ray has an Hα counterpart, thus suggesting a Be X-ray star association within the remnant. Lee et al. (2011) have performed a recent study utilizing the high spatial resolution of *Chandra* and find that this putative Be star is actually an extended knot of plasma. They find evidence of nonequilibrium plasma conditions and a marginal detection of Fe overabundance. Because it is seated within a complex environment, they conclude that IKT 25 is an example of a "prompt" Type Ia, whose progenitor system evolves to the supernova stage faster than typical (Borkowski et al. 2006).

DEM S 128 was initially identified through a survey of Hα emission nebulae (Davies et al. 1976). Inoue et al. (1983) reported the first X-ray observation of this remnant and detected an extended X-ray counterpart nearby to this Hα region, naming it IKT 24. Filipović et al. (2000) reported a continuum 843 MHz ATCA observation of this remnant and found significant radio emission. They compute radio spectral indices for sources coincident with the remnant and nearby X-ray sources RX J0105.5-7213, RX J0105.6-7211, and RX J0104.9-7210. They classify RX 0105.5-7213 as a background active galactic nucleus but are unable to classify the other two sources. They calculate a radio spectral index for DEM S 128 of $\alpha = -0.65$ suggesting an evolved SNR shock. Following this work, Filipović et al. (2005) observe the northern section

of the remnant at 2.37 GHz and show that the emission is constrained to a few bright spots that are uncorrelated with previous X-ray data, suggesting a complicated environment. Finally, Payne et al. (2007) report an S II/Hα ratio of DEM S 128 of 0.6, which is also consistent with the shell of an evolved remnant.

There is a paucity of observations on IKT 5. The first X-ray detection of IKT 5 was part of a large SMC survey by the *Einstein Observatory* (Inoue et al. 1983). In the optical, Payne et al. (2007) utilized long-slit spectroscopy to analyze IKT 5 along with other remnants in the SMC and found it to have a very high S II 6716 Å/ 673 Å line ratio. They also present a combined Hα and 843 MHz continuum image. Laycock et al. (2010) searched for X-ray binaries (XRB) in the SMC in the neighborhood of this remnant. They report finding an X-ray point source in the interior, labeled CXOU J004824-731918, but they conclude that due to the lack of a bright optical counterpart, this point source is likely not an X-ray binary. This leaves the possibility of another type of compact object.

The goal of our investigation is to conglomerate data at multiple wavelengths in order to better understand these potential Type Ia SNRs. Are they truly Type Ia remnants, with characteristic overabundance of Fe, or is there some other explanation of their X-ray 1 keV spectral feature? To what extent can their multiwavelength morphologies aid in determining their respective progenitor systems, if at all? What role do their environments play in determining their morphology? Does the environment of the remnant dominate morphology, or does the ejecta? Our goal is to provide insight to these questions with regard to IKT 5, IKT 25, and DEM S 128 and ultimately shed light on the SNR morphology dichotomy.

2. OBSERVATIONS

The observations of IKT 25 total 112 ks over two observations of on-axis time on the ACIS S-3 chip (observation IDs 9100 and 9810). In these same observations, another of these remnants, DEM S 128, was serendipitously detected on the ACIS S-2 chip (~6.′5 off-axis). Due to its front-illuminated nature, ACIS S-2 is less sensitive to the soft X-rays that dominate the emission of all three of these remnants. IKT 5 was also serendipitously observed as part of a deep-field observation searching for XRB in the SMC. As such, IKT 5 appears off-axis (~7.′5) for a total of 98 ks over three observations on the ACIS I-1 chip (observation IDs 7156, 8179, and 8481), which is also front-illuminated.

In order to analyze and extract images and spectra from these observations, we use the *Chandra* Interactive Analysis of Observations (CIAO) software package (Fruscione et al. 2006) version 4.4 with the Calibration Database (CALDB) version 4.4.8. All the data sets are reprocessed using the CIAO script *chandra_repro* in order to ensure the most modern and relevant calibrations were applied to the data sets. The observations of each remnant are merged using the *dmmerge* tool. The X-ray images were binned to the natural *Chandra* ACIS instrument resolution. The X-ray data were adaptively smoothed using the CIAO tool *dmimgadapt* using a Gaussian kernel. The X-ray images, adaptively smoothed, can be seen at the top of Figures 1–3.

To augment our analysis of these X-ray data, we examine the three remnants at different wavelengths. We analyze 20 cm data from the ATCA, which were reduced using MIRIAD (Sault et al. 1995). The infrared and optical data we present were taken with the *Spitzer Space Telescope*'*s* IRAC instrument, obtained through the *Spitzer* Heritage Archive, and optical data from the Magellanic Cloud Emission Line Survey (MCELS) in continuum-subtracted Hα, [S II], and [O III] bands. These particular wavebands have been included in order to qualitatively characterize the environments in which these SNRs are located.

3. X-RAY SPECTRAL ANALYSIS

Extraction regions for spectral analysis are determined through inspection of the X-ray images. The CIAO script *specextract* is used to extract spectra from regions, as well as produce the response matrices. The CIAO script *combine_spectra* is subsequently used to combine all the spectra from a given region into a single spectrum for analysis. For each remnant, there may be X-ray sources that are discrete and distinctive from the shocked plasma. In order for the X-ray plasma to be uncontaminated by these sources, we perform a point-source extraction to detect and exclude their contribution. To find these potential offenders, we used the CIAO tool *wavdetect* with wavelet transformation scales of 0.″5, 1″, 2″, and 4″. The output provides region files that encompass the 3σ extent of each source, where σ is the uncertainty in the point-spread function (PSF). To utilize this tool, we produced the expected off-axis PSF of *Chandra* using the *mkpsfmap* CIAO tool. After determination of point-source contributions, we chose extraction regions for each remnant based on suggestions from the apparent X-ray morphology. First, the X-ray emission of IKT 25 exhibits an apparent bipolar morphology roughly NW–SE, suggesting an analysis of regions along the axis of emission. This results in two extraction regions in the north (labeled A and B) and two in the south (labeled C and D), in addition to a region (the "Wisp") that includes a faint arc of emission evident in the east. Second, due to the low surface brightness of DEM S 128, we only use one X-ray extraction region for the entire remnant. Finally, the X-ray morphology of IKT 5 suggests two extraction regions: one in the north (northern) that corresponds to the more circular, diffuse emission surrounding the supposed point source, and one in the south (southern) that contains the wispy, more tenuous emission. The bottom of Figures 1–3 displays the X-ray data, with extraction regions overlaid.

A variety of thermal and nonthermal models are considered to find the best fit to these spectra using the *CIAO* fitting package, *Sherpa* (Freeman et al. 2001). We might expect some or all of these remnants to be in collisional ionization equilibrium (CIE) if they are older or in areas of enhanced density. In this case the plasma will be well described by the *xsvapec* model with the most up-to-date atomic processes in AtomDB 2.0.2 (Foster et al. 2012). If the plasma composing the SNR is younger or in a lower density regime, then the nonequilibrium model for singly shocked plasma, *xsvnei*, should accurately describe the spectra. The *xsvnei* model is used with an augmented line list from Kazik Borkowski that includes additional inner shell atomic processes (for a more complete explanation, see Badenes et al. 2006). A plane-parallel shock model, *xsvpshock,* is similar to *xsvnei*, but with a range of ionization timescales, which we might expect to see in regions where there are significant density gradients or complex ISM morphology. We fit these thermal models to the extracted spectra and also investigate contributions from nonthermal plasmas through the addition of a power-law component, using the *xspowerlaw* model. Elemental

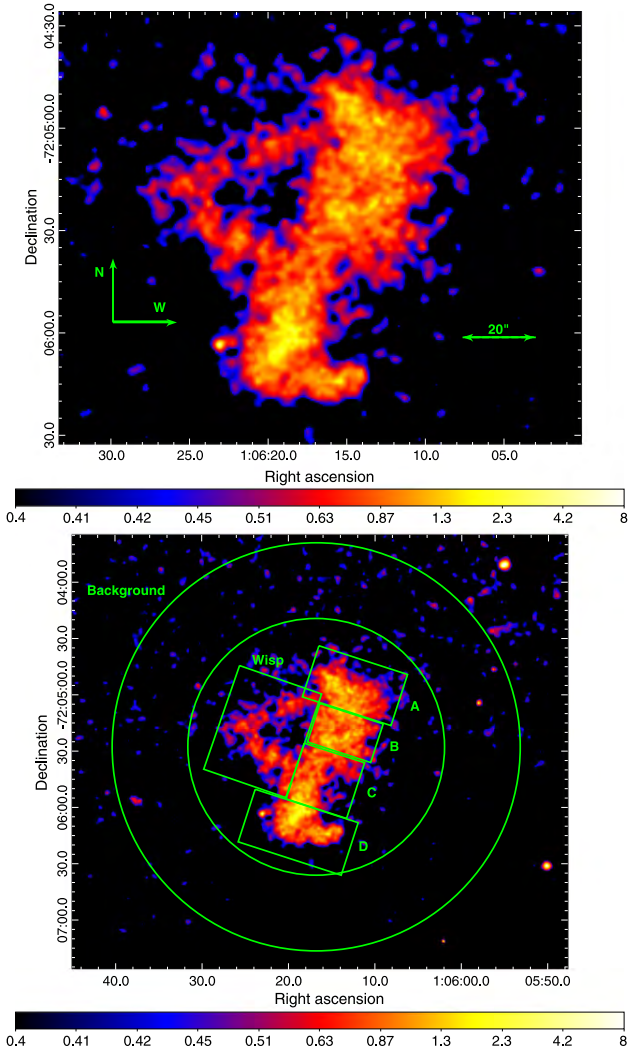

Figure 1. X-ray data of IKT 25. Broadband ACIS images (0.5–8 keV) of IKT 25, binned to the ACIS instrumental resolution (0.″5 per pixel) and adaptively smoothed using the *dmimgadapt* CIAO tool, with a kernel of 16 counts over scales from 0.5 to 16 pixels (top) and with spectral extraction regions overlaid (bottom). The color-bar scales are in counts/pixel.

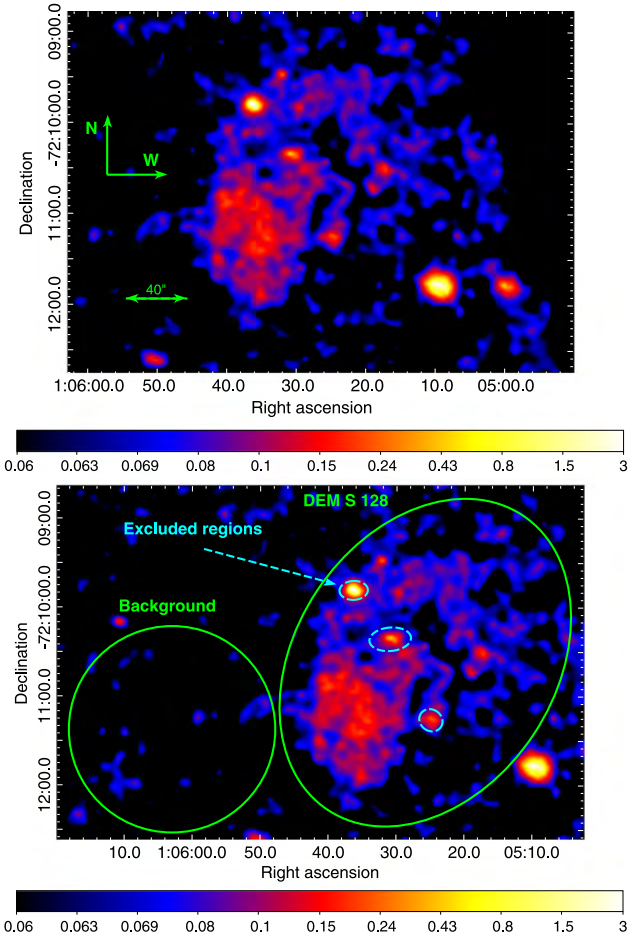

Figure 2. (a) X-ray data of DEM S 128. Broadband ACIS images (0.5–8 keV) of DEM S 128, binned to the ACIS instrumental resolution and adaptively smoothed, as in Figure 1. (b) X-ray image of DEM S 128 with spectral extraction regions overlaid. The color-bar scales of both images are in counts/pixel.

abundances are allowed to vary if statistically significant and are set to those of the SMC ISM per Russell & Dopita (1992): He 0.83, C 0.13, N 0.05, O 0.15, Ne 0.19, Mg 0.24, Al 0.80 (for *xsvapec* only), Si 0.28, S 0.21, Ar 0.16, Ca 0.21, Fe 0.20, and Ni 0.40, where a value of 1.0 signifies solar abundances. Since the majority of our X-ray emission exists between 0.7 and 1.0 keV, we pay particular attention to Fe-L shell emission lines and lines from Ne IX and Ne X in our fits, which are overabundant in the VDH04 fits.

The source spectral models are convolved through two separate absorption columns: one representing galactic absorption, *xstbabs*, with absorbers at galactic abundances and one representing absorption within the SMC, with SMC abundances, *xstbvarabs*. The galactic component is frozen at $N_H = 0.046 \times 10^{22}$ cm^{-2} for IKT 25 and DEM S 128 and at $N_H = 0.052 \times 10^{22}$ cm^{-2} for IKT 5 (Dickey & Lockman 1990), whereas the SMC component's hydrogen column density is allowed to vary. We choose *xstbabs* as a modern and complete absorption model, with abundances derived from Wilms et al. (2000) and photoionization cross-sections derived from Verner et al. (1996).

When performing spectral fitting, we use the Cash statistic (Cash 1979), which is a Poisson-likelihood statistic, as opposed to the χ^2 statistic. The latter assumes a Gaussian likelihood, whereas the Cash statistic better represents the distribution of counts per bin in the low-counts regime and is more appropriate for this investigation. In order to evaluate goodness-of-fit, we generate a distribution of best-fit statistics we expect, given the best-fit model and degrees of freedom. We construct this distribution by evaluating the best-fit model onto the spectral bins, adding in a Poisson noise component and evaluating the Cash statistic when the model is reapplied to the synthesized spectra. Repeating this process many times, we can construct a distribution of Cash statistics we might expect, given the model and degrees of freedom. If the statistic we derive from fitting the spectrum extracted from the observation is extreme compared to the distribution of statistics generated from the synthesized spectra, we rule out the fit. In our best-fit tables, Tables 1–3, we state the probability of finding a best-fit statistic lower than the one obtained in our fit, which we label 1 − (P-value).

In order to determine the statistical significance of additional model components, a variation of the likelihood ratio test

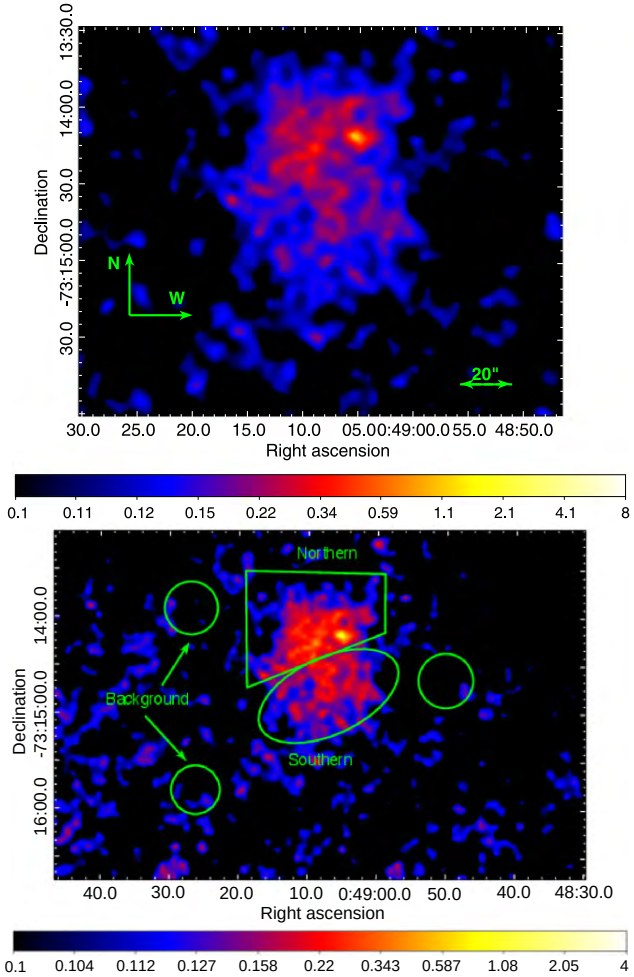

Figure 3. (a) X-ray image of IKT 5. Broadband ACIS images (0.5–8 keV) of IKT 5, binned to the ACIS instrumental resolution and adaptively smoothed, as in Figure 1. (b) X-ray image of IKT 5 with spectral extraction regions overlaid (bottom). The color-bar scales are in counts/pixel.

(LRT) is employed. As noted by Protassov et al. (2002), the LRT is not usable in the case when the simpler model is on the boundary of the parameter space of the more complicated model, as is the case when testing for an additional thermal model. This is because the null distribution used to judge the likelihood ratio is uncalibrated and, in general, analytically unknown. In order to solve this problem, we construct the null distribution of the LRT numerically by evaluating the likelihood ratio on synthetic spectra produced by adding a Poisson noise component to the best-fit simpler model. Due to computational limitations, we perform this 400 times for each spectrum. If the likelihood ratio is sufficiently high when compared to the constructed null distribution, we can be confident that the more complicated model is a better description of the spectrum, rather than an artificial improvement due to the more complicated model having more free parameters. We adopt a P-value of 0.1 to be the maximum for which we consider the more complicated model "better", i.e., the fit improvement has to be greater than the 90th percentile of the constructed null distribution to be considered a significant improvement over the simpler model. In this way, we numerically construct the LRT null distribution and restore its usefulness in distinguishing between a spectrum produced by one thermal component or by two thermal components. This method is similar to, but not identical to, the parametric bootstrapping described in Section 5.2 of Protassov et al. (2002).

4. RESULTS

4.1. IKT 25

For IKT 25, the best-fit models and their best-fit parameters are shown in Table 1. The spectra we obtained, with best-fit model overlaid, can be seen in Figures 4 and 5. Regions A, B, and D are best-fit with a CIE plasma model with temperature of ~1.0 keV. Region C is best fit with a two-temperature model with a CIE component at kT ~0.6 keV and an NEI component at kT ~ 1.0 keV. When we fit this region with a one-temperature CIE plasma model, it resulted in a temperature of around 1.0 keV, similar to the other three regions. Adding the NEI component decreased our statistic from 202/195 to 188/192, which was significant, with a P-value of 0.0025 (See Figure 8). In all regions we require an enhanced Fe abundance in order to fit the spectra, and in all regions the significance of the Fe overabundance was >5σ. With the Wisp, we found the best-fit model to be a two-temperature model as in Region C, with one important difference: we found a 5σ enhanced silicon abundance in addition to enhanced iron abundance. The improvement to the fit when compared to a single-temperature CIE model is significant, with a P-value of 0.0026 (Figure 8). The absorbing column density N_H varies greatly across the remnant, with Regions A, B, and D having a relatively small absorbing column density, at $<6 \times 10^{21}$ cm^{-2}. Regions C and the Wisp have a much larger absorbing column density at $\sim 1.5 \times 10^{22}$ cm^{-2}, and this higher absorbing column density is retained if only one thermal component is assumed.

4.2. DEM S 128

The best-fit model of the X-ray spectrum of DEM S 128 is given in Table 2 and is overlaid onto the extracted spectrum in Figure 6. With only one region extracted from DEM S 128, it is impossible to say anything about the spatial distribution of material in the SNR. However, in comparison to IKT 25, the absorbing column density is consistent with Regions A, B, and D at $\sim 3.5 \times 10^{21}$ cm^{-2}. Again, Fe was necessary to vary in the fit. As in IKT 25, the Fe abundance was enhanced at ~1.0 solar and was very significant at ~7 σ. All other elements were set to SMC abundance. Only one CIE thermal component was required, but the temperature was somewhat cooler than in IKT 25, at 0.65 keV.

4.3. IKT 5

The extraction regions for IKT 5 were chosen because the X-ray morphology suggests confinement in the north and extension toward the south. The best fits of the X-ray spectra obtained from the northern and southern regions can be found in Figure 7 and Table 3. As in IKT 25 and DEM S 128, we find an Fe overabundance in both the northern and southern regions of the remnant. The northern region has a ~6σ significant overabundance at 0.8 solar. The southern region has a higher Fe abundance at twice solar, but whose overabundance is much lower significance, at only ~2.5 σ. The northern region is well fit by a 0.94 keV equilibrium plasma. The southern region contains a lower-temperature equilibrium plasma at 0.56 keV

Table 1
Best-Fit Parameters for IKT 25 by Extraction Region

Region	Best-Fit Model	cstat/dof	1 - (P-value)	$N_{H,\mathrm{SMC}}$ (10^{22} cm^{-2})	kT_{vapec} (keV)	A_{Fe}	$\mathrm{norm}_{\mathrm{vapec}}$ (10^{-5} A)[a]	kT_{nei} (keV)	τ_{nei} (10^{11} cm^{-3} s)	$\mathrm{norm}_{\mathrm{nei}}$ (10^{-5} A)	A_{Si} Percentile	F-test P-value
A	$\mathrm{tbabs_{gal}} \times \mathrm{tbvarabs_{SMC}} \times$ vapec	202/195	75.0%	$0.58^{+0.15}_{-0.10}$	$0.95^{+0.02}_{-0.02}$	$1.2^{+0.2}_{-0.2}$	$6.1^{+0.7}_{-0.7}$	...	...	...	...	...
B	$\mathrm{tbabs_{gal}} \times \mathrm{tbvarabs_{SMC}} \times$ vapec	204/195	24.4%	$0.32^{+0.08}_{-0.08}$	$0.92^{+0.02}_{-0.03}$	$0.8^{+0.2}_{-0.1}$	$6.2^{+0.5}_{-1.0}$	...	...	...	...	...
C	$\mathrm{tbabs_{gal}} \times \mathrm{tbvarabs_{SMC}} \times$ (vapec + vnei)	188/192	10.6%	$1.4^{+0.6}_{-0.4}$	$0.68^{+0.04}_{-0.04}$	$0.7^{+0.2}_{-0.1}$	$1.2^{+0.2}_{-0.2}$	$0.98^{+0.05}_{-0.05}$	$2.8^{+0.2}_{-0.2}$	$1.4^{+0.2}_{-0.8}$	0.0026	
D	$\mathrm{tbabs_{gal}} \times \mathrm{tbvarabs_{SMC}} \times$ vapec	189/195	86.8%	$0.27^{+0.08}_{-0.07}$	$1.03^{+0.01}_{-0.02}$	$0.8^{+0.1}_{-0.1}$	$8.9^{+0.4}_{-0.7}$	...	...	...	...	...
Wisp	$\mathrm{tbabs_{gal}} \times \mathrm{tbvarabs_{SMC}} \times$ (vapec + vnei)	219/191	89.0%	$1.3^{+1.3}_{-0.3}$	$0.58^{+0.04}_{-0.04}$	$0.7^{+0.2}_{-0.1}$	$1.7^{+0.5}_{-0.4}$	$0.9^{+0.2}_{-0.1}$	>2.0	$0.9^{+0.4}_{-0.4}$	$1.3^{+0.3}_{-0.2}$	0.0025

Note. Spectral-fitting results by region listed in Figure 1. The remnant and regions are listed in the first two columns, with the next column indicating the best-fit model. Errors shown are analogous to 1σ. Abundances are shown relative to solar, with solar values equal to 1.

[a] Normalization parameter, where $A = [10^{-14}/(4\pi D^2)] \int n_e n_H dV$, D is the distance to the SMC, and the integral is the emission measure.

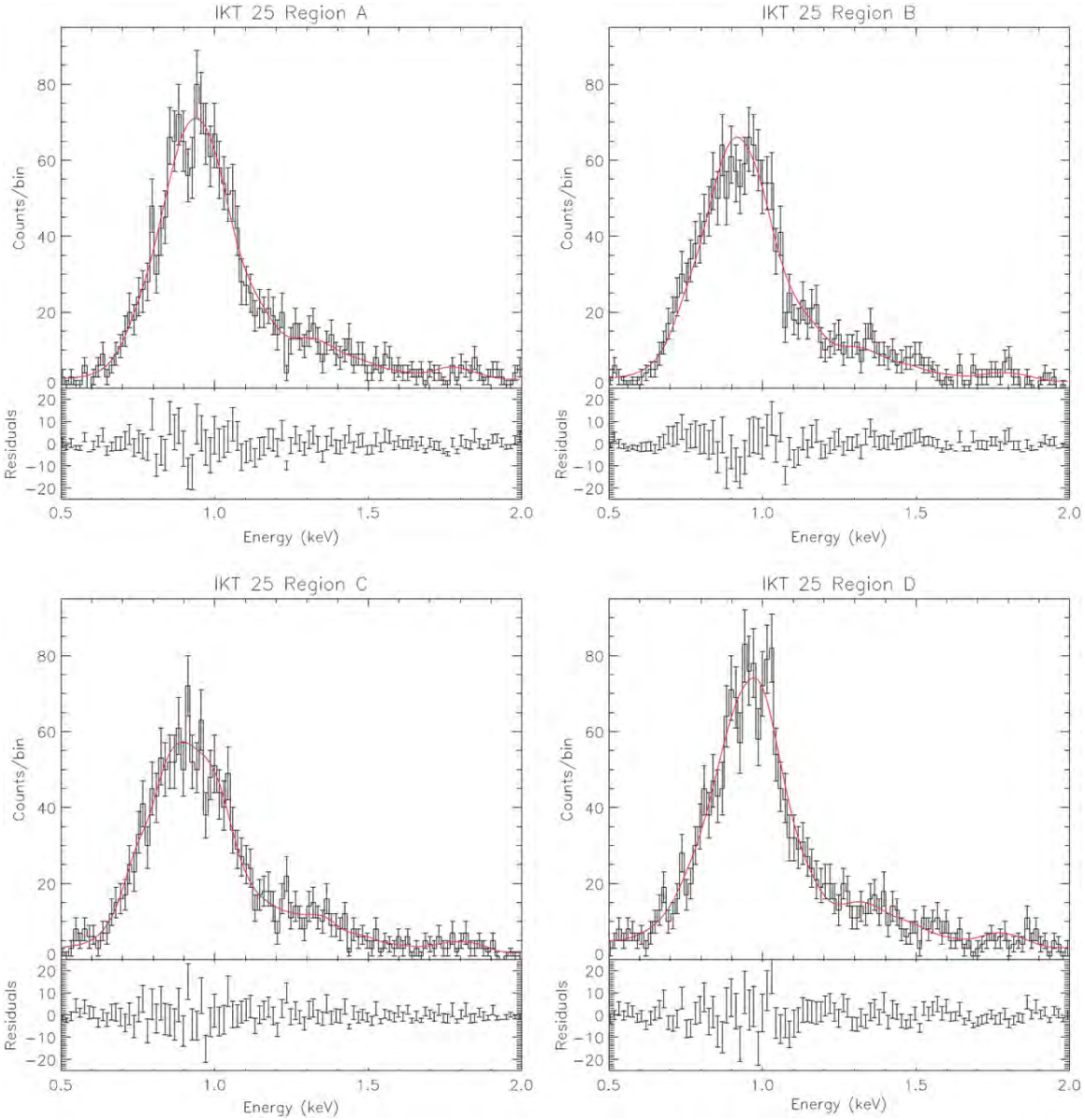

Figure 4. X-ray spectra extracted from IKT 25 from Regions A, B, C, and D in Figure 1 in black with best-fit models corresponding to the best-fit model in Figure 1 overlaid in red, as well as the residuals of the fit. The uncertainties presented are Poisson, and indicate the 68% error range to be somewhat analogous to the Gaussian case.

combined with a higher-temperature nonequilibrium plasma at 0.98 keV.

4.4. Derived Physical Characteristics

Using the parameters of our spectral fits we can calculate additional characteristics such as plasma density and shock velocity in order to learn more about these remnants and under what conditions they formed. Solving the Rankine–Hugoniot relations in the strong shock case with $\gamma = 5/3$ gives the post-shock temperature as a function of shock velocity, $kT = (3/16)\,\mu\, m_p\, v^2$, with the average mass per particle $\mu = 0.6$. We assume that $T_e \sim T_{\rm ion}$, as expected through Coulomb collisions in a plasma with a temperature of $\sim 10^6$ K and $n_e \sim 1\,{\rm cm}^{-3}$ (Draine 2011). If the electrons and ions are not in temperature equilibrium, then the calculated velocities signify lower bounds. The density is found using the norm parameter for each component, where norm $=[10^{-14}/(4\pi D^2)]\int n_e n_H dV$, where D is the distance to the source, in this case the SMC. The value $\int n_e n_H dV$ is the emission measure, where n_e and n_H are the electron and proton densities, and V is the volume of emitting plasma. A value of 61.3 kpc is used for D (Hilditch et al. 2005), and we assume that $n_e = 1.2 n_H$. We include a filling factor, f, which ranges from 0 to 1, to account for the fraction of the volume actually filled with X-ray-emitting plasma. We can also estimate the age of the remnant from the equilibrium shock velocities. Assuming that each remnant can be described by a Sedov solution (Spitzer 1998), the time since shock heating can be calculated as $t = (2/5)R/v$, where R is the estimated shock distance from the center. In Table 4, we detail the physical results calculated from our best-fit models.

Table 2
Best-Fit Parameters for DEM S 128

Best-Fit Model	cstat/dof	1 - (P-value)	$N_{H,\mathrm{SMC}}$ (10^{22} cm^{-2})	kT_{vapec} (keV)	A_{Fe}	$\mathrm{norm}_{\mathrm{vapec}}$ (10^{-5}A)[a]
$\mathrm{tbabs_{gal}} \times \mathrm{tbvarabs_{SMC}} \times$ vapec	219/200	12.4%	$0.35^{+0.14}_{-0.12}$	$0.65^{+0.03}_{-0.03}$	$0.9^{+0.2}_{-0.1}$	15^{+3}_{-2}

Note. Spectral-fitting results of DEM S 128 with extraction and background regions and Figure 2. The remnant and regions are listed in the first two columns, with the next column indicating the best-fit model. Errors shown are 1σ. Abundances are shown relative to solar, with solar values equal to 1.
[a] Normalization parameter, where $A = [10^{-14}/(4\pi D^2)] \int n_e n_H dV$, D is the distance to the SMC, and the integral is the emission measure.

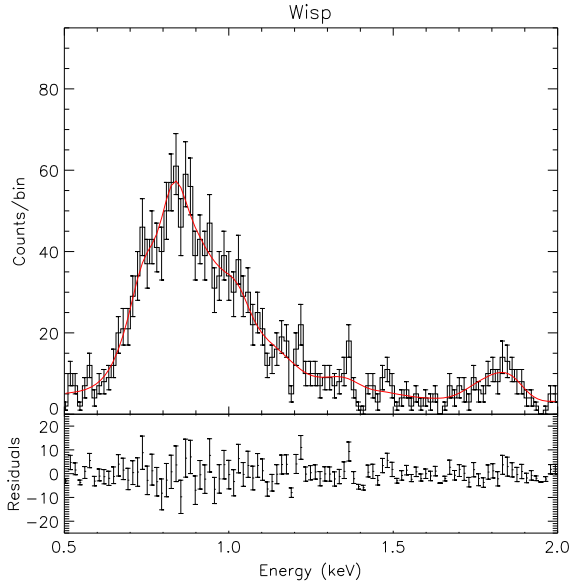

Figure 5. X-ray spectra extracted from IKT 25 from the Wisp region in Figure 1 in black with best-fit models corresponding to the best-fit model in Figure 1 overlaid in red, as well as the residuals of the fit. The uncertainties presented are Poissonian, and indicate the 68% error range to be somewhat analogous to the Gaussian case.

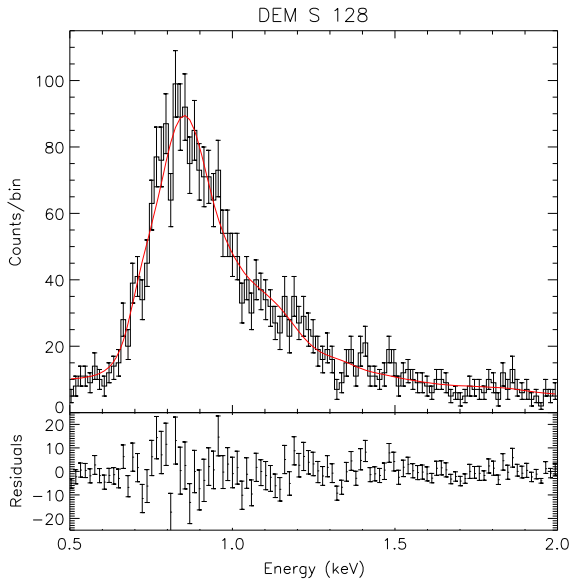

Figure 6. X-ray spectra extracted from DEM S 128 in black with best-fit models corresponding to the best-fit model overlaid in red. The uncertainties presented are Poissonian and indicate the 68% error range to be somewhat analogous to the Gaussian case.

It should be noted that in all three of these remnants, we find exotic environments that, at least in some cases, modify the plasma of the remnants asymmetrically, as detailed in the Discussion section of this paper. It is possible that none of these remnants are accurately described by a Sedov solution for this reason. In an effort to minimize this deviance from an idealized Sedov solution, we only use regions for each remnant where we have determined that the complicated environment has a minimized impact on the development of the SNR to determine its physical characteristics.

For IKT 25, the velocities derived from the fit are ~900 km s^{-1} across every region. Region C has a relatively low density, ~0.15 cm$^{-3}/f^{1/2}$, compared to Regions A, B, and D, which are >0.25 cm$^{-3}/f^{1/2}$. The Wisp has the lowest density in the remnant, with two components, both of which are <0.1 cm$^{-3}/f^{1/2}$. Therefore, even though Regions C and the Wisp exhibit the largest absorbing column densities, the X-ray-emitting plasma is relatively tenuous. DEM S 128 exhibits a relatively slow shock (~750 km s^{-1}), low density at <0.1 cm$^{-3}/f^{1/2}$, and in our sample has the largest physical X-ray size, suggesting that it is the oldest of our three remnants. IKT 5 has a low density, more consistent with DEM S 128 at ~0.1 cm$^{-3}/f^{1/2}$, even though its temperature remains relatively high.

5. DISCUSSION

5.1. IKT 25

In comparison to van der Heyden et al. (2004), we find that the temperatures across the remnant are somewhat hotter, ~1.0 keV compared to VDH04's finding of 0.6 keV. They do not examine the spatial dependence of the absorption column density and find a global absorbing column density of 4.1×10^{21} cm^{-2}, which, while consistent with our Regions A, B, and D, we find to be very low compared to our Region C and Wisp fits, whose absorbing column density is as high as 1.5×10^{22} cm^{-2}. Unlike VDH04, we do not find any evidence for enhanced Ne in the remnant. This is likely a consequence of the models in this paper being more advanced than those used in VDH04. In particular, the modeling of Fe-L shell ions from 0.8 to 1.0 keV has improved immensely in APED. The additional lines significantly increase the total line flux contribution from species in this energy range, thus decreasing the importance of the Ne lines in comparison to the newly added suite of Fe lines. When comparing to Lee et al. (2011), we find a cooler temperature than their 2.0 keV. Lee et al. (2011) also do not examine the spatial variation in the absorbing column density. Instead, they hold the column density across the remnant fixed to the value of their global fit, 9.1×10^{21} cm^{-2}. In Regions B and D, we find the absorbing column density to be as low as $\sim 3 \times 10^{21}$ cm^{-2}, with higher absorbing column density $\sim 1.5 \times 10^{22}$ cm^{-2} in Region C and

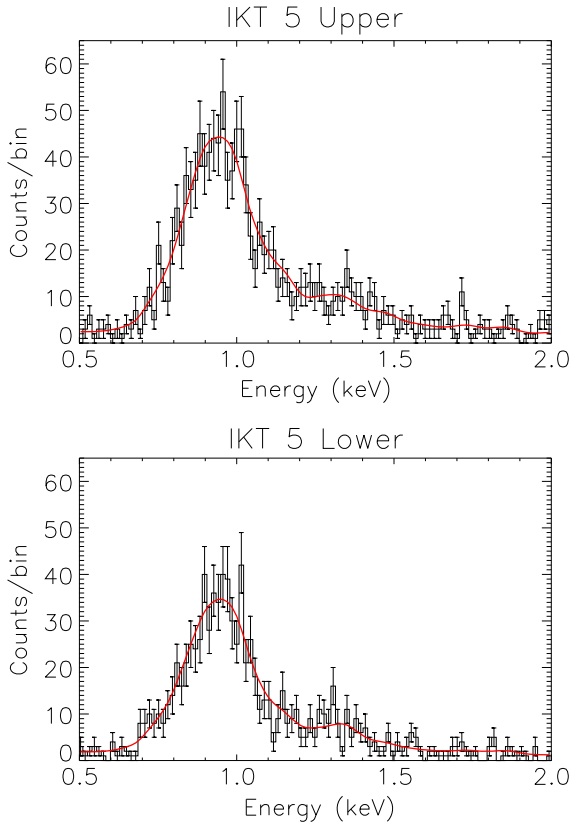

Figure 7. X-ray spectra extracted from IKT 5 in Figure 3 in black with best-fit models corresponding to the best-fit model in Figure 3 overlaid in red, by region. The uncertainties presented are Poissonian and indicate the 68% error range to be somewhat analogous to the Gaussian case.

the Wisp. In addition, our Fe overabundance is found to be more significant. Our norm-averaged Fe abundance across Regions A–D is 1.0 ± 0.1, which is 8 σ significance overabundant, whereas their norm-averaged Fe abundance across analogous regions Bar01–Bar04 is $\sim 1.08 \pm 0.32$, only 2.75 σ significance overabundant. It should be noted that a direct abundance comparison to Lee is difficult because they use the wrong abundances for the SMC. In particular, the abundances quoted in Table 1 of Lee et al. (2011) actually match the Table 1, column 8 values of Russell & Dopita (1992), which are the errors in the SMC abundances, not the abundances themselves, therefore rendering the results suspect. Using the improved statistical approach with accurate abundances and up-to-date line lists, we have more tightly constrained physical parameters and detect a more robust Fe enhancement for IKT 25, in comparison to previous studies.

Our X-ray results indicate that, with the exception of enhanced Fe, our remnant is ISM-dominated. We frame our X-ray results with data from other wavelengths to qualitatively probe how this remnant interacts with its environment. We use our IR and optical data (Figure 8) as images to compare with our X-ray and radio data for further insight into the emission of these remnants. From the radio contours of IKT 25 (Figure 9 (a)), we see evidence of a supernova (SN) blast wave traveling through material that is roughly anticoincident with the X-ray emission of the remnant. The radio emission is highly coincident with the IR emission in the northeast. Synchrotron emission in the lowest-density regions of the shock may explain the radio emission, whereas shock-heated material with subsequent cooling emission explains the IR, optical, and X-ray emission, albeit at different densities. The optical emission shows primarily cooling lines from regions in the shell with densities much higher than those in the X-ray plasma. The IR emission is roughly anticoincident with Regions A, B, and D and coincident with the Wisp region. The presence of significant IR emission suggests the existence of a local enhancement of the ISM density, which would give rise to the much higher line-of-sight (LOS) absorption column density in the Wisp region. The Wisp is also the only region in any of our remnants with enhanced Si, which is found to be >5σ. This enhancement is quite evident in the Wisp spectrum as the large bump at 1.8 keV Si XIII, especially when compared to all other spectra. This strongly suggests an enhancement of Si ejecta in this region. Its existence in the Wisp suggests that the supernova blast wave in this region is transitioning from the adiabatic phase to the radiative phase, and it contains only small pockets of gas at X-ray-emitting temperature with a low filling factor, which is consistent with a local enhancement of ISM density. The overabundance of Si in addition to Fe strongly suggests a Type Ia designation.

The bipolar morphology of IKT 25 may be due to asymmetry in the explosion mechanism of the progenitor system or modification by the environment. In either case, and especially for an asymmetric explosion, one might expect older plasma toward the center, with more recently shocked gas in Regions A and D. In this scenario we must be careful with the derived radii and velocities in Regions B and C, as they may be affected by LOS projection. In other words, much of the emitting plasma in B or C may actually be at a large radius, comparable to Regions A and D, yet just appear closer to the center in the X-ray data due to projection onto the plane of the sky. However, as seen from the X-ray spectral fit, there is a large column density associated with Region C. Inspection of the optical data reveals a band of dense material stretching across Region C, thus corresponding to the absorption seen in X-rays. In fact, the combination of X-ray, optical, IR, and radio data display a clear spherical geometry for this remnant. The band of material that is coincident in optical and radio wraps around the spherical remnant and is anticoincident with the X-ray emission, except for that in Region C. This suggests that this X-ray emission does not originate at large radii toward the observer, but must exist closer to the center of the remnant in this region. This constraint cannot be placed on Region B. For this reason, we only compare ages from the internal Region C with those found in A and D. For Regions A and D, we approximate the age using a Sedov solution, resulting in an age estimate of around 6000 yr. The ionization parameter in Region C implies a shock timescale of longer than this, at around 20,000 yr, depending on the assumed filling factor of the plasma. Therefore, the age structure of the remnant is consistent with a bipolar or directional flow of X-ray-emitting material away from the center of the remnant and toward the locations of Regions A and D. Given the large amount of IR and optically detected material located in the band surrounding the X-ray emission, it is still difficult to determine if the X-ray-emitting plasma is following a bipolar morphology due to a preferred explosion direction or pressure confinement from material in the environment.

Lee et al. (2011) have suggested that IKT 25 is produced by a so-called "prompt" Type Ia explosion mechanism. Our

Table 3
Best-Fit Parameters for IKT 5 by Extraction Region

Region	Best-Fit Model	cstat/dof	1 − (P-value)	$N_{H,\mathrm{SMC}}$ (10^{22} cm^{-2})	kT_{vapec} (keV)	A_{Fe}	$\mathrm{norm}_{\mathrm{vapec}}$ (10^{-5} A)[a]	kT_{nei} (keV)	τ_{nei} (10^{11} s cm^{-3} s)	$\mathrm{norm}_{\mathrm{nei}}$ (10^{-5} A)	F-test P-value Percentile
Northern	$\mathrm{tbabs}_{\mathrm{gal}} \times \mathrm{tbvarabs}_{\mathrm{SMC}} \times$ vapec	227/197	77.5%	$0.3^{+0.1}_{-0.1}$	$0.94^{+0.03}_{-0.03}$	$0.8^{+0.2}_{-0.1}$	$6.3^{+0.6}_{-0.6}$	…	…	…	…
Southern	$\mathrm{tbabs}_{\mathrm{gal}} \times \mathrm{tbvarabs}_{\mathrm{SMC}} \times$ (vapec + vnei)	221/194	79.1%	$0.23^{+0.08}_{-0.08}$	$0.56^{+0.03}_{-0.03}$	$2.0^{+1.3}_{-0.7}$	$0.6^{+0.8}_{-0.8}$	$1.0^{+0.1}_{-0.1}$	$1.7^{0.8}_{-0.3}$	$1.8^{1.0}_{0.2}$	0.0517

Note. Spectral-fitting results by region listed in Figure 3. The remnant and regions are listed in the first two columns, with the next column indicating the best-fit model. Errors shown are 1σ. Abundances are shown relative to solar, with solar values equal to 1.

[a] Normalization parameter, where $A = [10^{-14}/(4\pi D^2)] \int n_e n_H dV$, D is the distance to the SMC, and the integral is the emission measure.

Table 4
Physical Parameters of the SNR

Remnant	Region	$v_{shock,cie}$ (km s^{-1})	Radius (pc)	Sedov age (yr)	$n_{e,cie}$ (cm$^{-3}/f^{1/2}$)	t_{shock} (yr $\times f^{1/2}$)	$v_{shock,nei}$ (km s^{-1})	$n_{e,nei}$ (cm$^{-3}/f^{1/2}$)
IKT 25	Region A	899	14.5	6300	0.25	⋯	⋯	⋯
	Region B	885	⋯	⋯	0.45	⋯	⋯	⋯
	Region C	761	⋯	⋯	0.15	20,000	913	0.17
	Region D	936	14.3	6000	0.25	⋯	⋯	⋯
	Wisp	703	⋯	⋯	0.08	⋯	875	0.06
DEM S 128	⋯	755	21.9	11,000	0.08	⋯	⋯	⋯
IKT 5	Upper	894	13.9	6100	0.10	⋯	⋯	⋯
	Lower	691	14.1	⋯	0.05	38,000	923	0.08

Note. Physical parameters derived from the fit parameters in Tables 1–3. Shock velocity was calculated using the temperature from Tables 1–3.

Table 5
List of Point Sources in DEM S 128

J2000 Coordinates		Previously Reported Name (If Applicable)	Radio Coincident?
R.A.	Decl.		
01:05:36.3	−72° 9′ 48.″9	2XMM J010536.3-720948	No
01:05:30.9	−72° 10′ 21.″5	⋯	Yes
01:05:24.9	−72° 11′ 16.″1	⋯	Possible
01:05:9.7	−72° 11′ 48.″0	CXO J010509-721146	No
01:04:59.9	−72° 11′ 47.″7	⋯	No
01:05:50.5	−72° 12′ 37.″1	⋯	No
01:05:33.0	−72° 13′ 31.″5	⋯	No

Note. A list of the point sources within and around the supernova remnant DEM S 128. The point sources were detected using the CIAO tool *wavdetect*. Previously discovered point sources with names are given in the rightmost column.

analysis supports this idea. Indeed, IKT 25 shares a great deal with the first two SNRs to be classified in this way, DEM L238 and DEM L249 (Borkowski et al. 2006). As in the Borkowski et al. remnants, the ionization parameter is large when compared to its Sedov age, although it should be noted that both DEM L238 and DEM L249 have X-ray shells, whereas ours do not have well-defined shells in the X-ray. If we combine the results from all five regions of IKT 25, specifically the Fe abundance, the probability that they are consistent with or less than the SMC abundance of 0.2 solar is vanishingly small, equivalent to a $\sim 10\sigma$ significance. The global norm-averaged overabundance of greater than 8σ of Fe for IKT 25 and the presence of enhanced Si in the Wisp also argues strongly for the Type Ia designation.

5.2. DEM S 128

Aside from the absorbing column density, we find different physical parameters for DEM S 128 than those determined in VDH04. As with IKT 25, we find a significantly enhanced Fe abundance (7σ). All other elements are consistent with SMC ISM values, which contradicts the overabundance of Mg and Si reported in VDH03. An overabundance of these species should be seen as clear line signatures at 1.3 and 1.8 keV, respectively, which is not observed in the spectrum (Figure 6). Our enhanced Fe abundance and lack of Mg argue more strongly for a Type Ia designation.

As in the case of IKT 25, the X-ray spectrum of DEM S 128 suggests it is ISM-dominated, aside from Fe. In order to form a qualitative understanding of the interaction of DEM S 128 with its surroundings, we turn to other wavelengths for additional information. When examining IR data for DEM S 128, we see that there is very little in the way of extended sources. We observe an absence of dense shell emission from the SN blast wave, in stark contrast to IKT 25. In fact, we see no IR emission that is obviously associated with this SNR whatsoever. This may suggest a highly rarefied medium, which is consistent with the low density derived from the X-ray emission and Type Ia designation. However, it should be noted that the presence of plasma in CIE, as suggested by our fits, is inconsistent with this picture.

However, there are a number of discrete radio sources that are coincident with X-ray emission. Our point-source analysis of the X-ray image revealed seven point-source detections. These sources are diagrammed in the center panel of Figure 10, which also overlays the radio data as white contours. The positions of these objects are given in Table 5. Of the seven, two were previously identified in X-ray point-source catalogs, 2XMM J010536.3-720948 and CXO J010509-721146. Most of these X-ray point sources have no coincident radio emission greater than five times the local background flux. Intriguingly, one X-ray point source, labeled Source 2, does exhibit strong coincident radio emission. This object is only slightly extended when compared to the beam size of this midresolution radio image. Unfortunately, there are only a total of 69 X-ray source counts, which is not enough to spectrally analyze this point source to confirm its nonthermal nature. However, the off-axis nature of the X-ray observation leads to a large PSF and questionable discreteness of these sources. Also, high-resolution radio data over multiple frequencies would determine the spectral index, which should be flat, to be consistent with a PWN. On-axis, longer-duration *Chandra* observations combined with higher-resolution radio data could confirm that this source is indeed a PWN, contradicting the Type Ia designation. Further complicating the classification of DEM S 128 is its close positional coincidence with the star-

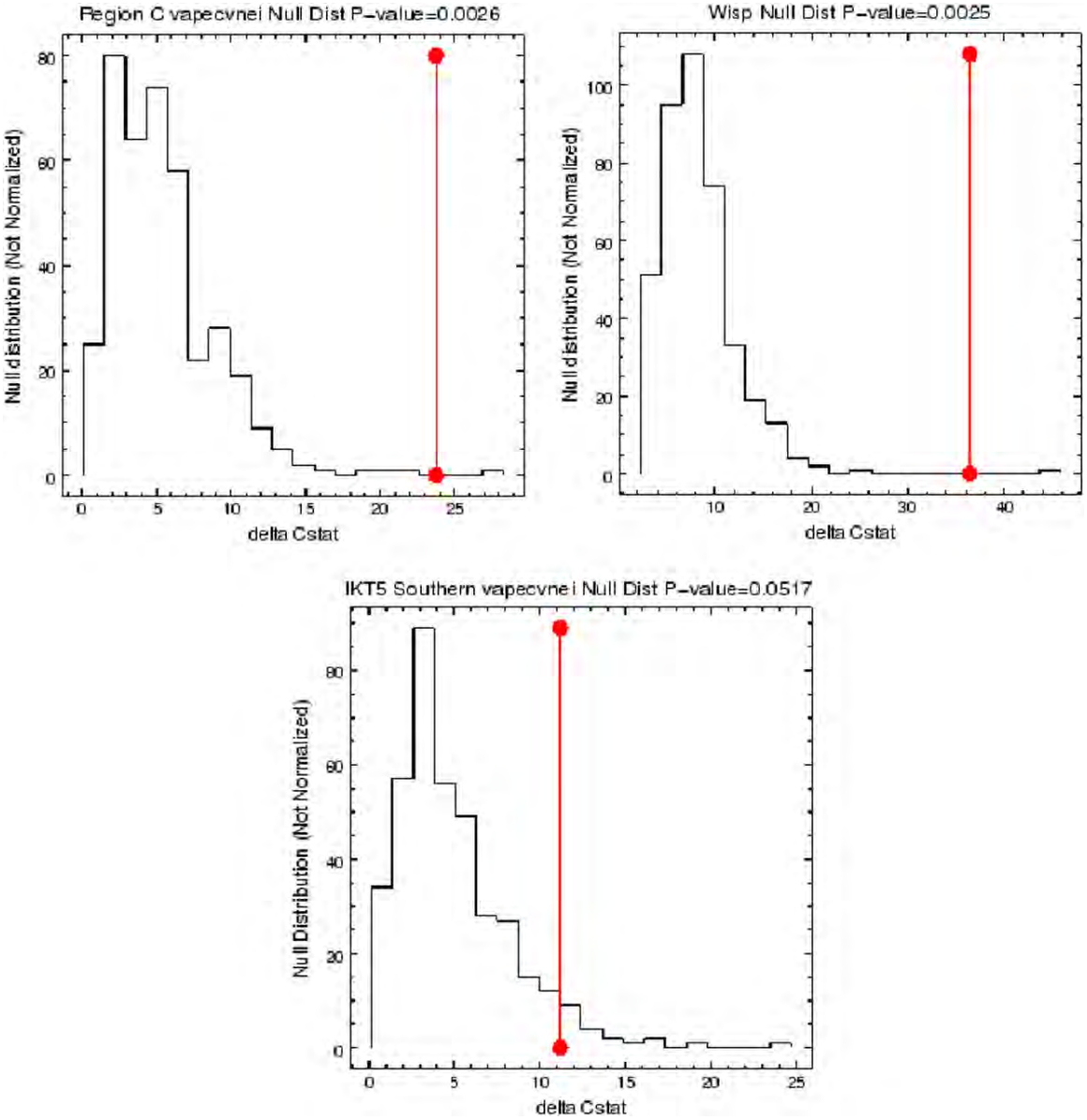

Figure 8. Results of the parametric bootstrapping method we replace the F-test with, as described in Section 3. All of these were constructed using 400 simulated spectra produced by adding a Poisson noise component to each fit's respective best-fit one temperature model. (a) The results for the parametric bootstrapping of IKT 25 Region C (see Table 1 for final fit parameters). (b) The results for the parametric bootstrapping of the IKT 25 Wisp region (see Table 1 for final fit parameters). (c) The results for the parametric bootstrapping of the IKT 5 southern region (see Table 3 for final fit parameters).

forming region (SFR), DEM S 124. If DEM S 128 is a member of this SFR, it seems likely that it is a CC remnant. This association would also explain the rarefied medium as being due to strong stellar winds.

The optical emission in of DEM S 128 is presented at the bottom of Figure 9. There is an optical circular shell filled with emission, but the center of this shell is some 45 pc spatially separated to the north of the X-ray remnant with no overlap. This optical feature is closer to the position of the original source, labeled DEM S 128 by Davies et al. (1976), but the X-ray remnant is more consistent with the position of the source reported by Inoue et al. (1983). An arc of optical emission appears to surround the X-rays, suggesting that the hotter gas is contained within this feature, but the high level of field confusion evident in the optical may make this association purely coincidental. If the radio and X-ray bright source is a PWN, it strongly indicates that DEM S 128 is of CC origin. This suggests that DEM S 128 is not a Type Ia SNR at all, but rather is the product of a CC explosion that produced the overabundance of Fe observed in the X-ray spectrum.

5.3. IKT 5

The X-ray results in this remnant are perhaps the most perplexing of the three remnants. The northern region has an Fe overabundance at 0.8 solar, which is significantly above the SMC abundance by about 4σ, whereas the southern region has an Fe abundance of twice solar, but the error bars on this particular region are large enough to be consistent with SMC ISM. As in Region C and the Wisp region of IKT 25, the southern region's CIE fit is relatively cool at 0.56 keV, whereas

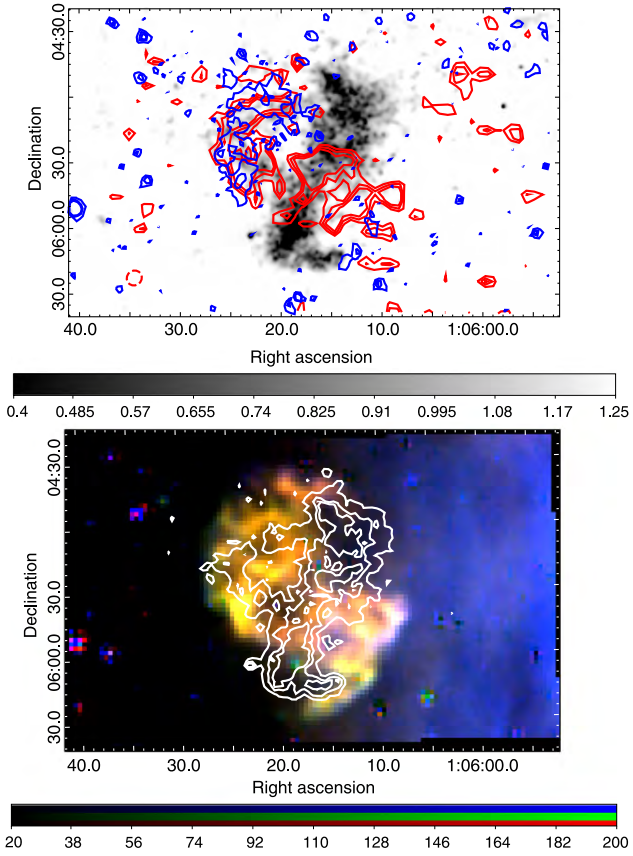

Figure 9. IKT 25 in other wavelengths. IKT 25 X-ray data in linear grayscale; the blue overlaid contours are 8 μm IRAC *Spitzer* data, and the red overlaid contours are ATCA 20 cm flux (top). The 8 μm IRAC contours are in units of 0.8, 1.0, and 1.2 MJy/Sr (~4σ, 5σ, and 6σ), whereas the radio contours are in units of 90, 120, and 150 μJy /beam (~3σ, 4σ, and 5σ). Optical MCELS RGB image of IKT 25, with ACIS contours overlaid (bottom). The red, green, and blue are continuum-subtracted [S II], Hα, and [O III], respectively.

the NEI component is at 1.0 keV. The values of the absorbing column density across IKT 5 found by VDH04 are consistent with our results. VDH04 find a very high ionization timescale, and while this is consistent with our Upper Region, which is in CIE, it is inconsistent with our fit result in the Lower Region, which has a component out of ionization equilibrium with a timescale that is smaller than the lower limit listed in VDH04. As with IKT 25, VDH04 find enhanced Ne, which we do not require in order for a good fit. Again, this is mostly due to the overlap of the Fe-L shell and the Ne-K shell in energy. The X-ray results on their own, as with IKT 25 and DEM S 128, suggest a Type Ia origin.

To explore this classification further, we perform a point-source analysis on IKT 5, given previous suggestions of a point source (van der Heyden et al. 2004; Laycock et al. 2010). We detect a source within the remnant that is coincident with the CXOU J004824-731918 source reported in Laycock et al. (2010). Figure 11 (upper right) shows the 3σ *wavdetect* psf extent as a green ellipse with high-energy, 2.0–8.0 keV emission in white contours. The peak of the high-energy emission is coincident with the location of the point source, suggesting that this source is not simply a bright knot of emission from the SNR. Given the Laycock et al. (2010) conclusion that the point source is likely not an XRB, the possibility exists that this source is a PWN or compact central

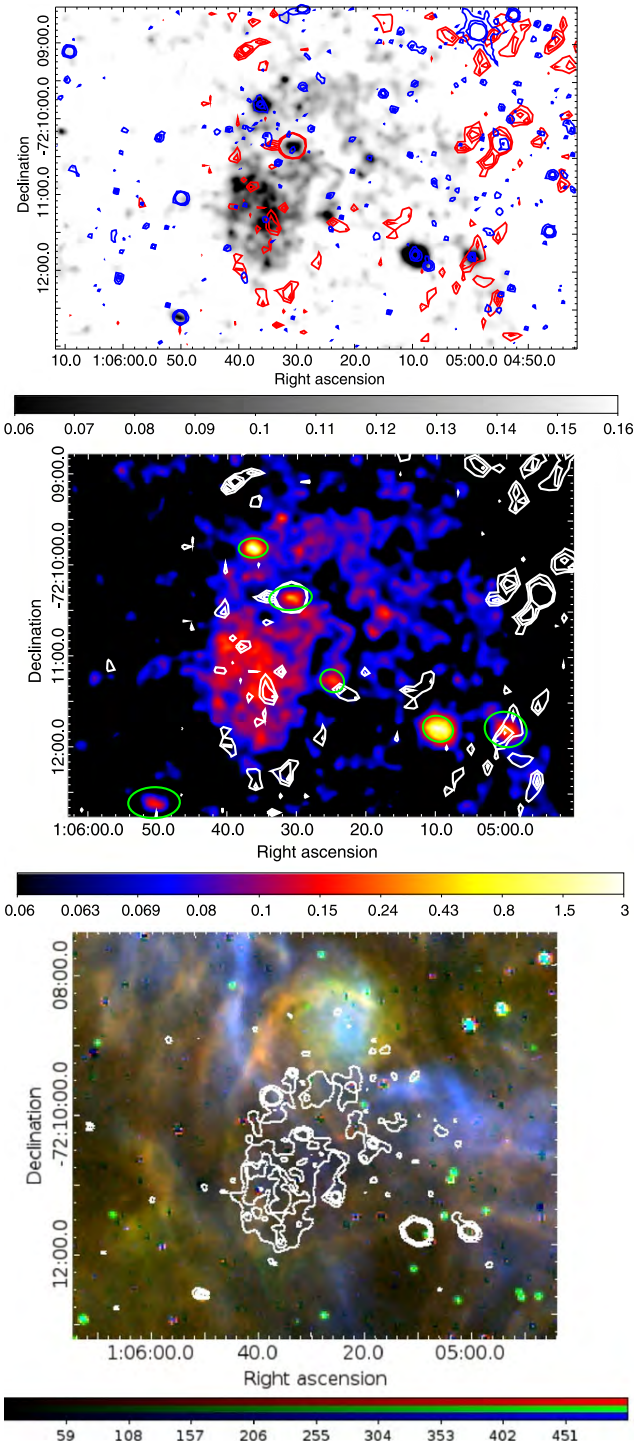

Figure 10. DEM S 128 X-ray data in linear grayscale; the blue overlaid contours are 8 μm IRAC *Spitzer* data, and the red overlaid contours are ATCA 20 cm flux (top). The 8 μm IRAC contours are in units of 0.8, 1.0, and 1.2 MJy/Sr (~4σ, 5σ, and 6σ), whereas the radio contours are in units of 90, 120, and 150 μJy /beam (~3σ, 4σ, and 5σ). DEM S 128 in the ACIS 0.5–2.0 keV waveband is in color, and the 20 cm radio is in white contours in units of 90, 120, and 150 μJy (middle). The green regions in the X-ray image are detected point sources, with labels indicating previously detected point sources. Optical MCELS RGB image of DEM S 128, and with ACIS contours overlaid (bottom). The red, green, and blue are continuum-subtracted [S II], Hα, and [O III], respectively.

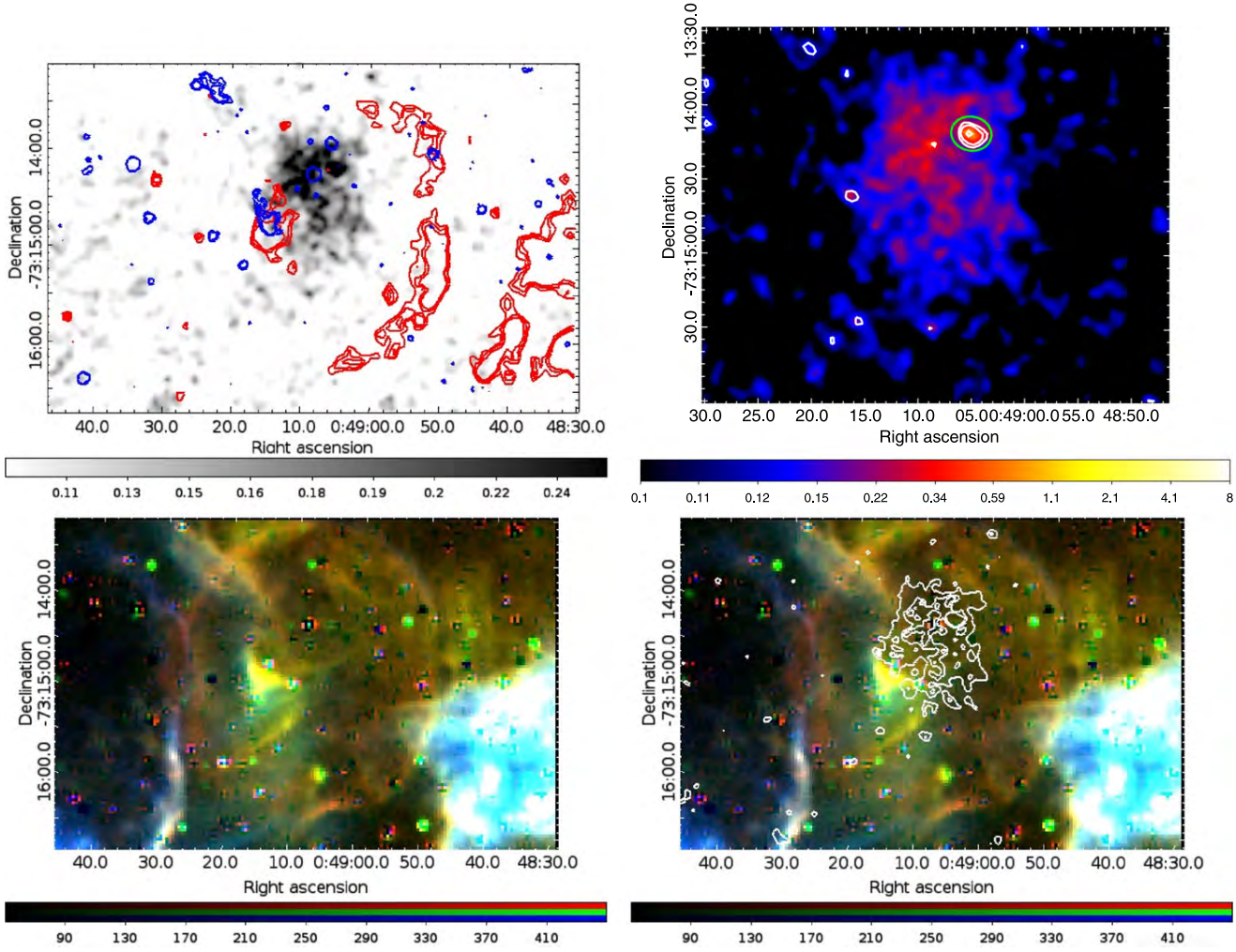

Figure 11. IKT 5 data in linear grayscale; the blue overlaid contours are 8 μm IRAC *Spitzer* data, and the red overlaid contours are ATCA 20 cm flux (upper left). The 8 μm IRAC contours are in units of 0.8, 1.0, and 1.2 MJy/Sr (~4σ, 5σ, and 6σ), whereas the radio contours are in units of 90, 120, and 150 μJy /beam (~3σ, 4σ, and 5σ). The X-ray images are detected point sources in white and green contours in units of 0.12, 0.15, and 0.3 counts/pixel of the ACIS data from 2.0–8.0 keV (upper right).IKT 5 in the MCELS optical band. The red, green ,and blue are continuum-subtracted [S II], Hα, and [O III], respectively (lower left). Optical MCELS RGB image of IKT 5, with ACIS contours overlaid (lower right).

object. Spectra extracted from just the point-source region were too low significance to perform meaningful spectral fits to verify this possibility. Longer, on-axis *Chandra* observations are necessary in order to further constrain the nature of this point source, yet the current characteristics challenge a typical Type Ia designation.

As in the IKT 25 and DEM S 128 cases, only Fe was overabundant, indicating that this is a highly ISM-dominated remnant. Figure 11 (upper left) shows that to the southeast of the X-ray remnant there is a small, diffuse knot of infrared emission that is roughly anticoincident with the X-ray emission in the southern region. We find from the shorter-wavelength IR images (not presented here) that this knot is actually unresolved point-source emission from a star cluster in the area and is likely not associated with the remnant. Also evident is an IR source in the middle of the remnant, coincident with a known red supergiant 2MASS J00490818-7314155 (Massey & Olsen 2003). It is unclear to what extent any of the IR emission in this field is associated with IKT 5.

The radio observation for IKT 5 is also shown in the upper left panel of Figure 10. The hard X-ray point source found in our analysis is not detected in the radio, making a PWN within the remnant questionable. However, the telescope array was optimized for diffuse emission. An observation using an array configuration optimized for spatial resolution is necessary to determine the strength of the point-source radio emission. In addition, further to the west of the remnant there is a half-shell in the radio consistent with shocked gas. This half-shell appears to have its center positionally consistent with the X-ray remnant. The optical emission completes this western radio shell in Hα and [S II] (Figure 10, bottom left). The optical image also reveals a secondary, inner optical bubble that appears just exterior to the X-ray emission. The inner bubble of this "double bubble" structure could be the SN shock front. This volume would then be filled with hot, X-ray-emitting gas. The outer, larger bubble is clearly also shocked gas, but is far outside the remnant. Such a shock could be due to the progenitor system. A massive star progenitor could have blown a cavity with its strong stellar wind. The ~50 pc physical size of this bubble is consistent with typical wind speeds (1000 km s^{-1}) and lifetimes (10^5–10^6 yr) of massive stars. The inner SN blast wave is in the process of catching up with

the outer bubble, which has a head start on the order of the lifetime of the massive star.

Our analysis suggests that IKT 5 may not be of Type Ia origin. The detection of the possible X-ray point source with surrounding high-energy emission is indicative of a leftover compact object, thus being consistent with the picture of a massive progenitor, as are the combined optical and radio data. However, the large Fe abundance argues against at least a typical CC SNR. In addition, the current lack of coincident radio emission argues that the potential compact object is unlikely to be a PWN, yet higher-resolution data are needed for verification. As with DEM S 128, the X-ray observation of IKT 5 was well off-axis, thus leading to a poor PSF and questionable point-source detection. Given the environmental conditions present in the multiwavelength analysis, there is stronger evidence of a CC origin for IKT 5. However, we cannot rule out the possibility that IKT 5 is another member of the same class SNR as IKT 25 and DEM s 128. It is important to acquire higher-quality, on-axis, longer-exposure X-ray data to ensure the nature of this point source and its high-energy emission, as well as high-resolution radio data. This would clarify the classification of this SNR and identify the central compact object.

6. SUMMARY

By applying the most modern X-ray plasma models available, in addition to using the Cash statistic, we have analyzed these remnants in the low-counts regime. The best-fit spectral models of these three SNRs indicate that they are both moderately aged and strongly ISM-dominated. However, despite the information lost in their advanced age, there is significant emission indicative of Fe overabundance in all the remnants we analyzed. The extent of these enhancements is too much to be due to the fluctuation of the ISM (Russell & Dopita 1992). This Fe overabundance is the biggest piece of evidence that points toward these three remnants being Type Ia SNRs. However, it is important to note that as the plasma models utilized in X-ray spectral fitting develop, in particular with the release of APEC version 3.0, there will be more support for Fe lines in the Fe-L shell, and the true abundance of Fe may be found to be somewhat less than reported in this paper. While the Fe content of each remnant argues for a Type Ia classification, these objects also display characteristics of CC remnants, such as dense environments, local star-forming regions, and possible progenitor point sources. Although we did not require varying oxygen abundance in the fit, when we allow the oxygen to vary, these remnants yield a lower abundance of oxygen than is usually produced from CC SNe, with [O/Fe] $\lesssim$0.5. Such a ratio has been achieved in nucleosynthesis models of low-metallicity progenitors with a mass of $\lesssim$15 $M_{\odot}$, which might be found in the SMC.

Lopez et al. (2011) make the case for ejecta-dominated Type Ia SNRs being more symmetric than CC SNRs, which was in conflict with IKT 25, DEM S 128, and IKT 5's tentative Type Ia classification by VDH04, especially compared to highly symmetric CC remnants in the SMC. Our analysis has shown that the apparent contradiction of these remnants evident in VDH04 with the study of Lopez et al. (2011) is only skin-deep. With the current X-ray data, it is uncertain what types of SN explosion were the progenitors of IKT 25, IKT 5, and DEM S 128. While we confirm that there is a significant Fe overabundance through X-ray spectroscopy, each has oddities that preclude their being a "classical" Type Ia SNR. In addition, these remnants show a high degree of ISM domination in their X-ray spectra, indicating a high degree of morphological alteration by the environment. If these remnants are Type Ia SNRs at all, they likely all originated from prompt Type Ia progenitor systems, which are fundamentally different than those studied by Lopez et al. (2011), so that even morphological comparison between these three remnants and their oxygen-rich CC cousins in the SMC may not be appropriate.

This research has made use of data obtained from the *Chandra* Data Archive and the *Chandra* Source Catalog and software provided by the *Chandra* X-ray Center (CXC) in the application packages CIAO, ChIPS, and Sherpa. The infrared data were obtained from the *Spitzer* Heritage Archive.[3] We obtained the optical data from the Magellanic Cloud Emission Line Survey.[4]

REFERENCES

Badenes, C., Borkowski, K. J., Hughes, J. P., Hwang, U., & Bravo, E. 2006, ApJ, 645, 1373
Borkowski, K. J., Hendrick, S. P., & Reynolds, S. P. 2006, ApJ, 652, 1259
Cash, W. 1979, ApJ, 228, 939
Davies, R. D., Elliott, K. H., & Meaburn, J. 1976, MmRAS, 81, 89
Dickey, J. M., & Lockman, F. J. 1990, ARA&A, 28, 215
Draine, B. T. 2011, in Physics of the Interstellar and Intergalactic Medium (Princeton, NJ: Princeton Univ. Press)
Filipović, M. D., Haberl, F., Pietsch, W., & Morgan, D. H. 2000, A&A, 353, 129
Filipović, M. D., Payne, J. L., Reid, W., et al. 2005, MNRAS, 364, 217
Flanagan, K. A., Canizares, C. R., Dewey, D., et al. 2004, ApJ, 605, 230
Foster, A. R., Ji, L., Smith, R. K., & Brickhouse, N. S. 2012, ApJ, 756, 128
Freeman, P., Doe, S., & Siemiginowska, A. 2001, Proc. SPIE, 4477, 76
Fruscione, A., McDowell, J. C., Allen, G. E., et al. 2006, Proc. SPIE, 6270, 62701V
Hilditch, R. W., Howarth, I. D., & Harries, T. J. 2005, MNRAS, 357, 304
Hughes, J. P., & Smith, R. C. 1994, AJ, 107, 1363
Inoue, H., Koyama, K., & Tanaka, Y. 1983, in IAU Symp. 101, Supernova Remnants and their X-ray Emission, ed. J. Danziger, & P. Gorenstein (Dordrecht: Reidel), 535
Laycock, S., Zezas, A., Hong, J., Drake, J. J., & Antoniou, V. 2010, ApJ, 716, 1217
Lee, J.-J., Park, S., Hughes, J. P., Slane, P. O., & Burrows, D. N. 2011, ApJL, 731, L8
Lopez, L. A., Ramirez-Ruiz, E., Huppenkothen, D., Badenes, C., & Pooley, D. A. 2011, ApJ, 732, 114
Massey, P., & Olsen, K. A. G. 2003, AJ, 126, 2867
Payne, J. L., White, G. L., Filipović, M. D., & Pannuti, T. G. 2007, MNRAS, 376, 1793
Protassov, R., van Dyk, D. A., Connors, A., Kashyap, V. L., & Siemiginowska, A. 2002, ApJ, 571, 545
Russell, S. C., & Dopita, M. A. 1992, ApJ, 384, 508
Sault, R. J., Teuben, P. J., & Wright, M. C. H. 1995, in ASP Conf. Ser. 77, Astronomical Data Analysis Software and Systems IV, ed. R. A. Shaw, H. E. Payne, & J. J. E. Hayes (San Francisco, CA: ASP), 433
Spitzer, L. 1998, Physical Processes in the Interstellar Medium (Weinheim: Wiley-VCH)
van der Heyden, K. J., Bleeker, J. A. M., & Kaastra, J. S. 2004, A&A, 421, 1031
Verner, D. A., Ferland, G. J., Korista, K. T., & Yakovlev, D. G. 1996, ApJ, 465, 487
Wilms, J., Allen, A., & McCray, R. 2000, ApJ, 542, 914

[3] The *Spitzer* Heritage Archive can be found at http://sha.ipac.caltech.edu/applications/Spitzer/SHA/
[4] http://astro.wsu.edu/worthey/html/mcsurvey.html